AGARDograph No. 138

on

Ballistic - Range Technology

Edited by

T. N. Canning, A. Seiff and C. S. James
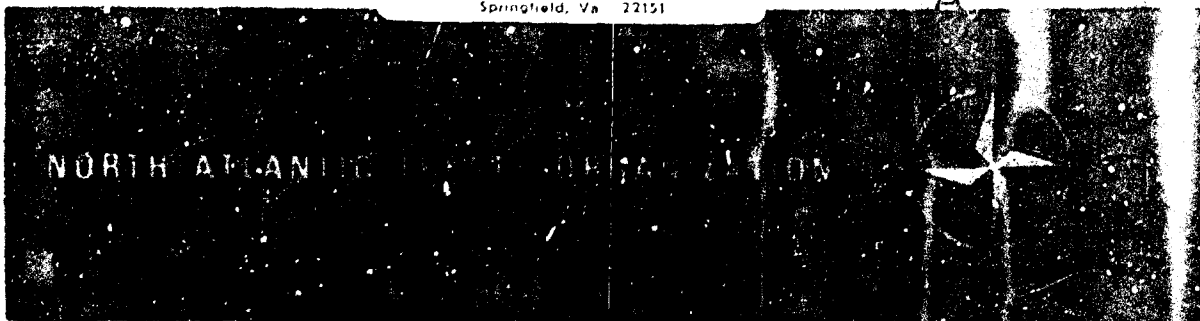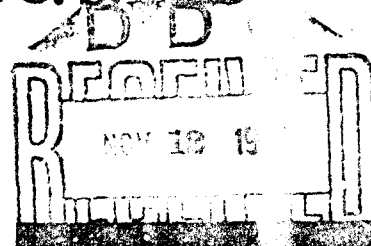
**DISTRIBUTION AND AVAILABILITY
ON BACK COVER**

Best
Available
Copy

NORTH ATLANTIC TREATY ORGANIZATION

ADVISORY GROUP FOR AEROSPACE RESEARCH AND DEVELOPMENT

(ORGANISATION DU TRAITE DE L'ATLANTIQUE NORD)

BALLISTIC-RANGE TECHNOLOGY

by members of the staffs of

Ames Research Center
National Aeronautics and Space Administration
Moffett Field, California, USA

and

Defence Research Establishment, Valcartier
Quebec, Canada
(Formerly Canadian Armament Research and Development Establishment)

Edited by

Thomas N. Canning, Alvin Seiff and Carlton S. James

PREFACE

Ballistic ranges as they exist today have evolved through the efforts of many individuals over the past 30 years. Their earlier use was primarily directed toward studying the flight of bullets and artillery shells. The application of the ballistic range to problems of supersonic flight of winged vehicles was given great impetus in the 1940's by Dr A.C.Charters at the Ballistic Research Laboratories, Aberdeen, Maryland. Many experimental aerodynamic studies were thus made possible, which were well beyond the capabilities of wind tunnels of the day. The further extension of the flight régime to hypersonic speeds, by use of a countercurrent airstream through which the aerodynamic models could be fired, was proposed in 1947 by Mr H. Julian Allen, of NASA-Ames Research Center, Moffett Field, California. This concept, together with his enthusiastic support of aeroballistic testing at Ames since that time, has been invaluable. Many other contributions of individual engineers and scientists in many laboratories throughout the world have added to the performance, the versatility, and the accuracy of data attainable in ballistic facilities. It is impractical to list all, but the names of many appear in credits in the text and as authors of cited references.

This book evolved from a recommendation by Professor Wilbur C.Nelson, of the University of Michigan, that the state-of-the-art of ballistic-range testing be described in a formal text. His review of the resulting manuscript, and a review by the staff of the US Naval Ordnance Laboratory, White Oak, Maryland, have been very helpful. The authors of individual chapters are members of the Hypersonic Free-Flight Branch at NASA-Ames Research Center and members of, or consultants to, the Aerophysics Division at the Defence Research Establishment, Valcartier, Quebec, Canada; formerly called the Canadian Armament Research and Development Establishment. The name change has been in effect for only a short time and is therefore not reflected throughout the book.

An acknowledgment of appreciation is given to Miss Toshiko Kato, Hypersonic Free-Flight Branch secretary, for preparation of the manuscript and to Mr Alfred H.Paulsen, of the Ames Graphics and Exhibits Branch, for supervision of figure preparation.

The forerunner of the ballistic range has doubtless existed as an experimental device since prehistoric times. The hunter or warrior, practicing with his weapons, improved his effectiveness by careful observation of the flight of stones, spears, darts, and arrows. There is no evidence of flagging interest in the use of ballistic ranges for missile development from that time to the present.

In the case of scientific research and development, on the other hand, the range achieved prominence during the Renaissance. The long arduous attack on the Aristotelian picture of kinetics, the development of the theories of impetus, and the final establishment of modern notions of inertia, all involved frequent recourse to observations of missiles under progressively better-controlled conditions and with fewer incorrect preconceptions. To contend that such experimentation was crucial would be an overstatement; but as improved descriptions of kinetics were developed, verification was sought in study of hurled and falling objects.

Once the modern picture of rigid-body mechanics became established, the scientific value of the ballistic range decreased for a while, but towards the end of the 19th century, Ernst Mach, among others, pioneered in the observation of flow fields using shadowgrams, interferograms, and schlieren photos of supersonic bullets. Even then, the motivation was strongly towards the study of aerodynamics of projectiles. Progress in photography and other technologies was evidenced in further European development of ranges in which series of pictures were made of gun-launched models in order to study motions of projectiles in detail. More recently in the United States of America and in Canada interest has broadened into studies of airplanes, guided missiles, and lifting bodies suitable for atmospheric entry at hyperbolic speeds. 'Higher-performance guns were a necessity for some of these studies, encouraging the development of light-gas guns starting in the late 1950's.

The attainment of muzzle velocities in the neighborhood of Earth-orbital speed using the light-gas gun made possible almost complete simulation of ballistic-missile aerodynamics as well as imitation of their wakes (a return to problems of weaponry).

Despite the growing popularity of the ballistic range as a tool for modern technical and scientific work, the experimental results obtained therein have not been accepted as widely as they perhaps deserve to be. The degree to which definitive tests of theoretical models or accurate simulation of large-scale events can be obtained in the ballistic range is not widely understood. Similarly, the scientific and technical communities are not properly aware of the accurately controlled environment available for testing physical theories.

It is felt that the graduate student can use the collated technology herein to gain appreciation of the opportunities presented by the ballistic range for experimental research, and to acquaint himself as well with the problems involved. Further, it is intended that the book guide the preliminary design of new ballistic ranges so that they may fulfill their intended purpose economically. It is also hoped that experimenters will find useful reference material so that they may exploit their own ranges more fully. Lastly, it is hoped that the user (and potential user) of experimental data obtained in ballistic ranges will be aided in evaluating the applicability and accuracy of results in terms of his own problems.

Thomas N. Canning

CONTENTS

CHAPTER 3.   MODEL AND SABOT DESIGN AND LAUNCHING TECHNIQUES

CHAPTER 4.   TERMINAL BALLISTICS

CHAPTER 5.   COUNTERFLOW FACILITIES

CHAPTER 6.   SYSTEMS FOR MEASUREMENT OF MODEL POSITION, ATTITUDE, AND VELOCITY

CHAPTER 7.   AERODYNAMICS OF BODIES FROM MOTION ANALYSIS

CHAPTER 10. MICROWAVE STUDIES

CHAPTER 11. POINT MEASUREMENTS IN THE WAKE

CHAPTER 12. CONVECTIVE-HEATING MEASUREMENTS

CHAPTER 1

MODERN BALLISTIC RANGES

AND THEIR USES

by

Thomas N. Canning and Alvin Seiff

NASA-Ames Research Center

MODERN BALLISTIC RANGES
AND THEIR USES

Thomas N. Canning and Alvin Seiff

Laboratory facilities such as ballistic ranges and wind tunnels invariably are conceived and developed to meet particular existing or anticipated needs. The need may be purely intellectual as in the case of electron and ion accelerators for nuclear research, or it may be very practical as in most engineering facilities - like the ballistic range - where problems of immediate concern to engineering advancement can be studied and solved. Occasionally, the ballistic range serves to answer purely intellectual questions as well.

Until the early 1940's, the emphasis in ballistic-range studies lay almost exclusively in perfection of various spin-stabilized shell for weapons. Gyroscopic stabilization of these projectiles, which were usually aerodynamically unstable in nose-forward flight, resulted in intricate yawing motions composed of precessions and nutations. Analysis of the real motions of bullets to determine the complete aerodynamic force and moment systems was a challenging task which should not yet be considered complete in all details. Analysis of these motions also yielded the aerodynamic drag force, which exerts a first-order influence on range, and the lift force, which influences dispersion.

In the past quarter century, however, the use of the ballistic range has broadened, until the study of the original ballistic problems has perhaps assumed secondary importance. Development of new uses has been stimulated by problems of vehicles proposed to fly at very high speeds in the atmosphere for military, commercial, and scientific purposes. These efforts include the development of transonic, supersonic, and hypersonic airplanes and missiles. A particular field of intense interest has been atmosphere entry of long-range missiles and space vehicles after flight outside the atmosphere. Emphasis has therefore shifted toward research in such disciplines as hypersonic aerodynamics, aerodynamic heating, and materials behavior under severe thermal and mechanical stress.

To say that these new missions stimulated development of the new techniques and uses of the range does not adequately imply the intimate connection between need and use. The ballistic range, in concert with other devices such as shock tubes, arc-jets, and electronic computers, made possible the swift advance of flight technology; for without these tools, prohibitively expensive and time-consuming full-scale flight-testing would have been required. Alternatively, reliance on inadequate simulation provided by more conventional facilities would have led to sometimes inaccurate and incomplete descriptions of the problems, and therefore inappropriate solutions. The advancements in capability which have kept the modern ballistic range equal to its task may be grouped in three classes: higher gun performance, new instrumentation, and greater range of flight-chamber environment.

The remainder of this chapter is intended as a look at the features of modern ballistic ranges and the kinds of research done in them. As such, it serves as a short preview of the topics covered in the remaining chapters and relates the chapters to one another.

1.1 GUNS

Until the 1950's the highest performance guns used the gases generated by gun powder to fire projectiles for range tests. While the powder gas gun still retains the advantage of operational simplicity and continues to be useful as a research tool at low and intermediate speeds, it does not provide the high speeds demanded by many studies of current interest. A considerable literature exists dealing with the construction and operation of the powder gun. Therefore, the discussion of guns in this book is limited to light-gas guns, which use highly compressed hydrogen or helium to propel research models in the laboratory.

By substituting hot hydrogen or helium for the gun-powder gases (low versus high molecular weight and high versus low sound speed), muzzle velocities have risen from around 2 to about 6 km/sec for fairly slender (i.e., delicate) metal models. For bluff (and potentially stronger) models the speed increase has been roughly from 3 to 9 km/sec and a few tests have been accomplished at 11 km/sec.

The modern gun operates in much the same way as does a child's pop-gun. The propellant gas is rapidly compressed by means of a free piston in a long cylinder (the pump tube). When the propellant pressure exceeds a preselected level, the gas is admitted to the breech of the launch tube, where it forces the model to accelerate to high speed. During the model's traverse of the launch tube the piston continues to compress the reservoir of hydrogen by virtue of its momentum. This results in a programmed variation of hydrogen pressure in the reservoir (at the launch-tube breech), which significantly reduces the peak acceleration and increases the ultimate muzzle velocity attainable. The very bulk and complexity of this system probably rule out military or sporting service, and the light-gas gun will probably remain a laboratory tool.

1.2 MODELS

The design and construction of the model and its carrier in the gun barrel, (called the sabot), are at the very heart of the successful test. The model must have the external form of the object to be simulated, and it must withstand the enormous launch acceleration, on the order of 10^6g, without damage. Its surface qualities and center of mass must frequently simulate those of the vehicle as well. In the case of terminal ballistics studies it is usually made of the same material as the actual projectile or meteoroid. The chemistry of the model surface may be prescribed by the need to provide the correct constituents in the wake. Furthermore, it is clear that the model must survive the rigors of flight through the test section. One severe test is with-standing convective heating rates that are 10 to 100 times those in full-scale flight.

A combination of rational design and empiricism has been developed to meet these seemingly impossible demands, and the general approach is outlined in Chapter 3 along with copious examples of successful designs.

1.3. PHOTOGRAPHIC STATIONS AND FLOW PHOTOGRAPHY

To record the position and attitude history of the model flight, most modern ballistic ranges use photographic stations. These respond automatically to the approach of the model, and fire either a very short-duration spark or a spark and an electro-optical shutter (Kerr cell) to expose the film, most often with a silhouette image of the model, as described in Chapter 6. Lasers and X-ray tubes are being used as well. Position and attitude references within the field of view are also recorded on the film to permit accurate measurements of three linear coordinates and at least two angular coordinates in each pair of orthogonal photographs. The time intervals between spark or shutter firings are measured to fractional-microsecond accuracy, in modern practice usually by electronic counter-chronographs.

The usual optical arrangement to make a shadow picture, namely, a spark and film on opposite sides of the flightpath, produces an important bonus - it makes key features of the flow field visible in the photograph. This basic shadowgraph, its variations, and other systems for flow visualization (Schlieren, interferometer) are described in Chapter 8. Such photographs can reveal the nature of the flow in great detail and have been the basis for understanding of high-velocity-flow configurations and phenomena. In fact, many range studies have consisted almost solely of careful scrutiny of many shadowgrams in order to arrive at empirical descriptions of the flow. An excellent example is in the study of laminar-turbulent transition of the boundary layer, and another is the study of conditions for attached or separated flow. The photographs also sometimes permit the tracing of Mach waves and streamlines. These and other uses of flow visualization are developed in Chapter 8, along with the theory of flow visualization, which makes the interpretation of flow photographs both rational and potentially quantitative.

Not to be overlooked either is the unequivocal recording of the condition of the model in flight. Simply because a model is undamaged when first photographed is no reason to expect it to maintain this perfect con-dition. The intense convective heating resulting from high-speed flight; will in many cases raise metal surfaces to the melting point or plastic surfaces to the boiling point. Shadowgraphs frequently record these features and so add to the observable phenomena available for study (e.g., quantitative use has been made of the determination of the onset of melting in measurement of heat-transfer rates, as described in Chapter 12).

1.4 MOTION ANALYSIS

The combination of shadowgraph photography and accurate reference systems means that the flight of any object through the range can, at least in principle, be recorded so accurately and completely as to enable determination of the complete aerodynamic force and moment system. The analysis of motion histories has evolved from early empirical, subjective observations of what constituted satisfactory flight behavior to meticulous curve-fitting programs which "find" that set of coefficients for the linearized equations of motion of lightly damped, slightly asymmetric, rolling bodies which best matches the observed data (Chapter 7). The evolution in data analysis since 1940 has consisted mainly of a gradual elimination of restrictions inherent in the equations. This progress has been permitted in no small part by the development of high-speed computers.

Until quite recently, analysis of nonlinear systems has been accomplished only by patching together "equivalent linear systems." It presently appears practical to relax the restrictions in data analysis still further to permit fitting of numerical solutions of highly nonlinear equations of motion directly to the trajectory data. Early efforts in this major development are outlined in Chapter 7, but the problem has by no means been completed.

Prediction of large-scale flight characteristics on the basis of small-scale flight tests is generally quite successful when the test data are taken at comparable values of Reynolds number, Mach number, and other simulation parameters, and when all degrees of freedom essential to the flight case are recognized and included. Such additional factors as surface roughness, surface temperature and ablation, and Knudsen number may enter as well. No laboratory aerodynamic testing device excels the ballistic range in permitting simultaneous duplication of Reynolds number, Mach number, and enthalpy. As pointed out later, simulation of nonequilibrium real-gas flows may deteriorate as a consequence of small model scale. These latter effects are usually of importance only in cases where the gas state and kinetics are the object of study. Comparison of ballistic-range tests of the Apollo command module with results from wind tunnels and from actual entries shows little evidence that aerodynamic behavior is affected by these chemical and kinetic differences in the flow fields.

Chapter 7 shows a detailed comparison of lift, drag, and stability data, using the AGARD model (HB-2), obtained in ranges and wind tunnels. Where disagreements are found, they are easily explained. Thus the comparisons both with other laboratory techniques and with large-scale flight vehicles validate the force measurements made in the range (if indeed they should be questioned).

1.5 MODIFICATIONS OF THE TEST ENVIRONMENT

The essential ingredients of the modern ballistic range are: (1) a light-gas gun; (2) models to be tested; (3) photographic stations to record the flights; (4) a chronograph to provide accurate records of operation of the photographic stations; and (5) a butt or target to stop the projectile. Beyond this, the special purposes of the range begin to dictate the detailed design of the basic parts and selection of additional features and equipment.

1.5.1. Variable Pressure, Temperature, and Composition

An important variation of the basic ballistic range is its enclosure in a steel tube to permit variations in the composition, pressure, and temperature of the test gas, first practiced at Ballistic Research Laboratories, Aberdeen, Maryland. The range of pressures thus achievable extends from about 10^{-6} atmosphere to several atmospheres, while the minimum temperature is limited only by liquefaction of the gas used. Pressure control yields direct control over Reynolds number; temperature control, which varies the speed of sound, gives independent control of Mach number. At low temperature, high Mach numbers are easily achieved. Substitution of exotic gases for air permits simulation of flight at other planets or the fundamental study of gas-property effects on gas dynamics.

Pressure control is invaluable in terminal-ballistic work as well. With the range tank evacuated, the influence of aerodynamic shock waves on the target is eliminated and the loss in projectile speed between gun muzzle and target is minimized.

The tank, pumps, and piping represent only part of the cost of this valuable improvement of the basic ballistic range. The entire photographic and reference system must be adapted to the pressure tank, while the gun muzzle must be coupled into it as well. Further, special tanks, structures, and valves are frequently required to absorb and contain the gun-muzzle blast and stop the sabot parts before they enter the test area. Some of these complications are treated in Chapter 6.

1.5.2 Countercurrent Airstream

A modification to the test environment which increases both the speed and Mach number capabilities of the ballistic range is to incorporate a supersonic airstream blowing towards the gun (Chapter 5). This was first applied at Ames Research Center. The counterflow was initially an airstream blowing at a Mach number of two from a large reservoir and discharging to atmosphere. The free-stream temperature was about 175°K so that the depressed speed of sound - 250 meters per second - and the velocity added directly by the airflow made hypersonic testing feasible with ordinary guns using smokeless powder. For example, a muzzle velocity of 2 km/sec yielded a Mach number of 10.

Another interesting counterflow facility, called the Atmospheric-Entry Simulator, used the density distribution within a long, continuously expanding nozzle to create a laboratory simulation of the altitude variation of density in the Earth's atmosphere. When high-speed models of entry bodies are fired through this simulated atmosphere, the heating history of entry bodies is remarkably well simulated, except for effects of radiation by the model surface and by the heated gases in the model flow field. This facility was built and used for several years at Ames Research Center.

As in the case of the pressure-vacuum tanks, the counterflow feature requires that other aspects of the design be compromised. Most important, the test-range length is limited to the length of test section in which a high-quality supersonic airflow can be maintained. Viscous effects produce a turbulent boundary-layer flow on the walls which ultimately fills the test section. The deceleration of the stream produced by this boundary layer effectively reduces the cross-sectional area of the tube; therefore the test section must be constructed with a slowly increasing cross section to compensate.

To match the ever-increasing speeds of interest, countercurrent streams of higher Mach number and higher enthalpy are called for. Preheating the working fluid to permit such performance with a simple blowdown wind tunnel becomes increasingly difficult and expensive. An alternative approach is to use a large shock-tube wind tunnel. In this device the air can be heated to a stagnation temperature of several thousand degrees Kelvin and expanded to much higher speeds and Mach numbers than possible in the earlier unheated blowdown flows. The flow duration is of course orders of magnitude shorter than that possible in the simple blowdown tunnel but is nevertheless quite compatible with the short observation times needed (milliseconds) with fast moving projectiles in available test section lengths. This type of counterflow was first introduced at Ames, and the largest such facility has a test section 23 meters in length by 1.2 meters in diameter. Test speeds up to 13 km/sec have been obtained, and 16 km/sec appears possible.

1.6 SPECIAL MEASUREMENT TECHNIQUES

As the speeds attainable have increased along with the controllability of the test environment, additional kinds of experiments have become possible; these new studies usually have required introduction of new types of instrument into the range. A few examples of these new experiments and their necessary instruments will illustrate the expanding research possibilities presented.

1.6.1 Thermal Radiation from Gases

The air near the path of a blunt, high-speed model is intensely heated by the passage of the bow wave. Temperatures above $10,000^{\circ}K$ can be attained; and even at speeds around 4 km/sec, where the maximum temperatures are only about $4000^{\circ}K$, the gas becomes luminous. The model itself may become luminous by virtue of intense convective heating. Other phenomena which emit measurable radiation occur in the wakes and in the impact processes at the target.

Introduction of radiometers (Chapter 9) to measure these thermal emissions has become a principal field of investigation in ballistic ranges. It has permitted verification of theoretical calculations of the thermodynamic and chemical properties of the immediate flow fields of the bodies and their wakes. Several contributions to the literature of molecular physics have come from such studies. In particular, the thin layer of hot gas which forms over the face of a nearly flat-nosed body is a well-characterized sample of hot uncontaminated gas (outside the region into which products of ablation diffuse). The emission from such shock layers has been successfully used in establishing some of the fundamental radiative properties of nitrogen, oxygen, and carbon dioxide, and mixtures thereof.

Simulation of radiative effects in full-scale flow fields is reasonably good except that nonadiabatic effects, important at very high speeds for large blunt vehicles, do not affect the flow importantly at model scale. Similarly the small scale of the tests degrades the simulation of chemical-kinetics effects. For the most part, however, the emphasis in radiation measurements is properly placed on testing theoretical estimates of radiation rather than on simulation of full-scale events.

An exception to this is in studying the spatial distribution of radiation within the shock layer of bluff bodies, particularly at large angles of attack. The difficulty of calculating such flows makes even the somewhat questionable simulation in the range quite desirable.

Another example of radiometry in the range is measurement of the thermal emission resulting from impact of projectiles into targets. The emission has been related to, among other more obvious variables, the ambient-gas composition and pressure.

Since the duration of events in the ballistic range is extremely short (the entire flight usually requires only a few milliseconds), very high-frequency-response radiometers must frequently be used. The design and absolute spectral calibration of these radiometers is detailed in Chapter 9.

1.6.2 Microwave and Other Techniques for Measuring the Wake

The heated flows produced by passage of the models are characterized by increased electron density as well as by radiative emission and absorption. One of the more powerful techniques for studying the electrical properties of plasmas is microwave interferometry (Chapter 10). The opportunity to study simulated wakes of entry bodies in the laboratory has led many investigators to install microwave equipment in enlarged variable-pressure ranges to measure electron-density, turbulence spectra, and flow-velocity variations along wakes as influenced by the usual aerodynamic parameters and by the material of which the model surface is made.

If short-wavelength equipment is used, careful design of lens systems can yield sufficient spatial resolution to determine the radial distribution of free electrons in the wake with modest accuracy.

The linear electron density of the wake, that is, the number of free electrons per unit length, is most easily determined by measurement of the power dissipation in a resonant cavity through which the model has been fired.

The study of flow fields and wakes, using microwave techniques, shares the imperfect simulation which limits the study of thermal emission. If the nondimensional fluid mechanical parameters such as Mach and Reynolds numbers are simulated, the absolute air density must be greater than in full-scale flight by the scale factor. Thus the equilibrium chemical and thermodynamic properties (as well as three-body-collision chemical reactions) are not faithfully scaled. The tests are best viewed as elaborate exercises in verification of complete theoretical models, which can presumably apply to the case of full-scale vehicles.

Radar can be utilized as well. Several ranges have been equipped to allow a CW microwave radar beam to "look" uprange from a reflector near the butt. The signal return can yield measurements of the model velocity, deceleration, and radar cross section (the apparent size of the model and its ionized flow field). By mounting the microwave antenna on the gun muzzle to establish a standing-wave system in the barrel, the time-history of projectile travel in the gun barrel itself can be measured. The resulting measurements of acceleration are invaluable to the ballistician, because he can deduce the actual propellant pressure history, as discussed in both Chapters 2 and 10.

A variety of instruments, in addition to the microwave interferometer, are available to measure the plasma and gas-dynamic properties of model wakes in the ballistic range. A whole family of these instruments is being established to make local "point" measurements in wakes (Chapter 11). Most of these devices are taken from earlier technology and are simply adapted to the ballistic-range environment (e.g., Langmuir Probes, hot-wire anemometers, microphones). One technique merits particular mention because of its utility in measuring flow speed in turbulent gases. This is the marking of a filament of the moving gas by discharging a high-voltage spark through it; then after suitable time delays, additional discharges are produced along the same, but progressively more distorted, filament. Stereoscopic photographs of the entire sequence record the changes in the filament shape with time, and thus indicate the velocity distribution existing at that station of the wake.

1.6.3 Heat-Transfer Measurements and Telemetry

Although high levels of convective aerodynamic heating occur in ballistic-range tests - larger by the scale factor than on large scale vehicles at the same velocity and Reynolds number - the measurement of neat transfer is not readily accomplished. Several different approaches have, however, been successfully developed and applied (Chapter 12). One conceptually simple method is to decelerate the model aerodynamically within the range to a low speed (by selection of the model mass and scale, and the ambient density and range length), and to recover it at the end of flight in a sensitive calorimeter which records the total heat content. Differentiation of the data from a number of firings at different muzzle velocities permits the determination of heating rate as a function of velocity. Another method, involving shadowgraph detection of the onset of ablation of low-melting alloy models (aluminum has been used), has already been alluded to. The companion phenomenon to heat transfer, boundary-layer skin friction, has been successfully measured by testing slender models whose drag is predominantly skin friction, and correcting measured total drag for the wave- and base-drag contributions.

In one application the drag of long and short thin tubular models with sharp leading edges was measured. The differences in drag and wetted area were used to derive the incremental skin-friction drag.

A potential method of measuring heat transfer, which has challenged many investigators over the years, is the use of telemetry to transmit from the free-flight model a signal proportional to temperature rise of a sensor placed at a selected location. Telemetry, of course, would have applications to many other measurements, including pressures and accelerations. The meager success of many vigorous efforts to develop transducers and miniature transmitters does injustice to the skill and determination of the engineers involved. The critical problem which has blocked complete success is that of producing frequency-modulation transmitters and pressure gages - not to mention batteries - capable of withstanding peak accelerations approaching 10^6g (required in the gun to achieve interesting speeds). The prospects of achieving useful results are further dimmed by the possibility of interference with and severe attenuation of the radiated signal by the thin plasma sheath surrounding the test body at the high flight velocities of interest in heat-transfer work.

One rudimentary telemetry system has successfully transmitted temperature data from tiny models fired at speeds up to 6 km/sec. No active electronic parts were included in the model; rather, a thermocouple at the model surface was connected directly to a small coil. The small current through the coil (resulting from rising surface temperature) produced a magnetic field, which was measured using multiple-turn coil antennae through which the model flew at high speed. Details are given in Chapter 12.

1.7 TYPICAL RANGES

During the last two decades the ballistic range has expanded its place in the family of engineering and scientific laboratory tools. Its qualities have complemented those of wind tunnels, arc-jets, and shock tubes, both by improving laboratory simulation of large-scale flight at very high speeds and by providing freedom from some of the imperfections inherent in other test devices.

In order to indicate the breadth of acceptance and application of the hypervelocity ballistic facility, a brief listing has been prepared of laboratories in which light-gas guns are used. The listing is limited to Western Europe and North America and is far from complete.

The elaborate array of ballistic-range facilities suggested by these entries attest to their wide use in governmental and industrial laboratories. The lengths of the ranges extend from a few meters to several hundred meters; the sizes of light-gas guns used range from less than 10 mm to over 100 mm in caliber and permit muzzle velocities over 10 km/sec. The purposes to which these ranges have been applied are diverse, and it is expected that they will become more so with the passage of time.

TYPICAL MODERN BALLISTIC RANGES

Facility	Application	Dimensions			Photographic stations (Number of orthogonal units)			Micro-wave	Radio-meter	Pressure range atm	Comments
		Length m	Dia-meter m	Gun size mm	Shadowgraph	Schlieren	X-ray				
NOL 1000ft Hyper-ballistics Range[a]	Aerodynamic stability Wake study	305	3	50-100	37	-	5	3	12	$1-4 \times 10^{-4}$	270 meters usable for stability.
NOL Pressurized Range	Aerodynamic stability Wake study	87	1	13-400	32	2	4	-	-	$6-2 \times 10^{-4}$	Controlled temperature section; 7-meter section for continuous wake study.
CARDE Range No.5[b]	Aerodynamic stability	120	3	-	Varies	-	11	-	-	- -	Nonorthogonal X-ray stations for model position.
RARDE Pressure Range[c]	Aerodynamic stability	22	0.6	6	16	-	-	-	-	$10-10^{-5}$	
LRBA Tunnel Hyperbalistique[d]	Aerodynamic stability	75	1.2	-	12	-	-	-	-	$7-4 \times 10^{-5}$	
VKF 1000ft Hyper-velocity Range[e]	Aerodynamic stability	305	3	63	43	-	-	-	-	$1-10^{-4}$	270 meters usable for stability.
NASA-Ames Aero-dynamic Facility[f]	Aerodynamic stability	25	1	7-38	16	-	-	-	-	$1-10^{-3}$	Part of M = 7, shock-driven countercurrent wind tunnel.
MIT Range A[g]	Wake study Aerophysics	30	0.3-1.5	20	5	1	-	Varies	Varies	$1-10^{-8}$	Stainless-steel construction; can be kept clean.
ISL Aero-ballistic[h]	Wake study Aerophysics	8.5	2	20	13	-	-	Varies	-	-	
NOL Aerophysics Range	Aerophysics	100	12	9	Varies	-	-	-	Varies	$1-1 \times 10^{-4}$	Mach-Zehnder interferometer. 4 rotating-mirror cameras.
GM-AC-DRL Aero-physics Range B[i]	Wake Study Aerophysics	55	0.6-2.5	20	5	3	-	Varies	4	-	
NOL Shock Interaction	Aerophysics	26	1	40	6	1	-	-	-	$1-4 \times 10^{-3}$	Shock tube used to generate planar shock-wave that intercepts model at test section
NASA-Ames Radia-tion Facility	Aerophysics	8	1	7-38	4	-	-	-	4	$1-10^{-3}$	Part of M = 7, shock-driven countercurrent wind tunnel.
VKF Counter-flow Range	Aerophysics	2	0.5	13	3	-	-	-	-	-	Part of shock-driven countercurrent wind tunnel.
Boeing Aero-ballistic Range[j]	Aerophysics Impact	10	0.75	13	6	1	1	-	1	-	
NOL Impact Range	Impact	10	2	13	-	-	3	-	-	$1-2 \times 10^{-3}$	1 rotating-mirror camera.
NRL Range No.1[k]	Impact	15	1	-	2	-	9	-	-	-	
GM Ballistic Range A	Impact	5	0.3	6-8	3	-	-	-	-	-	$V_m \leqslant 10$ km/sec.
Douglas Range A[l]	Impact	1	0.3	13	3	-	-	-	-	$1-1.3 \times 10^{-8}$	
Douglas Range B	Impact	30	3	6-20	3	-	-	-	-	$10-4 \times 10^{-3}$	Telemetry.
GM-AC-DRL	Impact	3	1.5x2	57	2	-	-	-	-	-	Gun attitude adjustable.
NASA-Ames Impact Range	Impact	7	1	6	6	-	1	-	1	$1-10^{-3}$	$V_m \leqslant 11.3$ km/sec.

[a] US Naval Ordnance Laboratory, White Oak, Silver Spring; Maryland 20910, USA
[b] Canadian Armament Research and Development Establishment; P.O. Box 1427; Quebec 2, P.Q., Canada
[c] Royal Armament Research and Development Establishment; Fort Halstead, Sevenoaks, Kent; England
[d] Laboratoire de Recherches Balistiques et Aerodynamiques; Vernon (Eure); France
[e] ARO, Inc., von Kármán Gas Dynamics Facility; Arnold Engineering Development Center; Arnold Air Force Station, Tennessee 37389, USA
[f] Ames Research Center; National Aeronautics and Space Administration; Moffett Field, California 94035, USA
[g] Massachusetts Institute of Technology; Lincoln Laboratory; Lexington, Massachusetts 02173, USA
[h] Institut Franco-Allemand de Recherches de Saint-Louis; 12, rue de l'Industrie; Saint-Louis (Haut-Rhin); France
[i] General Motors Corporation, AC Electronics; Defense Research Laboratories; 6767 Hollister Ave.; Goleta, California 93017, USA
[j] The Boeing Company, Aero-Space Division; P.O. Box 3707; Seattle, Washington 98124, USA
[k] US Naval Research Laboratory; Washington D.C. 20390, USA
[l] McDonnell-Douglas Aircraft Company, 3000 Ocean Park Blvd.; Santa Monica, California 90406, USA

CHAPTER 2

THE LIGHT-GAS-GUN MODEL LAUNCHER

by

Robert E. Berggren and Robert M. Reynolds

NASA-Ames Research Center

THE LIGHT-GAS-GUN MODEL LAUNCHER

Robert E. Berggren and Robert M. Reynolds

2.1 INTRODUCTION

The conventional powder gun - the forerunner of the present day ballistic-range model launcher - has been the object of theoretical and experimental research for two centuries. The foundations for formal systematic research on guns were laid by Robins[2.1] and Lagrange[2.2], who formulated the basic problems of classical internal ballistics. Many other notable names form the roster of those early workers who made significant contributions to the fascinating study of ballistics: Poisson[2.2], Résal[2.3], Hélie[2.4], Sarrau[2.5], Moisson[2.6], Hugoniot[2.7], Gossot and Liouville[2.8], Charbonnier[2.9], Röggla[2.10], Love and Pidduck[2.11], Cranz[2.12], and many others. Historical reviews of the earlier development of ballistics are given by Cranz[2.12], Corner[2.13], Thornhill[2.14], Hunt[2.15], and Nelson[2.16].

With the introduction of the free-flight ballistic range the gun became a laboratory tool which provided a convenient means for generating high speeds for the study of the physics of flight. Early ranges were used by Charbonnier[2.9], Cranz[2.12], and Fowler et al.[2.17], to investigate the aerodynamics of spinning shells. Since that period, a large number of modern ballistic ranges have evolved to study many aspects of flight at high speeds, not necessarily related to the weapons of ordnance. As the flight speeds of interest increased, new classes of projectile launchers were required, but the conventional powder gun has remained an important test device for research at speeds below approximately 3 km/s.

The powder gun is limited to such speeds because of the high molecular weight of powder gas. In accelerating a projectile by the expansion of a heavy gas, a large share of the total available energy of the gas is expended in accelerating the gas itself and thus the energy available for accelerating the projectile is relatively small; even with a very light projectile the maximum velocities attainable are relatively low. A much more favorable distribution of energy between the gas and the projectile, giving higher projectile velocities, is obtained with the use of a light gas such as hydrogen or helium.

The first gun utilizing a light propellant gas (helium) was developed by Crozier and Hume[2.18], in 1946 at the New Mexico School of Mines. Since that time, a large variety of "light-gas" guns have evolved, differing mainly in the manner in which the propellant gas is compressed to the high pressures and temperatures required to produce high speeds. Early further development of the type of gun introduced by the New Mexico group was made by Charters, et al.[2.19], at Ames Research Center (1955). Development of a second type of light-gas gun was carried out at the same time at the US Naval Ordnance Laboratory under the direction of Z.I. Slawsky[2.20], [2.21]. Further improvements in the technology of light-gas guns have since been made by many ballistic laboratories in the United States, Canada, and England, with the result that this type of model launcher has become an invaluable tool to generate flight speeds up to 11 km/s. The development of the high-speed computer and new instrumentation techniques have aided greatly in obtaining a better understanding of the complex internal ballistic processes, as evidenced by the large gains in velocity that have been achieved in the last decade, but much remains to be learned.

A number of other methods for accelerating projectiles or discrete particles have been explored and are well documented in the literature. Scully, et al.[2.22] report the attainment of velocities up to 20 km/s with small silicate spheres (10^{-8} to 10^{-6}gm) with an electrothermal gun. The spheroids are accelerated by aerodynamic drag in a stream of dense lithium plasma which is energized by an electric arc discharge. Small charged particles (0.1 to 10 microns diameter) have been accelerated electrostatically to velocities as high as 28 km/s, as reported by Friichtenicht et al. in Reference 2.23. Kronman and Kineke[2.24] report that discrete particles of larger mass (0.01 to 1.0 gm) have been accelerated with explosive shaped-charge techniques to approximately 21 km/s. Electromagnetic accelerators of a variety of types have been tested but have not produced results to date that would make this launcher competitive with the light-gas gun. A novel innovation to the two-stage light-gas gun has been developed by Howell and Orr[2.25], whereby spherical projectiles are given an additional increment in velocity as they are impulsively accelerated through a convergent section attached to the muzzle of the gun. Velocities in excess of 11 km/s have been obtained by this technique. A new development by Godfrey and Moore (reported in Reference 2.26), utilizing a light-gas gun in which the propellant gas is compressed in a controlled manner by an explosive lens, has produced velocities up to 12.2 km/s and shows promise of achieving substantially higher velocities. A brief description of this gun is contained in Section 2.7.

The light-gas gun has proven to be a particularly versatile device in comparison with other launchers because it has the capability of launching models of complex shape having a wide range of weights, sizes, and materials. It has the advantage that high velocities may be achieved under conditions which subject the model to relatively low accelerations and stresses. Although this gun has not produced velocities as high as desired, its present capabilities encompass a flight regime of interest for much present day research. Photographs of two representative light-gas guns may be seen in Figures 2.1 and 2.2.

Preceding page blank

This chapter will be confined to a discussion of the light-gas gun with major emphasis on the two-stage gun now in wide use as a laboratory model launcher.

2.2 SYMBOLS

a	speed of sound
A	cross-sectional area
b	co-volume term
c	modified speed of sound (see Equation (2.114))
d	diameter of projectile
D	diameter of gun components
f	factor in real-gas equation of state
F	factor in real-gas relations (see Equation (2.114))
G	mass of gas
h	enthalpy
k	factor in real-gas equation of state
l	length of projectile
L	length of gun components
m	mass
M	molecular weight
N	number of moles
p	pressure
$\mathcal{R}$	universal gas constant
R	gas constant for a mole of gas $= \mathcal{R}/M$
s	specific entropy
S	entropy
t	time
T	temperature
u	velocity
U	projectile velocity at muzzle of launch tube
v	specific volume
V	volume
w	cylinder wall ratio $= \dfrac{\text{outer diameter of cylinder}}{\text{inner diameter of cylinder}}$
x	distance
α	acceleration
β	factor in real-gas equation of state
γ	ratio of specific heats
ρ	density

σ	Riemann function
σ_y	yield stress
$\bar{a}, \bar{u}, \bar{t}$, etc.	nondimensional quantities defined in text
$\tilde{p}$	average pressure

Subscripts

a	ambient conditions
b	conditions at base of pump piston
c	conditions at entrance of transition section, or conditions in powder chamber
e	conditions at entrance to launch tube
f	final conditions at point specified which affect motion of the model in barrel (see Equation (2.134))
g	gas conditions
p	relating to piston or pump tube
r	reservoir conditions
R	conditions at release of model (diaphragm rupture)
s	relating to projectile, conditions at base of projectile, or launch tube
v	conditions at vertex of parabolic characteristic lines of similarity solution
o	initial loading or starting conditions
1	length or time corresponding to condition when first rare faction wave returns from reservoir and reaches projectile base
*	sonic conditions

2.3 SIMPLE LIGHT-GAS GUN

In the following paragraphs the fundamental problem of the expansion of an ideal propellant gas in a simple gun, consisting only of a reservoir and gun barrel, will be examined. The relationships which govern the expansion process will be developed and the factors that predominate in the determination of the projectile motion, the selection of the propellant gas, and the geometrical configuration of the gun will be considered.

2.3.1 Basic Parameters Influencing Projectile Velocity

The basic factors which determine the motion of a projectile or "shot" as it is accelerated in the bore of a gun under ideal conditions are related by Newton's equation of motion, as follows, with the notation shown in Figure 2.3:

$$\alpha = \frac{du_s}{dt} = \frac{p_s A_s}{m_s} , \qquad (2.1)$$

or, in terms of the distance traveled,

$$\alpha = u_s \frac{du_s}{dx_s} = \frac{p_s A_s}{m_s} . \qquad (2.2)$$

Not considered at this point are the retarding forces due to friction between the model and bore, and the pressures developed on the front face of the model by residual gases in the bore.

In virtually all guns, the pressure, p_s , acting on the base of the model during launch is not constant but varies over a wide range, and is some function of x or t . The launch velocity or muzzle velocity, U , achieved by accelerating the model through the entire barrel length, L_s , is obtained by integrating Equation (2.2):

$$U = \left[\frac{2A_s}{m_s} \int_0^{L_s} p_s dx_s \right]^{1/2} \qquad (2.3)$$

For purposes of simplification, consider an ideal case in which the model is accelerated by a base pressure, $\tilde{p}_s$, which is constant during the entire launch. (For the real case, $\tilde{p}_s$ represents the average pressure for the full launch distance). Equation (2.3) then becomes:

$$U = \left[\frac{2A_s}{m_s} \tilde{p}_s L_s\right]^{1/2} . \tag{2.4}$$

In terms of a nondimensionalized barrel length and model length this becomes, for a cylindrical projectile,

$$U = \left[\frac{2\tilde{p}_s}{\rho_s} \frac{L_s/D_s}{l_s/D_s}\right]^{1/2} . \tag{2.5}$$

Projectile velocities can be maximized, then, by maximizing $\tilde{p}_s$ and L_s/D_s and minimizing ρ_s and l_s/D_s. With a gun of specified bore diameter, the velocity is seen to increase with an increase in barrel length. However, increasing gun size by scaling up all dimensions proportionately will not result in increased performance, at least for the ideal conditions considered here, since the values of l_s/D_s and L_s/D_s remain unchanged.

It is informative to compute the launch velocities that might be attained under conditions of pressure, barrel length, model length, and density in Equation (2.5) that appear to be reasonable or realistic. Velocities calculated for several representative model weights and base pressures are plotted as a function of launch-tube length in Figure 2.4. Model density for all cases is 1 gm/cm^3, a value about equal to that of the plastics frequently used. Several typical model lengths were chosen ranging from ½ to 4 barrel diameter (calibers) long. The launch tube was limited to lengths no greater than 400 calibers, although construction of barrels appreciably longer than this is quite feasible. If one chooses an average base pressure of 10 kilobars, a value well within the strength capabilities of certain plastic models, a one-caliber-long model is accelerated to almost 30 km/s in the 400 caliber distance. This velocity is approximately three times greater than that actually achieved for this type of model. The primary reason is that the gun configurations in use at this time have not produced constant base pressures for lengths as long as 400 calibers, or an average pressure for this length where the peak pressures are low enough to be withstood by the model or the gun itself. An average base pressure of 1.5 kilobars, more representative of that attainable presently, is used for a second case. Actually it is difficult to maintain even this lower value of pressure for launch distances greater than 200 to 300 calibers (as will be shown in a later section) without producing peak pressures which are very much greater than the average value. The problem of achieving high launch velocities, then, is, in part, one of developing methods whereby acceptable pressures can be applied to the model for extended distances. One factor of primary importance in achieving this is the proper selection of propellant gas, and the effect of gas properties as well as other considerations will be examined in the following sections.

2.3.2 Expansion of Gas in Constant-Diameter Tube – Gas Properties

With the thought in mind that maintaining a high base pressure during the entire launching process is an important factor in obtaining high velocities, it is appropriate to examine briefly the behavior of a gas during the process of expansion to determine which parameters most strongly influence the relationship between the pressure and velocity.

Consider the case of the simple launcher shown in Figure 2.5, consisting of a reservoir and launch tube (or barrel) of the same bore diameter. The reservoir contains a perfect gas at initial conditions p_r, ρ_r, and T_r, separated from the projectile by a diaphragm. The launch-tube bore is evacuated to eliminate the retarding effects of any gas ahead of the projectile. When the diaphragm is ruptured in some manner, the subsequent expansion of the gas will accelerate the model, and part of the potential energy of the gas will be converted to kinetic energy in both the gas and projectile. If this expansion process is continued for a sufficiently long time, the limiting conditions will be reached where (neglecting friction and other losses) all potential energy will be converted to kinetic energy and the pressure will have decreased to zero. The limiting speed is termed the escape speed of the gas. The expansion process is nonsteady and one-dimensional, and the assumptions are made that the changes in the flow are continuous and that the process is isentropic. The fundamental relations which apply are:

Conservation of mass,

$$\frac{\partial \rho}{\partial t} + \rho \frac{\partial u}{\partial x} + u \frac{\partial \rho}{\partial x} = 0 . \tag{2.6}$$

Conservation of momentum,

$$\frac{\partial u}{\partial t} + u \frac{\partial u}{\partial x} + \frac{1}{\rho} \frac{\partial p}{\partial x} = 0 . \tag{2.7}$$

Constancy of particle entropy,

$$\frac{\partial s}{\partial t} + u \frac{\partial s}{\partial x} = 0 . \tag{2.8}$$

Isentropic process,

$$p = f(\rho) . \tag{2.9}$$

A solution to the nonlinear partial differential equations is possible using the "method of characteristics" given in Reference 2.27

Introducing the speed of sound relationship,

$$a^2 = \left(\frac{\partial p}{\partial \rho} \right)_s ,$$

into the conservation of momentum equation, (2.7), gives

$$\frac{\partial u}{\partial t} + u \frac{\partial u}{\partial x} + \frac{a^2}{\rho} \frac{d\rho}{dx} = 0 . \tag{2.10}$$

Multiplying the continuity equation, (2.6), by a/ρ and combining with Equation (2.10) leads to two equations which, when rearranged, become:

$$\frac{\partial(u + \sigma)}{\partial t} + (u + a) \frac{\partial(u + \sigma)}{\partial x} = 0 , \tag{2.11}$$

$$\frac{\partial(u - \sigma)}{\partial t} + (u - a) \frac{\partial(u - \sigma)}{\partial x} = 0 , \tag{2.12}$$

where, σ , the Riemann function, is defined as

$$\sigma = \int_0^\rho \frac{a}{\rho} d\rho , \tag{2.13}$$

and $\sigma = 0$ when $\rho = 0$.

Equations (2.11) and (2.12) are known as characteristic equations in which the fluid properties are defined in the $x-t$ plane along lines having slopes $dx/dt = (u \pm a)$. Along the $dx/dt = (u + a)$ curves the flow properties are related by

$$d\rho = -\frac{\rho}{a} du \tag{2.14}$$

or, in terms of pressure,

$$dp = - \rho a \, du . \tag{2.15}$$

For the $dx/dt = (u - a)$ characteristic lines,

$$d\rho = \frac{\rho}{a} du \tag{2.16}$$

or

$$dp = \rho a \, du . \tag{2.17}$$

The directions or velocities represented by $dx/dt = u \pm a$ are the paths in the $x-t$ plane of disturbances or acoustic waves which propagate upstream at the speed of sound, a, relative to the particle speed, u .

When a projectile is accelerated by an expanding gas, an infinite number of acoustic waves originate continuously in the gas at the base of the projectile and propagate upstream at velocity $(u - a)$ causing a continuous drop in pressure. In a sense, increasing projectile and fluid velocity is gained at the expense of a diminished pressure. It can be seen from Equations (2.15) and (2.17) that *the rate of change of pressure with velocity is dependent upon ρa , termed the acoustic impedance*. To obtain a high increment in velocity for a given incremental pressure drop requires that the acoustic impedance be low. This is a fundamental relationship, then, that governs the selection of the propellant gas to be used in a high-speed gun.

An expression for the acoustic impedance in terms of the reservoir conditions can be obtained from the following equation of state, sound speed equation, and isentropic relations:

$$p = \rho \frac{R}{M} T \tag{2.18}$$

$$a^2 = \gamma RT \tag{2.19}$$

$$\frac{a}{a_r} = \left(\frac{\rho}{\rho_r}\right)^{(\gamma-1)/2} = \left(\frac{p}{p_r}\right)^{(\gamma-1)/2\gamma} \tag{2.20}$$

$$\frac{du}{dp} = \pm\frac{1}{\rho a} = \pm\frac{a_r}{\gamma p_r}\left(\frac{p_r}{p}\right)^{(\gamma+1)/2\gamma} \tag{2.21}$$

or

$$\frac{du}{dp} = \pm\left(\frac{R T_r}{\gamma M p_r^2}\right)^{1/2}\left(\frac{p_r}{p}\right)^{(\gamma+1)/2\gamma} . \tag{2.22}$$

It can be seen that, for a fixed value of reservoir pressure, p_r and pressure ratio, p_r/p, a reduction in γ and an increase in reservoir sound speed will increase the velocity gained with a given pressure loss. The sound speed is the more important factor since it can be varied over a wide range while the variation in γ for suitable propellant gases is quite limited. A reduction in acoustic impedance is also obtained by reducing the molecular weight of the gas. The requirement of a low molecular weight gas to obtain high projectile velocities can be readily appreciated when one considers that in the process of accelerating a projectile a substantial portion of the total available potential energy of the gas is expended in accelerating the gas itself. A gas must thus be chosen which requires the least energy to achieve a given gas velocity and this then dictates a gas of low molecular weight. Equation (2.22) shows also that increasing reservoir temperature will serve to reduce the acoustic impedance. Note that an increase in reservoir pressure, p_r, adversely affects the acoustic impedance by increasing the density, ρ_r.

To gain further insight into the manner in which pressure is diminished in exchange for increasing velocity in an expansion, let us examine again the characteristic Equations (2.11) and (2.12). Integration of the expression for the Riemann function, σ, for a perfect polytropic gas gives the simple relation:

$$\sigma = \frac{2a}{\gamma - 1} . \tag{2.23}$$

The quantities $(u + \sigma)$ and $(u - \sigma)$, referred to as Riemann invariants, are thermodynamic functions which remain constant along the characteristic lines of slope $(u + a)$ and $(u - a)$. Thus:

$$u + \sigma = u + \frac{2a}{\gamma - 1} = \text{constant} , \tag{2.24}$$

along downstream characteristics having slope $dx/dt = (u + a)$, and

$$u - \sigma = u - \frac{2a}{\gamma - 1} = \text{constant} , \tag{2.25}$$

along upstream characteristics having slope $dx/dt = (u - a)$.

These disturbance paths are illustrated in the $x-t$ diagram of Figure 2.6, for a simple launcher having an infinitely long reservoir of the same diameter as the barrel.

The conditions in the barrel can be related to the conditions in the undisturbed region in the reservoir where the flow velocity is zero, along downstream characteristics by:

$$u + \frac{2a}{\gamma - 1} = \frac{2a_r}{\gamma - 1} . \tag{2.26}$$

Combining this equation with the isentropic relation

$$\frac{p}{p_r} = \left(\frac{a}{a_r}\right)^{2\gamma/(\gamma-1)} ,$$

gives the relationship between pressure and flow velocity for the expansion of a perfect gas:

$$\frac{p}{p_r} = \left[1 - \left(\frac{\gamma - 1}{2}\right)\frac{u}{a_r}\right]^{2\gamma/(\gamma-1)} , \tag{2.27}$$

or

$$\frac{u}{a_r} = \frac{2}{\gamma - 1} \left[1 - \left(\frac{p}{p_r}\right)^{(\gamma-1)/2\gamma} \right].$$

(2.28)

In the limit $\gamma \to 1$ these equations reduce to

$$- \log_e \frac{p}{p_r} = \frac{u}{a_r},$$

(2.29)

as noted in Reference 2.28. Curves of Equation (2.27), presented in Figure 2.7 for several values of γ, show that the pressure ratio is highly sensitive to changes in the velocity ratio. If the flow velocity is very much less than the sound speed, there is only a small reduction in pressure below the initial reservoir pressure, but as flow velocity is increased to values greater than the reservoir sound speed, the pressure reduction becomes exceedingly great. Thus, in a realistic gun in which the maximum reservoir pressure, p_r, is limited by the strength of the reservoir, the propelling pressures can be maximized during expansion only by choosing a propellant gas having a high sound speed. It can also be seen again that the "best" propellant should have a low ratio of specific heats, γ.

The limiting velocity of an expanding gas is reached if the gas is expanded completely to zero pressure. This "escape velocity" can be seen from Equation (2.28) to be:

$$u_{esc} = \left(\frac{2}{\gamma - 1}\right) a_r.$$

(2.30)

This represents a theoretical maximum to which a projectile could be accelerated in a constant-bore gun under ideal conditions, without losses, if the launch tube were infinitely long to allow complete expansion of the gas to zero pressure.

Table 2.1 gives the physical properties of several gases that have been used as propellants. Hydrogen and helium are clearly superior to powder gas in fulfilling the requirements of a low acoustic impedance, ρa, and a high sound speed, a. At the high pressure, more representative of gun conditions, the two light gases are closely competitive in these properties. However, in regard to low molecular weight and a low ratio of specific heats, γ, hydrogen is substantially superior. Thus, in a given gun, hydrogen will achieve the highest ultimate performance, or, when used under comparable conditions to produce the same performance, will have the advantage of operating at considerably lower temperatures than those required for helium. As a consequence, at high-performance levels the erosion of the launch tube surfaces with hydrogen can be very much less – as much as an order of magnitude less – than for helium. This can be the difference between a tolerable rate of deterioration of the launch tube and an unacceptable rate requiring frequent replacement of eroded components. Erosion should be minimized for the added reason that the metallic vapor is a contaminant which can degrade performance by increasing the molecular weight of the propellant gas. Helium, while second best to hydrogen, is still an important propellant, since considerations of safety, in certain situations, outweigh the advantages gained with hydrogen.

2.3.3 Gas Dynamics Related to Model Motion

2.3.3.1 Infinite-Length Reservoir – Constant-Diameter Tube

The motion of the projectile, as given by Newton's law (Equation (2.2), Section 2.3.1), can be combined with the unsteady isentropic expansion relation, Equation (2.27), to obtain:

$$\frac{du_s}{dt} = u_s \frac{du_s}{dx} = \frac{p_s A_s}{m_s} = \frac{p_r A_s}{m_s} \left[1 - \left(\frac{\gamma - 1}{2}\right)\frac{u_s}{a_r} \right]^{2\gamma/(\gamma-1)}.$$

(2.31)

The expression for distance becomes:

$$x_s \frac{p_r A_s}{m_s} = \int_0^{u_s} u_s \left[1 - \left(\frac{\gamma - 1}{2}\right)\frac{u_s}{a_r} \right]^{-2\gamma/(\gamma-1)} du_s.$$

(2.32)

Changing x_s and u_s to a dimensionless form $\bar{x}_s$ and $\bar{u}_s$:

$$\bar{x}_s = \frac{p_r A_s x_s}{m_s a_r^2}$$

(2.33)

$$\bar{u}_s = \frac{u_s}{a_r}$$

(2.34)

and, completing the integration, one obtains the following expression for distance (see References 2.19, 2.29, and 2.30):

$$\bar{x}_s = \frac{2}{\gamma - 1} \left\{ \frac{\frac{2}{\gamma + 1} - \left[1 - \left(\frac{\gamma - 1}{2} \right) \bar{u}_s \right]}{\left[1 - \left(\frac{\gamma - 1}{2} \right) \bar{u}_s \right]^{(\gamma+1)/(\gamma-1)}} + \frac{\gamma - 1}{\gamma + 1} \right\} . \tag{2.35}$$

For time, where

$$\bar{t} = \frac{p_r A_s t}{m_s a_r} . \tag{2.36}$$

one obtains:

$$\bar{t} = \frac{2}{\gamma + 1} \left\{ \left[1 - \left(\frac{\gamma - 1}{2} \right) \bar{u}_s \right]^{-(\gamma+1)/(\gamma-1)} - 1 \right\} \tag{2.37}$$

and by combining Equations (2.35) and (2.37):

$$\bar{x}_s = \frac{2}{\gamma - 1} \left\{ 1 + \bar{t} - \left[1 + \left(\frac{\gamma + 1}{2} \right) \bar{t} \right]^{2/(\gamma+1)} \right\} . \tag{2.38}$$

These are the basic relationships for projectile velocity, as a function of distance and time, for unsteady isentropic flow of an ideal gas in a gun with an infinitely long reservoir, of the same diameter as the launch tube. Equation (2.35) is plotted in Figure 2.8, for various values of γ.

2.3.3.2 Finite-Length Reservoir – Constant-Diameter Tube

Consider now, the acceleration of a projectile by the expansion of gas from a reservoir of finite length. As in the previous section, let the reservoir diameter be the same as the barrel diameter.

At $t = 0$, representing the start of projectile acceleration, an expansion wave travels rearward at the speed of sound of the reservoir gas, a_r, setting the gas in motion, which in turn causes a decrease in pressure. Upon reflection from the rear wall of the reservoir, this acoustic wave will return in a downstream direction at a velocity $(u + a)$, acting to retard the motion of the reservoir gas and further reduce the reservoir pressure. If the launcher barrel is sufficiently long, the "reflected" rarefaction will, on arriving at the base of the projectile, lower the base pressure and projectile acceleration to values below those which would have occurred had the rarefaction not caught up with the projectile. The characteristic lines for this case are shown in Figure 2.9. The reservoir length, L_{r1}, which will cause the first reflected rarefaction to catch the projectile just as the projectile leaves the muzzle of the launcher depends on projectile mass, launch-tube length, and the gas conditions. Any reservoir of length L_{r1} or greater can be considered as "effectively" infinite because the projectile will have left the barrel before receiving communication from the gas signaling the existence of a reservoir wall. Heybey[2.30] developed an analytical relationship for the point at which the first reflected wave reaches the projectile base, as a function of the reservoir length L_{r1}. This is given (in a different form) as a function of projectile velocity in Equation (2.39) below, for the expansion of an ideal gas in a constant diameter tube.

$$\bar{L}_{r1} = \frac{p_r A_s L_{r1}}{m_s a_r^2} = \frac{2}{\gamma + 1} \left\{ \left[1 - \left(\frac{\gamma - 1}{2} \right) \frac{u_{s1}}{a_r} \right]^{-\frac{1}{2}(\gamma+1)/(\gamma-1)} - 1 \right\} . \tag{2.39}$$

In the limit $\gamma \rightarrow 1$ Equation (2.39) becomes

$$\bar{L}_{r1} = e^{\bar{u}_s/2} - 1 . \tag{2.40}$$

It may be noted that this relationship is part of a general analytical solution to the longstanding Lagrange Ballistic Problem solved by Heybey by tracing the flow properties with a network of characteristic lines. Previous to this, Love and Pidduck[2.11] and Kent[2.31] had derived restricted "special" solutions to the Lagrange problem. A relationship for the distance traveled by the projectile at the time the first reflected wave reaches the projectile base can be obtained as a function of the reservoir length L_{r1} by combining Equations (2.39) and (2.35) to give:

$$\bar{x}_s = \frac{4}{\gamma^2 - 1} \left[\left(\frac{\gamma + 1}{2} \right) \bar{L}_{r1} + 1 \right]^2 - \left(\frac{2}{\gamma - 1} \right) \left[\left(\frac{\gamma + 1}{2} \right) \bar{L}_{r1} + 1 \right]^{4/(\gamma+1)} + \frac{2}{\gamma + 1} . \tag{2.41}$$

A plot of the barrel length, where $\bar{x}_s = \bar{L}_s$, is presented in Figure 2.10 as a function of the effectively infinite chamber length, for several values of γ (as given in Reference 2.28). Here, it is seen that for this criterion the chamber length is a nearly linear function of barrel length.

2.3.3.3 *The Effects of Chambrage*

When a gun has a reservoir diameter that is larger than the barrel or launch-tube diameter, as sketched in Figure 2.11, it is said to have "chambrage" or chamberage. In the expansion process in a chambered gun, rarefaction waves originating at the projectile base and moving toward the reservoir are partially reflected at the transition section, proceeding as compression waves directed back toward the projectile. The portion of the rarefaction not reflected is transmitted through the transition section to the reservoir, reflecting from the breech wall and lowering the reservoir pressure. The proportion of the rarefaction wave that is reflected at the transition section, towards the projectile, as a compression wave increases as the ratio D_r/D_s increases, approaching complete reflection as $D_r/D_s \rightarrow \infty$. This is in contrast to the situation in the constant-diameter gun (no chamberage) with an infinitely long reservoir, in which neither rarefactions or compressions can be reflected to the projectile. Hence, with other factors being equal the performance of a highly chambered gun would be expected to exceed that of a gun with smaller or no chamberage.

One other significant difference between the gas dynamics of the chambered gun and one with no chamberage is due to the quasi-steady flow in the transition section of the chambered gun, which is described by the following equation:

$$u \, du \; = \; -\frac{dp}{\rho} \; . \tag{2.42}$$

It is readily seen that for the chambered gun it is a low "ρ" as a function of pressure which is required to minimize the loss in pressure exchanged for an increase in velocity, rather than low "ρa" requirement for the constant-diameter gun.

The most extensive treatment of the chamberage problem has been given by Seigel in References 2.28 and 2.32 to 2.34. Stephenson[2.35] presents some particular solutions, using Seigel's approach, for guns having helium as the propellant gas, and Vasiliu[2.36] and Zondek[2.37] have obtained solutions for the chambered gun using the method of characteristics in a digital computer program. The detailed analysis of the chamberage problem will not be considered here. We will be content, instead, to briefly outline the problem and summarize some of the conclusions regarding chamberage, leaving it to the interested reader to delve further into the references.

While the flow processes in the reservoir and launch tube may be readily treated by the one-dimensional characteristics equations previously outlined, the flow in the transition section joining the two bores is two-dimensional as well as unsteady. Seigel simplifies the problem by assuming that the flow at the entrance and exit planes of the transition section is one-dimensional, and that the time rates of change of mass and energy of the gas in the transition section are negligible. Hence, at any instant of time, the quasi-steady continuity and energy equations may be used to relate the conditions at the entrance to those at the exit of the transition section:

$$\rho_c A_r u_c \; = \; \rho_e A_s u_e \; , \tag{2.43}$$

and

$$h_c + \frac{u_c^2}{2} \; = \; h_e + \frac{u_e^2}{2} \; . \tag{2.44}$$

For an ideal gas, in a gun having an infinitely long reservoir $(L_r = \infty)$ with chamberage, the following equations are applied:

$$a \; = \; \left(\frac{\gamma - 1}{2}\right)\sigma \; , \qquad \frac{p}{p_{r_0}} \; = \; \left(\frac{\sigma}{\sigma_0}\right)^{2\gamma/(\gamma-1)} \; ,$$

$$h \; = \; \left(\frac{\gamma - 1}{4}\right)\sigma^2 \; , \qquad \frac{\rho}{\rho_{r_0}} \; = \; \left(\frac{\sigma}{\sigma_0}\right)^{2/(\gamma-1)} \; , \tag{2.45}$$

$$u_c + \sigma_c \; = \; \sigma_0 \; , \tag{2.46}$$

and

$$u_r + \sigma_r \; = \; \sigma_0 \; . \tag{2.47}$$

(Equations (2.45) and (2.46) relate the conditions of the gas at the entrance of the transition section and at any point in the reservoir, respectively, to those of the gas in the undisturbed region of the reservoir where u_{r_0} is considered to be 0).

(Continuity)

$$\frac{A_r u_c}{A_s u_e} = \frac{\rho_e}{\rho_c} = \left(\frac{\sigma_e}{\sigma_c}\right)^{2/(\gamma-1)} . \tag{2.48}$$

(Momentum)

$$\frac{u_c^2}{2} + \frac{\gamma-1}{4}\sigma_c^2 = \frac{u_e^2}{2} + \frac{\gamma-1}{4}\sigma_e^2 . \tag{2.49}$$

(In the barrel)

$$\frac{\partial}{\partial t}(u \pm \sigma) + (u \pm a)\frac{\partial}{\partial x}(u \pm \sigma) = 0 . \tag{2.50}$$

(Equation of motion)

$$\frac{m_s du_s}{dt} = p_{r_0} A_s \left(\frac{\sigma_s}{\sigma_o}\right)^{2\gamma/(\gamma-1)} . \tag{2.51}$$

For the limiting case of infinite chamberage $(D_r/D_s = \infty)$ and infinite reservoir length $(L_r = \infty)$, application of the preceding equations by the method of characteristics leads to the results shown in Figure 2.12. It is readily seen that for infinite reservoir length, according to this simplified analysis, the effect of chamberage increases with projectile velocity. However, increasing chamberage from unity to infinity (case shown) gives, as a maximum, an increase in velocity of $a_r/2$ over that of the gun with no chamberage.

For the more general case of finite chamberage and reservoir lengths, Seigel presents, in Reference 2.28, results calculated using both the method of characteristics, outlined herein, and the method of von Neumann and Richtmyer[2.38]. The variation of $\bar{u}_s$ as a function of $\bar{x}_s$ was calculated for all combinations of chamberage equal to 1, 2, 5, and ∞, with various reservoir lengths, expressed as $G/m_s = 0.25$, 0.5, 1, 2, 5, and ∞, and for $\gamma = 1.1$, 1.4, and 1.67. The parameter G/m_s is the ratio of the mass of gas initially loaded in the reservoir to the projectile mass, and is related to the nondimensional reservoir length, as follows:

$$\frac{G}{m_s} = \frac{\rho_r A_r L_r}{m_s} = \gamma \frac{A_r}{A_s} L_r . \tag{2.52}$$

A typical plot of Seigel's results, for $\gamma = 1.4$ and $G/m_s = 5$, is shown in Figure 2.13. When compared at equal values of G/m_s, the calculations indicate the following:

(1) During the early stages of motion of the projectile, $\bar{x}_s$ small, while only a few reflections of the acoustic waves have occurred between the reservoir and projectile, increased projectile velocities result from increased chamberage. The largest gains in velocity occur with the initial increases in chamberage; that is, beyond a value of chamberage of 4 $(A_r/A_s = 16)$ only negligibly small additional increases in velocity may be obtained.

(2) As the expansion is allowed to proceed to larger values of $\bar{x}_s$, the effect of chamberage gradually diminishes, resulting ultimately in the same projectile velocity for all values of chamberage.

2.4 TWO-STAGE PISTON-COMPRESSION GUN

The simple single-stage gun described in Section 2.3, consisting of a reservoir of gas of constant volume, is not capable of providing the highest model velocities frequently required. Even with an infinite size reservoir the projectile base pressure drops rapidly from its initial peak, as the model accelerates (as seen in Figure 2.7), so that the average base pressure is, for many cases, too low to yield the desired velocity. Further, the models to be launched are often of complex shapes or are composites of several materials, encased for support in in a multiple piece carrier (sabot), and hence are relatively fragile (see Chapter 3). Thus the allowable peak base pressure (equal to reservoir pressure, p_r, in this case) is often limited by model strength and may be very much lower than the strength capability of the reservoir. The decrease in base pressure caused by the expansion of the propellant gas can, in principle, be counteracted by the addition of energy to the gas after start of model motion. The reservoir pressure, if initially limited by the strength of the model, may then be increased progressively until the reservoir strength is reached, in a manner to give a more uniform pressure history at the base of the projectile. In a single-stage gun, the energy can be augmented by electrical means, using an arc discharge (Refs. 2.39 to 2.42), or by chemical means, using combustible gases or explosives (Refs. 2.43 to 2.46).

The addition of energy to the propellant gas during the time that the model is being launched can be effectively accomplished with a two-stage light-gas gun, as sketched in Figure 2.14. The two-stage gun has two gas

chambers: energized gas in the first stage compresses the light propellant in the second stage, which in turn accelerates the projectile. In some cases the two gas regions are separated only by a diaphragm, and the second-stage propellant gas is compressed and heated, as in a shock tube, by shock waves generated as the first-stage gas expands into the second stage. However, for the conditions required in a high-performance launcher, a more effective transfer of energy is made between the first and second stages by means of a free piston. Compressed helium (see Reference 2.47) or combustible mixtures of hydrogen and oxygen with helium (see References 2.21 and 2.48) have been used as first-stage driver gases, but more generally the first-stage propellant is a gun powder gas. The operation of a typical two-stage gun, then, starts with the ignition and burning of a solid gunpowder propellant. The gas generated from this combustion drives the piston, which, in turn, compresses hydrogen or helium in the second stage to high pressures and temperatures. A diaphragm which serves to isolate the model from the light gas ruptures at some specified pressure and the model accelerates through the barrel or launch tube. The significant factor to be noted concerning the operation of the two-stage gun is that the compression or pumping process continues during a substantial part of the time that the model is being launched, adding energy to sustain the base pressure.

Two-stage piston-compression guns can be grouped into two general classes according to the manner in which the propellant gas is compressed and heated. In one type, the piston speed is low, and compression occurs nearly isentropically; in the other, the piston speed is high, and compression is accomplished by the strong shock waves which precede the piston. There are considerable differences in the pressure and temperature histories that occur with each type, as well as differences in gun geometry. A discussion of the relative merits of each type is presented in the following sections.

2.4.1 Isentropic-Compression Guns

When the second-stage propellant gas is compressed nearly isentropically (not considering viscous effects or heat transfer to the walls), the pressure in the reservoir rises smoothly and continuously, as shown in Figure 2.15. This is accomplished by driving the piston at a slow speed in relation to the gas sound speed so that strong shock waves are not formed, (see fluid-dynamics text, e.g., References 2.27 or 2.49). A reasonably smooth pressure rise during compression becomes important in launching models to high velocity when the pressure applied to the base of the model approaches the limit of the model's strength. In this case, large pressure jumps associated with strong shock waves can result in model failure.

The energy necessary to compress the propellant gas is provided by the kinetic energy of the "free" piston. With a low piston speed, a high piston mass is needed to provide the energy, so guns employing isentropic compression are sometimes referred to as "heavy-piston" guns.

The gas properties during compression are related to the initial properties by the following isentropic expressions:

$$\left(\frac{p}{p_o}\right) = \left(\frac{V_o}{V}\right)^\gamma = (\text{Comp. Ratio})^\gamma = \left(\frac{\rho}{\rho_o}\right)^\gamma = \left(\frac{T}{T_o}\right)^{\gamma/(\gamma-1)} = \left(\frac{a}{a_o}\right)^{2\gamma/(\gamma-1)}. \qquad (2.53)$$

These relations are plotted in Figure 2.16. The high sound speeds required for high performance can be achieved with a large volume (high compression ratio) pump tube. Sound speeds and temperatures developed by compressing isentropically to an arbitrary pressure of 10 kilobars from a range of initial gas-loading pressures (representative of a large number of guns in current operation) are given in Figure 2.17.

2.4.2 Shock-Compression Guns

The method of heating a gas by shock compression has been used successfully in the operation of a number of two-stage guns. Typically, a light piston is accelerated by the first-stage driver gas to relatively high speeds, 1500 to 3000 m/s, to produce the desired strong shock waves in the second-stage propellant gas. The effect of piston speed on the pressure, density, and temperature ratios may be seen by examining the approximate relationships for a strong normal shock (i.e., $p_2/p_1 \gg 1$):

$$\frac{p_2}{p_1} \simeq \frac{\gamma(\gamma + 1)}{2}\left(\frac{u_2}{a_1}\right)^2, \qquad (2.54)$$

$$\frac{\rho_2}{\rho_1} \simeq \frac{\gamma + 1}{\gamma - 1}, \qquad (2.55)$$

$$\frac{T_2}{T_1} \simeq \left(\frac{\gamma - 1}{\gamma + 1}\right)\frac{p_2}{p_1}, \qquad (2.56)$$

$$U_{\text{shock}} \simeq \left(\frac{\gamma + 1}{2}\right)u_2, \qquad (2.57)$$

where U_{shock} denotes the shock speed, and subscripts 1 and 2 refer to the conditions ahead of and behind the shock, respectively. (For exact shock relations, see, for example, References 2.49 to 2.51.)

During operation of such a gun, the shock traveling at a speed up to approximately $(\gamma + 1)/2$ times the piston speed, moves through the length of the pump tube, is reflected from the end of the pump, and travels rearward to be reflected by the piston. The shock may make several oscillations between piston and end of reservoir, further compressing and heating the gas. (Pressure, temperature, and density relations for multiple shock transits and reflections are given in Reference 2.52). Model motion begins upon rupture of a diaphragm separating the propellant gas from the model. Diaphragm rupture is generally designed to occur at the first or second shock reflection. During the time that the model is accelerated, the back and forth motion of the shock continues and may reflect from the base of the model several times, producing large and rapid pressure increases at the model base. A time-distance plot describing the motion of the piston, shock, and model is given in Figure 2.18. A plot of model base pressure during launch (Fig. 2.19) serves to show that the relatively violent shocking process exposes the model to large and rapid pressure fluctuations. Model damage may occur not only from the high peak pressures but also from the rapid rate of change in pressure which generates compressive and tensile stress waves within the model (see Reference 2.53).

Nonisentropic heating of the propellant gas yields higher temperatures than obtained by isentropic compression for the same increase in pressure. Baker[2.54] has shown that as an upper limit under ideal conditions a 30% increase in temperature is calculated for a piston velocity of 1800 m/s over that attained by isentropic compression to the same pressure. Real-gas effects, however, may reduce this gain. Stollery and Maull[2.55] show that for shock compression of air, real-gas effects will lower temperatures and increase the pressures so that if a comparison is made at equal final pressures, the temperature gained with a real gas will be significantly less than the ideal case.

The shock-compression gun has been widely used by a number of laboratories. A two-stage shock-compression gun described in Reference 2.56 uses a powder charge in a helium chamber for a first stage, with a light piston separating the first- and second-stage gases to transfer energy between the two stages. An example of such a gun used at Ames Research Center is shown in Figure 2.20.

In the combustion-driven shock-compressed light-gas gun, developed at the Naval Ordnance Laboratory (Ref. 2.21), the first-stage driver gas (helium) is energized by the combustion of a H_2-O_2 mixture. Expansion of the heated gas mixture upon rupture of a diaphragm separating the first and second stages, serves to shock compress and heat the second-stage propellant gas. (Other guns of this type are described in References 2.57 and 2.58.)

Further description of the design and performance of shock-heated light-gas guns, including analytical methods for computing velocity may be obtained from References 2.35, 2.41, and 2.58 to 2.63.

2.4.3 Comparison of Shock- and Isentropic-Compression Guns

The higher temperatures generated by shock-heating allow one to use a smaller-volume pump tube having a lower compression ratio than the isentropic gun. Further, the light piston used with the shock-heated gun provides some advantage in that the forces imposed on the high pressure end of the second stage, when the piston decelerates to rest, are generally less than the pressures resulting from deceleration of the heavy piston of the isentropic gun, making possible a somewhat simpler construction. The shock-compression gun, thus, may require less laboratory space and be more economical to construct and operate, but the difference need not be great.

On the other hand, it has been demonstrated through actual experience with both types and by analytical comparisons (see Lemcke, Reference 2.64) that the slow-piston isentropic gun has the capability of achieving higher model velocities. Temperatures as high as those achieved by shock heating can be attained isentropically, simply by increasing the size of the compressor to obtain a high compression ratio. The important advantage to be gained by isentropic compression is the more favorable pressure history at the base of the moving model, resulting generally in lower peak pressures (and more slowly varying pressures) imposed on the model to obtain comparable average base pressures. Thus, the model is subjected to lower stresses to obtain the same velocity. This means that fragile saboted models as well as rugged simple models can be launched to substantially higher velocities by a gun which has a more nearly isentropic mode of compression. Guns in present use are in many cases a compromise between the two types.

2.4.4 Two-Stage Isentropic-Compression Gun

From considerations given previously it was seen that it is desirable that the propellant gas be compressed isentropically. In the following section (2.4.5) it will also be seen that, ideally, the gas should be compressed in a manner which will result in a constant driving pressure at the base of the model throughout its full length of travel in the barrel. Although these requirements, strictly speaking, cannot be readily achieved, this has, however, become a widely accepted goal in the design and operation of laboratory model launchers. (In practice, a departure from constant base pressure operation is intentionally made to obtain higher velocities: the launch tube length is extended beyond that distance over which base pressures can be held relatively constant, to obtain an additional increment in velocity from further expansion of the gas to some low pressure at which the model acceleration becomes insignificant). The class of light-gas gun, in use currently, in which the compression process can be made to most closely approach the ideal conditions is the two-stage isentropic-compression gun, two types of which are described in the following discussion.

The first type of two-stage isentropic-compression gun is shown in Figure 2.21. (See, e.g., References 2.19, 2.39, and 2.62). The basic operation is that described in Section 2.4. A gunpowder propellant provides the energy to accelerate a relatively heavy piston to the required velocity to compress the light gas (in most cases, hydrogen). The piston generally reaches its maximum velocity at a time, or position in the pump tube, when the

second-stage pressure is still only a small fraction of the final value (at this time the expanding powder gas has dropped in pressure to about this same low value). Further compression of the hydrogen results from the kinetic energy of the piston, and thus the piston mass and velocity must be sufficient at this point to provide the energy required for compression. This gun has a square-ended or a relatively abrupt transition from the end of the pump to the breech of the launch tube. To prevent damage to this end a sufficient quantity of hydrogen must be loaded initially so that the piston will decelerate almost to rest when it reaches this point. To provide a buffer which will insure some margin of safety, a quantity of gas substantially larger than that necessary to launch the projectile must be used. This has the effect of lowering the compression ratio of the pump with the result that peak temperatures are reduced. This buffer may be eliminated by using an expandable transition section (see Reference 2.39), so that only the quantity of gas dictated by the launching requirements is needed. The expandable end section acts to stop the piston and is replaced after each firing.

Another type of two-stage isentropic gun presently in wide use is shown in Figure 2.22. The geometry of this gun, developed by Curtis[2.65], is similar to that of the gun previously discussed except for two important features: (1) the transition between pump tube and launch tube is made with a slender taper section (total included angle of taper generally between 6 and 16 degrees), and (2) the heavy piston is made of a deformable but relatively incompressible plastic such as polyethylene. During the compression cycle the piston enters the taper and starts to deform. The retarding forces imposed by the tapered wall as well as the rising gas pressure act to decelerate the piston to rest. These forces are frequently of approximately equal values. The piston comes to rest typically as its front face reaches the breech of the launch tube, although in some cases, with a relatively small mass of gas and high piston velocities, a portion of the piston may be driven into or even through the launch tube. If the transition section is sufficiently strong and massive there is relatively little damage incurred during each shot. A gradual deterioration occurs but usually many rounds may be fired before replacement is necessary. The taper, then, provides the means for stopping the piston without the need for any additional gas buffer, and only that quantity of gas required to launch the model is necessary. Thus, for a pump tube of given size, the tapered transition section enables one to maximize compression ratio in a manner that is not destructive to the gun. The slender taper also provides a gradual transition to give smoother flow. However, shock waves traveling through the pump tube are strengthened in the convergent taper (References 2.66 and 2.67). Additional shock waves may also be generated when the piston enters the taper. The front face of the piston must increase in velocity as it intrudes into the taper (the increase in velocity being inversely proportional to the change in area for an incompressible piston) and if the acceleration is great enough the compression waves generated will quickly coalesce into shock waves. These shock waves may serve to increase the model velocity but also produce the undesirable abrupt increases in base pressure.

Curtis suggests an additional factor that might result in increased model performance with the use of a slender taper. This is related to the fact that the front face of the piston increases in velocity as it traverses the taper, reaching much greater velocities than that portion of the piston in the constant diameter section of the pump. It is suggested the gas particles will be accelerated to sufficiently high velocities that the additional kinetic energy thus gained will add substantially to the total available energy, serving to lessen the ultimate pressure drop occurring between the reservoir and model. This effect will, of course, be greater with guns having relatively high piston speeds but may not be significant for guns having large values of chambrage that operate with very slow pistons.

The effects of gun geometry and variations in operating conditions on model performance with the deformable-piston isentropic-compression gun will be discussed in Section 2.5.

2.4.5 Ideal Isentropic Compression – Constant Base Pressure

In concept, or ideally, the maximum velocity that can be imparted to a particular model in a gun of fixed length results when the highest propellant pressure consistent with the steady-load strength characteristics of the model is maintained at the base of the model during the full launching time. In the sense of producing the highest possible performance, then, the application of a constant base pressure, resulting in uniform acceleration of the model for the full launch time, is regarded to be an ideal cycle for gun operation, and was first considered for use in a two-stage gun by Curtis[2.65], Charters[2.68], Wilenius[2.69], and Smith[2.70]. Subsequent extensions of these solutions and/or other considerations relating to the constant base-pressure cycle have been published in References 2.28, and 2.71 to 2.79. At this point we will not be concerned with the practical difficulties or limitations arising from application of this concept, such as the adverse dynamic effects (destructive shock waves in the model) which may occur with the sudden application of pressure to the base of the model at the start of the launching cycle. We wish to examine here the requirements for producing flow in a gun barrel that will maintain a constant pressure at the projectile base.

2.4.5.1 Gas Conditions for Uniform Acceleration in Unchambered Gun

To meet the requirements for constant pressure at the projectile base, the basic one-dimensional equations for unsteady flow (given in Section 2.3.2) must be satisfied:

Continuity Equation

$$\frac{\partial \rho}{\partial t} + \rho \frac{\partial u}{\partial x} + u \frac{\partial \rho}{\partial x} = 0 . \tag{2.6}$$

Momentum Equation

$$\frac{\partial u}{\partial t} + u\,\frac{\partial u}{\partial x} + \frac{1}{\rho}\,\frac{\partial p}{\partial x} = 0 \ . \tag{2.7}$$

Stanyukovich[2.80] was the first to show that the assumption $u = u(t)$, that is, gas velocity is a function of time only rather than time and distance, leads to

$$u = \alpha t \ , \tag{2.58}$$

as an exact solution of Equations (2.6) and (2.7), which satisfies the imposed requirement that the pressure be constant on the surface of the projected body (for elaboration on this point and demonstration that the same conclusion is reached by other lines of reasoning, see References 2.28, 2.69, 2.70, and 2.74).

To visualize the physical consequences of Equation (2.58) in the operation of a gun consider a column of gas and projectile being uniformly accelerated in a barrel by a piston, as sketched in Figure 2.23. The pressure in the first layer of gas at the base of the projectile, p_s , is constant, and dependent only on the acceleration, α , and the projectile mass, m_s , since $p_s A_s = m_s \alpha$. Similarly, at any other layer in the gas the pressure is also constant (a different constant), since that layer must accelerate the mass of gas and projectile ahead of it. Hence, along any given particle path the pressure will be constant. There will be no relative motion of the gas particles in one part of the flow with respect to any other part, so no expansion or compression waves will be generated. In the Lagrangian coordinate system, then, the flow is steady and there is no change in velocity with respect to distance. Velocity is a function of time only.

For an Eulerian coordinate system with its origin $x = 0$ fixed at the barrel entrance, and with $t = 0$ when $x = 0$, the projectile motion in the gun barrel is simply defined by

$$u_s = \alpha t = \frac{p_s A_s}{m_s}\, t \ , \tag{2.59}$$

and

$$x_s = \frac{\alpha t^2}{2} = \frac{p_s A_s t^2}{2m_s} = \frac{u_s^2}{2\alpha}. \tag{2.60}$$

The variation of enthalpy required for the constant base pressure solution is obtained by combining Equations (2.7) and (2.58) with the isentropic relation $dh = dp/\rho$, giving

$$h - h_s = \frac{\alpha^2 t^2}{2} - \alpha x \ , \tag{2.61}$$

where h_s is the initial enthalpy when $x = t = 0$, which is the enthalpy of the gas at the base of the projectile.

For an ideal gas subject to an isentropic process ($a^2 = \gamma p/\rho$ and $p\rho^{-\gamma} = $ constant) Equation (2.61) becomes:

$$a^2 = a_s^2 + \left(\frac{\gamma - 1}{2}\right)\alpha^2 t^2 - (\gamma - 1)\,\alpha x \ . \tag{2.62}$$

(This equation, also, was first given by Stanyukovich[2.80].) The expressions for pressure, density, and temperature are then easily obtained by use of the isentropic relations for an ideal gas:

$$\left(\frac{a}{a_s}\right)^2 = \left(\frac{p}{p_s}\right)^{(\gamma-1)/\gamma} = \left(\frac{\rho}{\rho_s}\right)^{\gamma-1} = \frac{T}{T_s} \ . \tag{2.63}$$

Thus,

$$\frac{p}{p_s} = \left[1 + \left(\frac{\gamma - 1}{a_s^2}\right)\left(\frac{\alpha^2 t^2}{2} - \alpha x\right)\right]^{\gamma/(\gamma-1)} \tag{2.64}$$

and

$$\frac{\rho}{\rho_s} = \left[1 + \left(\frac{\gamma - 1}{a_s^2}\right)\left(\frac{\alpha^2 t^2}{2} - \alpha x\right)\right]^{1/(\gamma-1)} . \tag{2.65}$$

In this form it is readily seen that the gas conditions at any point depend only on the constants p_s, a_s, α, and γ, and on the distance from the point of interest to the projectile base, $x_s - x$ (since $\frac{1}{2}\alpha^2 t^2 - \alpha x = \alpha(x_s - x)$). The gas conditions are invariant with time *at a prescribed distance from the projectile base*. This is illustrated in the sketch shown in Figure 2.24.

It is convenient to nondimensionalize Equations (2.62) to (2.65) by referring all the variables to the constant acceleration and the quantities at the base of the projectile. Thus,

$$\bar{p} = \frac{p}{p_s}, \quad \bar{\rho} = \frac{\rho}{\rho_s}, \quad \bar{T} = \frac{T}{T_s}, \quad \bar{a} = \frac{a}{a_s},$$

$$\bar{t} = \frac{\alpha t}{a_s}, \quad \bar{x} = \frac{\alpha x}{a_s^2}, \quad \bar{u} = \frac{u}{a_s} = \bar{t}. \tag{2.66}$$

Hence, Equations (2.62), (2.64), and (2.65) become:

$$\bar{a}^2 = \bar{T} = 1 + (\gamma - 1)\left(\frac{\bar{t}^2}{2} - \bar{x}\right), \tag{2.67}$$

$$\bar{p} = \left[1 + (\gamma - 1)\left(\frac{\bar{t}^2}{2} - \bar{x}\right)\right]^{\gamma/(\gamma-1)}. \tag{2.68}$$

and

$$\bar{\rho} = \left[1 + (\gamma - 1)\left(\frac{\bar{t}^2}{2} - \bar{x}\right)\right]^{1/(\gamma-1)}. \tag{2.69}$$

These, then, express the manner in which the gas properties must vary along the length of the gas column behind the projectile in order to maintain a constant pressure at the base of the projectile.

Using the subscript e to denote the conditions at the entrance to the gun barrel, that is, for the position in the barrel where $x = \bar{x} = 0$, the preceding equations become:

$$\bar{a}_e^2 = \bar{T}_e = 1 + \left(\frac{\gamma - 1}{2}\right)\bar{t}_e^2, \tag{2.70}$$

$$\bar{p}_e = \left[1 + \left(\frac{\gamma - 1}{2}\right)\bar{t}_e^2\right]^{\gamma/(\gamma-1)}, \tag{2.71}$$

$$\bar{\rho}_e = \left[1 + \left(\frac{\gamma - 1}{2}\right)\bar{t}_e^2\right]^{1/(\gamma-1)}. \tag{2.72}$$

These relationships are shown in Figure 2.25, for both hydrogen and helium. It is seen that the pressure, p_e, must increase, at an ever-increasing rate, as the projectile traverses the barrel. The total length of travel over which constant acceleration is possible, then, is limited by the maximum pressure that can be withstood by the barrel. To maximize this length the pressure ratio must be minimized. Since $\bar{t}_e = \alpha t_e / a_s$, increasing the sound speed of the gas at the projectile base will result in lower required pressures as a function of time, for the same α and γ. Also, in the limit as $\gamma \to 1$, $p_e = e^{\bar{t}_e^2/2}$, which indicates that for values of $\bar{t}_e$ up to approximately 2.1 the pressure ratio required is minimized by minimizing γ. The desirability of maximizing the sound speed and minimizing the specific heat ratio is thus the same conclusion indicated in the analysis of isentropic expansion of a gas from a fixed reservoir.

It is of interest now to examine the equations of the characteristic lines for the case of uniform acceleration flow. As shown in Section 2.3.2, Equations (2.6) and (2.7) can be rewritten in the form

$$\frac{\partial}{\partial t}(u \pm \sigma) + (u \pm a)\frac{\partial}{\partial x}(u \pm \sigma) = 0,$$

$$\begin{matrix} (2.11) \\ \text{and} \\ (2.12) \end{matrix}$$

where the Riemann invariants $u \pm \sigma$ are functions which remain constant along characteristic lines having slopes $dx/dt = u \pm a$, respectively. The equations for the characteristic lines, both for Eulerian and Lagrangian coordinate systems, have been derived and extensively discussed for uniform acceleration of ideal gases in References 2.28, 2.71, and 2.73. Herein, we will consider only the equations in the Eulerian coordinates.

Equations (2.58) and (2.62) give the relations for u and a:

$$u = \alpha t, \tag{2.58}$$

$$a^2 = a_s^2 + \left(\frac{\gamma - 1}{2}\right)a^2 t^2 - (\gamma - 1)\,\alpha x \ . \tag{2.62}$$

From Equations (2.24) and (2.25) of Section 2.3.2 we have:

$$u \pm \sigma = u \pm \frac{2a}{\gamma - 1} = \text{constant along a characteristic} \ . \tag{2.73}$$

Since $u = 0$ when $t = 0$ (Eq.(2.58)), letting $t = 0$ in Equation (2.62) provides the convenient parameter:

$$a_0^2 = a_s^2 - (\gamma - 1)\,\alpha x_0 \ . \tag{2.74}$$

(Note: a_0 is simply the local speed of sound at a point on any characteristic when $u = t = 0$ and $x = x_0$) . Thus,

$$x_0 = \frac{a_s^2 - a_0^2}{\alpha(\gamma - 1)} , \tag{2.75}$$

from Equation (2.74), is the x coordinate at which the characteristic line intersects the x-axis . Equation (2.73) can then be written as:

$$\frac{\gamma - 1}{2} u \pm a = \pm a_0 \ . \tag{2.76}$$

or

$$\left(\frac{\gamma - 1}{2} u \pm a_0\right)^2 = a^2 \ . \tag{2.77}$$

Substitution of Equations (2.58) and (2.62) in the equation (2.77), and nondimensionalizing the terms by Equations (2.66), gives

$$\bar{x} = \frac{\bar{t}^2}{2} - \frac{\gamma - 1}{4}\left[\left(\bar{t} \mp \frac{2\bar{a}_0}{\gamma - 1}\right)^2 - \frac{4}{(\gamma - 1)^2}\right] , \tag{2.78}$$

as the general expression for the net of characteristic lines (negative sign used for $u + a$ characteristic, positive sign for the $u - a$ characteristic). *All* the characteristic lines are *identical parabolas*, having their major axes parallel to the x-axis. The locus of their vertices is given by

$$\bar{t}_v^2 = \frac{2}{3 - \gamma}\left[1 - (\gamma - 1)\bar{x}_v\right] , \tag{2.79}$$

which is also a parabola. Since at the vertex of any characteristic line $d\bar{x}/d\bar{t} = 0 = u \pm a$, so $u = \mp a$ at this point, Equation (2.79) is the path along which the flow conditions are sonic. Thus, sonic conditions are attained at the projectile base (where $\bar{x} = \bar{t}^2/2$) when $\bar{t} = \bar{t}* = 1$ and at the barrel entrance ($\bar{x} = 0$) when $\bar{t}* = \sqrt{\{2/(3 - \gamma)\}}$.

Equation (2.73) might also be written as

$$\frac{\gamma - 1}{2} u \pm a = \frac{\gamma - 1}{2} u_s \pm a_s \ . \tag{2.80}$$

relating the characteristic lines to the point at which they meet the projectile path. Substitution of Equations (2.58), (2.62), and (2.66) as before, leads to the equations noted on the characteristics net shown in Figure 2.26. The segments of the characteristic lines of interest are most easily calculated from these equations, which are simply different forms of Equation (2.78).

Referring to Figure 2.26, it is evident that the $u - a$ characteristic lines intersect the $\bar{t}$-axis at a positive slope for $\bar{t} > \sqrt{\{2/(3 - \gamma)\}}$. Since $d\bar{x}/d\bar{t} = u - a$ on these lines, the positive slope indicates that $u > a$, or the flow velocity must become supersonic at the barrel entrance. Theoretically this is allowable for a constant diameter (unchambered) gun, but it cannot be realized physically in a gun having chamberage. In the latter case, the flow velocity at the entrance to the launch tube cannot exceed the sonic velocity, since the flow becomes "choked" by the area transition from reservoir to launch tube. Hence, the constant base pressure solution, presented in Figure 2.26, sometimes called the "similarity solution", applies for all values of time and distance only to the constant diameter (unchambered) gun.

2.4.5.2 Uniform Acceleration in Chambered Gun

For $\bar{t} < \sqrt{\{2/(3-\gamma)\}}$ the flow velocity at the barrel entrance is subsonic, and the reservoir conditions required to produce a constant-base-pressure flow are readily obtained by applying the quasi-steady continuity and energy equations (see Figure 2.27 for notation):

$$a_r^2 = \frac{\gamma - 1}{2} u_e^2 + a_e^2 . \tag{2.81}$$

or, nondimensionalized,

$$\bar{a}_r^2 = \frac{\gamma - 1}{2} \bar{u}_e^2 + \bar{a}_e^2 . \tag{2.82}$$

With $\bar{u}_e = \bar{t}_e$ from Equations (2.66) and $\bar{a}_e^2 = 1 + \frac{1}{2}(\gamma - 1)\bar{t}_e^2$ from Equation (2.70),

$$\bar{a}_r^2 = 1 + (\gamma - 1)\bar{t}_e^2 = \bar{T}_r . \tag{2.83}$$

Using the isentropic relations previously noted,

$$\bar{p}_r = \left[1 + (\gamma - 1)\bar{t}_e^2 \right]^{\gamma/(\gamma-1)} , \tag{2.84}$$

$$\bar{\rho}_r = \left[1 + (\gamma - 1)\bar{t}_e^2 \right]^{1/(\gamma-1)} . \tag{2.85}$$

Equations (2.83) to (2.85) then define the reservoir conditions required until sonic flow is reached at the barrel entrance, at which time

$$\bar{t}_e = \bar{t}_e^* = \sqrt{\left(\frac{2}{3 - \gamma} \right)}, \qquad \bar{p}_e^* = \left(\frac{2}{3 - \gamma} \right)^{\gamma/(\gamma-1)}$$

from Equation (2.71), and

$$\bar{p}_r^* = \left(\frac{\gamma + 1}{3 - \gamma} \right)^{\gamma/(\gamma-1)} ,$$

from Equation (2.83).

At this point it is of interest to define that $u - a$ characteristic line which has its vertex on the $\bar{t}$-axis, that is, with $\bar{x}_v = 0$. This line is known as the "limiting characteristic" of the similarity solution on which sonic flow is reached at the barrel entrance. Substituting $\bar{x} = 0$ and $\bar{t} = \sqrt{\{2/(3 - \gamma)\}}$ in Equation (2.78), one obtains $\bar{a}_0 = \sqrt{\{(3 - \gamma)/2\}}$. Using this value of $\bar{a}_0$ in Equation (2.78) then yields

$$\bar{x} = \frac{1}{2} \left[\sqrt{\left(\frac{3 - \gamma}{2} \right)} \bar{t} - 1 \right]^2 , \tag{2.86}$$

as the equation for the limiting characteristic. This is also shown in Figure 2.26.

Now for $\bar{t} > \sqrt{\{2/(3 - \gamma)\}}$, the flow velocity at the barrel entrance must remain sonic ($\bar{u}_e = \bar{a}_e = \bar{t}_e$); hence, in the region between $\bar{x} = 0$ and the limiting characteristic, the $u - a$ characteristics are no longer parabolas and must become tangent to the $\bar{t}$-axis , as shown in Figure 2.28. However, as shown in References 2.71 and 2.28, the paths of the $u + a$ characteristics in this region, along the segment $A - B$ in the sketch, may be assumed to be the same as those for an unchambered gun, at least in that portion of the region which can influence the conditions at the base of the projectile. (It has been verified by comparison with exact methods such as that of Reference 2.75 for $\gamma = 5/3$ (see also Reference 2.77) that this assumption results in negligible errors).

Again, along a $u + a$ characteristic, $u + \sigma$ is constant, so

$$u_e + \sigma_e = u_s + \sigma_s , \tag{2.87}$$

and thus for sonic flow at barrel entrance,

$$a_e + \frac{2}{\gamma - 1} a_e = \alpha t_s + \frac{2}{\gamma - 1} a_s , \tag{2.88}$$

or in nondimensional terms, using Equations (2.66),

$$\bar{a}_e^2 = \left[\frac{\gamma - 1}{\gamma + 1}\left(\bar{t}_s + \frac{2}{\gamma - 1}\right)\right]^2 .$$ (2.89)

The more general expression,

$$u + \sigma = u_s + \sigma_s ,$$ (2.90)

gives:

$$\frac{\gamma - 1}{2}\bar{u} + \bar{a} = \frac{\gamma - 1}{2}\bar{u}_s + 1 .$$ (2.91)

Then, from Equations (2.66) and (2.67),

$$\frac{\gamma - 1}{2}\bar{t} + \left[1 + \frac{\gamma - 1}{2}\left(\bar{t}^2 - 2\bar{x}\right)\right]^{1/2} = \frac{\gamma - 1}{2}\bar{t}_s + 1 .$$ (2.92)

At $\bar{x} = 0$, $\bar{t} = \bar{t}_e$, and the above equation becomes

$$\bar{t}_s = \bar{t}_e + \frac{2}{\gamma - 1}\left[\left(1 + \frac{\gamma - 1}{2}\bar{t}_e^2\right)^{1/2} - 1\right] .$$ (2.93)

Substitution of this equation into Equation (2.89) gives

$$\bar{a}_e^2 = \left\{\frac{2}{\gamma + 1}\left[\frac{\gamma - 1}{2}\bar{t}_e + \left(1 + \frac{\gamma - 1}{2}\bar{t}_e^2\right)^{1/2}\right]\right\}^2 = \bar{T}_e .$$ (2.94)

$$\bar{p}_e = \left\{\frac{2}{\gamma + 1}\left[\frac{\gamma - 1}{2}\bar{t}_e + \left(1 + \frac{\gamma - 1}{2}\bar{t}_e^2\right)^{1/2}\right]\right\}^{2\gamma/(\gamma - 1)} .$$ (2.95)

$$\bar{\rho}_e = \left\{\frac{2}{\gamma + 1}\left[\frac{\gamma - 1}{2}\bar{t}_e + \left(1 + \frac{\gamma - 1}{2}\bar{t}_e^2\right)^{1/2}\right]\right\}^{2/(\gamma - 1)} .$$ (2.96)

From Equation (2.82), with $\bar{u}_e = \bar{a}_e$,

$$\bar{a}_r^2 = \frac{\gamma + 1}{2}\bar{a}_e^2 .$$ (2.97)

so, from Equation (2.94),

$$\bar{a}_r^2 = \left\{\left[\frac{2}{\gamma + 1}\right]^{1/2}\left[\frac{\gamma - 1}{2}\bar{t}_e + \left(1 + \frac{\gamma - 1}{2}\bar{t}_e^2\right)^{1/2}\right]\right\}^2 = \bar{T}_r ,$$ (2.98)

$$\bar{p}_r = \left\{\left[\frac{2}{\gamma + 1}\right]^{1/2}\left[\frac{\gamma - 1}{2}\bar{t}_e + \left(1 + \frac{\gamma - 1}{2}\bar{t}_e^2\right)^{1/2}\right]\right\}^{2\gamma/(\gamma - 1)} ,$$ (2.99)

$$\bar{\rho}_r = \left\{\left[\frac{2}{\gamma + 1}\right]^{1/2}\left[\frac{\gamma - 1}{2}\bar{t}_e + \left(1 + \frac{\gamma - 1}{2}\bar{t}_e^2\right)^{1/2}\right]\right\}^{2/(\gamma - 1)} .$$ (2.100)

Equations (2.94 - 2.96) and (2.98 - 2.100) thus define the gas conditions required at the barrel entrance (sonic flow) and in the reservoir, as a function of time $(\bar{t}_e > \sqrt{2/(3 - \gamma)})$ at the barrel entrance, to produce a uniformly accelerated flow of an ideal gas in a chambered gun. The pressure-time histories, from Equations (2.71) and (2.95) for $\bar{p}_e$, and Equations (2.84) and (2.99) for $\bar{p}_r$, are shown in Figure 2.29 for both hydrogen and helium. The symbols on this figure indicate the time at which sonic flow is reached at the barrel entrance.

Comparison of Figures 2.25 and 2.29 indicates that the pressures required at the barrel entrance $(\bar{p}_e)$ of a chambered gun, due to the restriction to sonic flow at this point, are much higher, at times, $\bar{t}_e > \sqrt{2/(3 - \gamma)}$, than those for a gun with no chamberage.

2.4.6 Constant Base Pressure with Real-Gas Effects

All the solutions presented thus far have been based on the assumption that the gas is ideal and its properties can be related by the simple equation of state $pv = RT$ and the isentropic equation $pv^\gamma = $ constant. These equations adequately predict the behavior of the gas for a certain range of temperatures and densities, within which

there is no change in the number of particles constituting the gas or in the number of degrees of freedom of motion of the particles, and no significant intermolecular forces (either attractive or repulsive) acting between particles because of their proximity to one another. If, however, the process to which the propellant is subjected results in sufficiently high temperatures and/or densities as is usual in the operation of high performance light-gas guns, the foregoing conditions no longer exist; the gas no longer behaves in accordance with the ideal-gas relations, and is said to exhibit nonidealities or to act as a real gas. These effects must be taken into account to predict accurately the performance of a given gun. Unfortunately, little experimental knowledge exists of the actual state properties of hydrogen at these elevated temperatures and densities. However, a number of estimates have been made of the behavior of hydrogen gas at high densities, and the effect of this behavior on gun performance. Several of these will be discussed in the following paragraphs.

One state equation often used in considering real-gas effects is the Able-Noble, or "covolume", equation,

$$p(v - b) = RT , \qquad (2.101)$$

where the term b is a correction to the specific volume which accounts for the effective volume occupied by the gas molecules themselves, or in another sense, for the repulsive intermolecular forces occurring when the gas is at high densities. The Able-Noble equation is a reduced form of Van der Waal's equation of state

$$p = \frac{RT}{v - b} - \frac{a}{v^2} , \qquad (2.102)$$

with the term containing the intermolecular attractive-force constant "a" considered to be negligible. The relation between p and v along an isentrope for this gas is

$$p(v - b)^\gamma = \text{constant} , \qquad (2.103)$$

where the constant is a function only of the entropy. The sound speed is given by

$$a^2 = \frac{\gamma p v^2}{v - b} . \qquad (2.104)$$

Seigel[2.28] has compared the expansion of an Able-Noble gas with that of an ideal gas, in constant-diameter and chambered guns, for both infinite and finite reservoir lengths. It is shown that the expression for the acoustic impedance, as a function of p along an isentrope of an Able-Noble gas,

$$a\rho = \left[\frac{\gamma p_0^2}{RT_0} \left(\frac{p}{p_0} \right)^{(\gamma+1)/\gamma} \right]^{1/2} , \qquad (2.105)$$

is identical to that of the ideal gas, and hence, *in a constant-diameter gun*, the pressure-velocity histories for the expansion of the two gases will be identical, if started from the same initial temperature and pressure. There will be no difference in performance, even in guns having finite length reservoirs, so long as the ratio of propellant gas mass to projectile mass (G/m_s) is the same for both gases. The corresponding expressions for the densities as a function of pressure along the isentrope are not the same, however, for the two gases. For an ideal gas

$$\rho = \frac{p_0}{RT_0} \left(\frac{p}{p_0} \right)^{1/\gamma} , \qquad (2.106)$$

whereas for the Able-Noble gas

$$\rho = \frac{\dfrac{p_0}{RT_0} \left(\dfrac{p}{p_0} \right)^{1/\gamma}}{1 + \dfrac{b p_0}{RT_0} \left(\dfrac{p}{p_0} \right)^{1/\gamma}} . \qquad (2.107)$$

(Note: Equations (2.105) and (2.107) are easily derived from Equations (2.101), (2.103), and (2.104).) It is readily seen that, because of the covolume term b, the density as a function of pressure of the Able-Noble gas will be lower than that of the ideal gas for an expansion from the same initial conditions. As noted previously in Section 2.3.3.3, it is a low density as a function of pressure rather than a low acoustic impedance as a function of pressure which determines the relative merit of gases expanding through the transition section of a chambered gun. Hence, *in a chambered gun*, the pressure-velocity history of the expansion of an Able-Noble gas will be superior to that of the ideal gas. The performance of a chambered gun using a dense real gas in an effectively infinite-length reservoir will be better than that for an ideal gas, assuming both expansions proceed from the same initial conditions of pressure, temperature, and mass of gas.

Smith[2.70] applied the Able-Noble state and isentropic equations to the constant base pressure solution for a chambered gun. He observed that the sound speed of the Able-Noble gas is increased over that of the ideal gas when the molecular volume becomes significant (see Equation (2.104)), and hence that, when the initial propellant density is high, it is possible that sonic flow will not be attained at the barrel entrance for the real gas. His calculations show that in a chambered gun the real gas not only yields higher velocities, as compared to those produced using the same mass of ideal gas, but does so with lower required pressures in the reservoir and at the barrel entrance.

Another approximation for the behavior of dense real gases uses a semi-empirical entropic equation given below, which was first proposed by Seigel[2.81] as the following:

$$p^{(\beta-2)/\beta} (v - f) = k .$$ (2.108)

This equation has been fitted, in Reference 2.81, to match real-gas data for nitrogen and argon at high densities, and, in Reference 2.82, to match calculated data for real hydrogen at pressures up to 30.4 kilobars and temperatures up to 3500° K. The data of Reference 2.82 consists of an extrapolation of experimental data at lower densities obtained by Wooley, et al.[2.83]. This real gas data will be considered in some detail below. More recently calculations of hydrogen properties have been made by Baker, et al[2.84] using a Rowlinson equation of state which accounts for molecular volume and two body intermolecular forces. The results, given in tabular form for densities from 1 to 2000 amagats and temperatures from 500 to 3000° K, are reported to be in close agreement with that of Reference 2.82 except at the highest densities.

In the following analysis of the effects of a real gas on the constant base pressure solution the real gas relations of Reference 2.80 will be considered. The quantities β, f, and k in Equation (2.108) are constants along a given isentrope, but vary as the entropy is changed. It is convenient to nondimentionalize Equation (2.108) by referring the variables to the ambient condition $T_a = 300^\circ$ K and $p_a = 1.013$ bars . Thus,

$$\frac{p}{p_a}^{(\beta-2)/\beta} \left(\frac{v}{v_a} - \frac{f}{v_a}\right) = \frac{k}{p_a^{(\beta-2)/\beta} v_a} .$$ (2.109)

If p in the above equation is chosen as $p = p_{ro}$, the pressure in the gas when it is expanded isentropically to rest at a temperature of 300° K, then the complete real hydrogen gas behavior is defined as a function of entropy by the data of Figures 2.30 and 2.31. The resulting pressure-volume diagram is shown in Figure 2.32, and a comparison of the real- and ideal-gas isentropes is presented in Figure 2.33. It may be noted that for compression to a given final pressure a higher specific volume (with a correspondingly lower temperature) is realized with real hydrogen.

The following equations are easily derived for the relation between p and v given by Equation (2.108):

Sound speed

$$a^2 = \left(\frac{\partial p}{\partial \rho}\right)_s = \frac{\beta}{\beta - 2} p \frac{v^2}{v^2 - f} ,$$ (2.110)

Enthalpy

$$h - h_s = \int_{p_s}^{p} \left(\frac{dp}{\rho}\right)_s = \frac{\beta}{2} kp^{2/\beta} + fp - \left[\frac{\beta}{2} kp_s^{2/\beta} + fp_s\right],$$ (2.111)

Riemann function

$$\sigma = \int_{0}^{p} \left(\frac{dp}{\rho a}\right)_s = \{k\beta(\beta - 2)\}^{\frac{1}{2}} p^{1/\beta} ,$$ (2.112)

So

$$\frac{\sigma}{\sigma_s} = \left(\frac{p}{p_s}\right)^{1/\beta} .$$ (2.113)

The foregoing equations have been applied to the constant base pressure solution (previously discussed in Section 2.4.5) in References 2.78 and 2.79. The derivation proceeds in the same manner as that shown for the ideal gas, hence, it will only be outlined here. Because of the change in the state equation, it is convenient to nondimensionalize some of the terms in a different fashion. Except for the following, the notation and non-dimensional forms are as used previously for the ideal gas:

$$\bar{x} = \frac{p_s A_s}{m_s c_s^2} x$$

$$\bar{t} = \frac{p_s A_s}{m_s c_s} t \qquad \text{where} \quad c_s = \frac{(\beta - 2)a_s}{F + 1}$$

$$\bar{u} = \frac{u}{c_s}, \qquad \bar{a} = \frac{a}{c_s} \qquad \text{and} \qquad F = \frac{f}{v_a - f} . \tag{2.114}$$

For the real gas,

$$h_e - h_s = \frac{c_s \bar{t}_e^2}{2} . \tag{2.115}$$

and, with

$$\bar{u}_e = \bar{u}_e^\star = \bar{a}_e^\star = \bar{t}_e^\star . \tag{2.116}$$

when sonic conditions are attained at the barrel entrance, the equations providing the corresponding pressure and time are:

$$\bar{p}_e^{\star 2/\beta} \left[\bar{p}_e^{\star 2/\beta} - 1 + \frac{2F}{\beta} (\bar{p}_e^\star - 1) \right] = \frac{1}{\beta - 2} \left(F\bar{p}_e^\star + \bar{p}_e^{\star 2/\beta} \right)^2 . \tag{2.117}$$

$$\bar{t}_e^\star = \frac{1}{\beta - 2} \bar{p}_e^{\star - 1/\beta} \left(F\bar{p}_e^\star + \bar{p}_e^{\star 2/\beta} \right) . \tag{2.118}$$

Note that $\bar{p}_e^\star$ and $\bar{t}_e^\star$ are functions of β and F, which depend on the entropy of the gas at the initial conditions. The manner in which $\bar{p}_e^\star$ and $\bar{t}_e^\star$ vary with projectile base pressure, for various initial reservoir pressures (p_{r_0} is also a function of entropy, Figure 2.30), is shown in Figure 2.34. The effects of the real gas are quite startling. Whereas $\bar{p}_e^\star$ and $\bar{t}_e^\star$ are constant values depending on γ for an ideal gas ($\bar{p}_e^\star = 2.18$, $\bar{t}_e^\star = 0.224$ for $\gamma = 1.4$), it is seen that for many combinations of initial reservoir pressure and projectile base pressure the constant base pressure solution for real hydrogen gas indicates that sonic conditions may be attained at the barrel entrance at two different pressures and times. This implies that in a constant diameter gun the flow at the barrel entrance may first accelerate to sonic conditions at one value of $\bar{p}_e^\star$ and $\bar{t}_e^\star$, then continue to accelerate to supersonic velocities, and because of the manner in which the sound speed varies, the flow subsequently reaches a *different* sonic condition at another value of $\bar{p}_e^\star$ and $\bar{t}_e^\star$. Moreover, for some values of initial reservoir pressure there is a maximum value of projectile base pressure which will produce sonic conditions at the barrel entrance. For any base pressure greater than this maximum, at these initial reservoir pressures, the flow at the barrel entrance will remain subsonic at all times, and thus can be completely defined, even for a chambered gun, by the "similarity" solution $u = at$.

The general equation for the characteristic lines for the real hydrogen gas, constant-base-pressure solution is

$$\bar{x} = \frac{\bar{t}^2}{2} - \frac{1}{\beta(\beta - 2)} \left\{ \frac{\beta}{2} \left[(C \mp \bar{t})^2 - 1 \right] + F \left[(C \mp \bar{t})^\beta - 1 \right] \right\}, \tag{2.119}$$

where C is a constant, but a different value for each characteristic. As in the ideal-gas solution, this relationship applies at all times in the constant diameter gun, and at times less than $\bar{t}_e^\star$ in the chambered gun. Bixler and Seigel[2.79] have calculated the characteristic diagrams for flow in the constant diameter gun; these are compared with the ideal-gas solution in Figure 2.35. Again the real-gas effects produce startling results. The lines on which $u - \sigma$ is a constant, and $dx/dt = u - a$, in particular, are greatly changed in comparison with the ideal-gas characteristics, reversing direction twice and ultimately proceeding in a direction opposite to that for the ideal-gas characteristics. In accord with the discussion of the previous paragraph, there are two $u - a$ characteristics in Figure 2.35(b) having tangency points with the $\bar{x} = 0$ axis, corresponding to the two conditions for sonic flow at the barrel entrance when the initial reservoir pressure and projectile base pressure are appropriate. Similarly, as shown in Figure 2.35(c), when the base pressure exceeds that maximum value required to produce sonic flow at the barrel entrance for a given initial entropy, the $u - a$ lines have no tangency point along $\bar{x} = 0$ and all cross the $\bar{x}$-axis at a negative slope. Thus the flow at the barrel entrance in the latter case is subsonic at all times.

The equation for the real-hydrogen-gas pressure at the entrance to the barrel as a function of time, when the flow is not limited to sonic speed as for a constant diameter gun, is derived as

$$\bar{t}_e = \left\{ \frac{2}{\beta(\beta - 2)} \left[\frac{\beta}{2} \left(\bar{p}_e^{2/\beta} - 1 \right) + F \left(\bar{p}_e - 1 \right) \right] \right\}^{1/2} . \tag{2.120}$$

For the chambered gun, in which sonic conditions at the barrel entrance are a necessary restriction, the same assumption is made regarding the path of the $u + a$ characteristics as was made in the ideal-gas solution; namely, that they are the same, leading to the $\bar{p}_e - \bar{t}_e$ history for the real gas given by

$$\frac{\beta(\beta - 2)}{2}\,\bar{t}_e^2 \;=\; \frac{\beta}{2}\left[(\bar{t}_o - \bar{t}_e + 1)^2 - 1\right] + F\left[(\bar{t}_o - \bar{t}_e + 1)^\beta - 1\right], \tag{2.121}$$

where

$$\bar{t}_o \;=\; \frac{\bar{p}_e^{\,1/\beta}}{\beta - 2}\left(1 + F\bar{p}_e^{\,(\beta-2)/\beta}\right) + \bar{p}_e^{\,1/\beta} - 1 \;. \tag{2.122}$$

Similarly, consideration of the equations governing the expansion of the gas from the reservoir to barrel entrance leads to the following expressions for the required reservoir pressure as a function of time:

for the constant diameter gun,

$$\bar{t}_e \;=\; \left\{\frac{1}{\beta(\beta - 2)}\left[\frac{\beta}{2}\,(\bar{p}_r^{\,2/\beta} - 1) + F(\bar{p}_r - 1)\right]\right\}^{1/2}, \tag{2.123}$$

and for the chambered gun,

$$\frac{\beta}{2}\,\bar{p}_r^{\,2/\beta} + F\bar{p}_r \;=\; \frac{\beta}{2}\,\bar{p}_e^{\,2/\beta} + F\bar{p}_e + \frac{\beta}{2(\beta - 2)}\,\frac{(\bar{p}_e^{\,2/\beta} + F\bar{p}_e)^2}{\bar{p}_e^{\,2/\beta}}\;. \tag{2.124}$$

which must be solved in conjunction with Equations (2.121) and (2.122).

The foregoing equations have been solved by Bixler and Seigel for two values of projectile base pressure, 1.38 and 3.45 kilobars, over a range of initial reservoir pressure, and are compared with the ideal-gas solution in Figure 2.36. The effect of the real gas is to substantially reduce the differences between the pressure-histories required for the unchambered and chambered guns, both for $\bar{p}_e$ and $\bar{p}_r$. With increasing initial reservoir pressure (decreasing entropy) and model base pressure the solutions for the unchambered and chambered guns become, for all practical purposes, the same.

2.4.7 Piston Motion Required by Constant Base Pressure Solution

Having established in the preceding sections the required variation of pressure, density, and velocity with time (both at the entrance to the barrel and in the reservoir) for the constant base pressure solution, it is of interest to determine the pump piston motion necessary to satisfy these requirements. It should be noted that the constant-base-pressure solution does not consider the events occurring prior to the start of projectile motion at $t = 0$; it is assumed that the uniformly accelerated flow commences at time zero, with the desired gas conditions existant at the projectile base. This means that the gas conditions in the reservoir must also initially correspond to the desired base pressure conditions, requiring some form of compression or heating prior to this time. With the foregoing in mind, one may readily write the following relationships for piston motion for the ideal-gas case:

$$\begin{pmatrix}\text{Mass of gas}\\ \text{remaining in}\\ \text{reservoir at}\\ \text{time } t_e\end{pmatrix} = \begin{pmatrix}\text{Mass of gas}\\ \text{initially loaded}\\ \text{in reservoir}\end{pmatrix} - \begin{pmatrix}\text{Mass of gas}\\ \text{which was entered}\\ \text{barrel at}\\ \text{time } t_e\end{pmatrix}$$

or

$$\rho_r x_p A_r \;=\; \rho_s\,L_r A_r - \int_0^{t_e} \rho_e u_e A_s\,dt_e\;. \tag{2.125}$$

from which

$$\frac{x_p}{L_r} \;=\; \frac{\rho_s}{\rho_r}\left[1 - \frac{\displaystyle\int_0^{t_e} \rho_e u_e\,dt_e}{\rho_s\,\dfrac{A_r}{A_s}\,L_r}\right]. \tag{2.126}$$

where x_p is the distance between the front face of the piston and the end of the reservoir (or barrel entrance). Again nondimensionalizing terms, with

$$\bar{x}_p = \frac{p_s A_s x_p}{m_s a_s^2}, \qquad \bar{L}_r = \frac{p_s A_s L_r}{m_s a_s^2}, \qquad \bar{t}_e = \frac{p_s A_s}{m_s a_s} t_e,$$

$$\bar{\rho}_e = \frac{\rho_e}{\rho_s}, \qquad \bar{u}_e = \frac{u_e}{a_s}, \qquad \bar{A}_r = \frac{A_r}{A_s}. \tag{2.127}$$

So

$$\frac{\rho_s}{\rho_r} = \left(\frac{p_r}{p_s}\right)^{-1/\gamma} = \bar{p}_r^{-1/\gamma}, \tag{2.128}$$

and

$$\int_0^{t_e} \rho_e u_e dt_e = \frac{\gamma m_s}{A_s} \int_0^{\bar{t}_e} \bar{\rho}_e \bar{u}_e d\bar{t}_e, \tag{2.129}$$

and

$$\rho_s L_1 = \frac{\gamma m_s}{A_s} \bar{L}_r. \tag{2.130}$$

Hence, Equation (2.126) becomes:

$$\frac{\bar{x}_p}{\bar{L}_r} = \bar{p}_r^{-1/\gamma}\left[1 - \frac{\int_0^{\bar{t}_e} \bar{\rho}_e \bar{u}_e d\bar{t}_e}{\bar{A}_r \bar{L}_r}\right]. \tag{2.131}$$

where

$$\bar{A}_r \bar{L}_r = \frac{G}{\gamma m_s} = V_{r_0} = \text{dimensionless initial reservoir volume (See Equation (2.52)).} \tag{2.132}$$

When $\bar{x}_p$ becomes 0, all of the gas in the reservoir will have entered the barrel; hence

$$V_{r_0} = \int_0^{\bar{t}_{ef}} \bar{\rho}_e \bar{u}_e d\bar{t}_e = \int_0^{\bar{t}_e^\star} \bar{\rho}_e \bar{u}_e d\bar{t}_e + \int_{\bar{t}_e^\star}^{\bar{t}_{ef}} \bar{\rho}_e \bar{u}_e d\bar{t}_e. \tag{2.133}$$

where the first integral is for the subsonic portion of flow and the last integral is for sonic conditions at barrel entrance. That is:

For $0 < \bar{t}_e < \bar{t}_e^\star$, the flow at the barrel entrance is subsonic; so $\bar{u}_e = \bar{t}_e$, and $\bar{\rho}_e$ is given by Equation (2.72).

For $\bar{t}_e^\star < \bar{t}_e < \bar{t}_{ef}$, the flow at the barrel entrance is sonic; so $\bar{u}_e = \bar{a}_e$ and is given by Equation (2.94), and $\bar{\rho}_e$ is given by Equation (2.96).

Also, $\mathtt{U}_s$ is related to $\bar{t}_{ef}$ by Equation (2.93):

$$\mathtt{U}_s = \bar{t}_s = \bar{t}_{ef} + \frac{2}{\gamma - 1}\left[\left(1 + \frac{\gamma - 1}{2} \bar{t}_{ef}^2\right)^{1/2} - 1\right]. \tag{2.134}$$

Hence, Equation (2.133) becomes

$$V_{r_0} = \int_0^{\bar{t}_e^\star} \left[1 + \frac{\gamma-1}{2} \bar{t}_e^2\right]^{1/(\gamma-1)} \bar{t}_e d\bar{t}_e + \int_{\bar{t}_e^\star}^{\bar{t}_{ef}} \left\{\frac{2}{\gamma+1}\left[\frac{\gamma-1}{2} \bar{t}_e + \left(1 + \frac{\gamma-1}{2} \bar{t}_e^2\right)^{1/2}\right]\right\}^{(\gamma+1)/(\gamma-1)} d\bar{t}_e. \tag{2.135}$$

Equation (2.131) must also be evaluated in two steps, using $\bar{p}_r$ given by Equation (2.84) when $0 < \bar{t}_e < \bar{t}_e^\star$, or Equation (2.99) when $\bar{t}_e^\star < \bar{t}_e < \bar{t}_{ef}$. Thus, for $0 < \bar{t}_e < \bar{t}_e^\star$,

$$\frac{x_p}{L_r} = \left[1 + (\gamma - 1) \bar{t}_e^2\right]^{-1/(\gamma-1)}\left\{1 - \frac{1}{V_{r_0}} \int_0^{\bar{t}_e} \left[1 + \frac{\gamma-1}{2} \bar{t}_e^2\right]^{1/(\gamma-1)} \bar{t}_e d\bar{t}_e\right\}. \tag{2.136}$$

and for $\bar{t}_e^\star < \bar{t}_e < \bar{t}_{ef}$,

$$\frac{\bar{x}_p}{\bar{L}_r} = \left\{ \left[\frac{2}{\gamma+1} \right]^{1/2} \left[\frac{\gamma-1}{2} \bar{t}_e + \left(1 + \frac{\gamma-1}{2} \bar{t}_e^2 \right)^{1/2} \right] \right\}^{-2/(\gamma-1)} \left(1 - \frac{1}{\bar{V}_{r_0}} \int_0^{\bar{t}_e^*} \left[1 + \frac{\gamma-1}{2} \bar{t}_e^2 \right]^{1/(\gamma-1)} \bar{t}_e d\bar{t}_e \right.$$

$$\left. - \frac{1}{\bar{V}_{r_0}} \int_{\bar{t}_e^*}^{\bar{t}_e} \left\{ \frac{2}{\gamma+1} \left[\frac{\gamma-1}{2} \bar{t}_e + \left(1 + \frac{\gamma-1}{2} \bar{t}_e^2 \right)^{1/2} \right] \right\}^{(\gamma+1)/(\gamma-1)} d\bar{t}_e \right). \qquad (2.137)$$

The pump-piston velocity-time history may then be obtained by differentiating Equations (2.136) and (2.137); that is,

$$\bar{u}_p = \frac{d\bar{x}_p}{d\bar{t}_e}. \qquad (2.138)$$

The authors are not aware that a complete solution of the above equations has yet appeared in the literature. Wilenius et al.[2.71] have presented an approximate solution in which only the first term of Equation (2.135) is integrated with $\bar{t}_{ef}$ as the upper limit, to obtain $\bar{V}_{r_0}$, and only Equation (2.136) is solved (again with $\bar{t}_{ef}$ as the upper limit in the integral) to obtain the piston motion. From this the approximate base-pressure time history required for the pump piston was calculated using the relation

$$\bar{p}_b = \bar{p}_r - \frac{\bar{m}_p}{\bar{A}_r^2} \frac{d\bar{u}_p}{d\bar{t}_e}. \qquad (2.139)$$

While these are only approximate solutions, they are useful in illustrating qualitatively the following points concerning the achievement of a constant base pressure cycle of operation:

(1) In order that the base pressure be constant at the very beginning, the motion of the pump piston and projectile must commence simultaneously with both piston and projectile initially at rest. (This may be seen by differentiating Equation (2.136).)

(2) For an ideal gas, the maximum piston velocity is proportional to projectile velocity and is inversely dependent on the chamberage. When low chamberage ratios are used (e.g., less than diameter ratios of approximately 4), the maximum piston velocities become a very large fraction of the reservoir sound speed.

(3) Setting $\bar{x}_p = 0$ when all the reservoir gas has passed through the launch tube entrance (as assumed in the preceding derivation), requires that the pump piston have some final velocity (also strongly dependent on the chamberage) when it reaches the end of the reservoir.

(4) The base pressures required to drive the piston so as to produce the required piston motion are very high, almost as high as the reservoir pressure during the final stages of compression.

The preceding derivation of the piston motion has been shown, for simplicity, only for the ideal-gas case. A similar derivation can be made for the real-hydrogen-gas case, employing the relationships presented in Section 2.4.6. Although the magnitude of the piston velocities, accelerations, and base pressures would undoubtedly be different for the real- and ideal-gas cases, it is expected that the foregoing qualitative conclusions would remain unchanged.

It is apparent from the above requirements that constant-base-pressure flow cannot be precisely achieved but can only be approximated in the conventional two-stage free-piston gun. Smith's analysis[2.70] shows this quite clearly. He treats the mass-flow and reservoir-pressure requirements separately, and considers both the ideal gas and real (Able-Noble) hydrogen-gas cases. It is shown that matching of the mass-flow and pressure requirements in the later stages of the compression might be achieved by adjusting the mass of gas under compression. This can be accomplished in two ways, both of which start with an excess of gas in the reservoir. Either controlled leakage of some of the excess gas may be provided through bursting diaphragms in the reservoir or piston, or, portions of the excess gas may be progressively isolated (e.g., through ports which are subsequently covered by the piston) so as to remove it from the compression process. (This latter technique has also been studied by Winkler[2.74] in his analysis of the constant-base-pressure process.) However, in all cases shown by Smith, some mismatch between the mass-flow and pressure requirements must be accepted at the beginning of the launching cycle, even with later control of the gas mass.

In actual firings of present two-stage isentropic guns the ratios of maximum model base pressure to that pressure required for uniform acceleration (constant base pressure) to achieve the same velocity are frequently less than two when the guns are operated at conditions somewhat below maximum performance levels. However, at conditions used to obtain nearly maximum velocities this ratio may increase to values greater than five. The manner in which the individual variables can be adjusted to approach or approximate the constant-base-pressure process in conventional two-stage isentropic-compression guns is discussed more completely in Section 2.5.

2.4.8 General Computing Methods

Although the constant-base-pressure analyses may be applied to the selection of gun geometry and operating conditions in an effort to approach this desirable mode of operation, these analyses cannot be used to predict

actual gun performance when conditions deviate from the ideal, as is usually the case. Some general solution is necessary to predict performance over a wide range of gun geometries and loading conditions. A number of approximate methods have been developed (see, for example, References 2.19 and 2.28) which involve the numerical solution of a set of simultaneous equations using only a desk calculator. Predicted velocities compare well with experimental results at modest levels of performance, but these methods are limited to relatively low-performance levels and do not give necessary detailed information such as pressure histories. More accurate methods have been developed in which the nonlinear ordinary and partial differential equations of motion are numerically integrated by a high-speed digital computer.

Solutions may be readily obtained in this manner by writing the general equations in finite-difference form. The numerical scheme most widely used is based on the "q" method developed by von Neumann-Richtmyer (References 2.38 and 2.85). The quasi-one-dimensional hydrodynamic equations, valid within limits for changes in cross-sectional area, are most generally written in Lagrangian coordinates. The gun is divided into regions which may consist of the first-stage driver gas, piston, propellant gas, and model, each having a different equation of state. Each region is divided into a number of cells and mass points; the accuracy of this method is dependent, in part, on the number of cells chosen. The solution consists of numerical integration of the fluid dynamic equations over small intervals of time to determine the changes in pressure, density, internal energy, and velocity in each cell resulting from the influence of adjacent cells. The motion of these fluid elements and mass points, calculated with Newton's equation of motion, is determined by the pressure difference between adjacent cells. Stability requirements for the finite difference terms are given in Reference 2.85. An artificial viscosity term q (from which the "q" method derives its name) is added to the pressure term in the conservation equations and has the effect of spreading out the discontinuity at a shock wave to make the calculated variables continuous through the shock. An important feature of this method is that the presence and position of any shocks are known at each time interval and the overall effects of any shocks on the resulting performance are accounted for.

Equations for a two-stage gun analysis using the "q" method in Lagrangian coordinates are described by Piacesi, et al.[2.86] and Baer and Smith[2.87]. With numerical solutions of this type a real-gas equation of state can be used for the propellant gas, and estimates of the effects of friction and heat losses may also be readily included. A real-gas equation of state is used in Reference 2.78, which also includes calculations of friction and heat-transfer losses from an ideal gas to the gun walls. The "q" method computer program developed at the Naval Ordnance Laboratory has also been modified at Arnold Engineering and Development Center to include the effects of real gas, boundary layers, heat transfer, and piston friction. As shown in Reference 2.88, this program gives good results in comparison with experimental measurements. A numerical solution with equations written in Eulerian coordinates has been developed by Badhwar and Murphy[2.89, 2.90], with finite-differencing techniques given by Longley[2.91].

Digital machine programs have also been developed for analysis of the general two-stage gun problem using the method of characteristics. This method is readily adaptable to numerical solution with a digital computer for the case of isentropic flow of an ideal gas with friction and heat-transfer losses neglected. The use of this technique at Ames Research Center has provided results with good accuracy for isentropic-compression guns at velocities up to approximately 7.5 km/s. At higher levels of performance this particular program is inadequate, as are other methods which do not consider real-gas effects and losses.

When strong shocks must be considered, the method of characteristics becomes considerably more complex, although solutions can be obtained with the use of a third characteristic direction representing particle paths along which the entropy is constant (see Reference 2.27). A solution which might be adapted to the two-stage gun to handle shock waves is given in Reference 2.92.

2.5 ACTUAL GUN PERFORMANCE AND OPERATION

To aid in understanding the complex flow processes that occur during the operation of a light-gas gun so that performance can be optimized, it is expedient to explore, in a systematic manner, the many variables that influence performance. Virtually every ballistic-range laboratory has developed theoretical methods for this purpose. In most cases, the theories are based on ideal-gas relations and do not consider the various loss mechanisms such as fluid friction and heat transfer. These theories satisfactorily predict model velocities over a rather wide range of operating conditions, but, as the higher levels of performance are approached, where gas densities and temperatures rise to high values, the disparity between theory and the performance actually obtained becomes increasingly great. In some cases the results obtained experimentally actually contradict these theoretical predictions. To predict performance adequately under these conditions, real-gas effects and losses must be considered. More comprehensive theoretical treatments are being developed (see, for example, Seigel et al.[2.78] and Cable and DeWitt[2.88]) but, because of the complexity of the viscous flow processes and the lack of experimental data on the properties of hydrogen at high densities and temperatures, uncertainties exist which must be assessed experimentally.

Although extensive experimental studies have been made to determine the actual capabilities of light-gas guns, it would be an exceedingly ambitious task to attempt to optimize conditions experimentally for a wide range of velocities and model weights because of the interrelated effects of the large number of variables in gun geometry and loading conditions. These experimental studies have been of great value, however, in revealing, at the least, the basic trends of changes in variables, especially where the validity of theoretical predictions is uncertain. These efforts are aimed at obtaining a better understanding of the gas dynamics to aid in the final development of accurate computational methods.

A portion of the results of a systematic experimental study is presented in the following sections to illustrate the manner in which individual changes in the variables influence performance. The effects of changes in loading conditions for a two-stage isentropic-compression gun are given in Section 2.5.2 and changes in gun geometry are discussed in Section 2.5.3. The types of experimental measurements frequently made to determine gun performance are mentioned briefly in the following section.

2.5.1 Experimental Measurements

Measurements of maximum pressures generated in the first-stage driver gas are generally made to insure that the strength capabilities of the chamber are not exceeded. If gunpowder is used in the first stage, a time history of the chamber pressure is desirable to make certain that proper burning of the charge takes place. Pressure measurements are made most frequently with commercially available piezo-electric gages or with ballistic strain gages (for an example of the latter, see Reference 2.93).

Piston velocity, a primary factor in gun performance, is measured by means of simple wire probes inserted into the pump-tube bore at several positions along the length of the pump tube. A time measurement is obtained with electronic chronographs, as the electric probes are shorted by passage of the piston. Piston velocities given with the experimental data in the subsequent sections were obtained at a point somewhat before the start of the transition section, where the piston is near its peak velocity.

A time-resolved measurement of the reservoir gas pressure made at the point where the pressure becomes a maximum provides very important information for interior ballistic studies. Unfortunately this measurement is difficult to make with the use of standard gaging techniques without substantially reducing the strength of the gun in this critical area. Location of a pressure gage in the launch tube near the breech provides a convenient alternate position. The experimental data presented here do not include this measurement.

Perhaps the most meaningful diagnostic information is that obtained by measuring the position-time history of the projectile as it is being accelerated through the launch tube. This can be accomplished with a microwave reflectometer (see Chapter 10). With this information one can deduce the model acceleration-time history and thus obtain the resultant driving force acting on the model. If the friction between model and the wall of the barrel is neglected (a reasonable assumption for the plastic projectiles used) and if the barrel ahead of the model is evacuated, we then have a measure of the gas pressure acting on the model base throughout its travel in the barrel. One can then attempt to optimize loading conditions toward a constant base pressure. The measured base pressure history also provides additional important data with which to evaluate theoretical predictions. Comparison of measured muzzle velocities obtained in flight after launch with computed velocities is not sufficient to determine the accuracy of a theory. The final velocity is an integrated parameter of driving pressure and distance, and even though the calculated muzzle velocity may compare well with that measured, the pressure history (including maximum pressure) may be quite different. The model base pressure data presented in the following section were obtained by this microwave reflectometer technique as outlined in Reference 2.94.

Velocities are measured along the model trajectory from the muzzle of the gun. Most frequently this velocity is obtained by the standard techniques employing spark photography to measure distance and electronic chronographs to measure time (Chapter 6). To obtain an accurate value of muzzle velocity it is frequently necessary to account for the deceleration of the model occurring between the muzzle and the measurement stations.

Because of its ready accessibility to the authors, much of the experimental information presented herein was obtained with the Ames 7.1-, 25.4-, and 38.1-mm-bore-diameter guns, which are representative of the deformable-piston isentropic-compression gun. The dimensions of these guns, given in Table 2.2, are not considered to be optimum but are presented as examples of existing guns.

2.5.2 Effect of Loading Conditions

For any particular gun of fixed geometry the operating parameters or loading conditions that may be adjusted to achieve a desired velocity include:

1. Initial gas conditions
2. Piston velocity
3. Model release pressure
4. Piston mass
5. Model mass.

Large changes can be made in these conditions in various combinations to give the same velocity. However, the optimum condition that one would strive for is that of minimizing the maximum model base pressures to obtain the most uniform base pressure history possible and at the same time maintain gas reservoir pressures that are within the strength capabilities of the gun. Optimizing in this manner allows us, then, to test with a variety of models having the broadest range of strengths.

The reservoir pressure-time requirement for uniform base pressure is depicted by the dashed curve in Figure 2.37. A time history of reservoir pressure and base pressure representing conditions during firing is shown to indicate the manner in which these conditions might deviate from the desired conditions. (In this example, the effects of pressure gradients in the reservoir are neglected and thus the curves are a smoothed representation

of that actually encountered). The reservoir pressure depicted rises isentropically until it reaches the value at which the diaphragm ruptures, resulting in the start of model motion. For the case shown, the rate of rise of pressure (referred to as the pumping rate) is initially greater than the required ideal, with the result that the model base pressure then rises above that necessary for uniform acceleration. During the latter stages of compression, reservoir pressure drops rapidly as the piston decelerates to rest. However, this sudden decrease in pressure does not influence the model base pressure until later, because of the finite transmission speed of the expansion wave through the barrel. Thus the reservoir pressure need not be sustained for the full launch time.

The ideal pressure history shown applies for a particular model weight, but nondimensional similarity relationships can be used to account for changes in model weight. For uniform acceleration to the same velocity, an increase in model weight requires, with the same launch tube, a proportionate increase in base pressure, p_s, and model release pressure, p_R. From the constant-base-pressure equations (Section 2.4.5) it can be seen that an increase in base pressure necessitates a corresponding increase in reservoir pressure, p_r. By changing the initial loading pressure p_{r_0} (or gas mass G), in direct proportion, the pressure ratio p_r/p_{r_0} remains constant so that with ideal isentropic compression the same gas temperatures and sound speeds are maintained. With equal values of p_r/p_{r_0} the pressure rise time during launch will remain the same (as it must for equal acceleration to the same final velocity) if piston velocity is unchanged. Finally, the required adjustment in energy to compress the propellant gas is obtained by varying piston mass in direct proportion to gas mass. Ideally, then, the following similarity relationships can be used with a given gun to account for changes in model weight:

$$
\left.
\begin{array}{c}
\text{For equal } U \text{ with } \alpha = \text{constant} \\[4pt]
p_s,\ p_R,\ p_{r_0},\ G,\ m_p \sim m_s \text{ with} \\[4pt]
u_p \text{ unchanged.}
\end{array}
\right\}
\qquad (2.140)
$$

Real-gas effects encountered at high pressures, where sound speed is strongly influenced by density, will limit the region over which these relations apply. Further, the useful range of applicability is restricted because of the pressure limitations of both gun and model; for this reason a pump of fixed dimensions cannot be designed to achieve high performance over a wide range of model weights and strengths. If maximum performance is desired at relatively high model weights, the compressor size will, within limits, be made larger (to increase compression ratio) so that the gun can be operated more effectively at higher gas temperatures and sound speeds, within the given pressure restrictions.

The effects of variations in the gun-loading conditions are discussed in the following sections. It should be noted that the selection of the range of variables in the experimental data presented were made on the basis of other considerations and not specifically to test the validity of the similarity relationship for model weight noted above.

2.5.2.1 Initial Gas Conditions

When the choice is made of the propellant gas to be used, the ratio of specific heats, γ, and the molecular weight, $\bar{m}$, are therefore specified, leaving two remaining gas variables to be adjusted; the gas mass, G, and the initial temperature, T_{r_0}. At this point we will consider only the effect of G (or p_{r_0}) and T_{r_0} will be taken to be ambient. The question of increasing the initial temperature by heating the gas prior to compression will be discussed in Section 2.5.2.6.

Rather than examining the complete set of equations for general gun performance, it is helpful, in understanding the way in which the initial gas pressure (and other variables) influences the subsequent reservoir-pressure history, to consider the simplified case of isentropic compression in a constant-diameter closed-end pump tube. For a piston traveling at velocity u_p with initial reservoir volume V_{r_0} one can obtain, using the isentropic relations for pressure and volume, the following expression for the time rate of change of pressure:

$$
\frac{dp}{dt} = \frac{\gamma A u_p}{V_{r_0}} \left(\frac{p}{p_{r_0}}\right)^{1/\gamma} p \,. \qquad (2.141)
$$

This expression is at least indicative of the rate of pressure rise existing in the initial phases of the launch cycle when the total model motion is small and when the mismatch between desired and actual reservoir pressure for constant-base-pressure flow tends to be greatest. From this equation it is seen that the pumping rate at a particular value of p and u_p is inversely proportional to $p_{r_0}^{1/\gamma}$; an increase in p_{r_0} by a factor of 2 decreases dp/dt by a factor of 0.61 for a γ of 1.4. The rate of rise of pressure is also a function of p, rising more rapidly as the pressure level increases, as shown in Figure 2.38.

The effect of initial loading pressure, p_{r_0}, on the resultant base pressure, p_s, experienced by a model during launch is seen in Figure 2.39. Base pressures were measured during firings of the Ames Research Center 7.1 mm/39 mm gun (7.1 mm-bore launch tube and 39 mm-bore pump tube). Except for initial pressure, the loading conditions are nearly the same for both cases. The higher base pressures developed with the low gas loading result in a higher model velocity, but the difference in velocity cannot be attributed entirely to the fact that the pumping rate is increased with a lower p_{r_0}. Another primary factor is that the effective compression ratio is increased by decreasing p_{r_0} resulting in higher gas temperatures which can also serve to increase performance.

The variation of the maximum base pressures developed with changes in initial loading pressure (using hydrogen), obtained for two model weights from firings of the Ames 7.1 mm/39 mm gun, is shown in Figure 2.40. The 0.16 and 0.65 gram models are, for this bore diameter, equivalent to plastic(polycarbonate) cylinders 1/2 and 2 calibers long respectively. Piston mass, m_p, was held constant at 200 grams and diaphragm rupture (model release) pressure, p_R, at 690 bars. For constant values of piston velocity of 625 and 750 m/s it is seen that the maximum base pressures rise substantially as p_{r_o} is decreased, in accord with the increased pumping rate attendant with a decrease in p_{r_o}. This effect is much greater for the heavy model. With these test conditions, the maximum base pressures occurred shortly after diaphragm rupture when the model had moved only a short distance. The greater inertia of the heavy model results in a slower initial movement and because the pumping rate is high (particularly with low p_{r_o}) the base pressure rises to high values before a significant volume is opened behind the model.

The muzzle velocities achieved under these conditions are shown in Figure 2.41. It is seen again that the higher pressures and temperatures developed by reducing p_{r_o} result in increased model velocities. The rate of rise of velocity decreases as one approaches the lower tolerable limit of p_{r_o}, where the mass of gas becomes insufficient to maintain substantial base pressures for extended distances of model travel. As pointed out previously, the mass of gas required to supply constant base pressure is proportional to the model mass, so that higher initial loading pressures are required with increased model weight.

By cross-plotting the original data we obtain the variation of $p_{s_{max}}$ with p_{r_o} for a constant model velocity of 8 km/s with the light model and 6 km/s with the heavy model, as shown in Figure 2.42. Within the limits shown here one can reduce $p_{s_{max}}$ and yet achieve the same velocity by increasing p_{r_o} (u_p is increased simultaneously to maintain constant velocity).

Reservoir pressure histories were not measured during this test series, but to indicate the relation of maximum reservoir pressure, $p_{r_{max}}$, with changes in p_{r_o}, calculated values are presented in Figure 2.43. A reduction in p_{r_o} at constant piston mass and velocity produces an increase in $p_{r_{max}}$ in a manner similar to that seen for maximum base pressure $p_{s_{max}}$.

2.5.2.2 *Piston Velocity*

Piston velocity has a strong influence on the subsequent model base pressure history. The rate of rise of reservoir pressure is essentially a direct function of piston velocity (Eq.(2.141)) in the early stages of projectile motion when the mass-flow into the barrel is small.

Within limits, any desired piston velocity can be attained at one specified point in the compression cycle by proper selection of the powder charge. For example, the piston can be accelerated to the velocity required to give the desired pumping rate at the start of the model motion. There is, however, little control over the subsequent velocity history, except that the rate at which the piston decelerates during the latter part of compression may be varied by changing piston mass. In practice, as seen in Section 2.4.7, the piston velocity history cannot be matched to that required for constant base pressure for the full compression period. The actual velocity used, then, is that which will give the best overall match with the desired conditions.

The manner in which piston velocity influences the muzzle velocity attained is shown in Figures 2.44 and 2.45, for model weights of 0.16 and 0.65 gram, respectively. In this particular gun, piston velocity is determined at a position 1.5 m from the start of the transition section so that, depending upon the model release pressure, the piston will have decelerated somewhat before the start of the launching cycle. To examine the separate effects of changes in loading conditions, model release pressure and piston mass were held constant for both model weights, although the optimum requirements for each weight are necessarily different. Gas-loading pressure is presented as an independent variable and is expressed both in bars and as a ratio of gas-mass to model-mass, G/m_s. The latter is a classical nondimensional parameter of interest (see Section 2.3.3.3) – dependent upon the conditions desired, the required mass of gas is a function of the model mass and is useful in comparing guns of different sizes and configurations. The range of G/m_s (for ambient conditions) shown for the light model, Figure 2.44, is typical for this gun type but the same range was not covered for the heavy model. In this case piston mass, held constant for both model weights, was too low to provide the required energy for interest at the higher values of G/m_s. It is seen from both figures that, in general, model velocity increases rapidly with increasing piston velocity, along lines of constant p_{r_o}, but the rate of increase tapers off as u_p is raised. A combination of factors (which will be discussed in greater detail in following sections) may contribute to the gradual decrease in the slope of the U verses u_p curves at both high and low values of p_{r_o}; for example, as piston speed is increased to higher performance conditions, contamination of the propellant from erosion as well as other losses attendant with higher temperatures become increasingly significant (particularly at low values of p_{r_o}); at the lowest values of p_{r_o} there may be insufficient gas to provide substantial base pressures for an appreciable distance in the barrel; higher shock pressures generated as piston speed is increased may result in premature release of the model (this effect will be greater at high p_{r_o} and will have a larger influence on the velocity of the lighter model).

Maximum base pressures, $p_{s_{max}}$, measured for the test series shown in Figures 2.44 and 2.45, are correspondingly presented in Figures 2.46 and 2.47. Along lines of constant loading pressure the rate of rise of base pressure increases with increasing piston velocity. This effect is especially pronounced with the heavy model. For the test conditions and gun used, at high piston velocities the heavy model has moved, typically, less than 20 calibers at the time maximum base pressure is reached, indicating that the initial pumping rate at the start of the launch is much too high for these models.

When we add to Figures 2.46 and 2.47 the model velocities obtained for these conditions, in the form of lines of constant velocity, we obtain a most revealing picture. Within the limits of the test, the maximum base pressures are reduced by increasing, simultaneously, initial loading pressure and piston velocity. It is interesting to note that the model velocity can be maintained by moving in this direction even though the gas temperatures are steadily decreasing as p_{r_0} is increased. This may result, partly, from real-gas effects; that is, the reduction in sound speed with decreasing temperature may be partially offset by an increase in sound speed with increasing gas density at higher pressures (see Section 2.5.2.6). Secondly, the stronger shock waves produced with increasing piston velocity will enhance gas temperatures and pressures, although for these test conditions the shocks do not appear to produce a harmful rise in base pressure along the lines of constant model velocity.

In Figures 2.48 and 2.49 these data are plotted to show more clearly the variation of maximum base pressure with model velocity, for curves of constant p_{r_0}.

Shown in Figure 2.50 are two examples of the base-pressure time histories obtained using the microwave reflectometer, compared with corresponding theoretical calculations by the method of characteristics for an ideal gas. The curves in the upper portion of the figure represent the base pressure history of a 7.5-gm model accelerated to 7.63 km/s with a low value of initial pressure and piston speed in the Ames 25.4mm/102mm launcher. The improved pressure history shown in the lower portion of the figure resulted when the initial pressure and piston speed were both increased to obtain approximately the same model velocity, 7.32 km/s.

Calculated values of maximum reservoir pressure and the maximum pressure exerted by the piston on the wall of a 16^0-taper (included angle) transition section are given in Figure 2.51 as a function of piston velocity for several values of initial gas pressure, p_{r_0}. At the lowest piston velocities the maximum gas pressures are somewhat larger than the piston deformation pressures but the piston pressure becomes dominant at the higher piston velocities. With high initial gas loadings both gas and piston pressures are relatively low. At low loading pressures the reduced mass of gas has a smaller retarding effect on the piston so that the decelerating forces between the piston and the tapered wall rise rapidly, and at high piston velocities become much greater than the gas pressure. As will be seen later, the piston deformation forces can be reduced by decreasing the transition taper angle below the relatively high taper angle of this example.

2.5.2.3 Model Release Pressure

An additional important control over the model base pressure history is provided by varying the point in the compression cycle at which the model is released. This point is controlled by regulating the opening pressure of the valve isolating the pump from the model – in most cases this valve is simply a scored diaphragm and the pressure at which it ruptures is termed here, the model release pressure. Varying the release pressure changes not only the initial pressure felt by the model but the subsequent pressure history as well. From Equation (2.141) or Figure 2.38 it is seen that a reduction in release pressure results in a lower pumping rate at the start of model motion. The high base pressures experienced in the initial launching stage by the relatively heavy models (shown in Figure 2.47), which resulted from a pumping rate that was much greater than necessary to match the requirements for the initial motion of these heavy models, could thus be reduced by a reduction in model release pressure.

As stated previously, the reservoir and base pressures do not vary in the relatively smooth manner depicted in Figure 2.37. Instead, compression and expansion waves, generated by acceleration and deceleration of the piston, create pressure and velocity gradients which perturb the pressure curve predicted for isentropic compression. Strong shock waves generated at high piston speeds produce pressure gradients large enough to substantially change the time at which the diaphragm ruptures. The variation of reservoir pressure with time during compression, for a typical case, is shown in Figure 2.52. If the release pressure chosen was that occurring at time t_2 it is seen that a shock reaching the diaphragm at time t_1 would cause premature release of the model. Thus, the arrival of a shock at the diaphragm, of sufficient strength to cause diaphragm rupture, when the pumping rate is lower than desired, might then substantially affect the model base pressure and resultant velocity.

The effect of release pressure on the model base pressure history is shown in Figure 2.53 for two firings of the Ames 25.4mm/102mm gun. Release pressure was varied from 1.38 to 0.69 kilobars, with other loading conditions held constant. It can be seen that, even though the velocities obtained were approximately the same, a much more favorable base pressure history is obtained with the lower release pressure. In both cases base pressures rise very soon after start of model motion to substantially higher pressures than the release pressure, indicating that the pumping rate is greater than that required to match the model motion during the initial period of model travel.

The results of firings made with the 7.1mm/39mm gun to determine the influence of release pressure on the maximum base pressures developed for a wider variety of conditions are shown in Figure 2.54. The shots at the lowest value of rupture pressure were made without the use of a diaphragm. Some initial frictional restraint of the model, estimated to be of the order of 50 to 100 bars, was provided by making the models 0.2 to 0.3 mm larger than the bore diameter. A substantial decrease in maximum base pressure is generally noted with a decrease in rupture pressure. The data point for the 0.32 gram model at 0.3 kilobars showing a contrary trend is thought to be (for unexplained reasons) an unusual result peculiar to this particular shot and not representative of a normal round under these conditions.

The model velocities obtained for this test series are given in Figure 2.55. Except for one set of conditions with a light model, there is a surprisingly small variation in velocity over the full range of release pressures. The substantial loss in velocity incurred with decreasing release pressure with the 0.16 gram model and the lighter

piston is attributed to the following factors: the initial pressure, p_{r_o}, of 1.52 bars is relatively high for this light model in comparison with the other examples shown, resulting in a comparatively low pumping rate at the start. Movement of the model is too great during the initial stages to receive full benefit of the higher reservoir pressures eventually developed. (However, it is seen from Figure 2.54 that the peak pressures developed were very low). The low piston mass also resulted in more rapid piston deceleration. When p_{r_o} is lowered to 0.52 bars and piston mass increased to 200 grams, the variation in model velocity with rupture pressure becomes small. The heavy model test series resulted in essentially no change in model velocity. In this case, the initia acceleration of the higher inertia model is low enough so that the model travel is relatively small during the time that is required to reach an effectively high pumping rate. Within reasonable limits, then, the model velocity is relatively insensitive to changes in the timing of the diaphragm burst.

A final comparison of the effect of release pressure on normalized base pressure is given in Figure 2.56. Here, the base pressures presented in Figure 2.54 are normalized by dividing by the calculated effective constant base pressure necessary to achieve the measured velocities given in Figure 2.55. This ratio serves as a figure of merit for a particular firing, indicating how closely base pressure conditions approach the ideal, $p_{s_{max}}/p_{s_{avg}} = 1$. The advantage obtained by operating at relatively low release pressures for the loading conditions used in these tests is clearly evident. Although an appreciable reduction in velocity occurred with the light model at $p_{r_o} = 1.52$ bars, when release pressure was reduced to the minimum test value (see Figure 2.55), this firing approached most closely the desired constant base pressure conditions. In this case, as well as most of the other shots, lowering the release pressure resulted in a reduction in maximum base pressure that was proportionately greater than the reduction in velocity.

Operating with relatively low release pressures provides an effective means of reducing the high base pressures occurring in the early stages of model motion that result from a pumping rate that is too high to match the initial starting requirements. It should be noted, however, that for very light models which allow high initial pumping rates and models capable of withstanding high maximum pressures, the highest velocities are obtained with relatively high release pressures.

2.5.2.4 Piston Mass

In the type of gun under discussion, with the usual loading conditions, the piston reaches its maximum velocity prior to the start of the launching cycle. The first-stage driver gas, used to accelerate the piston, has by this time expanded to a low pressure and does not significantly contribute additional energy to the piston. Thus the major portion of the energy required to compress the propellant gas is supplied by the piston kinetic energy. The piston velocity, however, is specified by the pumping rate required to give the desired base pressure and so piston mass becomes an important variable in making up the energy requirement. Piston velocity must be reasonably matched to the pumping requirements during the early stages of model motion to limit a large initial pressure over-ride. Piston mass becomes an important factor in the later stages of compression in that it determines the rate at which the piston decelerates. A heavy piston maintains a higher pumping rate toward the end of the compression stroke, serving to maintain higher base pressures in the later stages of model travel. This effect can be seen in Figure 2.57, which shows the base pressure histories recorded during two launches with different piston masses. The less rapid deceleration of the heavier piston produces higher reservoir pressures which result, in this case, in higher base pressures throughout most of the launch. It should be noted that the 150 gram piston is comparatively light for the test conditions so that doubling piston mass in this case has a greater effect on the final velocity than would occur if the weights were closer to the optimum values.

The variation of model velocity with piston mass is presented in Figure 2.58 for several different launch conditions. With an initial pressure of 0.50 bars and a piston speed of 600 m/s a gain in muzzle velocity of 12% is realized for the 0.16 gram model when piston mass is increased from 150 to 300 grams. A further increase in mass shows no additional benefits. For the same change in piston mass but with an initial pressure of 1.52 bars and a piston velocity of 700 m/s a gain of approximately 40% in model velocity is realized for the 0.65 gram model. The larger increase in velocity obtained with the heavy model occurs because the 150 grams piston is farther from optimum conditions for this model than it is for the light model. The increased energy necessary to launch the heavy model with a greater gas mass requires a corresponding boost in piston mass. There is insufficient data to ascertain the optimum value of piston mass for these conditions but it appears that the primary gain has already been realized.

The curve identified by the square symbols, in Figure 2.58, is the result of a series of firings with the 0.16 gram model, made with powder charge mass held constant. Thus, as piston mass is increased, the piston velocity decreases, but the kinetic energy remains approximately constant. Actually, the resultant kinetic energy increased by 14% for the 250 gm piston and by 19% for the 350 gm piston. Even so, a continual loss in velocity occurred as piston mass was increased. The higher velocity realized with the 150 gram piston was obtained at the expense of greater maximum pressures (see Figure 2.59). It is seen in Figure 2.60 that a piston mass of 250 to 300 grams for the constant powder mass case gives the minimum ratio of maximum to average pressure. For the light model with constant piston velocity no improvement in normalized base pressure is shown by increasing piston mass above 150 grams.

The calculated effect of piston mass on the reservoir pressure and the pressure exerted by the piston on the tapered walls in decelerating to rest is shown as a function of piston velocity in Figure 2.61, for constant p_{r_o} 0.76 bars and m_s 0.76 gm. It should be noted that the transition-section taper angle for these data is 8 7 degrees — in contrast to the similar calculations for a 16-degree-taper transition section given in Figure 2.51 for the effect of initial loading pressure. Comparison of these two figures at the common condition of p_{r_o} 0 76 bars and m_p 200 gm shows that the maximum pressures generated are appreciably higher for the shorter (16°) taper section, particularly so for the piston deceleration pressures.

2.5.2.5 Model Mass

It has been seen in a number of the foregoing discussions that variations in model mass have a significant effect on model performance. For example, the change in model velocity and base pressure occurring with two different model weights over a limited range of initial gas pressures was given in Figures 2.40 and 2.42. The effect of varying piston velocity for several model weights, while holding p_{r_0} constant is shown in Figures 2.62 to 2.64. One can see that, at a particular set of loading conditions, increasing model mass results in higher reservoir and base pressures with reduced velocities.

To achieve *equal velocities* with models of different mass (in a particular gun) by maintaining the same acceleration history requires that the model base pressure be increased in direct proportion to the increase in model mass. According to the similarity relations (Eq. 2.140) discussed in the introduction to Section 2.5.2 this may be accomplished by a proportionate increase in release pressure, reservoir pressure, gas mass, and piston mass (with piston velocity history remaining the same). Unfortunately, the range of velocity and model mass over which these relations can be used may be quite restricted because of limitations in the tolerable model and reservoir pressures; or, interestingly, it can be stated in another way that, as the desired velocity is increased, the range of model mass over which constant base pressure conditions can be approximated becomes increasingly small.

In the operation of a conventional two-stage gun, the result is that with models of equal strength large deviations from the ideal are experienced at a lower velocity with the heavier model. Under these conditions, the above similarity relations cannot be used and the loading conditions must be, in effect, optimized for each model weight and velocity. In an effort to obtain high velocities with the high inertia models, the tendency frequently is to use loading conditions which result, initially, in a much greater pumping rate than that needed to match the required mass flow into the barrel at the start of model motion. In this situation, a reduction in model release pressure (contrary to that suggested by the similarity relations) provides a very effective method of lowering the initial pumping rate so that the base pressures at the start of launch can be kept within the strength of the model. Moreover, as seen in Section 2.5.3, reducing release pressure will not, for a relatively heavy model, result in a significant loss in velocity.

As mentioned previously, the experimental data given in this chapter are presented to indicate the manner in which individual changes in loading conditions influence performance, but the parameters have not been varied over the range required to optimize conditions for the spectrum of model weights and strengths normally encountered in ballistic-range tests. However, assuming that conditions are optimized, the best that can be achieved with models of *equal pressure capability*, as model weight is increased, is a reduction in velocity proportional to the square root of the increased mass. Unfortunately, the loss in velocity realized with models of increased weight may frequently be substantially greater than this, for in many tests, the heavier models tend to be complex configurations with less pressure capability than the simpler, lighter configurations.

To illustrate the relationship between velocity and model mass currently being achieved with light-gas guns, typical performance data from a number of laboratories in the United States, Canada, and England are given in Figure 2.65. Information from the VKF-Arnold Engineering Development Center has not been included because of internal security restrictions. Model velocity is plotted as a function of model mass, but to compare results of different size guns, the mass is divided by D_s^3. These velocities are representative of those being achieved at the present time with a large assortment of models of widely varying strengths in a variety of guns having considerably different geometries. The velocities do not necessarily represent the optimum or maximum capabilities of each launcher. However, the envelope of the maximum velocities attained for various model weights illustrates how velocity is sacrificed as model weight is increased. It should be noted that, if one is concerned with achieving a high model kinetic energy rather than high velocity, model energy is increased with increasing weight; the kinetic energy of the heaviest model shown, for $m_s/D_s^3 = 4.0$ gm/cm^3 at 4.18 km/s, is 40 times that of the lightest model, with $m_s/D_s^3 = 0.26$ gm/cm^3 at 11.29 km/s.

The lowest mass model (0.26 gm/D_s^3) which achieved the highest velocity was a polyethylene plastic (specific gravity 0.95) cyclinder approximately 1/3-caliber long, about the minimum practical length that can be successfully launched. With lengths below 1/3 caliber, problems of attitude stability and gas leakage past the model during launch are enountered. Thus, further reductions in model weight to achieve higher velocities with comparable driving pressures can only be made with the use of lower-density materials having the necessary dynamic strength. (See Chapter 3 for further discussion of model materials). Often test requirements dictate the use of a high-density material such as steel, or tungsten, as a portion of the model, and in this case the relative launch weight may be reduced by making the test model small in relation to the bore size (termed a sub-caliber model) so that the weight of the sabot, constructed of appreciably lighter material, constitutes a large fraction of the total projectile weight. This requires the use of a larger bore gun, but may be necessary to achieve the desired velocity.

2.5.2.6 Propellant Gas Temperature

It was seen in the ideal equations presented in Section 2.3 (e.g., Equations (2.21) and (2.22)) that increasing the sound speed by increasing temperature will produce a gain in velocity. As has been stated previously, high temperatures can be achieved by using large volume pump tubes to obtain a high compression ratio. Other methods considered by many laboratories have been those of preheating the gas in some manner prior to compression or by increasing temperatures by chemical or electrical means during compression. The ideal equations show that the maximum gas temperature will be doubled if the initial temperature before compression is doubled. Numerous calculations have been made (see, e.g., References 2.63, 2.76, and 2.95 to 2.97) indicating that large gains in

velocity can be achieved by additional heating, but experimental tests made to verify these calculations have resulted in little or no gains. Stephenson and Anderson[2.96] report a 9% increase from 8.38 to 9.15 km/s when T_{r_0} was doubled. Swift and Baker[2.98], in conducting an extensive series of tests with several methods of heating, noted small gains in velocity when operating at moderate performance levels, but found essentially no increase in velocity with an increase in T_{r_0} from 290° to 1000° K when firing at higher levels of performance. Cable[2.47] reports no gain in velocity with preheating to 425° K. Berggren and Mitvalsky conducted a series of tests at Ames (unpublished) with similar results; in these tests the pump tube of a high-compression-ratio isentropic-compression gun was raised to 700° K by ohmic heating. A comprehensive parametric study was made to optimize conditions in an effort to increase the maximum performance. The results, however, produced no increase in velocity, and in many cases a degradation in performance was noted.

There may be a number of factors contributing to these disappointing results. Losses by heat transfer to the walls, for one, increase with temperature and result in increasing disparity between ideal calculated performance and that actually achieved, as temperature is raised; but this could be only partly responsible for the above results in that essentially no gain in velocity was noted. Serious erosion of the bore surfaces was noted with preheating in the Ames tests and it is thought that the resulting contamination of the propellant by metallic vapors, causing an increase in molecular weight, may have degraded performance. A most significant factor may be related to real-gas effects. For example, the influence of high gas density on the sound speed may override the effects of high temperature.

The real-gas temperatures produced during the later stages of compression in a light-gas gun are considerably below those computed for an ideal gas at comparable pressures. However, at these high pressures, strong intermolecular repulsive forces in the real gas serve to reduce the gas density, and this effect offsets the reduced temperature so that a net increase in the speed of sound is realized. Calculations were made using Seigel's semi-empirical entropic relation, Equation (2.108), for which the speed of sound is given by Equation (2.110). The results of these calculations, Figure 2.66, made for realistic gun conditions, show that: (1) the sound speed increases with increasing pressure faster than for the ideal case, and (2) the speed of sound increases more slowly, as the initial temperature of the gas is raised, than is predicted from ideal-gas behavior. In fact, if the real-gas curves in Figure 2.66 are extrapolated to higher pressures, they may actually cross over, resulting in a reduction of sound speed with increasing initial temperature. Such a "reversal" has been predicted by Swift and Baker[2.98] using a somewhat different real-gas model and occurred at a significantly lower pressure than an extrapolation of Figure 2.66 might predict.

The question of the effect of high temperatures at high densities in light-gas-gun operation can only be estimated at this point and will not be resolved until an experimentally verified equation of state is available. The discrepancy between the ideal predicted performance and that obtained experimentally with preheating serves, however, to point out the necessity of accounting for losses and real-gas effects in calculating performance.

2.5.2.7 Powder Charge

The quantity of gun powder used is that necessary to accelerate the piston of given mass to the desired velocity at a specified point in the compression cycle. If piston velocity is measured near this point, the relation between powder charge and velocity can be easily determined experimentally. An estimate of the powder pressure, p_c, developed during burning may be obtained with the following relation for a closed chamber (see Reference 2.13):

$$p_c V_c = m_c RT , \qquad (2.142)$$

where m_c is powder charge mass and V_c is powder chamber volume. Powder burns at essentially constant temperature with the result that RT, for any particular powder, remains nearly constant. Depending on the ratio of the charge mass to chamber volume, typical values of RT for a nitrocellulose gun powder may vary from 5 to 11 kilobars cm^3/gm (the low values result when charge mass is small in relation to chamber volume). Equation (2.142) is valid if a relatively fast-burning powder is used so that burning is completed before the piston moves an appreciable distance. A fast powder may not always be desirable, however. To minimize peak powder pressures in a gun having a relatively small powder chamber volume it may be necessary to use a powder that burns more slowly and continues to burn as the piston moves, opening up additional volume. Maximum accelerations of the piston may thus be reduced by a slow-burning powder, minimizing the formation of shocks in the propellant gas ahead of the piston. Further considerations relating to the calculation of chamber-powder pressures and the powder-charge geometry are discussed in Section 2.5.3.5.

2.5.3 Effect Of Gun Geometry

The interrelation of the many variables of changing gun geometry and loading conditions on the resulting internal gas dynamics makes it difficult to pinpoint an optimum gun configuration — one which produces the desired launch velocities with the lowest resultant pressures. Further, a particular gun may be near optimum only for a limited range of model weights, and so, in many cases, the gun configuration chosen for general laboratory use to launch a large variety of models is at best a compromise.

Parametric studies made thus far have not been sufficiently broad in scope to enable one to select an optimum design. Theoretical parametric studies of the effect of gun geometry, which have been helpful in revealing trends, have been made using the ideal-gas relations (see, e.g., Reference 2.99). However, because of the uncertain effects of the various losses and gas non-idealities at high temperature and density, in the following discussion of gun geometry we will rely as much as possible on experimental evidence obtained with existing guns.

Geometries representative of the two-stage guns in present use at a number of laboratories are given in Table 2.2 along with the velocities obtained for the typical loading conditions listed. Model velocities achieved with these guns were also plotted in Figure 2.65. Gun dimensions listed in Table 2.2 are defined in Figure 2.67. It is most interesting to note the extreme variance in the geometries of these guns. This is due, in part, to the differing test requirements of the various laboratories. However, there are also large differences in the relatively high-performance guns which have achieved velocities near the envelope of the curve of Figure 2.65. From the wide range in initial gas pressures and piston speeds shown in Table 2.2, one can deduce that there are considerable differences in the extent of shock heating; some guns operate with nearly isentropic compression while others, in varying degrees, approach the shock compression mode of operation.

2.5.3.1 Launch-Tube Size

Since the launch-tube bore diameter chosen establishes the overall size of the gun and its cost, this diameter is generally made no larger than necessary to fulfill the anticipated test requirements for model size. To obtain maximum velocities, the launch-tube length is determined, not by considerations of the maximum length over which a reasonable base pressure can be maintained constant, but instead, is made longer to take advantage of further expansion of the gas to low values. The point at which the driver gas expands to such a low value that its force no longer exceeds those due to bore friction and pressure ahead of the model depends on the pumping capabilities and loading conditions. A practical maximum length for existing guns has been determined by experience to be in the range of 300 to 400 calibers. The results of a test series performed at Ames Research Center (unpublished) with a 5.6-mm-bore launch tube and 45-mm diameter by 6.7-meters-long pump tube are shown in Figure 2.68. Of the four lengths tested, the highest velocities were obtained with a barrel 325 calibers long. These tests were conducted with loading conditions held constant at values normally used with a shorter barrel. To properly define a maximum limit, however, the loading conditions should be optimized for each launch tube length, requiring an increase in gas mass and piston energy as the length is extended. It is expected that, had this been done in this test series, the maximum velocity may have shifted to somewhat longer barrel lengths. Microwave reflectometer measurements of models during launch in the Ames 7.1-mm gun, which has a launch tube length of 357 calibers, show that in some cases the model is still accelerating, although at a low rate, as it reaches the muzzle. Thus, a longer length would give a slight increase in velocity. However, only a small percentage increase in velocity is obtained beyond lengths of approximately 250 calibers; barrels longer than this may not be warranted in instances where maximum velocities are not required.

2.5.3.2 Pump-Tube Volume

The ideal-gas relations show that for a specified mass of gas, increasing pump-tube volume to obtain an increase in compression ratio will result, without limit, in continually higher temperatures and sound speeds and, therefore, higher model velocities. However, as seen in Section 2.4.6, the reservoir requirements are changed when a real gas is considered. Because of the large intermolecular repulsive forces at high densities, the real gas has a higher enthalpy than the ideal gas when expanded from the same temperatures and pressures. The required temperatures and pressures calculated for a real gas are lower than for the ideal case, to maintain the same base pressure. An indication of the effect of this on the required pump-tube volume can be seen in Figure 2.69, taken from Reference 2.78. Model velocities are calculated for an ideal and real hydrogen gas as a function of pump-tube length. The results are presented for a 20-mm-bore launch tube, 6.86 m long, and a 102-mm-diameter pump tube. Maximum reservoir pressure was limited to 17.25 kilobars. With relatively short pump-tube lengths, substantially higher velocities are predicted for the real gas. A particularly significant result is that the rate of gain in velocity diminishes as length is increased for the real-gas case, and that at longer lengths little benefit is derived from increasing length.

There is substantial experimental evidence to show that pump-tube length (or volume) cannot be increased indefinitely to obtain further gains in velocity. Several examples to support this, as well as instances where an increase in pump-tube volume improved performance, are discussed below – with launcher dimensions listed in succeeding tabulations. (It should be noted that the ratio V_r/V_s, given in these tabulations, is a useful guide in comparing the relative reservoir volume of guns of different scale but its value becomes distorted and less meaningful when comparing guns having appreciably different launch-tube lengths (in terms of calibers); in practice, relatively small changes in performance result with changes in L_s/D_s for values greater than approximately 200.)

Launcher	D_s (mm)	D_r (mm)	L_r (m)	D_r/D_s	L_s/D_s	V_r/V_s
I_a	5.6	32.5	12.2	5.82	273	269
I_b	5.6	32.5	6.1	5.82	273	135
I_c	5.6	32.5	3.74	5.82	273	83
II_a	5.6	45.0	6.7	8.04	264	296
II_b	5.6	45.0	4.19	8.04	264	185

The 5.6mm/32.5mm isentropic-compression gun, listed as Launcher I_a, was constructed at Ames with an exceptionally large volume pump tube (12.2 m long) in an effort to obtain high performance. With this pump, a mass of gas five times the weight of 1/2-caliber-long plastic model required an initial loading pressure of 0.52 bars. Although extreme temperatures were developed during compression, as evidenced by the substantial erosion that

occurred during each firing, the launch velocities obtained were no higher than those achieved with several other lower-compression-ratio guns at the laboratory. To reduce the intolerably high erosion, the pump-tube length was decreased to 6.1 m (listed as Launcher I_b), then finally to 3.74 m (Launcher I_c). An appreciable reduction in erosion was noted with each decrease in length. (The temperatures calculated for isentropic compression of a perfect gas to 13.8 kilobars from an initial pressure of 0.52 bars in the 12.2-m tube, and for the same mass of gas in the 3.74-m tube, are 5400° K and 3920° K, respectively). In spite of the large reduction in temperature, there was no discernible decrease in the velocities attained; in fact, the 3.74-m configuration has produced, with a light (0.045 gm) model, the highest velocity (11.3 km/s) yet achieved with a conventional two-stage light-gas gun. Because of the serious erosion encountered with the longest pump tube, it is reasoned that the inability to obtain higher performance with this configuration may be due, at least in part, to greater contamination of the hydrogen by the vaporized or molten metallic particles.

A 5.6mm/45mm gun at Ames (Launcher II_a), having a pump tube 6.7 m long, was also modified by shortening the pump to 4.19 m (Launcher II_b). The maximum velocities obtained after modification, with the light models generally used, are at least as high under comparable conditions as those achieved with the longer pump. It should be noted that although the compression ratio for Launcher II_a was somewhat greater than that for I_a, the erosion occurring at the entrance to the launch tube was much less severe for II_a (not sufficient to present a significant operational problem) than for I_a. Reasons for this difference, which may be attributable to a difference in chambrage, are discussed in Section 2.5.3.3.

Both guns I_a and II_a appear to be, however, beyond the limit for which an increase in pump-tube volume will produce an increase in performance at the model masses of interest. Yet, with appreciably smaller volume pumps, experience has shown that an improvement in performance is obtained with an increase in reservoir volume. For example, a 5.6-mm gun at Ames gave an increase in velocity from 7.3 to 8.5 km/s for a particular saboted model configuration when the pump-tube-volume ratio (V_r/V_s) was increased from 58 (Launcher III_a) to 98 (Launcher III_b).

Launcher	D_s (mm)	D_r (mm)	L_r (m)	D_r/D_s	L_s/D_s	V_r/V_s
III_a	5.6	20	5.54	3.58	218	58
III_b	5.6	32.5	3.51	5.68	218	98
IV_a	6.35	25.4	1.52	4.00	200	19
IV_b	6.35	25.4	6.1	4.00	200	77
V_a	7.1	39.3	10.7	5.53	357	129
V_b	7.1	39.3	5.8	5.53	357	70

It should be noted that for Launcher III, volume was increased by an increase in chambrage and a decrease in pump-tube length. RARDE reported a gain in performance (Reference 2.47) with a 6.35mm/25.4mm gun when the pump tube-volume ratio (V_r/V_s) was increased from 19 to 77 by quadrupling pump length (Launchers IV_a and IV_b). A 350% increase in reservoir volume made by increasing both pump-tube length and diameter in a 12.7-mm launcher at the AEDC made possible an improved mode of operation whereby 30% heavier models are launched to the same velocity with a 50% reduction in peak base pressure. Gun dimensions for this case may be obtained from Reference 2.100.

A very limited study of the effect of pump-tube volume was made with the Ames 7.1mm/39.3mm gun by shortening the pump tube from 10.7 m to 5.8 m long (Launchers V_a and V_b). The effect on model velocity of the change in length, with mass of gas held constant for both cases, is shown in Figure 2.70. A gain in velocity was obtained with the shortened pump although the difference diminishes at the higher piston speeds. Attendant with this gain in velocity is a substantial increase in maximum model base pressure, Figure 2.71. At values of G/m_s of 2.5 and 3.8, the models broke up during launch in the shortened gun; the base pressures shown are values measured prior to model failure. The increase in base pressure is due, at least in part, to a difference in pumping rate for equal piston speed and gas mass that results when volume is changed. From Equation (2.141) of Section 2.5.2, it was seen that dp/dt is inversely proportional to V_{ro} and $p_{ro}^{1/\gamma}$, resulting in a pumping rate for the short tube approximately 1.2 times that of the longer pump. The decrease in maximum pressure noted for the short gun at the highest piston velocity may be due to premature diaphragm rupture (because of higher shock pressures developed with an increase in initial pressure). Normalized maximum base pressure, $p_{s_{max}}/p_{s_{avg}}$, is plotted in Figure 2.72, as a function of model velocity to indicate the relative efficiency of launch for the two gun configurations. Although the apparent scatter or lack of consistent trend would make any fairing of the data questionable, it can be seen that the longer pump tube definitely provides the more favourable launch conditions in these tests.

An examination of Table 2.2 will reveal that there is a large variation in pump-tube geometry, even with the guns which have achieved velocities near the envelope of the velocity curve given in Figure 2.65. High velocities have been obtained with both the small volume pumps operating with relatively higher gas densities and the large compressors which generate considerably higher temperatures. The parameters lacking to make a meaningful comparison between these guns are the reservoir and base pressures produced in each case to obtain a given velocity.

2.5.3.3 Chambrage

From theoretical considerations (ideal gas) discussed in Section 2.3 it is indicated that a gain in performance is realized from chambrage when the pump-tube diameter is increased to three to four times the launch-tube diameter. However, the computations of Reference 2.79 indicate that with real hydrogen gas the difference in reservoir conditions for the chambered and unchambered gun, to maintain constant base pressure, is for high-performance conditions, not large enough to be of practical significance. Other considerations, then, can be used to determine a suitable value of D_r/D_s. For example, lack of laboratory space may limit pump-tube length, requiring a relatively large diameter tube to provide the desired reservoir volume. Because of space limitations, guns having diameter ratios up to at least 10 have been used with good results.

As the diameter is increased for a pump-tube of specified volume, with mass of gas held constant, piston velocity must be decreased to maintain the same pumping rate; that is

$$\frac{u_{p_1}}{u_{p_2}} = \left(\frac{D_{r_2}}{D_{r_1}}\right)^2.$$

(2.143)

The slower piston in a larger diameter pump will generate weaker shock waves and thus compress the gas in a more nearly isentropic manner. Further, with a larger-diameter, shorter pump the piston can be accelerated from rest to the proper velocity with a lower value of acceleration. This is significant in that the time required for compression waves to form shocks is a function of the piston acceleration (See, e.g., Rudinger, Reference 2.101). The fact that the piston acceleration is directly related to the pump-tube length can be reasoned as follows. If the piston is accelerated uniformly to the desired peak velocity, the acceleration will vary directly as the velocity squared and inversely with distance traveled; that is,

$$\frac{\alpha_1}{\alpha_2} = \left(\frac{u_{p_1}}{u_{p_2}}\right)^2 \frac{x_{p_2}}{x_{p_1}}.$$

(2.144)

To maintain the same pumping rate, piston velocity must vary inversely with distance traveled, or

$$\frac{u_{p_1}}{u_{p_2}} = \frac{A_2}{A_1} = \frac{x_{p_1}}{x_{p_2}},$$

(2.145)

(for equal pump-tube volumes). Thus the piston acceleration is proportional to pump-tube length, or

$$\frac{\alpha_1}{\alpha_2} = \frac{x_{p_1}}{x_{p_2}} = \frac{L_{r_1}}{L_{r_2}}.$$

(2.146)

It is of interest to compare further two 5.6-mm-bore guns in use at Ames (Launchers I_a and II_a) having approximately the same pump-tube volume but different values of chambrage. It was stated that the erosion occurring with the smaller diameter pump was far beyond acceptable limits, while that experienced with the other was not sufficient to be of concern. Having approximately equal compression ratios, the two guns would, with isentropic compression, produce the same gas temperature. Considering that the surface area to volume ratio is greater for the smaller diameter pump it would be predicted that the attendant convective losses would be greater and the mean gas temperature somewhat lower than with the large diameter pump. The greater erosion associated with the small bore pump is thought to be due, at least in part, to its higher piston velocity (approximately 700 to 900 m/s, as compared to 350 to 450 m/s) with greater shock heating. Further evidence of greater shock compression in the smaller bore gun is indicated by the slightly higher maximum velocities attainable in this gun with simple models capable of withstanding the higher peak pressures generated.

Consider again that piston velocity varies inversely as the square of the pump-tube diameter if volume, gas mass, and pumping rate are held constant. To provide the same piston energy, then, the mass of the piston must vary as the fourth power of the diameter ratio,

$$\frac{m_{p_2}}{m_{p_1}} = \left(\frac{D_{r_2}}{D_{r_1}}\right)^4,$$

(2.147)

with the result that as diameter is increased piston mass ultimately becomes impractically high. The effects of pump-tube to launch-tube diameter ratio (D_r/D_s), piston velocity, and piston mass on the stresses developed at the end of the pump when the piston decelerates to rest must also be considered. The pressure at the wall of a tapered transition section increases with an increase in D_r/D_s and is proportional to the piston mass and the square of the piston impact velocity. The pressure relationships for this case are developed in Reference 2.102.

Average values of D_r/D_s, used in current guns, can be seen from Table 2.2 to be in the range of 4 to 5.

2.5.3.4 Pump-Tube to Launch-Tube Transition

The guns listed in Table 2.2 include a number that have a square-ended or abrupt transition section between the pump and launch tube, but the majority have a slender tapered transition of 15° (included angle) or less. The function of the tapered transition was discussed in Section 2.4.4.

Tests made at several laboratories have shown that with the use of a deformable piston and a slender tapered transition the maximum velocity can be substantially increased over that attainable with a gun having an abrupt transition (in which additional gas is used as a buffer to prevent damage to the end of the pump). RARDE tests (Reference 2.47) obtained (for a limited range of loading conditions) an increase of approximately 760 m/s when taper angle was changed from 60 to 16 degrees. Examination of the available firing results plotted in Figure 2.65 for the guns listed in Table 2.2 reveals that the highest velocities, that is, those within 1000 m/s of the envelope, were (with one exception) obtained using guns having taper angles less than 15°. The exception, at $m_s/D_s^3 = 1.74$ and a velocity of 7000 km/s, was obtained with a 60° taper utilizing an expendable transition section.

Although the slender-taper deformable-piston gun has achieved the best performance with present methods, the question arises as to whether there is an optimum angle for this slender taper. Calculations for isentropic compression of an ideal gas (Reference 2.76) indicate that an increase in velocity is obtained as taper angle is increased from approximately 3° to 11° (included angle). At angles from 11° to 16° a rapid decrease in velocity is noted. The predicted pressure exerted on the walls increases slowly at small angles as taper angle is increased, but rises rapidly at angles above approximately 8°. In experimental tests, Curtis[2.65] noted, for a limited range of test conditions, a slight increase in velocity (370 m/s) when taper angle was increased from 5.4° to 7.4°. The RARDE results at higher angles show no appreciable velocity difference between 9° and 16°. Additional tests at Ames at included angles of 8.7°, 12.4°, and 16° also show no essential difference in model base pressure as well as velocity for a variety of different model weights and loading conditions (see Figures 2.73 and 2.74).

Since there is seen to be no gain in performance at angles above approximately 8°, and that piston deformation pressures increase rapidly at angles above this value, it may be concluded that 8° included angle (or possibly slightly lower) is a suitable angle for the deformable piston gun.

2.5.3.5 Powder Chamber

With the typical mode of operation of a two-stage isentropic compression gun the sole function of the first stage is to accelerate a pump piston of given mass to a specified velocity at the start of the launch. Ideally, for isentropic compression, the first-stage pressure-time history should be such that the piston is accelerated relatively smoothly to minimize shock formation in the second-stage propellant. With gunpowder as the first-stage propellant, the kinetic energy of the piston is determined by the mass of the charge. For a specified charge mass, pressures generated during combustion can be limited (to minimize peak piston base pressure) by making the volume of the powder chamber large in relation to the charge volume. The relation between peak powder pressure and chamber volume for a fast-burning powder which burns completely before the piston moves appreciably can be estimated by Equation (2.142) of Section 2.5.2.7. As noted there, a more uniform piston acceleration history is obtained with a slow-burning powder which continues to burn as the piston travels through a substantial part of the pump tube. The volume opened up by the motion of the piston serves as additional chamber volume so that the initial chamber need not be as large. The motion of the piston may be calculated using the conventional propellant interior ballistics solutions of References 2.13, 2.14, or 2.103 (see also Wilenius, et al.[2.71]).

Powder-chamber volumes for the guns in current use are listed in Table 2.2, expressed as the ratio of powder-chamber volume to launch-tube volume V_c/V_s. Launch-tube volume is considered a meaningful parameter with which to normalize chamber volume (to compare guns of different sizes) since powder chamber volume is determined by the required powder charge mass, which depends on the mass of light gas to be energized, which in turn is a function of model mass, and which, finally, be related to launch-tube size. A wide variation in V_c/V_s is noted in the table. The two guns listed at the RARDE facility use compressed helium as a first-stage driver gas and should be exempted from this comparison. Values of V_c/V_s range typically from 3 to 8 but a number of cases differ widely from these values. With two 5.6-mm Ames guns having a V_c/V_s of 45.4 and 49.6 the pump piston can be satisfactorily accelerated to the required velocity with relatively low peak accelerations but the chamber volumes are considered to be unnecessarily large. The maximum density of loading (ratio of charge mass to chamber volume) for these guns is approximately 0.12 gm/cm³. The Ames 25.4-mm and 38.1-mm guns, on the other hand, are considered to have undesirably small chamber volumes ($V_c/V_s = 1.8$, and maximum $m_c/V_c \sim 0.25$ gm/cm³). A somewhat larger volume would reduce the need for the close control of the powder burning rates presently required with changes in charge mass and piston weight.

Variations in shape of the charge will produce changes in the burning rate and the peak pressures developed. This effect is more pronounced at high loading densities (Reference 2.13). For reproducible results it is necessary that the charge geometry be approximately the same for each firing. An example of the charge geometry used in light-gas guns is shown in Figure 2.75. The main charge is contained in a paper or cardboard tube and is ignited by an electrical primer. To provide uniform ignition when the charge is large in relation to the primer, it is sometimes desirable to use a booster consisting of a core of fast-burning powder extending through the length of the charge. A charge of relatively high fineness ratio, extending over a large fraction of the chamber length, is preferable to a compact charge located at the breech end of the chamber. The compact charge provides a greater distance for compression waves generated during combustion to form shocks which may affect the piston motion and add to the generation of shocks in the second-stage gas (see Reference 2.104).

2.5.3.6 Effects of Scale

From Equation (2.5), Section 2.3.1, it is seen that the velocity attainable under ideal conditions is:

$$U = \left[\frac{2\widetilde{p}_s}{\rho_s} \frac{L_s/D_s}{l_s/D_s}\right]^{1/2} . \tag{2.5}$$

A given velocity may be obtained with guns of different size by maintaining the same average propelling pressure, model density, and launch tube and model lengths expressed in units of the model diameter. The volume of gas required to produce the same base-pressure history must increase in direct proportion to the increase in the launch-tube volume. The required increase in volume is provided if pump-tube dimensions are also scaled up in direct proportion to the increase in launch-tube-bore diameter. Thus equal velocities may be achieved with guns of different size if all gun dimensions (including model and pump piston) are changed by the ratio of launch-tube diameters.

The motion of the model is determined by

$$\frac{du_s}{dt} = \frac{p_s A_s}{\rho_s A_s l_s} = \frac{p_s}{\rho_s l_s} ,$$

which shows that an increase in model length results in a proportionate decrease in acceleration. Therefore, for the same final velocity, the launch time will vary directly with changes in gun size. With a proportionate change in outside gun dimensions and wall thicknesses, equal stresses will result from operation at the same pressures.

To summarize, the same performance obtained from a gun of bore diameter D_{s_1} will be realized with a larger gun of diameter D_{s_2} if:

1. Gun dimensions are increased by D_{s_2}/D_{s_1}

2. Mass of model and piston are increased by $(D_{s_2}/D_{s_1})^3$

3. Mass of gas and powder charge are increased by $(D_{s_2}/D_{s_1})^3$,

with the result that:

1. Acceleration of piston and model will decrease by D_{s_1}/D_{s_2}

2. Time scale will increase by D_{s_2}/D_{s_1}

3. Pressures, stresses, velocities remain the same.

Because one can obtain (ideally) the same performance with guns of different sizes, small scale or pilot guns have been used to develop and proof larger more costly guns. Additional considerations regarding scaling, including experimental comparisons, are contained in References 2.77 and 2.88.

The range of gun sizes over which these scaling relations can be used with reasonable accuracy depends on the extent of possible nonscalable losses. Because of the complex nature of the nonsteady flow processes in guns, calculations of boundary layer and heat-transfer losses (influenced in a nonlinear manner by Reynolds number) made thus far have not been sufficiently rigorous to establish the effect of scale. In practice, the highest velocities have been obtained with small-bore guns, but this may be due principally to the added caution used in operation of large-bore guns and the reluctance to press the more expensive and potentially more dangerous equipment to the limits imposed on the smaller guns.

2.6 MECHANICAL DESIGN CONSIDERATIONS

2.6.1 Powder Chamber and Pump Tube – Low-Pressure Sections

The design of many of the various components making up a light-gas gun involves only application of standard practice. In those areas of the gun where the pressure loadings are relatively light, such as the powder chamber and most of the pump tube, the design is straightforward, primarily involving selection of tube-wall thicknesses and attention to joint details. Joints in these areas may be sealed by standard neoprene "O"-rings in accordance with practices recommended by their manufacturers. These seals are preferably located on journals or shoulders which serve to maintain concentricity of adjoining parts and permit some axial strain of joint retaining members without loss of seal effectiveness. One nonstandard seal arrangement which has proven particularly reliable is sketched in Figure 2.76.

Straightness of the pump tube is not a critical factor, since pump-piston speeds are relatively low, but it is desirable to have a reasonably smooth, honed, uniform-diameter bore, with no offsets or other discontinuities, throughout the length of the tube.

2.6.2 Pump Tube – High-Pressure Section

Since the performance of the gun is limited in part by the pressure capability of the high-pressure end of the pump tube, this section is designed to have maximum strength consistent with acceptable costs of construction. Of the several types of construction in general use the simplest is the single piece or monobloc thick-wall cylinder. The pressure at which local yielding is first reached at the inner wall is given by:

$$p_y = \frac{\sigma_y}{\sqrt{3}}\left(\frac{w^2 - 1}{w^2}\right),$$

(2.148)

where w = wall ratio = $\dfrac{\text{outer diameter of cylinder}}{\text{inner diameter of cylinder}}$

and σ_y = yield stress. This relation is developed from the maximum distortion energy theory of Von Mises, which is reported in Reference 2.105 to be the most appropriate of the various failure criteria for this application. Very little increase in pressure capability is realized for wall ratios greater than 5, but even with an infinite wall ratio the pressure at which yielding occurs is only $0.58\,\sigma_y$. If operation is limited to completely elastic conditions, the maximum pressures for ductile high-strength steels must be restricted to values of the order of 7.0 kilobars. For the high-pressure section of a light-gas gun, this is, however, an unnecessary restriction and the bore is allowed to yield to obtain an increase in operating pressure. When a cylinder is subjected to internal pressures greater than that required to produce yielding, plastic flow of the material begins at the bore and progresses toward the outside diameter as pressure is increased. Release of the pressure then results in residual tensile hoop stresses in the elastic outer fibers and compressive stresses in the inner fibers near the bore. In subsequent loadings, as pressure is increased, this compressive stress is first reduced to zero before a tensile stress is induced, and thus, the chamber can be pressurized elastically to the previous value at which the chamber has been prestressed before again reaching the tensile yield strength. This prestressing process, termed "autofrettage" (See References 2.106 to 2.109), is finally limited for elastic operation by the compressive yield strength of the material at the bore; auto frettaging beyond this limit results in reverse yielding at the bore. For cylinders having wall ratios greater than 2.2 (see Reference 2.110) this pressure is approximately twice the value given by Equation (2.148), or:

$$p_y = \frac{2\sigma_y}{\sqrt{3}}\left(\frac{w^2 - 1}{w^2}\right).$$

(2.149)

A further increase in maximum pressure can be made if reverse yielding at the bore is accepted. The pressure at which yielding has progressed to the outside wall in a monobloc cylinder (for all wall ratios), so that the cylinder is fully plasitc, is given by Equation (2.150). This relation can be used to obtain an estimate of the bursting pressure, although the actual bursting pressure will be somewhat higher because the ultimate material strength is not considered.

$$p_{max} = \frac{2}{\sqrt{3}}\,\sigma_y\,\log_e w.$$

(2.150)

Although cylinders are frequently auto frettaged during construction, this operation is commonly performed, in effect, in light-gas guns by subjecting the chamber to the actual pressures developed during firing.

Because of its relative simplicity, the monobloc is widely used in light-gas-gun construction. To allow extensive plastic flow the cylinders are made massive with wall ratios commonly in the range of 3.5 to 6.0. These ratios are based on the pump-tube diameter ahead of the tapered transition section if such a section is used. With a slender taper and relatively high-compression-ratio pump, peak pressures generally occur towards the small end of the taper where the wall ratios are much greater. Operation of this section under conditions producing extensive yielding requires the use of a highly ductile material. AISI 4340 (heat-treated to Rockwell C-38 to C-40) has proven to be an excellent high-strength steel of high ductility and good harden ability and is generally used in this application.

Although the slender taper transition section provides a means for decelerating the piston without severe damage during each firing, there is a gradual deterioration at the bore from high-performance shots with this configuration. Continued operation at conditions producing extreme gas and piston pressures results in local cracking of the bore material and the section is discarded when this cracking becomes pronounced. To minimize the hazard resulting from a possible complete failure, a thick-plate shield is sometimes placed over this section.

Another method of construction whereby a favorable residual stress distribution is induced in the pressure vessel to increase the maximum operating pressure consists of the assembly of two or more concentric cylinders having interference fits. The shrink-fit of an outer cylinder or jacket upon an inner cylinder or liner generates tensile hoop stresses in the jacket and compressive stresses in the liner. Relations for shrink-fit pressures and the stress distributions induced by this method can be obtained in standard design texts such as Reference 2.111. As with the auto frettage process, the maximum operating pressure for elastic operation, determined by the compressive yield strength of the bore material, is given by Equation (2.149). Again the pressure capability can be increased substantially if a portion of the cylinder is allowed to reach the plastic state. This may be accomplished by stressing the chamber during normal usage or by a separate auto frettaging procedure after construction, or by an alternate method wherein the cylinders are auto frettaged separately before assembly. An example of a compound structure of two cylinders is given by Cloutier in Reference 2.112,

in which the liner is considered to be three-quarters plastic and the jacket one-half plastic. With a wall ratio of five for the duplex structure and three for the liner, and a yield strength of 10.4 and 17.3 kilobars for the jacket and liner, respectively, the design pressure capability is computed to be 25.9 kilobars. In this case a high-strength steel, such as a maraging steel, is chosen for the liner material and a conventional gun steel for the jacket. Herein lies an advantage of compound construction - the possibility exists of using a costly, ultra-high-strength steel for the liner that may not be practical in a large monobloc cylinder. Further, a more uniform hardness can be achieved with heat treatment of the separate pieces used in a compound cylinder than can be obtained in the thick-wall monobloc. The greater complexity of the compound cylinder, requiring additional machining to close-tolerance interference fits and a shrink-fit operation, add to the initial cost of the unit. This may be partially offset by the fact that replacement of the cylinder, which may be necessary because of failure at the bore from high-performance firings, may require renewal of only the inner liner.

2.6.3 Launch Tube

Several factors other than a high-pressure capability dictate the design of the launch tube. To maintain proper stability of the model in the barrel (the model is often relatively short) and to insure an effective gas seal between the model and the wall, the launch-tube bore must be smooth and continuous. The high model velocities and relatively low model strengths also require that the bore be exceedingly straight, and because the launch tubes are frequently very long in relation to the bore diameter, it is difficult to produce barrels with the necessary straightness. The straightness requirement frequently specified for launch-tube construction, but often not attained, is that the bore shall not deviate from a mean centerline more than 1 part in 10^4 units of length. For many applications this is an unnecessarily stringent specification.

Gun barrels are typically machined from a solid forging using special deep-hole-drilling techniques to produce a relatively straight bore. If necessary, the barrels are mechanically straightened after the drilling operation.

The erosion encountered at the breech of the launch tube necessitates periodic replacement of the barrel. Failure and breakup of the model frequently produces sufficient damage to the bore (even with simple plastic models) to also require replacement of the barrel, unless some local repair can be made. It is desirable then, that the launch-tube construction be such that replacement can be made with minimum cost and effort.

One launch-tube design, made to satisfy the requirements for straightness and economical replacement can be seen in Figures 2.77 and 2.78. The design consists of a thin-wall seamless-tube liner supported externally by a heavy, split, rectangular block clamped by a double row of bolts. This bolted construction is sufficient to withstand the gas pressures except in the region of highest pressure at the breech end of the tube where a thick-walled jacket approximately 30 calibers long is used.

Jacket and split-clamp housing are generally constructed of AISI 4340 steel heat-treated to Rockwell C-40, and the liner is a commercially available seamless tube of an annealed alloy such as AISI 4130. A planing operation is used to machine the split clamp, including the semi circular groove in the separate halves which form the bore of the housing upon assembly. It is this operation, made possible with the split construction, that produces a straight bore launch tube; while it is difficult to bore or drill a long straight hole, it is relatively easy to machine an exceptionally straight groove on a planer if proper precautions are taken. With the larger launch tubes the bolts are tightened during assembly with a hydraulic bolt tensioner, which makes possible uniform loading of all bolts to nearly the yield point. A slight interference fit between the liner and both the jacket and split housing prevents movement of the liner during firing. The liners are purchased slightly oversized, in quantity lots from the same mill run to insure uniformity, and are sized to the precise outside diameter, if necessary, by a simple external honing operation. With a spare jacket and liner assembly held in reserve, replacement of a damaged gun liner can be made in a very short time and at a cost which is only a small fraction of the replacement cost of a conventional one-piece barrel. The fact that launch tubes can be rapidly and economically replaced leads to greater freedom in the selection of models - one can attempt to launch models of marginal strength at high-performance conditions without fear of substantial penalties in cost in the event of model failure.

This design has been used successfully at Ames Research Center in a range of gun sizes having bore diameters from 5.6 mm to 38.1 mm.

2.6.4 Coupling of Launch Tube to Pump Tube

Generally, the design of the joint between the pump and launch tubes entails the provision for three items:

(a) a quick-opening valve that will release the high-pressure gas, at a prescribed pressure, from the pump tube to the projectile base,

(b) an adequate seal to prevent escape of the hot, high-pressure gas through the joint, and

(c) external structural members to couple the launch and pump tubes together and carry the axial pressure and inertia loads developed when the gun is fired.

Although other types of quick-opening valves have been used successfully in the past, such as discs which fail in shear or members which part in half in tensile failure under the applied gas-pressure loadings, the petaling-diaphragm type valve is now in most general use. These diaphragms are made thick enough that they will not fail in direct shear, are prescored to provide a four-petal opening configuration which bursts at a pressure

dependent on the remaining depth at the scored section, and are machined from annealed type 304 stainless steel, which is sufficiently ductile that the petals will usually not tear off during the opening, or bursting, process. Their design is relatively straightforward and is detailed in Reference 2 113.

The problem of providing a seal at the critical joint between the pump and launch tubes, where the pressures and temperatures of the gas are near a maximum, has been a difficult one. Early attempts to employ neoprene "O"-rings at this joint met with only limited success. Some leakage nearly always occurred, with consequent erosion of areas adjacent to the seals, and in some cases the "O"-rings were completely extruded into the joint making it very difficult to disassemble the gun after firing. One successful solution has been to use a low-carbon steel ring as a seal, machined to size in the form sketched in Figure 2.79. The O.D. and I.D. of the seal ring have small clearance with the respective journals on the heat-treated pump and launch tubes so that the pieces readily assemble until the outer corners of the seal come to bear against the adjoining faces. The slant height of the seal cross section is made sufficiently long so that when an axial load is applied bringing the pump and launch tubes together, the seal is upset and will develop its yield strength in compression against the mating journals. The diameters of the seal ring and journals with which it mates must be precisely controlled, but when the parts are machined and assembled properly, it provides a very effective seal.

The structural coupling of the launch and pump tubes may be accomplished in several different ways. For smaller guns, either bolted flanges or threaded nuts, as sketched in Figure 2.80, are generally sufficient. Inherent in the bolted flange design is the disadvantage that many bolts are required to carry the pressure and inertia loads developed when the gun is fired, with consequent time-consuming assembly operations. The interrupted-thread nut is a good, simple design, but for large guns, the nut may be cumbersome to handle and difficult to torque when substantial preload forces are required to minimize axial separation of the joint for proper sealing. In this case, at the expense of additional complexity, mechanical or hydraulic torque multipliers may be used with the nut to provide the necessary preload.

A satisfactory method of joining pump tube to launch tube for larger guns, which allows quick and easy assembly and disassembly, employs a hydraulically constrained coupling, as shown in Figure 2.81. With this system hydraulic preload forces greater than the axial separating forces can readily be applied. The outer nut and retaining ring assembly threaded on the high-pressure end of the pump tube contains a hydraulic piston having an internal interrupted shoulder (like a spline in appearance). The shoulder nut threaded on the launch-tube breech has a mating external segmented shoulder. During assembly the launch tube and pump tube are brought together with the shoulder segments on the soulder nut aligned to slip between those on the piston. The outer nut and piston assembly is then rotated until the interrupted shoulder on the piston opposes the shoulder segment on the launch-tube nut. Application of hydraulic pressure between the piston and retaining ring moves the piston against the shoulder nut, forcing it and the launch-tube into firing position against the pump-tube face. The joint is restrained hydraulically in this manner during firing without the use of any secondary mechanical backup. Disassembly of the coupling involves simply the release of the hydraulic pressure, return of the piston to its start position, a slight rotation of the shoulder nut to realign the interrupted faces, and finally, the withdrawl of the launch-tube assembly through the piston. This particular design has been used successfully on guns having launch-tube bores up to 38.1 mm diameter.

A general consideration concerns the use of AISI 4340 steel, frequently chosen for gun structural members. Experience has shown that with mating parts of this same steel there is a tendency towards galling and seizing, with relative motion of the parts under high local contact pressures. For this reason, highly loaded threaded joints requiring many threads with large heavy nuts are preferably constructed with interrupted, rather than continuous threads. Such a joint can be assembled with rapidity and ease, and with a minimum of sliding motion between mating threads. The use of an anti-seizing lubricant is also helpful in reducing this tendency towards galling.

2.6.5 Mounting

The mounting structure used in the support and restraint of the gun will be dictated, in part, by the method chosen for moving and handling the separate gun components during disassembly, cleaning, and assembly operations. Separation and movement of components may be accomplished in a variety of ways: with launch tube or pump tube kept stationary and other (or all) components moved axially and/or laterally to provide clearance for cleaning and for assembly of expendable parts.

It is frequently expedient to provide vertical and horizontal adjustment at individual support points so that the bore of long tubes can be readily aligned with regard to direction and straightness, eliminating in many cases the requirement that the outside tube diameter be made concentric with the inside diameter, as well as reducing the precision required in machining and locating mounts and supports.

The methods successfully used to restrain the gun members during firing vary from that of rigid restraint, allowing essentially no gun motion, to that of no restraint in which components are allowed to slide freely. With the highly restrained system the most effective point to provide this restraint is in the vicinity of the high-pressure transition section, where the highest peak axial loads are developed, so that these high loads need not be carried through the tubes and joints of other gun members. However, except perhaps for small guns, a rigid restraint system is undesirable because of the high peak loads developed in the support structure. These loads may be reduced with the use of a flexible support system with, for example, torsion bars, which act to temporarily store strain energy. The support structure loads may be reduced to moderate values by allowing greater motion of the gun with a system that applies some frictional restraint through clamped supports. Going a step beyond this, many two-stage guns, both large and small, are fired satisfactorily with essentially no

restraint other than the friction resulting from the weight of the gun. During operation, as a consequence of the free piston, an end load is first applied at the powder chamber accelerating the gun rearward, but this is counteracted later, for the most part, by the impulse imparted by the piston to the high pressure end. Although the net impulse is not zero the momentum of the model and light gas is generally small compared to the piston momentum, and, because the inertia of the complete gun is relatively high, the total excursion of the gun is reasonably small. It should be noted that, in such a system where the gun is allowed to move, the tubes and joints must be designed to handle the additional inertia loads developed.

2.7 PROSPECTS FOR HIGHER PERFORMANCE

The need in certain types of studies for velocities higher than presently attainable in the laboratory leads one to speculate about future possibilities for substantially increasing speeds. Techniques employing electrostatic acceleration, explosively formed jets, explosively driven plates, acceleration by drag forces, and others (see Reference 2.114) show promise, and, as noted in the Introduction, have achieved velocities well above 20 km/s. However, in most cases the particles accelerated are restricted in size, shape, and material. What are the prospects for accelerating the variety of aerodynamic models that are now launched primarily with guns? Very large gains in velocity have been made with the light-gas gun during the last decade but the rate of gain has of late slowed appreciably. Further increases in velocity with the conventional two-stage light-gas gun are becoming increasingly difficult to achieve. This is not meant to imply that the limits of capability of this launcher have been reached. Higher performance will surely be realized with an improved understanding of the internal ballistics of guns so that loading conditions and gun geometry can be better optimized to produce more nearly constant base pressure conditions. Further gains would result with improvements in the strength of gun and model materials. Perhaps the most significant increases in performance will result from the technological development of new concepts.

One of the basic limitations of the conventional gun is related to the fact that the propellant gas is expanded from a fixed reservoir. Extreme reservoir pressures are required to maintain an effective base pressure as the distance between the projectile and the chamber becomes large. The large expansion ratios required could be decreased if: the reservoir of gas were made to follow behind the model in some manner; or, the pressure and temperature of the gas were enhanced in some other fashion, in the region directly behind the model. A number of attempts have been made to achieve these conditions but in most cases without notable success.

One exception which promises to give substantially higher speeds is a new concept developed by Godfrey and Moore employing an explosive lensing technique (see Figure 2.82 taken from Reference 2.26). This launcher is a form of light-gas gun in which the model is accelerated in two stages. The function of the first stage is to accelerate the projectile and a reservoir of gas from rest to at least some minimum velocity (greater than approximately 5 km/s) required for operation of the second stage. The first stage used for this purpose has been a linear explosive driver consisting of a reservoir of helium contained in a metal tube surrounded by a high explosive. The tube is collapsed inward by detonation of the explosive, producing, in effect, a conical piston which travels progressively toward the projectile at a constant velocity equal to the detonation velocity of the explosive. The model, and driver gas energized by shock compression, are accelerated into the second stage, and when a sufficient quantity of gas at the proper conditions of pressure and temperatures have been introduced, operation of this stage is started. Employing a unique explosive lens, which also generates a conical piston, the second stage then further accelerates the projectile to the desired final velocity. The lens consists of two explosives having different detonation rates – a thin layer of fast explosive surrounds the slow explosive placed contiguous to the barrel. The difference in detonation speeds results in a detonation front that is inclined to the axis of the barrel. The smaller the angle of inclination, the higher the speed at which the collapse point (acting as a piston) proceeds along the barrel. By proper selection of detonation rates and lens geometry the "virtual piston" can be programmed to accelerate at various prescribed rates to speeds well above the highest explosive detonation velocity. The "piston" motion can be tailored to accelerate the reservoir gas in a manner to maintain a high and reasonably constant base pressure for an appreciable distance. Upon completion of the detonation phase a small further increase in velocity is obtained by expansion of the reservoir gas. Velocities as high as 12.2 km/s (with a 0.17-gm model, 6.4 mm in diameter) have been obtained with this technique – the highest velocity yet achieved with a light-gas gun – and projections indicate that velocities in the 15 to 20 km/s range are feasible.

Techniques such as this which do not depend on launching a model from a fixed reservoir, or other schemes in which the driver gas can be further energized in the region behind the model to sustain a high base pressure, may provide the means for launching laboratory test models to substantially higher velocities than presently attainable.

REFERENCES

2.1   Robins, R.   *New Principles of Gunnery.* James Wilson, MD, London, 1742.

2.2   (Lagrange,   *Mouvement de Poulet dans l'Intérieur de Canon.* Extraites des Manuscripts de
      Joseph-Louis)   Lagrange. J. d'Ecole Polytech., Vol.21, 1832.
      Poisson, M.D.

2.3   Résal.   *Recherches sur le Mouvement des Projectiles dans les Armes à Feu.* Paris, 1864.

2.4   Hélie.   *Balistique Expérimentale.* Paris, 1865.

2.5   Sarrau,   *Recherches Théoriques sur la Chargement des Bouches à Feu.* Paris, 1882.

2.6   Moisson,   *Pyrodynamique.* Paris, 1887.

2.7   Hugoniot,   J d'Ecole Polytech, Paris, 1889.

2.8   Gossot, Liouville   Mém. Poudres 1905, 1914.

2.9   Charbonnier,   *Balistique Intérieure.* Paris, 1908.

2.10 Röggla,   Mitt. Gegenstände d.Artill. u. Genie-wesens, 1914.

2.11 Love, A.E.H.   *Lagrange's Ballistic Problem.* Phil. Trans. of the Royal Society, Series A,
      Pidduck, F.B.   Vol.222, 1922.

2.12 Cranz,   *Lehrbuch der Ballistik.* Berlin, 1926.

2.13 Corner, J.   *Theory of the Interior Ballistics of Guns.* John Wiley & Sons, 1950.

2.14 Thornhill, C.K.   *A New Special Solution to the Complete Problem of the Internal Ballistics of Guns.*
                                    AGARD Report 550, 1966.

2.15 Hunt, F.R.W.   *Internal Ballistics.* Her Majesty's Stationery Office, London, 1951.

2.16 Nelson, W.C.   *Selected Topics on Ballistics.* Pergamon Press, New York, 1959.

2.17 Fowler, R.H.   *The Aerodynamics of a Spinning Shell.* Phil. Trans. of the Royal Society, London,
      Gallop, E.G.   1920.
      Lock, C.W.H.
      Richmond, H.W.

2.18 Crozier, W.D.   *high-Velocity Light-Gas Gun.* J. Applied Physics, Vol.28, 1957.
      Hume, W.

2.19 Charters, A.C.   *Development of a Piston-Compressor Type Light-Gas Gun for the Launching of Free-
      Denardo, B.P.   *Flight Models at High Velocity.* NACA TN 4143, 1957. (originally issued as RM
      Rossow, V.J.   A55G11, 1955).

2.20 Slawsky, Z.I.   *Survey of NOL Hyperballistics Research.* NOL Report 1238, 1959.

2.21 Seigel, A.E.   *A Hypervelocity Gun Using a Shock-Compressed Steam-Heated Propellant.* NAVORD
      Slawsky, Z.I.   Report 4345, 1956.

2.22 Scully, C.N.   *Electrothermal Gun for Hypervelocity Ballistics Research.* Proceedings of the
      Escallier, E.A.   Seventh Hypervelocity Impact Symposium, 1965.
      Rosen, F.D.
      O'Keefe, J.D.

2.23 Friichtenicht, J.F.   *Electrostatic Accelerators – Experimental Techniques.* Proceedings of the Seventh
      Slattery, J.C.   Hypervelocity Impact Symposium, 1965.
      Hansen, D.O.

2.24 Kronman, S.   *Explosive Devices for Projecting Hypervelocity Pellets up to 21.0 Km/Sec.* Pro-
      Kineke, J.H. Jr   ceedings of the Fifth Hypervelocity Impact Symposium, 1962.

2.25 Howell, W.G.   *Results of Developmental Research on an Augmentation Technique for a Light-Gas
      Orr, W.R.   Gun.* Proceedings of the Fifth Hypervelocity Techniques Symposium, 1967.

2.26   Moore, E.T. Jr   *Explosive Hypervelocity Launchers.*   Physics International Co. NASA Contractor Report CR-982, 1968.   Also, Physics International Final Report-051, 1967.

2.27   Courant, R.   *Supersonic Flow and Shock Waves.*   Interscience Publishers, New York, 1948.
       Friedrichs, K.O.

2.28   Seigel, A.E.   *The Theory of High Speed Guns.*   NATO AGARDograph 91, 1965.

2.29   Seigel, A.E.   *The Rapid Expansion of Compressed Gases Behind a Piston.*   Ph.D. thesis, University of Amsterdam, 1952.

2.30   Heybey, W.   *A Solution of Lagrange's Problem of Interior Ballistics by Means of Its Characteristics Lines.*   NOL Memorandum 10819, 1950.

2.31   Kent, R.H.   *The Motion of the Powder Gas. I. A Special Solution for the Case of an Imperfect Gas.*   Aberdeen Report No. 36, 1936.

2.32   Seigel, A.E.   *The Effect of Optimum Chambrage on the Muzzle Velocity of Guns with a Qualitative Description of the Fundamental Phenomena Occurring During Gun Firing.*   NAVORD Report 2691, 1952.

2.33   Seigel, A.E.   *The Influence of Chamber Diameter on the Muzzle Velocity of a Gun with an Effectively Infinite Length Chamber.*   NAVORD Report 3635, 1954.

2.34   Seigel, A.E.   *Results of Chambrage Experiments on Guns with Effectively Infinite Length Chambers.*
       Dawson, V.C.D.   NAVORD Report 3636, 1954.

2.35   Stephenson, W.B.   *Theoretical Light-Gas Gun Performance.*   Arnold Engineering Development Center, AEDC-TR-61-1, 1961.

2.36   Vasiliu, J.   *Analysis of Chambered, Finite Length Hypervelocity Launchers by the Method of Characteristics. A Complete Solution.*   Republic Aviation Corp., Report RAC 1617, 1963.

2.37   Zondek, B.   *A Computing Program for the Interior Ballistics of a Hypervelocity Gun.*   US Naval Weapons Lab. Report 1743, 1964.

2.38   von Neumann, I.   *A Method for the Numerical Calculation of Hydrodynamic Shocks.*   J. of Applied
       Richtmyer, R.D.   Physics, Vol. 21, 1932.

2.39   Swift, H.F.   *NRL Hypervelocity Accelerator Development.*   Proceedings of the Sixth Hypervelocity
       Porter, C.D.   Impact Symposium, Vol. ?, 1963.
       Condon, J.J.
       Baker, J.R.

2.40   Kovitz, H.E.   *An Electrically Heated Light Gas Gun for Wake Ionization Studies and Preliminary Results.*   AVCO Everett Research Note 201, 1960.

2.41   Glass, I.I.   *Hypervelocity Launchers. Part 1: Simple Launchers.*   University of Toronto, UTIAS Review No. 22, 1962.

2.42   Glass, I.I.   *Hypervelocity Launchers. Part 2: Compound Launchers – Driving Techniques.*   University of Toronto Institute for Aerospace Studies, Review No. 26, 1965.

2.43   Glass, I.I.   *Shock and Combustion-Wave Dynamics in an Implosion-Driven Hypervelocity Launcher.*   University of Toronto Institute for Aerospace Studies, Review No. 25, 1965.

2.44   Sevray, P.A.L.   *Performance Analysis of UTIAS Implosion-Driven Hypervelocity Launcher.*   University of Toronto Institute for Aerospace Studies, TN-121, January 1968.

2.45   Crosby, J.K.   *Feasibility Study of an Explosive Gun.*   Stanford Research Institute Final Report
       Gill, S.P.   No. 2. Prepared for Ames Research Center under Contract NAS2-1361, 1966.

2.46   Moore, E.T.   *Recent Developments in the Use of Chemical Explosives for Hypervelocity Test*
       Godfrey, C.S.   *Devices.*   Proceedings of the Fifth Hypervelocity Techniques Symposium, University
       Waldron, H.F.   of Denver, 1967.

2.47   Cable, A.J.   *The Performance of the RARDE 1/4-In. Calibre Hypervelocity Launcher.*   RARDE Memorandum 14/64, 1964.

2.48   Waldron, H.F.   *Free Flight Facilities and Aerodynamic Studies at CARDE.*   IAS Preprint No. 60-90,
       McMahon, H.M.   1960.
       Letarte, M.

54

2.49	Liepmann, H.W. Roshko, A.	*Elements of Gasdynamics.* John Wiley & Sons, Inc., 1957.
2.50	Bradley, J.N.	*Shock Waves in Chemistry and Physics.* John Wiley & Sons, Inc., 1962.
2.51	Glass, I.I. Hall, J.G.	*Shock Tubes.* Handbook of Supersonic Aerodynamics, Section 18, NAVORD Report 1488, Vol.6, 1959.
2.52	Evans, C. Evans, F.	*Shock Compression of a Perfect Gas.* J. of Fluid Mechanics, Vol.1, Part 4, 1956.
2.53	Watson, J.D. Godfrey, C.S.	*An Investigation of Projectile Integrity Using Computer Techniques.* Proceedings of the Fifth Hypervelocity Techniques Symposium, University of Denver, 1967.
2.54	Baker, J.R.	*A Comparison of Shock and Isentropic Heating in Light-Gas Gun Compression.* US Naval Research Lab. Report 6063, 1964.
2.55	Stollery, J.L. Maull, D.J.	*A Note on the Compression of Air Through Repeated Shock Waves.* J. of Fluid Mechanics, Vol.4, Part 6, 1958.
2.56	Bioletti, C. Cunningham, B.E.	*A High Velocity Gas Employing a Shock Compressed Light Gas.* NASA TN D-307, 1960.
2.57	Lord, M.E.	*Performance of a 40-mm, Combustion Heated, Light Gas Gun Launcher.* AEDC-TN-60-176, 1960.
2.58	Knystautas, R. Leftheris, B.	*An Analysis of the Double Shock Compression Light Gas Gun Cycle.* CARDE TR 516/65, 1965.
2.59	Winter, D.F.T.	*Multiple Shock Compression Using a Piston of Finite Weight.* J. of Fluid Mechanics, Vol.8, Part 2, 1960.
2.60	Bull, G.V.	*Hypervelocity Research in the CARDE Free Flight Ranges.* Galbraith Building Opening Ceremonies, University of Toronto, 1961.
2.61	Stephenson, W.B. Anderson, D.E.	*Design of a Large, Two-Stage, Light-Gas Model Launcher.* AEDC TR-61-6, 1961.
2.62	Lukasiewicz, J. Stephenson, W.B. Clemens, P.L. Anderson, D.E.	*Development of Hypervelocity Range Techniques at Arnold Engineering Development Center.* AEDC TR-61-9, 1961.
2.63	Stephenson, W.B. Knapp, R.E.	*Performance of a Two-Stage Launcher Using Hydrogen.* AEDC TDR-62-32, 1962.
2.64	Lemcke, B.	*An Investigation of the Performance of a Compression Heater for Use with Gun Tunnels or Hypervelocity Launchers.* Aeroelastic and Structures Research Lab. MIT Report 1010, 1963.
2.65	Curtis, J.S.	*An Accelerated Reservoir Light-Gas Gun.* NASA TN D-1144, 1962.
2.66	Bird, C.A.	*The Effect of Wall Shape on the Degree of Reinforcement of a Shock Wave Moving into a Converging Channel.* J. of Fluid Mechanics, Vol.5, Part 1, 1959.
2.67	Laporte, O.	*On the Interaction of a Shock with a Constriction.* Los Alamos Scientific Lab., University of California, LA-1740, 1954.
2.68	Charters, A.C.	*The Free-Flight Range. A Tool for Research in the Physics of High Speed Flight.* ARS Preprint 1984-61, 1961.
2.69	Wilenius, G.P.T.	*Slow Piston Gun Development at CARDE.* ARPA, CARDE, ARGMA Symposium on Aeroballistic Ranges. CARDE TM-Q-646/61, 1961.
2.70	Smith, F.	*Theory of a Two-Stage Hypervelocity Launcher to Give Constant Driving Pressure at the Model.* RARDE Report (B) 5/63, 1963.
2.71	Wilenius, G.P.T. Cloutier, M. Cowen, P.L.	*A Theoretical Analysis of a Constant Base Pressure Light-Gas Gun.* CARDE TN 703/62, 1962.

2.72   Curtis, J. S.   *An Analysis of the Interior Ballistics of the Constant Base Pressure Gun.* Proceedings of the Third Hypervelocity Techniques Symposium, Denver, 1964.

2.73   Winkler, E. H.   *The Presentation of the Propellant Flow in a Constant Acceleration Gun by the Method of Characteristics.* NOL TR 64-69, 1964.

2.74   Winkler, E. H.   *The Constant Acceleration Gas Gun Problem.* NOL TR 64-111, 1964.

2.75   Somes, J.   *Analytical Solution of a Special Gun Problem.* Naval Weapons Lab. TM K-45/64, 1964.

2.76   Charters, A. C.   *High Velocity Guns for Free Flight Ranges. The High Temperature Aspects of Hyper-velocity Flow.* AGARDograph 68, 1964. Also, General Motors Corp., Defense Research Curtis, J. S.   Lab. TM62-207, 1962.

2.77   Lukasiewicz, J.   *Constant Acceleration Flows and Applications to High-Speed Guns.* AEDC-TR-66-181, 1966.

2.78   Seigel, A. E.   *Wall Friction, Heat Transfer, and Real-Gas Propellant Effects in High Speed Guns.* Piacesi, R.   Proceedings of the Fourth Hypervelocity Techniques Symposium, Tullahoma, 1965. Bixler, D. N.

2.79   Bixler, D. N.   *Calculations of the Flow Conditions in a Constant Base Pressure Launcher with a* Seigel, A. E.   *Real Hydrogen Gas Propellant.* NOL TR 66-157, 1966.

2.80   Stanyukovich, K.   *Unsteady Motion of Continuous Media.* Pergamon Press, London, 1960, pp. 605-607.

2.81   Seigel, A. E.   *A Convenient and Accurate Semi-Empirical Entropic Equation for Use in Internal Ballistic Calculations.* NAVORD Report 2695, 1953.

2.82   Bixler, D. N.   *Calculated Thermodynamic Properties of Real Hydrogen up to 30,000 Atmospheres and* Piacesi, R. 3500° *K.* NOL TR 65-209, 1965. Seigel, A. E.

2.83   Wooley, H. W.   *Complication of Thermal Properties of Hydrogen in its Various Isotopic and Ortho-* Scott, R. B.   *Para Modifications.* National Bureau of Standards Research Paper RP1932, Vol. 41, Brickwedde, F. G.   1948.

2.84   Baker, J. R.   *Theoretical Thermodynamic Properties of Gases at High Temperatures and Densities* Geatches, W. H.   *with Numerical Results for Hydrogen.* NRL Report 6675, September 27, 1968. Swift, H. F.

2.85   Richtmyer, R. D.   *Difference Methods for Initial Value Problems.* Interscience Publishers, Inc., New York, 1957.

2.86   Piacesi, R.   *Computer Analysis of Two-Stage Hypervelocity Model Launchers.* NOL TR 62-87, 1963. Gates, D. F. Seigel, A. E.

2.87   Baer, P. G.   *Experimental and Theoretical Studies on the Interior Ballistics of Light Gas Guns.* Smith, H. C.   Sixth Symposium on Hypervelocity Impact, Cleveland, Ohio, 1963.

2.88   Cable, A. J.   *Optimizing and Scaling of Hypervelocity Launchers and Comparison with Measured* DeWitt, J. R.   *Data.* AEDC TR-67-82, 1967.

2.89   Badhwar, L. K.   *A New Interior Ballistics Computation System for Light Gas Guns.* Computing Murphy, J. R. B.   Devices of Canada, Report 9825/R1, 1965.

2.90   Murphy, J. R. B.   *Interior Ballistics Calculations Systems for Light Gas Guns and Conventional Guns.* Badhwar, L. K.   The Fluid Dynamic Aspects of Ballistics, AGARD Conference Proceedings No. 10, 1966. Lavoie, G. A.

2.91   Longley, H. J.   *Methods of Differencing in Eulerian Hydrodynamics.* Los Alamos Scientific Lab., University of California, LAMS-2379, 1960.

2.92   Vasiliu, J.   *Piston Motion and Shock Wave Formation in a Free-Piston Cycle – A Computer Solution.* Republic Aviation Corp., Report RAC 2553, 1964.

2.93   Dimeff, J.   *A Piston-Type Strain Gage for Measuring Pressures in Interior Ballistics Research.* Carson, J. A.   Review of Scientific Research, September 1955. Charters, A. C.

56

2.94 Hruby, R.J.
Sander, R.C.
Berggren, R.E.
Microwave Technique for Measuring Projectile Time History in Light-Gas Guns. IEEE Second International Congress on Instrumentation in Aerospace Simulation Facilities. Stanford University, August 1966.

2.95 Anderson, D.E.
Prince, M.D.
Design of Light-Gas Model Launchers for Hypervelocity Research. AEDC-TDR-62-97. 1962.

2.96 Stephenson, W.B.
Anderson, D.E.
Performance of Two-Stage Light-Gas Model Launchers. IAS Thirtieth Annual Meeting, New York, January 1962.

2.97 Eckerman, J.
McKay, W.L.
Performance of a Three-Stage Arc Heated Light Gas Gun. Proceedings of the Sixth Symposium on Hypervelocity Impact, Cleveland, Ohio, Vol.1, August 1963.

2.98 Swift, H.F.
Baker, J.R.
Hypervelocity Capability and Impact Effect Program. Final Report, NRL Memorandum Report 1677, 1966.

2.99 Collins, D.J.
Charters, A.C.
Christman, D.R.
Sangster, D.K.
Parametric Studies of Light-Gas Guns. Fifth Hypervelocity Techniques Symposium, University of Denver, March 1967.

2.100 Cable, A.J.
DeWitt, J.R.
Lukasiewicz, J.
Prepared Comments on the Calculation and Measurement of the Performance of Hypervelocity Launchers. Fifth Hypervelocity Techniques Symposium, University of Denver, 1967.

2.101 Rudinger, George
Wave Diagrams for Nonsteady Flow in Ducts. D. van Nostrand Co., New York, 1955.

2.102 Leech, C.
Piston Extrusion in Light-Gas Guns. CARDE TR 580/67, 1967.

2.103 Fleming, D.
Williams, R.
An Interior Ballistics System for a Propellant Driven Piston. CARDE TM 626/61, 1961.

2.104 Johnson, R.
Shock Phenomenon in Gas Gun Propellant Chambers as a Function of Charge Length. CARDE TN 1605/64, 1964.

2.105 Brooks, P.N.
A Comparative Review of Strength Criteria. CARDE TN 1583/63, 1963.

2.106 Davidson, T.E.
Barton, C.S.
Reiner, A.N.
Kendall, D.P.
The Autofrettage Principle as Applied to High Strength Light Weight Gun Tubes. Watervliet Arsenal WVT-RI-5907, 1959.

2.107 Dawson, V.C.D.
Seigel, A.E.
Reverse Yielding of Fully Autofrettaged Tube of Large Wall Ratio. NOL TR 63-123, 1963.

2.108 Dawson, V.C.D.
Limitations of the Autofrettage Process for High Strength Guns. Proceedings of the Third Hypervelocity Techniques Symposium, March 1964.

2.109 Dawson, V.C.D.
Residual Bore Stress in an Autofrettaged Cylinder Constructed of a Strain Hardening Material. NOL TR 64-25, 1964.

2.110 Dawson, V.C.D.
Seigel, A.E.
High Pressure Chamber Design. NOL TR 67-121, 1967.

2.111 Timoshenko, S.
Strength of Materials. Part II, 3rd edition, D. van Nostrand Co., New York, 1956.

2.112 Cloutier, M.
Design of High-Pressure Sections for Light-Gas Guns. CARDE TR 529/65, 1965.

2.113 Rast, J.J.
The Design of Flat Scored High Pressure Diaphragms for Use in Shock Tunnels and Gas Guns. NOL Report 6865, 1961.

2.114
Proceedings of the Seventh Hypervelocity Impact Techniques Symposium, Tampa, Florida, February 1965.

TABLE 2.1

Properties of Propellant Gases

Gas	p (bars)	γ	ρ (kg/m³)	a (m/s)	ρa (kg/m²s)	a/γ (m/s)	C_p (kJ/kg°K)	C_v (kJ/kg°K)	C_pT (kJ/kg)
Hydrogen	1*	1.40	0.0887	1,260	1.12×10^2	899	14.3	10.2	3,910
	2,000[†]	1.40	20.2	3,730	7.53×10^4	2,660	14.3	10.2	34,200
Helium	1*	1.67	0.176	971	1.71×10^2	583	5.19	3.11	1,420
	2,000[†]	1.67	16.8	4,440	7.46×10^4	2,660	5.19	3.11	29,700
Air	1*	1.40	1.27	330	4.19×10^2	236	1.01	0.722	274
	2,000[†]	1.40	291.	974	2.83×10^5	695	1.01	0.722	2,400
Gun Powder	1*	~1.25	1.23	318	3.91×10^2	254	1.48	1.18	405
	2,000[†]	~1.25	542.	681	3.69×10^5	545	1.48	1.18	1,850

*At T = 273° K.
[†]Isentropic compression neglecting caloric and thermal imperfections and intermolecular forces.

TABLE 2.2

Dimensions and Performance of Representative Laboratory Guns

Facility (1)	D_s (mm)	$\dfrac{L_s}{D_s}$	$\dfrac{D_r}{D_s}$	$\dfrac{L_r}{D_r}$	$\dfrac{V_r}{V_s}$	$\dfrac{V_r}{V_c}$	$\dfrac{V_c}{V_s}$	Transition angle (included) (deg)	p_{r_0} (bars hydrogen)	m_s (gm)	$\dfrac{G}{m_s}$	m_p (kgm)	u_p (m/s)	U (km/s)
Ames	5.6	273	5.82	115	82.90	1.67	49.60	14.6	2.76	0.0453	15.60	0.10	–	11.30
	[2]5.6	273	5.82	115	82.90	1.67	49.60	14.6	2.76	[3].0756	9.35	0.10	–	9.84
	5.6	264	8.04	93	184.50	4.06	45.40	11.8	1.59	0.0520	16.76	0.34	–	10.84
	5.6	264	8.04	93	184.50	4.06	45.40	11.8	1.03	0.0568	10.03	0.34	–	10.41
	7.1	357	5.53	273	129.20	36.80	3.51	8.6	0.50	0.1625	3.36	0.15	817	9.24
	7.1	357	5.53	273	129.20	36.80	3.51	8.6	1.03	0.5016	2.23	0.15	983	7.35
	12.7	300	5.07	246	105.00	27.50	3.82	8.9	0.69	0.9407	3.12	0.89	823	9.46
	12.7	300	5.07	246	105.00	27.50	3.82	8.C	1.03	3.170	1.39	0.89	879	6.72
	25.4	288	4.00	244	54.38	30.50	1.78	8.6	2.07	7.418	4.65	5.58	763	8.44
	38.1	256	4.15	208	58.30	31.90	1.83	3.6	2.07	15.205	7.30	22.70	786	9.07
	38.1	256	4.15	208	58.30	31.90	1.83	8.6	2.07	27.412	4.05	22.70	789	8.50
CARDE	38.1	312	2.67	95	5.77	6.34	0.91	14.2	[4]23.79	[3]50.0	6.17	9.08	869	5.21
	38.1	312	2.67	40	2.45	3.10	0.79	14.2	[4]59.65	[3]72.0	4.55	9.08	731	4.57
	101.6	207	2.67	41	3.10	6.60	0.47	33.4	[4]56.55	[3]1251.0	3.95	90.80	716	4.57
Douglas	7.6	200	5.13	182	124.00	3.57	34.70	11.8	1.72	0.21	5.86	0.30	731	8.84
	7.6	200	5.13	182	124.00	3.57	34.70	11.8	2.41	0.84	2.05	0.30	610	7.01
	12.7	200	4.00	120	40.15	4.64	8.65	3.6	3.45	1.00	3.69	0.40	762	9.14
	12.7	200	4.00	120	40.15	4.64	8.65	3.6	4.14	4 00	1.11	0.40	610	6.10
	19.1	240	4.67	100	43.60	10.00	4.36	6 6	6.90	[3]10.00	3.24	4.50	671	7.62
	19.1	240	4.67	100	43.60	10.00	4.36	6.6	9.66	14.00	3.24	4.50	610	6.40
	31.8	144	2.80	100	15.75	10.00	1.57	5.4	6.90	10.00	2.42	4.50	671	7.92
	31.8	144	2.80	100	15.75	10.00	1.57	5.4	9.66	[3]25.00	1.29	6.00	610	7.31
GM	5.6	200	4.53	145	67.60	1.70	39.80	7.5	4.00	0.0533	11.61	0.10	1050	10.80
	5.6	200	4.53	145	67.60	1.70	39.80	7.5	–	0.0322	–	–	–	10.30
	20.0	380	4.45	148	34.40	7.97	4.32	7.8	–	3.73	–	–	–	9.90
	20.0	380	4.45	148	34.40	7.97	4.32	7.8	4.70	[3]11.04	2.90	10.40	522	7.50
	60.0	332	4.23	141	28.10	8.27	3.40	7.7	–	87.0	–	–	–	8.90
	60.0	382	4.23	141	28.10	8.27	3.40	7.7	6.20	[3]500.0	1.89	252.00	436	5.90
NOL	12.7	480	4.00	60	8.06	1.02	7.90	41.2	28.62	[3]1 30	11.34	0.20	–	8.17
	12.7	480	4.00	60	8.06	1.02	7.90	41.2	28.62	[3]).66	8.88	0.20	–	7.30
	12.7	168	2.50	134	12.50	1.79	6.98	14.3	6.55	0.90	2.04	0.20	–	7.62
	12.7	168	2.50	134	12.50	1.79	6.98	14.3	7.93	[3]4.00	0.56	0.30	–	6.10
	32.0	338	3.17	128	12.30	21.70	0.57	8.7	20.00	[3]73.0	2.42	11.00	671	5.55
	32.0	338	3.17	128	12.30	21.70	0.57	8.7	21.72	[3]95.0	2.02	11.00	661	5.18
	50.8	480	4.00	129	17.50	17.60	0.99	9.5	14.83	[3]82.0	13.47	45.40	792	6.89
	50.8	480	4.00	129	17.50	17.60	0.99	9.5	18.28	[3]220.0	6.19	143.01	610	6.40
	50.8	480	4.00	89	17.50	17.60	0.99	9.5	18.28	[3]108.0	8.36	52.66	792	7.74
	50.8	480	4.00	89	17.50	17.60	0.99	9.5	28.62	[3]250.0	5.65	102.15	671	6.61
NRL	7.6	160	3.81	68	23.78	7.35	3.23	23.6	15.50	0.41	4.15	0.30	1000	9.20
	7.6	160	3.81	68	23.78	7.35	3.23	23.6	17.10	[3]0.72	2.60	0.35	600	7.00
	21.0	205	3.93	74	21.98	8.80	2.50	62.0	18.00	5.20	9.39	4.09	–	8.00
	21.0	205	3.93	74	21.98	8.80	2.50	62.0	15.10	[3]16.20	2.53	4.09	–	7.00
	63.5	161	3.28	81	19.04	6.66	2.86	3.0	[4]20.00	253.0	4.03	43.00	–	6.16
	63.5	161	3.28	81	19 94	6.66	2.86	3.0	[4]20.00	[3]447.0	2.28	43.00	–	4.85
RARDE	6.4	200	4.00	204	65.40	[5]0.24	269.00	74.0	7.91	0.08	21.51	0.03	1097	9.20
	6.4	200	4.00	204	65.40	[5]0.24	269.00	74.0	13.08	[3]1.36	2.09	0.07	1036	3.05
	25.4	96	5.00	55	71.87	[5]0.37	193.00	180.0	7.93	14.0	21.07	1.61	792	5.18
	25.4	96	5.00	55	71.87	[5]0.37	193.00	180.0	7.93	28.0	10.53	1.62	777	3.66

[1] Facility title and address given in Table 1.1

[2] Rifled launch tube

[3] Saboted model

[4] Helium propellant gas

[5] Helium first-stage driver gas
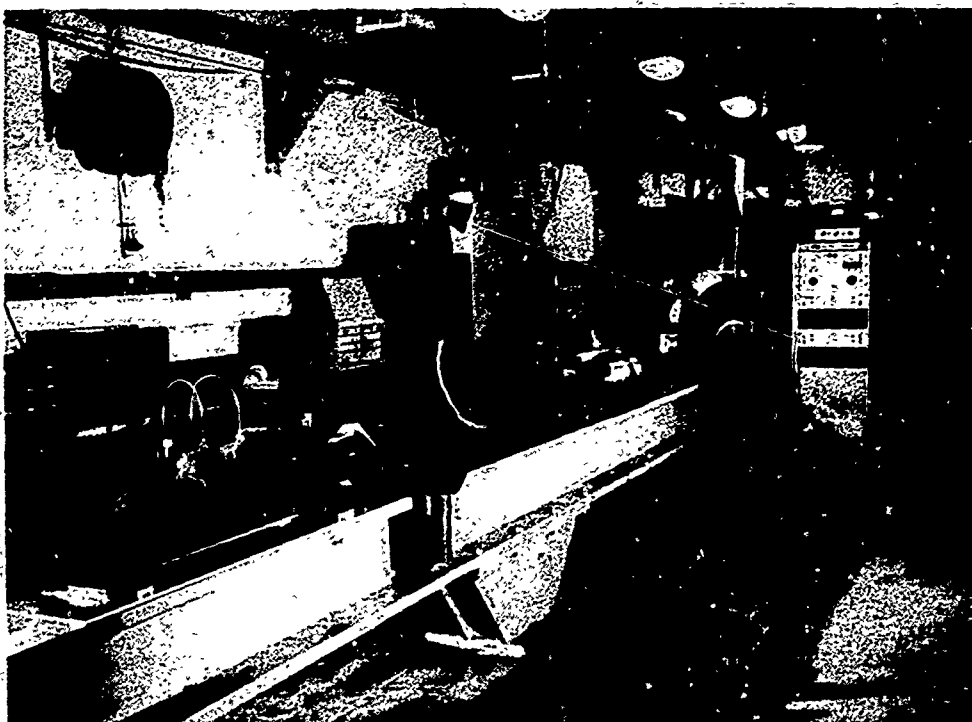
2.1   US Naval Ordnance Laboratory 12.7mm/50.8mm two-stage light gas gun
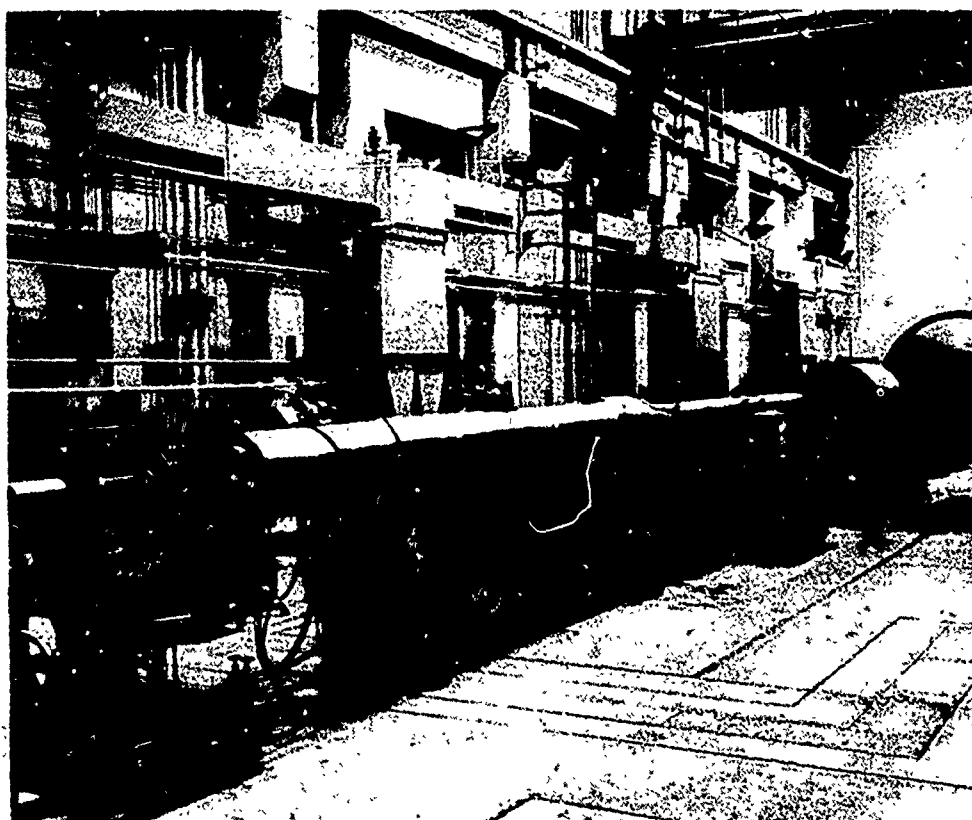
2.2   von Kármán Facility – Arnold Engineering Development Center 63.5mm/203mm two-stage light-gas gun
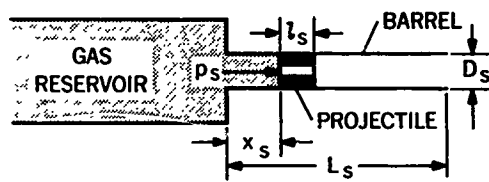
2.3 Simple light-gas gun
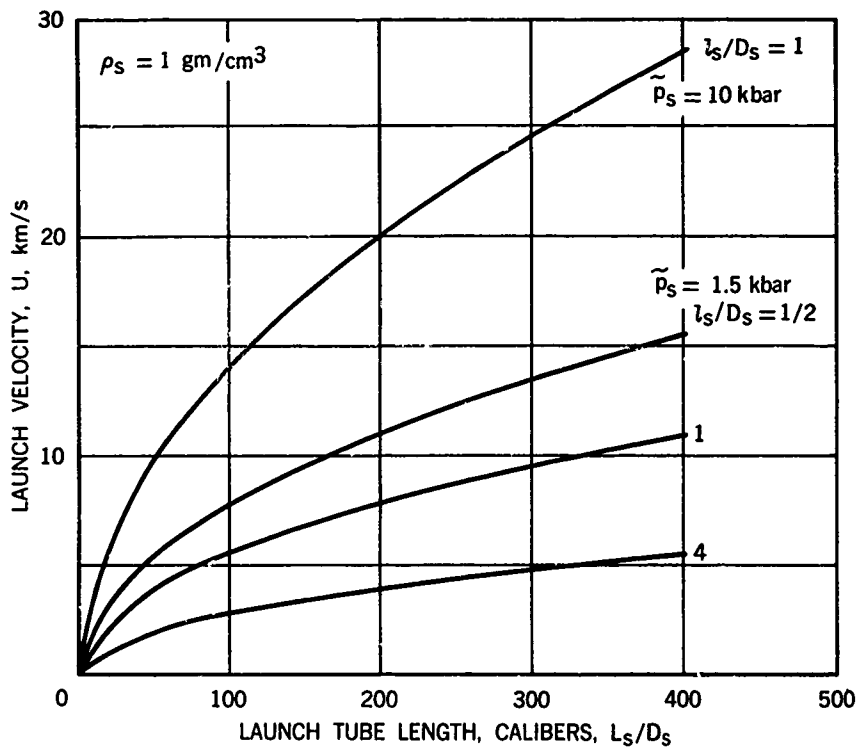
2.4 Maximum launch velocity as a function of launch-tube length for several values of base pressure and model mass
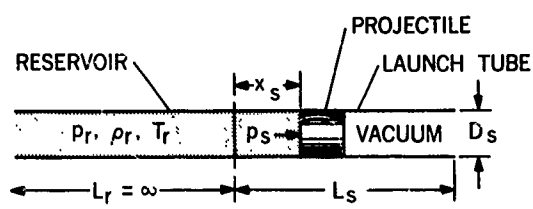
2.5 Simple constant-diameter gun
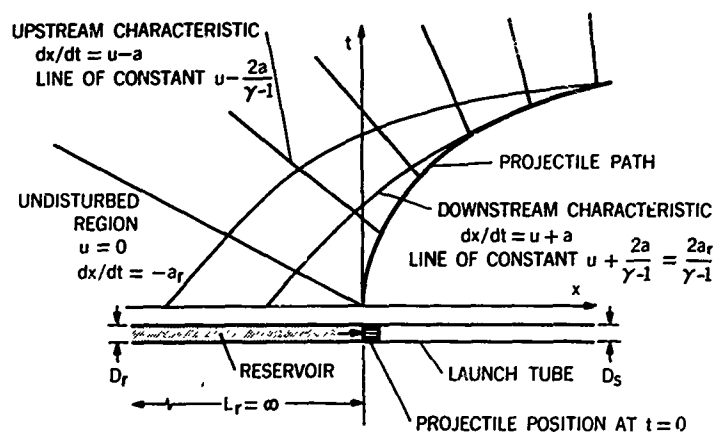
2.6 Acoustic waves in constant-diameter launcher with infinite-length reservoir
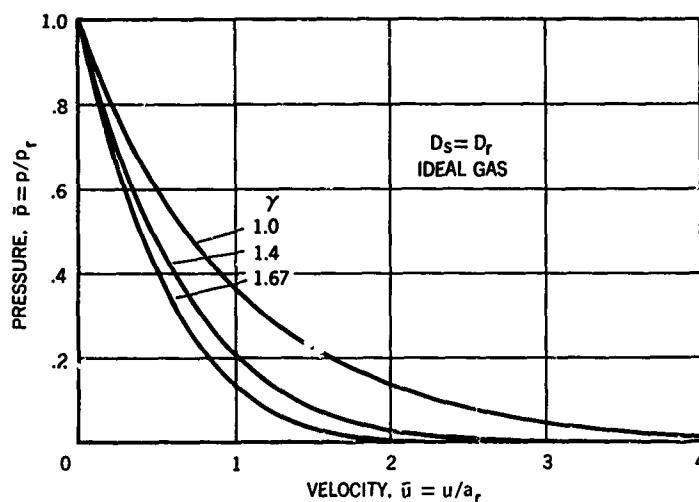
2.7 Variation of nondimensional pressure with velocity during expansion of an ideal gas in an infinitely long tube of constant diameter
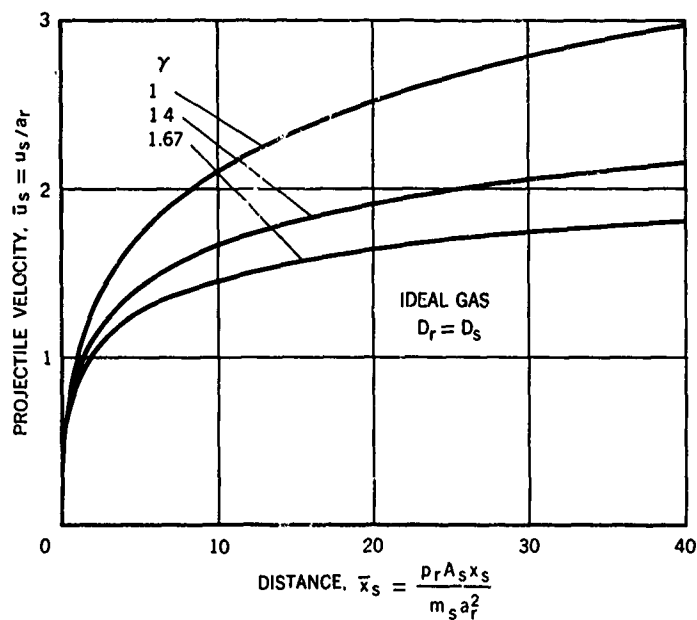
2.8 Variation of nondimensional projectile velocity with distance for the expansion of an ideal gas in an infinitely long tube of constant diameter
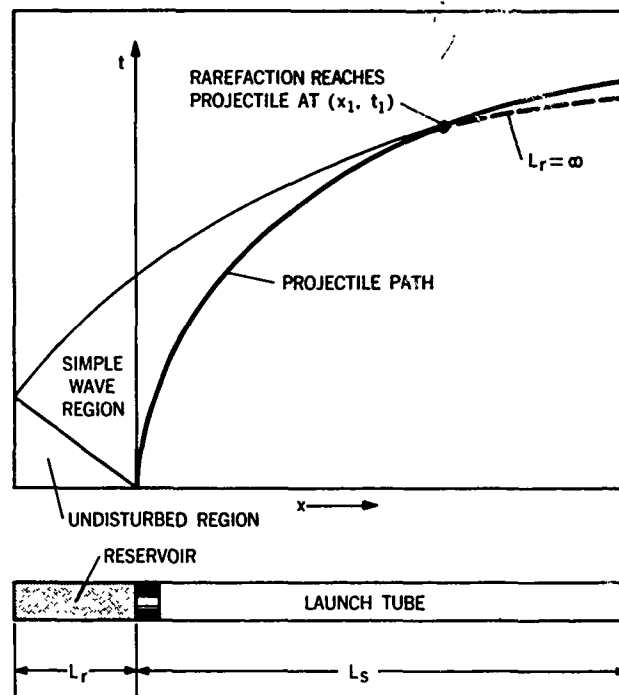
2.9   Acoustic waves in constant-diameter launcher with finite-length reservoir

$$\Gamma_{r_1} = \frac{p_r A_s L_{r_1}}{m_s a_r^2}$$
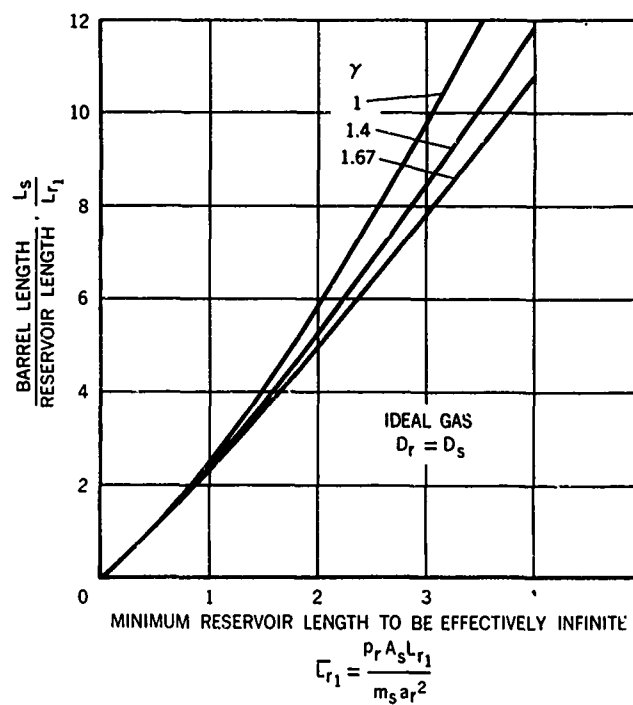
2.10   Minimum reservoir length to be effectively infinite as a function of normalized barrel length
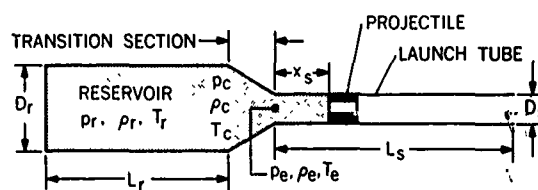
2.11   Simple light-gas gun with chambrage
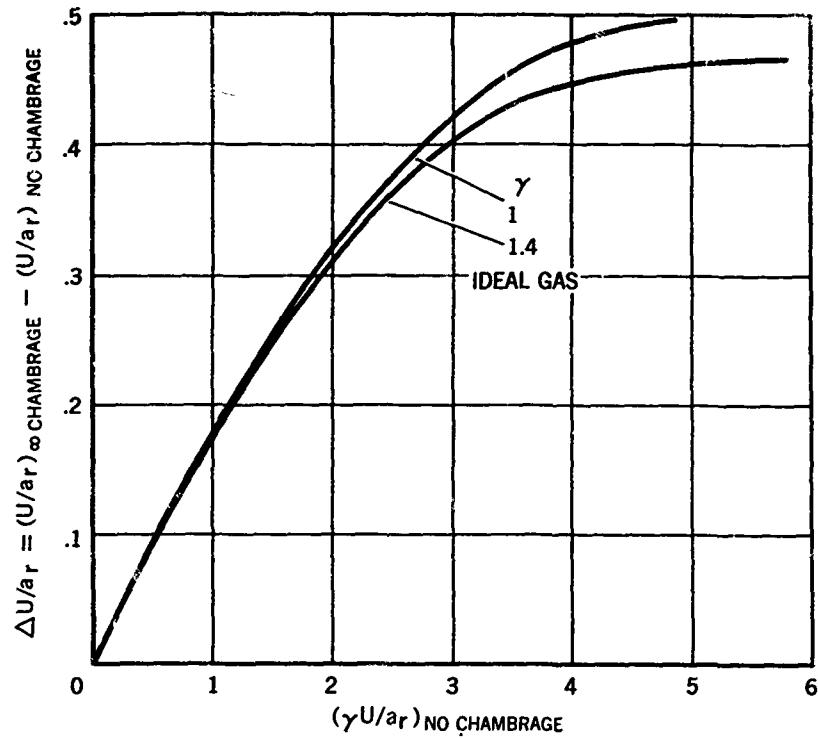
2.12 Increase in velocity due to chambrage for guns having infinite-length reservoirs. (From Seigel, Ref. 2.28)
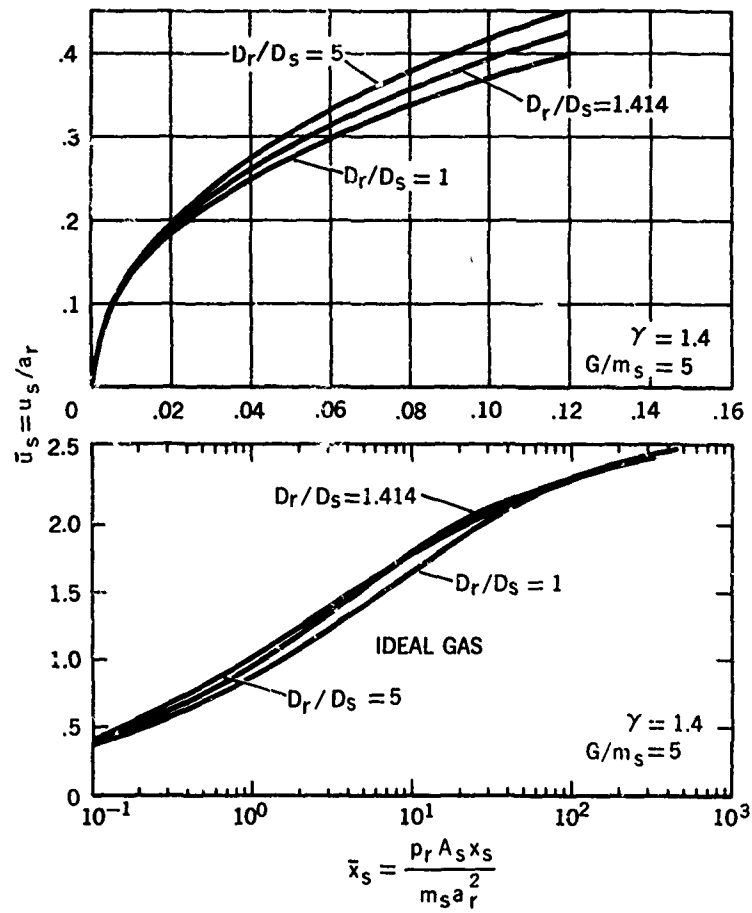
2.13 The effect of chambrage on the calculated performance of a gun with finite-length reservoir, for $\gamma = 1.4$ and gas-mass ratio, $G/m_s = 5$. (Data taken from Seigel, Ref. 2.28)
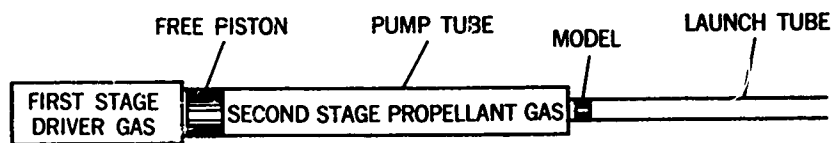
2.14 Two-stage light-gas gun
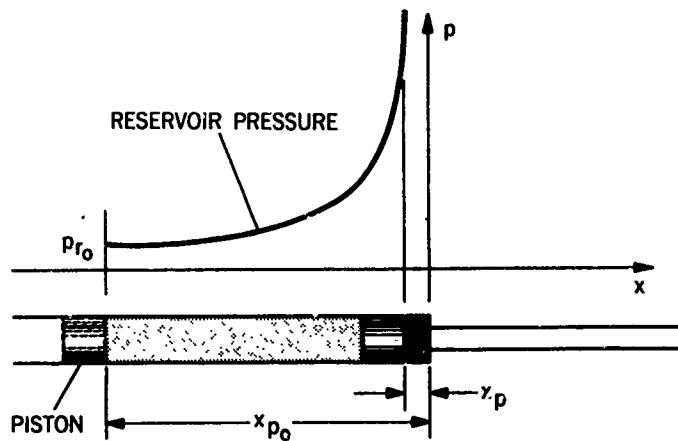
2.15 Reservoir-pressure history with isentropic compression of ideal gas
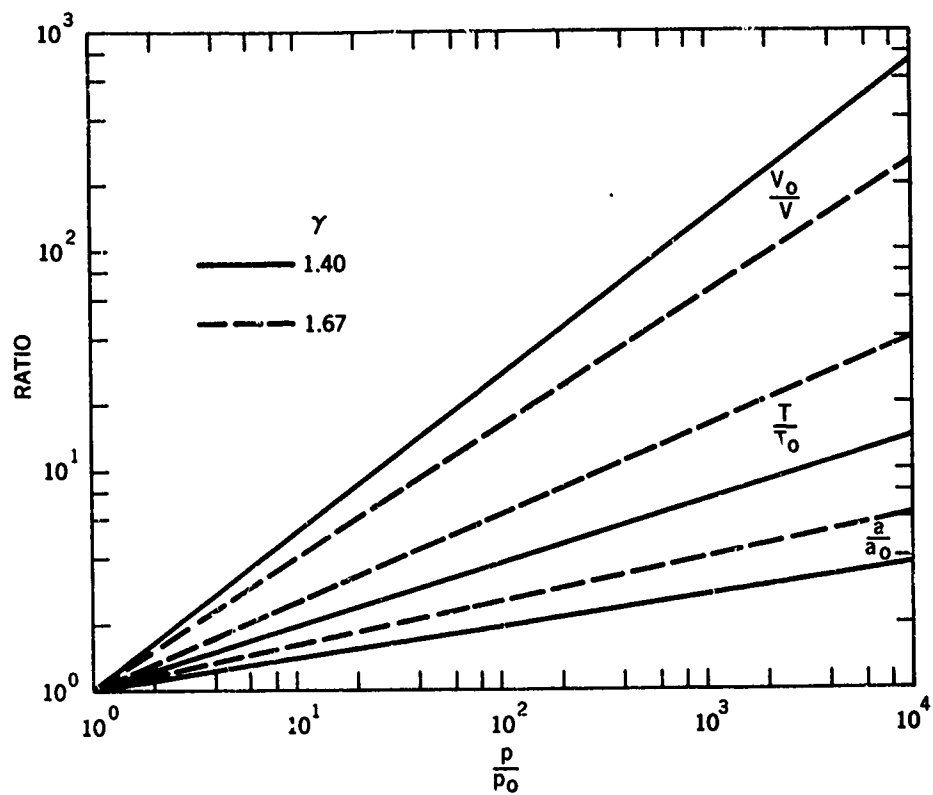
2.16 Variation of thermodynamic properties with isentropic compression
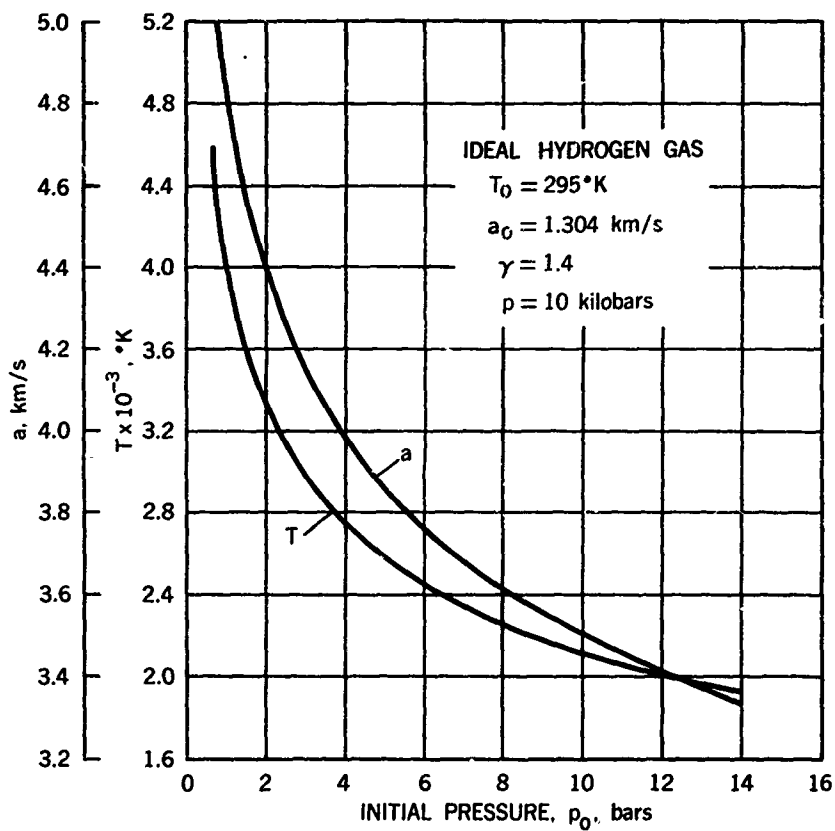
2.17   Isentropic compression of ideal hydrogen gas from initial pressure to 10 kilobars
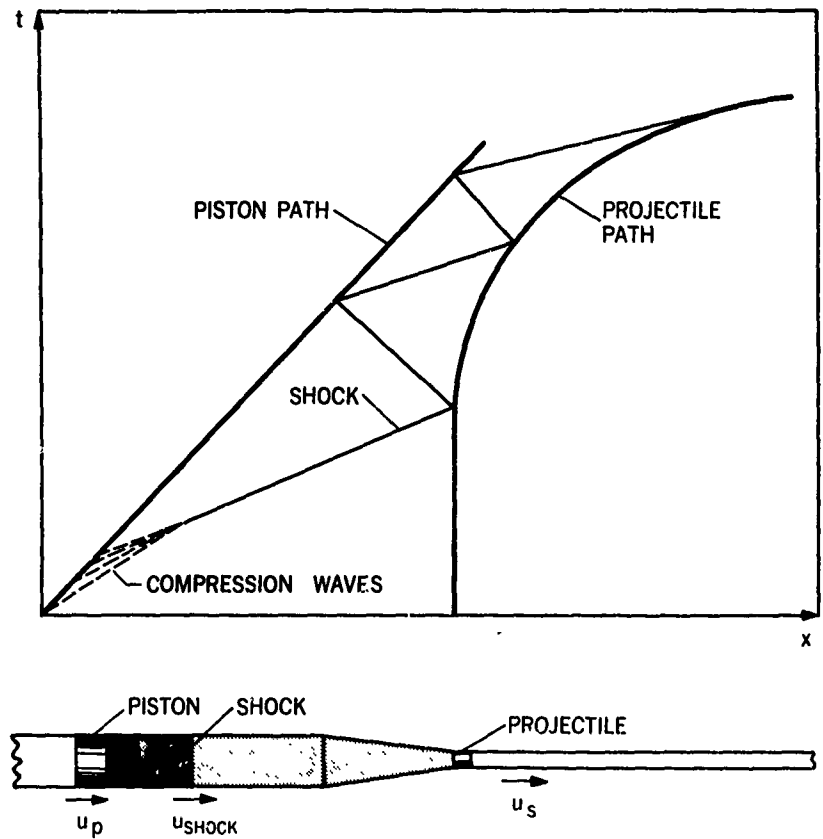
2.18   Acceleration of model by shock compression
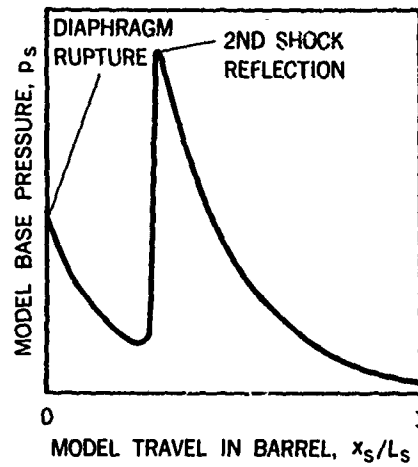
2.19   Example of model base pressure with shock compression

MAXIMUM VELOCITY FOR GIVEN LOADING CONDITIONS: 8.5 km/s
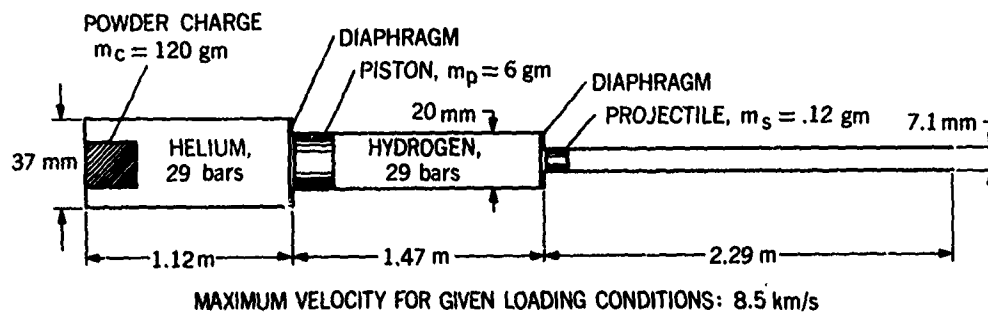
2.20   Ames Research Center 7.1 mm/20 mm two-stage shock-compression gun
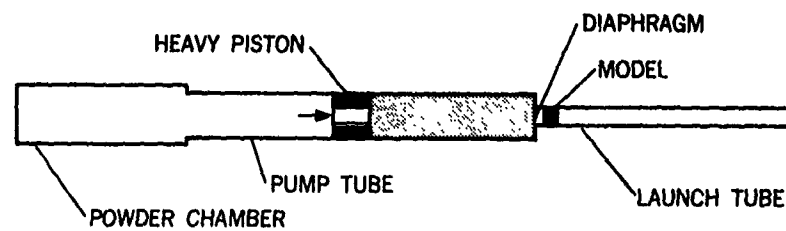
2.21   Two-stage isentropic-compression gun

2.22   Deformable-piston isentropic-compression gun

PISTON   PROJECTILE MASS, m_s

GAS p_s

$u = \alpha t$
$\alpha = $ CONSTANT
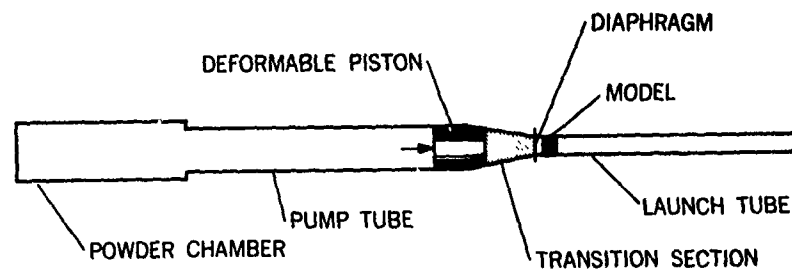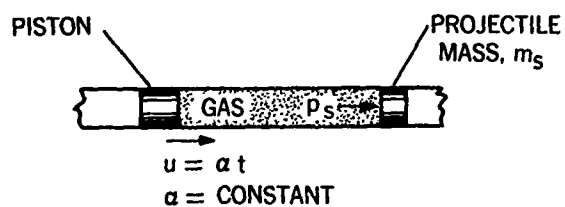
2.23 Uniform acceleration in constant-diameter tube

$\frac{p}{p_s} = f_1(x)$ AT $t = t_1$

$\frac{p}{p_s} = f_2(x)$ AT $t = t_2$

$(x_s - x)_2 = (x_s - x)_1$
$\Delta x_2 = \Delta x_1$
$\frac{p_2}{p_s} = \frac{p_1}{p_s}$, or $p_2 = p_1$

PROJECTILE AT TIME t_1

$p_s \rightarrow$

PROJECTILE AT TIME t_2
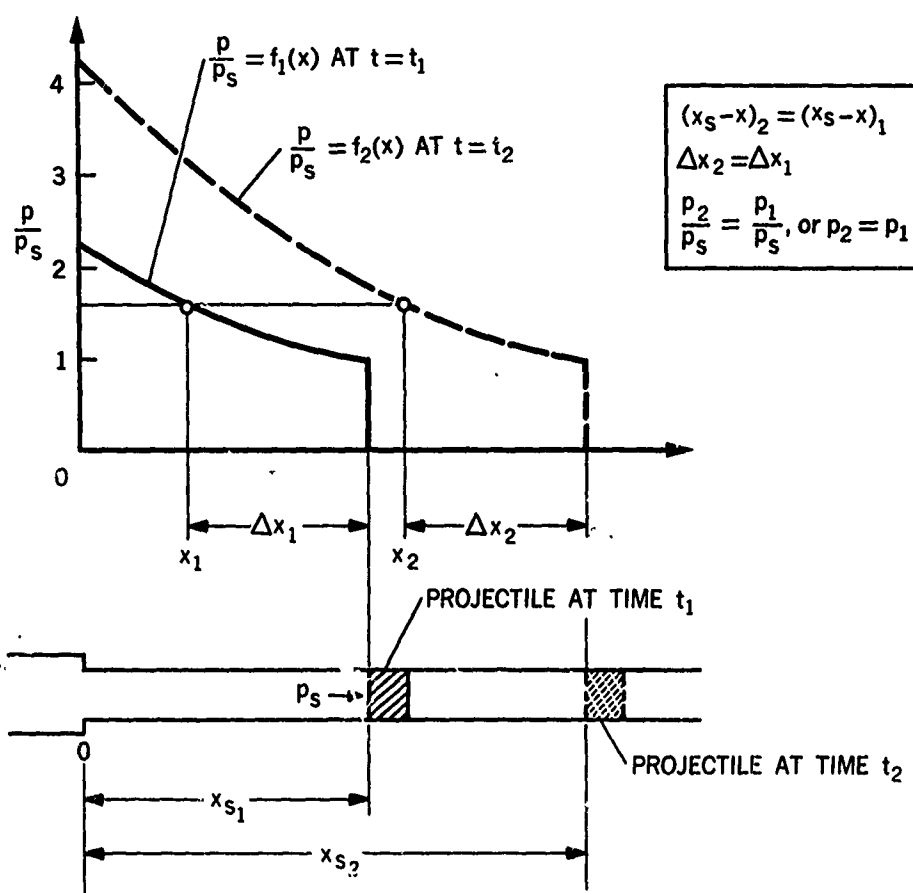
2.24' Constancy, with time, of pressure ratio, p/p_s, at a prescribed distance from the projectile base for constant-base-pressure flow
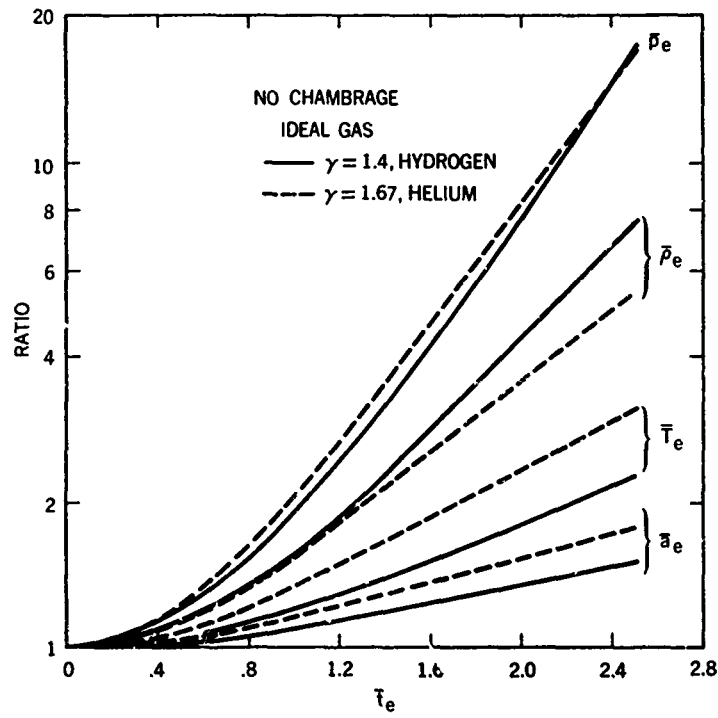
2.25 Gas conditions at entrance to barrel, as a function of time, as required by constant-base-pressure solution with isentropic compression

u + a LINES:

$$\bar{t} = \left\{ \frac{4}{3-\gamma}\left[\bar{x} + \frac{(\gamma-1)}{2(3-\gamma)}\left(\bar{t}_s + \frac{2}{\gamma-1}\right)^2 - \frac{1}{\gamma-1}\right]\right\}^{\frac{1}{2}} - \frac{(\gamma-1)\bar{t}_s + 2}{(3-\gamma)}$$

FOR: $\bar{x} < \bar{x}_s$

LIMITING u−a CHARACTERISTIC:

$$\bar{x} = \frac{1}{2}\left[\sqrt{\frac{3-\gamma}{2}}\ \bar{t}-1\right]^2$$

PROJECTILE PATH:

$$\bar{x}_s = \frac{\bar{t}_s^2}{2}$$

u − a LINES:

$$\bar{x} = \frac{\bar{t}^2}{2} - \frac{\gamma-1}{4}(\bar{t}-\bar{t}_s)^2 - (\bar{t}-\bar{t}_s)$$

FOR: $\bar{t} > \bar{t}_s$

SONIC FLOW PARABOLA: $\bar{t}^2 = \frac{2}{3-\gamma}\left[1-(\gamma-1)\bar{x}\right]$

SONIC FLOW AT BARREL ENTRANCE: $\bar{t} = \sqrt{\frac{2}{3-\gamma}}$
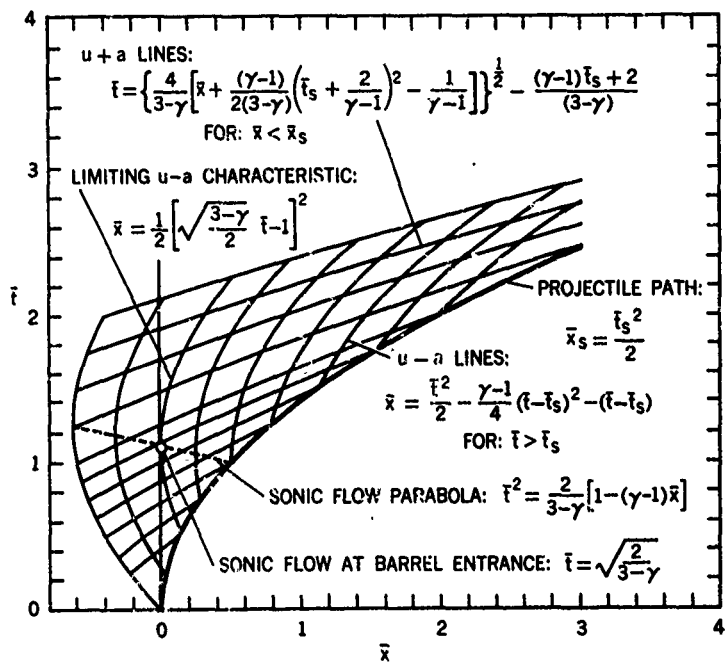
2.26 Characteristic lines for constant-base-pressure flow in an unchambered gun, $\gamma = 1.4$
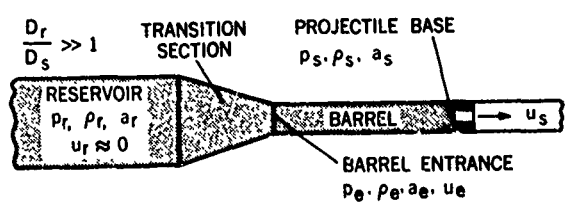
2.27 Flow parameters in chambered gun
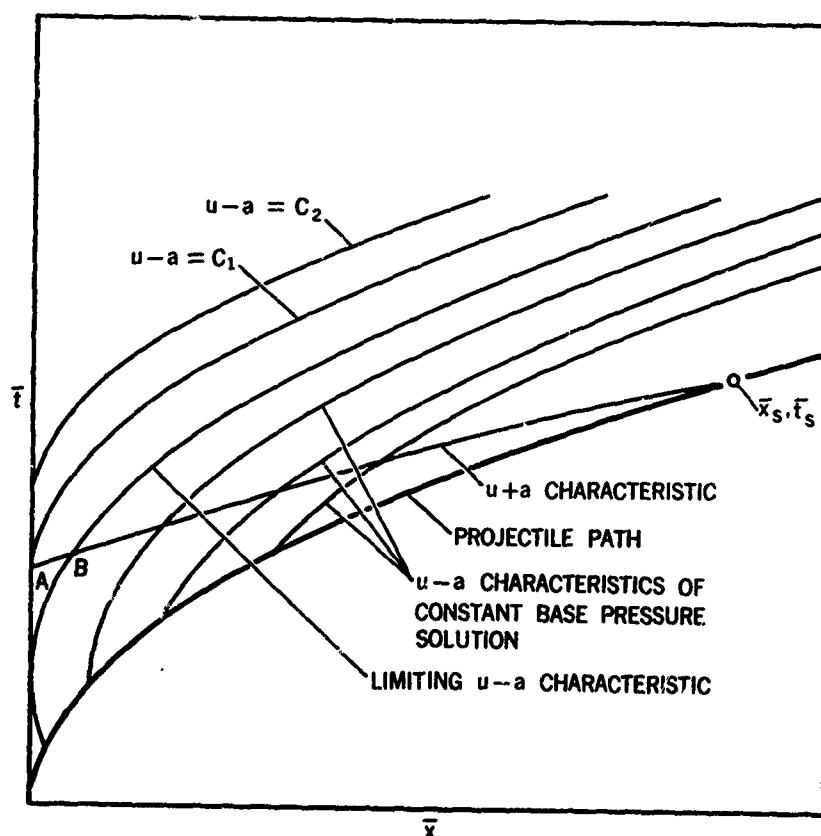
2.28 Characteristic lines for constant-base-pressure flow in a chambered gun
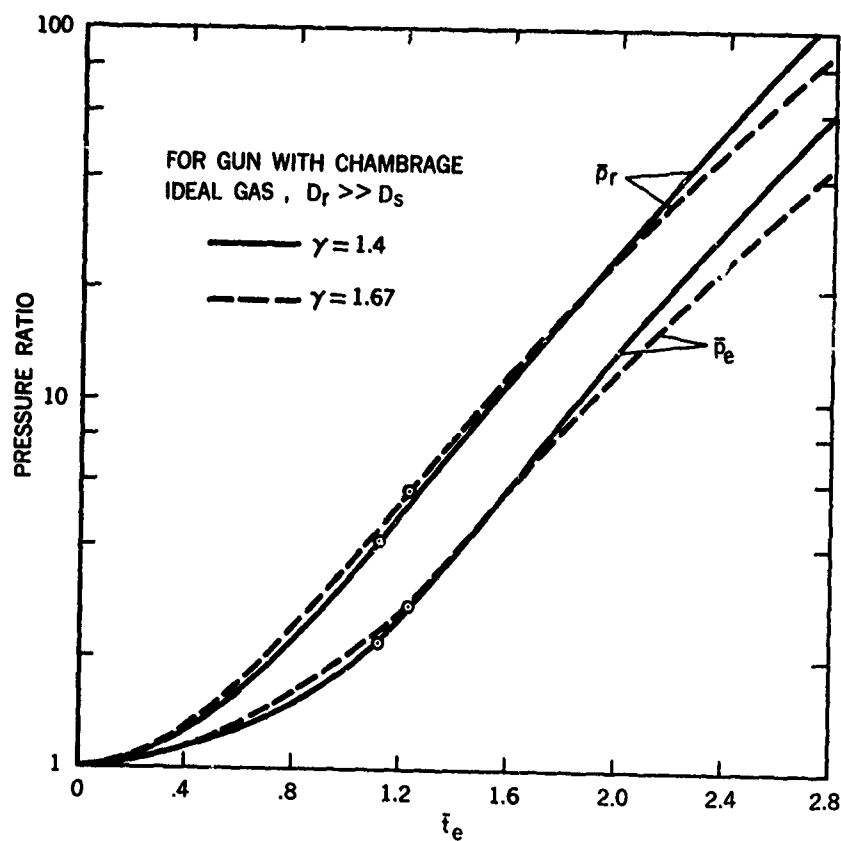
2.29 Pressure ratios in reservoir and at barrel entrance as a function of time, required by constant-base-pressure solution for a chambered gun
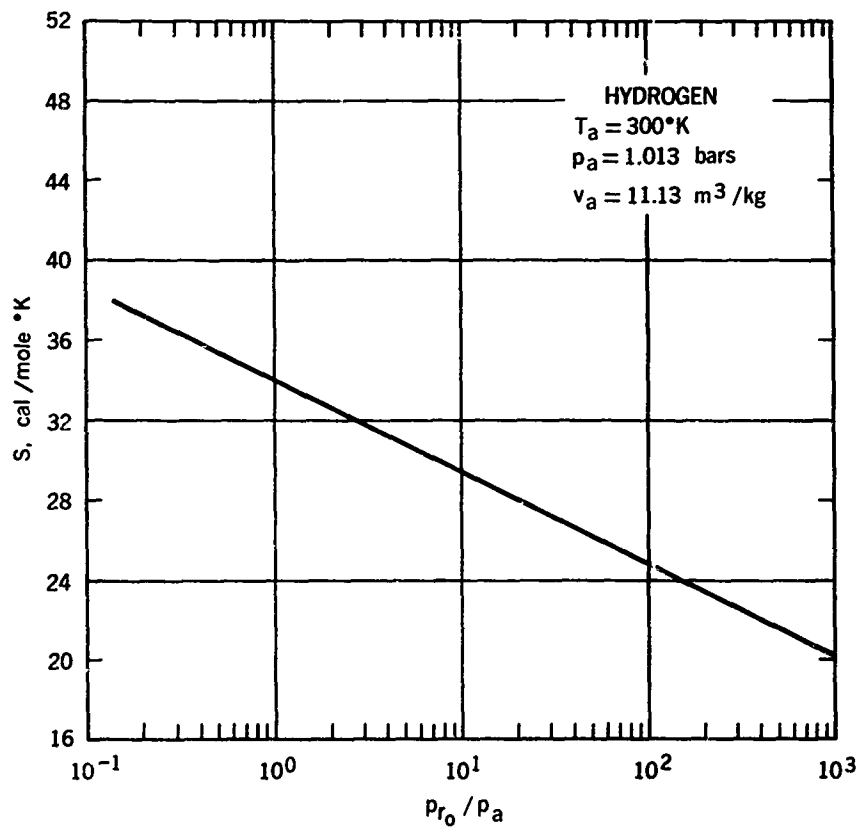
2.30 Entropy as a function of initial reservoir pressure at ambient conditions. (Data from Bixler, Piacesi, and Seigel, US Naval Ordnance Laboratory, Ref. 2.82)
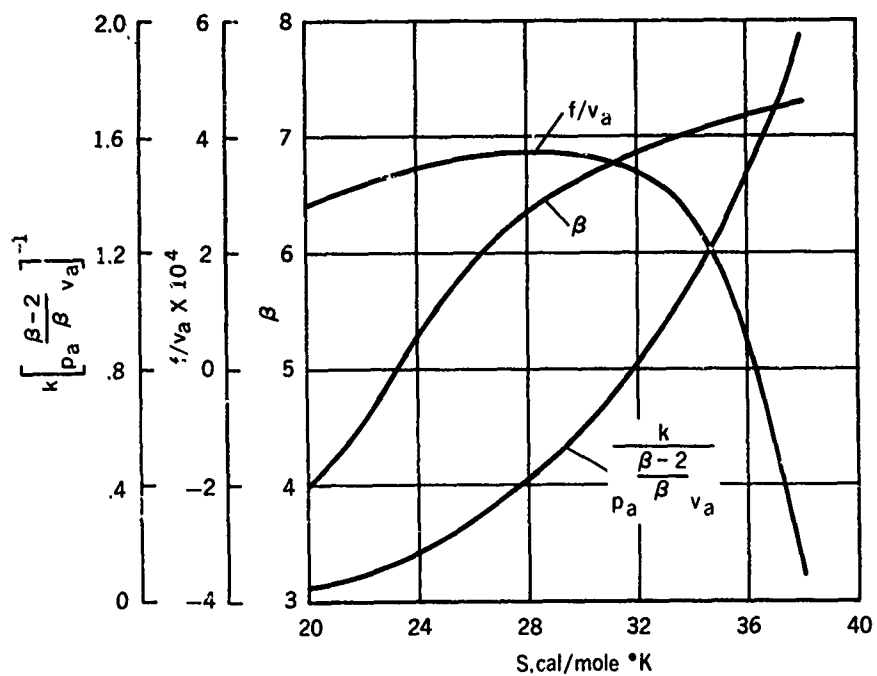
2.31 Constants in entropic equation which define behavior of real hydrogen gas. (From Bixler, Piacesi, and Seigel, US Naval Ordnance Laboratory, Ref. 2.82)
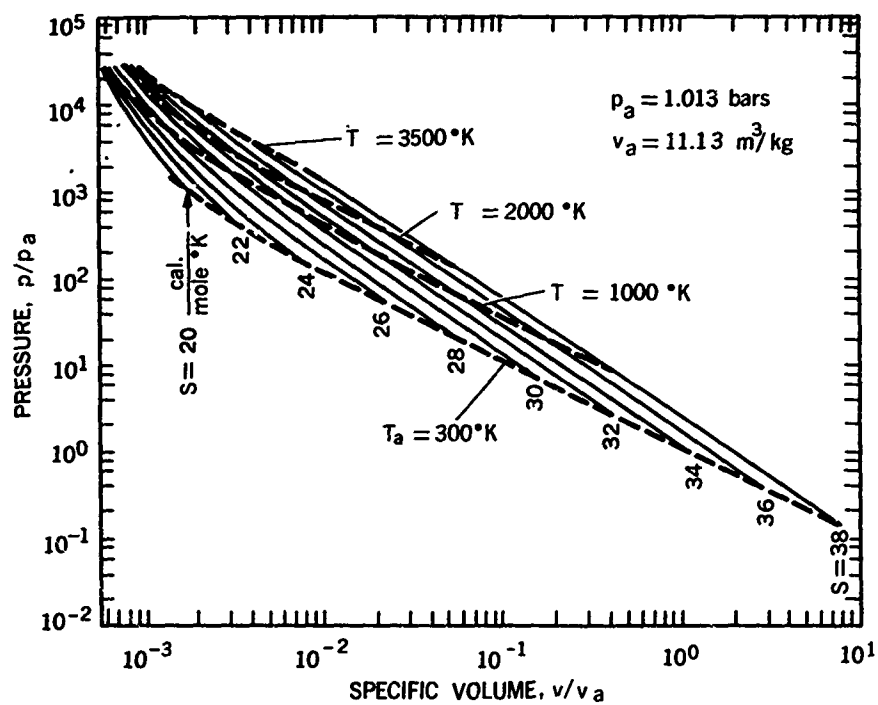
2.32 PV diagram for real hydrogen. (From Bixler, Piacesi, and Seigel, US Naval Ordnance Laboratory, Ref. 2.82)
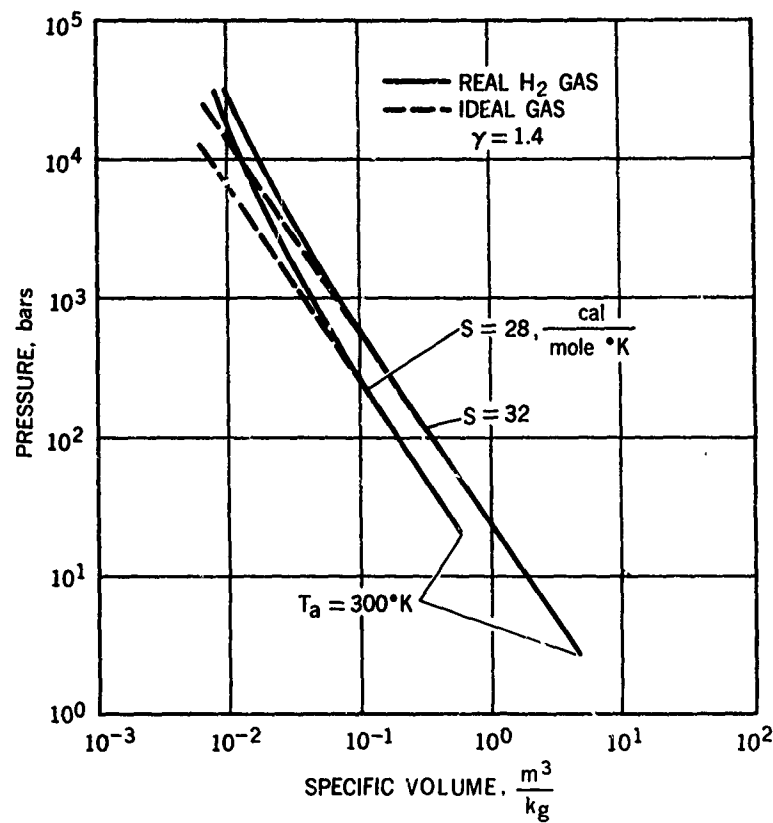
2.33 Comparison of real-gas and ideal-gas isentropes for hydrogen. (From Seigel, Piacesi, and Bixler, US Naval Ordnance Laboratory, Ref. 2.78)
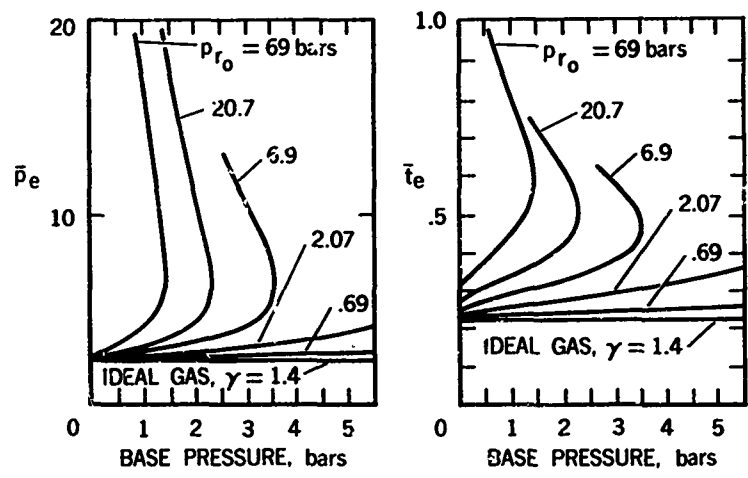
2.34   Pressure and time when flow at entrance of barrel reaches sonic speed; real hydrogen gas. (From Bixler and Seigel, US Naval Ordnance Laboratory, Ref. 2.79)

(a) IDEAL GAS ($\gamma = 1.4$)   (b) REAL HYDROGEN GAS   (c) REAL HYDROGEN GAS SUPERSONIC NEVER ACHIEVED AT $\bar{x} = 0$
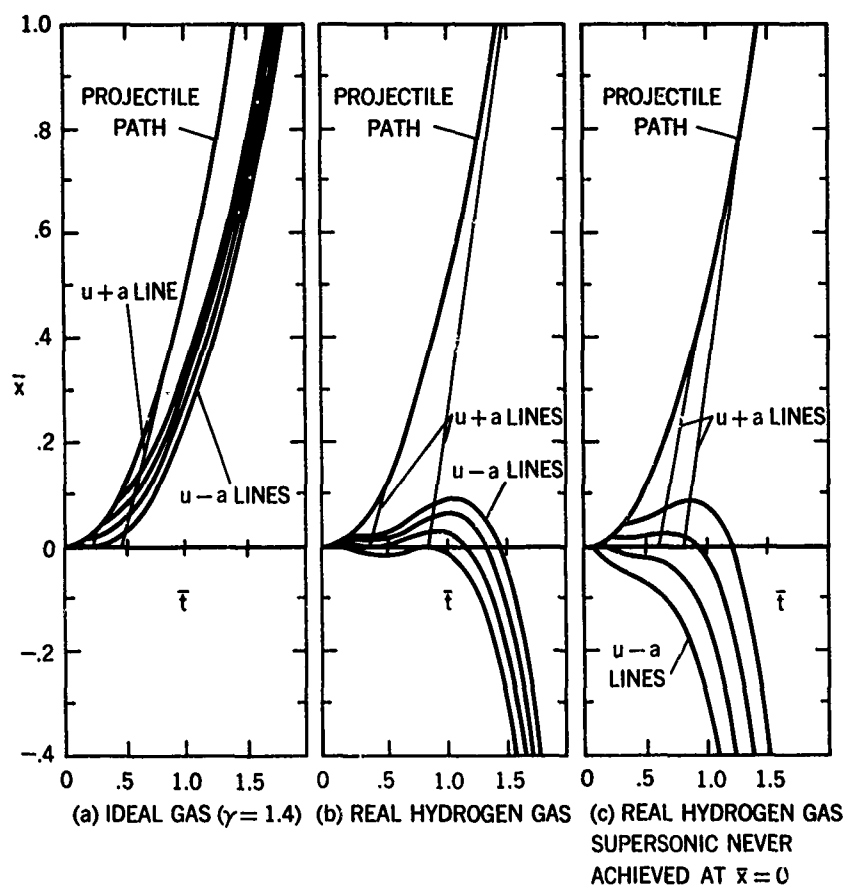
2.35   Characteristics diagram for a constant-base-pressure process in a straight tube. (From Bixler and Seigel, US Naval Ordnance Laboratory, Ref. 2.79)
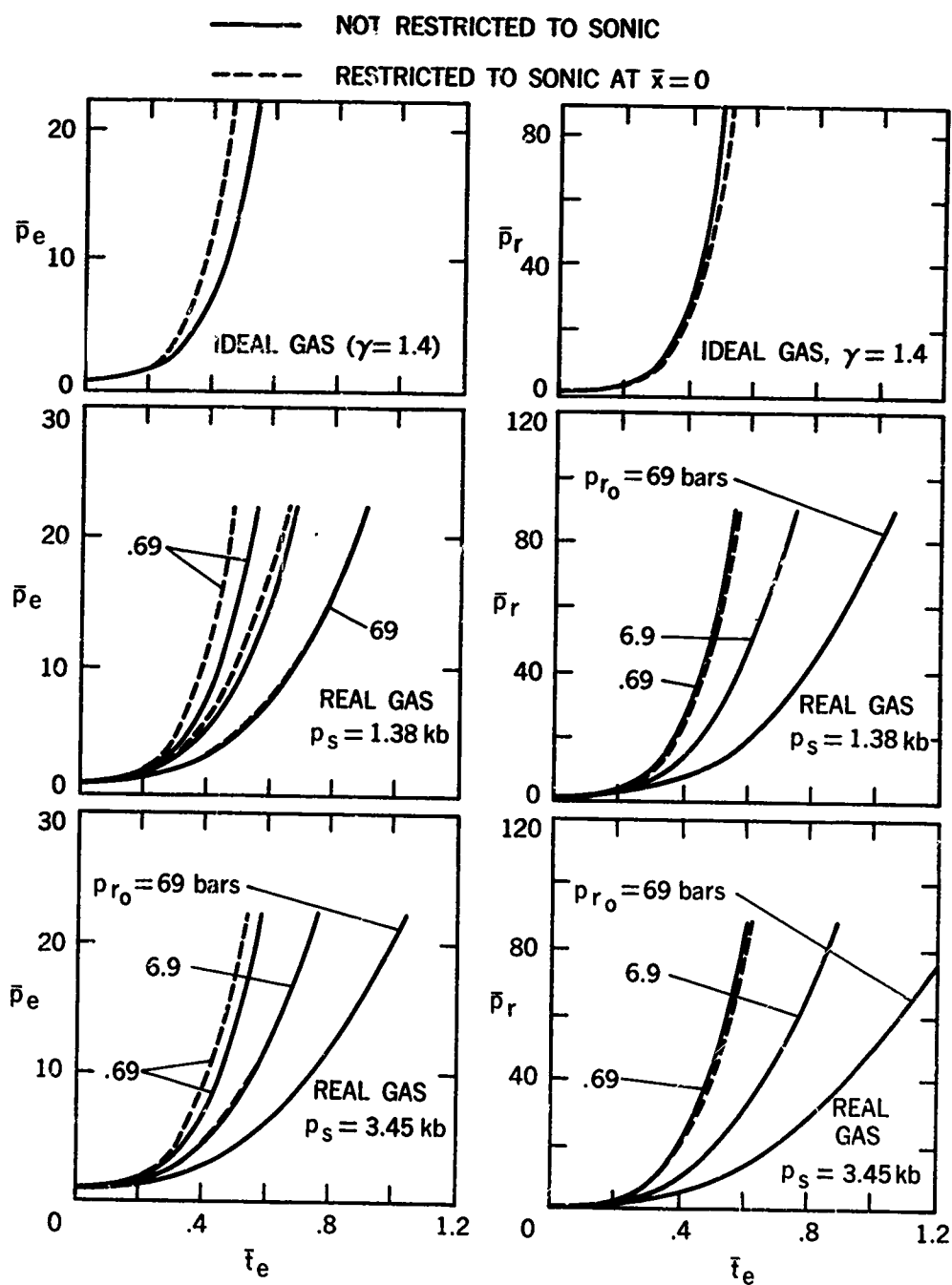
2.36 Pressure histories at the barrel entrance and reservoir in a constant-base-pressure solution for hydrogen gas. (From Bixler and Seigel, US Naval Ordnance Laboratory, Ref. 2.79)
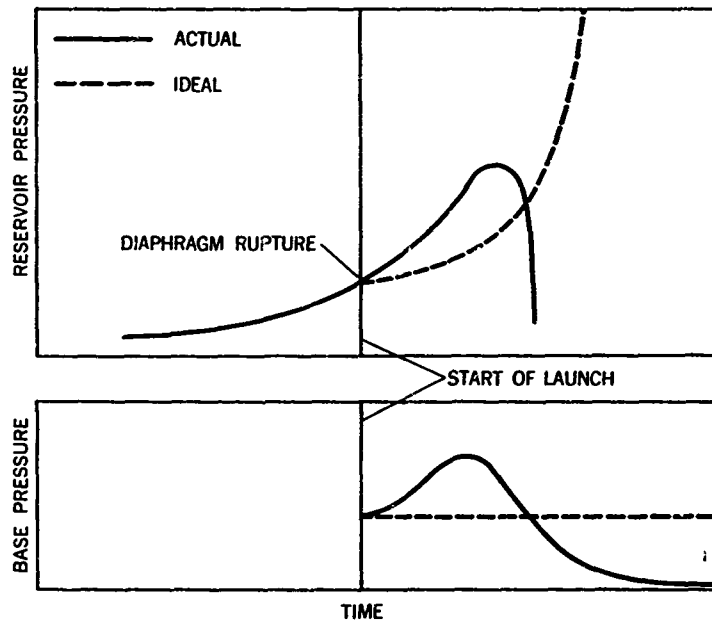
2.37 Example of actual reservoir- and base-pressure variation compared with ideal behavior
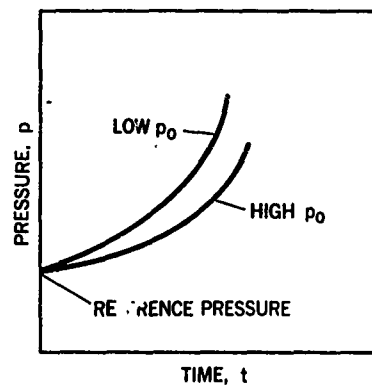
2.38 Effect of initial loading pressure on the rate-of-rise of pressure with isentropic compression, shown from some reference pressure
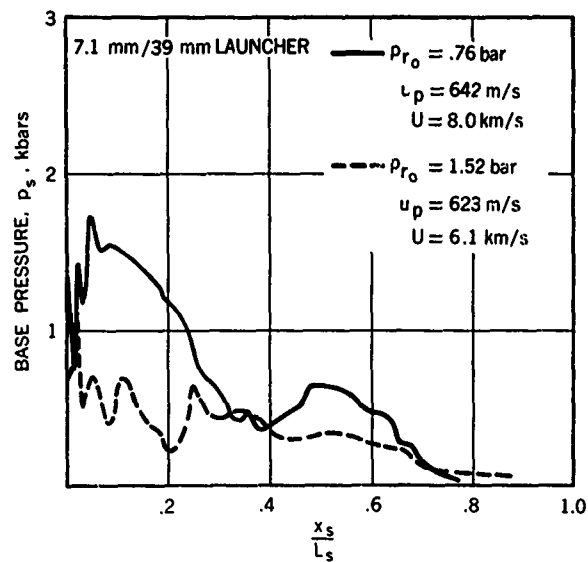
2.39 Effect of initial loading pressure on model base pressure during launch (experimental)
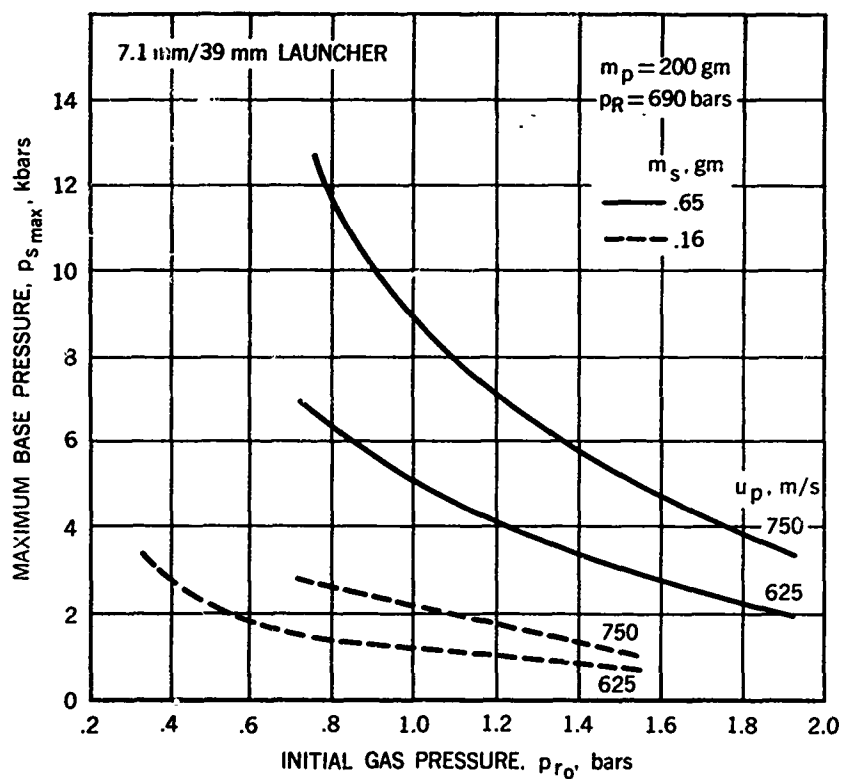
2.40   Effect of initial hydrogen pressure on maximum model base pressure, for two values of piston velocity
and model weight (experimental)
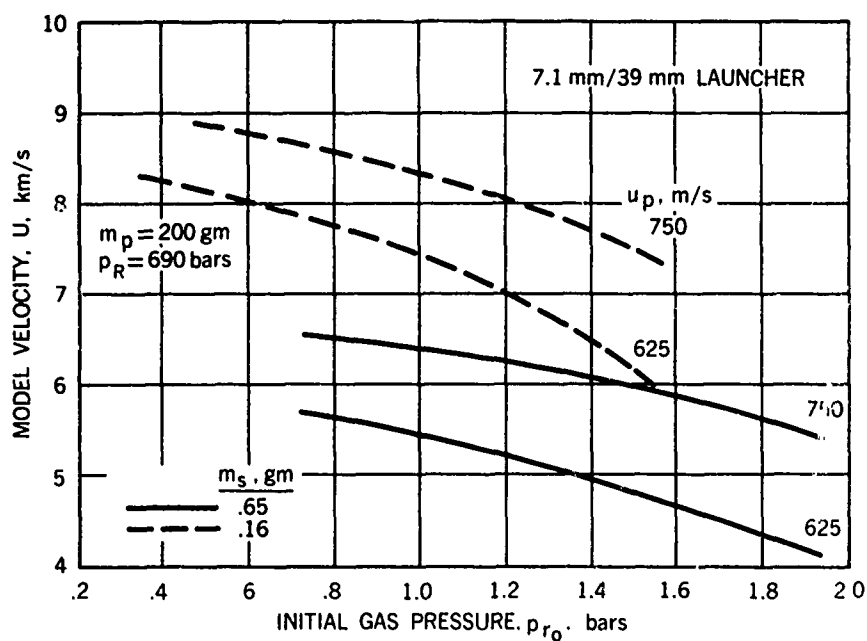
2.41   Variation of model velocity with initial hydrogen pressure, for two values of piston velocity and
model weight (experimental)
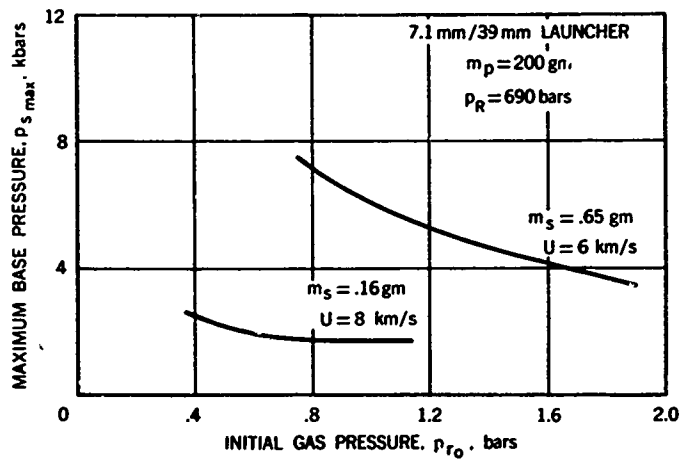
2.42 Effect of initial hydrogen pressure on the resultant maximum base pressure, at constant model velocity
(experimental)
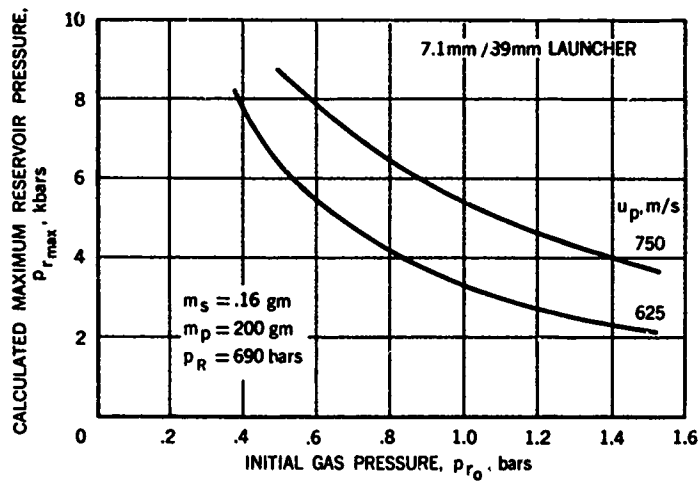
2.43 Variation of calculated maximum reservoir pressure with initial hydrogen pressure, at constant piston
velocity
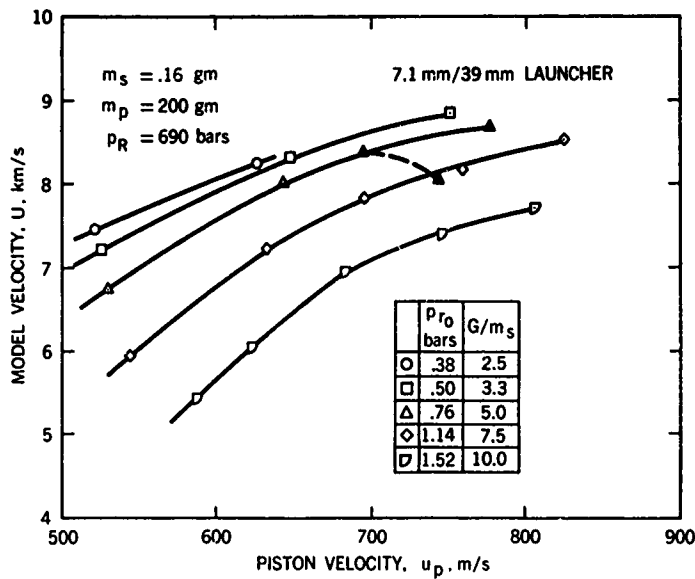
2.44 Variation of model velocity with piston velocity at constant values of initial hydrogen pressure, for a
relatively light model (experimental)
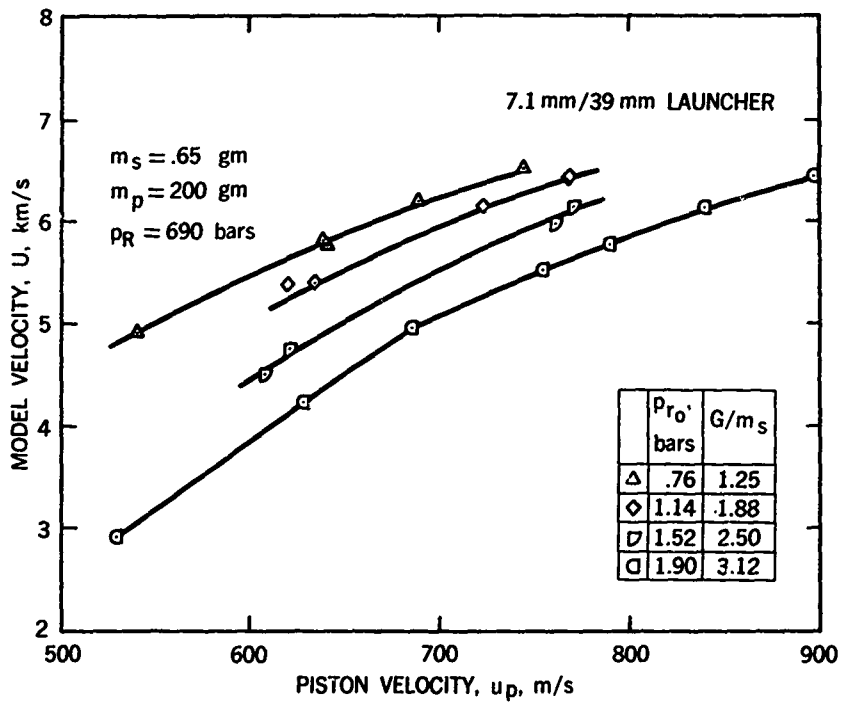
2.45 Variation of model velocity with piston velocity at constant values of initial hydrogen pressure, for a relatively heavy model (experimental)
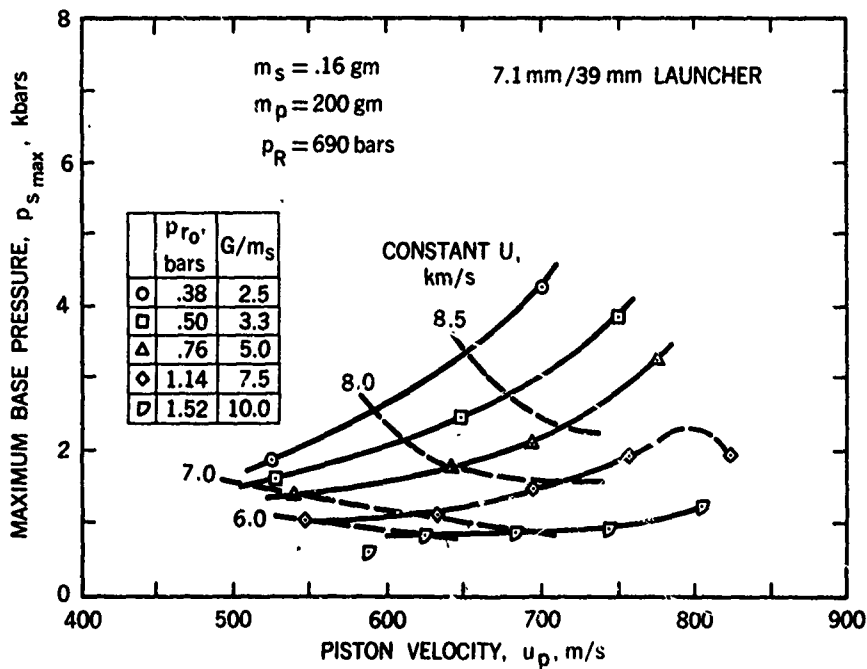
2.46 Variation of maximum base pressure with piston velocity at constant values of initial hydrogen pressure, for a relatively light model (experimental)
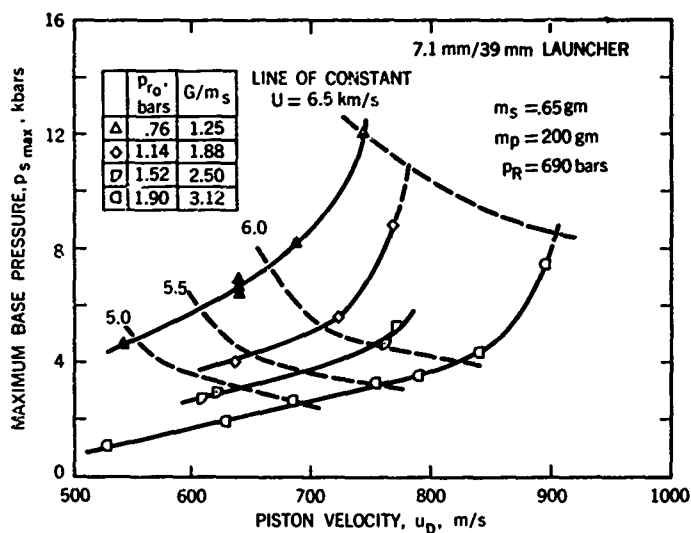
2.47   Variation of maximum base pressure with piston velocity at constant values of initial hydrogen pressure, for a relatively heavy model (experimental)
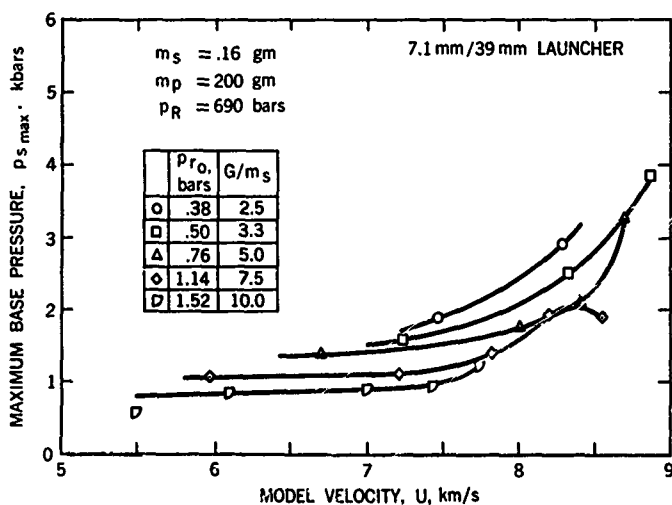
2.48   Variation of maximum base pressure with model velocity at constant values of initial hydrogen pressure, for a relatively light model (experimental)
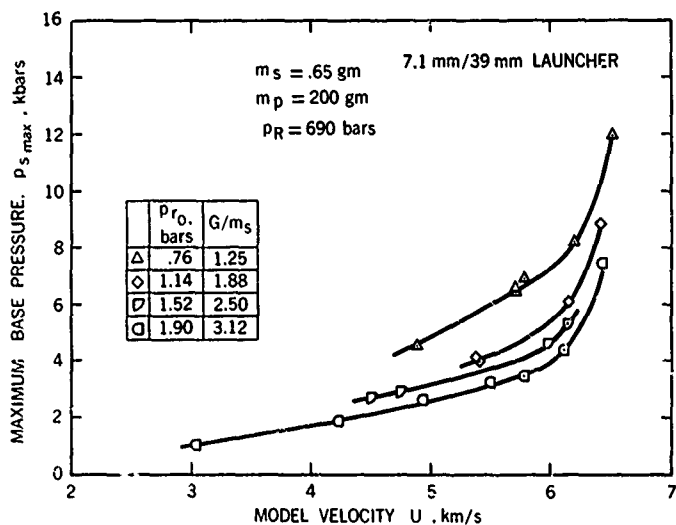
2.49   Variation of maximum base pressure with model velocity at constant values of initial hydrogen pressure, for a relatively heavy model (experimental)
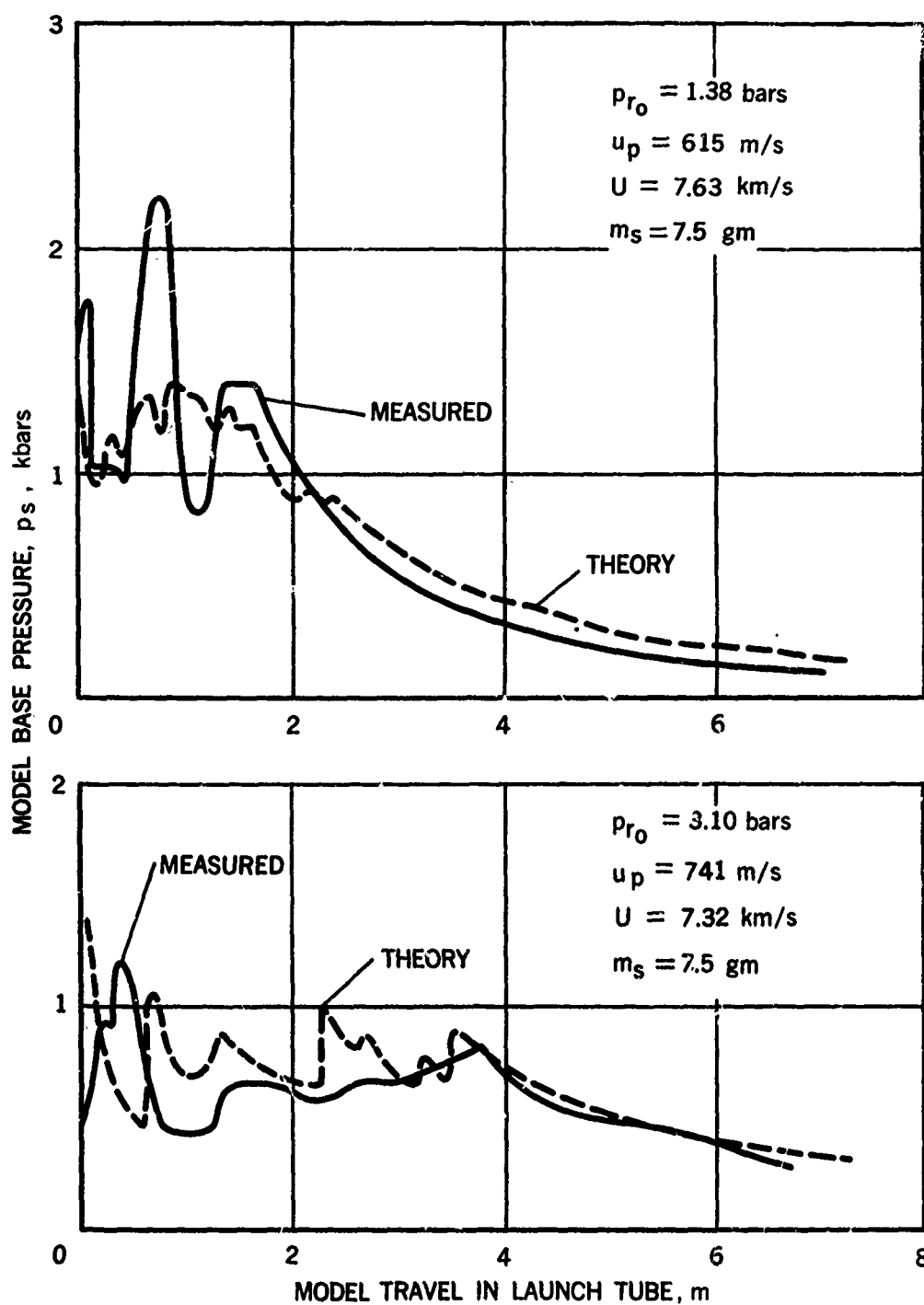
2.50 Example of base-pressure histories for two different initial reservoir pressures and piston velocities which give approximately the same model velocity; 25.4 mm/102 mm launcher
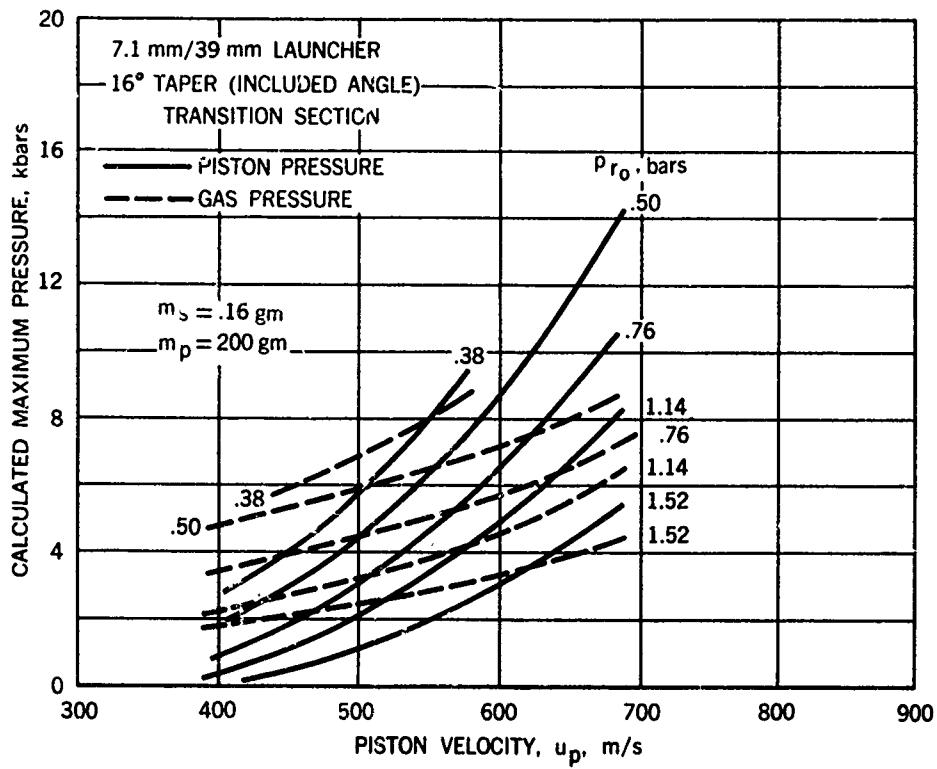
2.51 Calculated maximum pressures exerted on 16°-taper transition section by piston and gas as a function of piston velocity, for constant values of initial hydrogen pressure
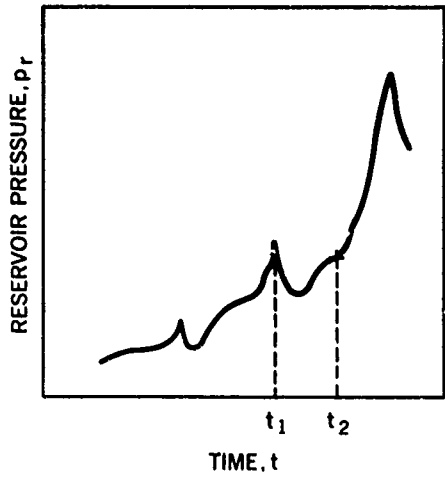
2.52 Example of variation of reservoir pressure during compression
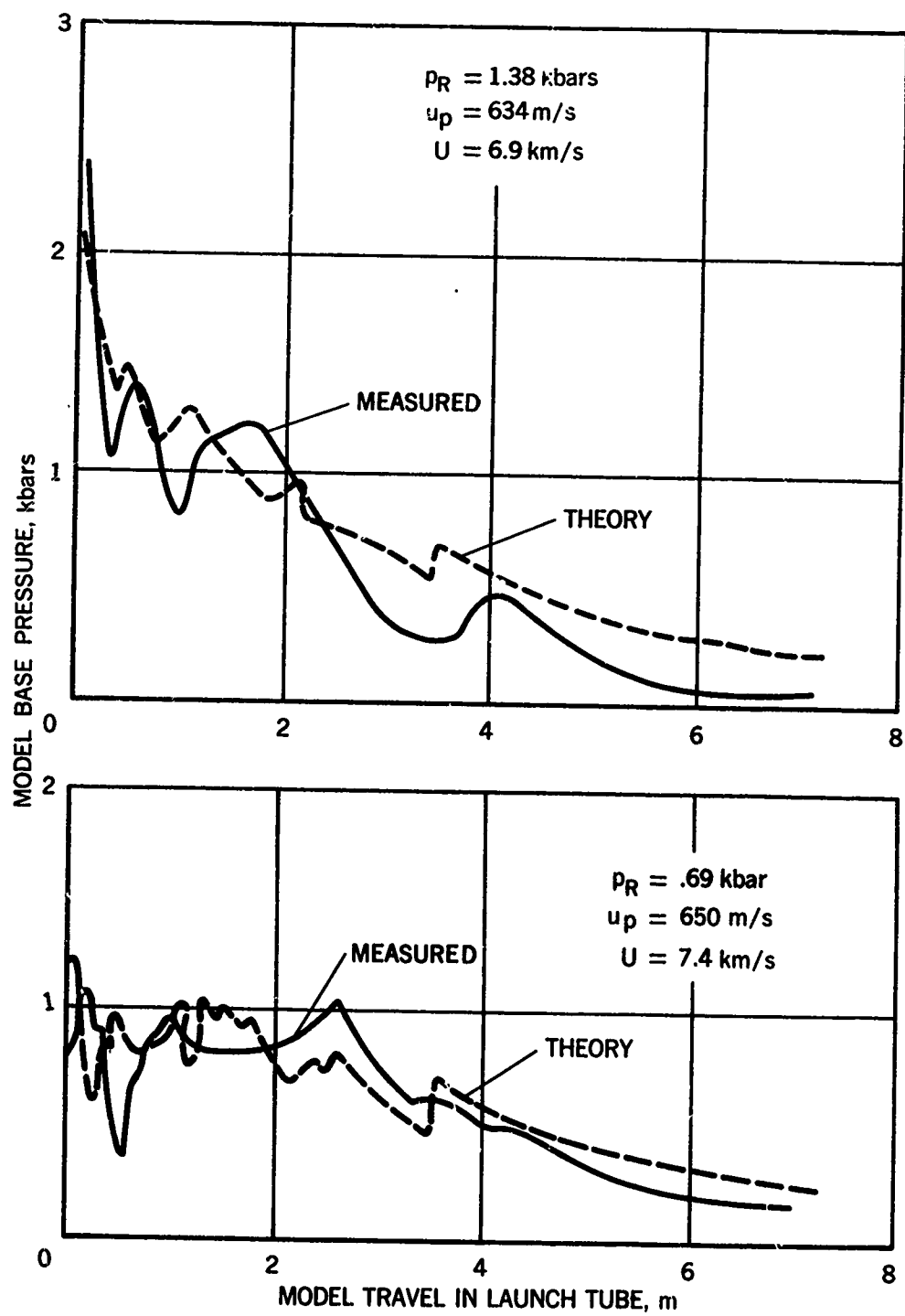
2.53 Effect of model-release pressure on the model-base pressure during launch; 25.4 mm/102 mm launcher
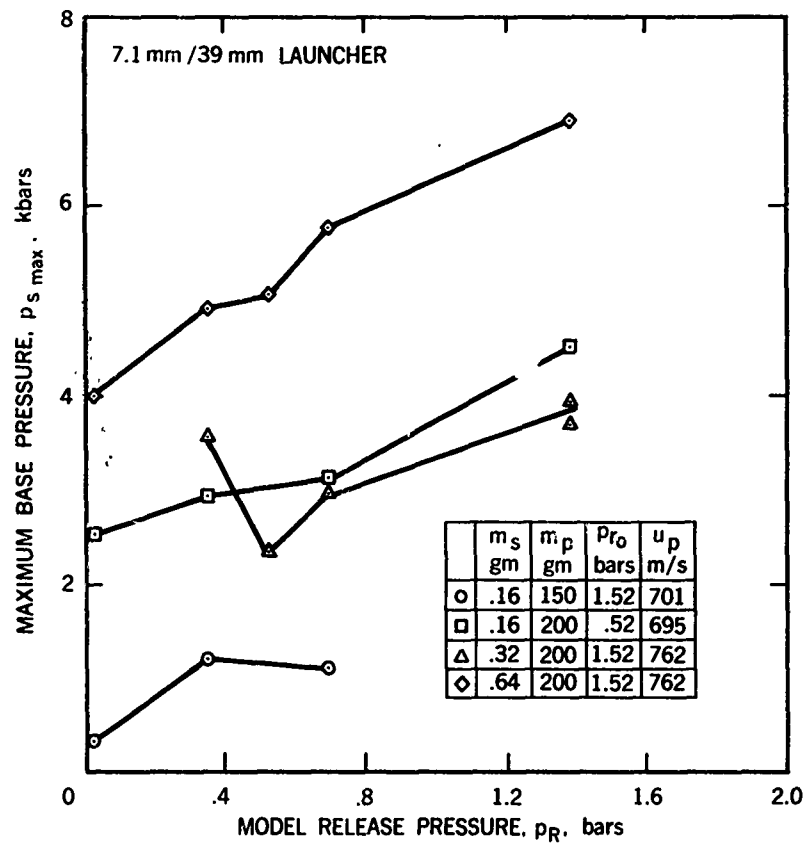
2.54 Effect of model-release pressure on maximum base pressure (experimental)
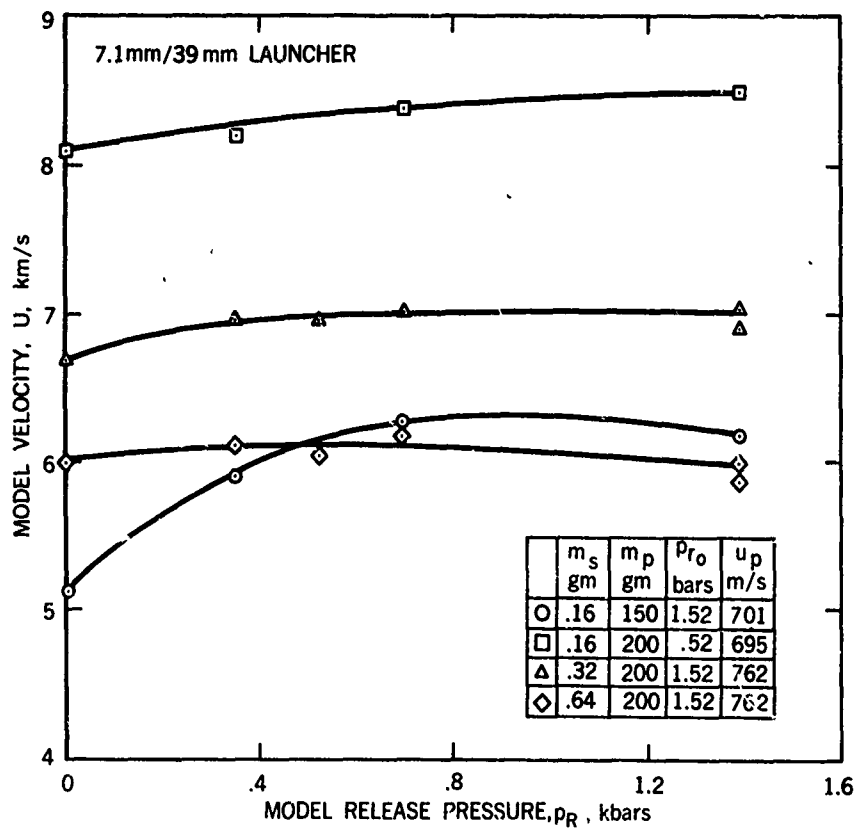
2.55 Effect of model-release pressure on model velocity for a variety of loading conditions (experimental)
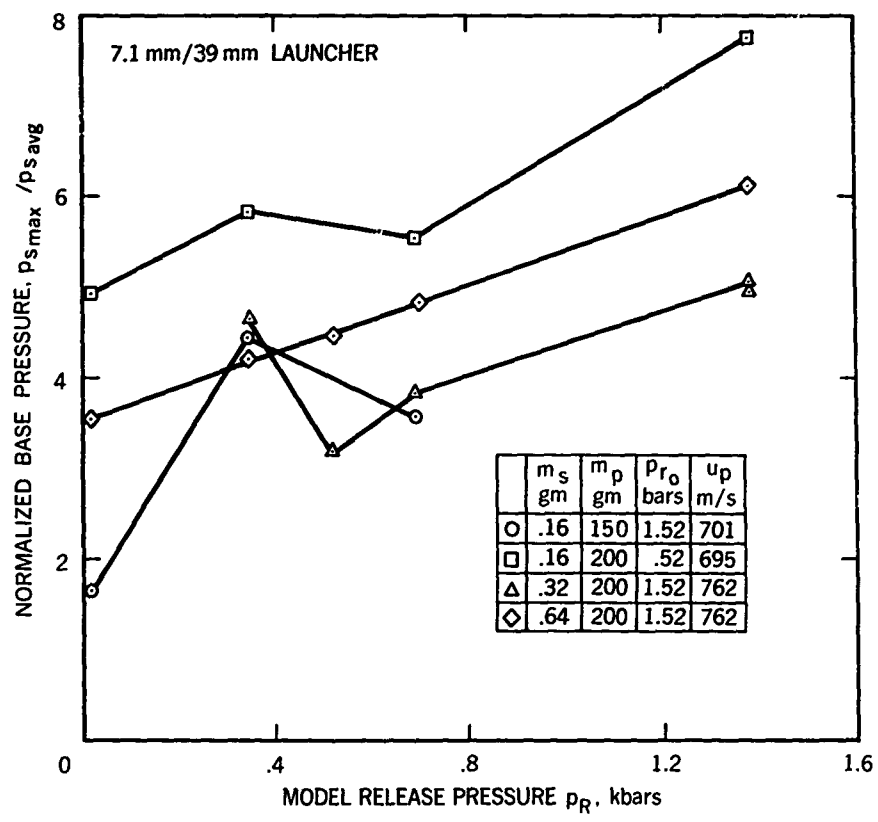
2.56   Effect of model-release pressure on normalized maximum base pressure (experimental)
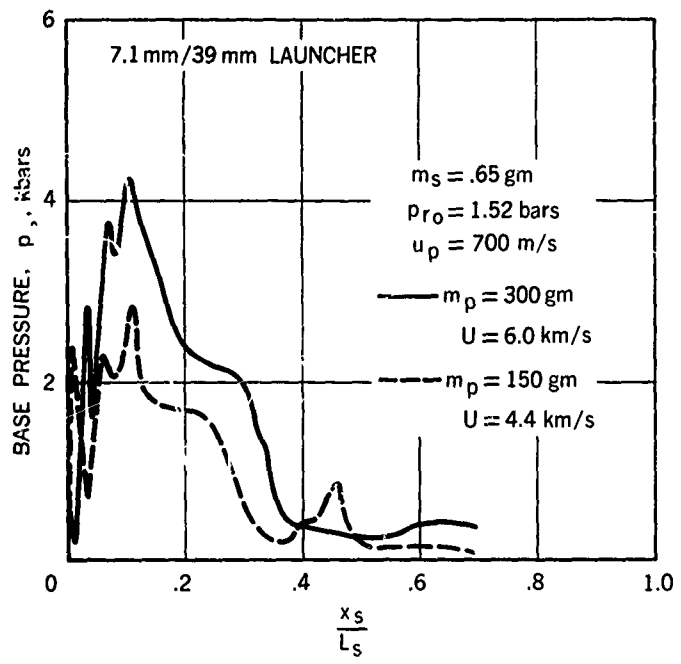
2.57   Effect of piston mass on model base pressure during launch (experimental)
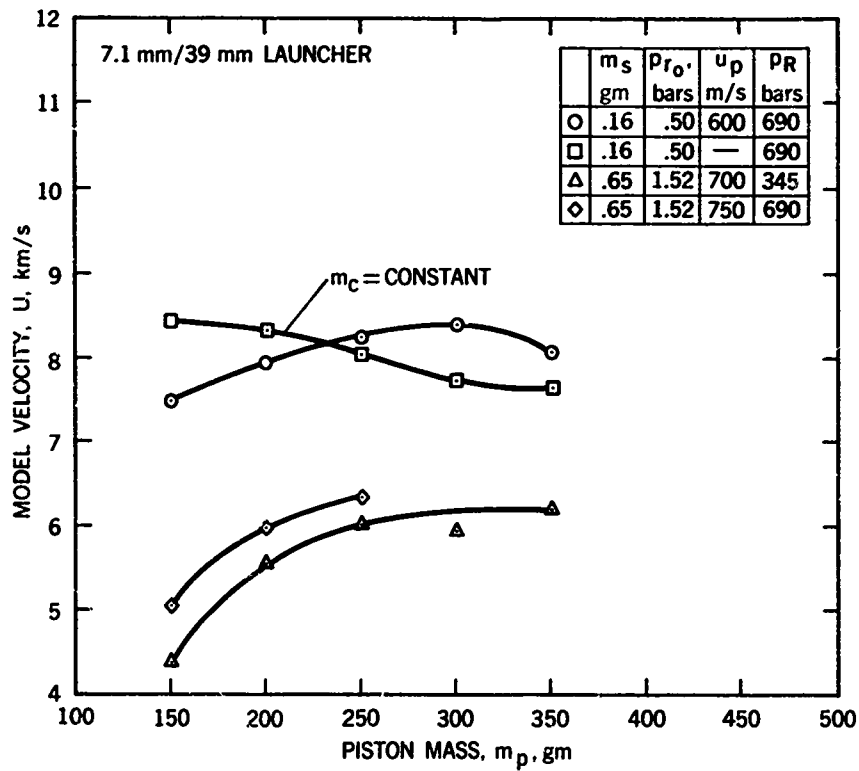
2.58   Effect of piston mass on model velocity for a variety of loading conditions (experimental)
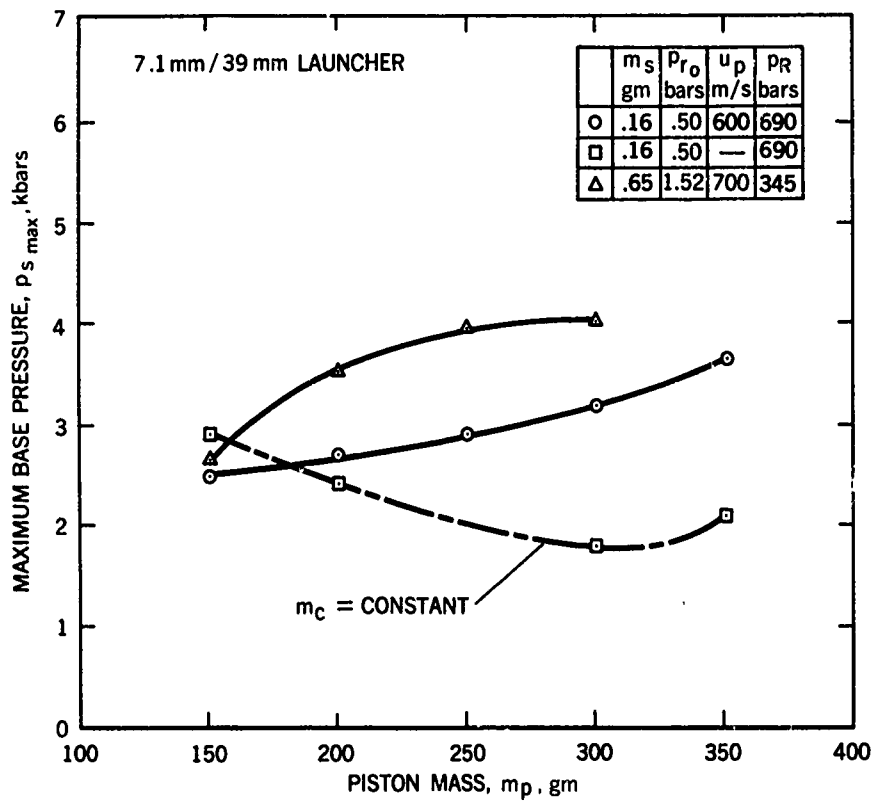
2.59   Effect of piston mass on maximum base pressure (experimental)
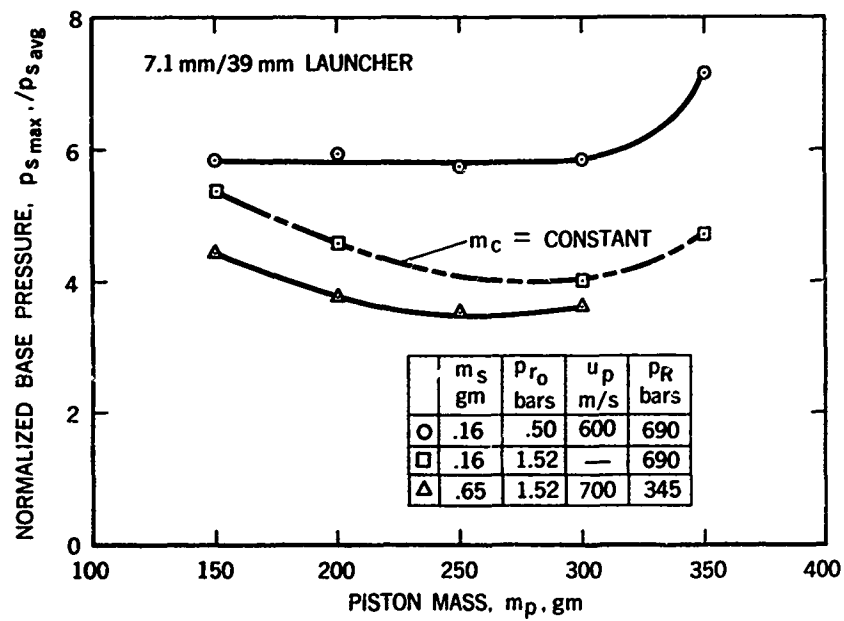
2.60 Effect of piston mass on normalized maximum base pressure (experimental)
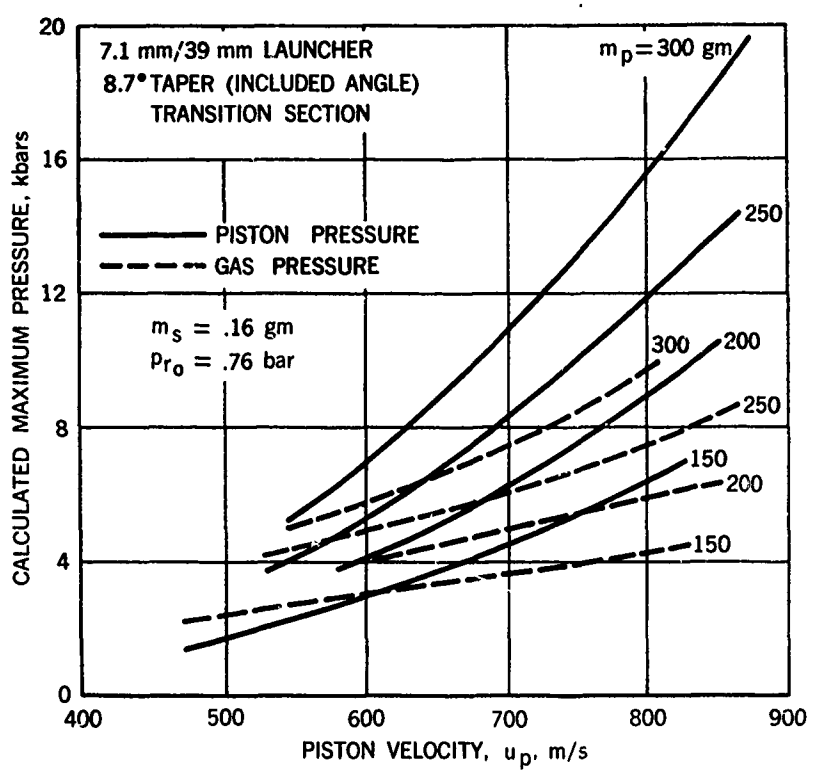
2.61 Calculated maximum pressures exerted on 8.7°-taper transition section by piston and gas as a function of piston velocity, for constant values of piston mass
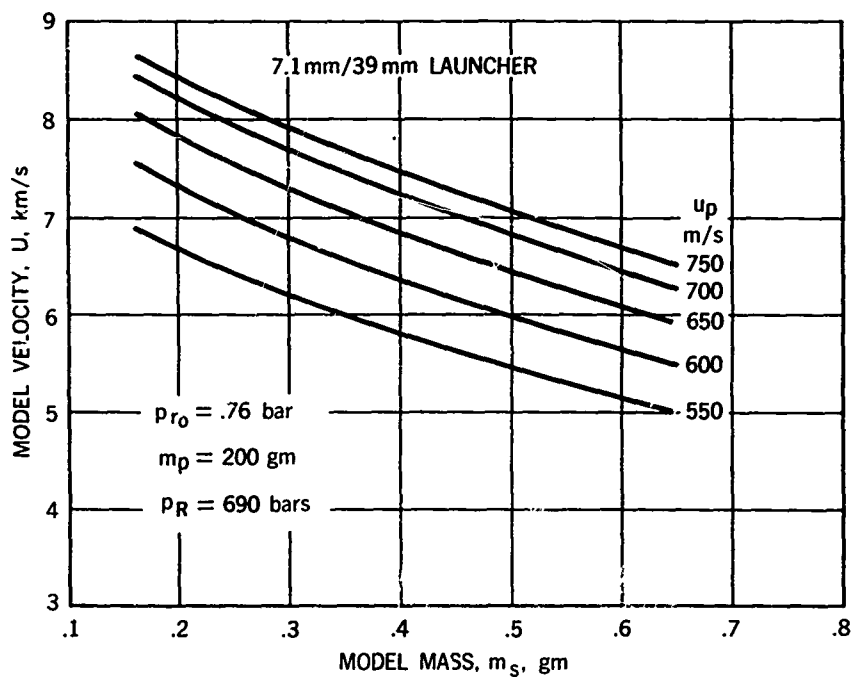
2.62   Effect of model mass on model velocity at constant values of piston velocity (experimental)
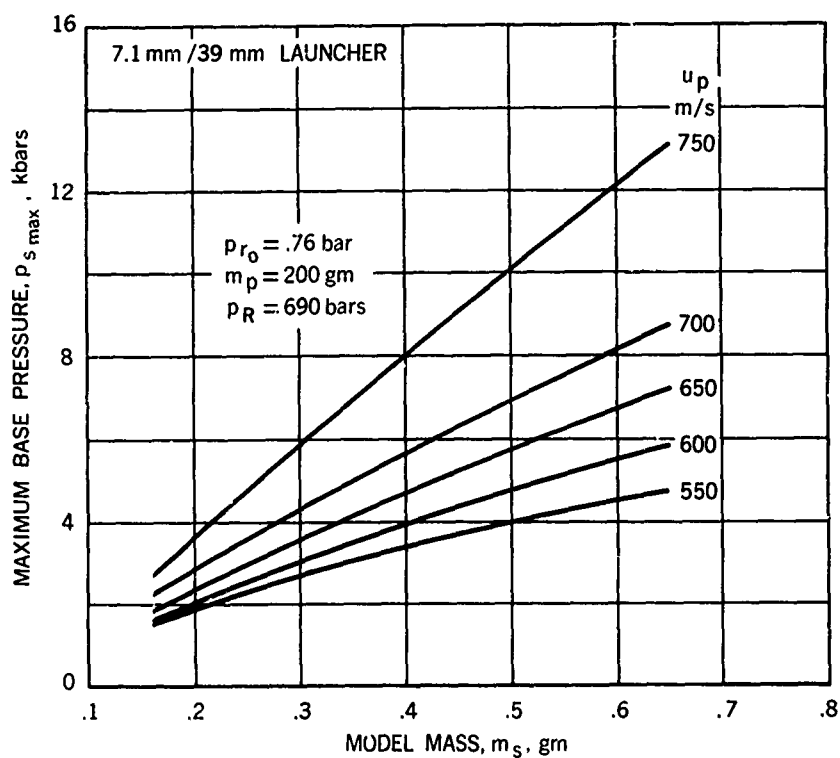
2.63   Effect of model mass on maximum base pressure at constant values of piston velocity (experimental)
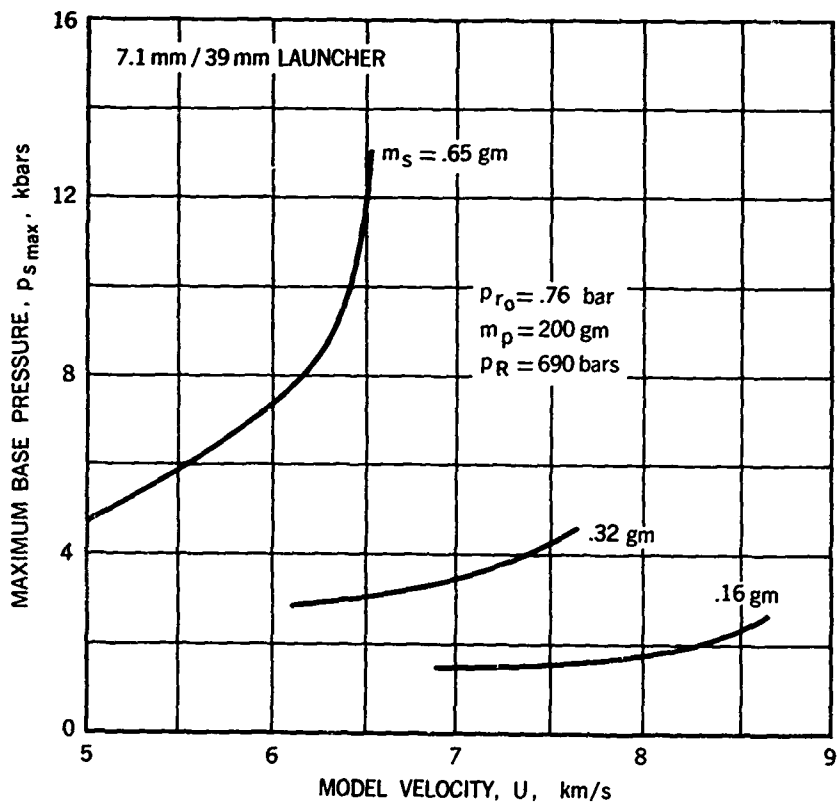
2.64   Variation of maximum base pressure with model velocity at constant values of model weight (experimental)
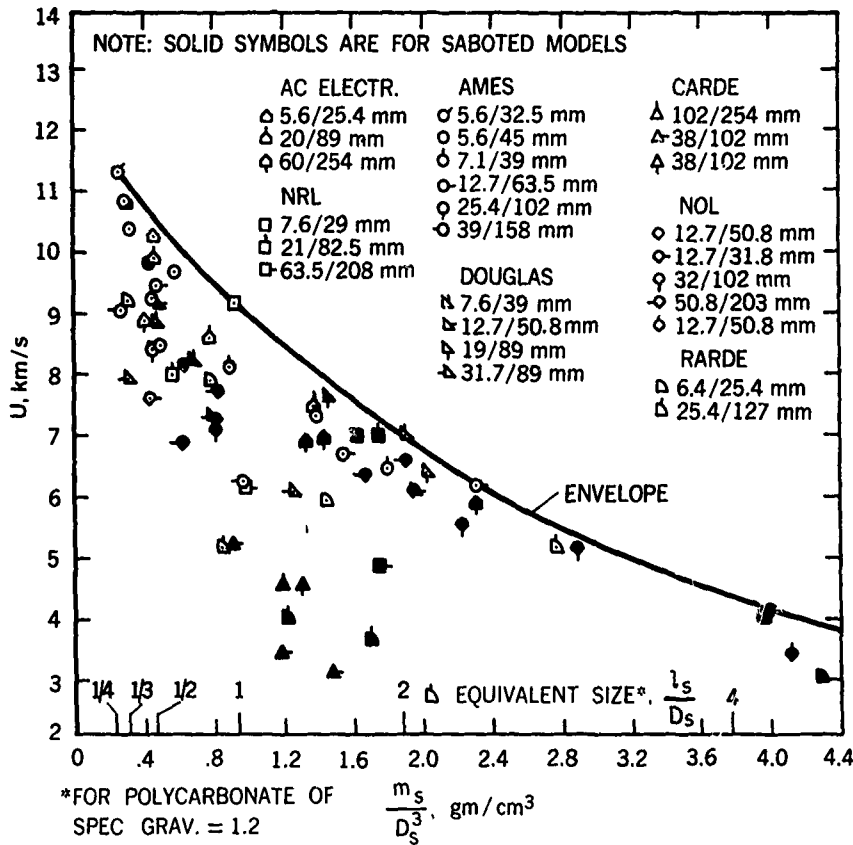
2.65   Launch velocities obtained for a wide variety of models with representative light-gas guns at a number
of research laboratories
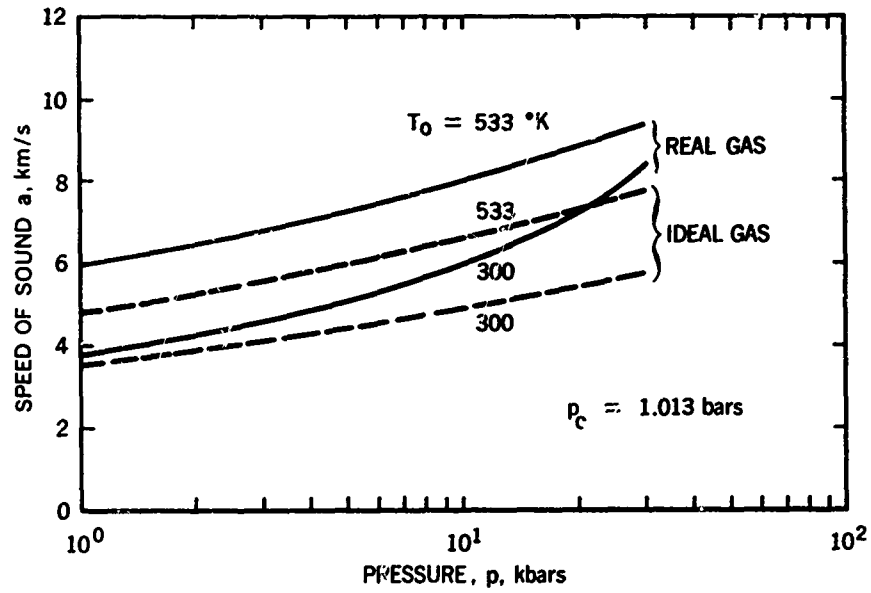
2.66   Comparison of speed of sound in ideal and real hydrogen, compressed isentropically to pressure, p, from initial pressure of 1.013 bars
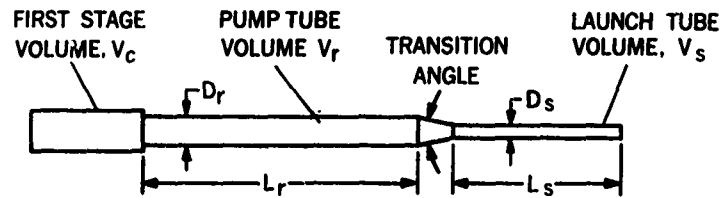
2.67   Notation for gun dimensions given in Table 2.2
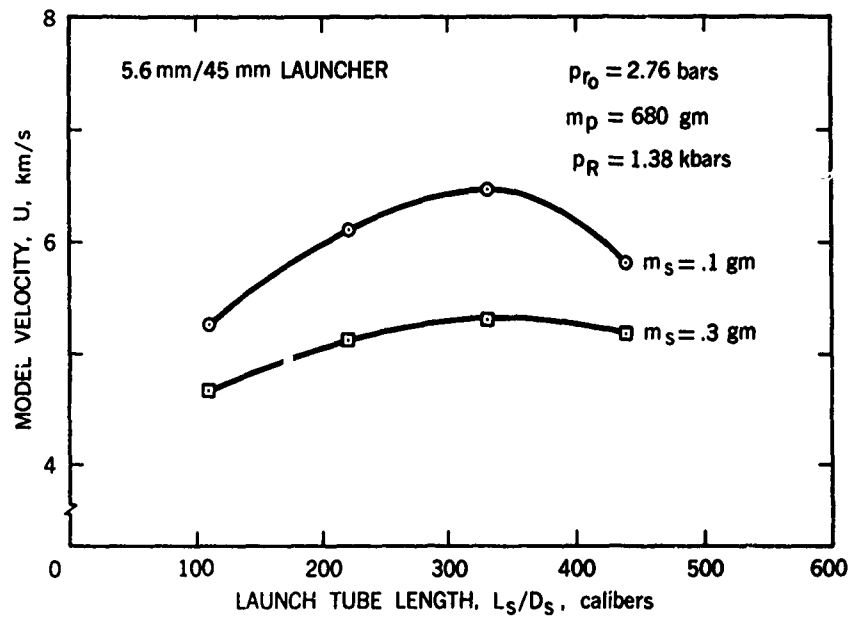
2.68   Effect of changes in launch-tube length on model velocity (experimental)
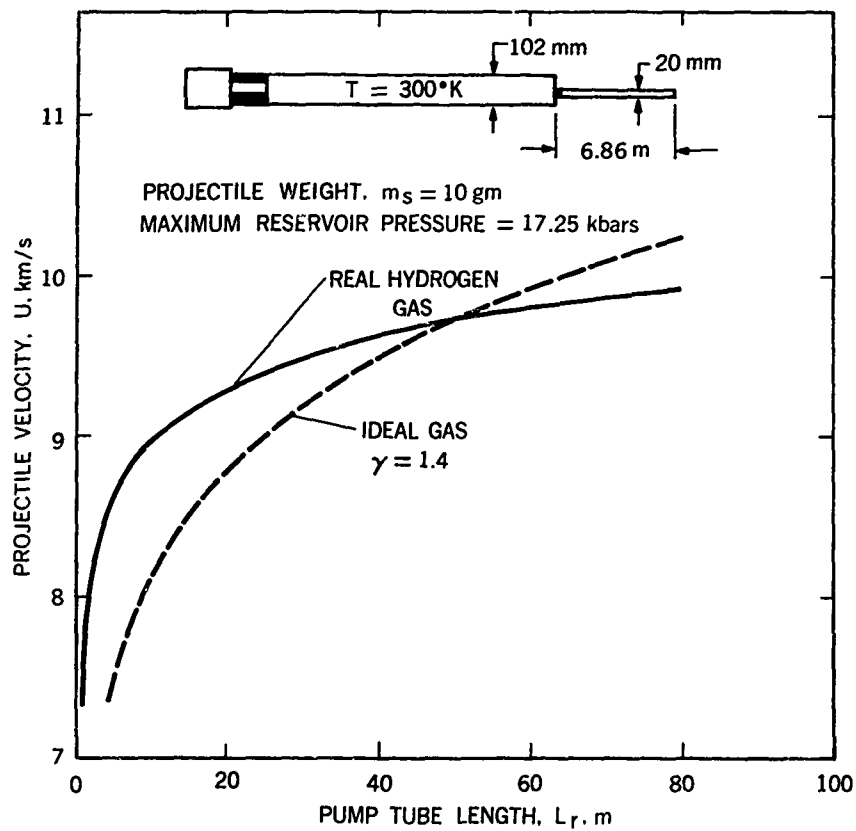
2.69   Effect of pump-tube length on calculated performance of gun operating with constant-base-pressure process. (From Seigel, Piacesi, and Bixler, US Naval Ordnance Laboratory, Ref. 2.78)
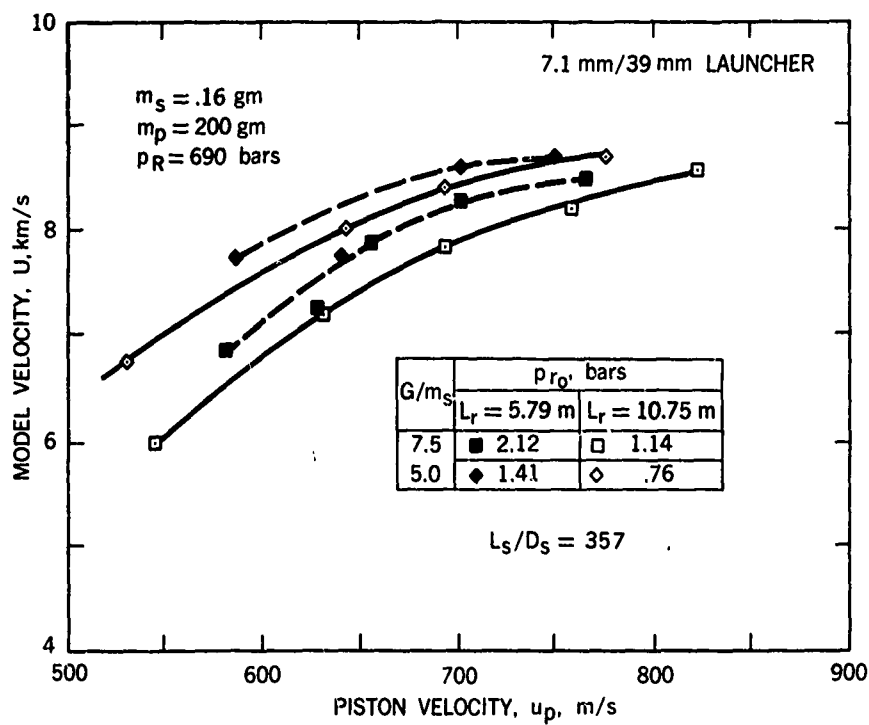
2.70   Effect of change in pump-tube length on variation of model velocity with piston velocity (experimental)
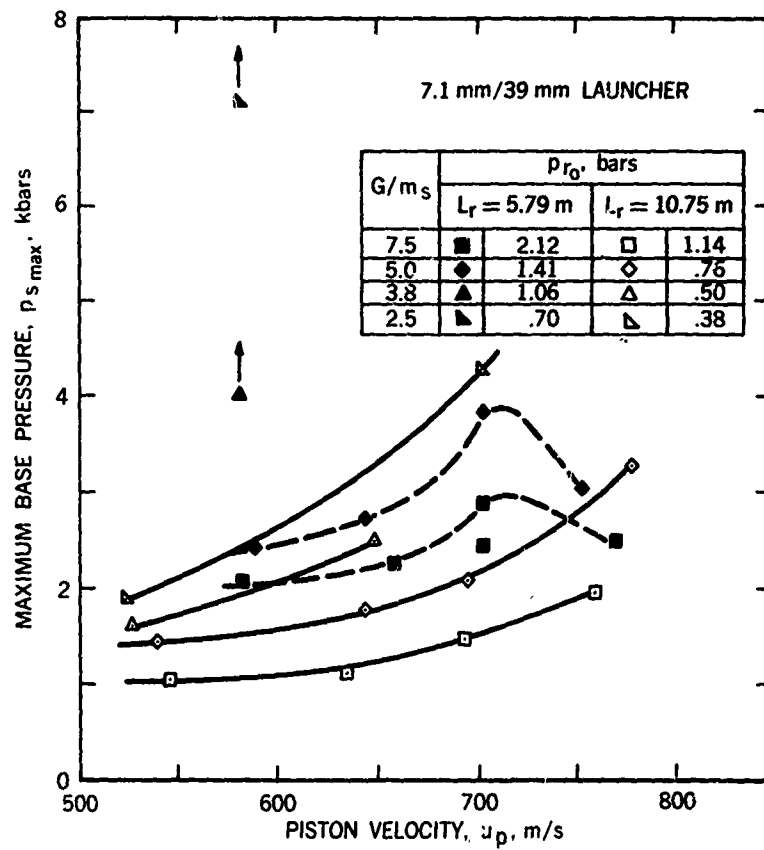
2.71 Effect of change in pump-tube length on variation of maximum base pressure with piston velocity (experimental)
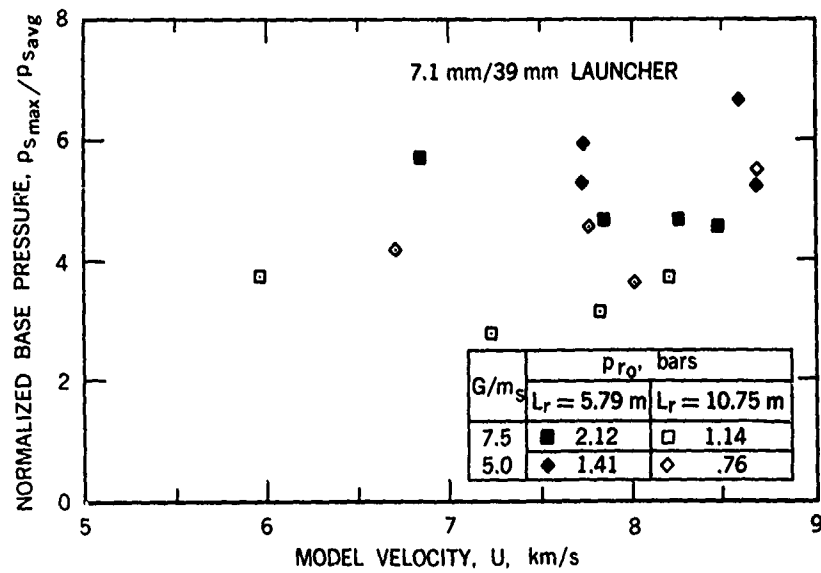
2.72 Effect of change in pump-tube length on variation of normalized maximum base pressure with model velocity (experimental)
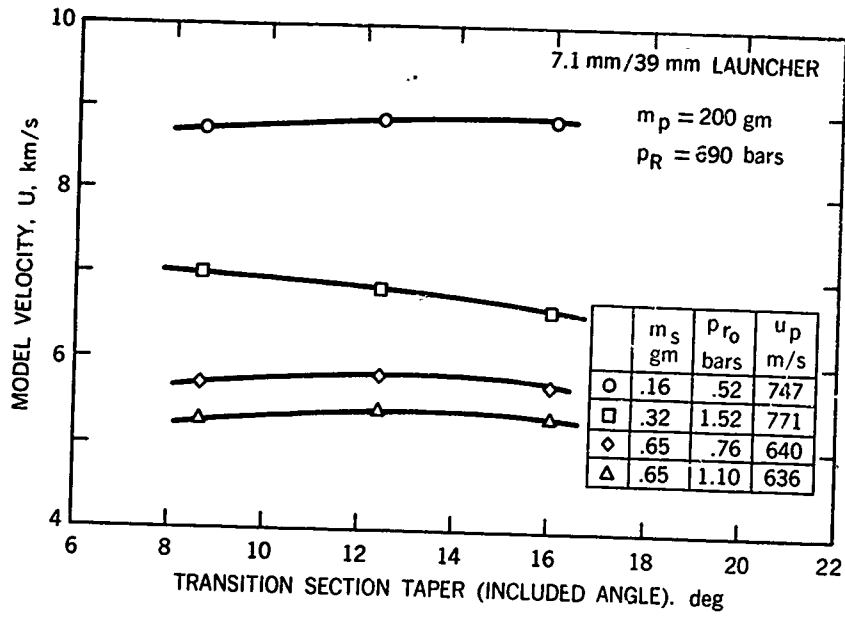
2.73 Effect of pump-tube to launch-tube transition-section taper angle on model velocity (experimental)
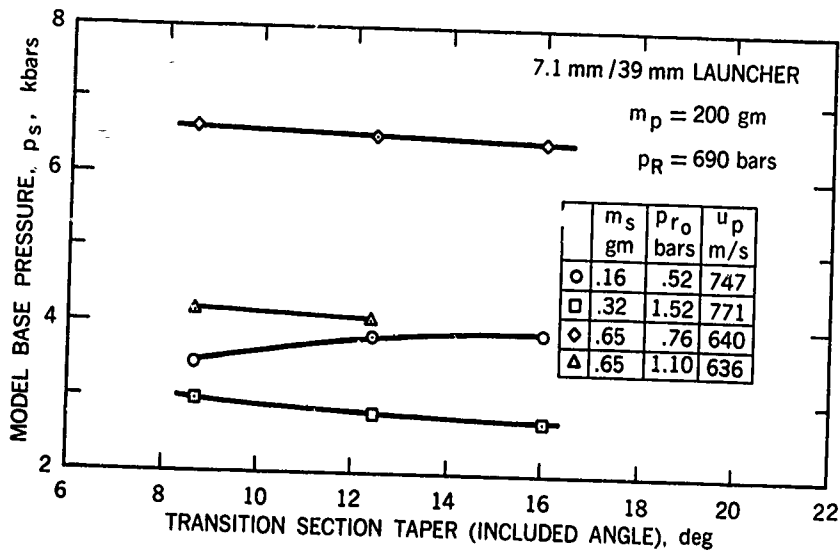
2.74 Effect of pump-tube to launch-tube transition-section taper angle on maximum base pressure (experimental)
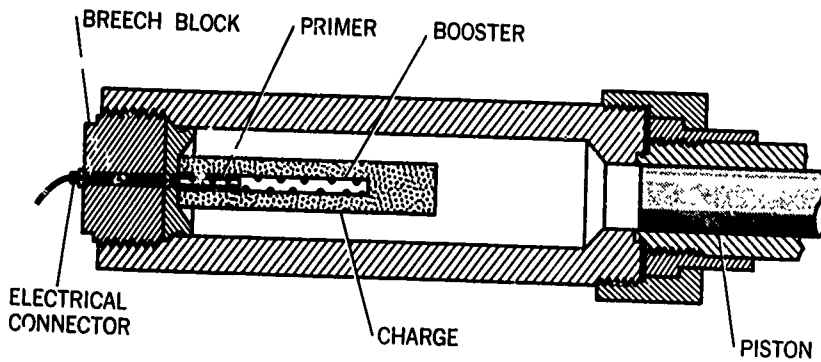
2.75 Light-gas gun powder chamber

.9 DIA. OF RING
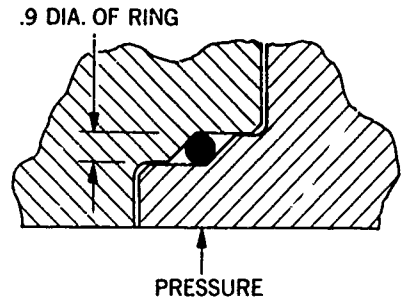
PRESSURE

2.76   O-ring seal at gun joint

CYLINDRICAL
BREECH   SPLIT CLAMP   LINER

SEAL SHOULDER
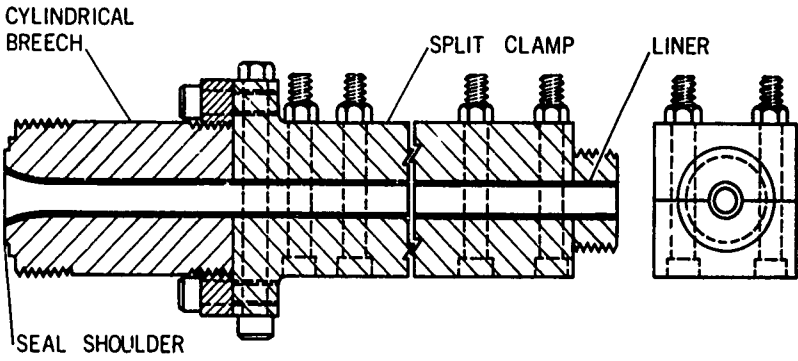
2.77   Split-clamp launch-tube design

2.78   Ames Research Center 25.4 mm/102 mm light-gas gun split-clamp launch tube

PETALING
DIAPHRAGM   STEEL SEAL

15°

PUMP TUBE   SPACER   LAUNCH TUBE

BEFORE ASSEMBLY   ASSEMBLED
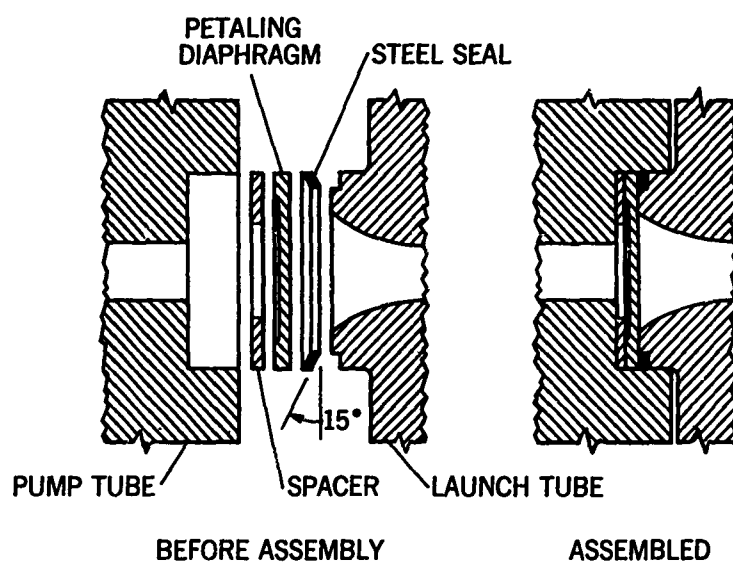
2.79   High-pressure gas seals

INTERRUPTED
THREAD

BOLTED FLANGE   THREADED NUT
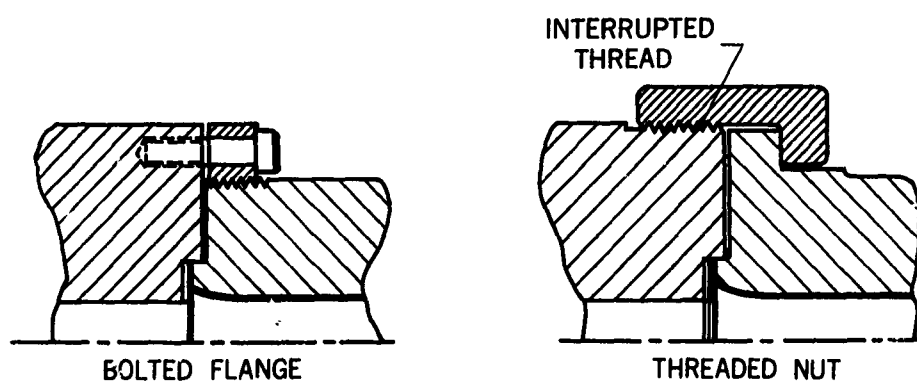
2.80   Launch- and pump-tube couplings for small guns

PALMETTO SEALS
OUTER NUT
PUMP TUBE
RETAINING RING
HYDRAULIC INLET
PISTON
INTERRUPTED SHOULDER (ASSEMBLED)
SHOULDER NUT
LAUNCH TUBE
PETALING DIAPHRAGM AND SEAL
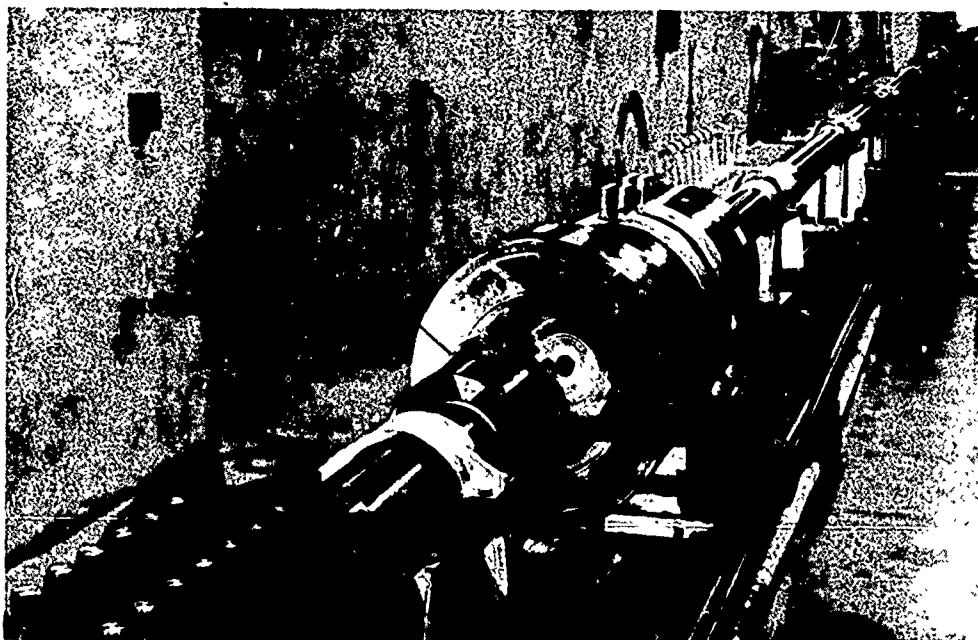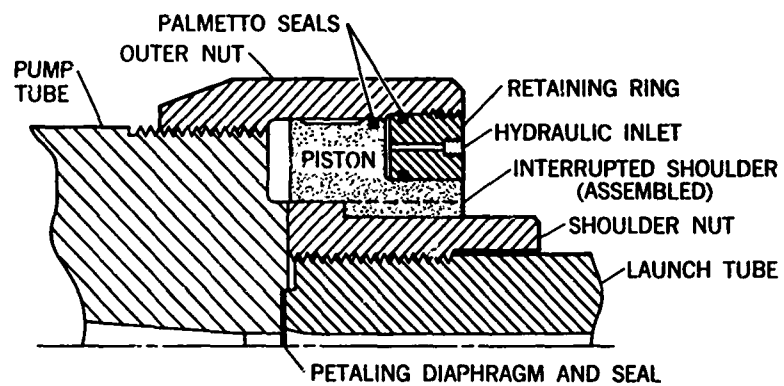
2.81   Ames Research Center 25.4 mm/102 mm light-gas gun launch-tube to pump-tube coupling

HELIUM
16.9 bars

NITROMETHANE
(6.4 km/s)

PROJECTILE

DETASHEET
(7.6 km/s)

DILUTED NITROMETHANE
(5.5 km/s)

DETONATOR

FIRST STAGE TAMPED
LINEAR EXPLOSIVE DRIVER

SECOND STAGE
EXPLOSIVE LENS

INITIAL CONFIGURATION
DETONATION WAVE VELOCITIES IN PARENTHESIS

DETONATION WAVE

SHOCK

CONSTANT-VELOCITY
VIRTUAL PISTON

HELIUM ~ 2 kb

FIRST-STAGE LINEAR DRIVER OPERATION

REFLECTED SHOCK AND DETONATION
ABOUT TO MEET

HELIUM ~ 8 kb

PHASED DETONATION WAVE

SECOND STAGE INITIATED
PROJECTILE AND DRIVER GAS BEING INJECTED INTO EXPLOSIVE LENS

PHASED DETONATION WAVE

ACCELERATING VIRTUAL PISTON

EXPLOSIVE LENS ACCELERATES PROJECTILE TO FINAL VELOCITY

2.82   Operation of a two-stage explosively-driven launcher. (From Moore, Physics International Co., Ref. 2.26\

CHAPTER 3

MODEL AND SABOT DESIGN
AND LAUNCHING TECHNIQUES

by

Charles E.DeRose and Peter F.Intrieri

NASA-Ames Research Center

MODEL AND SABOT DESIGN
AND LAUNCHING TECHNIQUES

Charles E. DeRose and Peter F. Intrieri

3.1 INTRODUCTION

In the preceding chapter, the operating principles and design of light-gas guns capable of accelerating projectiles to high velocities were discussed. Equally important to the ballistic range test is the projectile itself. The projectile usually consists of two parts, namely the part of interest in the test, the model, and its carrier in the gun, the sabot*. The model can be any body having the desired geometry and mass characteristics for which experimental data are required. The sabot alines and supports the model during the launching process.

It is necessary now to examine the design, construction and launching of the projectile. The designer's task is seldom an easy one, but represents the necessary first step in every successful ballistic range test. Many severe and often conflicting requirements must be satisfied before a successful design is achieved. The model must have the desired geometry, must withstand enormous launch accelerations, possess adequate aerodynamic stability (i.e., fly nose forward), and have the required mass and inertial characteristics dictated by test requirements. The sabot must also withstand the launch accelerations while supporting and protecting the model. Upon emerging from the gun it must also separate cleanly without imparting a large disturbance to the model and must not be allowed to hinder in any way the acquisition of data. It is seldom possible to achieve an *optimum* design which simultaneously satisfies all the imposed requirements. Rather, a successful combination of model and sabot is one which serves adequately to achieve the desired goals of the test. In a large number of cases this successful combination is not obtained through calculations alone, a development period of trial launches with some corrective redesign is often necessary to achieve the final useable configuration.

The purpose of this chapter is to discuss some of the basic principles cf model and sabot design and to present and analyze typical examples of successful designs. It is hoped that the material presented will convey the state of the art and will offer the reader an appreciation of the problems involved and possible solutions to these problems. The chapter proceeds as follows: first, a general discussion of the problems that direct the initial design will be presented. A truly general discussion here is difficult because of the individual nature of each test and facility combination. However, the basic problems can be outlined to illustrate how the resulting constraints dictate the design. Next, detailed calculations pertaining to the design of a particular configuration (a 10° half-angle cone) are presented to illustrate specifically the types of calculations performed in an actual model design. This particular example was chosen because most of the critical problems which can confront the designer are present, i.e., many conflicting requirements regarding model size, density, and inertia which require simultaneous solution, a relatively fragile model, high launch accelerations, complex sabot, heat protecting the model during flight, etc. The next two sections examine a number of actual designs of a variety of models and sabots which have been launched successfully at both low and high speeds. Here, the emphasis is on a detailed pictorial presentation where important features of individual designs are pointed out and discussed. Since the constraints on model design are usually more numerous and more severe for tests where the aerodynamic stability characteristics of the configuration are to be measured, the examples discussed are principally of this type. The next section is devoted to the subject of model measurement techniques. In this section, some of the methods used to determine a model's linear dimensions, weight, center-of-gravity position, moments of inertia and surface finish are discussed. The following section describes some of the auxiliary equipment used to separate the sabot from the model. These devices, while not directly a part of the design of models and sabots, are often required for successful testing, that is for example, to prevent sabot parts from entering the test area and to facilitate launching models in tests requiring low static pressure and other special situations. The chapter ends with a brief discussion of some of the techniques and equipment used in proof testing, that period of trial launches which precedes the use of the model for testing.

3.2 GENERAL DESIGN PROBLEMS

The design of particular models and sabots for ballistic-range tests is to some degree iterative. The constraints imposed by gun size, facility length, limits of operating pressure, number of photographic stations, and several lesser considerations determine how well the required data can be obtained in the desired flight regime. Usually, the design cycle is initiated by assuming an initial design based on prior experience which is then modified progressively as a result of various calculations.

---

* The word sabot is a French word which means wooden shoe (worn in various European countries). As used by ballisticians, it denotes the carrier or support used to launch various aerodynamic shapes and sub-caliber projectiles.

Preceding page blank

3.2.1 Initial Design Requirements

3.2.1.1 Design Conditions Imposed by Test Requirements

In tests where the aerodynamic coefficients governing the flight of a given configuration are to be measured, the mass and inertial characteristics of the model will have to be adjusted to meet both the velocity and density requirements of the test and the accuracy capabilities of the facility. If drag coefficient is to be determined, then the deceleration of the model must be large enough to be measured accurately, but not so large that it significantly alters the flight conditions[*]. Measurements of static stability, dynamic stability, and lift are possible only if there is sufficient definition of the model's pitching and swerving motion. In general, this requires that the wavelength of the pitching oscillations be less than two-thirds the length of the test section and that the swerve displacement be at least 20 to 30 times the measurement accuracy of the facility. To obtain the desired wavelength of oscillation, the model's size, moment of inertia, and center of gravity must be adjusted with respect to the free-stream density.

In tests aimed at studying the flow field around a model (such as, for example, boundary-layer transition), a primary design consideration is that of controlling the surface finish. Of course, these models must also be aerodynamically stable and capable of being flown at the desired flight attitude and velocity. Models for use in impact or flow-field radiation studies will be designed with the primary emphasis on shape, mass, and model material. A large amount of aerodynamic stability may have to be provided for these models since model attitude must be closely controlled in many of these tests; however, velocity changes during the flight are not usually a controlling factor.

The required velocity and Reynolds number of the tests put further constraints on model mass, dictate limits for model size, and narrow the choice of construction materials and assembly techniques. High velocity, in particular, causes the most problems in model design. In addition to extremely high accelerations that must be tolerated, heat-protective surfaces must sometimes be provided to keep the models from burning. In these tests a relatively simple design, that is, for example, solid homogeneous models constructed of high strength-to-weight ratio materials will usually afford the greatest assurance of success. Models for low speed tests generally offer a much wider choice of materials and can often be constructed of easy to machine sub-parts.

3.2.1.2 Design Conditions Imposed by the Facility

The facility to be used is the next important factor in model design. The length of the facility determines the amount of deceleration required for accurate drag measurements and puts boundaries on the wavelength of pitching oscillations. The density capability of the facility together with the velocity and Reynolds number desired may dictate the model size and hence the level of aerodynamic forces and accelerations that must be withstood. A facility which has a wide range of density capability allows greater flexibility in the design. The number of observation stations available, together with the precision with which the required measurements can be made, serve to establish limits for model deceleration and number of pitching and swerving oscillations. (To define the pitching and swerving oscillations of the model, it is desirable to have at least five observations per cycle of motion.)

Thus we see that the test objectives and facility can impose harsh requirements on the design of a ballistic model. We have not attempted to quantitatively define the design parameters involved, nor have we indicated specific solutions for satisfying the requirements; this will be done in Section 3.3 where we examine the design of a particular configuration for use at particular test conditions. However, it is clear at this point that most designs will result from a careful balance of numerous requirements, which in many instances are conflicting.

3.2.2 Structural Design Requirements for Model and Sabot

3.2.2.1 Model Considerations

One of the major problems in designing models and sabots is providing sufficient strength to survive the launching loads. The customary design procedure is to first calculate the constant acceleration in the gun (ideal operation) which would yield the desired velocity, given the length of the launch tube and the flight velocity desired. The appropriate equation is

$$A_{const.} = \frac{1}{2} \frac{V^2_{muzzle}}{l_{launch\ tube}} . \tag{3.1}$$

A factor which represents the ratio of the peak acceleration to this constant acceleration is then applied to estimate the maximum acceleration which will be experienced. This factor is usually determined from prior acceleration measurements in the gun (by microwave measurements during calibration of the gun for example) or from breech pressure histories in powder gas guns. This peak acceleration factor, is, of course, dependent on the type of gun, the muzzle velocity, and weight of the projectile; however, a good approximation is that it will be between 3 and 5.

---

[*] Changes in the flight conditions, that is, for example, Mach number, Reynolds number, are detrimental only if the desired aerodynamic coefficients vary with these changing conditions. However, this information is usually not known beforehand and so near-constant conditions during the flight are desirable.

Thus knowing the peak acceleration, a stress analysis is applied to critical sections of the model. It is assumed that the load across any section is that required to accelerate all the mass ahead of that section. Thus the stress analysis is fundamentally treated as a static loading; dynamic effects are very difficult to estimate and so are not usually considered in the initial design. Buckling of a particular section of the model may, however, be investigated and if a failure of this type is indicated it can be countered by thickening the walls (if possible) or by additional sabot support in this region.

It should be noted that although this structural analysis seems oversimplified, it has generally not been necessary to make it more complete. Instead it has been found that experience, plus a small number of trial or development launches (proof testing), can lead to successful designs. This in a sense is fortunate since the true nature of the loads imposed on the model during launch and the material's resistance to high-strain-rate stressing are not conclusively known. Exceptions to this procedure may arise when launchings are attempted at the highest possible velocities. Recently, attempts have been made by some experimenters to study theoretically the dynamic stress loading within very simple models and sabots[3.1]. The procedures are very complicated, however, and hence require a considerable investment of time, as well as access to electronic computers. Continuing research in this area of complete dynamic analysis is highly desirable and may in years to come prove a boon to the model designer.

Both the strength requirements and the model weight influence the choice of model material. A compromise to meet both requirements can sometimes be made by using two or more different materials in the construction or by hollowing a homogeneous model. Materials of high strength-to-weight ratio are usually of greatest advantage. Aluminum, magnesium, titanium, and high strength alloy steels are commonly used metals, while polycarbonate, polyamide, and polyethylene plastics are often chosen for sabots as well as for models. Table 3.1 shows the physical characteristics for some of the materials commonly used for ballistic models and sabots. Material cost is usually not an important factor in the selection since the quantity used in model construction is small. Machineability of the material, however, should be a consideration since accurate reproduction of the models is very important.

3.2.2.2 Sabot Considerations

As stated earlier the sabot is the supporting structure which is necessary to launch all sub-caliber models. The sabot alines the model in the gun, prevents model contact with the launch tube walls, and separates the model from the driving gases. It is frequently necessary to use models that are structurally weak relative to the predicted launch loads. In these cases, the sabot has been utilized to provide the necessary support for the weak sections. In fact, use of sabots which completely enclose the model has enabled successful launching of models which theoretically were too weak by factors of two or more. The use of the completely enclosing sabot, or a sabot that supports the internal structure of the model, extends the velocity capability of the model, but compromises the release process; this problem will be discussed in the next section.

Since the sabot must also withstand the accelerations during launch, the same type of stress analysis discussed previously in relation to the models is also usually applied to critical sections of the sabot. More specific discussion of these critical sabot sections and types of structural failure which can occur is given in Sections 3.3.2 and 3.4.

3.2.3 Design Considerations for Separation of Model From Sabot

While it is necessary for the sabot to support the model, seal off the driver gases, and keep the model alined and away from the launch tube walls, it is equally necessary to have the sabot separate from the model with minimum disturbance. The sabot, upon release of the model, should then veer away from the flight path of the model and not interfere with the acquisition of data (i.e., continue down range and trigger light sources in the observation stations which could cause double images on, and/or overexpose the photographic film, radiate light which could also blacken the film, follow the model too closely which could affect the wake flow and in turn affect the air pressure on the model base, damage parts of the instrumented test section such as vacuum lines, air lines, windows, measuring equipment, etc.). This separation of the sabot from the model is fully as important to the success of the test as protecting the model in the gun. These separation requirements lead toward a minimal, light-weight structure which generally conflicts with the requirement of maximum model support. The resulting compromise is usually a sensitive one and is frequently resolved only by proof firings.

3.2.3.1 Sabot Separating Forces

The way in which a sabot is designed to achieve a clean separation from the model upon emerging from the gun is fairly straightforward once one understands the forces available to accomplish the separation. Five types of separating force commonly used in ballistic range testing are: aerodynamic, propellant gas, internal elastic, centrifugal, and external mechanical.

Aerodynamic forces are most commonly used to separate segments of the sabot from the model. Pressure forces, acting on the beveled front face and/or hollow front section of the sabot pieces, force the pieces radially outward away from the model. Aerodynamic forces are also employed to achieve axial separation between a sabot base and the model. This method requires both a reasonably high air density and light-weight sabot segments (relative to model weight) to obtain good separation.

For sabot designs in which the front face cannot be shaped to utilize aerodynamic forces, an alternative is to use the pressure force of the propellant gas. Usually, in such cases, the sabot is split in two or more

pieces with a hole or cavity machined in from the base at the interfaces of base pieces and also fingers. This hole is filled with the high pressure propelling gas while the model and sabot are being accelerated in the gun. Upon leaving the launch tube, this high internal pressure forces these sabot pieces apart, away from the model. This same configuration can be used with a metal spring to produce the separating force (here the response time of the spring relative to the flight duration must be very short), but the gas pressure method is simpler and much more powerful.

Similar to the above design, internal elastic forces in the sabot material can also be used to provide a separating force. The segmented sabot is made slightly oversize and compressed when loaded into the launch tube. Upon leaving the barrel, the rebound of the material causes the segments to separate. This latter method is not as positive as the one employing the internal gas pressure, but may be of advantage when positive gas sealing is required.

The method of using centrifugal forces to separate sabot segments is extremely powerful, and does not rely on any internal or external pressure forces. However, its use is limited to those tests in which a high model roll rate is either desired, or is not detrimental to the test. This method is also dependent on the availability of a rifled launch tube. In the case of modern, light-gas guns, a rifled tube can be very expensive and difficult to obtain.

With some configurations, it is impossible to use the separating forces previously mentioned. In these cases, a mechanically-applied decelerating and deflecting force must be employed. This force is usually provided by a muzzle constri tor or sabot stripping plate. A retarding force may thus be applied to a full bore diameter sabot (base) to achi an axial separation between it and a subcaliber model. After the axial separation is achieved, a deflecting ramp can be used to divert the sabot away from the flight path of the model. A further discussion of this method will be presented in Section 3.7.

3.2.3.2 *Separation Dynamics*

After separation of the sabot segments from the model is achieved, some attention must be placed on the flight dynamics of the pieces. Hopefully, the pieces can be made light and of high drag shapes so that their deceleration is greater than that of the model. If this can be achieved, then the axial separation of model from sabot pieces can prevent any further interference. Heavy sabot segments which decelerate less than the model will usually have to be trapped by a sabot stripper – a plate with a hole on gun centerline large enough for only the model. Additional features of mechanical strippers and deflectors will be discussed in Section 3.7.

3.3 TYPICAL EXAMPLE OF DESIGN PROCEDURE

In the preceding section we discussed in general terms the types of problems associated with the design of models and sabots. Let us now examine a specific example to illustrate the actual design procedure in more detail. In doing this, we will describe the types of calculations that are made and give actual numbers to enhance the previous general statements.

The most demanding set of constraints is usually that imposed by aerodynamic stability tests, since all the constraints concerning model deformation and disturbance at launch are present together with others pertaining to scale, material, moments of inertia, and center-of-gravity location. Hence, let us consider the design of a 10^0 half-angle cone to be tested in a given flight regime for the purpose of measuring drag, static and dynamic stability and lift. The Mach number and Reynolds number range of the tests along with a description of the facility in which the tests are to be conducted are given in Table 3.2.

3.3.1 Model Design

If, first, it is assumed that the model will be of maximum size, compatible with the gun, i.e., 1.27 cm diameter, then the free-stream pressures will be:

$$P_\infty = 0.022 \text{ atm for } R_{e\infty} = 100,000$$

$$P_\infty = 0.22 \text{ atm for } R_{e\infty} = 1,000,000 \ ,$$

given $R_{e\infty} = \rho_\infty V_\infty d/\mu_\infty$, $\rho_\infty = P_\infty/RT_\infty$, $V_\infty = 5.2 \text{ km/sec}$, and $T_\infty = 290^0 \text{ K}$. It can be seen in Table 3.2 that these pressures are within the pressure capability of the facility, hence, the desired Reynolds numbers can be obtained in this facility with this size model.

For drag measurements, the deceleration must lie between some lower limit of measurability (Chapter 7) and an upper limit imposed by the requirement that test conditions do not vary significantly along the flight path (see footnote page 3-2). For these tests, it is desired to keep the change in Mach number to the order of 0.2.

A commonly used measure of the effect of drag on the trajectory is the distance decrement which is the difference in distance traveled, in a given time, between the actual model and a model with zero deceleration. For small changes in velocity, this distance decrement is given by

$$X_D = \frac{1}{2} At^2 = \frac{1}{2} \left[\frac{C_D \frac{1}{2} \rho_\infty V_\infty^2 S}{m} \right] t^2 \ , \tag{3.2}$$

where

A = deceleration, m/sec^2

C_D = drag coefficient

ρ_∞ = free stream density, kg/m^3

V_∞ = velocity, m/sec

m = model mass, kg

t = time, sec

S = model reference area, $\pi d^2/4$, m^2

d = model diameter, m.

The distance decrement may also be written

$$X_D = \frac{1}{2}\left[\frac{\Delta V_\infty}{t}\right] t^2 = \frac{1}{2} [\Delta V_\infty] t . \tag{3.3}$$

With $\Delta V_\infty = 0.2\, a_\infty = 0.2\,(344) = 68.8$ m/sec , and $t = l_{ts}/V_\infty = 23/5150 = 4.5 \times 10^{-3}$ sec (a_∞ is the speed of sound and l_{ts} is the length of test section), then the specified upper limit for the distance decrement for these tests would be

$$X_D = \frac{1}{2}[68.8]\,[4.5 \times 10^{-3}] = 0.155 \text{ m} \sim 16 \text{ cm} . \tag{3.4}$$

The lower limit of X_D , necessary for accurate drag measurements, depends on the accuracy with which distance measurements could be made in the facility and is estimated to be about 2.5 cm for the facility assumed here. This corresponds to an accuracy of 0.13 mm in the measurements of model position in the shadowgraphs and a time measurement accuracy of 0.02×10^{-6} sec.

The effects of the principal model parameters on the distance decrement can be displayed by rearrangement of Equation (3.2). For this purpose, we may assume that velocity is constant for the flight. Then velocity and time can be eliminated from the equation in favor of distance.

$$X_D = \frac{1}{4}\frac{C_D \rho_\infty S}{m} [l_{ts}]^2 . \tag{3.5}$$

Equation (3.5) gives explicitly the sensitive dependence of drag-measuring accuracy with test section length. Further, since model mass (m) varies directly with ($\rho_m d^3$), where ρ_m = model density , and S varies directly with d^2 , then

$$X_D \sim \frac{[C_D]\,[\rho_\infty]}{[\rho_m]\,[d]} [l_{ts}]^2 . \tag{3.6}$$

Equation (3.6) shows that the distance decrement varies inversely with model scale and model density, and directly with air density.

The minimum drag coefficient for this cone is estimated to be about 0.10. With this drag coefficient, a test section length of 23 meters, and a free stream air density 0.022 standard atmospheric density (to satisfy the lower Reynolds number requirement), the model weight must be 1.8 grams for $X_D = 2.5$ cm and 0.28 gram for $X_D = 16$ cm . Thus, an acceptable weight for this model would lie between 0.28 and 1.8 grams. Since the model volume is about 1.5 cm^3, this would require (for a solid model) materials having densities around 1 gram/cc (plastics). Since the weight of the model must vary directly with the free stream pressure to keep the distance decrement constant (see Equation (3.6)), the model for testing at 0.22 atm must weigh between 2.8 grams and 18 grams. These weights call for model materials with densities of metals. For both regions of this test, it is advisable to keep the model weight toward the heavy limit because the drag coefficient increases sharply with angle of attack. For example, C_D at 10° angle of attack is almost double that at 0°. Thus, to avoid a large change in velocity during flights experiencing moderate angles of attack (necessary for measurement of lift), the model weight must be larger than the minimum values given above.

In the test, the static stability of the configuration (as measured by the moment-curve-slope, C_{m_α}) will be determined from the wavelength of the pitching oscillations given by the relation

$$-C_{m_\alpha} = \frac{8\pi^2 I_y}{\lambda^2 \rho_\infty S d} , \tag{3.7}$$

where

I_y = moment of inertia about y-axis, kg-m^2

λ = wavelength of pitching oscillations, m

d = model reference diameter, m.

To obtain accurate stability data (in particular, dynamic stability) $1\frac{1}{2}$ to 2 cycles of motion are desired; i.e., the wavelength should lie between $\frac{2}{3} l_{ts}$ and $\frac{1}{2} l_{ts}$. The factors controll'ng the wavelength are given by Equation (3.7). Thus, in designing the model, C_{m_α} must be estimated, which requires knowing the position of the center of gravity. A homogeneous cone with a half angle of 10° has its theoretical center-of-pressure location about 0.31h from the base and its center of gravity at 0.25h from the base. With this center-of-gravity position further aft of the center of pressure, the configuration is aerodynamically unstable. Hence, the center of gravity must be placed forward of the 0.31h position either by hollowing the base of the cone or by ballasting the nose. The former method is usually preferred with plastic models because the plastic will usually not be strong enough to support heavy materials at the tip. The latter method, however, is frequently used with metal models. Since the desired weights of the models have already indicated use of plastic materials at the low Reynolds numbers, the method of hollowing the base is chosen for these models.

With the base of the model machined out as shown in Figure 3.1, the center of gravity is moved forward to 0.35h from the base. The static stability derivative, C_{m_α}, computed using Newtonian theory for this center-of-gravity position is –0.21 per radian (based on d). If nylon is used as model material ($\rho_m = 1.1$ grams/cc), the model would weigh 0.91 gram (acceptable for drag measurements at the lower Reynolds numbers), and have a pitch moment of inertia of 6.1×10^{-8} kg-m^2, which would result in a pitching-motion wavelength of 21 meters at a free stream pressure of 0.022 atm. This wavelength is about $0.9 l_{ts}$, which is greater than the prescribed upper limit for λ, and hence, would not yield accurate stability data. The desired wavelength should be from 12 to 15 meters.

Equation (3.7) can be expanded and the terms rearranged to obtain

$$\lambda \sim \left[\frac{1}{\sqrt{(-C_{m_\alpha})}}\right]\left[\sqrt{\left(\frac{\rho_m}{\rho_\infty}\right)}\right][d] . \tag{3.8}$$

It is seen from Equation (3.8) that reducing the model size is an effective way of reducing the wavelength. However, when the model size is reduced, the free-stream density must be proportionately increased to keep the Reynolds number constant; for a constant Reynolds number, the wavelength is proportional to $d^{3/2}$. These changes also increase the distance decrement in the drag analysis, so these limits must be rechecked. However a $\frac{2}{3}$ size model, base diameter of 0.84 cm, tested at 0.034 atm ($R_{e\infty} = 100,000$) would have a wavelength of 12 meters (acceptable) and a distance decrement of 6.9 cm (also acceptable).

. For measurements of dynamic stability, at least three well defined peaks in the pitching oscillations are necessary, which, for this facility, would require a wavelength of 16 meters or somewhat less. With the 0.84 cm diameter nylon model, we satisfy this requirement also.

To determine lift (as measured by the lift-curve slope, C_{L_α}), the displacement of the model's swerving motion about a mean line, Z_{swerve}, is measured. The appropriate equation is

$$Z_{swerve} = \frac{C_{L_\alpha}\alpha_{max}\rho_\infty S\lambda^2}{8\pi^2 m} . \tag{3.9}$$

For a 0.84 cm diameter nylon model at 0.034 atm pressure, assuming a theoretical value of $C_{L_\alpha} = 1.78$ per radian, and a maximum angle of attack, $\alpha_{max} = 10^\circ$, the maximum swerve displacement would be 0.5 cm. This amount of swerve should yield accurate results since the accuracy of these measurements in this facility is of the order of 0.13 mm or about $2\frac{1}{2}$ percent of the maximum displacement. Equation (3.9) can be rearranged to obtain

$$Z_{swerve} \sim \frac{[C_{L_\alpha}][\alpha_{max}][d]}{[-C_{m_\alpha}]} \sim \frac{[\alpha_{max}][d]}{[\text{static margin}]} , \tag{3.10}$$

where the static margin, for small angles of attack, may be written

$$\text{static margin} = \frac{x_{cg} - x_{cp}}{d} \approx -\frac{C_{m_\alpha}}{C_{L_\alpha}} . \tag{3.11}$$

It can be seen from Equations (3.10) and (3.11) that the swerve depends only on the model size and the amplitude of pitching oscillation for a given static margin.

Since it was specified that data ' obtained at Reynolds numbers from 100,000 to 1,000,000, models having different densities will be required. Using the basic model geometry shown in Figure 3.1 and the various scaling equations, the set of models of Table 3.3 can be formulated.

As can be seen in Table 3.3, three models, all the same size but of different materials, will cover the test range. The use of similar models but of different materials will usually result in low machining cost and good accuracy in reproduction. A single group of form tools can be used to machine all the models. Also, with the model size and geometry constant, a common sabot design can often be used.

The models just described will satisfy the test requirements but only if (1) they can be launched at the desired velocity without damage, and (2) if they survive the aerodynamic heating and pressure loading during the flight with no significant change in shape. To determine whether a structural failure of the model (and/or sabot) is likely to occur during launch, a simplified stress analysis is performed at critical sections in the model and sabot. This analysis involves calculation of the compressive stress at sections A-A and B-B (see Figure 3.2) and possibly at other intermediate sections. In these calculations the ultimate compressive strength

as determined from static tests is usually used as a criterion to predict model failure. The possible increase in strength due to rapid strain rates in the actual dynamic loading serves as an unknown safety factor. For the desired velocity of about 5 km/sec, a maximum acceleration of about 1×10^6 gravities occurs with the particular light gas gun to be used. At these conditions, the calculations indicate that the base (annulus) of the nylon model would fail in compression when the acceleration forces are applied only on the base, but that the steel and aluminum models would survive. However, it can be seen that if the plastic model is supported along its entire base area (internal cavity and base annulus) by means of an internal plug in addition to being supported externally along the skirt, much higher launch accelerations can be sustained. (As indicated in Figure 3.2, a fillet is used to alleviate stress concentration.) This example illustrates how sabot design can be used to overcome structural deficiencies in a model. Because plastics are much weaker than metals, the design of sabots for use with plastic models is more critical than for those used with metal models.

Other types of structural failures which might occur, particularly with the nylon model are: buckling of the thin skirt; bending or breaking off part of the model nose by convergence of stress waves in the tip or rarefaction waves produced within the model during the launch accelerations; and shearing off part of the model due to lateral accelerations developed by irregularities in the launch tube. These types of failures, however, are very difficult to investigate analytically; therefore, their occurrence is determined by trial launches. Here, again the importance of a good sabot design in achieving successful launches of fragile models can be demonstrated; in many cases it was found that complete encapsulation of plastic models within sabot "fingers" prevents these types of failures from occurring. Examples of plastic-cone models which used this type of sabot in actual tests will be presented later in this chapter.

In cases where hollowing the base of the model is not sufficient to move the center of gravity forward a desired amount, or where the nose of the model will burn because of high heating rates during the flight (the latter will probably occur for both the aluminum and steel models at the test conditions of this example), the designer will often use a bimetallic model such as the one shown in Figure 3.3. In cases where heating is not a problem, the important properties of the nose ballast material are that it has relatively high density, high strength-to-weight ratio, and is machinable. Sintered tungsten alloys are commonly used for this purpose. In tests where heating is important, metals which have very high melting temperatures (and also meet the other requirements just mentioned) such as tungsten, tantalum, and molybdenum are used. The problem of determining whether or not a material will burn during flight will be discussed in Section 3.5 where other solutions to this problem will also be discussed.

For the bimetallic model shown in Figure 3.3, it is again important that a simple stress analysis be made to insure that a structural failure does not occur at the joint of the two materials during launch. Stresses at the lower sections of the model will also increase due to the increased weight at the tip. Thus, the calculations of the compressive stress at sections A-A and B-B must be repeated. The design of the joint between the ballasting tip and the afterbody is critical. Considerations which can help prevent failure of this joint are to use fine threads for a screw attachment, and to achieve nearly zero clearance at both the base of the nose and the base of the screw so that the weight of the nose is distributed over the maximum available cross-sectional area. Other types of failures which have been known to occur and therefore should be examined analytically are: failure of the screw in tension or shear at section C-C or shearing of the screw threads of either material. Examples of several successful bimetallic model designs will be presented and discussed in Section 3.5.

3.3.2 Sabot Design

Several aspects concerning the design of sabots for the models of this example have already been implied in the previous discussion. The sabot shown in Figure 3.4 provides the internal pusher plug and complete encapsulation required for the plastic models, while the sabot for the homogeneous metal models (Fig.3.5) pushes only on the base annulus and uses shorter fingers.

A stress analysis is also required for the sabot to determine where failures might occur. Typical analyses performed are the following: compression at section D-D, bending along section E-E, and shearing along section F-F. These stress calculations are again based on the peak acceleration, or its equivalent, the peak gas pressure on the base of the sabot.

The front section of the sabot for the plastic model, by enclosing the model completely, acts to prevent buckling of the thin skirt and in addition supports the delicate tip. As shown, the front section of these sabots is split into four segments (fingers) to facilitate a cleaner separation from the model while shear pins, machined integral with the fingers, are provided to prevent differential axial movement of the segments during launch. The segments are separated aerodynamically by the pressure forces acting on the beveled front face. These four segments are usually machined from polycarbonate plastic (Lexan), a material chosen for its excellent strength and light weight. The base of the sabot could be either polycarbonate or polyethylene and is machined to fit the cavity of the model accurately. After the front segments have separated, the base piece being a full 1.27 cm diameter, decelerates behind the model in flight due to its higher drag. The base is not split into segments and so serves as a gas seal.

For the metal models, an aluminum insert is used in the plastic base to distribute the high stress under the thin base annulus of the model into the plastic. Because of the higher tip strength of the homogeneous metal models, complete encapsulation of the model in the sabot may not be necessary. Hence, an appreciable reduction in total projectile weight is achieved with consequent advantages in gun performance.

The models and sabots described in this section represent a configuration that has been successfully launched and tested. The final configurations, as used, were the hollow plastic and hollow bimetallic (tantalum nose, aluminum afterbody) models. The sabot shown in Figure 3.4 was the type used. The model shape in this example is simple, but the conditions of the test impose very critical requirements on the final design.

For models of more complicated geometry, the same general approach to design can be followed. Ordinarily however, the more complex shapes will be more difficult to launch without damage and so may be limited to lower speeds. Th. configurations that have been successfully launched are so varied that a complete comprehensive discussion would be impossible. As an example, Figure 3.6 shows the variety of models tested at only one laboratory. The approach in the next two sections will be to select a number of representative shapes and show how their design was directed.

3.4 MODELS AND SABOTS FOR LOW-SPEED TESTS

In the low-speed range, arbitrarily defined here to extend to 2000 meters/second (a velocity which is easily attainable using powder-gas guns), there exists a great deal of freedom in the type of model which can be tested and in the type of des'gn and construction that can be used. For example, large models are feasible in this speed range because of the wide availability of large-bore guns. The advantage of large size permits the use of very intricate models with some degree of economy; and the low speed, with its low-acceleration loads, allows these frequently fragile models to be launched without damage. (Size however, must be compatible with facility length and pressure capability as was discussed in the example in Section 3.3)

To attain a successful design for model and sabot, even for this rather forgiving low-speed regime, one must first estimate the forces and stresses which will be applied to the model during launch and in some cases also during flight. The stress analysis for the more complex models must consider a number of additional failure modes. Consider the example of Figure 3.7.

For the model:

(a) Compression at the base.

(b) Shear at wing and tail root joints.

(c) Compression at body joints, especially between different materials.

(d) Column stability of body (determine whether supporting fingers are needed).

(e) Deformation of tail.

For the sabot:

(a) Bending along section AA (both stress level and deflections are important. Excessive deflection of base can distort rear fins or other thin sections.)

(b) Compression across section BB.

(c) Shear across section CC.

(d) Column stability of member L.

In addition to consideration of model strength, difficult design problems might be encountered in ballasting, obtaining the required model density, and in devising a sabot that will support the model during acceleration and release it cleanly with min'mum disturbance. Let us examine some specific cases n which these problems were solved and successful designs were obtained.

3.4.1 Models Assembled from Individually-Machined Sub-Parts

Starting with models used for testing in the transonic to low-supersonic speed range (velocities up to about 500 m/sec), we will examine a series of models produced by assembling easy-to-machine sub-parts. Let us first consider two examples of models having wings and tails. Figure 3.8 shows an example of an airplane-like model tested at velocities up to 500 m/sec (Ref.3.2). The relatively low launching loads expected allowed the construction of this model to be kept simple and therefore economical. The model was constructed of four separate pieces, namely, a nose, body, wing and tail section which were pinned together. The body, wing, and tail section were 2024 aluminum. The nose was bronze to move the center of gravity forward for aerodynamic stability. To minimize the amount of bronze, the aft section of the body was hollowed out. The materials selected here were chosen merely on the basis of density, machinability and availability; strength of materials was only a secondary consideration, even for the aft section of the body which was hollow. The model size and weight were dictated by the facility used (an instrumented length of 20 meters at atmospheric pressure), the wavelength of oscillation in pitch (12 meters), and by the availability of a 7.6 cm diameter launch tube. The separate sections of this model were assembled using a press fit. The alinement of the nose and aft sections with the rest of the body was maintained by the long studs used for the press fit. In addition, steel pins were used to assure that the joints did not separate. Because the sections for the fins were quite thin, they were machined from a solid piece of aluminum and so were integral with the cylindrical aft section of the body.

The sabot used to launch this model is shown in Figure 3.9 and consisted of a steel-faced, cast, hollow plastic cup with four foamed-plastic fingers. The sabot base was cast to allow inexpensive reproduction without resorting o repetitive machining of large diameter plastic stock. The plastic was reinforced with glass fiber to strengthen the crown. The hollow design was used to minimize weight so the sabot would decelerate behind the model after launch. The thin skirt also served as a gas seal. The steel plate cast in the front face of the

sabot was used to distribute the acceleration loads into the plastic. The sabot fingers were cut from very light, rigid-foam plastic and were used to aline the model initially for loading into the gun. The accelerating forces kept the model alined during the launch (the fingers probably collapsed during this initial part of the acceleration) and the model emerged from the muzzle essentially free of all restraint.

A slightly different design approach was used for the model shown in Figure 3.10. This configuration was used to study drag at transonic speeds. It was designed to be launched from a 7.6 cm diameter gun into air at one atmosphere pressure. Again, multiple-piece construction was used but in this case, the wing and tails were glued into slots cut in the body. A commercially available epoxy glue which had a thick non-running consistency worked well for this application. The design philosophy here was that the glue joint offered more restraint than pinned construction because of the extremely thin sections and large contact area inside the body. Steel was used for the wings and tails to obtain sufficient stiffness in these thin sections. A long brass nose was used with an aluminum body and a hollow magnesium aftersection to provide static aerodynamic stability; maximum stability was desired because of the requirement to measure drag at small angles of attack.

Because of this model's low drag and relatively heavy weight, a solid sabot base was used. The base was machined from nylon and a brass front face was used to distribute the load from the small diameter model base into the plastic. This simple sabot was possible because of the large difference in aerodynamic deceleration between model and sabot which assured quick axial separation. Foam plastic fingers were used with this model also, merely to keep the model alined during loading. This sabot offered nearly disturbance-free launches.

Both of the preceding models are examples of a potentially large group of multi-piece winged models that can be launched using simple sabots and temporary, weak, alinement fingers. This type of sabot arrangement offers the advantage of permitting the largest possible model for a given size gun (the wing span is limited by gun bore only) and the least chance of damage to the delicate wing and tail sections. The requirement that deceleration of the sabot base be much greater than that of the model is usually easily met with these slender winged bodies.

The sabots just discussed are examples of simple types which can be used to launch winged configurations. However, much more complex sabots must sometimes be used to launch very intricate and fragile models. One such example which gave consistently good results is shown in Figure 3.11 along with the model[3.3]. As shown in this figure, this sabot is made in four segments which are separated aerodynamically from the model by the high ram air pressure inside the cylinder when the sabot emerges from the muzzle. This separation process removes the segments from the flight path of the model. The long length of this sabot gives good alinement within the gun and supports the model well during launch. These cylindrical sabots are of course more costly than the simpler type shown in Figure 3.9, but their cost can be insignificant compared to that of the highly complex models they must launch.

Another low speed model and sabot combination is shown in Figure 3.12 (Ref.3.4). This model differs from those discussed previously in that it has very high drag and in addition had to be made very lightweight. These two factors combine to give the model a low ballistic coefficient ($m/C_D S$), which usually results in high deceleration. The model construction was dictated primarily by the desire to launch the configuration at a velocity of about 800 m/sec into still air at low static pressure (0.01 atmosphere). To afford maximum strength and light weight, the body, skirt (or drag ring), and upper struts were machined from a solid block of 2024 aluminum (a tape-controlled milling machine was used for this particular operation). The lower struts which would not experience high loading, were soldered in place after machining the rest of the model. The nose was made of bronze for ballast.

Because of the high-drag/low-weight characteristics of this model, of primary concern was the design of an appropriate sabot. To achieve minimum weight the sabot was cast in rigid polyurethane foam. To assure positive separation from the model, the sabot was forcibly decelerated by shearing off the outer wall material (approximately 0.05 cm thick) of the sabot at the muzzle of the gun. No alinement fingers were used here because of the natural, self-positioning characteristics of the skirt. The model base was fastened to the sabot with a small amount of wax, which kept the model alined until the launching loads were applied. The base of the model which experienced high loading during the launch was supported on a polycarbonate plastic pedestal, while the lightly loaded skirt was supported on the polyurethane foam. This was done to equalize the compressive strain at the two points to prevent distortion.

Figure 3.13 shows a model of the Apollo launch-escape configuration with its sabot[3.5]. The model consisted of three principal parts; namely, the tower, the music-wire supports, and the blunt-face capsule. The tower and capsule sections were constructed from 7075-T6 aluminum with tungsten-alloy ballasts; the struts were made of 1.5 mm music wire and were press fit into the base of the tower and capsule. The model was launched at speeds from 200 to 400 m/sec into air at one atmosphere using a 57 mm powder-gas gun.

The sabot was made of polyethylene to minimize weight and consisted of six pieces. The two-piece base had shear pins to prevent differential movement of the halves during launch. The four fingers were used here to aline the long front section of the model but not to support it; all compression was taken through the music-wire supports into the base*. This was done to eliminate possible interference between the fingers and the base of the tower section during the separation process. Separation of the fingers was initiated by aerodynamic forces acting on the beveled front faces.

---

* When fingers were not used slight misalinement of the model in the gun caused permanent bending of the music-wire supports.

All of the above models were launched using smooth-bore guns and so the model roll rates obtained were usually quite small. In cases where a high model roll rate is desired or where large centrifugal forces must be utilized to achieve positive sabot separation, rifled launch tubes are used[3.6,3.7]. Examples of models which were launched from a 37 mm diameter rifled, powder-gas gun to obtain high roll rates are shown in Figure 3.14. These models were used to measure the rolling moment developed by trailing-edge spoilers, (as shown, various size spoilers, were used)[3.6]. To achieve a low axial moment of inertia which in this case was necessary so the spoilers could produce a high roll acceleration, the body was constructed from relatively lightweight materials (i.e., aluminum with a hollow magnesium aft section). This bimetallic construction gave an aerodynamically stable configuration. The cruciform tails were made of steel to afford maximum stiffness and were silver soldered into slots cut in the aft section of the body. The trailing-edge spoilers were machined separately, pinned in place for alinement, and then silver soldered. This technique permitted easy selection of spoiler height after the models were built and was found to be satisfactory up to a launch velocity of 1000 m/sec.

The sabot used with these models was made of six parts – a rifled aluminum base that was keyed to the model to produce the rotation, four rifled nylon fingers and a copper obturation cup to prevent powder gas leakage. Since both the sabot base and fingers were rifled, the resulting high spin rate of the configuration caused rapid radial separation of the fingers from the model. The fingers were not keyed to the base since the rifling grooves provided the necessary alinement.

3.4.1.1 Gas Seals

At this point, it is worthwhile to digress a bit from model and sabot design and discuss various types of auxiliary seals and obturation cups which are often used to prevent the propelling gas from leaking around or through the sabot. These gas seals are most often used when the sabot is of the split-base type (see for example, Figure 3.13), or where it is desirable to have a loose fitting sabot in the gun initially to minimize any radial compression of the model and sabot during travel through the launch tube. (Due to erosion by the driver gas, most launch tubes develop a taper of several thousandths of a cm during normal use). These seals can take many forms and the choice is usually made on the basis of material, weight, size and condition of the gun, as well as personal experience and preference.

A very simple type of gas seal is a thin disk of neoprene rubber (3 to 6 mm thick) and about 10 percent greater in diameter than the bore of the gun. The slight cupping of the rubber forms an effective seal to prevent gas from reaching the base of the sabot. Two other types of gas seal are shown in Figure 3.15. The first is a composite seal, simply made from polyester plastic and double-sided pressure sensitive tape. This plastic seal has worked remarkably well in many types of guns up to launch velocities of 8 km/sec. The other is the so-called obturation cup, which utilizes the high-pressure propellant gas acting in the hollow cavity to provide the seal. The cup may be integral with the sabot base or may be a separate part.

3.4.2 Investment-Cast Models

The method of model fabrication discussed thus far, i.e., assembly from individually machined sub-parts, is the preferred approach as long as these parts are easily generated by machine tools and the joints are sufficiently strong to survive the acceleration loads during launch. In many cases, however, models which do not lend themselves to straightforward machining techniques are required for testing. For these models of more complicated shape, the investment-casting technique has been used. This method of casting results in precisely duplicated models which are relatively inexpensive and require little or no finishing work. Both bronze and aluminum have been used successfully for these castings. To achieve a center-of-gravity position other than that of the homogeneous model, the models could be hollowed out and, if necessary, ballasting added. Figure 3.16 shows a group of five models that were produced by the investment-casting technique and were successfully launched at velocities up to 2000 m/sec.

One example of investment cast models is that of the X-15 research airplane[3.8]. This model and its sabot are shown in Figure 3.17. The model was cast of aluminum and was launched at velocities up to 1500 m/sec using a powder-gas gun with a 57 mm bore. The driver-gas pressure was used to separate the two halves of the sabot. The halves were held apart by the shear pin and the aluminum pieces of the sabot. The resulting gap provided the volume for the driver gas reservoir. No sabot fingers were used here; alinement was achieved by a pin in the base of the model, which was gripped by the aluminum inserts in the nylon base.

The two delta-wing models shown in Figure 3.16 were also cast of aluminum. The three-wing model is shown with its sabot in Figure 3.18 (Ref.3.9) (a shadowgraph of this model in flight is presented in Figure 6.75). This model used a three-piece nylon sabot with aluminum inserts to take the concentrated load from the small base area of the fuselage and wings. The sabot is separated from the model by the powder-gas pressure which acts on the walls of a centrally-drilled hole in the sabot. Axial movement of the three segments is prevented by the short, metal shear pins. In this design an O-ring on the outside of the sabot was used as an effective seal to prevent powder gases from flowing around the sabot. The four-wing model was essentially the same in construction and used a plastic sabot which was split into four segments [3.10].

A third example of a cast aluminum model is the glider-like model shown in Figure 3.19. This model proved difficult to launch at small or moderate angles of attack because of its light weight and long trailing wings. Because of the long wings even a small disturbance by the sabot would result in large initial angles of attack. A few low-angle-of-attack flights were obtained with this model and sabot combination indicating nearly perfect sabot separation in these cases. As shown in Figure 3.19 the sabot used for this model was made of nylon.

hollowed out at the front end, and used an aluminum pedestal screwed to the base to support the model. The sabot was split in halves and was separated by aerodynamic pressure forces acting inside the hollow front end. No alinement fingers were used - the pin in the base of the model served to hold and aline the model in the sabot until the launching loads were applied.

Another example of an investment-cast model is the half-cone, lifting-body model shown in Figure 3.20 (Ref.3.11). Bronze was used as the construction material to achieve the desired model density. This nonaxisymmetric shape trims, or flies, at a constant lifting attitude so the high weight was required to keep the flight trajectory within the walls of the facility. The model was cast with internal cavities which extended to the base to obtain the required center-of-gravity position without resorting to any internal machining or ballasting. The two pins in the base were added after the base was machined to position the model in the sabot and to provide a reference for determining the model's roll, pitch, and yaw attitudes. The sabot halves were separated from the model by the force of the driver gas trapped in the centrally-drilled hole.

3.4.3 Simple Machined Models

Other types of models which fall into the general category of being completely and easily machined are shown in the next two figures. The bimetallic model shown in Figure 3.21 was used to investigate boundary-layer transition on a highly swept wing[3.12]. This model represents a sector of the surface of a cone and thus was easily generated by machining and amenable to automatic machine polishing. The bimetallic construction was necessary to provide aerodynamic stability but resulted in an undesirable surface joint. This surface joint was a source of boundary-layer disturbance and is cited as an example of the unavoidable consequences of conflicting requirements.

Presented in Figure 3.22 are a group of models that consist of open-ended tubes. They are shown in two groups: the set shown in Figure 3.22(a) was used to study skin-friction drag[3.13] (the model on the right has a large ratio of surface area to frontal area, the model on the left is a tare model), and the other set was used to measure the drag of trailing-edge spoilers[3.6]. Both sets of models were launched successfully from rifled guns using solid metal pre-rifled bases as shown in Figure 3.22(b). In addition, the surfaces of the skin friction models were separated and protected from the lands of the rifling by a simple wrap of photographic film, held in place with cellophane tape during loading into the gun. A number of pre-rifled nylon supporting pieces were used with the solid metal base to launch the spoiler models. The centrifugal forces developed by the rifling quickly separated the sabot pieces from the model upon emergence from the gun.

The use of saboted models for ballistic testing is not limited to the sizes indicated thus far in this chapter. Large guns, such as the 127 mm, 178 mm, and 406 mm diameter guns used in high altitude research (HARP)[3.14,3.15] have launched very large saboted and instrumented models into the upper atmosphere. For example a model used in the 406 mm gun weighed about 84 kilograms and was launched at a velocity of approximately 2000 m/sec. The sabot base was aluminum with a steel insert and the supporting fingers were plywood. The capability of the 406 mm gun is impressive; models have been projected to a height of approximately 143 kilometers. Although these tests lie somewhat outside the realm of typical ballistic-range tests, they represent the largest models for use in ballistic research as well as the longest "instrumented" range.

3.5 MODELS AND SABOTS FOR HIGH-SPEED TESTS

Although the design approach outlined earlier is an almost essential companion to designing successful high speed models and sabots, it does not assure a priori that success will be obtained when the model is launched. This may be because the dynamic or transient loads imposed on the configuration during launch are not well enough understood to be evaluated accurately, or it may be because a failure mode has been overlooked entirely. Therefore, it can be said that the design of models and sabots for use at high speeds is strongly guided by design techniques which have proven successful in the past – i.e., the design is highly empirical.

It is therefore very pertinent to review designs which have been successful. In doing so we will examine some relatively complex and fragile models which have worked well at speeds up to 8 km/sec, as well as some simple configurations which have been launched at speeds up to 11.3 km/sec.

3.5.1 Design and Construction of Typical Models

The first configuration which we will consider is shown in Figure 3.23. Tests of this configuration were conducted in a pressurized ballistic range of the US Naval Ordnance Laboratory[3.16,3.17]. The models were homogeneous steel bodies, hollowed out to obtain aerodynamic stability. This type of construction results in the lightest possible model weight for a given material and represents the simplest approach to model design. The plastic sabot used to launch the models is also shown in Figure 3.23. Plastics are generally used as sabot material because they are sufficiently strong and lightweight, accommodate the small irregularities of the launch tube well, cause no appreciable wear of the launch tube, and because of their lightweight, inflict less damage to the test facility after emerging from the gun. Polycarbonate plastic (Lexan) is used widely because it has both a higher impact strength and a high modulus of elasticity than most other plastics. This type of sabot has proven very successful in launching models at high speeds and so is common in ballistic-range work. It features four polycarbonate fingers which fit around the model and are separated from it by aerodynamic forces acting on the beveled front faces. Polycarbonate pins are used to prevent longitudinal shifting of the fingers in the gun. The thin titanium plate distributes the model weight into the base of the sabot fingers. The separate polycarbonate base piece is also commonly used to more evenly distribute the pressure loads to the base

of ⸱e fingers and also as a gas seal. In this particular sabot, linen-phenolic inserts were used to aline the
l in the sabot fingers (rather than thickening the fingers to mate to the model) which results in a lower
⸱ al weight and a lower ballistic coefficient, m/C_DS , for each of the fingers, both of which provide for
better separation of the fingers from the model. In later sections of this chapter it will be seen that the
same basic components as these just described were used in other sabot designs; therefore, in these cases, it
will be necessary only to present a photograph of each sabot and to point out important modifications.

A different design approach to the configuration just described is illustrated in Figure 3.24 (Ref. 3.18,
3.19). The aftersection of each of these models was solid and was machined from 7075-T6 aluminum; the front
sections of the models with and without afterbody were machined from phosphor bronze and titanium, respectively, to
obtain the same center-of-gravity location (0.48d from the nose) as the model discussed previously. As can be
seen, the nose ballast materials were attached to the aluminum aftersections by means of a screw of the ballast
material. The small screw on the base of the flat-based model was used to secure the model to the sabot and
the point on the base of the screw served as a measurement reference in the shadowgraph pictures. The sabots
for these models differed from the one shown in Figure 3.23 in that they were made in two pieces; a hole drilled
i⸱ the center allowed gases inside the sabot to separate the two halves from the model upon emergence from the
gun.

Figures 3.25, 3.26 and 3.27 show sketches of three other bimetallic models. The noses of all three were
machined from a sintered tungsten alloy and threaded into an aftersection machined from 7075-T6 aluminum. The
configuration shown in Figure 3.25 (Ref. 3.20) was launched using a sabot machined from ethyl cellulose plastic,
split in two pieces, and having a hemispherical aluminum load-bearing insert under the model. The model is shown
in one half of the sabot in Figure 3.25. The ballasted-sphere model[3.21] shown in Figure 3.26 was launched from
a caliber 50 deformable piston light-gas gun similar to the one described in Reference 3.22 using the sabot shown.
The noses of the first two models launched with this type of sabot broke off for a rather obscure reason. Each
of these first two sabots had an oversized hole to accommodate the stud at the base of the model, which in this
case was necessary to define the model's angle of attack in the shadowgraphs. Although the sabot held the model
in place by gripping it above the maximum diameter, the model could pitch a few degrees in the sabot before the
stud made contact with the wall of the hole. This skewed attitude led to shearing of the screw that held the
nose to the aftersection. In succeeding tests the diameter of the hole in the sabot was made the same as that
of the stud and resulted in successful launches being obtained. Tests of this model at 4 km/sec through air at
one atmosphere were precluded because the tungsten-alloy nose material came apart or spalled under the high-
heating rates experienced during flight. A shadowgraph from one of these flights showing this spallation is
presented in Figure 8.37.

The configuration shown in Figure 3.27 (Ref. 3.23) was launched at velocities of 3 km/sec and 4.6 km/sec into
still air at a static pressure of 0.4 atmosphere. The models launched at 4.6 km/sec survived the launch but the
tungsten-alloy nose material, as in the preceding example, spalled under the high-heating rates experienced in
flight. A successful method of heat protection for the model was therefore devised and will be described in
Section 3.5.2 of this chapter. These models were initially launched by means of the sabot shown in Figure 3.27.
However, the models were so statically stable that they had to be canted in the sabot by as much as 15° to
obtain data at angles of attack above about 5°. Unlike the case of the ballasted sphere, the noses of these
models did not break off as a result of the model's skewed attitude in the gun.

A different design approach was necessary for the configuration shown in Figure 3.28 (Ref. 3.24) to keep the
nose screw of the model from repeatedly breaking off at the joint during launch. Note the very small scale of
these models – 3 mm body diameter. A separate steel machine screw, which is stronger than the tungsten alloy,
was used to fasten the tungsten-alloy nose to the 7075-T6 aluminum aftersection. One end of this steel screw
extended through the nose and was machined to form the center of the front face; the other end was hemispherical
and bottomed, with essentially zero clearance, into the hole machined in the aluminum section. This trimetallic
design permitted these small models to be successfully launched at speeds up to 6.5 km/sec. While the resultant
velocity (i.e., model velocity plus countercurrent flow velocity) was high (8.2 km/sec), the free-stream density
for these tests was low ($\rho_{\infty} = 0.03$ atmosphere), and no spalling of the nose material was evident in the shadow-
graph pictures. A photograph of the four-piece sabot (three polycarbonate fingers and a partly hollow polyethy-
lene base seal) used to launch these models is presented in Figures 3.28.

A trimetallic model design was also used successfully for the configuration shown in Figure 3.29 (Ref. 3.25).
In this case also, a steel machine screw was used to attach a rather large nose piece machined from a tantalum
alloy containing 90 percent tantalum and 10 percent tungsten (Ta – 10w), to an aftersection machined from
7075-T6 aluminum. This combination of materials, in addition to the hollowing of the base shown, gave the
desired center-of-gravity position. Sintered tungsten alloy was originally used as the nose material but it
blunted significantly during the flight and was so replaced with the tantalum alloy which survived the flight
with little blunting. These models were launched in the nose-forward attitude using the sabot shown at the
left in Figure 3.29. To help prevent possible separation of the nose from the aftersection during the launch,
the two polycarbonate fingers of the sabot were designed to completely encapsulate the model. By this technique,
the tip is strengthened against convergence of stress waves. It is interesting to note that this technique of
encapsulating a model within a sabot was used in early ballistic-range work to prevent "curling" or bending of
the tip of a slender cone when launched at relatively low speeds from powder gas guns.

To test their stability in a backward orientation, these models were launched in the base-forward attitude
by means of the sabot shown at the right in Figure 3.29. To provide support for the model in this attitude,
aluminum inserts contoured to match the model geometry were screwed to the inside of the polycarbonate fingers. This

rigid support prevented the model from being driven through the base of the sabot by the launch acceleration and permitted successful launching of the model at a velocity of 4 km/sec with no damage to the sharp tip.

Figure 3.30 shows a sketch of an Apollo-Type command module model, where a radial movement of the center of gravity of approximately 0.045 d was required to produce a trim angle of attack of 30 degrees (Ref.3.26). This radial offset of the center of gravity was achieved by use of a cylinder of sintered tungsten alloy and a cylinder of magnesium pressed into a block of 4340 steel before machining the assembly to the desired geometry with a smooth external surface. This model was made heavy to limit the flightpath curvature due to lift. The polycarbonate sabot used to launch the models at the natural trim attitude was split in two pieces along its plane of symmetry as shown in Figure 3.30. Two small peened-over sections of the sabot lip (180° apart) held the model in the sabot before launch.

One of the most complex and fragile models ever tested at speeds above 6 km/sec in a ballistic range is illustrated in Figure 3.31 (Ref.3.27). This small-scale model of an Apollo command capsule used a passive telemetry system (see Chapter 12) to measure afterbody heating during flight. Each model was constructed from no less than eight parts, which were glued together with epoxy glue. All electrical connections in the model were soft-soldered. A photograph showing the individual components along with an assembled model is presented in Figure 3.31. Several of these models were launched successfully at velocities up to 6.1 km/sec and the desired in-flight data were obtained. A sketch of the sabot used to launch the models is also shown in Figure 3.31.

3.5.2 Methods of Heat Protection

For speed above about 4 km/sec and for lower speeds when the free-stream density is high, a primary concern, particularly for pointed bodies such as cones, may be heat protection during flight. The need for heat protection is evidenced by melting or ablation leading to unacceptable rounding of sharp-tipped models, chemical burning of models in flight (Chapter 8), or spalling of model surfaces. There are three ways in which the model designer can solve these problems. One is to use metals that can be subjected to very high heating rates without melting. Whether or not a particular metal will melt during flight at particular test conditions can be ascertained by use of the following equation derived by Carslaw and Jaeger in Reference 3.28 for the time to reach melting temperature

$$ t_m = \left[\frac{(T_m - T_0)K}{2\dot{q}} \right]^2 \frac{\pi}{k} , \qquad (3.12) $$

where

t_m time to reach melting temperature at a particular point on the cone surface

T_m melting temperature

T_0 initial temperature

K thermal conductivity

k thermal diffusivity

and $\dot{q}$ is the stagnation point heating rate, which depends on test conditions and model geometry and is given by the equation $\dot{q} = C_H \frac{1}{2} \rho_\infty V_\infty^3 S$, where C_H is the heat-transfer coefficient, ρ_∞ and V_∞ are the free-stream density and velocity, respectively, and S is the model base area. The heating rate, $\dot{q}$, along the sides of the cone varies as $1/\sqrt{x}$ (x is axial distance along the cone). It is seen from Equation (3.12) that the time required to reach melting temperature is greatest for materials that have a high-melting temperature, high thermal conductivity, and low thermal diffusivity. Since the thermal diffusivity, k , is equal to the thermal conductivity, K , divided by the product of the material density, ρ_m , and specific heat, c , it is helpful to write Equation (3.12) in the form

$$ t_m = \frac{(T_m - T_0)^2 K \rho_m c \pi}{4 \dot{q}^2} . \qquad (3.13) $$

It is seen from Equation (3.13) that a material having a high value of the product of $\Delta T^2 K \rho_m c$ will have the longest flight time before starting to melt. Since the time to melt varies as the square of the melting temperature, metals with very high melting temperatures such as tungsten (3680°K), tantalum (3320°K), and molybdenum (2900°K) are the best metals to use for this purpose. It is important to recall here that these dense metals are also good ballast materials.

The second approach to the heat protection problem is to use plastics which undergo ablation during flight. The ablation gases coming off the model surface inhibit convective heating and minimize the mass loss. Plastics such as polytetrafluoroethylene (Teflon), Acetal (Delrin), Polycarbonate (Lexan), Polyethylene, Nylon, and Phenolic Nylon, have performed very satisfactorily in this respect. The amount of nose blunting and surface recession they experience is often acceptable to speeds of 10 km/sec. It is important to state here that all aerodynamic measurements such as static and dynamic stability, drag, lift, etc., made from flights where ablation of the surface is taking place at a high rate, must be considered as aerodynamic characteristics of "ablating" models. The aerodynamic characteristics of slender bodies are known to be strongly influenced by ablation. Nonablating models of the same geometry may have significantly different aerodyanmic characteristics (see, for

example, References 3.29 and 3.30). A study of the feasibility of obtaining aerodynamic data on ablating slender cones in a ballistic range is presented in References 3.31 and 3.32.

The third approach to the heat-protection problem is to use plastics but still not forfeit the advantages of metals. Thin ablative heat shields have been applied over metal bodies to combine heat protection through surface ablation and the high physical strength afforded only by metals. However, bonding these thin plastic coatings to metal models is not always simple and requires development of techniques to obtain good strength without weakening the metal structure. In the following paragraphs, examples are given of particular materials and model and sabot designs used successfully in high-speed tests where high heating rate was one of the problems to be overcome.

A solution of the first type, that is, metals with high melting temperatures, was used for the models shown in Figures 3.32 (Refs.3.31,3.32), and 3.33 (Ref.3.33). For the 10° half-angle cone (Fig.3.32) a tantalum nose was threaded into the aluminum aftersection. These slender cones have been successfully launched at speeds up to about 6 km/sec into still air at a range pressure of 0.04 atmosphere and experienced little blunting of the nose during flight. The sabots used to launch these models are also shown in the figure.

The 6° $20'$ half-angle cone shown in Figure 3.33 used a pure tungsten nose silver-soldered to a hollow, titanium alloy aftersection to alleviate tip blunting. Since these two materials could not be threaded together because it is nearly impossible to machine threads on pure tungsten, a silver soldering technique was used to join the two materials. The soldering method used was unique in that the silver-solder adheres to the pure tungsten stud but forms a mechanical junction with the titanium alloy aftersection by means of two rings machined into the walls of the hole which accommodates the stud. The sabots used to launch these models (Fig.3.33) are seen to be nearly identical to those presented in Figure 3.23. These four sabot fingers were made of linen-phenolic to provide strength and minimize weight and used a separate two piece cylindrical center section to accommodate the model. Use of the center section enabled straight-forward machining of the model cavity from one end.

A homogeneous plastic 30° cone, an example of the second heat protection method, the ablating model, is shown in Figure 3.34; this model was successfully launched at high speed and survived the high-heating conditions of the flight with no significant nose blunting or surface recession[3.34]. These models were made of solid polytetrafluorethylene (Teflon), a relatively weak material (Table 3.1)*. Successful high-speed launching of these solid Teflon cones was not attained until the completely encapsulating sabot shown in Figure 3.34 was used; all other attempts failed. Note in Figure 3.34 that it was necessary to make the polyethylene base piece (also, gas seal component of this sabot) very thin (1.2 mm) so that it would decelerate rapidly relative to the model.

Acetal plastic (Delrin) has also been used successfully at high-speed, and survived the heating during flight with little nose blunting and surface recession in the slender cone configuration shown in Figure 3.35 (Refs. 3.31,3.32). The sabot base piece used to launch these models at velocities up to 6 km/sec was polyethylene. It is interesting to note that gun performance limited the velocity of these tests rather than any structural limitation of the model-sabot combination.

The third and sometimes most desirable method of heat protection in high speed flight, that of using a relatively thin plastic coating over a metal model, is illustrated by the two configurations, in Figures 3.36 (Ref. 3.35) and 3.37 (Ref.3.23). The first configuration, a 30° half-angle cone, used a polyethylene outer sleeve which was injection molded over an aluminum (7075-T6) core. The models were then re-machined and trimmed to give the desired dimensions and were launched using the sabots shown in Figure 3.36. The polyethylene sleeve survived launching, provided heat protection to the model, and suffered little shape change during the course of the flight.

A much thinner plastic coating was found to provide a successful heat shield for bimetallic models of the configuration shown in Figure 3.37. The coating consisted of vinylidene fluoride polymer sprayed onto the model surface to a thickness of about 0.04 cm. The models were re-machined and trimmed to give a final coat thickness of about 0.02 cm. As can be seen from a comparison of Figure 3.37 with Figure 3.27, these configurations are the same but use different materials for the aftersections. The plastic-coated models required titanium alloy since the heat-curing cycle of the plastic was found to anneal the aluminum so that it deformed severely during the launch. The strength of the titanium alloy was not affected by the curing. Since titanium is heavier than aluminum, the size of the tungsten alloy front section was adjusted to achieve the same center-of-gravity location as for the earlier models. The coated models survived the heating with no significant nose blunting or surface recession. This is demonstrated by the shadowgraphs of one of these models at the first and last observation stations of the Ames Prototype Hypervelocity Free-Flight Facility shown in Figure 3.37.

3.5.3 Models For Maximum Speed Tests

Ballistic range tests such as those conducted to study radiation emitted by the shock layer ahead of a model (and also by the wake flow), to study impact phenomena, and also to study ablation and/or spalling of bodies simulating the behavior of meteorites, usually require the maximum model velocity attainable using the best guns available. Launching models from presently available light-gas guns at speeds above about 7.5 km/sec produces accelerations in excess of about 2×10^6 gravities; therefore only very small simple models can be used successfully. Fortunately, useful data can be obtained using these models. In this section, some representative examples of models of this type will be discussed.

* A cone with a half angle greater than 19.5° is aerodynamically stable - no ballasting is necessary

An important category of models here is the full caliber plastic model launched without a sabot. Most of these models, especially those used to make radiation measurements, consist of a short cylinder of plastic with the front face contoured to the particular shape of interest, such as flat, spherical or conical. The cylinder length for these models is usually about one-third caliber, or greater, for stability in the launch tube.

A sketch representing two full-bore plastic models, one of the type that achieved the highest velocity ever attained by an undamaged model in a light gas gun (11.3 km/sec), and also of the type frequently used in gas cap radiation studies, is presented in Figure 3.38. The full-bore right circular cylinders are machined from high-density polyethylene, polycarbonate, or other plastics. The model which achieved the highest velocity was successfully launched from a .22 caliber gun into a quiescent nitrogen atmosphere at a static pressure of about 1 torr (Ref.3.36).

At times, however, meteorite simulation studies and impact studies require firing very small (sub-caliber) models. In these cases a sabot is necessary. Figure 3.39 shows photographs of one such "model" and sabot combination which was launched successfully at speeds of about 8 km/sec from a caliber 30 deformable-piston light-gas gun at range pressures of about 0.03 atmosphere. The models were spherical particles of crystalline aluminum oxide (Al_2O_3) of from 400 to 700 microns diameter. Despite the high g loading, the very small weight of the particles kept stress levels below the strength of the materials. It was concluded in Reference 3.37 that mechanical breakup or disintegration of these aluminum oxide microspheres occurred during flight at these test conditions due to the thermal stress induced in the sphere by the temperature gradient in the particle. The thermal stress induced in the sphere was calculated using the following equation given by Timoshenko in Reference 3.38:

$$\sigma_T = 0.771 \frac{\alpha E}{2(1-\nu)} (T_m - T_0) ,$$ (3.14)

where

T_m melting temperature

T_0 initial temperature

α temperature coefficient of expansion

E elasticity modulus

ν Poisson's ratio,

and was found to be about an order of magnitude greater than the maximum tensile strength of the aluminum oxide, which is approximately 40,000 lb/in^2.

The serrated sabot used in these tests offers very high resistance to differential shearing of the four pieces. A further description of this interesting sabot type and its use are presented in Reference 3.39. A photograph of a cone model with a four-piece serrated sabot taken from this reference is presented in Figure 3.40.

Other examples of small saboted metal or glass spheres and a saboted thin polyethylene disc which have been successfully launched at speeds of about 9 km/sec are presented in Figures 3.41 to 3.44; pertinent information concerning the models and sabots are given in the table in each of the figures. An adhesive with little impact strength was used to hold the 600 micron diameter steel sphere in a small cavity on the front face of the sabot shown in Figure 3.41 before launch. The sabots shown in Figures 3.41 and 3.42 were separated from the models by aerodynamic forces acting on the front face. The sabots shown in Figures 3.43 and 3.44 were fired from a rifled launch tube and upon emergence from the gun, the centrifugal forces split and separated the sabot pieces from the models.

3.6 PHYSICAL MEASUREMENTS OF MODELS

A very important aspect of ballistic range testing of models is the determination of their physical characteristics prior to the test. The physical properties include dimensions and angles, mass, and moments of inertia. Accurate measurement of these properties is essential, since errors incurred here can lead to significant errors in the final results. Some of these properties are easy to measure accurately – e.g., diameter with a micrometer; others are very difficult to characterize, e.g., surface roughness. A discussion of some of the techniques used to make these measurements will be given in the following paragraphs.

3.6.1 Determination of Model Mass

The mass of a model is easily and accurately determined by use of a good analytical balance of either the equal-arm type (Fig.3.45(a)) or the substitution type (Fig.3.45(b)). For the equal-arm type, the model is placed on one of the pans and known weights added on the other pan until equilibrium is reached. The sum of the known weights is then equal to the model mass. For the substitution type, the model is placed in a pan, and known weights, which are built into the balance, are removed from the same end of the balance beam until equilibrium is achieved. Both types of analytical balances are easily accurate to 0.1 milligram, which, for models of the sizes described earlier, provides accuracy to a small fraction of one percent.

3.6.2 Determination of Model Center of Gravity

The center of gravity of a model can be determined by use of a modified analytical balance of the equal-arm type (see Figure 3.46). As shown in this figure, a plate which holds the model is attached to one end of the balance beam at an accurately known distance from the fulcrum. (The pan on this end of the beam is not needed and is therefore removed.) Known weights are placed in the pan at the opposite end of the balance beam until equilibrium is achieved. The distance between the model's center of gravity and the base of the model (front face of the plate) is then computed using the following equation:

$$X_{CG} = X_R \frac{m - m_{tare}}{M} - X_L . \tag{3.15}$$

where (see sketch in Figure 3.46)

M   model mass

m   sum of known weights necessary to achieve balance equilibrium

m_{tare} sum of known weights necessary to achieve balance equilibrium with no model

X_R distance from fulcrum to support point of pan

X_L distance from fulcrum to base of model.

The distances X_R and X_L are accurately determined by prior calibration of the balance using models with known centers of gravity such as accurately machined right circular cylinders. By this method, the centers of gravity of models can be determined to within 0.025 mm. This precision is usually quite adequate, however, the error in this measurement should always be compared to the model's static margin to assess its effect on the final results.

3.6.3 Determination of Model Moments of Inertia

To determine the aerodynamic stability characteristics, the moments of inertia of the model must be known. A simple method for measuring the moment of inertia of a body is by the use of a torsion pendulum. The period of oscillation of a torsion pendulum is

$$T = 2\pi \sqrt{\left(\frac{I + I_0}{C_0}\right)} . \tag{3.16}$$

where

I_0 tare moment of inertia (should be small relative to model)

C_0 constant, dependent on wire diameter and length

I moment of inertia of model.

A sketch of a typical torsion pendulum setup is shown in Figure 3.47. By placing cylinders of known moments of inertia in the holder, the value of C_0 and I_0 can be determined by measuring the periods of oscillation. Then, by measuring the period with the model in the holder, the moment of inertia of the model can be computed. With sensibly chosen torsion wires and calibration cylinders, values of the model moment of inertia can be determined accurate to a fraction of one percent[*].

A photograph of an apparatus used for moment-of-inertia measurements is presented in Figure 3.48. The wire and holder with a model attached are seen to the right in the figure. The model holder has a polished face which reflects a light beam from a fixed source to a photocell. The light beam serves to trigger the electron's counter. To eliminate the problem of centering the oscillation, the counter is triggered on alternate pulses emitted by the photocell. This method gives the time for one complete cycle.

3.6.4 Surface Finish Measurements

In ballistic-range tests intended to study boundary-layer transition on a model (see for example, Figure 3.21), the surface finish of the model must be controlled very precisely. This requires very accurate measurements of the amount and type of surface roughness present or produced on the model by machining, polishing, etc. For accurate measurements of surface roughness it is almost imperative that the techniques used do not mark, alter, or destroy the surface in any way. The use of instruments which contact the surface for example and trace the profile of roughness in the manner of a phonograph needle has been shown to be both inaccurate and damaging to the surface. Photomicrographs of the paths traced along the surface show that, even with a very light bearing force (on the order of a fraction of a gram), the sensing contact produces a furrow in the surface. Thus, it plows through the small grain roughness which is of interest in boundary-layer-transition work and in addition, leaves a scratch on the surface which has a width of the order of the tip diameter of the sensor and a depth which is proportional to both the bearing force of the sensor and the hardness of the model material.

---

[*] Length and diameter of the wire should be such that the period of oscillation is of the order of 1 to 2 seconds.

Two methods of surface finish measurements which meet this requirement and give accurate results are the multiple-beam interferometer and the wire shadow method. Both of these methods are described in detail in Reference 3.40. The first method uses green light with a wavelength of 5461 Å to produce a fringe pattern whose contour lines represent an elevation height of 274×10^{-6} mm. The second method, the wire shadow technique, utilizes a line shadow cast obliquely on the surface in question. Irregularities in the surface will produce an irregular shadow whose deviations can be measured with a microscope.

3.7 SABOT SEPARATION DEVICES AND SABOT TRAPS

As discussed in earlier sections of this chapter, the four basic methods used by the designer to achieve adequate separation between model and sabot before the model reaches the test area are:

(a) Design sabot parts which will produce large lift and/or drag forces and thus cause these pieces to fly away from the line of boresight and/or decelerate quickly behind the model. Success of this technique depends primarily on the ambient pressure outside the muzzle of the gun.

(b) Use the pressure force of the propellent gas acting in cavities at interfaces of the sabot base pieces and also sabot fingers to separate these pieces radially away from the model.

(c) Provide mechanical devices to decelerate the sabot and deflect it to one side. These devices will have their greatest use at very low ambient pressures.

(d) Use a sectioned sabot in a rifled barrel. The high tangential velocity of each piece carries it away from boresight and is independent of ambient pressure.

In some sabot designs employing the first method (i.e., aerodynamic forces), the sabot fingers separate radially from the model initially but then remain in close formation around the model during the entire flight. These segments can usually be stopped short of the test section by allowing them to impact into a steel plate which has a hole in the center large enough to allow only the model. A shallow-angle steel cone with a similar hole is sometimes added to the flat plate to make the initial impact oblique (and therefore less violent), and to force the sabot pieces radially outward. Of course this sabot trap will only be successful if there is a sufficiently high air density to provide an initial radial separation of the fingers.

For tests at low pressures, where the aerodynamic forces might not be adequate, a small tank with a higher static pressure can be used between the test section and gun[3.41]. A tank of this sort can be, in its simplest form, merely a length of tubing such as is shown in Figure 3.49. The entry and exit to this tank are sealed using thin plastic diaphragms. The entry diaphragm which is usually at the muzzle of the gun is broken either by the model and/or sabot or by the compressed air ahead of it. In the tank the high pressure air separates the sabot from the model, and the sabot segments are caught by the sabot trap as before. The model flies into the test section through the second diaphragm. In some tests, models cannot be permitted to fly through even these thin diaphragms because of the possibility of damage to sharp tips, leading edges or surface finish. In these cases the plastic diaphragms can be ruptured on signal with punches or exploding wires, or they might be replaced by quick-opening valv.

Extra care must be taken with this air-tank procedure to insure that the model receives negligible angular disturbance during the sabot separation process. If the model is pitched and enters the low pressure test section with excessive pitching rate, there could be insufficient restoring moment at this lower pressure to prevent the model from tumbling. If this disturbance is unavoidable but fairly repeatable it might be possible to adjust the muzzle position and air tank pressure so the model enters the low-pressure section at nearly maximum pitch amplitude (and low pitching rate), thus limiting the final amplitude.

In counter-flow facilities, as mentioned in Chapter 5, the shock-tube-wind-tunnel receiver tank (dump tank) has been used as the high-pressure sabot-separation tank. With the counter-flow air stream, the exit diaphragm (between the test section and the dump tank) is removed by the tunnel flow. Also, in this type of facility, the static pressure of the still air in the dump tank can be adjusted so that the dynamic pressure experienced by the model flying in this still air is equal to the dynamic pressure experienced during flight through the counter-flow air stream, hence, the model experiences no large changes in restoring moment in moving from one regime to the other.

For the case of a solid sabot base, it is often necessary to mechanically remove the piece from the flightpath using some type of sabot decelerator together with a deflector. The most successful devices for diverting these sabots are the contracting tube with a deflecting section or separate ramp[3.41,3.42]. The decelerator is a muzzle extension of contracting bore diameter with gas-release ports, Figure 3.50. The model and sabot enter this contracting section which then squeezes and decelerates the sabot base during the entire travel through the barrel extension. The driving gases are diverted out the ports in the wall. The model, which must be subcaliber, leaves the sabot and continues at launch speed. The sabot then strikes a deflecting ramp, or is deflected by the barrel (see Figure 3.50) and is diverted off the flight line of the model and into a retaining plate. The ramp and deflecting barrel are positioned so that the model passes undisturbed into the range. Another version of this simple sabot decelerator is merely a plate, with a subcaliber hole, attached to the muzzle of the gun which decelerates the sabot by shearing off a thickness of the sabot's outer wall material. This type of decelerator was used to separate the model and sabot shown in Figure 3.12.

As noted earlier, separation of a finger type or split sabot from the model can be achieved using a rifled launch tube in tests where model spin is either desirable or not detrimental. In impact studies, where positive separation is demanded and only the model must strike the target, rifled barrels have been used at velocities up to 9 km/sec.

3.8 PROOF TESTING

With a newly designed model and sabot, it is usually necessary to conduct proof tests. When these tests are made, frequently the initial design is not completely successful; i.e., it fails to put the model into flight undeformed and intact, or it imparts excessive disturbance to the model at sabot separation, or the sabot does not separate widely enough from the model. Quite often,when a new design is tried only fragments of the model and/or sabot will pass through the instrumented stations of the test facility. In these cases, it is very difficult to determine the exact cause of model and/or sabot failure.

In such cases, additional instrumentation is often required, usually to obtain more information on events occurring near the gun muzzle For example, if the condition of the model and sabot can be determined just as they emerge from the gun, it may be possible to conclude whether a structural failure occurred in the model or in the sabot, and whether the failure is due to a misalinement in the launch tube or whether the entire problem is in the model-sabot separation sequence. To accomplish this, X-ray photographs have been taken at the muzzle to determine the structural integrity and relative orientation of the parts.

The use of X-ray photography is advantageous, since such pictures can be taken in the presence of very bright muzzle flashes, which would completely blacken ordinary visible light photographs. An example of an X-ray photograph is presented in Figure 3.51. Also, a series of X-ray photographs taken at various distances from the gun muzzle in separate launchings of identical model-sabot combinations is presented in Figure 6.27. However, pictures like these are not easily obtained, and usually require a significant investment of time and effort in setting up the equipment, devising and testing suitable triggers, etc.

Pictures near the muzzle have also been obtained with high speed motion pictures cameras, looking toward the muzzle with telescopic lenses from a safe distance. The muzzle flash can provide back lighting for such pictures, and the sabot separation sequence can be recorded in silhouette. However, the number of frames is limited, even with cameras operating at 5000 to 7000 frames per second and frequently the model is not seen until it emerges from and outruns the muzzle blast. The critical events may by this time already be past.

Yaw cards (Chapter 6) are also useful for diagnosing separation difficulties. The relative positions and attitudes of model, sabot fingers, sabot base, etc., can be well identified, and used as a basis for constructing motion histories of the parts. These can give considerable insight as to whether the separation is taking place as planned. Model failures can also be diagnosed in this way – e.g., a bent or broken tip is conspicuously evident, as are other missing or separated sections of models. A problem with yaw cards is that they are normally torn into small pieces by the muzzle blast, and these pieces must be painstakingly gathered and fitted together. At very high launch velocities, the cards are essentially demolished, and the parts may not be recoverable and may even burn. Hence, this technique has very definite limitations.

When the development process is successfully completed, which may take several iterations in the design, and the model is launched in good condition, at the proper attitude and with small disturbance, the end objective of the design work described in this chapter has been achieved. Then it is possible to proceed, using these models to conduct the various types of tests which will be discussed in the following chapters.

REFERENCES

3.1 Watson, J.D.
Godfrey, C.S.
An Investigation of Projectile Integrity Using Computer Techniques. PITR-67-10, Physics International Co., 1967

3.2 DeRose, Charles E.
Boissevain, Alfred G.
An Exploratory Investigation in a Ballistic Range of the Stability Derivatives of a Simple Airplane Configuration at Low Supersonic Speeds. NASA TN D-139, Dec. 1959.

3.3 Warren, H.R.
Templin, R.J.
Cheers, B.
Aeroballistic Range Measurements of the Performance and Stability of Supersonic Aircraft. Presented at 26th annual meeting of IAS, Jan. 27-30, 1958.

3.4 DeRose, Charles E.
Ballistic-Range Tests of a Drag-Ring Configuration at Mach Numbers Around 2. NASA TN D-4291, Dec. 1967.

3.5 Kruse, Robert L.
Short, Barbara J.
Comparison of Free Flight and Wind Tunnel Data for Apollo Launch Escape Vehicle at Mach Numbers 0.7 and 1.2. NASA TM X-1196, Jan. 1966.

3.6 Canning, Thomas N.
DeRose, Charles E.
Drag and Rolling-Moment Effectiveness of Trailing-Edge Spoilers at Mach Numbers 2.2 and 5.0. NACA RM A55F15, Oct. 1955.

3.7 Boissevain, Alfred G.
Experimental Investigation of the Damping in Roll of Cruciform Triangular Wing-Body Combinations at Mach Numbers from 1.5 to 6.0. NACA RM A54B15a, April 7, 1954.

3.8 Boissevain, Alfred G.
Intrieri, Peter F.
Determination of Stability Derivatives from Ballistic Range Tests of Rolling Aircraft Models. NASA TM X-399, Jan. 1961.

3.9 Seiff, Alvin
Wilkins, Max E.
Experimental Investigation of a Hypersonic Glider Configuration at a Mach Number of 6 and at Full Scale Reynolds Numbers. NASA TN D-341, Jan. 1961.

3.10 Sammonds, Robert I.
The Shock Wave Patterns on a Cranked Wing Configuration. NASA TN D-346, Nov. 1960.

3.11 DeRose, Charles E.
The Aerodynamic Characteristics of a Blunt Half-Cone Entry Configuration Obtained from Ballistic Range Tests at Mach Numbers near 3. NASA TM X-578, Oct. 1961.

3.12 Chapman, Gary T.
Transition of the Laminar Boundary Layer on a Delta Wing with 74° Sweep in Free Flight at Mach Numbers from 2.8 to 5.3. NASA TN D-1066, Aug. 1961.

3.13 Sommer, Simon C.
Short, Barbara J.
Free-Flight Measurements of Turbulent Boundary Layer Skin Friction in the Presence of Severe Aerodynamic Heating at Mach Numbers from 2.8 to 7.0. NACA TN 3391, March 1955.

3.14 Murphy, Charles A.
Bull, Gerald V.
Edwards, Howard D.
Upper Atmosphere Winds Measured by Gun-Launched Projectiles. BRL Memorandum Report No. 1747, May 1966.

3.15 Marks, S.T.
Pilcher, J.O. II
Brandon, F.J.
The Development of a High Acceleration Testing Technique for the Electronic Instrumentation of HARP Projectile Systems. BRL Memorandum Report No. 1738, March 1966.

3.16 Jaffe, Peter
Hypersonic Ballistic Range Results of Two Planetary Entry Configurations in Air and Carbon Dioxide/Nitrogen Mixtures. TR No. 32-543, JPL, 1964.

3.17 Crogan, Leonard E.
Summary Report on R-71 Program. NASA CR 55543, NOL, Jan. 1964.

3.18 Intrieri, Peter F.
Free-Flight Measurements of the Static and Dynamic Stability and Drag of a 10° Blunted Cone at Mach Numbers 3.5 and 8.5. NASA TN D-1299, 1962.

3.19 Compton, Dale L.
Free-Flight Measurements of Drag and Static Stability for a Blunt-Nosed 10° Half Angle Cone at Mach Number 15. NASA TM X-507, 1961.

3.20 Kirk, Donn B.
Miller, Robert J.
Free-Flight Tests of Fifth-Stage Scout Entry Vehicle at Mach Numbers of 5 and 17. NASA TN D-1425, 1962.

3.21 Short, Barbara J.
Dynamic Flight Behavior of a Ballasted Sphere at Mach Number from 0.4 to 14.5. NASA TN D-4198, 1967.

3.22 Curtis, John S
An Accelerated Reservoir Light-Gas Gun. NASA TN D-1144, 1962.

3.23 Intrieri, Peter F.
Study of the Stability and Drag at Mach Numbers from 4.5 to 13.5 of a Conical Venus-Entry Body. NASA TN D-2827, 1965.

3.24 Kirk, Donn B.
    Chapman, Gary T.
Free-Flight Tests of a Blunt-Nosed Flare-Stabilized Body at Speeds to 8.2 km/sec. Journal of Spacecraft and Rockets. Vol.3, No.3, March 1966, pp.374-377.

3.25 Malcolm, Gerald N.
Stability and Drag Characteristics at Mach Numbers of 10 and 26 of a Proposed Slender Atmospheric Probe. NASA TN D-3917, 1967.

3.26 DeRose, Charles E.
Trim Attitude, Lift and Drag of the Apollo Command Module with Offset Center-of-Gravity Positions at Mach Numbers to 29. NASA TN D-5276, June 1969.

3.27 Yee, Layton
Free-Flight Measurements of Heat Transferred to the Apollo Afterbody With and Without Heat Shield Ablation. NASA TM X-1096, 1965.

3.28 Carslaw, H.S.
    Jaeger, J.C.
Conduction of Heat in Solids. Clarendon Press, Oxford, 1947, First ed.

3.29 Syvertson, C.A.
    McDevitt, J.B.
Effects of Mass Addition on the Stability of Slender Cones at Hypersonic Speeds. AIAA Journal, Vol.1, No.4, 1963, pp.939-940.

3.30 Chrusciel, G.T.
    Chang, S.S.
Effects of Ablation on Hypersonic Aerodynamic Stability Characteristics. AIAA Paper 66-410, 1966.

3.31 Intrieri, Peter F.
    Kirk, Donn B.
    Terry, J.E.
Ablation Testing in Ballistic Ranges. AIAA Paper No.68-385, April 1968.

3.32 Intrieri, Peter F.
    Kirk, Donn B.
    Chapman, Gary T.
Ballistic Range Tests of Ablating and Nonablating Slender Cones. AIAA Paper 69-179, Jan. 1969.

3.33 Crogan, Leonard E.
Drag and Stability Data Obtained from Free-Flight Hypersonic Firings of Both Sharp and Blunt-Nosed 12-degree 40-Minute Total Angle Cones at Several Range Pressures. TR 63-36, NOL, 1966.

3.34 Intrieri, Peter F.
Experimental Stability and Drag of a Pointed and a Blunted 30° Half-Angle Cone at Mach Numbers from 11.5 to 34 in Air. NASA TN D-3193, 1966.

3.35 Compton, Dale L.
    Cooper, David M.
Measurements of Radiative Heating on Sharp Cones. AIAA Journal, Vol.3, No.1, Jan. 1965, pp.107-114.

3.36 Denardo, B.Pat
Penetration of Polyethylene into a Semi-Infinite 2024-T351 Aluminium up to Velocities of 37,000 Feet per Second. NASA TN D-3369, 1966.

3.37 Collins, Daniel,J.
    Sangster, David K.
    Rogers, Walter K.
Feasibility Study on Small Particle Ablation Using a Free-Flight Range. CR-66-2128, General Motors DRS and Sandia Corp., Nov. 1966.

3.38 Timoshenko, S.
    Goodier, J.H.
Theory of Elasticity. 2nd ed. McGraw-Hill, 1951, pp.416-421.

3.39 Curtis, John S.
Sabots. CTN64-04, General Motors DRL, Aug. 1964.

3.40 Wilkins, Max E.
    Darsow, John F.
nishing and Inspection of Model Surfaces for Boundary-Layer-Transition Tests. SA Memo 1-19-59A, Feb. 1959.

3.41 Solnoky, P.
Some Recent Developments in Projectile Launching Techniques at Canadian Armament Research and Development Establishment. CARDE TM 727-62, Oct. 1962.

3.42 Teng, R.N.
Advances in Light-Gas Gun Model Launching Techniques. AIAA Journal Vol.5, No.11, Nov. 1967, pp.2082-2084.

TABLE 3.1

Physical Characteristics of Commonly used Materials

(Ref.: Materials in Design Engineering, Materials Selector Issue, Vol.60, No.5)

Material	Density (g/cc)	Ultimate Strength		Strength/weight ratio
		$\left(\dfrac{\text{newtons}}{\text{m}^2} \times 10^{-6}\right)$	$\left(\dfrac{\text{lbf}}{\text{in}^2} \times 10^{-3}\right)$	$\left(\dfrac{\text{newtons}}{\text{m}^2} \times 10^{-6}\right)$
Metals				
Tungsten	19.4	1520	(220)	78
Tantalum TA-10W	16.8	1100	(160)	65
Steel 4340	7.8	1980	(287)	254
Titanium 7Al-4Mo (Heat treat, max)	4.5	1380	(200)	307
Aluminum 7075 T6	2.8	572	(83)	204
Aluminum 2024 T3	2.8	483	(70)	172
Magnesium AZ63A	1.8	276	(40)	153
Plastics				
Fluorocarbon Teflon	2.2	45	(6)	20
Polycarbonate Lexan	1.2	65	(9)	54
Polyamides Nylon 66	1.1	83	(12)	75
Polyethylene High mol. wt.	0.94	37	(5)	39

TABLE 3.2

Model, Facility, and Test Requirements

Model	10° half-angle cone	
Test Conditions:	Mach number 15	
	Reynolds number (based on model diameter) from 100,000 to 1,000,000	
Facility:	instrumented length	23 meters
	shadowgraph stations	16 orthogonal pairs
	station spacing	1.5 meters
	pressure capability	1 atm to 0.001 atm
	air temperature	290^oK
Gun:	1.27 cm diameter light gas gun (deformable-piston, isentropic-compression)	

TABLE 3.3

Model Characteristics

R_{e_∞} (based on d)	100,000	500,000	1,000,000
Model dia. (cm) Model material	0.84 Nylon	0.84 Aluminum	0.84 Steel
Weight (gram)	0.27	0.63	1.80
ρ_∞ (atm)	0.034	0.17	0.34
I_y $(kg\text{-}m^2)$	0.8×10^{-8}	1.8×10^{-8}	5.1×10^{-8}
X_D $(C_D = 0.10)$ (cm)	6.9	14.7	10.4
λ (m)	12	8	10
Z_{swerve} (cm)	0.5	0.5	0.5
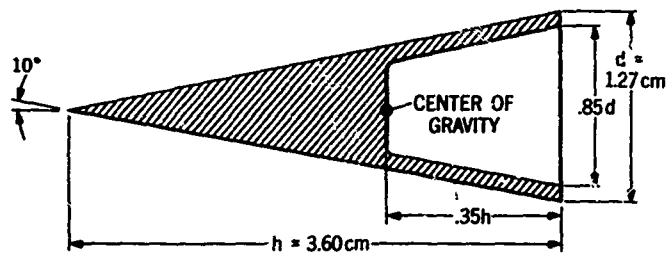
Fig. 3.1 Sketch of cone hollowed out for aerodynamic stability
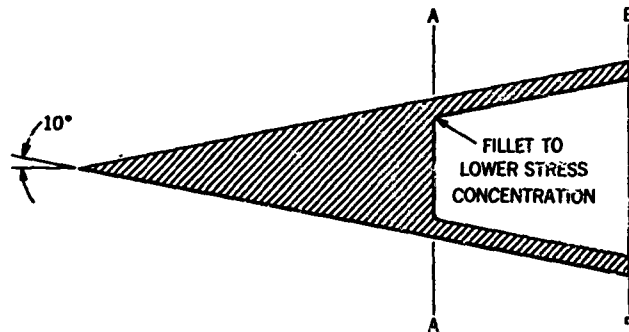
Fig. 3.2 Sketch of critical sections for stress analysis
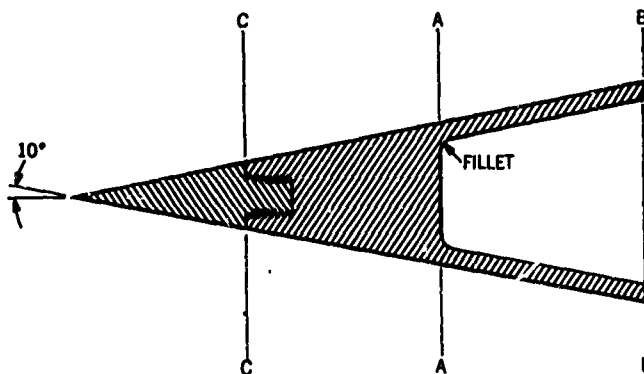
Fig. 3.3 Sketch of bimetallic hollow-base model
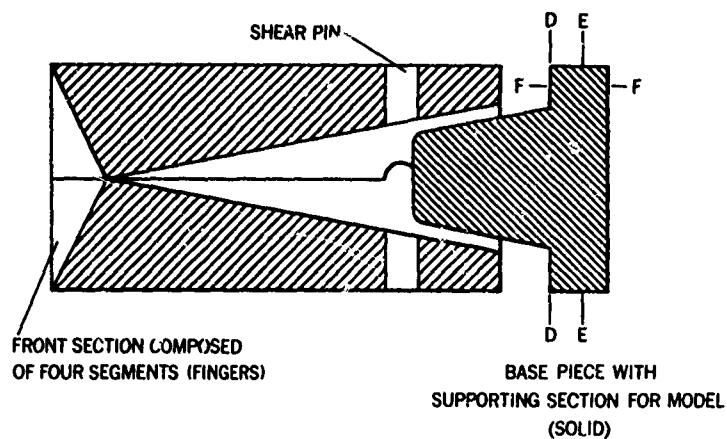
Fig. 3.4 Sketch of enclosing sabot for plastic cone model
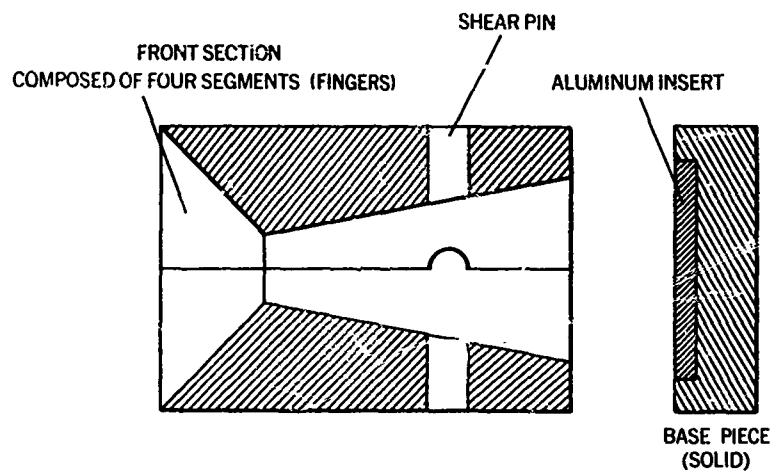
Fig. 3.5   Sketch of semi-enclosing sabot for metal cone model
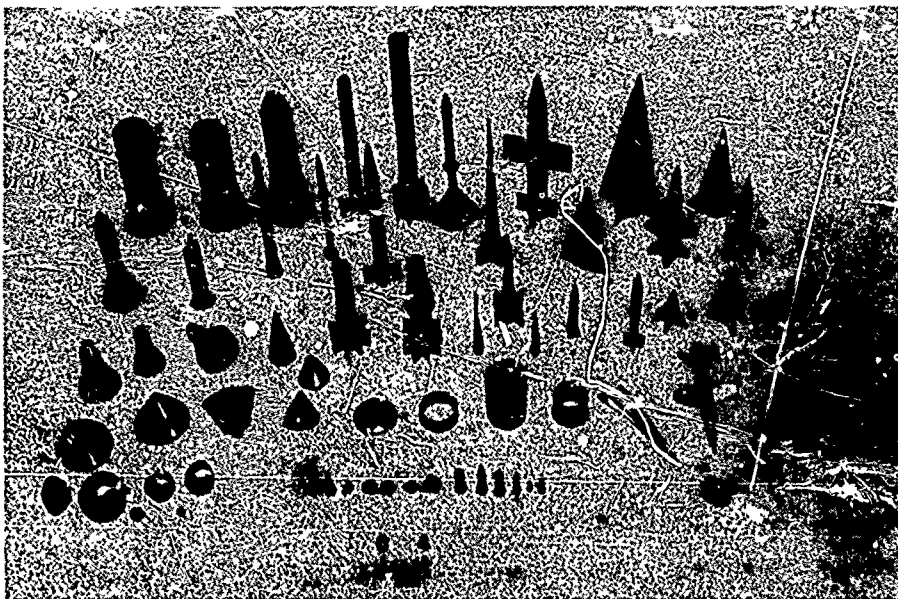
Fig. 3.6   Photograph showing variety of models tested at Hypersonic Free-Flight Branch, Ames Research Center
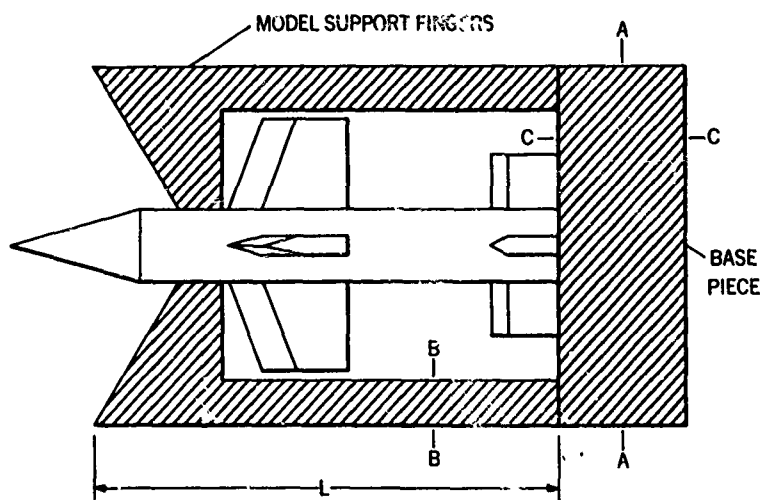
Fig. 3.7   Sketch of critical sections for stress analysis
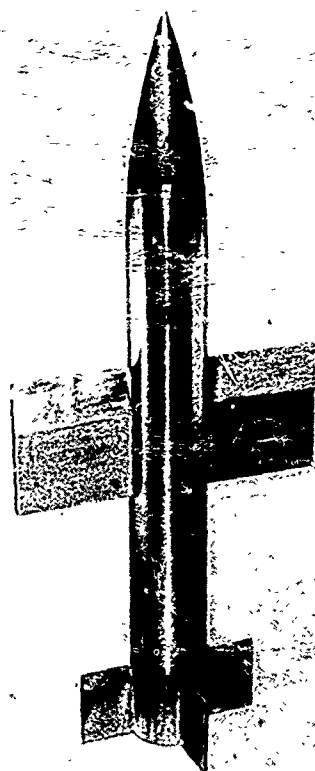
V_m, km/s	ρ, atm	GUN	PEF
0.5	1.0	76mm POWDER GAS	3.2

Fig. 3.8   Photograph of airplane-type model
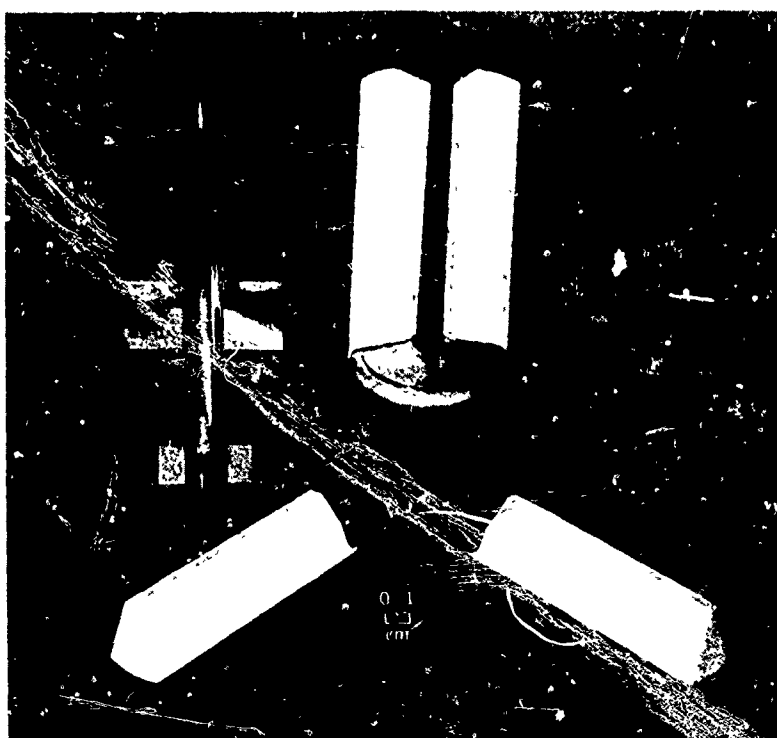
Fig. 3.9   Photograph of airplane-type model with sabot
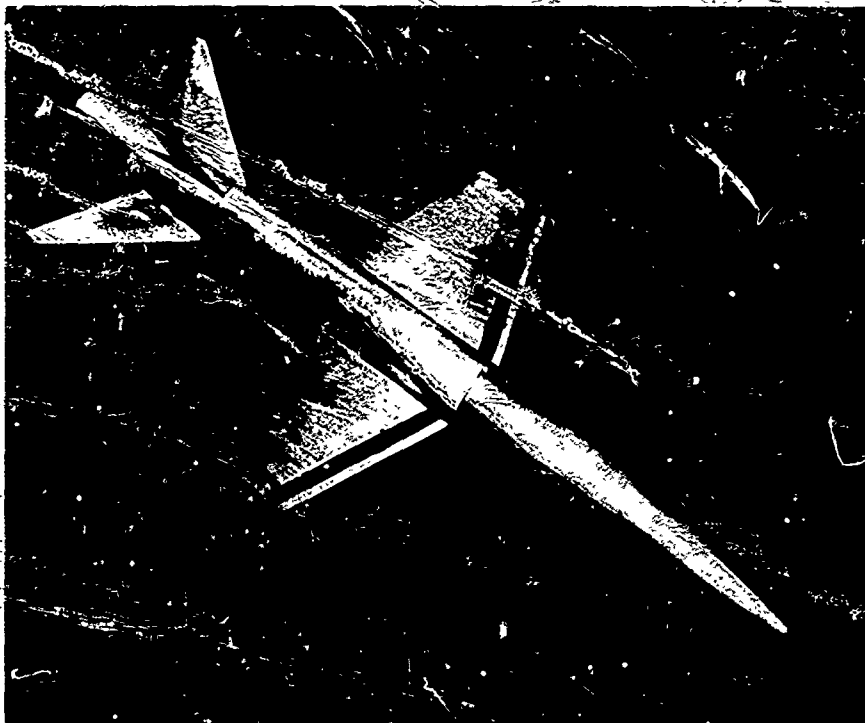
V_m, km/s	ρ, atm	GUN	REF
0.4	1.0	76mm POWDER GAS	NONE (AMES)

Fig. 3. 10   Photograph of winged-body model
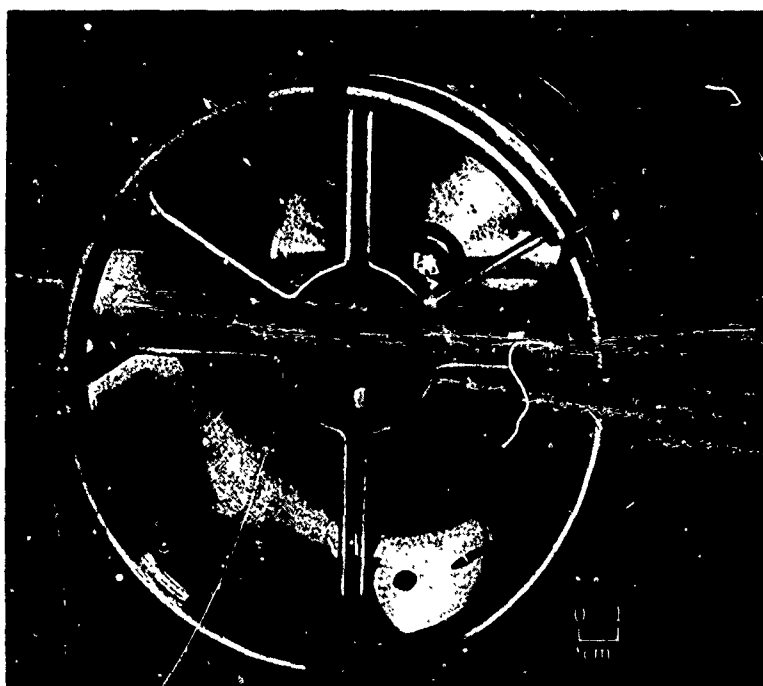
Fig. 3. 11   Cylindrical sabot for winged models.   (Courtesy of Canadian Armament Research and Development Establishment.)
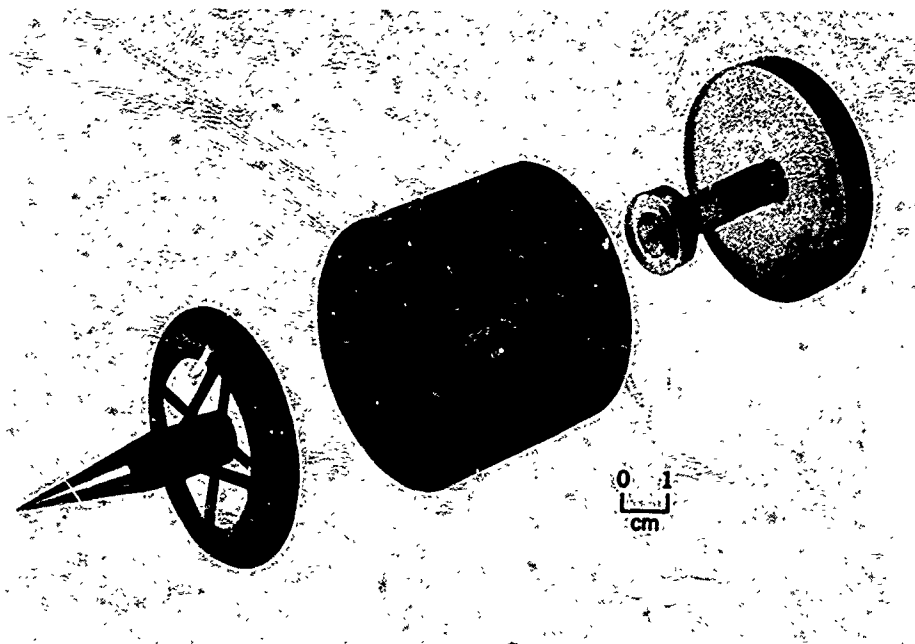
V_m, km/s	ρ, atm	GUN	REF
0.8	0.01	57 mm POWDER GAS	3.4

Fig. 3.12   Photograph of Martin Mars-Probe model and sabot
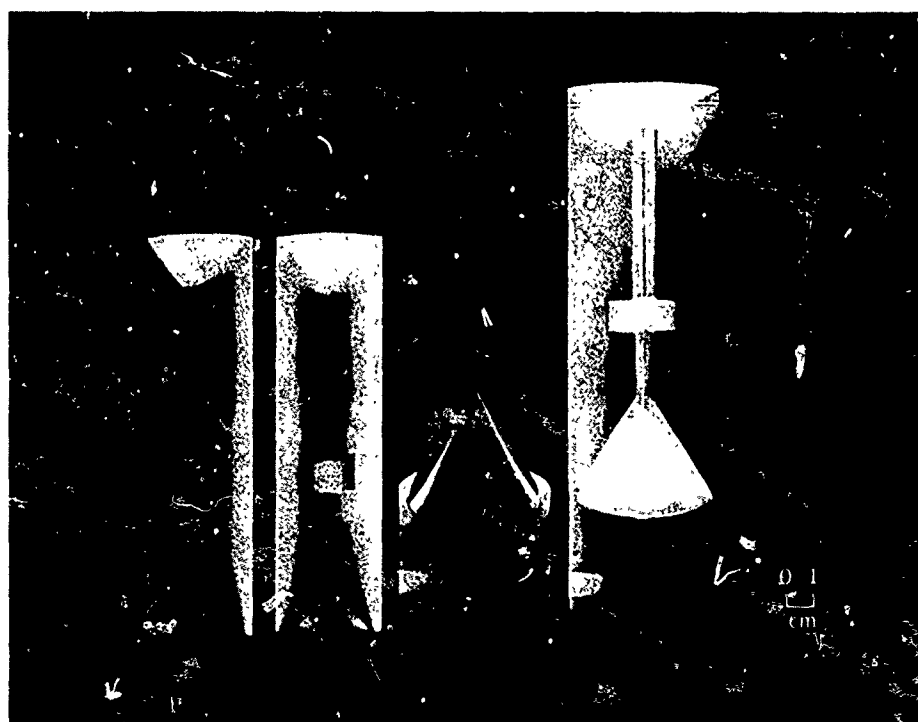
V_m, km/s	ρ, atm	GUN	REF
0.4	1.0	57 mm POWDER GAS	3.5

Fig. 3.13   Photograph of Apollo launch-escape-configuration model and sabot

126
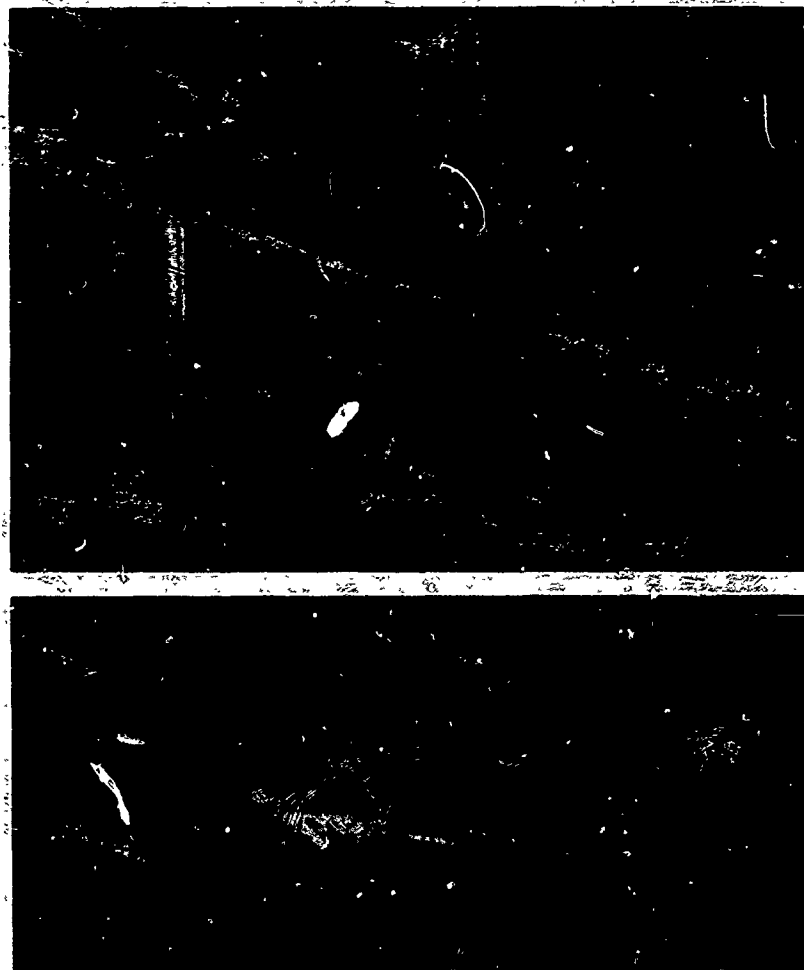
V_m, km/s	V_R, km/s	ρ, atm	GUN	REF.
0.8	1.3	0.1-1.0	37mm RIFLED POWDER GAS	3.5

Fig. 3. 14   Photograph of trailing-edge-spoiler models and model-sabot combination

(a) Composite seal   (b) Obturation cup
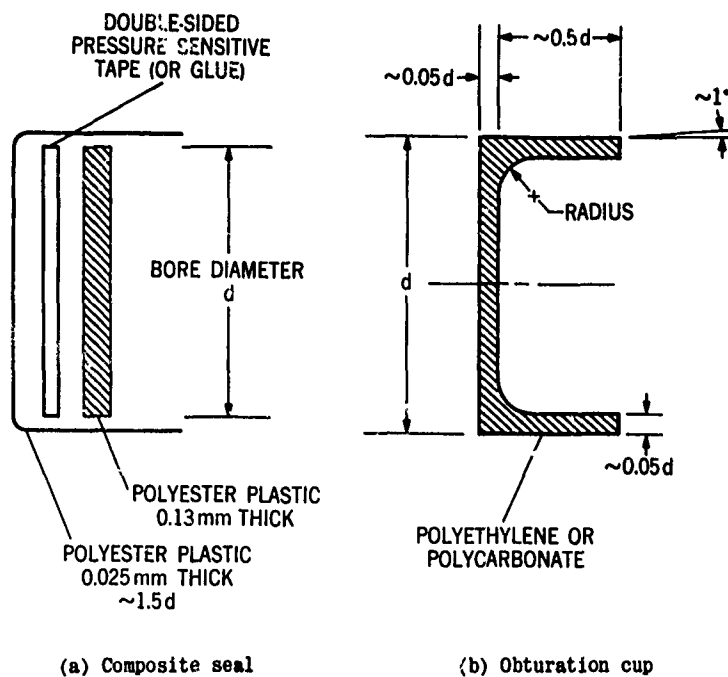
Fig. 3. 15   Sketch of two types of gas seals

Fig. 3. 16   Photograph of five investment-cast models
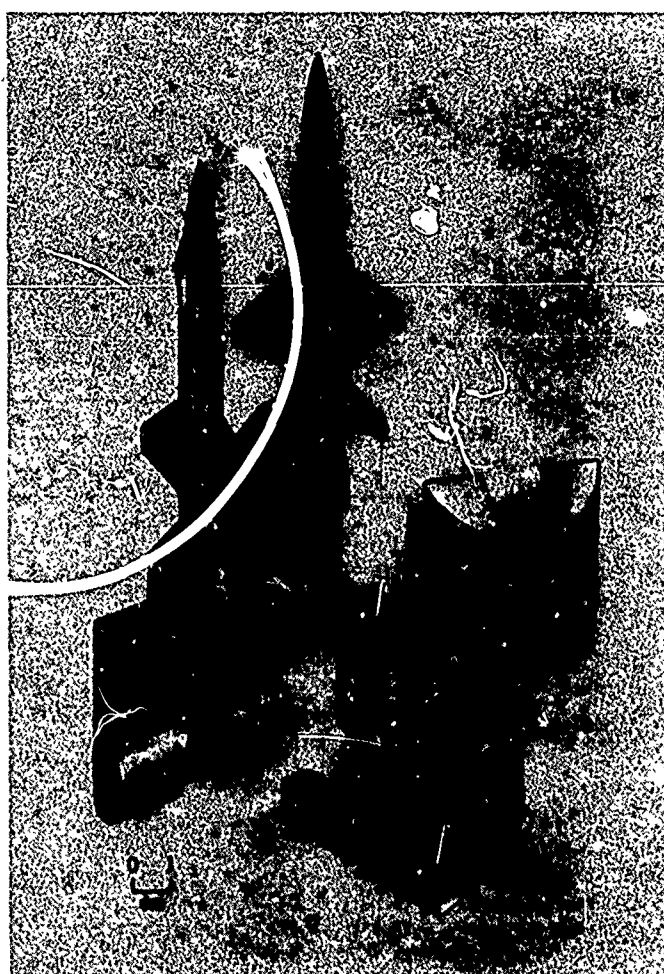
V_m, km/s	ρ, atm	GUN	REF
1.5	1.0	57 mm POWDER GAS	3.8

Fig. 3. 17   Photograph of X-15 research-airplane model and sabot .

V_m, km/s	V_R, km/s	ρ, atm	GUN	REF
1.3	1.8	0.1	57 mm POWDER GAS	3.9

Fig. 3. 18   Photograph of three-wing-airplane model and sabot

V_m, km/s	ρ, atm	GUN	REF
0.6	1.0	45 mm POWDER GAS	NONE (AMES)

Fig. 3.19   Photograph of hypersonic-glider model and sabot
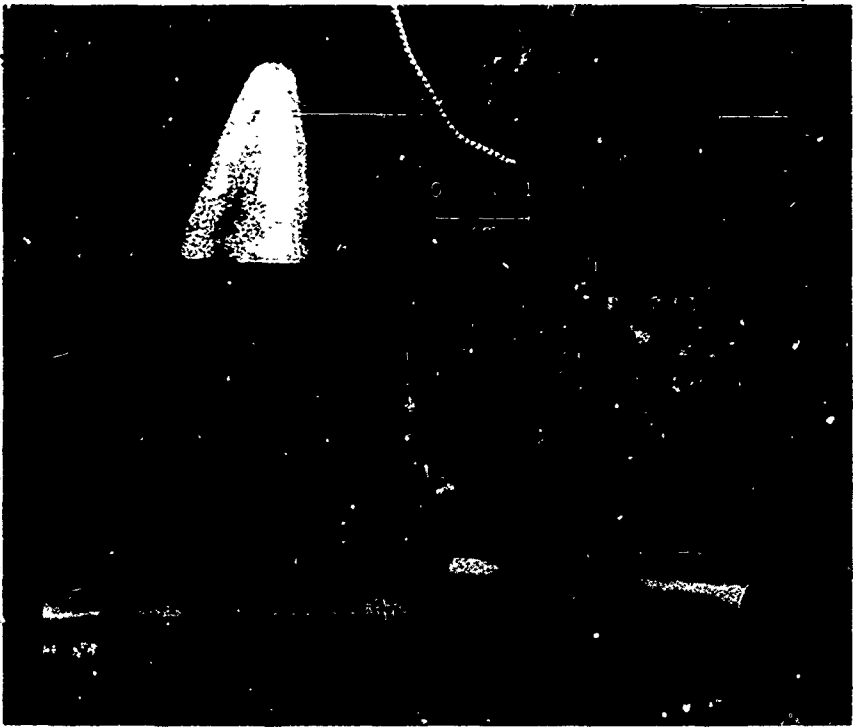
V_m, km/s	ρ, atm	GUN	REF
1.1	0.07	45mm POWDER GAS	3.11

Fig.3.20   Photograph of half-cone lifting-body model aud sabot

V_m, km/s	ρ, atm	GUN	REF
1.4	1.0	57mm POWDER GAS	3.12

Fig.3.21   Photograph of 74°-swept-back delta-wing model and sabot

V_m, km/s	V_R, km/s	ρ, atm	GUN	REF
1.3	1.8	1.0	37 mm RIFLED POWDER GAS	3.13

(a) Photograph of skin-friction-drag models

V_m, km/s	V_R, km/s	ρ, atm	GUN	REF
0.8	1.3	0.1-1.0	37 mm RIFLED POWDER GAS	3.6

(b) Photograph of spoiler-drag models

Fig. 3.22   Photograph of two varieties of open-ended-tube models
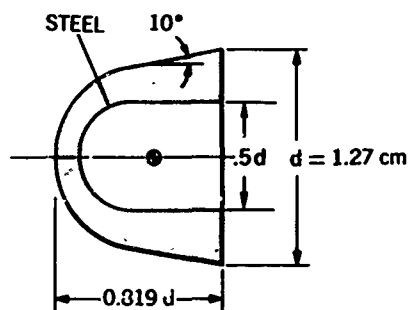
(a) Sketch of model
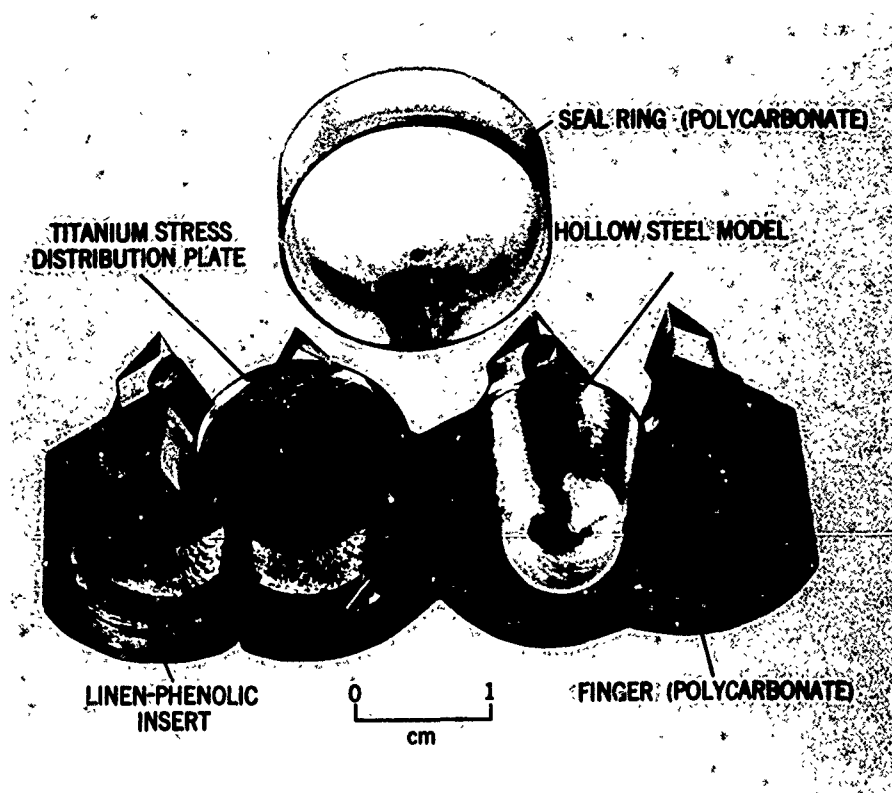
(b) Photograph of model with sabot

V_m, km/s	ρ, atm	GUN	REF
4.7	.12	20 mm TWO-STAGE LIGHT GAS	3.16, 3.17

Fig. 3.23   Short blunt cone, hollow base.   (Courtesy of Jet Propulsion Laboratory and US Naval Ordnance Laboratory.)

(a) Sketch of model   (b) Sketch of model with afterbody
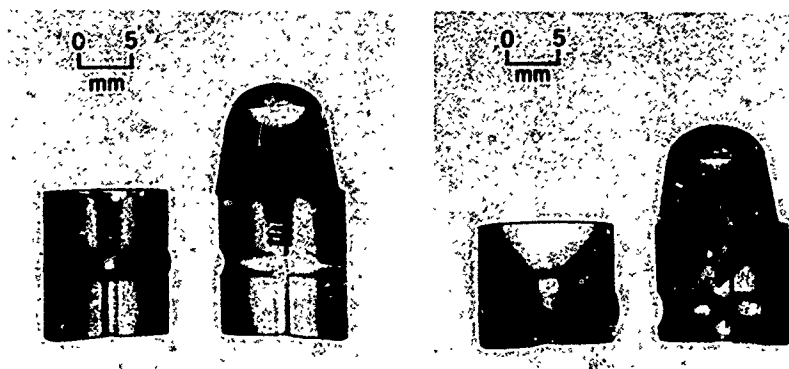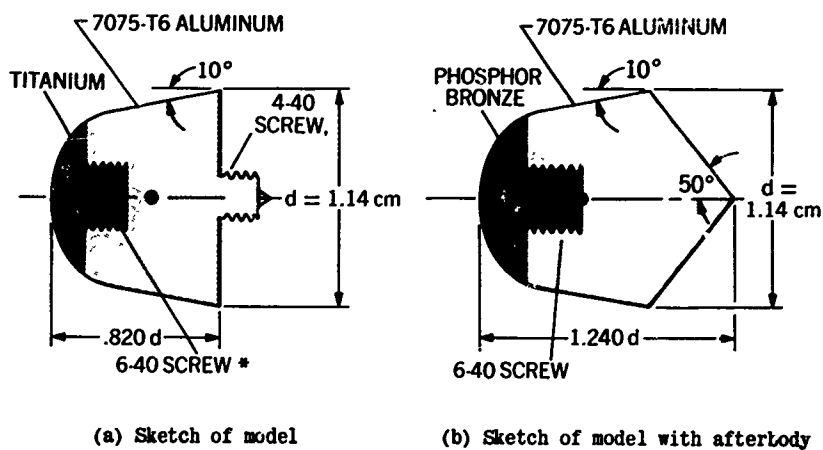
(c) Photographs of models with sabots

*SCREW THREADS DESIGNATED IN THIS CHAPTER
ARE AMERICAN STANDARD FINE-THREAD SERIES.

V_m, km/s	ρ, atm	GUN	REF
3.0	.1	12.7 mm SINGLE-STAGE LIGHT GAS	3.18, 3.19

Fig. 3.24   Short blunt cone (ballasted)
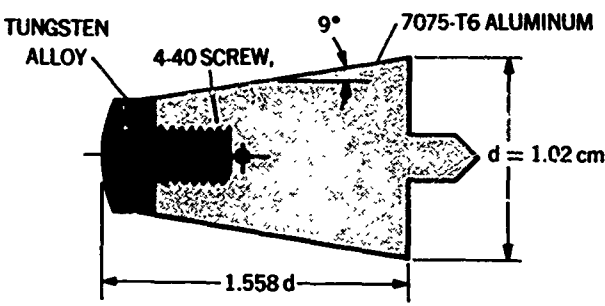
(a) Sketch of model
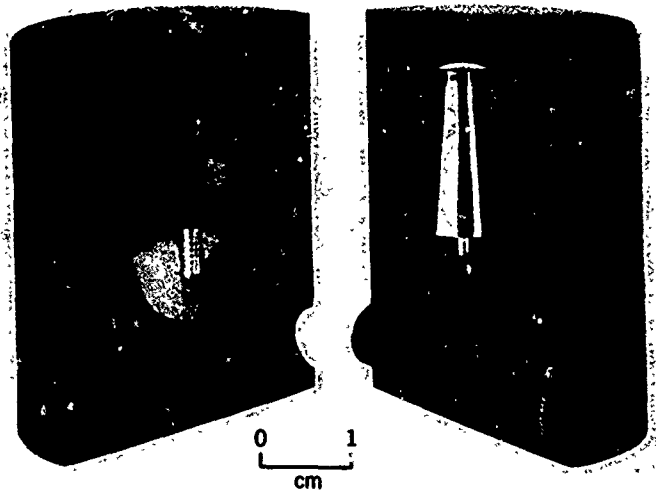
(b) Photograph of model with sabot

V_m, km/s	V_R, km/s	ρ, atm	GUN	REF
3.0	3.7	.38	37 mm SINGLE-STAGE LIGHT GAS	3.20

Fig. 3.25   Blunt-nosed 9^0 cone
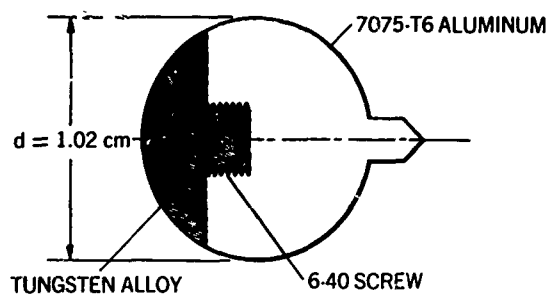
(a) Sketch of model

(b) Photograph of model with sabot

V_m, km/s	ρ, atm	GUN	REF
5.0	.25	12.7 mm DEFORMABLE-	3.21
4.0	1.0	PISTON LIGHT GAS	

Fig. 3.26   Ballasted sphere
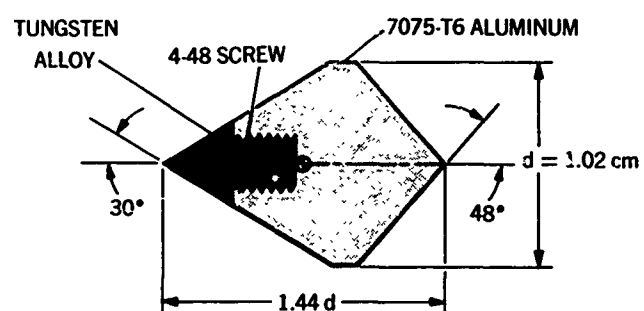
(a) Sketch of model
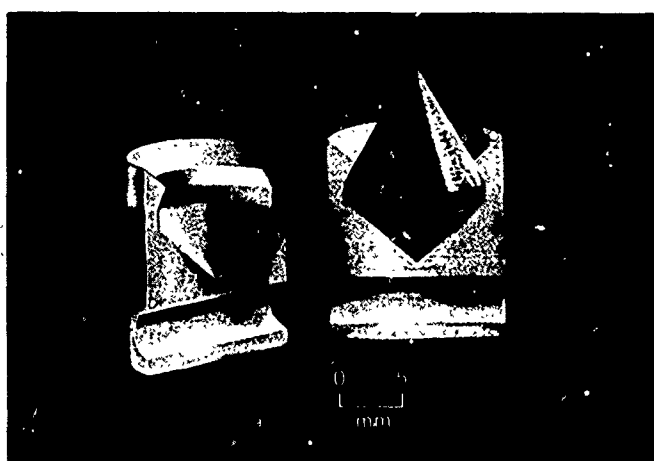
(b) Photograph of model with sabot

V_m, km/s	ρ, atm	GUN	REF
3.0	.4	12.7 mm DEFORMABLE-PISTON LIGHT GAS	3.23

Fig. 3. 27   Conical body
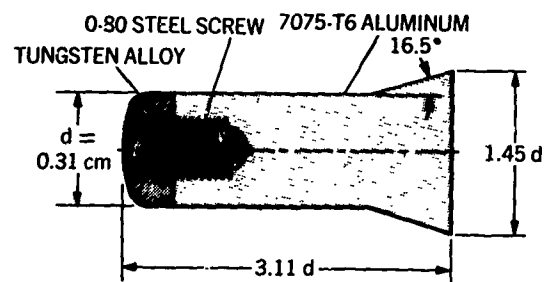
(a) Sketch of model
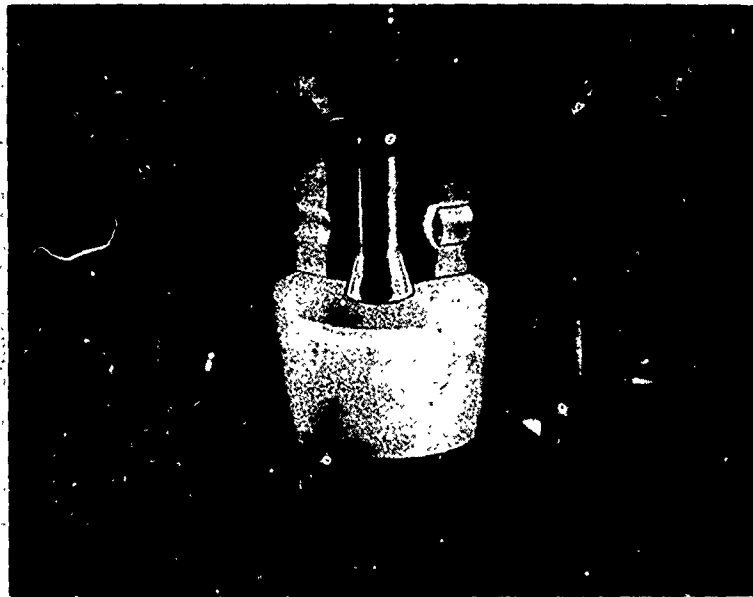
(b) Photograph of model with sabot

V_m, km/s	V_R, km/s	ρ, atm	GUN	
6.4	8.2	.03	12.7 mm DEFORMABLE-PISTON LIGHT GAS	3.24

Fig. 3. 28   Blunt-nosed flare-stabilized body
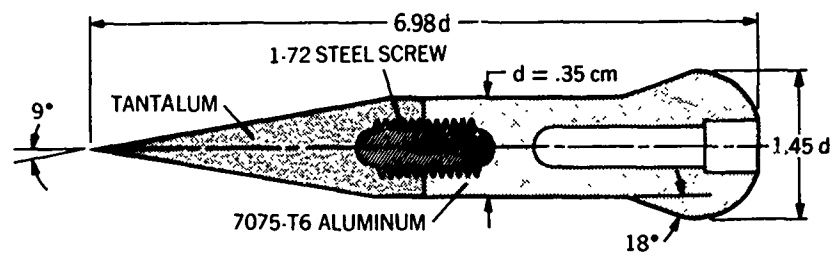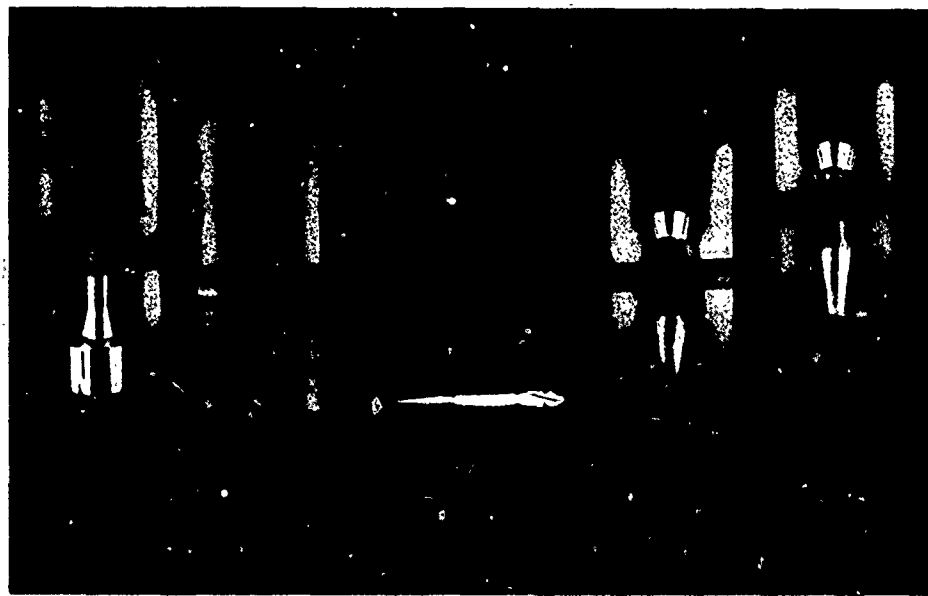
(a) Sketch of model

(b) Photograph of models with sabots

V_m, km/s	V_R, km/s	ρ, atm	GUN	REF
3.8	5.7	.12	12.7 mm DEFORMABLE-PISTON LIGHT GAS	3.25

Fig. 3. 29   Sharp-nosed flare-stabilized body
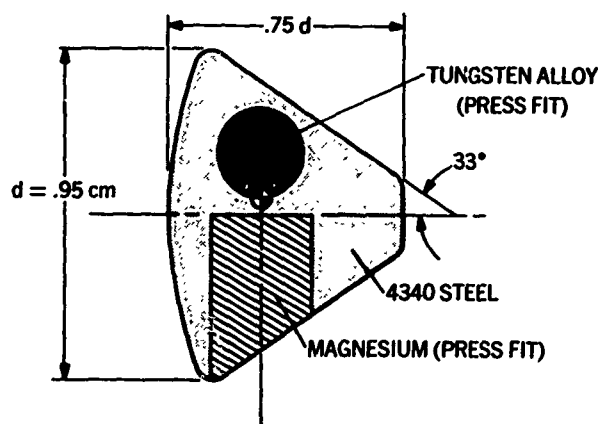
(a) Sketch of model
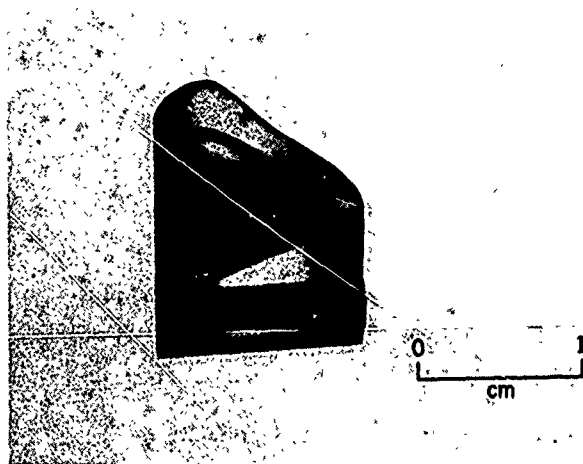
(b) Photograph of model with sabot

V_m, km/s	V_R, km/s	ρ, atm	GUN	REF
4.9	—	.1	12.7 mm DEFORMABLE-PISTON LIGHT GAS	3.26
4.9	7.6	.02		

Fig. 3.30   Apollo-type body

COPPER RING
(CALORIMETER)

BORON NITRIDE

HOT JCT (RING),

CONSTANTAN
DISK

ALUMINUM

$d = .75$ cm

(ALUMINUM,
NYLON OR
POLYCARBONATE)

COLD JCT

INSULATION

4 TURN COIL

MODEL WEIGHT: ~ 0.3 g

(a) Sketch of model

OBTURATION CUP
(POLYCARBONATE)

DISK
(NEOPRENE)

2 CUTS 90°
.025 cm OF BASE

SABOT
(NYLON)

MODEL

2.54 cm

(b) Sketch of model with sabot
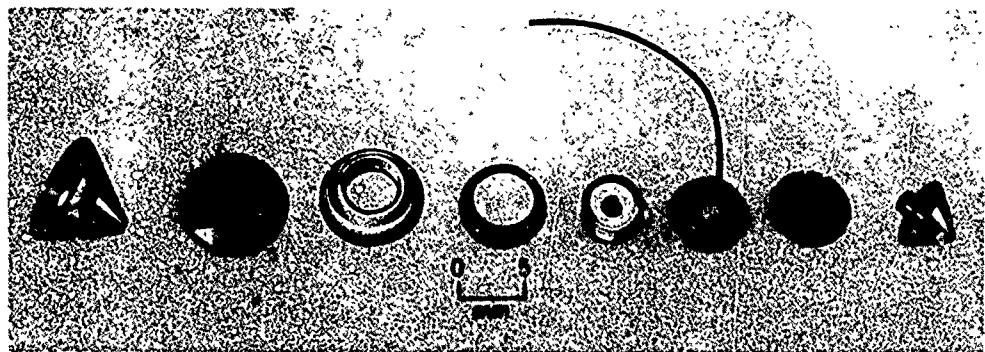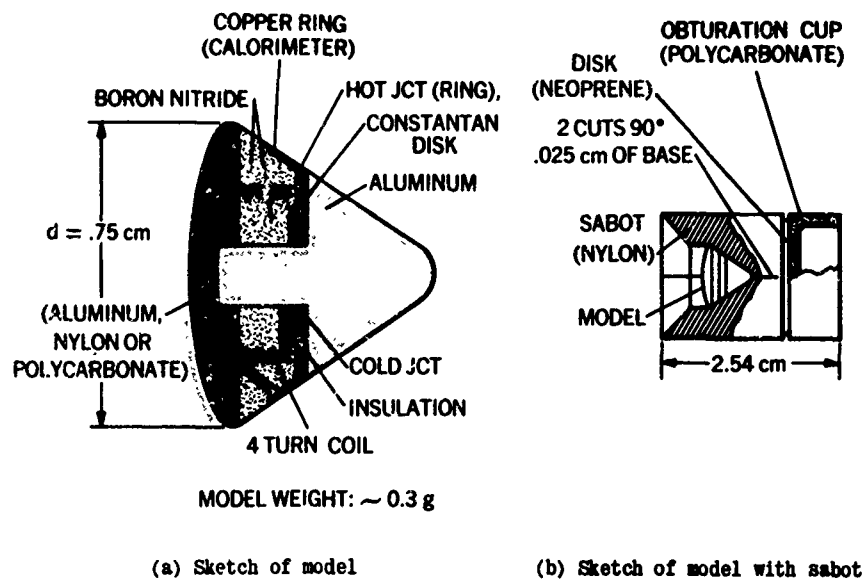
(c) Photograph of model components and assembled model

V_m, km/s	ρ, atm	GUN	REF
6.1	.13	15.2 mm DEFORMABLE-PISTON LIGHT GAS	3.27

Fig. 3.31   Passive-telemetry model
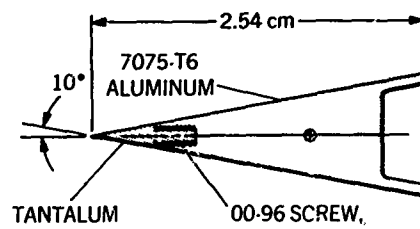
(a) Sketch of model
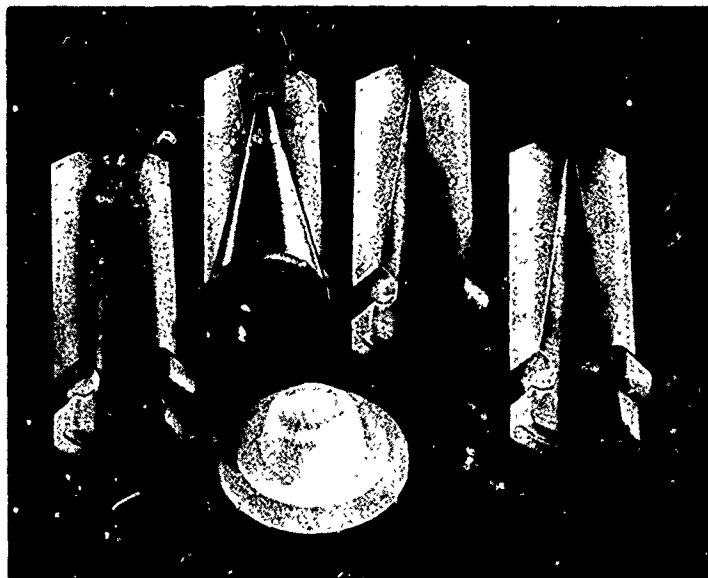
(b) Photograph of model with sabot

V_m, km/s	ρ, atm	GUN	REF
5.7	.04	12.7mm DEFORMABLE-PISTON LIGHT GAS	3.31, 3.32

Fig. 3.32   Sharp-nosed 10° cone

SILVER SOLDER RINGS (TWO)
TUNGSTEN
KENTANIUM K151A
6°20'
6°20'
2.54 cm
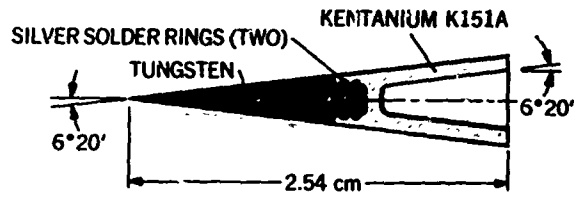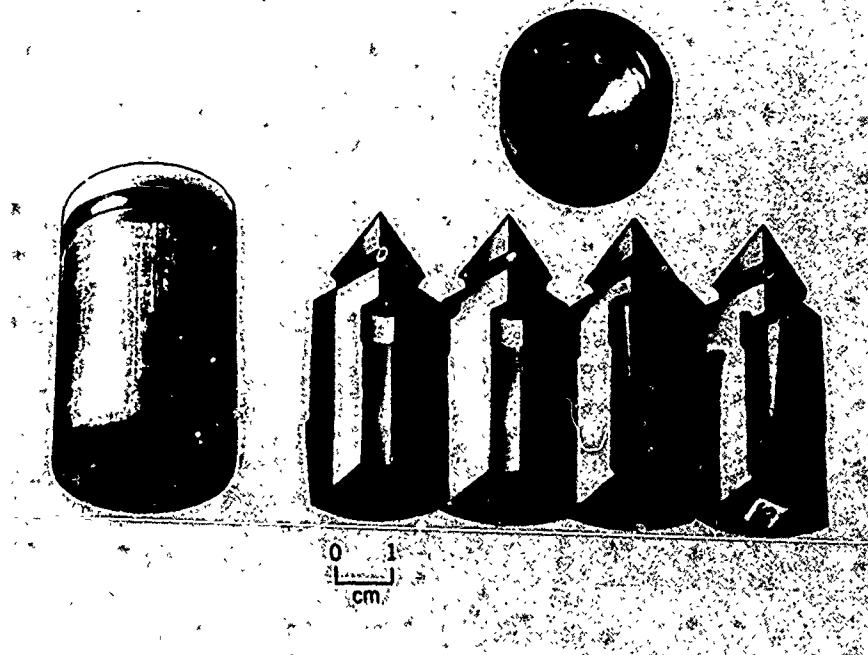
(a) Sketch of model

(b) Photograph of model with sabot

V_m, km/s	ρ, atm	GUN	REF
3.0	1	31.7 mm SINGLE-STAGE LIGHT GAS	3.33

Fig. 3.33   Sharp-nosed 6° 20' cone.   (Courtesy of US Naval Ordnance Laboratory.)
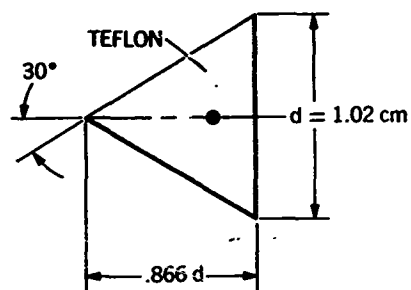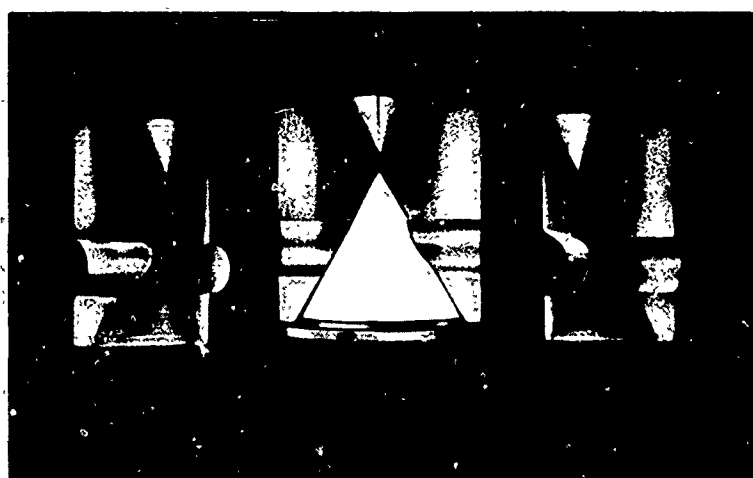
(a) Sketch of model

(b) Photograph of model with sabot

V_m, km/s	V_R, km/s	ρ, atm	GUN	REF
7.0	8.8	.02	12.7 mm DEFORMABLE-PISTON LIGHT GAS	3.34

Fig. 3.34   30° Teflon cone
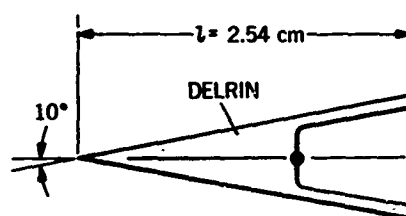
(a) Sketch of model
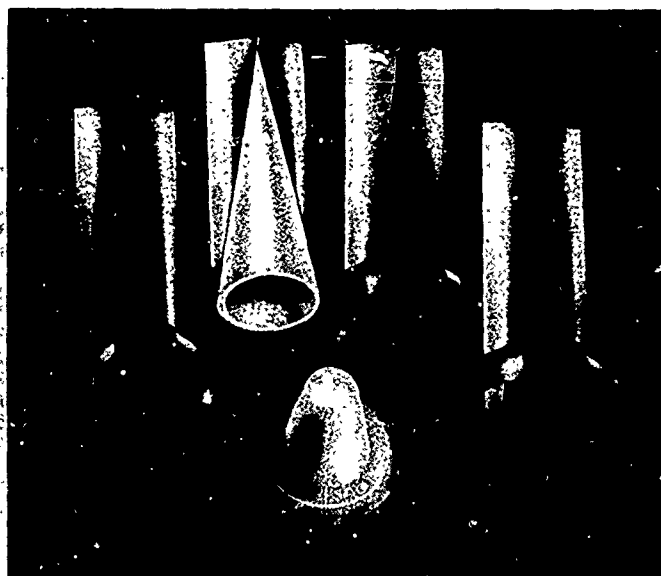
(b) Photograph of model with sabot

V_m, km/s	ρ, atm	GUN	REF
5.7	.04	12.7 mm DEFORMABLE-PISTON LIGHT GAS	3.31, 3.32

Fig. 3.35 10° Delrin cone

(a) Sketch of model   (b) Sketch of model with sabot
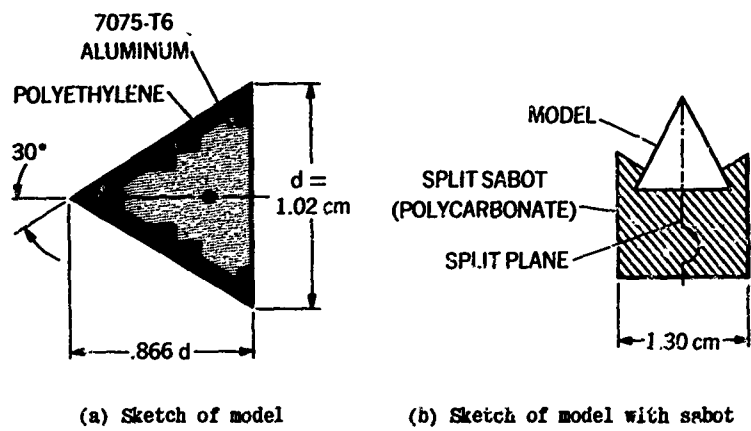
V_m, km/s	ρ, atm	GUN	REF
7.3	.026	12.7 mm DEFORMABLE-PISTON LIGHT GAS	3.35

Fig. 3.36 30° cone with injection-molded plastic shell
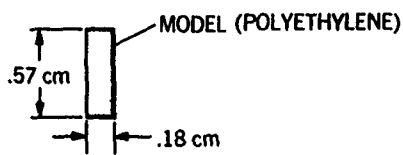
$MASS_{MODEL}$ = .0453 gm

V_{MODEL} = 11.3 km/s

P = 1·20 mmHg

GUN = 22 CALIBER DEFORMABLE PISTON LIGHT GAS (SMOOTH BORE)

REF = 3.36

Fig. 3.38   Sketch of thin right-circular-cylinder model.
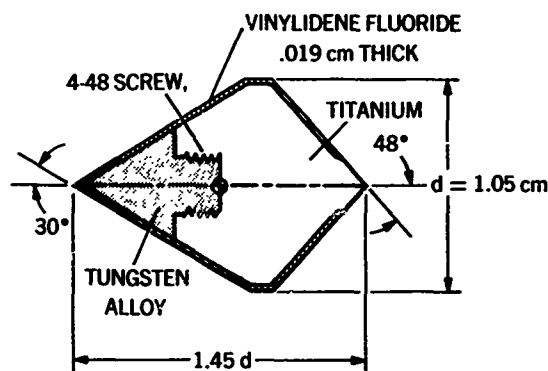
(a) Sketch of model
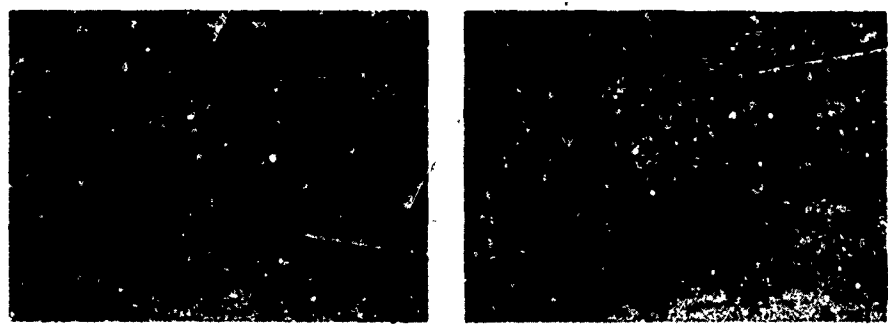
First station (x = 0)   Last station (x = 12.2 m)

(b) Sh.dowgraphs showing negligible tip blunting

V_m, km/s	ρ, atm	GUN	REF
4.6	.4	12.7 mm DEFORMABLE-PISTON LIGHT GAS	3.23

Fig. 3.37   Conical body with thin plastic coating
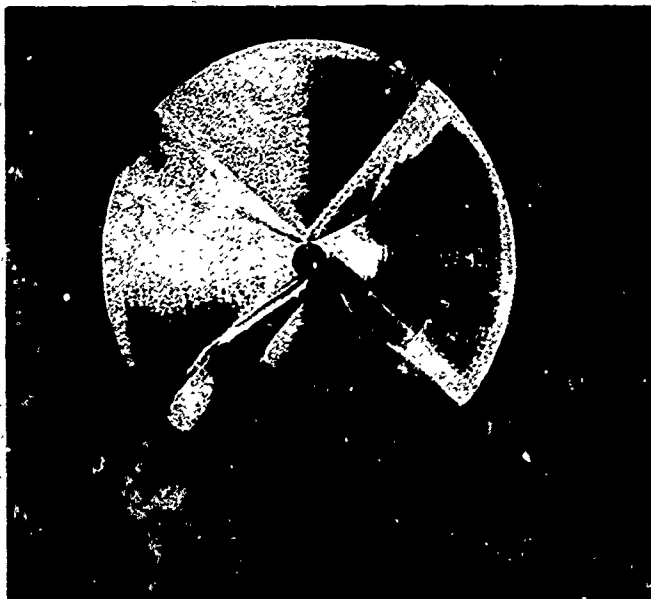
(a) Front view of sabot with model
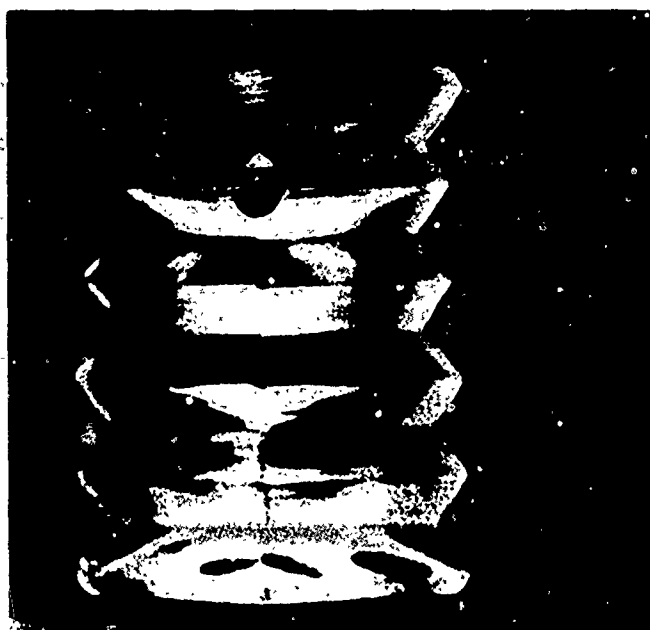
(b) Segmented view of sabot with model

V_m, km/s	ρ, atm	GUN	REF
8	.03	7.6 mm TWO-STAGE LIGHT GAS	3.3

Fig.3.39   Photographs of model (700-micron Al_2O_3 sphere) with serrated sabot.   (Courtesy of General Motors Defense Research Laboratories.)
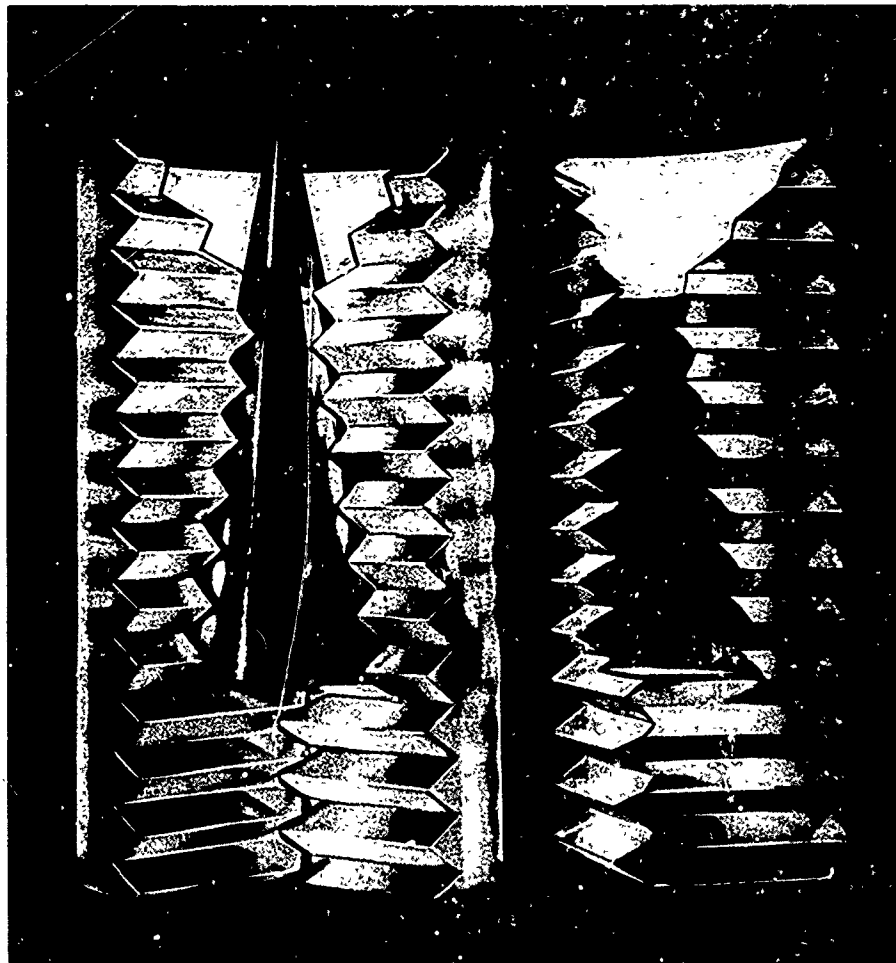
Fig.3.40   Photograph of cone model with serrated sabot. (Courtesy of General Motors
Defense Research Laboratories.)

600 μ
STEEL SPHERE

.32 cm diam   POLYCARBONATE SABOT
(2-PIECES)
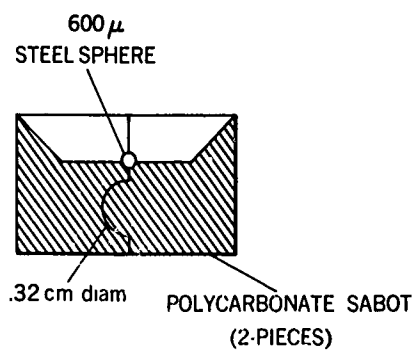
d_{MODEL} = 600 μ
$MASS_{MODEL}$ = .001 g
$MASS_{SABOT}$ = .980 g
d_{SABOT} = 1.31 cm
l_{SABOT} = .81 cm
V_{MODEL} = 8.3 km/s
P = .05 atm
GUN = 50 CALIBER DPLG*
REF = NONE (AMES)

* DEFORMABLE-PISTON
LIGHT GAS

Fig.3.41   Sketch of sabot for 600-micron steel sphere

2 CUTS 90° APART WITHIN
.025 cm OF BASE

.16 cm
DRILL

NYLON   .025 cm
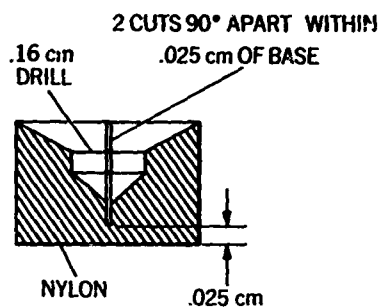
$d_{MODEL} = .16$ cm

$MASS_{MODEL} = .0060$ g

$MASS_{SABOT} = .080$ g

$d_{SABOT} = .54$ cm

$l_{SABOT} = .33$ cm

$V_{MODEL} = 9.4$ km/s

$P = 28$ mmHg

GUN = 22 CALIBER DPLG*
       (SMOOTH BORE)

REF = NONE (AMES)

Fig. 3.42   Sketch of sabot for 1600-micron aluminum sphere.

2 CUTS 90° APART WITHIN
.025 cm OF BASE

.025 cm

POLYCARBONATE
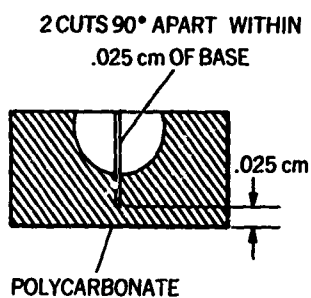
$d_{MODEL} = .32$ cm

$MASS_{MODEL} = .0374$ g

$MASS_{SABOT} = .0875$ g

$d_{SABOT} = .57$ cm

$l_{SABOT} = .28$ cm

$V_{MODEL} = 8.8$ km/s

$P = 1.6$ mmHg

GUN = 22 CALIBER DPLG* (RIFLED)

REF = NONE (AMES)

Fig. 3.43   Sketch of sabot for 3200-micron Pyrex-glass sphere

MODEL (1/6th CALIBER
POLYETHYLENE CYLINDER)

2 CUTS 90° APART WITHIN
.025 cm OF BASE

SABOT (POLYCARBONATE)
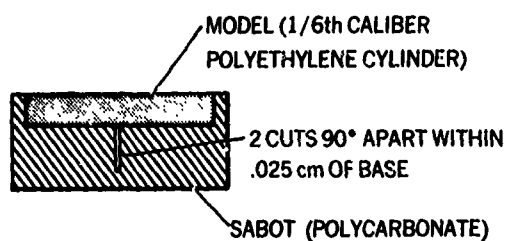
$l_{MODEL} = .08$ cm

$d_{MODEL} = .51$ cm

$MASS_{MODEL} = .0161$ g

$MASS_{SABOT} = .0595$ g

$d_{SABOT} = .58$ cm

$l_{SABOT} = .25$ cm

$V_{MODEL} = 9.8$ km/s

$P = 1.70$ mmHg

GUN = 22 CALIBER
       DPLG* (RIFLED)

REF = NONE (AMES)

Fig. 3.44   Sketch of thin cylinder model with sabot
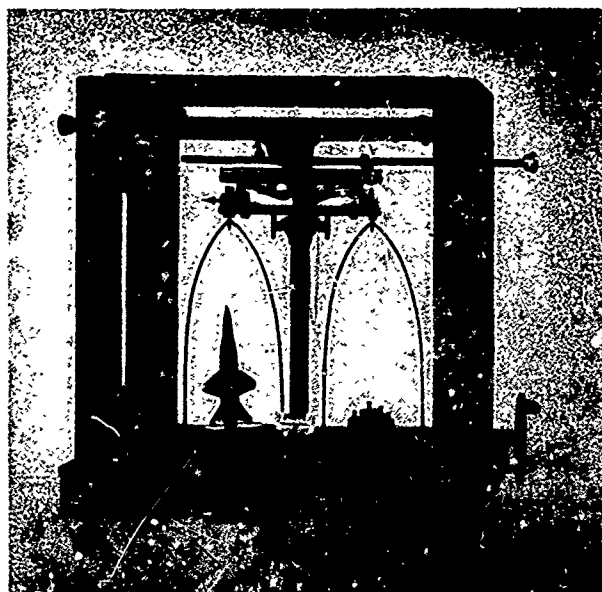
(a) Equal-arm type
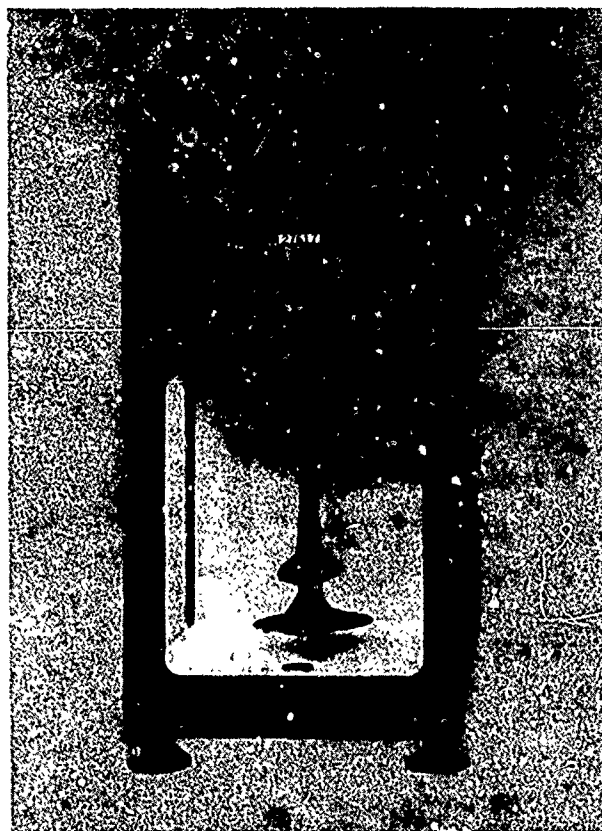
(b) Substitution type.

Fig.3.45   Two types of analytical balances for measuring model mass.
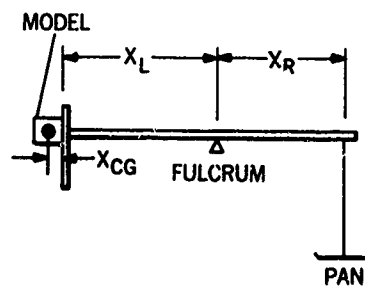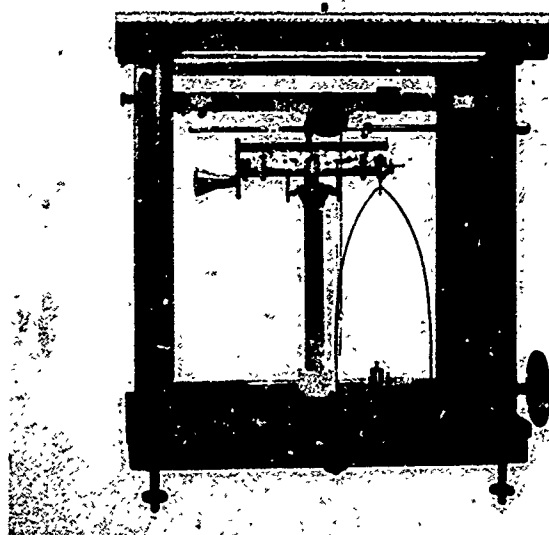
Fig.3.46   Equipment for the determination of model center of gravity
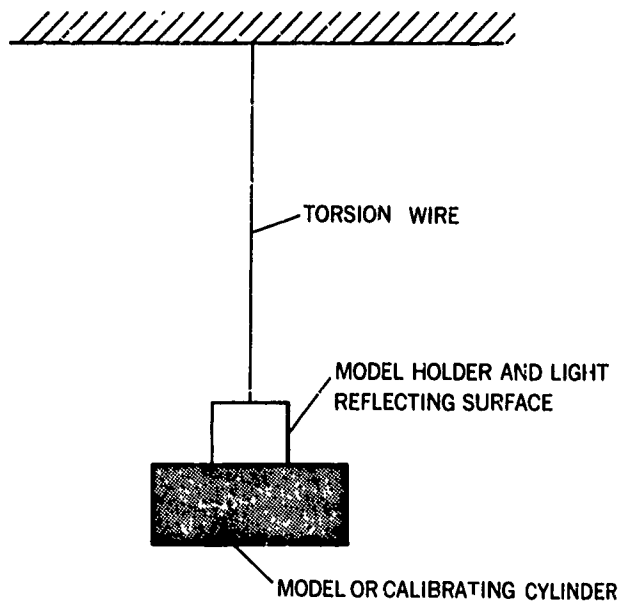
Fig.3.47   Sketch of torsion-pendulum setup for moment-of-inertia measurements
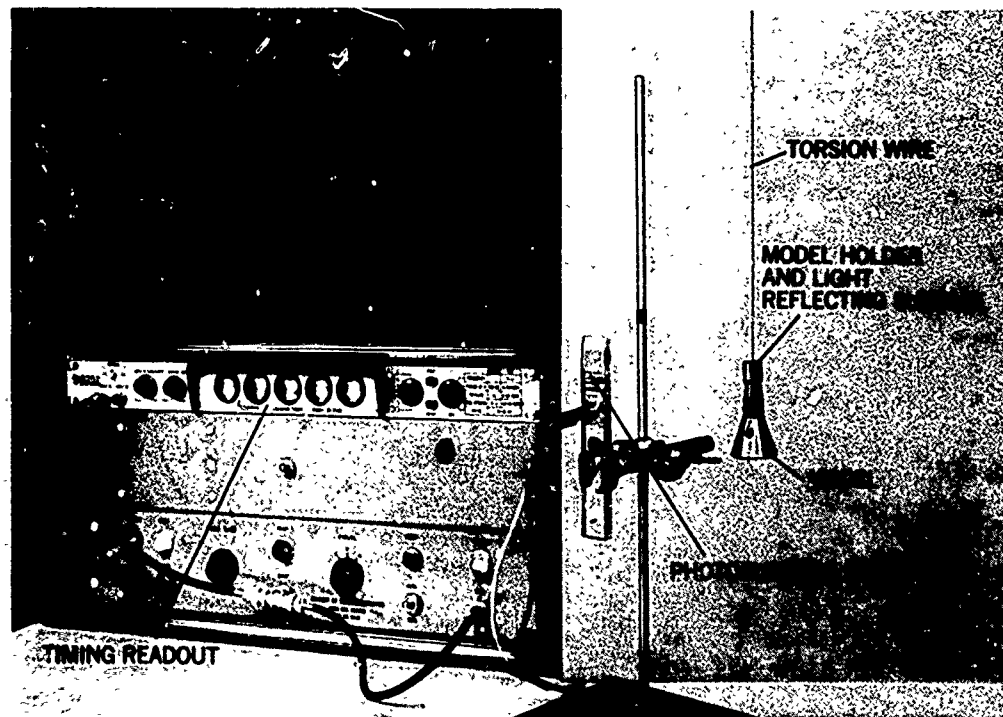
Fig.3.48   Photograph of moment-of-inertia apparatus
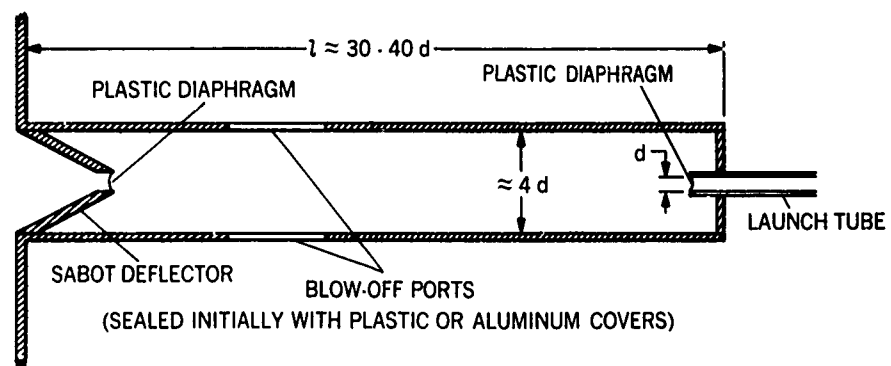
Fig.3.49   Sketch of simple sabot-separating tank

GAS-PRESSURE RELEASE PORTS

CONTRACTING SECTION   DEFLECTING RAMP

1°

GAS-PRESSURE RELEASE PORTS

CONTRACTING SECTION   DEFLECTING SECTION

1°
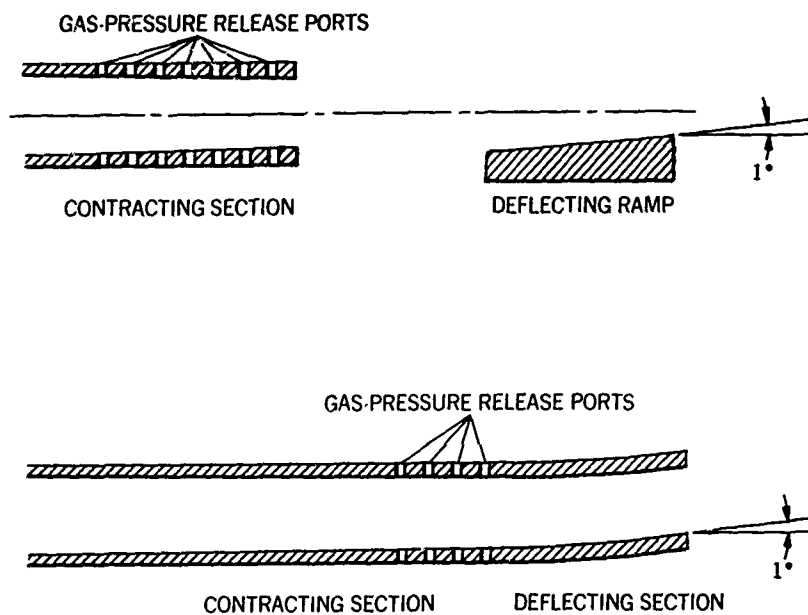
Fig.3.50   Sketch of two types of sabot decelerators and deflectors
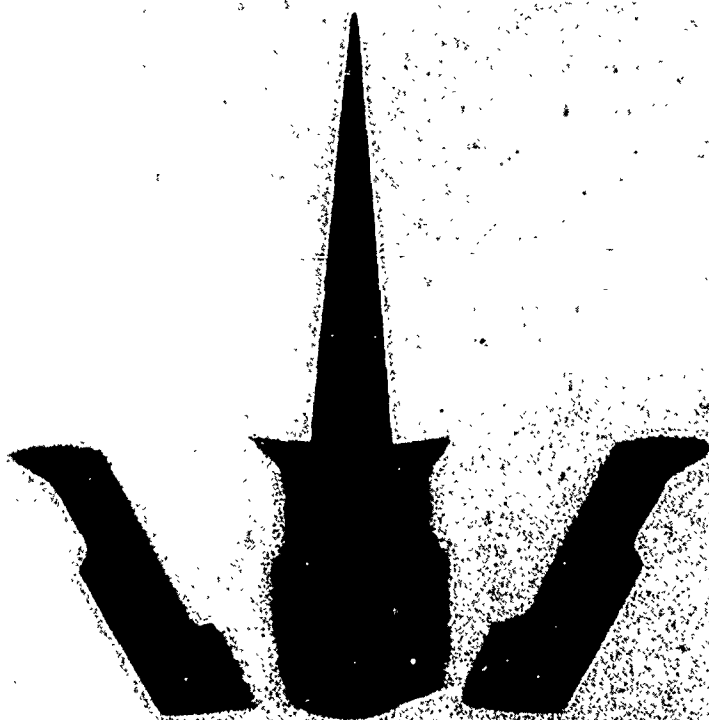
Fig.3.51   X-ray shadowgram showing separation of sabot from model. (Courtesy of von Kármán Gas Dynamics Facility, Arnold Engineering Development Center.)

CHAPTER 4

TERMINAL BALLISTICS

by

James L. Summers and B. Pat Denardo

NASA-Ames Research Center

TERMINAL BALLISTICS

James L. Summers and B. Pat Denardo

4.1 INTRODUCTION

Studies of terminal ballistics, or impact and penetration phenomena, have been motivated by interests in subjects as diverse as meteor craters on the moon and planets, armoring of military vehicles, meteoroid protection of space vehicles, and solid state physics of materials at extremely high pressures. To study impact, it is necessary to have an impacting object, the projectile, in high-velocity, relative motion compared to the target object or material. Aside from the study of natural impact craters, such as the aforementioned meteor craters, the most evident method of studying such phenomena is to set the projectile in motion in a gun, and to direct it at the target under controlled conditions of velocity and environment. Other means of putting the projectile in motion can be devised – e.g., use of high explosives, use of rockets, use of electrostatic forces to accelerate small particles – but it seems clear that the gun and the ballistic range comprise the basic laboratory approach to impact studies.

Classification of impact investigations by velocity ranges has some value in both discussions of the phenomena which control the impact process and in equipment needed to perform the research. In the lowest velocity range, within usual experience, the impacts may be either elastic or inelastic and penetration or permanent damage may or may not occur. This range is below the velocities generally associated with guns and need not concern us. The range of moderate velocities, associated with usual guns, is a range in which damage and penetration occur, but strong shock waves are not formed in the target material. The higher velocity range, referred to as the hyper-velocity impact range, is characterized by the formation of very strong shock waves in the target, and pressures measured in millions of atmospheres. Special high performance guns (light gas guns) and partially evacuated ranges are required to work in this regime.

While some elements of the ballistic range used for impact studies are the same as those discussed in Chapters 2 and 6, namely the guns and part of the instrumentation, other elements are essentially different and specialized. Spark photographs are used here primarily to measure the velocity and attitude of the model in flight so as to define these conditions at the instant of impact. The bulk of the instrumentation will be grouped around the target, and may include ultra high-speed cameras to time resolve the externally visible impact processes, luminosity detectors, and other electro-magnetic emission detectors. Simple or multiple ballistic pendulums may be provided to measure the momentum components of the impact. Special screens placed to catch and record the distribution of material ejected either forward or backward from the impact region may be installed. And, of course, primary emphasis is put on target recovery, measurement, and examination.

In this chapter, we will discuss these techniques which are special to the performance of impact studies. We will also, for completeness, describe various arrangements of the basic equipment essential to doing impact work in ballistic ranges. Since the nature of the research determines the kind of instrumentation needed, we will begin by briefly reviewing the kinds of research objectives which may be satisfied in impact studies.

4.2 AREAS OF IMPACT RESEARCH

Specific areas of hypervelocity impact research that can be studied in the ballistic range include the basic phenomenology of cratering, impact performance of complex space structures, and the properties of materials at very high pressure.

In studies of the phenomenology of cratering, a further classification is made on the basis of the thickness of the target specimen, because the phenomena observed depend very markedly on this parameter. Targets may vary from thicknesses of only a fraction of the characteristic dimension of the impacting projectile, to very thick, many times greater than this dimension, and are classified as thin, thick, and semi-infinite. Target materials include virtually all known substances; metals, minerals, plastics, and organic substances. The proceedings of several symposia covering this area of research are listed in References 4.1 through 4.8.

A second area of research, the evaluation of the performance of complex space structures when impacted by very high speed particles, is primarily a matter of assessing how much damage results from the impact of a known mass at a known speed into a variety of structures. Of course, tests of this kind often suggest improvements in design which increase the structure's resistance to damage. Examples of space structures include vehicle structural components, fuel cells, solar cells, heat shields, propulsion units, and space-suit materials. References 4.9 through 4.12 describe the results of some of the many experiments in this field.

A third area of research involves the study of the properties of matter at the high pressures attained behind the shock wave produced either by an explosive device or the impact of a high velocity projectile. The velocity of shock propagation and of the mass of material behind the shock front permits the determination of the density and pressure in the shock-compressed zone. The experimentally determined relation between these two quantities is generally termed the "Hugoniot" of the material under test, after the Rankine-Hugoniot relations describing the conditions across a shock wave. The equation of state of the material, which can then be determined, is of value in all scientific studies of solids at very high pressure (as, e.g., studies of planetary interiors). An excellent treatise on this subject is given in Reference 4.13 including both analytical and experimental treatments.

4.3 DESIGN AND ARRANGEMENT OF BALLISTIC RANGES FOR IMPACT STUDIES

The ballistic range is well suited to impact research because the flight characteristics of the projectile prior to impact and the test conditions at the target during impact are all precisely known and, generally, widely controllable. The modern light-gas gun has the capability of launching impact projectiles at very high velocities which are sometimes required for this type of research. These projectiles can range in shape from very low fineness-ratio discs, through spheres and short cylinders, to high fineness-ratio rods and cones. This is achieved by employing sabots which protect, support, and guide the projectile down the gun barrel (see Chapter 3). The structural integrity of the projectile after launch, its velocity at impact, and its angle of 'nclination when contact is made with the target are all established in the ballistic range through the use of photographic stations (see Chapter 6). Projectile materials can range from light plastics to heavy metals with corresponding densities varying from less than one to about 22 grams per cubic centimeter. Modest velocities (about 3 km/sec) are even achievable with foamed plastic projectiles having densities less than 0.1 gram per cubic centimeter. Projectile sizes may range from the diameter of the largest bore gun suitable to the range to as small as a few microns and, if desired, small particles can be launched in multiple quantities. The lower practical limit in size is generally determined by the useable sensitivity of the in-flight diagnostic instrumentation employed. Target environment is readily controllable and the standard procedure is to introduce into the impact chamber the proper composition of gas at the required pressure and temperature levels. Other test conditions such as target stress level, pressure differential possibly due to liquid containment, irradiation from a variety of sources, artificial gravity, and possibly other conditions can all be provided if desired. Finally, the variety of diagnostic instrumentation employed in the ballistic range suitable for studying the impact event itself, seems to be limited only by the ingenuity of the experimenter.

The general layout of a ballistic range intended for impact research exclusively would differ from those previously described in that the flight range would be shorter and less well instrumented, and the impact chamber, instead of being simply a place to stop the projectile, would be large in order to contain targets of sufficient size as well as to allow the necessary amount of time to study the transient impact effects thoroughly. A minimum of two photographic stations are required in the flight chamber in order to determine the projectile velocity. However, it is good practice to instrument the flight range with four to six orthogonal stations so that the aforementioned quantities, projectile velocity, attitude, integrity, etc., can be accurately determined. The impact chamber is normally built with the back or a sidewall mounted on hinges so that access to the entire chamber is provided without interference. This allows not only easy installation of massive targets but also access room for the installation and adjustment of instrumentation such as ballistic pendulums. A high-speed shutter [4.14] is often installed ahead of the target chamber to insure that sabot or pump piston particles or products of combustion from the launcher, all of which may result from somewhat less than perfect operation, do not enter the test area to inflict possible damage to the target or obscure the impact results. A photograph of a typical ballistic range installation showing a six-station flight range and large impact chamber is shown in Figure 4.1. The fast-closing shutter is located between the flight range and impact chamber.

Occasionally, unusual operating procedures or techniques are devised to accomplish a certain goal. One such technique reverses the role of the projectile and target in that the projectile is stationary and the target is moving. Thus, projectiles that cannot be launched because of configuration or strength considerations, are suspended in front of the launching device, and the targets of sufficient dimensions, are shot at them. The targets are then decelerated and finally stopped as gently as possible in some suitable catcher and then examined and measured. This technique has been employed to study the effects of impact of filaments having fineness ratios of the order of 1000 and of projectiles of foam and particulate matter having essentially no strength [4.15, 4.16]. This technique must be limited, of course, to conditions such that the damage suffered by the target during the deceleration and recovery is small compared to the impact crater produced. An extension of this technique is to launch a projectile at the moving target and after impact recover the target as before [4.17]. The impact velocity is then the vector sum of the projectile and target velocities. The additional problems that arise using this counterfiring technique are the timing and accuracy problems of the two launchers.

A vertical gun and flight range constitute a special facility for studying the effects of impact in target materials of such low strength that they are unable to support themselves in an upright position suitable for testing with horizontal launchers. Fluids and particulates are two such classes of strengthless materials. In such a facility also, the effects of gravity on the cratering process can be studied by employing a target-support table which can be accelerated vertically with respect to the launcher. By allowing the target to drop away from the launcher, controlled accelerations between zero and one earth gravity can be given to the target. Accelerations greater than this can be imposed on the target if it is accelerated towards the launching device. Gravity scaling relations for meteoroid impact occuring on the planets and their satellites are

a motivating problem for the use of such sophisticated facilities. Figure 4.2 is a photograph of a vertical firing facility in which the gun has been lowered to the horizontal for maintenance. This particular launcher can be operated from horizontal to vertical in 15° increments.

4.4 MEASUREMENTS IN IMPACT RESEARCH

Once the capability of conducting hypervelocity impact research is developed, the next problems are those of acquisition and analysis of data. The measurements to be made can be divided into two categories: static and dynamic. By static measurements, we mean those which can be made well after the completion of the events. On the other hand, the dynamic parameters must be measured during or immediately after the event while the transient effects are still being felt.

Static target measurements include the basic crater parameters: penetration, diameter, volume, mass loss, and shape. Penetration is the maximum depth of the crater measured from the undisturbed target face. This quantity is readily measured with a depth gage. The crater diameter is the average distance across the crater in the plane of the undisturbed surface and usually includes the total damaged area. This dimension is measured with a filar microscope or precision micrometer, depending on the crater size, after the crater lip has been carefully machined down to the undisturbed target surface. The volume of the crater is once again measured with reference to the undisturbed target face. Two of the acceptable methods for measuring this parameter are determination by liquid measure and by a casting technique. The first is accomplished by using a calibrated burette containing a mixture of water and a wetting agent. The second method is considerably more time consuming, but more accurate on small craters. First a casting is made of the crater. This casting is then projected on the screen of an optical comparator and tracings of several profile views are made. The tracings are then mechanically integrated and averaged to determine the volume. This method is restricted to craters whose surfaces are rather smooth, since the casting cannot be extracted cleanly from pitted crater surfaces. Crater mass loss is determined simply by weighing the entire target prior to installation in the impact chamber and again following the impact. Standard analytical balances are best suited for this measurement. For thin targets, measurements of diameter of perforation, mass loss, etc., can be made using similar techniques.

Other static measurements include target material changes such as hardness, grain and crystal structure, color, and change of state. Deformation of surrounding target areas is an additional parameter of this group. A variety of standard metallurgical techniques and devices are available for quantitative measurement of these parameters.

Finally, certain static measurements can be made of the target ejecta and spray. Ejecta is that portion of the target and projectile emitted uprange from the target face; whereas spray is that portion emitted to the rear or downrange. Both ejecta and spray can include material that is solid, melted, or vaporized. The spatial distributions of particles of ejecta and spray can be determined by allowing the particles to impinge on suitably placed witness plates, termed spray catchers (Figures 4.3 and 4.4), which are essentially heavy yaw cards (see Chapter 6). Careful examination of, and tests on the captured particles can reveal the same material changes previously mentioned: hardness, grain structure, etc.

Dynamic measurements include observations of the motion of the target during impact, a measure of the momentum transferred, which can be measured with the classic ballistic pendulum (Figure 4.5). For hypervelocity impact in thick targets, the quantity of ejecta can be so large as to result, in most cases, in the target momentum being substantially greater than that of the impacting projectile [4.16].

Both the momentum and the velocity of the target ejecta and spray can be measured dynamically. The velocity distributions can be studied through the use of high-speed cameras while the momentum is best evaluated with special ballistic pendulums. Actually, a rather sophisticated ballistic pendulum setup can be arranged to determine target, ejecta, and spray momentum on a single shot for yielding the division of momentum of the system (Figure 4.6). Particle size distribution is more difficult to measure, especially if the particle velocity is high. For the lower velocities, the particle may be caught in some soft, undamaging material and then measured. At higher velocities, unfortunately, even the softest and most porous of materials will cause particle breakup. If, however, particle size is sufficiently large and photographic resolution sufficiently high, the requisite information can be obtained from film records. Usually, however, the scale of the laboratory event is small enough to preclude the use of the above technique.

Crater growth history, another dynamic measurement, can be determined through the use of ultra high-speed cameras or sequential flash X-ray systems. Visible, thermal, or X-radiation emitted as a result of the impact can be studied with electronic and spectroscopic devices such as are described in Chapter 9. Shock velocity and free-surface velocity, required for determining the equation of state of target materials, can be measured with electrical closure-type pin gages or by the argon flash-gap technique. The pin gages are placed in the target sample from the rear surface at different distances from the face of the sample to be impacted. As the shock wave travels into the sample, the pin gages close in succession giving rise to spaced signals on a cathode-ray oscilloscope. The shock-wave velocity is then computed from the pin-gage spacings and oscilloscope sweep rate. A similar array of spaced pin gages located at the rear surface of the sample is used to determine the free-surface velocity. All pin gages must be carefully located so that there is no mutual interference.

The argon flash-gap technique makes use of the fact that this gas will glow brightly when strongly shocked. The following description of the technique is greatly simplified and is meant to illustrate the principle only. The test sample to be impacted is constructed with a groove of fixed width, but of tapering depth, which laterally traverses the rear face of the sample. As the shock wave proceeds into the sample from the impacted face, it will reach the deepest part of the groove first and then proceed laterally along the groove bottom to the shallowest part. The shock-wave velocity in the test sample can then be determined from (1), the angle between the plane of the shock-wave and the groove bottom, and (2), the lateral closing velocity along the groove bottom. This lateral movement of the shock-wave is made visible by inserting a transparent strip of acrylic plastic (Lucite or Plexiglass) into the groove but spaced away from the bottom to provide a gap of a fraction of a millimeter. Argon gas is flooded into this gap. As the shock-wave proceeds along the groove, the bottom moves as a free surface and generates a shock-wave in the argon gas, causing it to glow brightly. When the free surface strikes the acrylic strip, the acrylic becomes opaque and acts as a sharp cutoff optical shutter. Thus, a streak camera viewing the test sample from the rear and with its film moving normal to the groove, would record a sharply defined streak on the film. If appropriate fiducial marks are located on the rear of the test sample for film calibration purposes, then the lateral velocity of the shock-wave, and hence the propagation velocity of the shock-wave, can be computed from the camera speed and film-streak angle. A second acrylic strip with an argon flash gap, but located on the plane portion of the test sample rear surface and at an angle to it so that the closing distance from the free surface varies along its length, provides similar information for determining the free-surface velocity. The pin-gage and flash-gap techniques give experimental results in substantial agreement. Both methods are described in detail in Reference 4.13.

Many special techniques have been developed to study impact phenomena. Among these are the methods wherein substitute materials are employed for the projectile, target, or both. Particulate material is often used for the target material because binders of different strengths can be employed to vary the strength of the target from a few pounds per square inch to several thousand pounds per square inch. Also, if the targets are made up of colored layers of material, the movement of the target material caused by the impact of a projectile is readily traced as can be seen from Figure 4.7. References 4.19 and 4.20 describe the results of some investigations where particulate material has been used to study the impact process.

Another scheme devised to study cratering phenomena at meteoric velocities, beyond the capability of the launching devices, is to substitute for the desired test projectile, a simulating projectile made of denser material. For a given impact velocity, this denser projectile will produce a higher shock pressure and thus be somewhat representative of the desired projectile impacting at a higher velocity. Such a simulation results in cratering data suitable for engineering purposes, but because of the fundamental differences in the Hugoniot properties of the desired test projectile and its simulating counterpart, one cannot duplicate accurately all aspects of the cratering process.

While the above discussion is not extensive, it indicates some of the key techniques employed in laboratory studies of impact. Certainly, many additional experimental techniques have been devised, and others will be, to study particular features of impact problems. The reader is referred to the references given for more detailed discussions of some of these techniques.

REFERENCES

4.1   Proceedings of the First Hypervelocity Impact Symposium, The Rand Corp., Santa Monica, Calif., early in 1955.

4.2   Proceedings of the Second Hypervelocity Impact Symposium, Naval Research Laboratory, Washington, D.C., May 1957.

4.3   Proceedings of the Third Hypervelocity Impact Symposium, Armour Research Foundation of the Illinois Institute of Technology, Chicago, Illinois, October 7-9, 1958.

4.4   Proceedings of the Fourth Hypervelocity Impact Symposium, Air Proving Ground Center, Air Research and Development Command, US Air Force, Eglin Air Force Base, Florida, April 26-28, 1960.

4.5   Proceedings of the Fifth Hypervelocity Impact Symposium, Colorado School of Mines, Denver, Colorado, October 30-31, November 1, 1961.

4.6   Proceedings of the Sixth Hypervelocity Impact Symposium, The Firestone Tire and Rubber Co., Cleveland, Ohio, April 30, May 1-2, 1963.

4.7   Proceedings of the Seventh Hypervelocity Impact Symposium, The Martin Company, Tampa, Florida, November 17-19, 1964.

4.8   Proceedings of AIAA Hypervelocity Impact Conference, Cincinnati, Ohio, April 30-May 2, 1969.

4.9 Nysmith, C. Robert   *Preliminary Investigation of Impact on Multiple-Sheet Structures and an*
     Summers, James L.   *Evaluation of the Meteoroid Hazard to Space Vehicles.* NASA TN D-1039, 1961.

4.10 Nysmith, C. Robert   *An Experimental Investigation of the Impact Resistance of Double-Sheet*
     Summers, James L.   *Structures at Velocities to 24,000 Feet per Second.* NASA TN D-1431, 1962.

4.11 Nysmith, C. Robert   *Penetration Resistance of Double-Sheet Structures at Velocities to 8.8 km/sec.*
     NASA TN D-4568, 1968.

4.12 Summers, James L.   *The Resistance of a Variety of Composite Space Structures to Hypervelocity*
     Nysmith, C. Robert   *Impact.* Proceedings of AIAA 5th Annual Structures and Materials Conference, Palm Springs, April 1-3, 1964, pp.386-393.

4.13 Seitz, Frederick   *Solid State Physics.* Academic Press, Inc., New York and London. Vol.6, 1958,
     Turnbull, David   pp.1-63.
     (Editors)

4.14 Denardo, B. Pat   *Simplified Rapid Opening Mechanical Gate Valve.* The Review of Scientific
     McGee, James E.   Instruments, Vol.37, No.10, October 1966, p.1403.

4.15 Nysmith, C. Robert   *Investigation of the Impact of Copper Filaments into Aluminum Targets at*
     Summers, James L.   *Velocities to 16,000 Feet per Second.* NASA TN D-1931, 1964.
     Denardo, B. Pat

4.16 Fish, Richard H.   *The Penetration of Porous Projectiles in Aluminum and Plastic Targets.* NASA TN
     D-4505, 1968.

4.17 Kinard, William H.   *A Technique for Obtaining Hypervelocity Impact Data by Using the Relative*
     Collins, Rufus D. Jr   *Velocities of Two Projectiles.* NASA TN D-724, 1961.

4.18 Denardo, B. Pat   *Measurements of Momentum Transfer from Plastic Projectiles to Massive*
     Aluminum Targets at Speeds up to 25,600 Feet per Second. NASA TN D-1210, 1962.

4.19 Gault, Donald H.   *Impact Cratering Mechanics and Structures.* Presented at the Conference on
     Quaide, William L.   Shock Metamorphism of Natural Materials, Goddard Space Flight Center, Greenbelt,
     Oberbeck, Verne R.   Maryland, April 1966.

4.20 Quaide, William L.   *Thickness Determination of the Lunar Surface Layer from Lunar Impact Craters.*
     Oberbeck, Verne R.   J. of Geophys. Res., Vol.73, No.16, August 15, 1968, pp.5247-5270.
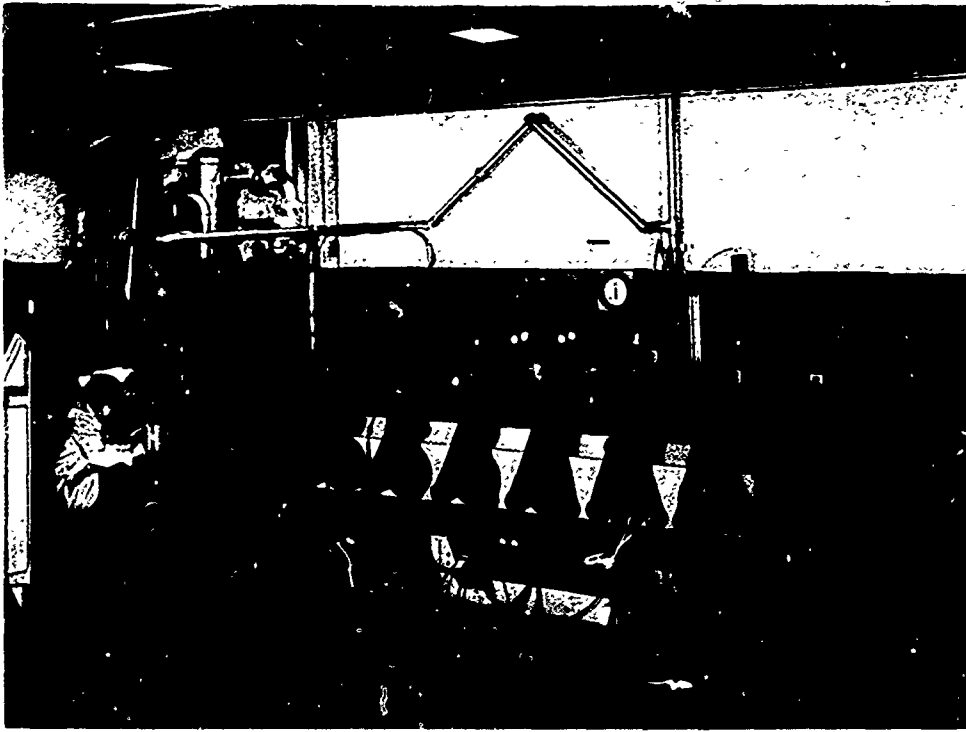
Fig. 4.1   Ballistic range for impact research

Fig. 4.2   Vertical ballistic range (lowered to the horizontal
position for maintenance)

Fig. 4.3   Ejecta pattern on catcher

Fig. 4.4   Spray pattern on catcher
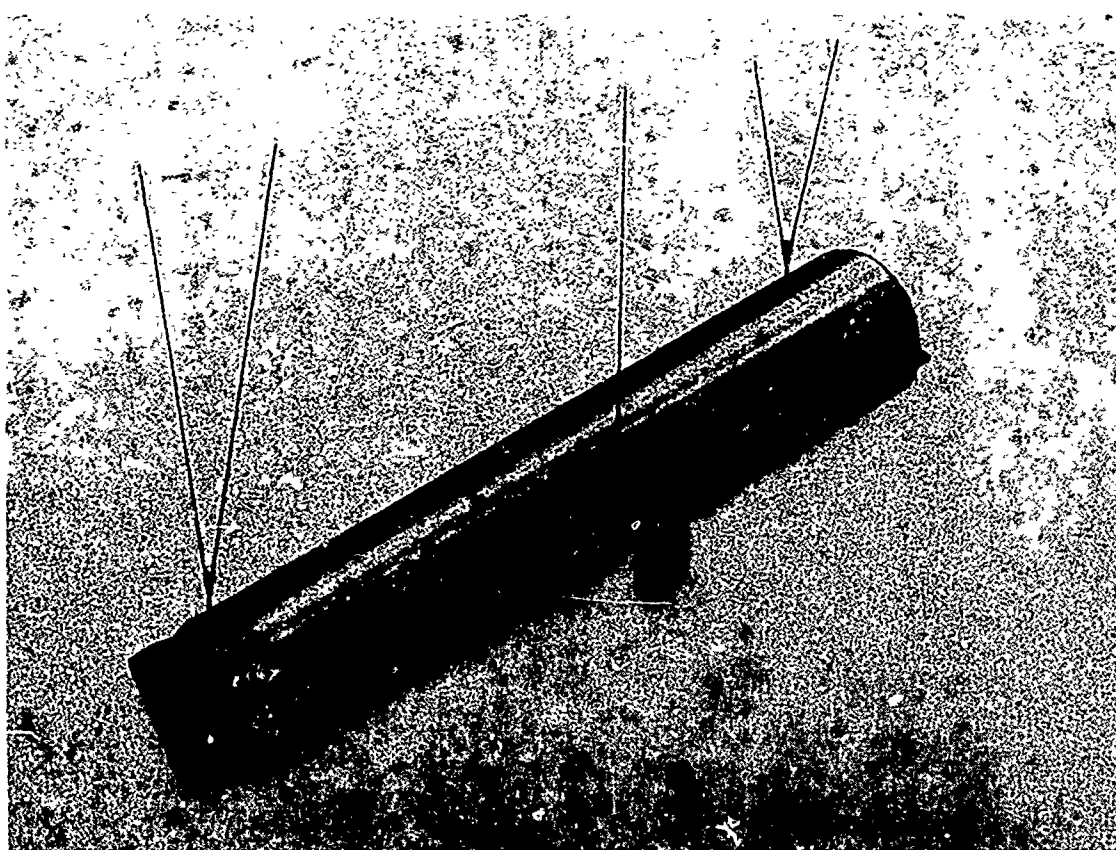
Fig.4.5   Classical five-wire ballistic pendulum

TARGET

SPRAY CATCHER

SPRAY PENDULUM

EJECTA CATCHER

TARGET PENDULUM

PROJECTILE

EJECTA PENDULUM
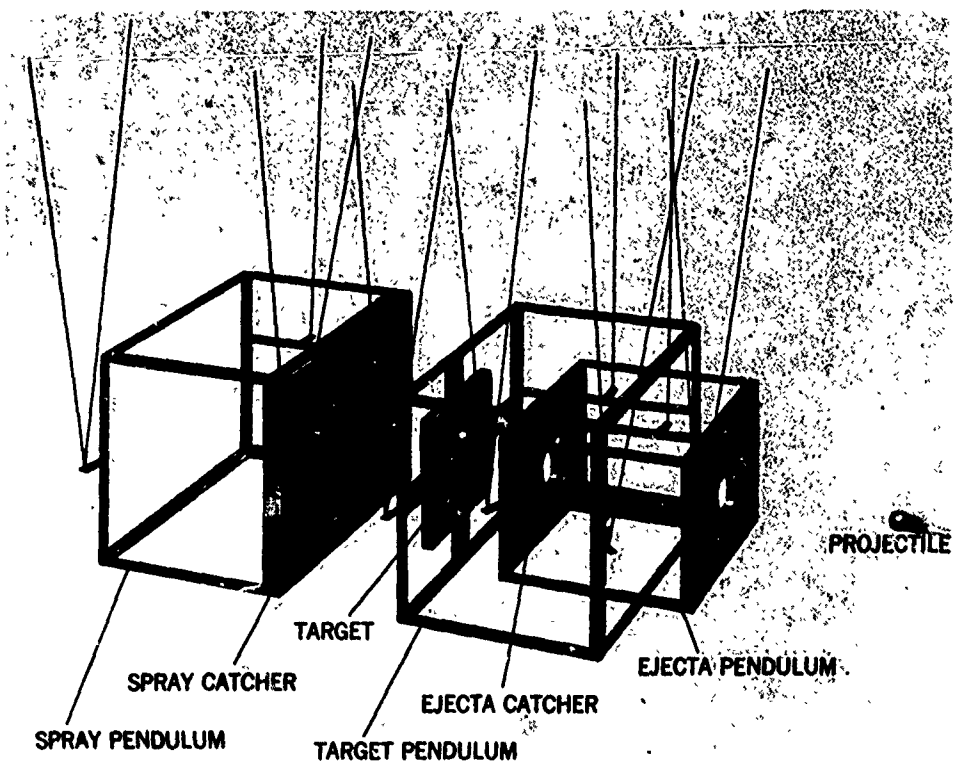
Fig.4.6   Multiple-ballistic-pendulum system
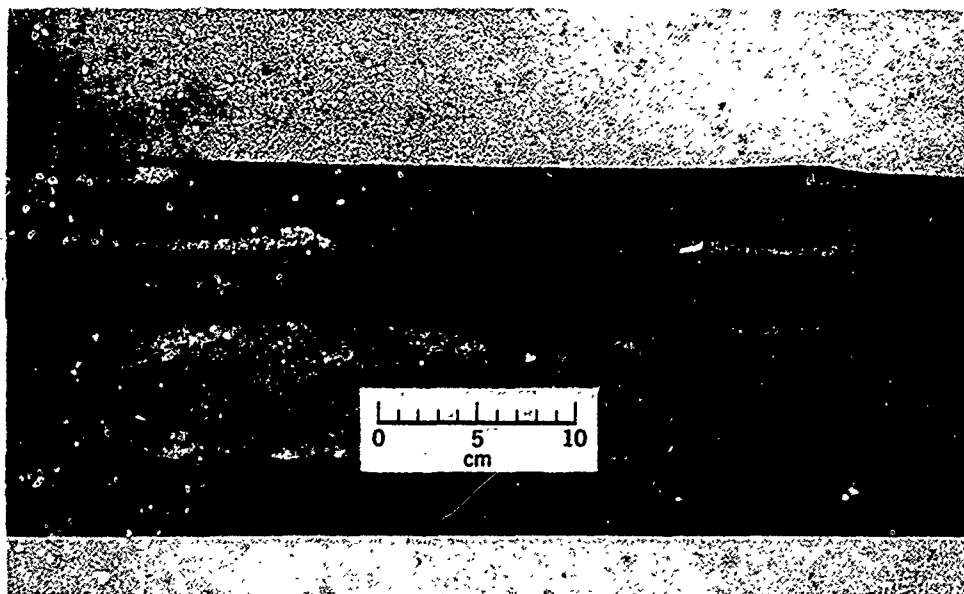
Fig. 4. 7   Sectioned particulate target

CHAPTER 5

COUNTERFLOW FACILITIES

by

Robert J. Carros and Charles E. DeRose

NASA-Ames Research Center

COUNTERFLOW FACILITIES

Robert J. Carros and Charles E. DeRose

5.1 INTRODUCTION

In ballistic testing, the maximum velocity is limited by structural limitations of the model and sabot and by the velocity capabilities of the gun. Though these limits have been steadily pushed higher through changes in gun operating cycles and design, availability of stronger materials for model and sabot construction, and advanced construction techniques, the interest in very high-speed phenomena motivated by space vehicles and basic research problems seem always to demand a velocity higher than that available. To satisfy this demand, for aerodynamic studies, a test section with a high-speed airstream may be combined with a conventional ballistic range to produce what has been called a counterflow facility. With this combination facility, the airstream velocity is added directly to the model velocity.

Typically, the counterflow facility consists of a long test section (by usual wind-tunnel standards) in which a supersonic airstream of near-constant stream properties is established. The model is launched upstream through this test section so that the total velocity experienced is equal to the sum of the model launch velocity and the airstream velocity. Data are recorded photographically as in conventional ballistic facilities, the only additional factor being that of accurately determining the airstream properties – pressure, temperature, and velocity.

The major advantage of the counterflow facility is that of increasing the velocity capability for aerodynamic testing with a given gun-model combination. However, it is not the only benefit realized. By control of the free-stream temperature, the Mach number can be varied considerably. Extremely high Mach numbers can be obtained by using a cold stream. Free-stream temperatures in the order of 100° K are easy to obtain and, with the speed of sound at this temperature around 200 meters/second, it is seen that a reasonable model velocity of 6 km/sec can yield Mach numbers of the order of 30 or more. In the same vein, a change in the free-stream temperature brings about a change in Reynolds number capability. Hot airstreams generated with high-energy drive systems produce low Reynolds numbers, while, conversely, cold airstreams will be characterized by high Reynolds numbers.

Another benefit is that the total model flightpath can be lengthened by the use of a high airstream velocity coupled with a low model velocity. Since the model flightpath length relative to the airstream is equal to

$$L_T = L_{ts} + V_t \left(\frac{L_{ts}}{V_m} \right) \tag{5.1}$$

$$L_T = L_{ts} \left(1 + \frac{V_t}{V_m} \right), \tag{5.2}$$

where V_m = velocity of model alone, m/sec

V_t = velocity of tunnel airstream, m/sec

L_{ts} = length of test section, m

L_T = total resultant flightpath length, m

it can be seen that the total flightpath length can easily be stretched out far beyond the actual test-section length. This capability contributes generally to the accuracy of aerodynamic measurements which improve with increasing range length, and in particular can be important when conducting tests to determine static and dynamic stability of a model where flightpath lengths must be of the order of two or more wave-lengths of pitch oscillation.

The counterflow type of facility also affords the capability – with suitably designed nozzles and test section – of permitting model flights through a variable density profile. Simulation of an earth entry for a space probe can be accomplished by a facility of this type. This kind of facility is highly restricted in the breadth of its research, but it is unique in offering a predetermined density, temperature, and velocity variation along the model flightpath.

Finally, another variation of a counterflow facility can be used to study the effect of blast waves on models in free flight. The use of a free-flying model allows the opportunity to observe the results of both a shock wave's dynamic effect on the model, and its aerodynamic effect on the bow shock wave, boundary layer, and wake, etc. The facility for this kind of study is essentially a launch gun firing a model into a shock tube.

All of the aforementioned capabilities are extensions of the basic capability of a conventional ballistic facility. At the same time, the use of a counterflow airstream complicates the testing and increases the cost of building and operating the facility. However, the difficulties can be largely overcome, and the benefits that this type of facility can offer in the form of greatly increased testing range are, for certain applications, well worth the effort.

. To illustrate the operating parameters and some of the inherent problems involved with operating a counterflow facility, we will examine the two major varieties in use. The first type will be designated the continuous flow facility - typified by the blow-down, unheated reservoir, wind tunnel. By continuous flow, we mean that the airflow duration is very long compared to the time of flight of the model. Flow times may be of the order of a minute or two which permits manual control of the test section conditions and the gun-firing sequence. The second type will be called the short-duration facility, in which the airflow times are only slightly longer than the flight time of the model. Typical of this latter type is the shock-tube-driven wind-tunnel configuration. Here, timing is of the utmost importance and most events in the launch procedure must be preprogrammed and sequenced by electronic control.

5.2 LONG-DURATION COUNTERFLOW BALLISTIC FACILITIES

5.2.1 General Description

Perhaps the simplest form of counterflow ballistic facility is one that utilizes a supersonic blow-down wind tunnel. The supersonic tunnel used in this way differs from a conventional blow-down tunnel mainly in the longer test section and the greater number of observation stations. Lengthening of the test section requires a divergence to the tunnel walls to account for boundary-layer growth. A maximum airstream velocity of approximately 0.6 km/sec can be attained without heating the supply air. This stream velocity of 0.6 km/sec for a Mach number 3 airflow, for example, when combined with a model velocity of 3 km/sec, results in a test Mach number of 18. (When an unheated air supply is expanded to a Mach number 3 airstream, the resultant sound speed is approximately 0.2 km/sec). The airstream density is relatively high (for this Mach number, 0.076 times the density in the air reservoir). The minimum density depends on the diffuser and exhaust conditions of the wind tunnel. For example, specification of atmospheric exhaust pressure with a blow-down wind tunnel determines the minimum reservoir pressure at which the tunnel will operate.

The complications to the testing introduced by combining a ballistic range and supersonic blow-down tunnel are not great. The first consideration is of course that of introducing the test model into the airstream at the proper time. This, fortunately, can be done quite easily, requiring no electronic sequence timers, since the time-of-model flight through the test section is very short, only a few milliseconds, compared to the long airflow duration of the order of a minute. The test operator can very easily fire the gun at a time when airflow has been properly established in the test section. Details of operation and instrumentation of a ballistic range will be found in other sections of this book and details of wind-tunnel operation and instrumentation can be found in the literature (see, for example, Reference 5.1), and will not be discussed here.

5.2.2 The Ames Supersonic Free-Flight Wind Tunnel

The facility described in this section was proposed by H.Julian Allen in 1946 as a means of extending the range of Mach numbers for laboratory aerodynamic testing beyond what was then available in wind tunnels. The Supersonic Free-Flight Wind Tunnel, placed in operation at the Ames Laboratory of National Advisory Committee for Aeronautics (NACA) in 1949, is shown schematically in Figure 5.1 and was the first counterflow ballistic facility. A brief description of the facility will be given here and a more complete description is contained in Reference 5.2.

5.2.2.1 Description of Facility

Air from an unheated reservoir, available to a maximum pressure of 6 atm, was expanded to Mach number 2 through a two-dimensional nozzle and exhausted to atmosphere. The most striking differences between this tunnel and a conventional supersonic blow-down tunnel was the test section length and the number of windowed observation stations. The test section originally was approximately 4.6 meters long and contained four vertical and three horizontal observation stations. After an initial operating period of five years demonstrated that the facility was both technically feasible and valuable, the test section was modified in 1955 to increase its length to approximately 7.3 meters with nine orthogonal photographic stations spaced at intervals of 0.915 meters. An additional interchangeable nozzle was added at this time for Mach number 3 airflow. The test section width originally was approximately 30 centimeters and height was approximately 61 centimeters, while the modified test section was approximately 43 cm wide by nominally 51 cm high. A photograph of the test section is shown in Figure 5.2.

The unusual length of the test section does not introduce any fundamental difficulties. It has been found that such a long supersonic flow can be established and maintained, with no more unsteadiness than is usual to supersonic wind-tunnel flows. Interestingly enough, it is found that when the reservoir pressure is reduced to the minimum levels that will sustain supersonic flow, the downstream end of the test section may lose supersonic flow while the upstream end retains it. However, the most important problem associated with the long test section is the growth of the thick turbulent boundary layer on the walls. This boundary layer would, in a long enough test section, ultimately fill the channel and leave no core of turbulence-free air for testing. The Supersonic Free-Flight Wind Tunnel and the subsequent Ames counterflow facilities were designed so that

this would not occur within the test section, and this specification in effect determined the minimum width dimensions of the facilities.

The time-average boundary-layer thicknesses in the Supersonic Free-Flight Wind Tunnel were calculated to be between 10 and 13 cm depending on stream Mach number and Reynolds number. With the final test section dimensions, this left a turbulence-free core at least 18 cm wide by about 36 cm high at the downstream end of the test section (station 1). This width was easily adequate for testing, since the model dispersion is least at this end of this test section, which is the end nearest the launching gun.

The displacement effect of the boundary layer also had to be considered, since for a uniform test-section cross section it would effectively diminish the area available for supersonic flow and thus reduce the Mach number with distance from the nozzle. To avoid this source of stream nonuniformity, the upper and lower blocks of the test section were designed to diverge and to compensate on two walls for the boundary-layer displacement thickness on four walls. Displacement thicknesses were calculated to be of the order of 2.5 cm at the downstream end of the test section, and the divergence allowed on the upper and lower blocks was slightly greater than 5 cm on each, giving a downstream end height of the channel of about 61 cm actual as compared to 51 cm nominal. As the stream Mach number and reservoir pressure were varied, this setting was not perfect, but represented a compromise or best average position, which was weighted in favor of the test condition most often used – the Mach number 3 airflow near maximum reservoir pressure. Some axial pressure variation thus remained for some flow conditions, and this will be described in a later section. It was not deemed practical or necessary to make the test section adjustable to best fit the airflow condition being used on each run.

The diffuser section had two right angle bends to greatly reduce the amount of daylight reaching the photographic film to prevent fogging. Furthermore, all surfaces in the diffuser and test section were painted with flat black paint to reduce the light reflecting back to the test section and the shadowgraph film. Curved vanes were located at the first bend in the diffuser to turn the air smoothly.

The model-launching gun was mounted on an "I" beam anchored to the floor of the diffuser. The beam and gun mounts were arranged so that the center'ine of the gun was coincident with the axis of the tunnel test section. A model catcher located in the settling chamber was filled with fireproof cotton waste backed up by several thick steel plates.

As in a conventional blowdown tunnel, pressure and temperature were measured from which the necessary stream properties were obtained. The instrumentation used to record data pertaining to the model was identical to that used in a ballistic range and is described in detail in other sections of this book.

5.2.2.2 Range of Test Conditions

The range of test conditions that were available in the Supersonic Free-Flight Wind Tunnel are shown in Figures 5.3 and 5.4. The test Mach number range is given for model-launching velocities to 6 km/sec. This velocity is well within the capability of modern light-gas guns which have operated to a maximum speed of 11.3 km/sec at Ames Research Center in 1966. The original Supersonic Free-Flight Wind Tunnel, however, never operated beyond a model-launching velocity of 3.7 km/sec corresponding to a maximum test Mach number of 21. There were three reasons for this limitation. First, the peak utilization of the original facility occurred before the present high level of gun capability was developed. Second, the gun beam provided in the facility was not long enough to accommodate the greater lengths of any but small-caliber light-gas guns. Third, the self-luminosity of the flow fields at very high speeds tends to fog the shadowgraph pictures and obliterate the model image (see for example, Figure 6.33 in Chapter 6). All of these problems could have been overcome, and, in fact, steps were required and were taken to modify the shadowgraph stations to overcome the third problem even at velocities of 3.7 km/sec; but at the same time, the higher performance, short-duration counterflow facilities were being developed, so emphasis was placed on them and use of the Supersonic Free-Flight Wind Tunnel was phased out.

The Mach number for a test utilizing the airstream is the sum of the stream Mach number and the model Mach number. (The sound speed is 0.253 km/sec for an air reservoir at room temperature with the Mach 2 airstream, and 0.204 km/sec with the Mach number 3 airstream). A test program using the facility air-off and air-on can, in principle, easily cover a range of supersonic Mach numbers up to 33.

The Reynolds number capability is shown in Figure 5.4 and extends over a wide range to a maximum of approximately 10 million per centimeter. Early in 1959 the Supersonic Free-Flight Wind Tunnel was connected to a 9½-atm air-supply reservoir. This increased the maximum Reynolds numbers available by a factor of 1.5.

5.2.2.3 Effect of Airstream Variations on Tests

The airstreams in supersonic wind tunnels are invariably imperfect and surveys of the airflow in the long test section of the Ames Supersonic Free-Flight Wind Tunnel disclosed a number of departures from uniform flow. A brief description of these and their effect on the aerodynamic data obtained from the facility will now be discussed.

The observed longitudinal variation of Mach Number, shown in Figure 5.5, was small, being only approximately ± ½% at M = 2 and ± ¾% at M = 3. The growth of the boundary layer, as discussed in Section 5.2.2.1, is responsible for the observed decrease in Mach number at the downstream (station 1) end of the test section for the

M = 3 condition and demonstrates that the cross-sectional area of the test section was insufficient to accommodate the thickened boundary layer. On the other hand, the small variation observed in the Mach number at the M = 2 condition shows that, in this case, the test-section area was adequate to allow for the boundary-layer growth. Early during calibration some adjustments were made to the cross-sectional area, by increasing the height dimension, to select the best setting that would result in the most favorable Mach number distribution for both the M = 2 and M = 3 conditions. Since the total test Mach number was high (for example, for a rather modest model velocity of 1.5 km/sec the total Mach number is approximately 10.5 for the M = 3 airstream) the small Mach number variation observed was not sufficient to effect aerodynamic data.

Closely associated with the Mach number variation are variations in the static and dynamic pressures. These are shown in Figure 5.6. The static-pressure-gradient results in buoyancy forces which are small compared to the drag forces and therefore do not affect the data significantly. The dynamic pressure varied approximately 0.7% at M = 2 and 1½% at M = 3 and this variation did cause some scatter in the results.

The variation of Mach number, static pressure, and dynamic pressure across the stream at station 1 is shown in Figure 5.7 for M = 2 and Figure 5.8 for M = 3. The variation in the central 5-centimeter core of the flow, where most model flights take place at this station nearest the gun, was small. From shadowgraph photographs showing the boundary layer and from oscillations observed in the manometer used to read total head pressures, as shown in Figure 5.9, it was evident that the boundary layer was approaching to within 5-centimeters of the tunnel centerline and was undoubtedly the cause for the variations observed in Figures 5.7 and 5.8.

Measurements of airstream angularity were attempted using cones that were pivoted so that they could become aligned with the stream. Photographs of the cones, made with a high-speed motion-picture camera, showed that they oscillated with an amplitude of about ±2 degrees at frequencies matching the natural frequency of the cones. Since the frequency of variation of the stream angle was several times that of the natural frequency in pitch of the test models, the pitching response of the test models to the stream angle variation was weak. Furthermore, the effect of stream angularity on a moving model is less than on a stationary model, as shown by the ratio

$$\frac{u_a}{V_a + V_m},$$

(5.3)

where u_a = lateral velocity component of airstream

V_a = airstream velocity relative to earth

V_m = model velocity relative to earth

which defines stream angle relative to a moving model. For example, a model flying at a Mach number of 3 in the Mach number 3 airstream (total test Mach number of 6) would experience only one-half the stream angle that a stationary model would experience. It was concluded that the influence of the observed stream-angle variation and the variations observed in Mach number, static and dynamic pressures were small and resulted in no important errors.

5.2.3 Atmosphere-Entry Simulators

5.2.3.1 Description of Facility

A second and rather specialized counterflow facility to simulate the velocity history and heating of entry vehicles coming into the earth's atmosphere has been mentioned in the Introduction. This type of facility makes use of a long contoured nozzle to dynamically establish a density profile along the nozzle axis which presents to the free-flight model flying upstream a variation similar to that encountered by a vehicle entering the atmosphere. The degree of simulation of entry aerodynamic heating which results has been shown to be surprisingly complete [5.3].

Such a facility was built at Ames Research Center and placed in operation in 1960. It consists of a high-pressure air reservoir, the specially contoured test-section nozzle, a vacuum tank, and a light-gas model-launching gun. Figure 5.10 is a schematic diagram of this facility and Figure 5.11 is a photograph of the air reservoir, test section, and large diameter piping leading to the vacuum sphere. The expanding test section was approximately 12 meters long, and during airflow, the air density varied exponentially with distance to simulate the variation with altitude in the atmosphere. Approximately three decades of density variation occurred within the test section so that an altitude interval of about 45 km in the earth's atmosphere was simulated. The actual air densities were larger than atmospheric by the scale factor of the model tested in order to achieve Reynolds number and heating simulation [5.3].

Airflow was supplied by a 0.48-cubic-meter high-pressure vessel initially pressurized up to 45 atm with air at room temperature. Mechanically rupturing the diaphragm between the reservoir and test section initiated flow which was exhausted into a 9¾ meters diameter vacuum sphere. The test section was instrumented with 12 orthogonal pairs of shadowgraph stations, as well as with static pressure transducers located at the sidewall to define the actual variation of air density with distance.

The model-launching gun used with this facility was a two-stage, light-weight piston (shock-heated) light-gas gun, with launch tube diameters of 12.7 and 20mm. The gun is required to launch the model at the velocity at which the vehicle to be simulated enters the atmosphere. A more detailed description of this facility will be found in Reference 5.4.

5.3 SHORT-DURATION, HIGH-ENERGY AIR SUPPLY SYSTEMS

The facilities in Section 5.2 all operate with room temperature air supplies and, as a result, are limited to airstream velocities of about 0.6 km/sec. When very high test speeds are desired, in the range from 10 to 15 km/sec, it would seem desirable to attempt to realize a larger speed increment from the airstream. In order to do so, it is necessary to utilize high-energy, heated reservoir types of drive systems. As the airstream velocity is increased, the required temperature of the reservoir quickly exceeds the limits of standard construction materials. Figure 5.12 shows the reservoir temperature required to produce a given stream velocity. The assumption is made that the airstream produced has a constant Mach number 7. The only way to obtain the high airstream velocities desired (from 2 km/sec and above) is to operate the facility in a manner in which the reservoir air is held for an extremely short time. As ballistic tests normally have flight times in the milli-second range, the use of a high-energy, short-duration-type of facility seems particularly attractive.

Although a number of possible approaches to a short-duration, high-energy supply are conceivable, at this writing there exists experience with only one – the reflected-shock (tailored-interface) shock tube [5.5-5.13]. Other possibilities which have not been developed would include arc-heated air supplies (hot-shot wind-tunnel type), piston compression reservoir heaters[5.14-5.18], and electrical resistance heated air supplies. The latter two types were seriously reviewed at Ames Research Centre prior to the construction of the facilities described later, and were judged to have considerable problems. Still another possibility that was considered to the extent that development tests were carried out was the use of gun-powder gases as a shock-tube driver system. Thus, although the remaining discussion is restricted to combustion-heated and cold helium shock-tube drivers, the basic concept need not be restricted in the reader's mind to this approach.

5.3.1 Shock-Tube Wind-Tunnel Configurations

The one type of system which has been applied to high-performance counterflow ballistic testing uses a shock-tube driver to supply air for a wind-tunnel test section, as in Figure 5.13. As shown in the figure, the shock-tube driven, counterflow ballistic range is composed of six component parts.

The first two, the driver and shock-tube, create the reservoir of high-temperature test gas. The driver section is filled with high-pressure gases such as hydrogen or helium, and the shock-tube, with low-pressure air (or other test gas). The two sections are separated by the main diaphragm, the explosively-triggered rupture of which starts the gas-compression cycle. The driver performance may be enhanced by heating the driver gas just prior to bursting the main diaphragm, either by chemical reactions in the driver (e.g., burning hydrogen), electrical heating, or compression heating. Basic theory and operation of shock tubes can be found in numerous reports, examples of which are References 5.5 to 5.13. The emphasis here will be on special aspects relating to their use as a counterflow air-supply system.

These first two tubes represent the high-pressure section of the facility and must be constructed to hold and seal against an internal pressure measuring as high as 1000 to 2000 atm. This high pressure is required for reasonable airstream densities in the test section if airstream velocities above 3 km/sec are contemplated.

Beyond the shock-tube, the end of which is the high-energy reservoir, are the nozzle section, test section and receiver tank, the low-pressure section of the facility. Here the pressure has to be reduced initially to the order of 100 microns of mercury (0.00013 atm) to permit the airflow to be established. This level of vacuum requires very careful attention to seals, piping, and valves, and a good quality mechanical vacuum pumping installation. As noted in Figure 5.13, the volume of the receiver tank is preferably designed to contain all of the gas without raising the resultant pressure above the safety limit of the glass windows in the test section. Frequently, in the case of a large, high-pressure facility, a blow-off diaphragm will be added to vent excess gas; otherwise, the volume of the receiver tank might be excessive.

The test section is an area that represents the greatest compromise in initial design. To assure constant stream conditions over the long test section, the cross-sectional area must increase to compensate for the boundary-layer growth. Unfortunately, the boundary-layer growth is dependent upon the pressure and enthalpy levels of the airstream. Therefore, the divergence rate of the walls must be set for a special range of tunnel running conditions. Airstreams generated by conditions off these design points will result in either an expanding or contracting airstream, which results in complications in reducing the aerodynamic data (see Chapter 7, Section 10.2). The wider the range of stream conditions designed for, the more nonuniform will be the off-design airstreams. In order to maintain airstream uniformity, the range of conditions must be limited or else adjustable walls provided. Wall adjustment, however, is incompatible with the requirement for good vacuum sealing.

5.3.1.1 Gas Compression Cycle

To illustrate the operation of the drive system, the sketches in Figure 5.14 show schematically the time history of the gas cycle. The description is intended only to define the various phases of the gas-compression cycle, which follows bursting of the main diaphragm.

174

5.3.1.2 *Tailoring Requirement*

To utilize a shock-tube-drive system in a counterflow facility, the stagnation region, or reservoir, must remain at constant pressure for a long enough time to complete the model flight. A constant reservoir condition can be accomplished by operating the shock-tube in a "tailored" condition. This means that the returning shock wave that brings the air and driver gas to zero velocity also leaves these two gases at the same pressure. With no pressure differential across the air/driver-gas interface, the reservoir will remain at nearly constant pressure until the expansion wave arrives to end the cycle. Testing time is then dependent upon the arrival of this expansion wave, a fact which leads to designs favoring long driver tubes.

Operating the shock-tube in a "tailored" mode limits the operation to a unique set of stagnation enthalpy conditions. The "tailoring" requirement

$$\frac{\gamma_4}{\gamma_1}\left(\frac{p_2}{p_1}\right)\left(1 - \frac{(p_2/p_1)-1}{\gamma_1 M_s^2}\right) = \left(\frac{a_4}{a_1}\right)^2\left(1 - \frac{\gamma_4-1}{a_4/a_1}\frac{M_s}{2}\frac{(p_2/p_1)-1}{\gamma_1 M_s^2}\right)^2 . \tag{5.4}$$

where γ = ratio of specific heats, C_p/C_v

p = pressure, newtons/m^2

M_s = shockwave Mach number

a = speed of sound, m/sec

subscripts

1 = initial loading conditions in shock-tube

2 = conditions behind shockwave

4 = conditions in driver tube just prior to bursting main diaphragm

essentially reduces to the fact that given the acoustical ratio (a_4/a_1) across the main diaphragm and the specific heat ratios, γ_4, and γ_1, there is only one M_s that will "tailor". While this seems like a limiting factor, in reality it merely sets the nozzle throat diameter and operating points for a given driver gas in the facility.

The counterflow facility that is shock-tube-driven may be constructed with a single nozzle contoured for a specific Mach number and still allow the free-stream velocity to be varied by changing the reservoir enthalpy. This makes it unnecessary to change the complete nozzle to change test-section air velocity. Only the throat diameter need be changed, and this can be done by changing a throat insert. The required relation between reservoir enthalpy and throat area ratio is shown in Figure 5.15 (Ref.5.19). The throat blocks are machined to match the specific reservoir conditions dictated by the "tailoring" requirements and the driver-gas conditions available.

5.3.1.3 *Shock-Tube-Drive Capabilities*

The shock-tube-drive system is able to develop high-energy reservoirs, and consequently, high-velocity airstreams. Figure 5.16 shows the relationship of shock-wave Mach number in the shock tube and airstream velocity in the test section. Indicated on this plot are typical "tailored" operating points – two for cold driver gases, and two for commonly used combustion-heated-helium drives. Thus, it is apparent that not only can a high-stream velocity be established by a shock-tube-drive system, but that the stream velocity can be varied over a wide range.

In a facility with the nozzle Mach number fixed, varying the airstream velocity is necessarily accompanied by changes in the speed of sound and free-stream temperature in the test section. The variable free-stream temperature, however, rather than being a disadvantage, actually permits a wide range of total Mach numbers and Reynolds numbers to be obtained.

5.3.2 Limitations of the Shock-Tube Wind Tunnel in a Counterflow Facility

The advantages of this type of test facility to extend the testing range are, unfortunately, accompanied by operating problems which put definite limits on its use. First, there is the necessity for timing the arrival of the model to match the establishment of the airstream. While at Ames Research Center, this has not been a major problem area, for some guns there could be enough uncertainty in launch time to make timing a problem.

Another major problem with the shock-tube drive is that of contamination of the airstream. When the reservoir is established and airflow is started through the nozzle, there is a tendency for the driver gas to mix with the air at the interface and flow through the nozzle before the end of the predicted clean-flow period. Small amounts of driver-gas contamination cannot be detected by pressure measurements and therefore the true air test time may not be conclusively known. The use of other techniques to determine when contaminated flow begins is therefore required.

For aerodynamic testing, small contamination is not too serious, but it can introduce serious errors into the measurements of shock-layer radiation from models, for example. In addition to chemical contamination, it is also found that because of the violent nature of diaphragm opening and high-stagnation enthalpy at the nozzle,

metal appears in the airstream in the form of small particles. Again, the amount of this type of contamination is not enough to affect most aerodynamic measurements, but may have important consequences in some tests, for example, boundary-layer transition testing if the particles hit and roughen the model surface.

Another operating problem is that of accurately determining the airstream properties. Since running time is in the millisecond range, fast-response gages are necessary. These gages have an electrical output and require calibration periodically. Unfortunately, such calibration is frequently static in nature while the use of the gage is dynamic. The method used to assure accurate results is to use redundant gages and average the results (eliminating any obviously wrong values).

Parallel with this problem of stream measurement is the additional one of stream calibration prior to testing. Pitot and static pressure measurements need to be made across the instrumented section of the facility in order to relate wall measurements to centerline values. Because of the required test-section length, stream calibration needs to be performed at many stations and at many pressure and enthalpy settings in order to determine the axial variation of the stream. This lengthwise calibration causes the stream calibration to be a long and involved procedure.

A final disadvantage of a counterflow facility is that it is much more expensive to build and requires more facility time and more man-hours per test than a conventional still air ballistic range. The cycle time per test is necessarily lengthened by the requirement to disassemble, clean, reassemble, and charge gases into the long tubes. There are also numerous expendable parts required. Typically, two preformed diaphragms and a mechanism for opening the main diaphragm are expended for each test.

5.3.3 Facility for Shock-Wave Impingement Effects on Free-Flight Models and Flow Fields

Before continuing with the counterflow facilities described above, let us examine a unique ballistic range using the shock tube driver without a nozzle. This type of facility[5.20] uses a shock-tube with a single photographic station to study the effect of shock wave impingement on models in free flight. The model is launched into the shock tube so as to be in the field of view of the window at the same time as the shock wave. Multiple photographs are made of the interaction of the normal shock wave with the model and its wake.

The critical factor in testing with this type of facility is in timing the arrival of the model and shock wave to coincide at the instrumented station. For windows of the order of 0.5 meter in length and model velocities of 5 km/sec, the time allowable for coincidence of model and shock wave at the test station is 100 μsec. This degree of timing accuracy is achieved by using a short shock tube and a long flight range, as is shown in Figure 5.17. The model is launched and its velocity is measured with a series of detectors. With this velocity information, the arrival time of the model at the window is computed. This information is fed to a delay unit which then fires the shock tube so as to produce a normal shock wave at the predicted time of arrival of the model at the window.

The photographic information obtained can be related to shock Mach number and model velocity. A very wide range of shock Mach numbers can be utilized as there is no necessity to tailor the drive conditions. The model velocity also can be varied almost at will as the only requirement is timing for one point in space and not over a protracted test-section length.

5.3.4. Hypervelocity Free-Flight Aerodynamic Facility

Of the four high-performance, short-duration, counterflow facilities which have been built at Ames Research Center[5.21], we will choose the largest for discussion and description in detail. It is called the Hypervelocity Free-Flight Aerodynamic Facility. The facility is shown in the sketch in Figure 5.18. The general structural arrangement is designed to allow approximately 0.025 sec of usable flow time in a test section 23 meters long. The test section is large enough to allow model excursions of ±20 cm and remain within the photographic field of view. Models up to 3.8 cm in diameter are possible with the largest available gun. The guns are interchangeable on a fixed, prealigned gun beam 46 meters long.

5.3.4.1 Operating Range and Boundary-Layer Correction

The airstream capabilities of this test facility are shown in Figure 5.19. These values are functions of the present operating pressure limit (680 atm) and the preselected Mach number of the airstream (M = 7).

Three interchangeable nozzle throat inserts are available to match the three different reservoir enthalpy conditions: H_s = 1870 joules/g (cold helium/air drive), H_s = 4670 joules/g (combustion-heated helium/air drive), and H_s = 7500 joules/g (another mixture of combustible gases with helium/air drive). As is noted in the figure, these reservoir conditions give airstream velocities of 1.8, 2.9, and 3.7 km/sec.

The two combustion-heated drives differ in the mixture of gases loaded, thus yielding end products of combustion having different final temperatures, molecular weight, and values of γ. As an example, for a reservoir enthalpy of 4670 joules/g, the mixture loaded is

$$4.5(H_e) + 3.5(N_2) + 1.0(O_2) + 3.0(H_2) \tag{5.6}$$
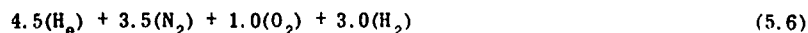
For convenience and economy, air is used instead of N_2 and O_2.

$$4.5(H_e) + 4.43(air) + 0.07(O_2) + 3.0(H_2) \qquad (5.7)$$

This combustion mix will tailor in this facility at a shock-wave Mach number of about 5.8.

The combustion-heated helium drive is used in preference to a cold hydrogen drive (which gives approximately the same stagnation enthalpy) in the interest of safety. In the combustion mode, hydrogen is used but in relatively small quantities. While some degree of hazard exists with the possibility of detonation instead of smooth burning occurring with the H_2, O_2, H_e mixes, operating results have shown consistently good burning with the driver geometry available.

The driver tube for this facility is 0.43 meter inside diameter and 23 meters long (length/diameter = 53.5). Ignition of the combustible mixture is accomplished by heating a single 0.38-mm-diameter tungsten wire with a pulse from a 90 microfarad bank of capacitors charged to 14.5 kV. Used in this manner, the wire is heated and not exploded, thus giving a line ignition down the center of the tube. The wire is installed with sufficient tension to keep the sag below 1 cm.

The pressure capability of the shock tube and driver tube is rated at 2040 atm with a safety factor of 1.5. This rating gives a good allowance for any adverse burning conditions.

Higher velocities than the 3.7 km/sec shown can be obtained by adjusting the constituents of the combustion drive. However, as is noted in the figures, the free-stream density drops rapidly with increasing stream velocity and aerodynamic testing in airstreams above 4 km/sec would be highly limited for this particular facility. Obtaining a higher free-stream density at higher airstream velocities by increasing the reservoir pressure is possible but is presently limited due to operating limits imposed by the main diaphragm (at 680 atm, this diaphragm is 1.27-cm thick, 304 stainless steel).

Another limitation on the use of a wider range of shock wave drives is that of maintaining uniform test-section conditions. As mentioned earlier, the test section must be constructed with a diverging test section to compensate for boundary-layer growth. The rate of the boundary-layer growth with distance has been calculated for this facility and is shown in Figure 5.20. These slopes are based on flat-plate turbulent boundary-layer growth at a distance of 37 meters from the leading edge.

The divergence rate built into this facility is 0.007 cm/cm, which matches the boundary-layer growth at $N_s = 10$ at 700 atm. This divergence rate was chosen as it was intended to operate the facility at high pressure at high-reservoir enthalpies. Lower pressures were contemplated for use with the lower reservoir enthalpies.

The result of operating off design is shown in Figure 5.21. To prevent the possibility of confusion with regard to this figure, it must be realized that the airflow is from station 16 to station 1, while the model flies from station 1 to station 16. This figure is so constructed so as to indicate the density experienced by the model at the time it passes through each station. This record of free-stream density shows clearly an expanding stream where the boundary-layer-growth rate is less than the wall-divergence rate. In this particular example, the stream effectively expands more than predicted by differences in boundary-layer correction. Figure 5.22 shows the stagnation-pressure record for this test. Indicated on the record are the pressures, which, when translated downstream, affected the flow at the time the model appeared in the stations. Thus, the rising reservoir pressure alone created a 18-percent change in the stream pressure that affected the model from station 1 to station 16. It is possible that a modification to the reservoir pressure history by varying the shock-tube loading so as to decrease pressure with time could be used to compensate for expansion of the airstream in the off-design operation. Success of this type of operation could greatly enhance the operating range of the facility.

5.3.4.2 General Test Range Capabilities of this Shock-Tube Facility

A general picture of the range of conditions that can be presently covered is shown in Figure 5.23. The results are based on a rather cautious maximum model velocity of 6 km/sec (compared to a maximum-recorded gun velocity of 11 km/sec) and a maximum model diameter of 3.8 cm. This choice is made to allow for the use of models with more complex shapes and greater weights than the minimum length plastic cylinders used in highest velocity firings; that is to say, it perhaps represents the usual velocity of the kinds of models of interest in aerodynamic testing. As can be seen, the velocity capability has been increased by more than 50% while still retaining a useful range of Reynolds number. The advantage of the counterflow airstream is even more pronounced when the model velocity is restricted by structural limitations to a value lower than 6 km/sec. However, because of the short running time of this facility, a minimum model velocity of approximately 2 km/sec is required if a countercurrent airstream run through the full length of the test section is desired.

5.3.4.3 Time and Coordination Problems

This imposition of a minimum model velocity is but one of the ramifications arising from the facility's short run time. To illustrate, Figure 5.24 shows a time-distance plot of the operation of this facility. This time history was taken from a test in which the airstream velocity was 2.9 km/sec and the model velocity was

3.7 km/sec. As shown on the diagram, with perfect timing, a minimum model velocity of 1.2 km/sec could be accommodated. However, to be realistic, leaving about 2 to 3 msec on both ends for timing margin, the minimum model velocity rises to the practical value of about 2 km/sec.

Expanding more on this timing problem, the example shown in Figure 5.24 was made with a relatively small gun, 1.27 cm diameter. This gun, for the velocity shown in the example, normally takes 0.042 sec between the signal to fire the gun and arrival of the model at station 1. From the time-history plot, it is seen that the gun is fired at the same time that the main diaphragm was ruptured. It is fortunate that this gun is fairly consistent in this time of model arrival as this type of coordination is the poorest possible. The greatest variation in time in the operation of these light-gas guns is in the time to burn the gun powder and set the compression piston in motion. With a larger gun requiring a longer time to place the model at station 1, the timing of the opening of the main diaphragm is determined by make-switches triggered by the pump piston after it is in motion. Smaller guns, which will have to be fired after the main diaphragm is ruptured, will have smaller errors in time because of the smaller overall time of operation.

While the timing is critical, this facility has been sized to allow a usable test time plus sufficient excess to cover expected irregularities in the operating cycle for all model velocities above the minimum 2 km/sec. Scatter in the time for the shock wave's arrival at the nozzle has been observed to be of the order of 1 msec. The gun's operation is less accurate, giving uncertainties of up to 5 msec for the worst case. These times show that, for an adverse summation of timing errors, the model can be placed outside the flow time at either the start or end of the flight.

5.3.4.4 *Airstream Properties and Calibration*

To accurately determine the stream parameters, four dynamic measurements are made during the gas-cycle process. These are: driver pressure at the time of diaphragm opening; velocity of the shock wave in the shock tube, reservoir pressure near the end wall of the shock tube, and test-section wall pressure. These measurements, along with previously measured air pressure in the shock tube and the loading pressure in the driver tube, give sufficient data to permit some redundancy in stream calculations.

The basic method of computing the free-stream conditions is to calculate the stagnation enthalpy from the knowledge of the shock-wave Mach number and the stagnation pressure measured (see Figure 5.25). This high-energy air is then assumed to expand isentropically to the free-stream pressure measured. This process can be traced on a Mollier diagram and yields a value for free-stream static temperature and enthalpy. The difference in enthalpy between stagnation conditions and free-stream conditions gives the value of free-stream velocity directly,

$$H_s - H_\infty = \frac{V_\infty^2}{2000} , \qquad (5.8)$$

where H_s = reservoir enthalpy, joules/gram

H_∞ = free-stream enthalpy, joules/gram

V_∞ = free-stream velocity, meters/sec.

Free-stream enthalpy and temperature may be used to compute the speed of sound and stream Mach number. With this, all parameters concerning the airstream are known.

Commercially available pressure transducers (quartz crystals) are used in the driver and shock tube to measure pressure. These cells are mounted in a standard holder (standard for this facility) so that only one hole configuration is bored in the tubes. A sketch of the holder is shown in Figure 5.26. An example of the driver pressure record is shown in Figure 5.27; the record is from a combustion-heated driver-gas test and shows the smooth burning that seems to be typical for this facility. This pressure is not used directly in any stream condition calculations, but it is necessary in determining smoothness of burning, pressure ratio across the main diaphragm, and for establishing timing relationships between ignition and rupture of diaphragm.

Two separate records are taken of the pressure in the reservoir region; the pressure transducers are placed slightly back from the diaphragm. These records are shown in Figure 5.28. The first trace shows the value of p_2, the pressure behind the shock wave as it travels towards the nozzle. The second trace shows the complete pressure history in the stagnation region. An accurate measure of p_2 from the expanded trace is useful in checking the value of shock Mach number obtained by velocity measurements.

The velocity of the shock wave is measured using piezoelectric crystals in a holder as is shown in Figure 5.29. The pressure-sensitive detectors are relatively simple to construct and rugged; some in the stagnation region have survived 50 tests over a period of two years and are still in good working order.

The final measurement required is that of free-stream pressure. The wall static pressure is measured using commercial unbonded-strain-gage cells mounted in a holder, as shown in Figure 5.30. The special holder is necessary to prevent shock and vibration of the tunnel structure from affecting the signal. The trace of a typical pressure history is shown in Figure 5.31.

With the preceding measurements, a time-distance diagram can be constructed as was shown previously in Figure 5.24. Correlating this with the time history of model position, the airstream properties can be computed for that time and position occupied by the model during its flight.

In order to define the properties of the airstream completely, measurements of stream properties across the test section at each station would be necessary. This procedure, if done for even an abbreviated set of flow conditions, would be a long and laborious task. Therefore, to date, stream calibrations have been performed only at stations 1, 8, and 15, with the flat-plate assembly shown in Figure 5.32.

The design philosophy applied to this calibration rig was to obtain as much stream information with each test as possible. Thus, the five static-pressure measurements from the flat plate, along with one wall measurement, give a fairly complete cross-stream record. This is complemented further by measurements using the two pitot probes.

Plotted in Figure 5.33 are calibration records of free-stream static pressure as a function of time from three tests at nominally the same drive conditions. To equate all measurements, the pressure is shown as the ratio of free-stream static pressure, p_∞, to stagnation pressure, p_s. As seen, the centerline pressure can differ from the sidewall pressure by as much as 20% at station 1 to almost perfect agreement at station 8.

At all stations, the central core, that is, the center 30 cm, seems to be fairly uniform. Also, station 8 seems to be not only at about the average static pressure for the entire length, but also, its sidewall pressure measurement reflects very accurately the centerline conditions.

This calibration at three distinct stations gives the end points and center of what is then assumed to be a smooth variation with distance. To check this assumption, an additional stream calibration was made by firing a sphere into the counterflow airstream and measuring its deceleration. The drag coefficients of a sphere is known and, because of a controlled small change in velocity, should be constant for the flight. By dividing the flight into segments and requiring the drag coefficient to be a preset constant value, a measurement of free-stream density can be made. The results of this method produced the tunnel density profile shown in Figure 5.21.

Along with the general determination of stream properties, some notice must be taken of possible stream contamination which, as noted earlier, could escape pressure-measurement detection. In an effort to minimize the travel of metal particles through the nozzle and into the test section, a simple modification has been made to the basic structure of the shock-tube end. This modification is primarily a baffle plate preceding the nozzle throat supported on posts. Solid metal particles traveling down the shock tube will either impact on the plate or on the end of the shock tube. No direct path is available to a heavy particle from the shock tube into the nozzle throat. The flow area available around the plate is made large with respect to the throat area so that gas velocities are low. Observations of stagnation pressures in the reservoir region and static pressures in the test section for similar tests have shown no discernible effect of the presence of this plate on the air-flow. The only drawback to this plate is that it will suffer considerable damage from models, being directly in the line of sight of the gun.

Since the problem of stream contamination by the driver gas is potentially very serious, a great effort has been expended on developing means of detecting and measuring its extent. To date, the most effective, but difficult, method is that utilizing gas sampling valves and a gas chromatograph.

The gas-sampling valves are normally closed valves sealing off a previously evacuated chamber. These valves are placed in the test section within the usable core of the flow. At a preset time, the valves open for a period of 1 msec and then close, trapping a sample of gas. With multiple valves set for staggered times, a timewise sampling of the gas in the stream can be accomplished. Immediately after the test, the gas is analyzed with a gas chromatograph. The gas chromatograph can easily separate out small traces of the light gases, hydrogen and helium, from the heavier gases making up air. This gives an accurate measure of the onset of driver-gas contamination. The operating problem with this equipment is to prevent leakage into the sampling chamber before the sample is analyzed.

5.3.4.5 Operating the Facility

Because of the large size of this counterflow facility, routine operations such as separating the joints, cleaning the tubes, and installing diaphragms can become major operations. Therefore, in the design, thought was devoted to mechanizing these operations and reducing the crew size needed to perform them. Reducing the cycle time was also, of course, an objective. As a result, all connections between the driver and shock tube are made up hydraulically. Photographs of the facility (Figures 5.34 and 5.35) show the hydraulic system and the methods of connection used on this structure. Only one bolt needs to be tightened to assemble the facility-that located at the nozzle joint.

Cleaning the tubes is achieved by first separating the tubes, then translating the shock tube laterally using hydraulic rams. Then a cleaning patch over a diameter-size plug is drawn through the tubes using a capstan drive. Two men can assemble this facility in about one-half hour, and disassemble and clean it in about one hour. Without the time and manpower-saving function of the hydraulic system, testing would be considerably slower and would require larger crews.

REFERENCES

5.1 Pope, Alan — *Wind Tunnel Testing.* John Wiley & Sons, 1954.

5.2 Seiff, Alvin — *A Free-Flight Wind Tunnel for Aerodynamic Testing at Hypersonic Speeds.* NACA TR 1222, 1955.

5.3 Eggers, A.J.Jr — *A Method for Simulating the Atmospheric Entry of Long-Range Ballistic Missiles.* NACA TR 1378, 1958.

5.4 Hamaker, Frank M. — *The Ames Entry Simulator and Its Application to the Determination of Ablative Properties of Materials for Ballistic Missiles.* NASA TM X-394, 1960.

5.5 Nagamatsu, H.J.
Geiger, R.E.
Sheer, R.E. Jr — *Hypersonic Shock Tunnel.* General Electric Res. Lab. Report 59-RL-2164. January 1959.

5.6 Glass, I.I,
Patterson, G.N. — *A Theoretical and Experimental Study of Shock-Tube Flow.* J.Aeron. Sci., Vol.22, No.2, 1955, pp.73-100.

5.7 Whittliff, C.E.
Wilson, M.R.
Hertzberg, A. — *The Tailored-Interface Hypersonic Shock Tunnel.* Cornell Aeron. Lab. Report AD-1052-A-8, 1958.

5.8 Russo, A.L.
Hertzberg, A. — *Modifications of the Basic Shock Tube to Improve its Performance.* Cornell Aeron. Lab. Report AD-1052-A-7, August 1958.

5.9 Hertzberg, A.
Smith, W.E.
Glick, H.S.
Squire, W. — *Modifications of the Shock-Tube for Generations of Hypersonic Flow.* Cornell Aeron. Lab. Report AD-789-A-2, March 1955.

5.10 Hertzberg, A. — *The Shock Tunnel and its Application to Hypersonic Flight.* Cornell Aeron. Lab. Report AD-1052-A-5, June 1957.

5.11 Whittliff, C.E.
Wilson, M.R. — *Shock Tube Driver Techniques and Attenuation Measurements.* Cornell Aeron. Lab. Report AD-1052-A-4, August 1957.

5.12 Squire, W.
Hertzberg, A.
Smith, W.E. — *Real Gas Effects in a Hypersonic Shock Tunnel.* Cornell Aeron. Lab. Report AD-789-A-1, March 1955.

5.13 Alpher, R.A.
White, D.R. — *Ideal Theory of Shock Tubes with Area Change near Diaphragm.* General Electric Report 57-RL-19664, January 1957.

5.14 Cox, R.N.
Winter, D.F.T. — *A Theoretical and Experimental Study of an Intermittent Hypersonic Wind Tunnel Using Free Piston Compression.* ARDE Report (B) 9/61.

5.15 Bray, K.N.C.
Pennelegion, L.
East, R.A. — *A Progress Report on the University of Southampton Hypersonic Gun Tunnel.* Dept. of Aeron. Res., Univ. of Southampton, ARC Tech. Report No.457, 1958.

5.16 East, R.A. — *The Performance and Operation of the University of Southampton Hypersonic Gun Tunnel.* U.S.A.A. Report No.135, August 1960.

5.17 Stalker, R.J. — *An Investigation of Free Piston Compression of Shock Tube Driver Gas.* National Res. Council of Canada, Mech. Engr. Report MT-44, May 1961.

5.18 Kamimoto, G.
Mori, T.
Kimura, T. — *An Analysis of the Piston Motion in a Hypersonic Gun Tunnel.* Dept. of Aeron. Eng., Kyoto Univ., Japan, C.P.5, January 1964.

5.19 Yoshikawa, Kenneth K.
Katzen, Elliott D. — *Charts for Airflow Properties in Equilibrium and Frozen Flows in Hypersonic Nozzles.* NASA TN D-693, April 1961.

5.20 Merritt, D.L.
Aronson, P.M. — *Free Flight Shock Interaction Studies.* U.S. Naval Ordnance Lab., January 24, 1966. AIAA Paper No. 66-57.

5.21 Seiff, Alvin — *Ames Hypervelocity Free-Flight Research.* Astronautics and Aerospace Engineering, Vol.1, No.11, December, 1962, pp.16-23.
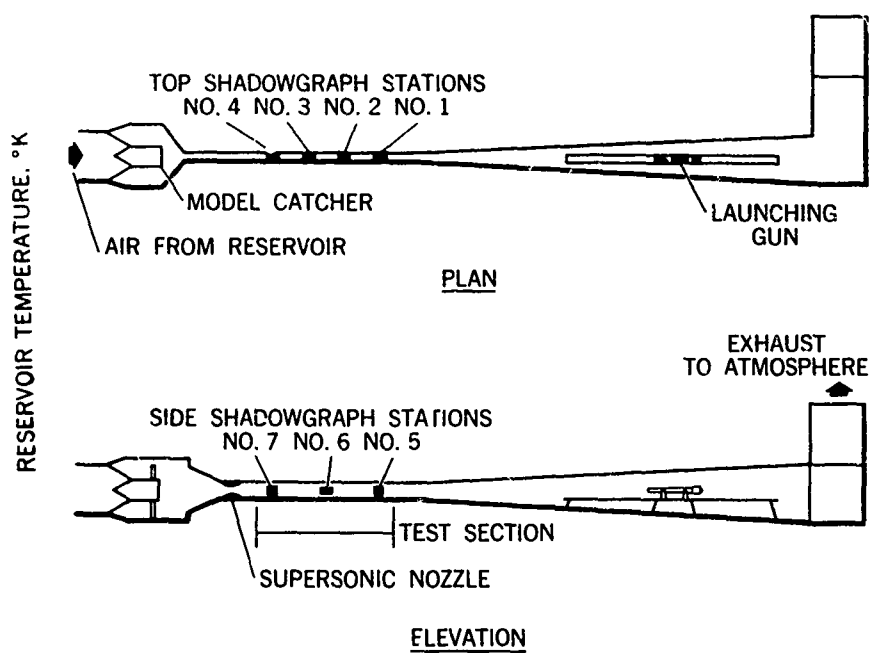
5.1 General arrangement of the Ames Supersonic Free-Flight Wind Tunnel
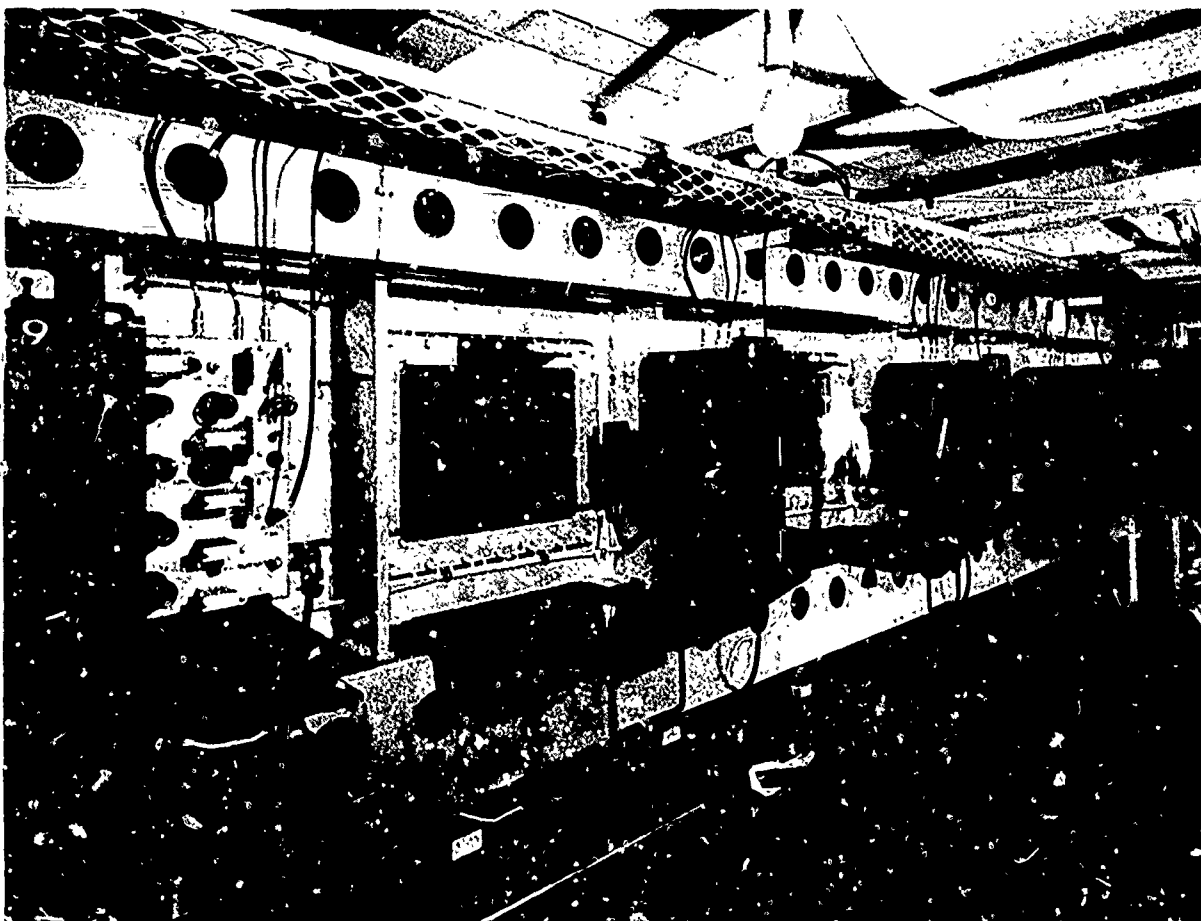
5.2 Photograph of the test section of the modified Ames Supersonic Free-Flight Wind Tunnel

Figure 5.3 (graph)
- Y-axis: TEST MACH NUMBER (0 to 40)
- X-axis: MODEL VELOCITY RELATIVE TO EARTH, km/s (0 to 6)
- Curves labeled: M=3 AIR FLOW IN TUNNEL, M=2 AIR FLOW IN TUNNEL, NO AIR FLOW IN TUNNEL
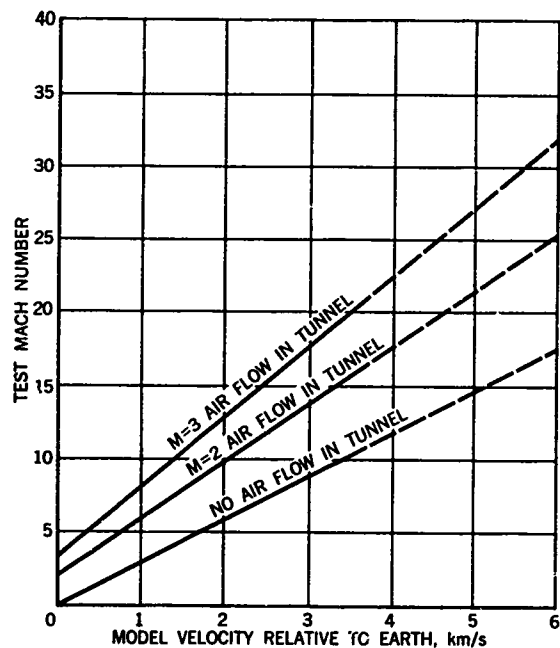
5.3 Test Mach-number capability of the
Ames Supersonic Free-Flight Wind Tunnel
for model velocities to 6 km/sec

Figure 5.4 (graph)
- Y-axis: REYNOLDS NUMBER PER CENTIMETER (10×10^6 scale)
- X-axis: TEST MACH NUMBER (0 to 40)
- Curves labeled: M=2 AIR FLOW RESERVOIR PRESSURE OF 6 ATMOSPHERES, NO AIR FLOW, M=3 AIR FLOW RESERVOIR PRESSURE OF 6 ATMOSPHERES

5.4 Reynolds-number capability of the
Ames Supersonic Free-Flight Wind Tunnel
for model velocities to 6 km/sec

Figure 5.5 (graph)
- Upper plot Y-axis: FREE-STREAM MACH NUMBER, M_∞ (2.8 to 3.1)
- Lower plot Y-axis: FREE-STREAM MACH NUMBER, M_∞ (1.8 to 2.1)
- X-axis: STATION NUMBER (1 to 9)
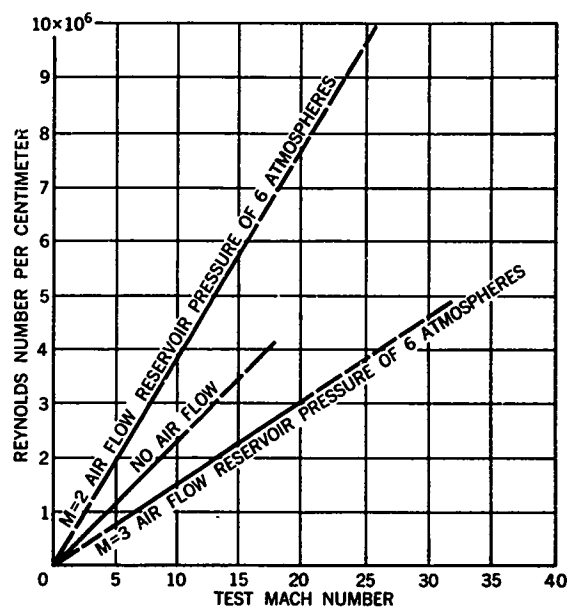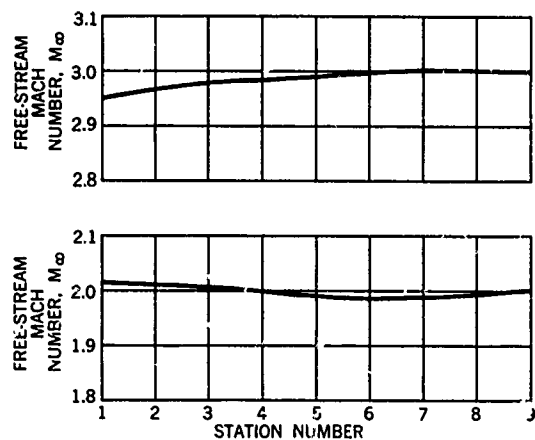
5.5 Variation of Mach number along the
tunnel-centerline axis for nominal
Mach numbers of 2 and 3

Figure 5.6 (graph)
- Upper plot left Y-axis: FREE-STREAM STATIC PRESSURE, P_∞ cmHg (M=2, 24 to 28); right Y-axis: FREE-STREAM STATIC PRESSURE, P_∞ cmHg (M=3, 11 to 15)
- Curves: FREE-STREAM MACH NUMBER, $M_\infty=2$; FREE-STREAM MACH NUMBER, $M_\infty=3$
- Lower plot Y-axis: FREE-STREAM DYNAMIC PRESSURE, q_∞ cmHg (67 to 77)
- Curves: FREE-STREAM MACH NUMBER, $M_\infty=2$ STAGNATION PRESSURE, $P_S=207$ cmHg; FREE-STREAM MACH NUMBER, $M_\infty=3$ STAGNATION PRESSURE, $P_S=399$ cmHg
- X-axis: STATION (1 to 9)
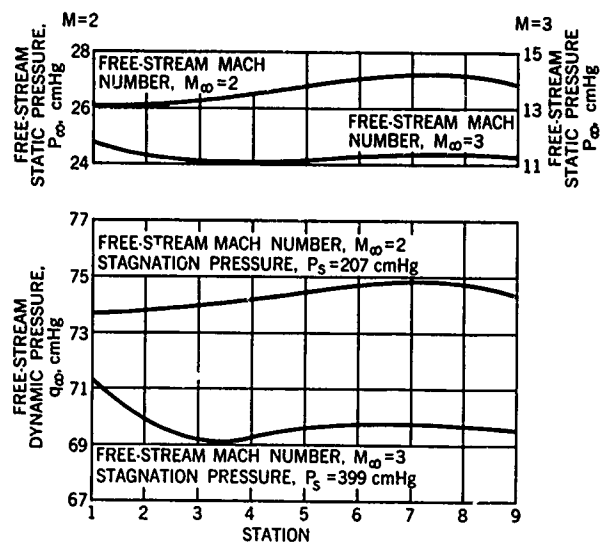
5.6 Variation of P_∞ and q_∞ along the
tunnel-centerline axis for nominal
Mach numbers of 2 and 3
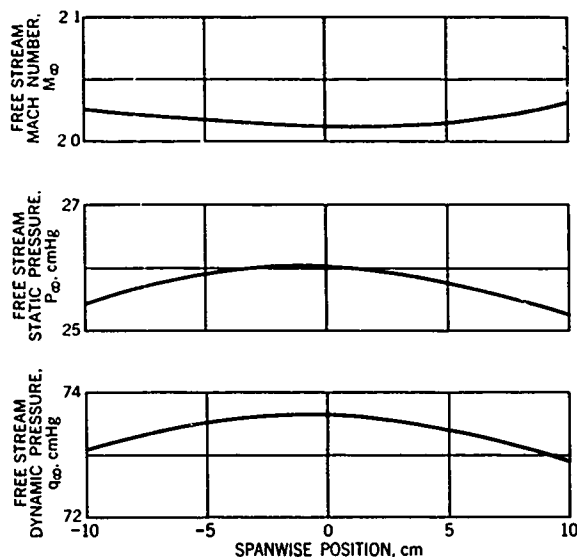
5.7 Variation of M_∞, p_∞ and q_∞ across the tunnel test section, at station 1 and on the centerline in the vertical direction, for nominal conditions of $M = 2$ and $p_{stag.} = 207$ cm Hg.
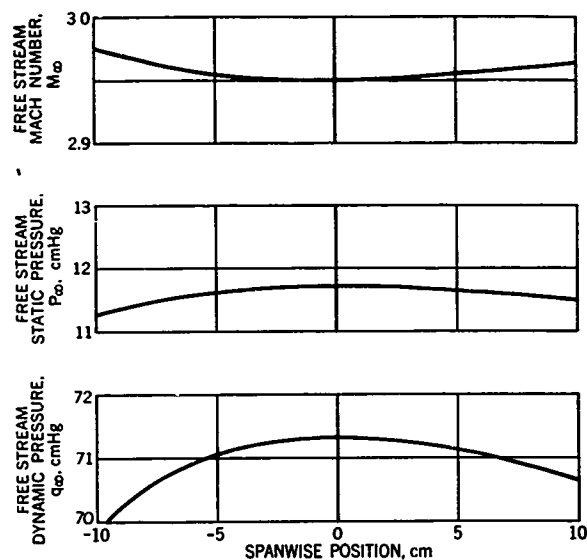
5.8 Variation of M_∞, p_∞ and q_∞ across the tunnel test section, at station 1, and on the centerline in the vertical direction, for nominal conditions of $M = 3$ and $p_{stag.} = 400$ cm Hg.
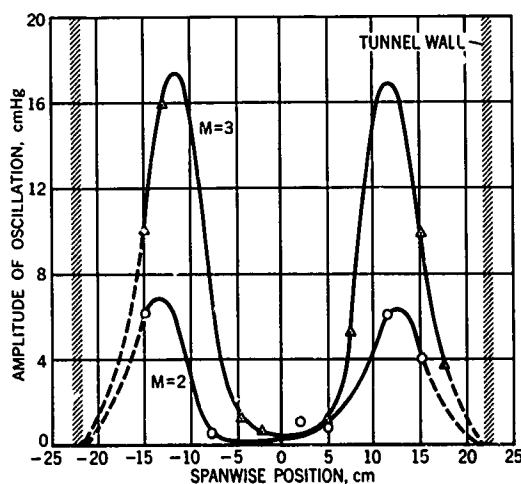
5.9 Amplitude of oscillation of the mercury manometer column used to measure the total-head pressure across centerline of tunnel at station 1, $M = 2$, $M = 3$
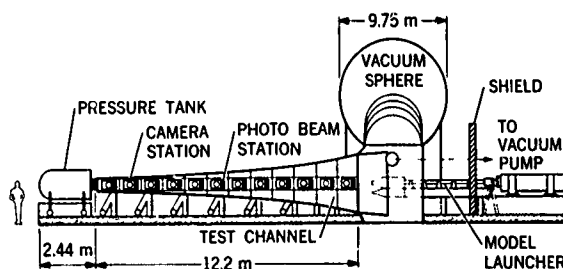
5.10 Schematic diagram of the Ames Atmosphere Entry Simulator

5.11   The Ames Atmosphere Entry Simulator

FREE STREAM MACH NUMBER = 7
RESERVOIR PRESSURE = 100 atm
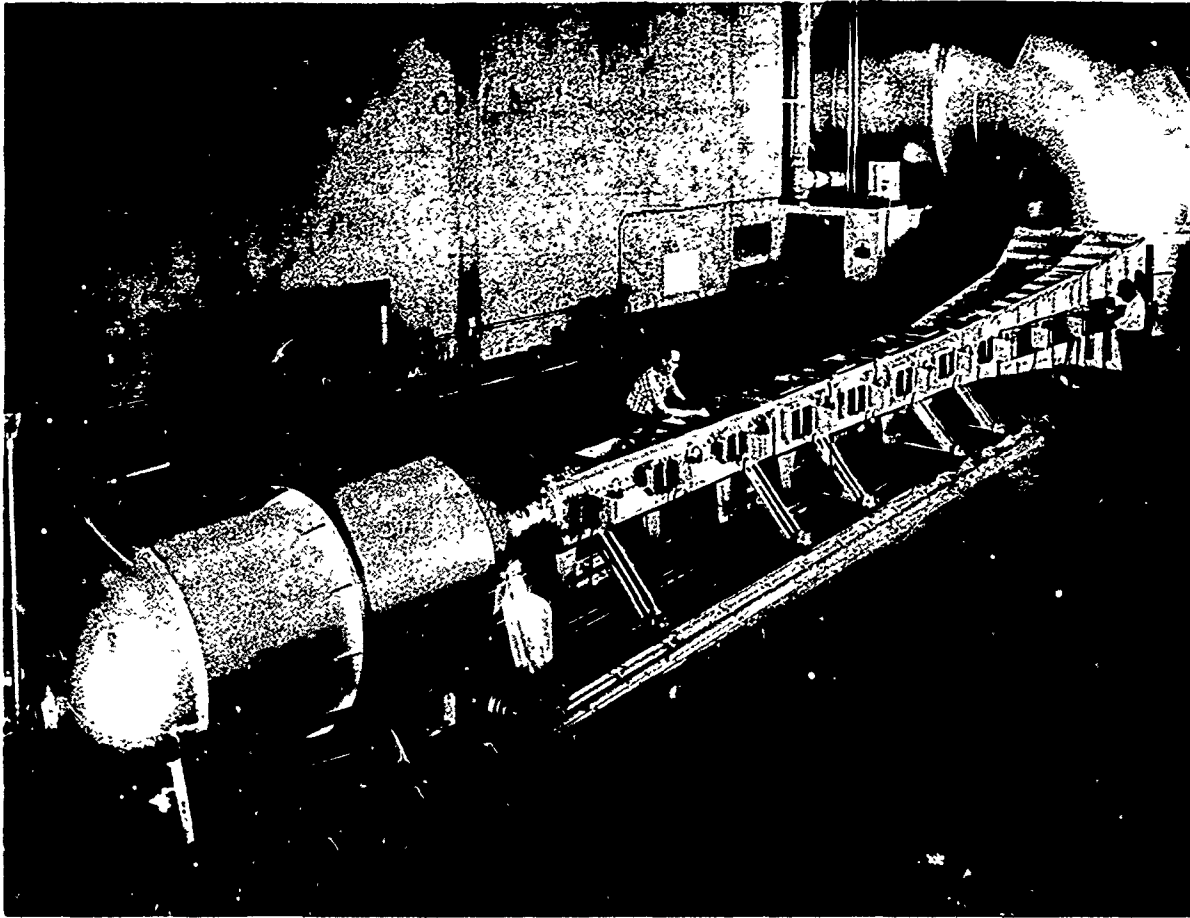
RESERVOIR TEMPERATURE, °K

AIR STREAM VELOCITY, km/s
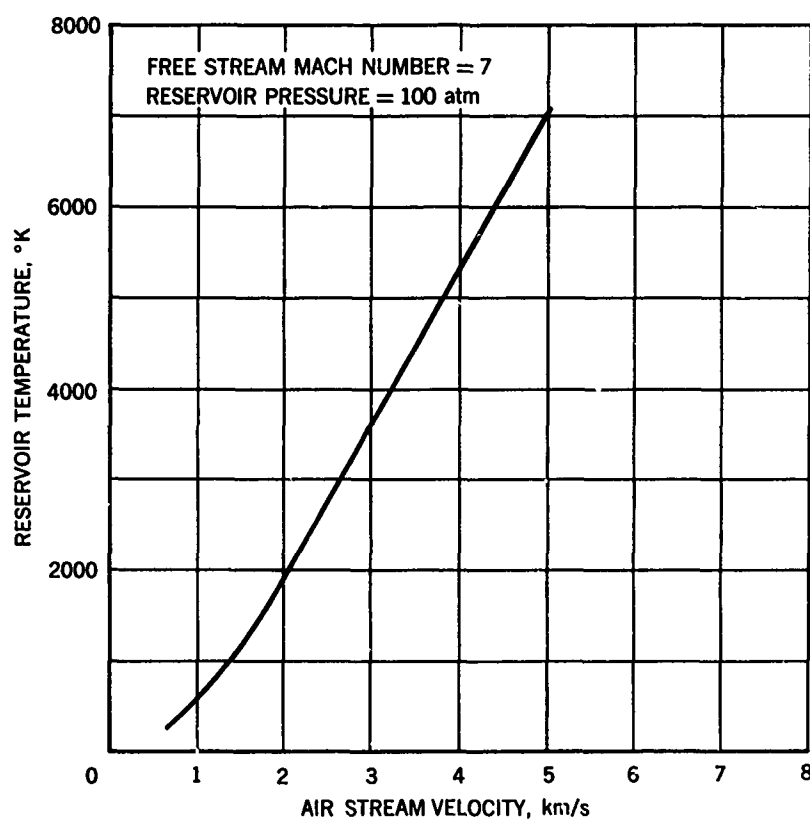
5.12   Air-stream velocity versus reservoir temperature
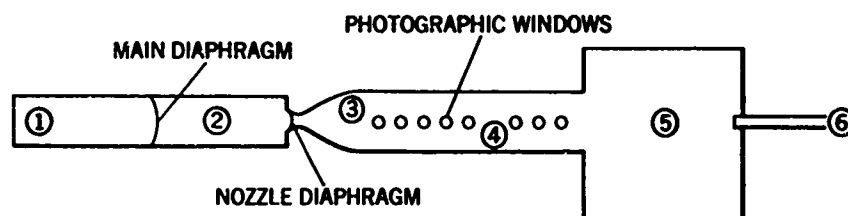
① DRIVER SECTION-HIGH PRESSURE GAS

② SHOCK-TUBE SECTION-LOW PRESSURE TEST GAS (AIR)

③ NOZZLE

④ TEST SECTION

⑤ RECEIVER TANK — SUFFICIENT VOLUME TO CONTAIN THE DRIVER AND TEST GAS AT SPECIFIED PRESSURE.

⑥ LAUNCH GUN

5.13   Shock-tube-driven counterflow ballistic facility

(a) TIME 0

(b) MAIN DIAPHRAGM REMOVED

(c) SHOCK WAVE REACHES END OF SHOCK TUBE, RETURNING SHOCK WAVE BRINGS GAS TO REST.

(d) TUNNEL FLOW BEGINS AFTER NOZZLE DIAPHRAGM BREAKS

(e) GAS CYCLE ENDS WHEN EXPANSION WAVE REACHES NOZZLE TO DROP RESERVOIR PRESSURE
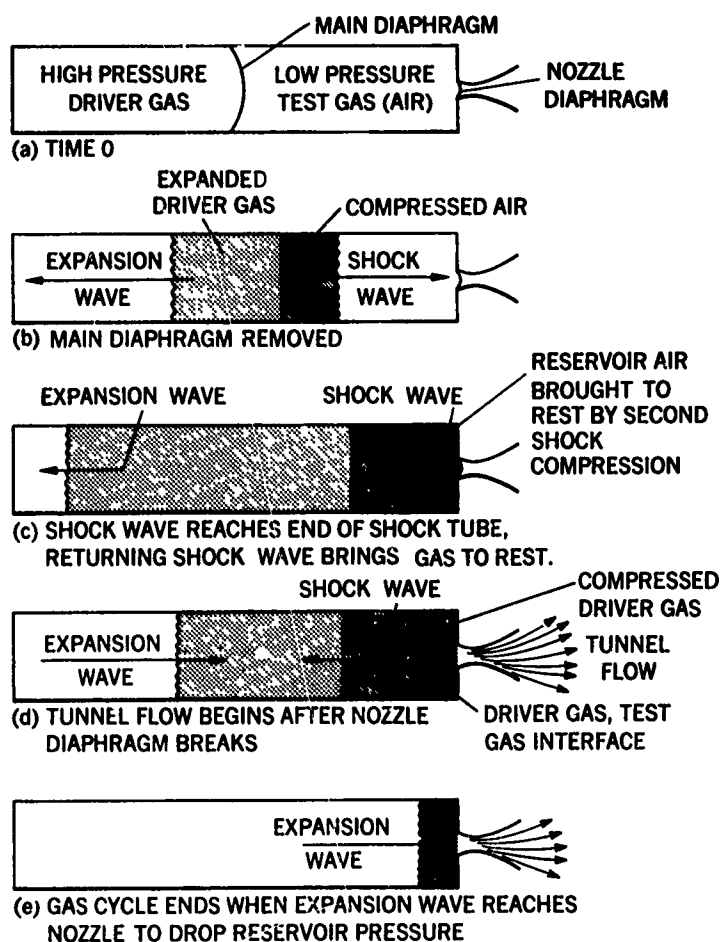
5.14   Shock-tube drive gas-compression cycle
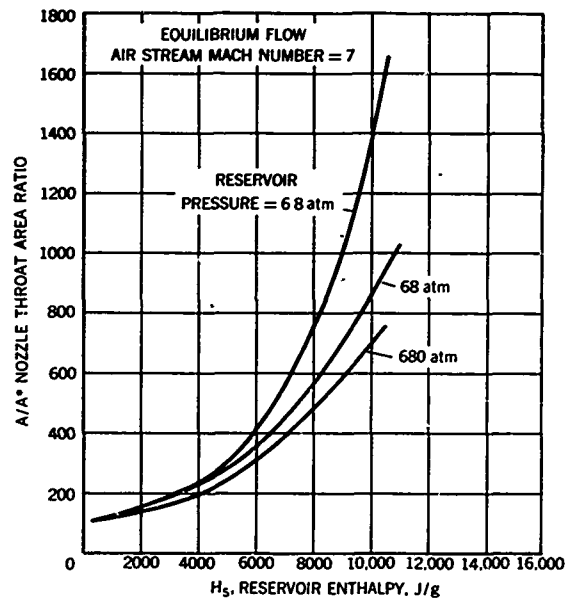
5.15   Nozzle-throat area-ratio variation with reservoir enthalpy
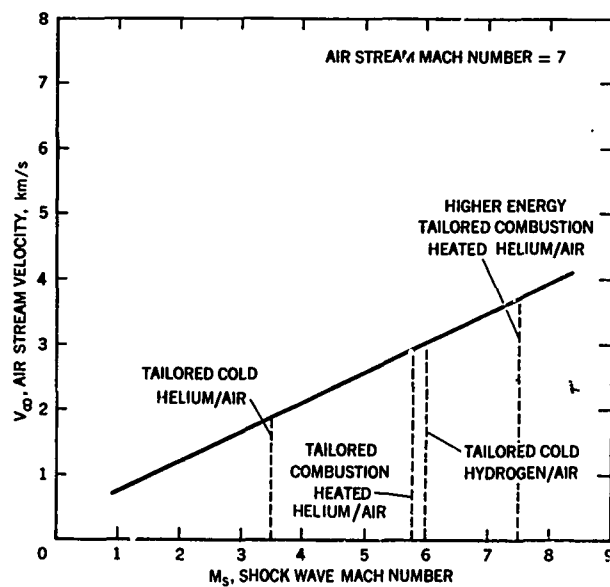
5.16   Air-stream velocity versus shock-wave Mach number
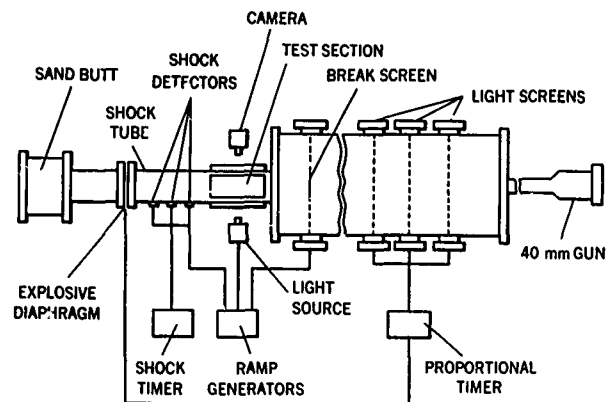
5.17   Ballistics range shock-interaction facility.   (Courtesy of David L.Merritt and Phillip M.Aronson, free
flight shock interaction studies, AIAA paper no.66-57, New York, January 24-26, 1966)

5.18   Ames Hypervelocity Free-Flight Aerodynamic Facility

(a) FREE STREAM DENSITY CAPABILITIES

(b) FREE STREAM PRESSURE CAPABILITIES
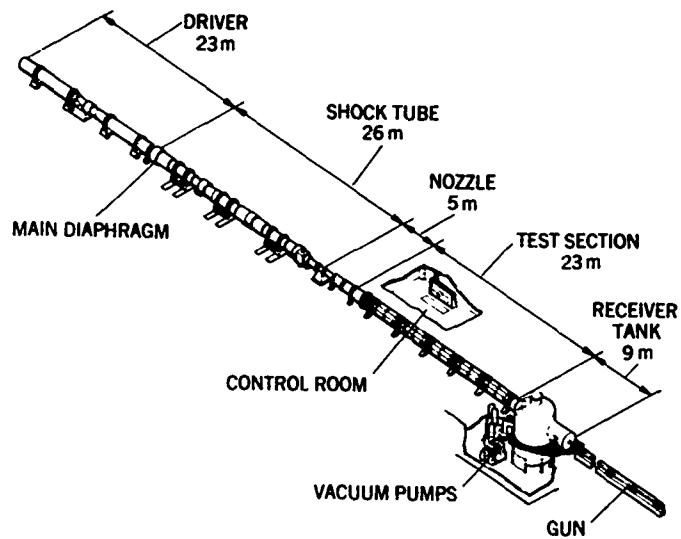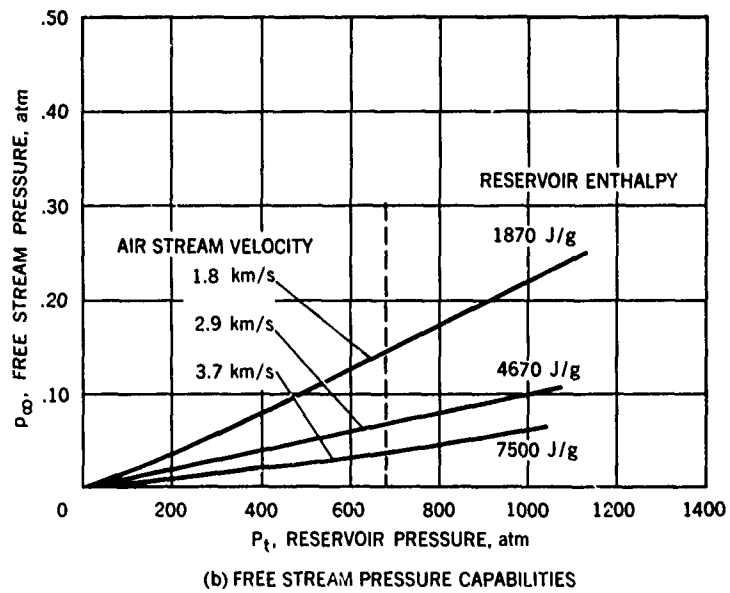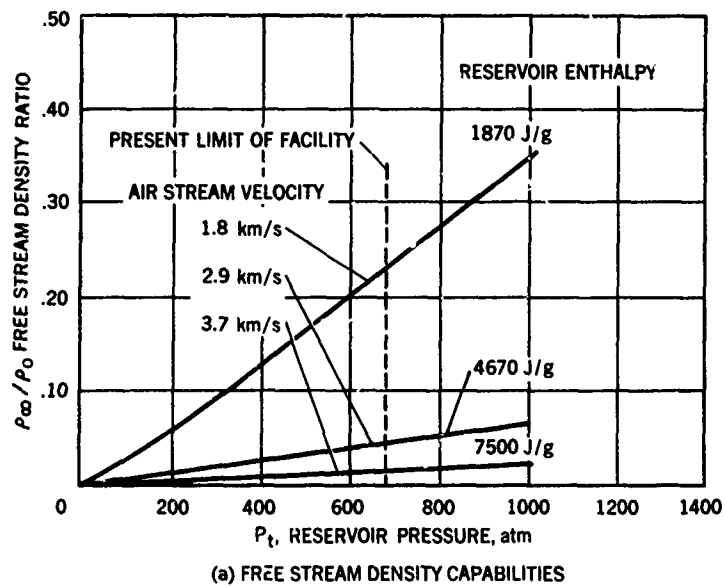
5 19   Test-section capabilities of Ames HFF Aerodynamic Facility
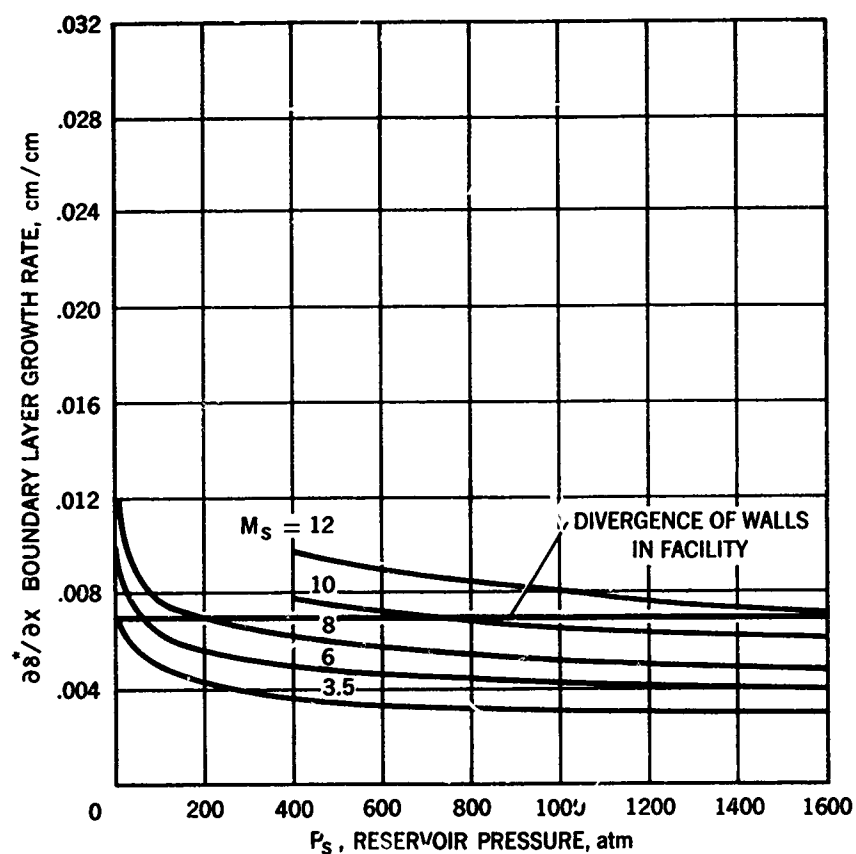
5.20   Boundary-layer growth rate calculated for Ames HFF Aerodynamic Facility
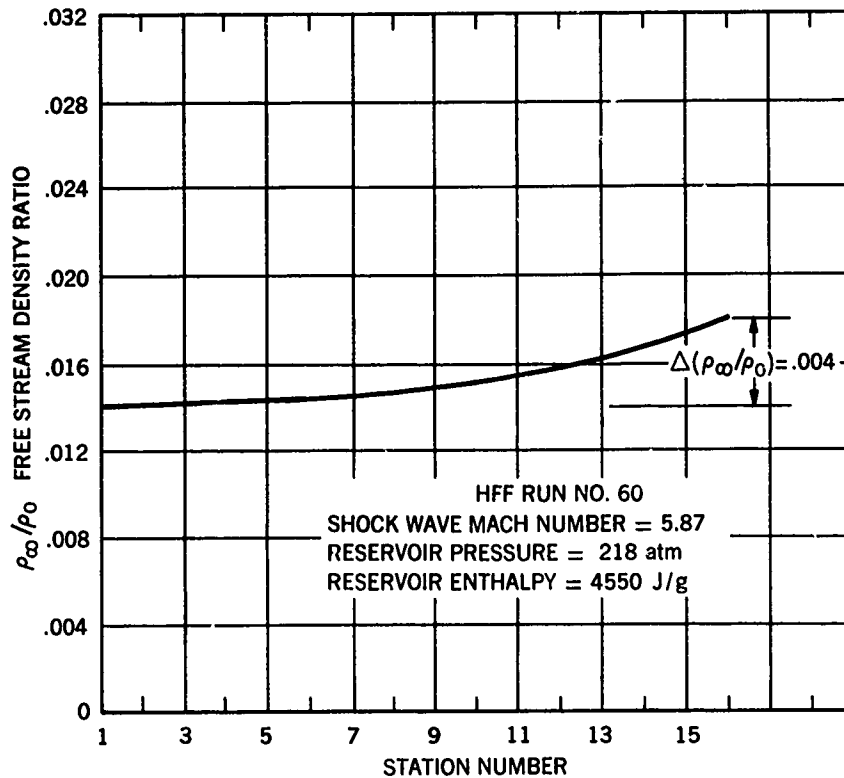
5.21   Density variation in Ames HFF Aerodynamic Facility
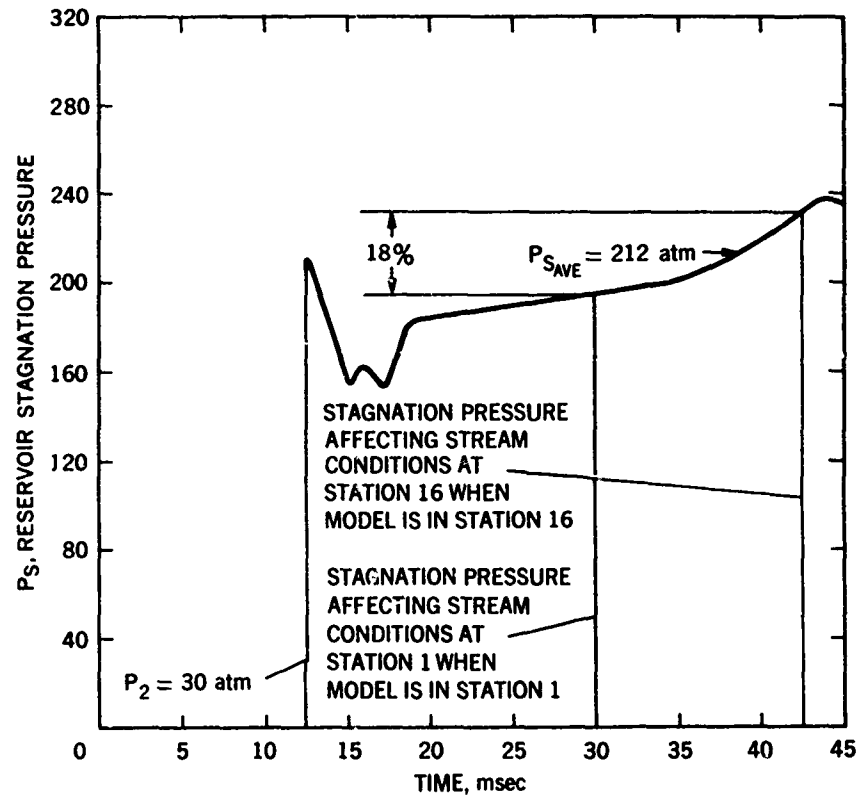
5.22   Stagnation-pressure time-history for HFF run 60
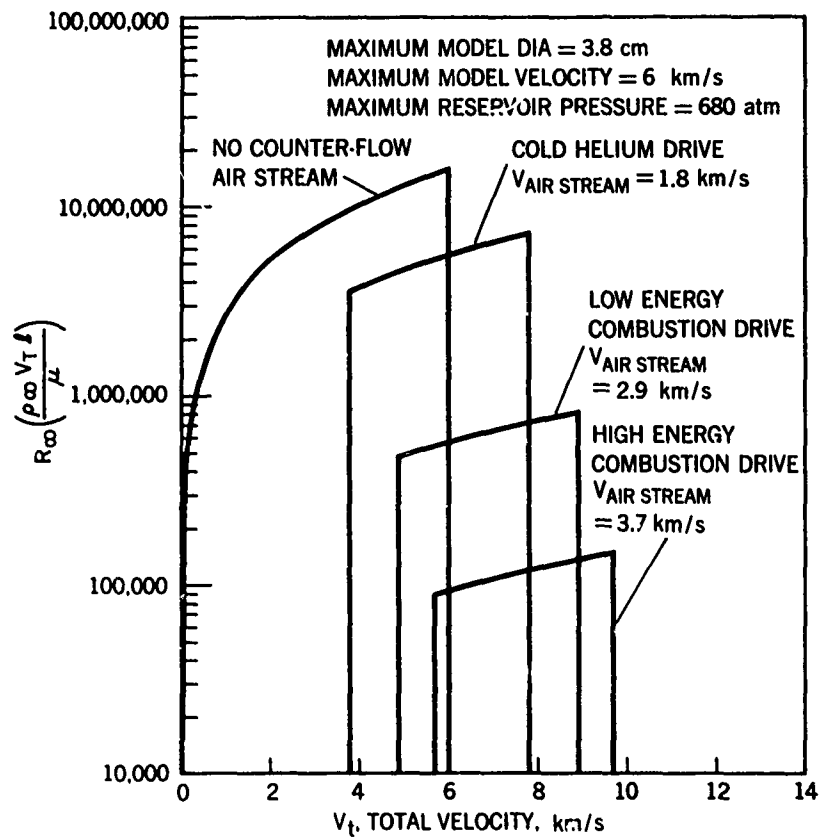
5.23   Test-range capabilities of Ames HFF Aerodynamic Facility
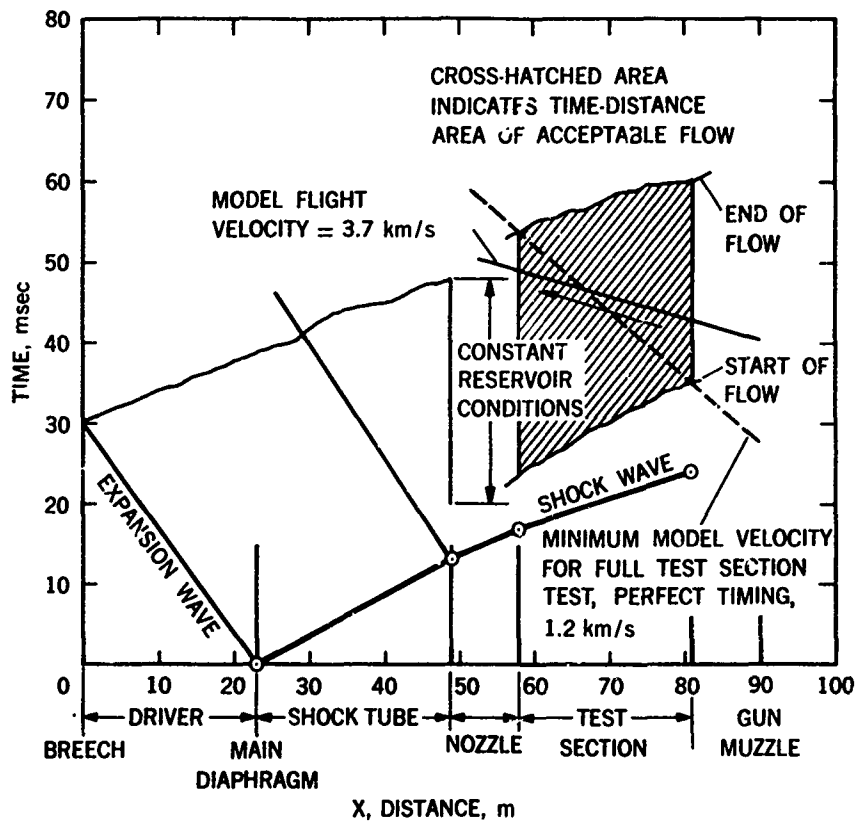
5.24   Timing relationship for Ames HFF Aerodynamic Facility
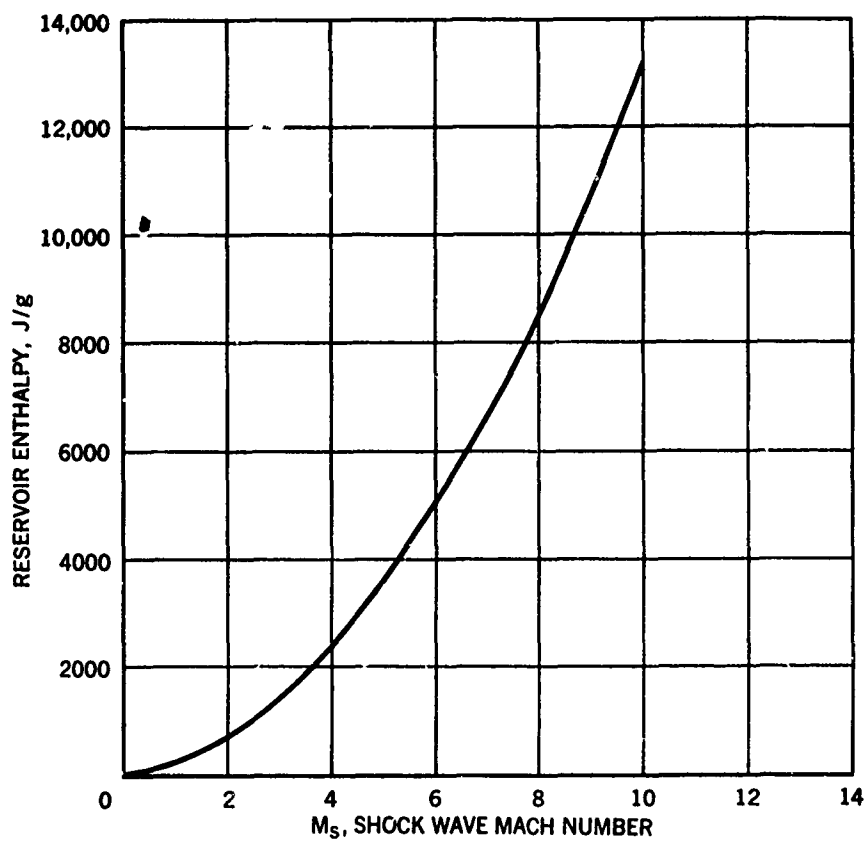
5.25   Reservoir stagnation enthalpy as a function of shock-wave Mach number

25.4 mm

HFF STANDARDIZED WALL
INSTRUMENT PLUG

57 mm

66 mm

PRESSURE
TRANSDUCER
ADAPTOR

TRANSDUCER
PACKING SCREW

3 mm DIAMETER
PRESSURE PORT
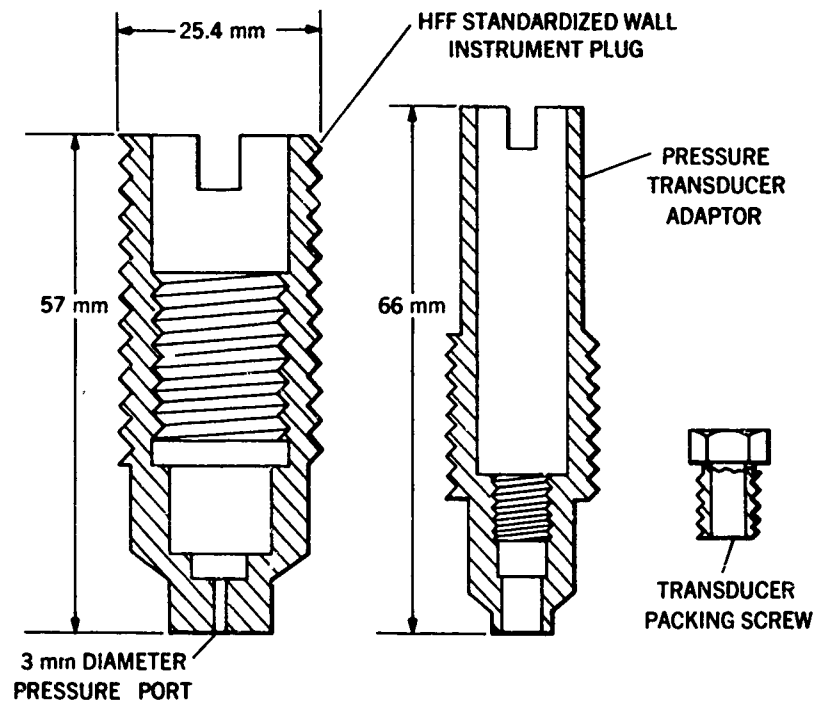
5.26   Shock-tube and driver-tube pressure-transducer holder

FIRST SPIKE OCCURS WHEN
DIAPHRAGM IS RUPTURED

SECOND SPIKE OCCURS WHEN
DIAPHRAM PEDALS REBOUND
AND STRIKE INSIDE OF DRIVER TUBE

PRESSURE

20 msec
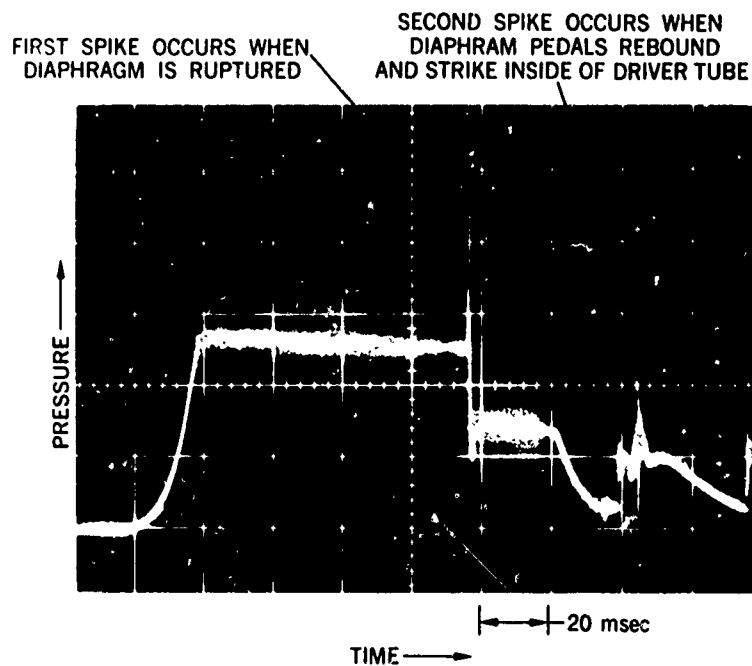
TIME

5.27   Driver-pressure time-history (combustion-heated helium)
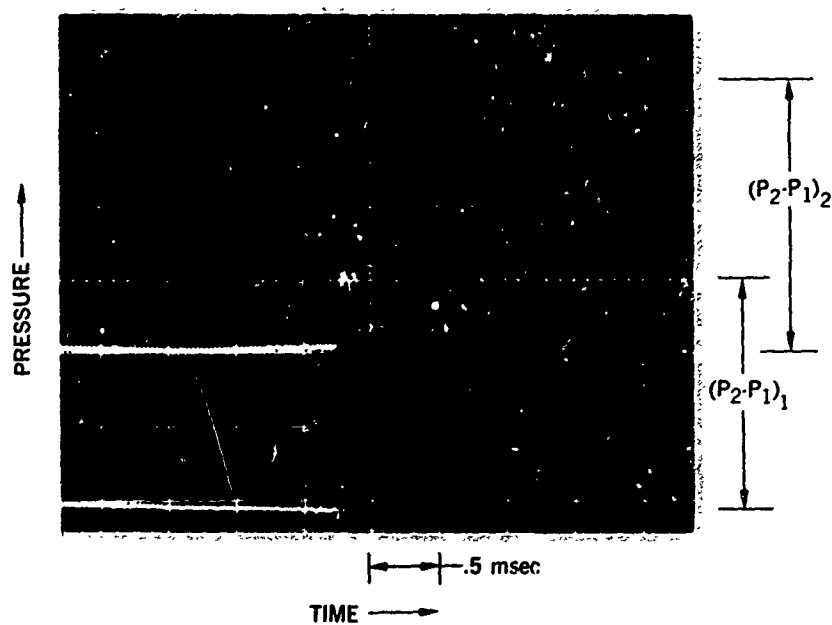
(a) EXPANDED RESERVOIR PRESSURE TIME HISTORY
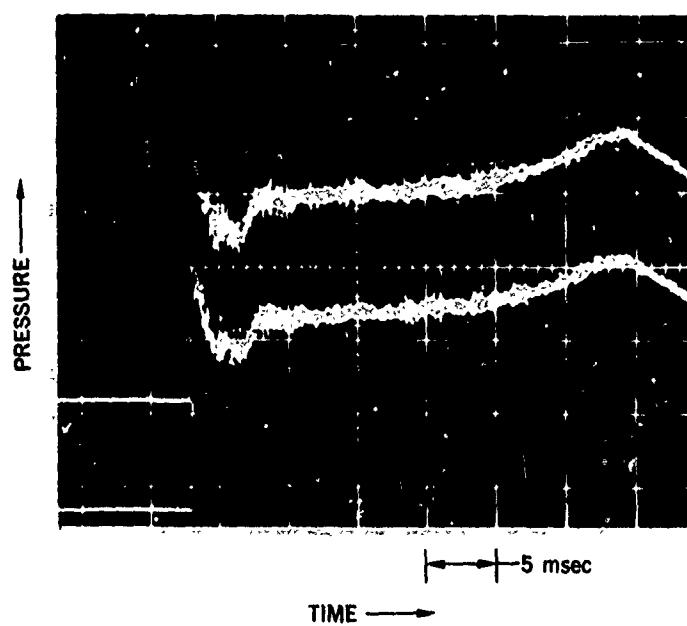
(b) REGULAR RESERVOIR PRESSURE TIME HISTORY

5.28 Reservoir-pressure time-history

INSTRUMENT PLUG, STAINLESS STEEL

1 cm

SPACER WASHER, BRASS

FRONT
ASSEMBLY
SCREW,
STAINLESS
STEEL

PRESSURE
DISC, RUBBER

FLUOROCARBON INSULATOR AND PRESSURE SEAL

SHOCK DETECTOR HOLDER,
STAINLESS STEEL

NEGATIVE
ELECTRODE, BRASS

PROTECTIVE
DISC, BRASS

FLUOROCARBON INSULATOR CUP

POSITIVE ELECTRODE, BRASS

PIEZOELECTRIC CRYSTAL GLUED TO
ELECTRODE WITH CONDUCTING EPOXY
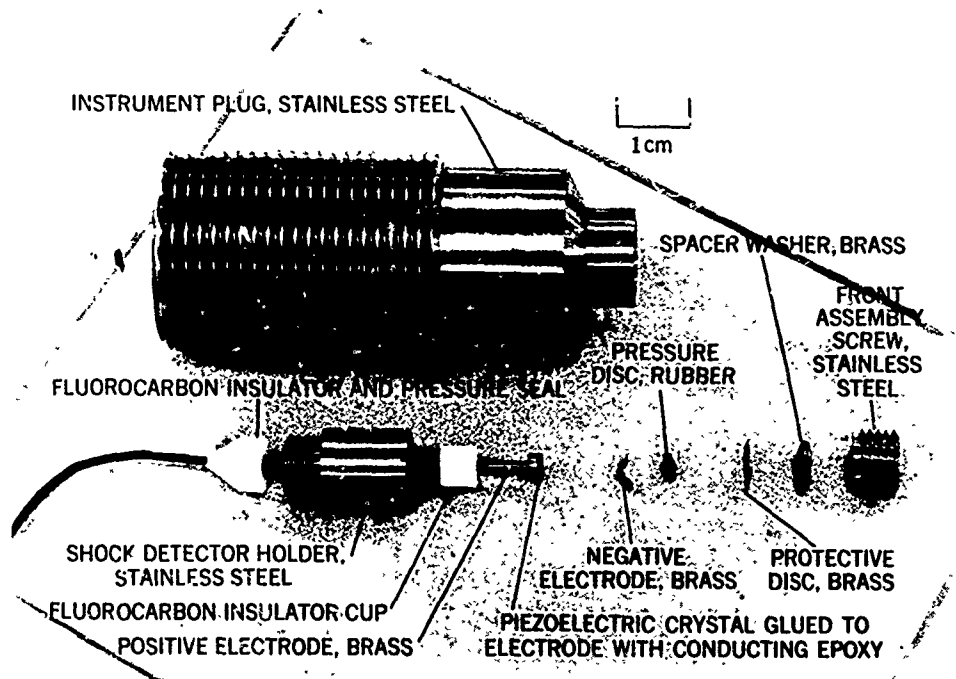
5.29   Photograph of piezoelectric-shock-detector components and holder

TEST SECTION WALL ADAPTER

0   5
cm

SILICONE RUBBER PADS FOR
SHOCK INSULATION

TRANSDUCER ASSEMBLY
CYLINDER

PRESSURE TRANSDUCER HELD
IN WITH THREADED PLUG

O-RINGS FOR SHOCK MOUNTING, NOT FOR SEALING

STATIC PRESSURE CELL HOLDER

VACUUM CAP WITH SEALED ELECTRICAL PLUG
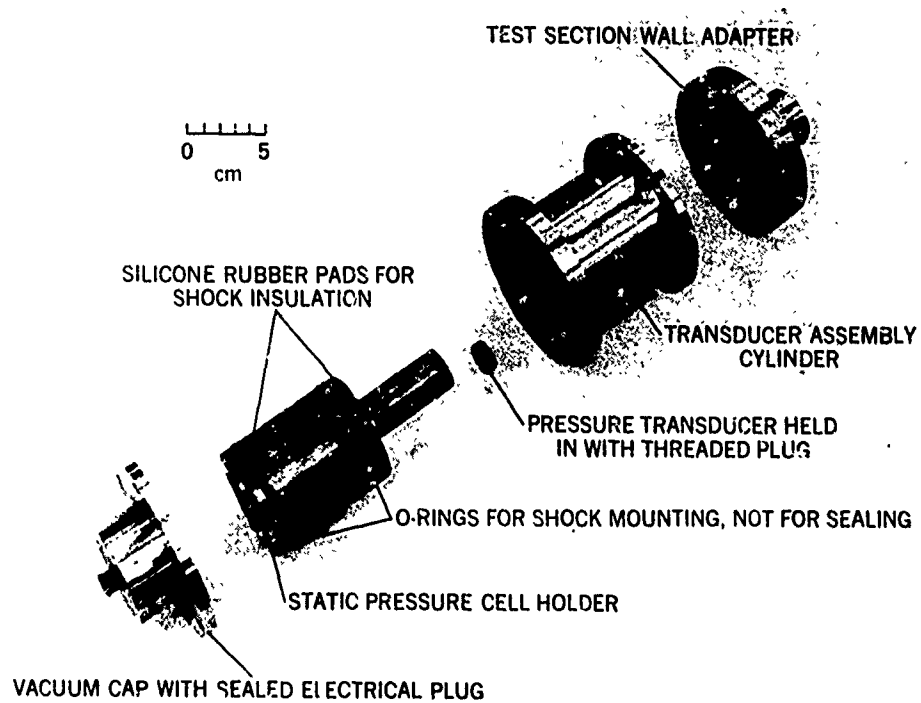
5.30   Photograph of static-pressure-transducer holder

SHOCK WAVES INDICATE MODEL PASSAGE
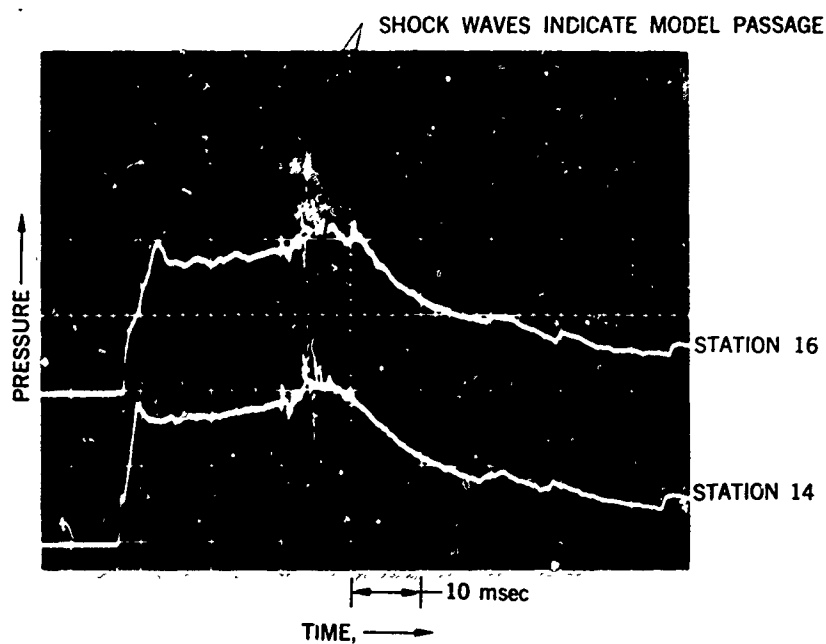
5.31   Air-stream static-pressure records
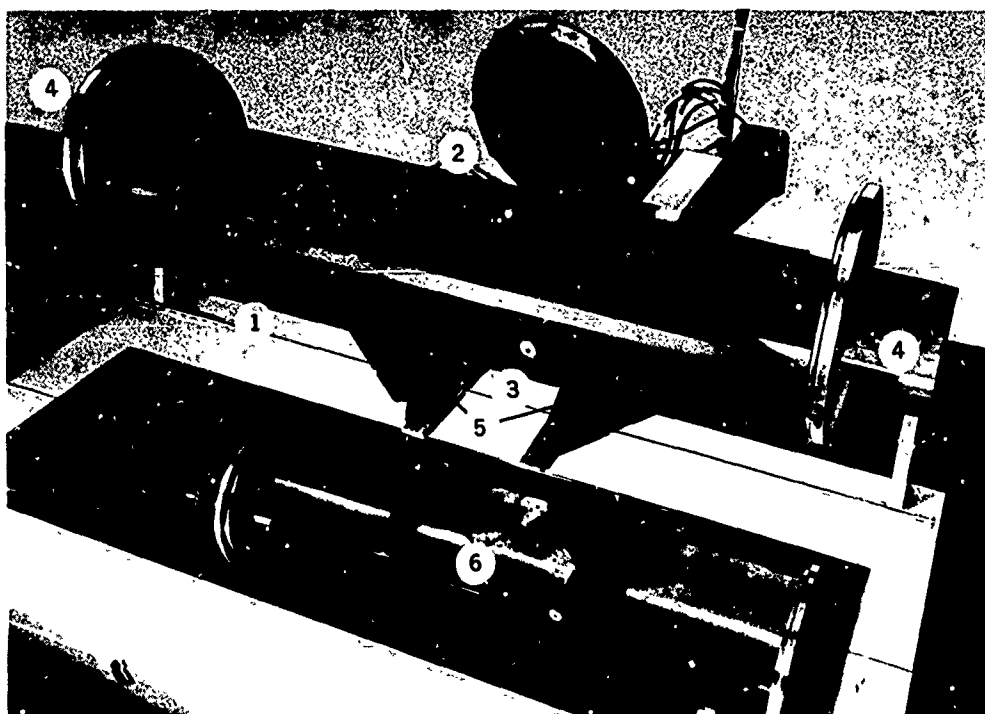
1. REPLACEABLE LEADING EDGE

2. 5 STATIC PRESSURE CELLS ON 7.6 cm SPACING

3. ONE OF TWO PITOT PRESSURE CELL HOLDERS

4. WINDOW PLATES WITH SLIDING VACUUM SEALS
   FOR END SUPPORT

5. CENTER SUPPORTS FOR RIGIDITY

6. PROVISION FOR OTHER PITOT PRESSURE CELL
   HOLDER AND ALTERNATE STING

5.32   Photograph of air-stream-calibration flat plate
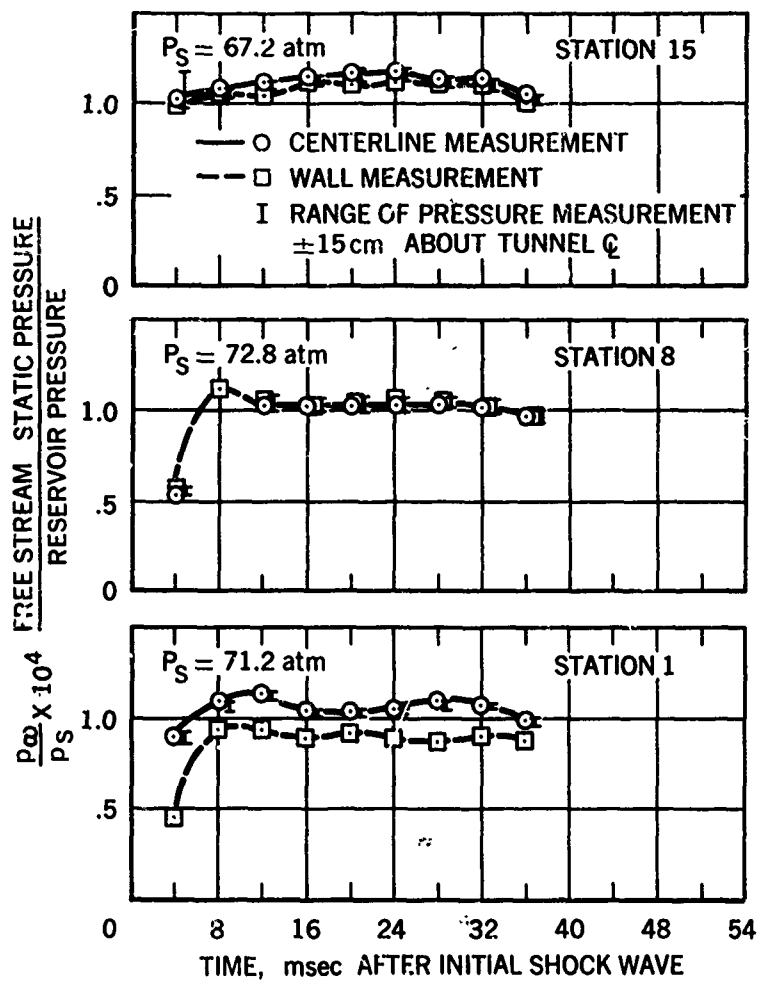
5.33   Air-stream-calibration records for three stations
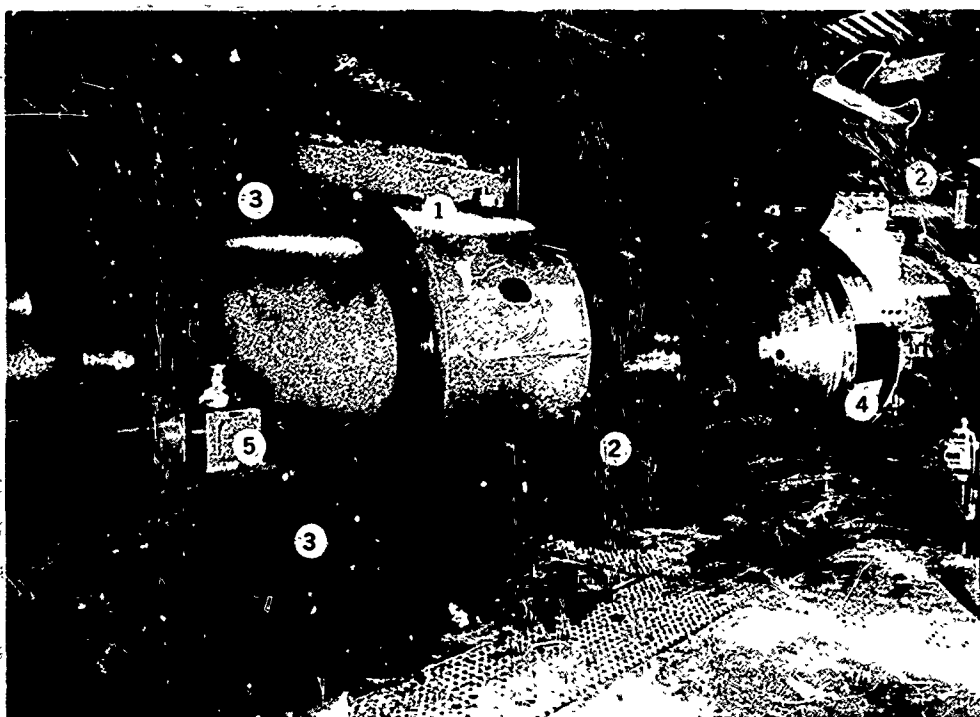
1 SHOCK TUBE, DRIVER-TUBE COUPLING NUT
2 HYDRAULIC RAMS FOR ROTATING COUPLING NUT
3 HYDRAULIC RAMS FOR TRANSLATING COUPLING NUT
4 INTERRUPTED THREADS ON DRIVER TUBE
5 CAPSTAN DRIVE UNIT FOR PULLING CLEANING PATCHES THROUGH TUBES

5.34   Photograph of Ames HFF Aerodynamic Facility, main diaphragm section
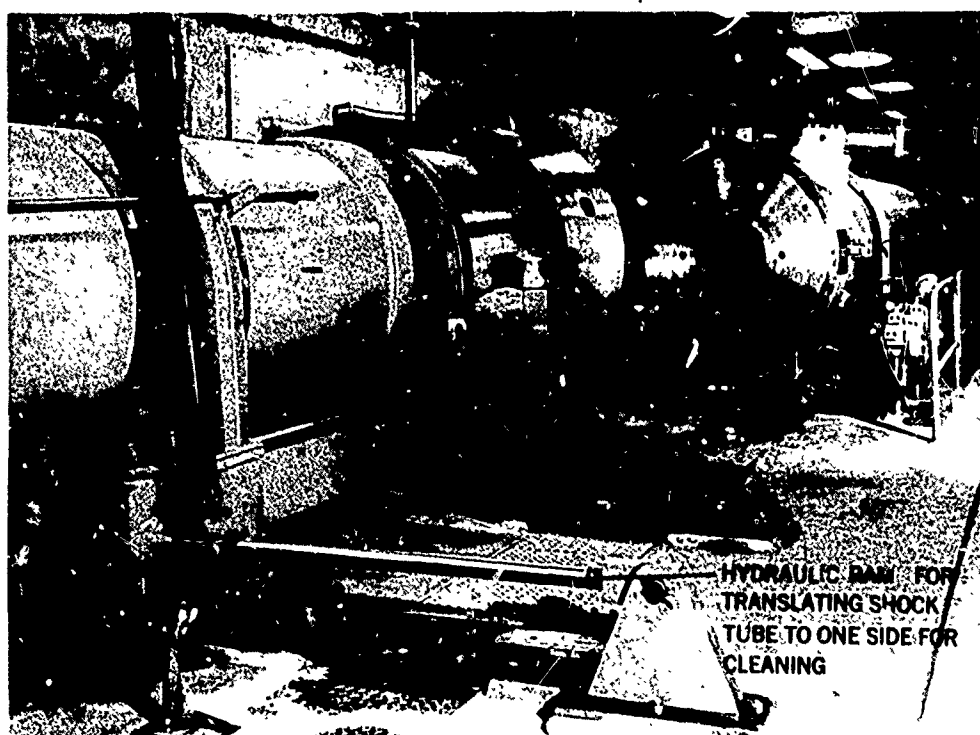
5.35   Photograph of Ames HFF Aerodynamic Facility, shock-tube-transfer hydraulic system.

CHAPTER 6

SYSTEMS FOR MEASUREMENT OF
MODEL POSITION, ATTITUDE, AND VELOCITY

by

C. S. James, R. J. Carros, A. G. Boissevain,
R. I. Sammonds, and M. E. Wilkins

NASA-Ames Research Center

Preceding page blank

SYSTEMS FOR MEASUREMENT OF
MODEL POSITION, ATTITUDE, AND VELOCITY

C. S. James, R. J. Carros, A. G. Boissevain
R. I. Sammonds, and M. E. Wilkins

6.1 INTRODUCTION

The data-gathering process for a great many aeroballistic-range tests consists of recording the position, attitude, and time of arrival of a model at several accurately surveyed points along its flightpath. One of the earliest and simplest approaches to this task utilized the yaw card – a sheet of paper through which the model flies. In the environments of most tests of current interest this approach is inapplicable, although it still finds limited use. Most current data-gathering systems for documenting projectile motion in ballistic ranges are fundamentally photographic in concept. This is a rather obvious choice because it is a convenient form of measurement capable of fast response and high precision, it does not disturb the phenomena being observed, and it can provide visualization of the projectile and its surrounding flow field. In general, such data-gathering systems are laid out in the form of measuring stations set at intervals along the flightpath. The measurements are repetitive and it suffices therefore to discuss the geometric arrangement and operation of the components of a single measuring "station".

The components which typically make up a photographic measuring station are the following:

(a) A point source of high-intensity, short-duration light. This is most often in the visible spectrum, but is sometimes an X-ray source;

(b) A system of optics (i.e., mirrors, lenses, prisms, etc.) for collimating and directing the light across the flightpath and onto a photographic film or projection screen;

(c) A photographic film, or camera, for recording the transient image of the model and flow field;

(d) An optical shutter for limiting the duration of light incident on the photographic film;

(e) A trigger subsystem which is capable of sensing the arrival of the model and initiating the action of the light source and shutter;

(f) Fiducial markers which are photographed simultaneously with the model, and which form a part of the range spatial reference system.

In addition to these components, there is a chronograph system which receives signals from enough stations, at the times of passage of the model, to provide the necessary time increments for the calculation of velocity and deceleration. Many geometric arrangements are possible, and there are alternative choices of components as well. The selection of a particular system, therefore, is dictated by factors such as the types of studies to be emphasized, the velocity range to be covered, the model scale, and cost. Counterflow capability also strongly constrains total range length and the placement of station components. In turn, the constraint on total range length usually results in more severe requirements on precision in the measurement of time increments and model position. (cf. Section 7.11)

In the sections which follow, after a brief description of the use of the yaw card, representative optical arrangements and components of the photographic measuring station are discussed in relation to the environments in which they must function. The final section considers the requirements for extracting the desired numerical data from the exposed photographic film.

6.2 THE YAW CARD – C. S. James

The most economical and least sophisticated of all measuring stations is the yaw card. As the name implies, it consists simply of a sheet of paper hung in a plane normal to the flightpath with its center on the launcher bore sight. As the model flies through the paper, it punches out a hole which registers the frontal silhouette of the model at that instant. Figure 6.1 is a typical puncture from a finned projectile. From the shape and dimensions of the hole and the known geometry of the model the angles of yaw and roll may be inferred. Model position is obtained from the relationship of the hole to the bore line or some other suitable reference. The time of model passage may be determined most simply, perhaps, through the use of an electrically conducting grid painted directly on the yaw card. This grid then becomes a break switch when the model penetrates the paper. The most satisfactory paper for yaw card use is a short-fibered, relatively low-strength and lightweight paper which will punch out easily and cleanly without tearing, and which will minimize the disturbance to the model. The "construction" paper, used by children in school projects, works well.

One or two yaw cards, strategically placed, can be surprisingly useful in diagnosing model and sabot-launching problems, as indicated in Section 3.8, or can indicate whether or not sabot pieces have flown downrange. The yaw card's usefulness in the vicinity of the gun is limited by its vulnerability to muzzle blast, although shredded yaw cards frequently can be reassembled to yield valuable data. In this regard, distinctively patterned and colored cards make the sorting job easier. By the use of multiple cards mutually related through spacial-reference and chronograph systems, all necessary measurements may be obtained for the determination of aerodynamic forces and moments. This technique has been used at the U.S. Naval Ordnance Laboratory (NOL)[6.1] and is used in the Aero-ballistic Range at the Canadian Armament Research and Development Establishment (CARDE)[6.2], which is a large enclosed range having available 80 such stations with capacity for 2.7-m by 3.7-m yaw cards. Figure 6.2 shows a typical station.

The precision of measurement to be expected from a yaw card system depends rather strongly on the configuration flown. In particular, accurate yaw angles are easily obtained with slender shapes, but difficult with bluff shapes. Roll angles are easily measured with finned configurations; while auxiliary means, such as a colored index which leaves a wipe mark on the yaw card may be required for a body of revolution. The potential accuracy anticipated for ideal conditions in the CARDE facility is stated as 0.1 degree for attitude angles, 0.25 degree for roll angle, and 1.6 mm for position. Limitations on the use of yaw cards are the possibility of damage to delicate models from impact with the yaw card, and the effect of the impact on model motion.

6.3 OPTICAL ARRANGEMENTS OF THE PHOTOGRAPHIC MEASURING STATION - C.S. James

Several types of optical system are used in ballistic-range testing – often for specialized purposes other than observing projectile motion (e.g., flow visualization). These which employ light transmitted through the flow field, and which therefore view the model in silhouette, include the shadowgraph, the schlieren, and the interferometer[6.3, 6.4]. Systems which view the model by reflected light or by the luminosity of the event itself include various forms of high-speed framing and streak cameras[6.5, 6.6, 6.7]. A hybrid technique, which in a sense employs both transmitted and reflected light, is that of holography[6.8, 6.9]. Holography is basically a form of interferometry and is a relatively new technique. While it has not yet been exploited to any extent in ballistic ranges, it appears to hold much promise for the future in that it is potentially capable of recording on film a stereoscopic representation of a model and flow field which can be reconstructed after the event and viewed from different vantage points.

Where the emphasis is on position and attitude measurement at multiple stations, the shadowgraph system is invariably chosen over other systems for reasons of dependability, accuracy, and simplicity. While the shadowgraph is not as sensitive to density modulations in the projectile flow field as the schlieren, nor as quantitative in this respect as either the schlieren or the interferometer, stable optical alignment is easily obtained. The shadowgraph can provide high local contrast both in the model silhouette, which is desirable for angle- and position-reading accuracy, and in the features of the flow field, which is helpful in resolving much of the fine structure present. Among the major ballistic ranges of the world, therefore, differences in their primary optical systems are invariably those of configuration, chosen in each case to meet particular requirements, rather than of optical principle.

6.3.1 Shadowgraph Configurations

The simplest form of shadowgraph consists of a point source of light and a photographic film situated on opposite sides of the flightpath. Since, in general, the model axis will not be parallel to the film plane, it is desirable to provide two orthogonal systems in order to record two projections of the model. Such a configuration is illustrated in Figure 6.3. The entire arrangement may be built inside a pressure vessel so that no optics are needed except for a small quartz window in the cannister which contains and isolates each spark-light source from the pressure and humidity variations in the range tank. Aside from its simplicity, the principal advantage of this so-called direct-shadow configuration lies in its ability to resolve much of the detail present in both the inviscid and viscous flow field surrounding the model. The light field is uniformly conical and of uniformly varying intensity since there are no optics to degrade it. A typical shadowgram is shown in Figure 6.4.

The flightpath corridor, shown by cross-hatching in Figure 6.3 can be made reasonably large in relation to the tank dimensions, for this configuration. It is limited principally by film size and the illumination angle obtainable with the light source. The large flight corridor can be an advantage particularly at downrange stations where it is needed to accommodate dispersion in model flightpaths. The magnification depends on the ratio of distances of the film and of the model from the light source, while the sensitivity in recording density changes in the flow field depends on distance of the film from the model. By varying the distance of the film plane from the flightpath, then, some control of both effective sensitivity and magnification can be exercised. A modification of this direct shadowgraph, which substitutes a plane mirror for one of the light sources, is employed in the Aerodynamics Range[6.10, 6.11] of the Ballistic Research Laboratories (BRL), and in the 285-foot Pressurized Ballistic Range[6.12] of the Naval Ordnance Laboratory (NOL). Figure 6.5 is a schematic of the NOL configuration. Where internal space is limited, which is the case with the 0.9 meter-diameter NOL facility, this arrangement can sometimes be an advantage in simplifying the placement of components, or in minimizing the need for windows. The economics of substituting a mirror for a light source could also be advantageous. On the other hand, the resolution of the flow field by the vertical light beam will be somewhat degraded by the mirror. Figure 6.6 shows the two orthogonal views of a model in the NOL range. An advantage of this arrangement is that both pictures are made at the same instant. With two light sources, small differences in their timing are possible, which translate into uncertainties of model position and velocity unless chronographs are used for each.

For aerodynamic testing at subsonic and supersonic speeds up to a Mach number of 10 or 12, the direct shadowgraph is quite satisfactory. Somewhere in the Mach number 10 to 12 range, depending on the bluffness of the model, its material, and on free-stream density, the model shock layer and wake begin to radiate with sufficient intensity to cause fogging of the photographic film. At the same time, the increased model velocity causes the model to move enough during the 0.2-to 0.6-μsec effective duration of the typical spark-light source to produce undesirable blur of the photographic image.

The remedies for these problems are to selectively attenuate the light from the model shock layer, allowing only that from the shadowgraph source to reach the film, and to shorten the effective duration of the exposure to minimize the motion blur. Various methods have been devised to accomplish these improvements.

Wavelength filtering in the visible and ultraviolet spectrum is a means of selective attenuation. To be effective, the output of the light source should be strong in a portion of the spectrum where the radiative output from the projectile is weak, and where the sensitivity of the photographic film is high; and the filter must have a reasonably narrow transmission band. These are difficult requirements to meet with an unfocused system where the entire photographic film must be covered by the filter. Some success in exploiting this technique with focused systems (cf. Section 6.4.2) has been reported, however[6.13, 6.14].

If the shadowgraph system uses an X-ray source, filtering becomes a simple matter, but flow visualization is lost. Pulsed-X-ray sources of sufficiently short duration (less than 10^{-7} sec) are available[6.15] which can cope quite well with the motion blur problem in, say, the 5 to 10 km/sec velocity range. The CARDE Range 5 utilizes a direct X-ray shadowgraph system which is nonorthogonal[6.16]. A sketch of the configuration is shown in Figure 6.7(a). With this arrangement, both views of the model appear on one sheet of film, which is doubly exposed. Figure 6.7(b) is a representative station photograph. X-ray systems can be used in undarkened ranges ard near the gun for launch and sabot-separation diagnostics.

Another method of achieving selective attenuation is to image the shadowgraph light source at an aperture placed in front of the film, as illustrated in Figure 6.8. The light from the model, originating at a shorter object distance, will not be in focus at the aperture; hence, it will be largely blocked from striking the film. A shutter in conjunction with the aperture will further block long-duration light from the model wake or from muzzle or impact flash, and can be used to reduce motion blur. The additional components add to the cost, and to the complexity of alignment, operation, and maintenance. Furthermore, the addition of an electro-optical shutter (transmissivity typically less than 0.4; cf. Section 6.5.2) usually requires the substitution of a much brighter light source to produce acceptable pictures.

If the aperture alone is sufficient to attenuate the unwanted light, the motion-blurring may be reduced by shortening the duration of the light pulse. Pulsed light sources of 10^{-8} sec or less duration are currently available (cf. Section 6.4). This approach has been taken with considerable success at the Lincoln Laboratory Re-Entry Simulating Range[6.17]. Figure 6.9 is a shadowgraph taken in that facility, which uses essentially the configuration of Figure 6.8 in conjunction with a magnifying camera to obtain greatly magnified shadowgrams. The 20-nsec exposure reduces motion blurring to the extent that spalled surface fragments from the sphere moving at 5.9 km/sec are clearly discriminated.

The optical arrangement of Figure 6.8 is called a focused shadowgraph. In addition to its usefulness as a means of selective attenuation, another valuable use, for which it was originally exploited, is the control of the effective shadowgraph sensitivity of the system. The position of the object plane imaged on the film may be adjusted by moving the film toward or away from the focusing lens. If the object plane is made to coincide with the model flight path, the shadowgraph sensitivity is minimum (ideally zero). Departure of the object plane from the flightpath increases the sensitivity. This device is frequently of value in reducing the optical distortion of the flow field in regions of strong density gradient, as, for example, the nose region of a bluff body in supersonic flight (see Chapter 8 for a further discussion).

The focused shadowgraph of Figure 6.8 has been illustrated with lens optics. Lenses permit close coupling and axial alignment of components, and are adaptable to direct magnification of the shadow image. Mirrors, on the other hand, are more economical for a large field of view, and avoid possible problems of striae or chromatic aberration. Figure 6.10 is the mirror-optic counterpart of Figure 6.8. The necessary departure from an axisymmetric lightpath introduces additional aberrations, in the usual installation, which can be troublesome if accurate measurements of projectile position are required. (See Reference 6.3 for a discussion). Illustrated in Figure 6.10 is a means of avoiding aberrations due to nonsymmetry of the optical path, which can be economically feasible for a modest field of view. If the light source and its image lie respectively on the parallel axes of the large parabolic collimating and focusing mirrors shown by the dashed lines, each mirror will operate as an axisymmetric component with a vignetted field. For the same focal length, a mirror diameter slightly more than twice that of the smaller full-field mirror (f/number slightly less than half) is required. But since only a small portion of the surface is used, a mirror of this diameter can be cut into sectors, as shown in the insert of Figure 6.10, to provide four (or more) components, thus offsetting in part the higher cost of the larger parabolic mirror. The dashed circles indicate the equivalent working area of the smaller full-field mirrors. The apex of each sector from the large mirror can be used as a reference for alignment by placing it at point A in the figure.

Two alternative noncollimated but focused shadowgraph configurations, which utilize single optical elements to focus the conical light field, are shown in Figures 6.11 and 6.12, together with representative shadowgrams from each. The first of these[6.18] makes use of a Fresnel lens inside the range tank, with the other components located externally; while the second[6.19] uses a spherical-segment mirror and folds the light field to contain it entirely within the range tank. In the second case, the light field is intercepted twice by the model and two images are

registered on the photographic film. Both of these version retain the advantage of attenuating light from the model flow field by differential focusing, and require one less optical element than the configurations of Figures 6.8 and 6.10. While they are both adapted to a relatively wide field of view, a wide field calls for a large lens or mirror, and the economics of such large components are usually against high optical quality. To overcome this weakness, both versions utilize the large focusing elements not as objectives to produce an image of the projectile on the film, but rather as efficient light-gathering screens. A small objective lens is then placed at the aperture to re-image on the film the shadows of the projectile and its flow field which fall on the screen.

An advantage that all focused shadowgraphs have over the direct shadowgraph is that the film size may be independently specified to strike the best compromise between cost, storage, and handling limitations, on the one hand, and the requirements of film-reading accuracy, on the other.

A simple shadowgraph configuration which has been used for many years in large ballistic ranges is sketched in Figure 6.13. It is an outgrowth of the direct shadowgraph, which, through the use of a camera, allows film size to be independently chosen. Because there are no expensive optics, this configuration is economical for covering a large flight corridor. Light from the source casts a shadow of the model and of the flow field onto a projection screen placed on the opposite side of the flightpath. The screen is usually coated with glass beads which reflect each incident ray approximately back on itself. A camera, placed as close to the light source as practicable, photographs the visible image on the screen. The camera, then, sees both the focused silhouette image from the screen and a displaced defocused image of the directly illuminated model. Figure 6.14(a) is a downrange view of the Ballistic Research Laboratories (BRL) Transonic Range[6.20], which uses this configuration. Figure 6.14(b) is a representative shadowgram.

In its capacity as a reflector, the beaded screen performs a function similar to that of the spherical-segment reflector in Figure 6.12(a), but its light-gathering efficiency is considerably lower and it does not have the selective light-attenuation capability of the focused shadowgraph. It has been found[6.19] that the efficiency of this type of reflector can be improved considerably if a lenticular motion-picture screen is used and mounted on a cylindrical support. Such a screen, when flat, reflects light as would a cylindrical reflector. If the cylindrical support is curved, with the proper radius, in the orthogonal plane, the screen will then act as a spherical reflector. Difficulties with beaded screen in variable-pressure range enclosures due to dust adhesion have been reported[6.21]. The repeated pressure cycling between vacuo and atmospheric tends to work dust particles into the inter-bead voids, reducing the reflection efficiency of the screen.

A novel arrangement of optical components for a focused shadowgraph[6.22], illustrated by Figure 6.15, permits orthogonal viewing in an enclosed range with a single light source, and a single shutter and camera. Some of the more expensive components are thus eliminated, and possible timing uncertainty resulting from operation of two light sources is avoided. Figure 6.15(a) illustrates very simply the principle involved. A projectile flying a path, normal to the page, which falls within the dashed boundary will intercept two bundles of rays, A and B, of a collimated light beam. Bundle A will be intercepted after reflection from the mirror, while bundle B will be intercepted before reflection. Since these bundles are incident on the projectile at right angles to each other, two orthogonal shadows of the projectile (and flow field) will be cast on the film. Figure 6.15(a) is itself a workable system which can be used with either a point source or a collimated beam.

Figure 6.15(b) is the focused version of this arrangement. Light from the source, collimated by lens L1, passes the flightpath in one direction; is routed around the range structure by mirrors M1 and M2; passes the flightpath in a direction normal to the first; and finally is focused at the aperture of the camera by lens L4. Lenses L2 and L3, working together, focus an inverted image of the projectile at a point slightly displaced from the projectile itself. The image is also rotated a quarter of a turn by the mirrors M1 and M2. Lenses L2 and L3 are spaced two focal lengths apart so that the light beam emerges recollimated from L3. The projectile and its inverted rotated image are focused in the film plane by lens L4. Fiducial wires are placed as shown to provide a position and angle reference. The shadowgram, then, consists of two images moving in opposing directions and diametrically displaced from the center.

Photographic stations of this configuration are installed on two small ranges at Ames Research Center. Figure 6.16 is a representative shadowgram from one of these stations. Figure 4.1 shows one of the installations.

6.4 LIGHT SOURCES – R.J.Carros

Since much of the data collected in ballistic ranges is on film, the development of light sources suitable to the task has been an important factor. The light sources are usually required to be of very short duration to effectively "stop" high-speed models in their flight. Because the duration is short, the intensity must be correspondingly high, to bring about photographic exposure. The development of suitable light sources has been evolutionary, over a period of several decades.

We will describe some types which represent the best state of development available in 1968. Undoubtedly, further developments will be made.

For purposes of classification, we will divide the discussion into sections on spark gaps, laser sources, X-ray sources, and other sources. In terms of overall usefulness to date, the first class is by far the most important.

6.4.1 Spark Gaps

To illustrate the requirement for short duration, consider for example a model traveling at a velocity of 3 kilometers per second, It will move 3 millimeters in 10^{-6} seconds. It is clear then that for even such moderate model velocities, a light source of less than one microsecond duration is required to limit blurring. Because of the short duration, the source must also be very bright to expose the photographic film properly. A light source which meets these requirements – and is perhaps the one most widely used in ballistic range facilities – is the capacitance-discharge spark gap, or Libessart spark, which consists of a pair of electrodes connected across a high-voltage capacitor. The spark is discharged on command at the desired instant by a voltage pulse applied to a trigger electrode. A circuit diagram of this system is shown in Figure 6.17. The trigger voltage pulse ionizes the air in the vicinity of the main electrodes making it conductive. The energy stored in the capacitor is then discharged into the gap, vaporizing some electrode material and heating it and the air in the current path to very high temperatures, in the order of tens of thousands of degrees Kelvin. The hot plasma becomes the source of the spark gap light. Values commonly used for the voltage and capacitance are in the order of 7,000 volts and 0.12 microfarads, providing a stored energy of about 3 joules.

A photograph of a spark gap light source of this type is shown in Figure 6.18. The cylindrical cover has been removed to show the array of capacitors around the electrodes and the charging resistors and trigger pulse transformer The principal electrodes shown disassembled in the lower part of the photograph are made of aluminum because both aluminum atoms and aluminum oxide molecules are efficient radiators at the plasma temperatures. A 1-mm diameter hole is drilled on axis at the apex of the ground electrode to allow the light to leave the gap. The 1-mm diameter is a compromise between the light-quantity and point-source requirements. The trigger electrode, also shown in the figure, is made from stainless steel.

Care must be exercised in the design and construction of the spark gap light source to keep the inductance of the system low so that the natural frequency of the capacitor-discharge loop will be high and the light duration, consequently, short. A good part of this is accomplished by placing the capacitors close to the electrodes thus keeping the path length to the electrodes as short as possible. The importance of low inductance in the circuit has been emphasized in the literature[6.23, 6.24]. The effective duration of the source described above is approximately 0.3 microsecond, which is commonly measured at the half-height of the peak light output. An oscilloscope record of the light output of this type of spark, as a function of time, is shown in Figure 6.19. References 6.23 through 6.27 include some examples of other short duration spark gap light sources.

The radiated spectral power as a function of wavelength for the type spark gap of Figure 6.18 is shown in Figure 6.20. Also shown in Figure 6.20 for comparison are two curves of the spectral radiance of a blackbody radiating at temperatures of $20,000^{\circ}$ K and $23,000^{\circ}$ K. This comparison suggests that the spark gap light source is radiating nearly as a blackbody at a temperature above $20,000^{\circ}$ K. To test this conclusion, the following experiment was performed. Two high-voltage electrodes with a common ground electrode were arranged as shown in the schematic diagram in Figure 6.21. The spacing of each high-voltage electrode from the ground electrode was approximately 2.5 mm, which is the same spacing as that of the principal electrodes in the spark gap light source of Figure 6.18. The high-voltage power supply was used to charge the capacitors and a trigger pulse amplifier was used to supply the trigger voltage to fire the sparks at the desired time. The voltage signal, from the 1P28 photomultiplier tube with S-5 response, is a direct measure of the spark gap light output and was recorded on an oscilloscope.

First, capacitor A only was charged (switch open). Spark A was then fired and the output recorded by the oscilloscope camera. A record obtained is shown in Figure 6.22(a). Then both capacitors were charged to the same voltage as in the first step and both spark gaps were fired simultaneously from the common trigger pulse to record the signal shown in Figure 6.22(b). These measurements were made for charging voltages of 3.5, 4.0, 4.5, 5.0, and 5.5 kilovolts. The data obtained from the oscilloscope records were reduced to the form shown in Figure 6.23. The percentage of light output from spark gap B transmitted through the plasma in spark gap A is over 60% at 3.5 kilovolts, but diminishes rapidly with increasing voltage to a level of 18% at a charging voltage of about 5 kilovolts and greater. One may then conclude that the plasma in gap A has considerable opacity to the radiation from gap B and that the plasma in gap A is behaving as a nearly blackbody at a temperature slightly greater than $20,000^{\circ}$ Kelvin. Therefore, to increase its luminous output, it would be necessary to increase the plasma temperature.

6.4.2 Lasers

As noted earlier, one approach to rejecting from the spark photograph light emitted by the model flow field is to use spectral filtering in the light path. This approach is particularly favored by a laser light source which produces intense light at a single frequency. All other frequencies can thus be blocked by the filter. Lasers can be switched to provide light durations of the order of 10 nanoseconds. A schematic diagram showing a laser as a light source, and the placement of the filter in a filtered focused shadowgraph system is shown in Figure 6.24. The system is otherwise unchanged from those discussed earlier. Since the laser output is a small diameter beam, a diverging lens is used to spread the light to the diameter required to cover the desired field at which point it is again collimated. It is necessary to pulse the flash tube of this type laser typically 500 microseconds prior to photographing the event. During this period of 500 microseconds, the so-called pumping action takes place and light intensity builds up to a peak. Therefore, a timing arrangement to start the laser must be provided. Timing of the photograph, however, is determined by operation of the Kerr cell, which is switched open when the model arrives at the photographic station. The usual timing signal would therefore be applied to the Kerr cell. Ballistic-range facilities which have used laser light sources include US Naval Ordnance Laboratory, MIT Lincoln Laboratory, General Motors Corporation, and Laboratoire de Recherches Balistiques

et Aérodynamiques (cf. References 6.17, 6.28, 6.29). A shadowgram made with a laser system in use at the US Naval Ordnance Laboratory is shown in Figure 6.25. The double image is a result of the geometry of the photographic system, as indicated in Figure 6.12(a). Lasers are not presently used widely in ballistic range photographic systems, however, because the "state of the art" is such as to present some problems including maintenance, non-uniform or mottled background in the photograph, and starting the operation of the flash tube 500 microseconds before use. Maintenance involves replacement of some components within the laser such as the flash tube, Kerr cell, mirrors, windows, and ruby rod which may become damaged after only a few hundred pulses due to the high energy levels in the laser. Some of the literature refers to the requirement that optics in the laser photographic system, such as range windows and mirrors, be maintained very clean to prevent scattering of the light which would result in a mottled background in the photograph. A mottled background may also be caused by non-uniform light emission from the laser rod. However, laser rods can be chosen selectively to minimize this problem. The relatively high initial cost of the laser may also limit its use to only a few selected stations to examine such details as model integrity, ablation, and shock shape on radiating models. All things considered, the laser has very attractive potentialities and, as research and development continues, the laser will most likely see increasing use in ballistic range facilities.

6.4.3 X-ray Sources

Still another source of electromagnetic radiation used to produce an image on photographic film is the X-ray source. Since radiation from the X-ray will pass through film covers opaque to visible light, radiation from the model shock layer can be blocked in an X-ray picture. Short duration or "flash" X-ray systems are commercially available. They consist of a high-voltage supply, a pulser, an X-ray tube, and a trigger system. A block diagram of a typical system is shown in Figure 6.26. The pulser is charged to the desired voltage from the high-voltage supply. Upon receiving a signal from the trigger system the pulser discharges to the X-ray tube which in turn emits radiation to photograph the event.

In addition to the use of this system to photograph self-luminous models, a second, perhaps more important, use of these systems has been to photograph the model and sabot in the vicinity of the launching gun muzzle where radiating gun gases make conventional photographic techniques unusable. The photographs in Figure 6.27 illustrate this use. They show a sequence of X-ray photographs of a model and sabot emerging from the launch gun muzzle and follow the process of early sabot separation. Photographs of this type are extremely valuable when launching problems are being experienced.

The laser light source with appropriate filters to prevent gun gas radiation from exposing the film is also potentially useful to obtain photographs near the gun.

It is a disadvantage of X-ray systems, used to obtain photographs of a model downrange, that they do not make any of the flow field characteristics visible. Hence, the penalty for this approach to photographing models in luminous flow fields is the loss of flow visualization.

6.4.4 Other Light Sources

Although the spark, X-ray, and laser are most often used in ballistic range photographic systems, other light sources have been used and have application in some special circumstances. These light sources include flash lamps, flood lamps, carbon-arc search lights, self-luminosity of models or surrounding flow fields, and explosive light sources. Flash lamps have been used singly or in groups of two or more and pulsed sequentially to either back light or front light an event to be recorded by either a single exposure or a motion picture camera. The flood lamp and carbon-arc search light (as used in Reference 6.30) may also be used for front or back lighting an event. The luminosity from a radiating model is also used as a light source in some photographs made for radiation studies; see for example Figure 9.1. All of these light sources are of long duration and therefore a shutter must be used to limit the exposure time and to stop motion of the event. These sources are then, with the exception of self-luminosity, limited to test circumstances where the event motion is relatively low speed so that the shutter may remain open long enough to sufficiently expose the film but yet not long enough to record event motion (blur) on the photograph. As described in the following section, image-intensifier-type cameras are often used to photograph a self-luminous event. Explosive light sources have short duration and therefore are suitable for photographing high-speed events. The explosive light source described in Reference 6.31 has a duration of 3×10^{-8} seconds and contains a few tenths of a gram of lead azide and PETN, which when detonated have sufficient energy to produce luminosity by shock compression of the air. For additional information on light sources, the reader is referred to such publications as Proceedings of International Congresses on High-Speed Photography and the Journal of the Society of Motion Picture and Television Engineers.

6.5 SHUTTERING – A.G.Boissevain

The "shuttering" provided by the short duration of the spark gap light source (about 0.3 microsecond for a capacitance discharge spark) effectively stops the motion of low velocity models and the necessary image sharpness for measurement is obtained. At increasingly high velocities, shuttering to achieve shorter exposures becomes necessary to limit motion blurring and thus retain image quality. Furthermore, as has been noted, when light from the model shock layer and wake must be rejected to preserve useful images, active shutters may also be required. These factors have led to a requirement for electro-optical or electromechanical shutters in modern, high performance ballistic range optical systems.

Other reasons for shuttering may also arise. Fog exposure of the film may occur due to a variety of causes, including room light, muzzle flash from the gun, flow field emission from sabot parts, light flashes from model

and sabot impacts, light from adjacent shadowgraph stations and from station-triggering light screens, and luminosity carried in the flow of counter-flow facilities. These problems can in some cases be overcome by simple solutions, such as limiting the time the film is uncovered or creating a spectral mismatch between the unwanted light source and the film response. As an example of the latter, the use of red photobeams and red-insensitive film is mentioned. The use of shutters, however, can largely overcome all of the above problems.

Shuttering systems can be grouped broadly as electromechanical and electro-optical. In the following paragraphs, several types within each class will be discussed briefly and their usual applications indicated.

6.5.1 Electromechanical Shutters

6.5.1.1 Moving-Film and Rotating-Mirror Cameras

High velocity events such as ballistic range models in flight can frequently be photographed without blur by means of a moving film or rotating mirror camera system. The principle is simply one of holding the model image stationary on the film for a long enough time to bring about exposure. The two sketches in Figure 6.28 show typical operation. For maximum effectiveness the film velocity or equivalent mirror rotational speed must be carefully matched to that of the model image to avoid blur in the direction of movement. While cameras employing this principle are commercially available, they may, for particular applications, have to be designed to meet test requirements and built to order or modified (cf. References 6.5, 6.6).

6.5.1.2 Spectrograph Shutters

For radiation studies in a ballistic range, a series of luminous events occur which may require shuttering to isolate the event of interest. An unshuttered spectrograph may superpose some response to all the events from the gun-muzzle flash to the impact of the model. Photomultiplier tubes and other radiometers that produce signals in the form of voltages are not of concern in this respect since such signals can be time-resolved by oscilloscope presentation.

In order to protect a spectrographic film from sources of light, other than the ones of interest, total blockage of the light is desirable. The spectrographic entrance slit is usually a convenient place for a shutter since the slit width is small. A shutter that takes advantage of this fact is sketched in Figure 6.29. A single current-carrying wire acting as the shutter is placed over the slit. Placed adjacent to this flexibly mounted wire is a fixed wire connected in series with the first such that the current flow is in the same direction in both wires. Discharging a capacitor through this circuit causes the wires to repel one another and the one which is free is rapidly displaced. A similar effect can be achieved by placing the shutter wire in a strong magnetic field parallel to the direction of light. This same concept can be used to close a slit that is initially open by providing a mechanical stop to the displaced conductor. Closing times on the order of 5×10^{-6} seconds can be obtained[6.32]. A modification of the design which permits the shutter to open and then close is to use the moving wire to displace a slide with a second slit cut into it. As this slide is pushed past the fixed slit, the shutter effectively opens and closes[6.33, 6.34].

A similar shutter, but on a larger scale, is one in which a light, stiff blade with appropriate openings is placed in tracks across an aperture. An explosive charge then drives the blade across the aperture[6.35, 6.36]. The dimensions of the openings in the blade can be matched to the translational rate of the blade to give a specified opening rate, open dwell time, and closing time. Figure 6.30 shows the salient features. A shutter of this type has closed a 3 mm hole in 1×10^{-4} seconds.

Another technique for shuttering spectographic openings is shown in Figure 6.31. In this arrangement an explosive squib is oriented so that the gases generated blow against a bi-stable shutter. Its usual mode of operation is to close the aperture after the event of interest. A closing time of about 3 milliseconds from receipt of signal for a 40 mm-diameter hole has been achieved.

There are several other types of shutter that depend on blocking out the incoming radiation by an irreversible action. One of these consists of a tube through which the light passes. On receipt of a signal an explosive charge, wrapped around the tube, causes it to collapse. (This technique may also be applied to locking gas flow into a container). A light foil cylinder can be made to collapse in a similar manner by placing it within a short coil. Discharging a capacitance through the coil causes the foil to collapse. Another approach uses shock loading from an explosive to destroy the transmissivity of a normally clear sheet of glass or plastic placed in the optical train[6.37]. The use of an exploding wire to activate a shutter is discussed in Chapter 9, and shown schematically in Figure 9.6.

6.5.2 Electro-Optical Shutters

Electro-optical shutters include Kerr cells and image-converter tubes.

6.5.2.1 Kerr-Cell Shutters

The method of operation of Kerr cells has been well discussed in the literature[6.38]. Briefly, they have the capability of rotating plane-polarized light on application of a high voltage across a pair of plates along two sides of the cell. The cell is placed in the light path between crossed polarizers, which normally block the light. When voltage is applied to the cell, rotation of the polarization of the light by the cell permits it to pass through the second polarizer. Hence, the shutter is opened when the voltage is applied.

The rotation of the plane of polarization by the cell is a function of the type of Kerr-effect fluid it contains, the magnitude of the voltage gradient impressed at right angles to the light path, and the length of the plates. These factors are adjusted to bring about 90° rotation of the plane of polarization.

Kerr cell shutters may be placed at the image of the light source in focused shadowgraph systems, where the aperture required is small. The duration of the light pulse which they pass depends on the duration of the applied high voltage pulse, which can be as short as one or two nanoseconds. These shutters have the disadvantage, however, of heavily absorbing light, especially at short wave-lengths. Since they pass only plane polarized light, a loss of 50% of the incident intensity is inherent. Further losses occur by absorption in the fluid and by reflection and absorption at the polarizers. The transmission through the fluid drops rapidly with wavelength below about 3500 Å. The polarizer transmission also falls off in the ultraviolet. Figure 6.32 shows the measured transmission of a representative shutter at the present state of the art as a function of wavelength. The sharp reduction at 3200 Å is probably due to absorption of the Kerr effect fluid. Unfortunately, much of the energy of a typical spark unit is at wavelengths shorter than 3000 Å (0.30μ), as shown in Figure 6.20

It should be noted that the Kerr cell and polarizers act as a refractive optical unit and can introduce aberrations and distortion into the optical system.

If the polarizers are made of crystal, their acceptance angle is small (on the order of 10 degrees), which limits the f/number of the optical system with which it is to be used. The size of the polarizer largely determines the cost of the whole unit because its cost varies as the cube of the dimension. Cost of the cell itself is not so critically dependant on size.

The improvement in picture quality made possible by the use of Kerr-cell shutters is shown in Figure 6.33. The two photographs are of the same burning aluminum model in flight. The optical system used is a parallel light focused shadowgraph of the type shown schematically in Figure 6.10. In obtaining the first picture, a 3 mm aperture was placed around the image of the source. In the second, the aperture was replaced by a 20-nanosecond-exposure Kerr cell.

6.5.2.2 *Image-Converter Cameras*

In an image-converter tube, the photons of an image focused on its receiving screen cause the proportional emission of electrons. Application of a voltage pulse directs these electrons, and effectively amplifies them in the process, to the emitting screen of the tube where they activate the phosphors of the screen, which emit photons, forming a duplicate of the image existing on the receiving screen at the time of the voltage pulse. Voltage pulses as short as a few nanoseconds in duration have been used successfully. Shuttering is achieved by operating on the electrons rather than on the photons[6,7].

One form of image converter tube uses deflection plates to translate the beams of electrons to one side, allowing consecutive pictures of the same event to be recorded on the emitting screen without overlap. Figure 6.34 shows three sequential photographs of a model taken with such an image converter camera. The exposure of each image was 0.2 microsecond and the time delay between exposures was 5 microseconds.

6.6 SPATIAL REFERENCE SYSTEMS — R.I.Sammonds

Since one of the most basic uses of ballistic ranges is to record motion histories of models flown through them, both out of interest in the motion itself and for determination of the aerodynamic forces and moments acting on the models, it is important to provide the means for accurate position and attitude measurement in the spark photographs. The means for doing this are the spatial reference systems.

The accuracies demanded of these systems are, in some cases, the greatest that the ingenuity of the system designer can provide. The reason is simple: Accuracy in the measuring system is essential to accuracy of the aerodynamic data obtained. The more accurate the measuring system, the more marginal the cases that can be treated. Accurate systems are especially necessary in very short ranges, such as counterflow facilities, where the combination of maximum measurement precision and lightweight model design may be required to make possible the collection of accurate results. On the other hand, short ranges make it easier to maintain high accuracy. Accuracies achieved in these systems have been better than 0.1 mm (100 microns) in the three linear coordinates, and better than 0.1° in attitude angles.

Spatial reference systems are generally based on the following properties and principles:

(a) The straightness of wires drawn taut (e.g. grid wires), and the straightness and verticality of plumb lines;

(b) The accurately known form of catenaries;

(c) The dimensional stability of statically determinate steel structures;

(d) The principle of self-recording of random small changes in optical alignment and shifting of the reference system itself.

Where reduced accuracy is acceptable, the reference system may be established and aligned using surveyors' instruments and thereafter presumed stable so that subsequent distortions are not recorded. In such cases,

distance fiducial marks can be placed in the photographic or yaw card stations, using a steel measuring tape, and the range centerline can be established by identifying the extension of the gun axis (boresite) at each station without any instruments other than the practiced eye of a technician.

On the other hand, ranges required to produce the best possible translational and rotational histories must be equipped with stable and accurate fiducial systems. Although most systems depend on similar concepts, their actual configurations are largely dictated by the type and size of test section, the type of shadowgraph system, and the accuracies required. Because of the adaptation of fiducial systems to conform to other range requirements, the descriptions to follow will be of particular systems which have proven reliable. The systems have been adapted to both direct-projection and focused shadowgraphs and to parallel and conical light beams. We will first examine a collimated (parallel) light system, which may be either direct-projection or focused.

6.6.1 Fiducial System for Collimated Light Field

In collimated light systems, the downrange distance, x , between adjacent stations is conveniently determined from images in the shadowgraph pictures of plumb lines hanging at carefully gaged locations along a continuous steel rod. The lateral and vertical displacements, y and z , may be measured relative to taut wires above and beside the flight path running roughly parallel to the range axis. The plumb lines provide a reference direction for the pitch angle, θ , in the side photographs, and the taut wire above the flight path provides a reference for the yaw angle, ψ . Such a system, in which the photographic station components lie outside the range enclosure, or test section, is illustrated in Figure 6.35 where the complete arrangement of bars, plumb bobs and wires for two stations is shown schematically. The other station components are deleted for clarity.

All plumb-line pairs are at identical spacing, S , as shown in Figure 6.35. This spacing is determined by the grooves machined in the sleeves on the rod. The spacing, S' , between corresponding plumb lines in adjacent stations, determined by the spacing of the sleeves along the rod, is also constant. The rods from which the plumb lines are suspended are offset longitudinally (i.e., in the flight direction) a small amount so that the line images will not be superimposed in the shadowgraph picture. The two catenary wires, on the opposite sides of the flightpath, are adjusted for proper position and tension so that they have the same sag and are parallel. Again the wires are offset slightly (vertically) so that the two images are displaced in the shadowgraph. The taut wires above and below the flightpath are arranged in pairs, two above the flightpath and two below. These wires are installed so that the two pairs are parallel and have the same spacing, t . The pairs are offset laterally so that their images are not superimposed. Typical shadowgrams with this arrangement are shown in Figure 6.36 where wires, A , C , and F are the plumb lines and catenary, respectively, on the side of the test section nearest the film and B , D , and E are the plumb lines and catenary on the other side. Similarly, H and J are the taut wires above and G and I the taut wires below.

The principle underlying this particular fiducial system stems from the necessity of accurately locating the model in space when the light beams are neither exactly collimated nor perpendicular to the range centerline. Although it is entirely possible to have the optical system perfectly collimated and aligned, it is more practical to install a fiducial system that can be used to correct the model position for small angular variations due to misalignment and lack of collimation. This, in fact, is the reason for the multiple wire system described here. With this system of reference wires, the calibrated spacing between the plumb lines and the taut wires on the sides of the range nearest to the film plane can be related to the spacing of these wires in the shadowgraph picture to determine the magnification of the optical system. Further, relating the spacing of the plumb lines and taut wires on either side of the range, in the shadowgram, (corrected for magnification) will indicate the accuracy of collimation of the light beams. Relating the amounts of offset of the plumb lines, catenaries and taut wires, as measured from the shadowgram, to the calibrated offset distances will determine the alignment of the optics. The working equations for these corrections are developed in detail below.

Referring to Figure 6.37, it can be seen that the mathematical expressions necessary to determine the model orientation in space, $\Delta x, y, z$, corrected for light angularity and lack of collimation ($\epsilon_1 \neq \epsilon_2$) are as follows:

$$\Delta x = AM - (y + \Delta y_1) \epsilon_x \tag{6.1}$$

$$z = FM + (y + \Delta y_2) \epsilon_z \tag{6.2}$$

$$y = GM - (z + \Delta z) \epsilon_y . \tag{6.3}$$

where ϵ_x , ϵ_y , ϵ_z are small-angle approximations for $\tan \epsilon$. Since each equation has two unknowns in it, we can determine y by substituting Equation (6.2) into Equation (6.3), which gives

$$y = \frac{GM - \epsilon_y (FM + \Delta z + \Delta y_2 \epsilon_z)}{1 + \epsilon_y \epsilon_z} . \tag{6.4}$$

Similarly, substituting Equation (6.3) into Equation (6.2) and rearranging we get

$$z = \frac{FM + \epsilon_z (GM + \Delta y_2 - \Delta z \epsilon_y)}{1 + \epsilon_y \epsilon_z} , \tag{6.5}$$

and substituting Equation (6.4) into Equation (6.1) gives

$$\Delta x = AM - \epsilon_x \left[\frac{GM + \Delta y_1 - \epsilon y \; (FM + \Delta z - \Delta y_1 \epsilon_z + \Delta y_2 \epsilon_z)}{1 + \epsilon_y \epsilon_z} \right] , \qquad (6.6)$$

where

$$\epsilon_x = \epsilon_1 + K_1 \; (AM - AB) = \frac{AB - AB_c}{W_1} + K_1 \; (AM - AB)$$

$$\epsilon_y = \epsilon_4 + K_2 \; (GM - GH) = \frac{GH - GH_c}{W_3} + K_2 \; (GM - GH)$$

$$\epsilon_z = \epsilon_3 - K_1 \; (FM + EF) = \frac{EF - EF_c}{W_2} - K_1 \; (FM + EF)$$

and

$$K_1 = \frac{\epsilon_2 - \epsilon_1}{BD} = \frac{BD - BD_c}{W_1(BD)}$$

$$K_2 = \frac{\epsilon_5 - \epsilon_4}{HJ} = \frac{HJ - HJ_c}{W_3(HJ)} .$$

The definitions and the use of K_1 and K_2 assume linear variation in the angularity of the light beams.

For this analysis, the length increments AM, AB, and BD are measured in the plane formed by the plumb lines A and C; increments EF and FM are measured in the vertical plane containing the catenary wire, F; and increments GH, HJ and GM are measured in the horizontal "plane" containing the taut wires G and I. In reducing a set of test data, however, these lengths, or distances, are measured on the photographic film (e.g., Figure 6.36) so that the apparent distances between plumb lines, catenary wires, etc., must be corrected for the magnification of the image-forming optical system in order to determine the true distances used in the foregoing equations. This can be accomplished (Fig.6.37) by taking ratios of the known calibrated spacings of the plumb lines in the horizontal view, AC_c, and the taut wires in the vertical view, GI_c, to the apparent distances, AC_a and GI_a, read from the photographic film. The true distances are then obtained from .

$$
\left.
\begin{aligned}
AM &= AM_a \left(\frac{AC_c}{AC_a} \right) ; \quad AB = AB_a \left(\frac{AC_c}{AC_a} \right) ; \\
BD &= BD_a \left(\frac{AC_c}{AC_a} \right) ; \quad EF = EF_a \left(\frac{AC_c}{AC_a} \right) ; \\
FM &= FM_a \left(\frac{AC_c}{AC_a} \right) ; \quad GM = GM_a \left(\frac{GI_c}{GI_a} \right) ; \\
GH &= GH_a \left(\frac{GI_c}{GI_a} \right) ; \quad HJ = HJ_a \left(\frac{GI_c}{GI_a} \right) ,
\end{aligned}
\right\}
\qquad (6.7)
$$

where $\dfrac{AC_c}{AC_a}$ is the magnification factor for the side film (horizontal view) and $\dfrac{GI_c}{GI_a}$ is the magnification factor for the bottom film (vertical view).

Since both Δx and z are determined from the side film, the assumption has been made that the magnification at this film plane is the same in both the horizontal (Δx) and vertical (z) directions. However, for certain optical systems where spherical aberration and coma effect due to off-axis mirrors are a problem the above assumption may lead to significant errors in the determination of EF and FM. A discussion of this problem is given at the end of Section 6.6.1.1.

6.6.1.1 Optical Distortion of Fiducial System

If the optical system includes windows through which light must pass, and if the windows are not perpendicular to the light path, or if the surfaces of the windows are not parallel (prism effect), or if distortions are present due to imperfections in the glass, error can arise in Δx y, and z. The nonperpendicularity of the light path with respect to the window can come about from either systematic or random causes. If the range walls containing the windows are flared, as they are in a counterflow facility to allow for boundary layer growth, the windows are systematically inclined. If during construction of the tunnel the window walls are not aligned perfectly, there will be random variations in the window inclination. Although these errors are generally quite small the equations for Δx, y, and z (Equations (6.4) through (6.6)) will now be modified to account for

the refraction of the light through the windows. Consider the pair of windows included in the shadowgraph station schematic of Figure 6.38. We can see that

$$\Delta x = AN - (y + \Delta y_1) \tan \epsilon_x ,$$

where $AN = AM + MN$

and MN is obtained as follows:

Since the angles ϵ_x and ϵ_t are small, the following relations apply:

$$i = \epsilon_x - \epsilon_t \; ; \; \mu = \frac{i}{r} \quad \text{(Snell's law of refraction)}$$

$$y' \approx t .$$

Thus, from the law of sines,

$$\frac{x'}{\sin(i-r)} = \frac{x'}{i - \frac{i}{\mu}} = \frac{y'}{\sin(90^0 - i - \epsilon_t)} = \frac{y'}{1} = t$$

or

$$MN = x' = t\left(i - \frac{i}{\mu}\right) = t(\epsilon_x - \epsilon_t)\left(1 - \frac{1}{\mu}\right) ;$$

thus

$$\Delta x = AM + t(\epsilon_x - \epsilon_t)\left(1 - \frac{1}{\mu}\right) - \epsilon_x(y + \Delta y_1) . \tag{6.8}$$

Substituting for y (Eq. (6.4)) we get

$$\Delta x = AM + t(\epsilon_x - \epsilon_t)\left(1 - \frac{1}{\mu}\right) - \epsilon_x \Delta y_1 - \epsilon_x \left[\frac{GM - \epsilon_y (FM + \Delta z + \Delta y_2 \epsilon_z)}{1 + \epsilon_y \epsilon_z}\right] . \tag{6.9}$$

This now corrects Δx for the longitudinal taper of the test section and angularity of the light rays. If the convergence angle of the range walls remains constant and the windows are of uniform thickness, the correction due to ϵ_t will be the same for all stations and thus would not affect the relative model position.

If the windows have a component of inclination in a plane normal to the range axis, then corrections similar to that for Δx may be required also for y and z. Figure 6.39 has been drawn to represent the case where the window pairs are inclined by angles of ϵ_y and ϵ_z with respect to the vertical and horizontal light beams (which might occur, for example, if the range enclosure became warped or twisted about its axis). The situation is analogous to a perturbation of the light rays of Figure 6.37 due to the presence of windows. Thus,

$$y = GM + t\epsilon_y\left(1 - \frac{1}{\mu}\right) - \epsilon_y (z + \Delta z) ,$$

$$z = FM - t\epsilon_z\left(1 - \frac{1}{\mu}\right) + \epsilon_z (y + \Delta y_2) .$$

Substituting each of these equations into the other gives

$$y = \frac{GM - \epsilon_y\left[FM + \Delta z + \epsilon_z \Delta y_2 - t\left(1 - \frac{1}{\mu}\right)(1 + \epsilon_z)\right]}{1 + \epsilon_y \epsilon_z}$$

$$z = \frac{FM + \epsilon_z\left[GM + \Delta y_2 - \epsilon y \Delta z + t\left(1 - \frac{1}{\mu}\right)(\epsilon_y - 1)\right]}{1 + \epsilon_y \epsilon_z} .$$

Substituting this value of y into the basic equation for Δx (Eq. (6.8)) gives,

$$\Delta x = AM + t(\epsilon_x - \epsilon_t)\left(1 - \frac{1}{\mu}\right) - \epsilon_x \Delta y_1 - \epsilon_x \left\{\frac{GM - \epsilon_y\left[FM + \Delta z + \epsilon_z \Delta y_2 - t\left(1 - \frac{1}{\mu}\right)(1 + \epsilon_z)\right]}{1 + \epsilon_y \epsilon_z}\right\} . \tag{6.10}$$

This set of equations corrects y and z for light angularity and Δx for both wall convergence and light angularity. As previously stated, however, these corrections may be so small in actual practice that they can be ignored.

Minor irregularities in the windows and mirrors, as well as spherical aberration due to the use of spherical mirrors, and the coma effect due to an off-axis optical system cause distortions in the shadowgraphs that can lead to significant errors. These distortions can be compensated for by mapping the field of view of each station using a calibrated grid or perforated plate placed on the axis of the range (flightpath). The grid is photographed with the shadowgraph system. Measurements made on the photograph are then compared with the known dimensions of the grid.

6.6.2 Fiducial System for Conical Light Field

Conical projection shadowgraphs, like those described in Section 6.3.1, are often used. For a conical light field several types of reference system are feasible. For instance, where reflecting surfaces (CARDE Aeroballistic Range[6.2] and NOL 1000 ft Hyperballistics Range[6.12]) or fresnel lenses (VKF 1000 ft Hypervelocity Range[6.18]) are used, marks or grids can be fastened to them which, when related to the surveyed position of the light source provide by themselves a good earth-fixed reference. A notched fiducial bar located at the intersection of the side and bottom film planes (BRL Aerodynamics Range[6.11], and NOL Pressurized Ballistics Range[6.12]) can also be used to establish the origin and orthogonality of the local station coordinate system. Each self-contained station of this type is aligned to the optical axis (centerline) of the range through reference to the two faces of the fiducial bar[6.11]. Systems of this nature rely on the stability of the mounting system and no account is taken of short-term shifts of the station components relative to the range axis. Where accuracy demands improved inter-station relationship, an auxiliary reference system consisting of plumb lines accurately spaced at each station, and a catenary wire, similar to that previously described for the collimated light system, can be added.

If the conical light field is produced by a point light source and there are no distorting optical elements between the light source and the fiducial references, the position and attitude of the model in the station coordinate system, as they appear in the shadowgram, need only be corrected for magnification due to the conical projection in order that they be determined accurately. However, since the magnification of a model image may differ from point to point on the film (significant for long bodies at high angle of attack) the projected angle shown in the shadowgraph picture may be distorted. This distortion must be taken into consideration when determining the corrected angle.

Once the position and attitude of the model have been established within each station coordinate system, they must then be related to determine the overall model motion and trajectory. In a rigid system, this would be accomplished directly by having aligned the stations in the range shell. However, when a secondary reference system (range coordinates) is used to improve the interstation relationship, the model position and attitude previously determined with respect to the station coordinate system must be translated and rotated into the secondary reference system.

The working equations for these operations are developed in detail below in two parts. Section 6.6.2.1 covers the equations necessary to accurately locate the position and attitude of the model in the station coordinate system, and Section 6.6.2.2 derives the equations necessary to relate the model position and attitude in each station to the range coordinate system in order to determine the overall model motion and trajectory. If a rigid system is under consideration then only the first part is needed.

6.6.2.1 Station-Coordinate System

The particular system under consideration is a simple direct shadowgraph which uses grid wires adjacent to the orthogonal film planes to establish the station reference system. The station axes ($\Delta x'$, y', and z'), shown in Figure 6.40, are defined as follows:

The y' axis is the line passing through the side spark perpendicular to the side film and is positive to the right when looking downrange. The z' axis is the line passing through the top spark perpendicular to the bottom film and is positive upwards. The y' axis and the z' axis intersect at $0'$, the origin of the station coordinate system, thus forming the $y'-x'$ plane. The $\Delta x'$ axis is the line passing through $0'$ perpendicular to the $y'-z'$ plane and is positive downrange. Grid wires just above the side and bottom film planes mark the intersections of the $\Delta x'-y'$ plane, the $\Delta x'-z'$ plane and the $y'-z'$ plane with the side and bottom films. The plane containing the bottom grid wires is parallel to the $\Delta x'-y'$ plane and the plane containing the side grid wires is parallel to the $\Delta x'-z'$ plane. Thus, the grid wires form a precisely orthogonal set of reference lines.

The apparent model position and orientation (Δx_a, y_a, z_a, θ_a, ψ_a), as measured from the shadowgram, are corrected for the conical light projection (magnification) within the station coordinate system in the following manner:

In the notation of Figure 6.41, the relationship for the magnification of the coordinates of a single point, m, is

$$\frac{y'}{y_a} = \frac{C_b - z'}{F_B}, \qquad \frac{z'}{z_a} = \frac{C_S - y'}{F_S} = \frac{\Delta x'}{\Delta x_a}, \tag{6.11}$$

where the subscript, a, stands for the apparent values read from the film. At this point, it should be noted that the film platens must be very flat in order that the apparent values of Δx, y, and z may be accurate. Any waviness in the film will show up as a waviness in the image of the grid wire in the shadowgram.

Solving Equations (6.11) simultaneously gives expressions for the location of the model in the station coordinate system.

$$\Delta x' = \Delta x_a \left(\frac{z'}{z_a}\right) = \Delta x_a \left(\frac{C_S F_B - y_a C_B}{F_S F_B - y_a z_a}\right),$$

$$y' = y_a \left(\frac{C_B F_S - z_a C_S}{F_S F_B - y_a z_a}\right),$$

$$z' = z_a \left(\frac{C_S F_B - y_a C_B}{F_S F_B - y_a z_a}\right), \tag{6.12}$$

where C_S, F_S, C_B, and F_B are calibrated values. The magnification of the coordinates of two points on a model will be different if they are at different distances from the film plane. It would also appear from this analysis that it would be impossible to determine unequivocally the magnification of a model if there were no specific points through which the light rays from both sparks would pass; for instance, a large diameter sphere. However, by suitable mathematical manipulation, it is possible to arrive at an expression that can be used to determine the sphere diameter

$$d = 2r = 2\left[\frac{\sin \phi_3}{\cos \phi_4}\left(\frac{C_B - C_S \tan \alpha_u}{1 - \tan \alpha_u \tan \phi_4}\right)\right], \tag{6.13}$$

where, with reference to Figure 6.42,

$$\phi_3 = \frac{1}{2}\left[\tan^{-1}\left(\frac{OC}{F_B}\right) - \tan^{-1}\left(\frac{OA}{F_B}\right)\right],$$

$$\phi_4 = \frac{1}{2}\left[\tan^{-1}\left(\frac{OC}{F_B}\right) + \tan^{-1}\left(\frac{OA}{F_B}\right)\right],$$

$$\alpha_u = \frac{1}{2}\left[\tan^{-1}\left(\frac{OD}{F_S}\right) + \tan^{-1}\left(\frac{OF}{F_S}\right)\right].$$

where OA, OC, OD, and OF are measured from the film and F_S, F_B, C_S, and C_B are calibrated values.

Concomitantly, when the magnification at the nose of a body differs from that at the base, the result is a distortion of the angular position of the model projected onto the film. This angle distortion can be quite large for long bodies at high angles of attack; it also changes with Δx, y, and z. The equations relating the apparent angles of pitch, θ_a, and yaw, ψ_a, and the true angles of pitch, θ', and yaw, ψ', and the projected pitch angle, θ'_p (in the station coordinate system) are as follows:

$$\psi' = \tan^{-1}\left[\frac{(C_S-y')(C_B-z') \tan \psi_a +(C_S-y')(\Delta x'\tan \psi_a -y') \tan \theta_a}{(C_S-y')(C_B-z') - (\Delta x'\tan \theta_a -z')(\Delta x'\tan \psi_a -y')}\right]$$

$$\theta'_p = \tan^{-1}\left[\frac{(C_S-y')(C_B-z') \tan \theta_a +(C_B-z')(\Delta x'\tan \theta_a -z') \tan \psi_a}{(C_S-y')(C_B-z') - (\Delta x'\tan \theta_a -z')(\Delta x'\tan \psi_a -y')}\right]$$

$$\theta' = \tan^{-1}\left[\tan \theta'_p \cos \psi'\right] = \tan^{-1}\left[\frac{\tan \theta'_p}{\sqrt{(1 + \tan^2 \psi')}}\right]$$

$$\alpha'_r = \tan^{-1} \sqrt{(\tan^2 \psi' + \tan^2 \theta'_p)}, \tag{6.14}$$

where the angle convention is shown in Figure 6.43. Since the angles of yaw and pitch are dependent on each other, it is necessary to decide on some angle sequence in order to derive the above equations. For this particular analysis, the model was assumed to have first yawed through some angle, ψ', and then pitched through some angle, θ'. In this manner, the apparent angle of yaw, ψ_a, seen in the bottom film, is a direct projection of the true angle of yaw, ψ', whereas the apparent pitch angle, θ_a, in the side film, is the projection of the angle, θ'_p.

6.6.2.2 Range-Coordinate System

The relationship of the photographic stations to one another may be accomplished by a second reference system, somewhat like that described in Section 6.6.1, supported from the range structure. A system consisting of plumb lines, suspended from a calibrated steel rod, and a single catenary wire, is shown in Figure 6.44. One plumb line is photographed in the side view of each station, while the catenary is photographed in both views. The model position and attitude, determined with respect to each station coordinate system, may then be translated (x_0, y_0, z_0) and rotated $(\epsilon_1, \epsilon_2, \epsilon_3)$ into the common range coordinate system in the following manner.

The local range axes, Δx, y, and z (Fig. 6.44) are determined by the catenary wire, stretched the length of the range under a known tension, and the plumb lines. The vertical plane containing the catenary and parallel to the plumb line is the Δx-z plane. The y-z plane is the plane perpendicular to the Δx-z plane which contains the plumb line. The origin, O, of the local range coordinate system is defined to be the point at which the catenary wire intersects the y-z plane. The sign convention for the range axes is the same as that for the station axes. (Correction must be made for the sag of the catenary wire when determining z values for the entire range).

The equations to accomplish the translation and rotation of the model center-of-gravity coordinates from station axes to range axes are:

$$\left. \begin{aligned} \Delta x_{CG} &= \Delta x'_{CG} + x_0 + y'_{CG}\epsilon_1 + z'_{CG}\epsilon_2 \\[2mm] y_{CG} &= y'_{CG} + y_0 - \Delta x'_{CG}\epsilon_1 - z'_{CG}\epsilon_3 \\[2mm] z_{CG} &= z'_{CG} + z_0 - \Delta x'_{CG}\epsilon_2 + y'_{CG}\epsilon_3 \ , \end{aligned} \right\} \qquad (6.15)$$

where

$$\left. \begin{aligned} \Delta x'_{CG} &= \Delta x' + l\cos\psi'\cos\theta' \\[2mm] y'_{CG} &= y' + l\sin\psi'\cos\theta' \\[2mm] z'_{CG} &= z' + l\sin\theta' \ , \end{aligned} \right\} \qquad (6.16)$$

and l is the distance from a measurement-reference point on the model axis ($\Delta x'$, y', z') to the center of gravity of the model ($\Delta x'_{CG}$, y'_{CG}, z'_{CG}). The coordinates x_0, y_0, and z_0 are the range-system coordinates of the station-system origin, O'. The angles, ϵ_1, ϵ_2, and ϵ_3, are, respectively, the angles of yaw, pitch, and roll of the station system with respect to the range system.

In order to solve these equations for Δx_{CG}, y_{CG}, and z_{CG} it is necessary first to determine x_0, y_0, and z_0 and ϵ_1, ϵ_2, and ϵ_3. If we notice that these equations for Δx_{CG}, y_{CG}, and z_{CG} hold not only for the center-of-gravity location at the model but for any point in space, we need only find a point, or points, one or more of whose range coordinates are known and all of whose station coordinates are known in order to solve for x_0, y_0, and z_0. To accomplish this, we define two points, Q and W, illustrated in Figure 6.45.

Define Q to be the point of intersection of the plumb line with the $\Delta x'$-y' plane and define W to be the point of intersection of the catenary wire with the y'-z' plane. Further, let H_Q be the distance from Q to the side film. Since Q is on the plumb line, all of whose points are by definition in the y-z plane, it follows that $\Delta x_Q = 0$. The station coordinates of Q (see also Figure 6.41) are:

$$\left. \begin{aligned} \Delta x'_Q &= \Delta x_{Qa}\frac{F_S - H_Q}{F_S} \\[3mm] y'_Q &= -F_S + C_S + H_Q \\[2mm] z'_Q &= 0 \ . \end{aligned} \right\} \qquad (6.17)$$

Similarly, since W is on the catenary wire, we have $y_W = z_W = 0$ and the station coordinates of W are given by:

$$\left. \begin{aligned} \Delta x'_W &= 0 \\[3mm] y'_W &= y_{W_a}\left(\frac{C_B F_S - z_{W_a}C_S}{F_S F_B - y_{W_a}z_{W_a}}\right) \\[3mm] z'_W &= z_{W_a}\left(\frac{C_S F_B - y_{W_a}C_B}{F_S F_B - y_{W_a}z_{W_a}}\right) \ . \end{aligned} \right\} \qquad (6.18)$$

We may now use equations (6.15) to solve for x_0, y_0 and z_0 as follows:

$$\left. \begin{aligned} x_0 &= \Delta x_Q - \Delta x'_Q - y'_Q\epsilon_1 - z'_Q\epsilon_2 &= -\Delta x'_Q - y'_Q\epsilon_1 \\[2mm] y_0 &= y_W - y'_W + \Delta x'_W\epsilon_1 + z'_W\epsilon_3 &= -y'_W + z'_W\epsilon_3 \\[2mm] z_0 &= z_W - z'_W + \Delta x'_W\epsilon_2 - y'_W\epsilon_3 &= -z'_W - y'_W\epsilon_3 \ . \end{aligned} \right\} \qquad (6.19)$$

Substituting these values of x_0, y_0 and z_0 into Equations (6.15) and adding Δz (the correction for catenary sag) to z_{CG} gives:

$$\left.\begin{aligned}
\Delta x_{CG} &= \Delta x'_{CG} - \Delta x'_Q + z'_{CG}\epsilon_2 + (y'_{CG} - y'_Q)\,\epsilon_1 \\[2mm]
y_{CG} &= y'_{CG} - y'_W - \Delta x'_{CG}\epsilon_1 - (z'_{CG} - z'_W)\,\epsilon_3 \\[2mm]
z_{CG} &= z'_{CG} - z'_W - \Delta x'_{CG}\epsilon_2 + (y'_{CG} - y'_W)\,\epsilon_3 + \Delta z\ .
\end{aligned}\right\} \qquad (6.20)$$

Note that there is a slight error in z_{CG} due to the fact that Δz is calculated at the plumb line instead of at W. However, this error is sufficiently small (0.25 mm) regardless of station size or configuration, as long as the plumb line is within a few centimeters of the y'–z' plane, that it may be neglected.

We are now ready to compute ϵ_1, ϵ_2, and ϵ_3, where again ϵ_1 is the angle of yaw of the station coordinate system with respect to the range coordinate system, ϵ_2 is the angle of pitch, and ϵ_3 is the angle of roll. The sign conventions for these angles are as follows:

ϵ_1 is positive when the Δx axis, viewed from above, is rotated clockwise from the $\Delta x'$ axis.

ϵ_2 is positive when the z axis, viewed from the side spark, is rotated counter clockwise from the z' axis.

ϵ_3 is positive when the z axis, viewed looking along the direction of the positive x axis, is rotated clockwise from the z' axis.

Notice, first, that these angles are small, and thus we can reasonably make the assumption that they are independent of each other; and second, that ϵ_3 and H_Q cannot be measured from either the side or bottom film. Therefore, ϵ_3 must be calculated from independent mechanical measurements made in the range, from which we also obtain H_Q, the distance between the plumb line and the side film platen. The assumption is made that although the range may bend about the y and z axes, or change length due to expansion or contraction, it is not as likely to twist about the Δx axis importantly. Additional reference wires could be included to eliminate this assumption, but actual measurements have shown that twisting is negligible in the only case studied by the authors.

From Figures 6.46 and 6.47 we can see that the apparent values of ϵ_1 and ϵ_2 are given by:

$$\left.\begin{aligned}
\tan\epsilon_{1_a} &= \frac{Y_L - Y_R}{X_{GRID}} \\[3mm]
\tan\epsilon_{2_a} &= \frac{Z_L - Z_R}{X_{GRID}}\ ,
\end{aligned}\right\} \qquad (6.21)$$

and z_{W_a} and y_{W_a} are given by

$$\left.\begin{aligned}
y_{W_a} &= C_1 Y_L + C_2 Y_R - Y_{GRID} \\[2mm]
z_{W_a} &= C_1 Z_L + C_2 Z_R\ ,
\end{aligned}\right\} \qquad (6.22)$$

where C_1 and C_2 are constants depending on the grid wire spacing. Using the Equations (6.14) and the assumption that ϵ_1 and ϵ_2 are small angles we may now solve for ϵ_1 and ϵ_2 as follows:

$$\left.\begin{aligned}
\epsilon_1 &= \frac{(C_S - y'_W)(C_B - z'_W)\tan\epsilon_{1_a} + (C_S - y'_W)(\Delta x_W \tan\epsilon_{1_a} - y'_W)\tan\epsilon_{2_a}}{(C_S - y'_W)(C_B - z'_W) - (\Delta x'_W \tan\epsilon_{1_a} - y'_W)(\Delta x'_W \tan\epsilon_{2_a} - z'_W)} \\[4mm]
\epsilon_2 &= \frac{(C_S - y'_W)(C_B - z'_W)\tan\epsilon_{2_a} + (C_B - z'_W)(\Delta x'_W \tan\epsilon_{2_a} - z'_W)\tan\epsilon_{1_a}}{(C_S - y'_W)(C_B - z'_W) - (\Delta x'_W \tan\epsilon_{1_a} - y'_W)(\Delta x'_W \tan\epsilon_{2_a} - z'_W)} - \frac{dz}{dx}\ .
\end{aligned}\right\} \qquad (6.23)$$

where dz/dx represents the slope of the catenary at the plumb line.

Since Equations (6.14) determined the model attitude angles in the station coordinate system $(\psi', \theta'_p, \theta', \alpha'_r)$, these angles must be corrected for the rotation of the station. Thus

$$\psi = \psi' - \epsilon_1$$

$$\theta_p = \theta'_p - \epsilon_2$$

$$\theta = \tan^{-1}(\tan\theta_p \cos\psi)$$

and
$$\alpha_r = \tan^{-1}\sqrt{(\tan^2\psi + \tan^2\theta_p)}\ . \qquad (6.24)$$

6.6.2.3 *Non-Orthogonal Projection*

Although most ballistic ranges have orthogonal-viewing shadowgraph stations it is sometimes desirable, or necessary, to use other viewing geometries. One facility in particular, the 122-meter CARDE Range 5 uses a non-orthogonal arrangement such that two light sources produce two images of the model on one piece of film[6;16] (see Figure 6.7) The proper location of the light sources, film plane and the fiducial system, consisting of two plumb lines and two catenary wires, result in geometrical relationships through which the spatial location and attitude of the projectile can be determined. This "stereo" system is explained in detail in Reference 6.16. There are, however, no real differences in principle between this system and that discussed in Section 6.6.2.1.

6.6.3 Error Sources and Determination of Accuracy

Systematic errors in recording on photographic film the position and attitude of a model in space are incurred to the degree that the recording system does not conform to the geometric relationships assumed for it. Such errors are introduced by optical refraction of light rays and by misalignment of the photographic and fiducial elements of the system. These errors must be accounted for by calibration, either through calculation, or by direct comparison of quantities measured in space with those deduced from measurements on the film. The calibration itself is, of course, subject to small residual systematic errors.

Significant random errors also may accrue from various sources. If a vibration environment exists, care must be exercised to prevent transient distortions of the reference system. Such problems may arise, for instance, in counter-flow facilities, and in transonic or subsonic tests where shock waves and pressure fields about the model may disturb an exposed reference system.

Apart from the effects of dimensional changes in the photographic film during processing, errors can arise if the film is allowed to curl or is not held precisely in the image plane during exposure. This is particularly true of a conical projection system. Complete or partial compensation for film misalignment can sometimes be effected by appropriate design and placement of the reference grid, as, for example, in a focused shadowgraph.

The accuracy of the system, once installed and calibrated, may be assessed by the consistency of the data which it produces or by artificial tests. The accuracy of the y and z measurements, for instance, can be checked by photographing catenary wires stretched through the range. A heavy projectile having low drag can be used to check the distance measurement, Δx, as well as the y and z measurements. This technique is particularly effective if the range can be evacuated.

If accurate account is kept of the apparent residual errors in the motion fit to the measured coordinates in all the stations for all the tests, systematic errors at a given station can be identified (cf. Section 7.11.5). Once the bias inserted into the results by a given station error is well documented, an arbitrary correction can be applied to the measurements made at this station. The running account of residual errors also permits early detection of changes in optical alignment and other shifts in the system which might degrade overall performance.

It should be noted that the two fiducial systems described in detail, herein, are designed to get the maximum accuracy available from the facility. The degree of attention to be given to accurate measurement systems depends entirely on the uses intended for the facility under consideration.

6.7 TIME- AND VELOCITY-MEASURING DEVICES - C.S.James

The most rudimentary ballistic-range test requires the simple determination of a velocity, while a more elaborate test usually calls for a complete time history of the projectile flight, through which various photographic and photometric measurements may be mutually related and used to study the projectile behavior. Time intervals of interest vary from several seconds for a large outdoor range to a fraction of a microsecond for a short enclosed range. In some tests, time resolution to the nearest 10^{-9} sec or less is desirable.

The one feature common to all modern ballistic time-measuring devices is an electrical or electronic time base. This time base can be simply the frequency of the power source, or it can be an oscillator controlled by a tuning fork or crystal, depending on the precision required. Beyond this common point considerable variety is found in the manner with which current systems meet their particular requirements. Some of these are purely electronic[6.1, 6.39, 6.40, 6.41]; others are fundamentally optical[6.42, 6.43, 6.44, 6.45]. They may be single-channel units capable of measuring one time interval, or multichannel units capable of measuring 50 or more time intervals[6.18]. Some units measure the time interval required to move a given distance[6.40, 6.42, 6.43]; others measure the distance covered in a given time interval[6.46].

While electronic counting or optical recording techniques are employed in the large majority of systems, two additional methods may be identified. Oscilloscopes, as opposed to counters, have been used both in interior ballistics, in conjunction with microwave interferometry[6.41, 6.47], and, to a limited extent, in the aerodynamic range[6.45, 6.48] to record and display time increments. Doppler Radar techniques, which have long been useful in large outdoor ranges over great distances, have found increasing application in the laboratory[6.39, 6.49, 6.50]. Applicability of this method in enclosed ranges is enhanced as the techniques for producing and transmitting microwave beams of shorter wavelength and narrower beam width improve.

Representative systems which utilize each of these techniques are described briefly in the following sections.

6.7.1 Electronic-Counter Chronograph

The electronic-counter chronograph, because of its flexibility, reliability, and simplicity of operation is the most widely used time-measuring device in ballistic-range work. Commercial units are available which are capable of recording, in digital form, time increments as long as 1 sec to as many as seven significant figures, on the one hand, or of resolving a time increment to the nearest 10 or 20 nsec, on the other. A typical hookup for a single-channel counter is shown in Figure 6.48 where the optical arrangement represents half of a typical orthogonal-viewing photographic station. The counter, together with those at all other stations, is started by a signal from a point in the launcher cycle, or from a sequencer or other reliable source. The counter is stopped upon the arrival of the projectile at the photographic station by a signal either from the shutter, if one is used, or from the light source. The element which controls the precise time of film exposure is selected as the signal generating element to minimize error in the time-position-attitude relationship. The interstation time increment is obtained by subtraction of adjacent counts. There are other ways of connecting and starting the counters, but the one described is believed the most reliable, in terms of both minimizing data loss due to individual station malfunction, and of accuracy in time measurement by minimizing the uncertainty due to tallied or untallied fractional counts.

While there is great flexibility in the single-channel counter, manual reading is a potential source of error when many photographic stations and counters are employed. A solution to this problem is the multiple-event digital chronograph developed for the VKF 1000-foot hypervelocity range[6.18, 6.51], which receives annunciation of projectile arrival at any of 59 measurement stations and presents the corresponding times in tabular form immediately after the shot. This system incorporates a principal 10-MHz counter which is gated by the event signals to record successive time intervals, and a secondary counter which continues the time base count while each recorded interval in the principal counter is being unloaded to a core storage. Events must be separated by at least the cycle time for this operation, which is 50×10^{-6} sec. Time-interval resolution is 2×10^{-7} sec.

6.7.2 Optical Chronographs

Chronographs have been designed which combine optical recording with an electronic time base. One design uses a rotating prism as the time-position link. Another employs a reel-type streak camera for this purpose.

6.7.2.1 Rotating-Prism Chronograph

A rotating prism chronograph[6.45] was employed in the first Ames Supersonic Free-Flight Wind Tunnel and served four photographic stations. Figure 6.49 is a schematic of this system, showing one of the photographic stations. The time base in this system was an electronic oscillator which controlled the pulsing of a mercury-arc lamp (Mazda BH-6) usually at 50 kHz. Light from the pulsed lamp and from each spark source was directed along a common vertical path to a rotating prism and brought to focus on a strip of 35-mm film held against the inner 4.5-meter circumference of a stationary cylindrical drum. Through the combined pulsing of the lamp and rotation of the prism a train of exposed spots, or pips, was spread along the film. The spacing of adjacent pips represented one period of the oscillator, 20 μsec. The firing of each station spark put an additional pip on the film. A segment of such a 35-mm film record is reproduced in Figure 6.50. Flight time of the projectile between stations was determined by counting the full and interpolating the fractional time-base intervals between station pips.

To realize the maximum precision of the system and yet not risk loss of data by overlapping of the record, it was necessary to spread the record of station pips over the full circumference of the drum, but no more. To do this required a reasonably good prediction of the velocity of the projectile, so that the proper rotational speed of the prism could be established. Overlap of the record was prevented by opening a magneto-mechanical shutter just prior to the arrival of the projectile at the first station, and then quenching the pulsing lamp after the prism has subsequently made one complete turn. With a good film record this system was capable of time resolution to the nearest 10^{-7} sec over a total period of 4 msec with the prism turning at 15,000 rpm.

6.7.2.2 Streak-Camera Chronograph

The streak-camera chronograph was developed at the US Naval Research Laboratory (NRL) and evolved from a drum-camera "streak-spot" technique[6.52]. As presently constituted, it is in use both at NRL[6.42, 6.43] and at the Air Force Materials Laboratory[6.44]. In essence, the chronograph functions as follows: As a projectile moves past each successive recording station, its shadow image is projected onto a moving strip of film, together with a time-base reference. The separation of shadow images on the film is interpreted as projectile transit time between recording stations.

A schematic of the arrangement, with one recording station, is shown in Figure 6.51. The system consists of a Fastax streak camera, a pulsed-light source, an illuminated slit at each recording station, and a system of mirrors which, together with the camera lens, project the images of the pulsed source and slits onto the moving film. The time base is a 10 kHz signal generator, which in the one system controls the pulsing of a flash lamp, and in the other controls a shutter which chops the steady output of a tungsten-iodine lamp. The pulsed light is brought to focus on the moving film by the camera lens and produces a train of timing pips. The vertical slit at each recording station is normal to the projectile trajectory and is illuminated from across the flight-path by a steady light source. The image of the slit is rotated into a horizontal direction by a three-mirror system so as to be normal to the direction of film motion when the camera is operated in its normal erect orientation. Lightpath extenders are placed where needed to make all optical path lengths equal. This permits all

images to be focused in the film plane by the single camera lens and ensures equal magnifications. It also ensures that the transmission times from slits to film are equal. The Xenon winker lamps are discussed in a subsequent paragraph.

As the film moves, the slit image from each station sweeps out an exposed band along the film strip. When the projectile, or any other object on the trajectory, passes the recording station, its shadow moves across the illuminated slit producing a shadowgram on the film. Under ideal conditions, prior knowledge of the projectile velocity, together with the optical magnification of the system, allows matching the speed of the film and that of the projectile image, so that there is no spatial distortion of the shadowgram. In practice, mismatches occur which produce moderate fore-shortening or lengthening of the image. This does not significantly affect the time-measuring function of the system.

Figure 6.52 is a portion of a film record, obtained in the NRL facility, for a spherical projectile and several sabot pieces. The film and image motion are from right to left. The spaces between the timing marks in the middle of the film strip each represent 100 μsec. The lower band is from a slit at the first station, while the upper bands are from slits at succeeding stations. At this portion of the film record the model and sabot cluster have passed the first two stations, and their images appear in the first two bands. The horizontal displacement of the projectile images in these bands, measured to the scale of the timing marks, represents the elapsed time of flight between recording stations. With a 1.5-m interval between recording stations, velocity is measured to 0.25 percent accuracy using this system. The number of bands which can be put on one 35-mm film strip depends on the slit length and on the magnification. At NRL as many as six bands are put on one film; and by using three cameras with a common time base and placing the shadowgraph from a common slit on two camera films simultaneously, 16 recording stations have been instrumented.

An advantage which this system has, of particular significance to terminal ballistic studies, is that all objects passing the slits while the camera is recording are photographed. Thus, the space and time separation of sabot fragments, or other debris, from the projectile can be ascertained. Another advantage is that synchronization of the cameras with the projectile flight is required only to the extent that the flight occur while the film is moving near peak speed. The projectile is effectively "self-detected" at each recording station, so that no independent sensor-trigger system is needed.

A limitation of the system is the demagnification required to match the speed of the projectile image with that of the film. The maximum translational speed of the film is about 70 meters/sec. To match this with the image speed of a projectile moving at 7-km/sec requires a magnification of 0.01, so that a projectile of, say, 5-mm diameter would produce an image of 0.05-mm diameter on the film. Smaller images than that become difficult to resolve.

It is of interest to note that, with this magnification, an allowance of 3 mm for the length of the slit image on the film would permit monitoring a trajectory 300 mm in width.

A versatile auxiliary device, used in conjunction with the streak camera, to record the times of occurrence of supplementary events is called a "Winker System"[6.43, 6.44]. An auxiliary slit is imaged on the film in the same alignment as the velocity measurement slits. Behind this slit is placed a row of eight small Xenon flash lamps each of which can be caused to discharge, through a thyratron circuit, by an event supplemental to the projectile flight, such as a flow visualization photograph or a radiometric measurement. The lamp discharge places a mark on the film, relating the time of that event to the projectile flight. The lateral position of the mark on the film is directly related to the position of the Xenon lamp in the row, thus identifying the event. The arrangement of this winker system appears in Figure 6.51.

6.7.3 Oscilloscopes as Chronographs

Oscilloscopes have been used to advantage in ballistics where it is desirable to record a large number of time intervals or to obtain a continuous time record of a characteristic such as velocity. Current application appears to be limited almost exclusively to interior ballistic studies[6.41, 6.47, 6.53], but the principle is equally applicable to range work.

6.7.3.1 Raster-Display Recording

The feature which gives the oscilloscope the necessary flexibility in meeting the usually conflicting requirements of precision on the one hand and total recording time on the other is the use of a raster display[6.47]. This may be accomplished without any electronics external to the oscilloscope in the following manner. A dual-trace scope is used (Tektronix 545 with type CA plug-in unit) with the horizontal sweep controlled by the delaying-sweep time base. The saw-tooth signal of the main time base is used as a triggered ramp generator and connected to one of the dual-trace input channels. The signal to be recorded is connected to the other input channel, and the plug-in unit set to add the inputs algebraically. A sketch of this hookup is shown in Figure 6.53. The record may then appear as shown in Figure 6.54, where the horizontal time scale is effectively folded back on itself many times. By knowing the sweep rate, a continuous velocity history – or a number of discrete velocities – is obtained. The vertical modulation of the trace may contain information as well. The number of sweep lines which can be resolved, hence the recording time, depends primarily on the amplitude characteristics of the recorded signal. If one line per millimeter can be resolved, then a total recording test time of 40 milliseconds would be possible with a 4- by 10-cm display and the sweep rate of Figure 6.54. If the record could be read to the nearest 0.2 mm, say, then corresponding time resolution would be 2 μsec. With increased sweep rate, the resolution could be improved by perhaps 2 orders of magnitude but with a corresponding reduction of total recording time.

For the arrangement described, the flyback time is likely to be a significant fraction of the sweep time and therefore must be accounted for. In addition, the nonwriting interval may cause loss of data. To avoid this problem, raster generators have been developed[6.41, 6.53, 6.54] which are substituted for the internal time bases and produce sweep patterns, such as those in Figure 6.55 which permit continuous writing. A block diagram of the generator[6.41] used to produce the sweep pattern of Figure 6.55(a) is shown in Figure 6.56. The staircase voltage signal is applied to one vertical channel of the dual-trace plug-in and added to the data signal, as before. The synchronous triangular voltage signal is applied to the horizontal channel. In addition, the accuracy of the system is improved by placing timing marks along the raster. This is done by applying short negative pulses from a time-mark generator to the cathode of the display tube. Figure 6.57 is an example of the record from such a system. In many circumstances the timing marks could be applied, alternatively, to one of the vertical channels. Reference 6.54 describes a similar raster generator which produces the sweep pattern of Figure 6.55(b).

6.7.3.2 Circular-Sweep Interval Interpolation

Another use has been made of the oscilloscope purely for the measurement of time intervals; namely, for interpolating within the least count of an electronic-counter chronograph[6.48]. The oscilloscope was made to have a five-radius circular sweep display to operate in conjunction with four spark-shadowgraph stations and a set of 1.6 MHz counter chronographs[6.45]. The sweep function is driven by a 400 kHz oscillator to give one revolution for each four counts, or 2.5 μsec. The start-and-stop pulses, defining the interval to be measured, are fed simultaneously to the z-axis grid of the oscilloscope and to the counter. A sweep frequency less than the counter frequency was purposely chosen to eliminate the ambiguity, which would arise with a synchronous frequency, as to whether or not a count was recorded if a start or stop pulse occurred very close to an instant of counter triggering. A radius-control circuit decreases the radius of the oscilloscope circle after receipt of each pulse. This serves to differentiate between start and stop pulses and identifies the spark station originating the pulse. The angular separation of successive bright spots on the oscilloscope trace represents a fraction of 2.5 μsec. The whole number of 2.5 μsec intervals is deduced from the counter reading. To locate the center of the circles and facilitate the angle measurements a sixth innermost circle is fully exposed. Figure 6.58 is a typical oscilloscope record giving three time intervals. Figure 6.59 is a block diagram of the system as it would be used to record four successive time intervals.

Comparison of this system with the rotating prism chronograph described earlier has established an accuracy for this system equal to or better than $\pm 10^{-7}$ sec. Uniformity of the sweep rate was such that angular positions could be read to an accuracy equivalent to $\pm 2.5 \times 10^{-8}$ sec. Use of higher-frequency counters would permit a higher rotation rate of the circular sweep and correspondingly greater potential accuracy.

The radius control circuit of the oscilloscope could be made to produce a spiral raster in which case the oscilloscope would be used in a manner analogous to that described in the first example. This would obviate the need for counters, but would greatly shorten the total recording time for a given accuracy. Using the 400 kHz sweep rate as an example, if one-millimeter spacing to a maximum radius of 50 mm were achieved, a 125 μsec recording period would be available.

6.7.4 Doppler-Radar Measurement of Velocity

The Doppler-Fizeau principle has been applied in the ballistic range using CW microwave radar to measure velocity directly from determination of the Doppler frequency, in a head-on orientation of the incident beam and the projectile. The use of this technique and its application to drag determination is treated in Chapter 10. It is sufficient to mention here that such systems have been developed[6.39, 6.55] which are capable of measuring velocities of small projectiles in relatively small range enclosures (e.g., 2-m dia) over distances measured in tens of meters to an accuracy approaching 0.1%.

Doppler radar may also be applied in an interferometer mode, as is now done in the study of interior ballistics (cf. Chapter 10). A unique application of this mode to range measurements, which allows the determination of a time-distance history and at the same time provides sequential triggering of range photographic stations has been employed at the Deutsch-Französisches Forschungsinstitut, Saint-Louis[6.50]. The system is capable, in principle, of measuring both velocity and distance. Used as an unbalanced interferometer to measure distance increments, it is coupled with counter chronographs to obtain a time-distance history. With this combination, accurate measurements of drag are more readily obtained than by the direct measurement of velocity because it does not require an accurate measurement of the time-varying Doppler frequency.

A schematic and block diagram of the arrangement is shown in Figure 6.60. The microwave antenna is placed near the butt end of the range, and its transmitted signal is directed uprange by a metal reflector which is apertured to allow passage of the projectile. The reflected signal from the moving projectile follows the reverse path back to the antenna. The wavelength, λ, of the transmitted signal is 3.16 cm (frequency of 9.5 GHz) in the installation. The photographic stations are spaced along the flightpath at multiples of the half-wavelength, $n_D \lambda / 2$. Ahead of the first station is a photoscreen separated from it by a distance $n_o \lambda / 2$. The reflected signal received by the antenna is mixed with a portion of the output signal. The resulting signal which oscillates at the Doppler frequency, f_D, is amplified and fed through a gate to a step counter which has stored in it the numbers n_o and n_D. When the projectile passes the photoscreen, the gate opens allowing the Doppler signal to reach the step counter which sends a signal to a pulse distributor at the end of n_o half-cycles of the Doppler signal and every n_D half-cycles thereafter. The pulse distributor, in turn, triggers the photographic light sources and counter chronographs in order. At the end of the flight, the projectile penetrates a trigger screen which closes the gate. The design of the microwave unit permits the use of a low-power klystron

of about 20 mW output to track accurately a 3-cm-diameter projectile from a distance of 15 m. Smaller projectiles with sharp tips require higher transmission energies. A velocity-distance relationship having scatter as low as 0.01 to 0.02% has been obtained with this system, so that accurate drag measurements are possible.

6.7.5 Precision Requirements

The precision requirement of a time-measuring system depends in part on the accuracy demanded in the derived quantities of interest, in part on the accuracy of related measurements, and in part on the magnitude of the time interval to be measured. While a comprehensive treatment of error analysis, as it relates to data reduction, is given in Chapter 7, it is useful here to illustrate precision requirements which may be placed on the time-measurement system by considering, in a simplified manner, two example situations – one in which only velocity is to be determined, and one in which drag is to be determined.

Suppose that one is interested in measuring the velocity of a projectile, over a distance interval of 5 meters, to an accuracy of 1 part in 10^3, or 0.1%; and suppose further that the anticipated distance measurement error is, say, 5 parts in 10^4. It can be shown that to good approximation the uncertainty in velocity is

$$\frac{\epsilon(V)}{V}\bigg|_{max} = \frac{\epsilon(t)}{t} + \frac{\epsilon(x)}{x} , \tag{6.25}$$

where $\epsilon(t)/t$ is the uncertainty in the measured time increment and $\epsilon(x)/x$ is the uncertainty in the measured distance increment. It follows, therefore, that the tolerable error in time, $\epsilon(t)/t$, is 5 parts in 10^4, or equal in this example to the anticipated distance error. For a velocity of 1 km/sec, time must be measured to the nearest 2.5 microsecond; for a velocity of 10 km/sec, time must be measured to the nearest quarter of a microsecond.

As a second example, suppose now that one must determine the drag coefficient of a 1-cm-diameter aluminum sphere flying at a velocity, V, of 5 km/sec in an atmosphere whose density, ρ, is 0.1 atmosphere. The determination is to be made by measuring the time increments, t_1, and t_2, required to cover two successive distance intervals, x, of 5 meters each. Suppose, further, that the drag coefficient, C_D, must be determined within an accuracy of 1%. The governing equation may be written

$$\frac{1}{V^2} \frac{\Delta V}{t} = C_D \frac{\rho A}{2m} , \tag{6.26}$$

where, because $\Delta V \ll V$,

$\quad$ V may be taken as the average velocity over the combined intervals,

$\quad$ ΔV is the difference between the two measured velocities: $(x/t_1) - (x/t_2)$,

$\quad$ t is the time interval over which the velocity changes by ΔV,

$\quad$ A is the projected frontal area of the sphere,

$\quad$ m is the mass of the sphere.

The value of C_D is taken as 0.9 for this example. The computation may be greatly simplified if it is assumed that

1. All of the measurement error resides in t ; that is, all measured quantities not involving t are exactly known;

2. The quantities involving t may be decoupled and the error limitation in each treated separately. (Care must be taken in making this assumption. For the present example, it is justifiable).

It can then be stated that

$$\frac{\epsilon(t)}{t} = \frac{\epsilon(V^2)}{V^2} = \frac{\epsilon(\Delta V)}{\Delta V} \leqslant 0.01 . \tag{6.27}$$

At a velocity of 5 km/sec the time required to fly 5 meters is 10^{-3} sec, so that

$$\epsilon(t)_t \leqslant 0.01 \times 10^{-3} = 10^{-5} \text{ sec} .$$

Similarly, by neglecting second-order terms in $\epsilon(t)$, it can be shown that

$$\epsilon(t)_{V^2} \leqslant 0.01 \times \frac{t}{2} = 5 \times 10^{-6} \text{ sec}$$

and that

$$\epsilon(t)_{\Delta V} \leqslant 0.01 \frac{t_2 - t_1}{2} = 7.6 \times 10^{-8} \text{ sec} .$$

It is clear that the error limitation on ΔV determines the permissible error in t.

If the configuration in this example were a slender cone ($C_D = 0.01$) the permissible error in t, $\epsilon(t)_{\Delta V}$, would be only 0.6×10^{-9} sec; and if finite errors in other measured quantities were to be compensated for, this number would be still smaller. Present-day technology would be hard put to meet such a requirement. As a practical matter, however, the accuracy limitations of related measurements must be considered in arriving at a realistic requirement for the precision of time measurement. For example, it is clear from Equation (6.25) that there is little to be gained by requiring a higher order of precision in the time measurement than is attainable in the distance measurement.

In practice, it is found that error limits such as these just calculated can be greatly relaxed if redundant measurements are obtained (e.g., several successive measurements of V or ΔV) and treated simultaneously by a least-squares[6.56] technique. This permits the derived quantity to be determined with an accuracy greater than that of the individual measurements, provided that the measurement errors are random. This subject is treated in detail in Chapter 7.

6.7.6 Sources of Systematic Error

The primary sources of systematic error in time measurements related to ballistics are the accuracy of the time base, differences in transmission time of time-mark signals to the recording device, and the relationship of the time-mark signal to the related distance measurement. Differences in transmission times of electronic signals can usually be reduced to the order of 10^{-8} sec by use of components having the same characteristics, and transmission lines of the same characteristics and length. If the transmission is optical or electrical, a difference in path length of 3 meters introduces a time difference of 10^{-8} seconds or more, which should be accounted for if that order of precision is required. The relationship of the time-mark signal to the distance mark is likely to introduce the greatest uncertainty if not given careful attention, particularly if the projectile is not photographed. Differences in the rise characteristics of light sources, the circuit constants of electronic shutters or sensors, or the sensitivity and directionality of sensors, can introduce time biases as great as 10^{-6} or 10^{-5} sec. Such biases can be minimized if the wave forms and strengths of the signal outputs are matched to each other and to the needs of the electronic counters so that all will operate with similar characteristics.

6.8   SENSORS AND SEQUENCERS FOR INSTRUMENT AND TEST-FUNCTION CONTROL – C.S. James

The extremely short duration of the typical ballistic-range tests, which may last one second for a low-speed flight in a long range, or 10^{-3} sec for a high-speed flight in a short range, is a dominant factor in the design of the equipment used in the conduct of the test. This is particularly true of a short-duration counterflow facility where proper timing of the counterflow generation, launcher cycle, and data gathering is critical. A problem inherent in ballistic-range testing, therefore, is that of coordinating these functions.

Two types of controller have evolved for this purpose: sequencers, which provide a programmed series of command signals to prescribed functions; and sensors, which provide a command signal upon detection of some characteristic of the event. The sequencer tends to be simpler, and more reliable when the time of the event or the rate at which it takes place can be controlled or accurately predicted. When this is not the case, sensors are more reliable. More often than not both types are found in a given facility, with the sequencer coordinating the operational components of the range, and initiating the event, and with sensors controlling the instrumentation. Frequently the two modes of control are directly coupled. For example a sensor may be used to initiate one or several time-delay circuits, which in turn control subsequent functions.

6.8.1   Sequencers

The sequencers used in ballistic ranges are almost all either electromechanical or electronic in operation. Motor-driven cams operating mechanical switches have some application. Electronic time-delay circuits are most often used where time increments must be short and precise. Multichannel electronic counter circuits and capacitor charge circuits have been built[6.57, 6.58] which can provide considerable flexibility in controlling complex instrumentation over periods ranging from a few microseconds to several minutes. In addition to its control function, the sequencer may also contain the time base[6.57].

Sequencers which are not based upon the time-delay principle, and which might be classified as hybrids, have found some application. One such device[6.59] is used to synchronize a reel-type cine camera with the event. An induction probe is placed near the teeth of the drive sprocket and used to count a preselected number of frames during film acceleration before initiating the event. Another example is the microwave Doppler system described in Section 6.7.4, in which preselected numbers of half-waves of the microwave signal are counted to determine the proper moment for initiating each of the photographic light sources. This system effectively slaves the "sequencer" to the progress of the event.

6.8.2   Sensors

A great amount of ingenuity has been applied in the development of sensing devices. In principle, anything that is capable of responding to some phenomenon associated with the event is a potential sensor. In ballistic ranges the most important sensing function is to trigger the photographic and other data-gathering stations which must operate at the precise moment the projectile passes. Several sensors developed for this purpose are discussed here to illustrate a variety of operating principles. Some of these have found widespread application, while others have found only limited application.

6.8.2.1 Early Systems

Among the early sensors were single-or multiple-strand breakwires, printed circuits, and foil switches. These circuits were interrupted by the projectile - or momentarily connected by it in the case of the foil switch. The projectile must make physical high speed contact with these sensors, with attendant possibility of damage to the projectile. Figure 6.61 is a micro-flash photograph of a projectile, triggered by a multi-strand breakwire, and damage due to the impact is evident on the projectile nose. For situations where projectile damage is of minor consequence, these sensors find application because of their simplicity (e.g., printed circuits painted directly on yaw cards).

Microphones, or pressure switches, have been used as sensors, which respond to the projectile bow shock wave. Their action thus depends on distance away from the flightpath and projectile Mach number. For Mach numbers much above 2, projectile dispersion can cause significant timing uncertainty.

6.8.2.2 Light-Decrease Systems

The term "light decrease" can be used to classify a group of sensor-trigger systems which respond to the interruption or attenuation of a beam or screen of light by the projectile. In this context the word "light" refers to virtually the entire portion of the electromagnetic spectrum from microwave to X-ray. The first systems made use of visible light as do most systems now in use. A steady light source and a photo-sensor are placed on opposite sides of the flightpath. Light from the source is collimated by a two-dimensional lens, or a three-dimensional lens apertured with a slit, to form a screen across the flightpath. The light is then focused onto the sensor by another lens. Figure 6.62 is a sketch of this arrangement. A projectile passing through this screen interrupts part of the light, causing the sensor to respond with an electrical pulse which is amplified and used as a trigger signal. Mirrors are often used in place of the lenses to produce folded optical paths or to make wide screens.

The width of the screen and the size of the projectile determine the strength of the output signal in relation to electrical and optical noise. It is desirable, therefore, to use a screen no wider than is necessary to ensure its penetration by the projectile. For some applications, particularly near the gun, a narrow beam will suffice, in which case the entire beam may be interrupted. To retain the advantage of a narrow beam and still get effectively a wide screen, a folded multipass optical path can be used. Two such arrangements are shown in Figure 6.63. Optical alignment and optical noise due to vibration become more critical with these arrangements, however, and shielding from stray light may be more difficult. The strength of the output signal depends also on the thickness of the light screen in relation to the length and shape of the projectile. For maximum signal strength the thickness of the screen should be no more than the length of the projectile, and for some shapes (e.g., slender cones), considerably less.

Measures to reduce the noise level of the system are sometimes required. These may include the use of a filtered D.C. power supply for the light source, to eliminate any ripple present; use of a photodiode sensor and transistorized trigger circuitry to eliminate microphonic noise in the electronics; shock mounting of optical components to isolate them from vibration; and shielding of the sensor from stray light. Optical noise due to vibration may be minimized by taking care to overfill each optical component, including the sensor, with the incident light by an amount slightly greater than the vibration amplitude of the beam to prevent momentary vignetting, chopping, or extinction of the peripheral rays.

A problem with the visible light system which can arise, particularly when it is used with a direct shadowgraph installation, (Section 6.3.1) is the protection of the shadowgraph film from fogging by the light source in the sensor-trigger system. Shielding is often ineffective. The usual solution, noted earlier, is to use a red filter in front of the light source, a sufficiently red-sensitive sensor, and orthochromatic film in the shadowgraph. There is a case here, however, for shifting the operating region of the sensor-trigger to the infrared. Photodiodes are available which have their peak sensitivity in the near infrared, and have microsecond response time. (An operating infrared system is described in a subsequent paragraph).

When a sensor is used to control a photographic station, there is an advantage to orienting it in such a way that it triggers at the moment the projectile is at the desired point in the field of view, so that no time delay is needed. This obviates the necessity of predicting projectile velocity and pre-setting time delays, and improves the reliability of the system. One way to accomplish this without interfering with the photographic function is to direct the light screen diagonally across the field of view of the photographic station as is shown in Figure 6.64. (The light-increase feature is discussed in Section 6.8.2.4). A configuration which works well with the direct shadowgraph and which can be integrated into the photographic station to give accurate positioning of the projectile in the photographs is that of Figure 6.65. The light source is housed in a canister between the film platens and about half way from their midpoint to their downrange edge. It is covered with a red filter and shielded with a rectangular slit such that it produces a fan-shaped light screen whose width just matches the effective photographic corridor (see Figure 6.3). A series of spherical-segment strip mirrors distributed along an arc between the photographic light sources focuses this light onto two or more photo-sensors. Each sensor is paired with two mirror segments. With the fan-shaped light screen, however, the signal strength varies in proportion to the distance of the projectile from the light source. A very similar arrangement, used in the NOL Hyperballistic Range, makes use of the large photographic station reflector to focus the fan-shaped photoscreen back across the flightpath onto the sensor, as shown schematically in Figure 6.66 (see also Figure 6.12(a)). The photoscreen light source and sensor are placed on opposite sides of the photographic light source.

An extremely simple wide-view light screen has been used for many years on open ranges at CARDE[6.2]. It consists of an apertured photocell placed directly below the flightpath to view the sky. A cylindrical lens is used to image the aperture slit at a height of approximately 2.5 meters above the photocell, the image dimensions being about 2.5 cm by 3 m. Indoors, the illumination has been provided by a back-lighted frosted diffuser and, more recently, by a linear infrared source of about 7 mm width. The infrared operation avoids fogging of photographic film. The sensor used is a 61SV lead sulphide photoconductive cell having a sensitive surface approximately 7 mm square, so that the effective screen thickness is about 7 mm at all points. In the range three cells are used to increase the width of coverage of the flight corridor. Figure 6.67 shows the relation of this light screen to other components in the Aeroballistic Range (cf.Figure 6.2).

When other sources of light can reach the sensor, for example, from the projectile flow field, gun-muzzle flash, or projectile impacts, light-decrease systems fail or become unreliable. Various approaches to the use of light-decrease systems under such conditions have been tried. Where the radiation is from the projectile flow field, a focused system analogous to the focused shadowgraph of Figure 6.8 may provide sufficient attenuation of the flow-field radiation to operate satisfactorily. Near the gun muzzle, where projectile dispersion is small, a visible-light system utilizing a narrow laser beam has been successful[6.60]. By utilizing three means of attenuating the muzzle flash – collimation, polarization, and wavelength filtering – and by interrupting the entire laser beam, a sufficiently high signal-to-noise ratio has been obtained.

Other regions of the spectrum, which permit use of a detector not sensitive to visible light, have also been employed. Some effort was put on the development of a CW X-ray beam attenuation device at the Ames Research Center with poor results. The use of X-ray scattering rather than attenuation might have proved more successful. The microwave region of the spectrum has, on the other hand, been used in "light-decrease" systems with good success[6.29, 6.61, 6.62, 6.63]. Two modes of operation have been developed. In one, the projectile interrupts one leg of a balanced interferometer circuit, upsetting the balance and producing a positive signal. In the other, the projectile simply attenuates the microwave beam. The interferometer circuit tends to be the more sensitive, but also the more complex both in construction and in use because it must be balanced before each firing. The interferometer mode does not function on a true "light-decrease" principle, strictly speaking.

An interferometer system has been developed to trigger the 38 photographic stations in the Hyperballistic Tunnel at the Laboratoire de Recherches Ballistiques et Aérodynamiques[6.61, 6.62]. This system is sketched in Figure 6:68(a). The microwave signal is generated by a klystron and separated into two branches. Ninety percent of the energy is directed into the antenna branch consisting of waveguides G1, cigar antennae E1 and E2, and waveguide G2. The other ten percent of the energy is directed into a regulation branch containing an attenuator and a dephaser. The two branches are rejoined by a T terminal and fed to a crystal detector. Since much of the energy directed to the antenna branch is dissipated in the transmission between the antennae, it is necessary to attenuate the energy passing through the regulation branch to match the amplitudes of the two signals. Before each firing the amplitude and phase of the signal in the regulation branch are adjusted to nullify the signal in the antenna branch. The crystal detector thus senses no signal. The passage of a projectile between the antennae disturbs this equilibrium both in amplitude and phase. The resulting signal (Fig.6.68(b)) is sensed by the detector, amplified, and used to trigger the photographic station. The system is operated at a frequency of 10 GHz (3-cm wavelength), and a microwave power of 50 mW. The antennae are approximately 70 cm apart. With this arrangement the system will detect a metal cylinder 3 cm in diameter and 3 cm long within an ellipsoid joining the antennae and having a maximum diameter of about 10 cm. If the cylinder is a transparent plastic (Plexiglass), the region of sensitivity is about doubled, that is, the ellipsoid has a maximum diameter of 20 cm.

An example of a microwave attenuation system is one developed at the Royal Armament Research and Development Establishment[6.63]. At present it is a two-station system operating at 9.5 GHz (3.16-cm wavelength), and is used to obtain X-ray photographs and to measure velocity. The antenna horns are mounted inside a 2.5-meter-diameter range tank on a swinging support to absorb blast loads (Fig.6.69). The transmitting horns are rectangular in section with the short dimension equal to the short dimension of the waveguide. The long side is oriented in a plane normal to the flightpath and flared to a width of 5 cm. This produces a narrow beam which opens to about 10 cm 0.3 meter away. The receiving horns have a 10-cm square opening and are separated from the transmitting horns by about 0.3 meter. Figure 6.70 is a block diagram of the microwave circuit. In normal operation a simple unmodulated wave is transmitted which results in a steady output from the crystal detector until the beam is interrupted by the projectile. For alignment purposes, the wave is modulated with a 3 kHz square wave which is monitored with an oscilloscope. The antennae are adjusted for separation and direction to give maximum power transfer, which occurs when separation is a multiple of the wavelength. With this system, however, tuning is not critical, and once adjusted the system is stable over a long time period. The system has good axial resolution in detecting small opaque projectiles (30 mm long by 6 mm diameter). Projectile shape is not critical. The system is less reliable with transparent (plastic) projectiles, at least at velocities less than 1.5 km/sec.

In the Aerophysics Range at General Motors Defense Research Laboratories[6.29], where transverse focused microwave probes are used for wake ionization studies, part of the transmitter energy for the probe is diverted through a pair of horn antennae a few centimeters uprange of the probe antennae to produce a trigger beam which is used to activate the probe recording instrument. The probes operate at frequencies of 35 GHz and 70 GHz.

6.8.2.3 Light-Increase Systems

When event luminosity is of sufficient intensity to hamper or defeat a light-decrease sensor, the sensor-trigger system can be made to respond to a light increase instead. If the luminous source is a moving projectile, the sensor must be masked to restrict its view angle to detect the projectile at the selected point in its trajectory. A device used in the AEDC 1000-Foot Hypervelocity Range[6.13], to prevent stray light from

prematurely triggering the system, is shown schematically in Figure 6.71. The field of view of the sensor is confined within the slotted opening of an optical cavity in the opposite range wall. The cavity is formed by two exponentially curved sheets of metal joined along a common seam and closed at the ends. The interior surfaces are coated with a non-reflecting black paint. The shape of the cavity prevents light rays entering it from returning to the exterior. Optical noise from stray light is thus reduced to near zero. The sensor responds when the luminous source (model) is within its fan-shaped field of view. If the structure walls opposite the sensor are effectively blackened and, if stray light is not intense, the system operates reliably without the cavity. Since dust is a good light scattering agent, maintenance can be reduced and system reliability improved if the components of the system are arranged such that both the window covering the sensor and the background surfaces viewed remain as dust free as possible. Gravity can be exploited here.

6.8.2.4 Dual-Mode Systems

Systems which can respond to either light increase or decrease are useful, since they are capable of operating over a wide range of ambient densities and velocities without fore knowledge of the luminous output of the model. Some light-decrease systems can be adapted to respond to a light increase as well. For example, in the arrangement of Figure 6.66 the sensor can view a luminous projectile as well as the reflected image of the light source and will respond in either mode. In all of the arrangements illustrated in Figures 6.62 through 6.65 a defocused image of the luminous projectile shock layer will be swept across the face of the sensor. Given an appropriate detector circuit, these systems can be operated as light-increase or dual-mode systems. There are usually problems associated with achieving sufficient sensitivity and directional selectivity of such systems to ensure reliable operation, however. One method of improving both of these factors is shown in Figure 6.64, where a second focusing mirror is placed to sweep a more sharply focused projectile image over the sensor. The sharpness of focus permissible will be tempered by the width of flightpath coverage required for reliability. This mirror is placed in such a way that the image which it forms will pass the sensor slightly ahead of that formed by the light-decrease mirror. In addition, the light-decrease mirror may be shielded to restrict its field of view to the collimating strip mirror.

If the system is to operate on either a light-decrease or a light-increase signal, the detector circuit must be designed to respond to either mode. One way to achieve this capability is demonstrated by a parallel light screen system recently installed in the NOL Hyperballistics Range[6.64] to supplement the lower sensitivity system of Figure 6.66. The output amplifier of the phototube sensor modifies the sensor output according to its polarity, as illustrated in Figure 6.72. If the projectile is nonluminous, the amplified phototube output is as shown in Figure 6.72(a). If the projectile is luminous, the phototube output is of opposite polarity in which case the amplifier distorts the signal to produce an over-shoot of the proper polarity from which the trigger pulse is taken, as shown in Figure 6.72(b). The trigger pulse then occurs at slightly different times in the two modes.

With a sensor-trigger system which will respond to either a light increase or a light decrease, the system may, under just the right circumstances, fail to respond if light reaching the sensor from a luminous projectile shock layer is just sufficient to replace that blocked from the photoscreen light source. A system which avoids this difficulty by responding to a light increase for both luminous and non-luminous projectiles is in use in the Hypersonic Range at the Royal Armament Research and Development Establishment[6.65] (Fig.6.73). The sensor, a 1P21 photomultiplier, views the flightpath diagonally across the photographic station. It is restricted by apertures to a field of view 9 cm high by 2.5 cm thick, in the flight direction. The region of the flightpath is imaged on the sensor cathode by a lens. Light from a small 48-watt coiled-filament lamp mounted near the sensor is directed, by two plane mirrors, along a path nearly coincident with that viewed by the sensor. The two paths intersect at the flightpath, where a magnified image of the lamp filament is focused by a lens placed near the lamp. The image size, being approximately 9 cm by 1 cm, coincides closely with the field of view of the sensor. When a projectile enters this field of view the sensor will respond either to light from the lamp reflected by the projectile or to light emitted from the projectile if it is luminous. The signals are of the same sign, but larger in the latter case.

6.8.2.5 Electromagnetic and Electrostatic Sensors

Sensing devices to detect projectiles, where extraneous light, vibration, or other noise sources are troublesome, have been developed at the Naval Research Laboratory[6.43, 6.44, 6.52]. These devices must be placed close to the trajectory.

One can be made to discriminate between two or more projectiles. It is electromagnetic in principle and consists of two coaxial and collateral solenoids which surround the trajectory. A direct current in the outer solenoid produces a strong magnetic field which has its axial gradient along the trajectory. A conducting but non-magnetic projectile moving through this field, experiences a continually changing field strength which induces an internal eddy current. This eddy current in turn produces a secondary magnetic field which counters slightly the strength of the primary field, thereby inducing an emf in the inner solenoid. A projectile of magnetic materials locally strengthens the primary field more than the eddy current weakens it, so that the emf induced in the inner solenoid is of opposite sign to that induced by a conducting non-magnetic projectile. As the projectile passes through the magnetic field, the induced emf in the inner solenoid varies as a sine wave, changing sign at the moment the projectile reaches the center of the field. This sign change is used as the detection signal. A nonconducting projectile or fragment induces no emf.

Another device operates on the same electrostatic principle as the Liebessart spark. It requires a projectile velocity high enough to ionize part of the gas in the shock layer. Two electrodes face each other across the

trajectory with the gap electrically stressed to 90% or more of its breakdown voltage by a pulse-forming network. As the projectile passes through the gap, its conducting shock layer triggers a spark in the gap, which discharges the pulse network and produces a detection signal. This technique has proven successful in detecting projectiles of 1.55-mm to 5-mm diameter moving at 4 km/sec, with an electrode spacing of approximately 2.5 cm, 1 kV across the gap, and range pressures up to 5.3 mb. Both coaxial blunt-ended rods and parallel rods or bars have been used successfully as electrodes.

6.8.2.6 Reliability Considerations

More often than not, sensor-trigger systems are subjected to noise fields or spurious signals of various kinds, and if multiple units are closely spaced or operated·from a common power supply, there is the likelihood of mutual interference.

Radio-frequency noise from the discharge of sparks, from high-voltage generators, or from other sources, can enter the system through power lines and exposed conductors and components, including elements of the sensors themselves. Optical noise from adjacent light sources, or from the system's own light source due to supply current ripple, can cause spurious triggering. The reliability of the system depends on the degree of success with which it can be isolated from such disturbances. Methods of isolation include shielding from RF and visible radiations, electrical and optical filtering, use of short cabling, shock mounting and massive construction to attenuate vibration, and use of transistorized circuits to avoid microphonic sensitivity. With optical systems particularly, there is often an optimum viewing direction. Other measures have been discussed throughout this section.

Advantage can sometimes be taken of the shape of the sensor output pulse both to reduce timing uncertainty and to discriminate between true and false signals. A typical pulse is sketched in Figure 6.74. The rise time of the pulse (time separation between O and C) is a function of the projectile shape and velocity, the penumbra of the light screen or viewing aperture, and the sensor response characteristic. If the trigger responds to the magnitude of the sensor signal, it will be delayed by this variable rise time, or a large fraction of it. The timing uncertainty can be reduced by designing the trigger to respond to the maximum in the first derivative of the signal at B, or in the second derivative at A. False signals having the same rise time (i.e., the same frequency) but lower amplitude can be discriminated against by triggering on the larger-magnitude derivative of the true signal at B.

The best possible application of all of these techniques is sometimes insufficient to reduce false triggering from spurious signals to an acceptable level. Also, with counterflow facilities, luminous transients and bits of debris in the counterflow may pass the sensors causing premature triggering. In such cases, a blanking circuit may be employed so that a signal pulse from the sensor is accepted only within a short time increment when the projectile is in flight. At all other times, the blanking circuit prevents the trigger pulse from being formed. This technique may be applied in a number of different ways. For example, a blanking voltage applied to one or more triggers in the range may be removed by a signal taken from the launching gun, time-delayed to allow the projectile to approach the first sensor. If there is a series of trigger or photographic stations which mutually interfere, the blanking circuit may be arranged such that the signal from each station unblanks the next successive station[6.40]. An alternative approach is to control the entire blanking function with a sequencer. To prevent multiple triggering of a photographic station by sabot fragments or other debris passing the sensor, a single-shot thyratron trigger circuit, self-resetting after a suitable time delay, is sometimes used. Where the light source is energized by a capacitor, this may also be accomplished by preventing the capacitor from recharging.

6.9 INTERPRETATION OF THE PHOTOGRAPHIC RECORD – M.E.Wilkins

The optical systems and their components described thus far produce (usually) a shadow picture of the model and certain distance measuring references or fiducial marks. After the picture is developed, the picture is used to measure positions and angles of the model as they were at the instant of exposure. The picture may also be used to study the flow configuration about the model in flight, and that aspect is discussed in Chapter 8. In this section, we consider the accurate measurement of the positions and angles.

Many factors contribute to the accuracy of the final results – the type of film used, the size and shape of the reference points of both the model and fiducial system, the quality of the photographs, the instruments used for making measurements on the film, and the judgment of the person reading the film.

6.9.1 Film Selection

The emulsion selected must achieve adequate contrast with the light available and should have a minimum grain size for clarity of enlarged images. Of great importance is the dimensional stability of the film base during development and storage. Glass photographic plates offer the best dimensional stability since glass is affected by only thermal changes (0.0009 % per $^{\circ}$C). Polyester-base films are affected by both thermal and humidity changes; in thermal expansion about three times that of glass, and from about 0.0015 to 0.0035 % per 1% change in relative humidity over a range of film base thickness of 7 to 2½ mil (0.178 to 0.064 mm) respectively. Polyester-base films, however, are usually sufficiently stable for precise work. Acetate-base film is approximately 50% less stable than the polyester in both thermal and humidity changes[6.66], [6.67], [6.68].

6.9.2 Model Reference Points

The design of the model should provide at least one reference point and line which will define its position and attitude on the film. Many models have natural references, e.g., pointed noses. All axially symmetrical bodies have a well-defined axis of symmetry. Cruciform wings provide excellent roll position references. In some cases, however, references are best added to the model. For example, a ballasted sphere might require a small pin protruding at the base to indicate the axis location, and an axially symmetric body might also, in certain cases, benefit from such a pin. Two or more pins placed off the axis of symmetry may be needed to determine the roll position. An example of a particularly difficult configuration on which to make position and attitude measurements is given in Figure 6.75. The model has an ogive-cylinder body with three highly swept wings spaced 120° apart. Since the wings extend from the tip to the base of the body, a projection of the model will not disclose the body except for the nose tip. Consequently, a base plug (in this case a screw which also served to hold the model to the sabot during launch) was attached to the base of the body to identify the model axis. The nose tip was used as a reference for x, y, and z measurements from fiducial references which do not appear in the figure. The tip and the base plug were used to define the angles of pitch and yaw, and thus to compute the position of the model center of gravity from the measured position of the tip. The roll angle was obtained from the projected positions of the model wing tips and the base plug. In this case the base plug is necessary to obtain the roll angle accurately. (One wing tip was clipped for positive identification). Assuming that distortions due to the diffraction and the refraction of light are the same along both wing edges, measurements are made from the axis (base plug) to each wing tip. Subtracting these two measurements cancels the optical distortion, and the two possible roll angles can be determined. (An orthogonal view is necessary to select the correct angle). This example will make clear both the need for and types of approaches to measuring aids designed as part of the model.

When more than one possible reference point exists on a model, the best choice may not always be immediately evident. The choice usually depends upon how well one point is visible in all the shadowgraphs of that test. For example, for the model shown in Figure 6.75, the x, y, and z measurements would have been made to the base plug instead of to the nose tip but the base plug image was occasionally partially obscured by flow coming off a wing. When a series of photographs is taken of a model at different stations, the same reference point or points on the model should be used in each. This compensates for systematic distortions in the location of the point due to refraction and diffraction. Similarly, readings of the film from several stations of the same test should be done by one person, so that subjective differences in selecting the reading point will not be introduced.

6.9.3 Fiducial System Reference

At each shadowgraph station it is necessary to relate the position of the model to that of the measuring reference system, so that the overall motion from station to station can be defined. This is most easily accomplished by allowing part of the reference system to be photographed with the model (cf. Figs.6.4, 6.7(b), 6.11(c)). The fiducial reference photographed should define the direction along which measurements are made. Plumb lines and taut wires are frequently used for this purpose. Symmetry of the part photographed is valuable, since it obviates the need to estimate the position of an edge. (Edges are indefinite in shadowgraph pictures because of diffraction, finite light-source size, etc.) Thus, measurements to the end of the image of a rod or column are not reliable unless a correction can be applied for the error due to diffraction or unless the error is compensated by being repeated in all stations. Wires, notches, spherical beads, and pinholes can be used to advantage. Where a direction reference (for angular measurements) is required, taut wires, straight edges, or pairs of pinholes are desirable. The best reference systems also provide information from which changes in optical alignment, magnification, etc., can be corrected.

6.9.4 Film Measurement

Given the images of the model and measurement references on film, the problem is narrowed to accurate measurement of distances and angles between them. For negatives of moderate size film (say up to 25 cm) machines are available to make measurements to a scale reading accuracy of about 0.002 mm (2 microns). However, with larger film sizes sometimes used in conical light field shadowgraph systems, up to 0.5 meter, for example, accuracy and ease of measurement are more difficult to obtain.

The degree of accuracy obtainable is frequently limited by the quality of the photograph from which measurements are to be taken. It is obvious that with even the most precise measuring instruments relatively poor accuracy will be obtained from blurred or indistinct images. Since the photograph of a model in flight must always have a finite time of exposure, some motion of the model is always present in the picture. Additionally, sharpness of the image is reduced by various effects such as finite light source size, and diffraction. These effects should be minimized by design wherever possible, but it is clear that the sharpness of the photographic image will often be the limiting factor in the accuracy obtained.

A simple technique for reading film is illustrated in Figure 6.76. It consists of laying a transparent grid over the film negative to be read. (In this case the grid is a glass photographic replica of an accurate master grid - the numbers have no significance here being actually spaced one inch (2.54 cm) apart.) The fiducial reference consists of a straight edge appearing at the top of the picture with vee notches every 0.6-inch (1.524 cm). After aligning the grid marks with the reference images, the coordinates of all the necessary points are read from the grid, possibly with the aid of a magnifying glass. Angles may be measured with a protractor or deduced from the coordinates. This process can be quite rapid and is frequently accurate enough to produce excellent results (linear dimensions accurate within 0.2mm). However, it allows opportunities for human error and, for high precision, involves more labor than required if more mechanized equipment is used.

A mechanical film reader consists basically of a film holder and a reticuled viewer, with provision for accurate relative motion in one or more linear or angular coordinates. The measurements of distances and angles are given by accurately machined lead screws, micrometers, etc. The determination of which parts should move is a design consideration which will not be pursued here. The measurement of the displacement will be discussed briefly, followed by some observations about optical viewers.

The translational movement of either the viewer or the film is usually effected by means of the calibrated lead screw which is in effect the length standard of the measurement. Backlash in the gearing mechanism should be eliminated to the extent possible. If present it can be compensated for by making all measurements from the same direction.

An alternative method of measurement which is free of backlash problems makes use of the moiré fringe counting technique[6.69]. Moiré fringes are produced when light passes through two transparent gratings mounted face to face with the rulings inclined to one another at a small angle. The fringes are observed to be nearly perpendicular to the rulings. When one grating is moved in a direction perpendicular to the lines with the other remaining fixed, the fringes move across the field at right angles to the direction of grating movement. The spacing of the fringes represents a magnification of the spacing of the ruling. Hence, a visual or an optical scanning count of the fringes passing a particular point is a measure of the number of rulings passing that point. A pair of gratings is required for each direction in which measurements are to be made. (Angular measurements may also be made with radial gratings.)

Another design choice in film viewers is the choice between microscope viewing of the images and enlarged image projection onto a screen. The microscope type (Fig.6.77) is probably the simpler of the two. The microscope is carriage-mounted and focused on the film, backlighted with a diffuse light source. The microscope has a reticule (usually 90° cross hairs) for alignment on the model and measurement references. The microscope may have a calibrated rotating reticule so that angles may be determined with the microscope alone or the film holder may rotate for angular measurements.

In the projection type (Fig.6.78) a high intensity point light source is used to project the film image onto the screen which contains the reticule. The reticule can be physically fixed on the screen and the screen rotated to obtain angular measurements, or an image of the reticule can be optically projected onto the screen and the image rotated. The latter method has more versatility. The image may be a shadow of cross hairs giving a dark line reference, or an image of an illuminated slit which provides a bright line reference. By use of filters the color of the illuminated slit can be chosen to give contrast with the film image.

It is possible to eliminate the human judgment factor at least in part, by use of a scanning densitometer which is programmed to locate the model and reference profiles by measuring relative densities of the film and to output the desired coordinate information on punch cards or tabulation sheets. This approach is useful for certain applications and is being increasingly exploited where many frames of cine film must be read. But accuracy, using this approach, appears difficult to achieve in the ballistic range where photographic exposures often vary considerably from one station to another and where the photographs may also include extraneous markings, such as smears on windows, fingerprints, blemishes on the film, etc., which can cause such a reading instrument to misinterpret what it sees. At present, the reading of ballistic-range film usually requires human judgment to choose the coordinate positions of the various references.

6.9.5 Design Considerations for Comfort and Speed in Reading

Since numerous measurements to high precision are required on many negatives, film reading is a slow and laborious task. In the design of a manual film reader, consideration of comfort and ease of operation can lead to improved speed and accuracy of reading.

The moving parts of a film reader, whether manually or motor driven, should be geared so as to provide relatively fast motion as well as exceedingly slow motion in approaching a reference line or point. When the distance between references is quite large, it is desirable to cover the major part of the distance as quickly as possible.

The direction of motion should be related to its control in the sense expected by the operator. It adds to the difficulties and is time consuming if the image moves in the opposite of the expected or natural direction.

6.9.6 Summary

With well designed film readers, well exposed pictures, a good measurement reference system, and care, linear coordinates accurate to 0.05 mm can be routinely obtained. Angular accuracy depends on the base length of the model being measured, and can be estimated from the linear accuracy. For example, on models 10 cm long, the angular accuracy implied by cumulative positional errors of 0.05 mm at either end is only 0.001 radian or 0.06°, while with a model with a reading length of 1 cm, the error would be 0.6°. The most essential ingredient to the acquisition of quality data, after the precautions of system design have been taken, is the motivated, conscientious reader.

REFERENCES

6.1 May, Albert
     Williams, T.J.
Free-Flight Ranges at the Naval Ordnance Laboratory. US Naval Ordnance Laboratory Rept NAVORD 4063. July 18, 1955.

6.2 Morgan, K.
Velocity Instrumentation in the CARDE Aeroballistic Range. Canadian Armament Research and Development Establishment Tech. Rept. 456/65. July, 1965.

6.3 Holder, D.W.
     North, R.J.
     Wood, G.P.
Optical Methods for Examining the Flow in High-Speed Wind Tunnel. AGARDograph 23. November, 1956.

6.4 Tanner, L.
The Design and Use of Interferometers in Aerodynamics. ARC R & M 3131, HMSO, London, 1959.

6.5 Keen, Stanley M.
Application of the "Slit-Aperture" Camera for Observation and Data Acquisition in Projectile Studies. Proc. Fifth International Congress on High-Speed Photography, Washington, DC. 1960, SMPTE 1962, pp.375-378.

6.6 Lecomte, C.
Utilization d'une Camera a Miroir Tournant pour la Photographie de Maquettes à Grand Vitesse. Proc. Sixth International Congress on High-Speed Photography, The Hague, September 17-22, 1962; Tjeenk Willink & Zoon NV-Haarlem, 1963, pp.434-442.

6.7 Meninger, R.C.
     Butenbach, R.W.
Millimicrosecond Photography with an Image Converter Camera. IRE National Convention Record, Part V, May, 1957, p.88.

6.8 Brooks, Robert E.
New Dimension for Interferometry. Electronics (McGraw-Hill), May 15, 1967, pp.88-93.

6.9 Wuerker, Ralph E.
Research on Electrostatic Charged Droplet Streams. US Air Force Aerospace Research Laboratories Rept. ARL 67-0211, October, 1967.

6.10 Charters, A.C.
      Thomas, R.N.
The Aerodynamic Performance of Small Spheres from Subsonic to High Supersonic Velocities. Jour. Aero. Sci., Vol.12, No.4, October, 1945, pp.468-476.

6.11 Braun, Walter F.
The Free-Flight Aerodynamics Range. US Army Ballistic Research Laboratories Rept. No.1048, July 1958.

6.12 Anon.
Aero and Hydro-Ballistics Research Facilities. US Naval Ordnance Laboratory Rept. NOL R 1264, July, 1967.

6.13 Lukasiewicz, J.
      Stephenson, W.B.
      Clemens, P.L.
      Anderson, D.E.
Development of Hypervelocity Range Techniques at Arnold Engineering Development Center. Arnold Engineering Development Center TR-61-9, June, 1961.

6.14 Anderson, R.Wayne.
High-Speed Photography Using Ultraviolet Radiation to Eliminate Visible Light Masking in Self-Illuminating Events. Proc. Fifth International Congress on High-Speed Photography, Washington DC, October 16-22, 1960, SMPTE, 1962.

6.15 Dyke, W.P.
      Grundhauser, F.J.
      Collins, F.M.
      Stunkard, N.W.
Recent Developments in Flash Radiography at Hypervelocities. Advances in Hypervelocity Techniques. Plenum Press, New York, 1962. Proc. Second Symposium on Hypervelocity Techniques, Univ. of Denver, March 20-21, 1962.

6.16 Léger, E.G.
      Beaulieu, R.
Stereo Flash X-ray Photo Attitude Station for Use on Ballistic Ranges. Canadian Armament Research and Development Establishment Tech. Rept. 563/67, April, 1967.

6.17 Clay, W.G.
      Slattery, R.E.
      Ferdinand, A.P.
      Kilcline, C.R.
Application of Nanosecond Light Pulses to Ballistic Range Measurements. AIAA Jour., Vol.5 No.2, February, 1967, pp.364-365.

6.18 Clemens, P.L.
      Hendrix, R.E.
Development of Instrumentation for the VKF 1000-Ft Hypervelocity Range. Advances in Hypervelocity Techniques. Plenum Press, 1962, Proc. Second Symposium on Hypervelocity Techniques, Univ. of Denver, March 20-21, 1962.

6.19 Cords, Paul H. Jr
      Thurston, Paul A.
      Noyes, William R.
A Modern Reflective Shadowgraph System for Use in High-Velocity Aeroballistic Ranges. Proc. Fifth International Congress on High-Speed Photography, Washington DC, October 16-22, 1960. SMPTE, 1962. Lib. of Congress catalog card 57-9846.

6.20 Rogers, W.K.
The Transonic Free-Flight Range. US Army Ballistic Research Laboratories Rept No.R-1044, June, 1958.

6.21 Clemens, P.L.
      Kingery, M.K.
Development of Instrumentation for a Hypervelocity Range. Arnold Engineering Development Center TN-60-230, December, 1960

6.22 Morrison, R.H.   Ames Research Center, Moffett Field, Calif: Private communication, March,1968.

6.23 Nolan, Philip   *High Intensity, Fractional-Microsecond Light Sources.* Proc. Fifth International Cong. on High-Speed Photography, Washington DC, October 16-22.1960, SMPTE, 1962.

6.24 Moden, J.C.   *Short-Duration Spark Light Sources of Extreme Luminance.* Proc. Fifth International Cong. on High-Speed Photography, Washington DC, October 16-22,1960, SMPTE, 1962.

6.25 Fischer, Heinz   *Improved Nanosecond Light Sources.* Proc. Sixth International Cong. on High-Speed
     Gallagner, C.C.   Photography, The Hague, September 17-22, 1962, Tjeenk Willink and Zoon NV-Haarlem,
     Tandy, Peter   1963, pp.152-157.

6.26 Charters, A.C.   *The Spark Photography Range.* Proc. Sixth International Cong. for Applied Mechanics, Paris, France, September,1946.

6.27 Kovasznay, Leslie, S.G. *High Power Short Duration Spark Discharge.* The Review of Scientific Instruments, Vol.20, No.9, September, 1949.

6.28 Lankford, John L.   *Feasibility Study of the Determination of Shock Detachment Distance and Ablation on Luminous Bodies Using a Laser Light Source.* US Naval Ordnance Laboratory TR 67-18, February 1,1967.

6.29 Anon.   *Aerospace Research Capabilities.* General Motors Defense Research Laboratories, TR 63-223, April,1964. (Revised).

6.30 Boissevain, Alfred G.   *Experimental Investigation of the Damping in Roll of Cruciform Triangular Wing-Body Combinations at Mach Numbers from 1.5 to 6.0.* NACA RM A54B15a, April,1954.

6.31 Liddiard, T.P., Jr   *An Explosive Light Source of Low Energy for 30-Nanosec Schlieren or Shadowgram
     Jacobs, S.J.   Photography.* Jour. Soc. Motion Picture and Television Engineers, February,1965.
     Kabik, I.

6.32 Dike, R.S.   *Quick Closing Light Shutter.* Review of Sci. Instr., Vol.36, No.8, August,1965,
     Kemp, E.L.   pp.1256-7.

6.33 Pirroni, J.S.   *High-Speed Electromagnetic Shutter.* Review of Sci. Instr., Vol.38, No.3, March,
     Stevens, R.R.   1967, pp.382-3.

6.34 Kendall, P.A.   *High-Speed Electromechanical Shutter for Time-Resolved Spectroscopy.* Applied Spectroscopy. Vol.18, No.2, 1964.

6.35 Denardo, B.P.   *Simplified Rapid Opening Mechanical Gate Valve.* Review of Scientific Inst.,
     McGee, J.E.   Vol.37, No.10, October,1966.

6.36 Schmitz, F.A.   *Explosive High-Speed Shutter.* Review of Sci. Inst. Vol.37, No.4, April,1968.
     Nims, D.J.

6.37 Chace, W.G.   *Exploding Wire Blast Shutter.* Applied Optics, Vol.2, No.4, April,1963.
     Fish, C.V.

6.38 Jenkins, Francis A.   *Fundamentals of Physical Optics.* McGraw-Hill, 1957, Lib. of Congress catalog card
     White, Harvey E.   56-12535.

6.39 Musal, H.M. Jr   *Millimeter Radar Instrumentation for Studying Plasma Effects Associated with
     Primich, R.I.   Hypersonic Flight.* Proc. of the IEEE First International Congress on Instrumenta-
     Blore, W.E.   tion in Aerospace Simulation Facilities, Paris, September 28-29,1964, PL Clemens,
     Robillard, P.E.   ed. (cf.GM-DRL Rept.TR 64-02J, August,1964).

6.40 Palkin, S.N.   *Issledovaniye unosa massy legkoplavkikh modeley na ballisticheskoy ustanovke.* In
     Reznikov, B.I.   Aerofizicheskiye Issledovaniya Sverkhzvukovykh-Techenii. Izdatel'stvo "Nauka",
     Studenkov, A.M.   Moscow, 1967, pp.274-283. (available also as NASA Technical Translat: TTF-11,
     Bykov, V.N.   309, November, 1967)

6.41 Hruby, Ronald, J.   *Microwave Technique for Measuring Projectile Time History in Light-Gas Guns.*
     Sander, Ronald, C.   Proc. IEEE Second International Congress on Instrumentation in Aerospace Simula-
     Berggren, Robert E.   tion Facilities, Stanford Univ., August 29-31,1966. P.L. Clemens, ed.

6.42 Hall, Donald A.   *New Technique for Measurement of Velocity of High-Speed Objects.* Proc. Fifth
     Atkins, W.W.   International Congress on High-Speed Photography, Washington DC, October 16-22,
     1960, SMPTE, 1962, pp.372-374.

6.43 Swift, H.F.   *Hypervelocity Capability and Impact Research - Electroballistic Program.* US Naval
     Baker, J.R.   Research Laboratory Memo Rept.1623, July,1965.

6.44 Swift, H.F.   *The Air Force Materials Laboratory Hypervelocity Ballistic Range.* US Air Force
                        Materials Laboratory TR 67-2, January, 1967.

6.45 Seiff, Alvin   *A Free-Flight Wind Tunnel for Aerodynamic Testing at Hypersonic Speeds.* NACA
                        Rept. 1222, May, 1955.

6.46 Struth, Wolfgang   *Kurzzeitaufnamen von Schüssen mit Hyperschallgeschwindigkeit in Reagierende Gase.*
                        Proc. Sixth International Congress on High-Speed Photography, The Hague, September
                        17-22, 1962, Tjeenk Willink and Zoon NV-Haarlem, 1963, pp.443-449.

6.47 Pennelegion, L.   *Microwave Interferometry Studies in Free-Piston Gun Tunnels. Advances in Hyper-
                        velocity Techniques.* Plenum Press, 1962, Proc. of Second Symposium on Hyper-
                        velocity Tech. University of Denver, March 20-21, 1962.

6.48 Kerwin, William J *Chronograph Times Supersonic Models.* Electronics, April, 1957, pp.152-155.

6.49 Koch, Bernhard   *Mesure Radioélectrique de la Vitesse des Projectiles.* L'Onde Electrique Vol.32,
                        1952, pp.357-371.

6.50 Koch, B   *Synchronizierung Ballistischer Reihenaufnahmen Mittels Radioelektrischer
     Simon, G.   Geschwindigkietmessung.* Proc. Sixth International Congress on High-Speed Photo-
                        graphy, The Hague, September 17-22, 1962, Tjeenk Willink and Zoon NV-Haarlem,
                        1963, pp.409-412. (See also: Giraud, M.; Koch, B.; and Simon, G.: "En Vol Libre
                        par Photographies Successives Déclenchées et Synchronisées par Radar". Proc.
                        Seventh International Congress on High-Speed Photography, Zurich, September 12-18,
                        1965, Verlag Dr. Othmar Helwich, Darmstadt, 1967, pp.225-229).

6.51 Clemens, P.L.   Arnold Engineering Development Center: Private communication, August, 1968.

6.52 Bailey, S.O.   *Facilities and Instrumentation of the NRL Hypervelocity Laboratory.* US Naval
     Clark, A.B.J.   Research Laboratory Rept.5271, February 18, 1959.
     Hall, D.A.
     Swift, H.F.

6.53 Knapp, R.E.   *Experimental Projectile Kinematic Studies in a Two-Stage Light-Gas Gun.* Arnold
     Hendrix, R.E.   Engineering Development Center TR 65-60, March, 1965.

6.54 Anderson, G.F.   *An Experimental Method for Measuring Continuously the Velocities of the Shock and
     Kelly, J.G. Jr   Contact Discontinuities in a Shock Tube.* Proc. IEEE Second International Congress
                        on Instrumentation in Aerospace Simulation Facilities, Stanford Univ. August 29-31,
                        1966. P.L. Clemens, ed.

6.55 Gates, D.F.   *A Doppler Radar System to Obtain Water Impact Drag Coefficients.* Proc. of the
     Haislmaier, R.J.   IEEE Second International Congress on Instrumentation in Aerospace Simulation
     Hill, L.L.   Facilities, Stanford Univ., August 29-31, 1966. P.L. Clemens, ed.

6.56 Shinbrot, Marvin   *A Least-Squares Curve Fitting Method with Applications to the Calculation of
                        Stability Coefficients from Transient Response Data.* NACA TN-2341, 1951.

6.57 Graves, Kenneth E. *Versatile Sequence Timer and Timing Generator for High-Speed Cameras.* Proc.
     Silberberg, George C. Sixth International Congress on High-Speed Photography, The Hague, September 17-22,
                        1962, Tjeenk Willink and Zoon NV-Haarlem, 1963, pp.413-422.

6.58 Wenig, Jacob   *A Time Delayed Generator for High-Speed Phenomena.* Proc. Sixth International
                        Congress on High-Speed Photography, The Hague, September 17-22, 1962, Tjeenk Willink
                        and Zoon NV-Haarlem, 1963, pp.423-426.

6.59 Hall, D.A.   *Synchronization of a High-Speed Prism Camera by Frame-Counting Technique.* Jour.
     Bailey, S.O.   SMPTE, Vol.68, March, 1959, pp.151-152.

6.60 Christman, D.R.   *Development and Application of High Velocity Impact Range Instrumentation.* Proc.
     McMillan, A.R.   IEEE Second International Congress on Instrumentation in Aerospace Simulation
     Gehring, J.W.   Facilities, Stanford Univ., August 29-31, 1966. P.L. Clemens, ed.

6.61 Berton, J.   *Etude de Barrière Hyperfréquence pour le Déclenchement de Photographies dans le
                        Tunnel de Tir.* Laboratoire de Recherches Balistiques et Aérodynamiques Note 1023
                        EAS - PV 1.

6.62 Loyen, R.   *L'Equipment de Déclenchement des Prises de Vues Photographiques de Tunnel Hyper-
                        balistique de Vernon.* Technique et Science Aéronautiques et Spatiales, January -
                        February, 1966, pp.31-35.

6.63 Fuller, P.W.W.   Royal Armament Research and Development Establishment: Private communication, July, 1968.

6.64 White, E.L.   *Projectile Detection of Luminous and Nonluminous Bodies.* IEEE Transactions on
     Fedenia, J.N.   Aerospace and Electronic Systems, Vol.AES-2, No.1, January, 1966, pp.13-20.

6.65 Wall, C.R.   *Photography of Projectiles of Near Orbital Velocities.* Proc. Sixth International Congress on High-Speed Photography, The Hague, September 17-22, 1962. Tjeenk Willink and Zoon NV-Haarlem, 1963, pp.506-572.

6.66 Anon.   Kodak Tech Bits, 1964, No.3. A Kodak Publication for Scientists and Engineers. Sales Service Division, Eastman Kodak Company, Rochester, NY 14650.

6.67 Anon.   The Kodak Compass, A Bulletin on Industrial Reproduction Processes and Materials, No.2, 1963. Sales Service Division, Eastman Kodak Company, Rochester, NY 14650.

6.68 Anon.   Kodak Professional Color Lab Letter, Summer 1968. Vol.5, No.3. Professional, Commercial, and Industrial Markets Division, Eastman Kodak Company, Rochester, NY 14650.

6.69 Guild, J.   *Diffraction Gratings as Measuring Scales.* Oxford Univ. Press (London), 1960.

Fig.6.1   Yaw-card puncture made by a finned projectile (courtesy of US Naval Ordnance Laboratory)

Fig.6.2   Yaw-card station in the CARDE Aeroballistic Range. In the foreground is a shadowgraph velocity
station with an infra-red light screen (courtesy of Canadian Armament Research and Development
Establishment)
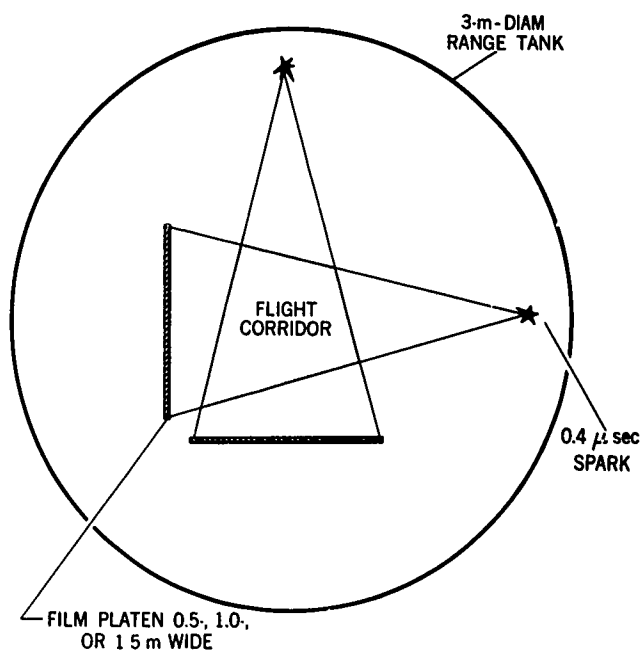
Fig.6.3   Schematic of shadowgraph configuration in the Ames Pressurized Ballistic Range.
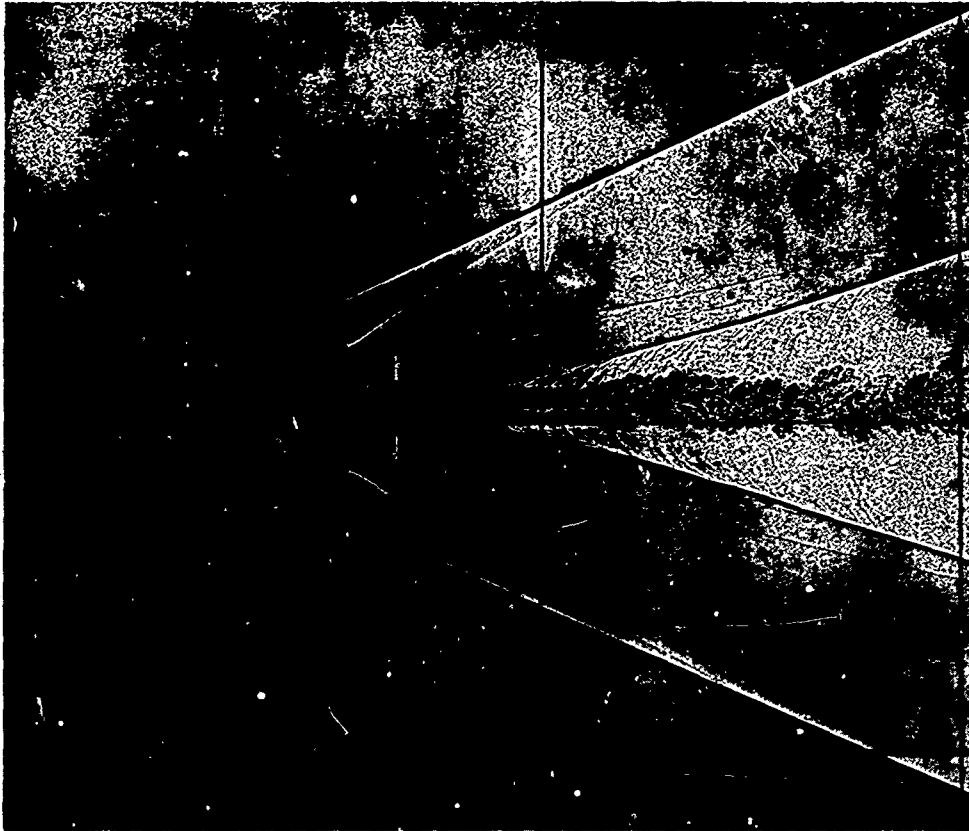
Fig.6.4   Shadowgram of slender cone obtained in the Ames Pressurized Ballistic Range.   Mach No. = 3.
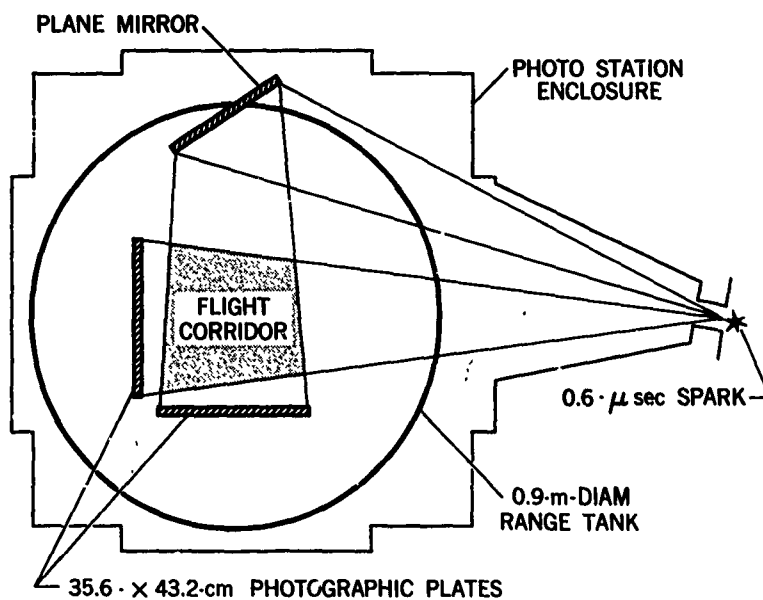
Fig.6.5   Schematic·of shadowgraph configuration in the NOL Pressurized Ballistics Range.

(a) horizontal light beam.
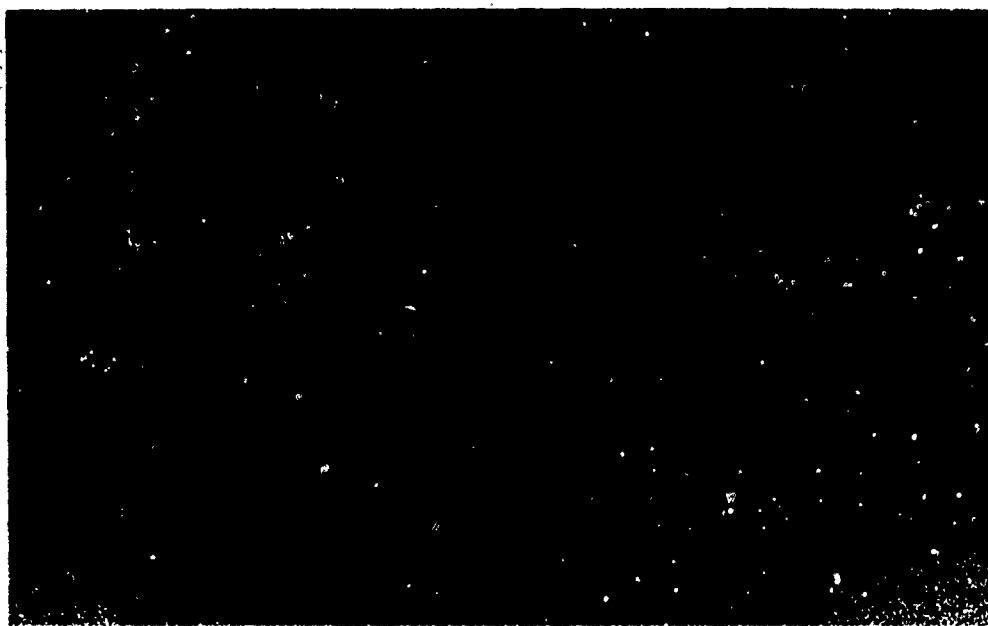
(b) vertical light beam.

Fig.6.6   Orthogonal shadowgram of a finned 10-deg. cone in the NOL Pressurized Ballistics Range.   Mach number: 5; range pressure: 436 mm Hg.   (courtesy of US Naval Ordnance Laboratory)
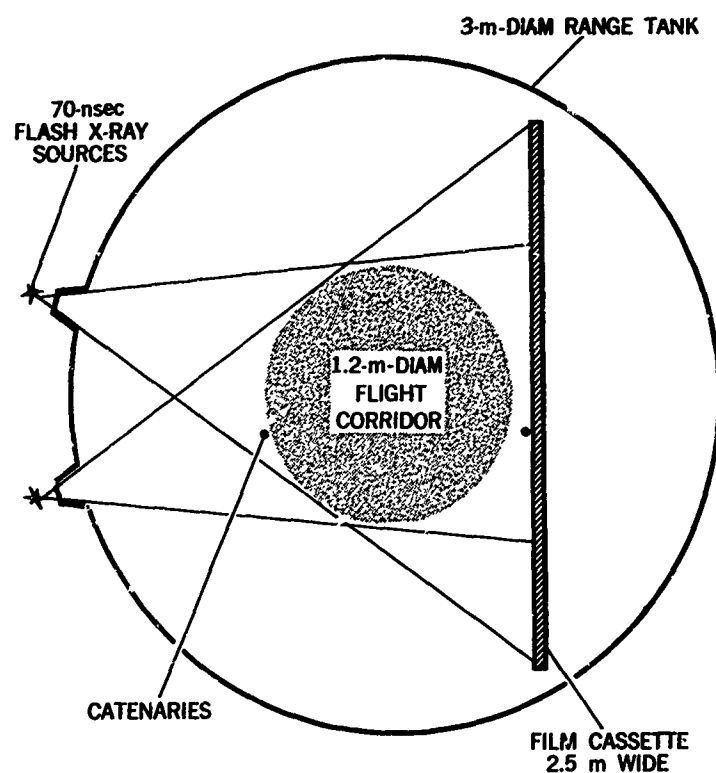
Fig.6.7(a) Schematic of nonorthogonal shadowgraph configuration in CARDE Range 5 (courtesy of Canadian Armament Research and Development Establishment)

Fig.6.7(b) X-ray shadowgram of a cone in flight; taken in CARDE Range 5. Velocity, 4.5 km/sec; Film exposure, 50 nsec (courtesy of Canadian Armament Research and Development Establishment)
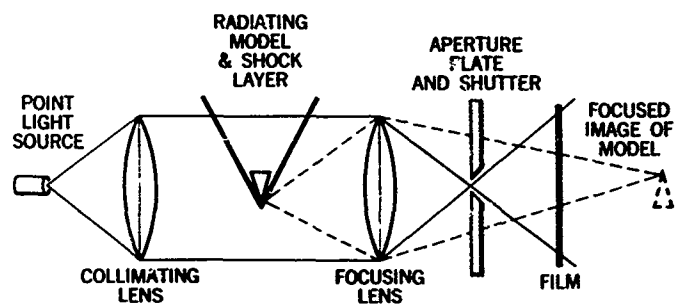
Fig.6.8   Schematic of a focused shadowgraph using lens optics
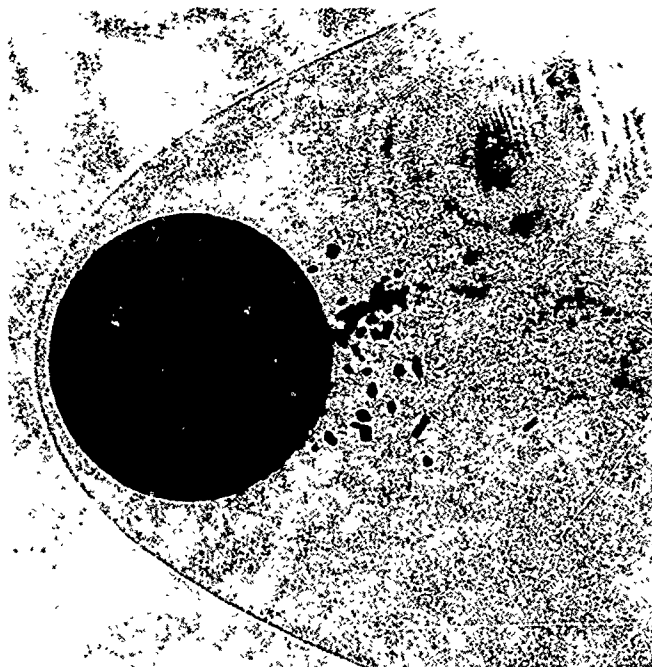
Fig.6.9   Shadowgram of a 4.8-mm-diameter phenolic sphere, exposed with a 20 nsec pulse of a ruby laser. Sphere
is moving at 5.9 km/sec in air at 40 torr. Spalled surface fragments are visible in the wake
(courtesy of Massachusetts Institute of Technology – Lincoln Laboratory)
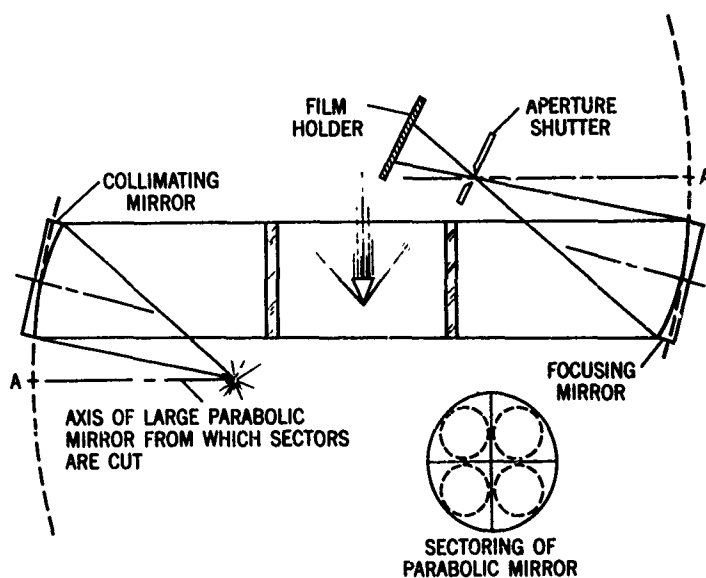
Fig.6.10   Schematic of a focused shadowgraph using mirror optics
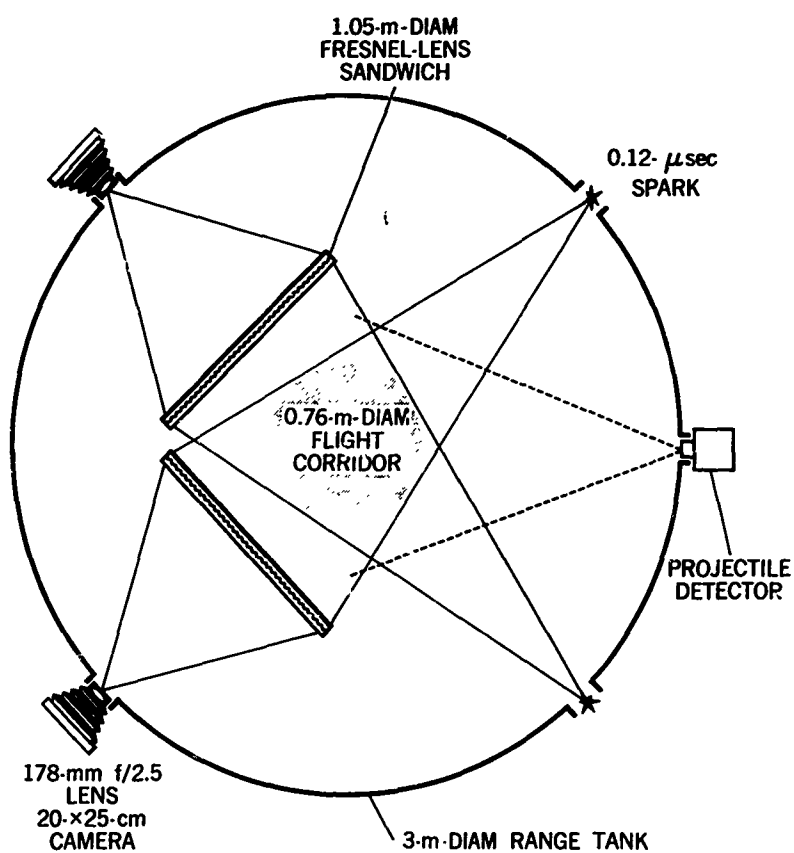
Fig.6.11(a)   Schematic of shadowgraph configuration in the von Kármán Gas Dynamics Facility 1000-ft
Hypervelocity Range

Fig.6.11(b)   Uprange view of Fresnel-lens shadowgraph stations in the VKF 1000-ft Hypervelocity Range
(courtesy of von Karman Gas Dynamics Facility, Arnold Engineering Development Center)
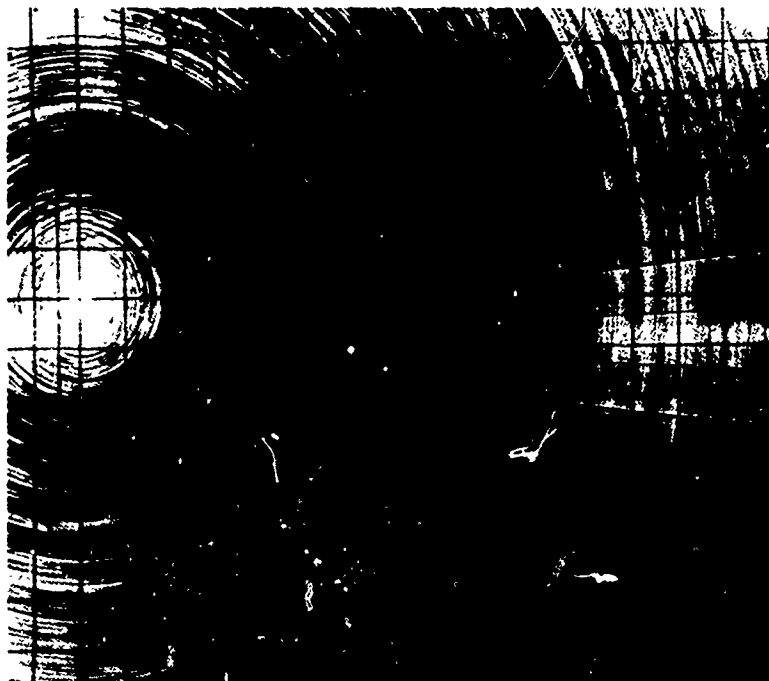
Fig.6.11(c) Fresnel-lens shadowgram of a 6-deg-semi-angle cone in the VKF 1000-ft Hypervelocity Range. Model base diameter: 20 mm; velocity: 5.1 km/sec; range pressure: 0.2 atm. (courtesy of von Kármán Gas Dynamics Facility, Arnold Engineering Development Center)
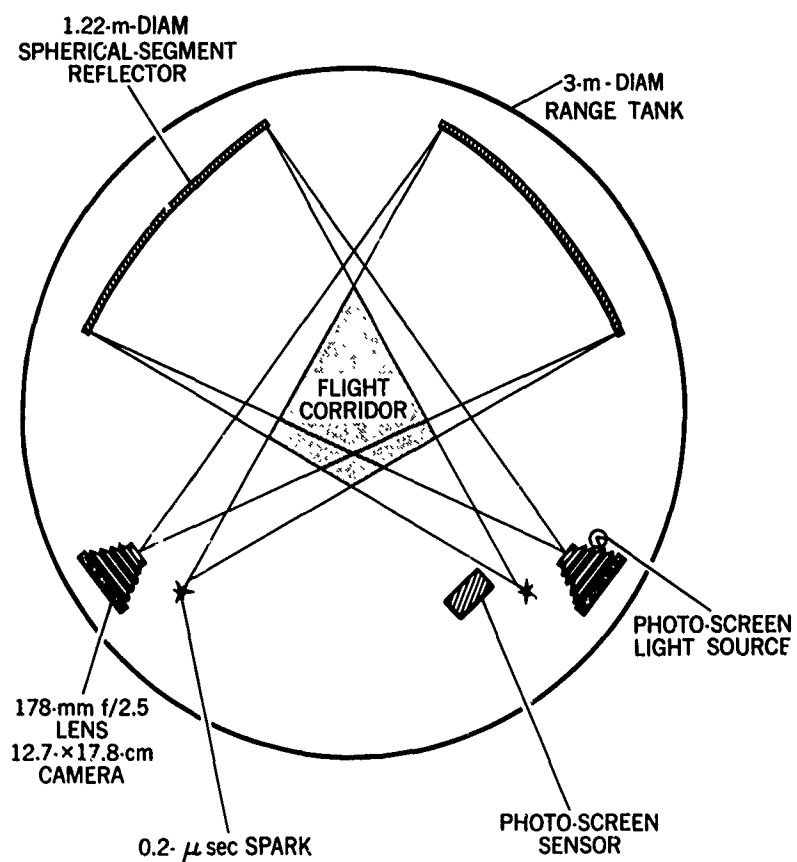
Fig.6.12(a) Schematic of shadowgraph configuration in the NOL 1000-ft Hyperballistics Range
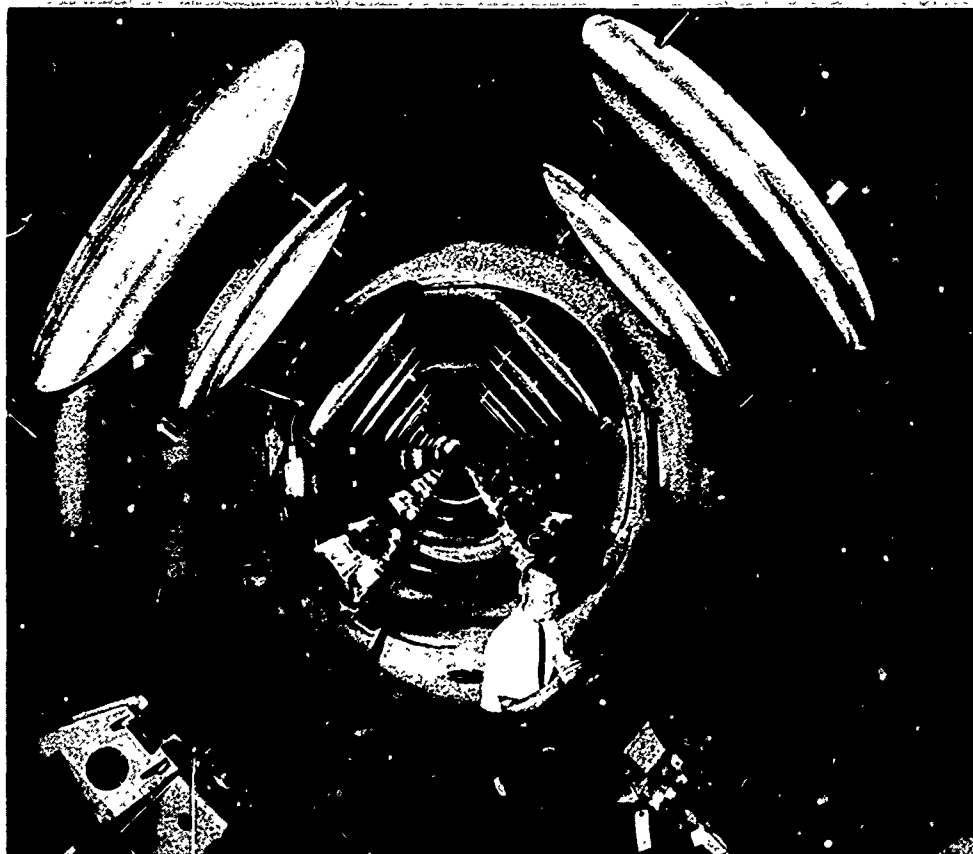
Fig.6.12(b) Uprange view of reflector shadowgraph stations in the NOL 1000-ft Hyperballistics Range
(courtesy of US Naval Ordnance Laboratory)
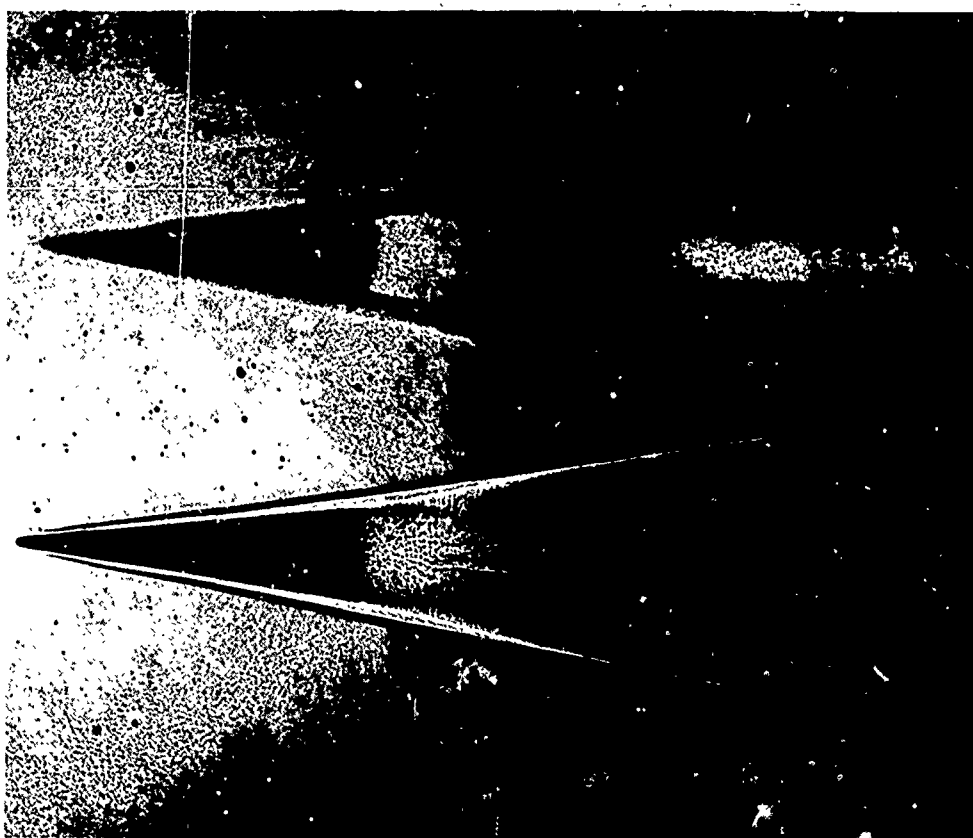
Fig.6.12(c) Reflector shadowgram of slender cone in the NOL 1000-ft Hyperballistics Range. Model base
diameter: 32 mm; velocity: 3.4 km/sec; range pressure: 1 atm. See also Figure 6.25
(courtesy of US Naval Ordnance Laboratory)
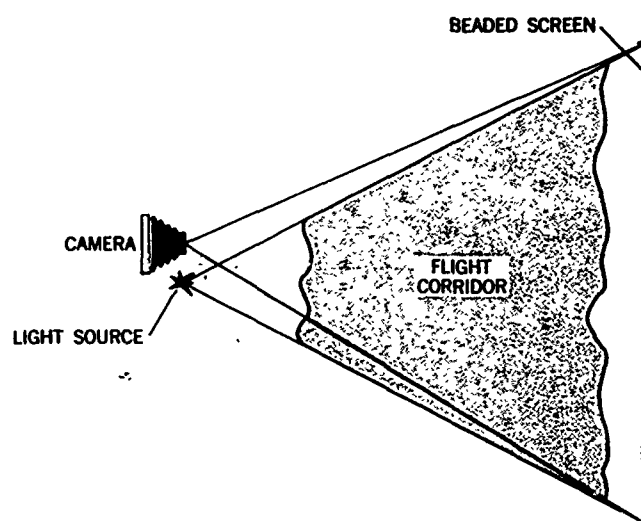
Fig.6.13   Schematic of a reflective-screen shadowgraph

Fig.6.14(a)   Downrange view of the BRL Transonic Range (courtesy of US Army Ballistic Research Laboratories)
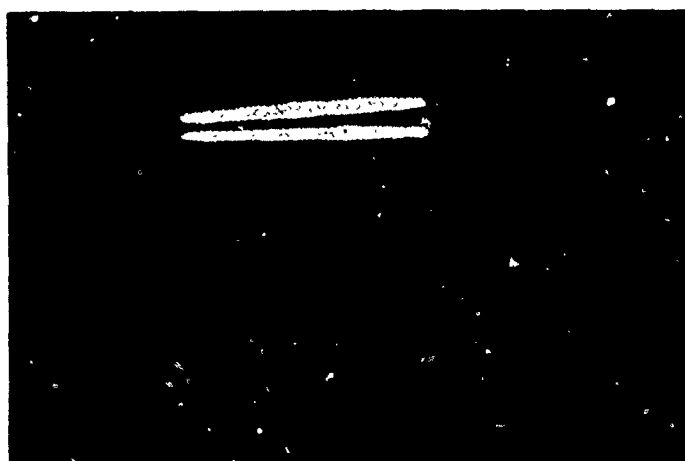
Fig 6.14(b)   Shadowgram of a double-cone model taken in the BRL Transonic Range.   Model diameter: 157 mm;
velocity: 616 m/sec (courtesy of US Army Ballistic Research Laboratories)
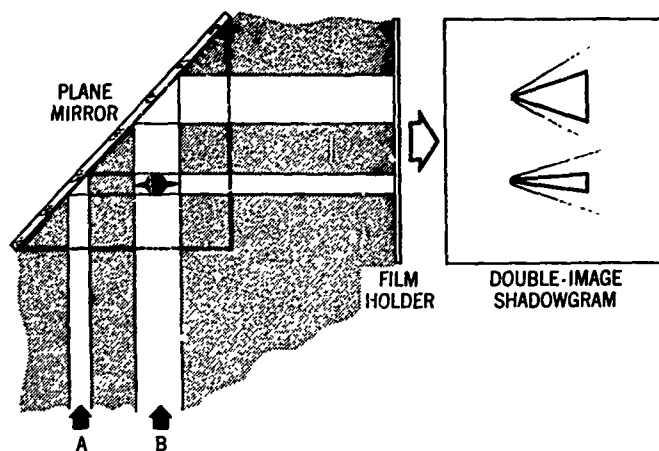
Fig.6.15(ε)   A simple orthogonal-view shadowgraph
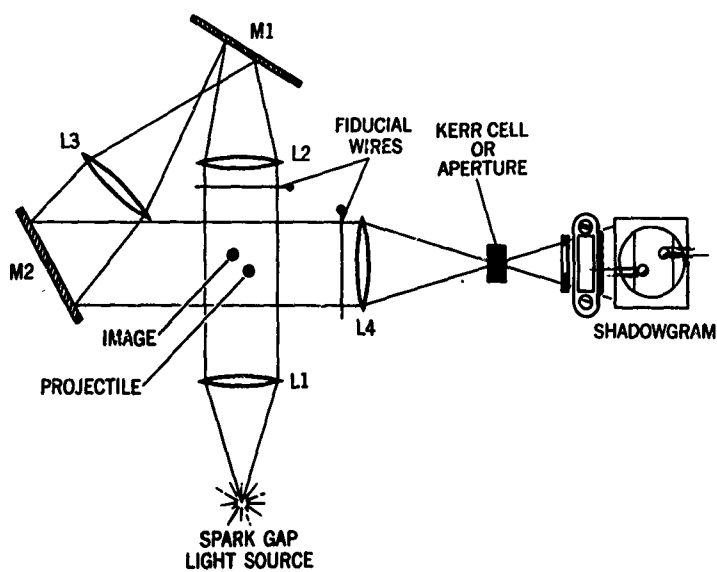
Fig.6.15(b)   Schematic of a focused orthogonal-view shadowgraph using a folded light path
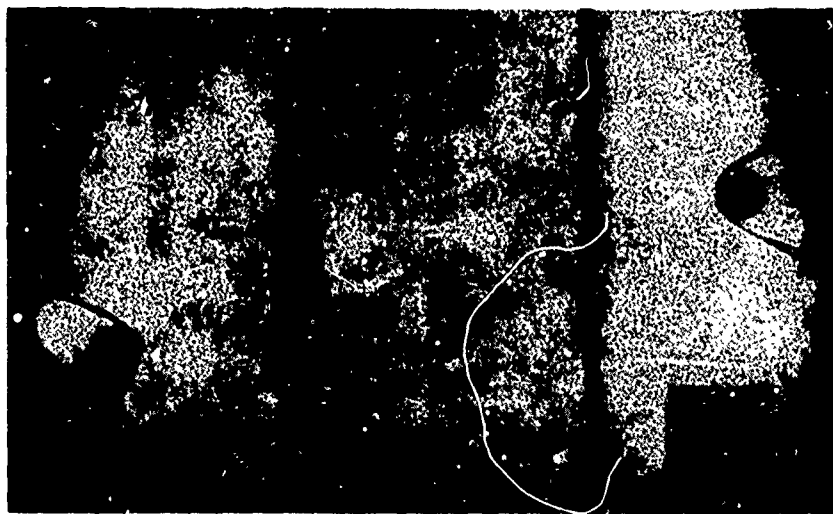
Fig.6.16   Shadowgram obtained in a small range using the configuration of Figure 6.15(b)
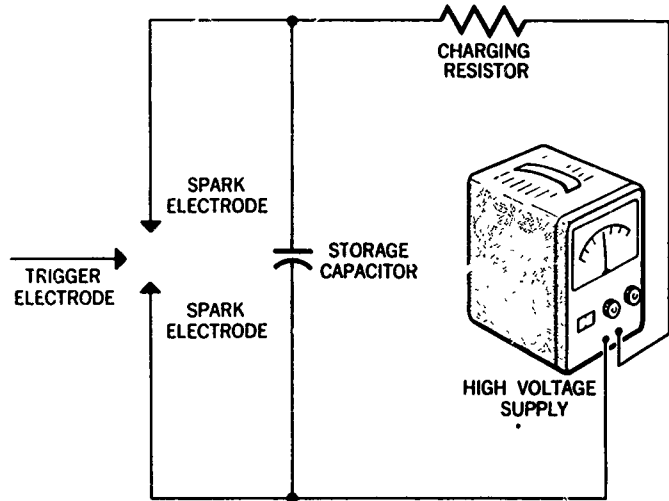
Fig.6.17   Schematic circuit diagram of capacitor-discharge-spark-gap light source
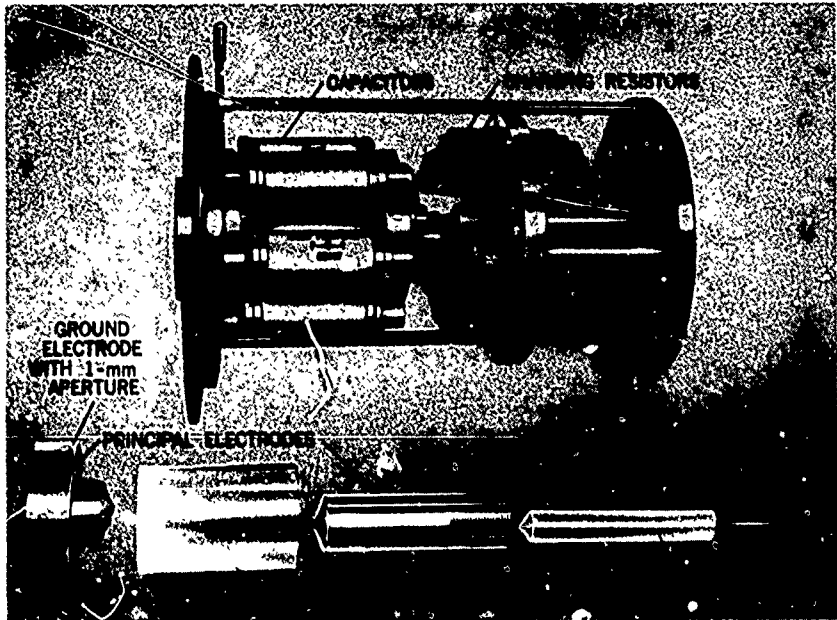
Fig.6.18   Capacitor-discharge-spark-gap light source
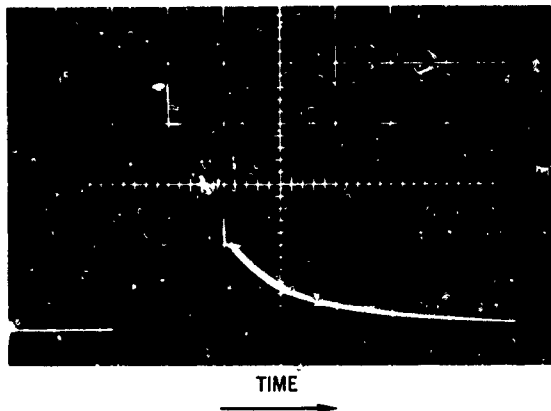
Fig.6 19   Light flux as a function of time of a capacitor-discharge-spark-gap light source, time scale: 0.2
microseconds per division
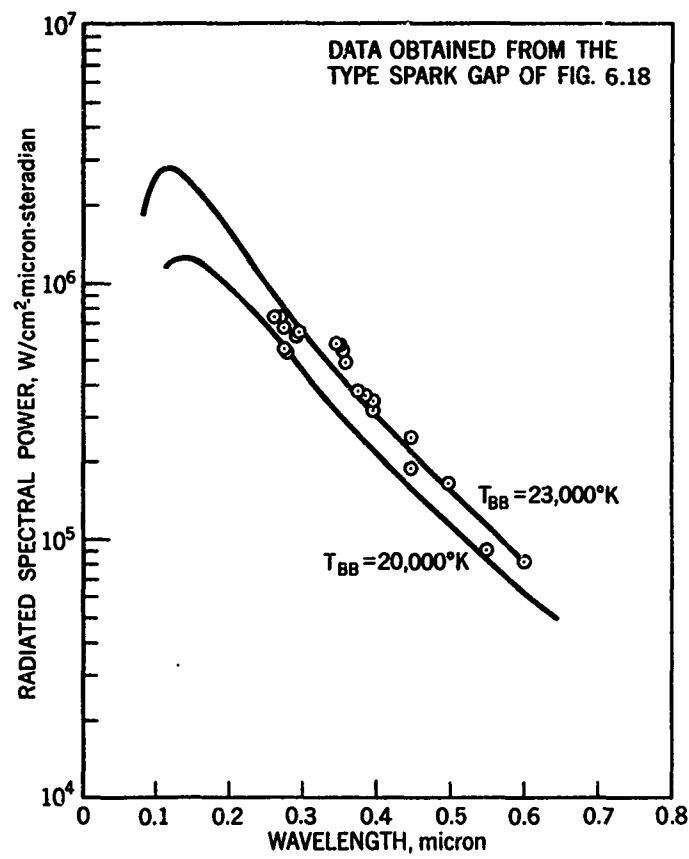
Fig. 6.20 ' Radiated power as a function of wavelength for the type of spark gap of Figure 6.18
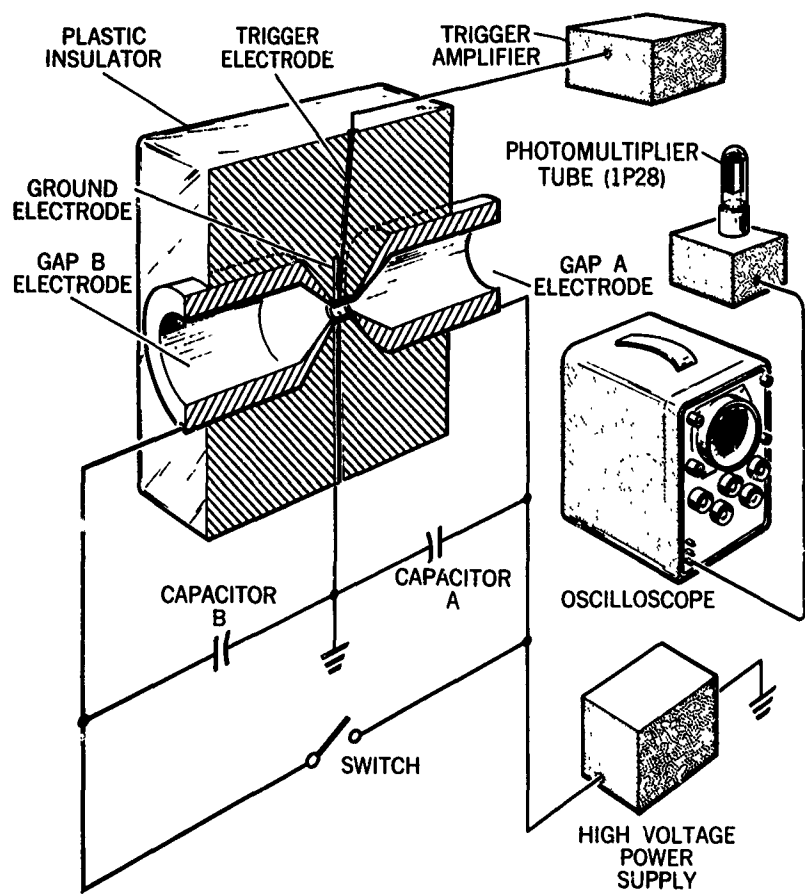
Fig. 6.21   Schematic diagram of apparatus for spark-gap absorptivity test

(a) Light output with capacitor A charged

(b) Light output with capacitor A and B charged

CAPACITORS B+A

CAPACITOR A

TIME
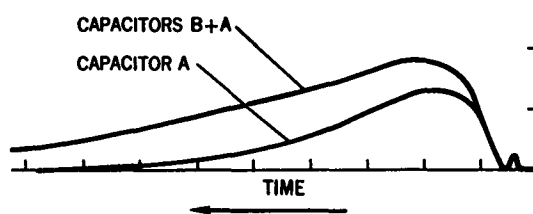
(c) Tracing of curves (a) and (b) from above

Fig.6.22   Light-output records from spark-gap absorptivity tests

PERCENTAGE OF REAR-GAP LIGHT
PASSING THROUGH FRONT GAP

REAR-GAP ENERGY PENETRATING
FRONT GAP PLASMA, percent

CAPACITOR CHARGING VOLTAGE, kV
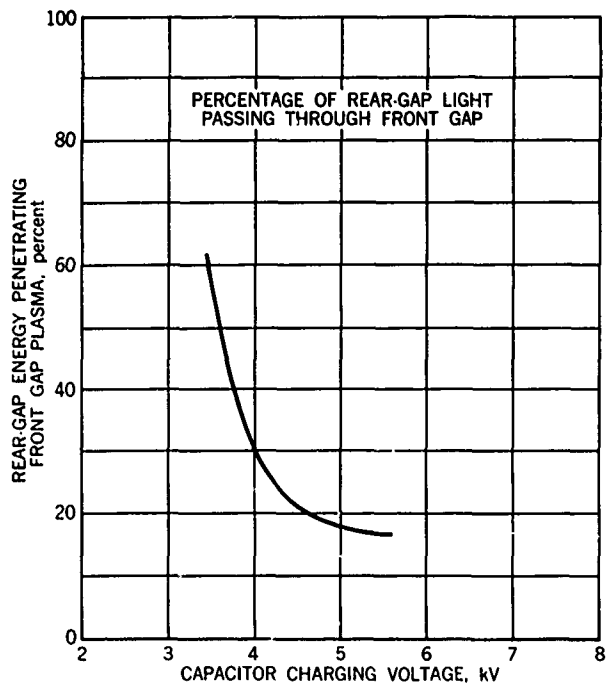
Fig.6.23   Percentage of light from gap B being transmitted through gap A as a function of capacitor charging
voltage
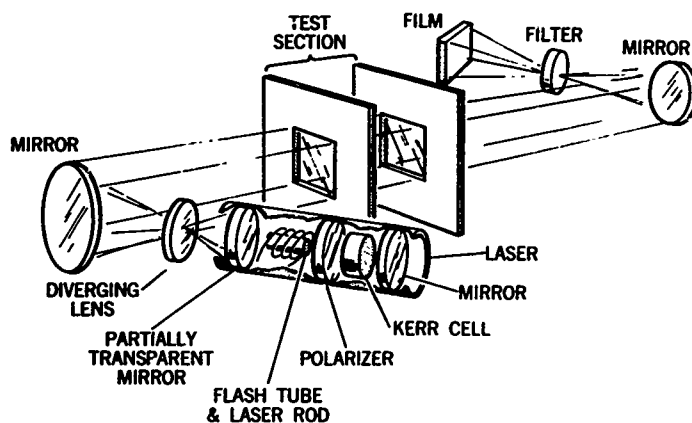
Fig.6.24   Schematic diagram of laser - shadowgraph system

Fig.6.25   Laser shadowgram from the NOL 1000-ft Hyperballistics Range; velocity of 5.2 kilometers per second, and pressure of 33 millimeters of mercury (courtesy of the US Naval Ordnance Laboratory, White Oak, Maryland)
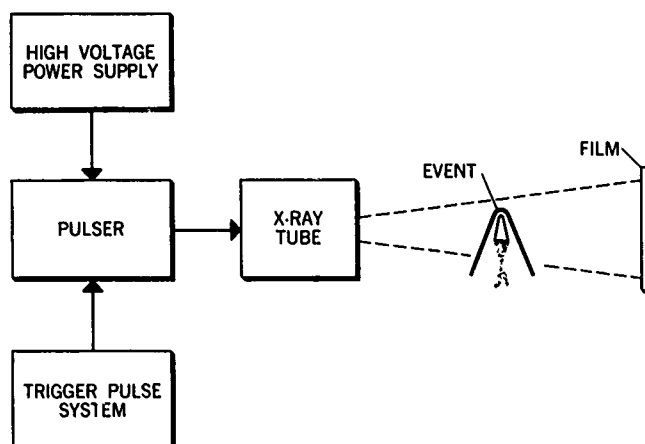
Fig.6.26   Schematic diagram of X-ray photographic system

Fig. 6.27 X-ray photographs of a model and sabot taken near the muzzle of the launch gun in the Ames Pressurized
Ballistic Range
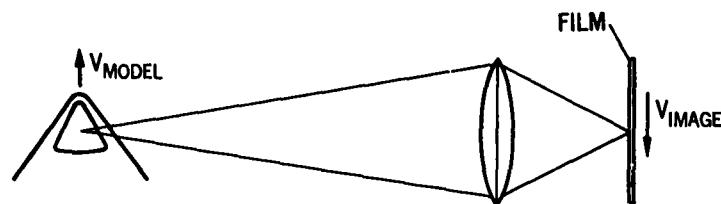
(a) Moving-film camera
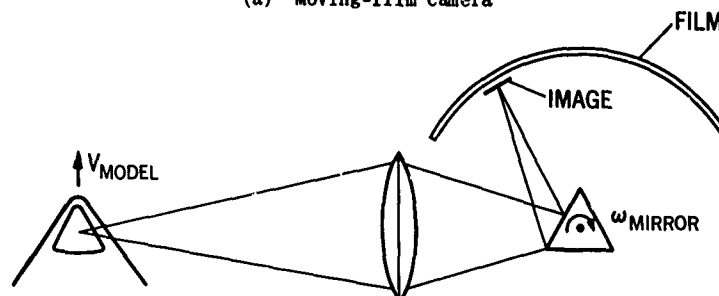
(b) Rotating-mirror camera

Fig. 6.28 Image-movement compensation
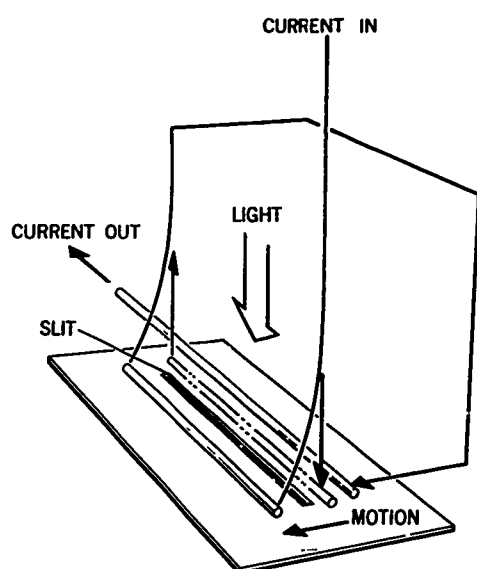
Fig.6.29   Galvanometer impulse shutter
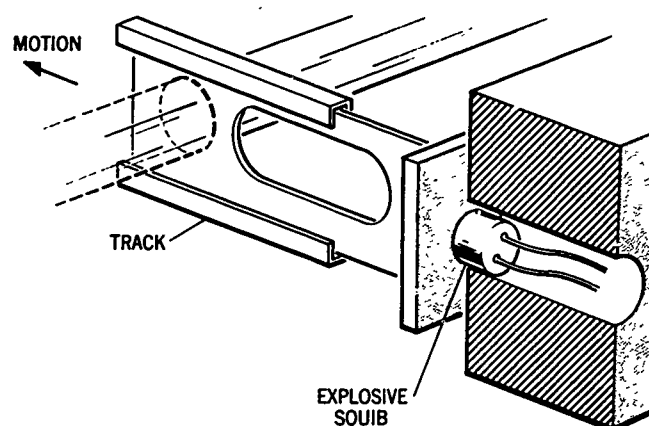
Fig.6.30   Explosively-driven blade shutter
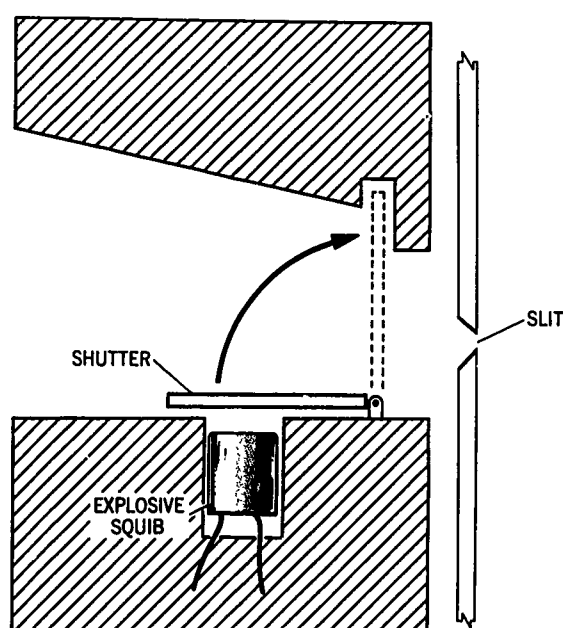
Fig.6.31   Explosively-driven pivoting shutter
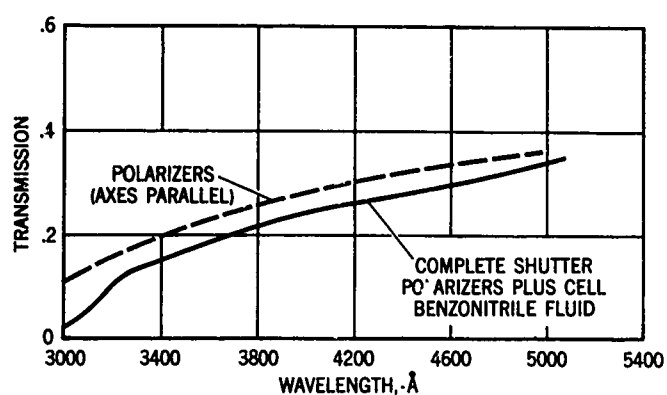
Fig.6.32   Spectral transmissivity of polarizers and complete Kerr-cell shutter

(a)   3-mm aperture at secondary image of source
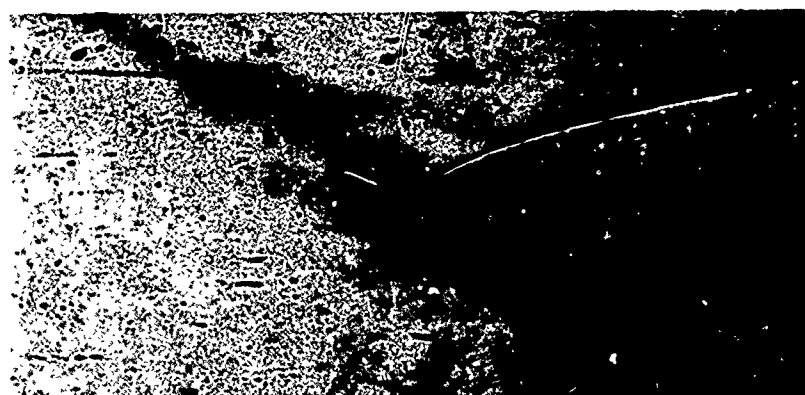
(b)   20-nsec Kerr-Cell shutter at secondary image of source

Fig.6.33   Focused shadowgram of burning aluminum model.   Velocity 6.0 km/sec; range density 0.25 atmosphere
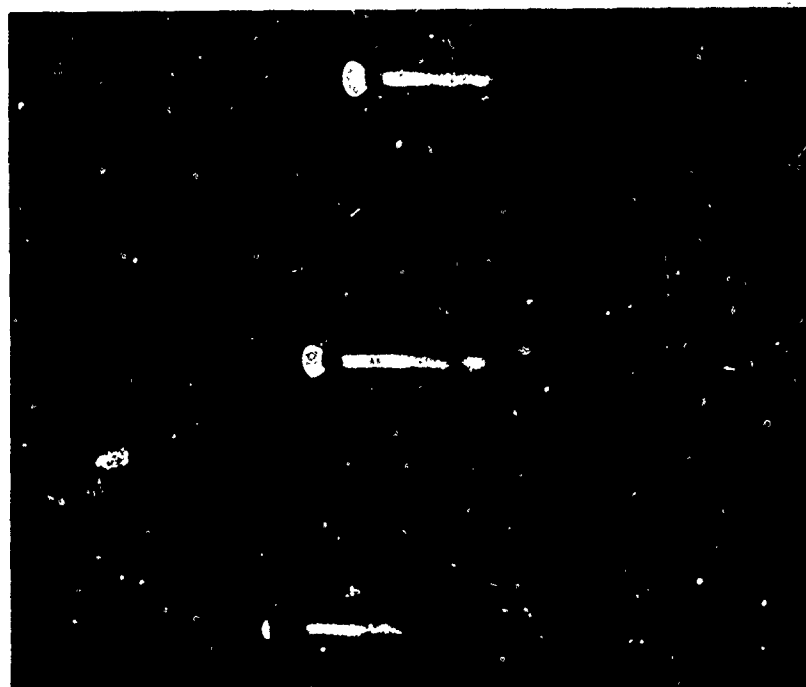
Fig 6 34   Sequential image-converter photographs of 13-mm-diameter polyethylene slug.   Velocity: 7.1 km/sec; range density: 0.1 atmosphere
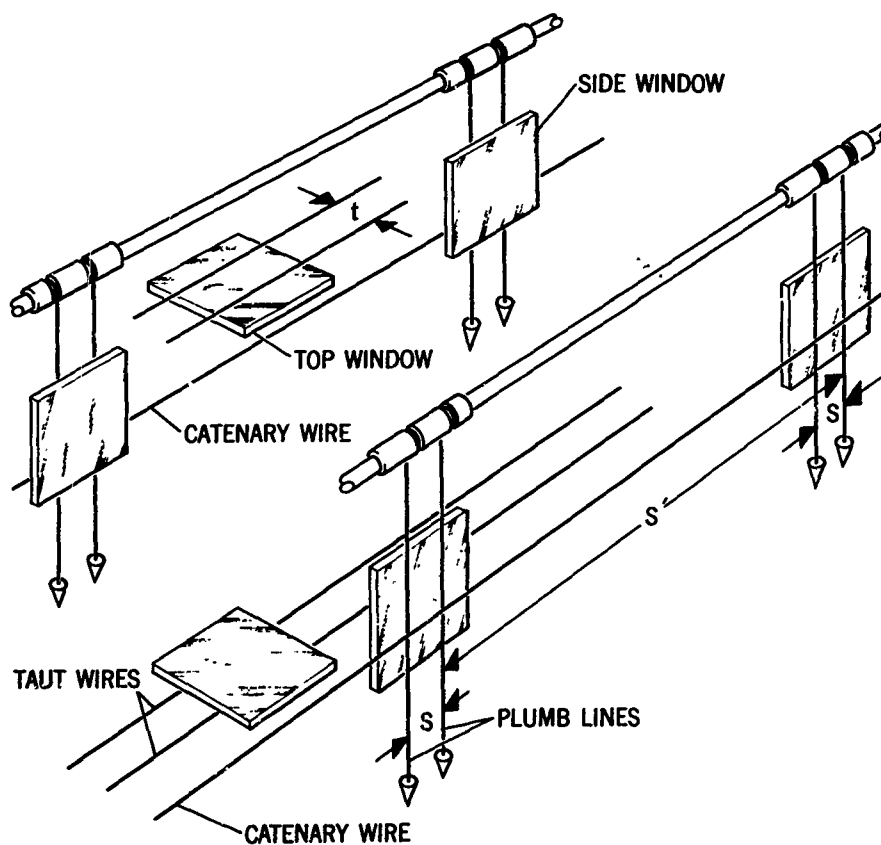
Fig.S.35   Schematic drawing of fiducial system used with collimated light
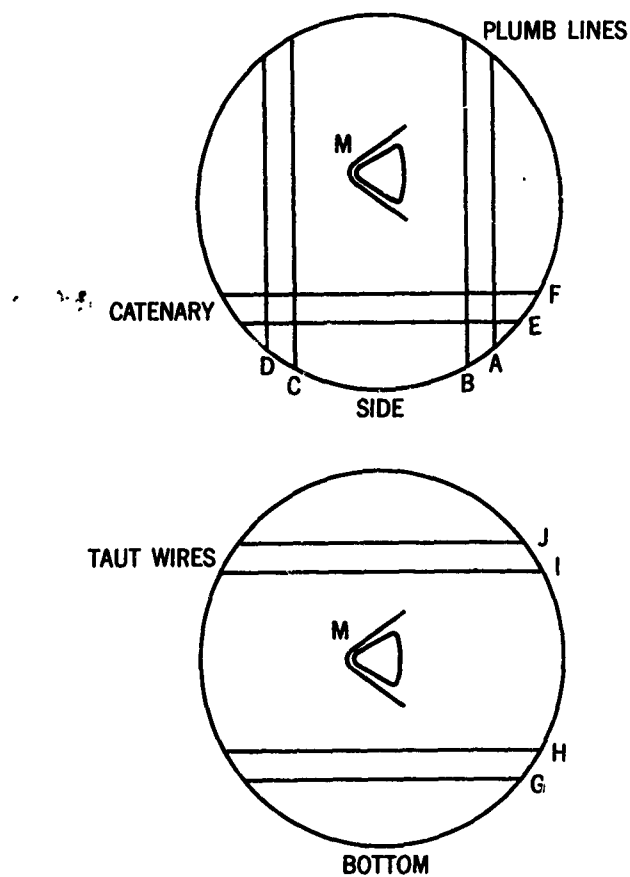
Fig.6.36   Images of fiducial wires in the side and bottom shadowgrams (circular window apertures)
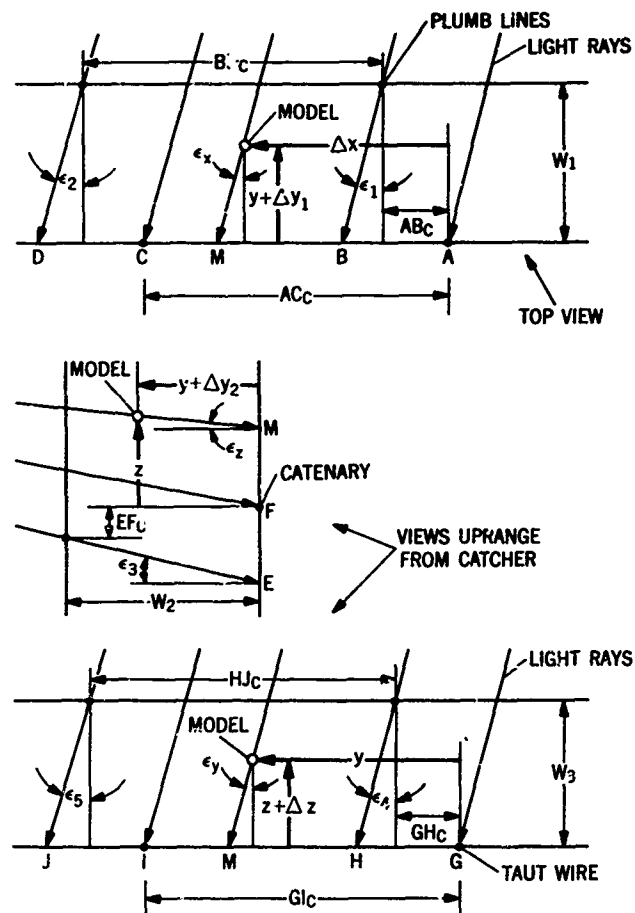
Fig.6.37 Relationships between light rays, measurement references, and model-image location in one near-parallel-light shadowgraph station
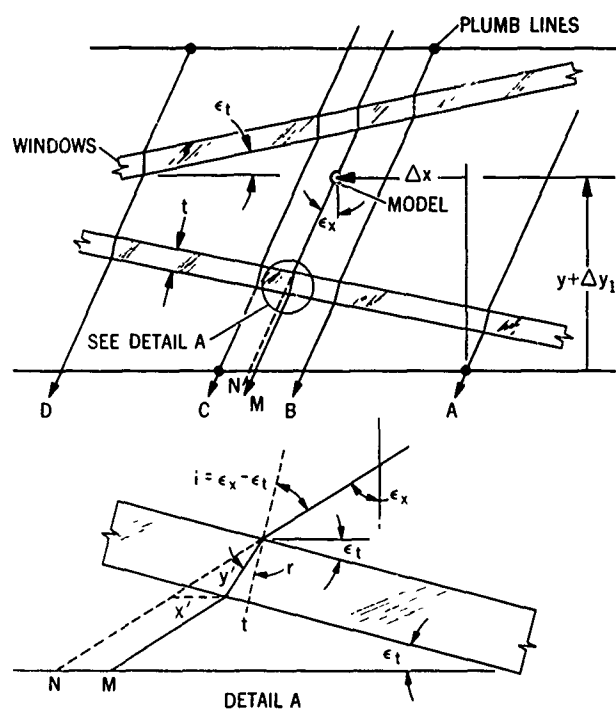
Fig 6 38   Ray diagram illustrating the lateral displacement of a beam of light through two nonparallel glass windows
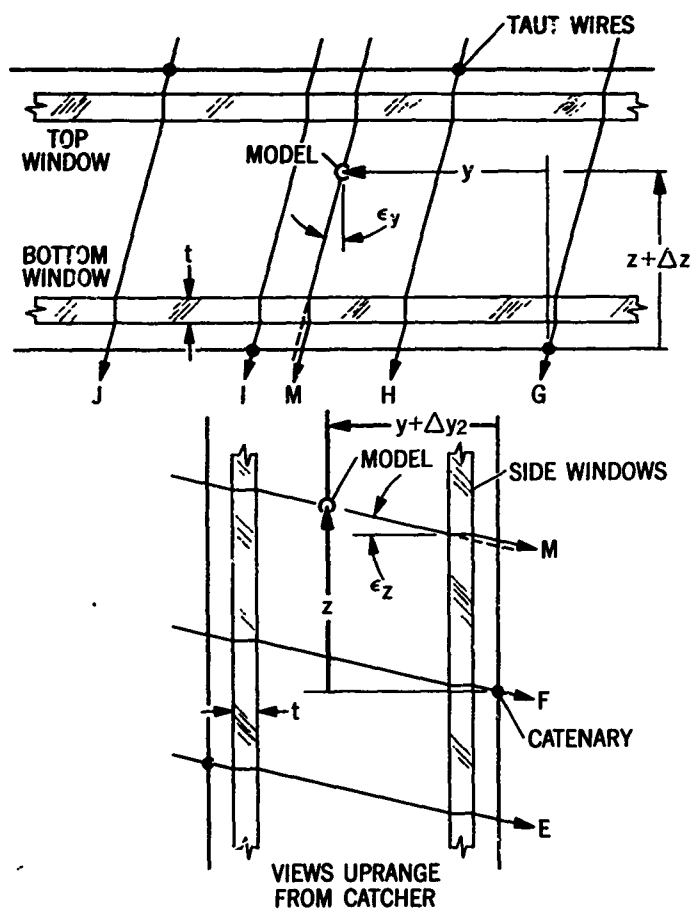
Fig.6.39   Ray diagram illustrating the displacement of light beams through two parallel glass windows
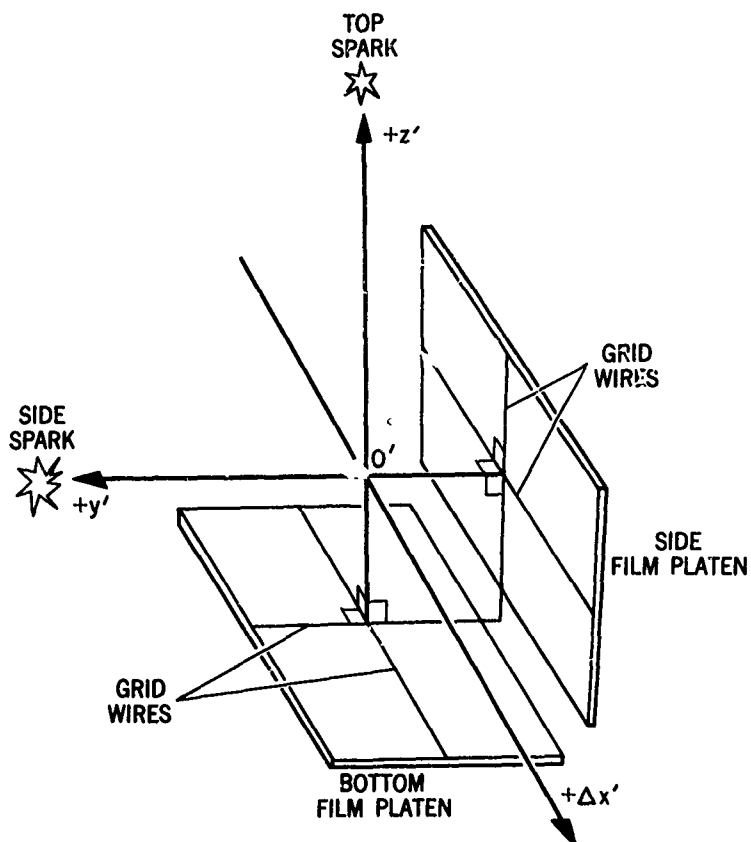
Fig.6.40   Schematic drawing of the station-coordinate system for a conical-projection direct shadowgraph
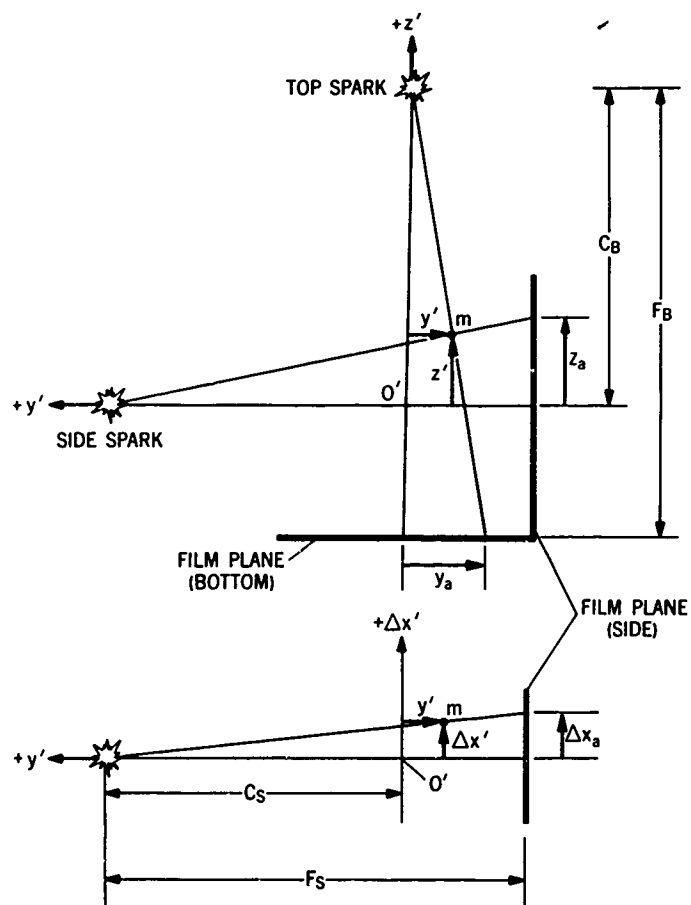
Fig.6.41   Ray diagram illustrating the magnification of the model image due to conical projection
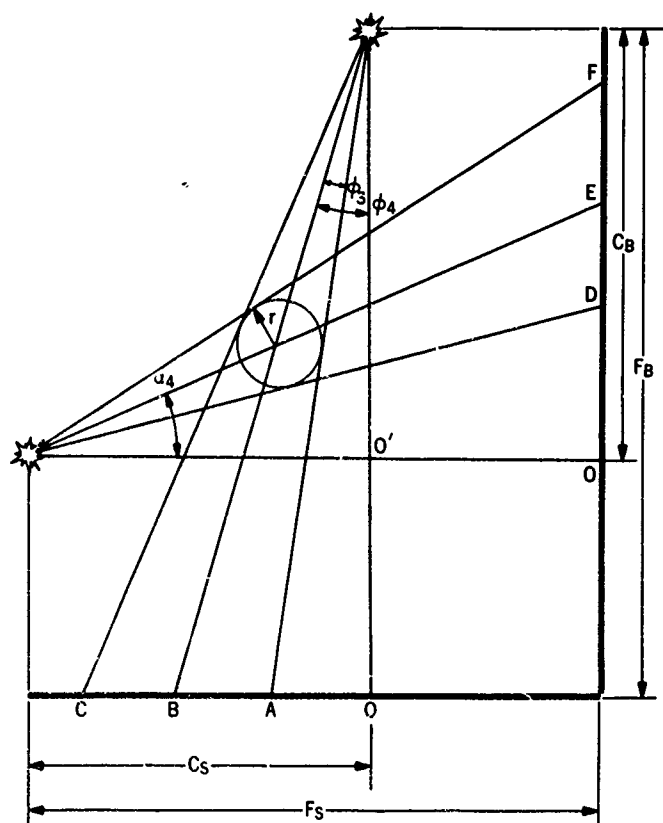
Fig.6.42   Illustration of the paths of the light rays about a sphere in a conical projection
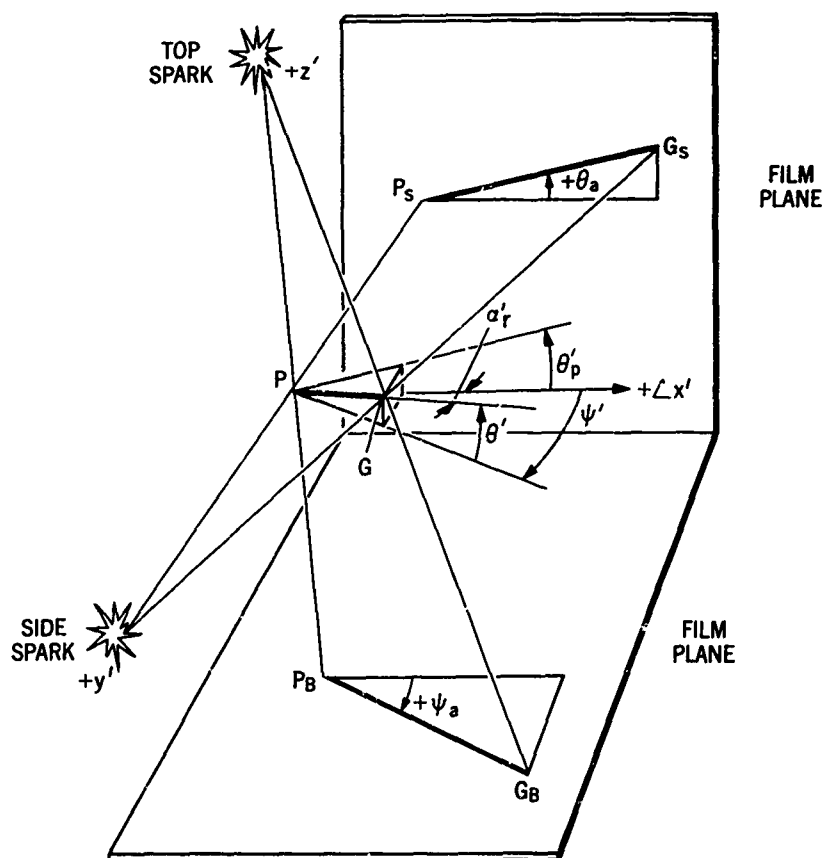
Fig.6.43 Ray diagram illustrating the distortions of the model attitude due to conical projection
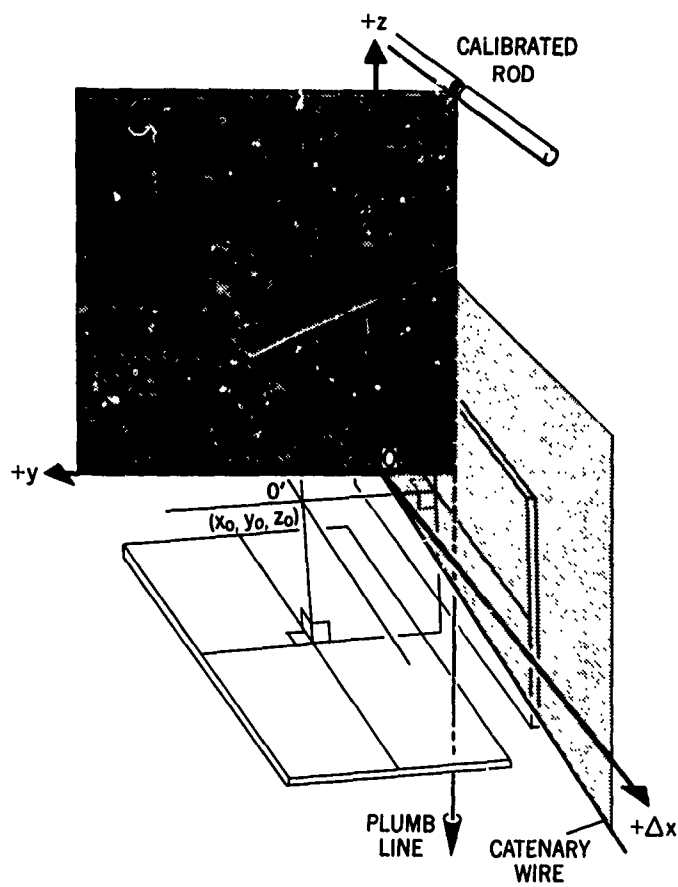
Fig.6.44 Relationship of the range- and station-coordinate system for a conical-projection direct shadowgraph
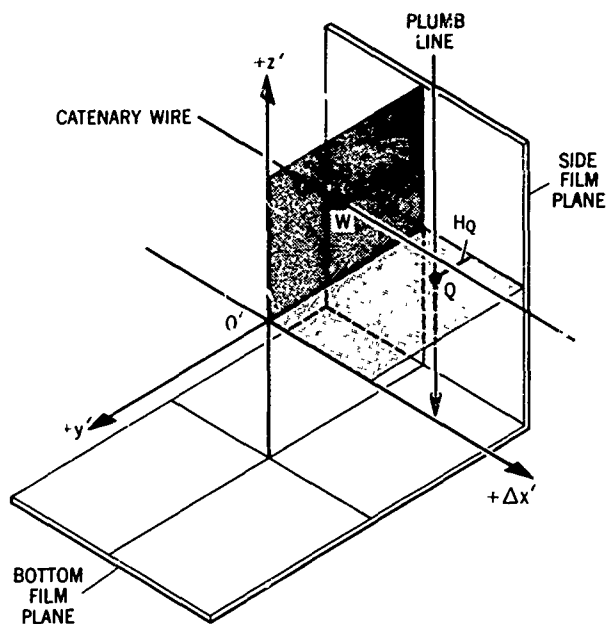
Fig.6.45 Location of the W and Q points in the station-coordinate system
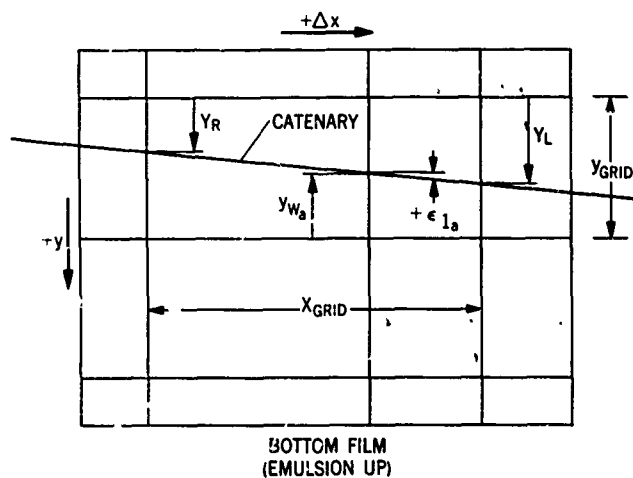
Fig.6 46 Wire images in the bottom film used to determine the apparent angle of yaw of the station-coordinate system with respect to the range-coordi' 'e system
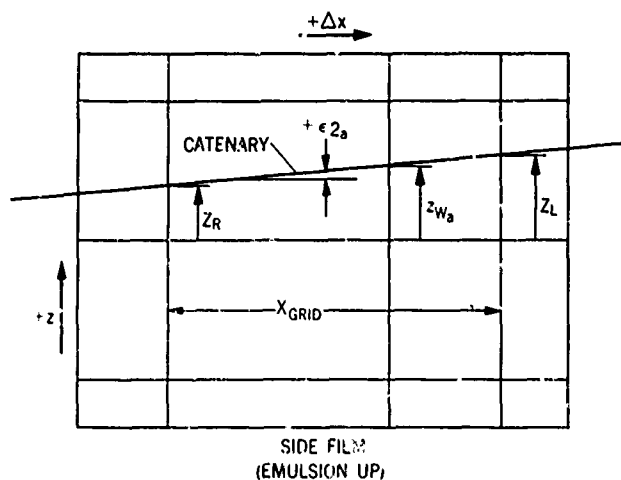
Fig. 6 47 Wire images in the side film used to determine the apparent angle of pitch of the station-coordinate system with respect to the range-coordinate system
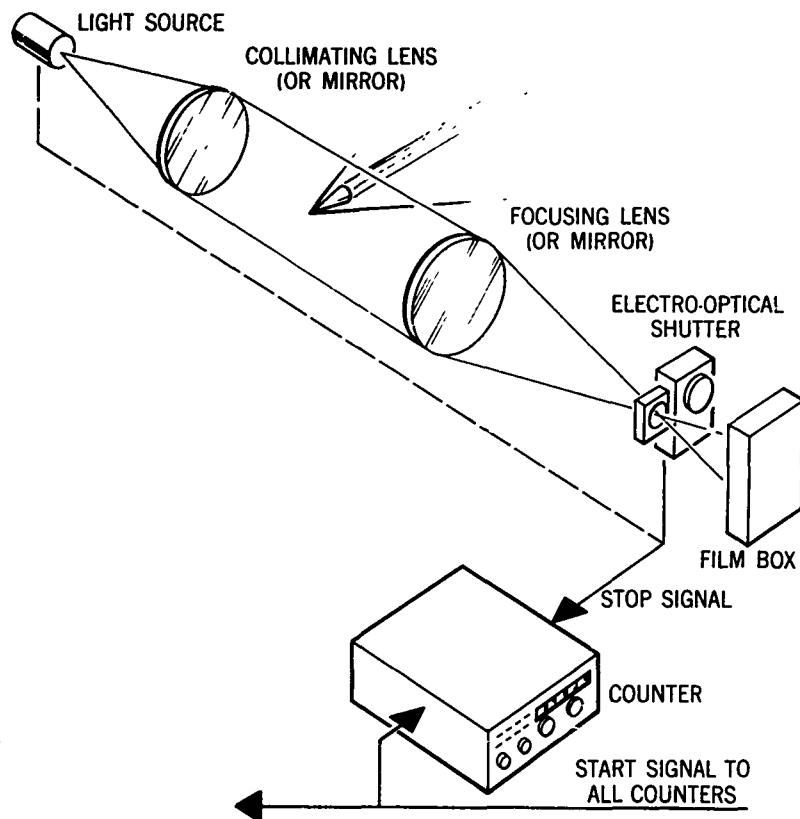
Fig.6.48   Hook-up of a one-channel electronic counter
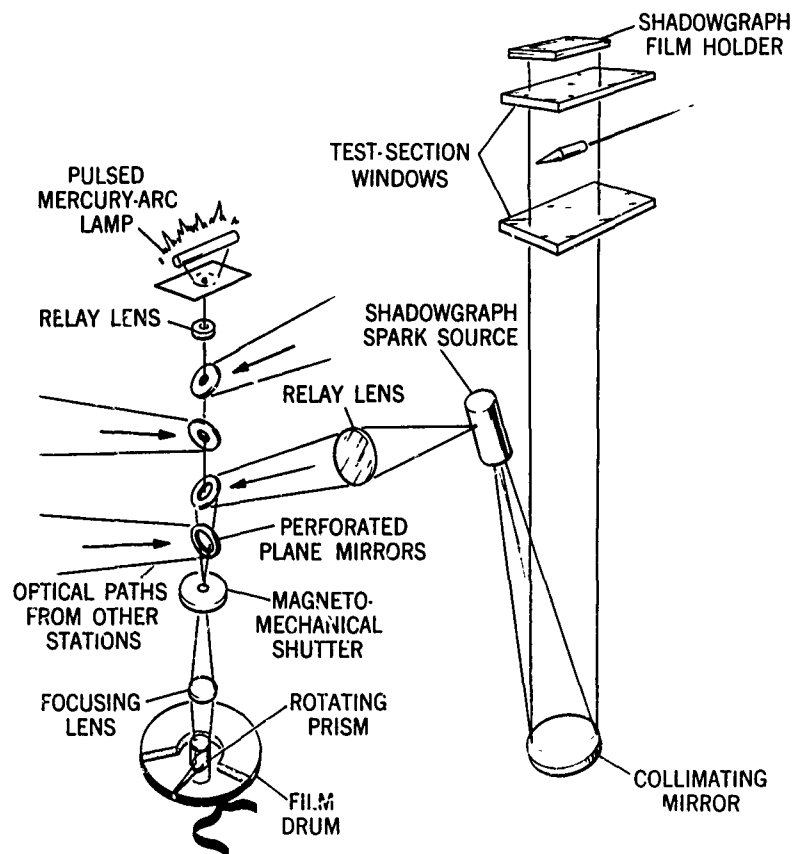
Fig.6.49   Sketch of a rotating-prism optical chronograph

254
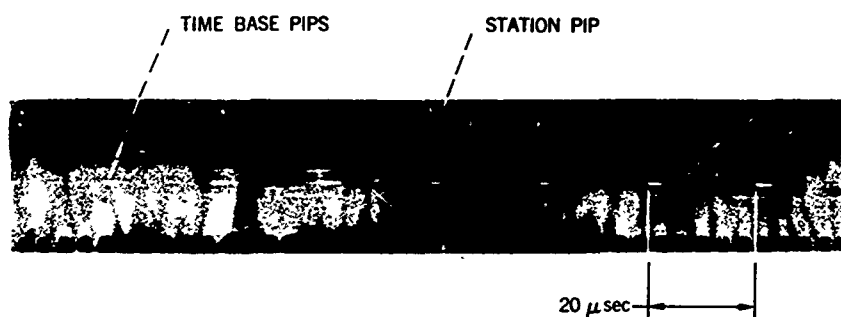
Fig.6.50   Segment of chronograph film record
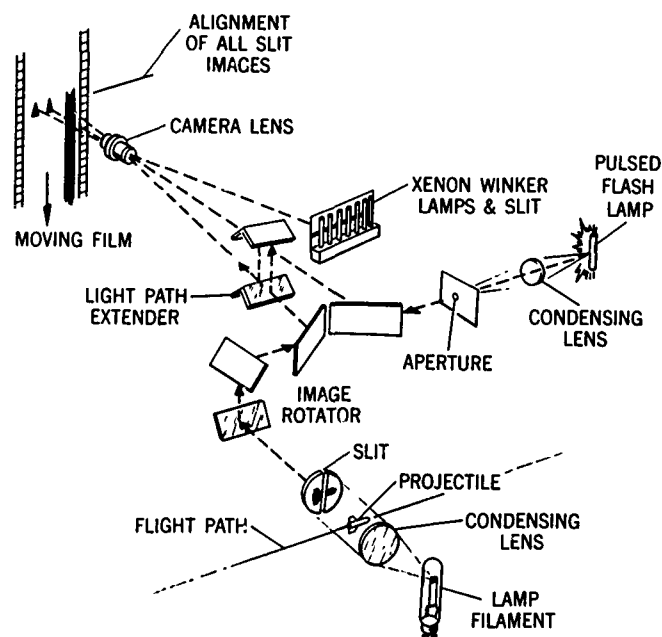
Fig.6.51   Sketch of a streak-camera optical chronograph
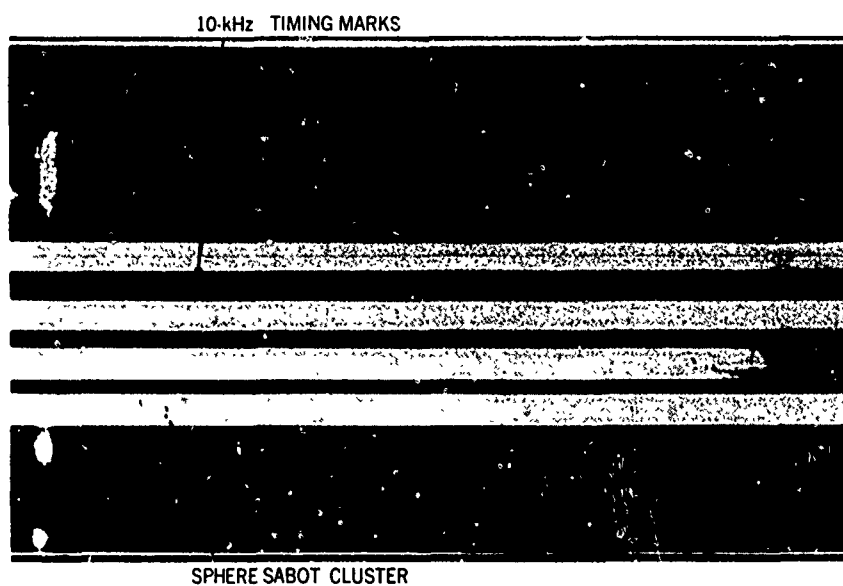
Fig 6 52   Portion of the film record from a streak-camera chron raph showing shadow images of a 4.8-mm-diameter
aluminum sphere and segments of its sabot. The velocity of 5.76 km/sec was determined from this
record courtesy of US Naval Research Laboratory
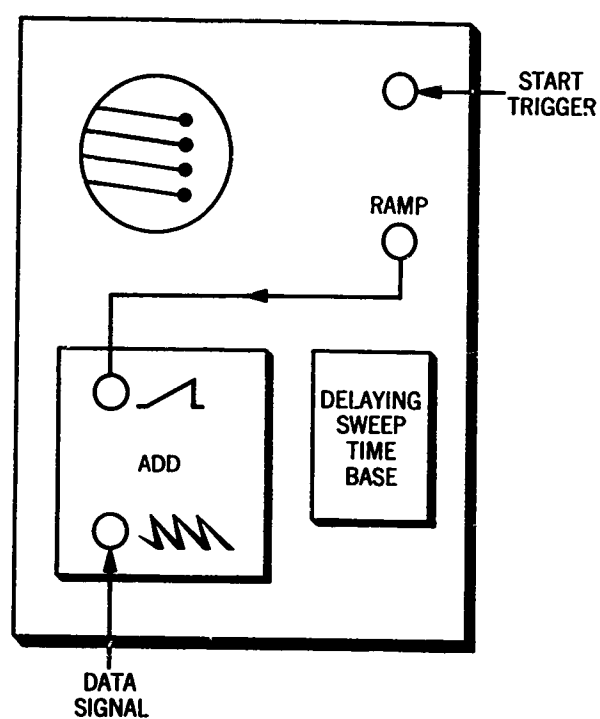
Fig.6.53   Oscilloscope hook-up for raster display (after Pennelegion, National Physical Laboratory, England)
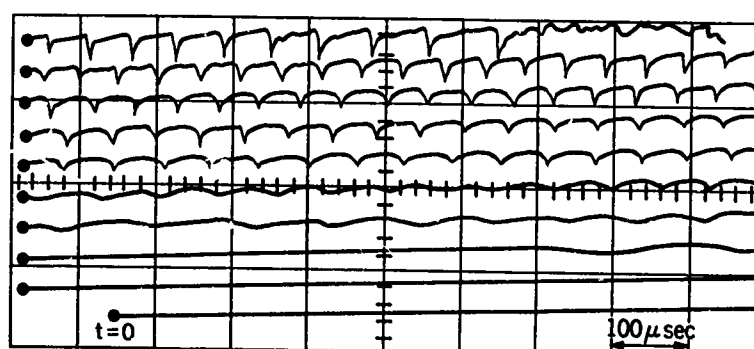
Fig.6.54   Raster-display oscilloscope record (after Pennelegion, National Physical Laboratory, England)
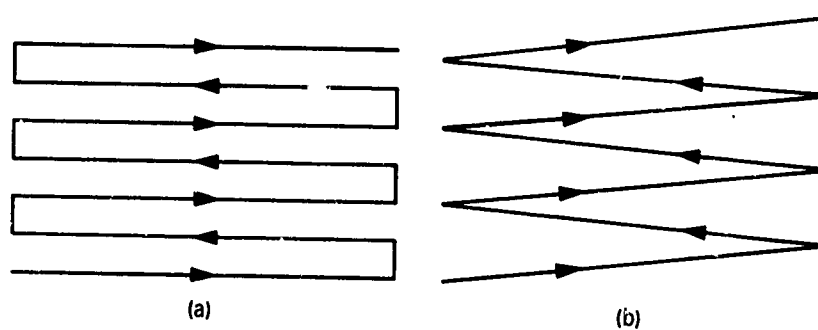
Fig.6.55   Alternative raster patterns
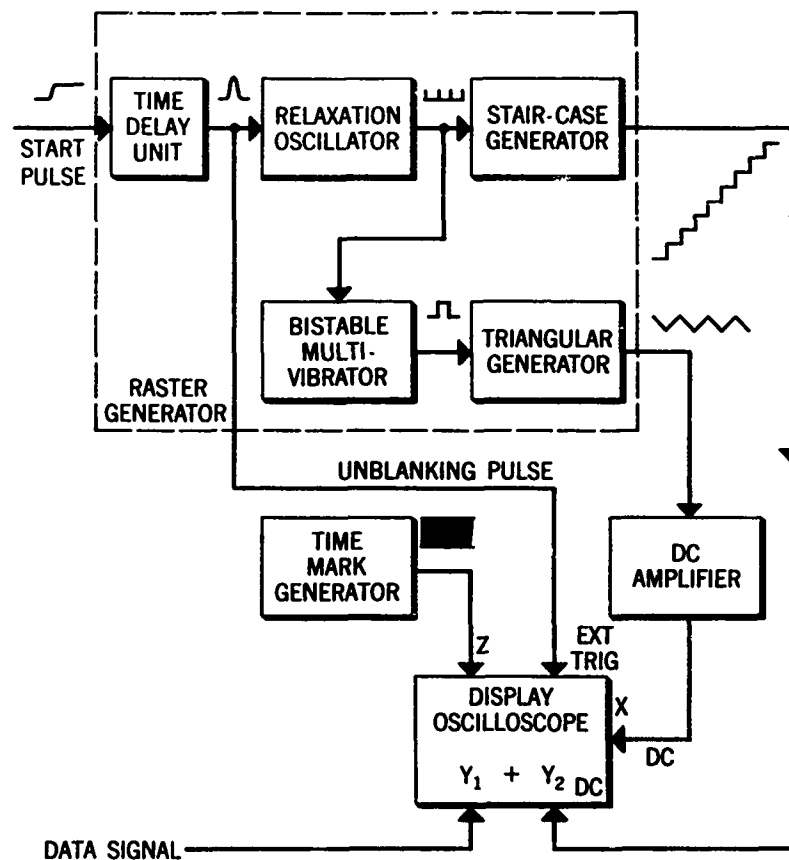
Fig.6.56 Block diagram of oscilloscope hook-up with external raster generator
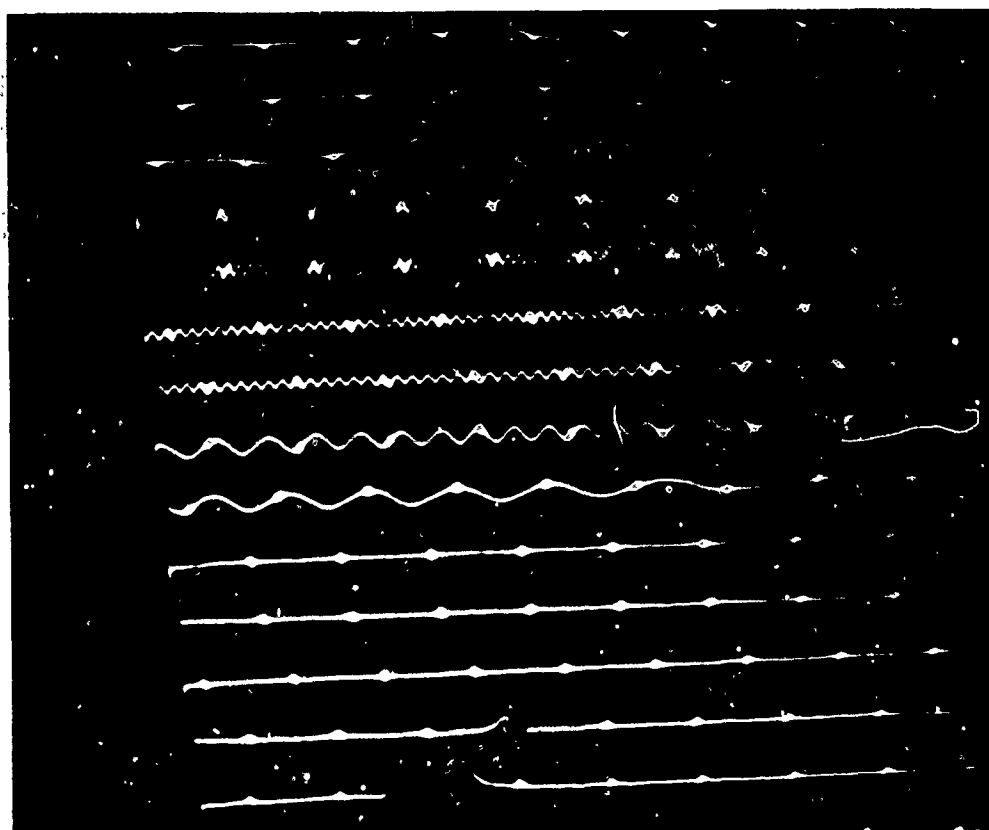
Fig 6 57 Oscilloscope record obtained with hook-up of Figure 6.56

Fig.6.58   Circular-sweep oscilloscope record
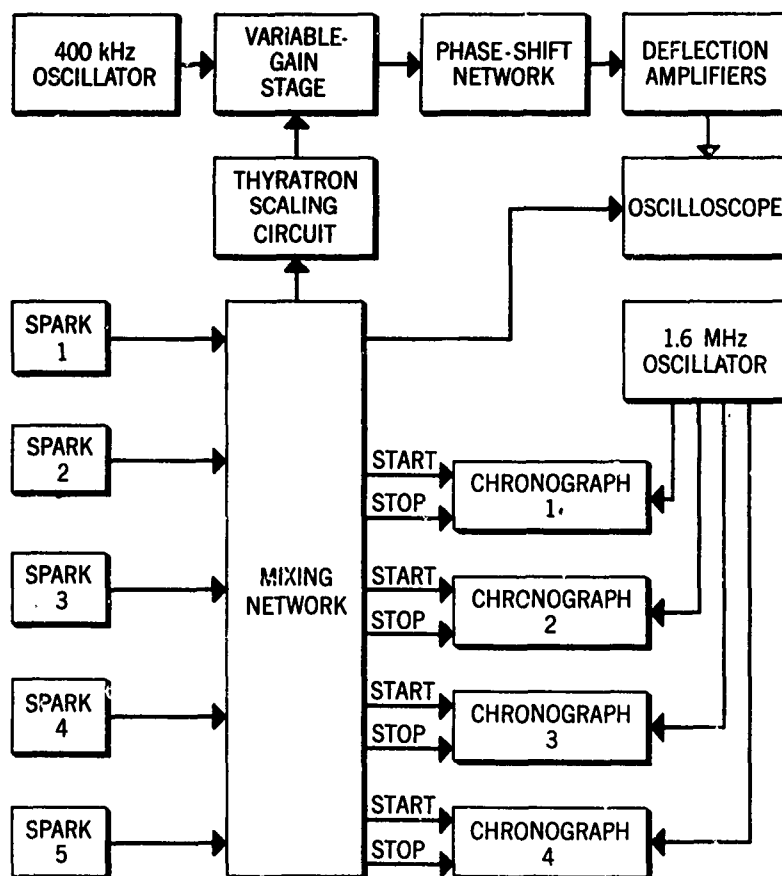
Fig.6.59   Block diagram of circular-sweep chronograph system

STOP-TRIGGER
SCREEN

LIGHT-SCREEN
START TRIGGER

FILM PLATENS

$\lambda = 3.16$ cm

f_D

AMPLIFIER

f_D

GATE

f_D

STEP
COUNTER
n_0, n_D

PHOTOGRAPHIC SPARKS

N   N-1   3   2   1

$n_D \frac{\lambda}{2}$ $n_D \frac{\lambda}{2}$ $n_D \frac{\lambda}{2}$ $n_0 \frac{\lambda}{2}$

C_{N-1} C_2 C_1 C_0

COUNTER
CHRONOGRAPHS

IMPULSE DISTRIBUTOR

f_D / n_D
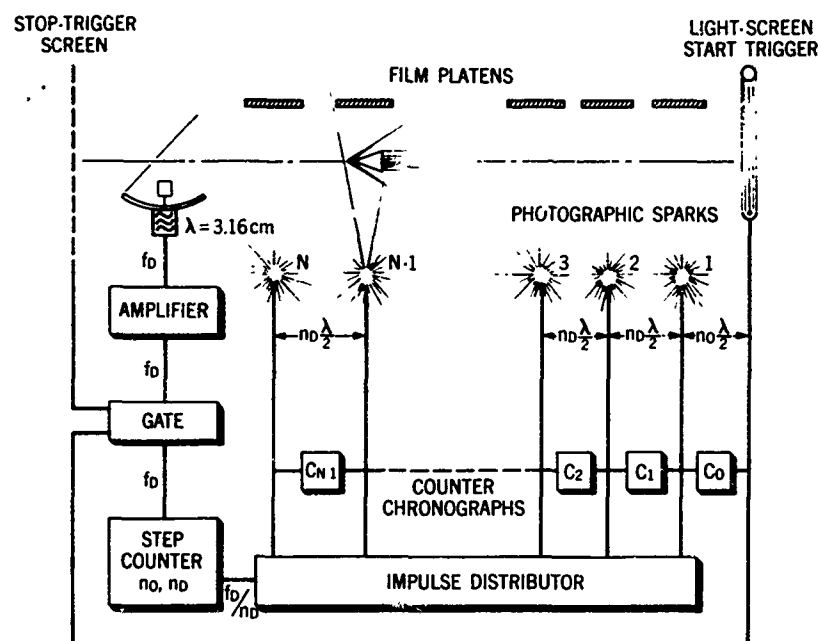
Fig. 6.60   Schematic of microwave-Doppler range instrumentation at ISL (courtesy of Deutsch-Französisches
Forschungsinstitut, Saint-Louis)

Fig. 6.61   Multi-strand breakwire used to trigger microflash photograph of projectile. (Courtesy of US Naval
Ordnance Laboratory)

LIGHT
SOURCE

SLIT APERTURED
COLLIMATING LENS

SLIT APERTURED
FOCUSING LENS

PHOTO
SENSOR
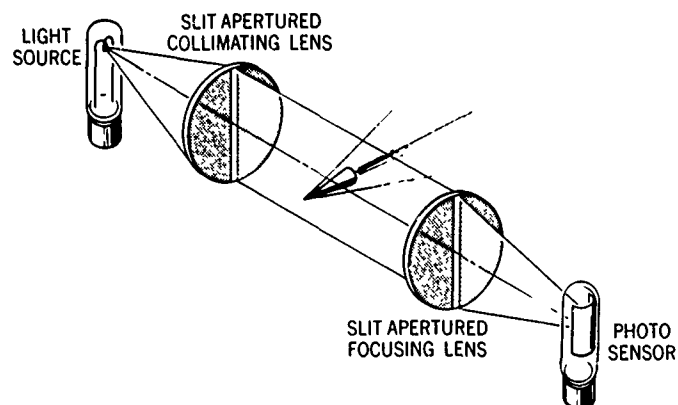
Fig 6 62   Arra ...ment of a typical light-screen projectile detector

APERTURED
COLLIMATING
LENS

INTERIOR
LIGHT RAY

LIGHT
SOURCE

PHOTO
SENSOR

APERTURED
FOCUSING
LENS

(a) Using lenses and prisms

COLLIMATING
STRIP
MIRROR

LIGHT
SOURCE

PLANE
STRIP
MIRRORS

PLANE
STRIP
MIRRORS

PHOTO
SENSOR

FOCUSING
STRIP
MIRROR

(b) Using spherical and plane strip mirrors
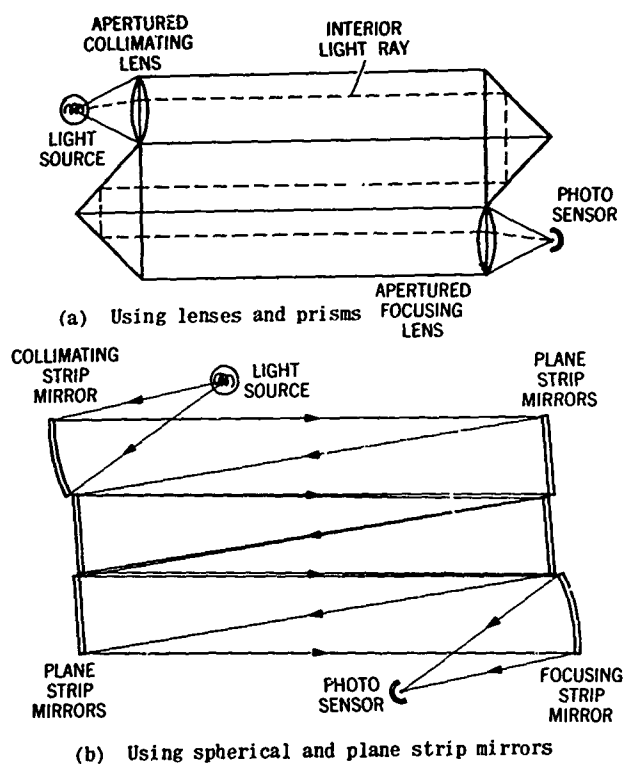
Fig.6.63   Alternative arrangements of a folded multi-pass light screen

COLLIMATING
STRIP
MIRROR

PHOTO SCREEN
LIGHT SOURCE

WINDOWS

PHOTO
SENSOR

LIGHT
INCREASE

LIGHT
DECREASE

FOCUSING
STRIP MIRRORS
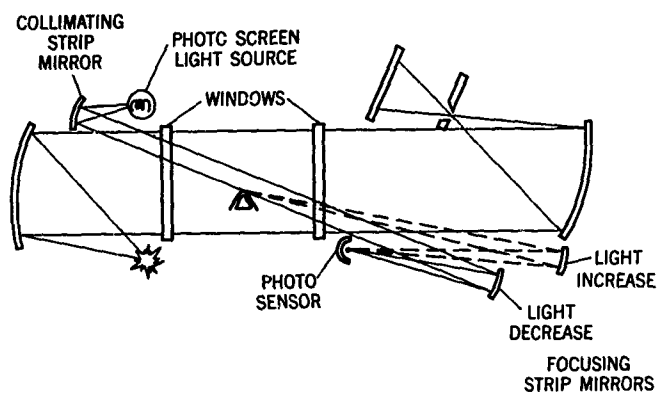
Fig.6.64   Schematic of a shadowgraph station with diagonal zero-time-delay light screen

SPHERICAL
STRIP
MIRRORS

PHOTOGRAPHIC
LIGHT SOURCE

3-m-DIAM
RANGE TANK

PHOTO
SENSORS

FILM
PLATEN

PHOTO SCREEN
LIGHT SOURCE

PHOTOGRAPHIC
LIGHT SOURCE

FILM
PLATEN
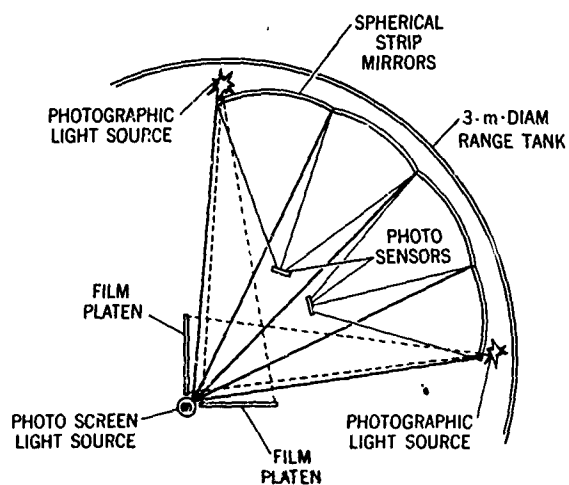
Fig.6.65   Sketch of multi-path zero-time-delay light screen used in the Ames pressurized ballistic range

1.22·m-DIAM
SPHERICAL-SEGMENT
REFLECTOR

SLIT

LIGHT
SOURCE

SENSOR
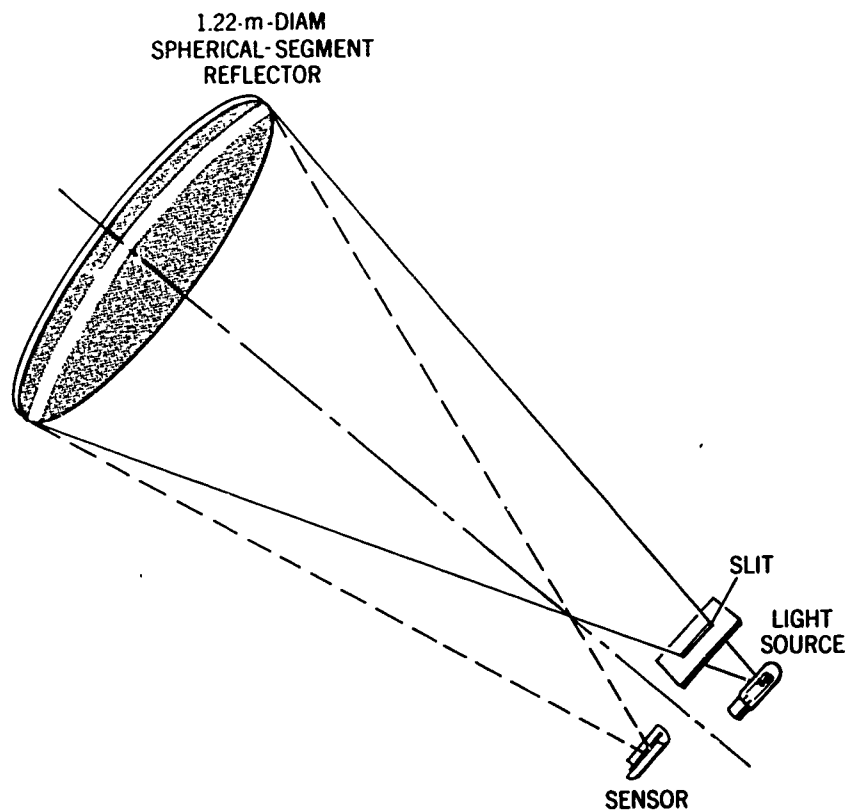
Fig.6.66   Zero-time-delay light screen used in the NOL 1000-ft hyperballistics range.   (Courtesy of US Naval
Ordnance Laboratory)

6·×6·m
RANGE ENCLOSURE

YAW CARD FRAME

I.R. SOURCE
ACTIVE SURFACE

NOMINAL
FLIGHT
CORRIDOR

BEADED
SCREEN

CAMERA

LIGHT
SOURCE

I.R. SENSORS
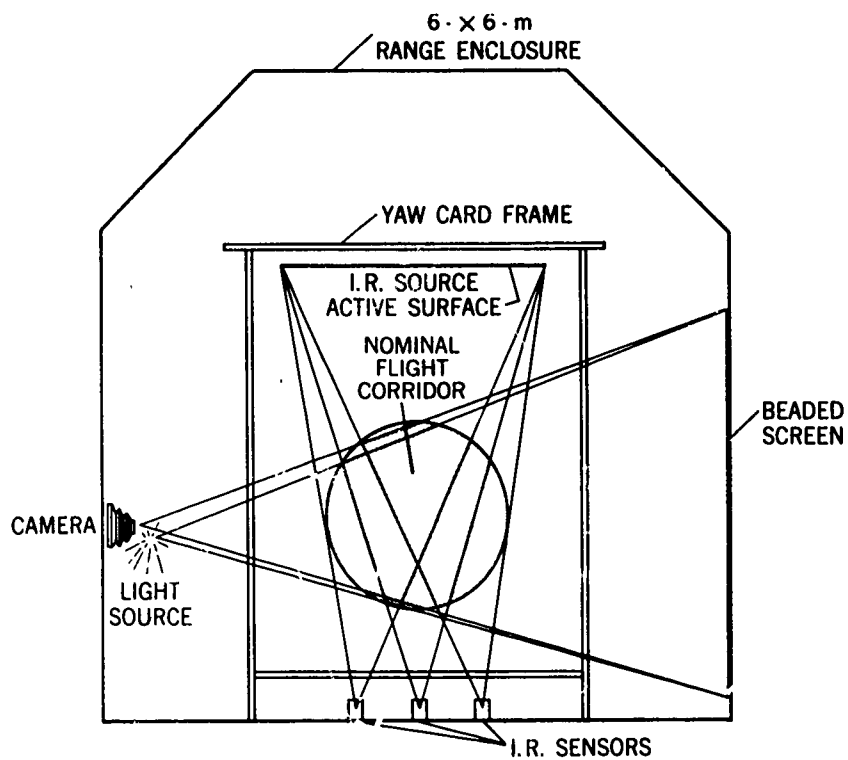
Fig 6 67   Schematic of CARDE Aeroballistic Rang Station.   (Courtesy of Canadian Armament Research and
Development Establishment)
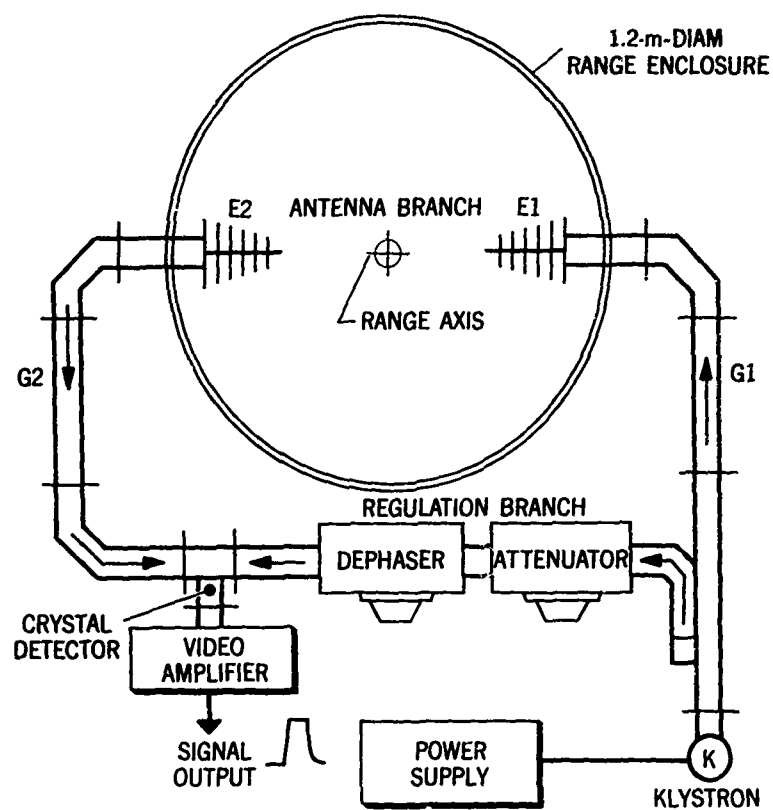
(a) Sketch of the apparatus
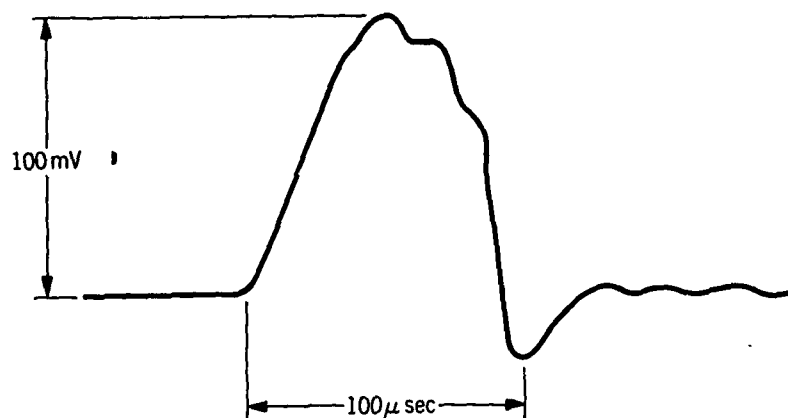
(b) Oscillogram of a typical output signal

Fig.6.68   Microwave-interferometer trigger developed at LRBA. (Courtesy of Laboratoire de Recherches Ballistiques et Aérodynamiques de Vernon)
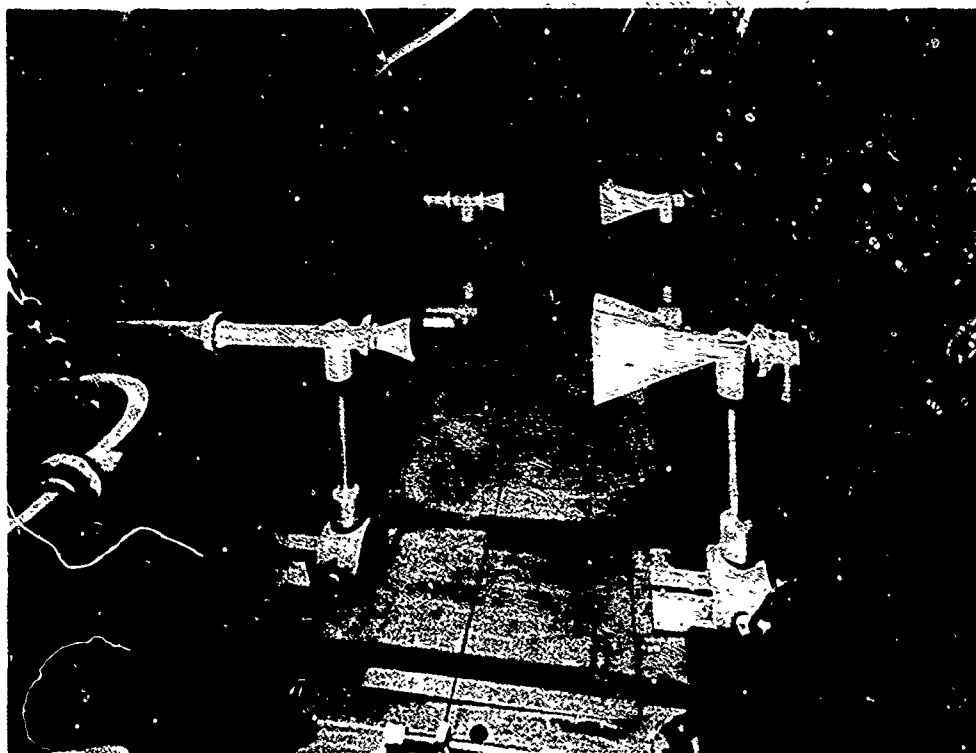
Fig.6.69 Microwave-attenuation-trigger antenna horns on swinging support in range tank. (Courtesy of Royal
Armament Research and Development Establishment. "Britisn Crown copyright reserved.
Reproduced with the permission of The Controller, Her Brittanic Majesty's Stationery Office")
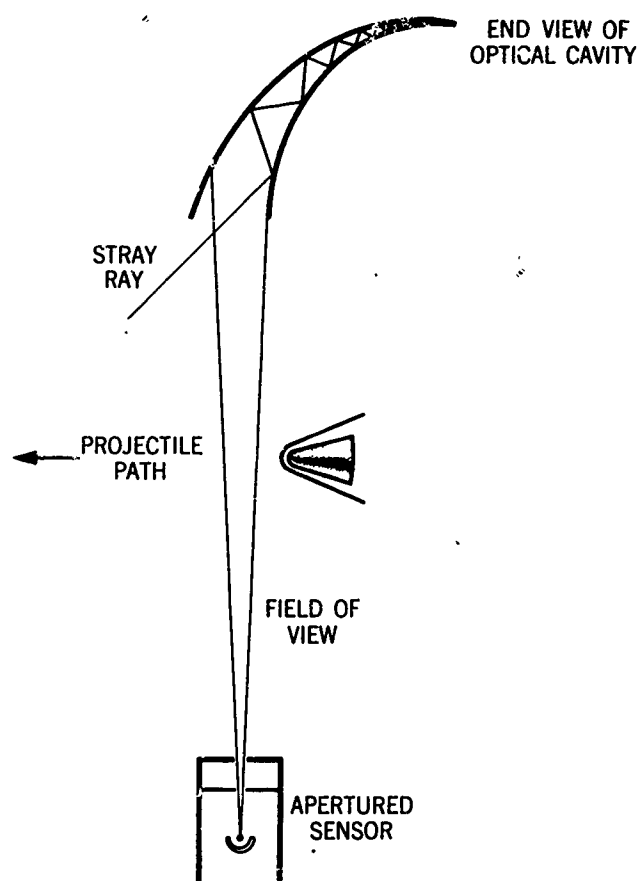
Fig.6.71   Schematic of an optical-radiation projectile detector

(a) LIGHT-DECREASE TRIGGERING

(b) LIGHT-INCREASE TRIGGERING
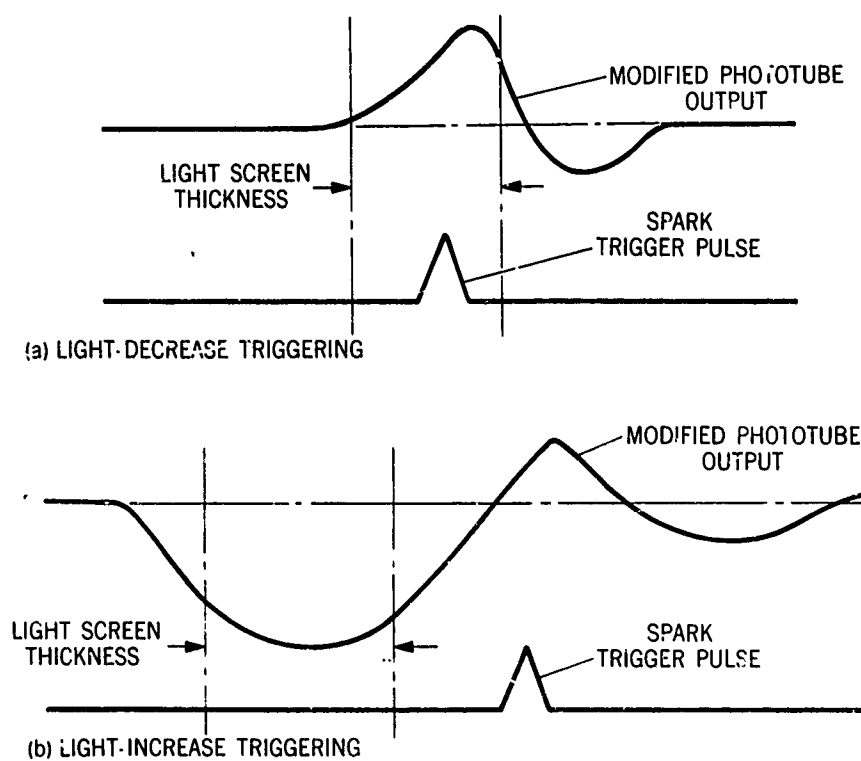
Fig.6.72   Dual-mode triggering. (Courtesy of US Naval Ordnance Laboratory)
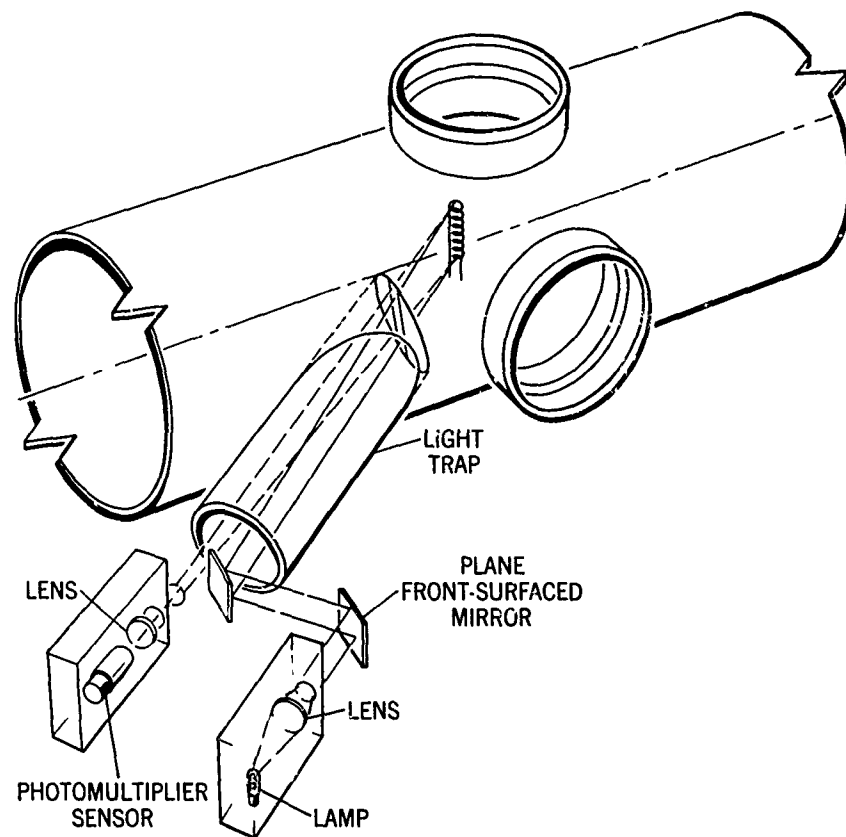
Fig.6.73   Light-increase sensor which responds to luminous or nonluminous projectiles (after Wall, Royal Armament Research and Development Establishment)
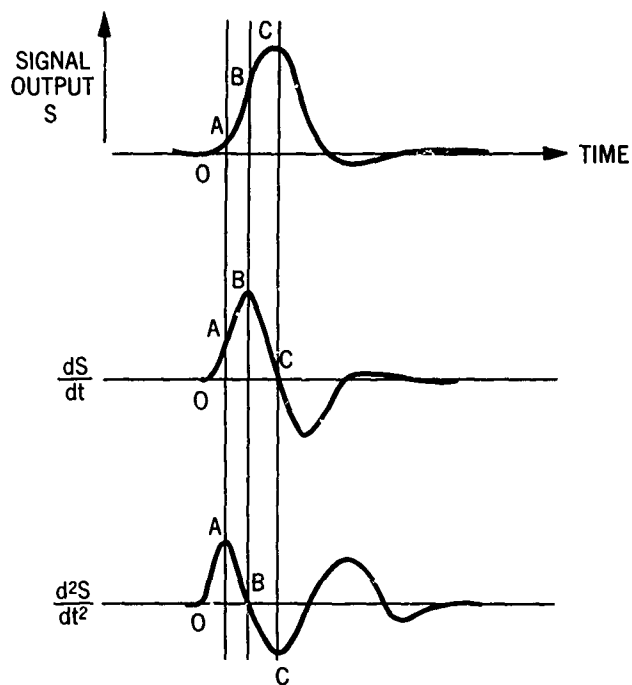
Fig.6.74   Triggering points on a typical sensor-output-signal trace

WING ATTITUDE

(VIEWED FROM ASTERN)
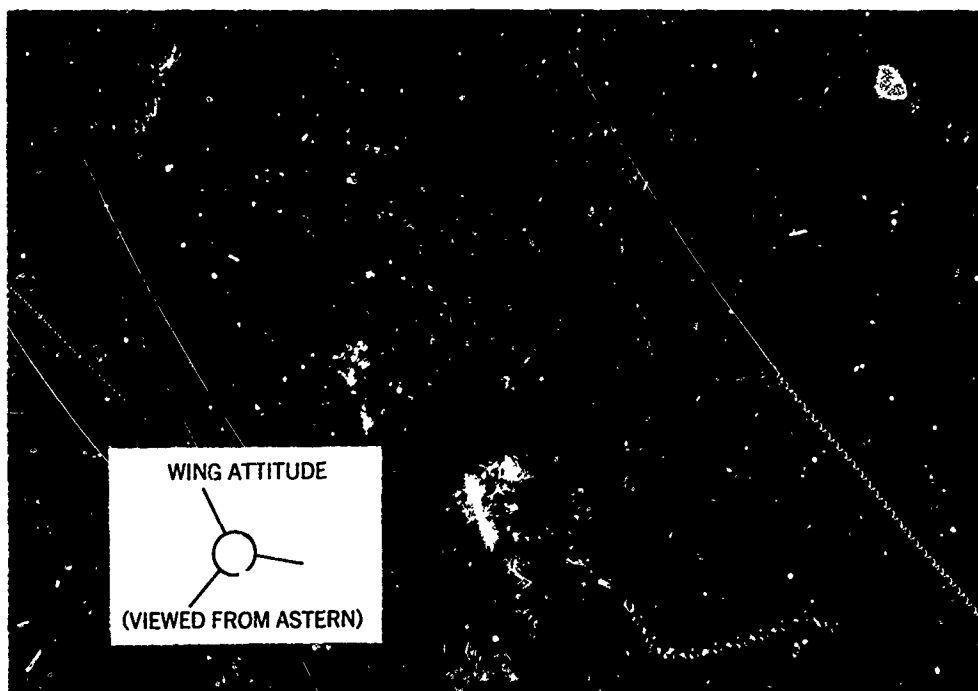
Fig.6.75   Shadowgram of three-wing model
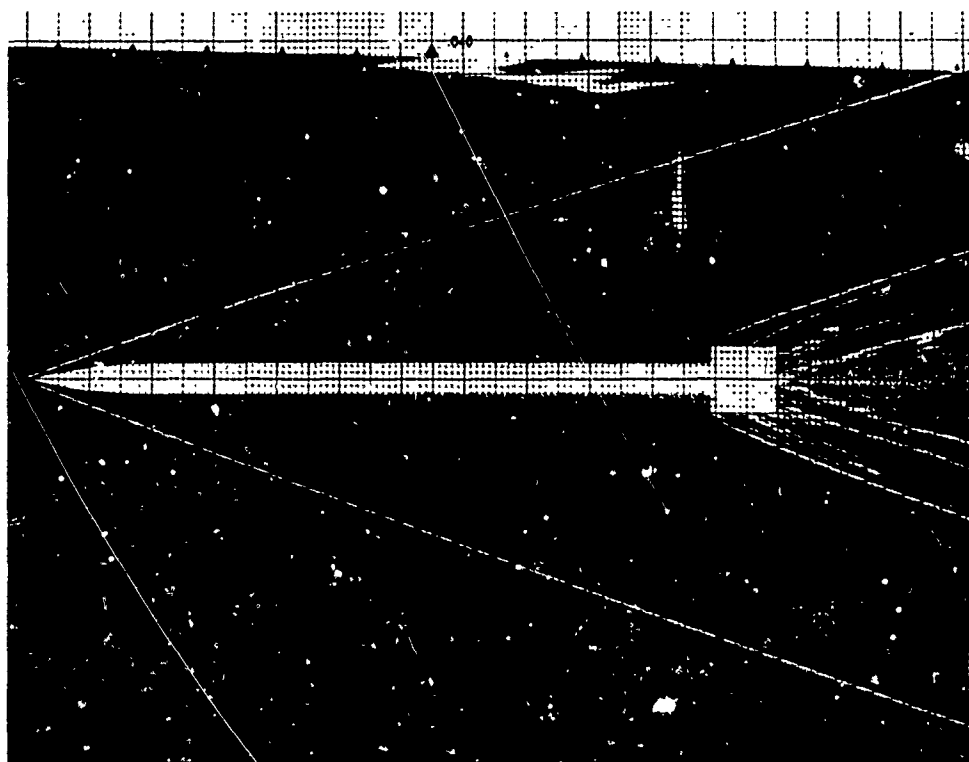
Fig.6.76   Photograph of glass grid superimposed on shadowgram negative

266
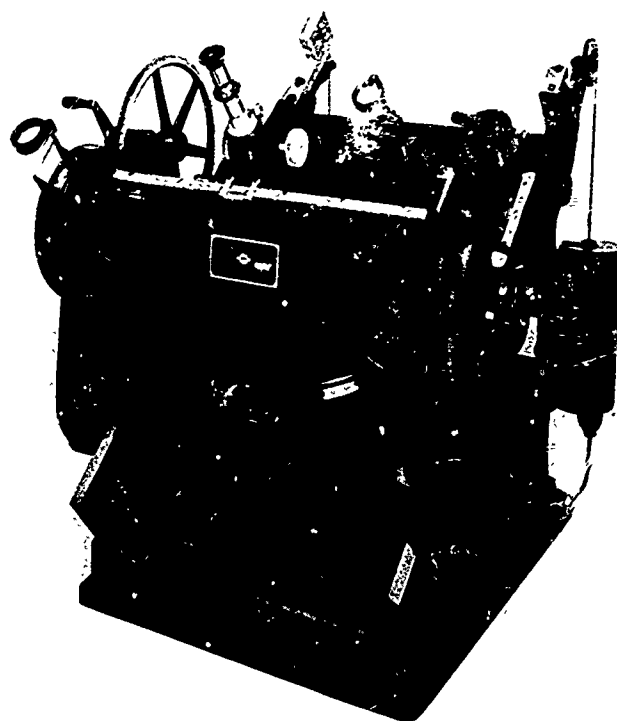
Fig. 6.77   20.3- by 25.4-cm film reader with microscope
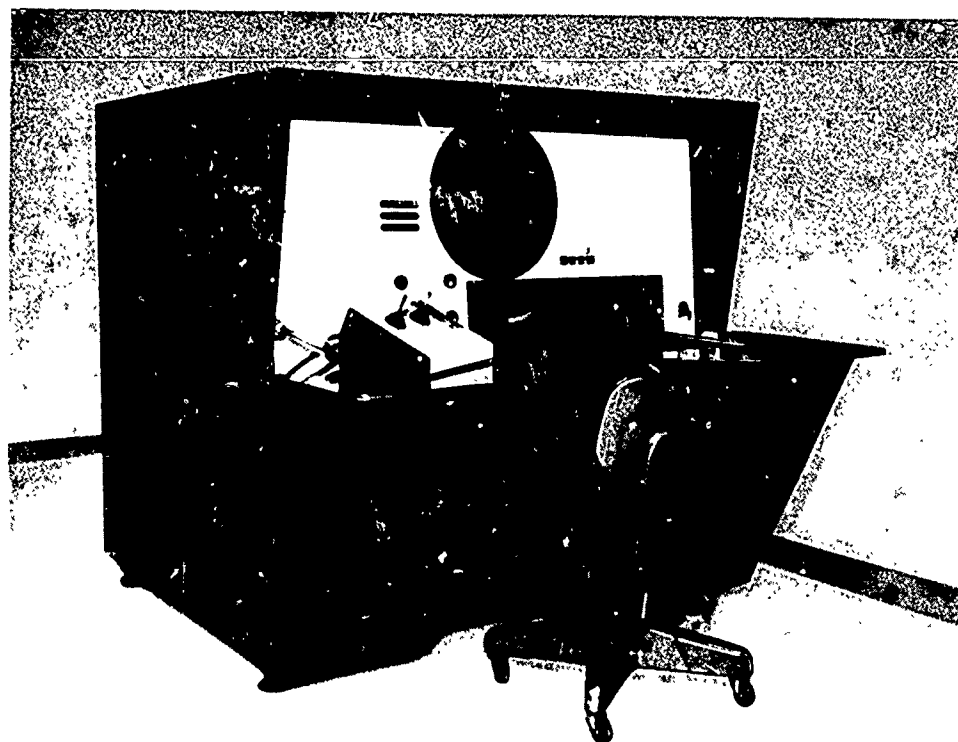
Fig. 6.78   50.8- by 50.8-cm film reader with viewing screen

CHAPTER 7

AERODYNAMICS OF BODIES FROM MOTION ANALYSIS

by

Gary T. Chapman, Donn B. Kirk,
and Gerald N. Malcolm

NASA – Ames Research Center

AERODYNAMICS OF BODIES FROM MOTION ANALYSIS

Gary T.Chapman, Donn B.Kirk,
and Gerald N.Malcolm

7.1 INTRODUCTION

The purpose of this chapter is to examine a number of techniques for determining the aerodynamic character-
istics of bodies in free flight in a ballistic range. The measurements from which the aerodynamics are to be
deduced usually consist of angular and linear position data from photographic records of a model in flight,
such as shadowgraphs; they could conceivably be acceleration data obtained from onboard accelerometers, or
velocity data obtained from onboard integrating accelerometers or rate gyros. With gun-launched models, the
accelerations and velocities are not usually measured, since at the present state of development accelerometers
and transmitters cannot withstand the launch loads imposed by the gun (see Chapter 12). The discussions in
this chapter will therefore be restricted to the analysis of angular and linear position data as functions of
either time or distance traveled.

There are basically two approaches to the problem of obtaining aerodynamics of bodies from such data. The
first is to curve-fit the position and angular orientation data and differentiate the fitted curves twice to
obtain the appropriate accelerations. These accelerations are directly related through Newton's laws of motion
to the aerodynamic forces and moments acting on the body. This technique presents no problems in mathematics,
but does require data of very high precision. The second approach is to consider the differential equations
which govern the motion and perform the appropriate integrations to obtain solutions for the position and
angular orientation as functions of time or distance. These solutions are then curve-fit to the data to yield
the aerodynamic characteristics of the body. This approach does lead to problems in mathematics. The differen-
tial equations are highly nonlinear and in general cannot be solved in closed form.

Much work has been done by many people on this latter approach. The original contributions in this field
were by Lanchester[7.1] at the turn of the century. His work was mainly restricted to the analysis of airplane-
type motions in which he considered only small deviations from a steady-state glide-path, linear aerodynamics,
and small roll rates. Since ballistics studies generally involved high roll rates and symmetric bodies, the
ballistician had to take a somewhat different approach from Lanchester's. The original analysis of symmetric
spinning bodies was conducted by Fowler and his associates in 1920 (References 7.2 and 7.3). Because the two
areas, aerodynamics and ballistics, originally had so little in common, they developed independently. With
the arrival of guided missiles, in particular, airplane-launched missiles, the aerodynamicist was confronted
with the same problems as the ballistician and was not familiar with ballistics or ballistic terminology.
Bolz[7.4], Nicolaides[7.5] and Charters[7.6] did much to alleviate this situation. They made an attempt to merge
the approaches of the ballistician and the aerodynamicist and to clarify the differences in nomenclature
between the two. All of this work was predominantly for linear aerodynamics. The introduction of nonlinear
aerodynamics was done by such people as Murphy and Rasmussen in the early 1960's[7.7,7.8].

With the advent of the electronic computer, the application of many of the above procedures was greatly
enhanced; but even more importantly a completely different approach to the problem was made possible. That
approach is to curve-fit the position and angular orientation data using the differential equations directly
by employing numerical integrations. A method for applying this technique is described in Section 7.8.2.

Much of the work in the field of dynamics, in particular, ballistics and aerodynamics, has been to describe
the motion, given a set of aerodynamic coefficients. Although some attention will be directed to this problem,
throughout most of this chapter emphasis will be placed on the inverse problem. That is, given the equations
for the motion, determine the aerodynamic coefficients which best describe that motion. This problem is not
nearly as unique since it is not known a priori what the functional relationships will be. For instance, it
is necessary to assume either that the aerodynamics are linear or nonlinear, and if nonlinear, the form they
take.

Because the discussions will be focused on ballistic range data reduction procedures, the derivations of the
equations of motion will incorporate assumptions that are pertinent to this type of facility. For example,
because ballistic ranges are normally short, the direction of the gravity vector can be assumed not to change.
Major assumptions which are implicit in all of the material will be specifically pointed out.

The chapter begins with a discussion of the different coordinate systems used in analyzing free flight data.
Once these have been established, the differential equations of motion are derived by considering several ways
of writing the equations for flight dynamics and combining these with appropriate expressions for the applied
forces and moments. With the equations of motion derived, the various techniques for deducing drag, static and
dynamic stability, lift, and rolling moment coefficients (both linear and nonlinear) from the measured data are

discussed. Typical examples are presented and some of the results compared to conventional wind tunnel measurements. The chapter concludes with a section on error analysis and an appendix treating the method of least squares using differential corrections.

7.2 NOTATION

A	reference area

C_i — force or moment coefficient; i can take the values $x, y, z, \bar{x}, \bar{y}, \bar{z}, D, L, N, S, l, m,$ or n. Some particular coefficients that appear frequently are:

C_D drag coefficient, $\dfrac{\text{drag}}{\frac{1}{2}\rho V^2 A}$

C_L lift coefficient, $\dfrac{\text{lift}}{\frac{1}{2}\rho V^2 A}$

C_m pitching moment coefficient, $\dfrac{\text{moment}}{\frac{1}{2}\rho V^2 A l}$

C_{i_k} — partial derivative of C_i with respect to a variable k; k can take the values $\alpha, \dot{\alpha}, \beta, \dot{\beta},$ $p, \dot{p}, q, \dot{q}, r,$ or $\dot{r}$ (refer to Equation (7.74)). Some particular derivatives that appear frequently are:

C_{L_α} lift-curve slope, $\partial C_L/\partial\alpha$

C_{m_α} moment-curve slope, $\partial C_m/\partial\alpha$

$C_{m_q} + C_{m_{\dot\alpha}}$ damping-in-pitch derivative, $\partial C_m/\partial(ql/V) + \partial C_m/\partial(\dot\alpha l/V)$

C_{N_α} normal-force-curve slope, $\partial C_N/\partial\alpha$

$C_{i_{kp}}$ — partial derivative of C_{i_k} with respect to the roll rate p (Magnus terms)

C_{1_0} — value of C_1 at zero angle of attack

$\vec{F}$ — force vector

F_c — Coriolis force

F_i — component of force

g — gravitational constant

H_n — damping moment coefficients, $n = 0, 1, 2, \ldots$

H_{0_e} — effective linear damping

h_n $=$ $\dfrac{1}{2+n}\dfrac{H_n}{H_0}\alpha_a^n$ (Equation (7.201))

I — moment of inertia: for an axially symmetric body, $I_{\bar{y}} = I_{\bar{z}} = I$; for a general body oscillating in one plane, I is the moment of inertia about an axis perpendicular to that plane

$I_{\bar{x}, \bar{y}, \bar{z}}$ — roll, pitch, and yaw moments of inertia in body-fixed coordinates

$I_{\tilde{x}}$ — roll moment of inertia in fixed-plane coordinates ($I_{\tilde{x}} = I_{\bar{x}}$)

K — $\rho A/2m$

K_s — $\rho A l/2I$

l — reference length

$\dot{M}$ — moment vector

M_n — static moment coefficients, $n = 0, 1, 2, \ldots$

$\hat{M}_n$ — $-M_n/(\rho V^2 A l/2)$

$M_{l,m,n}$ — moment components in body-fixed coordinates

$\tilde{M}_{l,m,n}$	moment components in fixed-plane coordinates
M_∞	Mach number
m	mass
$m_n \quad =$	$\bar{M}_n \ddot{x}_a^n/M_0$ or $M_n \alpha_a^n/M_0$
p,q,r	components of angular velocity in body-fixed coordinates
$\tilde{p},\tilde{q},\tilde{r}$	components of angular velocity in fixed-plane coordinates
P	roll-rate parameter, $(I_{\bar{x}}/I)p = (I_{\tilde{x}}/I)\tilde{p}$
Q_i	generalized force or moment
q_i	generalized coordinate
R_∞	Reynolds number
SD	standard deviation
T	total kinetic energy
$[T]_{A_1/A_2}$	transformation matrix from A_2 coordinate system to A_1 coordinate system
t	time
u,v,w	linear velocity components in earth-fixed coordinates
$\bar{u},\bar{v},\bar{w}$	linear velocity components in body-fixed coordinates
$\tilde{u},\tilde{v},\tilde{w}$	linear velocity components in fixed-plane coordinates
$\vec{V}$	velocity vector
V	magnitude of velocity vector, $|\vec{V}|$
x,y,z	earth-fixed coordinates
$\bar{x},\bar{y},\bar{z}$	body-fixed coordinates
$\tilde{x},\tilde{y},\tilde{z}$	fixed-plane coordinates
$\hat{x},\hat{y},\hat{z}$	trajectory coordinates
α,β	projection of resultant angle of attack onto x-z plane, onto x-y plane
$\bar{\alpha},\bar{\beta}$	angle of attack and angle of sideslip in body-fixed coordinates
$\tilde{\alpha},\tilde{\beta}$	angle of attack and angle of sideslip in fixed-plane coordinates
α_a	defined by $\alpha_a^2 = \frac{1}{2}[(\alpha_m)_k^2 + (\alpha_m)_{k+1}^2]$ where k denotes peak number
α_m	maximum angle of attack
α_R	resultant angle of attack
α_{rms}	root-mean-square angle of attack
Γ	gamma function
γ_1,γ_2	angles relating trajectory axes to earth-fixed axes
θ,ψ,ϕ	projected angles
θ_E,σ,ψ_E	Euler angles
$\theta_{ME},\psi_{ME},\phi$	modified Euler angles
θ_a,θ_l	the direction of flight with respect to the local meridian and the geographical latitude of a given facility (Equation (7.71b))

λ	wavelength of oscillation
ξ	dynamic-stability parameter (Equation (7.104))
ρ	density of test medium
σ_m	maximum resultant angle of attack
σ_0	minimum resultant angle of attack
τ	period of oscillation
$\bar{\bar{\omega}}$	angular velocity
ω	frequency
ω_E	magnitude of earth's angular velocity (7.3×10^{-5} rad/sec)

Subscripts

cg	center of gravity
cp	center of pressure
D	drag
eff	effective
exp	experimental
L	lift
l,m,n	designation of moment orientation; that is, roll, pitch, and yaw, respectively
N	normal force
o	initial value
s	side force
$(\cdot)$	derivative with respect to time
$(\ )'$	derivative with respect to distance

7.3 COORDINATE SYSTEMS

The discussions in this chapter will involve a number of different coordinate systems, each of which has certain advantages in specific applications. For example, an inertial system is desirable for writing the equations of motion of a body in flight since the equations become much more complicated in an accelerating coordinate system. Other systems are more useful for obtaining experimental flight measurements and for describing the aerodynamic forces and moments acting on the body. Coordinate systems are also chosen to take advantage of certain degrees of body symmetry. Several of the more important ones will be described in the following sections.

7.3.1 Earth-Fixed Axes

Strictly speaking, earth-fixed axes are not inertial because of the earth's rotation. However, because of their convenience they can be used for writing the equations of motion if care is taken. An earth-fixed axis system is shown in Figure 7.1. It is a right-handed cartesian system with the z-axis aligned with the gravity vector. The x-axis is in the general direction of the flight (i.e., downrange). The origin is arbitrary. The flight path is assumed short, so the change in direction of the gravity vector due to curvature of the earth's surface can be neglected.

In this coordinate system, position measurements of the model center of gravity and angle measurements with respect to axes fixed in the model are made. The figure shows that the model flightpath is not in general along the x-axis; hence, the velocity has components u, v, and w.

As a result of the earth's rotation, an apparent force (Coriolis force) acts on a model in flight. In ballistic range testing, this can normally be neglected, but can become important for long-flight-distance or low-speed testing.

7.3.2 Body-Fixed Axes

A body-fixed axis system is one of several systems introduced to provide a reference frame for angular measurements and, hence, for writing the equations of angular momentum. It may also be used to define aerodynamic forces and moments. This system, designated by $\bar{x}, \bar{y}$, and $\bar{z}$, is shown in both Figure 7.2(a) and 7.2(b), along with the earth fixed axes (x,y,z), the components of angular velocity (p,q,r), and the components of linear velocity $(\bar{u}, \bar{v}, \bar{w})$. The body-fixed axes are normally chosen to be principal axes through the center of gravity (products of inertia are zero). The virtue of this coordinate system is that it greatly simplifies the equations of angular momentum. For airplane-like configurations, the $\bar{x}$-axis corresponds to the longitudinal axis (tail-to-nose), the transverse $\bar{y}$-axis to the direction of the right wing (perpendicular to the plane of symmetry) and the $\bar{z}$-axis intersects the other two forming a right-handed system.

There are two sets of angles which are commonly used in this system. First there are the Euler angles shown in Figure 7.2(a) which are defined as:

(i) Rotate about the x axis, θ_E (precession). This forms a new axis N (called the nodal axis) in the y-z plane. Note that the nodal axis is the line of intersection of the moving $\bar{y}$-$\bar{z}$ plane with the fixed y-z plane.

(ii) Pitch about the N axis, σ (nutation).

(iii) Roll about the $\bar{x}$ axis, ψ_E (spin).

Second, there are modified Euler angles shown in Figure 7.2(b) which are defined as:

(i) Yaw about the z axis, ψ_{ME}.

(ii) Pitch about the new y axis, θ_{ME}.

(iii) Roll about the $\bar{x}$ axis, ϕ.

Note that neither set of angles forms an orthogonal set or is commutative.

Another important set of angles used in the description of the forces and moments is $\bar{\alpha}, \bar{\beta}$, and α_R, referenced to the velocity vector. These angles are defined by

$$\left. \begin{aligned} \bar{\alpha} &= \sin^{-1}(\bar{w}/V), \quad \text{angle of attack} \\ \bar{\beta} &= \sin^{-1}(\bar{v}/V), \quad \text{angle of sideslip} \\ \alpha_R &= \cos^{-1}(\bar{u}/V), \quad \text{resultant angle of attack (has significance only for axisymmetric bodies).} \end{aligned} \right\} \quad (7.1)$$

7.3.3 Model-Oriented Fixed-Plane Axes

For axisymmetric bodies, simpler equations are obtained if a coordinate system which takes advantage of the axial symmetry is used. Of the three principal axes, only one is uniquely defined for axisymmetric bodies, the $\tilde{x}$ axis. There is an infinite selection of principal axes normal to the axis of symmetry. Hence, the $\tilde{y}$ axis may be chosen perpendicular to $\tilde{x}$ and contained in the x-y plane in a direction such that, when $\tilde{x}$ and x coincide, so do $\tilde{y}$ and y. The $\tilde{z}$ axis is then chosen to form a right-handed system. This system is shown in Figure 7.3. Again, the angles of interest are the modified Euler angles defined as:

(i) Yaw about the z axis, ψ_{ME}.

(ii) Pitch about the $\tilde{y}$ axis, θ_{ME}.

(iii) Rotate about the $\tilde{x}$ axis, ϕ. Note here that only the body rotates – not the $\tilde{y}$ and $\tilde{z}$ axes.

The angles of attack and sideslip, and their resultant are defined as

$$\left. \begin{aligned} \tilde{\alpha} &= \sin^{-1}(\tilde{w}/V) \\ \tilde{\beta} &= \sin^{-1}(\tilde{v}/V) \\ \alpha_R &= \cos^{-1}(\tilde{u}/V). \end{aligned} \right\} \quad (7.2)$$

The relationship between these angles and the modified Euler angles is shown in the upper portion of Figure 7.4.

In ballistic range work, a set of "projected" angles is also defined, which is similar to the modified Euler angles. The only difference is that the polar angle, θ_{ME}, is replaced by its projection on the x-z plane to correspond to the angle seen in side-view photographs (ψ_{ME}, as defined, is the angle seen in top-view photographs). This set of angles will be designated as ψ, θ, and ϕ, where $\psi = \psi_{ME}$ (Fig. 7.3).

7.3.4 Model-Oriented Nonrolling Axes

Another axis system introduced in Reference 7.9 but not used here is convenient with axisymmetric models, and has the advantage of allowing a simple angular momentum equation to be derived in an exact manner. It has the disadvantage of being difficult to visualize and requires that ballistic range data be transformed before being analyzed.

7.3.5 Trajectory Axes

Another useful coordinate system has one axis along the local velocity vector, $(\hat{x})$, and the other two perpendicular to the local velocity vector, $(\hat{y}, \hat{z})$. The $\hat{y}$ and $\hat{z}$ directions are chosen such that $\hat{y}$ lies in the x-y plane perpendicular to $\hat{x}$, and $\hat{z}$ forms a right-handed system. This system is illustrated in Figure 7.5. The angles locating these axes are γ_1 and γ_2, analogous to ψ_{ME} and θ_{ME}.

These coordinates are useful for axisymmetric bodies and/or planar motion in writing the aerodynamic forces and, in some cases, the equations of linear momentum. In tests in a ballistic range, the angles γ_1 and γ_2 are normally very small and hence certain simplifications are possible.

7.3.6 Relationships Between Systems

Since it is sometimes necessary to transform one coordinate system to another, we will give some transformation relations, both exact and approximate, before we proceed to the equations of motion.

The transformation matrix is that matrix which operates on a vector in one coordinate system to produce the vector in another system. For example, the forces in the body-fixed coordinates $\vec{F}_B$ transform to earth-fixed coordinates $\vec{F}_E$ by

$$\vec{F}_E = [T]_{E/B} \vec{F}_B , \qquad (7.3)$$

where $[T]_{E/B}$ is the transformation matrix. This transformation matrix preserves the magnitude and direction of the vector; that is, it simply relates the vector to a different coordinate system. Hence, these matrices have the properties of a unitary matrix, that is, the inverse is equal to the transpose,

$$(T_{ij})^{-1} = (T_{ji}) = (T_{ij})^T . \qquad (7.4)$$

Hence, it follows that $(T_{ij})_{A/B} = (T_{ij})_{B/A}^T$.

The transformation matrix for body-fixed to earth-fixed coordinates (using modified Euler angles) is

$$[T]_{E/B} = \begin{pmatrix} \cos\theta_{ME}\cos\psi_{ME} & \sin\theta_{ME}\cos\psi_{ME}\sin\phi - \sin\psi_{ME}\cos\phi & \sin\theta_{ME}\cos\psi_{ME}\cos\phi + \sin\psi_{ME}\sin\phi \\ \cos\theta_{ME}\sin\psi_{ME} & \sin\theta_{ME}\sin\psi_{ME}\sin\phi + \cos\psi_{ME}\cos\phi & \sin\theta_{ME}\sin\psi_{ME}\cos\phi - \cos\psi_{ME}\sin\phi \\ -\sin\theta_{ME} & \cos\theta_{ME}\sin\phi & \cos\theta_{ME}\cos\phi \end{pmatrix} . \qquad (7.5)$$

For body-oriented fixed-plane coordinates to earth-fixed coordinates, it is

$$[T]_{E/FP} = \begin{pmatrix} \cos\theta_{ME}\cos\psi_{ME} & -\sin\psi_{ME} & \sin\theta_{ME}\cos\psi_{ME} \\ \cos\theta_{ME}\sin\psi_{ME} & \cos\psi_{ME} & \sin\theta_{ME}\sin\psi_{ME} \\ -\sin\theta_{ME} & 0 & \cos\theta_{ME} \end{pmatrix} \qquad (7.6)$$

and for trajectory coordinates to earth-fixed coordinates, it is

$$[T]_{E/T} = \begin{pmatrix} \cos\gamma_1\cos\gamma_2 & -\sin\gamma_1 & \cos\gamma_1\sin\gamma_2 \\ \sin\gamma_1\cos\gamma_2 & \cos\gamma_1 & \sin\gamma_1\sin\gamma_2 \\ -\sin\gamma_2 & 0 & \cos\gamma_2 \end{pmatrix} . \qquad (7.7)$$

It is possible to obtain relations between any combination of these systems using appropriate matrix multiplication.

These matrices will now be considered for small angles (except ϕ); that is

$$\sin(a) = a$$
$$\cos(a) = 1$$

Then the transformation matrices become

$$[T]_{E/B} \begin{pmatrix} 1 & \theta_{ME}\sin\phi - \psi_{ME}\cos\phi & \theta_{ME}\cos\phi + \psi_{ME}\sin\phi \\ \psi_{ME} & \cos\phi & -\sin\phi \\ -\theta_{ME} & \sin\phi & \cos\phi \end{pmatrix} \qquad (7.8)$$

$$[T]_{E/FP} \begin{pmatrix} 1 & -\psi_{ME} & \theta_{ME} \\ \psi_{ME} & 1 & 0 \\ -\theta_{ME} & 0 & 1 \end{pmatrix} \qquad (7.9)$$

$$[T]_{E/T} = \begin{pmatrix} 1 & -\gamma_1 & \gamma_2 \\ \gamma_1 & 1 & 0 \\ -\gamma_2 & 0 & 1 \end{pmatrix} . \tag{7.10}$$

Note that in these last three transformations, it would be consistent with the small-angle assumption to replace θ_{ME} and γ_2 by their projected values (on the x-z plane).

Another transformation matrix which is of interest is that between the trajectory coordinates and the body-oriented fixed-plane coordinates. This is obtained by the appropriate operations on Equations (7.6) and (7.7) (i.e., $[T]_{PP/T} = [T]_{PP/E} \cdot [T]_{E/T} = [T]_{E/PP}^T \cdot [T]_{E/T}$). The result to first order is

$$[T]_{PP/T} = \begin{pmatrix} 1 & \psi_{ME} - \gamma_1 & -\theta_{ME} + \gamma_2 \\ -\psi_{ME} + \gamma_1 & 1 & 0 \\ \theta_{ME} - \gamma_2 & 0 & 1 \end{pmatrix} . \tag{7.11}$$

The interpretation of the elements of this matrix is straightforward. If one calculates the components of velocity in the fixed-plane system using the first order matrix, the result is

$$\vec{V}_{PP} - [T]_{PP/T} \cdot \vec{V}_T$$

or

$$\begin{pmatrix} 1 & \psi_{ME} - \gamma_1 & -\theta_{ME} + \gamma_2 \\ -\psi_{ME} + \gamma_1 & 1 & 0 \\ \theta_{ME} - \gamma_2 & 0 & 1 \end{pmatrix} \cdot \begin{pmatrix} V \\ 0 \\ 0 \end{pmatrix} = \begin{pmatrix} V \\ (-\psi_{ME} + \gamma_1) V \\ (\theta_{ME} - \gamma_2) V \end{pmatrix} = \begin{pmatrix} \tilde{u} \\ \tilde{v} \\ \tilde{w} \end{pmatrix} . \tag{7.12}$$

Since the angle of attack and angle of sideslip are defined as

$$\left. \begin{aligned} \tilde{\alpha} &= \sin^{-1}\left(\frac{\tilde{w}}{V}\right) \approx \frac{\tilde{w}}{V} \\ \tilde{\beta} &= \sin^{-1}\left(\frac{\tilde{v}}{V}\right) \approx \frac{\tilde{v}}{V} , \end{aligned} \right\} \tag{7.13}$$

then to first order

$$\left. \begin{aligned} \tilde{\alpha} &= \theta_{ME} - \gamma_2 \\ \tilde{\beta} &= -\psi_{ME} + \gamma_1 . \end{aligned} \right\} \tag{7.14}$$

These angles are the off-diagonal elements in the transformation (7.11). They can be better visualized by referring to the lower portion of Figure 7.4. This is a view looking aft along the earth-fixed x axis at the y-z plane. A unit vector along the model axis, $\tilde{x}$, has a projection $0-A$, labeled $\vec{\Omega}$, with components θ_{ME} and ψ_{ME}. A unit vector along the total velocity vector appears as a projection $0-B$ and is called $\vec{\gamma}$. The components of $\vec{\gamma}$ are $\dot{y}/V$ and $\dot{z}/V$, which are essentially equal to γ_1 and $-\gamma_2$. The vector $B-A$ between the velocity vector and the model axis $\tilde{x}$ is called the resultant angle of attack, $\tilde{\alpha}_R$, and has components $\tilde{\alpha}$ and $\tilde{\beta}$. Therefore

$$\vec{\alpha}_R = \vec{\Omega} - \vec{\gamma} . \tag{7.15}$$

This is an exact expression when velocity components are used. Also shown in this figure is the angle, ϕ, which one would observe between the coordinate axes and a canard on the nose of the body.

The coordinate systems necessary for motion analysis are now defined, and their relationships to one another have been given. We can now proceed to the development of the equations of motion for a body in free flight.

7.4 EQUATIONS OF MOTION

The equations of motion will be developed in three steps. First, the dynamics of a body in free-flight will be expressed in several forms. Second expressions for the aerodynamic forces and moments will be obtained. Then the forces, moments, and flight dynamics will be combined to obtain the differential equations of motion.

7.4.1 Flight Dynamics

7.4.1.1 Introduction

The behavior of a rigid body in flight is governed by Newton's laws of motion. Although there are various ways of expressing these laws, the simplest is to write the equations of conservation of linear and angular momentum within an inertial reference frame

$$\frac{d(m\vec{V})}{dt} = \vec{F} \tag{7.16}$$

and

$$\frac{d([I]\vec{\omega})}{dt} = \vec{M} \ . \tag{7.17}$$

where m is the mass of the body, $\vec{V}$ is its velocity vector, $\vec{F}$ is the force vector acting on it, $[I]$ is the moment of inertia (a 2nd rank tensor), $\vec{\omega}$ is the angular velocity vector, and $\vec{M}$ is the moment vector. To apply these equations in a moving coordinate system one needs the transformation

$$\left(\frac{d\vec{A}}{dt}\right)_m = \left(\frac{d\vec{A}}{dt}\right)_f + \vec{\omega} \times \vec{A}_f \ , \tag{7.18}$$

where $\vec{A}$ is any vector quantity, m denotes the moving system and f the fixed system. An example of the type of quantity produced by the 2nd term is the Coriolis acceleration which appears in the equations of motion expressed in earth-fixed coordinates.

Another formulation of the momentum equations is that of Lagrange. It will be used more extensively in the following development than the basic form given above.

7.4.1.2 Lagrangian Equations

The Lagrangian equations of motion are derived in textbooks on dynamics[7.10]. These equations greatly simplify the handling of the pitching and yawing motion of a body in free flight. The Lagrangian equations are

$$\frac{d}{dt}\left(\frac{\partial T}{\partial \dot{q}_i}\right) - \frac{\partial T}{\partial q_i} = Q_i \ . \tag{7.19}$$

Here T is the total kinetic energy of the system; q_i is the ith generalized coordinate; $\dot{q}_i$ is the time rate of change of q_i; Q_i is the force tending to change q_i; and t is time. There are as many such equations as there are degrees of freedom, the subscript i representing, therefore, the ith degree of freedom. For free flight of a rigid body there are six degrees of freedom, three translational and three rotational.

The total kinetic energy of a rigid body in free flight is written as

$$T = \tfrac{1}{2}m(\dot{x}^2 + \dot{y}^2 + \dot{z}^2) + \tfrac{1}{2}I_{\bar{x}}p^2 + \tfrac{1}{2}I_{\bar{y}}q^2 + \tfrac{1}{2}I_{\bar{z}}r^2 \ , \tag{7.20}$$

where m is the model mass, $I_{\bar{x}}$, $I_{\bar{y}}$, and $I_{\bar{z}}$ are the moments of inertia about the three principal axes, p, q, and r are the angular rates about the principal axes and $\dot{x} = u$, $\dot{y} = v$, and $\dot{z} = w$ are the components of velocity in the earth-fixed axis system. Note that in using earth-fixed axes some energy has been ignored due to the non-inertial character of the earth-fixed coordinates. The only important term here is the Coriolis acceleration which we will discuss under the section on forces.

For a body with axial symmetry

$$I_{\bar{y}} = I_{\bar{z}} = I \tag{7.21}$$

and hence the total kinetic energy can be written as

$$T = \tfrac{1}{2}m(\dot{x}^2 + \dot{y}^2 + \dot{z}^2) + \tfrac{1}{2}I_{\bar{x}}p^2 + \tfrac{1}{2}I(q^2 + r^2) \ . \tag{7.22}$$

Note that any body which has a plane of mass symmetry and trigonal or greater rotational (mass) symmetry can be considered to be axially symmetric with respect to its moments of inertia ($I_{\bar{y}} = I_{\bar{z}}$).

7.4.1.3 Equations of Linear Momentum

The equations of motion in the x, y, and z directions can be obtained as follows: Let x be the first generalized coordinate,

$$\frac{d}{dt}\left(\frac{\partial T}{\partial \dot{x}}\right) - \frac{\partial T}{\partial x} = Q_x \ . \tag{7.23}$$

Using Equation (7.20),

$$m\frac{d^2x}{dt^2} = Q_x = F_x \ ; \tag{7.24}$$

similarly,

$$m \frac{d^2 y}{dt^2} = F_y \tag{7.25}$$

and

$$m \frac{d^2 z}{dt^2} = F_z . \tag{7.26}$$

In vector form these equations can be written

$$m \frac{d^2 \vec{R}}{dt^2} = \vec{F} . \tag{7.27}$$

Note that the mass, m, has been taken outside the differential operator. This can be done not only if the mass is a constant, but also if the velocity (relative to the body) of the mass that leaves the body is very small. In that case, its contribution to the change in momentum can be neglected. Most of the problems to be treated will be for constant mass but some cases will be considered with variable mass where this momentum assumption is thought to be valid.

These equations can alternately be written in the trajectory coordinates described earlier. The result for the component of force along the velocity vector is

$$m \frac{d^2 \hat{x}}{dt^2} = F_{\hat{x}} \tag{7.28}$$

and that normal to the velocity vector is

$$m \left(\frac{d\hat{x}}{dt} \right)^2 \vec{R}_c / R_c^2 = \vec{F} (F_{\hat{y}}, F_{\hat{z}}) . \tag{7.29}$$

The term on the left side of this equation is the centrifugal force term (R_c is the radius of curvature of the flight path) which arises from the non-inertial character of the trajectory coordinates.

7.4.1.4 Equations of Angular Momentum

The Lagrangian equations of angular motion can be written with each of the three sets of angles which have been introduced. The angular momentum equations will be written (at least in part) using all three sets so that similarities and differences can be seen. First, however, one must obtain the angular velocities in terms of the angles for each of the systems. They are listed in the following table.

Euler Angles	Modified Euler Angles	Fixed-Plane Modified Euler Angles
$p = \dot{\psi}_E + \dot{\theta}_E \cos \sigma$	$p = \dot{\phi} - \dot{\psi}_{ME} \sin \theta_{ME}$	$\tilde{p} = \dot{\phi} - \dot{\psi}_{ME} \sin \theta_{ME}$
$q = \dot{\sigma} \cos \psi_E + \dot{\theta}_E \sin \sigma \sin \psi_E$	$q = \dot{\theta}_{ME} \cos \phi + \dot{\psi}_{ME} \cos \theta_{ME} \sin \phi$	$\tilde{q} = \dot{\theta}_{ME}$
$r = -\dot{\sigma} \sin \psi_E + \dot{\theta}_E \sin \sigma \cos \psi_E$	$r = \dot{\psi}_{ME} \cos \theta_{ME} \cos \phi - \dot{\theta}_{ME} \sin \phi$	$\tilde{r} = \dot{\psi}_{ME} \cos \theta_{ME}$

Since the Euler angles and the modified Euler angles are more general in that they do not require axial symmetry, they will be considered first. The total kinetic energy using the Euler angles is

$$T = \tfrac{1}{2}m (\dot{x}^2 + \dot{y}^2 + \dot{z}^2) + \tfrac{1}{2}I_{\bar{x}} (\dot{\psi}_E + \dot{\theta}_E \cos \sigma)^2 + \tfrac{1}{2}I_{\bar{y}} (\dot{\sigma} \cos \psi_E + \dot{\theta}_E \sin \sigma \sin \psi_E)^2 +$$
$$+ \tfrac{1}{2}I_{\bar{z}} (-\dot{\sigma} \sin \psi_E + \dot{\theta}_E \sin \sigma \cos \psi_E)^2 \tag{7.30}$$

and the total kinetic energy using the modified Euler angles is

$$T = \tfrac{1}{2}m (\dot{x}^2 + \dot{y}^2 + \dot{z}^2) + \tfrac{1}{2}I_{\bar{x}} (\dot{\phi} - \dot{\psi}_{ME} \sin \theta_{ME})^2 + \tfrac{1}{2}I_{\bar{y}} (\dot{\theta}_{ME} \cos \phi + \dot{\psi}_{ME} \cos \theta_{ME} \sin \phi)^2 +$$
$$+ \tfrac{1}{2}I_{\bar{z}} (\dot{\psi}_{ME} \cos \theta_{ME} \cos \phi - \dot{\theta}_{ME} \sin \phi)^2 . \tag{7.31}$$

It is straightforward to substitute both of the above expressions for T into the Lagrangian equations (7.19) and arrive at the equations of angular momentum. However only those equations using modified Euler angles will be listed here. For the ψ_{ME} coordinate, we get

$$\frac{d}{dt} \left(\frac{\partial T}{\partial \dot{\psi}_{ME}} \right) = \frac{d}{dt} [I_{\bar{x}} (\dot{\phi} - \dot{\psi}_{ME} \sin \theta_{ME}) (-\sin \theta_{ME}) + I_{\bar{y}} (\dot{\theta}_{ME} \cos \phi + \dot{\psi}_{ME} \cos \theta_{ME} \sin \phi) (\cos \theta_{ME} \sin \phi) +$$
$$+ I_{\bar{z}} (\dot{\psi}_{ME} \cos \theta_{ME} \cos \phi - \dot{\theta}_{ME} \sin \phi) (\cos \theta_{ME} \cos \phi)] = Q_{\psi_{ME}} \tag{7.32}$$
$$= [M_m \sin \phi + M_n \cos \phi] \cos \theta_{ME} .$$

for the θ_{ME} coordinate.

$$\frac{d}{dt}\left(\frac{\partial T}{\partial \dot{\theta}_{ME}}\right) - \frac{\partial T}{\partial \theta_{ME}} = \frac{d}{dt}\left[I_{\bar{y}}\left(\dot{\theta}_{ME}\cos\phi + \dot{\psi}_{ME}\cos\theta_{ME}\sin\phi\right)(\cos\phi) + \right.$$

$$+ I_{\bar{z}}\left(\dot{\psi}_{ME}\cos\theta_{ME}\cos\phi - \dot{\theta}_{ME}\sin\phi\right)(-\sin\phi)] +$$

$$+ I_{\bar{x}}\left(\dot{\phi} - \dot{\psi}_{ME}\sin\theta_{ME}\right)\left(\dot{\psi}_{ME}\cos\theta_{ME}\right) +$$

$$+ I_{\bar{y}}\left(\dot{\theta}_{ME}\cos\phi + \dot{\psi}_{ME}\cos\theta_{ME}\sin\phi\right)\left(\dot{\psi}_{ME}\sin\theta_{ME}\sin\phi\right) +$$

$$+ I_{\bar{z}}\left(\dot{\psi}_{ME}\cos\theta_{ME}\cos\phi - \dot{\theta}_{ME}\sin\phi\right)\left(\dot{\psi}_{ME}\sin\theta_{ME}\cos\phi\right) = Q_{\theta_{ME}} = M_m\cos\phi - M_n\sin\phi \qquad (7.33)$$

and for the ϕ coordinate

$$\frac{d}{dt}\left(\frac{\partial T}{\partial \dot{\phi}}\right) - \frac{\partial T}{\partial \phi} = \frac{d}{dt}\left[I_{\bar{x}}\left(\dot{\phi} - \dot{\psi}_{ME}\sin\theta_{ME}\right)\right] +$$

$$+ I_{\bar{y}}\left(\dot{\theta}_{ME}\cos\phi + \dot{\psi}_{ME}\cos\theta_{ME}\sin\phi\right)\left(\dot{\theta}_{ME}\sin\phi - \dot{\psi}_{ME}\cos\theta_{ME}\cos\phi\right) +$$

$$+ I_{\bar{z}}\left(\dot{\psi}_{ME}\cos\theta_{ME}\cos\phi - \dot{\theta}_{ME}\sin\phi\right)\left(\dot{\psi}_{ME}\cos\theta_{ME}\sin\phi + \dot{\theta}_{ME}\cos\phi\right) = Q_{\phi} = M_l . \qquad (7.34)$$

These equations represent a set for the angular momentum. They are general in the sense that they apply to an arbitrary rigid body.

A more widely used form for the equations of angular momentum of an airplane-like configuration can be obtained from (7.17) and (7.18). First let $\vec{\omega} = \vec{\omega}(p,q,r)$. Then note that the cross-product needed in (7.18), $\vec{\omega} \times I\vec{\omega}$, can be represented by the determinant

$$\begin{vmatrix} \vec{l} & \vec{m} & \vec{n} \\ p & q & r \\ I_{\bar{x}}p & I_{\bar{y}}q & I_{\bar{z}}r \end{vmatrix} .$$

The resulting equations are:

$$\left. \begin{array}{l} I_{\bar{z}}\dot{r} = pq\left(I_{\bar{x}} - I_{\bar{y}}\right) + M_n \\[2mm] I_{\bar{y}}\dot{q} = pr\left(I_{\bar{z}} - I_{\bar{x}}\right) + M_m \\[2mm] I_{\bar{x}}\dot{p} = qr\left(I_{\bar{y}} - I_{\bar{z}}\right) + M_l . \end{array} \right\} \qquad (7.35)$$

In comparison to (7.32), (7.33), and (7.34), these equations are much simpler. Because (7.32)-(7.34) are so complicated, we will treat some specialized cases which result in many simplifications.

7.4.1.5 Planar Motion

For the case of planar motion (an oscillation confined to a single plane, here arbitrarily the x-z plane) ψ_{ME} is identically zero and since there can be no roll, $\dot{\phi} = 0$. Note that the results obtained will apply to any planar motion since in the absence of an important gravity force, the x-z plane can be rotated to the plane of motion. With these conditions (a single degree of rotational freedom) the equation for angular momentum is

$$I_{\bar{y}}\ddot{\theta}_{ME} = M_m . \qquad (7.36)$$

7.4.1.6 Small Angular Motion

There are a number of subcases in this category and several of them will be considered. First assume that the angles θ_{ME} and ψ_{ME} (but not necessarily ϕ) and the angular rates and accelerations are small. Hence,

$$\sin\psi_{ME} = \psi_{ME}$$

$$\sin\theta_{ME} = \theta_{ME}$$

$$\cos\psi_{ME} = \cos\theta_{ME} = 1 .$$

With these restrictions and neglecting products of small terms, the equations of angular momentum in terms of the modified Euler angles reduce to the following:

$$I_{\bar{y}}\left(\ddot{\theta}_{ME}\sin\phi\cos\phi + \ddot{\psi}_{ME}\sin^2\phi\right) + I_{\bar{z}}\left(\ddot{\psi}_{ME}\cos^2\phi - \ddot{\theta}_{ME}\sin\phi\cos\phi\right) = M_m\sin\phi + M_n\cos\phi \qquad (7.37)$$

$$I_{\bar{y}}\left(\ddot{\theta}_{ME}\cos^2\phi + \ddot{\psi}_{ME}\sin\phi\cos\phi\right) + I_{\bar{z}}\left(-\ddot{\psi}_{ME}\sin\phi\cos\phi + \ddot{\theta}_{ME}\sin^2\phi\right) = M_m\cos\phi - M_n\sin\phi \qquad (7.38)$$

$$I_{\bar{x}}\ddot{\phi} = M_l .$$
(7.39)

If, in addition, we assume there is no rolling torque ($M_l = 0$), (7.39) can be solved and

$$\phi = A + Bt .$$
(7.40)

If this result is substituted into (7.37) and (7.38) the result is

$$I_{\bar{y}}[\ddot{\theta}_{ME}\sin(A+Bt)\cos(A+Bt) + \ddot{\psi}_{ME}\sin^2(A+Bt)] + I_{\bar{z}}[\ddot{\psi}_{ME}\cos^2(A+Bt) - \ddot{\theta}_{ME}\sin(A+Bt)\cos(A+Bt)]$$
(7.41)

$$= M_m \sin\phi + M_n \cos\phi .$$

and

$$I_{\bar{y}}[\ddot{\theta}_{ME}\cos^2(A+Bt) + \ddot{\psi}_{ME}\sin(A+Bt)\cos(A+Bt)] + I_{\bar{z}}[-\ddot{\psi}_{ME}\sin(A+Bt)\cos(A+Bt) + \ddot{\theta}_{ME}\sin^2(A+Bt)]$$
(7.42)

$$= M_m \cos\phi - M_n \sin\phi .$$

The left hand sides of these two equations are linear with variable coefficients and are coupled.

Finally, if it is assumed that the angle ϕ is also small, the equations become

$$\left.\begin{array}{l} I_{\bar{z}}\ddot{\psi}_{ME} = M_n \\ I_{\bar{y}}\ddot{\theta}_{ME} = M_m . \end{array}\right\}$$
(7.43)

All of the coupling has now been removed from the left hand sides.

7.4.1.7 Axially Symmetric Bodies

A more restricted but often encountered case will now be considered, namely, that of an axially symmetric body. Noting that $I_{\bar{y}} = I_{\bar{z}} = I$, the kinetic energy can be expressed in terms of Euler angles as

$$T = \tfrac{1}{2}m(\dot{x}^2 + \dot{y}^2 + \dot{z}^2) + \tfrac{1}{2}I_{\bar{x}}(\dot{\psi}_- + \dot{\theta}_E\cos\sigma)^2 + \tfrac{1}{2}I(\dot{\sigma}^2 + \dot{\theta}_E^2\sin^2\sigma) .$$
(7.44)

The following equations of angular momentum can then be obtained.

$$\frac{d}{dt}[I_{\bar{x}}(\dot{\psi}_E + \dot{\theta}_E\cos\sigma)\cos\sigma + I\dot{\theta}_E\sin^2\sigma] = Q_{\theta_E}$$
(7.45)

$$\frac{d}{dt}[I\dot{\sigma}] + I_{\bar{x}}(\dot{\psi}_E + \dot{\theta}_E\cos\sigma)\dot{\theta}_E\sin\sigma - I\dot{\theta}_E^2\sin\sigma\cos\sigma = Q_\sigma$$
(7.46)

$$\frac{d}{dt}[I_{\bar{x}}(\dot{\psi}_E + \dot{\theta}_E\cos\sigma)] = Q_{\psi_E} .$$
(7.47)

These equations represent the most general case for an axially symmetric body. Noting that $\dot{\psi}_E + \dot{\theta}_E\cos\sigma = p$ and, defining a new parameter

$$P = \frac{I_{\bar{x}}}{I}p ,$$
(7.48)

then (7.45), (7.46), and (7.47) can be written as

$$\frac{d}{dt}(IP\cos\sigma + I\dot{\theta}_E\sin^2\sigma) = Q_{\theta_E}$$
(7.49)

$$\frac{d}{dt}(I\dot{\sigma}) + IP\dot{\theta}_E\sin\sigma - I\dot{\theta}_E^2\sin\sigma\cos\sigma = Q_\sigma$$
(7.50)

$$\frac{d}{dt}(IP) = Q_{\psi_E} .$$
(7.51)

A special case using these equations is for zero roll torque ($Q_{\psi_E} = 0$) and for zero precession torque ($Q_{\theta_E} \equiv 0$). With these restrictions, (7.49) and (7.51) become

$$IP\cos\sigma + I\dot{\theta}_E\sin^2\sigma = \text{constant} \equiv Ib$$
(7.52)

$$IP = \text{constant} ,$$
(7.53)

and hence, (7.50) becomes

$$\frac{d}{dt}(I\dot{\sigma}) + \frac{IP(b - P\cos\sigma)}{\sin\sigma} - \frac{I\cos\sigma(b - P\cos\sigma)^2}{\sin^3\sigma} = Q_\sigma .$$
(7.54)

Note that even for this restricted case the problem is highly nonlinear even if the right hand side of the equation is linear. This equation remains nonlinear even for small angles (i.e. σ small).

For the case of σ small, (7.54) reduces to

$$I\ddot{\sigma} + IP\frac{(b-P)}{\sigma} - I\frac{(b-P)^2}{\sigma^3} = Q_\sigma .$$ (7.55)

For planar motion $b = P = 0$ and (7.55) reduces to

$$I\ddot{\sigma} = Q_\sigma .$$ (7.56)

Note the left hand side of the equation is linear.

One other case that is of interest is that for which the moments are all conservative. Here the sum of the kinetic energy plus the potential energy is constant. This case is developed in Reference 7.8 and will not be discussed here.

Next the momentum equations using modified Euler angles in fixed-plane axes will be considered. Noting that $I_{\tilde{y}} = I_{\tilde{z}} = I$, the total kinetic energy is

$$T = \tfrac{1}{2}m(\dot{x}^2 + \dot{y}^2 + \dot{z}^2) + \tfrac{1}{2}I_{\tilde{x}}(\dot{\phi} - \dot{\psi}_{ME}\sin\theta_{ME})^2 + \tfrac{1}{2}I(\dot{\theta}_{ME}^2 + \dot{\psi}_{ME}^2\cos^2\theta_{ME}) .$$ (7.57)

Substituting into the Lagrangian Equations (7.19) one obtains for $\psi_{ME}, \theta_{ME},$ and ϕ respectively

$$\frac{d}{dt}[-I_{\tilde{x}}(\dot{\phi} - \dot{\psi}_{ME}\sin\theta_{ME})\sin\theta_{ME} + I(\dot{\psi}_{ME}\cos^2\theta_{ME})] = \tilde{M}_n\cos\theta_{ME}$$ (7.58)

$$\frac{d}{dt}(I\dot{\theta}_{ME}) + I_{\tilde{x}}(\dot{\phi} - \dot{\psi}_{ME}\sin\theta_{ME})\dot{\psi}_{ME}\cos\theta_{ME} + I\dot{\psi}_{ME}^2\sin\theta_{ME}\cos\theta_{ME} = \tilde{M}_m$$ (7.59)

$$\frac{d}{dt}[I_{\tilde{x}}(\dot{\phi} - \dot{\psi}_{ME}\sin\theta_{ME})] = \tilde{M}_l .$$ (7.60)

These are the basic equations using modified Euler angles, and are similar to those with Euler angles. Consider the case where $\tilde{M}_l = 0$ (no roll torque). One obtains

$$(\dot{\phi} - \dot{\psi}_{ME}\sin\theta_{ME}) = \tilde{p} = \text{constant} \equiv \frac{I}{I_{\tilde{x}}}P .$$ (7.61)

Substituting this in the remaining two equations yields

$$-IP\dot{\theta}_{ME}\cos\theta_{ME} + I\ddot{\psi}_{ME}\cos^2\theta_{ME} - 2I\dot{\psi}_{ME}\dot{\theta}_{ME}\sin\theta_{ME}\cos\theta_{ME} = \tilde{M}_n\cos\theta_{ME}$$ (7.62)

and

$$I\ddot{\theta}_{ME} + IP\dot{\psi}_{ME}\cos\theta_{ME} + I\dot{\psi}_{ME}^2\sin\theta_{ME}\cos\theta_{ME} = \tilde{M}_m .$$ (7.63)

If these equations are now linearized, the result is

$$I\ddot{\psi}_{ME} - IP\dot{\theta}_{ME} = \tilde{M}_n$$ (7.64)

$$I\ddot{\theta}_{ME} + IP\dot{\psi}_{ME} = \tilde{M}_m ,$$ (7.65)

where it has been assumed that

$$\left.\begin{array}{c} \cos\theta_{ME} \approx 1 \\ \sin\theta_{ME} \approx \theta_{ME} \end{array}\right\}$$ (7.66)

and products of small terms have been neglected. Note that it is convenient to express (7.64) and (7.65) as a single equation in the complex plane (since $\dot{\theta}_{ME}$ and $\dot{\psi}_{ME}$ are orthogonal). This is done simply by multiplying (7.64) by $i(\sqrt{(-1)})$ and then collecting real and imaginary parts.

$$I\dot{\tilde{\Omega}} - iIP\dot{\tilde{\Omega}} = \tilde{M} ,$$ (7.67)

where

$$\dot{\tilde{\Omega}} = \dot{\theta}_{ME} + i\dot{\psi}_{ME}$$ (7.68)

and

$$\tilde{M} = \tilde{M}_m + i\tilde{M}_n .$$ (7.69)

There is another method (although not discussed here) of developing the dynamic equations of motion of a symmetric body which employs the nonrolling axes mentioned in Section 7.3.4 (Ref.7.9). This approach is advantageous in that a simple, exact differential equation for pitching motion can be obtained, but it is not as convenient to use since measured data must be expressed in an inconvenient reference frame.

With the above several formulations of the dynamic equations of motion available to us, it remains to consider the applied forces and moments which make up the right hand sides of these equations.

7.4.2 Forces and Moments

7.4.2.1 Introduction

The forces and moments acting on a body in flight can originate from a number of different sources, including pressure and shear forces, gravitational force, buoyancy force, Coriolis force, and electromagnetic force. In ballistic range tests, aerodynamic forces are usually dominant, and for tests of low flight velocity and/or long duration, gravity and Coriolis forces can become important. Buoyancy and electromagnetic forces are negligible and will not be considered. The bulk of the discussion in this chapter will be concerned with aerodynamic forces and moments. However, since gravity and Coriolis forces are sometimes considered, they will be described briefly now.

If the coordinate system is earth-fixed as described earlier, the gravity vector is always aligned with the z-axis and hence the gravity force can be written as

$$F_{z\ grav} = mg .$$
(7.70)

The Coriolis force is given by

$$\vec{F}_c = 2m (\vec{\omega}_E \times \vec{V}) ,$$
(7.71a)

where $\vec{\omega}_E$ is the rotational velocity of the earth ($\omega_E = 7.3 \times 10^{-5}$ rad/sec), and m is the mass of the body in flight. Equation (7.71a) can be expanded to obtain

$$F_c = 2m\omega_E V (\sin\theta_l + i \cos\theta_l \sin\theta_a) ,$$
(7.71b)

where the first term is along the y axis and the last term is along the z axis, θ_l is the geographical latitude of the facility ($0°$ at the equator) and θ_a is the direction of flight (i.e. the angle between the earth-fixed x axis and the local meridian · due east yields $\theta_a = 90°$).

7.4.2.2 Aerodynamic Forces and Moments

The aerodynamic forces and moments are defined in body-fixed axes normally chosen to be principal axes through the center of mass. This coordinate system, with related forces and moments, is shown in Figure 7.6. The force components produce moments M_l, M_m, M_n about the $\bar{x}$, $\bar{y}$, and $\bar{z}$ axes, respectively.

The aerodynamic forces and moments are in general quite complicated. The aerodynamic force coefficients are expressed as $C_{force} = Force/\frac{1}{2}\rho V^2 A$ and the aerodynamic moment coefficients as $C_{moment} = Moment/\frac{1}{2}\rho V^2 A l$, where ρ is the density of the fluid through which the body is flying, V is the flight velocity, A is the reference area, and l is the reference length. They are functions of flight speed, conditions of the test gas, model scale, and geometry. They also depend to some degree on the flight history. If the dependence on history were strong, a correlation of results would be next to impossible. In practice this dependence is not strong. Therefore, the "aerodynamic hypothesis" will be invoked; that is, the forces on a body in free flight can be expressed in terms of the body's instantaneous motion. This can be done in two ways; in terms of velocity ratios $\bar{u}/V$, $\bar{v}/V$, $\bar{w}/V$, p, q, and r and derivatives thereof or, equivalently, in terms of the angles represented by the velocity ratios $\bar{u}/V$, $\bar{\beta}$, $\bar{\alpha}$, p, q, r. In the work to follow the latter will be used.

The aerodynamic hypothesis should apply when the flight distance in a cycle of oscillatory motion is many times the length of the body, the usual situation both in full-scale flight and in ballistic ranges. Despite this simplifying assumption, there remain many variables on which the forces may depend. We will write this functional dependence as

$$F_i = C_i (R_\infty, M_\infty, \bar{\alpha}, \bar{\beta}, \dot{\bar{\alpha}}, \dot{\bar{\beta}}, p, q, r \ldots) \frac{1}{2}\rho V^2 A ,$$
(7.72)

where $C_i (R_\infty, M_\infty, \ldots\ldots)$ is the ith force coefficient (for example, $i = \bar{x}, \bar{y}, \bar{z}$) and R_∞, M_∞ are Reynolds number and Mach number.

Similarly, for the moments

$$M_j = C_j (R_\infty, M_\infty, \bar{\alpha}, \bar{\beta}, \dot{\bar{\alpha}}, \dot{\bar{\beta}}, p, q, r \ldots) \frac{1}{2}\rho V^2 A l ,$$
(7.73)

where C_j is the jth moment coefficient (the subscript j becomes l, m, n for moments about the $\bar{x}, \bar{y}$, and $\bar{z}$ axes, respectively).

For well-behaved aerodynamic coefficients (i.e., smooth, continuous and single-valued functions) the coefficients can be expanded in a Taylor series as follows:

$$C_i = C_{i_0} + C_{i_\alpha}\bar{\alpha} + C_{i_\beta}\bar{\beta} +$$

$$+ C_{i_{\dot{\alpha}}}\frac{\dot{\bar{\alpha}}l}{V} + C_{i_{\dot{\beta}}}\frac{\dot{\bar{\beta}}l}{V} +$$

$$+ C_{i_p}\frac{pl}{V} + C_{i_q}\frac{ql}{V} + C_{i_r}\frac{rl}{V} +$$

$$+ C_{i_{\dot{p}}}\frac{\dot{p}l^2}{V^2} + C_{i_{\dot{q}}}\frac{\dot{q}l^2}{V^2} + C_{i_{\dot{r}}}\frac{\dot{r}l^2}{V^2} +$$

$$+ C_{i_{\alpha p}}\bar{\alpha}\frac{pl}{V} + C_{i_{\beta p}}\bar{\beta}\frac{pl}{V} +$$

$$+ C_{i_{\dot{\alpha}p}}\frac{\dot{\bar{\alpha}}l}{V}\frac{pl}{V} + C_{i_{\dot{\beta}p}}\frac{\dot{\bar{\beta}}l}{V}\frac{pl}{V} +$$

$$+ C_{i_{pp}}\left(\frac{pl}{V}\right)^2 + C_{i_{qp}}\frac{ql}{V}\frac{pl}{V} + C_{i_{rp}}\frac{rl}{V}\frac{pl}{V} +$$

$$+ C_{i_{\dot{p}p}}\frac{\dot{p}l^2}{V^2}\frac{pl}{V} + C_{i_{\dot{q}p}}\frac{\dot{q}l^2}{V^2}\frac{pl}{V} + C_{i_{\dot{r}p}}\frac{\dot{r}l^2}{V^2}\frac{pl}{V} +$$

+ higher order terms. (7.74)

Here i is used as a general subscript for both forces and moments (for example, $i = \bar{x}, \bar{y}, \bar{z}, l, m, n$). The second-order subscripts denote derivatives which have been nondimensionalized (e.g., $C_{i_\alpha} = \partial C_i/\partial\bar{\alpha}$, $C_{i_{\dot{\alpha}}} = \partial C_i/\partial(\dot{\bar{\alpha}}l/V)$, $C_{i_{\alpha p}} = \partial^2 C_i/\partial\bar{\alpha}\,\partial(pl/V)$, etc.). The terms involving $\dot{p}$, $\dot{q}$, and $\dot{r}$ are included for completeness since, under center of gravity translation, they are required to keep the force system invariant. They are neglected in practice, however, because they are small, and will not be carried along any further in this chapter.

The terms in the above equation can be interpreted as follows:

C_{i_0} — trim coefficients (e.g., the axial force $C_{\bar{x}_0}$)

C_{i_α}, C_{i_β} — initial static force or moment curve slopes (e.g. initial normal-force-curve slope)

$C_{i_{\dot{\alpha}}}$, $C_{i_{\dot{\beta}}}$ — damping coefficient due to rates of change of angle of attack and sideslip

C_{i_p}, C_{i_q}, C_{i_r} — damping due to model roll, pitch, and yaw

$C_{i_{\alpha p}}$, $C_{i_{\beta p}}$, ... — Magnus terms. (A body traveling in, say, the x direction and spinning about the z axis experiences a force in the y direction due to the spin; forces of this type are called Magnus forces.)

These coefficients depend on Mach number, Reynolds number, and perhaps on other test conditions, but not on $\bar{\alpha}$, $\bar{\beta}$, p, q, r and their derivatives. In any ballistic range test there will be a change of Mach number, Reynolds number, etc., over the length of flight. One could expand the coefficients about the values at the center of the flight trajectory to yield a mean value.

$$C_{i_K} = C_{i_K}\big|_{mean} + \frac{\partial C_{i_K}}{\partial M_\infty}\Delta M_\infty + \frac{\partial C_{i_K}}{\partial R_\infty}\Delta R_\infty + \ldots$$

For most of the material covered here, the following assumptions will be made:

$$\frac{\partial C_{i_K}}{\partial M_\infty}\Delta M_\infty \ll C_{i_K}\big|_{mean}$$

$$\frac{\partial C_{i_K}}{\partial R_\infty}\Delta R_\infty \ll C_{i_K}\big|_{mean}.$$

Therefore, for all flight conditions

$$C_{i_K} = C_{i_K}\Big|_{mean} \ .$$

Note that these assumptions may be satisfied in two ways: either the derivatives are small (normally they are except at certain critical conditions such as in the transonic regime); or there is little change in conditions along the instrumented flight path. For example, the velocity loss is small.

In general, (7.74) states that there are 126 aerodynamic coefficients (first-order plus Magnus terms). However, depending on the degree of symmetry exhibited by the particular body under consideration many of the terms are zero cr equal to other terms. The reader should be aware at this point that although these symmetry arguments are based on good mathematical and physical concepts, there are some recent experimental data[7.11] which show that under certain conditions an (apparently) axisymmetric body at some angle of attack and zero yaw experiences nonzero side forces. These forces are not understood at present. With this in mind conventional symmetry arguments will be presented.

7.4.2.3 Mirror Symmetry About One Plane (Airplane-like)

Mirror symmetry was considered in a very general mathematical fashion by Maple and Synge[7.12] and a good physical description is given by Charters[7.6]. Under the conditions of mirror symmetry many of the coefficients in (7.74) are zero. In addition Magnus terms can be ignored for airplane configurations because roll rates are normally of the order of pitching rates and hence the Magnus terms are 2nd order.

The force and moment coefficients can be written as[*]

$$
\left.
\begin{aligned}
C_{\bar{x}} &= -C_{\bar{x}_0} - C_{\bar{x}_\alpha}\bar{\alpha} - C_{\bar{x}_{\dot{\alpha}}}\frac{\dot{\alpha}l}{V} - C_{\bar{x}_q}\frac{ql}{V} \\[1em]
C_{\bar{y}} &= C_{\bar{y}_\beta}\bar{\beta} + C_{\bar{y}_{\dot{\beta}}}\frac{\dot{\beta}l}{V} + C_{\bar{y}_p}\frac{pl}{V} + C_{\bar{y}_r}\frac{rl}{V} + \left[C_{\bar{y}_0}\right] \\[1em]
C_{\bar{z}} &= -C_{\bar{z}_0} - C_{\bar{z}_\alpha}\bar{\alpha} - C_{\bar{z}_{\dot{\alpha}}}\frac{\dot{\alpha}l}{V} - C_{\bar{z}_q}\frac{ql}{V} \\[1em]
C_l &= C_{l_\beta}\bar{\beta} + C_{l_{\dot{\beta}}}\frac{\dot{\beta}l}{V} + C_{l_p}\frac{pl}{V} + C_{l_r}\frac{rl}{V} + \left[C_{l_0}\right] \\[1em]
C_m &= C_{m_0} + C_{m_\alpha}\bar{\alpha} + C_{m_{\dot{\alpha}}}\frac{\dot{\alpha}l}{V} + C_{m_q}\frac{ql}{V} \\[1em]
C_n &= C_{n_\beta}\bar{\beta} + C_{n_{\dot{\beta}}}\frac{\dot{\beta}l}{V} + C_{n_p}\frac{pl}{V} + C_{n_r}\frac{rl}{V} + \left[C_{n_0}\right] \ .
\end{aligned}
\right\}
\tag{7.75}
$$

These then represent the linear force and moment coefficients for airplane-like configurations. The minus signs on $\bar{x}$ and $\bar{z}$ are in conformity with standard practice. There remain 27 coefficients.

7.4.2.4 N-gonal Symmetry Plus Mirror Symmetry

This notation simply means that the configuration has a plane of symmetry and has N indistinguishable orientations of roll about its axis of symmetry located $2\pi/N$ radians apart. Magnus terms will be retained now since p can be large. Again Maple and Synge[7.12] have given the results which follow (as well as for the N-gonal case without mirror symmetry, e.g., canted fins), and a good physical description of a configuration with $90°$ roll symmetry (N = 4) has been given by Charters[7.6]. It will suffice here to state that for linear aerodynamics any model with trigonal or greater rotational symmetry can be considered axially symmetric. This additional symmetry allows many more coefficients to be set to zero and also yields

$$
\left.
\begin{aligned}
C_{\bar{y}_\beta} &= -C_{\bar{z}_\alpha}, & C_{\bar{y}_{\dot{\beta}}} &= -C_{\bar{z}_{\dot{\alpha}}}, & C_{\bar{y}_r} &= C_{\bar{z}_q}, \\[1em]
C_{\bar{y}_{\alpha p}} &= C_{\bar{z}_{\beta p}}, & C_{\bar{y}_{\dot{\alpha} p}} &= C_{\bar{z}_{\dot{\beta} p}}, & C_{\bar{y}_{qp}} &= -C_{\bar{z}_{rp}}, \\[1em]
C_{n_\beta} &= -C_{m_\alpha}, & C_{n_{\dot{\beta}}} &= -C_{m_{\dot{\alpha}}}, & C_{n_r} &= C_{m_q}, \\[1em]
C_{n_{\alpha p}} &= C_{m_{\beta p}}, & C_{n_{\dot{\alpha} p}} &= C_{m_{\dot{\beta} p}}, & C_{n_{qp}} &= -C_{m_{rp}}.
\end{aligned}
\right\}
\tag{7.76}
$$

---

[*] The bracketed terms in (7.75) are ideally zero. In some sections of this chapter, however, they will be retained to account for small asymmetries.

Hence, due to trigonal symmetry or greater the force and moment coefficients become

$$
C_{\bar{x}} = -C_{\bar{x}_0} - C_{\bar{x}_{pp}}\left(\frac{pl}{V}\right)^2
$$

$$
C_{\bar{y}} = -C_{\bar{z}_\alpha}\bar{\beta} - C_{\bar{z}_{\dot{\alpha}}}\frac{\dot{\beta}l}{V} + C_{\bar{z}_q}\frac{rl}{V} + C_{\bar{z}_{\beta p}}\bar{\alpha}\frac{pl}{V} + C_{\bar{z}_{\dot{\beta}p}}\frac{\dot{\alpha}l}{V}\frac{pl}{V} - C_{\bar{z}_{rp}}\frac{ql}{V}\frac{pl}{V} + \left[C_{\bar{y}_0}\right]
$$

$$
C_{\bar{z}} = -C_{\bar{z}_\alpha}\bar{\alpha} - C_{\bar{z}_{\dot{\alpha}}}\frac{\dot{\alpha}l}{V} - C_{\bar{z}_q}\frac{ql}{V} - C_{\bar{z}_{\beta p}}\bar{\beta}\frac{pl}{V} - C_{\bar{z}_{\dot{\beta}p}}\frac{\dot{\beta}l}{V}\frac{pl}{V} - C_{\bar{z}_{rp}}\frac{rl}{V}\frac{pl}{V} - \left[C_{\bar{z}_\zeta}\right]
$$

$$
C_l = C_{l_p}\frac{pl}{V} + \left[C_{l_0}\right]
$$

$$
C_{\bar{m}} = C_{m_\alpha}\bar{\alpha} + C_{m_{\dot{\alpha}}}\frac{\dot{\alpha}l}{V} + C_{m_q}\frac{ql}{V} + C_{m_{\beta p}}\bar{\beta}\frac{pl}{V} + C_{m_{\dot{\beta}p}}\frac{\dot{\beta}l}{V}\frac{pl}{V} + C_{m_{rp}}\frac{rl}{V}\frac{pl}{V} + \left[C_{m_0}\right]
$$

$$
C_n = -C_{m_\alpha}\bar{\beta} - C_{m_{\dot{\alpha}}}\frac{\dot{\beta}l}{V} + C_{m_q}\frac{rl}{V} + C_{m_{\beta p}}\bar{\alpha}\frac{pl}{V} + C_{m_{\dot{\beta}p}}\frac{\dot{\alpha}l}{V}\frac{pl}{V} - C_{m_{rp}}\frac{ql}{V}\frac{pl}{V} + \left[C_{n_0}\right] \quad .
$$

(7.77)

Again, the bracketed terms are ideally zero but are retained to allow for small asymmetries.

7.4.2.5 Drag and Lift Forces for Airplane-like Configurations

The expressions for aerodynamic forces and moments given so far have been in terms of the body-fixed coordinate system. Another frequently used set of aerodynamic force coefficients are those oriented relative to the velocity vector. For airplane-like configurations these are drag, lift, and side force. The drag component is along the velocity vector; the lift force is normal to the velocity vector and the $\bar{y}$ axis; and the side-force forms a right-hand system. These forces can be written by transformation of the forces in the body-fixed axis system:

$$
F_D = -F_{\bar{x}}\cos\bar{\alpha}\cos\bar{\beta} - F_{\bar{y}}\sin\bar{\beta} - F_{\bar{z}}\sin\bar{\alpha}\cos\bar{\beta}
$$

$$
F_L = F_{\bar{x}}\sin\bar{\alpha} \qquad\qquad - F_{\bar{z}}\cos\bar{\alpha}
$$

$$
F_S = F_{\bar{x}}\cos\bar{\alpha}\sin\bar{\beta} - F_{\bar{y}}\cos\bar{\beta} + F_{\bar{z}}\sin\bar{\alpha}\sin\bar{\beta} \quad .
$$

An alternative is to express them through their own expansions.

$$
F_D = C_D\tfrac{1}{2}\rho V^2 A
$$

$$
= \left(C_{D_0} + C_{D_\alpha}\bar{\alpha} + C_{D_{\dot{\alpha}}}\frac{\dot{\alpha}l}{V} + C_{D_q}\frac{ql}{V}\right)\tfrac{1}{2}\rho V^2 A
$$

(7.78)

$$
F_L = C_L\tfrac{1}{2}\rho V^2 A
$$

$$
= \left(C_{L_0} + C_{L_\alpha}\bar{\alpha} + C_{L_{\dot{\alpha}}}\frac{\dot{\alpha}l}{V} + C_{L_q}\frac{ql}{V}\right)\tfrac{1}{2}\rho V^2 A
$$

(7.79)

$$
F_S = C_S\tfrac{1}{2}\rho V^2 A \quad .
$$

(7.80)

7.4.2.6 Drag and Lift Forces for Axially Symmetric Bodies

For axially symmetric bodies, the drag force is again along the velocity vector, but the lift is now defined as being normal to the velocity vector and in a plane such that there is no side force. It is difficult to express these forces in terms of body-fixed forces because of the Magnus terms. Ignoring Magnus terms, the drag and lift are related to the body-fixed forces through the resultant angle of attack, α_R

$$
\left.
\begin{aligned}
F_D &= -F_{\bar{x}}\cos\alpha_R + F_N\sin\alpha_R \\
F_L &= F_{\bar{x}}\sin\alpha_R + F_N\cos\alpha_R \\
F_S &= 0
\end{aligned}
\right\}
$$

(7.81)

where $\qquad F_N = |F_{\bar{y}} + iF_{\bar{z}}| \quad .$

Note that F_N is frequently referred to as normal force and $F_{\bar{x}}$ as axial force.

The drag and lift forces can also be written with their own expansions, and to first order including the Magnus terms

$$F_D = C_D \tfrac{1}{2}\rho V^2 A = \left(C_{D_0} + C_{D_{pp}}\left(\frac{pl}{V}\right)^2\right)\tfrac{1}{2}\rho V^2 A \tag{7.82}$$

$$F_L = \left[\left(C_{L_\alpha} + iC_{L_{\alpha p}}\frac{pl}{V}\right)(\bar\beta + i\bar\alpha) + \left(C_{L_{qp}}\frac{pl}{V} + iC_{L_q}\right)\frac{l}{V}(q + ir) + \left(C_{L_{\dot\alpha}} + iC_{L_{\dot\alpha p}}\frac{pl}{V}\right)\frac{l}{V}(\dot{\bar\beta} + i\dot{\bar\alpha})\right]\tfrac{1}{2}\rho V^2 A . \tag{7.83}$$

7.4.2.7 Coordinate Transformation of Angular Rates

A question which has not been considered up to this point is what happens to the rate terms in the force and moment expressions when rotations about the $\bar x$-axis are required in transforming from one reference frame to another; for example, from body-fixed coordinates to fixed-plane coordinates. The complex angle, $(\bar\beta + i\bar\alpha)$, when rotated to fixed-plane coordinates, is simply

$$e^{i\int\dot\phi\,dt}(\bar\beta + i\bar\alpha) = \tilde\beta + i\tilde\alpha .$$

Consider the rate terms by differentiating both sides with respect to time:

$$e^{i\int\dot\phi\,dt}(\dot{\bar\beta} + i\dot{\bar\alpha}) + i\dot\phi e^{i\int\dot\phi\,dt}(\bar\beta + i\bar\alpha) = \dot{\tilde\beta} + i\dot{\tilde\alpha} .$$

Rearranging and substituting $\tilde\beta + i\tilde\alpha$ for $e^{i\int\dot\phi\,dt}(\bar\beta + i\bar\alpha)$ we get

$$e^{i\int\dot\phi\,dt}(\dot{\bar\beta} + i\dot{\bar\alpha}) = (\dot{\tilde\beta} + i\dot{\tilde\alpha}) - i\dot\phi(\tilde\beta + i\tilde\alpha) .$$

Note that we have generated an additional term. Murphy[7.9] "avoids" this by including a term of opposite sign $(+i\dot\phi(\bar\beta + i\bar\alpha))$ in the force and moment expressions in body-fixed coordinates, and hence the second term disappears after transformation. Nicolaides[7.5] neglects the second term in the above equation completely. An important conclusion is that when rate coefficients are quoted, one should indicate what coordinate system they are applicable to.

7.4.3 Differential Equations of Motion

The momentum equations and expressions for the forces and moments may now be combined to obtain the equations of motion for use in analyzing experimental data.

7.4.3.1 Airplane-like Configurations

The equations of motion of an airplane-like configuration can now be obtained by combining the momentum equations (7.24), (7.25), (7.26), and (7.35) with the forces and moments given by Equation (7.75). The linear momentum equations for small angles and angular rates (except roll), neglecting gravity and Coriolis forces, then become

$$m\frac{d^2x}{dt^2} = F_x \simeq F_{\bar x} + F_{\bar z}\bar\alpha + F_{\bar y}\bar\beta$$

$$\simeq -\left[C_{D_0} + C_{D_\alpha}\bar\alpha + C_{D_{\dot\alpha}}\frac{\dot{\bar\alpha}l}{V} + C_{D_q}\frac{ql}{V}\right]\tfrac{1}{2}\rho V^2 A \tag{7.84}$$

$$m\frac{d^2y}{dt^2} = F_y \simeq -(F_{\bar z} - F_{\bar x}\bar\alpha)\sin\phi + (F_{\bar y} - F_{\bar x}\bar\beta)\cos\phi \tag{7.85}$$

$$m\frac{d^2z}{dt^2} = F_z \simeq (F_{\bar z} - F_{\bar x}\bar\alpha)\cos\phi + (F_{\bar y} - F_{\bar x}\bar\beta)\sin\phi \tag{7.86}$$

where $(F_{\bar z} - F_{\bar x}\bar\alpha) \approx -F_L$ is given by (7.79) as

$$F_L = \left(C_{L_0} + C_{L_\alpha}\bar\alpha + C_{L_{\dot\alpha}}\frac{\dot{\bar\alpha}l}{V} + C_{L_q}\frac{ql}{V}\right)\tfrac{1}{2}\rho V^2 A . \tag{7.87}$$

Now using the angle relationships developed earlier for small angles (Equation (7.14)), the angle of attack and sideslip in body-fixed axes can be written as

$$\bar\alpha = (\theta_{ME} - \gamma_2)\cos\phi + (\psi_{ME} - \gamma_1)\sin\phi \tag{7.88}$$

$$\bar\beta = -(\psi_{ME} - \gamma_1)\cos\phi + (\theta_{ME} - \gamma_2)\sin\phi . \tag{7.89}$$

Differentiate these equations to get $\dot{\bar\alpha}$ and $\dot{\bar\beta}$; then substitute the small angle expressions of p, q, and r (see table in Section 7.4.1.4), note that $\dot\gamma_2 \simeq -(1/V)\ddot z$ and $\dot\gamma_1 = (1/V)\ddot y$, and utilize (7.85) and (7.86) to arrive at

$$\dot{\alpha} = q - p\bar{\beta} + \frac{F_{\bar{z}} - F_{\bar{x}}\bar{\alpha}}{mV} \tag{7.90}$$

$$\dot{\beta} = -r + p\bar{\alpha} + \frac{F_{\bar{y}} - F_{\bar{x}}\bar{\beta}}{mV} . \tag{7.91}$$

Equations (7.35), (7.90), and (7.91) can be combined and after eliminating q and r and their derivatives, the following differential equations are obtained.

$$\left[C_{l_\beta}\bar{\beta} + (C_{l_{\dot\beta}} - C_{l_r}) \frac{\dot{\beta}l}{V} + C_{l_p} \frac{pl}{V} + C_{l_r} \frac{pl}{V} \bar{\alpha} \right] \frac{\rho V^2 A l}{2I_{\bar{x}}} +$$

$$+ \left(\frac{I_{\bar{y}} - I_{\bar{z}}}{I_{\bar{x}}} \right) \left(\frac{\rho V A}{2m} \right) \left[C_{\bar{y}_p} (\dot{\alpha} + p\bar{\beta}) \frac{pl}{V} - C_{L_0} (\dot{\beta} - p\bar{\alpha}) + C_{\bar{y}_0} (\dot{\alpha} + p\bar{\beta}) \right] = \dot{p} \tag{7.92}$$

$$\ddot{\alpha} + C_1\dot{\alpha} + C_2\bar{\alpha} + C_3\dot{\beta} + C_4\bar{\beta} - \frac{\rho V^2 A l}{2I_{\bar{y}}} C_{m_0} + \dot{p}\bar{\beta} -$$

$$- \frac{I_{\bar{z}} - I_{\bar{x}}}{I_{\bar{y}}} p \frac{\rho V A}{2m} \left(C_{\bar{y}_p} \frac{pl}{V} + C_{\bar{y}_0} \right) = 0 \tag{7.93}$$

$$\ddot{\beta} + C_5\dot{\beta} + C_6\bar{\beta} + C_7\dot{\alpha} + C_8\bar{\alpha} + \frac{\rho V^2 A l}{2I_{\bar{z}}} C_{n_0} - \dot{p}\bar{\alpha} +$$

$$+ \frac{I_{\bar{x}} - I_{\bar{y}}}{I_{\bar{z}}} p \frac{\rho V A}{2m} C_{L_0} + \frac{\rho V^2 A l}{2I_{\bar{z}}} C_{n_p} \frac{pl}{V} = 0 \tag{7.94}$$

where

$$C_1 = \frac{\rho V A}{2m} C_{L_\alpha} - \frac{\rho V^2 A l}{2I_{\bar{y}}} \frac{l}{V} (C_{m_q} + C_{m_{\dot\alpha}})$$

$$C_2 = - \frac{\rho V^2 A l}{2I_{\bar{y}}} C_{m_\alpha} - \frac{I_{\bar{z}} - I_{\bar{x}}}{I_{\bar{y}}} p^2$$

$$C_3 = \left(\frac{I_{\bar{z}} - I_{\bar{x}}}{I_{\bar{y}}} + 1 \right) p$$

$$C_4 = \left[- \frac{\rho V^2 A l}{2I_{\bar{y}}} \frac{l}{V} C_{m_q} - \frac{I_{\bar{z}} - I_{\bar{x}}}{I_{\bar{y}}} \frac{\rho V A}{2m} (C_{\bar{y}_\beta} + C_{D_0}) \right] p$$

$$C_5 = - \frac{\rho V A}{2m} (C_{\bar{y}_\beta} + C_{D_0}) - \frac{\rho V^2 A l}{2I_{\bar{z}}} \frac{l}{V} (C_{n_r} - C_{n_{\dot\beta}})$$

$$C_6 = \frac{\rho V^2 A l}{2I_{\bar{z}}} C_{n_\beta} + \frac{I_{\bar{x}} - I_{\bar{y}}}{I_{\bar{z}}} p^2$$

$$C_7 = \left(\frac{I_{\bar{x}} - I_{\bar{y}}}{I_{\bar{z}}} - 1 \right) p$$

$$C_8 = \left[\frac{\rho V^2 A l}{2I_{\bar{z}}} \frac{l}{V} C_{n_r} + \frac{I_{\bar{x}} - I_{\bar{y}}}{I_{\bar{z}}} \frac{\rho V A}{2m} C_{L_\alpha} \right] p .$$

In the above coefficients the following types of terms were deleted:

(i) Products of aerodynamic coefficients (because they always appear with $(\rho A l / 2I)^2$ or $(\rho A / 2m)(\rho A l / 2I)$ which are normally very small).

(ii) Certain rate terms which appear with other terms that are much larger; for example $(\rho A l / 2m)(C_{L_q} + C_{l_{\dot\alpha}}) \ll 1$.

(iii) Terms involving products of angles and/or angular rates, like $\bar{\alpha}\bar{\beta}$ or $\dot{\alpha}\bar{\beta}$.

Equations (7.84) (7.85), (7.86), (7.92), (7.93), and (7.94) are the equations of motion used for the analysis of airplane-like configurations. Note that for constant roll rate the right hand side of Equation (7.92) is zero as is the $\dot{p}$ term in (7.93) and (7.94). Note also that the last term in (7.93) and the last two terms in (7.94) are normally ignored.

Even for constant roll rate the coefficients C_1, C_2, C_4, C_5, C_6, and C_8 are not strictly constant since they contain velocity which will change because of drag. The coefficients can be made essentially constant by changing the independent variable from time to distance. This is accomplished as follows:

$$\frac{d}{dt} = u \frac{d}{dx}$$

$$\frac{d^2}{dt^2} = \frac{d}{dt}\left(u \frac{d}{dx}\right) = u^2 \frac{d^2}{dx^2} + \frac{du}{dt} \frac{d}{dx} \; ;$$

but

$$V \cong u \, ,$$

so

$$\frac{du}{dt} = -C_D \frac{\rho V^2 A}{2m} \, ,$$

and hence

$$\frac{d^2}{dt^2} = V^2 \frac{d^2}{dx^2} - C_D \frac{\rho A}{2m} V^2 \frac{d}{dx}$$

$$p(t) = Vp(x) \, .$$

Equations (7.85), (7.86), (7.93), and (7.94) now become

$$\frac{d^2y}{dx^2} = \frac{\rho A}{2m} C_D \frac{dy}{dx} + \frac{F_L}{mV^2} \sin\phi + \frac{F_{\bar{y}} - F_{\bar{x}}\bar{\beta}}{mV^2} \cos\phi \tag{7.95}$$

$$\frac{d^2z}{dx^2} = \frac{\rho A}{2m} C_D \frac{dz}{dx} - \frac{F_L}{mV^2} \cos\phi + \frac{F_{\bar{y}} - F_{\bar{x}}\bar{\beta}}{mV^2} \sin\phi \, . \tag{7.96}$$

Retaining the most dominant terms, the forces are given by

$$F_L = \frac{\rho V^2 A}{2} (C_{L_0} + C_{L_\alpha} \bar{\alpha}) \, , \qquad F_{\bar{x}} = -\frac{\rho V^2 A}{2} C_D \, ,$$

$$F_{\bar{y}} = \frac{\rho V^2 A}{2} (C_{\bar{y}_0} + C_{\bar{y}_\beta} \bar{\beta})$$

$$\bar{\alpha}'' + \bar{C}_1 \bar{\alpha}' + \frac{1}{V^2} C_2 \bar{\alpha} + \frac{1}{V} C_3 \bar{\beta}' + \frac{1}{V^2} C_4 \bar{\beta} - \frac{C_{m_0} \rho A l}{2 I_{\bar{y}}} = 0 \tag{7.97}$$

$$\bar{\beta}'' + \bar{C}_5 \bar{\beta}' + \frac{1}{V^2} C_6 \bar{\beta} + \frac{1}{V} C_7 \bar{\alpha}' + \frac{1}{V^2} C_8 \bar{\alpha} + \frac{C_{n_0} \rho A l}{2 I_{\bar{z}}} = 0 \, , \tag{7.98}$$

where

$$\bar{C}_1 = \frac{1}{V} C_1 - \frac{\rho A}{2m} C_D$$

$$\bar{C}_5 = \frac{1}{V} C_5 - \frac{\rho A}{2m} C_D \, .$$

The coefficients are now considered as constants, based on the assumption that the aerodynamic derivatives are invariant.

7.4.3.2 Axially Symmetric Bodies

To determine the differential equations of motion for axially symmetric bodies, we start with the Lagrangian dynamic equations. The Lagrangian equations for small angles and constant roll rate (Equation (7.67)), rotated to fixed-plane coordinates (and where $M_m = C_m \rho V^2 A l/2$ is obtained from Equation (7.77)), become

$$I\ddot{\vec{\Omega}} - iI_{\bar{x}}p\dot{\vec{\Omega}} = \tfrac{1}{2}\rho V^2 A l\left[\left(C_{m_{\alpha p}} \frac{pl}{V} - iC_{m_\alpha}\right)(\bar{\beta} + i\bar{\alpha}) + \left(C_{m_q} - iC_{m_{qp}} \frac{pl}{V}\right)\frac{l}{V} (\bar{q} + i\bar{r}) + \right.$$
$$\left. + \left(C_{m_{\dot{\alpha}p}} \frac{pl}{V} - iC_{m_{\dot{\alpha}}}\right)\frac{l}{V} (\dot{\bar{\beta}} + i\dot{\bar{\alpha}})\right] \, . \tag{7.99}$$

where $\dot{\vec{\Omega}} = \dot{\theta}_{ME} + i\dot{\psi}_{ME}$.

It should be noted that $C_{m_{\beta p}}$ and $C_{m_{\dot{\beta}p}}$ (Equation (7.77)) have been written here as $C_{m_{\alpha p}}$ and $C_{m_{\dot{\alpha}p}}$, which is the more common notation for those coefficients; for axisymmetric bodies, derivatives with respect to $\tilde{\alpha}$ or $\tilde{\beta}$ are equivalent. The same argument applies to writing $C_{m_{rp}}$ as $C_{m_{qp}}$.

Transforming the forces given by (7.82) and (7.83) into y and z directions and including gravity and Coriolis forces from (7.70) and (7.71), the linear momentum equations (7.24)-(7.26) become

$$\ddot{x} = -\frac{\rho V^2 A}{2m} C_D$$

$$\ddot{y} + i\ddot{z} = -\frac{\rho V^2 A}{2m} \left[\left(C_{L_\alpha} + iC_{L_{\alpha p}} \frac{pl}{V} \right) (\tilde{\beta} + i\tilde{\alpha}) + \right.$$

$$+ \left(C_{L_{qp}} \frac{pl}{V} + iC_{L_q} \right) \frac{l}{V} (\tilde{q} + i\tilde{r}) + \left(C_{L_{\dot\alpha}} + iC_{L_{\dot\alpha p}} \frac{pl}{V} \right) \frac{l}{V} (\dot{\tilde{\beta}} + i\dot{\tilde{\alpha}}) +$$

$$\left. + C_D (\gamma_1 - i\gamma_2) \right] + ig - 2\omega_E V (\sin\theta_l + i\cos\theta_l \sin\theta_a) \ . \tag{7.100}$$

Here γ_1 and γ_2 are the projections of the local flight path angle γ on the x-y and x-z planes, g is the acceleration due to gravity, and the last term is the Coriolis acceleration. Combining (7.99), (7.100), and (7.15) and making the following assumptions:

(i) Products of aerodynamic derivatives are small and may be neglected.

(ii) Multiple-term coefficients preceding the various derivatives of $\bar{\alpha}_R$ which are of the form $(1+a+b\ldots)$, where a, b, etc. are $\ll 1$, are treated as just 1.

(iii) The quantity $(\rho A/2m) C_D L$ is much less than one. For cases with small roll rates where Magnus forces and moments are not important, this can be relaxed to $(\rho A/2m)(\lambda/2\pi) C_D \ll 1$. Here, λ is the wavelength of the oscillatory motion and L is the length of the facility.

the equations of motion for axially symmetric bodies become:

$$\ddot{\vec{\alpha}}_R - B_1 \dot{\vec{\alpha}}_R - B_2 \vec{\alpha}_R = 0 \ . \tag{7.101}$$

where

$$\vec{\alpha}_R = \tilde{\beta} + i\tilde{\alpha}$$

$$B_1 = \frac{\rho VA}{2m} \left\{ -C_{L_\alpha} + \frac{ml^2}{I} (C_{m_q} + C_{m_{\dot\alpha}}) + i\frac{pl}{V} \left[-C_{L_{\alpha p}} + \frac{ml^2}{I} (C_{m_{\dot\alpha p}} - C_{m_{qp}}) \right] \right\} +$$

$$+ i\frac{I_{\tilde{x}}}{I} p$$

$$B_2 = \frac{\rho V^2 Al}{2I} \left(C_{m_\alpha} + iC_{m_{\alpha p}} \frac{pl}{V} \right) - \frac{\rho VA}{2m} \frac{I_{\tilde{x}}}{I} p \left(C_{L_{\alpha p}} \frac{pl}{V} - iC_{L_\alpha} \right) .$$

$$\ddot{y} + i\ddot{z} = -\frac{\rho V^2 A}{2m} \left\{ \left(C_{L_\alpha} + iC_{L_{\alpha p}} \frac{pl}{V} \right) (\tilde{\beta} + i\tilde{\alpha}) + \frac{l}{V} \left[(C_{L_q} + C_{L_{\dot\alpha}}) + \right. \right.$$

$$\left. + i (C_{L_{\dot\alpha p}} - C_{L_{qp}}) \frac{pl}{V} \right] (\dot{\tilde{\beta}} + i\dot{\tilde{\alpha}}) +$$

$$\left. + C_D (\gamma_1 - i\gamma_2) \right\} + ig - 2\omega_E V (\sin\theta_l + i\cos\theta_l \sin\theta_a) \ . \tag{7.102}$$

For clarity, the definitions of the derivatives appearing in the last two equations are as follows:

$$C_{m_\alpha} = \frac{\partial C_m}{\partial \alpha} , \quad \text{static moment-curve slope}$$

$$C_{m_q} + C_{m_{\dot\alpha}} = \frac{\partial C_m}{\partial (ql/V)} + \frac{\partial C_m}{\partial (\dot\alpha l/V)} , \quad \text{damping-in-pitch derivative}$$

$$C_{m_{\alpha p}} = \frac{\partial^2 C_m}{\partial \alpha \, \partial (pl/V)} , \quad \text{static Magnus moment coefficient}$$

$$C_{m_{\dot\alpha p}} - C_{m_{qp}} = \frac{\partial^2 C_m}{\partial (\dot\alpha l/V) \, \partial (pl/V)} - \frac{\partial^2 C_m}{\partial (ql/V) \, \partial (pl/V)} , \quad \text{dynamic Magnus moment coefficient}$$

$$C_{L_\alpha} = \frac{\partial C_L}{\partial \alpha} , \quad \text{lift-curve slope}$$

$$C_{L_q} + C_{L_{\dot\alpha}} = \frac{\partial C_L}{\partial (ql/V)} + \frac{\partial C_L}{\partial (\dot\alpha l/V)} , \quad \text{lift derivative due to pitching and plunging}$$

$$C_{L_{\alpha p}} = \frac{\partial^2 C_L}{\partial \alpha \, \partial (pl/V)} , \qquad \text{static Magnus force coefficient}$$

$$C_{L_{\dot\alpha p}} - C_{L_{qp}} = \frac{\partial^2 C_L}{\partial(\dot\alpha l/V)\,\partial(pl/V)} - \frac{\partial^2 C_L}{\partial(ql/V)\,\partial(pl/V)} , \qquad \text{dynamic Magnus force coefficient.}$$

Distance again proves to be a more convenient independent variable than time, since it eliminates (to second order at least) the velocity from the equations. The transformation of (7.101) proceeds as follows:

$$\dot{\vec\alpha}_R = \dot x \vec\alpha_R' \approx V \cos\gamma \vec\alpha_R' \approx V \vec\alpha_R' \qquad (\cos\gamma \approx 1)$$

$$\ddot{\vec\alpha}_R = V \frac{d\vec\alpha_R'}{dt} + \vec\alpha_R' \frac{dV}{dt} = V \frac{d^2\vec\alpha_R}{dx^2} \frac{dx}{dt} + \vec\alpha_R' \frac{d^2x}{dt^2}$$

$$= V^2 \left(\vec\alpha_R'' - C_D \frac{\rho A}{2m} \vec\alpha_R' \right)$$

$$p(t) = Vp(x) .$$

Then (7.101) becomes

$$\vec\alpha_R'' - \left\{ \frac{\rho A}{2m} \xi + i \frac{\rho A}{2m} pl \left[-C_{L_{\alpha p}} + \frac{ml^2}{I} (C_{m_{\dot\alpha p}} - C_{m_{qp}}) \right] + i \frac{I_{\tilde x}}{I} p \right\} \vec\alpha_R' -$$

$$- \left\{ \frac{\rho A l}{2I} (C_{m_\alpha} + iC_{m_{\alpha p}} pl) - \frac{\rho A}{2m} \frac{I_{\tilde x}}{I} p (C_{L_{\alpha p}} pl - iC_{L_\alpha}) \right\} \vec\alpha_R = 0, \qquad (7.103)$$

where ξ, which is called the dynamic stability parameter for unpowered flight at constant altitude, is defined as

$$\xi = C_D - C_{L_\alpha} + \frac{ml^2}{I} (C_{m_q} + C_{m_{\dot\alpha}}) . \qquad (7.104)$$

A similar transformation applied to (7.102), again assuming γ is small, leads to the following differential equation:

$$y'' + iz'' = -\frac{\rho A}{2m} \{ (C_{L_\alpha} + iC_{L_{\alpha p}} pl)(\tilde\beta + i\tilde\alpha) +$$

$$+ l[(C_{L_q} + C_{L_{\dot\alpha}}) + i(C_{L_{\dot\alpha p}} - C_{L_{qp}})pl](\tilde\beta' + i\tilde\alpha')\} +$$

$$+ \frac{ig}{V^2} - 2\frac{\omega_E}{V}(\sin\theta_l + i\cos\theta_l \sin\theta_a) . \qquad (7.105)$$

We will now allow for the possibility of small asymmetries.

7.4.3.3 Small Asymmetries

For the axially symmetric body case just considered, but with slight asymmetries in forces and moments which are body fixed, we can, following Nicolaides[7.5], simply add to the force and moment equations a term which rotates the asymmetry into the fixed-plane coordinates. The appropriate term to add to the right-hand side of (7.103) is

$$\left[-\frac{\rho A l}{2I} C_{m_{\delta_\epsilon}} + i \frac{\rho A}{2m} \frac{p}{V} \left(1 - \frac{I_{\tilde x}}{I} \right) C_{L_{\delta_\epsilon}} \right] \delta_\epsilon e^{ipx} , \qquad (7.106)$$

while the term to add to the right-hand side of (7.105) is

$$-\frac{\rho A}{2m} C_{L_{\delta_\epsilon}} \delta_\epsilon e^{ipx} , \qquad (7.107)$$

where $C_{L_{\delta_\epsilon}}$ and $C_{m_{\delta_\epsilon}}$ are the trim force and moment coefficients due to small asymmetries from, for example, a flap deflection δ_{ϵ}. If the body is externally axisymmetric but has a center of mass not on the axis of external symmetry, then only $C_{m_{\delta_\epsilon}}$ would have a value.

Equations (7.103) and (7.105), along with the additional terms given by (7.106) and (7.107), represent the equations normally used for analysis of axisymmetric bodies with small asymmetries. They are often referred to as the tricyclic equations, a term which gives a physical description of the solution of (7.103) plus (7.106).

7.5 DRAG ANALYSIS

Consider that a test has been conducted in a ballistic range and that time and distance data have been obtained at a number of discrete observation stations. It is desired to determine the drag coefficient governing the test model. We start with the momentum equation along the flight path, which is (neglecting gravity)

$$m \frac{d^2 \hat{x}}{dt^2} = F_{\hat{x}} = -D ,$$

where $\hat{x}$ is the distance traversed by the model c.g. and the drag, D, can be written

$$D = \frac{\rho A}{2} \left(\frac{d\hat{x}}{dt} \right)^2 C_D .$$

Note that the measured data are along the earth fixed axis, x, not along $\hat{x}$. However, x is related o $\hat{x}$ by

$$x = \int_0^{\hat{x}} \cos \gamma \, d\hat{x}$$

or

$$\hat{x} = \int_0^x \frac{dx}{\cos \gamma} ,$$

where γ is the angle between the x axis and the flight path. Extracting the drag coefficient from time and x-distance measurements using the above equations is a difficult task. In ballistic range testing, however, γ is normally less than a degree (1 ft swerve in 60 ft of travel). Hence, one can make the very good approximation that $\cos \gamma = 1$, and thus $\hat{x} = x$. The momentum equation can then be written

$$\frac{d^2 x}{dt^2} = \frac{dV}{dt} = -\frac{\rho A}{2m} V^2 C_D \qquad (7.108a)$$

or

$$\frac{dV}{dx} = -\frac{\rho A}{2m} V C_D . \qquad (7.108b)$$

This is the basic equation for determining the drag coefficient.

7.5.1 Case with Constant Coefficients

When the density, reference area, mass, and drag coefficient (ρ, A, m, C_D) are all constants, (7.108) can be integrated in a straightforward manner. From (7.108a),

$$V = \frac{V_0}{1 + V_0 K C_D (t - t_0)} . \qquad (7.109a)$$

Alternately from (7.108b)

$$\left. \begin{array}{l} \log_e V = \log_e V_0 - K C_D (x - x_0) \\[2mm] V = V_0 e^{-K C_D (x - x_0)} , \end{array} \right\} \qquad (7.109b)$$

where $K = \rho A / 2m$, and the initial conditions are $t = t_0$, $V = V_0$ at $x = x_0$.

Integrating again yields

$$t = t_0 + \frac{1}{V_0 K C_D} \left[e^{K C_D (x - x_0)} - 1 \right] . \qquad (7.110)$$

Any of these equations can be used to determine the drag coefficient, and different simplifications are employed which lead to varying degrees of accuracy. The simplest approaches will be considered first since they are amenable to hand calculations and then more complicated ones suitable for high speed digital computers will be discussed. (A brief discussion of drag determination is also given in Chapter 10, Section 10.2.3).

Method 1: The simpler methods are based on (7.109) rather than (7.110), and begin by calculating the velocity. The average velocity between stations $i - 1$ and i is given as

$$V_{AV} = \frac{x_i - x_{i-1}}{t_i - t_{i-1}} . \qquad (7.111)$$

For small velocity loss, this average velocity may be assumed to occur at the center of the distance interval, and the use of two adjacent intervals will give two velocities whose difference ΔV is a measure of the deceleration. Thus, data from two such intervals may be substituted into (7.108b) in difference form

$$\frac{\Delta V}{\Delta x} = -KV_{AV}C_D \tag{7.112}$$

to calculate C_D . Here V_{AV} is the average velocity over the double interval of three measuring stations.

Method 2: More accurately, the velocities calculated using (7.111) may be used in (7.109b) which may be written as

$$\log_e V = \log_e V_0 - KC_D x . \tag{7.113}$$

where x_0 has been arbitrarily set to zero. The slope of a plot of $\log_e V$ versus x is $-KC_D$. A least squares fit (see Section 7.12) of this linear equation to the $\log_e V$ versus x data will yield the drag coefficient.

This approach still retains a small error in that the average velocity does not occur at the center of the interval. The error can be almost entirely eliminated by a procedure suggested by Seiff[7.13]. This procedure is given next.

Method 3: First note that (7.109) and (7.110) can be combined to yield

$$\Delta t = \frac{1}{KC_D}\left(\frac{1}{V_f} - \frac{1}{V_0}\right). \tag{7.114}$$

where V_f is the velocity at the end of an interval, V_0 is the velocity at the beginning of an interval, and Δt is the time of flight over that interval. Next the average velocity for that interval is

$$V_{AV} = \frac{\Delta x}{\Delta t} = KC_D \Delta x \frac{1}{\left(\frac{1}{V_f} - \frac{1}{V_0}\right)} . \tag{7.115}$$

Now consider at what x position this average velocity occurs. Using (7.109),

$$V_{AV} = V_0 e^{-KC_D \kappa \Delta x} , \tag{7.116}$$

where $\kappa \Delta x$ is the x position in the interval (measured from the beginning of the interval) at which V_{AV} occurs ($\kappa = \frac{1}{2}$ for constant deceleration). Combining (7.115) and (7.116) yields κ as

$$\kappa = \frac{\log_e\left[\left(\frac{V_0}{V_f} - 1\right)\bigg/\log_e \frac{V_0}{V_f}\right]}{\log_e \frac{V_0}{V_f}}. \tag{7.117}$$

This then represents the fraction of the interval Δx at which the average velocity occurs and hence the point where V_{AV} should be plotted.

To apply this result, κ is first set equal to $\frac{1}{2}$. After the first approximation to the velocity-distance curve is obtained, κ can be evaluated for each interval and x positions adjusted accordingly. This new set of data can be treated as before and iterated to convergence. (Normally, a single iteration is sufficient.) This procedure is straightforward but requires precise calculation in evaluating κ from (7.117).

Method 4: Another approach is to use (7.110) to obtain the drag coefficient directly from the time-distance data. An approximate method for employing this equation is to expand the exponential and retain terms to order x^2 . Thus, setting $x_0 = 0$, we obtain

$$t = t_0 + \frac{1}{V_0} x + \frac{KC_D}{2V_0} x^2. \tag{7.118}$$

A least-squares fit will then yield the drag coefficient.

Method 5: Equation (7.110) could also be used without any expansion approximations even though C_D appears in an exponent by using either a differential correction procedure or some other numerical procedure to minimize the sum of the squares of the residuals of measured and calculated times at the given x locations. One method of minimizing residuals is to fix the value of the drag coefficient (use approximate value of C_D obtained from applying Equation (7.118) to start with) and fit (7.110) to the x-t data by least-squares (this is straight-forward) and obtain values for V_0 and t_0 . Next compute the sum of the squares of the time residuals, then change the drag coefficient a small amount and repeat the process. If the sum of the squares of the residuals increases, change the drag coefficient in the other direction and repeat the process. If the sum decreases continue to change C_D in the direction minimizing the sum of the squares of the residuals. Whenever the sum increases, C_D is changed in the other direction by a smaller increment. This process is assumed to converge when the increment becomes smaller than some prescribed value.

7.5.2 Cases with Variable Coefficients

7.5.2.1 Treatment of Drag Coefficient Dependent on Angle of Attack

At first glance it would appear that the drag coefficient determined assuming C_D constant (Section 7.5.1) would be of little value when C_D depends on angle of attack. However, this is not the case. Reference 7.14 showed that for axially symmetric bodies with drag coefficients which are quadratically dependent on angle of attack, i.e.,

$$C_D = C_{D_0} + C_{D_2}\alpha_R^2 . \tag{7.119}$$

a *mean line* (to be described) through a plot of $\log_e V$ versus x data determined an effective drag coefficient $C_{D_{eff}}$ given by

$$C_{D_{eff}} = C_{D_0} + C_{D_2}\alpha_{rms}^2 . \tag{7.120}$$

Here C_{D_0} is the zero-angle drag coefficient, α_R is the resultant angle of attack, and

$$\alpha_{rms} = \left(\frac{1}{x}\int_0^x \alpha_R^2\, dx\right)^{\frac{1}{2}} .$$

From (7.119) and (7.120) then, it is seen that $C_{D_{eff}}$ is that value of C_D which occurs at a resultant angle of attack equal to the root-mean-square resultant angle of attack of the flight in question. Therefore, for each flight or flight segment one obtains a value for $C_{D_{eff}}$ and α_{rms}. If these points are plotted as $C_{D_{eff}}$ versus α_{rms}^2 and a straight line is fit to them by least-squares, values for C_{D_0} and C_{D_2} are obtained and one then has an expression for C_D versus angle of attack.

If the drag coefficient cannot be expressed as a quadratic function of angle of attack but is instead of the form $C_D = C_{D_0} + C_{D_n}\alpha_R^n$, then the angle of attack at which to plot the effective drag coefficient is[7.15]

$$\alpha_{rmn} = \left(\frac{1}{x}\int_0^x \alpha_R^n\, dx\right)^{1/n}$$

and

$$C_{D_{eff}} = C_{D_0} + C_{D_n}\alpha_{rmn}^n .$$

The best value of n is found by a trial and error process.

A generalization of these ideas is possible. The drag coefficient is assumed to be monotonic (either increasing or decreasing with angle of attack) and can be represented by

$$C_D = C_{D_0} + C_{D_i}\alpha_R^i + C_{D_j}\alpha_R^j + \dots \tag{7.121}$$

where the exponents i, j, etc. are arbitrary. If this is substituted for C_D in (7.108b) and integrated once, then

$$\log_e V = \log_e V_0 - K\int_0^x C_D\, dx . \tag{7.122}$$

With the definition

$$C_{D_{eff}} = \frac{1}{x}\int_0^x C_D\, dx = C_{D_0} + C_{D_i}(\alpha_{rmi})^i + C_{D_j}(\alpha_{rmj})^j + \dots \tag{7.123}$$

where

$$\alpha_{rmi} = \left(\frac{1}{x}\int_0^x \alpha_R^i\, dx\right)^{1/i} \quad \text{etc.},$$

Equation (7.122) can be written

$$\log_e V = \log_e V_0 - K C_{D_{eff}} x . \tag{7.124}$$

Hence, a mean line through the $\log_e V$ versus x data would yield $C_{D_{eff}}$ and from several tests which had different values of angle of attack one could determine the coefficients C_{D_0}, C_{D_i}, etc. provided the angular motion had been analyzed and the appropriate angles determined. The quadratic and n^{th} power laws are special cases of this approach.

The term *mean line* has appeared several times and needs to be defined. It can best be visualized by considering the $\log_e V$ versus x plot in conjunction with an angle of attack versus x plot such as those shown in Figure 7.7. For a drag coefficient which is monotonic with angle of attack the mean line which yields the effective drag coefficient is that line which intersects the actual $\log_e V$ curve at x positions corresponding to maximum and minimum drag points and hence to the maximum and minimum angle-of-attack points as noted in the figure.

Note that in the present formulation the mean line is straight; hence, the pitching motion is assumed not to be excessively damped. Furthermore, in practice a least-square procedure is normally used to obtain $C_{D_{eff}}$ and this does not necessarily yield a mean line in the sense just described. It gives the mean line only if the angular motion is undamped and the least-squares fit extends over a flight path of many cycles of oscillation. For a half cycle of pitching motion, the result shown in Figure 7.8 occurs.

The deviations are normally small for cases of practical interest, however. Some examples of the error introduced by assuming that the least-squares line is the mean line have been obtained by numerical techniques. It was assumed that the drag coefficient was quadratically dependent on angle of attack and that the drag coefficient at zero angle of attack (C_{D_0}) was known exactly. The deduced value of C_{D_2} was found to depend on (i) the amount of damping present, (ii) the number of cycles of pitching motion, and (iii) the phase relation of the pitching motion to, say, a sine wave. The ratio C_{D_2} (deduced)/C_{D_2} (actual) is shown in the following table.

α_f/α_0	n = 0.5	n = 1	n = 2	n = 3	n = 5
0.9	0.70-1.30	0.92-1.08	0.98-1.02	0.99-1.01	0.99-1.00
0.7	0.70-1.30	0.90-1.07	0.96-1.01	0.97-1.00	0.98-1.00
0.5	0.67-1.29	0.86-1.06	0.92-0.99	0.93-0.98	0.95-0.97
0.1	0.54-1.22	0.58-0.98	0.65-0.83	0.68-0.79	0.71-0.78

n	= number of cycles of pitching motion
α_f	= angle-of-attack envelope at end of flight
α_0	= angle-of-attack envelope at start of flight

The quantity α_f/α_0 is proportional to the damping. The *range* of the numbers tabulated for the C_{D_2} ratio extends from the smallest to largest obtained as the phase relation was varied between $0°$ and $90°$. Note that if 2 or more cycles of pitching motion are available and modest damping is present, the error introduced into C_{D_2} is at most a few percent.

When the least-square curve fitting procedure is applied directly to the time-distance data rather than to $\log_e V$ versus distance data, the situation is more complicated. It cannot be shown exactly that the $C_{D_{eff}}$ concept carries over to this case since (7.108) cannot be integrated twice in closed form when the drag coefficient depends on angle-of-attack. However, for planar motion and small velocity loss the $C_{D_{eff}}$ concept can be proved valid. For quadratic drag, it can be shown to apply for nonplanar motion again assuming a small velocity loss. Since in most cases of practical interest the velocity loss is small, the effective-drag-coefficient concept is valid within the limits imposed by the small damping restriction.

7.5.2.2 Treatment of Variable Ambient Density

In counter-flow facilities, the model may encounter density variations along its flight path. Usually the density variations encountered are not extreme, deviating perhaps $\pm20\%$ from a given level. When this is the case, a very accurate estimate of the drag coefficient can be obtained exactly as before but using the *average* density over the length of the flight instead. That is

$$\rho_{AV} = \frac{1}{L} \int_0^L \rho(x)\, dx .\tag{7.125}$$

7.5.2.3 Treatment of Variable Model Mass

The problem of variable mass, which arises in the study of meteors, can also occur in the simulation of meteoric events in the laboratory by use of models. (To a lesser degree, mass variations occur with any model which ablates in flight.) The parameter of interest here is not the drag coefficient but rather the mass loss rate. If the mass loss rate is small, the drag coefficient and model reference area may be assumed constant. Further, it is assumed that the velocity of the mass leaving the body is small so that (7.108) is still applicable. Then differentiating (7.108) with respect to time and rearranging yields

$$\left.\begin{aligned}
\dot{m} &= -\rho V A C_D - m\,\frac{d^2V}{dt^2}\bigg/\frac{dV}{dt} \\[2mm]
\dot{m} &\approx \frac{2m}{V}\frac{dV}{dt} - m\,\frac{d^2V}{dt^2}\bigg/\frac{dV}{dt} .
\end{aligned}\right\}\tag{7.126}$$

or

If C_D is known from another source, the first of these equations should be used. These equations indicate that the distance versus time data must be differentiated three times to determine $\dot{m}$. Unless the data are very good, this procedure will not yield accurate information.

Given the functional dependence of the mass loss rate on velocity, one can obtain the mass loss rate more accurately. Consider the function

$$\dot{m} = -kV ,\tag{7.127}$$

where k is a positive proportionality constant which depends on model material, size, and freestream density. (This function approximates ablators with good convective heat transfer blockage at very high speeds.) Equation (7.127) can be integrated, yielding

$$m - m_0 = -kx ,\tag{7.128}$$

where at $x = 0$, $m = m_0$, $V = V_0$, and $t = t_0$.

By restriction to small mass loss, the reference area and drag coefficient are again assumed constant. Substituting the linear expression for m into (7.108) and integrating gives

$$\frac{V}{V_0} = \left(1 - \frac{k}{m_0} x\right)^{\rho A C_D / 2k}$$

(7.129)

Integrating again yields

$$t = t_0 + \frac{m_0}{k\left(1 - \frac{\rho A C_D}{2k}\right) V_0} - \frac{\left(1 - \frac{k}{m_0} x\right)^{1 - (\rho A C_D / 2k)}}{\left(\frac{k}{m_0} - \frac{\rho A C_D}{2m_0}\right) V_0} .$$

(7.130)

For small mass loss this can be expanded as follows:

$$t = t_0 + \frac{1}{V_0} x + \frac{\rho A C_D}{2m_0 V_0} \frac{x^2}{2} - \frac{\rho A C_D}{2m_0 V_0}\left(\frac{\rho A C_D}{2m_0} + \frac{k}{m_0}\right)\frac{x^3}{6} + \dots$$

(7.131)

Note that this equation is the same as that derived previously for constant mass (Equation (7.118)) to the order x^2. The information defining k occurs in the x^3 (and higher order) terms. Hence, well-defined data are again required, but less accuracy is needed than for the first method, since (7.131) uses the entire run to determine the coefficient k, while in the first method, the curvature in the velocity curve was considered locally.

In the event that the area changes importantly while the drag coefficient remains approximately constant (e.g., the case of an ablating meteor model with intermittent flange build-up and loss), one can deduce the mass-loss rate, provided the area change is known from shadowgraphs or other sources, by rearranging (7.108) to yield

$$\overset{.}{m} = \frac{-\rho A(x) C_D V(x)}{2 \, dV/dx} .$$

(7.132)

Since all of the quantities on the right side of this equation are known or measurable at various points along the trajectory, one can plot the mass versus time. The slope of this curve is the mass loss rate. Again, this slope involves effectively a third derivative of the time-distance data.

7.5.3 Correction for Swerving Flight Path

The assumption that flight path distance, $\hat{x}$, is equal to the distance along the x axis can be removed if the swerving motion of the model center of gravity has been analyzed to yield a flight path distance. To first order, an average value of $1/\cos\gamma$ is computed over each data interval and applied as follows:

$$\Delta\hat{x}_i = \Delta x_{exp_i}\left(\frac{1}{\cos\gamma}\right)_{AV_i} .$$

(7.133)

where

$$\left(\frac{1}{\cos\gamma}\right)_{AV} = \frac{1}{\Delta x}\int_x^{x+\Delta x} \frac{dx}{\cos\gamma} .$$

(7.134)

A good approximation to the flight path distance is then

$$\hat{x} = \sum_i \Delta\hat{x}_i .$$

(7.135)

This correction is time consuming and usually unnecessary. It need be considered only in cases where the swerve is very large, enough to significantly increase the total distance traveled.

7.6   STATIC AND DYNAMIC STABILITY ANALYSIS

A model designed so that its center of gravity is ahead of the center of pressure of the aerodynamic forces will oscillate when in free-flight. Normally orthogonal shadowgraphs are taken at a number of stations along the trajectory to define this oscillation. Frequently, small pins are included on the base of the model so that the roll orientation (and hence roll rate) can also be determined.

The types of motions obtained from ballistic range tests are many and varied. The easiest way to visualize the motion is via a crossplot of the angle of attack versus the angle of sideslip (α versus β). This is equivalent to watching the path traced by the nose of the model on a plane normal to the velocity vector. Examples of typical motions are shown in Figure 7.9. The upper left motion has essentially zero roll rate, the lower right motion has a high roll rate. The roll rate present can be measured by the amount of precession of the peak amplitudes.

From a knowledge of the angle history experienced by the model, it is possible to deduce the static and dynamic stability coefficients which governed the flight. A number of methods are available for doing this and will be discussed in the following sections.

7.6.1 Determination from Wavelength and Amplitude Variation

The first method to be considered is not sophisticated, but does lead to a good physical understanding of the problem. The following assumptions will be made.

(i) Static restoring moment is linear with angle of attack.

(ii) Dynamic stability parameter is constant with angle of attack.

(iii) Aerodynamic coefficients are constant over the trajectory portion analyzed (small Mach number and Reynolds number changes or insensitivity of coefficients to Mach number and Reynolds number).

(iv) Motion is planar, which implies that the roll rate is zero. This assumption is introduced to simplify the discussion, and will be dropped presently.

The static and dynamic stability parameters, C_{m_α} and ξ, are determined from the wavelength and the change in the maximum amplitude of the motion, respectively. Consider the differential equation of angular motion that is appropriate under the assumptions listed (simplified version of Equation (7.103)):

$$\alpha'' - K\xi\alpha' - K_s C_{m_\alpha}\alpha = 0 , \tag{7.136}$$

where

$$K = \frac{\rho A}{2m}$$

ξ = dynamic stability parameter (or damping parameter) for unpowered flight at constant altitude

$$K_s = \frac{\rho A l}{2I}$$

$$C_{m_\alpha} = \frac{\partial C_m}{\partial \alpha} = \text{static moment-curve slope.}$$

Equation (7.136) is of the form

$$\alpha'' + 2\eta\alpha' + \omega^2\alpha = 0 , \tag{7.137}$$

which is the differential equation for damped simple harmonic motion. The solution to this equation is

$$\alpha = e^{-\eta x}[A_1\cos(\omega^2 - \eta^2)^{\frac{1}{2}}x + A_2\sin(\omega^2 - \eta^2)^{\frac{1}{2}}x] . \tag{7.138}$$

Normally $\eta \ll \omega$ so the frequency can be approximated $(\omega^2 - \eta^2)^{\frac{1}{2}} \approx \omega$.

From (7.136) and (7.137) we can write

$$\xi = \frac{-2\eta}{K} = \frac{-2\eta}{\rho A/2m} \tag{7.139}$$

and

$$C_{m_\alpha} = \frac{-\omega^2}{K_s} = \frac{-2\omega^2 I}{\rho A l} .$$

The wavelength is

$$\lambda = \frac{2\pi}{\omega}$$

and C_{m_α} in terms of the wavelength becomes

$$C_{m_\alpha} = \frac{-8\pi^2 I}{\lambda^2 \rho A l} . \tag{7.140}$$

Note that this equation specifies that for linear aerodynamics (i.e., C_{m_α} = constant) the wavelength of the motion does not depend on the amplitude.

Making use of (7.138) and Figure 7.10, it is seen that

at $x_1 = 0$, $\alpha_1 = A_1$

at $x_2 = \lambda$, $\alpha_2 = e^{-\eta\lambda}(A_1\cos\omega\lambda + A_2\sin\omega\lambda)$;

but
$$\lambda = 2\pi/\omega.$$

so
$$\alpha_2 = e^{-\eta\lambda}(A_1 \cos 2\pi + A_2 \sin 2\pi) = A_1 e^{-\eta\lambda}$$

$$\frac{\alpha_2}{\alpha_1} = \frac{A_1 e^{-\eta\lambda}}{A_1} = e^{-\eta\lambda}.$$

Hence $\log_e\left(\dfrac{\alpha_2}{\alpha_1}\right) = \cdot\eta\lambda$ (logarithmic decrement in amplitude)

$$\eta = -\frac{1}{\lambda}\log_e\frac{\alpha_2}{\alpha_1}. \tag{7.141}$$

In terms of ξ, from (7.139),

$$\xi = \frac{\log_e\dfrac{\alpha_2}{\alpha_1}}{(\rho\lambda/4m)\lambda}, \tag{7.142a}$$

which can also be written as

$$\alpha_2 = \alpha_1 e^{(\rho A/4m)\xi\lambda}. \tag{7.142b}$$

Hence, knowing the wave length and the amplitude ratio, the static and dynamic stability parameters can be determined from (7.140) and (7.142).

Note that the dynamic stability parameter could also be determined using, for example, the ratio $|\alpha_3/\alpha_1|$ together with the distance between these peaks. This is not as accurate as using the ratio from every other peak due to the possibility that the model is oscillating about a trim angle of attack other than zero.

Assume next that the motion is not planar but the roll rate is small. The static and dynamic stability parameters can be determined exactly as before except now the wave length and amplitude ratio are determined from a plot of the resultant angle of attack (α_R) versus flight distance (note $\alpha_R \approx \sqrt{(\alpha^2 + \beta^2)}$).

Now assume in addition an arbitrary (but near-constant) roll rate which is presumed known. The expression for the static stability parameter is then given by the following equation, the first term of which is the same as (7.140):

$$C_{m_\alpha} = \frac{-8\pi^2 I}{\lambda^2 \rho Al} + \frac{2I}{\rho Al}\left(\frac{p}{2}\frac{I_x}{I}\right)^2.$$

In this case, however, there is no simple expression like (7.142) for obtaining the dynamic stability parameter.

7.6.2 Determination from Angle of Attack Variation Near a Peak

The pitching moment coefficient (C_m) and damping parameter (ξ) can also be determined by applying directly the differential equation of motion and determining the angular accelerations from the angle of attack history. This method can be applied to motions at all amplitudes (including tumbling motions) and is not limited to linear aerodynamics. While the method of the previous section requires that more than a cycle of oscillatory motion be defined, with three peak amplitudes to get dependable results, the method we will now present requires instead as many data points as possible in a quarter to half cycle of motion preferably containing a peak amplitude near its center. The assumptions made in this approach are:

(i) The Mach number or Reynolds number variations in the aerodynamic coefficients may be neglected.

(ii) The angular motion is accurately defined on both sides of a peak.

(iii) The motion is nearly planar. This assumption will be relaxed later.

The general differential equation of angular motion for planar flight is

$$\alpha'' = K(C_m)_D + K_s(C_m)_S. \tag{7.143}$$

where

$(C_m)_D$ = dynamic pitching moment coefficient

$(C_m)_S$ = static pitching moment coefficient

$$K = \frac{\rho A}{2m}$$

$$K_s = \frac{\rho Al}{2I}.$$

The half cycle of motion to be analyzed is represented in Figure 7.11 and can be considered as two segments, divided by the peak, where $\alpha' = 0$. If there is damping in the system, the $\alpha(x)$ curves on either side of

center will not be identical. The difference between the two curves is a measure of the damping. The shape of the curves $\alpha_1(x)$ and $\alpha_2(x)$ will reveal the nature of the pitching moment which produced the resulting motion.

We proceed as follows. Define

$$\alpha = \alpha_1(x), \quad x_1 \leqslant x \leqslant x_c$$

$$\alpha = \alpha_2(x), \quad x_c \leqslant x \leqslant x_2$$

and at

$$x = x_c$$

$$\alpha' = 0, \quad \alpha_1(x) = \alpha_2(x) = \alpha_m .$$

From (7.143)

$$\left.\begin{array}{l} \alpha_1'' = K(C_m)_{D_1} + K_S(C_m)_{S_1} \\[2mm] \alpha_2'' = K(C_m)_{D_2} + K_s(C_m)_{S_2} . \end{array}\right\} \tag{7.144}$$

At any given α the static moments are identical, that is

$$(C_m)_{S_1} = (C_m)_{S_2} = (C_m)_S .$$

From (7.144) then, at points of equal α,

$$\alpha_1'' + \alpha_2'' = K\left[(C_m)_{D_1} + (C_m)_{D_2}\right] + 2K_s(C_m)_S$$

or

$$(C_m)_S = \frac{\alpha_1'' + \alpha_2''}{2K_s} - \frac{K}{2K_s}\left[(C_m)_{D_1} + (C_m)_{D_2}\right] . \tag{7.145}$$

Thus, from values of the angular accelerations α_1'' and α_2'', if we could either evaluate or neglect $(C_m)_{D_1}$ and $(C_m)_{D_2}$, we could readily compute values for $(C_m)_S$. When the damping contributions to the total moment are zero or negligible, that is $(C_m)_{D_1} = (C_m)_{D_2} = 0$, then

$$\alpha_1'' = \alpha_2'' = \alpha''$$

and (7.145) reduces to

$$(C_m)_S = \frac{\alpha''}{K_s} . \tag{7.146}$$

An expression for $\alpha = \alpha(x)$ can be obtained by fitting a polynomial in x to the α versus x data. Differentiation of this expression twice yields values of $\alpha''(x)$ which lead directly to $C_{m_S}(x)$ through (7.146). By plotting C_{m_S} versus α for common values of x, $C_{m_S}(\alpha)$ is obtained.

Real systems have some damping, which is in general proportional to the angular rate,

$$(C_m)_D = \xi\alpha' ,$$

where ξ is again the dynamic stability parameter.

On substituting $(C_m)_{D_1} = \xi\alpha_1'$ and $(C_m)_{D_2} = \xi\alpha_2'$ into (7.144) we get

$$\left.\begin{array}{l} \alpha_1'' = K\xi\alpha_1' + K_S(C_m)_{S_1} \\[2mm] \alpha_2'' = K\xi\alpha_2' + K_S(C_m)_{S_2} . \end{array}\right\} \tag{7.147}$$

Subtracting these equations for points at a common value of α, remembering that $(C_m)_{S_1} = (C_m)_{S_2}$ at a given α, we get

$$\alpha_1'' - \alpha_2'' = K\xi(\alpha_1' - \alpha_2') ,$$

so that

$$\xi = \frac{\alpha_1'' - \alpha_2''}{K(\alpha_1' - \alpha_2')} . \tag{7.148}$$

Thus, the damping parameter can be calculated from the first and second derivatives of the angle of attack variations with x at points of common amplitude on both sides of the peak, α_m.

When the damping terms are retained, the static pitching moment is calculated as follows:

Equation (7.145) is written with the damping coefficients proportional to angular rate

$$(C_m)_s \; = \; \frac{\alpha_1'' + \alpha_2''}{2K_s} - \frac{K\xi}{2K_s} \; (\alpha_1' + \alpha_2') \; .$$

But ξ is defined by (7.148) so

$$(C_m)_s \; = \; \frac{\alpha_1'' + \alpha_2''}{2K_s} - \frac{\alpha_1'' - \alpha_2''}{2K_s(\alpha_1' - \alpha_2')} \; (\alpha_1' + \alpha_2')$$

and we obtain

$$(C_m)_s \; = \; \frac{\alpha_2''\alpha_1' - \alpha_1''\alpha_2'}{K_s(\alpha_1' - \alpha_2')} \; . \qquad\qquad (7.149)$$

The static and dynamic pitching moment coefficients can be obtained over a large angle of attack range by this technique if the observed motion of α versus x can be well represented mathematically. A polynomial of the form $\alpha = A_1 + A_2x + A_3x^2 + \ldots + A_Nx^{N-1}$ is fitted by least squares to the α versus x data. At each value of α, there will be two (meaningful) values of α' and α'', one for each side of the peak. Substituting these values in (7.148) and (7.149) gives the desired results. The method is least accurate in the low-angle portion of the α versus x curve where the acceleration is small and consequently the curvature approaches zero. An improvement to the results can be made by first locating the point of $\alpha' = 0$ by least-squares fitting the entire set of data. Then, two separate polynomials, one on each side of the peak, of the form $\alpha - \alpha_m = A_1x^2 + A_2x^3 + \ldots + A_Nx^{N+1}$ can be given zero slope and the same peak amplitude at this point.

Assume now that the motion is not planar but that the roll rate is small. Equations (7.148) and (7.149) then become

$$\xi \; = \; \frac{\alpha_{R_1}'' - \alpha_{R_2}''}{K(\alpha_{R_1}' - \alpha_{R_2}')} - \frac{\alpha_{R_1}\phi_1'^2 - \alpha_{R_2}\phi_2'^2}{K(\alpha_{R_1}' - \alpha_{R_2}')} \qquad\qquad (7.150)$$

$$(C_m)_s \; = \; \frac{\alpha_{R_2}''\alpha_{R_1}' - \alpha_{R_1}''\alpha_{R_2}'}{K_s(\alpha_{R_1}' - \alpha_{R_2}')} - \frac{\alpha_{R_2}\phi_2'^2\alpha_{R_1}' - \alpha_{R_1}\phi_1'^2\alpha_{R_2}'}{K_s(\alpha_{R_1}' - \alpha_{R_2}')} \; , \qquad\qquad (7.151)$$

where α_R again denotes the resultant angle of attack and ϕ' is the rotation rate of the resultant-angle vector in the α-β plane (Fig. 7.12). The subscripts 1 and 2 on α_R and ϕ' are interpreted exactly as in Figure 7.11. At a given value of α_R on each side of the peak angle there will be corresponding values for ϕ_1' and ϕ_2' just as there are for α_{R_1}' and α_{R_2}'.

For motions governed by a linear static moment and constant damping, one can analyze $\alpha_R(x)$, $\alpha(x)$, or $\beta(x)$ separately and obtain equally valid results within the limits of experimental error in angle readings. For motions governed by a nonlinear moment where the minimum α_R is more than about 20% of the peak α_R, only the $\alpha_R(\lambda)$ curve will yield meaningful results. However, since α_R does not go to zero as in a planar case, the range of α_R values to be analyzed should not go beyond the inflection points on either side of the $\alpha_R(x)$ curve.

The success of this method depends strongly on accurate angle readings. The damping coefficient is very sensitive to random error. The static pitching moment coefficient is much less sensitive and sometimes can be determined to a useful degree of accuracy even in the absence of a peak. However, without the motion history on both sides of a peak, one has no way of determining the dynamic moment. An example showing application of this method is given in Section 7.9.2.

7.6.3 Tricyclic Method

The methods discussed so far run into serious problems in cases where asymmetries are present or when an unknown roll rate exists. These cases require the more complete tricyclic equations of motion for proper treatment[7.5,7.16]. In discussing the tricyclic method, projected angles as defined in Section 7.3.3 will be used instead of modified Euler angles. To the order of the approximations that will be made, the two sets of angles are essentially identical.

The important assumptions of this method are:

(i) Basic axial symmetry with only slight asymmetry due to, for example, a control surface or offset center of mass.

(ii) Linear aerodynamics.

(iii) Constant roll rate.

(iv) Small angular displacements

(v) Small linear displacements due to swerve.

(vi) Small velocity change.

The differential equation of angular motion has been given in (7.103) and (7.106) and is reproduced here as follows.

$$\vec{\alpha}_R'' - \left\{\frac{\rho A}{2m}\xi + i\frac{\rho A}{2m}pl\left[-C_{L_{\alpha p}} + \frac{ml^2}{I}(C_{m_{\dot\alpha p}} - C_{m_{qp}})\right] + i\frac{I_{\tilde x}}{I}p\right\}\vec{\alpha}_R' -$$

$$-\left\{\frac{\rho Al}{2I}(C_{m_\alpha} + iC_{m_{\alpha p}}pl) - \frac{\rho A}{2m}\frac{I_{\tilde x}}{I}p(C_{L_{\alpha p}}pl - iC_{L_\alpha})\right\}\vec{\alpha}_R = Re^{ipx}. \qquad (7.152)$$

where

$$\vec{\alpha}_R = \beta + i\alpha$$

and

$$\xi = C_D - C_{L_\alpha} + \frac{ml^2}{I}(C_{m_q} + C_{m_{\dot\alpha}}).$$

Equation (7.152) can be written as

$$\vec{\alpha}_R'' - (\phi_1 + \phi_2)\vec{\alpha}_R' + \phi_1\phi_2\vec{\alpha}_R = K_3(\phi_3 - \phi_1)(\phi_3 - \phi_2)e^{\phi_3 x}, \qquad (7.153)$$

which has the solution

$$\vec{\alpha}_R = K_1 e^{\phi_1 x} + K_2 e^{\phi_2 x} + K_3 e^{\phi_3 x}. \qquad (7.154)$$

This is called the tricyclic equation, since it is equivalent to three rotating vectors in the α-β plane. This is shown in Figure 7.13, with the following nomenclature defined:

$$\phi_1 = \eta_1 + i\omega_1 \qquad\qquad K_1 = b_1 + ia_1$$

$$\phi_2 = \eta_2 - i\omega_2 \qquad\qquad K_2 = b_2 + ia_2$$

$$\phi_3 = ip \qquad\qquad\qquad K_3 = b_3 + ia_3.$$

If we write the components of $\vec{\alpha}_R$ in (7.154) we get

$$\beta = e^{\eta_1 x}(b_1\cos\omega_1 x - a_1\sin\omega_1 x) + e^{\eta_2 x}(b_2\cos\omega_2 x + a_2\sin\omega_2 x) + (b_3\cos px - a_3\sin px)$$

$$\alpha = e^{\eta_1 x}(b_1\sin\omega_1 x + a_1\cos\omega_1 x) + e^{\eta_2 x}(-b_2\sin\omega_2 x + a_2\cos\omega_2 x) + (b_3\sin px + a_3\cos px).$$

Note that from (7.152) and (7.153) we get the expressions

$$\phi_1 + \phi_2 = \frac{\rho A}{2m}\xi + i\frac{\rho A}{2m}pl\left[-C_{L_{\alpha p}} + \frac{ml^2}{I}(C_{m_{\dot\alpha p}} - C_{m_{qp}})\right] + i\frac{I_{\tilde x}}{I}p$$

$$\phi_1\phi_2 = \frac{-\rho Al}{2I}(C_{m_\alpha} + iC_{m_{\alpha p}}pl) + \frac{\rho A}{2m}\frac{I_{\tilde x}}{I}p(C_{L_{\alpha p}}pl - iC_{L_\alpha})$$

$$K_3(\phi_3 - \phi_1)(\phi_3 - \phi_2) = R.$$

Also,

$$\phi_1 + \phi_2 = \eta_1 + \eta_2 + i(\omega_1 - \omega_2)$$

$$\phi_1\phi_2 = \eta_1\eta_2 + \omega_1\omega_2 + i(\eta_2\omega_1 - \eta_1\omega_2).$$

We therefore have

$$\eta_1 + \eta_2 = \frac{\rho A}{2m}\xi \qquad\qquad (7.155)$$

$$\omega_1 - \omega_2 = \frac{\rho A}{2m}pl\left[-C_{L_{\alpha p}} + \frac{ml^2}{I}(C_{m_{\dot\alpha p}} - C_{m_{qp}})\right] + \frac{I_{\tilde x}}{I}p \qquad\qquad (7.156)$$

$$\eta_1\eta_2 + \omega_1\omega_2 = \frac{-\rho Al}{2I}C_{m_\alpha} + \frac{\rho A}{2m}\frac{I_{\tilde x}}{I}p^2 l\, C_{L_{\alpha p}} \qquad\qquad (7.157)$$

$$\eta_2\omega_1 - \eta_1\omega_2 = \frac{-\rho A}{2m}\frac{I_{\tilde x}}{I}pC_{L_\alpha} - \frac{\rho Al}{2I}C_{m_{\alpha p}}pl. \qquad\qquad (7.158)$$

In order to obtain numerical values for the desired aerodynamic coefficients one must obtain the coefficients in (7.154). A least squares procedure using differential corrections (described in the appendix) can be used to fit (7.154) to the experimental data, α and β, at various values of x. The constants a_1, a_2, a_3, b_1, b_2, b_3, η_1, η_2, ω_1, and ω_2 are determined from the fit. If one examines (7.155) thru (7.158), it will be noted that there are more aerodynamic coefficients to be determined than there are equations, a seemingly impossible

situation. However, for most ballistic range tests of aerodynamically stable projectiles launched from non-rifled guns, the model experiences low roll rates and the Magnus terms can usually be ignored. It will be shown later, after development of the displacement equations of motion, how some of these Magnus coefficients can be obtained. When the Magnus terms are negligible, it is very simple to obtain the remaining coefficients. From (7.155) the dynamic stability parameter ξ is

$$\xi = \frac{\eta_1 + \eta_2}{\rho A/2m} . \tag{7.159}$$

while from (7.156) with $C_{L_{\alpha p}}$, $C_{m_{\dot\alpha p}}$, $C_{m_{q p}}$, and $C_{m_{\alpha p}} = 0$,

$$\omega_1 - \omega_2 = \frac{I_{\tilde x}}{I} p . \tag{7.160}$$

Thus, the roll rate p is not an independent parameter but is fully determined by ω_1 and ω_2. From (7.157), since $\eta_1 \eta_2 \ll \omega_1 \omega_2$, we obtain

$$C_{m_\alpha} = \frac{-2\omega_1 \omega_2 I}{\rho A l} . \tag{7.161}$$

Equation (7.158) indicates that C_{L_α} can be obtained from

$$C_{L_\alpha} = \frac{\eta_1 \omega_2 - \eta_2 \omega_1}{\dfrac{\rho A}{2m} \dfrac{I_{\tilde x}}{I} p} . \tag{7.162}$$

However, the η's and ω's are usually not precise enough to define an accurate value of C_{L_α} from this expression. If C_{L_α} can be obtained from the swerve (displacement of the model trajectory) then one can express η_2 as a function of η_1, C_{L_α} and p (Equations (7.160) and (7.162)):

$$\eta_2 = \left(\eta_1 + \frac{\rho A}{2m} C_{L_\alpha}\right)\frac{\omega_2}{\omega_1} - \frac{\rho A}{2m} C_{L_\alpha} . \tag{7.163}$$

We therefore have to determine only nine independent coefficients rather than eleven. For the case where p is known from experimental measurements of the model roll rate, then from (7.160)

$$\omega_2 = \omega_1 - \frac{I_{\tilde x}}{I} p \tag{7.164}$$

and as a result

$$\eta_2 = \left(\eta_1 + \frac{\rho A}{2m} C_{L_\alpha}\right)\left(\frac{\omega_1 - (I_{\tilde x}/I)p}{\omega_1}\right) - \frac{\rho A}{2m} C_{L_\alpha} . \tag{7.165}$$

Then ω_2 and η_2 are functions of only ω_1 and η_1 and the measured values of p and C_{L_α}, and only eight unknown coefficients have to be determined.

7.6.3.1 Starting Solution

To initiate the least-squares-with-differential-corrections procedure, starting values for the unknown coefficients must be provided. The method used is a modification of Prony's method[7.17]. Fundamental to Prony's method is the following theorem: If

$$(\beta + i\alpha)_l = \sum_{j=1}^{3} K_j e^{\phi_j x_l} , \tag{7.166}$$

where

$$x = x_1, x_2, \dots x_n \qquad \text{(x locations of equally spaced points, } \Delta x \text{ apart)}$$

$$l = 1, 2, \dots n \qquad \text{(n = number of points, } \beta + i\alpha \text{),}$$

then $\beta + i\alpha$ satisfies the linear difference equation

$$(\beta + i\alpha)_{l+3} + Q_2 (\beta + i\alpha)_{l+2} + Q_1 (\beta + i\alpha)_{l+1} + Q_0 (\beta + i\alpha)_l = 0 , \tag{7.167}$$

where Q's are constants such that the roots of $h^3 + Q_2 h^2 + Q_1 h + Q_0 = 0$ are

$$h_j = e^{\phi_j \Delta x} .$$

This minimizes

$$\sum [(\beta + i\alpha)_{l+3} + Q_2 (\beta + i\alpha)_{l+2} + Q_1 (\beta + i\alpha)_{l+1} + Q_0 (\beta + i\alpha)_l]^2 \tag{7.168}$$

instead of

$$\sum \left[(\beta + i\alpha)_{\text{measured}} - (\beta + i\alpha)_{\text{calculated}} \right]^2 \ . \tag{7.169}$$

which means simply that the coefficients derived from the procedure are not the "best possible" coefficients but are good first approximations. To obtain values for the coefficients K_j and ϕ_j, the first step is to solve the following set of equations by the method of least squares for Q_2, Q_1, and Q_0 (see Equation (7.167)).

$$\left.\begin{array}{l}
(\beta + i\alpha)_4 + Q_2 (\beta + i\alpha)_3 + Q_1 (\beta + i\alpha)_2 + Q_0 (\beta + i\alpha)_1 = 0 \\[2mm]
(\beta + i\alpha)_5 + Q_2 (\beta + i\alpha)_4 + Q_1 (\beta + i\alpha)_3 + Q_0 (\beta + i\alpha)_2 = 0 \\[2mm]
\ \ \vdots \\[2mm]
(\beta + i\alpha)_n + Q_2 (\beta + i\alpha)_{n-1} + Q_1 (\beta + i\alpha)_{n-2} + Q_0 (\beta + i\alpha)_{n-3} = 0 \ .
\end{array}\right\} \tag{7.170}$$

With Q_2, Q_1, and Q_0 known, the cubic equation

$$h^3 + Q_2 h^2 + Q_1 h + Q_0 = 0 \tag{7.171}$$

is solved for roots h_1, h_2, and h_3, where

$$\begin{aligned}
h_1 &= e^{\phi_1 \Delta x} \\[2mm]
h_2 &= e^{\phi_2 \Delta x} \\[2mm]
h_3 &= e^{\phi_3 \Delta x} \ .
\end{aligned} \tag{7.172}$$

Then Equations (7.172) are solved for ϕ_1, ϕ_2 and ϕ_3, which are substituted into (7.166) to obtain K_1, K_2, and K_3 by a second least squares operation. However, since ϕ_3 is not independent of ϕ_1 and ϕ_2 for the tricyclic equation in question (i.e., $p = f(\omega_1, \omega_2) \Rightarrow \phi_3 = g(\phi_1, \phi_2)$) the procedure is slightly modified.

We assume initially that $\phi_3 = 0$ and therefore $h_3 = e^0 = 1$. We therefore have

$$(\beta + i\alpha)_l = K_1 e^{\phi_1 x_l} + K_2 e^{\phi_2 x_l} + K_3 \tag{7.173}$$

and $h^3 + Q_2 h^2 + Q_1 h + Q_0 = 0$ has unity as a root and we get $1 + Q_2 + Q_1 + Q_0 = 0$. If we eliminate Q_0 between this equation and (7.167), we have

$$[(\beta + i\alpha)_{l+2} - (\beta + i\alpha)_l] Q_2 + [(\beta + i\alpha)_{l+1} - (\beta + i\alpha)_l] Q_1 = (\beta + i\alpha)_l - (\beta + i\alpha)_{l+3} \ . \tag{7.174}$$

This equation is now solved by least squares for the coefficients Q_1 and Q_2. The exponentials $e^{\phi_1 \Delta x}$ and $e^{\phi_2 \Delta x}$ are now found to be the roots of

$$h^2 + (Q_2 + 1)h + (Q_1 + Q_2 + 1) = 0 \ . \tag{7.175}$$

So from

$$\left.\begin{array}{l}
h_1 = e^{\phi_1 \Delta x} \\[2mm]
h_2 = e^{\phi_2 \Delta x}
\end{array}\right\} \tag{7.176}$$

we can get ϕ_1 and ϕ_2. From ϕ_1 and ϕ_2 we can calculate ϕ_3 using the expression

$$\phi_3 = i \left[\frac{\Im(\phi_1) + \Im(\phi_2)}{I_{\tilde{x}}/I} \right] \ .$$

where $\Im$ denotes the imaginary part. The process is repeated with the new ϕ_3 until the coefficients remain essentially constant. The values of ϕ_j are then substituted into (7.166), and K_j solved for by a second least-squares procedure. Since equally-spaced data are required for Prony's method, they are either computed from the raw data using some interpolation scheme or obtained from hand fairings of the data.

7.6.3.2 Swerve Corrections

In ballistic range tests the angular measurements are normally made with respect to an earth-fixed axis system while the differential equations involve angles relative to the actual flight path. Hence a correction to the angular measurements may be required for the swerving of the trajectory. These corrections (which are usually small) can be computed by differentiating with respect to distance the $z(x)$ and $y(x)$ curves derived from the tricyclic lift analysis (Section 7.7.3). Figure 7.14 shows the relationship of the swerve trajectory, flight path angle, and measured angles in orthogonal planes.

$$\alpha = \theta + \tan^{-1} \frac{dz}{dx}$$

$$\beta = -\psi + \tan^{-1} \frac{dy}{dx} \ .$$

With this new set of angles the stability analysis could be performed again to give a better set of coefficients from the tricyclic analysis and then an iterative procedure set up between stability and lift analyses to obtain the best solution possible (that is, one would iterate until the angle corrections remained essentially constant).

7.6.3.3 Rotation of Coordinate Axes

One of the assumptions necessary in the derivation of the tricyclic equation (7.154) is that angular displacements are small so that the resultant angle of attack is simply the square root of the sum of the squares of the pitch and yaw angles:

$$\alpha_R = \sqrt{(\alpha^2 + \beta^2)} . \tag{7.177}$$

The exact expression for the resultant angle of attack (with α and β regarded as projected angles) is

$$\alpha_R = \tan^{-1}\sqrt{(\tan^2\alpha + \tan^2\beta)} . \tag{7.178}$$

These two equations agree closely for small angles. They agree exactly if either α or β equals zero. Thus, the error introduced by (7.177) can be reduced for near-planar motions by rotating the coordinate axes through an angle Φ to keep the angles in one plane small. To accomplish this, a peak amplitude near the middle of the flight is rotated into either the pitch or yaw plane, establishing the angle Φ, and then all data points are rotated through this angle. This concept is illustrated in Figure 7.15.

The error due to using the tricyclic analysis at large amplitudes (without rotating the data) is most evident in the dynamic stability parameter, ξ. Figure 7.16 demonstrates the magnitude of errors that are encountered for a typical case. Consider a test in a range which has 11 data stations at 1.22 meter intervals with test conditions such that $\rho A/2m = 0.002/m$ and the wavelength of oscillatory motion is 7.9 meters. Various values of ξ are considered at root-mean-square angles of attack of $20°$, $30°$, and $40°$ for a planar motion with $\Phi = 45°$ (the worst case). The figure shows the induced error $(\xi - \xi_{exact})$ as a function of ξ for the three values of α_{rms}. Note the near linear dependence of the induced error on ξ, and also the progressive increase in the error with increasing α_{rms}.

7.6.4 Nonlinear Static Restoring Moment

7.6.4.1 Introduction

One of the assumptions inherent in the tricyclic method (Section 7.6.3) is that the static pitching moment varies linearly with angle of attack. This is usually a good assumption at small angles of attack, but may not be true at larger angles of attack. In this section an examination will be made of nonlinear moments which contain various terms from a power series in angle of attack (or in resultant angle of attack).

$$M = -\Sigma M_n \alpha^{n+1} . \tag{7.179}$$

The term represented by $n = 0$ will be referred to as a linear moment. Similarly, $n = 2$ will be called a cubic moment; $n = 4$, quintic moment; etc. Care must be taken in using even powers of α since they result in a moment curve unsymmetrical about the origin. For axially symmetric bodies, we want a moment which is an odd function of α, and hence use even exponents in the form $M_3\alpha^3|\alpha|$, etc. It will be shown that the results from the tricyclic method previously developed can be used as a first step in finding the nonlinear coefficients.

It is worthwhile to consider just how nonlinearities in the static moment can be detected in ballistic-range data. These nonlinearities affect both the shape and frequency (or wavelength) of the model oscillation. It is found, however, that moderate nonlinearities have only a second-order effect on the shape. In most instances, the resulting wave form differs very little from a damped sine wave. This is illustrated graphically in Figure 7.17, where the wave form for a pure cubic moment $(M = -M_2\alpha^3)$ is compared to a sine wave having the same wavelength. This comparison is for planar motion with zero damping. It should be noted that the wave form corresponding to *all* nonlinear moments of the form $M = -M_0\alpha - M_2\alpha^3$, where both terms are stabilizing, would fall between the two curves shown in this figure.

Hence, the primary means for detecting nonlinearities in the static moment is by observing changes in the wavelength with amplitude of the pitching oscillation*. When the moment is nonlinear, the wavelength changes with amplitude as a consequence of the change in the mean slope of the pitching moment curve, C_{m_α} (see Equation (7.140)). Normally, the aerodynamic damping is small so the wavelength of the model oscillation is essentially constant during a given flight even though a nonlinear static moment exists. For this reason, a number of flights of a given configuration must be made having different peak amplitudes before the form of nonlinearity in the static moment can be determined.

A number of methods have been developed for analyzing ballistic-range data where a nonlinear static moment exists. Some of these methods will be detailed in the following sections. For clarity, the discussion will proceed from simple, very restricted systems toward a general solution with many of the restrictions dropped. First, however, it is useful to illustrate the influence of nonlinear static moments by considering a mechanical analogue.

---

* In at least one instance[7.18], the change in the wave form itself was used to determine the nonlinearities in the static moment.

7.6.4.2 Mechanical Analogue

The analogy between a spherical ball rolling over a contoured surface and the combined pitching and yawing motion of a model in flight is developed in Reference 7.19. A necessary assumption is that zero gyroscopic roll rate of the missile being simulated must be prescribed. Consider for simplicity an axially symmetric configuration. Then construct a bowl according to the equation

$$z = z_0 + A_0 r^2 + A_2 r^4 + \ldots$$

or

$$\frac{dz}{dr} = 2A_0 r + 4A_2 r^3 + \ldots .$$

where z is the height of the bowl surface and r is the distance from the bowl center. A ball rolling over this bowl would execute a motion equivalent to the α versus β motion of a model in free flight which was governed by the static moment

$$C_m = B_0 \alpha_R + B_2 \alpha_R^3 + \ldots .$$

where C_m denotes the moment coefficient at a given *resultant* angle of attack. In other words, C_m has the same form as $\frac{dz}{dr}$.

A number of bowls were made to check out the usefulness of this mechanical analogue. The contours of these bowls, and the static moments they correspond to, are shown in Figure 7.18. The bowls were placed directly below a motion-picture camera, and balls of different sizes and different materials were launched into them by rolling the balls down a chute. It was found that the surfaces of the bowls could be oiled in varying amounts to maintain a control on the damping in the system. Checks made with the "linear-moment" bowl, where an exact analytic solution exists, showed the bowl analogy to be valid.

The real interest in this analogy lay in examining the effect of a nonlinear static moment. One set of results for a linear-cubic moment where the linear term is destabilizing is shown in Figure 7.19. The two components of the resultant angle of attack make little sense by themselves, but the cross-plot of α versus β is completely understandable. The deflection away from the origin in this cross-plot is a characteristic of a nonspinning configuration that is statically unstable at small angles of attack. This mechanical analogue can often be helpful by intuitively revealing the type of static moment governing a particular model.

7.6.4.3 Static Moment Consisting of a Single Term

As an introduction to the treatment of nonlinear moments, we will consider a simple case where an exact solution exists. Consider the case of a single degree of freedom in pitch (planar motion), no aerodynamic damping, and a small velocity loss, and assume the static moment can be represented as

$$M = C_m \frac{\rho V^2 A l}{2} = -M_n \alpha^{n+1} , \qquad n \geq 0 , \tag{7.180}$$

so that

$$C_{m_\alpha} = \frac{-M_n (n+1) \alpha^n}{\frac{1}{2}\rho V^2 A l} . \tag{7.181}$$

The equation of motion to be considered is

$$I\ddot{\alpha} + M_n \alpha^{n+1} = 0 . \tag{7.182}$$

On multiplying this equation by $\dot{\alpha}$ and integrating, we obtain

$$\frac{I\dot{\alpha}^2}{2} + \frac{M_n \alpha^{n+2}}{n+2} = C .$$

To find C, we use the fact that $\dot{\alpha} = 0$ when $\alpha = \alpha_m$. Thus

$$C = \frac{M_n \alpha_m^{n+2}}{n+2}$$

and

$$dt = \left(\frac{(n+2)I}{2M_n}\right)^{\frac{1}{2}} \left(\frac{d\alpha}{\sqrt{(\alpha_m^{n+2} - \alpha^{n+2})}}\right) . \tag{7.183}$$

We can determine $\tau/4$ (where τ is the period of the oscillation) by integrating (7.183) from $\alpha = 0$ to $\alpha = \alpha_m$, that is,

$$\frac{\tau}{4} = \left(\frac{(n+2)I}{2M_n}\right)^{\frac{1}{2}} \int_0^{\alpha_m} \frac{d\alpha}{\sqrt{(\alpha_m^{n+2} - \alpha^{n+2})}} .$$

An expression for the period can be obtained in terms of gamma functions.

$$\tau = \left(\frac{2\pi I (n+4)^2}{(n+2)M_n \alpha_m^n}\right)^{\frac{1}{2}} \frac{\Gamma\left(\dfrac{n+3}{n+2}\right)}{\Gamma\left(\dfrac{n+3}{n+2}+\dfrac{1}{2}\right)} \,. \tag{7.184}$$

This is an exact relationship that shows the effect of the coefficients assumed in (7.180) and the maximum angle of attack. However, it does not provide much in the way of intuitive feel. This can be helped to some extent by introducing the concept of an "effective" angle of attack. First, consider the experimenter's situation. A number of firings have been made of a given configuration. The data have been analyzed as though the static moment were linear and the moment-curve-slope obtained. It is found that the moment-curve-slope is not a constant, but varies with the amplitude of the particular test. The question then arises, for what angles of attack are each of the moment-curve-slopes obtained true local values? That is, what is the effective angle of attack for each measurement?

Solving for M_n in (7.184) and substituting into (7.181) leads to the expression for C_{m_α}.

$$C_{m_\alpha} = \frac{-2\pi(n+1)(n+4)^2}{n+2}\left[\frac{\Gamma\left(\dfrac{n+3}{n+2}\right)}{\Gamma\left(\dfrac{n+3}{n+2}+\dfrac{1}{2}\right)}\right]^2 \left(\frac{\alpha}{\alpha_m}\right)^n \frac{2I}{\tau^2 V^2 \rho A l} \,. \tag{7.185}$$

For a linear moment, $n = 0$ and this equation reduces to (7.140):

$$C_{m_\alpha} \equiv C_{m_{\alpha_l}} = \frac{-8\pi^2 I}{\tau^2 V^2 \rho A l} \,. \tag{7.186}$$

We define the effective angle of attack α_{eff} as that angle at which the moment-curve-slope obtained from a linear analysis of a motion of amplitude α_m matches C_{m_α}. To obtain this angle of attack, we equate (7.185) and (7.186), substituting α_{eff} for α in (7.185). Thus,

$$\frac{\alpha_{eff}}{\alpha_m} = \left\{\frac{2\pi(n+2)}{(n+1)(n+4)^2}\left[\frac{\Gamma\left(\dfrac{n+3}{n+2}+\dfrac{1}{2}\right)}{\Gamma\left(\dfrac{n+3}{n+2}\right)}\right]^2\right\}^{1/n} \,. \tag{7.187}$$

This equation in effect gives the transformation from a plot of $C_{m_{\alpha_l}}$ versus α_m to a plot of C_{m_α} versus α, which can be integrated to obtain C_m. Figure 7.20 shows a plot of α_{eff}/α_m versus n. Note that for a cubic moment ($M = -M_2\alpha^3$), $C_{m_{\alpha_l}}$ should be applied at $0.489\,\alpha_m$. This value will also arise when a linear-plus-cubic moment is considered.

The one-term moment represented by (7.180) has zero slope through the origin, and thus does not allow initial static stability or instability at $\alpha = 0°$. Hence, this representation is not generally applicable, but was included as a simple introductory case.

7.6.4.4 Linear + Cubic Static Moment

Many real physical cases can be represented by the cubic case if a linear term is added to provide finite static stability or instability about the origin. We will still assume undamped angular motion, with only a small change in velocity, and consider a static moment represented by

$$M = C_m \frac{\rho V^2 A l}{2} = -M_0\alpha - M_2\alpha^3 \tag{7.188}$$

$$C_{m_\alpha} = -\frac{2}{\rho V^2 A l}(M_0 + 3M_2\alpha^2) \,. \tag{7.189}$$

It should be noted that three cases of interest exist depending on the signs of M_0 and M_2. These cases are shown in Figure 7.21.

Note that we are considering cases where a model in free flight is oscillating between $+\alpha_m$ and $-\alpha_m$. For a type 1 moment, α_m can be any value. For a type 2 moment, α_m must be less than α_1 or tumbling will occur, and for a type 3 moment, α_m must be greater than α_2 $\left(\text{defined by } \int_0^{\alpha_2} M\,d\alpha = 0\right)$ or the oscillation will take place about the trim angle (α_3) and never pass through zero.

Following the same approach as in the preceding section, we can obtain exact closed-form expressions for the effective-angle parameter, α_{eff}/α_m, in terms now of elliptic integrals. Defining $m_2 = M_2\alpha_m^2/M_0$, these expressions can be written as follows:

Type 1 and type 3 moments:

$$\frac{\alpha_{eff}}{\alpha_m} = \sqrt{\left(\frac{\pi^2(1+m_2)}{12m_2[K(k)]^2} - \frac{1}{3m_2}\right)} \qquad (7.190)$$

$K(k)$ = complete elliptic integral of the first kind

$$k = \sqrt{\left(\frac{m_2}{2(1+m_2)}\right)} .$$

Type 2 moment·

$$\frac{\alpha_{eff}}{\alpha_m} = \sqrt{\left(\frac{\pi^2(2+m_2)}{24m_2[K(k)]^2} - \frac{1}{3m_2}\right)} \qquad (7.191)$$

$$k = \sqrt{\left(\frac{-m_2}{2+m_2}\right)} .$$

These solutions are shown graphically in Figure 7.22. It is interesting to note that the value of α_{eff}/α_m obtained in the previous section for a pure cubic moment (0.489), is representative of nearly all linear-cubic moments of both type 1 and type 3. In fact, except in the vicinity of the singular points for types 2 and 3, a value of α_{eff}/α_m of 0.5 would be a fairly close approximation.

What is most important to note at this point is that exact expressions have been obtained which allow a transformation from $C_{m_{\alpha_l}}$ (equivalent linear system) versus α_m to a local C_{m_α} versus α and the unknowns M_0 and M_2 can be obtained from experimental data by a simple iteration procedure, which proceeds as follows: Assume that $C_{m_{\alpha_l}}$ and α_m have been obtained from a number of tests (e.g., using the tricyclic method). First $(\alpha_{eff})_i$ is assumed equal to $[0.5(\alpha_m)_i]$ and a least squares fit is made to the equations

$$(C_{m_{\alpha_l}})_i = \left(\frac{-2}{\rho V^2 A l}\right)_i [M_0 + 3M_2(\alpha_{eff}^2)_i] ,$$

solving for M_0 and M_2. Depending on the type of moment, either (7.190) or (7.191) is then applied to yield better values of the transformation to apply to each of the $(\alpha_m)_i$ and the least squares procedure is repeated. It is found that the iteration process converges very rapidly for any of the three types of moment.

7.6.4.5 General Power-Series Moment

We will now relax some of the assumptions of the preceding sections and obtain an expression for the case of a spinning symmetric missile governed by an arbitrary nonlinear moment in the *resultant* angle of attack. It is still assumed that aerodynamic damping is negligible and that there is no swerve of the flightpath; therefore,

$$\alpha_R \equiv \sigma .$$

We start with a body-fixed coordinate system denoted by $\bar{x}, \bar{y}, \bar{z}$, with the origin at the center of gravity. This system is related to the inertial coordinate system (x,y,z) by the Euler angles θ_E, σ, and ψ_E (see Figure 7.23). The body has constant angular velocity p about the $\bar{x}$ axis. We will consider that the restoring moment is given by the expression

$$M(\sigma) = C_m\frac{\rho V^2 A l}{2} = -\sum_n M_n\sigma^{n+1} .$$

The moment is completely arbitrary in that any of the coefficients M_n may be set equal to zero*. Following the development in Reference 7.8, it is found that the following differential equation governs the resultant angle of attack σ.

$$\frac{1}{8}\left(\frac{d\sigma^2}{dt}\right)^2 = \left(\sigma^2 - \frac{\sigma_m^2 + \sigma_0^2}{2}\right)\sum_{n=0}^{\infty}\frac{\bar{M}_n}{n+2}\frac{\sigma_m^{n+4} - \sigma_c^{n+4}}{\sigma_m^2 - \sigma_0^2} + \sum_{n=0}^{\infty}\frac{\bar{M}_n}{n+2}\left(\frac{\sigma_m^{n+4} + \sigma_0^{n+4}}{2} - \sigma^{n+4}\right) . \qquad (7.192)$$

Here σ_m and σ_0 are the maximum and minimum resultant angles of attack, and the $\bar{M}_n$ terms are the coefficients M_n modified to include the effect of spin. For the odd subscript terms $(\bar{M}_1, \bar{M}_3 \ldots)$. $\bar{M}_n = M_n/I$. For the even subscript terms, a general expression for $\bar{M}_n$ is exceedingly complicated. In most practical cases, however, the following expressions are essentially exact:

---

* It should be kept in mind that for the symmetric missile under consideration, the desired moment is an odd function of angle of attack. Since $\sigma > 0$, this poses no problem but for planar motion, note that terms like $M_1\alpha|\alpha|$ are implied.

$$\bar{M}_0 = \frac{M_0}{I} + \frac{P^2}{4}$$

$$\bar{M}_2 = \frac{M_2}{I} + \frac{P^2}{12}$$

$$\bar{M}_4 = \frac{M_4}{I} + \frac{17}{960} P^2$$

$$\bar{M}_{>4} = \frac{M_{>4}}{I} .$$

where

$$P = \frac{I_{\bar{x}}}{I} p .$$

By integrating (7.192) from σ_0 to σ_m, an expression for the frequency of oscillation can be obtained. Evaluating the resulting integral in closed form can be done only in special cases. However, an excellent approximation for the frequency can be obtained[7,8]:

$$\omega^2(t) = \frac{8 \sum_{n=0}^{\infty} \frac{\bar{M}_n}{n+2} \left[\frac{\sigma_m^{n+4} + \sigma_0^{n+4}}{2} - \left(\frac{\gamma_m^2 + \sigma_0^2}{2} \right)^{(n+4)/2} \right]}{(\sigma_m^2 - \sigma_0^2)^2} . \tag{7.193}$$

This equation is least accurate for the case of planar motion. It becomes increasingly more accurate as more and more circular motions are considered, and is exact in the limit of circular motion.

Because the equation is least accurate for planar motion, it is interesting to compare it in this limit with exact results and also with approximate results obtained by the Kryloff-Bogoliuboff technique[7,20]. For planar motion ($\sigma_0 = 0$, $p = 0$), (7.193) assumes the form

$$\omega^2(t) = \frac{4}{I} \sum_{n=0}^{\infty} \frac{M_n}{n+2} \left[1 - (\tfrac{1}{2})^{(n+2)/2} \right] \alpha_m^n . \tag{7.194}$$

The first comparison will be for the one-term moment of arbitrary power in angle of attack considered in Section 7.6.4.3 (i.e., $M = -M_n \alpha^{n+1}$). This comparison is shown in Figure 7.24. It is seen that the approximation given by (7.194) is superior to the Kryloff-Bogoliuboff approximation for all values of n greater than 2. It also agrees well with the exact results.

The other planar-motion comparison that will be shown is for a linear-cubic-quintic restoring moment:

$$M = -M_0 \alpha - M_2 \alpha^3 - M_4 \alpha^5 .$$

Exact results for this case are presented in Reference 7.21. For brevity, only the particular moment having stabilizing linear and quintic terms and a destabilizing cubic term will be considered. The comparisons are shown in the carpet plots (Fig. 7.25), where the dashes represent the exact solution and the solid lines a given approximation. Both approximations are fairly good, but results from (7.194) are clearly superior. Since (7.193) is least accurate for planar motion, it is apparently a very accurate representation.

7.6.4.6 Application to Free-Flight Data

Equation (7.193) shows the influence of maximum and minimum amplitudes, spinning rate, and an arbitrary set of restoring moment coefficients on the frequency of the motion. Before applying this equation to free-flight data, it is again convenient to transform from time to distance, which essentially removes velocity from the problem. If (7.193) is divided by V^2 and the terms of the series are written out explicitly, with only the dominant spin term retained, we obtain

$$\omega^2(x) = \frac{P^2(x)}{4} + \frac{1}{IV^2} \left\{ M_0 + \frac{8}{3} M_1 \left[\frac{\frac{\sigma_m^5 + \sigma_0^5}{2} - \left(\frac{\sigma_m^2 + \sigma_0^2}{2} \right)^{5/2}}{(\sigma_m^2 - \sigma_0^2)^2} \right] + \frac{3}{4} M_2 (\sigma_m^2 + \sigma_0^2) + \dots \right\} .$$

Recall that each of the unknown M_n's contains V^2 (for example, $M_0 = -C_{m\alpha} \rho V^2 A l / 2$), so M_n / V^2 is independent of velocity. If we now define

$$\hat{M}_n = \frac{-M_n}{\rho V^2 A l / 2} .$$

the $\hat{M}_n$'s are coefficients in a power series in C_m,

$$C_m = \sum_n \hat{M}_n \sigma^{n+1} ,$$

and are assumed to be constants. Then the above equation becomes

$$\omega^2(x) = \frac{P^2(x)}{4} - \frac{\rho A l}{2I}\left\{\hat{M}_0 + \frac{8}{3}\hat{M}_1\left[\frac{\frac{\sigma_\mathbf{m}^5 + \sigma_0^5}{2} - \left(\frac{\sigma_\mathbf{m}^2 + \sigma_0^2}{2}\right)^{5/2}}{(\sigma_\mathbf{m}^2 - \sigma_0^2)^2}\right] + \right.$$

$$+ \frac{3}{4}\hat{M}_2(\sigma_\mathbf{m}^2 + \sigma_0^2) + \frac{8}{5}\hat{M}_3\left[\frac{\frac{\sigma_\mathbf{m}^7 + \sigma_0^7}{2} - \left(\frac{\sigma_\mathbf{m}^2 + \sigma_0^2}{2}\right)^{7/2}}{(\sigma_\mathbf{m}^2 - \sigma_0^2)^2}\right] +$$

$$+ \frac{1}{12}\hat{M}_4(7\sigma_\mathbf{m}^4 + 10\sigma_\mathbf{m}^2\sigma_0^2 + 7\sigma_0^4) + \frac{8}{7}\hat{M}_5\left[\frac{\frac{\sigma_\mathbf{m}^9 + \sigma_0^9}{2} - \left(\frac{\sigma_\mathbf{m}^2 + \sigma_0^2}{2}\right)^{9/2}}{(\sigma_\mathbf{m}^2 - \sigma_0^2)^2}\right] +$$

$$\left. + \frac{5}{32}\hat{M}_6(3\sigma_\mathbf{m}^6 + 5\sigma_\mathbf{m}^4\sigma_0^2 + 5\sigma_\mathbf{m}^2\sigma_3^4 + 3\sigma_0^6) + \ldots\right\}. \tag{7.195}$$

From a set of flights made at about the same test conditions, assume that a converged solution for each has been obtained with the tricyclic method of analysis. Then values of all the parameters except $\hat{M}_n$ are known for each flight for use in (7.195). A decision as to the number of terms to be retained is made, and then the $\hat{M}_n$ can be calculated from the set of m simultaneous equations (one for each test flight or portion thereof) by the method of least squares, provided $m >$ number of unknowns. Note that $\omega^2(x) - [P^2(x)/4]$ is essentially equal to the product $\omega_1\omega_2$ given by the tricyclic analysis.

Although damping has been assumed negligible in deriving (7.195), the procedure still gives good results when damping is present if values of $\sigma_\mathbf{m}$ and σ_0 are determined as follows:

$$\sigma_\mathbf{m}^2 = \frac{1}{2}[\sigma_\mathbf{m}^2 \text{ (first peak)} + \sigma_\mathbf{m}^2 \text{ (last peak)}]$$

$$\sigma_0^2 = \frac{1}{2}[\sigma_0^2 \text{ (first minimum)} + \sigma_0^2 \text{ (last minimum)}] .$$

The question of which and how many terms to retain in (7.195) would seem to be critical. The possibilities are essentially unlimited, and there is no systematic way to make a choice a priori. Fortunately, however, a number of different assumed forms for the moment, when fit to the experimental data, turn out to yield nearly identical $C_\mathbf{m}(\alpha)$ curves. Hence, there is no unique representation for the moment that gives the "best fit" to the data but a number of choices which will give equally good fits.

This is illustrated by the following set of results, based on the experimental data of Reference 7.18. The data showed large nonlinearities, and it was decided that a four-term series representation of the moment was needed. The linear coefficient $\hat{M}_0$ was known from other sources and was not allowed to vary. All possible four-term moments, each containing $\hat{M}_0$, and three members of the set $(\hat{M}_1, \hat{M}_2, \hat{M}_3, \hat{M}_4, \hat{M}_5, \hat{M}_6)$ were fit to the experimental data using (7.195) and the method of least squares. The results are summarized as follows:

Powers of resultant angle of attack in assumed moment	Sum of the squares of the residuals
1-2-3-4	3.5×10^{-7}
1-2-3-5	4.9
1-2-3-6	6.6
1-2-3-7	8.5
1-2-4-5	6.6
1-2-4-6	8.4
1-2-4-7	10.4
1-2-5-6	10.2
1-2-5-7	11.6
1-2-6-7	12.4
1-3-4-5	2.4*
1-3-4-6	2.0*
1-3-4-7	1.9*
1-3-5-6	1.8*
1-3-5-7	2.0*
1-3-6-7	3.2
1-4-5-6	8.4
1-4-5-7	11.3
1-4-6-7	17.3
1-5-6-7	32.0×10^{-7}

Some of the moment represertations have much larger error sums than others, and can be rejected as inferior. However, among several of the better fits, there is little to choose. Figure 7.26 shows the envelope from the five moments that gave the smallest sum of the squares of the residuals, marked in the above table with stars. The moment curves are close enough together, out to $\sigma \cong 36^0$, that no real choice between them need be made.

7.6.5 Effect of Nonlinear Static Moment on Deduced Damping

The study of nonlinearities in aerodynamic moments has been extended in Reference 7.22 to allow nonlinearities to exist in both the static moment and the damping moment, and nonlinear damping moments will be treated in the next section. The study revealed that a nonlinear *static* moment could lead to apparent nonlinearities (and large errors) in the deduced damping even when the actual damping was in fact linear. This effect will now be discussed.

For this purpose, it is assumed that the motion is planar and that there is no swerve in the trajectory. The equation of motion considered, with distance as the independent variable, is

$$\alpha'' + H_0 \alpha' + \sum_{n \geq 0} \frac{M_n}{IV^2} \alpha^{n+1} = 0 . \tag{7.196}$$

Note again that since M_n contains V^2, M_n/V^2 is independent of velocity. The constant H_0 $(H_0 = - (\rho A/2m)\xi)$ is a measure of the damping and we desire to determine its value. First, we consider the (idealized) case where we have exact values of the angle of attack α_m at every peak. If the static moment were linear, these peak angles would fall on the exponential envelope $e^{-(H_0/2)x}$ and the logarithmic decrement would be constant with the value

$$\log_e \left| \frac{(\alpha_m)_k}{(\alpha_m)_{k+1}} \right| = \frac{\pi}{2} \frac{H_0}{\omega} , \tag{7.197}$$

where the subscript k denotes the peak number and ω is the frequency of the motion defined by

$$\omega^2 = \frac{M_0}{IV^2} - \frac{H_0^2}{4} \approx \frac{M_0}{IV^2} .$$

The difficulty that arises is when the static moment is nonlinear, the logarithmic decrement is no longer a constant. However, it is useful to analyze the data as though it were constant and an effective linear damping H_{0_e} is defined by the expression

$$\log_e \left| \frac{(\alpha_m)_k}{(\alpha_m)_{k+1}} \right| = \frac{\pi}{2} \frac{H_{0_e}}{\omega_1} , \tag{7.198}$$

where ω_1 is now a function of α_m, M_n, and H_0. An approximate relationship between the apparent damping and the actual damping, which is in excellent agreement with numerical integrations, is derived in Reference 7.22, for arbitrary nonlinearities in both the static and damping moment and is expressed as the ratio of two power series. The complete expression will be given later, but the expression for a linear plus cubic static moment (and constant damping) is as follows[*]:

$$\frac{H_{0_e}}{H_0} = \frac{m_0 + (5/8)m_2}{m_0 + (15/16)m_2} . \tag{7.199}$$

Here m_0 is +1 if the linear static term is stabilizing and −1 if it is destabilizing. Note that the definition of m_2 is now modified slightly, becoming

$$m_2 = \frac{M_2 \alpha_a^2}{M_0} ,$$

where α_a represents an "average" value of the maximum angle of attack; i.e., $\alpha_a^2 = \frac{1}{2}[(\alpha_m)_k^2 + (\alpha_m)_{k+1}^2]$. The physical import of (7.199) is shown in Figures 7.27-7.29, which give the variation of H_{0_e}/H_0 with m_2. The solid lines represent the case we are considering (exact knowledge of successive peak angles) and it is seen that a significant effect on the deduced damping is introduced by the nonlinear static moment. For the stable-stable case (Fig.7.27), the deduced damping is always less than the true damping and in the most extreme case (pure cubic moment), it is 2/3 of the true damping. For the stable-unstable case (Fig.7.28), the deduced damping is always greater than the true damping. The largest deviations of the deduced damping from true values occur with an unstable-stable static moment (Fig.7.29), for which the error is never *less* than 33 percent.

It is, of course, unrealistic to presume exact knowledge of successive peak angles of attack. In the real case, the damping would probably be obtained using the tricyclic solution developed earlier (Equation (7.154)) fitted to the discrete data points measured along the trajectory. Results obtained in this manner are indicated by the circular symbols in Figures 7.27-7.29. To obtain these results, a number of exact trajectories were generated for a variety of linear-cubic static moments and these "data" (50 points for each run) were analyzed by the tricyclic method. There is scatter in the results, which is expected when discrete data are being

---

[*] A similar approximate formula was derived in Reference 7.23 and can be written

$$\frac{H_{0_e}}{H_0} = \frac{m_0 + (3/4)m_2}{m_0 + (9/8)m_2} .$$

This proves to be less accurate than (7.199).

analyzed, but the results show consistent trends. For each of the three types of nonlinear moments, the discrepancy from the true damping coefficient is greater than for the "exact-data-at-every-peak" case. What is noted is that the percent error is just about double that of the first case considered. Again the worst case is that with an unstable-stable static moment. It appears that if a static moment of this type governs, the deduced damping will differ from the true damping by a factor greater than 3. This statement holds whether the motion is damped or undamped.

For the case where exact values of the angle of attack are known at successive peaks, the true damping can be derived by a procedure to be given in the following section. However, when discrete data are analyzed by linear methods, no precise method exists to correct the deduced damping. An approximate correction would be to double the error calculated by assuming the peaks known.

7.6.6 Nonlinear Damping Moment

7.6.6.1 Approximate Solution

Since the aerodynamic damping is one of the most difficult aerodynamic parameters to determine from ballistic-range tests, the definition of "second-order" effects produced by nonlinearities in the damping is even more difficult. An important reason for studying the subject has been developed by Tobak and Pearson[7.24], who indicate that static nonlinearity should be accompanied by nonlinear damping. There are, of course, ample practical reasons for defining nonlinear damping in cases where the sign of the damping coefficient changes, introducing limit cycles and other major effects on the motion. With the recent advances in shadowgraph optics (particularly Kerr-cell shutters, see Chapter 6) and more sophisticated methods of reading the pictures obtained, far better data are becoming available for analysis; this should lead to less scatter in the experimental results and allow some coefficients previously lost in the scatter to be determined.

We will briefly consider nonlinear damping coefficients, confining the discussion to planar motion and zero swerve. The differential equation considered is

$$\alpha'' + \left(\sum_{n \geq 0} H_n \alpha^n \right) \alpha' + \sum_{n \geq 0} \frac{M_n}{IV^2} \alpha^{n+1} = 0 \ . \tag{7.200}$$

The middle term represents the damping moment, the last term, the static restoring moment. Note again that $n = 2$ will be referred to as a cubic moment, etc. As discussed in the previous section, if the static moment is nonlinear, the logarithmic decrement (determined from successive peaks) is not constant. We will consider that we have exact data at every peak in the angle of attack, and that we will analyze the data as though the logarithmic decrement were constant, which again introduces the concept of an "effective linear damping" (H_{0_e}). An approximate expression relating the effective linear damping to the linear term in the actual damping has been derived in Reference 7.22 and is given as follows[*]:

$$\frac{H_{0_e}}{H_0} = \sum_{k \geq 0} \frac{\sum\limits_{n \geq 0} a_{kn} m_n}{\sum\limits_{n \geq 0} b_{kn} m_n} h_k \ , \tag{7.201}$$

where

$$h_k = \left(\frac{1}{2+k} \right) \frac{H_k}{H_0} \alpha_a^k$$

and

$$m_n = \frac{M_n \alpha_a^n}{M_0} \ .$$

The constants a_{kn} and b_{kn} are given in the following tables.

	Values of a_{kn}								
k n	0	1	2	3	4	5	6	7	8
0	2.0000	1.2732	1.0000	0.8488	0.7500	0.6791	0.6250	0.5821	0.5469
1	1.5349	1.0095	0.8065	0.6913	0.6143	0.5582	0.5147	0.4797	0.4510
2	1.2500	0.8398	0.6797	0.5875	0.5250	0.4788	0.4428	0.4136	0.3895
3	1.0568	0.7208	0.5894	0.5130	0.4608	0.4218	0.3912	0.3663	0.3453
4	0.9167	0.6323	0.5213	0.4565	0.4118	0.3784	0.3519	0.3301	0.3118
5	0.8102	0.5639	0.4679	0.4118	0.3731	0.3439	0.3206	0.3014	0.2851
6	0.7266	0.5092	0.4249	0.3756	0.3415	0.3156	0.2950	0.2779	0.2633
7	0.6589	0.4645	0.3894	0.3456	0.3152	0.2920	0.2735	0.2581	0.2450
8	0.6031	0.4272	0.3596	0.3202	0.2928	0.2720	0.2552	0.2413	0.2294
∞	0	0	0	0	0	0	0	0	0

[*] Note that (7.199) is a special case of this expression.

					Values of b_{kn}				
n \ k	0	1	2	3	4	5	6	7	8
0	1.0000	1.0000	1.0000	1.0000	1.0000	1.0000	1.0000	1.0000	1.0000
1	0.9593	0.9575	0.9542	0.9505	0.9468	0.9434	0.9399	0.9364	0.9337
2	0.9375	0.9346	0.9297	0.9243	0.9138	0.9135	0.9084	0.9038	0.8997
3	0.9247	0.9211	0.9155	0.9091	0.9027	0.8964	0.8905	0.8850	0.8797
4	0.9167	0.9127	0.9067	0.8998	0.8929	0.8861	0.8797	0.8735	0.8677
5	0.9115	0.9073	0.9011	0.8940	0.8868	0.8798	0.8729	0.8665	0.8603
6	0.9082	0.9039	0.8975	0.8904	0.8831	0.8758	0.8688	0.8621	0.8558
7	0.9060	0.9016	0.8953	0.8882	0.8808	0.8735	0.8664	0.8596	0.8530
8	0.9047	0.9003	0.8940	0.8868	0.8795	0.8722	0.8650	0.8582	0.8516
∞	1.0	1.0	1.0	1.0	1.0	1.0	1.0	1.0	1.0

An example of what this equation looks like in expanded form is given as follows, where all terms relating to a 1-3-5 static moment together with a 1-3-5 damping moment have been retained.

$$\frac{H_{0_e}}{H_0} = \frac{m_0 + 0.6250\,m_2 + 0.4583\,m_4}{m_0 + 0.9375\,m_2 + 0.9167\,m_4} + \frac{m_0 + 0.6797\,m_2 + 0.5213\,m_4}{m_0 + 0.9297\,m_2 + 0.9067\,m_4}\,h_2 +$$

$$+ \frac{0.7500\,m_0 + 0.5250\,m_2 + 0.4118\,m_4}{m_0 + 0.9188\,m_2 + 0.8929\,m_4}\,h_4 \; . \tag{7.202}$$

Equation (7.201) has been compared with the results from numerical integrations for many different nonlinearities in both the static and dynamic moments[7,22]. In all cases investigated, the approximate formula yielded results extremely close to the "exact" result. Of concern now is how the coefficients (M_n, H_n) in (7.200) can be extracted from experimental data.

7.6.6.2 Determination of Nonlinear Damping Parameters from Data

Equation (7.201) can be useful in determining the nonlinear damping parameters from a set of observed oscillations. Assume that a given oscillator is governed by (7.200). We wish to infer from observed oscillations the appropriate values of H_0, H_2, H_4, ... and M_0, M_2, M_4, ...

We assume that the frequency and maximum amplitudes for every half cycle of motion from each model flight can be accurately determined from the data. The effective linear damping for each half cycle is then computed by

$$H_{0_e} = \frac{2\omega}{\pi}\log_e\left|\frac{(\alpha_m)_k}{(\alpha_m)_{k+1}}\right| . \tag{7.203}$$

In addition, we assume that the damping is small so that $H_0/\omega \ll 1$. This assumption is normally satisfied in ballistic-range testing, and allows the simplification that the damping can be neglected in determining the static-moment parameters M_n .

By use of the approximation for the frequency developed earlier (Equation (7.194) transformed to distance), we can write

$$\omega^2(x) = \frac{M_0}{IV^2} + \sum_{n>0} A_n \frac{M_n}{IV^2}\,\alpha_a^n , \tag{7.204}$$

where

$$A_n = \frac{4}{n+2}\left[1 - \left(\tfrac{1}{2}\right)^{(n+2)/2}\right]$$

and

$$\alpha_a = \sqrt{\left(\frac{(\alpha_m)_k^2 + (\alpha_m)_{k+1}^2}{2}\right)} .$$

This formula is a good approximation for large and small nonlinearities, except in the vicinity of the singular points of static instability. By fitting this equation to a set of frequency versus amplitude data, the appropriate values of M_n can be obtained.

A similar but slightly more complicated situation exists for determining the damping parameters H_n . In this case, the static parameters play an important role, whereas in the determination of the static-moment parameters M_n , the effect of the damping parameters can be neglected. Rewriting (7.201) in a slightly different form, H_{0_e} is given by

$$H_{0_e} = B_0 H_0 + \sum_{k>0} B_k H_k \alpha_a^k , \qquad (7.205)$$

where B_k $(k \geqslant 0)$ is

$$B_k = \frac{1}{2+k} \frac{\sum\limits_{n \geqslant 0} a_{kn} M_n \alpha_a^n}{\sum\limits_{n \geqslant 0} b_{kn} M_n \alpha_a^n} .$$

Equation (7.205) is analogous in form to (7.204). In this case, however, the coefficients B_k are functions of $M_0, M_1, M_2, \ldots \ldots$ and α_a, whereas the coefficients A_n were constants. In the determination of the damping, however, the static parameters can be regarded as already determined by the use of (7.204). Hence, the coefficients B_n are functions of only α_a insofar as determination of the damping is concerned.

It is now useful to divide both sides of (7.205) by B_0, obtaining

$$\frac{H_{0_e}}{B_0} = H_0 + \sum \frac{B_k}{B_0} H_k \alpha_a^k . \qquad (7.206)$$

Because $B_0, B_1, B_2, \ldots$ all vary with α_a in a similar manner, the ratios B_k/B_0 vary slowly with α_a. Equation (7.206) can now be used to study a set of damping data in a manner analogous to studying frequency data with (7.204).

As a simple example, consider that a set of data for a given oscillator has been obtained and that the static moment, completely arbitrary, has been determined with the use of (7.204). Assume that the damping moment can be described by a linear term and a single arbitrary nonlinear term so that (7.206) appears as

$$\frac{H_{0_e}}{B_0} = H_0 + \frac{B_n}{B_0} H_n \alpha_a^n . \qquad (7.207)$$

where n is not known. Choosing a particular value of n determines B_n/B_0. Then on a plot of H_{0_e}/B_0 versus $(B_n/B_0)\alpha_a^n$, when the right value of n is chosen, the data will fall on a straight line. The slope of the line yields H_n, and the intercept of the line with the H_{0_e}/B_0 axis yields H_0. This will be true without regard to the particular form of the static moment.

For an arbitrary damping moment described by a given set of data over an amplitude range, there may be many combinations of the parameters $H_0, H_1, H_2, \ldots$ that will fit the data. This situation also occurred in determining the static-moment parameters. One must often settle for a member of a class of moments that gives a good fit. Thus, a certain amount of experience is useful in analyzing the data. For a set of data including small angles of α_a as well as large, one should plot the damping data as H_{0_e}/B_0 versus $(B_2/B_0)\alpha_a^2$ (or as a first try against α_a^2 since B_2/B_0 varies slowly with α_a). If the data fall on a straight line, the damping moment is a cubic as described by (7.207) with $n = 2$. If the data deviate from a straight line, which might be expected to occur at larger values of α_a, one can estimate the magnitude and sign of the next higher order damping term needed to fit the data. In such a manner the appropriate form of damping polynomial tends to suggest itself.

7.7 LIFT ANALYSIS

A model in free-flight normally develops lift which causes the center of gravity to follow a trajectory that deviates from a straight line. For airplane-like configurations, this is often troublesome in that the lift can cause the model to quickly fly out of the field of view. Even for axisymmetric bodies the lift usually causes the model to depart from bore sight of the gun. This can be explained as follows. Consider the simplified form of (7.105)

$$z'' = -\frac{\rho A}{2m} C_{L_\alpha} \alpha , \qquad (7.208)$$

where C_{L_α} is the lift-curve slope. Now assume for simplicity that the model emerges from the gun at zero angle of attack but is given an angular rate during separation from the sabot. A simple form for the angle of attack that satisfies these conditions is

$$\alpha = \alpha_m \sin \omega x .$$

Substituting this expression into (7.208) and integrating twice yields

$$z = \frac{\rho A}{2m} C_{L_\alpha} \frac{\alpha_m}{\omega^2} \sin \omega x + C_1 x + C_2 . \qquad (7.209)$$

If we make the initial conditions $z = z' = 0$ at $x = 0$, then

$$z = \frac{\rho A}{2m} C_{L_\alpha} \frac{\alpha_m}{\omega^2} \sin \omega x - \frac{\rho A}{2m} C_{L_\alpha} \frac{\alpha_m}{\omega} x . \qquad (7.210)$$

This equation indicates that even with zero vertical velocity upon emerging from the gun, a vertical velocity is acquired due to the lift. For this simplified case, the center of gravity oscillates about a straight line in phase with the angle of attack as shown in Figure 7.30. The presence of aerodynamic damping, gravity, etc. would cause the swerve oscillation to take place about a curved line. What is important to note here is that the magnitude of the deviation from some mean line is a measure of the lift. We will now consider various methods for determining the lift coefficient.

7.7.1 Determination from Displacement Variation Near a Peak

The most basic method for determining the lift coefficient as a function of angle of attack is by analysis of the lateral displacement history of the model mass center (which is caused by the lift). The deduced lateral acceleration is related to the angle of attack history to define $C_L(\alpha)$. For motions involving a small roll rate, an approach similar to that used for determining the moment coefficient in Section 7.6.2 can be used. For a planar motion in the x-z plane (ignoring gravity), the differential equation of motion is

$$z'' = - Kl(C_L)_D - K(C_L)_S ,$$ (7.211)

where

$(C_L)_D$ = dynamic lift coefficient

$(C_L)_S$ = static lift coefficient

$K = \rho A/2m .$

As with the angle of attack data, a desirable segment of vertical displacement data is one which brackets a peak deviation, and which can be considered as two sets of data about this maximum or peak. (The swerving motion peaks at very nearly the same x position as the angular motion; they peak at exactly the same x if damping is zero.)

The development of the equations is exactly analogous to that for angles and we have, at any given α,

$$-(C_L)_S = \frac{z_1'' + z_2''}{2K} - \frac{l}{2} [(C_L)_{D_1} + (C_L)_{D_2}] .$$ (7.212)

If we assume that $(C_L)_D = (C_{L_q} + C_{L_{\dot\alpha}})\alpha'$ we have

$$-(C_L)_S = \frac{z_1'' + z_2''}{2K} - \frac{l}{2} (C_{L_q} + C_{L_{\dot\alpha}})(\alpha_1' + \alpha_2') .$$ (7.213)

Usually, the contribution of the dynamic term to the lift coefficient is very small. Therefore, when z_1'' and z_2'' are determined (for points of equal angle of attack on either side of the peak), $(C_L)_S$ is effectively determined. If damping in lift is truly negligible, the two values of z'' are nearly identical. The deduced instantaneous values of $(C_L)_S$ are plotted against the instantaneous corresponding angles of attack to generate a curve of $C_L(\alpha)$. An example showing results from this method is given in Section 7.9.2.

7.7.2 Normal Force from Stability Data on Models with Different Centers of Mass

The normal-force-curve slope, C_{N_α} $(C_{N_\alpha} \approx C_{L_\alpha} + C_D)$, and the center of pressure location, x_{cp}, are often found by testing models of fixed external shape but with two different (known) center of mass locations. The two bodies would have the same values of C_{N_α} and x_{cp}, but the moment-curve slope, C_{m_α}, would be different. Values of C_{m_α} can be obtained experimentally for each of the bodies by methods already described. Then using the relationship between C_m and C_N,

$$C_{m_\alpha} = C_{N_\alpha} \left(\frac{x_{cg} - x_{cp}}{l} \right) ,$$ (7.214)

where l is the reference length, we have a pair of simultaneous equations for the two unknowns, C_{N_α} and x_{cp}.

7.7.3 Tricyclic Method

When the angular motion is not planar and involves precession due to spin, the tricyclic method discussed in Section 7.6.3 can be used for the analysis of the swerve and the determination of lift coefficients. A trim lift force may be included in this analysis, defined as follows:

C_{y_0} lift coefficient in y direction for $\beta = 0$ at $x = 0$

C_{L_0} lift coefficient in z direction for $\alpha = 0$ at $x = 0$.

These are components of the C_{L_δ} term in (7.107). They rotate with the body at a rate, p , and their resultant represents the force at zero angle of attack due to small asymmetries in the model.

The equation for displacement acceleration is (see Equation (7.105))

$$y'' + iz'' = -K\{(C_{L_\alpha} + iC_{L_{\alpha p}} pl)(\beta + i\alpha) + l[(C_{L_q} + C_{L_{\dot\alpha}}) + i(C_{L_{\dot\alpha p}} - C_{L_{qp}})pl](\beta' + i\alpha') + (C_{y_0} + iC_{L_0})e^{ipx}\} +$$

$$+ ig/V^2 - 2\frac{\omega_E}{V}(\sin\theta_l + i\cos\theta_l \sin\theta_a) \quad . \quad (7.215)$$

Note that the lift coefficients due to Magnus effects $(C_{L_{\alpha p}}, C_{L_{\dot\alpha p}}, C_{L_{qp}})$ are retained in this equation, but are exceedingly difficult to obtain experimentally unless very high roll rates are experienced. If these coefficients can be obtained, moment coefficients due to Magnus effects can be found from the stability analysis.

If we now integrate the above equation twice with respect to x we obtain

$$y + iz = -K\left\{C_{L_\alpha}\int_0^x\int_0^x(\beta + i\alpha)\,dx\,dx + iplC_{L_{\alpha p}}\int_0^x\int_0^x(\beta + i\alpha)\,dx\,dx + \right.$$

$$+ l(C_{L_q} + C_{l_{\dot\alpha}})\int_0^x(\beta + i\alpha)\,dx - l(C_{L_q} + C_{L_{\dot\alpha}})(\beta_0 + i\alpha_0)\,x +$$

$$+ ipl^2(C_{L_{\dot\alpha p}} - C_{L_{qp}})\int_0^x(\beta + i\alpha)\,dx - ipl^2(C_{L_{\dot\alpha p}} - C_{L_{qp}})(\beta_0 + i\alpha_0)\,x +$$

$$+ (C_{y_0} + iC_{L_0})\left(\frac{1 + ipx - e^{ipx}}{p^2}\right)\biggr\} + (y_0' + iz_0')\,x +$$

$$+ (y_0 + iz_0) + \int_0^x\int_0^x i\,\frac{g}{V^2}\,dx\,dx -$$

$$- 2\frac{\omega_E}{V_0}(\sin\theta_l + i\cos\theta_l\sin\theta_a)\int_0^x\int_0^x\frac{V_0}{V}\,dx\,dx$$

which, after terms are rearranged, becomes

$$y + iz = -K\left\{(C_{L_\alpha} + iplC_{L_{\alpha p}})\int_0^x\int_0^x(\beta + i\alpha)\,dx\,dx + \right.$$

$$+ l\left[(C_{L_q} + C_{L_{\dot\alpha}}) + ipl(C_{L_{\dot\alpha p}} - C_{L_{qp}})\right]\left[\int_0^x(\beta + i\alpha)\,dx - (\beta_0 + i\alpha_0)\,x\right] +$$

$$+ (C_{y_0} + iC_{L_0})\left(\frac{1 + ipx - e^{ipx}}{p^2}\right)\biggr\} + (y_0' + iz_0')\,x +$$

$$+ (y_0 + iz_0) + ig\int_0^x\int_0^x\frac{1}{V^2}\,dx\,dx -$$

$$- 2\frac{\omega_E}{V_0}(\sin\theta_l + i\cos\theta_l\sin\theta_a)\int_0^x\int_0^x\frac{V_0}{V}\,dx\,dx \quad . \quad (7.216)$$

The term

$$ig\int_0^x\int_0^x\frac{1}{V^2}\,dx\,dx$$

is the displacement in the vertical plane due to gravity. It can be calculated separately and added to z algebraically. If the precise flight time is known for a specific x location, the displacement due to gravity is simply $z_g = \frac{1}{2}gt^2$. The Coriolis term can be integrated directly since $V_0/V = e^{KC_Dx}$ (Equation (7.109)). The result is

$$- 2\frac{\omega_e}{V_0}(\sin\theta_l + i\cos\theta_l\sin\theta_a)\left(\frac{e^{KC_Dx} - KC_Dx - 1}{(KC_D)^2}\right) \quad (7.217)$$

and for small KC_D

$$\frac{e^{KC_Dx} - KC_Dx - 1}{(KC_D)^2} \cong \frac{x^2}{2} \quad . \quad (7.218)$$

This contribution to y and z can also be calculated separately and added algebraically to the y and z data.

If the Magnus terms are ignored, there are eight unknown coefficients in (7.216): C_{L_α}, $(C_{L_q} + C_{L_{\dot\alpha}})$, C_{y_0}, C_{L_0}, y_0', y_0, z_0', and z_0. All of these coefficients appear in a linear fashion and if the integrals of $(\beta + i\alpha)$ can be calculated in closed form and p is known, then the coefficients can be solved for by a standard least squares technique. The expressions for $(\beta + i\alpha)$ can be obtained in closed form from fitting (7.154) to the angle data in obtaining the static and dynamic stability. The roll rate p is also known from the stability reduction.

Some of the Magnus coefficients can now be found by using the stability and lift analyses together, provided the data are accurate and well-defined. From (7.216), values for $C_{l_{\alpha p}}$ and $(C_{L_{\dot\alpha p}} - C_{L_{q p}})$ can be obtained from a least-squares fit since they occur linearly as do the other coefficients. Then from (7.158), given C_{L_α}, we can calculate $C_{m_{\alpha p}}$. With (7.157), given $C_{L_{\alpha p}}$, we can calculate a slightly modified value of C_{m_α}. With (7.156), given $C_{L_{\alpha p}}$, we can obtain $(C_{m_{\dot\alpha p}} - C_{m_{q p}})$. Therefore, from the combined stability and lift analyses, we can derive all of the following coefficients: ξ, C_{m_α}, C_{L_α}, $C_{m_q} + C_{m_{\dot\alpha}}$, $C_{L_q} + C_{L_{\dot\alpha}}$, $C_{m_{\alpha p}}$, $C_{L_{\alpha p}}$, $C_{m_{\dot\alpha p}} - C_{m_{q p}}$, $C_{L_{\dot\alpha p}} - C_{L_{q p}}$, C_{y_0}, and C_{L_0}. For most ballistic range tests, however, the models are fired from smooth-bore guns so that the roll rates are small and the Magnus terms are negligible.

It is also possible to deduce the center of pressure, x_{cp}, and normal-force-curve slope, C_{N_α}, from measurements of a single model flight which define the lift, drag, and static stability coefficients. For small angles

$$C_{N_\alpha} \approx C_{L_\alpha} + C_D$$

and, as noted earlier,

$$C_{m_\alpha} = C_{N_\alpha} \left(\frac{x_{cg} - x_{cp}}{l} \right),$$

so that

$$\frac{x_{cp}}{l} = \frac{x_{cg}}{l} - \frac{C_{m_\alpha}}{C_{L_\alpha} + C_D}.$$

7.7.4 Nonlinear Lift

Another method for obtaining the lift coefficient, which can handle a case involving nonlinear lift, proceeds as follows. The lift coefficient is expressed as a polynomial in resultant angle of attack, α_R, as

$$C_L = \sum_{i=1}^{n} C_{L_{\alpha_i}} \alpha_R^i. \tag{7.219}$$

For simplicity in demonstration, we will use the two-term series

$$C_L = C_{L_\alpha} \alpha_R + C_{L_{\alpha_3}} \alpha_R^3. \tag{7.220}$$

In the α-β plane, with the y and z coordinate axes also shown, we define an angle ϕ (see Figure 7.31) as the angle between the resultant angle of attack α_R and the β (or $-y$) axis. The lift in the z direction is

$$C_{L_z} = C_L \sin\phi = C_{L_\alpha} \alpha_R \sin\phi + C_{L_{\alpha_3}} \alpha_R^3 \sin\phi \tag{7.221}$$

and in the y direction

$$C_{L_y} = C_L \cos\phi = C_{L_\alpha} \alpha_R \cos\phi + C_{L_{\alpha_3}} \alpha_R^3 \cos\phi. \tag{7.222}$$

The differential equations of motion (with no damping) in the z and y directions are

$$z'' = -KC_{L_z} + \frac{g}{V^2} \tag{7.223}$$

$$y'' = -KC_{L_y}, \tag{7.224}$$

where $K = \rho A/2m$ and g is the acceleration due to gravity. Substituting (7.221) and (7.222) into these equations, we get

$$z'' = -K(C_{L_\alpha} \alpha_R \sin\phi + C_{L_{\alpha_3}} \alpha_R^3 \sin\phi) + g/V^2 \tag{7.225}$$

$$y'' = -K(C_{L_\alpha} \alpha_R \cos\phi + C_{L_{\alpha_3}} \alpha_R^3 \cos\phi). \tag{7.226}$$

Integrating twice with respect to x we obtain

$$z = z_0 + z_0'x - KC_{L_\alpha} \int_0^x \int_0^x \alpha_R \sin\phi \, dx \, dx - KC_{L_{\alpha_3}} \int_0^x \int_0^x \alpha_R^3 \sin\phi \, dx \, dx + \frac{gt^2}{2} \tag{7.227}$$

$$y = y_0 + y_0'x - KC_{L_\alpha} \int_0^x \int_0^x \alpha_R \cos\phi \, dx \, dx - KC_{L_{\alpha_3}} \int_0^x \int_0^x \alpha_R^3 \cos\phi \, dx \, dx. \tag{7.228}$$

At each data station there are measured values for α, β, y, z; α_R can be calculated from

$$\alpha_R \cong \sqrt{(\alpha^2 + \beta^2)}$$

and ϕ can be obtained from

$$\phi = \tan^{-1}(\alpha/\beta) .$$

Thus, $\alpha_R \sin\phi$, $\alpha_R \cos\phi$, $\alpha_R^2 \sin\phi$, and $\alpha_R^2 \cos\phi$ can be plotted as functions of x and integrated graphically. With the integrals determined, a least squares technique can be used to find best values for all of the unknowns in (7.227) and (7.228).

7.8 NUMERICAL INTEGRATION OF EQUATIONS OF MOTION

The tricyclic method described earlier has been the most widely used means for obtaining aerodynamic coefficients from free-flight tests. Within the realm where the assumptions made in the derivation of the tricyclic equations were satisfied, the method was convenient and gave good results. Even when the assumptions were not satisfied, this method was normally applied first, and then the results were modified by some of the methods that have been described.

It is easy to see how this strong dependence on the tricyclic equations came about. The problem was to deduce the aerodynamic characteristics governing a body from discrete observations of its position and attitude in space. The complete differential equations governing the motion were presumed known. Since errors were certain to exist in the position and attitude data, a "best fit" of some kind was called for, preferably an iteration scheme that would search for this fit. A least-squares fit was the natural choice, and with it a differential correction technique would have to be used. For this to work, however, partial derivatives of each dependent variable (e.g. $\alpha, \beta, y, z, \ldots$) with respect to each unknown coefficient in the differential equations of motion had to be known at every data station.

At that period in time, electronic computers were too slow to consider numerical determination of these partial derivatives. The remaining choice was to get a closed-form solution (e.g. $\alpha = f(x)$) so that the various partial derivatives would also have closed-form expressions. A least-squares fit is then straightforward, although convergence of the iteration procedure cannot be guaranteed. The tricyclic equations are the implementation of this approach. Enough approximations and assumptions are introduced into the differential equations of motion so that a closed-form solution can be obtained.

It would be beneficial if the need for having a closed-form solution could be by-passed, and the data fit instead by *numerical* solutions to the differential equations. This would allow far more generality in the problem of obtaining the aerodynamic coefficients because, at least theoretically, the exact differential equations of motion could be used. Two such methods will be described. The first (Section 7.8.1) is an approximate method which has been successfully applied in the past to small-amplitude motions of airplane-type configurations[7.25]. It does not require a very sophisticated computer, but does have the drawback that it yields results which cannot be improved except by trial and error. The second method described (Section 7.8.2) eliminates this drawback by providing an iterative scheme for seeking the "best fit" to experimental data[7.26]. In this case a high-speed digital computer is essential. In practice, the first method can be used to obtain a starting solution for the more powerful second approach.

7.8.1 Approximate Method

In Section 7.4.3.1 we obtained a set of differential equations to describe the motion of airplane-type configurations (Equations (7.95)-(7.98)). Simplifying the nomenclature, these equations appear essentially as follows:

$$y'' = B_1 y' + B_2 \bar{\alpha} \sin\phi + B_3 \bar{\beta} \cos\phi \tag{7.229}$$

$$z'' = B_1 z' - B_2 \bar{\alpha} \cos\phi + B_3 \bar{\beta} \sin\phi \tag{7.230}$$

$$\bar{\alpha}'' = B_4 \bar{\alpha}' + B_5 \bar{\alpha} + B_6 \bar{\beta}' + B_7 \bar{\beta} + B_8 \tag{7.231}$$

$$\bar{\beta}'' = B_9 \bar{\beta}' + B_{10} \bar{\beta} + B_{11} \bar{\alpha}' + B_{12} \bar{\alpha} + B_{13} . \tag{7.232}$$

Here ϕ is the angle of roll about the model's $\bar{x}$ axis measured from the pitch plane (see Figure 7.2b). Presumably it is a known function of distance. These four equations form the basis for determining the aerodynamic coefficients from the flight records. The following results are obtained after integrating twice with respect to distance (ζ and η are dummy variables):

$$y(x) = y_0 + (y_0' + B_1 y_0)x + B_1 \int_0^x y \, d\eta + B_2 \int_0^x d\eta \int_0^\eta \bar{\alpha} \sin\phi \, d\zeta + B_3 \int_0^x d\eta \int_0^\eta \bar{\beta} \cos\phi \, d\zeta \tag{7.233}$$

$$z(x) = z_0 + (z_0' + B_1 z_0)x + B_1 \int_0^x z \, d\eta - B_2 \int_0^x d\eta \int_0^\eta \bar{\alpha} \cos\phi \, d\zeta + B_3 \int_0^x d\eta \int_0^\eta \bar{\beta} \sin\phi \, d\zeta \tag{7.234}$$

$$\bar{\alpha}(x) = \bar{\alpha}_0 + (\bar{\alpha}_0' + B_4\bar{\alpha}_0 + 3_6\bar{\beta}_0)x + B_4 \int_0^x \bar{\alpha}\,d\eta + B_5 \int_0^x d\eta \int_0^\eta \bar{\alpha}\,d\zeta + B_6 \int_0^x \bar{\beta}\,d\eta + B_7 \int_0^x d\eta \int_0^\eta \bar{\beta}\,d\zeta + B_e\frac{x^2}{2} \quad (7.235)$$

$$\bar{\beta}(x) = \bar{\beta}_0 + (\bar{\beta}_0' + B_9\bar{\beta}_0 + B_{11}\bar{\alpha}_0)x + B_9 \int_0^x \bar{\beta}\,d\eta + B_{10} \int_0^x d\eta \int_0^\eta \bar{\beta}\,d\zeta + B_{11} \int_0^x \bar{\alpha}\,d\eta + B_{12} \int_0^x d\eta\int_0^\eta \bar{\alpha}\,d\zeta + B_{13}\frac{x^2}{2} \quad (7.236)$$

To accurately evaluate the integrands in the above equations, a continuous history of $\bar{\alpha}$ and $\bar{\beta}$ must be obtained. Since the basic data $\psi_{ME}, \theta_{ME}, \phi, y, z$ are obtained only at discrete points along the trajectory, it must be assumed that a faired curve drawn through these observed points represents the true continuous trajectory of the model. For any x position, the angle of attack, $\bar{\alpha}$, and the angle of sideslip, $\bar{\beta}$, can then be determined from the observed parameters by use of the relationships defined in Figure 7.4.

$$\bar{\alpha} = (\theta_{ME} + z')\cos\phi + (\psi_{ME} - y')\sin\phi \quad (7.237)$$

$$\bar{\beta} = -(\psi_{ME} - y')\cos\phi + (\theta_{ME} + z')\sin\phi . \quad (7.238)$$

This method of obtaining a continuous record of $\bar{\alpha}$ and $\bar{\beta}$ is considered to be more accurate than to transform the measured points into $\bar{\alpha}$ and $\bar{\beta}$ and then fair the points.

Sets of redundant simultaneous equations are obtained by evaluating each of the equations (7.233) thru (7.236) at a number of x locations; since the required coefficients appear in a linear fashion, a straightforward application of a least-squares technique can be used to solve for them.

7.8.2 Iterative Approach[7.26]

As mentioned earlier, for a least-squares fit employing differential corrections to succeed, partial derivatives of each dependent variable with respect to every unknown coefficient must be known accurately at every data station. The problem of obtaining these partial derivatives can be successfully handled by the method of parametric differentiation. To illustrate the procedure, assume that the equations of motion governing a particular configuration are the two coupled nonlinear differential equations

$$\left.\begin{array}{l} \alpha'' + C_1\alpha' + C_2\alpha + C_3\alpha^3 + C_4\beta' = 0 \\[2mm] \beta'' + C_1\beta' + C_2\beta + C_3\beta^3 - C_4\alpha' = 0 . \end{array}\right\} \quad (7.239)$$

Note that C_1 is related to the damping moment, C_2 and C_3 define a linear-cubic static moment, and C_4 is related to the roll rate.

The initial conditions at $x = 0$ are

$$\alpha(0) = C_5$$
$$\alpha'(0) = C_6$$
$$\beta(0) = C_7$$
$$\beta'(0) = C_8 .$$

We want to determine the four aerodynamic parameters (C_1 to C_4) and the four initial conditions such that we obtain a least-squares fit to experimental $\alpha(x)$ and $\beta(x)$ data. The method of differential corrections will be used to do this (described in the Appendix). Assume that initial values of the unknowns, required to start the differential correction procedure, are available (previous section). Next we need the partial derivatives of both α and β with respect to the eight unknowns. No closed-form solution exists for these derivatives, but they can be obtained numerically by the method of parametric differentiation. First define the following notation:

$$P_i = \frac{\partial\alpha}{\partial c_i}, \qquad P_i' = \frac{\partial P_i}{\partial x} = \frac{\partial\alpha'}{\partial c_i}, \qquad P_i'' = \frac{\partial^2 P_i}{\partial x^2} = \frac{\partial\alpha''}{\partial c_i}$$

$$Q_i = \frac{\partial\beta}{\partial c_i}, \qquad Q_i' = \frac{\partial Q_i}{\partial x} = \frac{\partial\beta'}{\partial c_i}, \qquad Q_i'' = \frac{\partial^2 Q_i}{\partial x^2} = \frac{\partial\beta''}{\partial c_i} .$$

Note that it is explicitly assumed here that the order of differentiation can be reversed and that

$$\frac{\partial}{\partial c_j}\left(\frac{\partial\alpha}{\partial x}\right) = \frac{\partial}{\partial x}\left(\frac{\partial\alpha}{\partial c_j}\right), \quad \text{etc} .$$

For well-behaved functions, this is normally true. Now differentiate (7.239) with respect to C_i, to obtain the following 16 differential equations.

$$P_1'' + C_1 P_1' + (C_2 + 3C_3\alpha^2)P_1 + C_4 Q_1' = -\alpha'$$

$$P_2'' + C_1 P_2' + (C_2 + 3C_3\alpha^2)P_2 + C_4 Q_2' = -\alpha$$

$$P_3'' + C_1 P_3' + (C_2 + 3C_3\alpha^2)P_3 + C_4 Q_3' = -\alpha^3$$

$$P_4'' + C_1 P_4' + (C_2 + 3C_3\alpha^2)P_4 + C_4 Q_4' = -\beta'$$

$$P_5'' + C_1 P_5' + (C_2 + 3C_3\alpha^2)P_5 + C_4 Q_5' = 0$$

$$P_6'' + C_1 P_6' + (C_2 + 3C_3\alpha^2)P_6 + C_4 Q_6' = 0$$

$$P_7'' + C_1 P_7' + (C_2 + 3C_3\alpha^2)P_7 + C_4 Q_7' = 0$$

$$P_8'' + C_1 P_8' + (C_2 + 3C_3\alpha^2)P_8 + C_4 Q_8' = 0$$

$$Q_1'' + C_1 Q_1' + (C_2 + 3C_3\beta^2)Q_1 - C_4 P_1' = -\beta'$$

$$Q_2'' + C_1 Q_2' + (C_2 + 3C_3\beta^2)Q_2 - C_4 P_2' = -\beta$$

$$Q_3'' + C_1 Q_3' + (C_2 + 3C_3\beta^2)Q_3 - C_4 P_3' = -\beta^3$$

$$Q_4'' + C_1 Q_4' + (C_2 + 3C_3\beta^2)Q_4 - C_4 P_4' = +\alpha'$$

$$Q_5'' + C_1 Q_5' + (C_2 + 3C_3\beta^2)Q_5 - C_4 P_5' = 0$$

$$Q_6'' + C_1 Q_6' + (C_2 + 3C_3\beta^2)Q_6 - C_4 P_6' = 0$$

$$Q_7'' + C_1 Q_7' + (C_2 + 3C_3\beta^2)Q_7 - C_4 P_7' = 0$$

$$Q_8'' + C_1 Q_8' + (C_2 + 3C_3\beta^2)Q_8 - C_4 P_8' = 0 .$$

$$(7.240)$$

The initial conditions are

$$P_5 = Q_7 = 1$$
$$P_6' = Q_8' = 1 \qquad \text{at} \quad x = 0$$

all other

$$P_i = P_i' = Q_i = Q_i' = 0 .$$

Note that these are all linear differential equations with variable coefficients. However, both the variable coefficients and the right-hand sides are known from the numerical solution to (7.239). Hence numerical integration of (7.239) and (7.240) can yield values of α, β, and all partial derivatives. It is necessary to interpolate during the integration to obtain the values at the particular "x" locations where data exist. Corrections (ΔC_i) to the starting values of the eight unknown coefficients can then be obtained by solving the matrix equation

$$[A] \; [\Delta C] = [B] .$$
$$8 \times 8 \; 8 \times 1 \qquad 8 \times 1$$

where general elements of the A and B matrices are

$$A_{ij} = \sum_{\substack{\text{all data} \\ \text{stations}}} \left(\frac{\partial\alpha}{\partial c_i}\right)\left(\frac{\partial\alpha}{\partial c_j}\right) + \left(\frac{\partial\beta}{\partial c_i}\right)\left(\frac{\partial\beta}{\partial c_j}\right)$$

$$B_i = \sum_{\substack{\text{all data} \\ \text{stations}}} (\alpha_{exp} - \alpha_{calc})\frac{\partial\alpha}{\partial c_i} + (\beta_{exp} - \beta_{calc})\frac{\partial\beta}{\partial c_i} .$$

$$(7.241)$$

The subscript "exp" denotes experimental values, while "calc" denotes calculated values obtained from the numerical integration. New values of the coefficients are obtained by adding ΔC_i to the present values, and the iteration process is continued until any prescribed degree of convergence is reached.

Some miscellaneous notes relating to this technique should be listed.

(i) As a starting solution, an approach as outlined in the previous section is best. In many cases, however, results from the tricyclic method or even educated guesses from a hand-fairing of the data can be used.

(ii) Although a large number of differential equations can become involved, the time to analyze a given flight is not prohibitive. With the foregoing example, the time to get a converged solution (five iterations) for a 200 ft flight is about 90 seconds on an IBM 7090.

(iii) Any known functions of distance (such as variable density) can easily be incorporated. For example, in (7.239) if C_1 is replaced by $D_1 f_1(x)$, C_2 by $D_2 f_2(x)$, etc., it is possible to solve for D_i exactly as C_1 was solved for. The functions of distance may be either expressions or tabulations.

(iv) A number of different flights of a given configuration can be analyzed simultaneously to obtain the aerodynamic coefficients that best represent all flights. This would often be necessary to find terms that are nonlinear in angle of attack.

(v) Alternate approaches for numerically fitting differential equations to experimental data are discussed in References 7.27 and 7.28.

7.9 EXAMPLE CASES

7.9.1 Introduction

Examples showing application of some of the data reduction procedures that have been described will be given next. First the determination of aerodynamic coefficients from analysis of data points in the vicinity of a peak amplitude will be illustrated. This will be followed by examples illustrating the tricyclic analysis, and finally by an example applying the method of numerical integration of the equations of motion.

7.9 Analysis Using Angles and Displacements Near a Peak

An example application of the procedure described in Section 7.6.2 will now be given. A planar motion was generated numerically using nonlinear aerodynamic coefficients. A half cycle of motion bracketing a peak was then analyzed by the most complete version of the method in Section 7.6.2 (including damping) to see if the α versus x variation could be reduced to obtain the aerodynamic coefficients used to generate the motion. The α versus x segment analyzed is plotted in Figure 7.32. The center is found to be at $x = 18.4$ m where $\alpha = 24.89^\circ$. When both halves are plotted with the center as origin, the difference in the two curves can easily be seen as shown in Figure 7.33. Each curve is fitted with a polynomial of the form

$$\alpha - \alpha_m = A_1 x^2 + A_2 x^3 + A_3 x^4 + A_4 x^5 ,$$

where $\alpha_m = 24.89^\circ$. The C_m and ξ curves deduced are shown in Figures 7.34 and 7.35. With no random errors introduced into the α data, both results are very precise except at $\alpha < 10^\circ$, where the curvature in the angle data tends to vanish. With various degrees of random error (uniform error distribution), the deduced C_m curves remain fairly accurate but the ξ curves become poor rapidly as the maximum error is increased.

This example has also been used to illustrate the method for obtaining the lift coefficient as described in Section 7.7.1. The deduced C_L versus α curves are shown in Figure 7.36. Included are results for exact data (no random errors) and a case with random errors in both α and z. Above 10° both curves are very close to the exact curve.

7.9.3 Analysis Using Tricyclic Method

7.9.3.1 Data Reduction Procedure[7.29]

We will now discuss the overall procedure one might use for reducing data from a free-flight test utilizing the tricyclic analyses for stability and lift coefficients (Sections 7.6.3 and 7.7.3) and the direct t versus x analysis for drag coefficient (Section 7.5.1, Method 5). The emphasis here is on the interaction between the various reduction procedures which have previously been described.

A representative flow diagram for the order of the calculations in reducing ballistic range data is shown in Figure 7.37. The steps can be summarized as follows:

(i) Determination of drag coefficient by fitting x-t data with (7.110); correction of z and θ data for gravity effects.

(ii) Smoothing of experimental data. This smoothing procedure has not been discussed previously, but basically seeks to eliminate data points which lie well outside the standard deviation of the fit obtained. No exact criterion for rejection can be given but experience has shown that it is usually helpful to eliminate data points having residuals greater than about 2.25 standard deviations and replace them with the calculated values.

(iii) Determination of static and dynamic stability coefficients from angle data using tricyclic analysis (Equation (7.154)).

(iv) Rotation of orthogonal coordinate system to reduce inherent error in tricyclic analysis due to large angles.

(v) Determination of lift parameters from displacement data (Equation (7.216)) in conjunction with tricyclic analysis of angles.

(vi) Calculation of corrections to measured angles due to curvature (swerving) of the flight path.

(vii) Repeat stability analysis and continue with iterative scheme between stability and lift until angle corrections from swerve remain constant.

(viii) Smooth angle and displacement data and repeat any steps that are necessary.

7.9.3.2 Example, and Comparison of Free-Flight and Wind-Tunnel Results

An example of the application of the above procedures, and a comparison of results from free-flight and conventional wind tunnel tests of the same body shape at identical test conditions, is now made to illustrate the generally good agreement and to point up a common discrepancy in drag results[7.29]. The shape selected is the AGARD standard hypersonic ballistic correlation model HB-2. Free-flight data obtained in the Pressurized Ballistic Range at Ames Research Center[7.29] are compared to wind-tunnel data from Arnold Engineering Development Center (AEDC)[7.30,7.31] and some free-flight results from the Canadian Research and Development Establishment (CARDE)[7.32]. The model used in the Ames' tests (Fig.7.38) was ballasted at the nose to make it aerodynamically stable. The two pins on the base were used to measure the roll orientation and the small frustum on the base was gripped by the sabot during launch. The tests were conducted at a Mach number of 2.0 and a Reynolds number based on cylinder diameter of 1.7 million. A shadowgraph of this model in flight is shown in Figure 8.17.

Figure 7.39 shows a typical set of position, time, and angle data for the free-flight tests. Figure 7.39(a) shows the flight time as a function of distance and the resulting velocity decrease over the length of the range. Figures 7.39(b), and (c) show the displacement and angular measurements.

The total drag coefficient* as a function of angle of attack is shown in Figure 7.40. The Ames data are indicated by the circular symbols, through which a least-squares curve has been drawn, and the AEDC data are indicated by the dashed line. There is a significant difference in the level of C_D between the ballistic-range and wind-tunnel results although it is noted that the curves are roughly parallel. The wind tunnel total drag was obtained by combining the contributions of forebody and base drag measurements given in Reference 7.30. Sting effects on the base pressure were suspected to be the cause of the discrepancy (see, e.g., Reference 7.33). Therefore, the base drag coefficient was calculated from the flow-field configuration shown in shadowgraph pictures of the free flight models. More detail on base pressure estimation is given in Chapter 8, Section 8.5.4. This base drag coefficient, when added to the AEDC forebody drag, gave the shaded region in Figure 7.40 (the region brackets the results from four different flights analyzed in this manner). The agreement with the free-flight measurements of total drag is now excellent.

The lift-curve slope, c_3 deduced from the swerving motion of each model, is shown in Figure 7.41 plotted against pitching amplitude. These data indicate that the lift coefficient is linear with angle of attack at least to 7 degrees. The wind-tunnel result for lift-curve slope (deduced from normal and axial force measurements) is shown, together with a value obtained using the Ames-deduced base pressure in the axial force contribution. The agreement between free-flight and wind-tunnel results is very good.

A curve of normal force versus angle of attack was calculated from the measured lift and drag data where $C_L = 3.40\alpha$ and $C_D = 1.239 + 0.00249\alpha^2$ and $C_N = C_L\cos\alpha + C_D\sin\alpha$. The results are plotted in Figure 7.42 and are compared to AEDC wind-tunnel data and to ballistic-range data obtained at CARDE[7.32]. The CARDE results fall slightly lower throughout the angle of attack range.

The nonlinear pitching-moment coefficient was calculated by the method described in Section 7.6.4.6 with linear and cubic terms in resultant angle of attack chosen as most representative of the data. (Higher order polynomials were examined but gave nearly identical results.) One flight at low amplitude ($\sigma_m = 1.8°$) revealed a significant decrease in static stability, which is reflected in the lower initial slope of the Ames pitching-moment curve in Figure 7.43. The curves determined at AEDC and CARDE indicate slightly higher values for the pitching moment. Small differences in boundary-layer conditions or base pressure, as well as measurement inaccuracies, could contribute to the discrepancy.

As shown in Figure 7.39(c), the angular motions of these models were fairly heavily damped. The values obtained for the dynamic-stability parameter for unpowered flight at constant altitude,

$$\xi = C_D - C_{L_\alpha} + \frac{md^2}{I}(C_{m_q} + C_{m_{\dot\alpha}}) ,$$

are shown in Figure 7.44(a) while the values for $(C_{m_q} + C_{m_{\dot\alpha}})$ are given in Figure 7.44(b). The wind-tunnel result, from Reference 7.31, shows about 20% less dynamic stability than the free-flight results. The reduced frequencies ($\omega d/V$) for these two sets of tests were different (0.010 and 0.006, respectively) which might have an influence on the data.

It is concluded from these comparisons that ballistic range tests and wind tunnel tests will give closely comparable aerodynamic coefficients when the test conditions are similar, and that most discrepancies which occur can be explained in terms of known effects (e.g., sting interference effects, differences in boundary layer transition point, etc.).

---

* In the aerodynamic coefficients that are presented, the reference area is the cylinder cross-sectional area and the reference length is the cylinder diameter.

7.9.4 Analysis Using Numerical Integration of Equations of Motion

A series of ballistic-range tests of models of the Gemini capsule conducted in 1962 in the Ames Pressurized Ballistic Range, indicated that both the static moment and the damping moment governing the model oscillations were nonlinear functions of angle of attack[7.34]. Four of these flights were found to be essentially planar and were analyzed simultaneously with the method described in Section 7.8.2 using one-degree-of-freedom simulation given by

$$\alpha'' + (H_0 + h_2\alpha^2)\alpha' + (M_0 + M_2\alpha^2)\alpha = 0 . \tag{7.242}$$

The constants H_0 and H_2 define the nonlinear damping moment, while the constants M_0 and M_2 define the nonlinear static moment. Twelve unknown coefficients were sought; four aerodynamic parameters, and eight initial conditions, two for each flight. The solution converged as follows: $SD(\alpha) = 2.29^\circ, 1.40^\circ, 0.88^\circ, 0.75^\circ, 0.7426^\circ, 0.7424^\circ, 0.7424^\circ$. The data points for the four flights together with the fit obtained by this method are shown in Figure 7.45. Values of the four coefficients are as follows:

$$H_0 = \frac{-0.0199}{m} , \qquad H_2 = \frac{0.000344}{m \ deg^2} , \qquad M_0 = \frac{0.224}{m^2} , \qquad M_2 = \frac{-0.000404}{m^2 \ deg^2} .$$

Several points should be made at this time. The first is that the nonlinear static moment obtained by this analysis of four flights is in good agreement with that obtained using the method described in Section 7.6.4.6. This comparison is shown in Figure 7.46. No comparison with the nonlinear damping moment is possible; however, the value at $\alpha = 0^\circ$ is in good agreement with results in Reference 7.34.

Another point is that if one looks carefully at the fits to the experimental data shown in Figure 7.45, three of the motions are matched very well, while run 582 is not matched as well. For this run (although small-amplitude and hence small residuals) the fitted motion leads the data points at the early stations, reproduces the data well in the middle of the flight, and lags the data points at the end of the flight. When the analysis was first performed, it was not realized that any intentional difference existed between the models tested in the four flights. However, the model tested in run 582 turned out to have had no "simulated window cutouts", whereas the models for the three other flights did have these simulated windows. As discussed in Reference 7.34, the effect of the window cutouts was relatively minor, but when more than one flight is being analyzed at once as in the present case, minor differences in the aerodynamics can be detected. This kind of effect becomes more and more pronounced with increasing distance flown.

The three remaining runs, where the design model geometry *was* constant, were then analyzed together. As would be expected, the standard deviation in the fit did become better, $(SD(\alpha) = 0.7183^\circ)$ but the improvement was small due to the small amplitude of run 582. The values of the coefficients are now: $H_0 = -0.0180$, $H_2 = 0.000315$, $M_0 = 0.220$, $M_2 = -0.000380$. These coefficients generate moments that differ only slightly from the previous set. The static moment obtained from these coefficients is also shown in Figure 7.46.

7.10 MISCELLANEOUS TOPICS

In this section, two topics will be considered. The first is the study of rolling motions. In particular, reference will be made to cases where a roll torque exists and hence the assumption made previously of a constant roll rate is invalid. It is sometimes of interest to study either roll acceleration due to control deflections, or roll damping. Interest in these properties can be stimulated by practical problems of missiles with fins, or even bodies without fins which sometimes acquire rolling velocity due to small asymmetries.

The other topic is the treatment of density variations along the flightpath. This has been mentioned briefly in Section 7.5.2.2 on drag determination and Section 7.8.2 on numerical integration. The motivation for considering it is the countercurrent ballistic facility (Chapter 5), in which the density encountered by a model is never absolutely constant. Density variations with respect to pitching motions will be emphasized and practical methods of handling them will be indicated.

7.10.1 Determination of Roll Derivatives

The equation for the angular momentum about the $\bar{x}$ axis in terms of Euler angles is given as follows. Using the expression for the kinetic energy given by (7.30) in the Lagrangian equations, one obtains

$$I_{\bar{x}}(\ddot{\psi} + \ddot{\theta}_E\cos\sigma - \dot{\theta}_E\dot{\sigma}\sin\sigma) + (I_{\bar{z}} - I_{\bar{y}})\,[\dot{\theta}_E^2\sin^2\sigma\sin\psi_E\cos\psi_E -$$

$$- \dot{\sigma}^2\sin\psi_E\cos\psi_E + (\dot{\sigma}\dot{\theta}_E\sin\sigma)(\cos^2\psi_E - \sin^2\psi_E)] = Q_{\psi_E} .$$

This applies to a general body. In this section, we are going to consider (near-) axisymmetric bodies, but are going to allow small roll-producing asymmetries, like canted fins. It can still be assumed that $I_{\bar{y}} = I_{\bar{z}}$, and then the above equation reduces to

$$I_{\bar{x}}(\ddot{\psi}_E + \ddot{\theta}_E\cos\sigma - \dot{\theta}_E\dot{\sigma}\sin\sigma) = Q_{\psi_E} = L . \tag{7.243}$$

The moment L is of aerodynamic origin. Retaining the most dominant terms in (7.74), we can write

$$L = \frac{\rho V^2 A l}{2}\left(C_{l_0} + C_{l_p}\frac{pl}{V} + C_{l_\alpha}\bar{\alpha} + C_{l_\beta}\bar{\beta}\right). \tag{7.244}$$

Here C_{l_0} is the static rolling moment; it is normally produced by an asymmetry, like canted fins, deflected tabs on fins, etc. C_{l_p} is the damping due to roll, and C_{l_α} and C_{l_β} are changes in the rolling moment with angle of attack and sideslip.

Equation (7.243), with the moment given by (7.244), is difficult to solve in its present form since it is coupled to the motion in the other degrees of freedom. In practice, however, when rolling moment coefficients are to be determined, the model is rolled at a fairly rapid rate and, hence, the motion about the other axes tends to be small by comparison. It may then be permissible to assume that the terms in (7.243) involving θ_E and σ are small and can be neglected. With this assumption and a similar argument for terms with $\bar{\alpha}$ and $\bar{\beta}$, (7.243) and (7.244) are combined to obtain

$$\ddot{\psi}_E = \frac{\rho V^2 A l}{2I_{\bar{x}}}\left(C_{l_0} + C_{l_p}\frac{pl}{V}\right)$$ (7.245)

For consistency with previous discussions a change will be made to x dependence. Equation (7.245) then becomes (note that $\psi_E' = p$)

$$\psi_E'' - \frac{\rho A}{2m}\left(C_D + \frac{ml^2}{I_{\bar{x}}}C_{l_p}\right)\psi_E' = \frac{\rho A l}{2I_{\bar{x}}}C_{l_0} .$$ (7.246)

The solution to this is

$$\psi_E = a_0 + a_1 x + a_2 e^{-a_3 x} ,$$ (7.247)

where a_0 and a_2 are constants of integration, a_1 is the equilibrium roll rate given by

$$a_1 = \frac{-C_{l_0}}{\left(\frac{I_{\bar{x}}}{ml}C_D + lC_{l_p}\right)}$$ (7.248)

and

$$a_3 = -\frac{\rho A}{2m}\left(C_D + \frac{ml^2}{I_{\bar{x}}}C_{l_p}\right).$$ (7.249)

There are several alternatives to the application of these equations to obtain rolling moment coefficients. The most general is to seek a least squares fit of (7.247) to ψ_E versus x data, and hence obtain C_{l_0} and C_{l_p}. Since a_3 appears as an exponent, a least-squares procedure using differential corrections is required (see Appendix). The disadvantage to this approach is that the data must be very accurate or extend over a long distance to yield accurate rolling-moment coefficients. The reason is apparent if one considers an expansion of (7.247) for small values of $a_3 x$; that is

$$\psi_E = (a_0 + a_2) + (a_1 - a_2 a_3)x + \frac{a_2 a_3^2 x^2}{2} - \frac{a_2 a_3^3 x^3}{6} + \ldots$$ (7.250)

In order to obtain the four coefficients (a_0 to a_3), terms to order of x^3 must be retained. This means to obtain accurate values of the a's, the data must be accurate to a small term cubed ($a_3^3 x^3$). This is equivalent to being able to determine the third derivative of ψ_E accurately.

If the roll rate changes only a small amount over the instrumented range ($\psi_E' \cong$ constant), the total rolling moment is essentially constant and hence the solution to (7.246) can be written as

$$\psi_E = C_0 + C_1 x + \left[\frac{\rho A l}{2I_{\bar{x}}}C_{l_0} + \frac{\rho A}{2m}\left(C_D + \frac{ml^2}{I_{\bar{x}}}C_{l_p}\right)p_0\right]\frac{x^2}{2} ,$$ (7.251)

where p_0 is the average roll rate over the length of the test flight not far different from the initial roll rate C_1. A least-squares curve fit of (7.251) to ψ_E versus x data will yield a value of the total rolling moment (since C_D is known from the drag reduction) but will not permit separation of C_{l_p} and C_{l_0} terms. If two tests are conducted, identical in all respects except roll rate, and they both satisfy the assumption of small roll rate change, then it is possible to separate the two terms.

Under special test conditions we can make one of the coefficients dominant and neglect the other. Near zero roll rate the C_{l_0} term will dominate and the data can be curve fit using (7.251) to determine C_{l_0}. Similarly, for certain model geometries and very accurate model construction, the C_{l_0} term can be made very small and a curve fit using either (7.251), or (7.247) with the $a_1 x$ term dropped, will yield C_{l_p}.

7.10.2 Variable Density

When testing in a counter-current ballistic facility, the possibility exists that the density of the test medium may vary with both time and position within the facility. This makes extraction of the aerodynamic coefficients more difficult. As noted in Section 7.8.2, the integral method can handle this problem quite generally. However, it is useful to consider some of the more traditional techniques that have been applied in the past[7.35,7.36].

Typically, the density encountered by the model changes slowly with distance flown. In most instances, the density can be represented simply by $\rho = \rho_0 - ax$, with a change in density of less than 20% between the first and last data station. Under these circumstances, an effective method of accounting for the density variation is as follows: the data are first analyzed by the constant-density methods already described (using the *average* density over the trajectory) and values of both the aerodynamic coefficients and initial conditions are obtained. These values are then used with the *measured* density variation, in the differential equations of motion. The equations are numerically integrated to generate a motion which roughly approximates the motion obtained experimentally. This generated motion is then analyzed by the constant-density program (again using the average density) and the computed coefficients compared with the input values.

The values of C_D, C_{m_α}, and C_{L_α} obtained by the constant density analysis have been found to show very close agreement with input values, and thus require no adjustment. The computed value of the dynamic stability parameter ξ, however (and hence $(C_{m_q} + C_{m_{\dot{\alpha}}})$), differs significantly from its input value. It is found by repeating the process of generating a motion, then analyzing it with the constant-density program, for different values of ξ that a simple relationship exists between the actual and calculated values, namely

$$\xi(\text{actual}) - \xi(\text{calculated}) = \text{const.}$$

Thus, the value obtained from analyzing the experimental data can be corrected to obtain the proper value.

Note that the constant in the above equation applies to a *specific* set of data. What the equation means is that the constant-density program, applied to a given set of experimental data where the density varied slowly, introduces a certain error in ξ that is independent of ξ. It is probable that the foregoing approach would be of little use if the density variation encountered were either very large or highly nonlinear.

With an arbitrary density variation, if the successive peak angles of attack are known, the following equations may be applied. It has been shown[7.36] that the envelope of the angle of attack of a coasting body in free flight can be written as

$$\alpha_{\text{env}}(x) = \frac{C_0 e^{\frac{1}{2}\int B(x)\,dx}}{[-C_{m_\alpha}(x)\rho(x)V^2(x)/2]^{1/4}} \tag{7.252}$$

where

$$B(x) = \frac{\rho A}{2m} C_D J$$

$$J = \frac{1}{C_D}\left[-C_{L_\alpha} + \frac{ml^2}{I}(C_{m_q} + C_{m_{\dot{\alpha}}})\right]$$

$$= \left[\frac{\xi}{C_D} - 1\right].$$

Note that C_D has been assumed constant in deriving this equation, but that any of the other aerodynamic coefficients, as well as the density, can be arbitrary functions of distance*.

When both the aerodynamic coefficients and density are constants, (7.252) reduces to (7.142b), namely

$$\alpha_{\text{env}}(x) = C_1 e^{(\rho A/4m)\xi x}.$$

When the aerodynamic coefficients are constants, but the density variation is arbitrary, a simple expression can again be obtained for α_{env}. Equation (7.108) is integrated once to give

$$\dot{x} = \dot{x}_0 e^{-\int(\rho A/2m)C_D\,dx} = \dot{x}_0 e^{-(1/J)\int B(x)\,dx}.$$

Then

$$\dot{x}^{-J/2} = \dot{x}_0^{-J/2} e^{\frac{1}{2}\int B(x)\,dx}$$

and (7.252) can be written

$$\alpha_{\text{env}}(x) = \frac{C_2(\dot{x})^{-J/2}}{[\rho(x)V^2(x)/2]^{1/4}} = \frac{C_3(\dot{x})^{-\xi/2C_D}}{[\rho(x)]^{1/4}}. \tag{7.253}$$

With peak angles of attack presumed known, together with velocity and density variations, the parameter J can be easily determined from ballistic range data. If the density variation is not extreme, C_D and C_{L_α} can be determined from the constant-density program and hence $(C_{m_q} + C_{m_{\dot{\alpha}}})$ follows. For more extreme density variations, an approach like that described in Section 7.8 would have to be used to find the components of the parameter J.

---

* Note also that (7.252) is an asymptotic solution, and hence would not be accurate in cases like the first few cycles of motion during atmospheric entry. Pertaining to ballistic ranges, however, it is essentially exact.

7.11 ERROR ANALYSIS*

In closing this chapter, we will undertake to discuss how accurately aerodynamic coefficients can be determined from ballistic range tests[7.37]. This is a difficult question to answer, even partially. In the first place, the problem is statistical in nature. Instead of talking about a coefficient being accurate to within plus or minus some number, statements must be made concerning parameters like the standard deviation in the coefficient. A further concern is that errors that degrade the results can enter from a variety of sources, and some of these are not amenable to analysis. Errors can be introduced by

(i) Incorrect determination of physical characteristics of the model.

(ii) Incorrect determination of test conditions (pressure, temperature, etc.).

(iii) Erroneous time measurements.

(iv) Erroneous measurements of model position or attitude angle on the film.

(v) Incorrect position reference system calibration (Chapter 6).

(vi) Incorrect mathematical model used in analyzing raw data.

These errors can be either random or systematic. The random errors come principally from misreading the film. To consider how random errors affect the deduced aerodynamic coefficients, a simplified approach will be followed and it is assumed that angle-distance data satisfy the equation

$$\alpha = Be^{Dx} \cos(2\pi x/\lambda) . \tag{7.254}$$

Note that the constant D is proportional to the dynamic stability parameter ξ and the wavelength λ is proportional to C_{m_α} .

7.11.1 Dynamic-Stability Parameter

An approximate expression for the standard deviation in the dynamic-stability parameter can be derived as follows. The sum of the squares of the angle residuals (SSR) is defined by

$$SSR = \sum_i (\alpha_i - \alpha_{exp_i})^2 ,$$

where α_i is the value of α calculated from (7.254) at point x_i , and α_{exp_i} is the experimental value of α at this point. Differentiating this equation with respect to D and setting the result equal to zero gives

$$\frac{\partial(SSR)}{\partial D} = 2 \sum_i (\alpha_i - \alpha_{exp_i}) \frac{\partial \alpha_i}{\partial D} = 0 . \tag{7.255}$$

Assume B and λ are known exactly and that α_{exp_i} is given by

$$\alpha_{exp_i} = B_E e^{D_E x_i} \cos(2\pi x_i/\lambda_E) + \Delta\alpha_i , \tag{7.256}$$

where the subscript E denotes exact values and $\Delta\alpha_i$ is the experimental error in α at x_i . Now let $D = D_E + \Delta D$, substitute (7.254) and (7.256) into (7.255), expand the exponentials involving ΔD retaining only linear error terms, and solve for ΔD . This gives

$$\Delta D = \frac{B_E \sum_i \Delta\alpha_i x_i e^{D_E x_i} \cos(2\pi x_i/\lambda_E)}{B_E^2 \sum_i x_i^2 e^{2D_E x_i} \cos^2(2\pi x_i/\lambda_E)} .$$

The variance of D , which is the same as the variance of ΔD , can now be obtained.

$$VAR(D) = \frac{VAR(\alpha)}{B_E^2 \sum_i x_i^2 e^{2D_E x_i} \cos^2(2\pi x_i/\lambda_E)} .$$

Now expand the exponential retaining terms linear in x , assume that the data points are close enough together to allow replacing the summation by an integration, and neglect all oscillatory terms after integrating. The result is

$$VAR(D) = \frac{6 \ VAR(\alpha)}{B^2 \lambda^2 N^3 n \ (1 + 3\lambda DN/2)} .$$

---

* As a supplement to this section, the Appendix (Section 7.12) shows how a differential correction procedure can be used in estimating errors in the deduced coefficients.

where N is the number of cycles of motion being analyzed, and n is the number of data points per cycle. We want the standard deviation in the dynamic-stability parameter ξ. Since $\xi = 2D/K$ (Equation (7.139)) where $K = \rho A/2m$, the variance of ξ can be related to that of D as follows:

$$\text{VAR}(\xi) = \frac{4}{K^2} \text{VAR(D)} + \frac{4D^2}{K^4} \text{VAR(K)} .$$

The standard deviation is the square root of the variance, and the final result is

$$\text{SD}(\xi) = \sqrt{\left\{ \frac{24 \, [\text{SD}(\alpha)]^2}{B^2 K^2 \lambda^2 N^3 n \, (1 + 3K\lambda\xi N/4)} + \frac{\xi^2 [\text{SD(K)}]^2}{K^2} \right\}} . \tag{7.257}$$

A number of approximations have been introduced in deriving this expression. Nevertheless, the expression yields results that are in very good agreement with results from a Monte Carlo analysis. This is shown in Figure 7.47, where the standard deviation in ξ is plotted versus the number of cycles of motion being analyzed (N) for a variety of number of data points per cycle (n). Each data point represents the results of analyzing 20 cases having random errors in the angle data (using the tricyclic method of analysis, Section 7.6.3). It is noted that $\text{SD}(\xi)$ increases rapidly below $N = 1\frac{1}{2}$ as would be expected, due to the difficulty in being able to differentiate between damping and trim angle. Results from (7.257) are shown for two values of n.

7.11.2 Static-Stability Parameter

A similar derivation for the standard deviation in the static-stability parameter C_{m_α} assuming that B and D in (7.254) are known exactly yields

$$\frac{\text{SD}(C_{m_\alpha})}{C_{m_\alpha}} = \sqrt{\left\{ \frac{6 \, [\text{SD}(\alpha)]^2}{\pi^2 B^2 N^3 n \, (1 + 3K\lambda\xi N/4)} + \frac{[\text{SD}(K_1)]^2}{K_1^2} \right\}} , \tag{7 258}$$

where $K_1 = 2I/\rho Al$. This equation has also been investigated by analyzing many cases containing random errors. The results showed (7.258) to be valid and indicated similar trends to those shown in Figure 7.47, but the induced errors were exceedingly small (always less than 1%). An accurate measure of C_{m_α} is far easier to achieve than an accurate measure of ξ.

7.11.3 Lift-Curve Slope

The swerving deviations from straight-line flight are used to deduce the lift-curve slope. By treating the equation (simplified version of Equation (7.216))

$$z = z_0 + z_0'x - KC_{L_\alpha} \int_0^x \int_0^x Be^{Dx} \cos (2\pi x/\lambda) \, dx \, dx$$

in a similar manner as was done in the discussion of the dynamic stability parameter (presuming now that all constants except C_{L_α} are known exactly), the following equation for the standard deviation in the lift-curve slope is obtained:

$$\text{SD}(C_{L_\alpha}) = \sqrt{\left\{ \frac{16 \, \pi^4 \, [\text{SD}(z)]^2}{K^2 B^2 \lambda^4 (T_s + 1)} + \frac{2C_{L_\alpha}^2 [\text{SD}(\alpha)]^2}{B^2 (T_s + 1)} + \frac{C_{L_\alpha}^2 [\text{SD(K)}]^2}{K^2} \right\}} .$$

Here T_s is the total number of observation stations. The results of this equation have also been confirmed by a Monte Carlo analysis.

7.11.4 Drag Coefficient

The time-distance equation which determines the drag coefficient is (Equation (7.110))

$$t = t_0 + \frac{1}{V_0 K C_D} (e^{KC_D x} - 1) .$$

To obtain the standard deviation in C_D, the exponential is expanded and terms to order x^2 are retained. Again the derivation is similar to that for $\text{SD}(\xi)$, except here all three unknowns (C_D, V_0, t_0) are allowed to contain errors, so the resulting expression is more accurate than those previously given. The result is

$$\text{SD}(C_D) = \sqrt{\left\{ \frac{720(T_s - 3)! \, \{V_0^2 [\text{SD}(t)]^2 + [\text{SD}(x)]^2\}}{K^2 \Delta x^4 (T_s + 2)!} + \frac{C_D^2 [\text{SD(K)}]^2}{K^2} \right\}} . \tag{7.259}$$

Here Δx is the distance between data stations, assumed constant.

Some insight can be gained by considering a specific example.

$$T_s = 11 \text{ stations} \qquad SD(x) = 0.000114 \text{ m}$$

$$\Delta x = 1.22 \text{ m} \qquad SD(t) = 0.02 \,\mu\text{sec}$$

$$K = 0.00041/\text{m} \qquad V_0 \cdot SD(t) = 0.000122 \text{ m}$$

$$C_D = 1.0 \qquad SD(K) = 0 .$$

$$V_0 = 6100 \text{ m/sec}$$

Substituting these numbers into (7.259) leads to $SD(C_D) = 0.0187$. Twenty cases were generated using a uniform error distribution with standard deviations as listed. These cases were analyzed by Method 5 described in Section 7.5.1 and from these 20 cases, $SD(C_D) = 0.0198$, very close to 0.0187. The results for these cases, in order of increasing drag coefficient, follow.

C_D	$\Sigma(\Delta t)^2$ (sec^2)
0.953	0.58×10^{-14}
0.977	0.41
0.983	0.78
0.983	0.22
0.989	1.45
0.991	0.46
0.996	0.34
0.997	0.71
0.997	0.42
0.999	0.43
1.004	0.42
1.004	0.42
1.007	0.75
1.010	0.26
1.013	0.51
1.014	0.52
1.015	0.64
1.015	0.46
1.016	0.69
1.055	0.32×10^{-14}
Avg.	1.001 .

Also listed is the sum of the squares of the residuals for each case (ascribing all the error to time, none to distance). In about half of the cases, the calculated drag coefficient is within 1% of the actual value. There are two cases, however, where the calculated drag coefficient is off by a significant amount, about 5%. Note that the sum of the squares of the residuals for these two cases would not indicate that bad answers had been obtained. It is cases like these that prove perplexing when real data are being analyzed. Re-reading the position data on the film would probably improve the answers, but nothing can be done to get different time measurements.

7.11.5 Facility Calibration

It is obvious that poor position and angle calibrations of a ballistic facility can introduce errors in deduced aerodynamic coefficients. Furthermore, these errors are more likely systematic than random, which is a worse situation. What is interesting to point out here is how the facility calibration can be monitored in the process of determining aerodynamic coefficients.

Every run analyzed yields, among other things, differences between measured and calculated values at every data station. The drag routine gives time residuals (or equivalent $\Delta x = V \Delta t$ residuals), the stability routine gives angle residuals, and the lift routine gives y and z residuals. If these residuals are saved, station by station, from every run analyzed until there are enough of them to be statistically meaningful, then errors (or changes) in the facility calibration can be detected. If the errors at each station are random, the residuals should scatter about zero. If they scatter about a non-zero value, in all likelihood there is a calibration error. From the error indicated, a correction can be made. This analysis is most meaningful if done for a number of tests of a single configuration at given test conditions, since the variation in film reading accuracy between different configurations and free stream conditions would be eliminated.

Figure 7.48 shows the y residuals versus station number from 32 tests of sphere-cone models conducted in the Ames Hypervelocity Free-Flight Aerodynamic Facility. It is obvious that at some stations the scatter is not symmetrical about zero. The fact that the amount of the scatter is about the same at every station indicates that this is probably the reading accuracy, in this case $SD(y) \cong 0.015 \text{ cm}$. If the amount of scatter differed from station to station (stations assumed identical), it could be an indication that the equations used to analyze the motion were not sufficiently complete.

7.12 APPENDIX

7.12.1 Method of Least Squares Using Differential Corrections

The problem can be stated as follows: given a set of experimental data and the function relating the dependent and independent variables, find the unknown coefficients in the function such that a "best fit" to the experimental data is obtained. The method of least squares determines a best fit on the basis of minimizing the sum of the squares of the residuals (differences between experimental and calculated values).

The function can be written as

$$y = f(x; C_1, C_2, \ldots, C_r) , \tag{7.260}$$

where the C's are the unknown coefficients*. The sum of the squares of the residuals is then

$$SSR = \sum_{i=1}^{n} [y_{exp_i} - f(x_i; C, C_2, \ldots C_r)]^2 , \tag{7.261}$$

where n is the number of data points. Note that the errors have all been assumed to be in the dependent variable y. The minimization is achieved by taking the partial derivative of SSR with respect to each coefficient. These expressions are equated to zero, summed over all data points, and the resulting equations are solved simultaneously for the C's. This is straightforward if all the C's in the function, f, appear in a linear manner. A simple example is the case where f is a polynomial. Consider the three-term polynomial $y = C_1 x^2 + C_2 x + C_3$. The unknowns are obtained by solving the following three equations:

$$\begin{bmatrix} \sum_{i=1}^{n} x_i^4 & \sum x_i^3 & \sum x_i^2 \\ \sum x_i^3 & \sum x_i^2 & \sum x_i \\ \sum x_i^2 & \sum x_i & n \end{bmatrix} \begin{bmatrix} C_1 \\ C_2 \\ C_3 \end{bmatrix} = \begin{bmatrix} \sum_{i=1}^{n} x_i^2 y_i \\ \sum x_i y_i \\ \sum y_i \end{bmatrix} . \tag{7.262}$$

In many cases of practical interest, however, the coefficients appear in a nonlinear or transcendental manner. For these cases the straightforward approach does not work, but a technique employing what are commonly called differential corrections can be used instead. First an approximation to each coefficient must be available. The function f can then be expanded in a Taylor series about this approximate solution.

$$f(x; C_1, C_2, \ldots C_r) = f^0(x; C_1^0, C_2^0, \ldots C_r^0) + \sum_{j=1}^{r} \frac{\partial f^0}{\partial c_j} \Delta c_j .$$

The zero superscript refers to the approximate solution, and $\Delta c_j = c_j - c_j^0$. Substituting this into (7.261) yields

$$SSR = \sum_{i=1}^{n} \left[y_{exp_i} - f^0(x_i; C_1^0 \ldots C_r^0) - \sum_{j=1}^{r} \frac{\partial f_i^0}{\partial c_j} \Delta c_j \right]^2 . \tag{7.263}$$

Note that the Δc_j's appear in a linear manner and the minimization of SSR with respect to them is straightforward. The partial derivative of SSR with respect to Δc_k is

$$\frac{\partial (SSR)}{\partial \Delta c_k} = 2 \sum_{i=1}^{n} \left\{ \left[y_{exp_i} - f^0(x_i; C_1^0 \ldots C_r^0) - \sum_{j=1}^{r} \frac{\partial f_i^0}{\partial c_j} \Delta c_j \right] \frac{\partial f_i^0}{\partial c_k} \right\} = 0 . \tag{7.264}$$

In matrix form, then, we have

$$\underset{r \times r \ \ r \times 1}{[A] \ [\Delta c]} = \underset{r \times 1}{[R]} , \tag{7.265}$$

where $[A]$ is a square matrix with elements

$$A_{jk} = A_{kj} = \sum_{i=1}^{n} \frac{\partial f_i^0}{\partial c_j} \frac{\partial f_i^0}{\partial c_k} , \tag{7.266}$$

---

* Note that some of the C's might represent initial conditions and not appear explicitly in f; for example, if $y = \int_0^x \int_0^w g(w) \, dw \, dw$, then $y(0)$ and $y'(0)$ would also be unknowns.

ΔC is a column vector containing the corrections to the coefficients

$$\Delta c \simeq \begin{bmatrix} \Delta c_1 \\ \Delta c_2 \\ \cdot \\ \cdot \\ \cdot \\ \Delta c_r \end{bmatrix} \qquad (7.267)$$

and R is a column vector of the residuals

$$R = \begin{bmatrix} \sum_{i=1}^{n} (y_{exp_i} - f_i^0) \dfrac{\partial f_i^0}{\partial c_1} \\ \cdot \\ \cdot \\ \cdot \\ \sum_{i=1}^{n} (y_{exp_i} - f_i^0) \dfrac{\partial f_i^0}{\partial c_r} \end{bmatrix} \qquad (7.268)$$

Note that normally the partial derivatives that appear in the A and R matrices have closed form expressions and are hence easy to evaluate. A case was presented in Section 7.8.2, however, where numerical techniques were needed to obtain the partial derivatives.

Equation (7.265) may be solved by hand for simple cases or on a computer for complicated cases. Symbolically, the result is

$$\Delta C = [A]^{-1} R , \qquad (7.269)$$

where $[A]^{-1}$ is the inverse of $[A]$. New values of the coefficients are obtained by adding Δc_j to the present value.

$$C_j = C_j^0 + \Delta c_j . \qquad (7.270)$$

This new solution can now be considered as an approximate solution and the entire process repeated to obtain a better solution*. This process continues until changes in the coefficients, Δc_j , approach zero or in practice some small value. It is often easier to monitor the convergence process by computing the SSR for each iteration and when it stops changing within some prescribed limit, the solution is considered converged. When this point is reached, the best least squares set of coefficients has been obtained.

An additional benefit of a differential correction process of this type is the simplicity with which the accuracy of the various coefficients can be determined. It can be shown that after convergence, the elements of the $[A]^{-1}$ matrix are related to the variance (VAR) and covariance (COV) of the coefficients as follows:

$$\left.\begin{aligned} VAR(C_i) &= A_{ii}^{-1} \cdot VAR(y) \\ SD(C_i) &= [VAR(C_i)]^{\frac{1}{2}} \\ COV(C_i, C_j) &= A_{ij}^{-1} \cdot VAR(y) \qquad i \neq j . \end{aligned}\right\} \qquad (7.271)$$

Here A_{ij}^{-1} denotes the ij^{th} element of the $[A]^{-1}$ matrix. Thus if one can estimate the accuracy of the measured quantity y , the accuracy of the coefficients can be obtained. Note that the standard deviation of the least squares fit to the experimental data $(SD = \sqrt{(SSR/n)})$ is normally better than the true measuring accuracy.

If the parameters of interest are related to the coefficients (C_i) by a routine relationship, the following equations can be used in conjunction with (7.271) to find the accuracy in these parameters. Let a and b be constants.

$$VAR(aC_1) = a^2 VAR(C_1)$$

$$VAR(aC_1 \pm bC_2) = a^2 VAR(C_1) + b^2 VAR(C_2) \pm 2ab \, COV(C_1, C_2)$$

$$VAR(aC_1^2) \approx a^2 [4C_1^2 VAR(C_1) + 2 VAR^2(C_1)]$$

$$VAR(aC_1 C_2) \approx a^2 [C_2^2 VAR(C_1) + C_1^2 VAR(C_2) + 2C_1 C_2 COV(C_1, C_2) + VAR(C_1) VAR(C_2) + COV^2(C_1, C_2)]$$

$$VAR\left(\frac{aC_1}{C_2}\right) \approx \frac{a^2}{C_2^2} \left[VAR(C_1) + \frac{C_1^2}{C_2^2} VAR(C_2) - \frac{2C_1}{C_2} COV(C_1, C_2) \right]$$

$$VAR(e^{aC_1}) \approx a^2 e^{2aC_1} [VAR(C_1) + \tfrac{3}{2}a^2 VAR^2(C_1) + \tfrac{7}{6}a^4 VAR^3(C_1) + \dots] .$$

The two equations involving $VAR(aC_1^2)$ and $VAR(aC_1 C_2)$ are exact if C_1 and C_2 are normally-distributed random variables.

---

* There is no guarantee that this iteration procedure will not diverge. However, with reasonable initial estimates of the coefficients, convergence is normally obtained.

328

REFERENCES

7.1   Lanchester, F.W.   *Aerial Flight*. Vol.1 – Aerodynamics; Vol.2 – Aerodonetics. Const..., & Co. Ltd, London, England, 1907 and 1910.

7.2   Fowler, R.H.   *The Aerodynamics of a Spinning Shell*. Phil. Trans. Roy. Soc., London, 1920.
       Gallop, E.G.
       Lock, C.N.H.
       Richmond, H.".

7.3   Fowler, R.H.   *The Aerodynamics of a Spinning Shell, Part II*. Phil. Trans. Roy. Soc., Vol.222,
       Lock, C.N.H.   London, March 15, 1922, pp.227-247.

7.4   Bolz, R.E.   *A Method of Determining Some Aerodynamic Coefficients from Supersonic Free-Flight*
       Nicolaides, J.D.   *Tests of a Rolling Missile*. J. Aeron. Sci., Vol.17, No.10, October 1950. (Also BRL No.711, 1949.)

7.5   Nicolaides, J.D.   *On the Free-Flight Motion of Missiles Having Slight Configurational Asymmetries*. Report 858, BRL, 1953.

7.6   Charters, A.C.   *The Linearized Equations of Motion Underlying the Dynamic Stability of Aircraft, Spinning Projectiles, and Symmetrical Missiles*. NACA TN 3350, 1955.

7.7.   Murphy, C.H.   *The Effect of Strongly Nonlinear Static Moment on the Combined Pitching and Yawing Motion of a Symmetric Missile*. Report No.1114, BRL, 1960.

7.8   Rasmussen, M.L.   *On the Pitching and Yawing Motion of a Spinning Symmetric Missile Governed by an*
       Kirk, D.B.   *Arbitrary Nonlinear Restoring Moment*. NASA TN D-2135, 1964.

7.9   Murphy, C.H.   *Free Flight Motion of Symmetric Missiles*. Report 1216, BRL, 1963.

7.10   Timoshenko, S.   *Advanced Dynamics*. McGraw-Hill, New York, 1948.
       Young, D.H.

7.11   Curry, W.H.   *Some Comments on the Aerodynamic Characteristics of the Tomahawk Sounding Rocket*.
       (Sandia Corp.)   A Volume of Technical Papers Presented at AIAA Sounding Rocket Vehicle Technology
       Uselton, J.C. (AEDC)   Specialist Conference, Williamsburg, Va., 1967.

7.12   Maple, C.G.   *Aerodynamic Symmetry of Projectiles*. Quarterly of Appl. Math., Vol.VI, No.4,
       Synge, J.L.   January 1949.

7.13   Seiff, A.   *A New Method for Computing Drag Coefficients from Ballistic-Range Data*. J. Aero. Sci., Vol.25, No.2, February 1958, pp.133-134.

7.14   Seiff, A.   *Experimental Investigation of a Hypersonic Glider Configuration at a Mach Number*
       Wilkins, M.E.   *of 6 and at Full-Scale Reynolds Numbers*. NASA TN D-341, 1961.

7.15   Terry, J.E.   *Aerodynamic Characteristics of a Truncated-Cone Lifting Reentry Body at Mach*
       Miller, R.J.   *Numbers from 10 to 21*. NASA TM X-786, 1963.

7.16   Kelley, J.L.   *On the Motion of a Projectile with Small or Slowly Changing Yaw*. BRL Report No.446,
       McShane, E.J.   1944.

7.17   Shinbrot, M.   *A Least Squares Curve Fitting Method with Applications to the Calculation of Stability Coefficients from Transient Response Data*. NACA TN-2341, 1951.

7.18   Kirk, D.B.   *Free-Flight Tests of Fifth-Stage Scout Entry Vehicle at Mach Numbers of 5 and 17*.
       Miller, R.J.   NASA TN D-1425, 1962.

7.19   Canning, T.V   *A Simple Mechanical Analogue for Studying the Dynamic Stability of Aircraft Having Nonlinear Moment Characteristics*. NACA TN 3125, 1954.

7.20   Kryloff, N.   *Introduction to Nonlinear Mechanics*. Princeton University Press, 1947.
       Bogoliuboff, N

7.21   Kirk, D.B.   *A Method for Obtaining the Nonlinear Aerodynamic Stability Characteristics of Bodies of Revolution from Free-Flight Tests*. NASA TN D-780, 1961.

7.22   Rasmussen, M.L.   *A Study of Damping in Nonlinear Oscillations*. NASA TR R-249, 1966.
       Kirk, D.B.

7.23   Murphy, C.H   *On the Qu i-Linear Substitution Method for Missile Motion Caused by a Strongly Nonlinear Static Moment*. BRL Memo No.1466, April 1963.

| 7.24 | Tobak, M.
Pearson, W. | *A Study of Nonlinear Longitudinal Dynamic Stability.* NASA TR R-209, 1964. |

7.25 Boissevain, A.G.   *Determination of Stability Derivatives from Ballistic Range Tests of Rolling*
      Intrieri, P.F.   *Aircraft Models.* NASA TM X-399, 1961.

7.26 Chapman, G.T.   *A New Method For Extracting Aerodynamic Coefficients from Free-Flight Data.*
      Kirk, D.B.   AIAA Paper 69-134, January 1969.

7.27 Bellman, R.   *Quasilinearization, System Identification, and Prediction.* RAND Corporation
      Kagiwada, H.   RM-3812-PR, August 1963.
      Kalaba, R.

7.28 Goodman, T.R.   *System Identification and Prediction – An Algorithm Using a Newtonian Iteration*
                          Procedure. Quarterly of Applied Mathematics, Vol. XXIV, No. 3, October 1966,
                          pp. 249-255.

7.29 Malcolm, G.N.   *A Computer Program for Systematically Analyzing Free-Flight Data to Determine the*
      Chapman, G.T.   *Aerodynamics of Axisymmetric Bodies.* NASA TN D-4766, 1968.

7.30 Gray, J.D.   *Force Tests of Standard Hypervelocity Ballistic Models HB-1 and HB-2 at Mach 1.5*
      Lindsay, E.E.   *to 10.* AEDC-TCDR-63-137, August 1963.

7.31 Gray, J.D.   *Summary Report on Aerodynamic Characteristics of Standard Models HB-1 and HB-2.*
                          AEDC-TDR-64-137, July 1964.

7.32 Conn, H.   *Ballistic Range Measurements of the Cubic Normal Force and Pitching Moment of a*
                          Nonrolling Symmetric Missile. CARDE TR 569/67, January 1967.

7.33 Hruby, R.J.   *FM Telemetry and Free-Flight Techniques for Aerodynamic Measurements in Conven-*
      McDevitt, J.B.   *tional Wind Tunnels.* NASA TN D-3319, 1966.
      Coon, G.W.
      Harrison, D.R.
      Kemp, J.H. Jr

7.34 Kruse, R.L.   *Comparison of Free-Flight Measurements of Stability of the Gemini and Mercury*
      Malcolm, G.N.   *Entry Capsules at Mach Numbers 3 and 9.5.* NASA TM X-957, 1964.
      Short, B.J.

7.35 Intrieri, P.F.   *Experimental Stability and Drag of a Pointed and a Blunted 30° Half-Angle Cone*
                          at Mach Numbers from 11.5 to 34 in Air. NASA TN D-3193, 1966.

7.36 Sommer, S.C.   *Study of the Oscillatory Motion of Manned Vehicles Entering the Earth's Atmosphere.*
      Tobak, M.   NASA Memo 3-2-59A, 1959.

7.37 Chapman, G.T.   *Obtaining Accurate Aerodynamic Force and Moment Results from Ballistic Tests.*
      Kirk, D.B.   AGARD Conference Proceedings No. 10, The Fluid Dynamic Aspects of Ballistics,
                          September 1966, pp. 381-401.

BIBLIOGRAPHY

Boissevain, A.G.   *Experimental Investigation of the Damping in Roll of Cruciform Triangular*
                        Wing-Body Combinations at Mach Numbers from 1.5 to 6. NACA RM A54B15a, 1954.

Bolz, R.E.   *Dynamic Stability of a Missile in Rolling Flight.* J. Aeron. Sci., Vol. 19, No. 6,
                        June 1952.

Canning, T.N.   *Drag and Rolling Moment Effectiveness of Trailing-Edge Spoilers at Mach Number*
DeRose, C.E.   *2.2 and 5.* NACA RM A55F15, 1955.

Coakley, T.J.   *Fundamental Analysis of Various Dynamic Stability Problems for Missiles.* University
Laitone, E.V.   of California, Inst. of Eng. Res. Series 176, Issue 1, June 1961.
Maas, W.L.

Cranz, C.   *Lehrbuch der Ballistik.* Springer, Berlin, 1926.

Durand, W.F.   *Aerodynamic Theory, Vol. V.* Durand Reprinting Committee, CIT, 1943.

Friedrich, H.R.   *The Dynamic Motion of a Missile Descending Through the Atmosphere.* J. Aeron. Sci.,
Dore, F.J.   Vol. 22, No. 9, September 1955, pp. 628-632, 638.

330

Jaffe, P. *Obtaining Free-Flight Dynamic Damping of an Axially Symmetric Body (at All Angles-of-Attack) in a Conventional Wind Tunnel.* JPL Tech. Report 32-544, 1964.

Karpov, B.G. *The Accuracy of Drag Measurements as a Function of and Distribution of Timing Stations.* BRL Report No.658, February 1948.

Kent, R.H. *An Elementary Treatment of the Motion of a Spinning Projectile About Its Center of Gravity.* BRL Report No.85, 1937. (Revision by Kent and McShane, BRL Report No.459, 1944.)

Kopal, Z.
Kavanagh, K.E.
Rodier, N.K. *A Manual of Reduction of Spinner Rocket Shadowgrams.* Technical Report No.4, M.I.T., 1949.

Malcolm, G.N. *Stability and Drag Characteristics at Mach Numbers of 10 and 26 of a Proposed Slender Atmospheric Probe.* NASA TN D-3917, 1967.

McShane, E.J.
Kelley, J.L.
Reno, F.V. *Exterior Ballistics.* The University of Denver Press, 1953.

Moulton, F.R. *New Methods in Exterior Ballistics.* University of Chicago, 1926.

Murphy, C.H. *Analogue Computer Determination of Certain Aerodynamic Coefficients.* BRL Report No.807, 1952.

Murphy, C.H. *The Measurement of Non-Linear Forces and Moments by Means of Free-Flight Tests.* BRL Report 974, 1956.

Murphy, C.H. *On Stability Criteria of the Kelley-McShane Linearized Theory of Motion.* BRL Report No.853, 1953.

Murphy, C.H.
Hodes, B.A. *Planar Limit Motion of Nonspinning Symmetric Missiles Acted on by Cubic Aerodynamic Moments.* BRL Memo Report 1358, June 1961.

Nicolaides, J.D. *Variation of the Aerodynamic Force and Moment Coefficients with Reference Position.* BRL Technical Note No.746, 1952.

Nicolaides, J.D.
Bolz, R.E. *On the Pure Rolling Motion of Winged and/or Finned Missiles in Varying Supersonic Flights.* J. Aeron. Sci., Vol.20, No.3, March 1953, pp.160-168. (Also BRL Report No.799, 1952.)

Nielsen, K.L.
Synge, J.L. *On the Motion of a Spinning Shell.* Quarterly of Appl. Math., Vol.4, No.3, October 1946.

Perkins, C.D.
Hage, R.E. *Airplane Performance Stability and Control.* Wiley, New York, 1949.

Phillips, W.H. *Effect of Steady Rolling on Longitudinal and Directional Stability.* NACA TN 1627, 1948.

Rankin, R.A. *The Mathematical Theory of the Motion of Rotated and Unrotated Rockets.* Phil. Trans. of the Royal Soc., London, Series A, Vol.241, No.837, March 23, 1949, pp.457-485.

Rasmussen, M.L. *Determination of Nonlinear Pitching-Moment Characteristics of Axially Symmetric Models from Free-Flight Data.* NASA TN D-144, 1960.

Redd, B.
Olsen, D.M.
Barton, R.L. *Relationship Between the Aerodynamic Damping Derivatives Measured as a Function of Instantaneous Angular Displacement and the Aerodynamic Damping Derivatives Measured as a Function of Oscillation Amplitude.* NASA TN D-2855, 1965.

Rosser, J.B.
Newton, R.R.
Gross, G.L. *Mathematical Theory of Rocket Flight.* McGraw-Hill, New York, 1947.

Schmidt, L.E.
Murphy, C.H. *Effect of Spin on Aerodynamic Properties of Bodies of Revolution.* BRL Memo No.715, August 1953.

Smith, R.A. *A Simple Non-Linear Oscillation.* J. London Math. Soc., Vol.36, 1961, pp.33-34.

Turetsky, R. *Reduction of Spark Range Data.* BRL Report No.684, 1948.

Webster, A.G. *The Dynamics of Particles and of Rigid, Elastic, and Fluid Bodies.* Stechert-Hafner, New York, 1920 (B.G.Teubner, Leipzig, 1904).

Whittaker, E.T. *A Treatise on the Analytical Dynamics of Particles and Rigid Bodies.* 4th edition. Dover, New York, 1944.

Zaroodny, S.J.   *On Jump Due to Muzzle Disturbances.* BRL Report No.703, 1949.

Zaroodny, S.J.   *On the Mechanism of Dispersion and Short Ranges of Mortar Fire.* BRL Report No.668, 1948.
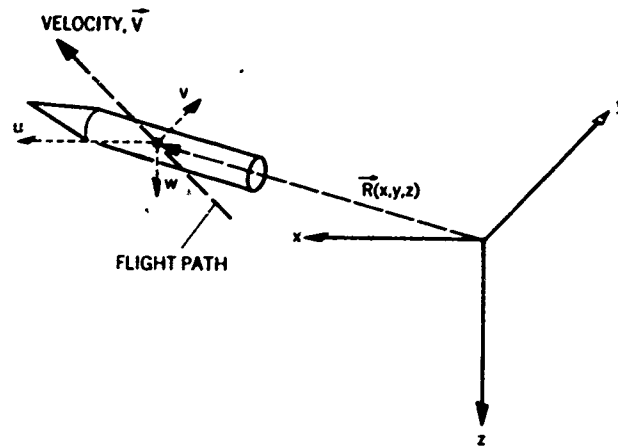
Fig. 7.1   Earth-fixed axes
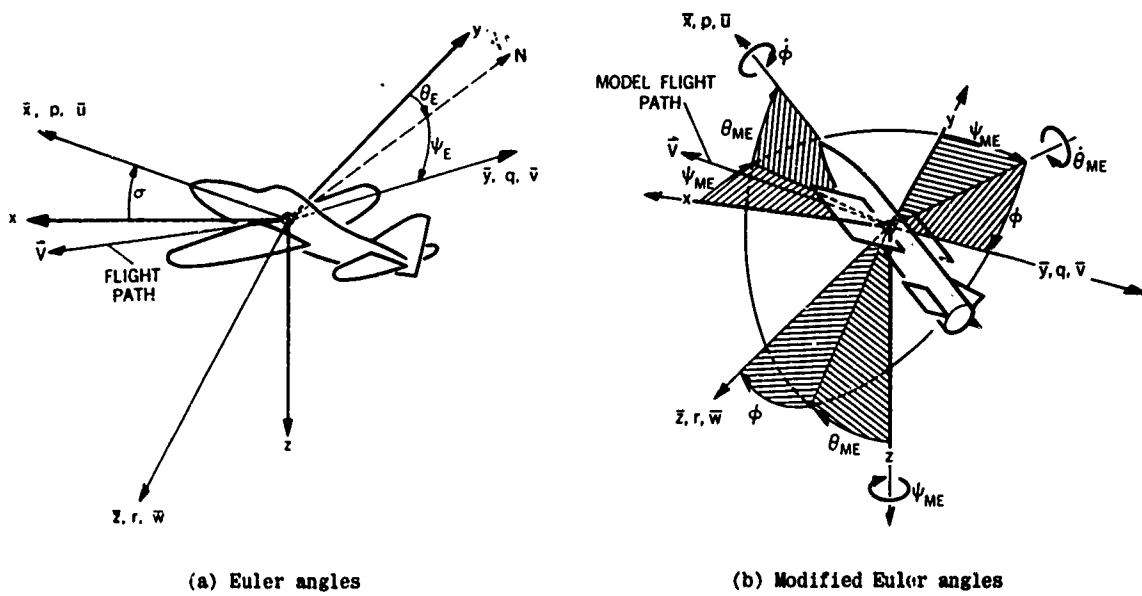
(a) Euler angles   (b) Modified Euler angles

Fig. 7.2   Body-fixed axes
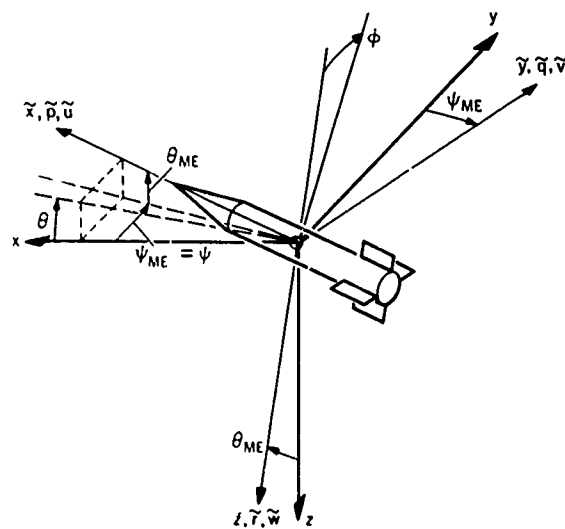
Fig. 7 3   Model-oriented fixed-plane axes

Fig.7.4 Angular relationships between model axes and flight direction

Fig.7.5 Trajectory axes

Fig.7.6 Aerodynamic forces and moments
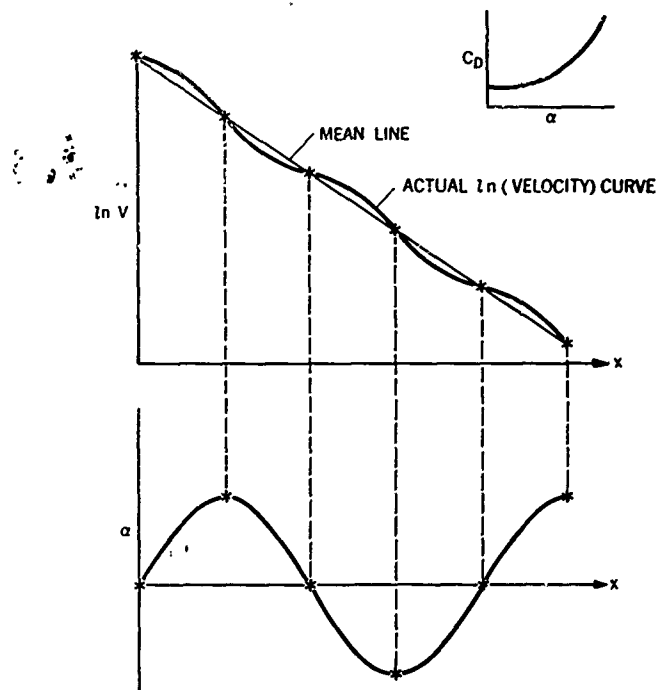
Fig.7.7 Variation of $\log_e V$ and angle of attack with flight distance
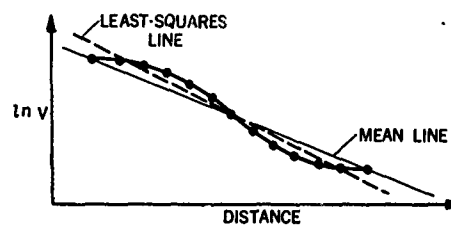
Fig.7.8   Mean line relative to least-squares line
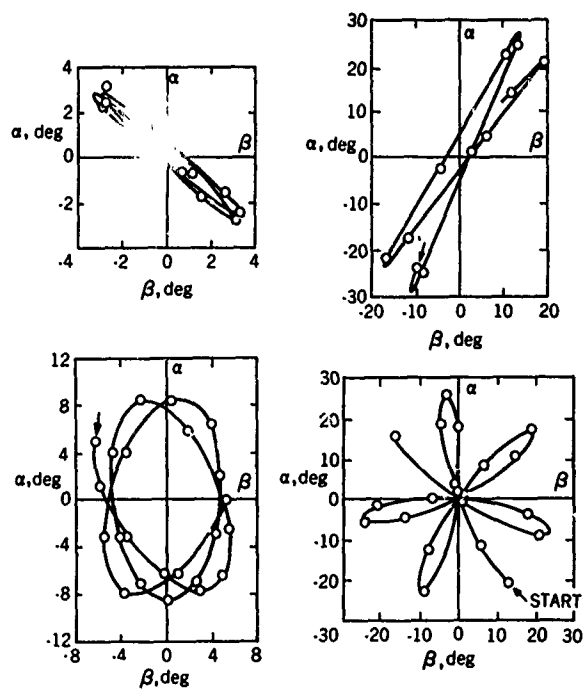
Fig.7.9   Typical angular motions
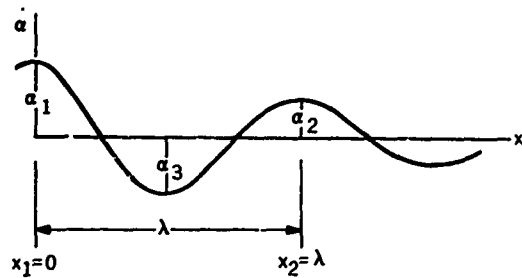
Fig.7.10   Angle variation with distance
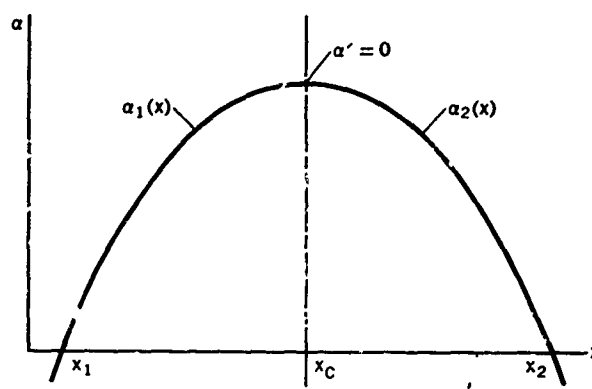
Fig.7.11   Sketch of peak
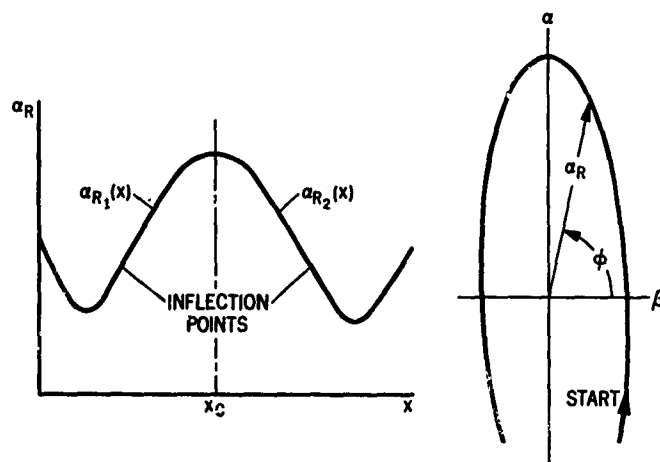
Fig.7.12   Sketch of resultant angle peak for a nonplanar motion
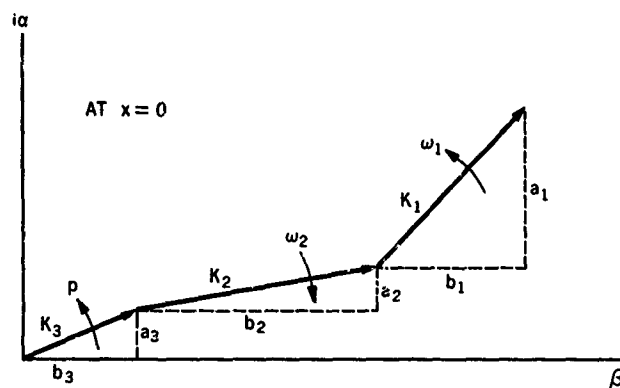
Fig.7.13   Three rotating vectors
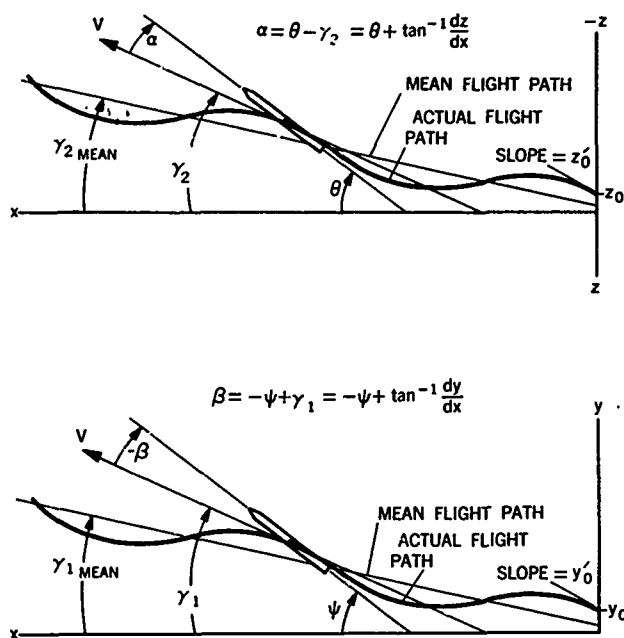
Fig. 7.14 Swerve corrections to measured angles
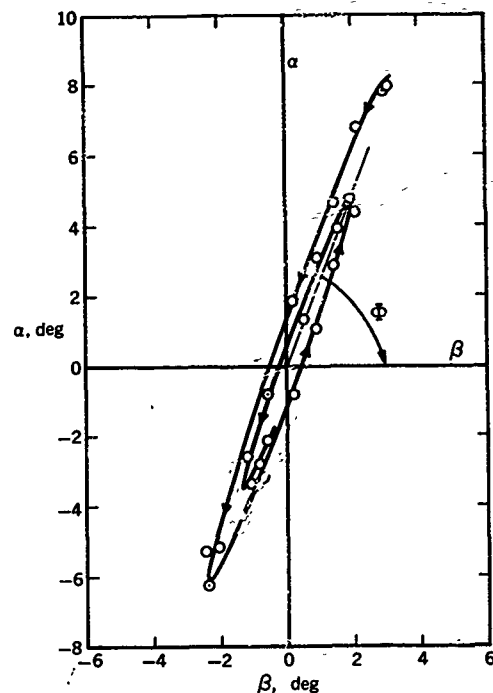
Fig. 7.15 Rotation of coordinate axes
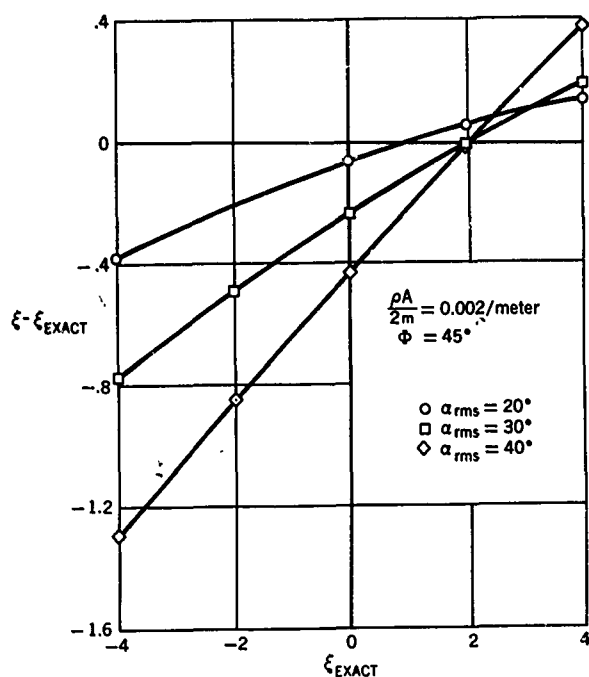
Fig. 7.16 Effect of large angles on deduced dynamic-stability parameter
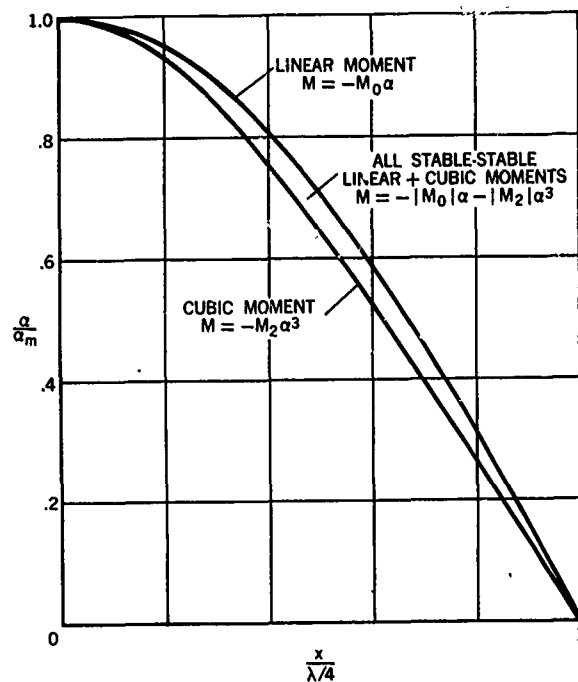
Fig. 7.17 Effect of nonlinear moment on wave-form of oscillation
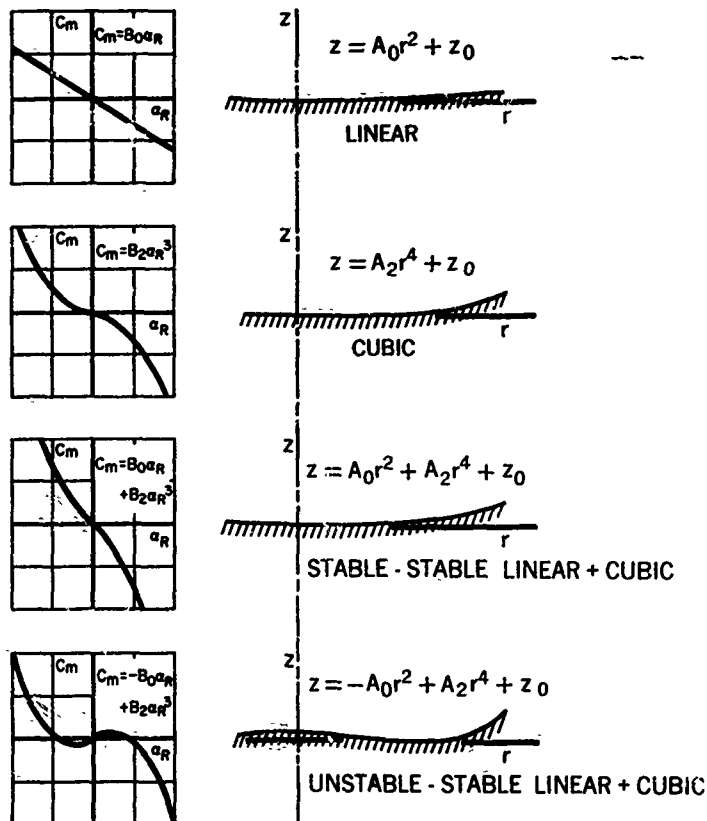
Fig. 7. 18   Moment curves and surface profiles
for analogue surfaces tested
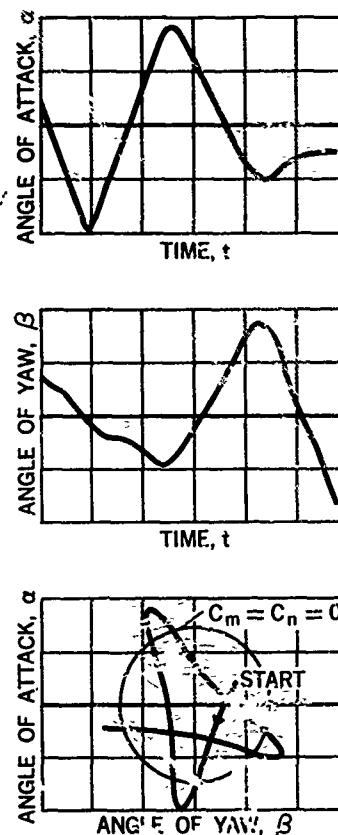
Fig. 7. 19   Pitch and yaw histories
for stable-unstable
linear + cubic case
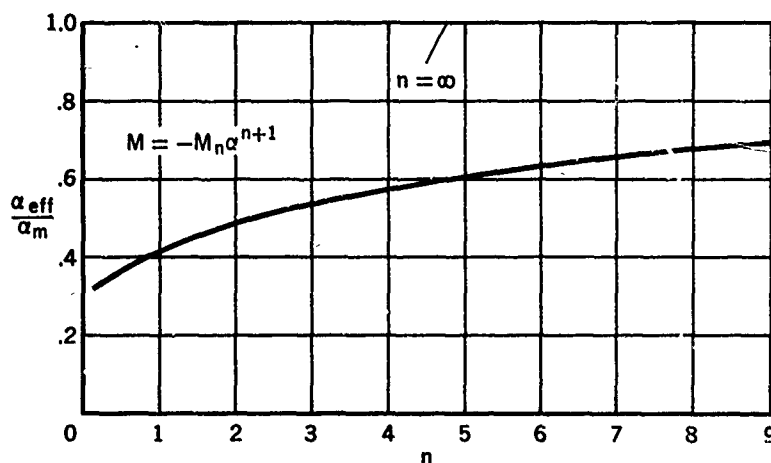
Fig. 7.20   Effective angle-of-attack parameter for a single-term nonlinear restoring moment.
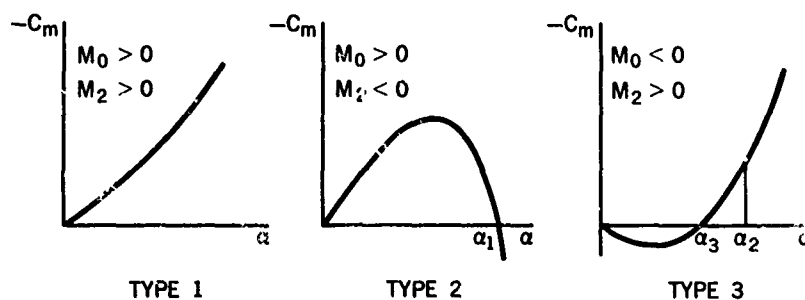
Fig. 7.21   Three types of linear + cubic moment
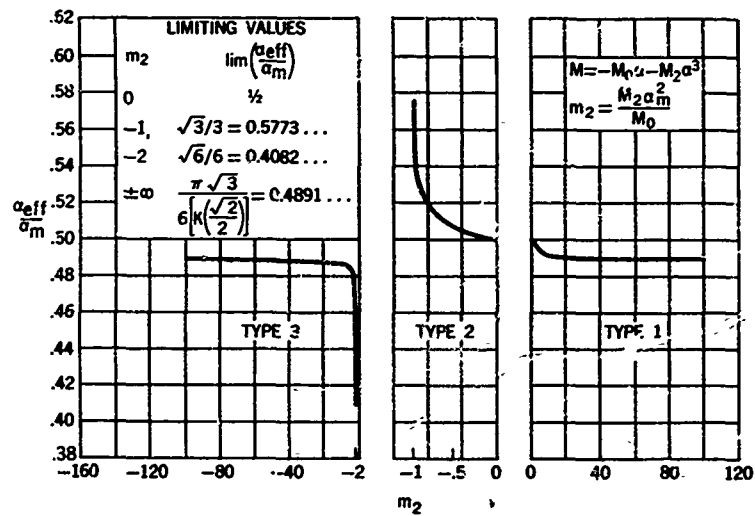
Fig.7.22   Effective angle-of-attack parameter for a linear + cubic restoring moment
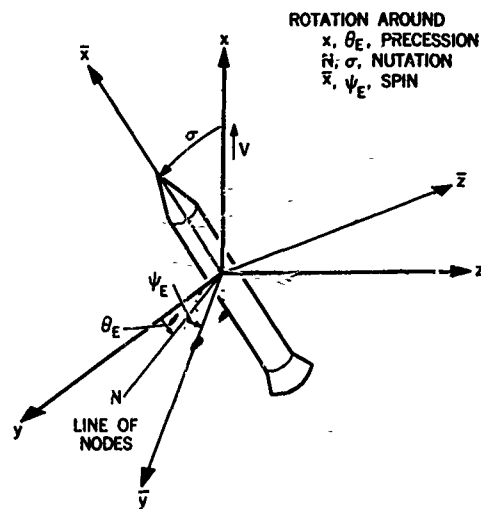
Fig.7.23   Euler angles
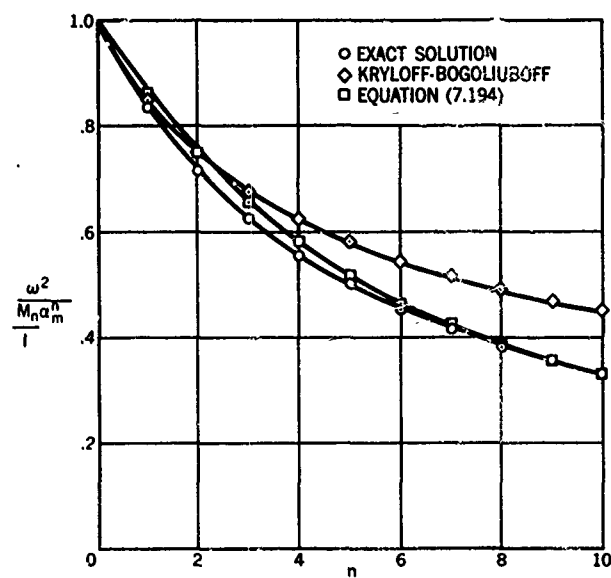
Fig.7.24   Comparison of approximate solutions with exact solution; $M = -M_n \alpha^{n+1}$
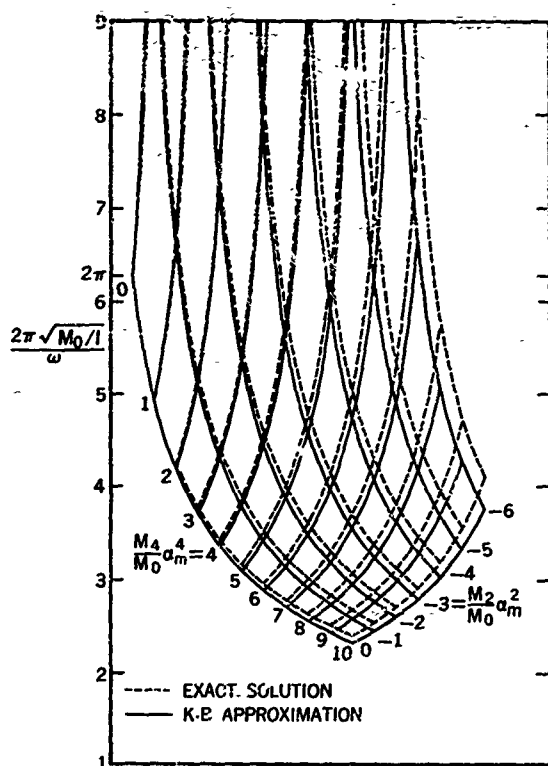
(a) K-B approximation versus exact solution
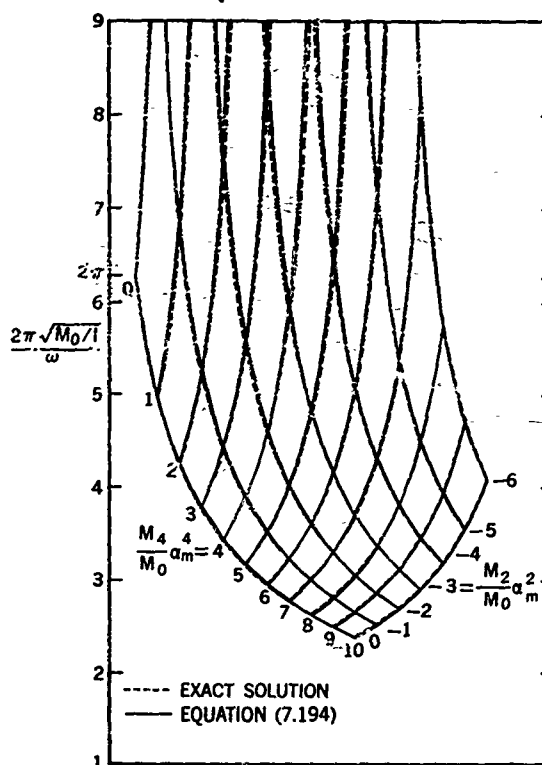
(b) Approximation of Reference 7.8 versus exact solution

Fig. 7.25   Carpet plots showing comparison of approximate solutions with exact solution; $M = -M_0\alpha - M_2'\alpha^3 - M_4\alpha^5$, $M_0 > 0$, $M_2 < 0$, $M_4 > 0$
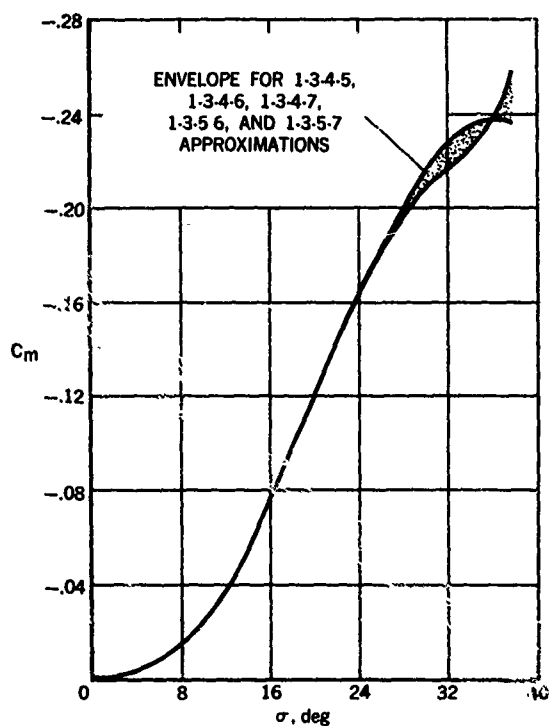
Fig. 7.26   Restoring-moment coefficients corresponding to various assumed moment representations
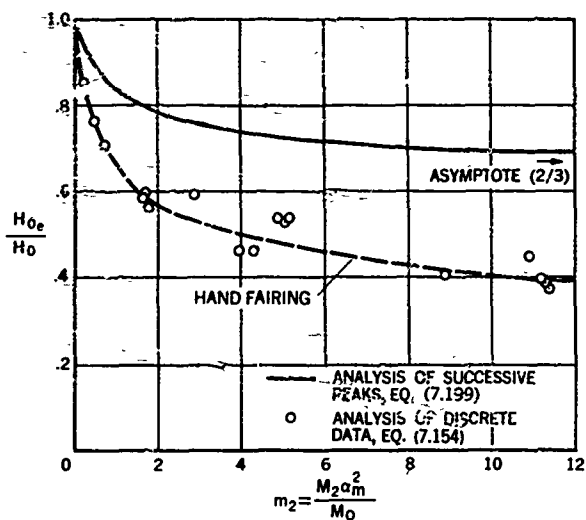
Fig.7.27   Effective damping parameter for
stable-stable linear + cubic static moments
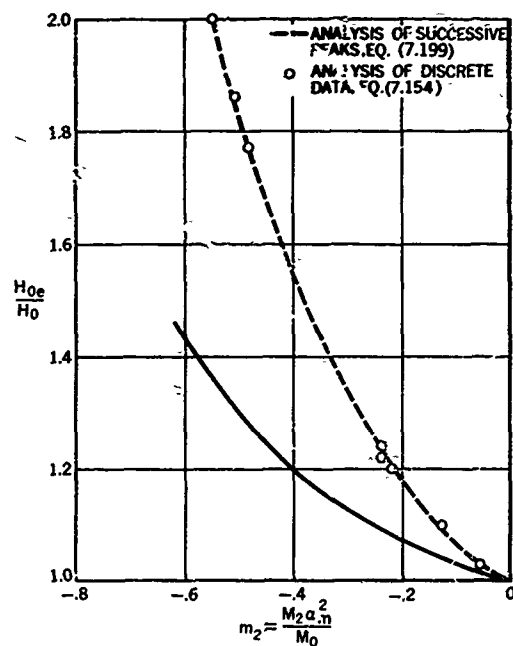
Fig.7.28   Effective damping parameter for
stable-unstable linear + cubic
static moments
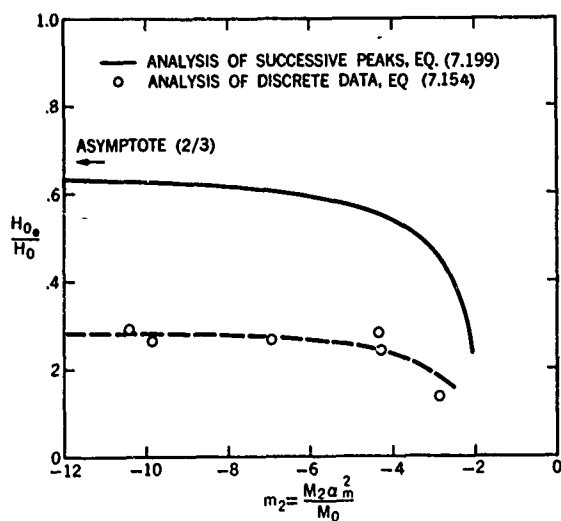
Fig.7.29   Effective damping parameter for
unstable-stable linear + cubic
static moments
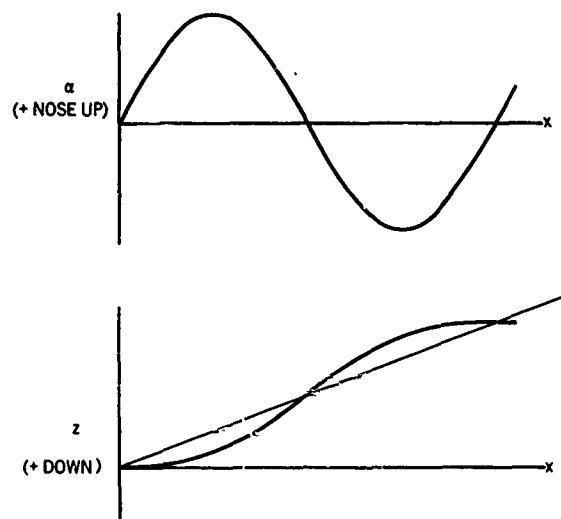
Fig.7.30   Angle and displacement history
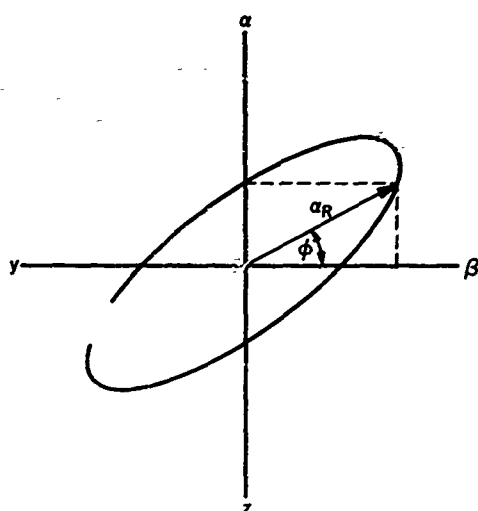
Fig.7.31   Definition of angle ϕ
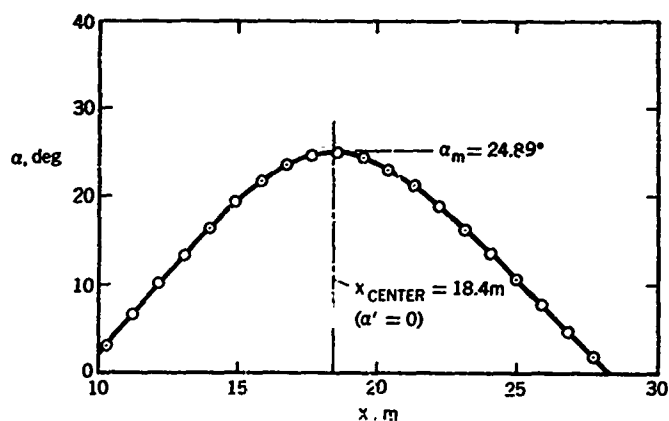
Fig.7.32   Angle of attack versus flight distance

O LEFT SIDE OF α vs x } IN FIG. 7.32
$\triangle$ RIGHT SIDE OF α vs x }
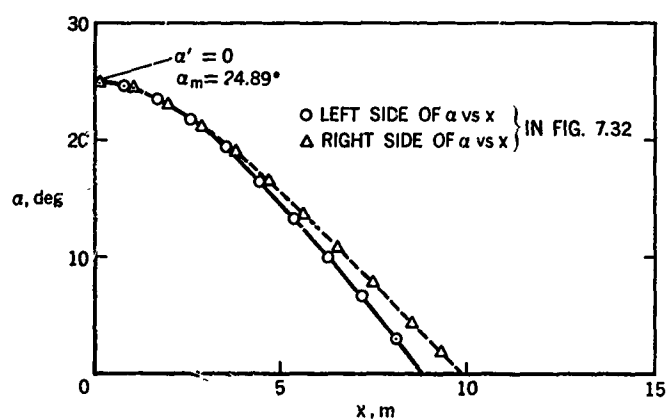
Fig.7.33   Angle of attack versus flight distance (folded about x_{center})

EXACT, $C_m = -0.0005\alpha - 0.00005\alpha^3$
NO RANDOM ERRORS
MAXIMUM RANDOM ERROR $= \pm 0.2$ deg } DEDUCED
MAXIMUM RANDOM ERROR $= \pm 0.4$ deg
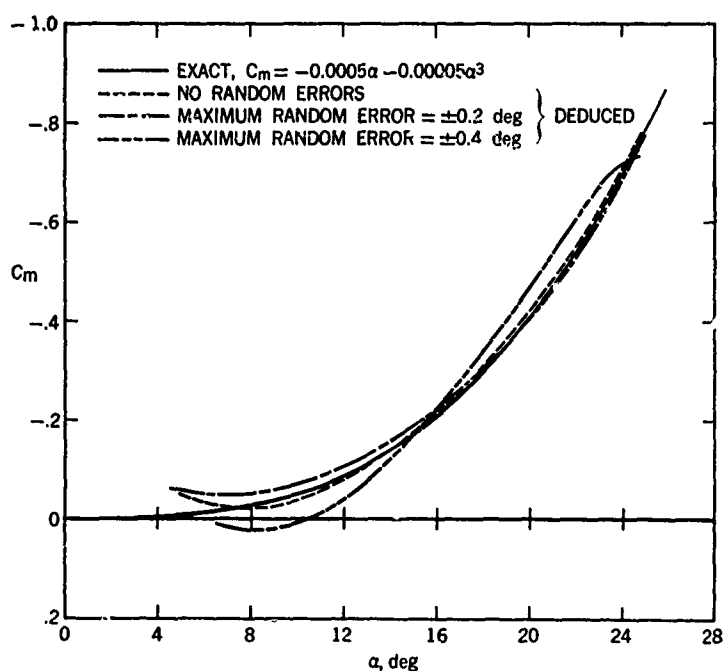
Fig.7.34   Pitching-moment coefficient versus angle of attack
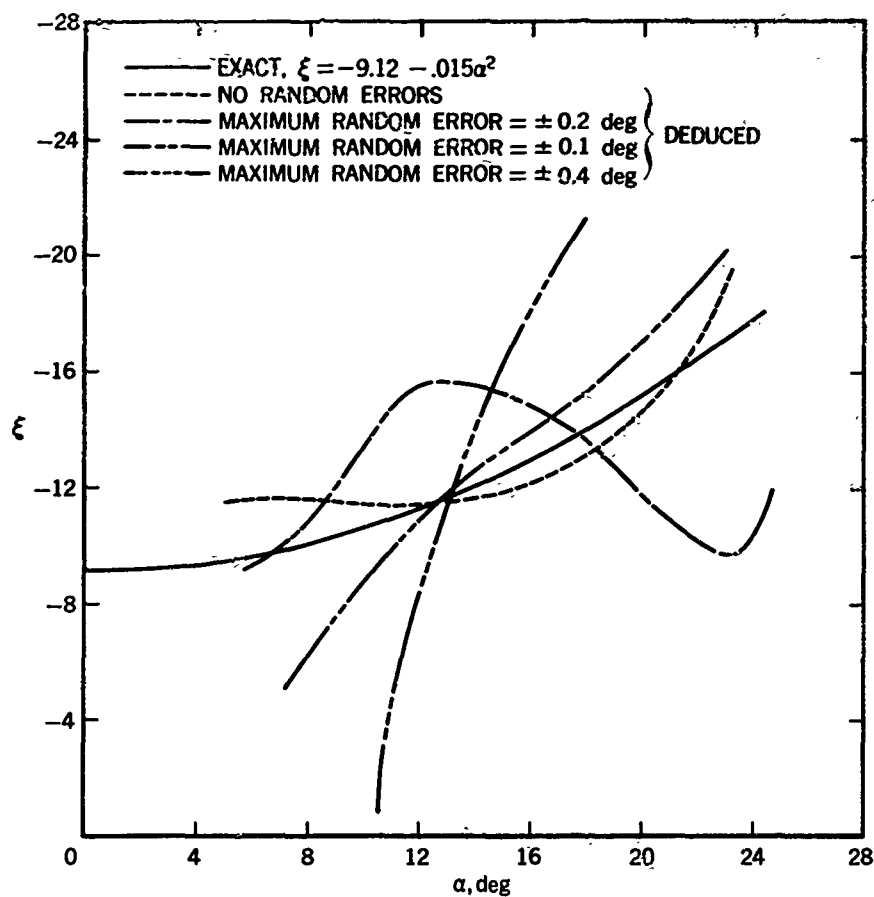
Fig.7.35   Dynamic-stability parameter versus angle of attack
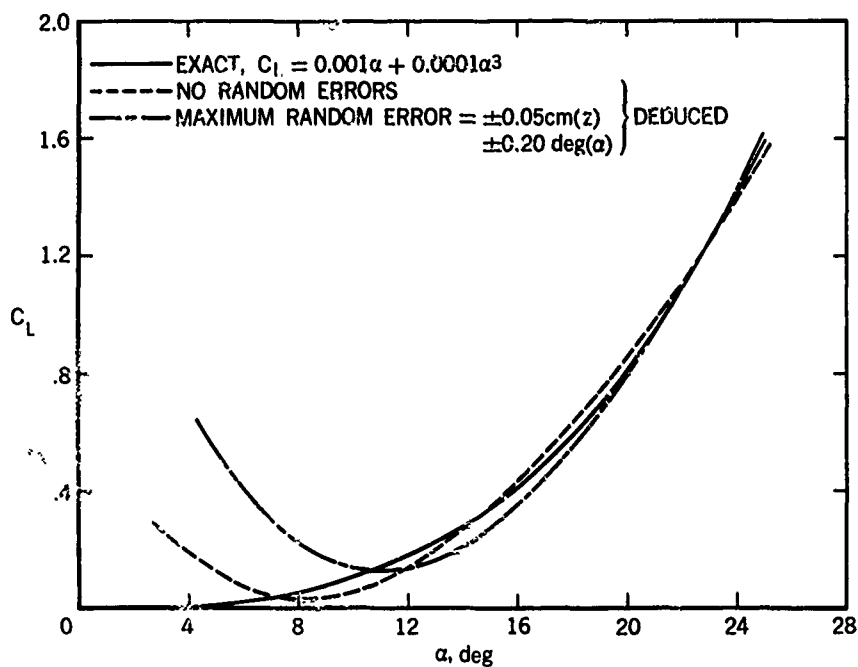
Fig.7.36   Lift coefficient versus angle of attack
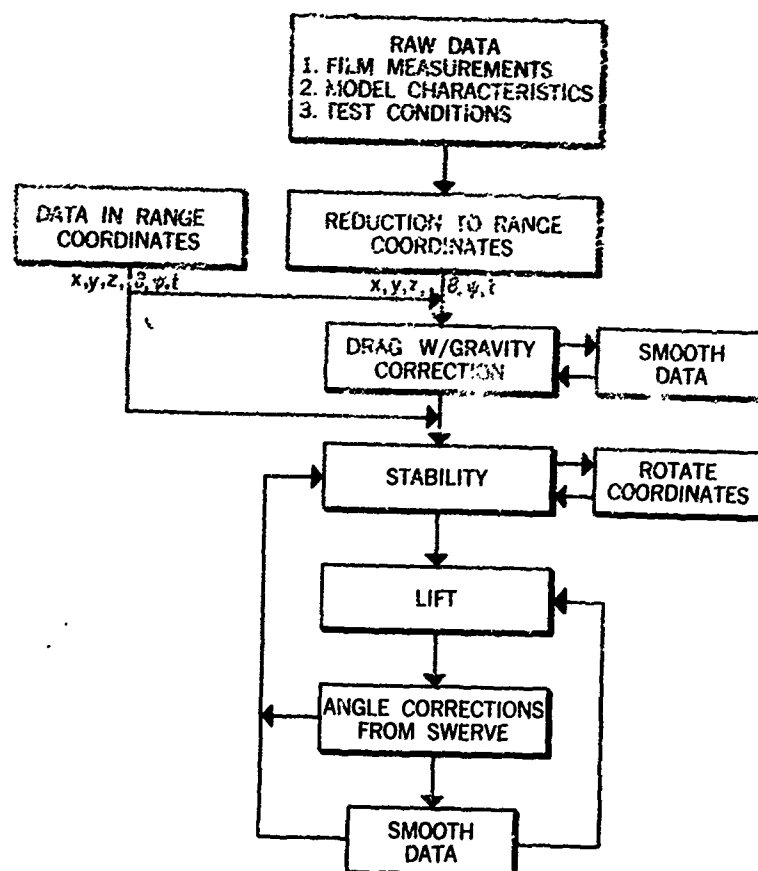
Fig.7.37   Flow chart of data-reduction procedure
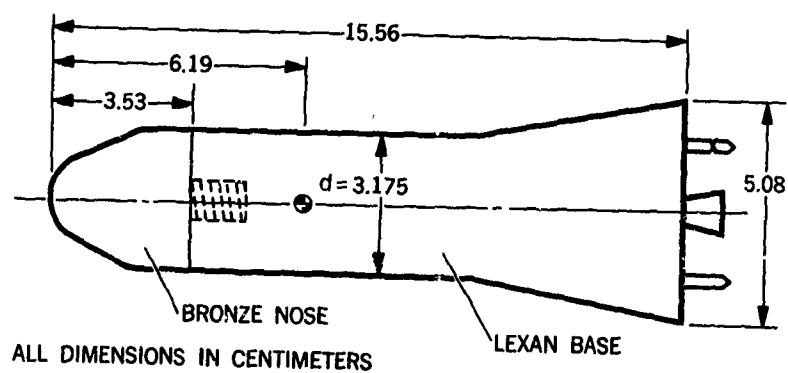
Fig.7.38   Model tested (AGARD HB-2)

344
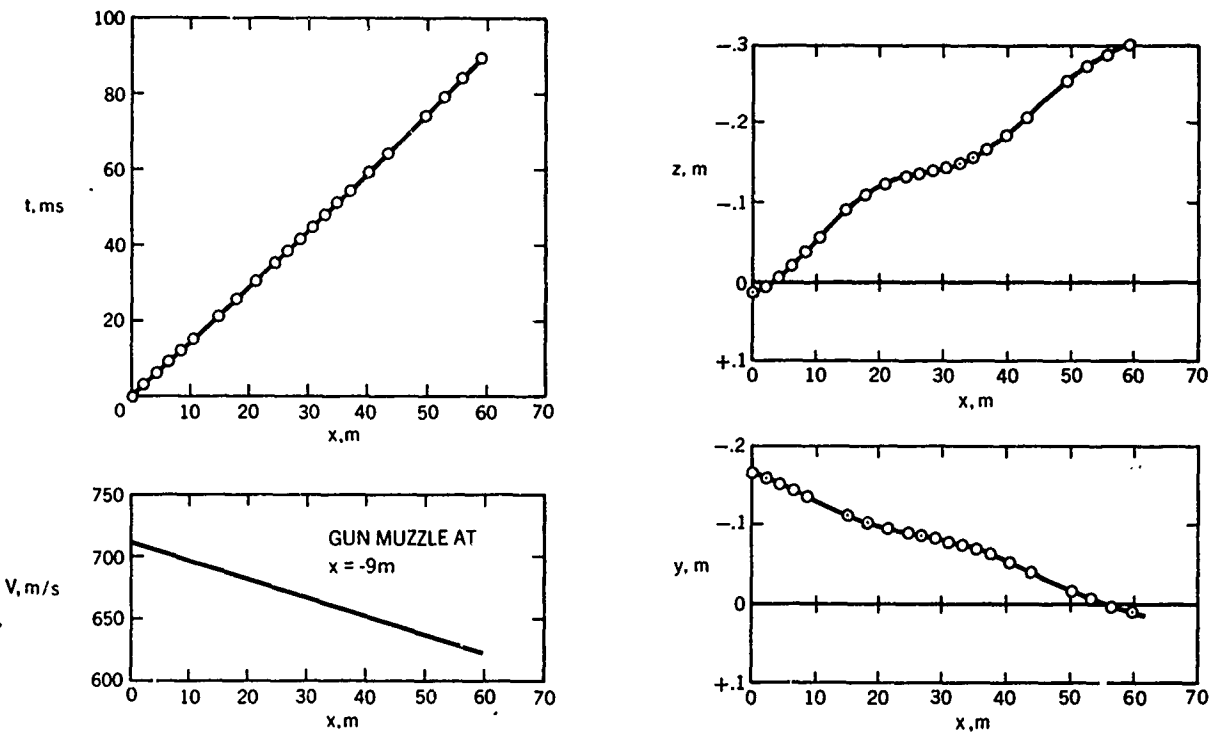
(a) Time and velocity versus distance

(b) Displacement versus distance
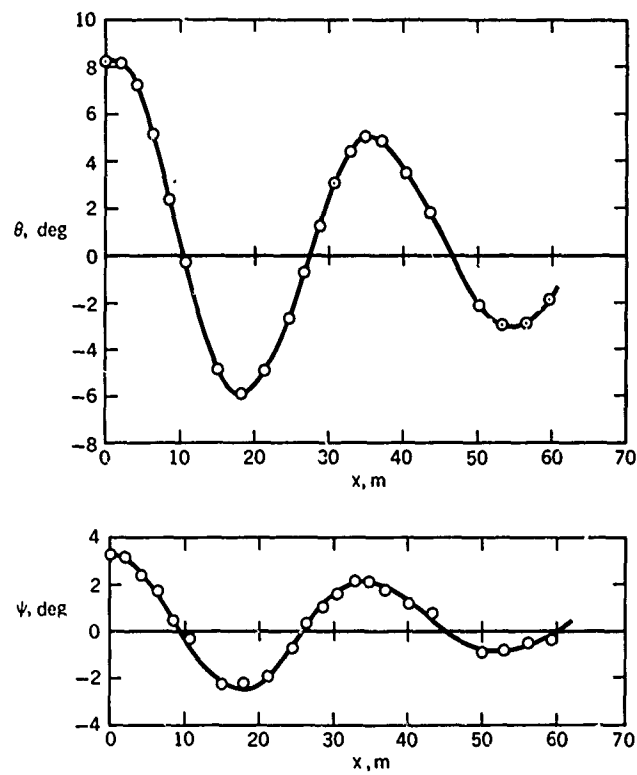
(c) Angular measurements versus distance

Fig.7.39   Typical ballistic-range data
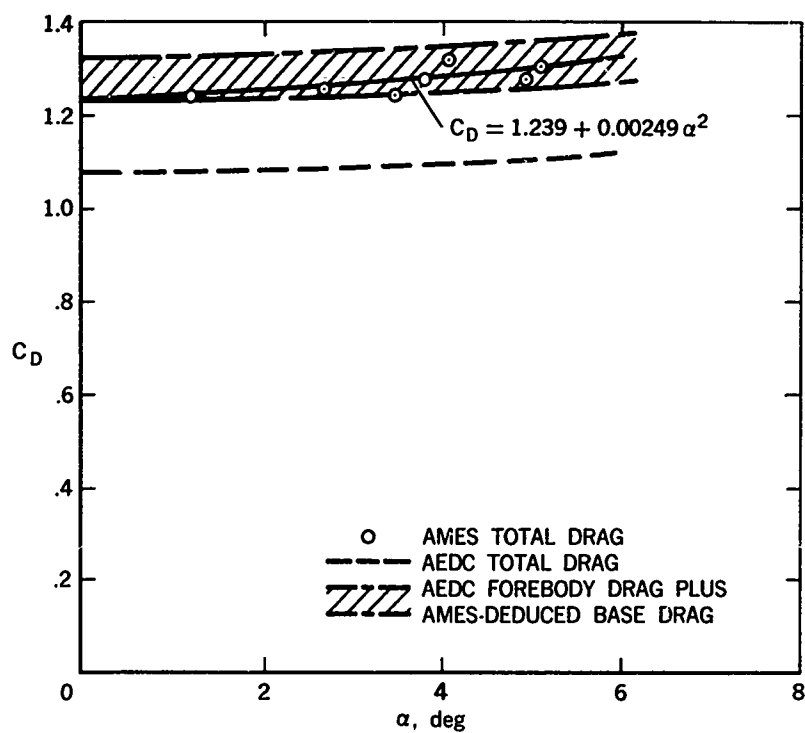
Fig.7.40   Variation of drag coefficient with angle of attack

Legend in figure:
○   AMES TOTAL DRAG
— — —   AEDC TOTAL DRAG
///   AEDC FOREBODY DRAG PLUS AMES-DEDUCED BASE DRAG

$C_D = 1.239 + 0.00249\,\alpha^2$

Axes: C_D (vertical), α, deg (horizontal)

Fig.7.41   Lift-curve slope

Labels in figure:
AEDC
AEDC WITH AMES BASE DRAG
$C_{L_\alpha} = 3.40$
○ AMES DATA

Axes: C_{L_α}, per radian (vertical), α_m, deg (horizontal)
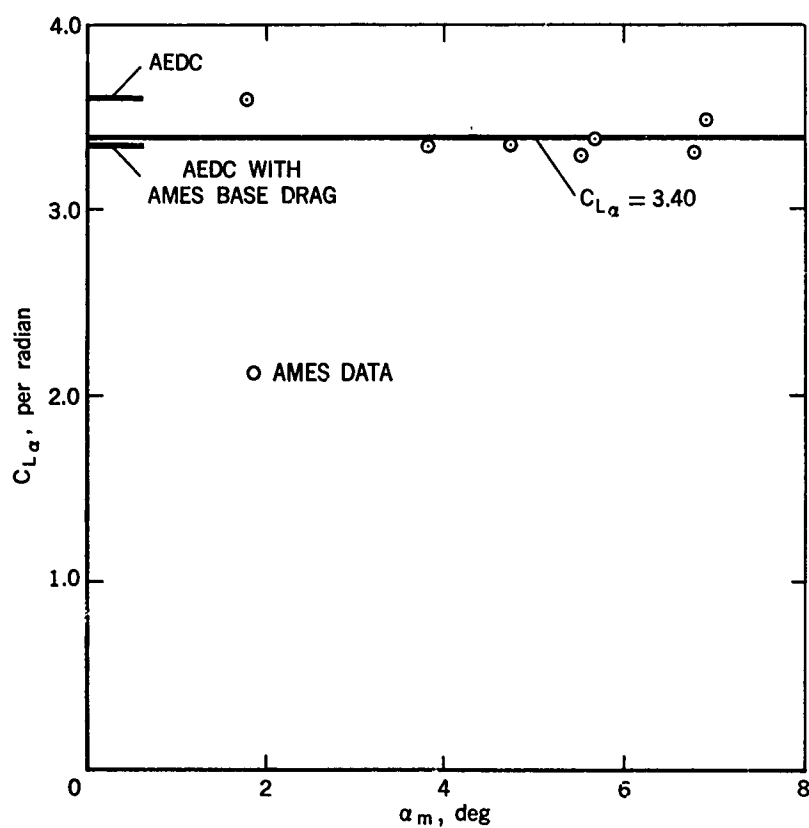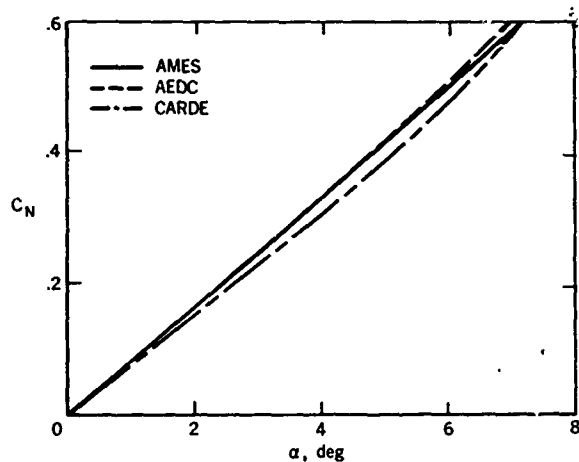
Fig.7.42   Variation of normal-force
coefficient with angle of attack
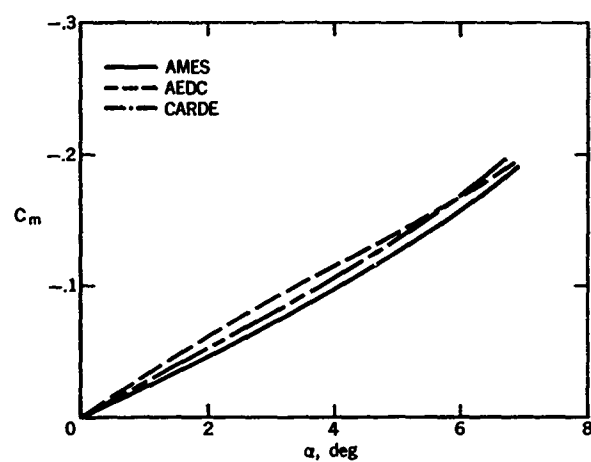
Fig.7.43   Variation of pitching-moment
coefficient with angle of attack
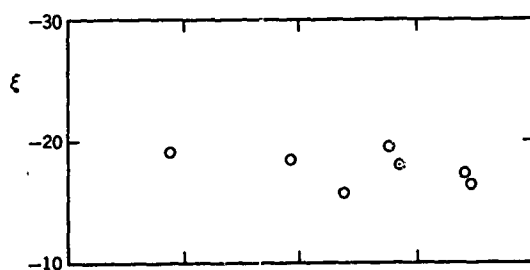
(a) Dynamic-stability parameter
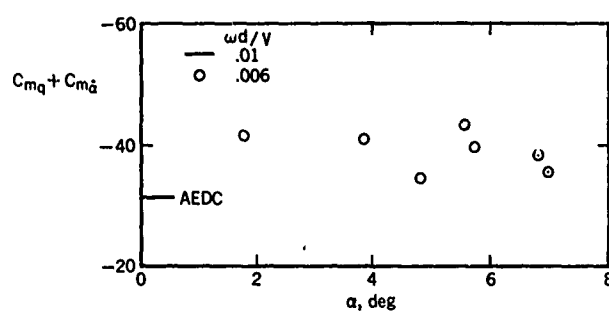
(b) Damping-in-pitch derivative

Fig.7.44   Aerodynamic damping parameters
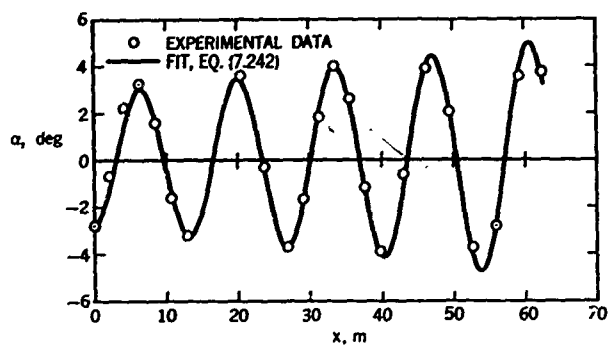
(a) Run 575
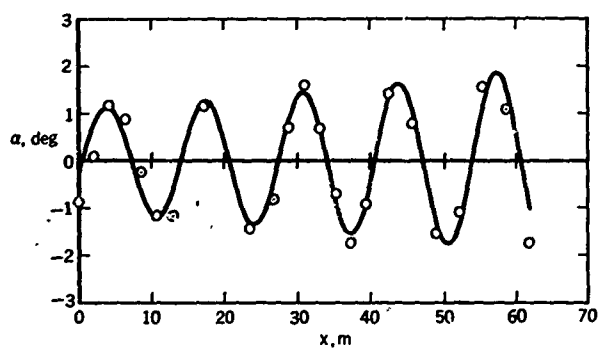
(b) Run 582
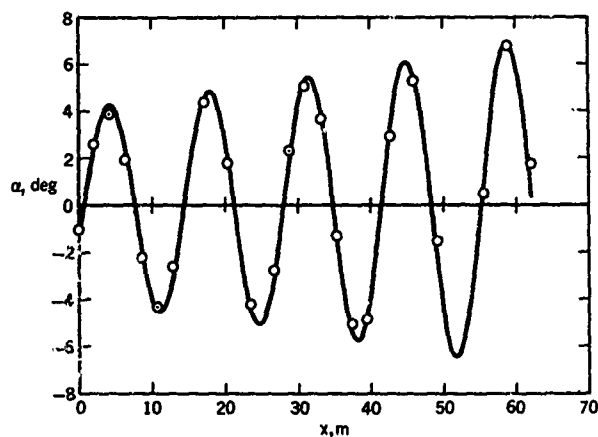
(c) Run 584
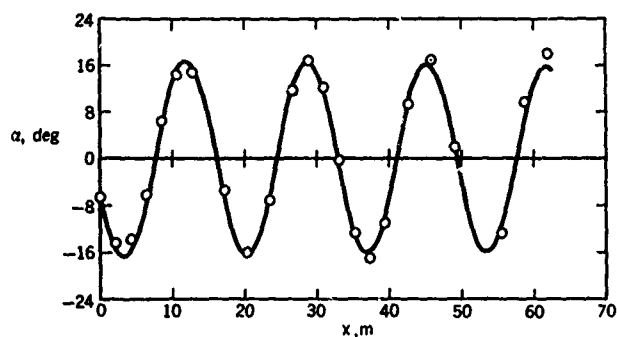
(d) Run 585

Fig. 7.45   Angle-of-attack histories for four Gemini flights
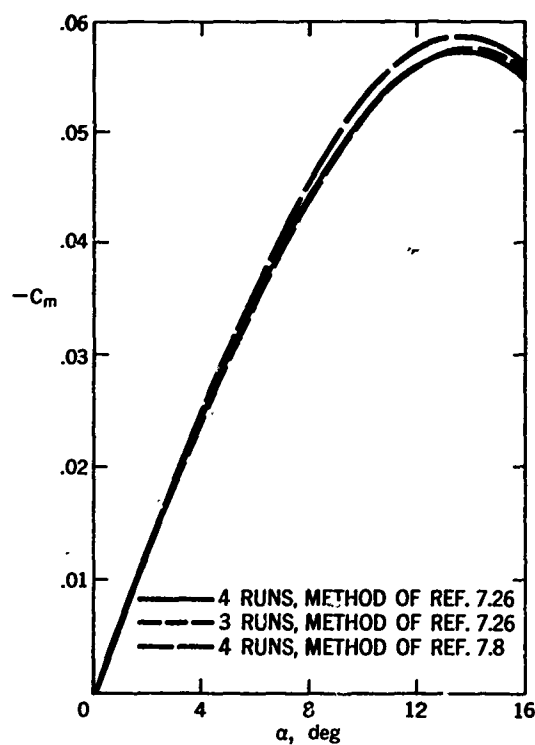
Fig.7.46   Pitching-moment coefficient versus angle of attack
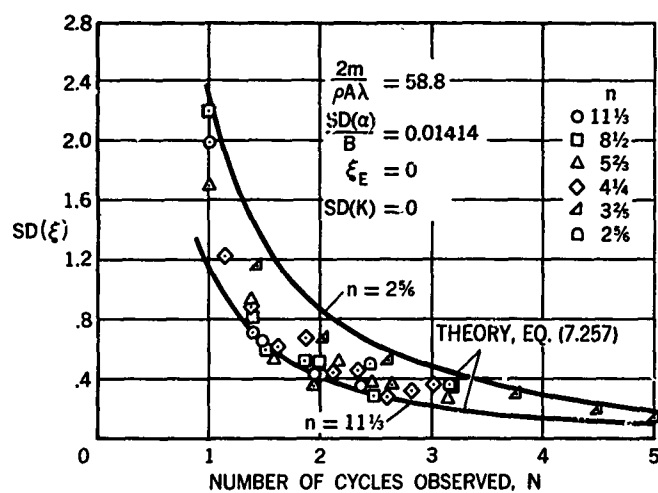
Fig.7.47   Standard deviation in dynamic-stability parameter
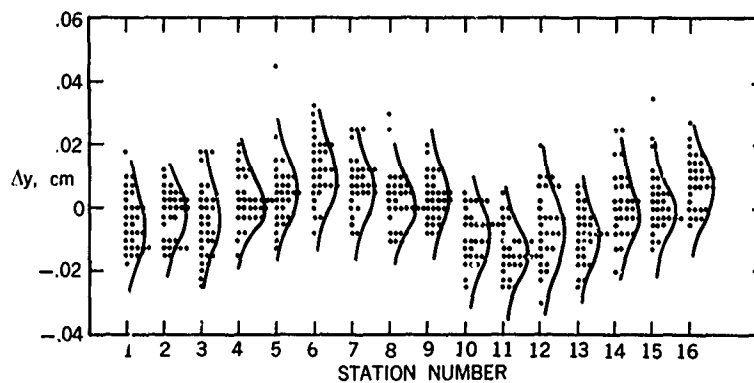
Fig.7.48   Differences between measured and computed lateral displacements

CHAPTER 8

SHADOW, SCHLIEREN, AND INTERFEROMETER PHOTOGRAPHS
AND THEIR USE IN BALLISTIC RANGES

by

Alvin Seiff

NASA-Ames Research Center

SHADOW, SCHLIEREN. AND INTERFEROMETER PHOTOGRAPHS
AND THEIR USE IN BALLISTIC RANGES

Alvin Seiff

8.1 INTRODUCTION

Spark shadow photographs are the means most often used to record the instantaneous position and attitude of models in flight through ballistic ranges. It has long been known that such pictures also make visible certain features of the flow field about the projectile. This was demonstrated as early as the 1880's by Ernst and Ludwig Mach and by C.V. Boys in their famous photography of bullets in flight at low supersonic speeds[8.1,8.2].

The ability of optical systems to make features of high speed gas flows visible has been invaluable in the history of fluid mechanics and the development of all kinds of devices to fly at high speeds in the atmosphere, from projectiles and missiles to aircraft and man-carrying spacecraft. Without the assistance provided by these pictures, our intuitive understanding of the nature of high speed flow would certainly be far less than it is today. It can properly be said that one of the key contributions of ballistic range studies has been the thousands of beautiful pictures of high speed flows they have provided.

Flow fields are made visible in photographs by virtue of the variations in the gas density, which result in variations in the refractive index. Light rays encountering the non-uniform medium are curved or bent, and hence intersect optical elements or the photographic film with altered directions or at altered locations. The velocity of light also is lowered in regions of high gas density compared to its value in the free stream. Different optical systems may be used to detect one or another of these effects of the flow field on the light rays and waves.

The three best known optical systems for this purpose are the shadowgraph, schlieren, and interferometer. Representative flow photographs recorded by these systems are shown in Figure 8.1*. The qualities of flow visualization demonstrated in these examples are well and widely known. Shadowgraph pictures, such as Figure 8.1(a), display the bow shock wave as a dark band of finite width with a light band on its inner boundary. They also show secondary shock waves, such as the strong waves trailing the body; outlines of supersonic expansions, e.g. at the base corner of the cone; turbulence in boundary layers and wakes, showing fine details of structure; and weak disturbance waves generated either by body-fixed disturbances or the irregular edge of a turbulent boundary, as at the edge of the base flow in Figure 8.1(a). In schlieren photographs, such as Figure 8.1(b), regions of the flow field with uniform density gradient are brightened or darkened, depending on direction of the gradient and the knife edge orientation. Thus, in Figure 8.1(b), the shock wave outlines a dark region about the cone within which the density gradient normal to the knife edge is nearly uniform. Light intensity gradations occur in such pictures wherever there are density gradients, as in the region surrounding the wake where pressure pulses occur. The appearance of the turbulent wake is noticeably different from that in shadowgraphs, but close inspection reveals the same structural features. In interferograms, such as Figure 8.1(c), fields of dark and light interference fringes are displaced or shifted by the density distribution due to the flow. Discontinuities in fringe slope occur at shock waves, and fringes in other locations may be sharply curved (notably in the expansion fan in this picture). The fringe displacements measured may be quantitatively interpreted in terms of the density distribution of the flow field. Turbulent regions, such as the wake in Figure 8.1(c), give irregularity of contour to the fringes.

Although not usually thought of as a means of flow visualization, self-luminous photographs (e.g. Figure 8.2) of very high speed flow fields (velocity greater than about 6 km/sec) certainly contain information about the flow, and we mention them here for completeness. Such pictures can provide an outline of the high temperature shock layer, show the dimensions of the base flow region, and indicate the development of turbulence in the wake. The wake flow visualization occurs at the speed represented in Figure 8.2 because of the injection into the flow of efficient radiators by ablation of the polycarbonate plastic model. Pictures of this kind, whose flow visualization properties will not be further discussed herein, are obtained with image converter cameras or Kerr cell shuttered cameras (Chapter 6). The radiative properties of high speed flows are discussed in Chapter 9.

In this chapter, we will first discuss the three optical systems normally considered for flow visualization, and the principles by which flow features are made visible. The nature of the images to be expected from particular flow configurations will be analyzed and compared with images observed, since understanding how the image is formed permits us to be more precise and confident in our interpretations. The basis will be laid for quantitative consideration where it is desired. Some remarks on the capabilities and limitations of the three systems in ballistic testing will be included. The second main topic will be a discussion of research uses of flow

---

* Flow photographs in this chapter which are not otherwise credited were obtained in the ballistic test facilities of the NASA Ames Research Center and its predecessor, Ames Aeronautical Laboratory of NACA.

visualization. These may be put into three classes: (1) The definition of flow configurations (studies of fluid mechanics). (2) The correlation of flow features with observed aerodynamic and flight behavior. (3) The indirect determination of properties of the flow or flowing gases. The second and sometimes the third categories constitute use of flow visualization in support of other test objectives. The first and third may represent uses of flow visualization as the principal approach to investigation. The third category will perhaps be obscure until some examples are given later in the chapter.

8.2   THE SHADOWGRAPH

Shadowgraph systems are widely used in ballistic ranges because of their simplicity and the excellence of flow visualization which they can provide.

8.2.1   Optical Arrangements

The simplest shadowgraph optical system consists of a spark source, approximating a point source, and a sheet of film. The spark firing is timed so that the model shadow falls on the film and light rays traverse the surrounding flow field, as in Figure 8.3. Sensitivity of the shadowgraph is determined by the distance from the model to the film, which also affects the magnification due to the conical light field.

The requirement for short spark duration, in the sub-microsecond range to prevent blurring of the image due to motion, has been discussed in Chapter 6. This requirement, imposed basically to permit accurate measurements of model position, is one of the factors which has led to the excellence of ballistic range shadowgraphs*. Since the gas velocities relative to the earth are equal to or smaller than model velocity, the flow configuration, including its small details such as turbulent eddies, are "stopped" along with the model. Thus, transient features of the flow are photographed in their instantaneous configuration, even in the simplest shadowgraph system, as long as the spark duration is short enough to stop model blur.

Some advantage is gained by collimating the light in shadowgraph systems. The model shadow is then recorded in true size (except for diffraction effects), and distortions due to yaw are avoided. (The latter arise in conical light fields when the model axis is not a uniform distance from the film plane, in which case the magnification is a function of position along the model axis). A single spherical or parabolic mirror will produce a nearly-parallel beam of light which can be passed through a test region to fall on the recording film, arranged as in Figure 8.4. The shadowgraph sensitivity depends, as before, on distance from the flow disturbance to the film, but the collimating mirror may be placed at any convenient distance from the flight path without any first order effects on sensitivity and magnification. It should be noted, however, that imperfections of the collimating mirror and the off-axis arrangement of the spark can affect the accuracy of position measurements, since a perfectly parallel light column is not practically attainable.

If an imaging mirror is added to this arrangement on the film side of the test section, the system is called a focused shadowgraph system (Figure 8.5). The film is now effectively located at its image plane (as indicated in the sketch), and the sensitivity of the shadowgraph may be varied by moving this position toward or away from the flight path of the model projectile. This is conveniently accomplished by moving the film plane toward or away from the imaging mirror. The shadowgraph can be adjusted for minimum sensitivity by placing the effective film location on the flight path. The sensitivity will not then be zero, however, because refraction occurs as the light rays both approach and leave the plane of flight, within the bow shock wave envelope. The plane of focus may even be placed on the far side of the model from the imaging mirror – an arrangement impossible except in focused systems. This reverses the direction of light displacements in the picture.

Shadowgraphs of a blunt body with various sensitivity settings are compared in Figure 8.6. Increasing the sensitivity broadens the shock wave image and makes visible some features not discernible at the minimum setting, specifically the trailing shock wave and base flow. At the highest setting, the bow shock wave image is wider than the shock layer, and it obscures the model front face. Thus, the sensitivity appropriate for one region may be inappropriate for another, and the proper setting depends on the flow feature of immediate interest.

The value of focused shadowgraphs for rejecting model and flow field luminosity has been noted earlier in Chapter 6. An aperture plate which blocks extraneous light at the focal plane of the second mirror is a particularly effective addition (Figure 8.5). The overall rejection ratio of such systems for light from the flow field can be as large as 10^4 compared to that which would fall on a photographic plate placed in the usual position near the flight path. A very mild illustration of this effectiveness has been included in Figure 8.6. The two focused shadowgraph pictures are clear, while the parallel light, unfocused picture is fog exposed, even though the test relative velocity was only 11,000 ft/sec, and the luminosity was limited to the stagnation region of the spherical nose. With blunter models at higher speeds, the parallel light picture would become blackened and the model shadow indiscernible.

In the progression of optical systems, described above, it is evident that the schlieren system is the next step, requiring only the addition of a knife edge at the focal point of the imaging mirror. Discussion of this optical system will be deferred until after a consideration of the theory of shadowgraph systems.

---

* By comparison, it was at one time conventional to use light sources of millisecond duration for flow photographs in wind tunnels.

8 2.2 Theory

A consideration of the processes by which light rays are redirected in compressible flow fields enables us to understand what we see in flow photographs, and opens the possibility of making quantitative interpretations. While we do not intend a comprehensive treatment of this subject, it will be of interest to describe quantitatively the effect of shock waves on light rays, and to write the equation governing the effect of regions of continuous but varying density. Consideration of these two topics provides the basis for understanding the images seen in shadowgraphs of shock waves, wakes, turbulence, boundary layers, separated flow boundaries, expansion-fan boundaries, streamlines of density-gradient discontinuity, and boundary-layer-induced sound or pressure fields – in short, all the phenomena normally displayed in shadowgraphs.

8.2.2.1 Shadowgraph Images of Shock Waves

The index of refraction, like the more familiar fluid properties, density, pressure, and temperature, is discontinuous at a shock wave because the density is discontinuous. Light rays intersecting the wave surface therefore behave as they do at the surface of a lens, i.e., they obey Snell's law,

$$\frac{\sin i}{\sin r} = \frac{c_1}{c_2},$$ (8.1)

where c_2, the speed of light within the shock layer, is slightly lower than c_1, the speed of light in the ambient atmosphere. The incident ray, where it is not normal to the shock surface, is therefore bent toward the normal on entering the disturbed flow field, and away from it on leaving (Figure 8.7), in both cases being deviated inward. Consequently, it intersects the shadowgraph film inward of its undisturbed location. Even this limited consideration is consistent with the shadowgraph image pattern typical of a shock wave, which is a dark (unexposed) band at the wave surface, with a brighter than normal band inside that (Figure 8.1a). The tangent ray (outermost boundary of the dark band) is not disturbed by the presence of the shock wave, except for diffraction effects. It therefore defines the location of the shock wave in space.

Let us now show that the presence of the dark and light bands can be fully predicted from elementary considerations, and derive expressions relating the width of the dark band to the strength of the shock wave. Consider an axially symmetric shock wave, shown in cross section in Figure 8.7 which, for simplicity, is assumed to be approximately cylindrical in the direction of flight so that all light rays lie and remain in the plane of the sketch. (Note that the equations written under this assumption apply exactly to a body of revolution in the plane of symmetry containing the incident ray direction, as well as to all spanwise stations of a cylinder in cross flow in a wind tunnel test). A further assumption is that the gas has uniform index of refraction within the shock layer. This assumption is made to isolate the effect of the shock wave alone on the light ray.

If we denote the deflection of the light ray at entry into the shock layer by δ_1, then

$$i_1 = r_1 + \delta_1,$$ (8.2)

and δ_1 is presumed small. The complement of i_1 is ϵ_1 and Equation (1) may be written

$$\frac{\cos(\epsilon_1 + \delta_1)}{\cos \epsilon_1} = \frac{c_2}{c_1}.$$ (8.3)

For non-ionized gases of constant composition, the speed of light may be related to the gas density through the expression

$$\zeta^{-1} = c/c_0 = 1 - G\rho,$$ (8.4)

where ζ is the index of refraction, c_0 is the speed of light in vacuum, and G is called the refractivity or the Gladstone-Dale coefficient[*]. Its value for undissociated air is 0.227 cm^3/gm. Since $G\rho \ll 1$,

$$c_2/c_1 = 1 - G(\rho_2 - \rho_1).$$ (8.5)

On expanding $\cos(\epsilon_1 + \delta_1)$ and combining Eqs. (8.3) and (8.5), we obtain

$$\cos \delta_1 - \tan \epsilon_1 \sin \delta_1 = 1 - G(\rho_2 - \rho_1).$$ (8.6)

With small angle approximations for δ_1, this may be solved to give

$$\frac{\delta_1}{\delta_{1t}} = -\frac{\tan \epsilon_1}{\delta_{1t}} + \left[\left(\frac{\tan \epsilon_1}{\delta_{1t}}\right)^2 + 1\right]^{\frac{1}{2}},$$ (8.7)

---

[*] For ionized gases, $c/c_0 = 1 - \alpha\lambda^2 n_e - G\rho$, where n_e is the electron number density, λ is the light wavelength, and α is a coefficient. At appreciable degrees of ionization, the change in the velocity of light due to free electrons tends predominate over that due to neutral gas particles. In such a case, with monochromatic light, Equation (8.7) will apply, but Equation (8.8) must be modified to read $\delta_{1t} = \left[2\left(\alpha\lambda^2 n_e - G\rho_1\right)\right]^{\frac{1}{2}}$.

where δ_{1t} is the deflection angle for grazing incidence ($\epsilon_1 = 0$),

$$\delta_{1t} = [2G\rho_1(\rho_2/\rho_1-1)]^{\frac{1}{2}}. \tag{8.8}$$

and $\delta_1/\delta_{1t} \to 0$ as $(\tan \epsilon_1)/\delta_{1t} \gg 1$.

Equations (8.7) and (8.8) relate the ray deflection angle on entry into the shock layer to the complement of the incidence angle ϵ_1, the ambient density ρ_1, and the shock strength as measured by the density ratio ρ_2/ρ_1. From symmetry, $i_2 = r_1$, and from Equation (8.1), it can readily be shown that the ray deflection on leaving the shock layer is equal to that on entering. Hence, the total angular deflection of the light ray, neglecting the refraction that occurs inside the shock layer, is twice the value given by Equations (8.7) and (8.8).

$$\delta = 2\delta_1 . \tag{8.9}$$

The linear deflection of the ray on the shadowgraph film, designated Δn in Figure 8.7, is just

$$\Delta n = B\delta . \tag{8.10}$$

for a distance B from the model to the film plane*. If we define the coordinate n to be zero at the projected actual position of the shock wave, then a light ray which would have intersected the film at n now falls instead at

$$n_f = n + \Delta n = n + B\delta(n) . \tag{8.11}$$

The coordinate n is related to the compliment of the incidence angle ϵ_1, as may be seen from Figure 8.7, by

$$\cos \epsilon_1 = 1 - n/R . \tag{8.12}$$

Equations (8.7) through (8.12) allow n_f to be calculated for all n. A representative example is given in the lower part of Figure 8.8. The dark band is predicted by these equations and is calculated for this example to be 2.5 mm wide, starting at the projected actual position of the shock wave, $n_f = 0$. Note that light intersecting the shock wave in the first few thousandths of a mm inside the tangent ray is directed 18.7 mm inside the flow field in the shadowgraph.

Normal or uniform exposure of the film is defined by the total energy per unit film area, E, provided by the light pulse from the shadowgraph spark. Outside the disturbed flow field, the energy falling on unit width of the film in elemental length Δn is $E\Delta n$. For rays originally separated by Δn which pass through the shock wave, their spacing on the film may be termed Δn_f, and the energy per unit area is $E(\Delta n/\Delta n_f)$. The ratio of this energy to the uniform energy per unit area is just $\Delta n/\Delta n_f$, which will be termed the average light amplification factor $\bar{A}$ over the zone Δn_f.

Since, as may be seen in Figures 8.8 and 3.9, there are two contributions to light intersecting the film at given n_f, one originating in the dark band and one outside it, Δn is the sum of two parts. For positive Δn_f, Δn_1 is negative (see Figure 8.8) and Δn_2 is positive, but both contribute positively to the exposure of the film, so we write

$$\bar{A} = \frac{-\Delta n_1 + \Delta n_2}{\Delta n_f} . \tag{8.13}$$

In the limit of very small Δn_f, the amplification factor at a point becomes

$$A = - dn_1/dn_f + dn_2/dn_f. \tag{8.14}$$

At the outer boundary of the light band, slopes and amplification factor become locally infinite[†]. Amplification factors for the example are plotted in the upper part of Figure 8.8. The bright region with $A > 2$ is a band 0.3 mm wide, beyond which A levels off to a value of about 1.5. A shadowgraph picture taken at approximately the conditions of the example is reproduced in Figure 8.10. The dark band on the axis of symmetry measures 2.6 mm wide on the original negative.

The above analysis is purposely simplified to give insight into the shock wave image-forming process. It is, however, a first order quantitative description of that process in shadowgraphs.

8.2.2.2 Refraction Within the Shock Layer

Now let us turn attention to refraction effects within the shock layer, and derive the governing equations. Then we will give a phenomenological discussion of images of flow features frequently visible in shadowgraph pictures, and how they are formed.

---

* Note in Figure 8.7 that the effective position of the model differs slightly from the actual position, being defined by the point of intersection of the extended incident ray with the extended emergent ray.

† Total light on the film remains finite, however, because infinite amplification occurs only along a line of zero width.

A wave front, proceeding along z across a region in which density and hence light velocity varies along y, will rotate, as indicated schematically in Figure 8.11, where yz has been chosen as the plane containing the light ray and the density gradient. Since the velocity c_2 is greater than c_1, the upper end of the wave front advances in time Δt by a distance $z_2 > z_1$, and rotates by an amount

$$\Delta\theta = \frac{\Delta z}{\Delta y},$$ (8.15)

where

$$\Delta z = (c_2 - c_1)\Delta t = z_1\left(\frac{\zeta_1}{\zeta_2} - 1\right),$$ (8.16)

and ζ_1 and ζ_2 are the local refractive indices. Since $\Delta\zeta = \zeta_2 - \zeta_1$,

$$\Delta z = -z_1\frac{\Delta\zeta}{\zeta_2}$$ (8.17)

and

$$\Delta\theta = -\frac{z_1}{\zeta_2}\frac{\Delta\zeta}{\Delta y}$$ (8.18)

In the limit of vanishing Δt, for which z_1 becomes infinitesimal, and for vanishing Δy, Equation (8.18) becomes the differential equation

$$\frac{\partial\theta}{\partial z} = -\frac{1}{\zeta}\frac{\partial\zeta}{\partial y}.$$ (8.19)

The rate of ray rotation along the direction of propagation is thus proportional to that component of the gradient of the index of refraction which is normal to the ray. Since $R_c d\theta = dz$, where R_c is the radius of curvature of the ray, we identify $\partial\theta/\partial z$ as $1/R_c$. The total rotation of a ray traversing the density field is obtained by integration of Equation (8.19) over z, where z is a curvilinear coordinate following the ray and y remains perpendicular to z. The angle of the ray at exit from the field is

$$\theta_e = \int_0^{\theta_e} d\theta = -\int_{z_i}^{z_f}\frac{1}{\zeta}\frac{\partial\zeta}{\partial y}\,dz$$ (8.20)

A bundle of rays, within which θ_e is constant will deliver the same energy intensity to the film as if it had been undeviated. Only where

$$\frac{\partial\theta_e}{\partial y} \neq 0$$ (8.21)

is the exposure affected. Differentiation of Equation (8.20) yields

$$\frac{\partial\theta_e}{\partial y} = \int_{z_i}^{z_f}\left[\frac{1}{\zeta^2}\left(\frac{\partial\zeta}{\partial y}\right)^2 - \frac{1}{\zeta}\frac{\partial^2\zeta}{\partial y^2}\right]dz + \frac{1}{\zeta_i}\left(\frac{\partial\zeta}{\partial y}\right)_i\frac{\partial z_i}{\partial y} - \frac{1}{\zeta_f}\left(\frac{\partial\zeta}{\partial y}\right)_f\frac{\partial z_f}{\partial y},$$ (8.22)

By use of Equation (8.4), this may be expressed in terms of the gas density,

$$\frac{\partial\theta_e}{\partial y} = \int_{z_i}^{z_f}\left[G^2(1-2G\rho)\left(\frac{\partial\rho}{\partial y}\right)^2 - G(1-G\rho)\frac{\partial^2\rho}{\partial y^2}\right]dz + G(1-G\rho_i)\left(\frac{\partial\rho}{\partial y}\right)_i\frac{dz_i}{\partial y} - G(1-G\rho_f)\left(\frac{\partial\rho}{\partial y}\right)_f\frac{\partial z_f}{\partial y}$$ (8.23)

Thus, $\partial\theta_e/\partial y$ depends on both first and second derivatives of density taken normal to the ray.

Exposure intensity on the film in a region between two rays, initially a distance dy apart, whose emergent angles differ by $d\theta_e$, depends on the separation with which they intersect the film, $dy + Bd\theta_e$. The local light amplification factor A may be expressed as

$$A = \frac{dy}{dy + Bd\theta_e} = \frac{1}{1 + B\partial\theta_e/\partial y}$$ (8.24)

Thus, when $\partial\theta_e/\partial y$ is negative, the rays are convergent and $A > 1$. With $\partial\theta_e/\partial y$ positive, the rays are divergent and $A < 1$.

8.2 2 3 Shadowgraph Images of Particular Flow Features

Ordinarily, in viewing shadowgraph pictures, we are less concerned with subtle variations in the light ampli-
fication factor than in the appearance of sharply delineated photographic features which arise where θ_e under-
goes discontinuous or nearly discontinuous change. Let us now consider in a more qualitative way the nature of
such interactions of the light field with particular density fielus, specifically Prandtl-Meyer expansions, tur-
bulent eddies, streamlines of density-gradient discontinuity, and laminar boundary layers.

In Prandtl-Meyer expansions, density is constant on Mach lines emanating from the expansion corner. A density
gradient exists normal to those lines. The expansion fan is bounded by an initial Mach line, inclined at the
initial Mach angle to the streamlines approaching the corner, and a final Mach line, inclined at the final Mach
angle to the streamlines leaving the expansion. The gradient is discontinuous at the initial Mach line and at
the final Mach line, so that the density distribution is of the type schematically indicated in Figure 8.12.
The coordinate y lies along the direction of the density gradient, in the plane which is normal to the inci-
dent ray direction. The bending of the light rays by this density profile is schematically indicated. The
disturbance is, for simplicity, collapsed to a plane, which may be regarded as its effective location, where
the emergent rays extended backwards intersect the incident rays. Since the density gradients outside the ex-
pansion fan are presumed small by comparison with those within the fan, rays passing outside the fan are indicated
as undeflected. Those passing through the fan are deflected toward the high density region. As a result, a
doubly-exposed light band occurs along and outside the initial Mach line, while an unexposed or dark band lies
along and inside the final Mach line. Since the light-ray deflection angles θ_e vary comparatively slowly in
the intervening region, the amplification factors, A, Equation (8.24), are near unity and the exposure is al-
most uniform. A shadowgraph in which an expansion fan originating at the model base corner may be compared with
the above description has been given in Figure 8.1(a)*.

Turbulence is recorded in shadowgraph systems as a collection of spot patterns whose size and shape show some
degree of regularity. These spots may be clustered in large, seemingly random, groupings, giving an irregular
outline to the boundary layer or wake (see, e.g., the wake of the model in Figure 8.1(a)), or in a single file
row in the early stages of development of a turbulent layer (Figure 8.13). The mere fact that turbulence is
visible in shadowgraphs, of course, is evidence of density fluctuations. If we assume that the eddy or vortex
is a basic element of turbulent flow, then the fact that pressure forces must be centrally directed in a vortex
to maintain circular motion, and that density will have the same direction of variation as pressure leads us to
expect a density distribution in an idealized eddy like that indicated in Figure 8.14. The light field passing
through this density pattern is deflected outward, yielding a bright ring around the eddy. Inside the bright
ring, there will be a dark center, with perhaps a spot of light at the center, depending on the sharpness of
the density minimum. The correspondence of this description with the spot patterns seen in Figure 8.13 may be
regarded as evidence for the existence of such density patterns in the flow.

The density distribution across a representative laminar boundary layer on a ballistic range model is like
that in Figure 8.15. The density rises near the wall because of cooling of the inner layers of the boundary
layer by the model surface, which is generally at a much lower temperature than the boundary layer recovery
temperature. As in the case of the turbulent eddy, the light field diverges on either side of the density
minimum, some light being refracted into the model shadow. The divergent region is a region of dimmer than
normal exposure. A band of convergent rays orginates near the boundary layer edge, to produce a bright band
which lies roughly along, but, depending on the shadowgraph sensitivity, possibly inside or outside the boun-
dary layer edge. Thus the boundary layer image is expected to comprise a region of reduced exposure near
the model surface and extending slightly inside it, with a bright band near the boundary layer edge†.

The existence of this pattern with attached laminar boundary layers is very difficult to determine, because
of two factors. First, the boundary layers are generally very thin - typically a few thousandths of an inch
thick. Second, wave diffraction patterns occur at the edge of the model shadow, and interfere with observa-
tion of the boundary layer image. However, separated laminar boundary layers are readily seen, as, e.g., at
the boundary of the base flow region in Figure 8.16. Primarily, a single bright band is recorded, presumably
the outward directed convergent rays of Figure 8.15.

Transition to turbulence can often be seen in following this line. The line develops irregularities and
gaps before the spot patterns typical of eddies begin to appear. However, a high contrast line pattern behind
the base is not always proof of laminar boundary layer coming off the base, since it has been observed that
such lines occur for a short distance beyond separation of a turbulent boundary layer (see baseflow region in
Figure 8.17). This may be the exposure intensification from inward directed light from the sublayer, which,
behind the model base falls on an already illuminated region of the film. The dissipation of the bright line
would then signify the disappearance of the sublayer, without a wall to bound it.

Streamwise vortices frequently occur in laminar boundary layers as an early stage of the transition to tur-
bulence. When these occur in a base flow region, they might be expected to leave an image on the film. Since
the density distribution in the vortex cross section is like that of Figure 8.14, extended along the length of
the vortex, the image pattern should consist of two bright lines surrounding the darkened vortex core. Several
patterns of this description can be seen in the base region of the cone in Figure 8.16, and are attributed to
streamwise vortices.

---

* An interesting but not typical feature of this picture is the large deflection which the light band takes near the
expansion corner. This is attributed to combined effects of the boundary layer and the expansion.

† A similar discussion with similar conclusions has been given by Holder and North[8.3] (see their Figure II-26 and its
discussion on page 28). They considered two-dimensional boundary layers with density profiles appropriate in wind
tunnels at zero heat transfer - i.e., they do not exhibit the upturn near the wall.

When secondary shock waves intersect a bow shock wave, as in Figure 8.18, streamlines crossing the bow wave above and below the intersection experience different total pressure losses (entropy increases). Since, at the dividing streamline, there must exist a common static pressure, it can be demonstrated from elementary considerations that the velocity and temperature are discontinuous at this streamline. It follows from the gas law that density is discontinuous, being higher on the inward side. Light rays will interact with this density jump just as they do with a weak shock wave. Hence, in Figure 8.18, we see that the streamline originating at the wave intersection point near the conical tip is visible downstream, and has the dark outer band, light inner band typical of shock wave images. Because there is a high velocity gradient across this streamline, it develops into a shear layer which can become turbulent, as in Figure 8.18.

Figure 8.19 is a somewhat more subtle (and more typical) example of the wave intersection phenomenon, wherein a large number of streamlines become marked by the intersection with the bow wave of wavelets generated by disturbances fixed on the model surface. This method of marking the streamline paths can be very valuable in studies of the flow field.

It has also been observed that a very strong expansion interacting with a shock wave will mark a streamline[8,4]. In this case, while density is continuous, the density gradient is discontinuous. Characteristics solutions performed on a large-angled cone cylinder showed that, along Mach waves emanating from the base corner of the cone, the density distribution was of the type shown in Figure 8.20. The discontinuity in gradient occured along the streamline crossing the bow wave at the point of intersection of the bow wave with the first Mach wave of the expansion. Light rays are deflected away from this streamline in both directions, leaving it marked as a dark band. This marking is observed to persist far downstream.

The above examples illustrate qualitative prediction of shadowgraph images, given the density distribution. When research objectives demand it, the predictions can be made quantitative.

8.2.2.4 Dimensional Distortion in Shadowgraph Flow Fields

If dimensions of the flow field are to be measured from shadowgraphs, it is important to consider at least qualitatively the details of the process by which the image is formed so that possible distortions can be evaluated. Flow field dimensions which have been obtained from shadowgraphs in past research include shock wave stand off distances, shock wave profiles, angles of embedded shock waves, convergence angles of wakes, angles of Mach wavelets from surface disturbances, initial and final Mach angles of expansion fans, thicknesses of turbulent boundary layers, thicknesses of wake minimum sections, and diameters of turbulent wakes far downstream. When primary research results depend on these measurements, it is important to evaluate the optical distortions, either inherent in producing the shadowgraph image of the feature being measured or in the surrounding flow. When large distortions are found to be present, it may be possible to correct the data from an optical analysis.

An example of large distortion may be of interest. In the course of some turbulent boundary layer studies, the writer desired to measure the boundary layer thickness from shadowgraphs of thin-walled tubes with sharp leading edges, having flow both inside and out (Figure 8.21). As a test for optical distortion, model image diameters were measured in the pictures. The model image diameters were found to be consistently larger than actual diameter, 3.8 cm, by as much as 0.25 cm. The measurements of boundary layer thickness therefore could not be accepted as valid, without considering the cause of the distortion and its effect.

It was known from previous calibrations that the light beams were accurately parallel, so simple magnification was not the cause. Pictures of stationary models in the test section showed that light diffraction (discussed below) caused an image enlargement of only about 0.05 cm. Analysis of light ray deflections at the shock wave and in the flow external to the boundary layer showed that they were opposite in direction and produced a net movement of the ray on the film of only a few thousandths of a cm in the vicinity of the model edge. Hence, none of these could explain the observed distortion. In the thick turbulent boundary layer, however, the density gradients were large near the wall, and the light path within the boundary layer on models of this diameter was long. By use of theoretical density profiles, refraction was estimated to cause outward ray displacement of 0.1 cm on each side of the body for rays passing just outside the temperature maximum near the model surface. Thus, the model diameter distortion was traced primarily to boundary layer refraction. Near the boundary layer edge, however, the mean density gradient was small, and the mean distortion calculated to be negligible. Hence, it was concluded that the most reliable measurement of boundary layer thickness was to be obtained by measuring the distance from the boundary layer edge on one side of the model to the boundary layer edge on the other side, and subtracting the actual model diameter. It should be pointed out that the distortion occurring in this example were larger than usual for turbulent boundary layers, for two reasons – because the boundary layers were very thick (artificially thickened by use of high drag trips); and because of the large model diameter.

Other quantitative uses of shadowgraph images are suggested by the theory, given earlier. One, which was proposed in Reference 8.5, is to determine the density ratio across a shock wave from the width of the dark band which it generates in the shadowgraph. It is evident that very accurate measurement and correction for diffraction effects would be required to give useful accuracy. Also suggested in that reference, but, to the writer's knowledge, untried in the intervening years, was the use of a wire grid of accurately known dimensions, superimposed on and photographed through a flow field to indicate ray angles induced by the flow field. These could be compared with predicted ray directions for confirmation of theoretical density distributions, or possibly used in an Abel-integral approach (see Interferometry) to deduce density profiles.

Other quantitative applications will suggest themselves to the interested investigator.

8.2.2.5 Diffraction Effects

The discussion of the theory and phenomenology of image formation in shadowgraph pictures would not be complete without some comments on diffraction effects. These occur at the model shadow edges, and at every sharp-edged dark band such as those indicated in Figures 8.12 and 8.20, as well as at the undeflected tangent ray at a shock wave surface. Diffraction, a wave interference phenomenon, produces fringe patterns at shadow edges in monochromatic light (see, e.g., Reference 8.6, page 197). The first fringe is bright, and its center lies at a distance $1.2 (B\lambda/2)^{\frac{1}{2}}$ outside the edge of the geometric shadow, where B is the distance from the object to the film, and λ is the wavelength of the light. (For example, with $\lambda = 5000$ Å and $B = 30$ cm, the distance to the fringe center is 0.33 mm outside the shadow edge). This bright fringe forms a border around the shadow, and diameters are naturally measured by the eye to its inner edge. Shadow images are accordingly found to be larger than the object, in perfectly parallel light.

In monochromatic light from a point source, a series of fringes would be observed, but in the multi-colored spectrum characteristic of a shadowgraph spark (Chapter 6), only the first bright fringe and the first dark fringe are usually seen, with an occasional suggestion of a second bright fringe. Typical of these patterns are those in Figure 8.22, photographed in a shadowgraph light beam with a razor blade and a thin-walled tubular model mounted on a supporting stand to serve as shadow forming objects. The first bright fringe seen around these stationary objects is the same kind of light pattern expected from a laminar boundary layer, and this similarity makes it difficult to distinguish one phenomenon from the other.

Theoretically, as noted above, one would expect fringes at the shadow edge caused by a shock wave or a density gradient discontinuity, and occasionally, in a print of suitable contrast, one can find a suggestion of a bright fringe at the appropriate edges of the dark band. Such fringes can be seen in original prints on Figures 8.10 and 8.13 at the outer edge of the bow shock wave dark band, and in Figure 8.16 at both edges of the final Mach wave of the base expansion fan. One should always keep diffraction effects in mind in studying and interpreting shadowgraph pictures, as they can be responsible for some of the subtler things seen, as well as for the easily measurable effect on apparent object diameters, even in the absence of flow.

8.3 SCHLIEREN SYSTEMS

Schlieren optical systems for flow visualization have been used far less extensively than shadowgraphs in ballistic ranges. Primarily, this is due to the excellence of flow visualization afforded by the simpler shadowgraphs under usual ballistic-range conditions. Schlieren systems require somewhat more care in their use, since the image of the light source must be carefully alined on the knife edge, and the pictures obtained may seem, in some respects, less informative than shadowgraphs. The masses of dark and light exposure which differentiate expansion from compression regions tend to dominate the picture, while many interesting details, such as noise fields due to turbulence tend to be lost. However, it has been often assumed that in some circumstances, schlieren pictures may possess higher sensitivity to flow features than shadowgraphs.

Schlieren photography has thus found application in ballistic range studies of laminar wakes, far downstream of bodies flying through low density air, and in some other problems as well. We will therefore briefly review schlieren systems, with attention to optical arrangement and basis of operation.

8 3.1 Optical Arrangements

The standard optical arrangement for a parallel light schlieren system is shown in Figure 8.23. The film is so located that the model image formed by the second mirror is in focus at the film plane. Then light rays refracted by the flow field are, in the image plane, returned approximately to their original locations relative to the model. Ideally, this cancels the shadowgraph effect, but in practice, this is not fully achieved, since rays passing through different parts of the flow field do not have the same effective plane of origin. Also, even a small error in focal position due, e.g., to the model flying out of the bore sight plane, can result in a shadowgraph image of the shock waves.

The image of the spark light source formed by the second mirror is partly occulted on the knife edge, thereby dimming the level of illumination on the film. The knife edge does not shadow any part of the film, however, because rays from all parts of the source image fall on all parts of the film. The sensitivity of the schlieren system depends on the width of the source image which is allowed to pass the knife edge. The sensitivity is increased by reducing the unccculted width of the source image. It follows that the position of the source image on the knife edge is required to be either stable or adjusted just prior to use.

Stability may be hard to achieve because of earth movement, thermal expansion, etc. An added fundamental difficulty is that conventional spark light sources do not fire at a fixed location on the electrodes, but rather, the spark moves about, finding a new location at each firing. Mercury filled discharge lamps also exhibit this behaviour when fired in short duration pulses. Note in Figure 8.24, from Reference 8.7, the progressive change in shape of the mercury arc column over a sequence of 12 firings in 110 microseconds.

If the source movements due to all causes are appreciable compared to source diameter, the sensitivity variations will be large. The effect of uncontrolled source position is illustrated in Figure 8.25, which is a schlieren picture inadvertently obtained in a focused shadowgraph system. In this case, the source image, intended to be centered in a circular aperture, moved onto the edge of the aperture. A schlieren visualization of the wake resulted, while the bow shock wave and discontinuity streamlines are shadowgraph images. The high sensitivity of the schlieren system to changes in light ray angles is well demonstrated by the appearance of rings in the focusing mirror. For shadowgraph use, this mirror has no detectable imperfections.

To overcome the problem of source movement within the electrodes, confined sparks have been developed. Reference 8.3 describes four configurations of confined sparks which have been used in wind tunnel schlieren systems, and Reference 8.8 indicates "a semi-confined spark between parallel electrodes in a quartz block" used in a ballistic range application of schlieren photography. Sketches of these confined spark sources are given in Figure 8.26. The dimensions used in the semi-confined gap were approximately 0.5 mm width by 5 mm length. Light from the spark is imaged on a smaller slit, which further restricts source movement, since the slit becomes the schlieren source. For maximum sensitivity, slits of very small width (e.g., 0.1 mm) have been used.

Other schlieren optical arrangements than the parallel light system of Figure 8.23 are possible and have been used. A single mirror, single pass, conical light system is shown in Figure 8.27. While having the advantage of requiring only one parabolic mirror, this arrangement has two conspicuous disadvantages: (1) The source must be placed more than twice the focal distance from the mirror, to satisfy the requirement for source image location on the mirror side of the flight path. This means that the light falling on the mirror and hence on the film is much less than in Figure 8.23 for mirrors of equal focal length and aperture. (2) The mirror is required to be severalfold larger than the intended field of view. Thus, this arrangement is in need of a large aperture mirror of short focal length - i.e., an expensive mirror.

Double light pass systems have been used in cases where high sensitivity is required. The parallel light system may be made a double pass system by replacing the second parabolic mirror by a flat mirror, just slightly inclined (away from normal to its incident rays) so that the source image formed by the first mirror does not fall directly on the source. The first (collimating) mirror thus becomes the image forming mirror for both the source and the model. The tilting of the flat mirror gives rise to a slightly displaced second (double) image, which degrades picture quality. This can be partially avoided by alining the flat mirror to return the source image precisely to the source, and using a half-silvered mirror near the source to reflect the source image to the side (Fig. 8.28). Half the light is then lost at each pass through the half-silvered mirror, and the picture brightness is reduced by ¾.

Conical multiple pass systems, Figure 8.29, have apparently been preferred for use in ballistic ranges because they eliminate the need for a good quality flat mirror, and are more compact. A single parabolic mirror is placed near the model flight path, and the spark source is located at twice the focal length from the mirror. If the source and its image are off axis, as shown, the double image problem occurs, but it may be minimized by flying the model near the mirror and by reducing the axis separation. The double image may be avoided by use of the half-silvered splitter mirror, with attendant light loss. Conical double-pass systems have been successfully employed to obtain laminar wake photographs at low ambient pressures (Figure 8.30 and Reference 8.8).

8.3.2 Theory

The basis for understanding the operation of schlieren systems has already been developed in the section on shadowgraphs. Here, we need consider only the special features of the schlieren arrangement and their effects specifically the knife edge, and the focus of the model image on the film plane.

Because of the focusing, ideally, light rays will intersect the film undeviated from positions relative to the model image they had near the model plane of symmetry. The effect of the density field thus will not be to displace the rays, but rather, to lighten or darken local exposure, through the action of the knife edge.

Refraction in the model flow field moves the image of the light source in its plane, the plane of the knife edge. Each point in the flow field is illuminated by light from all points of the source, so that though a single point P in the model's plane of symmetry, there passes a slender conical bundle of light rays, one ray from each point in the source. The point P and every point in the plane of symmetry is thus a point of virtual origin of an image of the light source. Now if all the rays passing through P are refracted through an angle θ_e, the source image formed by these rays is displaced, since the position of this image is governed entirely by the ray directions. For a parallel light system, the image movement is $f\theta_e$, where f is the focal length of the image forming mirror. More generally, f may be replaced by the image distance from the mirror. Thus, instead of a single image of the source, there is an image of the source for each point in the model image.

The refracted positions of the source images, when they are toward or away from the edge of the knife, will cause the light quantity passing the edge from the points P to change. This in turn changes the brightness of the image of P on the film. This action is illustrated in Figure 8.31. If the knife edge was originally set to pass an unrefracted width, w, of the image of a rectangular source, the change in intensity of light on the film at the image of the point P may be expressed as

$$\Delta I/I = f\theta_e/w , \tag{8.25}$$

where ΔI may be either positive or negative, depending on the direction of θ_e. Now, θ_e represents the total angular deflection of light rays passing through a given point in the plane of symmetry of the flow. Earlier, equations were given for the deflection θ_e in continuously varying regions (Equation (8.20)) and at the shock waves (Equations (8.7), (8.8), and (8.9)). These deflections combine to give the total deflection θ_e.

In schlieren photography, particular interest is directed toward the continuously varying density regions. Hence, Equation (8.20) is further developed in the following steps. First, it may be expressed in terms of the density gradient as

$$\theta_e = -\int_{z_i}^{z_f} (1 - G\rho) G \frac{\partial \rho}{\partial y} dz , \tag{8.26}$$

where $1 - G\rho \simeq 1$. Since only that component of θ_e which is perpendicular to the knife edge is effective in changing the exposure, y in Equation (8.26) may be taken as the coordinate perpendicular to the knife edge.

For a knife edge oriented parallel to the axis of a body of revolution in axially symmetric flow, we may express ρ as a power series in the coordinate r radial to the axis, so that

$$\frac{\partial \rho}{\partial r} = a_0 + a_1 r + a_2 r^2 + a_3 r^3 + \dots , \qquad (8.27)$$

where the constants are functions of the axial coordinate x. They are selected, and as many terms retained as necessary, to represent accurately the density gradient profile in a given cross section of the flow. Now $\partial\rho/\partial y$ is the component along y of $\partial\rho/\partial r$ (Fig. 8.32) and may be written as

$$\frac{\partial \rho}{\partial y} = \frac{\partial \rho}{\partial r} \cos\phi = \frac{y}{r}\frac{\partial \rho}{\partial r} = a_0 \frac{y}{r} + a_1 y + a_2 yr + a_3 yr^2 + \dots , \qquad (8.28)$$

where $r = (y^2 + z^2)^{\frac{1}{2}}$. For $G\rho \ll 1$, the integral of Equation (8.26) may be written, with the approximation that the ray path does not deviate far from a path of constant y, as

$$-\frac{\theta_e}{2G} = \int_0^{z_s} \frac{\partial \rho}{\partial y}\, dz = a_0 \int_0^{z_s}\frac{dz}{(y^2+z^2)^{\frac{1}{2}}} + a_1 y \int_0^{z_s} dz + a_2 y \int_0^{z_s}(y^2+z^2)^{\frac{1}{2}} dz + a_3 y \int_0^{z_s}(y^2+z^2)\, dz + \dots , \qquad (8.29)$$

which may be integrated to give

$$-\frac{\theta_e}{2G} = \left[a_0 y + \frac{a_2 y^3}{2}\right]\log_e\left[\frac{z_s}{y} + \left\{1 + \left(\frac{z_s}{y}\right)^2\right\}^{\frac{1}{2}}\right] + a_1 y z_s + \frac{a_2 y^2 z_s}{2}\left\{1 + \left(\frac{z_s}{y}\right)^2\right\}^{\frac{1}{2}} + a_3 y^3 z_s + \frac{a_3 y z_s^3}{3} + \dots . \qquad (8.30)$$

Thus, for a given density profile, the intensity variation over the schlieren field of view may be predicted. In principle, this can be used as a basis of comparison of theoretical density profiles with experiment.

Schlieren systems which are sensitive enough to detect continuous variations in density are normally saturated at the shock waves. Very large ray deflections can occur at the shock wave, just inside the tangent ray (see Figure 8.33, computed from Equation (8.7)). By Equation (8.25), with $\theta_e = \delta$, Figure 8.33 also represents relative light intensity on the film near the shock wave. When the ray deflection $f\delta$ exceeds either the unocculted width w of the source image in one direction (Figure 8.31) or the occulted width in the other direction, saturation occurs. There is then a region of uniform illumination just inside the shock wave, either at full available brightness or at zero exposure, depending on knife edge orientation relative to the ray deflections. The saturated zone may extend well inside the shock wave location. For example, in the case represented by Figure 8.33, the deflection is 0.0033 radian at n/R of 0.2. With a 3 meter focal length mirror, this would correspond to a source image displacement of 1 cm at knife edge. The example shown is, however, more severe than many cases of interest, since $\delta_t = 0.1$ radian corresponds to a normal shock wave with a density ratio of 5.5 at atmospheric ambient density.

If the focusing is imperfect, and in general it will be, some residual shadowgraph effect remains at the shock wave. Then the narrow dark band characteristic of the shock wave shadowgraph image is superimposed onto the schlieren effect, and quantitative interpretation becomes very complicated.

8.4 INTERFEROMETRY

An interferometer, as the name implies, is a device for measuring the interference between two coherent light beams, usually obtained by splitting and later recombining a single beam. In flow visualization applications, one beam, the active beam, is passed through the flow field, while the other, the reference beam, is passed around it. Unlike the other flow visualization systems discussed, the interferometer does not depend on or respond to refraction (literally, bending of the rays). Rather, it measures the retardation of waves locally (within small ray bundles) from their phase shift relative to the reference beam. Thus, the index of refraction, basically defined as the ratio of light velocity in vacuum to the velocity in the gaseous medium, is measured from the velocity itself rather than from ray deflection.

An interferometer requires exceptionally precise alinement, and also requires a monochromatic light source of very high intensity. Its optical surfaces must be very accurately ground, flat within fractions of the wavelength of light. Its supporting frame must be dimensionally stable against temperature changes and vibration isolated. As such, it is not the "rough and ready" instrument that the shadowgraph is, or even the schlieren. It is available in research only after careful design, development, and investment of time toward its perfection. Hence it is not considered a device for routine flow visualization in ballistic ranges. It is rather a special purpose instrument, quantitatively interpretable, and usually applied only to problems selected for careful study.

8 4.1 Optical Arrangement

The usual instrument employed in ballistic ranges (and wind tunnels) is the Mach-Zehnder interferometer. Although other optical arrangements have been used, they are in principle closely related to the Mach-Zehnder, and only the latter will be described here.

Figure 8.34 shows the basic arrangement of optics. Light from a monochromatic source is collimated to produce plane waves, of which half the intensity is reflected upward at the first half-silvered mirror to form the reference beam while the other half passes through the mirror and through the flow field to be examined. The two beams are recombined at the second half-silvered mirror where they may interfere if the instrument is well alined. Note that half the beam energies are lost at recombination. The image forming mirror, provided where the recombined beams emerge from the instrument, is in focus on the plane of the model, so that a sharp shadow image of the model is superimposed on the interference field and refraction effects are minimized.

Although it is not the purpose of this discussion to examine in detail the practical problems of such an interferometer, it must be noted that these problems are considerable. There are problems of the light source and problems of alinement and stability of alinement. (Numerous papers have been written on these subjects – see, e.g., References 8.9 through 8.13). The light source must be of short duration to prevent model motion during exposure. If a high voltage spark is used, its output must be passed through a prism or grating monochromator or an interference filter to select a restricted wavelength region to be admitted to the interferometer. The number of fringes of good contrast depends sensitively on spectral purity of the source. Unfortunately, the bulk of the light output of the source must for this reason be discarded, leaving adequate film exposure a problem, with restrictions on both the duration and spectral band width of the light pulse. Accordingly, some investigators (see e.g., Reference 8.13) have used rotating mirror cameras to hold the image stationary on the film and permit longer durations of exposure. The laser would seem an advantageous light source for an interferometer, being by nature monochromatic and intense. At this writing, no papers describing the use of a laser light source in a Mach-Zehnder interferometer have come to the author's attention, although a novel interferometer employing holographic techniques has been reported (Ref. 8.14).

For discernible interference between the active and reference beams, their wave fronts must be nearly parallel past the recombination of the beams. Alinement of the instrument to achieve this parallelism is affected by all four flat mirrors, the two on the right affecting the active beam; the two on the left, the reference beam. Thus, once alinement has been achieved, the mirrors must be rotated in pairs to retain it. Furthermore, the mirror rotation mechanisms must be capable of very fine and slow motion, and mechanically very smooth to achieve the perfection of alinement required. The alinement is also affected by mechanical vibration and thermal expansion, so that shock mounting and the use of low expansion materials such as Invar are desirable.

To initially aline the mirrors, both physical measurements for rough alinement and use of targets placed ahead of the first half-silvered mirror and viewed in the emergent beams are helpful. Alinement to equalize path lengths in the reference and active legs is needed if the source is not perfectly monochromatic, in which case the fringe contrast diminishes away from the equal-path-length fringe because of the superposition of many sets of fringes of slightly different spacing. For perfectly monochromatic light, the paths do not have to be equal, since interference need not be restricted on recombination to the same plane wave front which was split. That is, any pair of plane wave fronts can be made to interfere, depending only on their relative phase.

8.4.2 Theory of Fringe Formation

If two superimposed trains of plane waves of equal wavelength are perfectly parallel, they will produce a uniform intensity on a screen or film, depending on their phase. If they are in phase, their intensities add; out of phase, their intensities subtract; and intermediate phase conditions give intermediate intensities (Figure 8.35).

If the first beam is slightly inclined to the second, the relative phase of the two families of waves varies across the field. This is shown in Figure 8.36. Constructive interference occurs at intervals, shown by the long dashed lines. Half way between the lines of constructive interference, lines of destructive interference occur. If these wave trains fall on film or a screen, the alternation of bright and dark regions is termed a series of fringes, and the distance from one bright fringe to the next is the fringe spacing, s. From the geometry, it may be seen that when the wave fronts are inclined to one another by an angle ϵ, the fringe lines are inclined at $\epsilon/2$ to the ray directions and

$$\frac{\lambda}{2 \cos (\epsilon/2)} = s \tan (\epsilon/2) \tag{8.31}$$

With small angle approximations appropriate to the actual values of the angle ϵ, this may be written

$$s = \lambda/\epsilon \tag{8.32}$$

For example, with $\lambda = 5000 \overset{o}{A}$ and $s = 0.5$ cm,

$$\epsilon = \frac{5 \times 10^{-5}}{0.5} = 10^{-4} \text{ radians or } 0.0057^\circ ,$$

Thus it is seen that only a minute angularity of the beams is desired (corresponding, e.g., to a rotation of a 20 cm diameter mirror by 10^{-3}cm at its edges), and that small angle approximations for ϵ are indeed valid.

Now suppose that a local patch of one of these wave trains is delayed by having traversed a region of low light velocity. Further suppose, as an example, that this delay puts the wave system locally half a wave length behind its normal position. Locally, then, constructive interference is replaced by destructive, and vice versa

and the fringe pattern is shifted. The bright fringe becomes dark, and the dark becomes bright. Such a shift, when seen, may be interpreted as a phase shift of the wave train by $\lambda/2$ (or more generally, by any odd integral multiple of $\lambda/2$). Generalizing this observation, we may say that when the fringe shift is measured in units of the fringe space, it represents the phase shift in numbers of wavelengths. Thus

$$m = \Delta s/s, \qquad (8.33)$$

where m is the number of wavelengths of retardation of the wave fronts. It will be noted that the same fringe position would occur for all values of m which differ by integers, but if the fringe shifts can be followed from a region of no disturbance to the point in question, then a value can be assigned unambiguously to m.

The fringe shift is measured from the position which the fringe would take in the undisturbed ambient gas. Since this position is not marked in an interferogram of a disturbed flow, it must be determined by interpolation of the fringe positions on either side of the disturbed flow. Now in real interferometers, fringes are not perfectly straight, nor perfectly steady. They tend to swim about a little under the influence of air motion in the room. Hence, some error in measuring fringe shift arises from lack of knowledge of the exact position of the undisturbed fringe. Since the uncertainty will usually be less than one fringe space, it is of most concern when the fringe shifts are also of this order. When fringe shifts of many fringes occur, this source of error is less important.

Immediately behind shock waves, the value of $\Delta s/s$ is not always easy to determine, because the fringe shifts become large and the slopes are steep (see e.g., Figure 8.37). In such cases, one may either grossly reduce the ambient density (in ballistic ranges where ambient pressure may be controlled) to reduce the fringe shift and thus make it easier to trace the fringes, or use so-called white light fringes, obtained with a broader spectral band in the light source, to trace the fringes near the shock wave. With white light, only a few discernible fringes are obtained and the central fringe, because of its sharp contrast with its neighbors, can be readily traced across the flow field.

With the wave retardation determined to be $m\lambda$ from the picture, the remaining task is to make an interpretation in terms of the flow field density distribution responsible for the retardation.

8.4.3 Deduction of Flow-Field Densities

The test data to be analyzed will be either axially symmetric or three dimensional. The axially symmetric case is the easier to analyze, but in experimental practice, it is the harder to achieve, because the free-flight model in general will be at some angle of attack. Thus, for simple interpretation, a companion problem to analyzing the photograph is that of getting the photograph at small resultant angle of attack. One technique which has been used (Reference 8.15) is to place the interferometer station near an expected node in the oscillation (e.g., half a wavelength of the pitching motion from the origin of the pitch disturbance near the gun nuzzle). Spheres comprise a special case. Except near the viscous wake, they will always generate an axially symmetric flow at high supersonic speeds, regardless of attitude.

Let us then describe the procedure for analysis of axially symmetric interferograms*. We use the notation of Figure 8.32, and neglect the bending of light rays traversing the field. (This may not be permissible in all cases, but without this assumption, the analysis cannot be written explicitly. The analysis with ray deflection would necessarily be numerical, but it would proceed similarly to that given below.)

The time for a ray to traverse the flow cross section at the level y above the axis of symmetry is

$$t = 2 \int_0^{z_s} \frac{dz}{c}, \qquad (8.34)$$

where c is $c(z)$. In the absence of flow disturbance, a wave front would advance in the time t a distance $c_1 t$, c_1 being the light velocity in the ambient atmosphere, whereas in the flow field, the wave front advances by $2z_s$. The difference is the distance by which the wave front is retarded by the presence of the flow field.

$$m\lambda = 2c_1 \int_0^{z_s} \frac{dz}{c} - 2z_s \qquad (8.35)$$

The light velocity ratio, c_1/c, may be replaced by the inverse ratio of the indices of refraction, ζ/ζ_1, and ζ may be in turn be written as $1 + G\rho$, so that

$$2c_1 \int_0^{z_s} \frac{dz}{c} = \frac{2}{\zeta_1} \int_0^{z_s} (1 + G\rho)\, dz = \frac{2}{\zeta_1} \left[z_s + G \int_0^{z_s} \rho\, dz \right] \qquad (8.36)$$

---

* We will assume in this discussion that ionization does not occur in the flow and that the index of refraction is determined solely by gas density. If ionization is present, the expressions for index of refraction are modified (see footnote on page 353)

Equation (8.35) thus becomes

$$m\lambda = \frac{2G}{\zeta_1} \int_0^{z_s} \rho \, dz - \frac{2G\rho_1 z_s}{\zeta_1} \, . \tag{8.37}$$

(since $1/\zeta_1 - 1 = -G\rho_1/\zeta_1$). Solving for the integral, we obtain the equation relating the density distribution to the wave retardation.

$$\int_0^{z_s} \rho \, dz = \frac{m\lambda\zeta_1}{2G} + \rho_1 z_s \, . \tag{8.38}$$

Note that ζ_1 in this equation may usually be regarded as unity for practical purposes, and that m is experimentally determined from the interferogram (Equation (8.33)).

Given a density distribution, we can readily calculate $m(y)$ and hence the fringe shift distribution by means of Equation (8.38). The reverse problem – given $m(y)$, calculate $\rho(r)$ – is less convenient to solve. It is referred to in the literature as the Abel integral inversion problem. The usual approach to solution is to approximate the actual density distribution by a large number of linear segments, each linear segment corresponding to a thin annular zone. A second approach which will be described is to represent the density by a power series in r whose term coefficients are to be determined.

To perform the zone approximation solution, we first express the integral in terms of the radial coordinate r as independent variable to take advantage of the axial symmetry.

$$\int_0^{z_s} \rho \, dz = \int_y^{\sqrt{(y^2+z_s^2)}} \frac{\rho r/dr}{\sqrt{(r^2 - y^2)}} \, . \tag{8.39}$$

In this integral, which is performed along a light ray, y is a constant. The upper limit $\sqrt{(y^2 + z_s^2)} = r_s$. We replace the integral with a sum of terms, one for each zone. The subscript i is used to denote the number of the inner boundary of the zone, and $j = i + 1$ represents the number of the outer boundary. The density within the zone is represented linearly by

$$\rho = \rho_i + \frac{\rho_j - \rho_i}{r_j - r_i} (r - r_i) \, . \tag{8.40}$$

The contribution of the zone to the integral represented in Equation (8.38) may be obtained by inserting Equation (8.40) into the integral, it is found to be

$$\int_{r_i}^{r_j} \frac{\rho r \, dr}{\sqrt{(r^2 - y^2)}} = A_i \rho_i - B_i \rho_j \, . \tag{8.41}$$

where

$$A_i = r_j \frac{\sqrt{(r_j^2 - y^2)} - \sqrt{(r_i^2 - y^2)}}{r_j - r_i} - \frac{y^2}{2(r_j - r_i)} \log_e \frac{r_j + \sqrt{(r_j^2 - y^2)}}{r_i + \sqrt{(r_i^2 - y^2)}} \, ,$$

$$\tag{8.42}$$

and

$$B_i = r_i \frac{\sqrt{(r_j^2 - y^2)} - \sqrt{(r_i^2 - y^2)}}{r_j - r_i} - \frac{y^2}{2(r_j - r_i)} \log_e \frac{r_j + \sqrt{(r_j^2 - y^2)}}{r_i + \sqrt{(r_i^2 - y^2)}}$$

Note that y is determined by the location of the ray being analyzed, and r_i and r_j are known numbers for each zone. Hence, the coefficients A_i and B_i are known. The total integral along the ray is the sum of terms similar to Equation (8.41) for each of the zones traversed and may be written

$$\int_0^{z_s} \rho \, dz = \int_y^{r_s} \frac{\rho r \, dr}{\sqrt{(r^2 - y^2)}} = \sum_{i=1}^{N} (A_i \rho_i - B_i \rho_j) \tag{8.43}$$

Here, $i = 1$ at $r = y$, and N is the total number of zones between y and r_s. The value of the integral is obtained from the interferogram through Equation (8.38). Hence, the gas density at one zone boundary may be unknown in Equation (8.43) and be determined from it. This boundary is tangent to the position y of the ray being analyzed. The densities at all zone boundaries outboard of this will have been determined in sequence, progressing from the shock wave inward.

For the calculation to start, the density immediately behind the shock wave must be determined. If the flow field is known to be in chemical and thermodynamic equilibrium, this can be done most simply from a measurement of the shock wave inclination and reference to shock wave tables. If ρ_s is to be determined from the experiment, it is necessary to make a one zone calculation at the shock wave and to assume that $\rho = \rho_s = $ constant within the zone.

This leads to

$$\int_0^{z_s} \rho \, dz = \rho_s \int_y^{r_s} \frac{r \, dr}{\sqrt{(r^2 - y^2)}} = \rho_s \sqrt{(r_s^2 - y^2)} = \frac{m_y \lambda \zeta_1}{2G} + \rho_1 z_s \ . \tag{8.44}$$

from which ρ_s may be obtained. The zone for this determination, $r_s - y$, is chosen thin to minimize the variation of density within the zone. The density determined is more properly plotted at the center of the zone than immediately behind the shock wave.

Tables of coefficients for these calculations, corresponding to (but not identical to) A_i and B_i, have been published in Reference 8.16 for a 50 zone division of the flow field. The use of these tables can make the reduction less laborious. Of course, with modern electronic computers, the labor of this analysis is of less concern than it was formerly.

The series representation method – the second method noted earlier – is calculationally simpler but may present difficulties in cases where the density profile is not smooth. It is analagous to the approach used earlier to obtain expressions for flow deflection angles for schlieren and shadowgraph applications, Equations (8.27) through (8.30). Here, however, we represent the density rather than the density gradient by the power series,

$$\rho = \rho_0 + a_1 r + a_2 r^2 + a_3 r^3 + a_4 r^4 + \dots a_{n-1} r^{n-1} \ . \tag{8.45}$$

Note that in this expression, ρ_0 is the density on the axis of the flow, where $r = 0$, and is fictitious for stations of the flow where the body occupies the axis. Now, since we wish to evaluate $\int_0^{z_s} \rho \, dz$, we put Equation (8.45) in terms of z,

$$\rho = \rho_0 + a_1 \sqrt{(y^2 + z^2)} + a_2 (y^2 + z^2) + a_3 (y^2 + z^2)^{3/2} + a_4 (y^2 + z^2)^2 + \dots \ . \tag{8.46}$$

This expression may be substituted into the integral and evaluated term by term to obtain

$$\int_0^{z_s} \rho \, dz = \rho_0 z_s + \frac{a_1}{2} \left[z_s r_s + y^2 \log_e \frac{z_s + r_s}{y} \right] + a_2 \left[y^2 z_s + \frac{z_s^3}{3} \right] + $$

$$+ \frac{a_3}{4} \left[z_s r_s^3 + \frac{3}{2} y^2 z_s r_s + \frac{3}{2} y^4 \log_e \left(\frac{z_s + r_s}{y} \right) \right] + a_4 \left[y^4 z_s + \frac{2}{3} y^2 z_s^3 + \frac{z_s^5}{5} \right] + \dots \ . \tag{8.47}$$

Now for any given axial station of the flow, r_s may be measured from the interferogram, y is selected by the analyst, and $z_s = \sqrt{(r_s^2 - y^2)}$. Hence, the bracketed multipliers of the coefficients a_1, a_2, a_3, $a_4 \dots$ in Equation (8.47) are known numbers. By choosing a number of values of y for analysis at a given axial station of the flow, we may write Equation (8.47) as many times as we please, with values of the bracketed multipliers appropriate to each value of y chosen. If we write in this way the same number of equations as terms used to define ρ, we may solve these questions simultaneously to define ρ_0, a_1, a_2, etc., and hence obtain a representation of the density profile across the flow field at that station. If we write more simultaneous equations than the number of unknowns, then least squares methods may be used to obtain a best fit.

Although five terms have been retained in representing the density profile above, more or fewer terms can be retained. Sometimes, higher order terms in a series will improve the fit to a few measured points, but introduce physically unrealistic inflections in the curve. When the number of measured points is large, or the data are faired continuously, more terms in the series should be of advantage. This is a matter for study in individual applications. The picture of a slender cone shown in Figure 8.38 has been analyzed by the power series method to obtain the results shown in Figure 8.39 for one and two term approximations. The one term approximation, where density is regarded as constant along each light ray, but variable from ray to ray, already shows the character of the distribution and may be hand calculated very quickly. The one-term densities have been plotted both at y (the location at which fringe shift is measured) and at $(y + r_s)/2$ to bracket the position at which they would be expected actually to occur, and these two curves do indeed bracket the two term approximation. The two term approximation requires data at only two values of y to define a series of values of ρ_0 and a_1, hence was solved locally between every adjacent pair of fringe-shift measurements, of which there were 4 in all, corresponding to the fringes intersected by a plane normal to the model at the station analyzed. The locally derived segments, which are entirely independent, come very near to intersecting and forming a continuous curve. A fairing of these two term solutions is shown by the long dashed curve. The agreement of the two-term solutions and their fairing with conical flow theory is reasonable considering that the model was at an angle of attack at 1.25^0 and that it was the windward side which was analysed. Note that the sensitivity of the interferometer has permitted definition of detail even though the density is only a few percent above ambient.

8.4.4 Reported Applications

Because of the difficulty of the method, both experimentally and analytically, there have been comparatively few applications of interferometry to obtain quantitative density distributions around projectiles in ballistic ranges. There have been several applications to spheres, because the symmetry requirement is satisfied and

because of fundamental interest in flow about spheres. A beautiful interferogram of a 90 mm sphere tested at the Ballistic Research Laboratories at a Mach number of 5.7 and a range pressure of 0.05 atmospheres is shown in Figure 8.40. Results of analyses of the flow field of a sphere have been presented and discussed in References 8.17 and 8.18. It is difficult to achieve accurate spatial resolution in the forward part of the shock layer because it is thin (see especially Figure 8.37). On the other hand, density is slowly changing in this region, so that a high degree of spatial resolution may not be required, except for purposes of detailed comparisons with theory.

Cone flow fields also have been analyzed (Reference 8.19). When cones are slender, their fringe patterns are slowly varying and permit accurate measurement (Figure 8.38). When the cone angle is large, problems are analagous to those of other low fineness ratio bodies. Low ambient densities favor clear identification of fringe shifts, but may introduce non-equilibrium flow effects. These were the subject of study in Reference 8.20 which, while it was a study in an expansion tube, could equally have been performed in a ballistic range. Cones may be used to test the validity and accuracy of the analysis procedure and the instrument, since a wide range of theoretical solutions is available.

Interferometry has also been used to investigate density profiles in turbulent boundary layers on models in a ballistic range (Reference 8.15). Long conical and ogive-cylinder models were selected to maximize the boundary layer thickness, and precautions were taken to minimize the angle of attack at the interferometer station. Figure 8.38 is an interferogram from this investigation, and Figure 8.41 shows an enlargement of fringes in the boundary layer. The boundary layer fringe shifts are appreciable and indicate the presence of density variations associated with turbulence. The boundary layer fringes were analyzed assuming axial symmetry (which, because of the fluctuations, does not precisely obtain), and both the mean density profiles and the fluctuation levels were determined. It was also possible, with the aid of an energy balance, to deduce the heat transfer rate to the model from the measurements.

8.5 RESEARCH APPLICATION OF SHADOWGRAPH AND SCHLIEREN PICTURES

Now let us review some of the ways shadowgraph and schlieren photographs have been used in research in ballistic ranges, and thereby indicate how they may be used, in a general sense. The discussion which follows is organized under eight topics - Shock Wave Location and Shape, Boundary Layer Transition and Turbulence, Separated Flow, Base Flow Configuration and Base Pressure, Wakes, Determinations of Local Mach Number and Static Pressure, Density Ratios and Non-Equilibrium Flow, and Additional Phenomena (outside the other categories). A logical place to begin is with the most prominent features of supersonic flow fields, the shock waves.

8.5.1. Shock-Wave Location and Shape

From what has already been said, it is clear that the shock wave may be located in a shadowgraph or schlieren picture from the position of the last undisturbed light ray upstream of the wave, i.e., the ray tangent to the shock wave envelope. Measurements of the coordinates of a series of points along the bow shock wave require correction only for any magnification that may be present (or, in parallel light systems deviations of rays from perfect parallelism). Measurements of this kind have been used to test theoretical calculations of shock wave shape, and as inputs to the computation of downstream flow fields[8.21]. It has been found from such measurements that bow shock waves can often be well represented by power law expressions of the form $y = kx^m$, or by connection of a series of such expressions[8.22].

A second important property of bow shock waves is the stand off distance from blunt bodies, or the analagous property for cones, the stand off angle. This distance or angle may be directly measured from the above-noted criterion for location of the shock surface, but may be significantly in error if refraction in the shock layer distorts the location of the body surface. This error is minimized by (a) focusing the shadowgraph on the plane of flight, and (b) operating at low air densities. It may also be corrected by theoretical analysis of the emergent angle of the light ray tangent to the body surface. Particularly obvious errors will occur when the dark and light bands produced at the wave extend across the shock layer and overlap the model (Figure 8.6(c)). No useful measurement can be expected in such a case. For highest accuracy, correction for diffraction at the shock and model surfaces may be required. To illustrate that a useful degree of accuracy can be obtained without the latter corrections, but with the restriction of shadowgraph sensitivity and air density to give favorable conditions for such measurements, Figure 8.42 is reproduced from Reference 8.23.

In addition to bow shock waves, secondary or embedded shock waves are of significant interest. An example is the shock wave generated on a flared afterbody (Figure 8.43) or other stabilizing or control surface. From the standpoint of configuration aerodynamics, it is important to know the flow configuration, since the forces and stability are sensitive to the shock waves present. Since the light rays recording embedded waves traverse the bow shock wave and intervening density field, distortions of positions can be expected. The locations of embedded shock waves relative to adjoining body surfaces, however, should be recorded fairly accurately, since the distortions to the absolute location of the shock surface and body surface due to the surrounding flow field are similar.

Interest may also be directed to the interference of shock waves with downstream body surfaces. For example, when a bow shock wave impinges on or passes near the location of a body surface, the bow wave may be deflected (strengthened), as in Figure 8.44. Actually, in this case there is an intersection of the bow wave with an embedded shock wave, and reflection of the embedded wave off the bow wave may be observed. Also, emerging from the intersection, a discontinuity streamline appears and undergoes transition to turbulence. The embedded wave

is not formed on the leeward surface of the flare. In this example, the wave interaction occurs because of angle of attack, but on appropriate configurations, it may occur at the equilibrium flight attitude. Flow photographs document the occurrence and give details of the resulting flow configuration.

Figures 8.43 and 8.44 were obtained as part of the investigation reported in Reference 8.24.

8.5.2 Boundary-Layer Transition and Turbulence

A very rich and interesting use of shadowgraphs has been the observation and investigation of boundary layer transition phenomena. Under favorable conditions, this method of detecting transition is of great value, giving information not available from methods traditionally applied in wind tunnels. The optical method, developed in ballistic ranges, has therefore found application in wind tunnels also.

The visibility of turbulence in shadowgraphs, e.g., Figures 8.13 and 8.16, implies that the place where turbulence begins, the laminar-turbulent transition location, should be observable. However, since the turbulent boundary layer may be initially very thin, the question arises as to whether it can be detected in its early stages – i.e., the eddies might be initially too small to observe within the limits of diffraction at the model edge, film grain, etc.

Experience has shown[8.25, 8.26] that thin turbulent boundary layer conditions can occur under which discrete eddies cannot be individually identified. Under these conditions, however, the eddies collectively still give characteristic appearance to the boundary layer, and in addition may give indirect evidence of their presence by generating a field of sound waves which can be seen in the adjoining flow (see, e.g., Figure 8.45). Note in this figure that the noise field is bounded by a Mach wave at an inclination appropriate to the boundary layer edge Mach number. Tracing this wave to its point of origin identifies the forward limit of the boundary layer region which is generating a noise field. It may be assumed that this point is the instantaneous point of boundary layer transition.

The transition point obtained from such an observation may be compared with that given directly by the appearance of the thin turbulent boundary layer. In regions where discrete eddies cannot be resolved, models with thin turbulent boundary layers have been described as having a "hairy" appearance along their edges[8.25] (Figure 8.46). When the eddies are small, the density gradients are very large, and light may be refracted to much greater distances than the eddy diameter. Thus, in Figure 8.46, we see shadow filaments projecting well outside the boundary layer along the model's forward surfaces, beginning near the tip. A glance at the model base region leaves no doubt that the boundary layer is turbulent as it comes off the base. A sound field from the boundary layer can also be seen within the shock layer. If the limits of the hairy region coincide with the limits of the noise generating region, confirmation of two independent techniques for locating transition has been obtained.

A further test can be applied to the selected location of boundary layer transition on long models which attain appreciable boundary layer thickness. From selected individual photographs, one can measure the boundary layer thickness and plot it against streamwise distance on logarithmic paper to obtain, ideally for conical and cylindrical models, a straight line growth curve (see Reference 8.15 for plots of this kind). Extrapolation forward to the point where the theoretical laminar boundary layer thickness is matched will yield a transition point estimate which can be compared with the other two determinations.

It was implied above that the instantaneous location of transition to turbulence is time dependent. This is indeed the case. Views of the same model meridian in successive photographic stations generally show different locations of transition, and may also show the presence of short duration bursts of turbulence (Figure 8.47). These may proceed separately along the surface, precede a steadier turbulent boundary layer, or be superimposed on other bursts or on the steadier turbulent boundary layer. The mean location of transition may furthermore differ on different meridians, because of the presence of microscopic roughness elements along those meridians. Angle of attack also, for slender bodies, has a first order, determining influence on transition. Thus, no single picture can be taken as definitive of the boundary layer transition on a given model flight. Rather, the effects of unsteadiness, meridianal differences (due to surface roughness or tip asymmetry), and angle of attack must be carefully isolated in a series of pictures, normally requiring a series of test firings. The unsteadiness by itself leads to a region of intermittently laminar and turbulent boundary layer which has been identified, from ballistic range studies and from hot wire anemometer studies in wind tunnels, as the transitional boundary layer zone defined by other, time-averaging techniques of observing transition (see, e.g. Reference 8.26).

The fact that the noise-field-bounding Mach line may have a slope appropriate to the boundary layer edge Mach number indicates that the transition point generating this field is at least momentarily stationary, or moving slowly on the surface. In the case of bursts, however, the shock wave attached to their leading edges is seen to be much steeper than the stationary disturbance Mach angle, because bursts are in rapid movement backward along the surface. The slope of the wave may be used to determine the speed of movement of the upstream edge of the burst down the surface, which is found to be about 6/10 of the boundary layer edge velocity. It has also been found possible to define the shapes of bursts in profile and plan view from their shadowgraph images[8.27]. The profiles were obtained by careful thickness distribution measurements, while the plan dimensions were deduced from bursts wide enough to appear on two or more of the four visible meridians in simultaneous orthogonal shadowgraphs. Correlation of the measurements of a large number of bursts was necessary in order to arrive at a representative definition of shape. The shapes obtained by this technique were found to relate closely to shapes previously determined by other techniques in wind tunnels. The growth patterns of bursts were also deduced by relating size to distance from the model leading edge or from the observed disturbance point responsible for the bursts.

The measurement of turbulent boundary layer thickness from shadowgraphs is seemingly straightforward, except for difficulties posed by the irregularities of its outer edge, but it is also subject to certain optical inaccuracies. The edge irregularities, illustrated in the preceding figures, are an inherent feature of the turbulent boundary layer. The thickness at a given point and at a given instant is sharply defined, but like the transition point, the thickness at any station varies with time, and can be fully described only statistically. The simplest statistical approach is to measure the actual thickness at a large number of positions along the surface, plot these measurements, and let the eye fair a mean line. Whether a more formal approach is justified will depend on the quantity and quality of the data available.

Distortions of the boundary layer thickness recorded on film have been discussed earlier. They may arise from three sources: (a) eddy refraction, causing the eddy images to be larger or smaller than their actual diameters. (b) refraction in the steep density gradient of the inner part of the boundary layer, causing the model edge to be displaced. (c) refraction through the surrounding flow field, causing a (nearly equal) displacement of the boundary layer edge and the model edge. Of these three contributions, the third seems to be of least concern, being nearly self compensating. The second can be of major concern, as noted earlier. The first source of distortion, due to eddy refraction, can only be evaluated theoretically, or by comparison of boundary layer thickness measurements obtained with those given by a different measuring technique. Such comparisons are necessary if the measurements are to be regarded as more than a rough indication of the boundary layer thickness.

Additional features of the structure of the steady state turbulent boundary layer may be observed in shadowgraph pictures. The correspondence between the theoretical image of an eddy and the spot patterns seen in turbulent boundary layers has been noted in an earlier section. Close study of these patterns reveals that the spot images are nearly of uniform diameter for a wide variety of test conditions, and that they are arrayed in single file order during early stages of boundary layer growth (to Reynolds numbers of 10^7) (Reference 8.15). When the boundary layer thickness begins to exceed the diameter of a single spot, the spots are found in staggered rows, two deep. This process develops until as many as five spots are seen across the thickness of the boundary layer. At this stage, one can find repeated patterns where the spots are arrayed in slanted lines, inclined to the surface at about 45° (Reference 8.15). These configurations are thought to be related to "horseshoe vortices" reported from studies of low speed boundary layers by other visualization techniques, and which are also inclined to the surface in this way.

The use of flow visualization for transition and turbulent boundary layer studies is, of course, limited to favorable optical and fluid dynamic conditions. First of all, the Reynolds numbers must be large enough to generate turbulent flow (greater than about 10^6). In addition, the model to be studied must be large enough to develop appreciable boundary layer thickness (which is roughly proportional to the 0.8 power of the length of run along the model), since observation of thin boundary layers is difficult and may not be definitive. Third, shock waves should not lie so close to the body surface as to obscure a clear view of the boundary layer (studies of slender pointed bodies at very high speeds encounter difficulty in this respect). Fourth, the gas densities must be high enough to produce appreciable eddy refraction (note that this requirement is usually satisfied if the first requirement is satisfied). At low subsonic speeds, shadowgraph visualization of turbulence tends to be lost because the density gradients are small in low speed flow. Thus, the technique is not universally available. However, when it can be applied, it is a very powerful and informative one.

8.5.3 Separated Flow

Flow separation on ballistic range models is often associated with stabilizers, such as conical flares, forward facing steps (e.g., Figure 8.18), or backward facing steps, of which the blunt base is an almost universally present example. The photographic indications of flow separation are: (a) the boundary layer image may be seen to leave the surface. (b) An oblique shock wave may be formed by the turning of the external flow at the separation point. (c) Reattachment phenomena, such as additional shock waves or gathering compressions, may be seen at a reattachment point.

The details seen differ, depending on whether the boundary layer approaching the separation point is laminar (Figure 8.48) or turbulent (Figure 8.49). When it is turbulent, the separated region is conspicuously filled with turbulent eddies. When it is laminar, the shadowgraph image of the separated boundary layer appears as a smooth line bounding the separated region. Such a line is clearly visible on the bottom side of the model in Figure 8.48, extending from a separation point ahead of the midlength station of the model to a reattachment point near the center of the flare. The separation shock wave is weak but discernible, while the reattachment shock wave is stronger, and replaces the embedded wave which would, in the absence of separation, originate at the flare-cylinder intersection. (The background of turbulence in this picture comes from the boundary layer on the windows of the Supersonic Free-Flight Wind Tunnel, a counterflow facility where the photograph was obtained).

Another type of separation results from the inability of a flow to negotiate a convex corner; this type of separation is frequently seen at the sharp or slightly rounded corners of the face of blunt bodies. This is illustrated clearly at the outermost corner of the step in Figure 8.18. The thick turbulent region behind th' corner clearly indicates separation. Separations of this kind are often, unlike Figure 8.18, very local, with reattachment occurring immediately behind the corner, accompanied by a reattachment shock wave. Laminar separated regions of this kind are sometimes so thin that their presence can be definitely determined only from the presence of the reattachment shock wave. Figure 8.10 shows a very strong reattachment shock wave in a case where the separated streamline can be clearly seen.

8 5 4 Base-Flow Configuration and Base Pressure

Shadowgraph pictures contain a wealth of descriptive information on the configuration of base flows (see, e.g., Figures 8 16, 8.17, and 8.19). When a model terminates in a bluff base, the flow must expand to reoccupy the full cross section behind it. This process begins in a Prandtl-Meyer expansion fan at the base corner. As noted earlier, in the section on images of flow features and as may be seen in these pictures, the first and last Mach line of the expansion fan are made visible by the shadowgraph. The flow is turned toward the axis by the expansion, and the laminar (Figure 8 16) or turbulent (Figures 8.17 and 8.19) boundary layer coming off the model becomes the boundary of the dead air (separated flow) region behind the base, and leaves its image in the picture. If transition occurs along this boundary, that may be seen (Figure 8.16). The inward directed flow must be turned parallel to the main flow direction again, and this is accomplished in a compression region – usually not a single, discrete oblique shock wave. The multiple shock waves of the compression soon coalesce into a single shock wave, however. The boundary layer passes through a minimum section, usually termed the neck of the wake, near the region of origin of this closing shock wave. Beyond the minimum section, the boundary layer air and air subsequently entrained by it comprise the viscous wake.

Besides the conspicuous differences between laminar and turbulent base regions due to the visibility of turbulence, systematic differences in flow geometry also are found. Since turbulent boundary layers involve more mass flow, they tend to have a larger diameter wake neck at a given Reynolds number, and furthermore, the distance downstream from the base to the minimum section is different (Figure 8.50). (These two pictures were obtained at nominally equal test conditions. Differences in the boundary layer and wake were a result of microscopic differences in roughness and symmetry of the model tip. The different flow configuration is accompanied by a difference in base pressure).

The downstream distance to the neck is sensitive also to Reynolds number, particularly with laminar flow. At very low Reynolds numbers, the wake may actually be initially divergent. The angle of convergence of the wake is, in addition, Mach number dependent, becoming smaller at low Mach numbers, and slightly divergent under some subsonic flow conditions. This tendency for initial divergence at low supersonic Mach numbers is illustrated by Figure 8.18.

Although a low speed recirculating flow exists in the dead air region (and in separated flows generally), no evidence of this is provided in the shadowgraphs. An interesting phenomenon which is made visible is the formation of streamwise vortices in the separated laminar boundary layer, as an intermediate stage of transition to turbulence. Attention has already been called to these vortices, marked by dark cores bounded by light edges, in the base region of Figure 8.16. They can also be seen in the upper picture of Figure 8.50.

We can fully explain the lines bounding the Prandtl-Meyer expansion fans on the basis of earlier sections on particular flow features and diffraction effects. For example, the final Mach line of the fan is located along the inner boundary of the dark (unexposed) band (Figure 8.12). Diffraction may contribute a light fringe along this boundary of the band, to give it the appearance of a shock wave. It is believed that this pattern has in some cases led to discussion of a "lip shock wave" in the literature. It is, however, possible for a weak shock wave to form along an initially curved edge of the separated flow region, and shock waves may, in some instances, occur there.

The base pressure can be estimated from the image of the flow configuration by two independent methods. The first is based on a measurement of the angle through which the streamlines turn in coming off the model base to the direction of the boundary layer image behind the base [8,28]. This method has been applied in the example of the preceding Chapter. The boundary layer line image is considered the boundary for an inviscid Prandtl-Meyer expansion. (This may be in error to the extent that the boundary layer affects the expansion). The pressure and Mach number preceding the expansion are required, but for cones, e.g., these are readily available from theory. The measured turning angle may be used to enter tables of Prandtl-Meyer flow (e.g., for perfect air, Reference 8.29), to determine the pressure after expansion – the boundary pressure of the base region*. Since flow velocities in the dead air region are small, it is presumed that no large pressure difference can exist within it.

The second method requires measurement of the Mach angle after expansion, the angle between the final Mach line of the expansion and the streamline direction as given by the boundary layer image. From the Mach angle β, the local Mach number M may be calulated (sin $\beta = 1/M$). The ratio of local (base edge) static pressure to total pressure p/p_t is a function of the Mach number, available in tables for both perfect and real gases. Since the flow may be assumed isentropic except at the shock waves, the total pressure is calculable (for streamlines near the body surface) from the flow tables and shock wave tables, given the shock wave slope at the model apex. Hence, the base edge pressure may be computed. An advantage of this method is that it does not require knowledge of pressure and Mach number on streamlines approaching the model base, and hence may be applied in cases where theoretical solutions for the forebody flow field are not available.

8 5 5 Wakes

The visibility of turbulent wakes has been evident in many of the pictures discussed thus far. These pictures invariably show turbulent spot patterns, the spots being of remarkably uniform size. The grouping of the spot patterns into turbulent clusters gives irregularity to the edge of the wake, which, in many pictures, is strongly suggestive of a helical or "corkscrew" pattern.

* Although the expansion becomes three dimensional some distance away from the corner, it may be considered two-dimensional at radial distances from the corner small compared to the body base radius. To make the use of two-dimensional tables valid, then, it is necessary to measure the angles as close to their initial values as practicable. It is also emphasized that optical distortion of these angles can be present, as car flow distortion by the boundary layer.

Laminar wakes downstream of the trailing shock wave have not been seen as often in routine ballistic range testing because at the Reynolds numbers associated with fractional atmosphere ambient pressure, the boundary layer is seldom stable enough to run along the separated flow region and pass through the trailing shock wave system and remain laminar.

Interest in wakes very far downstream has been stimulated by observations of entry vehicles coming into the atmosphere, which may leave ionized trails thousands of feet long. A number of techniques have been applied in ballistic ranges for measuring the properties of these wakes. (Some are described in Chapters 10 and 11). Two areas of interest have been served by studies employing optical examination of wakes in shadowgraph and schlieren pictures. These are the Reynolds number of laminar-turbulent transition in the wake (at very low body length Reynolds number); and the rate of growth of wakes in the far downstream region.

For the study of these problems, the firing of the light source may be delayed until the model has traveled a desired distance (as much as 10^2 to 10^4 diameters) past the photographic station. Alternatively, the last station in the range may be used to trigger all the stations simultaneously to record the instantaneous config-uration at a series of positions along the wake[8.30]. The turbulent wake "diameters" measured from shadowgraphs are, of course, irregular and must be interpreted statistically.

The laminar wakes produced at very low range pressures (order of 0.01 atmosphere) are visible only in highly sensitive optical systems. Double pass schlieren systems have been used to make these flows visible. Figure 8.30 is one such picture, obtained with the knife edge horizontal, at a body length Reynolds number of about 60,000. First indications of transition appear about 10 diameters downstream of the base of the $12\frac{1}{2}^\circ$ half-angle cone. Although the base flow pattern is not strongly convergent, a trailing shock wave originates near the wake neck about 2 diameters behind the base. The rate of growth of the wake is seen to be slow within the region covered, and it appears that approximate measurements of the rate of growth of the laminar wake could be obtained from pictures of this kind. The experimental conditions of this photograph are further discussed in Reference 8.31.

8.5.6 Determination of Local Mach Number and Static Pressure

Whereever Mach wavelets are generated by body-fixed disturbances and recorded in flow pictures, e.g., Figure 8.51, especially on the upper surface of the sphere, it is possible to determine both the local Mach number and static pressure near the body surface. The local Mach number is determined from the angle β between the Mach wave and the local streamline direction, which at the surface is tangent to the body, by the well known relation-ship between Mach number and Mach angle, $M = 1/\sin \beta$. The static pressure may be calculated from the local Mach number with the assumption that the flow is isentropic except in passing through shock waves. (The effect of the shock waves on flow total pressure is calculable from shock wave theory, see, e.g., Reference 8.32, from the slopes of shock waves traversed by streamlines near the body surface).

To generate such Mach wavelets, shallow grooves may be machined on the body at selected locations. To avoid undue disturbance to the flow, they should be of the minimum depth needed to generate a visible wave. From a properly distributed set of these grooves, surface pressure distributions may be derived.

The Mach waves may remain visible well away from the surface where, in general, they become curved. If the stream direction and points of streamline crossing of the shock waves are known for off-surface locations, local Mach number and static pressure are, again, defined. A few streamlines may be marked by intersection with the bow wave of shock waves generated by accidental or purposely located disturbance generators near the model nose. The combination of marked streamlines and Mach waves would make it possible to obtain a considerable definition of the flow field surrounding a body, particularly a slender body at moderate supersonic Mach number.

In the past, these techniques have been used only occasionally to determine base pressures and surface Mach numbers at isolated points. They would seem to be capable of much more, in principle providing a way of obtain-ing from ballistic ranges information normally conceded to be outside their measurement capabilities.

8.5.7 Density Ratios and Non-Equilibrium Flow

Three techniques have been identified for determining indirectly the density ratios across bow shock waves. Two of these have been applied[8.33, 8.34]. Through comparison of the density ratios determined with equilibrium values given by theory, the presence of non-equilibrium flow can be investigated. One technique, limited to conical flow fields, is capable of giving relaxation times for non-equilibrium processes.

A technique applicable to blunt nose bodies, originally described in Reference 8.33, is based on the depen-dence of bow shock wave stand off distance on the density ratio at the shock wave in the stagnation region. (For spherical noses, the relation $\delta/R = 0.78(\rho_1/\rho_2)$ has been established as accurate within a few percent[8.23, 8.35]. Here, R is the body nose radius of curvature and ρ_1/ρ_2 the ratio of ambient to shock layer density in the stagnation region). Measurement of the stand-off distance of spherical-nosed bodies may thus be interpreted to define stagnation region gas density. Comparison of densities determined with those tabulated theoretically for chemical and thermodynamic equilibrium behind the shock wave (e.g., Reference 8.36) will indicate whether equilibrium is attained in the experiment. Calculations can also be made of density ratios with some of the degrees of freedom equilibrated to provide further interpretation of what is observed.

A related technique, applicable to shock waves on cones, can be used to determine relaxation times[8.34], [8.20]. In this case, it is the angular separation of the bow shock wave from the model face - the stand-off angle - which depends on the density ratio. The initial wave angle at the tip is determined by the unrelaxed gas and is therefore larger than the equilibrium angle. At large enough distances from the apex for the bulk of the flow in the shock layer to have equilibrated, the wave slope becomes asymptotic to the equilibrium slope. At low ambient pressures, equilibration may never occur within the physical length of the model, while at high ambient pressures, the non-equilibrium zone may be very local, confined to the region of the tip, and may not be observable. The intermediate regime, where shock wave curvature may be visible and measurable, leads through theoretical interpretation to the relaxation time[8.34].

Still another technique for determining density ratio is the measurement of the dark band width of the shock wave in shadowgraphs, discussed in an earlier section. This is directly an optical technique, since the index of refraction in the shock-compressed gas is the property determined, and is directly related to gas density (for velocities at which ionization may be neglected). When ionization becomes the dominant process affecting the index of refraction, experimental studies of the degree of ionization immediately behind the wave could concievably be approached on this same basis.

8.5.8 Additional Phenomena Sometimes Seen in Shadowgraphs

There are many interesting and informative phenomena seen occasionally in shadowgraph pictures which do not fall under the above headings. We will mention and show examples of some. These include evidences of high frequency oscillations in otherwise steady flows, unusual configurations in base flows; evidences of model damage, deformation, burning in flight, or surface spalling; and evidences of soot particle condensation from products of ablation of organic model materials.

High frequency oscillations have been recorded emanating from shallow spanwise or circumferential V-grooves, machined near model leading edges to act as boundary layer trips. An example occurs near the wing leading edge of the airplane model in Figure 8.52. There were several grooves a few thousandths of an inch deep machined parallel to and near the wing leading edge. The oscillation indicated by the train of waves coming from this vicinity, at a frequency of the order of 250 kilocycles/second, is believed to result from correlated pulsating flow into and out of the grooves. (The trip was effective in starting turbulence at a chord Reynolds number less than 10^6).

Unsteady waves have also been recorded in the stagnation region of blunt body shock layers[8.37], [8.38], in the absence of grooves or other intentionally placed roughness. These waves (e.g., Figure 8.53) are less regular than the waves of Figure 8.52, and their origin is uncertain. They are not always seen in such flows. One possible cause is unsteadiness of boundary layer transition. Another is minute grooves left on the surface in machining and polishing. It is not difficult to imagine oscillations rebounding across the thickness of the shock layer, compressions reflecting as compressions off the solid surface and as expansions off the shock surface, once a source of initial disturbance has been introduced[8.39].

An example of a very regular boundary layer transition process in the base flow of a blunt body is shown in Figure 8.54. Transition occurs at a nearly constant station around the wake periphery, and evidences of vortices transverse to the flow are presented by line images spanning parts of the base region. The profile views of these vortices, seen at the outer boundaries of this station of the wake, appear as small black cores. Pictures presented in this chapter have shown the diversity of processes by which laminar boundary layers become turbulent.

Experimenters will always inspect their shadow pictures closely for model damage, which may range from catastrophic to minute. Supersonic flow over a surface helps provide evidence of minor damage, such as upset joints, by generating Mach waves where the surface is not smooth and continuous. Note that the model in Figure 8.17 shows joint imperfections both at a forward station on the cylinder and at a station near the base of the flare, both of which are so small as to be almost imperceptible in the model shadow image. Figure 8.55, while not of very general significance, presents the intriguing picture of a model being pulled apart in flight by the drag force on the flare. The friction available on the nose plug was not sufficient to provide the incremental force needed to give the heavy nose the same deceleration as the drag force gave to the complete model.

Three kinds of model surface reaction to its thermodynamic environment are recorded in Figures 8.56 through 8.59. The model in Figure 8.56 had a titanium nose which was ignited in flight by aerodynamic heating and it burned chemically as it flew. The image of the flame was recorded as a bright streak exposure in the focused shadowgraph. Other models in this series were flown at the same conditions without igniting. The phenomenon in Figure 8.57 has been seen many times when heating rates become very large (greater than 10^4 watts/cm^2). Surface spalling is apparently induced in some materials at these rates, and small particles are explosively ejected from the surface to fly momentarily as small companions to the test model. The spalling has been observed to be continuous throughout the flight and surface erosion is clearly evident in later pictures. More intense spalling or material ejection is represented in the photograph of Figure 8.58. Here, the ejections are so large and frequent that the contour of the shock wave is affected over the entire field of view. Gas evolution may be the principle phenomenon here, since no clear evidence of large solid particles appears. Figure 8.59, shows a dark shadowed wake and is typically obtained when carbon-rich organic materials, such as polycarbonates (trade names - Lexan, Zelux), are used for models[8.40]. This wake is brightly luminous when scanned with radiometer instrumentation such as is described in Chapter 9, and has a grey body spectrum, at a temperature of about 4000°F, with molecular bands superimposed. The partial opacity in the shadowgraph, the grey body spectrum, and the high atom ratio of carbon in the material have indicated that carbon condensation occurs to form minute soot particles in the ablation products in the wake[8.40].

The above discussion is not comprehensive, but it suggests the nature of the many interesting, miscellaneous phenomena which occasionally appear in high speed flow pictures.

8.5.9 Correlation of Shadowgraphs With Other Data

The strongly supportive nature of what is seen in shadowgraphs and what is measured with other techniques needs little additional emphasis. For example, it is evident that if a change in Reynolds number changes the base region from laminar to turbulent, a change in drag coefficient is to be expected. If the location of transition to turbulent flow changes from test to test under similar flight conditions, the skin friction coefficient and drag coefficient may show significant changes[8.41]. If two model flights exhibit considerably different flow separations near the stabilizer, then their stability coefficients will probably differ. If a shock wave comes near to a body surface above a given angle of attack, non-linearity of the aerodynamics may follow. The interplay and correlation of shadowgraph study with other measurement techniques in ballistic range testing is continual. It is one of the more powerful aspects of the use of ballistic ranges for study of aerodynamics and fluid mechanics.

REFERENCES

8.1   Mach, Ludwig   *Further Research on Projectiles.* Kaiserlichen Akademie der Wissenschaften, Wien, Sitzungsberichte, 1896, pp.605-633.

8.2   Boys, C.V.   *Photography of Flying Bullets.* Journal of Photographic Society of Great Britain, April, 1892.

8.3   Holder, D.W.   *Optical Methods for Examining the Flow in High-Speed Wind Tunnels.* Agardograph 23, North, R.J.   November, 1956.
       Wood, G.P.

8.4   Seiff, A.   *Experimental Investigation of the Drag of 30°, 60°, and 90° Cone Cylinders at Mach*
       Sommer, S.C.   *Numbers between 1.5 and 8.2.* NACA Research Memorandum RM A52A14b, 1952.

8.5   Keenan, P.C.   *The Measurement of Densities in Shock Waves by the Shadowgraph Method.* NAVORD
       Polachek, H.   Report 86-46, 1946.

8.6   Strong, John   *Concepts of Classical Optics.* Published by W.H.Freeman and Co., 1958.

8.7   Briggs, R.O.   *Instrumentation of the Ames Supersonic Free-Flight Wind Tunnel.* NACA RM A52A18,
       Kerwin, W.J.   April, 1952.
       Schmidt, S.F.

8.8   Slattery, R.E.   *Some Instrumentation Techniques Used at the Re-Entry Simulating Range.* Inter-
       Clay, W.G.   national Congress on Instrumentation in Aerospace Simulation Facilities, September, 1964.

8.9   Zobel, T.   *Entwicklung und Bau eines Interferenzgerates zur optischen Messung von Dichtefeldern.* Available in translation as NACA TM 1184, 1947.

8.10   Winkler, E.H.   *Analytical Studies of the Mach-Zehnder Interferometer.* Parts I and II, NOL Reports 1077 and 1099, U.S. Naval Ordnance Laboratory, 1950.

8.11   Bennett, F.D.   *Effect of Size and Spectral Purity of Source on Fringe Pattern of the Mach-Zehnder Interferometer.* BRL Report No.742, October, 1950; also in J.Appl. Phys.22, 776, 1951.

8.12   Sleator, D.B.   *Monochromatic Light Source for Interferometry of High-Speed Gas Flows.* BRL Memoran-
       Bergdolt, V.E.   dum Report 594, April, 1952.
       Bennett, F.D.

8.13   Rowe, R.L.   *Interferometers for Hypervelocity Ranges.* Instrument Society of America Transactions. January, 1966.

8.14   Heflinger, L.O.   *Holograph Interferometry.* J. Appl. Phys., Vol.37, No.2, February, 1966.
       Wuerker, R.F.
       Brooks, R.E.

372

8.15   Seiff, A.   *An Investigation of Supersonic Turbulent Boundary Layers on Slender Bodies of Revo-*
        Short, B.J.   *lution in Free-Flight by Use of a Mach-Zehnder Interferometer and Shadowgraphs.*
                          NACA TN 4364, September, 1958.

8.16   Ladenburg, R.   *Interferometric Study of Supersonic Phenomena.* NAVORD Report 69-46.
        Van Voorhis, C.C.
        Winckler, J.

8.17   Sidney, R.   *Ballistic Missiles and Space Technology.* Pergamon Press, Vol.II, London, 1961, p.337.
        Kahl, G.D.

8.18   Bradley, J.W.   *An Interferometric Study of a ¼ Inch Sphere at Mach 9.66 in Air.* BRL MR 1665, June,
        Oskay, V.   1965.
        Patchell, J.R.

8.19   Giese, J.H.   *Interferometric Studies of Supersonic Flows About Truncated Cones.* BRL R 830,
        Bergdolt, V.E.   September, 1952.

8.20   Spurk, J.H.   *Interferometric Measurement of the Nonequilibrium Flow Field Around a Cone.* BRL
        Bartos, J.M.   Report No.1333, August, 1966.

8.21   Seiff, A.   *Calculation of Flow Fields From Bow-Wave Profiles for the Down-stream Region of*
        Whiting, E.E.   *Blunt-Nosed Circular Cylinders in Axial Hypersonic Flight.* NASA TN D-1147, November,
                          1961.

8.22   Seiff, A.   *A Correlation Study of the Bow-Wave Profiles of Blunt Bodies.* NASA TN D-1148,
        Whiting, E.E.   February, 1962.

8.23   Seiff, A.   *Recent Information on Hypersonic Flow Fields.* Gas Dynamics in Space Exploration,
                          NASA SP-24, December, 1962.

8.24   Kirk, D.B.   *Free-Flight Tests of a Blunt-Nosed Flare-Stabilized Body at Speeds to 8.2 Km/Sec.*
        Chapman, G.T.   J. of Spacecraft and Rockets, Vol.3, No.3, March, 1966, p.374.

8.25   Seiff, A.   *Some Experiments at High Supersonic Speeds on the Aerodynamic and Boundary-Layer*
        Sommer, S.C.   *Transition Characteristics of High-Drag Bodies of Revolution.* NACA RM A56I05,
        Canning, T.N.   January, 1957.

8.26   Jedlicka, J.R.   *Experimental Determination of Boundary-Layer Transition on a Body of Revolution at*
        Wilkins, M.E. $M = 3.5.$ NACA TN 3342, 1954.
        Seiff, A.

8.27   James, C.S.   *Observations of Turbulent-Burst Geometry and Growth in Supersonic Flow.* NACA TN
                          4235, April, 1958.

8.28   Charters, A.C.   *Determination of Base Pressure From Free-Flight Data.* Ballistic Research Laboratory
        Turetsky, R.A.   Report 653, March, 1948.

8.29   *Equations, Tables, and Charts for Compressible Flow.* Ames Research Staff, NACA
                          Report 1135, 1953.

8.30   Murphy, C.H.   *Growth of the Turbulent Wake Behind a Supersonic Sphere.* BRL Memo Rep.No.1388,
                          February, 1962.

8.31   Slattery, R.E.   *Physics of Fluids.* Vol.5, 1962, P.849.
        Clay, W.G.

8.32   Liepmann, H.W.   *Introduction to Aerodynamics of a Compressible Fluid.* Galcit Aeronautical Series,
        Puckett, A.E.   John Wiley and Sons, Inc., New York.

8.33   Schwartz, R.N.   *Shock Location in Front of a Sphere as a Measure of Real Gas Effects.* NAVORD Rep.
        Eckerman, J   3904, February, 1955.

8.34   Stephenson, J.D   *A Technique for Determining Relaxation Times by Free-Flight Tests of Low-Fineness-*
                          Ratio Cones, With Experimental Results in Air at Equilibrium Temperatures up to
                          $3440^o K.$ NASA TN D-327, September, 1960.

8.35   Inouye, M.   *Blunt Body Solutions for Spheres and Ellipsoids in Equilibrium Gas Mixtures.* NASA
                          TN D-2780, May, 1965.

8 36   Wittliff, C.E.   *Normal Shock Wave Parameters in Equilibrium Air.* Cornell Aero. Lab. Rep. CAL-111,
        Curtis, J T.   November 1961.

8.37   Canning, T.N.
       Sommer, S.C.   *Investigation of Boundary-Layer Transition on Flat-Faced Bodies of Revolution at High Supersonic Speeds.* NACA RM A57C25, June, 1957.

8.38   Kruse, R.L.   *Transition and Flow Reattachment Behind on Apollo-Like Body at Mach Numbers to 9.* NASA TN D-4645, July, 1968.

8.39   Morkovin, M.V.   *Note on the Assessment of Flow Disturbances at a Blunt Body Traveling at Supersonic Speeds Owing to Flow Disturbances in Free Stream.* Paper No.60, APM-10, J.Appl. Mechanics.

8.40   Page. W.A.   *A Survey of Thermal Radiation Studies of Ablating Bodies in the Ballistic Range.* NASA TN D-3741, February, 1967.

8.41   Carros, R.J.
       James, C.S.   *Some New Drag Data on the NACA RM-10 Missile and a Correlation of the Existing Drag Measurements at M = 1.6 and 3.0.* NACA TN 3171, June, 1954.

374
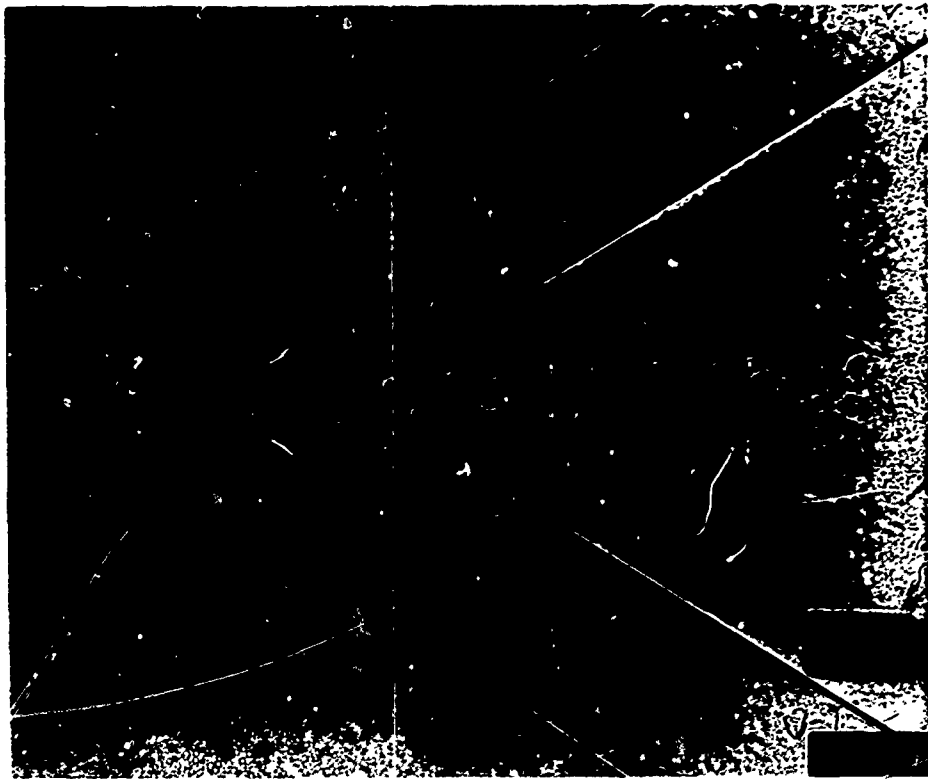
(a) Shadowgraph, $M = 2$, cone half-angle, 9.5^o

(b) Schlieren, $M = 1.8$, cone half-angle, 9.5^o, knife edge vertical. (Courtesy of US Army Ballistic Research Laboratory)
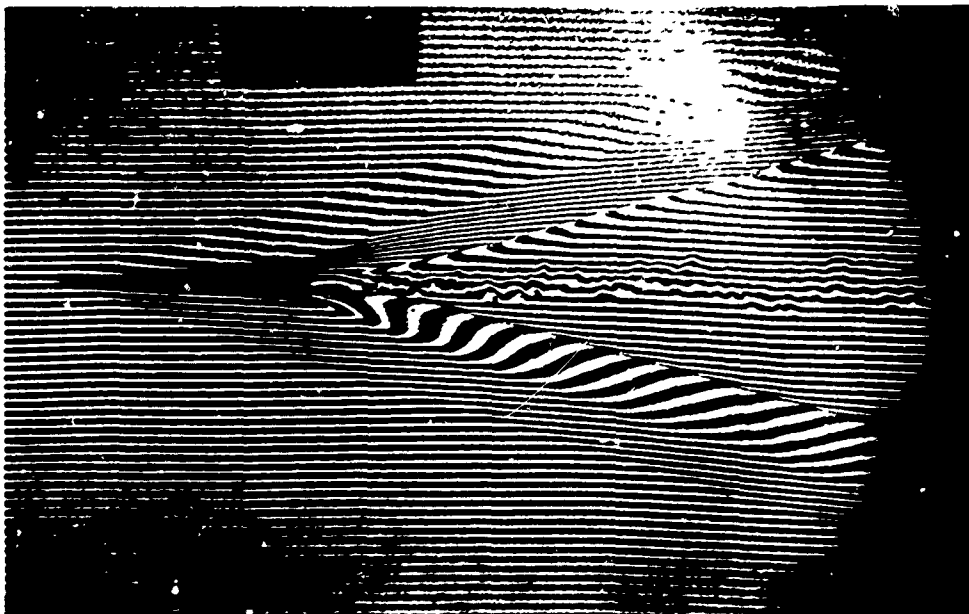
(c) Interferogram, M = 3.6, cone half-angle, 4.1°

8.1   Representative shadowgraph, schlieren, and interferometer pictures of cones.

8.2   Self-luminous photograph of an ablating polycarbonate round-nosed, large-angle cone at a velocity of 7 km/sec, ambient density of 0.066 atmospheres
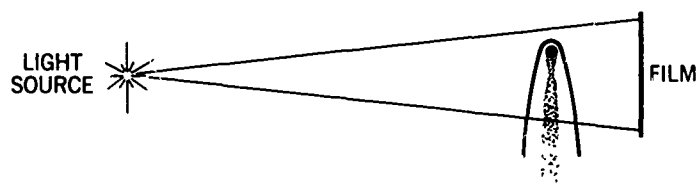
8.3   Conical-light-field shadowgraph
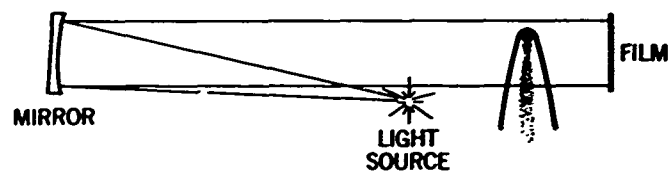
8.4 Parallel-light shadowgraph
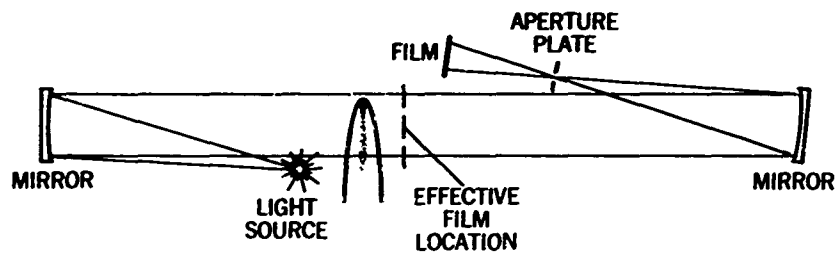
8.5 Focused shadowgraph
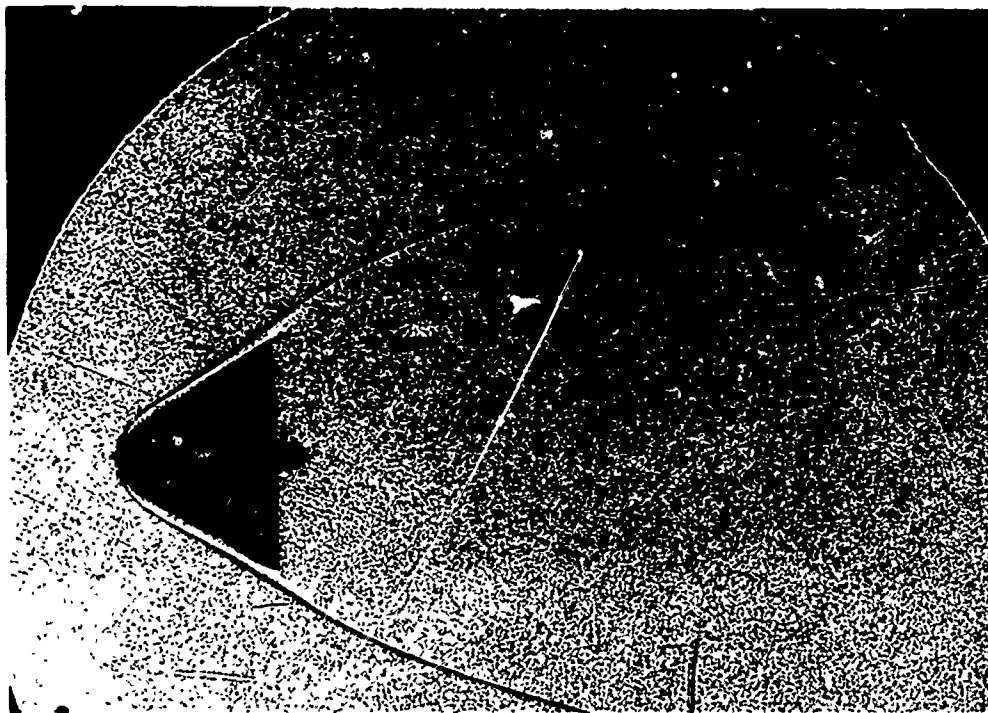
(a) Focused shadowgraph, low sensitivity
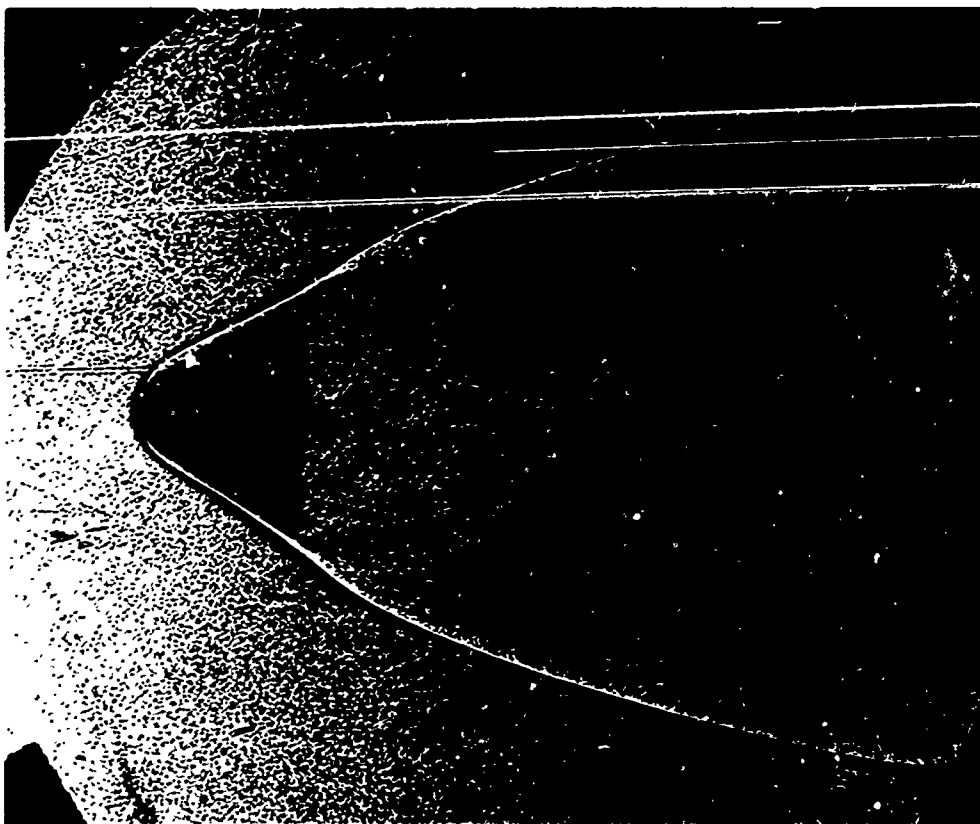
(b) Focused shadowgraph, intermediate sensitivity
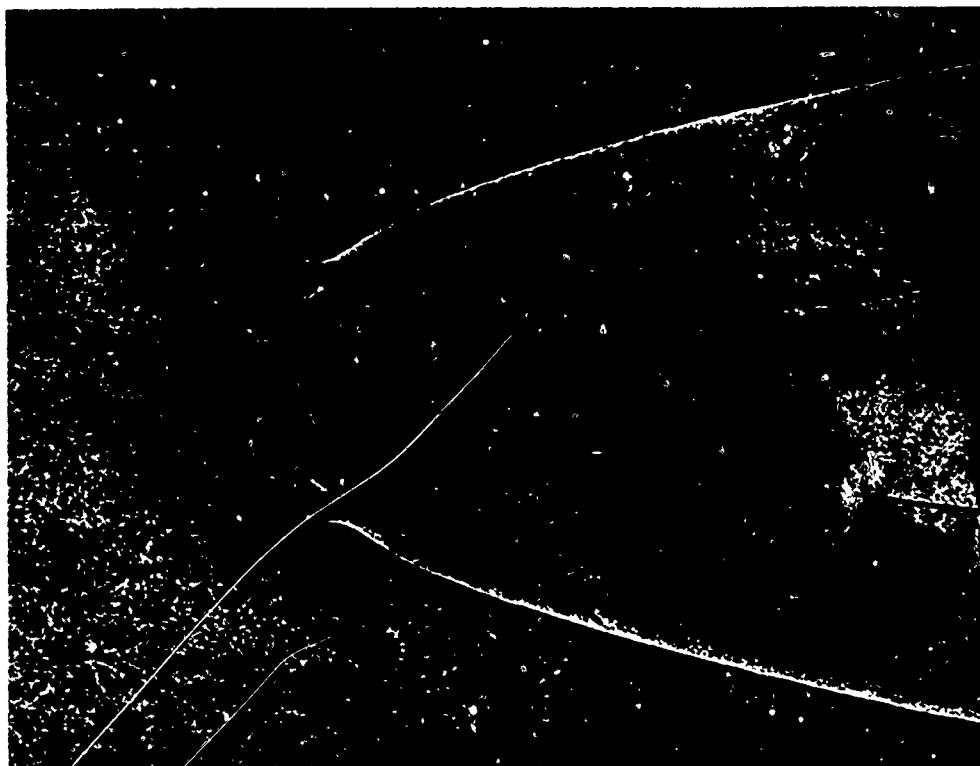
(c) Parallel-light shadowgraph (Figure 8.4), high sensitivity

8.6 Shadowgraph pictures of a round-nosed 30° half-angle cone with various sensitivity settings
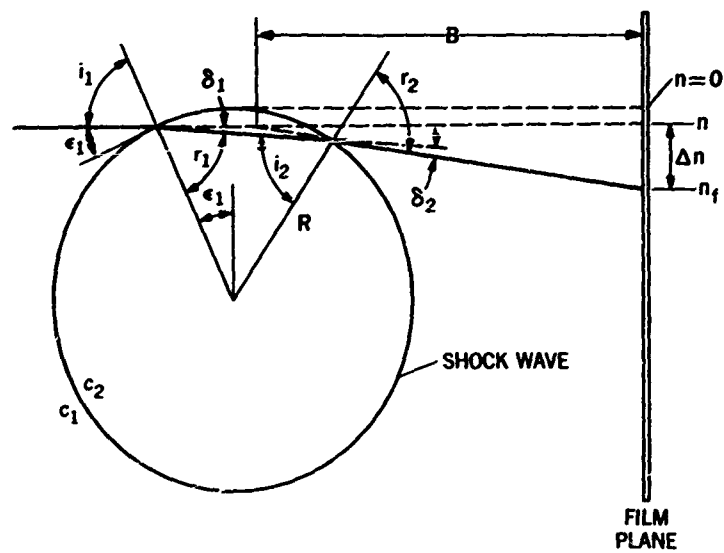
8.7 Light-ray deflections at a shock wave

NORMAL SHOCK WAVE
$\rho_1 = .00123 \ g/cm^3$
$\rho_2 / \rho_1 = 4.8$
$(V = 1.22 \ km/s)$
$R = 2.5 \ cm$
$B = 20 \ cm$
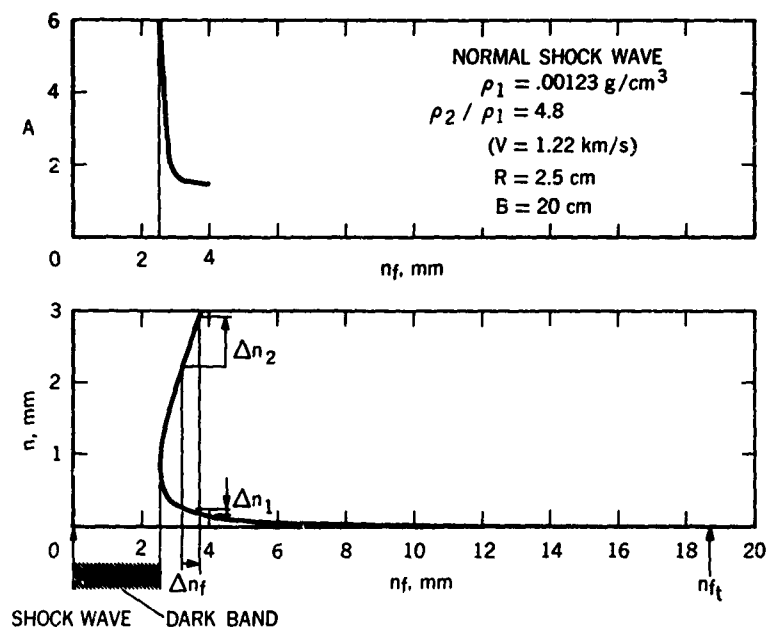
8.8 Example calculation of light-ray deflection at a shock wave, and light-amplification factors in the bright band

8.9 Two rays intersecting film at a common point

8.10 Shadowgraph showing shock-wave dark band width for conditions: velocity, 0.9 km/sec; 1-atm. ambient pressure; shock wave radius of curvature on axis of symmetry, 3.5 cm; and distance B from model to film approximately 30 cm
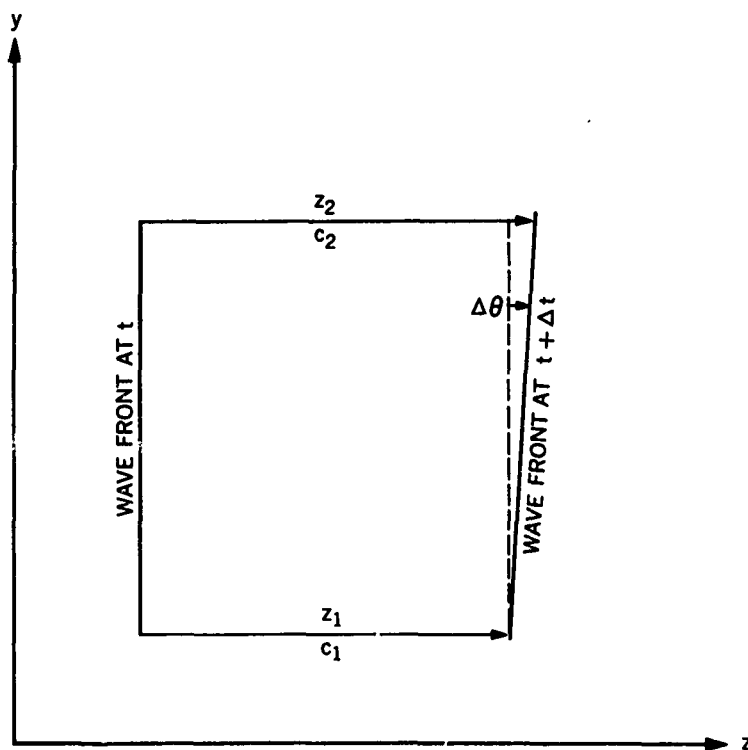
8.11 Wave-front rotation due to non-uniform light velocity
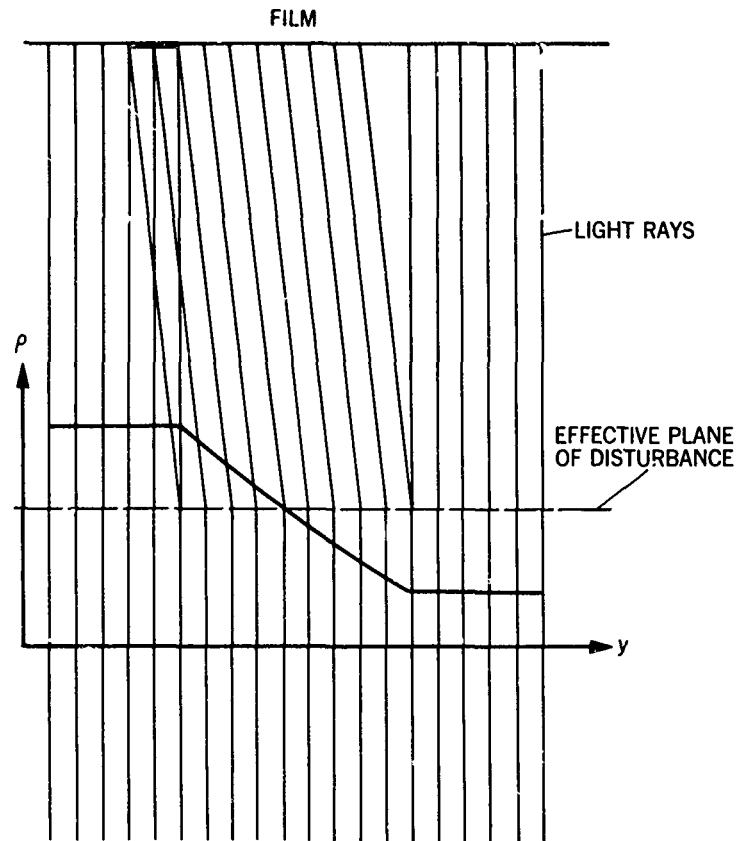
8 12   Schematic light ray paths in a Prandtl-Meyer expansion

8 13   Shadowgraph of a turbulent boundary layer on a slender body of revolution at M = 3.5, length Reynolds
number of 12 million
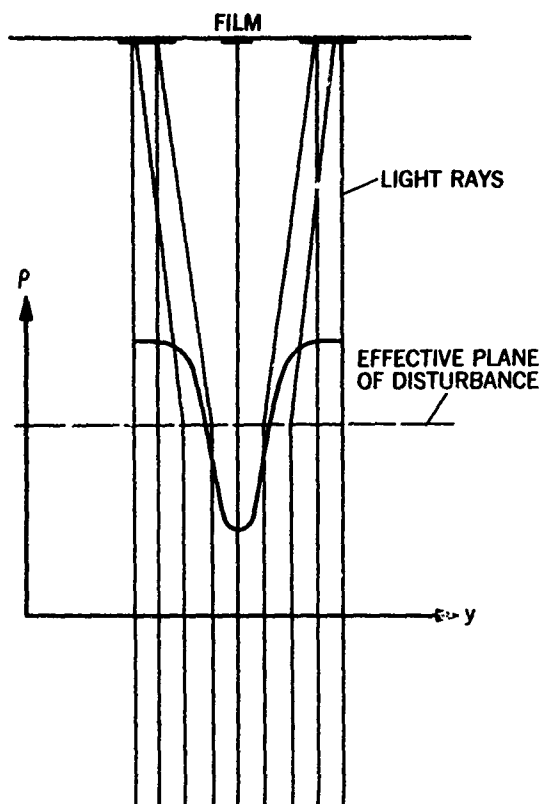
8.14   Light-ray paths in a turbulent eddy
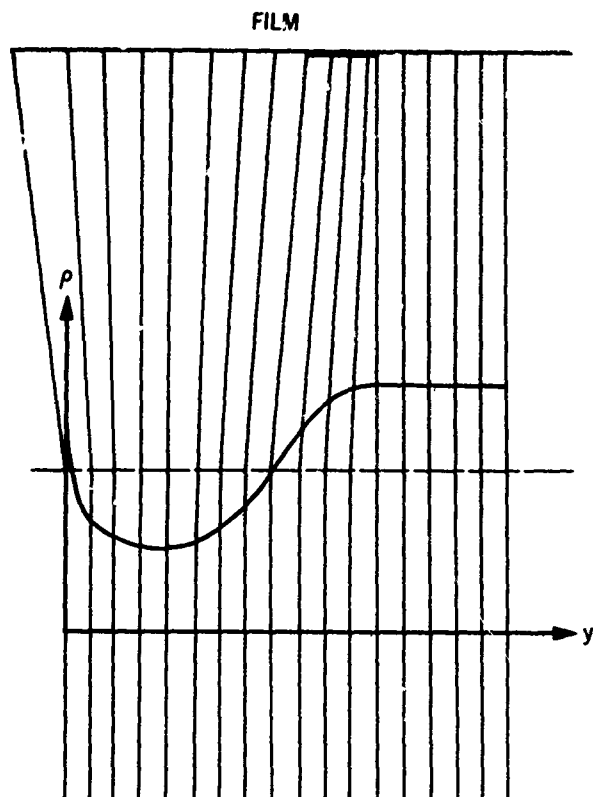
8.15   Light-ray paths in a cold-wall
        laminar boundary layer

8.16   Shadowgraph of 9.5°-half-angle cone at M = 4, showing separated laminar boundary-layer image behind base
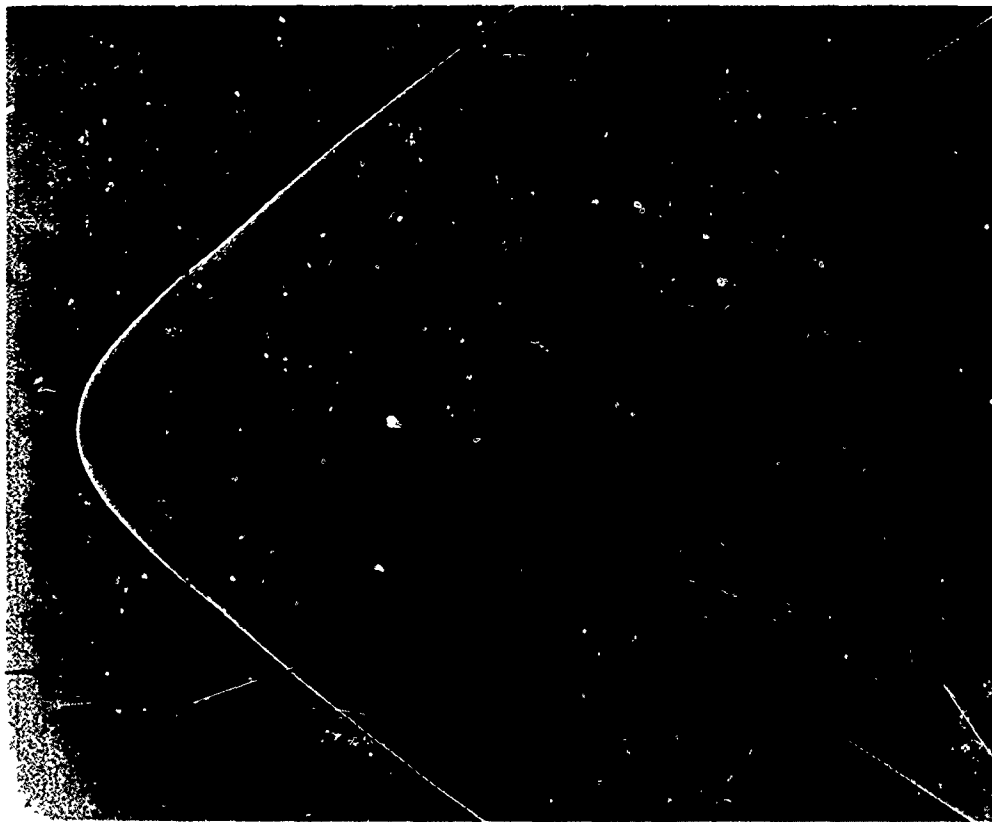
8.17 Line image in sublayer of a turbulent boundary layer behind the base of a flare-stabilized body
$(M = 2.06 , \quad Re = 6 \times 10^6)$

8 18 Image of a velocity-discontinuity streamline emanating from an intersection of shock waves
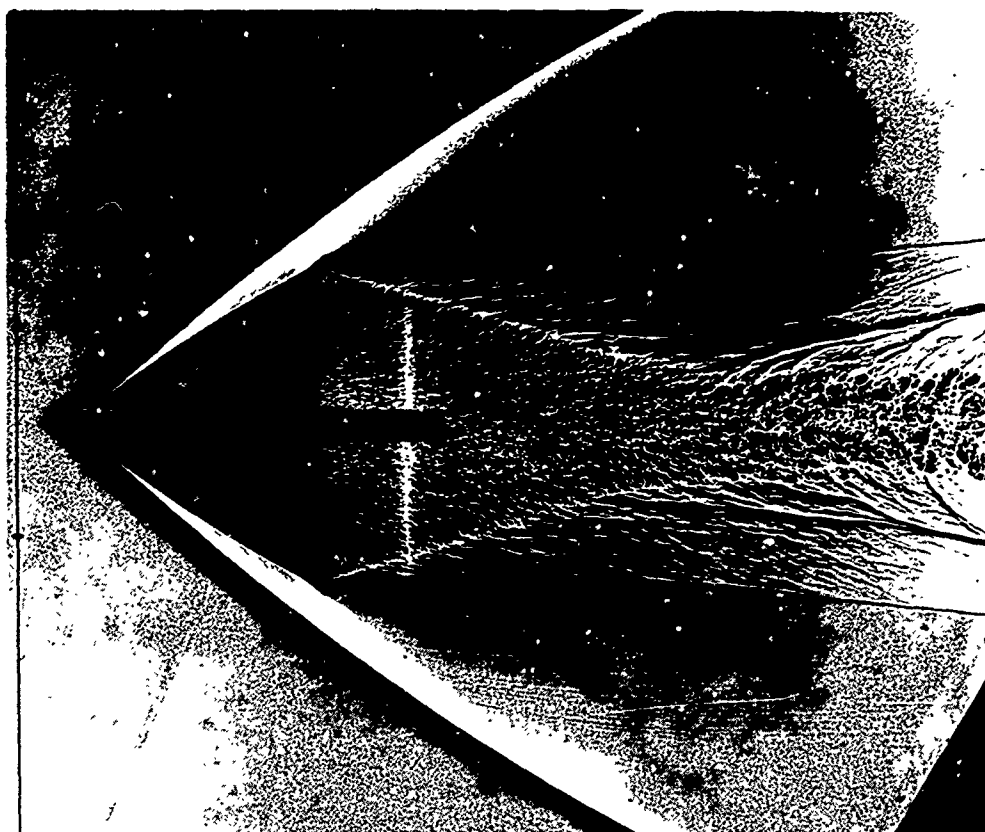
8.19   Marked streamlines, due to minute waves from body-fixed disturbances intersecting the bow wave
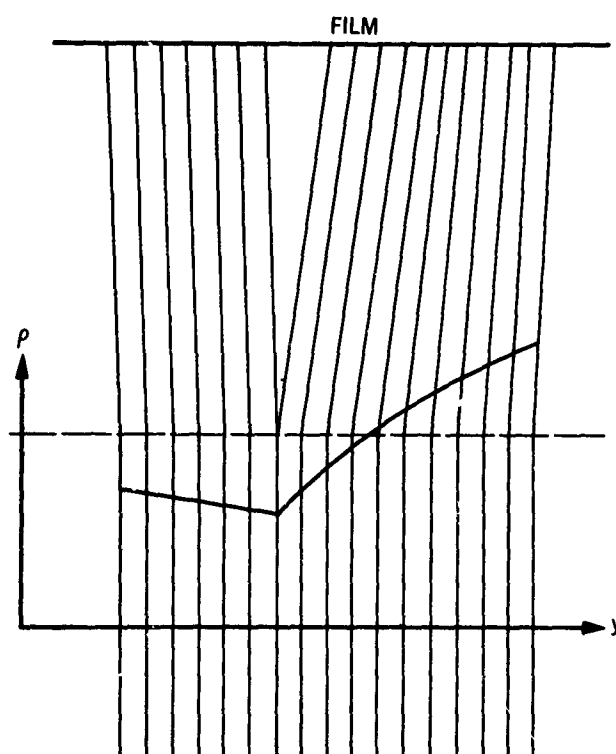
8.20   Light refraction at a streamline where density gradient is discontinuous
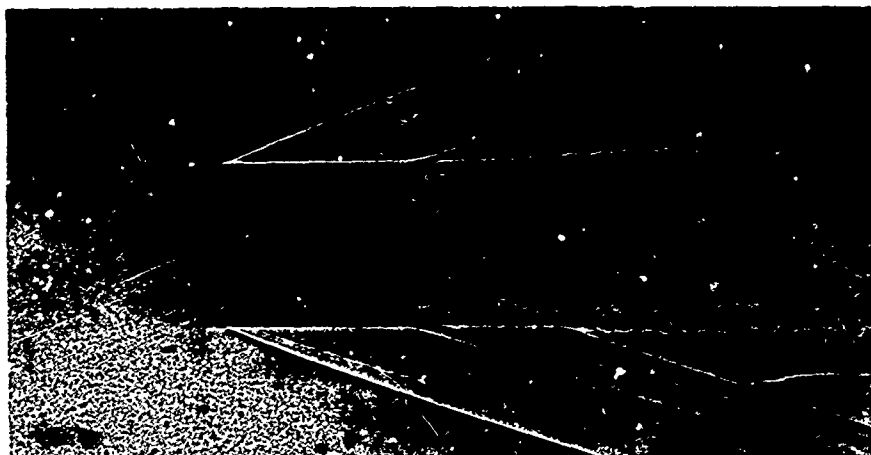
8.21 Shadowgraph of thin-walled tubular model with thick, turbulent boundary layer at $M = 3.8$, length Reynolds number of 4×10^6

8.22 Diffraction fringes at the edges of a razor blade (left), thin-walled tubular model with serrated leading edge (right), and metal stand in a parallel-light shadowgraph system
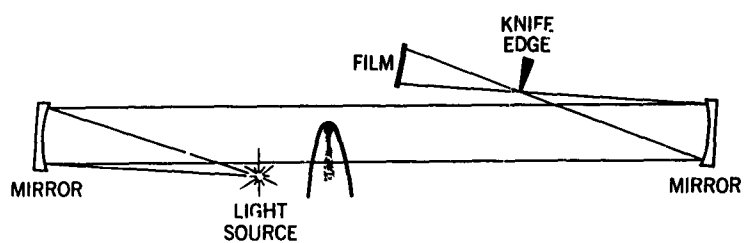
8.23 Parallel-light schlieren system

8 24 Shape variations of luminous region in a mercury-arc lamp (BH-6) when pulsed repeatedly at intervals of 10 microseconds
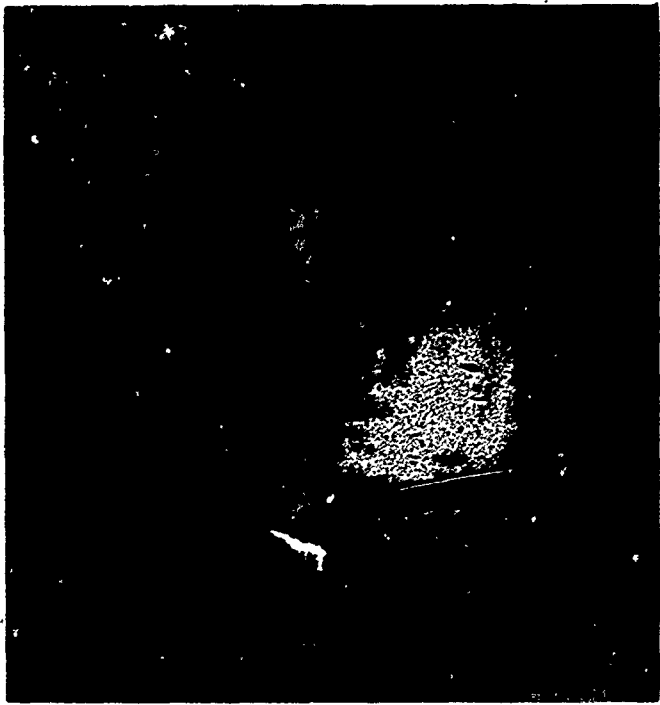
8.25   Schlieren effect obtained inadvertently in a focused shadowgraph system. Model, 30°-half-angle cone at
a velocity of 6 km/sec, ambient pressure, 100 mm mercury
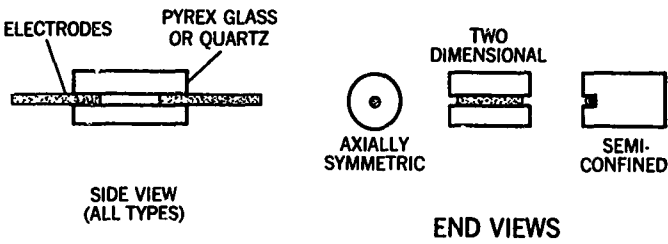
8.26   Sketches of confined spark gaps
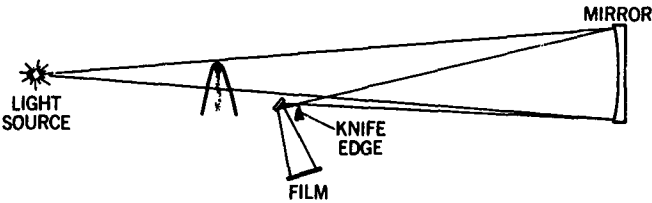
8.27   Single-mirror, single-pass schlieren system
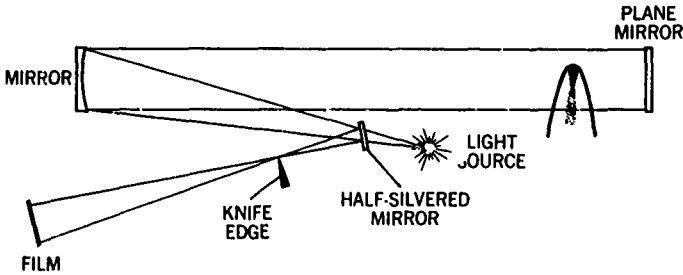
8.28   Double-pass, parallel-light schlieren system
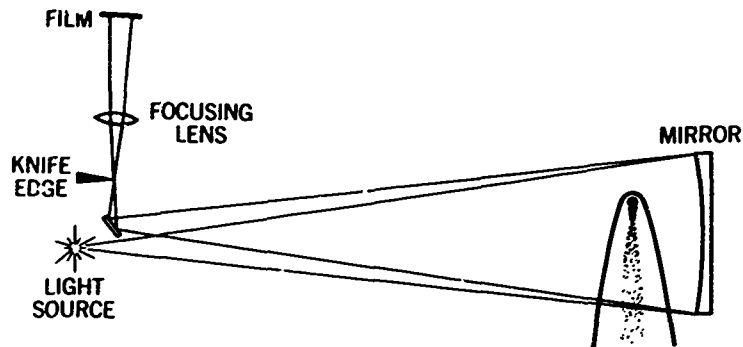
8.29   Double-pass, conical-light schlieren system
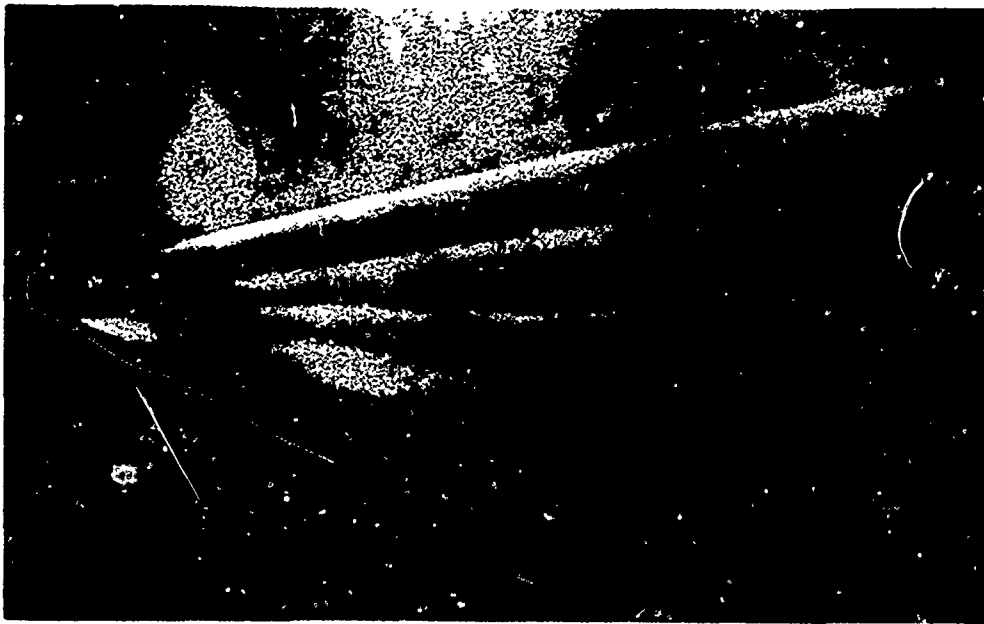
8.30   Schlieren photograph of a laminar wake at 0.013 atm. ambient pressure, undergoing initial stages of transition to turbulence. Model is a $12\frac{1}{2}^\circ$-half-angle cone at velocity of 2.4 km/sec
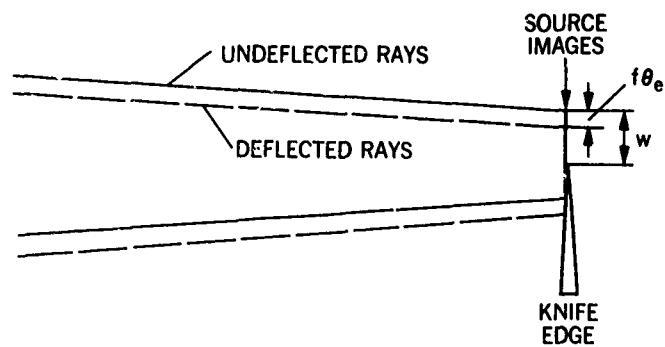
8 31   Action of the knife edge to differentially occult source images from various points in the flow field
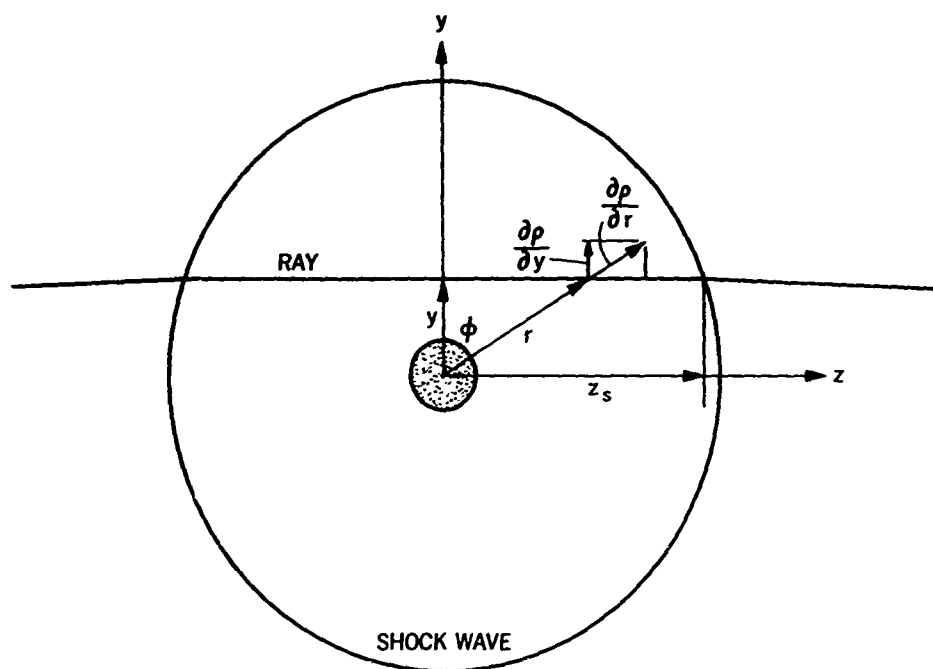
8.32   Notation for integrating Equation (8.26)
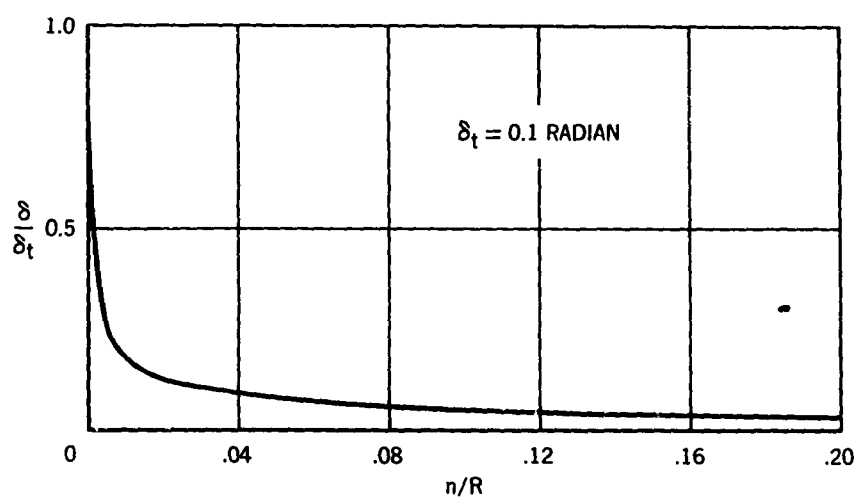
8.33   Relative deflections of rays passing through a shock wave as a function of normal distance from the tangent ray
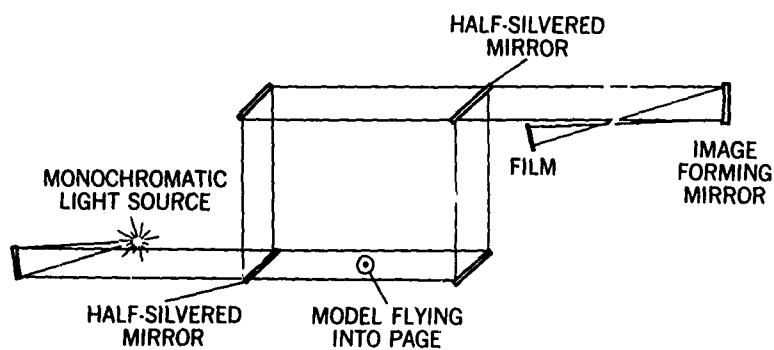
8.34   Optical arrangement, Mach-Zehnder interferometer

388
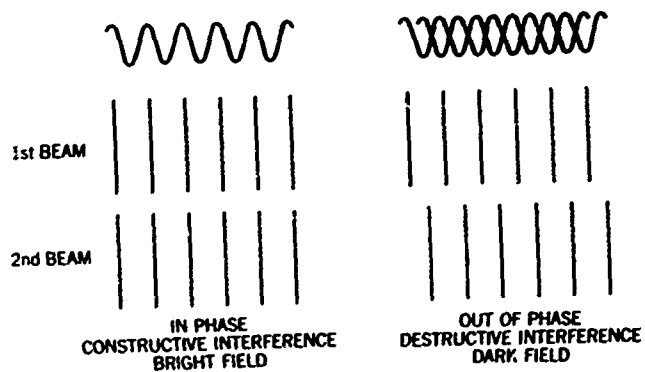
8.35   Interference between perfectly-parallel plane-wave trains
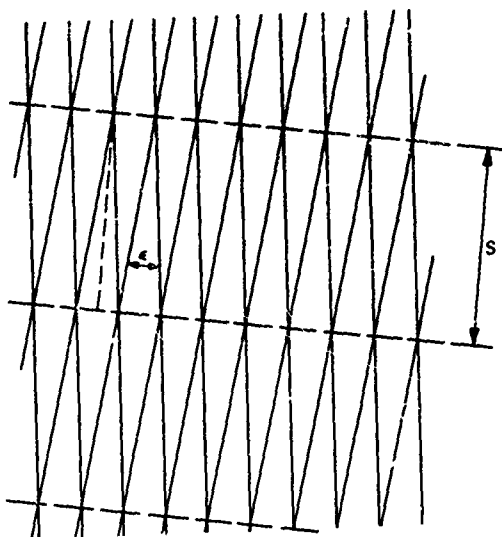
8.36   Interference between slightly inclined systems of plane waves
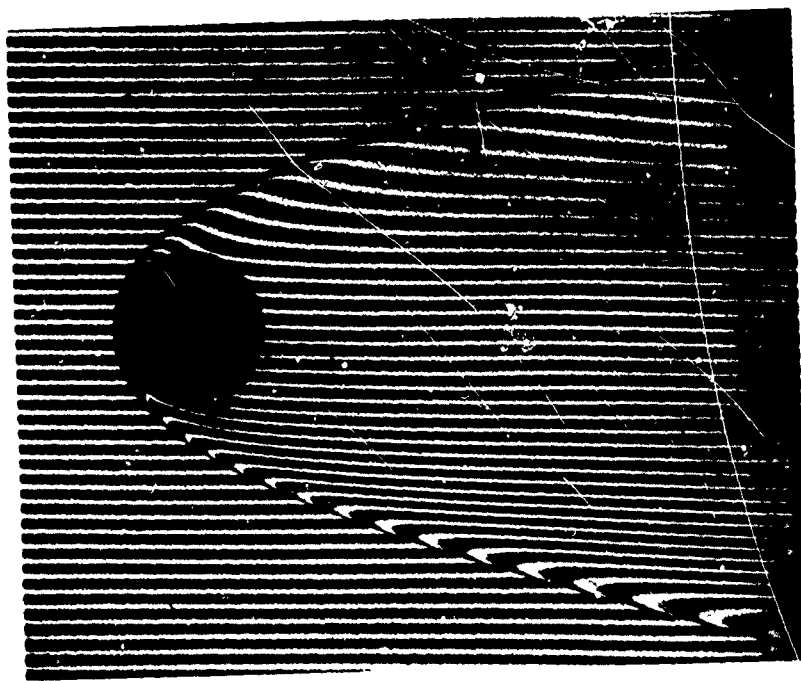
8 37   Interferogram of an aluminum sphere, 20 mm in diameter, at a velocity of 3.4 km/sec, range pressure of
0 1 atmosphere. (Courtesy of US Army Ballistic Research Laboratory)
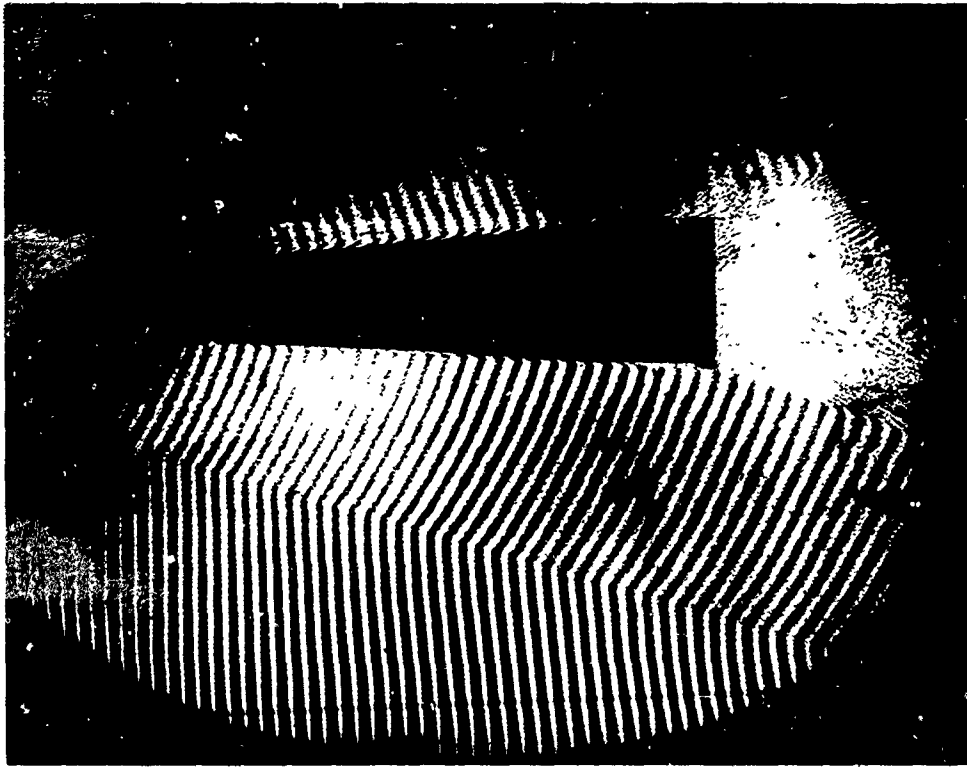
8.38   Interferogram of a cone in flight at 1.25 km/sec through air at one atmosphere pressure.   Cone half-angle, 3.58°, and length, 30.5 cm
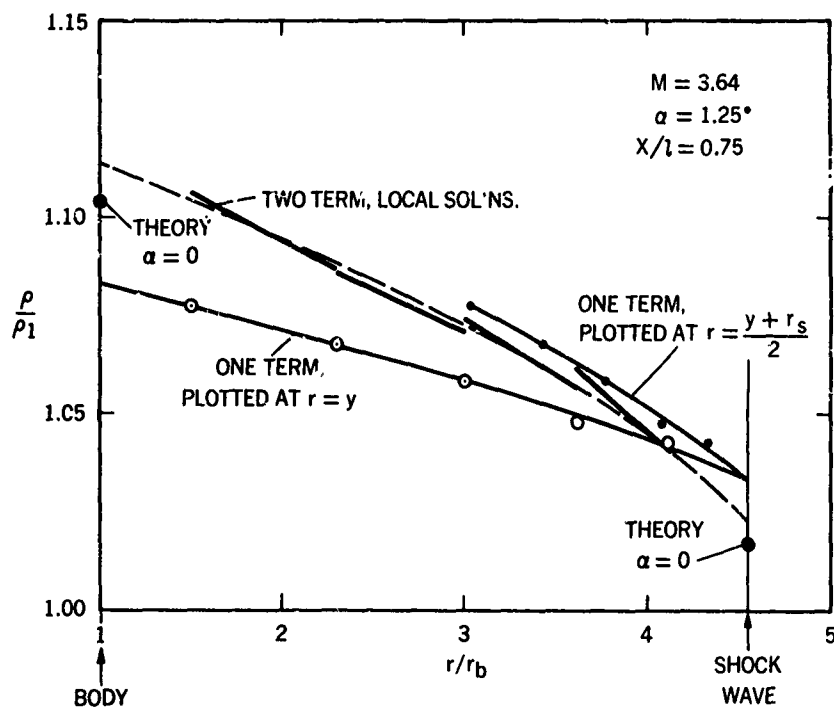
8.39   Density distributions, reduced by one-term and two-term series approximations from the interferogram of Figure (8.38)
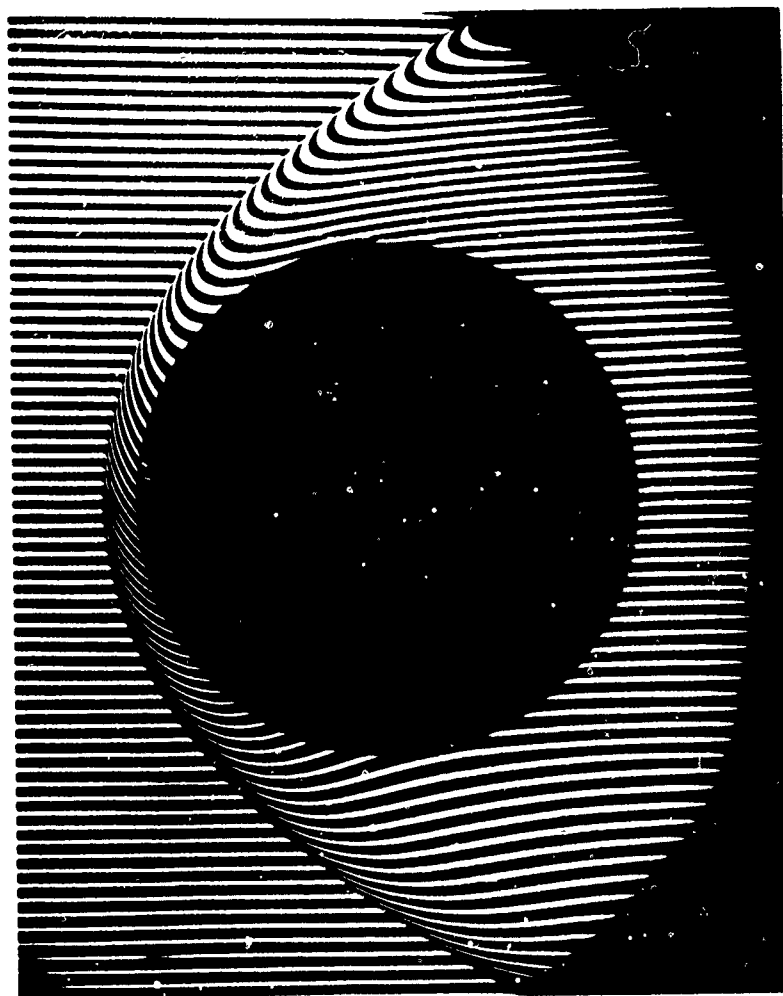
8.40   Interferogram of 8 9 cm-diameter sphere in flight at a Mach number of 5.7, range pressure of 0.05
atmospheres.   (Courtesy of US Army Ballistic Research Laboratory)
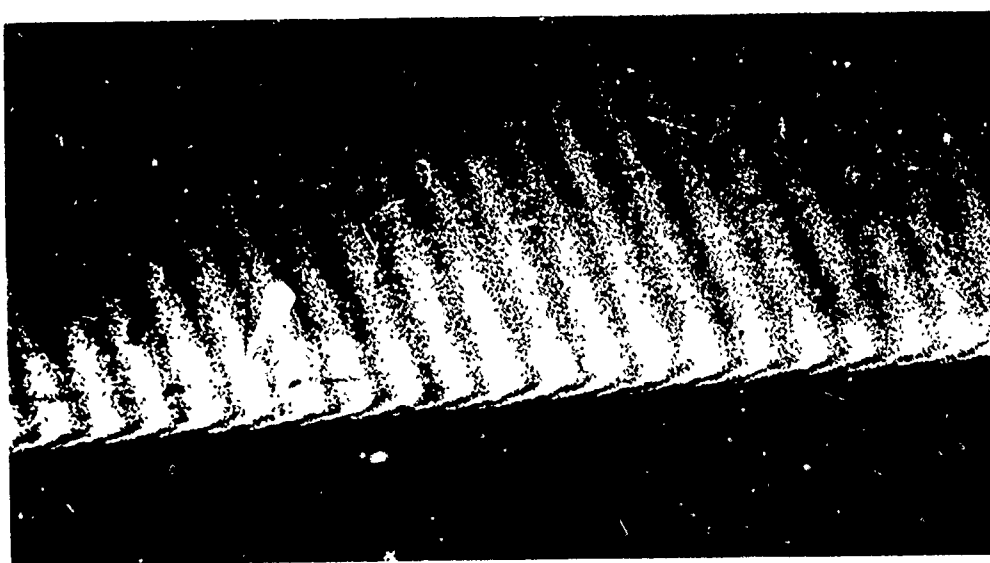
8 41   Enlargement of the fringes in the turbulent boundary layer along one edge of the model in Figure (8.38).
Boundary-layer thickness. 2 mm. Reynolds number, 25×10^6
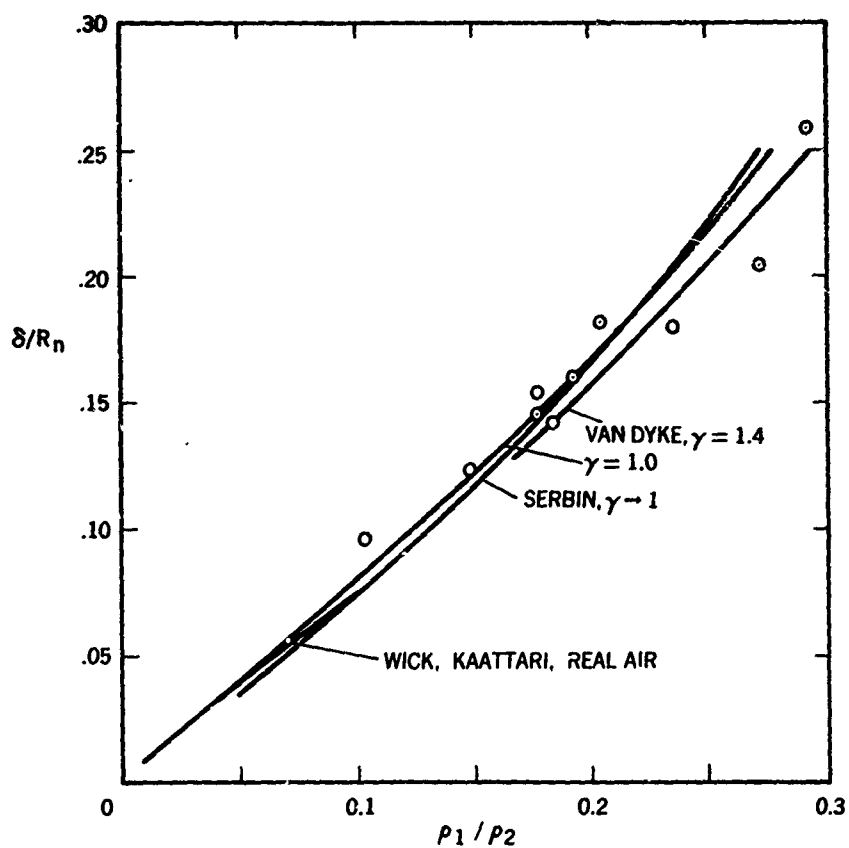
8.42 Comparison with theory of sphere shock-wave stand-off distances measured from shadowgraphs

8.43 Shadowgraph of a flare-stabilized body in flight at a Mach number of 5.2, showing the oblique secondary shock wave generated by the flare
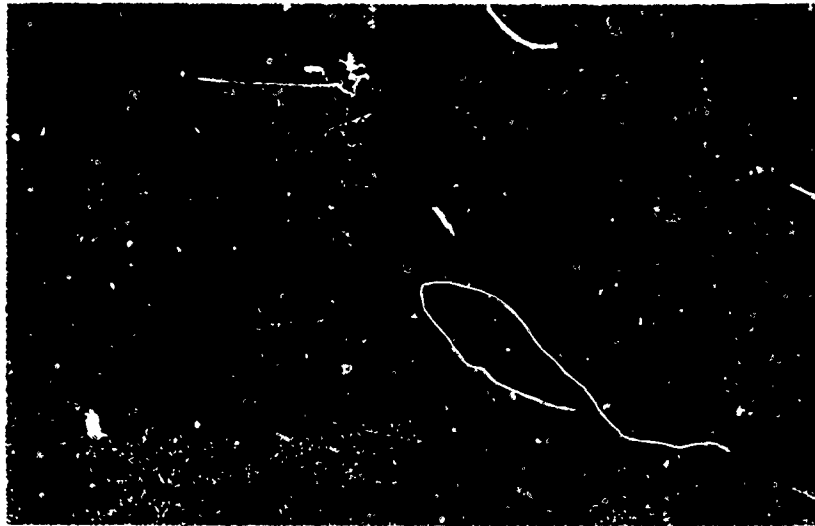
8.44 Interaction of the bow wave with the embedded shock wave from a downstream surface at a Mach number of 11, 18° angle of attack
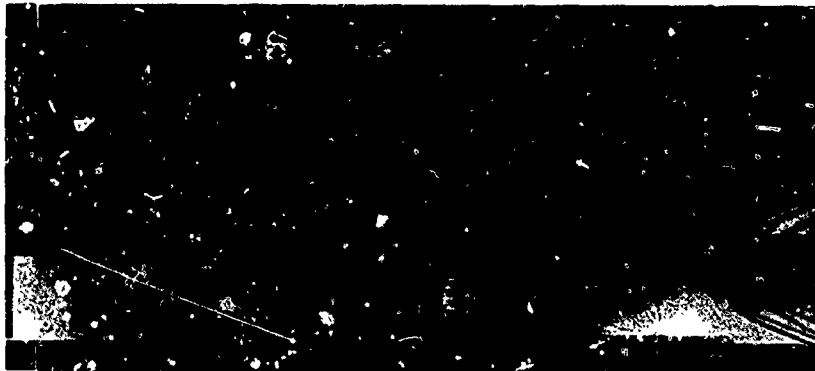
8.45 Acoustic field associated with boundary-layer turbulence on a slender body of revolution at a Mach number of 3.5
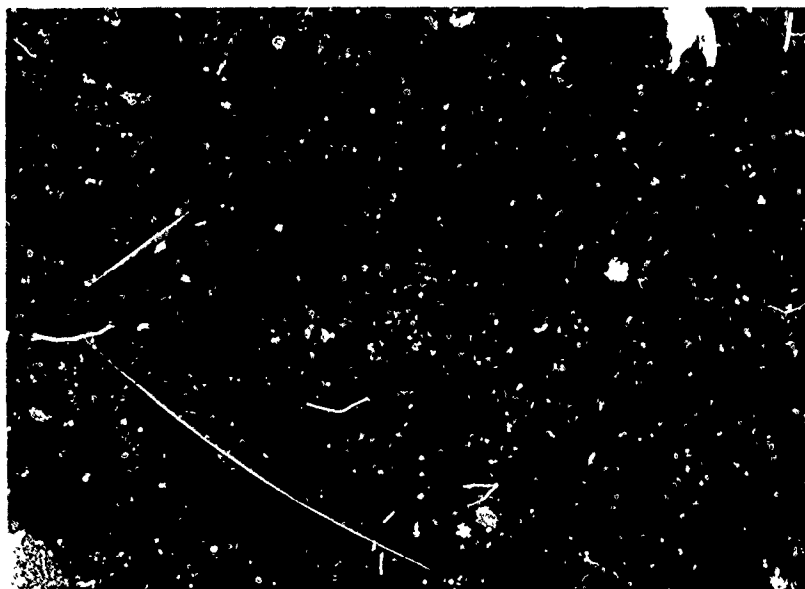
8.46 "Hairy" image at the model edge signifying the presence of turbulent boundary layer. Mach number 4, Reynolds number based on diameter. 3 ^ × 10^
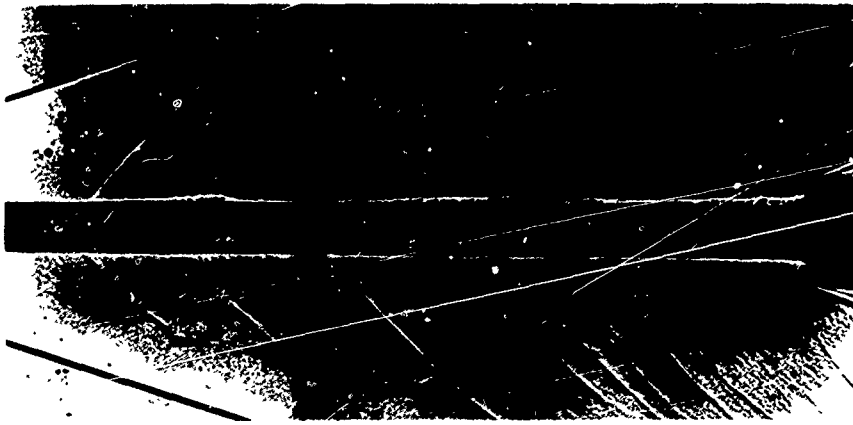
8.47   Shadowgraph of isolated bursts of turbulence on a slender body of revolution at a Mach number of 3.5
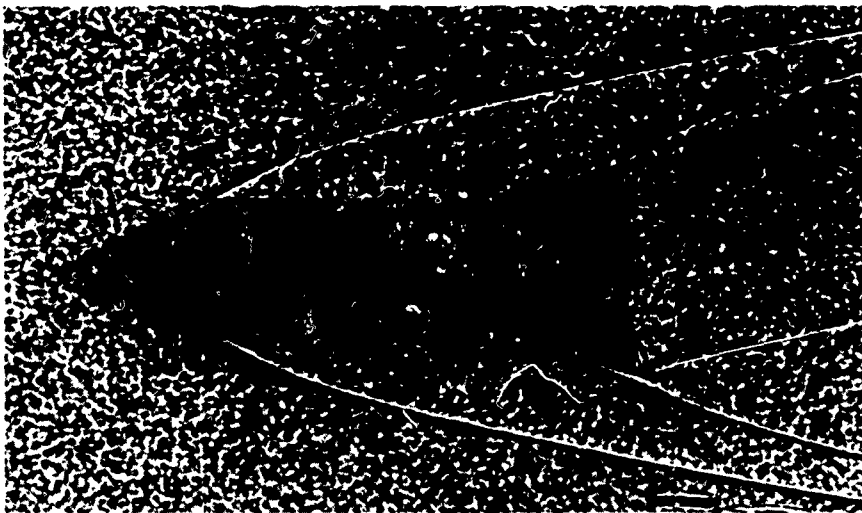
8.48   Laminar separation ahead of the flare on a flare-stabilized body at a Mach number of 15
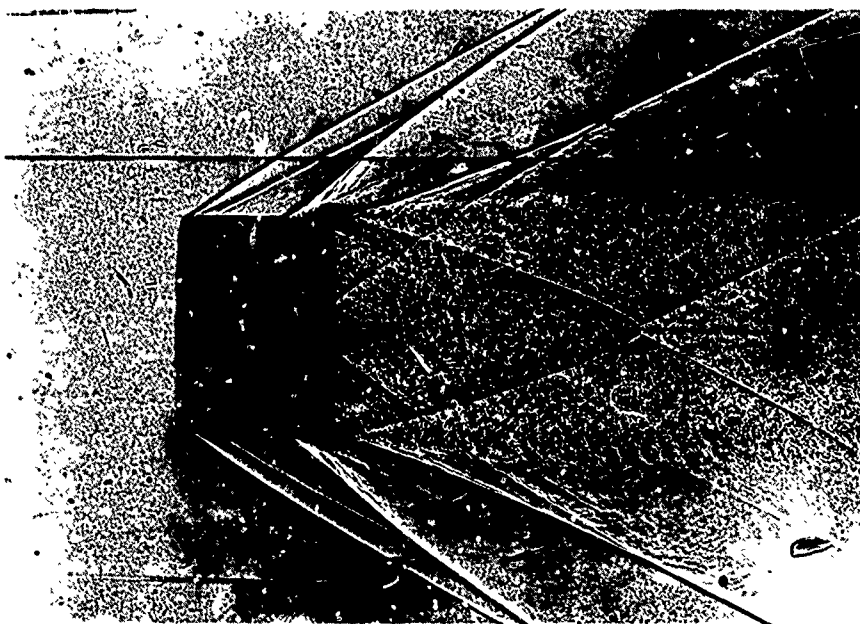
8.49   Turbulent separation in front of a step on a hollow-cylindrical model in flight at a Mach number of 2.2

394

8 50   Illustration of the influence of laminar-turbulent transition on length of the base-flow region and
thickness of the wake neck

8 51   Field of Mach waves generated by body-fixed disturbances on a sphere between the sonic point and separation
point at a flight Mach number of 1.4
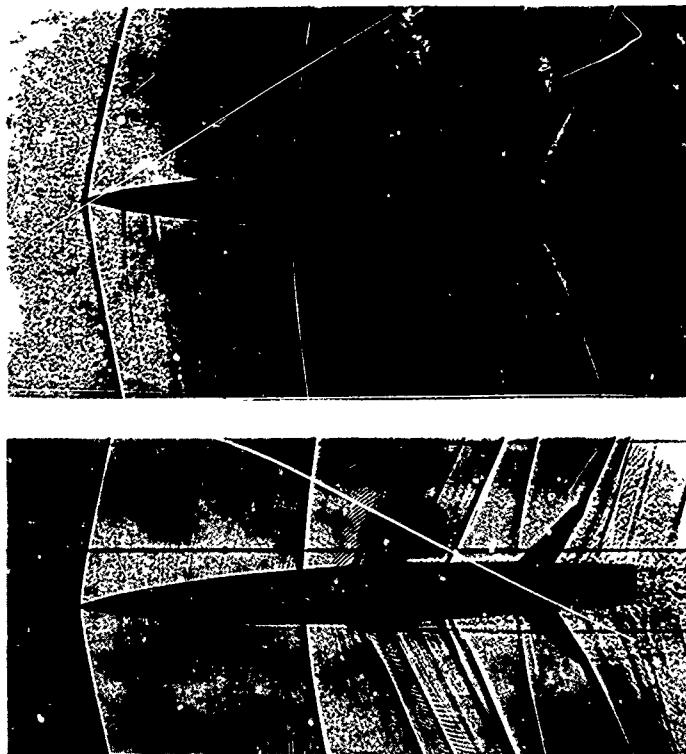
8 52   Field of high-frequency sound waves generated by shallow V grooves parallel to wing leading edge of an airplane model in flight at a low-supersonic Mach number (orthogonal views)
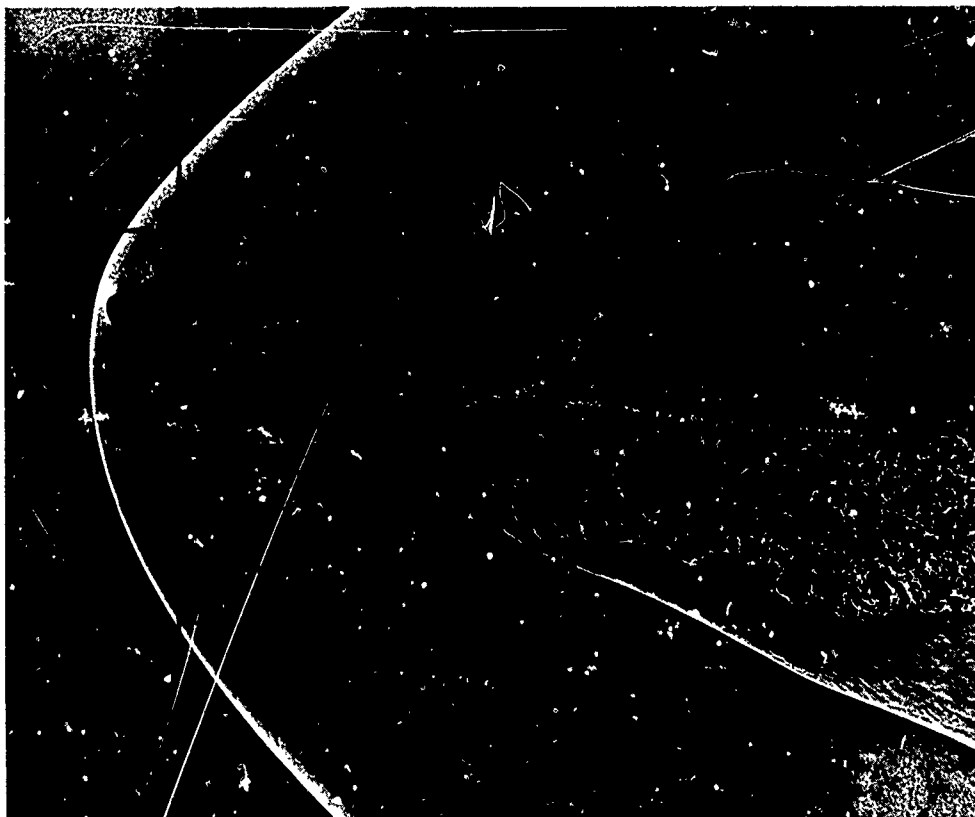
8.53   Oscillations in the stagnation region of a blunt-body flow at Mach number of 2.31. Reynolds number of 1.6×10^6
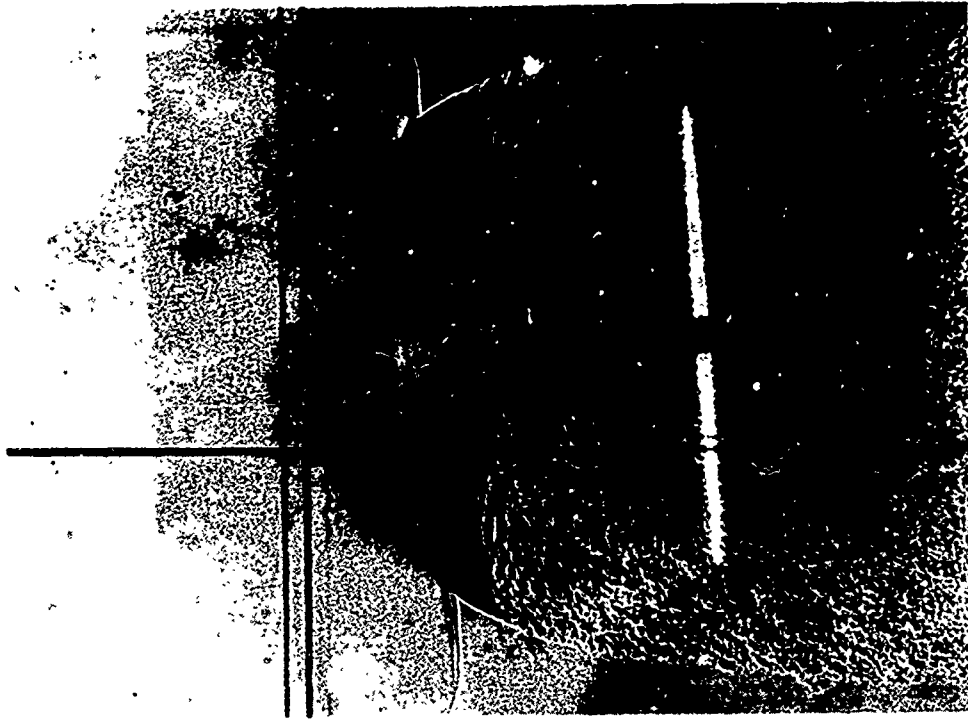
8.54   Transition effected by vortices transverse to the flow
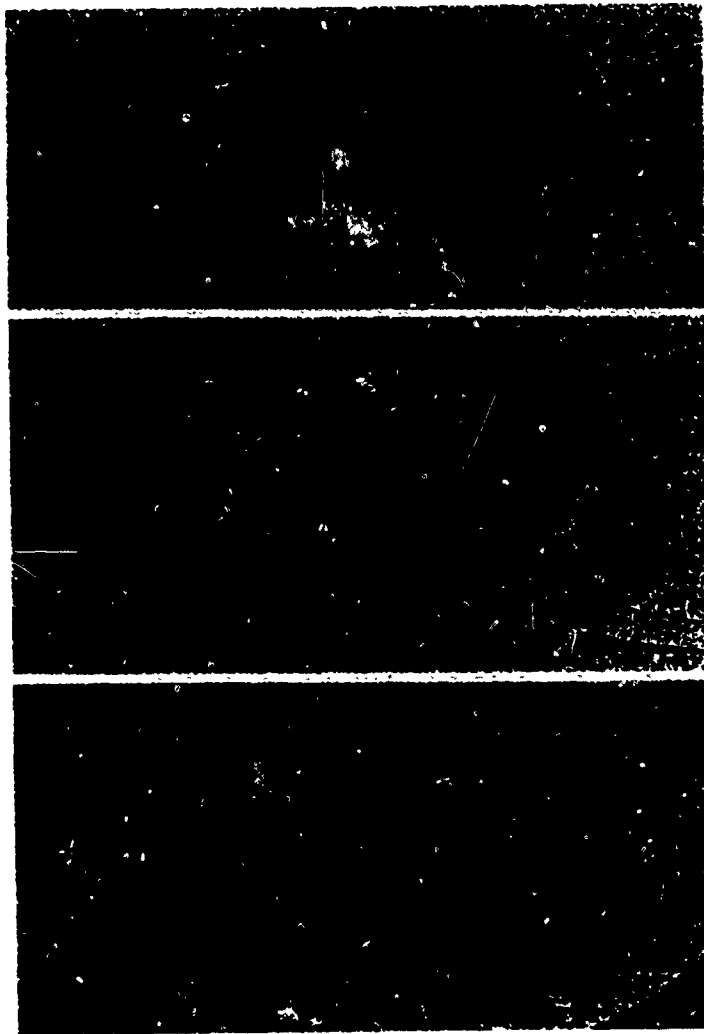
8 55   Successive views of a model being separated into its component parts by drag forces in flight
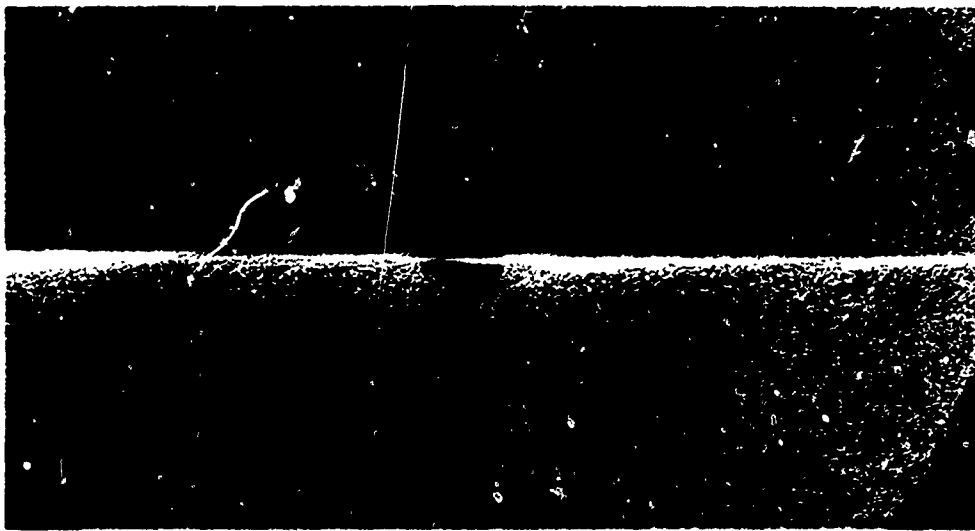
8.56   Model with titanium nose, burning chemically in flight at a velocity of 3 km/sec (M = 15)
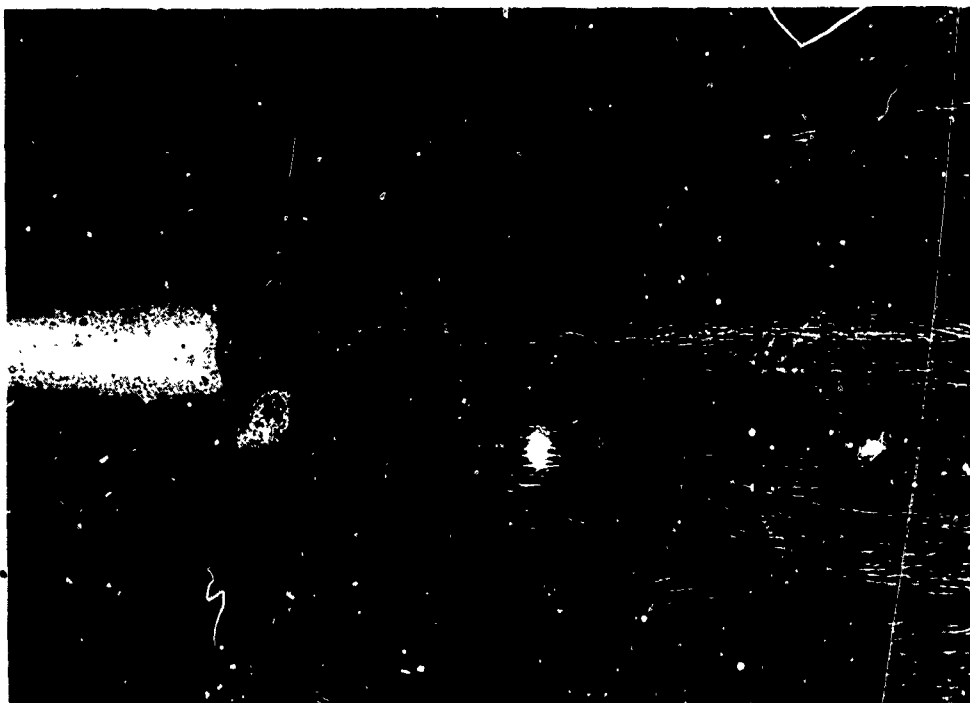
8.57   Sintered iron-tungsten nose undergoing surface spalling and ejecting small particles due to intense surface heat transfer at a velocity of 4 km/sec in atmospheric air
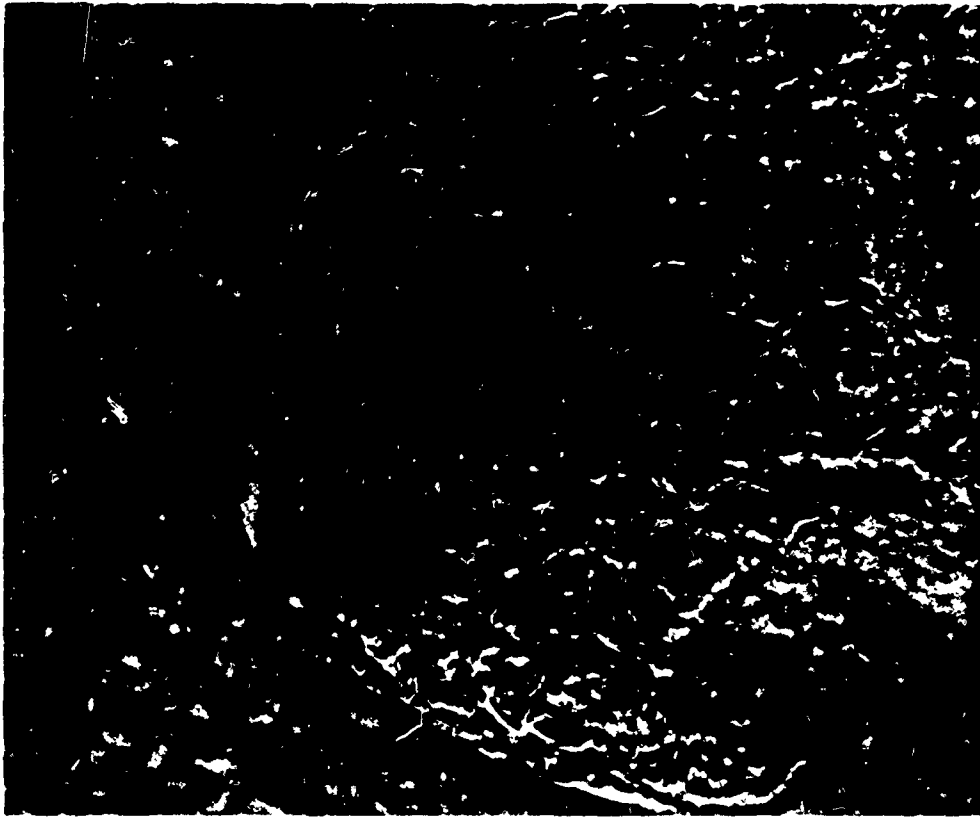
8 58   Plastic model in violent ablation at a relative velocity of 12 km/sec
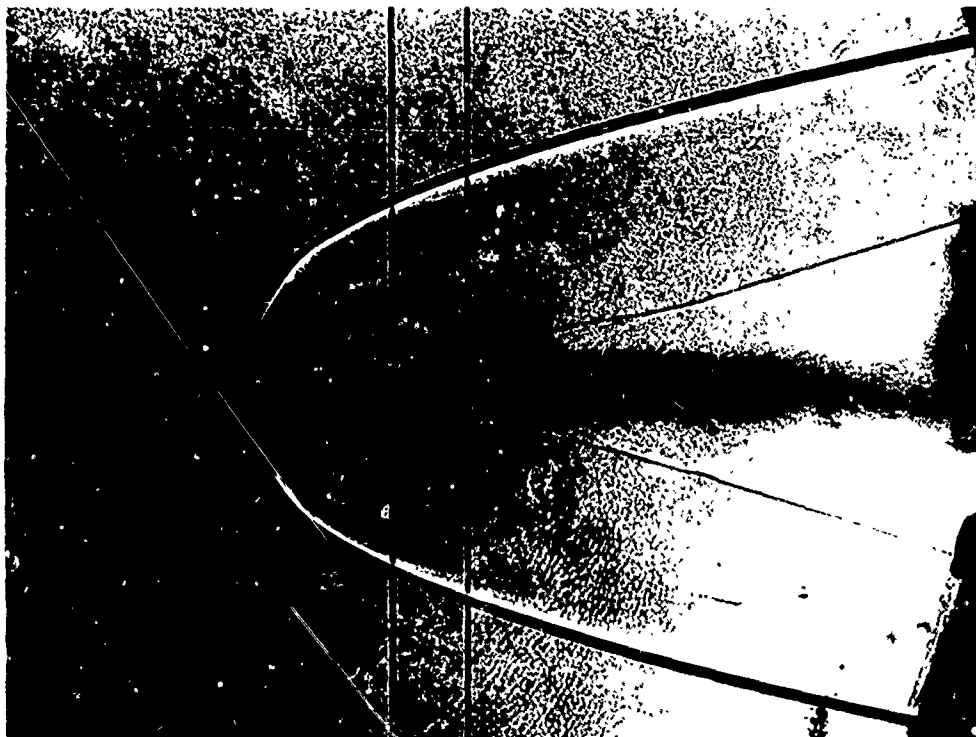
8 59   Shadowgraph of soot in the wake of an ablating polycarbonate model at a velocity of 5.8 km/sec and ambient pressure of 0.19 atm

CHAPTER 9

TECHNIQUES FOR OPTICAL RADIATION STUDIES
IN THE BALLISTIC RANGE

by

William A. Page

NASA-Ames Research Center

TECHNIQUES FOR OPTICAL RADIATION STUDIES IN THE BALLISTIC RANGE

William A. Page

9.1 INTRODUCTION

At the velocities reached by ballistic range models the temperature of the disturbed flow field is sufficiently high to excite electronic states in the molecules and atoms present. Much of the resultant characteristic photon emission appears in the spectral range amenable to observation and can be used by the researcher in several important ways: (1) to identify the species present in the shock layer, boundary layer and wake, (2) to study the basic radiative properties of high temperature gases, (3) to study the ablation of heat shields and the physical-chemical processes in the wakes of entry bodies, and (4) to provide basic data for estimating the radiative heating and entry signatures of entry vehicles. Historically, the fourth of these possibilities provided the initial motivation for opening this area of research.

The major purpose of the present chapter is to describe the experimental techniques and the instrumentation which have been developed for radiation studies in ballistic ranges and counterflow facilities. For convenience, emphasis is placed upon the experiences of the writer and his colleagues in the Hypersonic Free-Flight Branch at Ames Research Center, even though similar and very excellent research work has been performed elsewhere.

9.2 RADIATIVE PROPERTIES OF FLOW FIELDS ABOUT FREE-FLIGHT MODELS

Before we discuss instrumentation techniques for use in ballistic-range radiation studies, let us review the spatial features, spectral characteristics, emission intensities, etc., that are typical of the experimental events to be measured. The spatial distribution of the luminosity generated by ablating blunt projectiles flying at hypersonic velocities in a ballistic range has been recorded in image-converter photographs, such as Figure 9.1 from Reference 9.1. The camera, sensitive to the 0.38 to 0.60 micron spectral range, had an exposure time of 0.05 microsecond. A corresponding shadowgraph picture, Figure 1, shows density disturbances in the flow field, including the bow shock wave and the viscous wake.

Radiation is seen primarily in two locations — the shock layer behind the nearly normal part of the bow shock wave, and the viscous core of the wake beyond the wake recompression shock. The boundary layer along the model sides is also luminous. The radiation of the boundary layer has been shown to be associated with products of ablation, as has that from the wake. The turbulent structure of the wake somewhat further downstream can be identified from the luminosity pattern.

The time required for this event to pass a stationary observer (or instrument) placed to the side of the flightpath is extremely brief. The luminous shock layer of the typical 13-mm-diameter blunt-faced model is only about 3 mm thick. For the model velocity of 6.6 km/sec = 6.6 mm/μsec this layer passes a point in about 1/2 μsec; hence any instrument designed to measure the shock-layer luminosity separately from the emission from the model sides must respond to the radiation in a time period shorter than 1/2 μsec. Observations of the luminosity from comparable-sized regions of the wake require similar instrument rise-time capability. It is these very short observation times which place very stringent response requirements upon the radiometric instrumentation.

Three types of spectral features are to be expected in ballistic range tests of ablating bodies. As depicted in Figure 9.2, there can be, for example, an underlying continuum caused by the interaction of free electrons with atoms or ions[9.2] or by the presence of particulate carbon particles in the ablation products[9.1]. Mo~ ~~ radiation can be present, such as $N_2^+(1-)$ and $N_2(2+)$ systems in the shock-layer gases[9.3] or the CN (violet) or CN (red) systems normally present in the ablation species in the boundary layer and wake[9.1,9.4]. These radiating systems tend to extend over moderate spectral ranges in vibrational bands from 20 to several hundred Angstroms wide. Lastly, atomic-line radiation can be present, at discrete wavelengths. In this example spectrum, we have shown the bright carbon line at 2478 Å, and the sequence of strong nitrogen atom lines[9.5] which exist in the infrared portion of the spectrum.

Convincing identification of the various spectral features can be made with either a spectrograph using photographic film or with photoelectric scanning instruments. Experience has indicated that the required resolution for identification can be surprisingly low. For sufficiently intense atomic lines, for example, a resolution of about 10 Å will allow the lines to be recognized above the background continuum[9.6]. Some molecular bands can be identified with a similar resolution, particularly if they are of low intensity and are well dispersed over broad spectral ranges (examples are CN (red) (Ref.9.6) and $N_2(1-)$). The radiation from CN (violet), which has a sequence of concentrated band structures, can be recognised and even measured with a resolution of 100 Å (Ref.9.7). Actual requirements, of course, always depend upon such factors as the intensity of radiating systems with respect to noise and background sources, the presence of interfering species and their relative intensity, and prior knowledge of the species present, their purity, and the radiating sources and the other.

Representative emission levels are shown by the computed values in Fig.9.3. The computations are for the emission into 4π steradians from the shock layer of a 13-mm-diameter nonablating blunt model flying in air at various velocities. This shock layer has an effective radiating volume (to be discussed in Section 9.3.2.7) of about 0.060 cm^3. The emission will vary with the cube of model scale and approximately with the square of the free-stream density. The numbers given on the figure are for a free-stream density ratio, ρ_∞/ρ_0 of 0.08, which is about that required for thermodynamic equilibrium in the shock layer[9.8].

For the example, we have given the total radiation[9.9] in the spectral range $0.2 < \lambda < 1.2\mu$, the spectral range most readily measured. Also shown is the emission from a 5 Å region at the band head (3914 Å) of the $v = 0$ vibrational sequence of the $N_2^+(1-)$ molecular system[9.10], a typical molecular radiator. The emission from the single N atomic line at 8680 Å is also shown. This is the most intense atomic nitrogen line in this spectral range. The calculated emissions have been corrected for self-absorption, which is significant at the higher velocities shown on the figure. We will discuss the instrument sensitivity limits shown on the figure in a subsequent section.

9.3 MEASUREMENT TECHNIQUES

9.3.1 Spectrographic Techniques for Species Identification

As noted earlier, convincing species identification can be made by spectrographic observations using a photographic plate as the recording medium. Obtaining photographic spectra of ballistic-range events is difficult, however, because of the speed of movement of the radiation source.

A method for observing the flight of a ballistic-range model with a spectrograph is sketched in Figure 9.4. If the collection optics are arranged to focus a point along the model flightpath on the spectrograph input slit, then for a system free of diffraction effects the energy placed upon the photographic film from a source of height h, parallel to the spectrometer entrance slit, traveling at velocity V_∞, and which emits W watts in 4π steradians, in the spectral range $\Delta\lambda$, is given by

$$E, \text{ watt-sec/cm}^2 = \frac{(W/h)T_\lambda\psi_2}{4\pi V_\infty \sin\theta}\left[1 + \frac{D_2\Delta\lambda}{\omega_2}\right]^{-1}, \tag{9.1}$$

where T_λ is the system transmission, ψ_2 is the solid angle subtended at the camera mirror, D_2 is the spectrograph dispersion, ω_2 is the monochromatic image width of input slit on the film plane, and θ is the angle of view. Equation (9.1) results directly from consideration of: (1) The irradiance per unit area of the source which falls upon the input slit, (2) the actual velocity of the source image across the input slit, and (3) the effect of spectrograph dispersion on the area of film exposed. The equation, of course, assumes that the collimation mirror is filled with radiation from the collection mirror, that is, $\psi_1 < \psi$, and indicates that increasing energy per unit film area (i.e., exposure) follows from (1) brighter sources per unit height, (2) high system transmission, (3) a large value for ψ_2, (i.e., a low f-number for the camera optics), (4) a low model velocity (actually, since $W \sim V_\infty^n$, where $5 < n < 15$, a higher model velocity in fact will increase the exposure), (5) a value of θ approaching $0°$ (but there are practical limits to the gain obtained as the viewing angle approaches head-on because the model image at the spectrograph slit does not remain in focus during the exposure), and (6) using the widest slit which still provides adequate spectral resolution for species identification. It is interesting to note that the equation places no demands on the f-number of the collection or collimation optics other than the collection optics fill or overfill the collimator and be arranged so as to allow for some variation from test to test in the actual location of the model flightpath.

To demonstrate the use of Equation (9.1), consider the observation of the molecular system $N_2^+(1-)$ for the nonablating ballistic-range model having $d = h = 1.3$ cm considered in Figure 9.3. Let the spectrograph have $\psi_2 = 0.02$ ster (f/6.3), $T_\lambda = 1/4$, and $\omega_2/D_2 = 2$ Å (i.e., the image width of input slit on film is equivalent to 2 Å dispersion). Let $\Delta\lambda$ of the $N_2^+(1-)$ band head be 5 Å and let the observation be at right angles to the flightpath so that $\sin\theta = 1$. Since a value of $E = 1.0 \times 10^{-9}$ watt-sec/cm² is typical of that required for exposing the film[9.11], the required source intensity is

$$W, \text{ watts} = \frac{4\pi(1.3)(1 \times 10^{-9})}{1/4(0.02)}\left[1 + 5/2\right]V_\infty \tag{9.2}$$

$$= 1.1 V_\infty, \qquad V_\infty \text{ in km/sec.}$$

Equation (9.2) is plotted on Figure 9.2 and intersects the $N_2^+(1-)$ curve at about 10 km/sec, that is, a rather high model velocity would be required before this molecular band system would be adequately exposed on the photographic plate. A higher-speed spectrograph is of great advantage. If the camera optics are changed to f/2.0, for example, the velocity at which $N_2^+(1-)$ can be observed is reduced from 10 to 7.8 km/sec.

Spectrographic observation of even the brightest nitrogen atomic line (Fig. 9.3) is very difficult since not o̲ is the source intensity no higher than that of the molecular system discussed but the sensitivity of photographic ... is in the IR portion of the spectrum is less by factors of 10 or 20 than the sensitivity of films use ...

Most of the spectrographic observations made in the ballistic range have been of ablating models and the species most easily observed have been those from the ablation products. Prediction of the spectral intensity of these species is not nearly as straightforward as for the air shock layer species shown in Figure 9.3. Attempts at prediction have been made, however, and have had moderate success[9.4,9.12].

Figure 9.5 shows an example spectrum of an ablating polycarbonate model of 13-mm diameter flying in air at $\rho_\infty/\rho_0 = 0.12$ and at 9.4 km/sec. The spectrum was obtained[9.4] with a spectrograph, as described in the example given by Equation (9.2) above. The well-exposed and easily recognized spectral features are from ablation-product species, CN, C_2, NH, and several contaminant species, Cr, Ca^+, K, and Fe. (The contaminant species are present in the 1.8 km/sec countercurrent airstream of the Ames Prototype Hypervelocity Free-Flight Facility in which this spectrum was obtained.) The spectrum also contains the moderately exposed $\Delta v = 0$ bandhead of $N_2^+(1-)$ at 3914 Å. The film density for this air species is reasonably consistent with the prediction given on Figure 9.3. The spectrograph entrance slit was left open to both the shock layer and wake and the major source of the dominant emission from the ablation species is from the near wake. The total time-integrated emission from the ablation species is about 10 times greater than that from the air species in the shock layer. Thus, threshold velocities for spectrographic observations of ablation species are several km/sec lower than those for the shock-layer air species.

During a ballistic-range firing there can be luminous events caused by processes other than the passage of the model. Emission from the gun muzzle blast, from the model impacting the model catcher, or from sabot pieces following in the wake of the model can be recorded on the spectrograph plate. It may also be required to observe the emission from the shock layer free of interference from wake emission. Protection from these extraneous sources can be provided by use of a high-speed-shutter mechanism. The spectrum shown in Figure 9.5 was limited to the model and near wake by use of a shutter consisting of a sheet of thin brass shim stock, which was blown (by the use of a small explosive squib) over a rectangular hole located a short distance in front of the spectrograph slit. The shutter closed off the light path to the spectrograph in about 20 μsec after a 30 μsec delay from initiation of the squib.

Several other shutter designs have been reported in the literature[9.13,9.14]. One of the best designs is shown in Figure 9.6 (following Wurster[9.15],) and has demonstrated closure of a 2-mm-wide optical path of a spectrograph in 5 μsec or less. A capacitor charged to 3 kV, containing approximately 20 joules, is appropriate for exploding the wire. Such a shutter, if properly timed, allows the separation of radiation from the shock layer and the near wake. The shutter begins to close after a time delay dependent upon the spacing between the wire and the optical beam; for 1.5 cm, about 40 $\pm$ 2 microseconds is required after the pulse is applied to the exploding wire. Improvements to the performance of this shutter have been made by shortening the shock-tube length downstream of the flap.

9.3.2 Measurement of Absolute Radiation Intensities

9.3.2.1 Detectors

The multiplier phototube is the principal photon detector used in instrumentation designed for measuring the absolute intensity of optical radiation from ballistic-range-model shock layers, boundary layers, and wakes. The general characteristics and availability of this detector have led to its wide use in the observation of transient optical events. It exhibits high sensitivity, linear response over several decades of intensity, stability, and rise-time capabilities appropriate for use in the ballistic range. Photocathode materials are available which are sensitive to radiation from the vacuum ultraviolet (below 2000 Å) to an upper limit of about 1.2 microns. At longer wavelengths, photon energies are too low to overcome photocathode work functions and the most suitable type of detector is a liquid-nitrogen-cooled Indium Antimonide or Gold-doped Germanium crystal. These detectors exhibit rise times of $\sim 10^{-6}$ sec and are the most sensitive types presently available in the spectral range from 1 to 10 μ.

9.3.2.2 Threshold Sensitivity, Multiplier Phototubes

The threshold sensitivity of the multiplier phototube can be shown to be less than the minimum radiation signal of interest from ballistic-range tests for viewing arrangements where the photocathode is simply exposed to the radiation. For highest signal-to-noise ratio, correct operation of the phototube[9.16] is obtained when "shot noise," caused by the statistical fluctuations in the electron current from the photocathode, is dominant. The mean-square shot noise developed by an electron current, I, is given by

$$\overline{i^2} = 2eI \Delta f,$$ (9.3)

where e is the charge on the electron, and Δf, the frequency bandpass over which the mean square current is being observed. For the multiplier phototube the dominant current flowing from the photocathode is due to the signal itself. Hence, the signal-to-noise ratio is

$$\frac{S}{N} = \frac{I}{\sqrt{(\overline{i^2})}} = \frac{I}{\sqrt{(2eI \Delta f)}} = \sqrt{\left(\frac{I}{2e \Delta f}\right)}$$ (9.4)

This expression is recognized as nothing more than the square root of the number of electrons observed in a time interval given by $(2 \Delta f)^{-\frac{1}{2}}$, a quantity closely corresponding to the minimum time interval of observation (the instrument rise time). If S/N = 10, then the number of electrons observed is 100. Since the minimum time interval for observation must be $\sim 0.1 \mu$sec or less for reasonable spatial resolution along the model flightpath, the minimum photocathode signal current, I , is 10^9 electrons per second. For a photocathode quantum efficiency of 10 percent, (number of electrons generated from the number of incident photons) and for radiation at $\lambda = 4000$ Å, the minimum radiative power incident on the photocathode is

$$P_{min} = 10 \, Ih\nu = 10 \, Ihc/\lambda$$

$$= 10(10^9)6.625 \times 10^{-34}(3 \times 10^{10})/0.4 \times 10^{-4}$$

$$= 5 \times 10^{-9} \text{ watts.} \tag{9.5}$$

Only a fraction of the source emission is observed by the radiometer. A typical viewing distance from model to photocathode is 50 cm. For photocathode surfaces of 1.0 cm^2 this fraction is

$$F = 1.0/4\pi \, (50)^2 \approx 3 \times 10^{-5} \, .$$

Hence, the minimum observable source power is

$$W_{min} = 5 \times 10^{-9}/3 \times 10^{-5} = 1.7 \times 10^{-4} \text{ watts.} \tag{9.6}$$

This "minimum detectable signal power" has been placed on Figure 9.3 for comparison with the previously calculated power emitted by various shock-layer sources. It is observed that all features can be observed down to rather low model velocities, even for a spectral bandpass as narrow as 5 Å.

9.3.2.3 Threshold Sensitivity, Infrared Detectors

The threshold sensitivity of liquid-nitrogen-cooled Indium Antimonide and Gold-doped Germanium infrared detectors is controlled by the same phenomenon as for the multiplier phototube, namely, the "shot noise" from the detector current. However, near signal threshold, and for zero-bias conditions the dominant current developed in the detector arises from the 300° K background radiation. This current can be reduced by cooling the detector aperture and background environment and such techniques have improved the threshold sensitivity of the devices.

The steady current developed by the incident flux is given by

$$I = e\eta JA \, , \tag{9.7}$$

where η is the detector quantum efficiency, A is the detector area, and J is the incident flux in photons/cm^2 sec. As an example, consider an Indium Antimonide detector having a quantum efficiency of 1 , a detector area of 4 mm^2 , and which views a 300° K background through 2π sr . The spectral response extends from 1 to 5.5 microns and calculation of the flux of background photons, J_N , gives about 2×10^{16} photons/cm^2 sec. From Equ. (9.7) the computed current would be

$$I = (1.6 \times 10^{-19})(1)(2 \times 10^{+16})(0.04) = 1.28 \times 10^{-4} \text{ amps .}$$

This contrasts with an actual measurement of 6.0×10^{-5} amps, or about one-half the predicted value. The difference can be caused, for example, by a quantum efficiency of 1/2 or by an uncooled viewing solid angle somewhat less than 2π sr. Using Equations (9.3) and (9.7) we can write an expression for the signal-to-noise ratio

$$\frac{S}{N} = \frac{I_s}{\sqrt{(\overline{i^2})}} = \frac{e\eta J_s A}{\sqrt{(2eI\Delta f)}} \, . \tag{9.8}$$

where J_s is the signal flux, and I is the observed steady current due to the noise or background flux. Observed rise-time for actual detectors having A = 4 mm^2 is 1.0×10^{-6} seconds. Hence, if we demand S/N = 10,

$$J_s = \frac{S}{N} \frac{\sqrt{(2\Delta fI)}}{\eta A e} = \frac{10}{0.04}\sqrt{\left(\frac{6 \times 10^{-5}}{1.6 \times 10^{-19}(10^{-6})}\right)} = 5 \times 10^{12} \text{ photons/cm}^2 \text{ sec .} \tag{9.9}$$

For radiation at 5 microns, and for a source 50 cm from the detector, the minimum detectable power (for the observed fraction F of $0.04/4\pi(50)^2 = 1.3 \times 10^{-6}$ becomes

$$W_{min} = \frac{J_s Ahc}{\lambda} \frac{1}{F} = \frac{(5 \times 10^{12})(0.04)(6.625 \times 10^{-34})(3 \times 10^{10})}{(5 \times 10^{-4})(1.3 \times 10^{-6})}$$

$$= 6 \times 10^{-3} \text{ watts.} \hspace{3cm} (9.10)$$

This number is quite small and allows the surface radiation from typical ballistic-range models to be easily observed.

A low-input impedance preamplifier developed at Ames Research Center, NASA, which provides zero-bias conditions, a current gain of 10^3, and no degradation of IR detector rise-time capabilities, is depicted in Figure 9.7. The observed noise from the amplifier-detector combination is about twice the theoretical value for the detector alone as given by Equation (9.3).

9.3.2.4 Physical Arrangement

Multiplier phototubes can be mounted in any convenient position. Infrared detectors, on the other hand, are usually cooled with liquid nitrogen and are designed to be mounted vertically. Front-surfaced mirrors, however, can be utilized to direct radiation from the model in the appropriate direction. The arrangement in common use for observing the model luminosity with a multiplier phototube or infrared solid-state detector is sketched in Figure 9.8. The instrument assembly, called a radiometer, consists of: slits, used to reduce scattered light and to define the spatial field-of-view of the detector along the model flightpath; a spectral filter, (as appropriate for the spectral wavelength region under observation); the multiplier phototube, or other photon detector, its power supply and anode load resistor; a wide-band preamplifier (if needed); and an oscilloscope for display. The record of the detector signal as a function of time is photographically recorded. A typical radiometer record of an ablating polyethylene model is shown inset in Figure 9.8. The oscilloscope sweep may be started by either the signal itself (self-triggering) or, as in Figure 9.8, by an electrical signal obtained by a model detector located somewhat uprange of the radiometer. The first pulse on the oscillograph represents the model shock layer passing through the field-of-view, whereas the second is the radiation from the shock recompression zone in the near wake (cf. Fig.9.1). The additional rise on the first pulse represents the radiation from the model sides coming into the field-of-view.

9.3.2.5 Electrical Requirements

The rise-time capability of the radiometer is controlled by the RC time constant of the phototube anode coupling circuit. The capacity to ground of the anode itself, the wiring, and the input capacity of the amplifier connected to the anode all contribute to C. The wide-band preamplifier of the ballistic-range radiometers developed at the Ames Research Center[9,17] uses an effective load resistor of 2000 ohms, giving an observed rise-time of 0.060 μsec, which is equivalent to an RC constant about three times shorter. (The measurements were made using a GaAs infrared-light-emitting diode, Hewlett Packard HP4106, as the source.) Hence, the input capacitance is $C = \Delta t/R - 2 \times 10^{-8}/2000 = 10^{-11}$ farads = 10 picofarads, a small value difficult to further reduce. A diagram of the coupling circuit, the preamplifier, and the dynode power supply is shown in Figure 9.9. If the anode circuit is connected directly to the typical oscilloscope vertical deflection amplifier, having an input impedance of 10^6 ohms and an input capacity of 50 picofarads, on the other hand, a load resistor of 500 ohms or less must be placed in parallel across the oscilloscope terminals to obtain a similar time constant. The capacitance of cabling connecting the phototube anode to oscilloscope must also be considered, unless the cable is resistively terminated with its characteristic impedance ($\sim$ 100 ohms). Such small load resistors lead to large pulse currents in the anode circuit, which in turn changes the electron multiplication of the dynodes, unless the power supply providing dynode voltages has low output impedance. The effective impedance can be reduced by placing capacitors across the dynode voltage terminals to provide the energy required for the dynode current pulses without dynode voltage fluctuations and consequent changes in tube gain.

Excessive radiation falling on the photocathode, or excessive pulse current demands in the last dynode or anode circuit, leads to saturation where the output voltage is no longer linearly related to the incident radiation. Tests, using transient radiation sources, should be made to determine the linear range of operation, particularly as a function of the applied power supply voltage across the dynodes. Control of the maximum radiation falling on the photocathode is most easily accomplished by adjusting the distance from the photocathode to the model flightpath, or by the use of neutral density filters placed in the light path. Thin etched brass plates, having multiple holes on 1-mm centers, for example, with optical transmissions of one to ten percent, have been found particularly useful.

Stable and reproducible operation of multiplier phototubes also requires careful measurement and control of the high-voltage supply, since the tube gain depends critically upon applied voltage ($G = \delta^n$, where G = total current gain, δ = gain of single dynode stage, approximately proportional to applied voltage, and n = number of dynode stages). Differentiation of the equation gives $dG/G = n \, d\delta/\delta$; hence small changes in applied voltage are magnified by the number of dynode stages, n, in their effect on total gain.

Further details regarding the proper operation and calibration of multiplier phototubes can be found in Appendix A.

Liquid nitrogen cooled Indium Antimonide detectors are operated at zero bias and require a current preamplifier having low input impedance (< 100 ohms), and a current gain of 10^2 to 10^3, for providing an adequate electrical signal for oscilloscope display. As previously remarked upon, Figure 9.7 diagrams the preamplifier developed at NASA Ames Research Center, for this purpose.

9.3.2.6 Spectral Filtering

The usefulness of radiometers can be tremendously enhanced by spectral filtering. Attention can be directed to specific spectral regions, much narrower than the photocathode spectral response, or to radiation from individual species. If a sufficient number of filtered radiometers are used, it is possible to obtain low-resolution spectra over the spectral range for which photocathodes will respond. This spectral range is normally restricted (a) at short wavelengths, by either absorption in the intervening gases (for air, ~ 1800 Å) or by the phototube window transmission cutoff, (for fused silica ~ 2000 Å), and (b) at long wavelengths, by photocathode work functions, ~ 12,000 Å. The infrared limit can be further extended by the use of infrared detectors. Multichannel radiometers have been constructed using two filtering techniques.

Made-to-order interference filters were utilized in the 12-channel system shown schematically on Figure 9.10 The resultant spectral response curves, R_λ, which are the product of the spectral transmission of the filters and the spectral responsivities of the multiplier phototubes, are shown in the upper portion of the figure. Note that the spectral coverage extends from 0.20μ to 1.15μ and within this interval is almost complete. The lower portion of the figure shows the physical arrangement of the radiometer components consisting of slits, interference filters, neutral density filters (as required), and multiplier phototubes. They are positioned in a pie-shaped array so as to view the model from the side at a single point along the flightpath and over a reasonably small angular extent. Typical research results obtained by this multichannel radiometer are reported in References 9.2, 9.18, and 9.19.

Similar multichannel radiometers using various physical arrangements have been developed at almost all ballistic range laboratories.

Spectral filtering can also be obtained by utilizing the spectral dispersion of a prism or grating. Viewing a section of the focal plane of a spectrograph with multiplier phototubes or other photon detectors is a well-known technique for observing a selected region of the optical spectrum. An application of this technique to a multichannel ballistic-range radiometer is shown in Figure 9.11. The sketch shows 9 monochromator-radiometers of a total of 18, arranged in two tiers of 9 each, all positioned so as to view from slightly different angular positions the model flightpath at almost one point. Bausch and Lomb model 30-84-40 monochromators, with 1/4-meter focal length and 67 Å/mm reciprocal dispersion, individually provide filtering for each channel. Blocking filters are used to attenuate the second and higher order spectrum.

A particular advantage of dispersive filtering is that spectral adjustments are available. Not only can the set of monochromator-radiometers be arranged to cover the complete spectral range (see Ref.9.12) as was provided by the set of interference filter radiometers shown on the previous figure, but they can be set at selected wavelengths, with the appropriate spectral width, for study of specific radiating systems. An example of the measured and predicted spectral response of a single monochromator channel set to observe the 0.1 vibrational head of the CN (violet) molecular system at 4216 Å is shown in Figure 9.11. The slit function is trapezoidal, and, as is well known, determined by the width of the input and output slits of the monochromator. In this example, one slit opening is about 1/2 mm, giving the half intensity bandpass of 30 Å, whereas the other is about 1/3 mm, giving the wavelength extent of the sloped portion of the slit function.

9.3.2.7 Techniques for Theoretical Comparison, Shock-Layer Emission

One of the uses to which shock-layer radiometric observations in the ballistic range has been put is to establish the total emission characteristics of high-temperature air[9.8] and of CO_2-N_2-Ar mixtures[9.20,9.21]. Multichannel radiometers or single broadband multiplier phototubes have been used. Since the broadband phototubes, (S5 or S13 photocathodes for the ultraviolet range, S1 photocathode for the infrared range), do not respond uniformly over the spectral range covered, spectral corrections can be made by appeal to a theoretical relative spectral distribution, or to spectral measurements obtained by a set of filtered radiometers. Reasonable estimates of the total radiation in the spectral range from 0.2 to 1.1μ can be made from single phototube observations by this method. An S-5 phototube, for example, typically observes about 0.6 of the total radiation from air in this spectral range[9.8]. The emission outside this range, mainly in the vacuum UV portion of the spectrum, is not measured nor accounted for in this comparison.

Several different methods, varying in complexity, have been developed for comparing the radiometric observations with predictions. If the assumption is made that the gas is optically thin (which is typically the case for the spectral range observed and for the thin shock layers of ballistic-range models), then the spectral emission from the shock-layer volume viewed by the radiometer is

$$W_\lambda \text{, watts}/\mu = \int_V E_\lambda \, dV \tag{9.11}$$

where E_λ is the volume emission coefficient, watts/cm$^3\mu$, and is a function of the space coordinates of the volume element in the shock layer. The symbol V represents the observed shock-layer volume and is less than the total shock-layer volume for radiometers which view the model from the side as, for example, in Figure 9-8. Predictions for W_λ require knowledge of the thermodynamic properties in the shock layer as well as the emission properties of the shock-layer gases. Such predictions have been particularly successful when generated for comparison with the emission from a single radiating species, as will be discussed.

When it is desired to reduce the experimental observations directly to a volume emission coefficient, the expression utilized has been[9.8]

$$E_{t_\lambda} , \text{watts/cm}^3\mu = W_\lambda/V_{eff} . \tag{9.12}$$

where V_{eff} can be considered as an effective volume having the thermodynamic properties existing directly behind the normal part of the bow shock and which emits the observed radiation. The effective volume will be less than the total shock-layer volume, since (a) the observable volume is reduced by the bulge of the model face for radiometers viewing at right angles to the flightpath, and (b) almost everywhere in the shock layer the average emission per unit volume is less than that from the gas directly behind the bow shock. If we assume the shock wave is concentric with the spherical model nose, then the observed volume is defined by the body surface, the shock wave, the corner expansion fan and a cylindrical surface tangent to the model surface and parallel to the radiometer line of sight. The expression (in spherical polar coordinates, r, θ, ϕ) for the effective volume then becomes:

$$V_{eff} = \int_0^{\theta_m} \int_R^{r_2} \int_0^\pi r^2 (E_\lambda(\theta,r)/E_{t_\lambda}) \sin\theta \, d\phi \, dr \, d\theta + \int_0^\theta \int_{r_1}^{r_2} \int_0^\phi r^2 (E_\lambda(\theta,r)/E_{t_\lambda}) \sin\theta \, d\phi \, dr \, d\theta . \tag{9.13}$$

where r_2 is the shock wave radius, R is the body radius, r_1 is a point on the cylindrical surface given by

$$r_1 = R[\sin^2\theta \cos^2\phi + \cos^2\phi]^{-1/2} , \tag{9.14}$$

θ_m is the co-latitude of the model, and ϕ the limit of the integral defined as

$$\theta_m = \text{const} = \sin^{-1}\{[1 - (R/R + \delta)^2]^{1/2} [\sin \theta_m]^{-1}\} \tag{9.15}$$

or

$$\phi = \sin^{-1}\{[1 - (R/R + \delta)^2]^{1/2} [\sin \theta]^{-1}\} \tag{9.16}$$

as dictated by the intersection of the spherical and cylindrical surfaces bounding that part of the shock layer on the side opposite the radiometer. It should be noted that the effective volume depends upon the relative distribution of radiation through the shock layer, $E(\theta, r)/E_t$, and not upon the absolute intensity levels.

Calculations of the effective volume for an inviscid shock layer have been made for air, utilizing the relative variation in total radiation as predicted in Reference 9.22*, and letting the total shock-layer volume be defined as

$$V_{total} = \frac{2\pi R^3}{3} \left[(1 + \delta/R)^3 - 1 \right] \left[1 - (1 - \frac{1}{4} [R/d]^{-2})^{\frac{1}{2}} \right] , \tag{9.17}$$

where d is the model diameter and δ the shock standoff distance. The calculations account for the r variation in $E(\theta,r)$ by computing only $E(\theta,0)$ and $E(\theta,\delta)$ and letting $E(\theta,r)$ vary linearly for intermediate r values. The results for three model nose radius to diameter ratios are shown in Figure 9.12 as a function of shock-wave standoff distance.

Other approximations for the value of K have been given in the literature; in Reference 9.23 a value of K = 0.1 has been used for a spherical body.

9.3.3 Measurements of Radiation Distribution

As is evident from Figure 9.1, the radiative emission about a free-flight model has a complex spatial distribution. Air species and their dissociated and ionized products emit radiation in the shock layer; ablation species and reaction products with the free-stream gas emit radiation in the boundary layer; and both can emit radiation from the wake. Radiometric measurements are more valuable when spatial resolution of the flow field is possible; and the use of slits, which define a narrow field-of-view for the radiometer, is a convenient way of obtaining sufficient spatial resolution, so that, at least, radiation from the shock layer and wake are well separated. Slit widths, however, cannot be reduced indefinitely. In addition to limits imposed by diffraction phenomena, the radiometer must have sufficient rise-time capability to respond to a radiation source during the time it passes through the slitted field-of-view. For example, if the radiometer rise time is 0.1 μsec and the model velocity 8 km/sec, then the minimum allowable slit width is $8 \times 10^{+6}(0.1 \times 10^{-6}) = 0.8$ mm.

Other methods of obtaining spatial resolution have been developed. Because of the desire to know how shock-layer radiation is distributed across the front face of blunt bodies (for radiative-heating studies and for checking calculations such as those for the effective volume as discussed in the previous section), techniques have been developed for measuring the distribution. We describe, next, two methods which have produced useful results.

---

* The absolute emission predictions from this report are now considered obsolete. However, the relative variation with velocity and density is approximately valid. More up-to-date emission predictions can be found in Reference 9.9

In the first metnod a nearly head-on view of the model front face is imaged with a mirror and lens onto a plate, as depicted in Figure 9.13. Focal lengths and distances are adjusted so that the model image is in focus when located at the plate center. The flight off-axis angle of viewing makes the model image sweep across the plate as the model flies down the range. The center of the plate contains a hole (diameter ~ 3 percent of the model image diameter) behind which is located a multiplier phototube. When the model flies by, the phototube scans the radiative distribution across the model image, and if the alignment with the model flightpath is correct, the scan passes through the model line of symmetry giving the desired radiation distribution. The spectral range of operation depends upon the photocathode response and the transmission characteristics of the optical elements between the phototube and the model and, if desired, an interference filter can be placed in the optical train to study a specific radiating species. Successful measurements obtained by this "image dissection" method have been published in Reference 9.24.

Another method of obtaining head-on radiation-distribution measurements replaces the orifice plate described above with the photocathode of an image-converter camera. A model detector is positioned along the range to operate the camera when the model image is focused on the photocathode. Exposure times are about 1/4 microsecond. Standard step-wedge techniques are used to calibrate the film density versus intensity response and the result is a head-on photograph which gives the relative radiation distribution over all the model front face. In contrast to the image-dissection technique which has the advantage of linearity of response, the photographic method records the entire radiation distribution of the shock layer. The spectral response of the system depends again upon the photocathode response of the image-converter tube and the transmission of any optical elements in the light path. Filters can also restrict the spectral range if desired, as long as adequate intensity levels are available for exposure of the film at the output of the image-converter camera. An example of photographs obtained by this method is shown in Figure 9.14, along with flow-field shadowgraphs and a plot of the relative radiation distribution obtained from the densitometer traces of the image-converter camera negatives. The six bright horizontal lines in the head-on photographs are caused by the grid structure in the camera tube and do not represent emission from the shock layer. The method has also been used to measure relative radiation distributions on bodies at angle of attack and preliminary results are reported in Reference 9.25.

9.4 STUDIES OF BASIC RADIATIVE PROCESSES

Several additional ballistic-range radiometric techniques have been developed for studies in which the basic radiative processes taking place in the high-temperature gases of the model shock layer are of particular interest. The instrumentation developed has, in each case, been somewhat unique and different from conventional ballistic-range radiometric instrumentation.

9.4.1 Moving-Source Scanning Spectrometer

The quantitative study of basic radiative processes (i.e., molecular system oscillator strengths, continuum cross sections, etc.) require spectral measurements from gas samples having known thermodynamic properties. Conventionally, such measurements are performed in shock tubes or electric arcs using spectrographs or narrow-band radiometers essentially similar to those used in ballistic ranges. Quantitative studies of selected radiative processes have also been performed in the ballistic range using an instrument called the moving-source scanning spectrometer, described below.

The optical arrangement of the spectrometer is depicted in Figure 9.15. The instrument is a spectrograph with no entrance slit, and a photoelectric readout. As the model moves along the line of flight, the luminous shock layer acts as an entrance slit and by virtue of its movement, sweeps out the spectrum of the shock-layer emission on the exit slit. The measurement is made by a phototube located behind the exit slit. When the model material is chosen so that there is no discernible radiation from the wake in the spectral region being scanned, the shock layer is the only important source of radiation in the flow field, as can be seen in the image-converter photograph included in Figure 9.15. Nonablating metal models and some ablating plastic models have been successfully employed[9.2,9.3] and have given spectra free of wake effects. Successful measurements have been made of oscillator strengths of molecular band systems[9.3], and of cross sections of continuum radiative processes[9.2].

The design of a moving-source scanning spectrograph is based upon standard spectrograph relationships. Some of the practical design principles are: (1) A reasonably small angular collimator scan (5 to 10°) should be used to prevent significant change in the fraction of the shock-layer volume being observed. (2) One of the optical elements of the spectrometer should be masked down so that the remaining elements are underfilled with radiation during the scan. This feature prevents the instrument intensity calibration from being sensitive to variation in the model flightpath. (3) To maximize spectral resolution, the output slit width should be adjusted to just encompass a monochromatic image of the luminous shock layer (4) The spectral resolution is increased for larger collimator focal lengths. However, the spectral extent of the scan is reduced. In fact, the resolution and scan length are related, as can be appreciated by considering that the maximum number of spectral "resolution elements" obtainable is simply given by the luminous shock layer width along the flightpath divided into the length of the observed flightpath.

A four-channel scanning spectrometer, covering the spectral range $0.2 < \lambda < 1.9$, has also been constructed[9.26]. An example scan from this instrument, having about 25 Å spectral resolution, is shown in Figure 9.16. The model is flying through a 60-mm-Hg gas mixture of 27 percent CO_2 and 73 percent N_2 at 6.0 km/sec. Theoretical predictions for a transparent gas[9.10], for the expected molecular band radiation, are also shown on the figure for comparison purposes. It can be observed that there is a reasonable correspondence between theory and experiment

and that band systems of CH, NH, CN (violet), C_2 (Swan), and CN (red) are observed along with atomic lines from C and O . By using a longer focal-length collimator with this instrument, the spectral resolution has been increased to 4 Å, but at the cost of a much reduced spectral scan.

9.4.2 Measurements in the Vacuum-UV Spectral Range

At the high temperatures reached in vehicle shock layers during entry into planetary atmospheres an appreciable portion of the radiation contributing to vehicle heating lies in the vacuum-UV portion of the spectrum ($\lambda < 2000$ Å). Laboratory measurement of this radiation is particularly difficult since any intervening window material or gas containing nitrogen, oxygen, CO_2 , etc., is so strongly absorbing that the radiation detectors must be placed adjacent to the high-temperature gas sample being observed, or all of the absorbing gas must be removed from the light path by, for example, differential vacuum pumping.

The ballistic-range technique depicted in Figure 9.17 has been successfully developed for making vacuum-UV measurements[9.27]. To circumvent the difficulty introduced by intervening windows and gas, the ultraviolet radiation from the model shock layer is measured by a radiometer placed directly in the flightpath. The radiometer consists of an ultraviolet-sensing phosphor, sodium salicylate, sprayed on a quartz substrate, a turning mirror, and a calibrated multiplier phototube to measure the phosphorescent output. The measurement is made in the last few microseconds prior to model impact onto the detector. In practice, two detectors are placed in the model path ((Fig.9.17);; one is filtered with quartz or CaF_2 so as to allow determination (by taking the difference between the two readings) of the vacuum-UV radiation below the cutoff wavelength of the filter material. In this way, some resolution of the vacuum-UV spectral range can be obtained in the measurements.

Calibration of the detector system is done by determining the quantum efficiency of sodium salicylate as a function of wavelength (extensively reported in the literature), calibrating the multiplier phototube in the spectral range (~ 4200 Å) of the phosphorescent output, and considering the solid angles and distances from the model shock layer to the sodium salicylate detector screen and from the screen to the multiplier phototube cathode.

Measurements of vacuum-UV continuum and line radiation from nitrogen obtained by this method are reported in Reference 9.28. Because of the residual free-stream gas absorption between the model shock layer and detector at the required stream pressures and because of the desire to reach shock-layer temperatures above $13,000°$ K at moderate model-launch velocities (< 8 km/sec), a mixture of nitrogen and neon was used as the test gas. Neon is easily shock-heated to high temperatures and, furthermore, except for isolated narrow-spectral-line absorption, is optically transparent down to its photoionization edge at 575 Å. It was found, however, that for the 99 percent neon, 1 percent nitrogen mixture used, and for the conditions of the reported tests, thermodynamic equilibration of the gas in the shock layer was a problem. This problem, however, does not detract from the basic approach described to vacuum-UV radiometry in a ballistic range which will have additional applications as well.

APPENDIX

Radiometer Calibration Techniques

Roger A. Craig and William C. Davy
NASA-Ames Research Center

9.5 INTRODUCTION

This appendix contains a discussion of ballistic range radiometer calibration techniques. Emphasis is placed on problems which arise because of the significant differences between the intensity and time scale of the radiation from the ballistic-range event and from the available calibration sources. The discussion is based upon a previous treatment given by the authors in Reference 9.17.

A radiometer can be considered a transfer device, that is, a device whose response to the incident flux from the test is compared to its response to the incident flux from a calibration source of known intensity. To increase the reliability of this comparison, the calibration source should simulate as much as possible the intensity-time characteristics of the test source. The viewing geometry is matched if the sources are small compared to the distance to the detector, which is usually the case, and the distances are equal. However, the calibration source is often very much lower in intensity and almost always substantially longer in time duration than the ballistic-range event, requiring that the detector dynamic range, nonlinearities, and possible fatigue effects be known. Relating the test and calibration responses thus requires extrapolations which can be done with confidence only if the effects of changes in intensity and time duration on the instrument response are known.

In the following discussion we treat the mathematical relationship which defines the transfer comparison between test and calibration source, the practical techniques of spectral and absolute calibration, and the extrapolation of instrument-response characteristics from the calibration conditions to the test conditions.

9.6 RESPONSE EQUATION

The radiometer-response equation relates the radiometer signal output to the incident flux falling on the radiometer. This equation must apply in two instances: for the calibration condition and for the test condition.

The concept of a radiometer as a transfer device is easily seen when the response equations are proportioned and written in the form

$$\frac{\epsilon_T}{\epsilon_c} = \frac{\int_0^\infty R(\lambda)T(\lambda)J(\lambda)\ d\lambda}{\int_0^\infty R(\lambda)T(\lambda)L(\lambda)\ d\lambda}, \tag{9.18}$$

where ϵ_T and ϵ_c are the radiometer electrical signals (either voltages or currents) from the test and calibration, respectively;

$R(\lambda)$ is the relative spectral response of the detector;

$T(\lambda)$ is the relative spectral transmission of any spectral filter, if present; and

$J(\lambda)$ and $L(\lambda)$ are the spectral radiation intensities incident on the radiometer from the test and calibration, respectively, or alternatively the source emission if the "viewing" geometry is identical.

Before $J(\lambda)$ can be evaluated, ϵ_T and ϵ_c must be measured, the lower integral must be evaluated (by calibration of $R(\lambda)$, $T(\lambda)$, and knowledge of $L(\lambda)$), and the upper integral inverted. Note that $J(\lambda)$ occurs in the integrand of an integral equation. Without knowledge of the form of $J(\lambda)$, exact closed-form solution is never possible. If the relative spectral quality of $J(\lambda)$ is known, however, the integral can be evaluated by factoring out the ratio of absolute to the relative spectral quality. If the relative spectral quality is not known, all that is possible to report are the test results in terms of an effective average flux in the spectral response region of the radiometer.

We will now discuss techniques for determining the various quantities in Equation (9.18).

9.7 CALIBRATION TECHNIQUES

9.7.1 Spectral Calibration of Detectors

The detector relative spectral response, $R(\lambda)$, is determined by comparing its response at various wavelengths to that of another detector of known relative spectral response. It is of particular advantage to use

a comparison detector whose response is independent of wavelength, such as a blackened thermocouple*. The comparisons are made on an optical bench (cf. Fig.9.18) by utilizing along the bench: a radiation source such as a tungsten lamp, a monochromator or a set of narrow-band interference filters to generate radiation at various wavelengths, a chopping wheel, and an arrangement whereby first one and then the other detector can be placed in the optical beam. Special precautions are required to assure that the monochromatic beam is free of scattered radiation of other wavelengths, and the detector apertures are over-filled with radiation so that the detector responses are not critically dependent upon their exact positioning in the beam. Scattered radiation is reduced by using two monochromators in series, or by using an interference filter along with the monochromator.

It has been the experience of the authors that precise response measurements can most easily be made with a modulated beam, utilizing, for example, a chopping wheel (see Fig.9.18) and detecting the signal from the detector with a synchronous amplifier[9.31]. The authors use a Princeton Applied Research, Inc. model no. HR-8 amplifier. Modulating frequencies must be within the capabilities of the radiometer frequency response; for multiplier phototubes and InSb infrared detectors, 0.8 kHz, which avoids higher harmonics of the power-line frequency, is typically used. For thermocouple detectors, 5-20 Hz is typically used. A mechanical chopper allows the use of more stable AC amplifiers after detection, narrow electrical bandwidth to reject noise, and rejection of any background radiation not passing through the mechanical chopper.

9.7.2 Spectral Calibration of Filters

The filter transmission, $T(\lambda)$, is usually the quantity which dominates the determination of the spectrally sensitive range of the radiometer; and for this reason the degree to which it first delineates this region, and second, rejects the unwanted portion of the spectrum, must be investigated. Filter-transmission measurements are made by determining the ratio of the responses of a detector to nearly monochromatic radiation with and without the filter being positioned in the beam. Hence, the measurement system described in the foregoing section can be used. Absorption or interference-filter manufacturers normally will provide transmission calibrations of their filters upon demand. These calibrations are usually obtained on double-beam recording spectrophotometers. Sideband transmission below $T(\lambda) = 0.01$, however, is usually not well determined. If there are possible contributions to the integrals of Equation (9.18) in the filter sideband region, then it is necessary to request careful calibration of this region or determine the sideband transmission oneself.

The common circumstance when the sideband transmission is important is when the filter center wavelength is in the UV portion of the spectrum and the complete radiometer is exposed to a standard tungsten lamp for final calibration. Because the lamp radiation increases by a factor of 10^3 or 10^4 in the visible and IR portion of the spectrum, the product of $T(\lambda)\,L(\lambda)$ in the denominator of Equation (9.18) can have contributions to the integral in the visible and IR spectral regions unless the sideband transmission is quite low. Measurements of sideband transmission to as low as 10^{-5} may be required to evaluate the integral. For a specific case described in Reference 9.17, the radiometer output was almost entirely due to response of the detector in the sideband region. The sideband-transmission problem can also be reduced if an additional calibrated ultraviolet-transmitting, visible- and IR-blocking filter is placed in the beam to modify the spectral quality of the source during the calibration. The extra filter reduces the radiation in the unwanted region of the spectrum.

Care must be taken when measuring sideband transmission to insure the spectral purity of the transmitted beam, since any spurious radiation in the region of primary transmission can invalidate the results. It may be advantageous to reduce the dynamic range over which the detector is being used by using a calibrated neutral density filter when taking readings with the filter under measurement out of the beam. These readings must, of course, be corrected by dividing out the neutral filter transmission.

When a monochromator is used for the spectral filter of a radiometer, the monochromator spectral transmission (sometimes called the slit function) can in principle be measured as described above. Another technique, however, which is particularly applicable when the monochromator bandpass is narrow, is to scan a spectrally isolated atomic line (by turning the wavelength control of the monochromator) near the center wavelength of the bandpass. Atomic line radiation at various wavelengths can be obtained from gas discharge lamps (utilizing a monochromator or filters for isolation) of various types, such as low pressure mercury vapor, neon, or argon. Examples of such measurements are shown and discussed in References 9.17 and 9.32.

The sideband transmission of a monochromator tends to be nearly constant with respect to wavelength. For example, the grating monochromators used for the research measurements reported in Reference 9.32 exhibit a constant value of about 10^{-3}, which may not be adequately low for some applications. Additional blocking filters may be required. For prism monochromators, the dispersion (and hence, slit function) varies with wavelength and usually must be measured for each particular application. Reference 9.33 discusses slit functions of prism monochromators.

9.8 ABSOLUTE CALIBRATION

Once the relative value of the product $R(\lambda)T(\lambda)$ is known, an absolute calibration must be performed; that is, the radiometer response must be measured when the radiometer is exposed to an absolute calibration source. A source of known radiation intensity is required - usually a tungsten lamp for wavelengths between 0.25 and 2.5 microns and a heated "blackbody" cavity at longer wavelengths. For calibrated sources useful to 0.2 micron

---

* Information regarding the use of thermopiles as reference in the vacuum ultraviolet and in the infrared can be found in References 9.29 and 9.30.

there are short-lived tungsten lamps available[9.34]. Absolute calibration in the vacuum ultraviolet requires additional techniques and is beyond the scope of the present discussion. Some applicable vacuum UV techniques are discussed in References 9.27, 9.29, and 9.35.

9.8.1 Tungsten-Filament Standard Lamps

Calibrated tungsten lamps, for operation at fixed currents, either AC or DC, and traceable to the US National Bureau of Standards primary standards, can be purchased from several sources. There are available tungsten ribbon filament lamps. These lamps are to be used with spherical mirrors which image the filament onto a small aperture to isolate a small central portion of the filament (see Figure 9.20, to be discussed). The spectral reflectivity of the mirrors must also be measured. This can be easily done in a manner analogous to the filter transmission technique described in Section 9.7.2 The detector, however, must be physically moved from the incident to the reflected beam. The ribbon filament lamps are operated at high currents for use in the ultra-violet, and at a somewhat lower current for use in the infrared. The lower current provides longer operating life. Filament temperatures are from approximately 2200° K to 2500° K. Reference 9.36 discusses these lamps and calibration of the mirrors. Figure 9.19 contains a plot of the spectral irradiance at the radiometer aperture under typical radiometer calibration conditions.

Also available are coiled filament lamps[9.37], which are calibrated in terms of the specific intensity from the entire lamp (i.e., the lamp is not masked) falling onto a surface at a specified distance. These lamps are supplied calibrated as a function of wavelength at a prescribed lamp current. The filament temperatures of the coiled filament lamps are operated near 2900° K, substantially higher than that of the ribbon filament lamp. A plot of spectral irradiance is also shown on Figure 9.19 for typical calibration conditions. The life of the coiled filament lamps has been extended due to the presence of iodine within the envelope[9.38].

9.8.2 Infrared-Radiation Standards

As previously indicated, tungsten ribbon filament lamps, operated at lower temperatures, can be used for an irradiance standard in the infrared spectral range. The lamps are calibrated from 0.5 to 2.5 microns. The spectral range can be extended by using lower temperature blackbody radiation sources. Shown also on Figure 9.19 is the irradiance from a source operating at 1000° C (1273° K), of one cm^2 aperture. The distance from the aperture to the detector was taken to be 10 cm. Several such devices are commercially available.

9.8.3 Operating Practices, Tungsten-Filament Lamps

To increase the lifetime of the calibrated standard, the usual practice is to use a secondary, or working, standard. This working standard is an identical lamp which is purchased uncalibrated and which is compared to the standard and then used for routine calibrations. The function of the standard lamp then is to periodically check the performance of the working standard. References 9.36 and 9.37 give instructions for lamp operation. Not cited therein, but of interest, is the relationship between accuracy of current through the lamp to accuracy in radiant output. This relationship[9.17] for a tungsten filament lamp at temperatures greater than 1000° K is

$$\frac{\Delta i}{i} \cong 10^{-4} \, \lambda T \frac{\Delta L(\lambda)}{L(\lambda)} \, , \tag{9.19}$$

where $\Delta i/i$ is the fractional error in lamp current, $\Delta L(\lambda)/L(\lambda)$ is the fractional error in spectral irradiance, λ is the wavelength in microns, and T is the filament temperature in °K. For example, at a wavelength of 0.25 micron and a filament temperature of 2500° K, the precision in current control must be 16 times greater than the desired precision of the radiant flux. An additional need for precision arises because, in practice, there are three current measurements involved in the calibration of a radiometer: one for operation of the standard lamp, one for initial calibration of the working standard, and one for calibration of the radiometer. For calibration at 0.25 micron, with an expected precision of 5 percent, it is necessary to regulate and measure the lamp current to the order of 0.1 percent.

A typical calibration setup, utilizing a ribbon-filament lamp, a mirror train, an aperture, and a mechanical chopper, is shown in Figure 9.20. The pictured arrangement includes a 3-inch-diameter, 12-inch-focal-length spherical mirror for compact folding of the optical beam. The use of a coiled filament standard does not require imaging mirrors and their calibration. If a coiled filament lamp were used, it would be positioned at the aperture (image of the ribbon filament lamp) shown in Figure 9.20.

9.9 EXTRAPOLATION FROM CALIBRATION TO TEST CONDITIONS

The response equation (Eq. (9.18)) was written presuming that the absolute sensitivity of the radiometer is identical for both the calibration and test events. Since the signal intensities and time duration are different during calibration and testing, the extent to which this presumption holds must be investigated. It therefore becomes necessary to define the limits within which the radiometer output remains a known function of the incident flux Additionally calibration is usually done in a continuous, or steadily modulated mode with typical pulse lengths of 0.6 milliseconds (mechanically chopped at 0.8 kHz), whereas the test event is usually a single pulse of a few microseconds duration preceded by a long period of dark quiescence; thus it is also necessary to investigate and measure possible changes in sensitivity due to fatigue effects.

In addition to the time scale difference, there is also a difference in intensities. To emphasize this latter difference, compare at 0.391 μ, the source power of the $N_2^+(1-)$, $\Delta v = 0$ bandhead shown on Figure 9.3 with the calibration signal from Figure 9 19. At 50 cm, the equivalent source power for $\Delta \lambda = 5 \text{ Å}$ for the ribbon filament lamp is

$$V = 3 \times 10^{-5} (0.0005) 4\pi (50)^2 = 4.6 \times 10^{-5} \text{ watts}. \tag{9.20}$$

which is weaker by a factor of 10^6 than the test signal at $V = 7$ km/sec. Note that it is indicated from Figure 9.3 that this calibration signal is too weak to be measured with a multiplier phototube having a rise-time of 0.1 μ sec. Low-level signals such as this are measured by lengthening the rise-time of the radiometer by, for example, adding capacitance at the multiplier phototube anode (see Fig.9.9), or by use of a synchronous amplifier[9,31]

9.9.1 Dynamic Range, Multiplier Phototubes

Multiplier phototubes are inherently linear devices; a doubling of the photon flux doubles the output signal. However, there is an upper limit of useful dynamic range usually determined by one of several saturation phenomena, either from the associated electronics, or from the phototube itself. Multiplier phototubes commonly exhibit three types of saturation[9,39,9,40,9,41] photocathode, space charge, and reduction of dynode voltage. Photocathode saturation results from excessively high radiation fluxes incident on the photoemissive surface. Space-charge saturation is the result of high currents within the tube at the later dynode stages changing the electrostatic field between the dynodes. Dynode voltage reductions are the result of high currents within the tube which are drawn from the capacitors on the external voltage divider. If the charge depletion is significant, the voltage is reduced enough to change the overall amplification of the tube. It is often the case that the divider capacitors are chosen so that the limiting saturation observed during ballistic-range testing will be photocathode or space charge, but the limiting saturation observed during longer calibration pulses might be from reduction of dynode voltage. Thus, the saturation limits for both testing and calibration must be determined.

A simple method of determining the onset of saturation, and hence the linear dynamic range of the detector, is by measurement of the transmission of a filter. The incident intensity falling on the detector is increased as the filter transmission is measured over and over again until the transmission appears to increase, indicating saturation of the radiometer with the filter out of the beam. This, then, defines the maximum linear output from the radiometer, for the conditions of this measurement.

Saturation limits should be determined for the calibration conditions, with the mechanical chopper operating at the same rate as for the absolute calibration tests, as well as under conditions simulating the ballistic-range event, both in time duration and intensity. A practical method of performing this latter test is by use of a General Radio strobe lamp, Type 1531-A, which has a flash duration of about 3 μsec and which is intense enough to saturate the detector.

9.9.2 Dynamic Range, Infrared Detectors

Infrared detectors of the Indium Antimonide type, which are broad-band photodiodes, are not necessarily linear in response. The degree of nonlinearity depends on the diode characteristics of the particular detector, and the voltage developed across the detector terminals. If the detector is operated as a current source (i.e., terminated by a low resistance, $\sim 100 \, \Omega$ or less), the output will be linear over a wide range. The current amplifier developed at Ames Research Center (cf. Fig.9.7) is adjustable to obtain zero volts across the detector for the background conditions, and provides an input impedance of approximately $20 \, \Omega$.

Curves of output signal versus input radiation can be obtained in a direct manner by noting the output signal as the distance from detector to source is changed. The detectors examined, using the amplifier described above, have exhibited linear behavior over the entire operating range of the radiometer, from signals just discernible from the amplifier and shot noise (the limiting-noise sources) to signals just saturating the amplifier - a dynamic range of about 3 decades.

The authors have not yet made extensive measurements of fatigue effects of InSb radiometers. For the few detectors examined, the long-term stability has been excellent, the sensitivity has remained constant to within a few percent.

9.9.3 Fatigue Effects, Multiplier Phototubes

Fatigue effects[9,39] are defined as changes of multiplier phototube sensitivity due to the prior history of tube use. Generally these effects are the result of strong irradiance, high-ambient temperature, or high currents within the tube. The effects are not well understood and in some instances the sensitivity may not recover to the previous value for particularly severe exposures. Fatigue effects are always reduced by decreasing the irradiance level and the tube currents to as low a value as possible during calibration and use. The procedure used by the authors[9,17] to determine the extent of fatigue effects, and hence correct for it, simply compares detector response due to a steadily modulated source to that of a single short pulse from the same source after the tube has been dark-rested for a period of time. The test is repeated for various source intensities. These corrections have been found to be generally less than 10 percent for the majority of photo-tubes checked and may be positive or negative. Fatigue phenomena have been found to depend on the particular phototube; some phototubes show unusual sensitivity to fatigue effects and are rejected for use in any calibrated radiometer.

An additional fatigue effect has been observed when the radiometer is physically attached to the facility. Apparently the shock load from the ballistic-range gun can damage the tube. This problem can be avoided by using vibration isolative mounting or by remotely locating the radiometers.

REFERENCES

9.1 Page, William A. *A Survey of Thermal Radiation Studies of Ablating Bodies in the Ballistic Range.* NASA TN D-3741, 1967.

9.2 Cooper, David M. *Equilibrium Air Radiation from Shock Layers at 11.3 Km/sec.* AIAA J., Vol. 4, No. 12, Dec. 1966, pp. 2125-2130.

9.3 Reis, Victor H. *Oscillator Strengths for the $N_2(2+)$ and $N_2^+(1-)$ Systems from Observations of Shock Layers About Hypersonic Projectiles.* JQSRT, Vol. 4, 1964, pp. 783-792.

9.4 Borucki, William J. *Spectrographic Observations of Polycarbonate, Polyethylene, and Polyformaldehyde in a Ballistic Range, an Arc-Jet, and a Diffusion Flame.* AIAA J., Vol. 5, No. 7, July 1967, pp. 1329-1336.

9.5 Wiese, W.L. Smith, M.W. Glennon, B.M. *Atomic Transition Probabilities.* Vol. 1 – Hydrogen Through Neon. Natnl. Bur. Stds., 1966.

9.6 Whiting, Ellis E. *Mars Atmospheric Composition by Shock Layer Radiometry During a Probe Experiment.* AIAA Paper No. 67-293.

9.7 Reis, Victor H. *Oscillator Strength of the CN Violet System.* JQSRT, Vol. 5, 1965, pp. 585-594.

9.8 Page, William A. Arnold, James O. *Shock Layer Radiation of Blunt Bodies at Reentry Velocities.* NASA TR R-193, 1964.

9.9 Page, W.A. Compton, D.L. Borucki, W.J. Ciffone, D.L. Cooper, D.M. *Radiative Transport in Inviscid Nonadiabatic Stagnation-Region Shock Layer.* AIAA Selected Reprint Series, Vol. 7, Radiative Gas Dynamics, Robert J. Goulard, Editor.

9.10 Woodward, Henry T. *Predictions of Shock-Layer Radiation from Molecular Band Systems in Proposed Planetary Atmospheres.* NASA TN D-3850, 1967.

9.11 *Kodak Plates and Films for Science and Industry.* Kodak Scientific and Technical Data, No. P-9, 1967.

9.12 Stephenson, Jack D. *Measured and Predicted Ablation-Product Radiation in the Near Wake.* AGARD Conference Proceedings No. 19, Fluid Physics of Hypersonic Wakes, Fort Collins, Colorado, May 1967.

9.13 Weiss, H.H. *Exploding Thin Film Optical Switch.* Applied Optics, Vol. 4, No. 8, Aug. 1965, pp. 935-936.

9.14 Pirroni, J.S. Stevens, R.R. *High Speed Electromagnetic Shutter.* The Review of Scientific Instruments, Vol. 38, No. 3, March 1967, pp. 382-383.

9.15 Wurster, W.H. *High Speed Shutter for Spectrographs.* Review of Scientific Instruments, Vol. 28, New Series, 1957, pp. 1093-1094.

9.16 Hiltner, W.A. *Astronomical Techniques.* Vol. II of Stars and Stellar Systems: Univ. of Chicago Press, 1962. Chapter 6, A. Lallemand, Photomultipliers.

9.17 Craig, Roger A. Davy, William C. *Absolute Radiometers for Use in Ballistic Ranges and Shock Tubes,* NASA TN D-5360, 1969.

9.18 Compton, D.L. Cooper, D.M. *Measurements of Radiative Heating on Sharp Cones.* AIAA J., Vol. 3, No. 1, January 1965, pp. 107-114.

9.19 Davy, W.C. Craig, R.A Chapman, G.T. Compton, D.L. *Ablation Products Radiation from Cones.* AIAA, Vol. 2, No. 9, September 1964, pp. 1583-1589.

9.20 Arnold, J.O.
Reis, V.H.
Woodward, H.T.
Studies of Shock-Layer Radiation of Bodies Entering Planetary Atmospheres. AIAA J., Vol. 3, No. 11, November 1965, pp. 2019-2025.

9.21 James, C.S.
Experimental Study of Radiative Transport from Hot Gases Simulating in Composition the Atmospheres of Mars and Venus. AIAA J., Vol. 2, No. 3, March 1964, pp. 470-475.

9.22 Kivel, B.
Bailey, K.
Tables of Radiation from High Temperature Air. AVCO Everett Research Report 21, 1967.

9.23 Sadowski, C.M.
Dionne, J.G.G.
Trottier, G.
A Study of Shock-Cap Radiation from 1.0 inch Diameter Hypersonic Spheres. Part 1. Projectile Velocities to 17,000 ft/sec. CARDE TR. 491/64, April 1964.

9.24 Givens, J.J.
Canning, T.N.
Bailey, H.
Measurements of Spatial Distribution of Shock Layer Radiation for Blunt Bodies at Hypersonic Speeds. NASA TM X-852, 1964.

9.25 Reynolds, Robert M.
A Technique for Determining the Spatial Distribution of Relative Radiant Intensity in Shock Layers over Bodies at Angle of Attack at Hypersonic Speeds. NASA TM X-61224, 1968.

9.26 Whiting, Ellis E.
A New Four Channel Scanning Spectrometer for Ballistic-Range Radiometry. IEEE Transactions on Aerospace and Electronic Systems, Vol. AES-3, No. 3, May 1967.

9.27 Compton, Dale L.
Measuring Vacuum Ultraviolet Radiation from High-Temperature Nitrogen. IEEE Transactions on Aerospace and Electronic Systems, Vol. AES-3, No. 3, May 1967.

9.28 Compton, Dale L.
Measurements of Ultraviolet (575 $\overset{o}{A}$ – 1800 $\overset{o}{A}$) Radiation from Nitrogen at Temperatures from $13,000^\circ$ to $16,000^\circ$ K. AIAA Paper No. 66-422.

9.29 Johnson, R.G.
Madden, R.P.
On the Use of Thermopiles for Absolute Radiometry in the Far Ultraviolet. Applied Optics, Vol. 4, No. 12, Dec., 1965.

9.30 Eisenman, W.L.
Bates, R.L.
Merriam, J.D.
Black Radiation Detector. J. Opt. Soc. Am., Vol. 55, No. 6, June 1963.

9.31 Moore, Robert D.
Lock-In Amplifiers for Signals Buried in Noise. Electronics, June 9, 1962.

9.32 McKenzie, Robert L.
Arnold, James O.
Experimental and Theoretical Investigations of the Chemical Kinetics and Non-equilibrium CN Radiation Behind Shock Waves in CO_2-N_2 Mixtures. AIAA Paper No. 67-322.

9.33 Strieff, M.L.
Ferrisco, C.C.
An Investigation of the Slit Function of Infrared Littrow Type Monochromators. Paper Y-3, Symposium on Molecular Spectroscopy. Ohio State Univ. 1964.

9.34 Kostkowski, H.J.
Erminy, D.E.
Hattenberg, A.T.
New Spectral Radiance Calibrations. J. Opt. Soc. Am., Vol. 54, 1964, p. 1386.

9.35 Samson, J.A.R.
Absolute Intensity Measurements in the Vacuum Ultraviolet. J. Opt. Soc. Am. Vol. 54, 1964, p. 6.

9.36 Stair, R.
Johnson, R.G.
Halback, E.W.
Standard of Spectral Radiance for the Region of 0.25 to 2.6 Microns. J. Res. of the NBS – A. Physics and Chemistry, Vol. 644, No. 4, July-August 1960.

9.37 Stair, R.
Schneider, W.E.
Jackson, J.D.
A New Standard of Spectral Irradiance. Applied Optics, Vol. 2, No. 11, November 1963, pp. 1151-1154.

9.38 Zubler, E.G.
Mosby, F.A.
An Iodine Incandescent Lamp with Virtually 100% Lumen Maintenance. Illum. Eng., December 1959, p. 734.

9.39
Phototubes and Photocells, RCA Tech. Manual, PT 60, 1963.

9.40
Dumont Multiplier Phototubes. 4th ed. Dumont Labs, Div. of Fairchild, Clifton, New Jersey, June 1965.

9.41 Baker. D.J.
Wyatt, C.L.
Irradiance Linearity Correction for Multiplier Phototubes. Applied Opt., Vol. 3, No. 1, January 1964.

$$V_\infty = 6.6 \text{ km/s}$$
$$P_\infty/P_0 = 0.08$$
$$\Delta t = 0.05 \,\mu\text{sec}$$
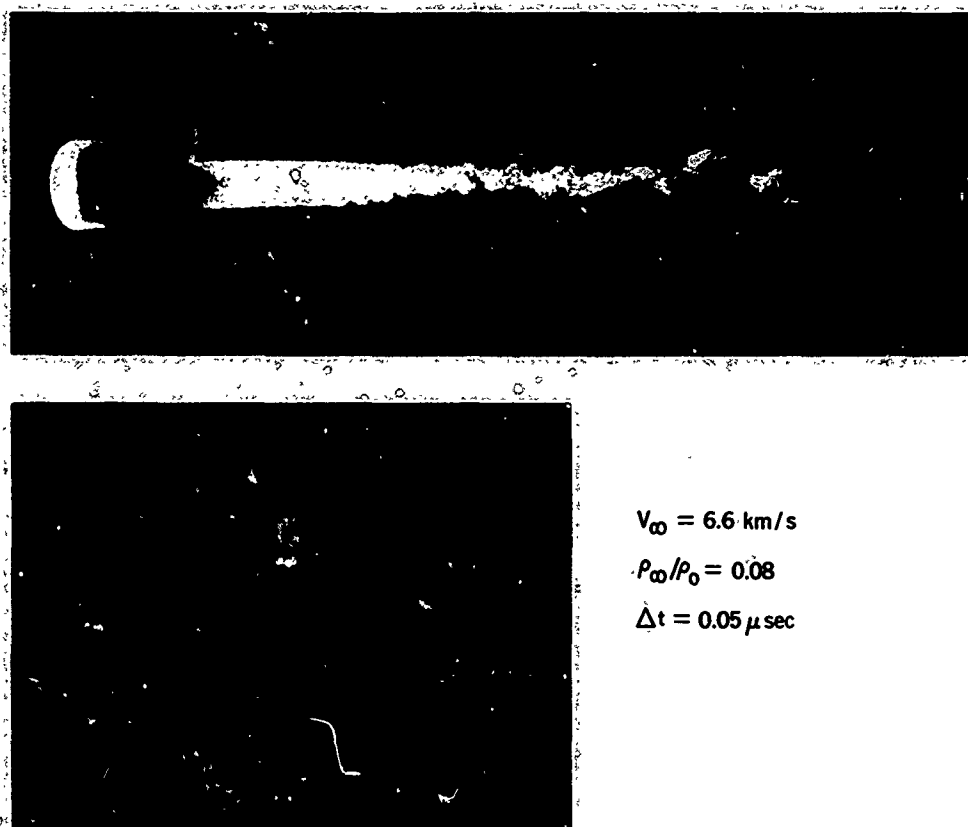
Fig.9.1   Image-converter photograph and shadowgraph of ablating blunt body.
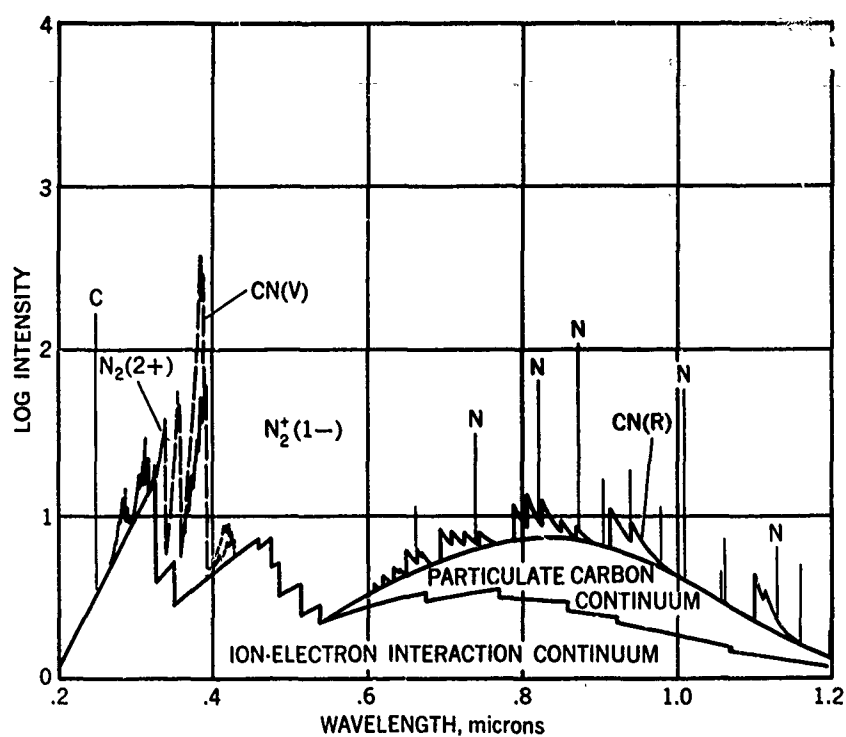
Fig.9.2   Spectral features of radiation from typical ablating ballistic-range model
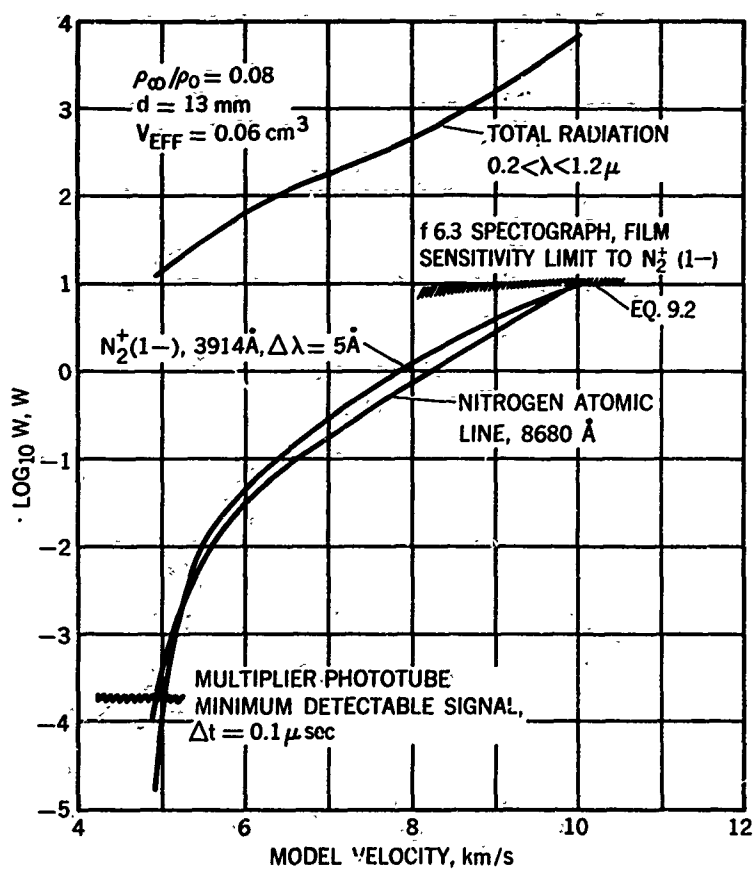
Fig.9.3   Emission from blunt-body shock layer
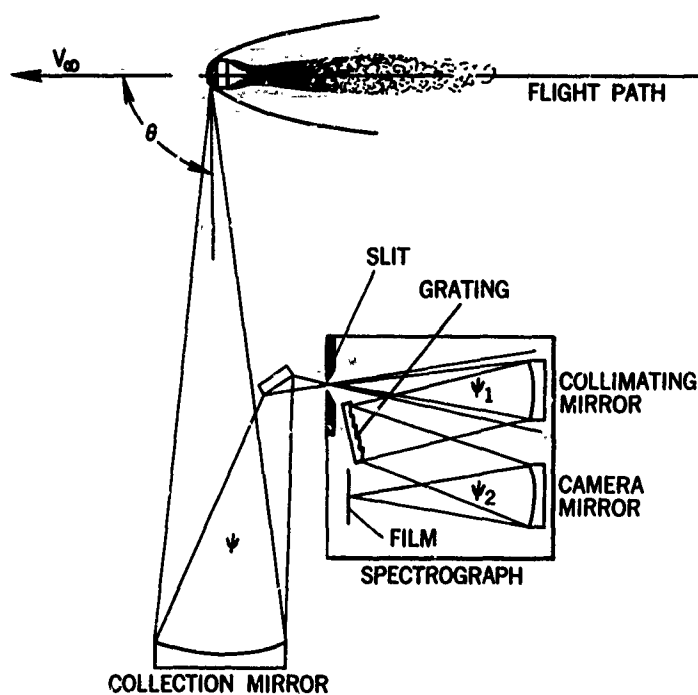
Fig.9.4   Arrangement for spectrographic observation of ballistic-range model

$N_2^+(1-)$

C_2(SWAN)

CN(VIOLET)

NH

Fe

Hg(CALIB.)

Ca⁺ K   Cr

.30   .35   .40   .45   .50   .55

WAVELENGTH, microns
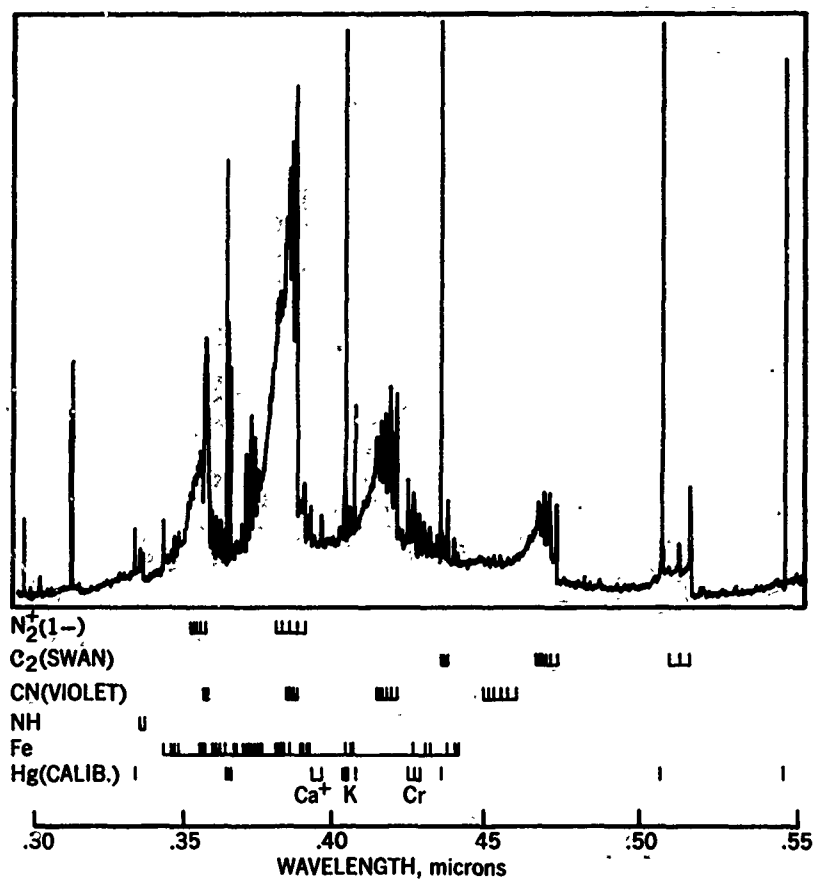
Fig. 9.5   Densitometer record of spectrum from ablating polycarbonate model; $V_\infty = 9.4$ km/sec , $\rho_\infty/\rho_0 = 0.12$,
$d = 13$ mm
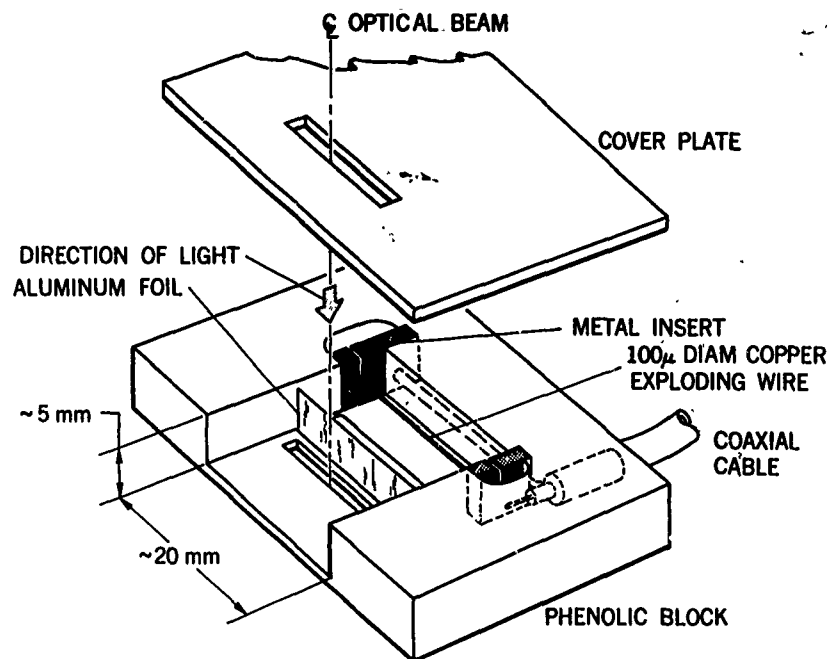
Fig. 9.6   Exploding-wire-driven spectrographic shutter

NOTES:

1. ALL RESISTOR 1/4 WATT UNLESS OTHERWISE SPECIFIED

2. VARIABLE CAPACATORS ARE FOR ADJUSTING
   FREQUENCY RESPONS.

Fig.9.7 Current amplifier for use with infrared detectors

Fig.9.8 Layout of ballistic-range radiometer

NOTE: ALL RESISTORS 1/2 WATT

Fig.9.9 Dynode power supply and signal amplifier for multiplier phototubes
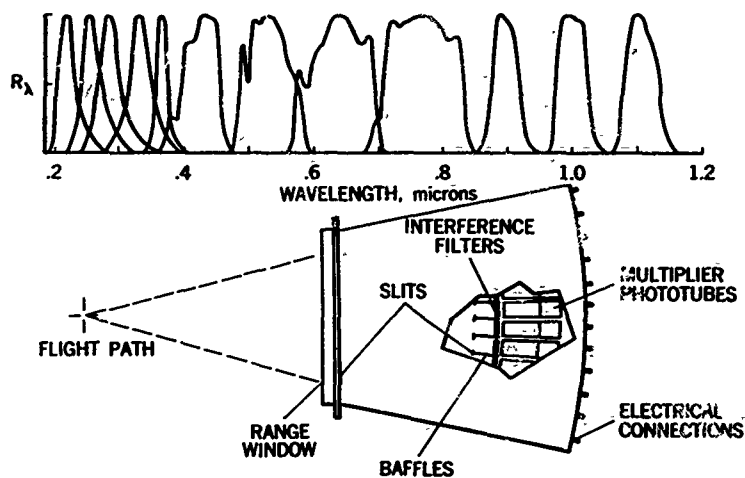
Fig.9.10   Schematic sketch of 12-channel ballistic-range radiometer using interference filters
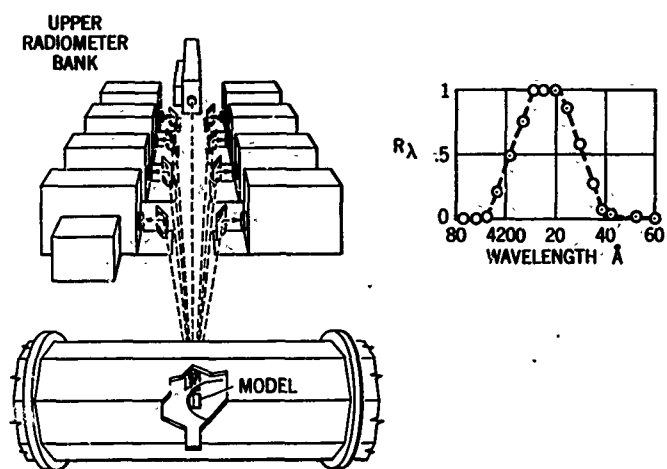
Fig.9.11   Schematic sketch of 18-channel ballistic-range radiometer using monochromator filters
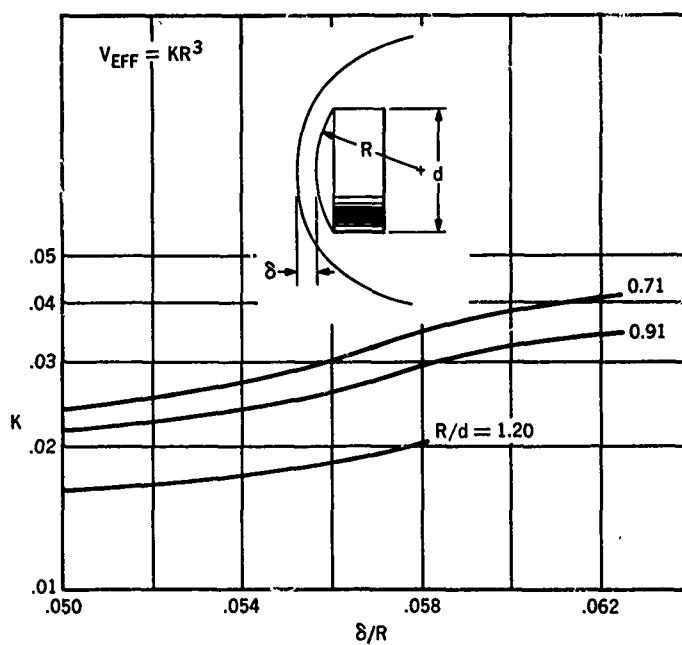
Fig.9.12   Effect of shock-standoff distance and model R/d on effective radiating volume
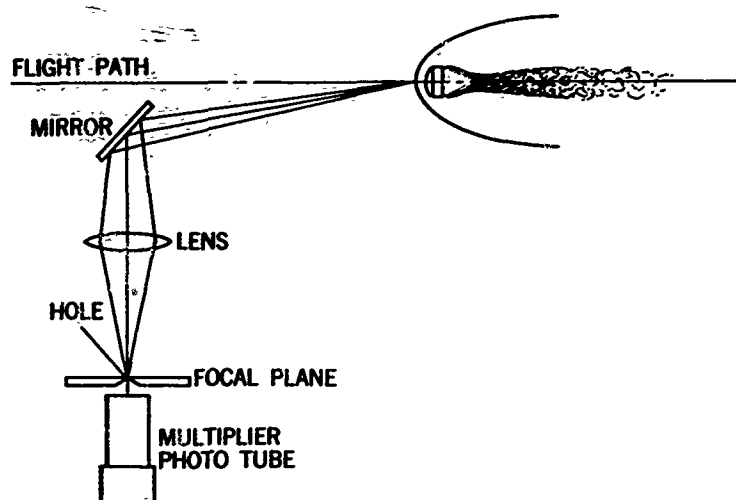
Fig. 9.13   Scanning method of measuring radiation distribution in shock layer

R/d = 0.67

R/d = 1.44

$V_\infty = 6.48$ km/s
$P_\infty = 10$ torr
$\frac{R}{d} = 1.44$

$V_\infty = 6.80$ km/s
$P_\infty = 5$ torr
$\frac{R}{d} = 0.67$

RELATIVE INTENSITY

$\frac{\text{RADIAL DISTANCE}}{\text{MODEL DIAM}}$ MODEL EDGE
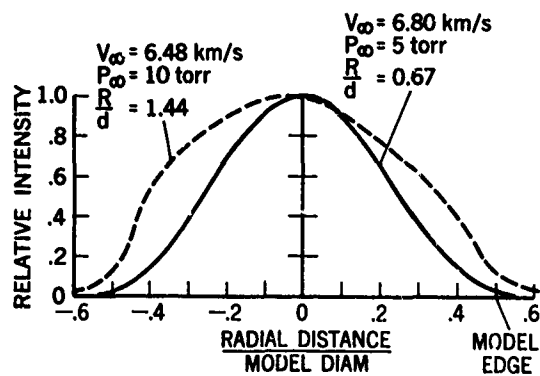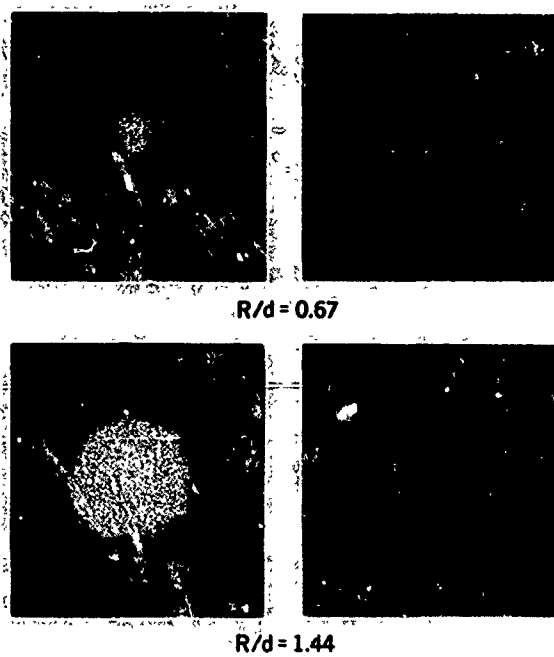
Fig. 9.14   Relative radiation distributions obtained from head-on image-converter photographs of hypervelocity
models.   50 % CO_2 - 50 % N_2 gas mixture for simulating Martian atmosphere
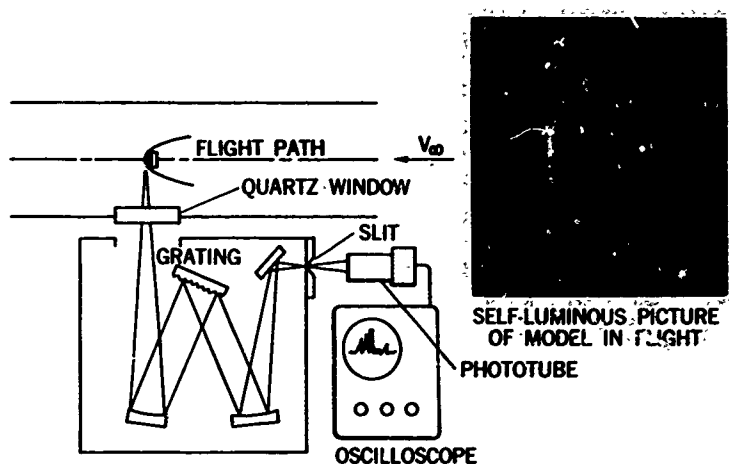
Fig.9.15　Sketch of moving-source scanning spectrometer
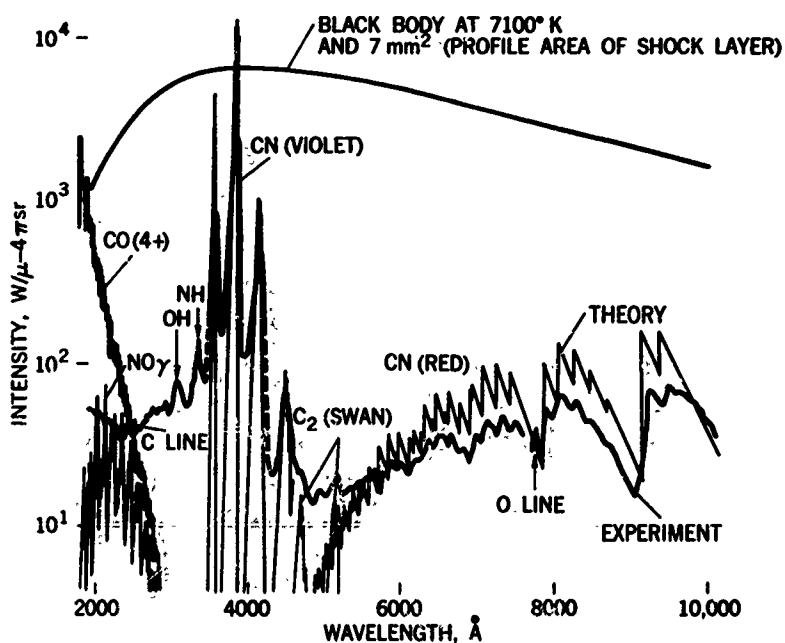
Fig.9.16　Equilibrium radiation from shock layer in simulated Martian atmosphere; $V_\infty = 6$ km/sec,, $\rho_\infty/\rho_0 = 0.08$, Gas composition - 27% CO_2 , 72.6% N_2 , 0.2% O_2
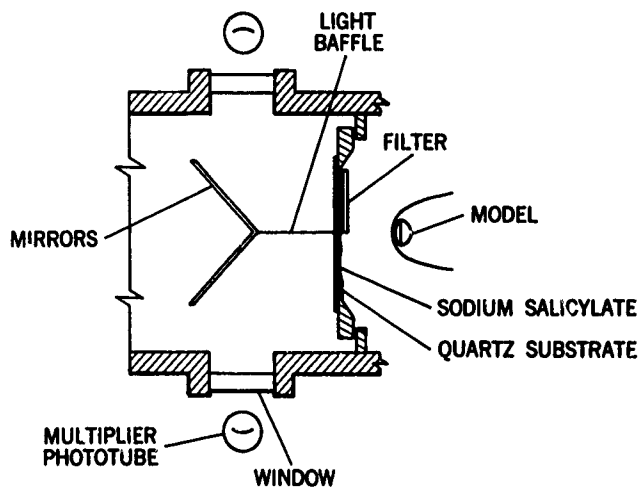
Fig.9.17　Geometry of detection system for vacuum-UV radiation
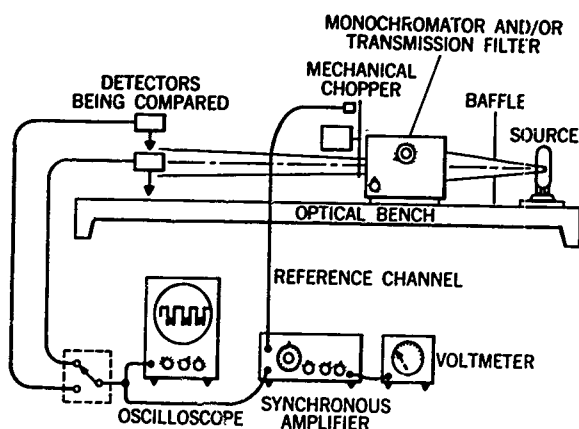
Fig.9.18   Optical and electrical-component arrangement for measuring spectral responses of detectors.
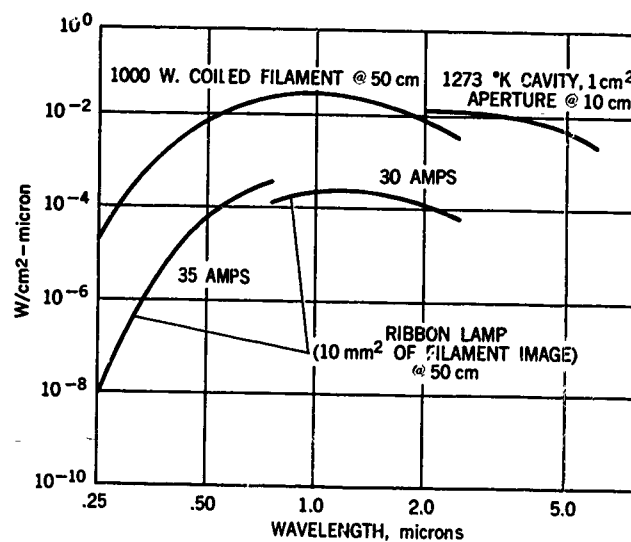
Fig.9.19   Spectral irradiance produced by various standard sources
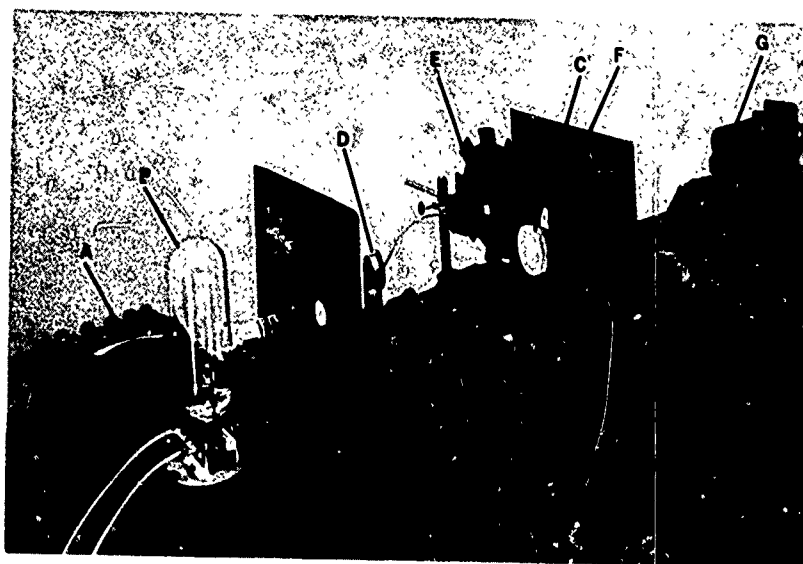
Fig.9.20   Calibration setup utilizing tungsten-ribbon lamp.   A. Precision ammeter;   B. Working standard lamp;
C. Spherical imaging mirror;   D. Flat mirror;   E. Mechanical chopper;
F. Aperture at filament image;   and G. Radiometer under test

CHAPTER 10

MICROWAVE STUDIES

by

M. Gravel, D. Heckman, and R. Tremblay

Canadian Armament Research and Development Establishment
Quebec, Canada

MICROWAVE STUDIES

M. Gravel, D. Heckman, and R. Tremblay

10.1 INTRODUCTION

The chapter which follows here is concerned with the use of microwave techniques in the ballistic range. A notable advantage of these techniques is that no physical disturbance is offered to the flow by microwave probes, and no disturbance of its plasma characteristics is produced by the low intensity microwave radiation which is employed. As will be shown, microwave techniques are not only applicable to the study of the hypersonic flow environment, but also have important roles to play in the development of light-gas-gun launchers. The aim of this chapter is not to discuss every possible application of microwave technology, but rather to concentrate on those techniques which are, or which have been, in routine productive use in ballistic facilities.

The following section begins by discussing Doppler radar techniques for measurements of the velocity and drag of various projectiles in controlled range atmospheres. Velocity measurements are again the subject of the third Section, but here the motion of the projectile as it travels down the launch tube of the gun is the object of measurement, through the use of cavity techniques as well as Doppler radar.

In the fourth section, considerable space has been devoted to a description of the hypersonic flow field and then to a rapid survey of some of the basic electron-producing mechanisms in such a flow. There is also a brief mention of the importance of the measurements of mean electron density distributions to the development of adequate models for complex chemically-reacting hypersonic flow fields. The Section closes with an introduction to the relationship between the microwave measurables such as the phase change and attenuation suffered by electromagnetic waves upon their passage through an ionized gaseous medium and the plasma characteristics of the medium, setting the stage for the discussion of microwave diagnostics to follow.

Section 5 is a description of the plasma sheath effect on the radar cross section for spheres as measured from the head-on aspect, and discusses the physical optics model which has been developed to explain the phenomenon. Section 6 describes the measurement of mean electron density and collision frequency using the microwave interferometer and microwave cavity, among the most productive of all microwave techniques used in the ballistic range.

Finally, in Section 7, the study of scattering of microwave radiation from wakes is introduced. Although not much information about results has yet been published concerning these techniques, their basic interest and practical importance should ensure continued effort in the near future.

10.2 KINEMATIC MEASUREMENTS USING DOPPLER RADAR

In hypersonic range facilities the Doppler radar technique is particularly useful to the aerodynamicist by providing accurate velocity and drag measurements[10.1]. Other kinetic parameters of interest such as oscillation frequencies, rolling rates and maximum angles of attack are better determined by photographic methods. However, amplitude variations appearing in Doppler radar signals can often be related to model oscillations.

The Doppler radar principle is well known[10.2]. The important point is that the electromagnetic signal returned from a moving target, having experienced the Doppler shift, can be beaten against a sample of original signal to yield the Doppler frequency which is relevant to the target velocity component along the line of sight. One interesting aspect of this technique is that continuous records can be obtained over a long portion of trajectory by operating in the continuous-wave mode. As a matter of fact, pulse radars are not really suitable for kinematic measurements in indoor ranges because of the short observation times available.

This section is devoted to the description of one Doppler radar system which has proved to be very useful for data acquisition in hypervelocity ranges. Some remarks are made concerning the accuracy with which velocity and drag measurements can be made using simple recording and data-processing techniques.

10.2.1 Doppler-Radar Apparatus

The type of apparatus being described here was developed at the Defense Research Telecommunication Establishment (DRTE), Canada, by Primich et al.[10.3]. The developments were initially made for the Canadian Armament Research and Development Establishment (CARDE) where extensive measurements have been made in 1.8-meter-diameter hypersonic ranges. More recently, the same technique has been introduced at the General Motors Defense Research Laboratories[10.4].

A schematic diagram of the apparatus mounted in the flight chamber of a hypervelocity range is shown in Figure 10.1. A continuous-wave electromagnetic signal enters the range through a polystyrene window especially designed for minimum reflection[10.5] and is deflected along the flight path of the projectile by a thin expendable microwave reflector. A proper lens[10.6] mounted in the aperture of the circular conical horn antenna ensures maximum gain for the aperture size being used. Typically, with a 30-db antenna operating at 35 GHz a beamwidth of about $6°$ is obtained.

As the projectile travels down the range into the radar beam, microwave energy is returned to the radar according to the reflection properties of the complex structure presented by the hypervelocity model and its associated plasma sheath. This back-scattered signal, whose frequency has been increased due to projectile motion, is converted in the radar head into the so-called "Doppler signal" whose frequency and amplitude depend upon the projectile velocity and effective scattering area respectively.

The heart of the system, as indicated in the block diagram in Figure 10.2, is a hybrid-T which permits the use of a single antenna for both transmission and reception, and which conveys the received signal into the balanced mixer where the Doppler frequency is extracted.

The Doppler signal, whose frequency is typically in the megahertz region, can be recorded on an oscilloscope triggered, for instance, by the passage of the projectile itself in front of a photocell. Oscilloscope records are very convenient both to obtain rapid estimates of the model velocity and to determine the magnitude of its radar cross section. However, accurate velocity and drag measurements usually involve recording on magnetic tape, necessitating often a second frequency reduction of the signal in order to fall within the frequency range of the tape unit.

The Doppler radar technique has been adopted for a number of reasons. One of these, as mentioned earlier, is that it provides continuous measurements. Another interesting feature is that the probing signal appears at a frequency which is high enough to permit the use of a bandpass filter so as to ensure, on one side, the rejection of high-frequency noise, and, on the other side, the rejection of the stationary background signal as well as low frequency signals that may come from vibrations of the test chamber. A typical bandpass filter accepts Doppler frequencies corresponding to model velocities ranging from 2.5 km/sec to 7.5 km/sec.

It should be pointed out that any important static reflections occurring inside the range may interfere with the radar beam and hence affect the phase and the energy distribution along the axis to such an extent that, for instance, the inverse square law dependence with distance could be slightly modified in a more or less random manner. This effect will result in a spatially dependent amplitude and phase modulation of the Doppler signal. Appropriate care must be taken lest this modulation adversely affect the accuracy of the results. Nevertheless, it has been shown[10.3] that when the radius of the test chamber is greater than one hundred wavelengths, the diverging angle of the radar beam can be made small enough to ensure that side wall reflections will occur only in the very far field, so leaving an appreciable working range rather free from interference. For example, in a 2-meter diameter test chamber, measurements at 35 GHz can be made over a good 10 meters without there being any necessity to cover the side walls with microwave absorbent material. However, the end wall facing the radar beam generally needs to be covered.

10.2.2 Free-Flight Velocity Measurements

When the radar beam is aligned along the trajectory, as in the present case, the classical Doppler frequency formula reduces to

$$f_d = \frac{2V}{c} f_0 ,$$ (10.1)

where f_0 is the radar frequency, V the velocity of the model and c the speed of light. From this equation a relative error formula immediately follows

$$\frac{\Delta V}{V} = \frac{\Delta c}{c} + \frac{\Delta f_0}{f_0} + \frac{\Delta f_d}{f_d} ,$$ (10.2)

whose first term on the right side indicates that the accuracy in velocity measurements can never exceed the accuracy with which the speed of light is known, say 1 part in 10^6 as per actual knowledge.

In current hypervelocity range application, the velocity need not be determined to an extremely high precision, and accuracy of 0.1% appears largely satisfactory. In order to achieve this, as the frequency stabilization required for the microwave source poses no problem, the only factor that matters is the precision with which the Doppler frequency is produced, recorded and analyzed.

Notice that the motion of the center of mass of the projectile is not the only mechanism responsible for the frequency shift produced in the range. Any irregularities arising in the axial phase distribution of the radar beam as well as any displacement of the scattering center of the projectile during the period of observation also contribute to the shift. Such phenomena arise, for example, from wall reflections or from model instabilities and associated variations of the ionized flow field. The true nature of these secondary phenomena as well as the exact influence they exert on the Doppler frequency production, are, unfortunately, very difficult to appreciate with confidence To be more specific, let it be said that these factors appear to the authors as being those that really limit the technique to the point that velocity measurements in hypervelocity ranges can hardly be

made to an accuracy better than 0.1%. Incidently that limit also corresponds to the point where the axial phase contraction due to antenna diffraction generally becomes apparent[10.7].

With conventional techniques of display and data processing, an error analysis is generally not difficult to carry out, because the characteristics of the recording equipment are well known. Values of frequency shift deduced from oscilloscope traces are not usually more accurate than 2% or 3%, due to uncertainties in sweep linearity. Comparatively, much better accuracy is obtainable with magnetic tape records because they cover a longer section of trajectory, and smoothing procedures can be used to eliminate some of the spurious effects.

Playback of magnetic tape records cannot be expected to be accurate to any better than 0.1% with actual apparatus. Increased accuracy in frequency measurement can be obtained however by mixing the Doppler frequency with a stable known frequency and recording the difference. The increase in accuracy is proportional to the ratio of Doppler frequency to difference frequency. There is a limit to this technique in that a certain number of cycles are required for analysis.

10.2.3 Drag Determination

The drag force, or deceleration force, experienced by a body of mass, M, traveling at a velocity, V, into an atmosphere of density, ρ_a, is defined by the formula

$$F_D = M \frac{dV}{dt} = -\frac{1}{2} \rho_a C_D A V^2 ,$$
(10.3)

where C_D is the so-called drag coefficient and A designates the cross-sectional area of the body relative to a plane perpendicular to the trajectory. From the knowledge of the velocity-time history, that equation can then be used to determine either the ballistic coefficient, $M/C_D A$, the drag area coefficient, $C_D A$, or the drag coefficient alone.

Perhaps the most-direct method of data processing with regard to the above equation is through the use of a frequency discriminator. Indeed, Doppler signals previously recorded on magnetic tapes or magnetic discs, can be played back into a frequency discriminator whose output voltage is proportional to the Doppler frequency, and hence the velocity. The behaviour of this voltage, as a function of time, can be predicted by integration of Equation (10.3).

Assuming $C_D A$ constant over the period of observation, one obtains

$$V(t) = V_0 (1 + a V_0 t)^{-1} ,$$
(10.4)

where $a = \rho_a C_D A / 2M$ and V_0 is the velocity at the time $t = 0$.

Because of the short time of observation available in hypervelocity ranges, the term $a V_0 t$ in the above equation is usually not large compared to unity, so that the first few terms in the power series expansion

$$V(t) = V_0 [1 - V_0 a t + (V_0 a t)^2 - \ldots]$$
(10.5)

often constitute a useful approximation. This is substantiated in Figure 10.3 which shows a frequency-discriminator trace that appears very close to a straight line. This is a simplified situation where only the linear term in the series expansion is needed to describe satisfactorily the velocity decay and, consequently, where the slope of the trace, in a good approximation, is directly proportional to $C_D A$.

When high-power terms in the series are significant, one must come back to equation (10.4) in which the parameter, a, must be determined using some curve-fitting technique. In this case, it may be found more convenient to rewrite equation (10.4) in the form

$$\frac{1}{V(t)} = \frac{1}{V_0} + at ,$$
(10.6)

which represents a straight line whose slope is also proportional to $C_D A$.

Comparing Equations (10.5) and (10.6) it appears that even if the slopes are measured with high accuracy, the exact formula (10.6) is to be preferred since the factor, V_0, appearing in the expression for the slope for Equation (10.5) limits the accuracy in $C_D A$, in that case, to the accuracy to which the velocity itself is determined.

Several other approaches can be taken in drag determination. The choice depends upon many factors such as the capability of the radar system, the recording method, the accuracy required and the rapidity with which the results must be obtained.

10.3 MICROWAVE STUDIES OF INTERIOR BALLISTICS

The use of microwave techniques to study interior ballistics in hypersonic launchers seems to have first been reported by L.Pennelegion[10.8,10.9] of the University of Southampton, England, who measured piston displacement and velocity in a hypersonic gun tunnel. More recently, microwave measurements of projectile kinematics inside

the launch tube of light-gas guns have been reported by several laboratories, notably Arnold Engineering Development Center (AEDC)[10.10,10.11,10.12], NASA Ames Research Center[10.13], and the Canadian Armament Research and Development Establishment (CARDE).

The technique considers the gun barrel as a circular wave guide. Microwave energy fed from the muzzle is transmitted down the barrel where it is reflected back from the front surface of the projectile. The motion of the latter changes the phase of the reflected signal, and the time required to produce a phase variation of 2π radians corresponds to the time taken by the projectile to move through half of a guide-wavelength. The distance-time data so obtained during the launch phase are differentiated twice to determine the time history of acceleration from which the driving pressure can be estimated by taking into account the mass of the projectile and an assumed friction coefficient inside the launch tube.

Because the gas processes in the pump tube of light-gas guns are very complex and not monitored, the pressure at the base of the projectile (or driving pressure) becomes a central factor in interior ballistics studies. Consequently, the microwave diagnostic technique under consideration appears to be very useful to ensure that the driving pressure is not going to exceed the mechanical tolerances of the gun or of the model being launched, or to study variation of this pressure with the aim of increasing the gun performance, or to assess the validity of theoretical models used to describe launching cycles.

In the following, some design considerations are given together with a brief description of two different microwave techniques that have been used for acquisition of interior-ballistics data. Typical results are included. For detailed discussion, the reader should consult the references.

10.3.1 The Gun Barrel as a Wave Guide

In an empty wave guide, the guide-wavelength, λ_g, is given by the formula

$$\lambda_g = \lambda[1 - (\lambda/\lambda_c)^2]^{-1/2} , \qquad (10.7)$$

where λ is the free-space wavelength, and λ_c is the cutoff wavelength for the propagation mode chosen. The guide wavelength is then always greater than the free-space wavelength and even increases to infinity as the cutoff condition is approached.

The cutoff wavelength of the different modes encountered in circular waveguides depends upon the ratio of the inner guide radius, r, to the free-space wavelength, λ. Figure 10.4 indicates cutoff ratios for a few of the lowest modes. When modes are being excited at frequencies below cutoff the rate of attenuation is very high and no electromagnetic power is carried down the guide, which in effect, behaves like a high-pass filter.

Equation (10.7) prescribes that the best spatial resolution is obtainable with the transmission mode that has the longest cutoff wavelength, namely the TE_{11} fundamental mode. Furthermore, the higher the frequency of the microwave source, the better is the resolution and the smaller is the attenuation rate. However, operation in the multi-mode frequency region requires the development of mode selectors in order to avoid mode interferences and signal ambiguities.

From the point of view of energy carried down the guide the TE_{11} mode also appears to be the most suitable one, not only because it accepts more energy than any other mode but also because its attenuation rate is generally lower. A good theoretical estimate of attenuation in gun barrels is, however, difficult to make due to uncertainties in surface conductivity and permeability. For instance, the state of ionization of the gas in the portion of the barrel located ahead of the projectile may well influence these parameters.

It should be pointed out that some particular shapes of projectile may exhibit matching properties with the incident signals, thereby reducing considerably the amplitude of the reflected signals. In general, when the sabot supporting the model is made from a dielectric material, the addition of a thin metal plate at the base contributes to increase the reflectivity. Sometimes it may be found more advantageous to operate in the TM_{01} symmetrical mode whose energy distribution pattern shows a relatively great concentration of energy at the center of the guide, in contrast to a broader pattern associated with the TE_{11} mode. However, the attenuation rate of the TM_{01} mode is typically two to three times higher than that of the fundamental mode, depending upon the frequency of operation.

10.3.2 The Microwave-Cavity Technique

The gun barrel can be transformed into a microwave cavity by terminating the muzzle end with a reflector, the other end being terminated by the projectile.

Different configurations are possible. The schematic diagram in Figure 10.5 shows an arrangement comparable to a hybrid-T in which the launch tube and the reflector form two arms, while the excitation and the detection circuits form the other two arms. Upon entering the barrel, the incident power divides itself between the reflector and the projectile arms. In principle, the system can be designed such that there is no direct energy coupling between the excitation and the detection arms. The signals reflected at both ends of the barrel add together in the output port with a phase depending upon the position of the projectile. The motion of this latter produces an amplitude modulation of the output signal, the modulation rate being proportional to the model velocity.

In actual design several important requirements must be met. From the point of view of mechanics it is necessary to insist on the condition that the presence of coupling holes should not seriously affect the strength of the barrel, and that the reflector should not present an obstacle to the passage of the model being launched. From the electrical point of view the couplers must provide an effective transfer of energy in and out of the gun barrel, without ambiguity and at the desired transmission mode. The design of these couplers is no doubt the most important task in this technique.

Figure 10.6 illustrates one configuration used at NASA Ames[10.13] on a 25.4-mm light-gas gun. The muzzle of the gun is terminated with a circular horn in the aperture of which is mounted the reflector. A hole located at the center of the reflector plate permits the model to escape. The purpose of the horn is to expand the incident microwave signal so that a large fraction of it is reflected back, despite the hole in the reflector. The system operates in the TE_{11} cylindrical mode (11.5 GHz) which is being excited by way of two magnetic-coupled slot apertures cut through the wall of the horn, diametrically across from each other. Another pair of slots located halfway between the first slots serves to extract the signal. In both cases the length of the rectangular waveguide connecting one pair of slots is equal to an odd multiple of half a guide wavelength in order to match the TE_{11} electromagnetic field configuration. The frequency of operation must be carefully chosen such as to minimize direct energy coupling between the exciting and receiving slots.

Operation in the TM_{01} symmetrical mode would require a slightly different arrangement.

10.3.3 The Doppler-Radar Technique

Because the open end of a gun barrel is similar to an open waveguide this aperture can be used as a low gain antenna both to pick up energy from an illuminating radar beam and to radiate back the signal reflected by the projectile inside the barrel. As viewed from the radar site, the motion of the projectile can be observed not only during the launch phase but also, in principle, for some time after its exit from the barrel.

At CARDE, where this technique has been used in conjunction with light-gas guns having bore diameters of 38 mm and 102 mm, the axial illumination is realized through the use of a thin microwave reflector mounted in the flight path to deflect the radar beam entering the range from the side (Fig. 10.7). This reflector is made sufficiently fragile to be blown out of the way by the shock wave ahead of the hypersonic projectile, leaving an open path for the model. The muzzle of the gun is made in the form of a circular horn in order to increase the coupling between the radar beam and the barrel. A satisfactory illumination is obtained when the muzzle is located in the far field of the radar antenna.

The signal returning to the radar consists, in the first part, of a static background reflection arising from the portion of incident beam which is not coupled to the barrel, and, in the second part, of a dynamic reflection caused by the moving projectile. While the former is cancelled out in the radar circuit prior to firing, the latter is beaten with a reference signal from the microwave source to obtain the Doppler shift from which the instantaneous model velocity is deduced.

The TE_{11} cylindrical mode is easily excited and somewhat favoured with the feeding technique considered here, because the field configuration of the illuminating beam has much in common with the field configuration of this mode. Operation at a frequency just below the cutoff frequency of the TM_{01} mode will ensure the existence of the fundamental mode alone. However in order to obtain a high spatial resolution it is preferable to operate at a frequency as high as possible. Static measurements made at CARDE have revealed that it is possible to operate at a frequency as high as twice the cutoff frequency of the TM_{01} mode without introducing intolerable modulation of the signals, arising from multimode interaction. For instance, satisfactory results have been obtained at 9.950 GHz in a 38-mm barrel, but at the same frequency in a 102-mm barrel, severe amplitude and phase modulation were observed.

Vibrations and gun recoil occurring during the launch phase generate large-amplitude low frequency signals. These signals can be removed with a high-pass filter at the cost of losing the first few cycles of projectile movement.

10.3.4 Data Processing and Typical Results

The same data processing methods can be used in both microwave techniques just described because the information appears in the same form, namely, a frequency-modulated signal whose amplitude, incidently, does not matter.

The method of analysis most commonly used is based on measuring the time increments of each successive cycle, or number of cycles, to obtain a distance-time history. Several ways of measuring these time increments have been employed. At AEDC, for example, after suitable pulse shaping, the time intervals between nodes in the recorded signal are read out digitally on electronic counters[10.11]. This method gives direct digital indication of time intervals corresponding to projectile displacements of half-wavelengths inside the barrel.

Direct display on an oscilloscope can be made, but single sweep records are not always convenient to perform a good diagnostic, due to the limitation in the number of Doppler cycles being resolved. To overcome this difficulty the signal can be displayed on the vertical axis and simultaneously recorded on a fast moving film from which the time interval data can be obtained. Another way is to use the oscilloscope in conjunction with a proper raster sweep-generator so as to obtain multi-sweep recordings (cf Section 6.7.3.1). An example of this type of data[10.13] is shown in Figure 10.8.

432

As the range of Doppler frequencies generally encountered in interior-ballistics studies does not exceed 300 kHz, the use of magnetic tapes for recording is very straightforward. For data analysis, the tape is usually played back at a much lower speed and the data are displayed on a strip chart recorder.

Another method of processing the Doppler signal is to pass it through a wide-band frequency discriminator and to display the output on an oscilloscope. This yields directly a velocity-time curve as shown in Figure 10.9. With this technique, the accuracy in displaying and reading the data remains comparable to that of previously-mentioned methods, but the results of acceleration should be more accurate because only one differentiation is required instead of two, and also because the curves do not need to be smoothed before differentiation.

The overall accuracy of the data is often difficult to establish precisely. Even with a well-stabilized microwave source and an accurate determination of the empty guide wavelength, there exist many imponderables such as spurious signals due to mismatch, change of guide wavelength due to the state of ionization of the hot gas ahead of the model, and possible reflection from the shock wave preceding the model.

Perhaps the first precaution to take against ionization is to make sure that the driving gases are well sealed by the projectile and cannot flow along its side and thus pass ahead of it. Also, the shock wave ionization is certainly reduced by evacuating the barrel to low gas pressure, say 100 microns Hg. However, in the presence of high projectile acceleration and velocity, additional precautions must be taken. For example, the barrel can be flushed with a gas that has a higher ionization level than air, such as helium. A getter gas can also be used that has a strong affinity for free electrons.

Despite some rather severe operating conditions, useful data have been derived using both microwave approaches discussed here. Two examples of acceleration histories obtained at Ames with the microwave cavity method are shown in Figure 10.10, along with theoretical predictions. Figure 10.11 shows typical velocity and base pressure curves obtained at CARDE, using the Doppler technique. Although, in both cases, the theoretical calculations were based on idealized models that do not take into account real-gas effects, heat losses and friction, the agreement is certainly remarkable, especially in the first part of the motion. It is believed that with good firing conditions velocities can be measured to an accuracy of 5 per cent, although the error in acceleration can hardly be reduced below 15 per cent. (cf Section 2.4.2)

Besides the study of projectile kinematics in the gun barrel, these microwave techniques can also be used to study the motion of the shock wave preceding the projectile down the barrel and even to study the motion of the piston in the pump tube. Several piston observations have been made at CARDE, utilizing a specially designed projectile slug that is semi-transparent to microwaves. Data have been obtained from the moment of firing up to the time of release of the slug.

10.4 HYPERSONIC-PROJECTILE PLASMAS AND MICROWAVE DIAGNOSTICS

The present section is intended to provide an elementary review of some of the characteristics of the flow field associated with hypersonic projectiles and also to provide an elementary discussion of the basis of the interaction of microwave radiation with plasmas.

The discussion begins with a brief description of the hypersonic flow field and then touches on the chemical dissociation and ionization processes which take place in shocked air. Some reference is made to work involving the theoretical computation of temperature, density, and chemical species concentrations for chemically reacting hypersonic flows. This was believed to be desirable because the results of measurements of electron density using microwave techniques to study the free electron population in hypersonic projectile environments in the ballistic range have proved to be extremely valuable in the construction of acceptable flow field models and chemical reaction schemes for the theoretical prediction of the thermochemical characteristics of hypersonic flow fields. The following subsection reviews the interaction of a microwave beam with a plasma, and shows how the phase shift and attenuation experienced by a plane wave on passage through a plasma are related to the electron density and collision frequency in that medium. The section closes with a discussion of a few of the particular problems which arise when microwave techniques are applied in the ballistic range.

10.4.1 Description of Plasma in the Projectile Vicinity and in the Wake

The interaction of microwaves with the flow field immediately adjacent to a hypersonic projectile or with the wake following the projectile is determined mainly by the density of free electrons in these regions. The electron density is in turn determined by the thermochemical histories of the fluid particles which pass through various parts of the flow field. For example, gas which has just passed through the normal part of the bow shock in front of a blunt body will be at a high temperature and the degree of ionization will be relatively high. However by the time this gas has expanded around the body and found its way into the wake, its temperature will have dropped considerably, recombination will have taken place and the degree of ionization will be lower, though still higher than that associated with other gas in the wake which passed through a relatively oblique portion of the bow shock.
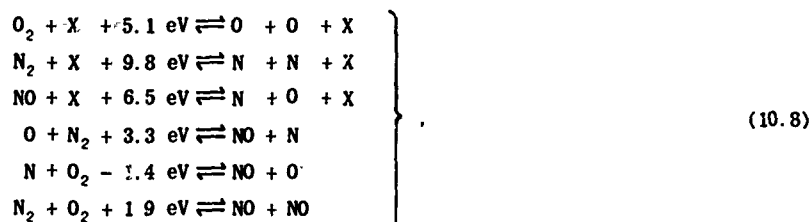
The purpose of this subsection is to briefly touch on some of the processes which play a role in determing the ionization in the flow field associated with a hypersonic projectile. First, the main divisions of the flow field are enumerated. Following, some of the features of the chemistry of hypersonic air flows concerned with the production and removal of free electrons are described.

Figure 10.12 illustrates schematically the flow fields in the neighborhood of a blunt axisymmetric projectile moving at hypersonic speeds. In the figure, the body is considered to be at rest and the gas is considered to be in motion over the body. Just in front of the body and trailing off to the sides is the bow shock. Behind the bow shock is the inviscid flow region, extending on down behind the body. Adjacent to the body is the viscous boundary layer, which separates at the base of the body. The free shear layers thus shed converge and merge at the "neck" region behind the body. The major part of the flow in the converging free shear layers passes through a recompression region at the neck (which coalesces into the trailing shock) and is turned parallel to the wake axis. The other part of the shear layer flow, that below the dividing streamline, is turned back by the high pressure region at the neck into the recirculation zone bounded by the dividing streamline, the stagnation point at the neck, and the base of the body.

The region downstream of the body forms the wake flow. The core of the wake is formed from that part of the shear layer flow which passes through the neck recompression region; the outer part of the wake is the continuation of the inviscid flow. Downstream of the recompression region the flow expands to ambient pressure. The inner wake core, which may be either laminar or turbulent depending on the location of transition, tends to diffuse into the outer inviscid part of the wake flow. Across the flow field there exists a profile of velocity variation. In the frame of reference of Figure 10.12, in which the air is considered to be flowing over the body at rest, it is customary to speak of a velocity deficit profile, where the flow velocity decreases from a maximum, or freestream value, at the bow shock to some value, V_c, on the wake axis (the velocity defect on the axis is, hence, $V_\infty - V_c$).

Associated with the various regions of the velocity field there are distributions of enthalpy, temperature, density and chemical species concentrations. The flow field is much influenced by the shape of the projectile. For example, in the case of a blunt body, some very high temperatures are developed in the region of the nose stagnation point, and the strong normal part of the bow shock processesses a considerable amount of gas, such that most of the momentum deficit and static enthalpy is located in the inviscid flow. In the case of a slender cone, the only high temperatures are those developed in the boundary layer, while the very oblique shock extending from the cone tip barely decelerates the flow. Thus behind a cone the inviscid enthalpy is very low compared with the enthalpy inside the wake core at the neck. Again, with blunt bodies, there is some cooling of the flow possible through the mechanism of expansion about the body. This mechanism is less important for slender cones and generally it is found that the enthalpy in the wake behind cones decays faster than it does in the wake behind blunt bodies. The effect of body shape is reflected in the distribution of chemical species and ionization in the flow, as well as in the variation of thermodynamic variables.

The processes governing the transfer of energy to gases passing through a strong shock wave are familiar ones. In the high-static-enthalpy region behind a shock, translational and rotational degrees of freedom of gas molecules are immediately equilibrated, followed slightly more slowly by excitation of vibrational degree of freedom, and then by dissociative processes. In the case of air, with shock velocities of less than 10 km/sec, the degree of ionization is small, and the coupling between dissociation and ionization is approximately one-way[10.14]. Therefore by making the approximation that air consists only of O_2 and N_2, the temperature, density, and molecular- and atomic-concentration profiles behind a shock are mainly determined by the following six dominant chemical reactions:

$$
\left.
\begin{aligned}
O_2 + X &+ 5.1 \text{ eV} \rightleftharpoons O + O + X \\
N_2 + X &+ 9.8 \text{ eV} \rightleftharpoons N + N + X \\
NO + X &+ 6.5 \text{ eV} \rightleftharpoons N + O + X \\
O + N_2 &+ 3.3 \text{ eV} \rightleftharpoons NO + N \\
N + O_2 &- 1.4 \text{ eV} \rightleftharpoons NO + O \\
N_2 + O_2 &+ 1 9 \text{ eV} \rightleftharpoons NO + NO
\end{aligned}
\right\}
\tag{10.8}
$$

where X represents any molecule or atom in the dissociating gas mixture. The concentrations of species in an air flow field determined with these reactions may then be used to compute electron density.

The competing ionization processes behind a shock (electron-impact, photoionization, charge exchange, electron attachment, and atom-atom, atom-molecule and molecule-molecule collisions) have been considered by Lin and Teare[10.14], who match theoretical predictions based on cross section data for the various processes with experimental shock tube measurements of Lin, Neal, and Fyfe[10.15]. According to their findings (Fig. 10.13) the most important group of ionization processes appear to be the atom-atom reactions, followed in approximately decreasing order of importance by photo-ionization, electron impact, atom-molecule and molecule-moecule collisions, depending on the shock velocity. The atom-atom processes are most predominant at low shock velocities (5 km/sec); however electron impact processes may become predominant at shock velocities greater than 10 km/sec. This has recently been confirmed by Wilson[10.16].

Among the atom-atom ionization processes, the N-O reaction

$$
N + O + 2.8 \text{ eV} \rightleftharpoons NO^+ + e
\tag{10.9}
$$

is the major contributor for shock speeds from 5 to 9 km/sec, although at 9 km/sec the contribution from

$$
N + N + 5.8 \text{ eV} \rightleftharpoons N_2^+ + e
\tag{10.10}
$$

becomes comparable to that from the N-O reaction.

The reaction

$$O + O + 6.9 \text{ eV} \rightleftharpoons O_2^+ + e \qquad (10.11)$$

is somewhat less important. Most workers dealing with the calculations of ionization in flows at re-entry velocities have considered only the first of these three electron producing reactions.

The inverse reactions (dissociative recombination of NO^+, N_2^+ and O_2^+) are the most important paths for disappearance of free electrons. The atomic ions are neutralized most efficiently by charge transfer processes with diatomic molecules, thereby producing diatomic ions which have a much higher probability of reaction with electrons than the atomic ions[10.17]. The effect of the presence of charge transfer reactions in the shock layer for a typical case of ballistic re-entry has been shown by Eschenroeder et al[10.17]. However in the wake of a re-entry body, when the wake temperature drops below a range of values extending from $700^\circ K$ to $950^\circ K$ (depending on pressure), the oxygen attachment reaction

$$O_2 + e + O_2 \rightleftharpoons O_2^- + O_2 \qquad (10.12)$$

becomes much faster than the two-body electron-ion recombination reactions[10.18,10.19]. This causes the electron density to drop below the positive ion density.

Examples may be found through the literature of nonequilibrium flow field calculations undertaken using pure air chemistry reaction schemes such as those sketched in the preceding paragraphs. There is no intention here to attempt a list of such contributions; however one or two sources will be given. An example of inviscid flow field calculations for the immediate vicinity of a blunt body are those of Hall, Eschenroeder and Marrone[10.20], while a description of a technique for nonequilibrium boundary layer computations for the case of sharp cones is given by Blottner[10.21]. A description of progress in computation of reacting laminar wake characteristics behind spheres and cones including a comparison of electron prediction with integrated electron density interferometer measurements is given in a number of reports from General Motors Defense Research Laboratories[10.22,10.23]. Certain attempts have also been made to compute species in turbulent reacting wake flow. Reference to these together with conclusions as to their usefulness are provided in two papers by Lykoudis[10.24,10.25]. Finally, a thorough review of the whole field of wake chemistry has just recently been undertaken by Eschenroeder, including discussion of the low temperature reaction schemes which influence electron population in the intermediate and far wakes[10.26].

The foregoing has been concerned only with the chemistry of pure air. In the presence of impurities, additional electron-influencing reactions are introduced into the chemistry, with the result that the observed electron density may be drastically changed from that obtained in the absence of impurities. In general, the effect of impurities is an initial enhancement of electron density near to the body, followed by a radically increased rate of electron cleanup in the wake. Contamination may arise from several sources. There is the dust arising from model and sabot impact which may remain in the atmosphere to affect subsequent shots, and impurities which may arise from dirt or ablation material from the model itself. Care must be taken also with the gases which are introduced into the range to form the atmosphere. A discussion of these problems has been given in a paper by Slattery, Clay, and Worthington[10.27]. At the present time, considerable controversy still surrounds the subject of range contamination and its effect on electron density levels in the wake.

Further discussion of flow field electron chemistry would take us beyond the scope of this Chapter on microwave studies. However, inclusion of the previous material is important to the realization that measurement of electron density has increased our understanding of the physics and chemistry of hypersonic flow, particularly in the wake. The mean electron density has been the point of comparison between the results of experimental measurements of integrated electron density obtained by microwave interferometer and cavity techniques. This has led to refinement of chemical reaction schemes on the one hand and to at least qualitative information about turbulent transport on the other.

10.4.2 Microwave Interaction with Plasma

From the point of view of employing microwave techniques to diagnose hypersonic flow fields, the ultimate aim of the theoretical analysis is to provide meaningful expressions for the various parameters of interest in the flow in terms of the microwave measurables such as the amplitude of the signals, their phase, their frequency shift and their change in polarization.

In the case of the ionized flow in the wake of projectiles generally studied in ballistic ranges, the gas is weakly ionized. This weak ionization leads to two basic simplifications.

First, the current contribution from the motion of ions may be neglected in comparison with the current contribution resulting from electron flow. In other words, it is only necessary to consider momentum conservation in the collision of electrons with ions of zero velocity. In addition we suppose that the electrons and ions retain their identity after the collision and the electrons are left with zero velocity. This yields $V_{ion}' = (M_{el}/M_{ion}) V_{el}$; i.e., the maximum ion current contribution is at most 1/2000 the electron current contribution for an electron-proton collision.

Secondly, in addition, weak ionization allows us to neglect the effect of electron-electron and electron-ion collisions in comparison with electron-neutral collisions.

One of the most useful descriptions of such an ionized gas medium, as far as microwave-plasma interactions are concerned, is obtained by assigning to it an effective dielectric coefficient. Most laboratory plasmas act like lossy dielectric materials through which microwaves can propagate, experiencing attenuation and phase shift. Refraction, reflection and change in polarization can also occur at boundaries or when inhomogeneities are present as in the case of dielectric materials. Hence, using this approach, the problem reduces to the classical one of electromagnetic-wave propagation in a medium having a complex dielectric coefficient.

According to Maxwell's equations, the relative dielectric coefficient, K, of a homogeneous medium possessing space charges can be expressed as a function of the electrical conductivity, σ, by the formula

$$K = 1 + \sigma/(j\omega\epsilon_0) .\tag{10.13}$$

where ω is the angular frequency of the electromagnetic signal, ϵ_0 is the electrical permittivity of free space, and j is $\sqrt{(-1)}$.

In a weakly ionized gas the conductivity, σ, can be determined from the equation of motion of the free electrons

$$m\frac{d\vec{V}}{dt} + \nu m\vec{V} = q_e\vec{E} .\tag{10.14}$$

where the symbols m, q_e, ν, and $\vec{V}$ designate respectively the mass, the charge, the collision frequency and the drift velocity of the electron, and $\vec{E}$ is the electric field strength. The term $\nu m\vec{V}$ represents the drag force resulting from collisions between free electrons and neutral atoms, while the term $q_e\vec{E}$ is the electrical component of the Lorentz force, the magnetic component being neglected since the drift velocity is much smaller than the speed of light.

Considering a harmonic time dependence and introducing the electron current density

$$\vec{J} = nq_e\vec{V} = \sigma\vec{E} .\tag{10.15}$$

where n is the free electron density, the solution for σ takes the form

$$\sigma = \frac{nq_e^2}{m(\nu+j\omega)} .\tag{10.16}$$

which leads to

$$K = 1 + \frac{nq_e^2}{m\epsilon_0}\left[\frac{1}{j\omega(\nu+j\omega)}\right] .\tag{10.17}$$

This expression can now be related to the complex propagation constant for a plane wave

$$\gamma = \frac{j\omega}{c}\sqrt{K} = \alpha + j\beta\tag{10.18}$$

in order to solve for the attenuation coefficient, α, and the phase coefficient, β. This yields

$$\left.\begin{aligned}\alpha &= \frac{\omega}{c}\left[-\frac{1}{2}\left(1-\frac{\omega_p^2}{\omega^2+\nu^2}\right) + \frac{1}{2}\sqrt{\left[\left(1-\frac{\omega_p^2}{\omega^2+\nu^2}\right)^2 + \left(\frac{\nu}{\omega}\frac{\omega_p^2}{\omega^2+\nu^2}\right)^2\right]}\right]^{1/2}\\ \beta &= \frac{\omega}{c}\left[+\frac{1}{2}\left(1-\frac{\omega_p^2}{\omega^2+\nu^2}\right) + \frac{1}{2}\sqrt{\left[\left(1-\frac{\omega_p^2}{\omega^2+\nu^2}\right)^2 + \left(\frac{\nu}{\omega}\frac{\omega_p^2}{\omega^2+\nu^2}\right)^2\right]}\right]^{1/2},\end{aligned}\right\}\tag{10.19}$$

where c is the speed of light and ω_p is the so-called angular plasma frequency defined by the formula

$$\omega_p^2 = \frac{nq_e^2}{m\epsilon_0} .\tag{10.20}$$

The exponential dependence of the electromagnetic wave in the plasma is then

$$\frac{E(x)}{E(0)} = e^{-\alpha x}e^{j(\omega t - \beta x)} .\tag{10.21}$$

When $\nu << \omega$ the equations indicate that $\alpha \to 0$ and the signal propagates without attenuation, as long as ω remains greater than ω_p. Indeed when $\omega < \omega_p$, the phase coefficient becomes imaginary, which results in attenuation. Thus, ionized gas behaves as a high-pass filter, the cutoff frequency being the plasma frequency.

Now, as regards the diagnostic potential of measurements of attenuation and phase coefficients, a simultaneous solution of Equations (10.19) leads to

$$\nu = \frac{2\omega\alpha\beta}{\beta_0^2 + \alpha^2 - \beta^2} \quad \cdot$$

$$\omega_p^2 = \frac{nq_e^2}{m\epsilon_0} = \left(\frac{\beta_0^2 + \alpha^2 - \beta^2}{\beta_0^2}\right)\left(\frac{4\omega^2\alpha^2\beta^2}{\beta_0^2 + \alpha^2 - \beta^2} + \omega^2\right) \tag{10.22}$$

$$\beta_0 = \frac{\omega}{c} \, .$$

which means that an estimate of ν and n is readily obtained.

If, for instance, we consider a slab of plasma of thickness, d , and make the assumption that the electron density and collision frequency remain reasonably constant over the thickness, then the signal, in passing through the plasma, is attenuated by a factor, $e^{-\alpha d}$, and experiences a phase shift of $(\beta - \beta_0)d$ radians. Denoting by A and A_0 the final and initial signal amplitudes respectively and by ϕ the experienced phase shift, we have

$$(\beta - \beta_0)d = \phi \qquad \text{or} \qquad \beta = \beta_0 + \frac{\phi}{d} \tag{10.23}$$

and

$$\frac{A}{A_0} = e^{-\alpha d} \quad \text{or} \quad \alpha = \frac{1}{d} \, ln \, \frac{A_0}{A} \tag{10.24}$$

which means that the microwave diagnostics of ν and n are based on the measurement of phase shifts and amplitude ratios.

Such an ideal case is not generally found in the study of real plasmas. The total attenuation and phase shift correspond to an integrated value of transmission coefficient through a generally nonuniform slab or cylindrical column. In such cases, values of n and ν can be determined only for simple variations of plasma properties.

10.4.3 Microwave Plasma Diagnostics in Free Flight Ballistic Ranges

Several methods of microwave diagnostics have been developed to study laboratory plasmas[10.28]. The study of the ionized flow field associated with hypersonic pellets poses, however, particular problems and is hampered by the short time available for observations. Also, the task of data analysis is often complicated by the "integrated" nature of the data.

The size of the pellets determines the spatial resolution required. Though there exists no definite criterion, a resolution of about one fifth of the model diameter is generally acceptable. With present launching facilities, ionized flow fields of interest for microwave probing are obtained with model sizes not exceeding a few centimeters diameter. As microwave beams cannot be focused into a region smaller than the wavelength, millimetric wavelengths must then be used in such studies.

Because the period of observation is not long enough to permit probe displacement in the flow field, it is often necessary to use an arrangement of several focused probes, mounted as a fence across the flight path, in order to ensure that all the important parts of the flow will be probed in a single flight. The fence configuration also permits allowance for the dispersion of the projectiles from one shot to another.

Depending upon the local free electron density, and upon the microwave frequency used, the different regions of a given flow field can then be probed. The upper density limit that can be sensed is determined by the critical electron density, while the lower limit is determined by the size of the flow and the sensitivity of the particular instrument used. Figure 10.14, from Heald and Wharton[10.28], indicates these two limits in the case of phase shift measurements involving a single pass, assuming a minimum detectable phase shift of 18 degrees. Nowadays, with stabilized equipment and low-noise detector crystals, a minimum phase shift of one degree is readily attainable. Of course, the sensitivity obtained with multipass probes, such as resonant cavities, permits measurements of much lower electron densities than is possible with single pass instruments.

When the results of microwave interactions are analyzed under the hypothesis of an underdense plasma, the upper electron density limit is generally taken to be about one order of magnitude below the critical density. This condition must be satisfied, for example, when experimental results are to be compared with theoretical calculations based on the Born approximation.

Regarding analysis of "integrated" signals, one of the two following approaches can generally be taken to infer the local properties of the plasma through which the probing wave has passed.

First, when the distributions of ionization can be represented by some realistic empirical laws involving adjustable parameters, the true distribution can be estimated by solving for the unique set of parameters that lead to the observed phenomena. This is the approach taken in the following section which is devoted to the study of the plasma sheath.

Second, when the form of the distribution cannot be assumed, one must proceed to the "inversion" of the integrated results, an operation which generally requires a large amount of precise input data to yield realistic distributions. As pointed out in section 10.6.1, this is the approach taken to deduce radial electron density distributions in wakes from multi-beam interferometer records.

10.5 MICROWAVE DIAGNOSTICS OF THE PLASMA SHEATH

It is well known that the layers of ionized gases created in front of a body traveling at high velocity through the atmosphere can greatly influence the propagation of electromagnetic signals. One striking evidence of this is the period of telecommunications blackout occurring during the re-entry of Mercury and Gemini vehicles, a phenomenon caused by an overdense electron population in surrounding gas layers.

In controlled flight experiments, such as in ballistic range facilities, the electromagnetic wave-plasma interaction can be used as a probe to measure the electron density in the plasma sheath in front of the model. This sort of diagnostic has been performed for instance at the General Motors Defense Research Laboratories (GM/DRL)[10.4] and at the Canadian Armament Research and Development Establishment (CARDE) with the help of continuous-wave Doppler radars of the type presented at the beginning of this Chapter. Observations consisted of dynamic head-on radar cross-section measurements at different model velocities and ambient pressures.

Spherical metal projectiles are particularly suitable for this type of experiment. Indeed, as metal objects, they are practically nonablative and absorb no electromagnetic energy; as spherical objects, they give rise to data not dependent upon flight attitude. All these properties result in better reliability in the measurements and greatly simplify the tasks of data analysis, theoretical predictions, and interpretation of the observed phenomena.

The choice of the radar frequency is an important factor in the experiment. It must be made such as to favor the interaction of microwaves with the plasma sheath over the range of velocities and ambient pressures covered in the ballistic range. This interaction mainly depends on two factors: the degree of ionization in the plasma sheath, and the size of the model.

Equations (10.19) indicate how the population of free electrons and their collision rate influence the propagation of electromagnetic waves. In particular, a strong interaction is predicted when the plasma frequency approaches the probing frequency, a condition which must be satisfied to ensure a good diagnostic capability. However, calculations of plasma frequencies in the ionized sheath of hypervelocity bodies are very complex and involve, among other things, the development of a chemical model that includes all important high temperature chemical reactions contributing to the production of free electrons. An appreciation of this problem is given in Section 10.4.1. Reference is made here to published tables[10.29,10.30] of plasma frequencies and electron collision frequencies encountered in front of hypersonic blunt bodies. These tables apply to rarified air, and cover all velocities and pressures of interest in ballistic range studies.

Projectile dimensions and firing conditions determine the thickness[10.31] of the plasma sheath. If, for instance, that thickness could be made such that the ionized sheath would behave as a quarter-wavelength transformer[10.32] over an appreciable region of the body, there is no doubt that the resultant phase interference would greatly reduce the back-scattering signal. The main point here is to deal with a sheath thickness that represents an important fraction of the radar wavelength. This condition not only ensures appreciable phase interference but also ensures that the projectile will be at least a few wavelengths in diameter, a condition which permits the neglect of diffraction phenomena[10.33,10.34] when developing a scattering model.

In the following sections, we first indicate a method of measuring head-on radar cross sections in hypersonic ranges. Next, some typical experimental results are examined using a simple physical-optics model with the aim of deriving the gross electron distribution along the plasma sheath.

10.5.1 Radar Cross Section Measurements

According to the well-known radar equation[10.35], the power density, p_r, returned to the radar by a target of effective area, σ, located at a distance, x, in the far field of the antenna is

$$p_r = \left(\frac{P_r G_r}{4\pi x^2}\right) \sigma \left(\frac{1}{4\pi x^2}\right) . \tag{10.25}$$

where P_r and G_r are the power transmitted by the radar and the gain of its antenna respectively. This equation assumes that all the electromagnetic energy intercepted by the area, σ, is radiated isotropically, and therefore leads to an inverse fourth-power-law dependence upon distance.

Figure 10.15 shows an oscilloscope record of the Doppler signal intensity obtained in a ballistic range as the projectile approaches the antenna. One can check the x^{-4} dependence of the amplitude of this signal, all over the far field region. (It will be recalled that the far field is usually considered to begin at a distance D^2/λ from the antenna, where D is the antenna diameter and λ the wavelength of the radiation.)

A dynamic calibration of the radar is needed to determine the absolute value of radar cross-section. This calibration consists of relating the amplitude and the frequency of the recorded signal to the amount of energy returned by the projectile. A very convenient way by which this can be achieved is through the use of an auxiliary microwave source, located up-range, that transmits to the radar a signal simulating in frequency and amplitude the signal returned by the projectile itself. Figure 10.16 illustrates a target simulator unit whose output power is controlled with a precision attenuator and whose operating frequency is maintained, by means of a phase locking circuit[10.36,10.4], above the radar frequency by an amount equal to the desired Doppler frequency. This latter is provided by a variable oscillator, and then added to a reference signal taken from the radar source. One notable property of this technique of frequency control is to provide a calibration which is invariant with respect to the usual frequency instabilities that may occur in the radar klystron; indeed, the frequency difference between the two klystrons is kept constant.

Upon radiating a power, P_s, from the simulator antenna, the power density produced at the radar antenna becomes

$$p_r = \frac{P_s G_s}{4\pi L_s^2},$$ (10.26)

where G_s refers to the gain of the simulator antenna and L_s designates its location in the radar beam. Under conditions of simulation, the two expressions for p_r given above are equal and lead to the simple formula

$$\sigma = 4\pi \left(\frac{G_s}{G_r}\right)\left(\frac{P_s}{P_r}\right)\left(\frac{x^4}{L_s^2}\right),$$ (10.27)

showing that the dynamic head-on radar cross-section can be determined at any point, x, of the trajectory from the knowledge of P_s. For convenience, a calibration can be done immediately prior to firing in order to relate the amplitude of the oscilloscope signal to P_s.

Typical experimental results obtained at CARDE with a 35 GHz CW Doppler radar are shown in Figure 10.17. The projectiles were 2.54-cm-diameter aluminum spheres launched in air at an ambient pressure of 76 mm Hg. The dynamic radar cross-section, σ, is given in decibels below the static value, σ_s, as a function of velocity. Each vertical segment on the figure corresponds to one observation. The solid curve drawn through the average of the experimental results, shows more clearly the behaviour of the cross section as a function of velocity.

The results indicate that the plasma sheath does not influence appreciably the backscatter until the projectile reaches a velocity of 3 km/sec. There then appears a strong absorption phenomenon which reaches the -12 db level at about 4.25 km/sec. At this point the ionized sheath acts as an anti-reflection dielectric coating, but beyond this point the addition of free electrons gradually transforms the dielectric coating into a conductor, thus increasing the radar cross-section. The increase can exceed the static value, as observed by GM/DRL[10.4] at higher velocities.

It should be mentioned here that in some cases free electrons can also be found in significant numbers ahead of the sheath, due to electron diffusion[10.37] through the shock front or to photo-ionization by ultraviolet radiation[10.38] emanating from it. A sufficiently thick spherical electron cloud ahead of the shock can very effectively refract radar energy away from the target and reduce backscattering[10.38]. Reduction as high as 20 db may occur in a typical re-entry condition.

In the ballistic range experiments under consideration, the mechanisms of electron production ahead of the shock front are not significant[10.39]; the microwave-plasma interaction remains confined to the plasma sheath. This interaction will now be examined on the basis of a simple physical optics model.

10.5.2 Physical-Optics Model

According to physical optics, the far-field-backscattering radar cross-section of a metallic body of large dimensions compared to the wavelength can be estimated by summing up, in a reference plane normal to the line of sight, all the signals reflected from each element of surface of the body. Upon extending the application of this principle to the axisymmetric plasma-projectile structure shown in Figure 10.18, the normalized head-on radar cross-section takes the approximate form

$$\sigma_N \simeq \left[\frac{\int_0^\infty F(y)e^{-2\gamma_1 G(y)}y\,dy}{\int_0^R (-1)e^{-2\gamma_1[G(y)+H(y)]}y\,dy}\right]^2,$$ (10.28)

where $F(y)$ is the complex voltage reflection coefficient of the structure at a radial distance y from the axis of symmetry, and γ_1 is the free space propagation constant.

It is difficult to estimate the function $F(y)$ because of the non-uniformity of the electron distribution within the plasma sheath. Moreover, these distributions are not well known; only in a few cases have detailed flow field calculations been made and published. Approximations must then be made, not only because of the lack of data but also because of the desirability of developing a method for which numerical calculations are not too involved.

As a first simplification, the distributions across the plasma sheath, in the direction parallel to the axis of symmetry, are approximated by averaged constant distributions. This is justified in the present case because the shock detachment distance represents only a fraction of the wavelength, and consequently no significant spatial resolution can be expected along the direction of sight. On the contrary, in the transverse direction, gradients can be seen as the dimensions involved are comparable to the wavelength and even longer.

Further simplification is obtained when the shock front curvature is approximated by a staircase function with steps much smaller than the wavelength. Then the element of integration appears as a small corona of radius, y.. According to the flow diagram in Figure 10.19, the voltage reflection coefficient of this plasma corona backed by a metal surface takes the form

$$F(y) = \frac{r_{12}(y) - e^{-2\gamma_2(y)H(y)}}{1 - r_{12}e^{-2\gamma_2(y)H(y)}}$$

(10.29)

where γ_2 is the plasma propagation constant and r_{12} the voltage reflection coefficient at the shock front where an abrupt discontinuity is assumed. These last two quantities can be calculated in terms of plasma frequency, ω_p, and electron collision frequency, ω, as follows:

$$\left.\begin{aligned} r_{12} &= \frac{\gamma_1 - \gamma_2}{\gamma_1 + \gamma_2} \\[2mm] \gamma_1 &= j\frac{2\pi}{\lambda} \\[2mm] \gamma_2 &= j\frac{2\pi}{\lambda}\left[1 + \omega_p^2\left(\frac{1}{j\omega(\nu + j\omega)}\right)\right]^{1/2} \end{aligned}\right\}$$

(10.30)

We recall that the stagnation values of plasma frequency and collision frequency are available from charts for hot equilibrium air[10.29,10.30] according to projectile velocity and pressure. However, outside of the stagnation region these frequencies must be estimated from detailed flow field calculations.

Results of detailed flow field calculations at CARDE verify that the radial distribution of free electrons in the plasma sheath of a sphere can be described approximately by the following two-parameter formula

$$n(y) = n(0)\,exp\,(-y/aR)^b,$$

(10.31)

where R is the radius of the sphere and a and b are parameters indicating the spreading of ionization and the decay rate, respectively. The interesting point with this simple formula is that even without prior knowledge of the values of a and b for a given experiment, it is still possible to analyze the radar results by adjusting these parameters so as to fit the data.

Figure 10.20 shows the results of a study of the influence of the parameters a and b for the flight conditions corresponding to the minimum value of the radar cross-section occurring in Figure 10.17. (For simplicity, the stagnation value of electron collision frequency was assumed constant throughout the sheath.) Some discussion of the uniqueness of the determination of a and b is in order. From Figure 10.20 it is apparent that there is an infinite number of ways to choose a and b such that the −12 db level in radar cross-section can be attained at a velocity of 4.4 km/sec. However, the unique set of parameters that one seeks is that for which the cross-section is a minimum at these conditions. Considering that the form of the electron distribution should not vary rapidly with velocity, so that the parameters a and b can be assumed constant over the velocity range of interest, different sets of parameters were tried, each of them being related to a point on segment XX, in Figure 10.20. In this way, it was found that the set, a = 0.474 and b = 4, provides a reasonably good match to the experimental data, as illustrated in Figure 10.21.

The same analysis was applied to some GM/DRL radar cross-section results[10.4] obtained at 10 torr using projectiles consisting of plastic slugs with spherical metal noses of 1.25-cm radius-of-curvature. The radial-electron-density function inferred from the radar data by the foregoing analysis is shown in Figure 10.22. Also shown on the figure are the results of a theoretical average distribution calculated at CARDE by Ellington for conditions at 10 torr on 2.5-cm-diameter spheres, using the reaction scheme described in Section 10.4.1. The agreement is remarkable.

In the light of this physical-optics model the mechanism of microwave-interaction with the plasma sheath of metal spheres is clearly indicated: The distribution of power-reflection coefficient along the shock front is a "pinched function" which covers only the central part of the front surface of the projectile when the strong reduction of radar cross-section first appears (at a velocity of 4.25 km/sec in the case considered here). As the velocity increases, the overdense disc of plasma extends over the Fresnel zones to give rise to successively destructive and constructive interferences between the signal reflected from the disc and that reflected from the part of the projectile which is not screened by overdense layers. The number of Fresnel zones, and hence the number of oscillations encountered as a function of velocity depends, of course, upon the radar frequency and the size and shape of the hypersonic body.

10.6 AVERAGE WAKE-ELECTRON-DENSITY AND COLLISION-FREQUENCY MEASUREMENT

As mentioned previously, the measurement of electron density distributions in the ionized wakes of hypersonic projectiles are of prime interest to the understanding of the electron-determining reaction mechanisms in the wakes and to the study of the radar return associated with re-entry objects.

One important result of the analysis presented in Section 10.4 is that only two plasma parameters really influence the propagation of microwaves through an underdense ionized medium, namely, the free electron density which is mainly responsible for phase shift, and the electron collision frequency which is mainly responsible for attenuation. For an accurate determination of these parameters in the wake of hypersonic projectiles launched in ballistic ranges, the most valuable microwave instruments have proved to be the single-pass interferometer and the resonant cavity.

10.6.1 Single-Pass Interferometer

The interferometric method consists in using a bridge circuit to yield the total phase shift experienced by the probing wave upon its passage through the plasma. Several types of microwave interferometers and display techniques have been described by Heald and Wharton[10.28] and others[10.40,10.41,10.42] The choice of the technique mainly depends upon the phase, space, and time resolution needed.

One technique adopted in ballistic range studies is to mount a microwave fence of adjacent focused beams in a plane perpendicular to the line of flight, (Fig. 10.23). By using dielectric lenses with small focal-length-to-diameter ratio, the microwave field is concentrated into a cylindrical region whose diameter is of the order of the wavelength, thus permitting the system to have a good spatial resolution. Electrical isolation of the beam is ensured by an appropriate spacing between the beams and, in certain cases, by alternating the polarization from one to another.

The choice of the operating frequency is governed by such factors as the spatial resolution required, the maximum electron density to be measured, and the availability of microwave components. For example, systems developed[10.43] using frequencies at 35 GHz and 70 GHz, have shown that electron densities in the range of 10^{10} to 10^{13} electrons/cm^3 can be measured with sufficient spatial resolution to permit the mapping of constant-electron-density profiles in axisymmetric wakes.

The measurements are made by recording both the amplitude and phase variations produced by the wake. The phase shift is obtained by comparing the transmitted signal with a reference signal through hybrid elements. A block diagram of a typical one-channel microwave interferometer is shown in Figure 10.24. In this type of interferometer, the reference signal provides a bias on the crystal detector to ensure operation in the linear region. By making the amplitude, $A(t)$, of the probing signal small compared to the bias, two components are obtained in phase quadrature, namely,

$$\left. \begin{array}{l} S_1(t) = A(t) \cos \phi(t) \\ \\ S_2(t) = A(t) \sin \phi(t) \end{array} \right\} , \tag{10.32}$$

t being time. The phase angle, $\phi(t)$, is then explicitly given by the formula

$$\phi(t) = \tan^{-1} \frac{S_2(t)}{S_1(t)} . \tag{10.33}$$

As shown in the figure, the amplitude, $A(t)$, is simply obtained through the use of a directional coupler.

Figure 10.25 shows results for $A(t)$ and $A(t) \sin \phi(t)$ obtained at CARDE from observations on a 2.5-cm-diameter polycarbonate (Zelux) sphere in a ballistic range at 4.6 km/sec, and at a pressure of 70 mm Hg. Both quantities are given as functions of time, or equivalently, as functions of axial distance in body diameters, x/D , behind the projectile. The regions of flow probed by each beam can be seen from the illustration at the bottom of the figure. The size of of the circles indicates the spatial resolution of the beams relative to the flow, and the arrows simply indicate the polarization. The strongest signals occurred in beams 3 and 4 which were located almost symmetrically about the axis of the flow. Because of the symmetry, both beams show similar amplitude and similar phase behavior. A strong absorption pulse is first observed when the sphere cuts the beams. In fact, this pulse reaches the cut-off level predicted by the pre-flight calibration. Immediately behind the projectile, when the beams are in the rarefied region, the transmission returns to the high level. A second absorption pulse follows immediately at the recompression shock, indicating an important increase of ionization at this point. With increasing distance behind the projectile the signal traces gradually reach their initial levels. The signals obtained from channels 1 and 2 were observed to behave differently, of course, according to the region of the flow that was probed.

The signals recorded give the sum of the variations occurring along the lines crossing the wake, they represent "integrated" results. Before applying Equations (10.22) of Section 10.4 to find the electron density, n , and the collision frequency, ν, it is necessary to solve the "integrals" and obtain the variation per unit length occurring at any point in the wake. The experimental measurements are then used to obtain an approximate analytical expression of the integral, the radial functions are deduced by assuming symmetry of revolution in the flow. The method for doing this is described in Reference 10.44. Unfortunately, while the technique is

fairly straightforward in principle, the stringent requirements in accuracy of the signals in various beams make it very difficult to obtain precise contour maps of electron density in practice, except for a relatively select set of conditions. The problem with the inversion technique is that relative errors of the order of 10 percent (which would be considered excellent for an integrated electron density measurement from one beam) can generate regions of apparent negative electron density and other anomalies in the deduced contour map[10.45].

Typical results obtained by the application of this method are shown in Figure 10.26. Contours of constant electron density in the region near the wake of a "Zelux" sphere are indicated. These results are the average of 5 firings under the same conditions. The increase of ionization at the recompression shock is well marked. In the region of the wake shown, most of the ionization seems to be confined to a cylinder having a diameter less than twice the body diameter.

From such rounds, valuable information can be deduced about the rate of recombination of the electrons, the influence of ablation products upon ionization, and so forth, over a wide range of firing conditions.

10.6.2 Resonant Cavity

The microwave interferometer is restricted to measurement of electron densities of 10^{10} electrons/cm^3 or greater. This sensitivity limitation of the interferometric method leads to the use of the resonant cavity method. Here, an increase in sensitivity of the order of the Q of the filled cavity can be obtained when plasma is occupying the total volume over which the field has significant values.

It is well known that the plasma introduced into a microwave resonator will change the resonant frequency, f_0, and will tend to lower the Q of the unperturbed cavity. The presence of a low-electron-density plasma (dielectric constant, ϵ, close to unity) with a low electron-molecule collision rate, ν, will shift the resonant frequency of the cavity by an amount $\Delta f = (f - f_0)$ such that

$$\frac{\Delta f}{f_0} \simeq \frac{1}{2[1 + (\nu/\omega)^2]} \frac{\int_{v'} (\omega_p/\omega)^2 |E|^2 dv'}{\int_v |E|^2 dv} \qquad (10.34)$$

and will modify the Q according to the relation

$$\Delta \frac{1}{Q} \simeq \frac{\nu/\omega}{1 + (\nu/\omega)^2} \frac{\int_{v'} (\omega_p/\omega)^2 |E|^2 dv'}{\int_v |E|^2 dv} \simeq \frac{2\nu}{\omega} \frac{\Delta f}{f_0} , \qquad (10.35)$$

where E is the local field in the unperturbed resonator, v is the volume of the resonator, and v' is the volume of the perturbing plasma. As before, ω_p and ω are the angular frequencies of the plasma and of the propagated signal, respectively. Knowing the field distribution and the parameters of the cavity which may be obtained from other indirect measurements, the electron density and electron-molecule collision frequency can be calculated for measured values of $\Delta f/f_0$ and $\Delta(1/Q)$.

In the resonant cavity method, systems can be built by using two types of resonators: UHF resonators (closed resonators) and quasi-optical microwave resonators (open resonators). Two typical examples of such systems, as well as their use for microwave-plasma-wake diagnosis, will now be presented.

10.6.2.1 Closed UHF Resonator

The closed cavity employed in plasma diagnostic experiments at UHF frequencies resonates in the TM_{010} mode, which has a longitudinal electric field parallel to the line of flight of the projectile. Entry and exit ports, provided to permit free passage of the projectile, are made with circular tubes of such a diameter that at the operating frequency the tubes are beyond propagation cutoff and the UHF field is thus confined inside the cavity. Figure 10.27 shows a diagram of a cavity used at Lincoln Laboratory, MIT, in which pellets of diameters varying from 4.7 mm to 12.7 mm were fired at speeds ranging up to re-entry velocities[10.19].

The wake electron density and collision frequency are derived from the change of the cavity transfer impedance. Two circuits are used: In the "standard" circuit used for plasma diagnosis in a high-electron-density wake (values of electron line density, N, ranging from 10^{12} to about 10^8 electrons/cm) the phase and the amplitude of the output signal from the cavity are compared with the corresponding values of the empty cavity. To measure electron line density from about 10^9 to about 10^5 electrons/cm, a "difference" circuit is employed. Here the output signal is balanced against the input signal of the cavity. Figure 10.28 shows the combination of the two systems, permitting measurement of the electron line density from 10^{12} down to about 10^5 electrons/cm.

By this method of measurement the plasma is characterized by the linear electron density, N, the number of electrons per unit length; that is, if the plasma column is located in the region of nearly constant electric field, then

$$N = \int_0^{\rho_e} n(r) \, 2\pi r \, dr , \qquad (10.36)$$

where ρ_e is the radius of the plasma column, and $n(r)$ is the radial distribution of volume electron density.

Relations for calculating the electron line density and the electron-molecule collision frequency are reproduced below (in the present nomenclature) from Reference 10.19.

For the "standard" circuit:

$$N = \frac{\pi\alpha^2 J_1^2(\alpha)m}{q_e^2\mu_0 Q_L} \frac{\sin\phi_1}{S_1}\left[\left(\frac{\cos\phi_1 - S_1}{\sin\phi_1}\right)^2 + 1\right] \quad \text{electrons/meter}$$

$$\nu = \omega \frac{(\cos\phi_1 - S_1)}{\sin\phi_1} \quad \text{collisions/sec,}$$

$$(10.37)$$

and for the "difference" circuit:

$$N = \frac{-\pi\alpha^2 J_1^2(\alpha)m}{q_e^2\mu_0 Q_L} \frac{S_2}{\sin\phi_2} \quad \text{electrons/meter}$$

$$\nu = -\omega\frac{(\cos\phi_2 - S_2)}{\sin\phi_2} \quad \text{collisions/sec.}$$

$$(10.38)$$

Here $\alpha = 2.405$ is the first root of $J_0(x) = 0$, J_0 and J_1 being respectively the Bessel functions of zeroth and first order; m, the electron mass; q_e, the electron charge; μ_0 the vacuum permeability and Q_L, the loaded Q of the cavity. S represents the normalized output amplitude and ϕ its phase shift. The subscripts 1 and 2 refer to results obtained with the standard circuit and difference circuit respectively. Detailed derivation of Equations (10.37) and (10.38) can be found in Reference 10.46.

It is clear from Equation (10.36) that this method yields no direct information either on the radial distribution of the electrons or on the plasma column diameter. Moreover the electron collision frequency, ν, for momentum transfer has been assumed constant. In order to obtain information about the plasma column diameter of the wake of a hypersonic projectile in free flight, as well as data on the transition from laminar to turbulent flow and the volume electron density, the projectile can be fired at right angles to the electric field within a cavity operating in TM_{010} mode (Fig. 10.29). The measuring circuit is the same as the previous one described.

Assuming a uniform cylindrical plasma distribution, Reference 10.47 gives for the electron density, n,

$$n = \frac{2m\epsilon_0\omega^2}{q_e^2}\left[1 - \frac{(\nu/\omega)\sin\phi}{\cos\phi - S_0}\right] \quad \text{elec/cm}^3$$

$$(10.39)$$

and for the electron wake radius, ρ_e,

$$\rho_e^2 = \frac{\alpha^2 J_1^2(\alpha)\delta c}{4\omega Q_L(1.189)} \frac{2\cos\phi - (1/S_0) - S_0}{(\omega/\nu)(S_0 - \cos\phi) + \sin\phi}$$

$$(10.40)$$

where δ is the height of the cavity (Fig. 10.29), ϕ is the phase shift of the output signal, S_0, the normalized signal amplitude, while the other symbols have been previously defined. The value of ν can be estimated by the relation

$$\nu = 2 \times 10^8 \times \text{(pressure in mmHg)}$$

$$(10.41)$$

or from measurements with the same technique at low electron density[10.47].

10.6.2.2 Open Microwave Resonators

The closed UHF resonator described in the previous section, while having excellent sensitivity (from about 10^{12} down to about 10^5 electrons/cm), has poor spatial resolution. If used with larger projectiles (4.7 mm to 12.7 mm was the diameter of the pellets fired in the UHF resonators of Ref. 10.46), part of the cavity, namely the entrance port, will physically interfere with the flow field, and cause reflections of the bow shock which may modify the distribution of ionization in the wake. The smaller cavity dimensions demanded by operation at higher frequencies lead to the same limitations.

At higher frequencies, the open microwave resonator can be used to overcome these difficulties. Primich, Hayami, et al.[10.48-10.52], have shown that quasi-optical microwave resonators can give sufficient spatial resolution, good sensitivity and negligible wake perturbation. Also by using a number of resonators displaced radially as in the focused multi-probe interferometer, the radial gradients can be determined. In this section a brief description of concentric focused Fabry-Perot resonators[10.52] will be presented, and their use as a plasma diagnostic instrument outlined. For a more detailed analysis of the various open resonators, the reader is referred to the paper by Boyd and Kogelnik[10.53].

The configuration of a focused Fabry-Perot resonator for plasma diagnosis is shown in Figure 10.30. It has been shown[10.51] that by an appropriate choice of reflector spacing, aperture radius, and reflector radius of curvature, such a microwave structure resonates in the dominant TEM_{00q} mode in which the field distribution is given by

$$E(x,y,z) = \frac{E_0 d_b(0)}{d_b(x)} \left\{ \exp\left[-2\,\frac{(y^2+z^2)}{d_b^2(x)} \right] \right\} \begin{array}{l} \times\ (\cos kx)\ \text{for even values of}\ q \\ \times\ (\sin kx)\ \text{for odd values of}\ q\ , \end{array} \tag{10.42}$$

where

$$d_b(x) = \left(\frac{d_r \lambda}{\pi}\right)^{1/2} \left(\frac{2R}{d_r} - 1\right)^{1/4} \left(1 + \frac{4x^2}{d_r^2\left(\frac{2R}{d_r} - 1\right)}\right)^{1/2} \tag{10.43}$$

is the spot size of the TEM_{00q} mode at coordinate x , defined by twice the value of $(y^2+z^2)^{1/2}$ for

$$\left| \frac{E(x,y,z)}{E_0} \right|^2 = \frac{1}{e} .$$

Here, λ is the wavelength of the unperturbed resonant signal, $k = 2\pi/\lambda$, $q = 2d_r/(\lambda-1)$ and other quantities are defined in Figure 10.30. The envelope of the field distribution at which $(E/E_0)^2 = 1/e$ is also shown in the figure.

Moreover, it has been shown[10.51] that for maximum sensitivity (which is directly related to the Q) the resonator must be operated at a d_r/R ratio near 1.9.

Using Equation (10.42) for the electric field of the unperturbed resonator, Hayami and Kelley[10.52] have found that the relative resonant frequency shift of the resonator due to the presence of the plasma cylinder can be represented by the relation

$$\frac{\Delta f}{f_0} = \frac{\pi^{\frac{1}{2}} D_p}{4 d_r} \frac{n_0}{n_c} F[x_0, y_0, D_p, d_b(0)] = \frac{1}{2Q} \tan \phi' , \tag{10.44}$$

where for a Gaussian radial density distribution

$$F = \frac{D_p}{(D_p^2 + d_b^2(0))^{1/2}} \exp\left(-\frac{4 y_0^2}{D_p^2 + d_b^2(0)}\right) \left\{1 \pm \cos 2kx_0 \exp\left[-\frac{kD_p}{2}^2\right]\right\} , \tag{10.45}$$

and for a uniform radial density distribution

$$F = \frac{2D_p}{\pi d_b(0)} \int_{-\pi/2}^{\pi/2} \left\{ \exp\left[-\left(\frac{2y_0 + D_p \sin\theta}{d_b(0)}\right)^2 \right] \left[\cos\theta \pm \frac{\cos 2kx_0}{kD_p}\sin(kD_p \cos\theta)\right] \right\} \cos\theta\, d\theta . \tag{10.46}$$

Here, n_0 represents the electron density at the plasma-wake center-line; n_c the critical electron density defined by $n_c = \omega^2 m\epsilon_0/q_e^2$; D_p the diameter of the plasma cylinder for a uniform distribution and the diameter to the $1/e$ point in density for a Gaussian distribution; $d_b(0)$ the diameter of the microwave beam to the $1/e$ point in power, at $x = 0$; Q , the unperturbed Q of the resonator; and ϕ the phase shift of the transmitted signal due to the perturbation of the resonator by the plasma. For other definitions refer to Figure 10.30.

Figure 10.31 shows a block diagram of the system for measuring Δf . The frequency of an oscillator is periodically swept through the bandpass of the cavity and the transmitted signal is displayed on an oscilloscope whose time base is related to frequency. As the wake passes through the cavity, the location of the successive resonant frequency peaks referred to the unperturbed cavity resonant frequency peak give the values of Δf (Fig. 10.31). The swept-frequency resonator system is limited in the first instance by its relatively slow response to a rate of change of frequency, thus forcing the system to sample the wake only at relatively long intervals of time during the passage of the wake. Secondly the determination of Δf is difficult because it is done by locating two maxima which are close and eventually this becomes a critical limitation when the system is used for measuring a small perturbation.

To overcome these limitations, a phase system (Fig. 10.32) can be used[10.52] for measuring the phase of the transmitted signal and thus for determining the value of Δf from Equation (10.44). The klystron is set at the resonant frequency before perturbing the resonator and the Q is measured under the same condition. The maximum rate of perturbation to which such a system can respond is related to the time response of the resonator itself, Q/ω_0 , (approximately 0.2 microsecond for a Q = 50,000 and operating frequency of 35 GHz) and to the rise time of the phase measuring system.

On the other hand, the sensitivity of the system can be increased by increasing the Q of the cavity, but this will cause a deterioration in time response of the system. A compromise between the maximum sensitivity and the desired time response is required.

10.7   SCATTERING OF MICROWAVES FROM HYPERSONIC WAKES

The microwave diagnostic techniques described in the preceeding section are useful to determine average electron distributions in hypersonic wakes. These distributions, in the case of laminar wakes, can be used in conjunction with an appropriate scattering model to predict reflection properties and values of radar cross section. In the case of turbulent wakes, however, the scattering depends not only upon averaged values of electron density but also upon spatial and temporal variations. Thus, scattering measurements can be regarded as a way to obtain information about the wake structure, in addition to assessing the validity of theoretical scattering models. The interest in this approach also arises from the fact that scattering measurements are the only type of radar measurements that can be made on the wake of hypervelocity objects moving into the earth's atmosphere, such as meteors and re-entering satellites or rockets.

Of particular interest is the case of scattering from largely underdense wakes in which the process of single scattering can be assumed. Then the signals arising from the different parts of the wake are independent from each other and the formulation of the problem is greatly simplified by using the Born approximation which yields accurate results in this case. This is very fortunate because the inclusion of multiple scattering processes, which are dominant in an almost critically-dense plasma, is a very difficult task that defies accurate formulation.

The purpose of this section is to indicate the type of information that can be obtained from radar scattering measurements on underdense wakes. This includes the observation of the laminar to turbulent wake transition, the measurement of the average turbulent wake velocity and a brief description of wake structure studies using well known scattering models applicable for underdense laminar and turbulent wakes. Particular attention is given to the study of the statistical behavior of the turbulent wake.

10.7.1   Laminar-to-Turbulent Wake-Transition Studies

The ballistic range has been the site of a considerable number of studies of the transition from laminar to turbulent flow in the hypersonic wake. In free-flight tests, photographs of the wake are obtained with the aid of optical systems, such as schlierens, and transition is identified on the photographs by irregularities in the images of the viscous wake core at some axial distance behind the body. The techniques are described in Chapter 8.

Wilson[10.54] has recently discussed the possibility that the viscous wake may sometimes be turbulent but appear laminar in a schlieren picture because the gas density is too low to produce adequate refraction of the light. This problem is aggravated in the case of blunt bodies by the high-temperature (low density) layer of gas formed around the viscous wake by that part of the "inviscid" flow which has been most highly heated by passing through the nearly normal part of bow shock wave. The outer limit of this hot, inviscid layer is fairly sharply defined in a schlieren photograph and may resemble a laminar-viscous wake even though there be an "invisible" turbulent viscous wake inside it. Only when the turbulence propagates radially to the outer (higher density) edge of the hot layer does the schlieren detect it. Radar waves, on the other hand, may penetrate the hot layer and be scattered by the turbulent core.

It has been reported[10.55] that backscattered radar signals have indicated the presence of turbulence in the wake, even when this could not be ascertained with certainty from schlieren photographs.

A convenient experimental approach is through the use of a focused-beam Doppler radar viewing the wake from an oblique angle. When the illuminated portion of the wake is laminar the reflections produced are mainly specular, and no significant signal is returned to the radar. However, at the time of transition, the appearance of turbulence in the radar beam can produce significant reflections in all directions, in particular towards the radar. Thus the transition is associated with the beginning of the detection of a random signal caused by the turbulence. It can be observed whether the wake is overdense or underdense.

10.7.2   Turbulent-Wake Velocity Measurements

Turbulent-wake velocity measurements can be performed on under-dense wakes using the same radar arrangement as described above for the observation of laminar to turbulent wake transition. The wake should be underdense enough to ensure that the backscattered signal contains all possible Doppler components corresponding to the velocity profiles existing in the wake.

Observations of the wakes of spheres made at GM/DRL[10.55] have shown strong backscatter exhibiting pronounced periodicity with random modulation. The mean periodicity was obtained by averaging data over small axial intervals and the wake velocity determined. An example of such data is presented in Figure 10.33. Recent sphere wake convection velocity measurements made with electrostatic probes appear to be in good agreement with the radar measurements[10.56].

There appears to be little prospect of measuring turbulent wake velocity behind slender bodies such as sharp cones by this technique. In contrast to returns from sphere wakes which exhibit strong periodicity with a superimposed amplitude modulation, the returns from cone wakes exhibit no periodicity[10.55]. The signals appear to be random with much lower fluctuation rates than those observed behind spheres.

10.7.3 Scattering by a Laminar Wake

As the different models launched in ballistic ranges are usually axisymmetric, the discussion is limited here to the case of underdense axisymmetric wakes. Assuming further that the collision frequency is much smaller than the angular radar frequency, then the dielectric constant of the plasma remains everywhere close to unity and can be represented by

$$K = 1 - \frac{n(\rho, z)}{n_c} , \qquad (10.47)$$

where n_c is the critical electron density and n is the local electron density at a point of radial coordinate ρ and axial coordinate z (see Figure 10.34).

The problem of scattering of plane electromagnetic waves incident at an arbitrary angle on such a dielectric structure has been formulated by Albini and Nagelberg[10.57,10.58] using the Born approximation. At large distances from the structure, the integral representation of the scattered electric field, E_s, takes the approximate form

$$E_s \simeq E_0 \left[\frac{k_0^2 \sin \chi}{4\pi n_c} \right] \left[\frac{\exp(jk_0 r)}{r} \right] I(n) , \qquad (10.48)$$

where

$$I(n) = \int_V n(\vec{r}') \exp[j(\vec{k}_i - \vec{k}_r) \cdot \vec{r}'] d^3\vec{r}' . \qquad (10.49)$$

E_0 is the amplitude of the incident electric field; k_0 the vacuum wave number; r the magnitude of $\vec{r}$, which is the vector from the scattering region to the point of observation directed along the line of sight to the point of observation; χ the angle between $\vec{r}$ and the direction of polarization of E_0; and $\vec{k}_i$ and $\vec{k}_r$ are vectors of magnitude k_0 oriented along the direction of incidence and the direction of the point of observation, respectively.

The differential scattering cross section, defined as the ratio of the power scattered into a differential element of solid angle divided by the magnitude of the incident power flux, is then given by

$$\sigma = \left[\frac{k_0^2 \sin \chi}{4\pi n_c} \right]^2 I(n)I^*(n) , \qquad (10.50)$$

where the asterisk denotes the complex conjugate.

Because of the assumed symmetry of revolution, the integration over the polar angle ϕ (see Figure 10.34) can be carried out, with the result[10.57]

$$I(n) = 2\pi \iint n(\rho, z) \exp(jk_0\gamma z) J_0(k_0\Omega\rho)\rho \, d\rho \, dz , \qquad (10.51)$$

where J_0 is the zero order Bessel function and

$$\gamma = \cos\theta - \cos\theta_0 \qquad (10.52)$$

$$\Omega = (\sin^2\theta + \sin^2\theta_0 - 2\sin\theta \sin\theta_0 \cos\phi_0)^{1/2} , \qquad (10.53)$$

and θ_0 and ϕ_0 are the angular coordinates of the direction of observation.

This form is very useful for studying the influence of various radial and axial distributions of the scattered field pattern. Several types of distributions have been considered by Albini[10.57], notably in the case where the electron density function can be written in the form

$$n(\rho, z) = A(\rho)B(z) . \qquad (10.54)$$

The inverse problem, which consists of determining the electron distribution from the analysis of experimental data obtained at different angles or different frequencies, is difficult to solve. One approximate approach is to assume some realistic parametric functions whose parameters can be adjusted so as to match experimental results, in a way similar to that taken in Section 10.5 to study the plasma sheath.

10.7.4 Scattering by a Turbulent Wake

Since the original paper of Booker and Gordon[10.59] in 1950, many studies have been reported on the problem of scattering of electromagnetic waves by numbers of randomly distributed scatterers. Under the same assumptions as in the case of the laminar wake discussed above, but considering further that the fluctuations in electron density arising with turbulence cause the scattered field to fluctuate, the average value of this field can be written[10.57] as

$$\langle E_s \rangle \simeq E_0 \left[\frac{k_0^2 \sin \chi}{4\pi n_c} \right] I(\langle n \rangle) , \qquad (10.55)$$

where

$$I(\langle n \rangle) = \int_V \langle n(\vec{r}') \rangle \exp[j(\vec{k}_i - \vec{k}_r) \cdot \vec{r}'] d^3\vec{r}' . \qquad (10.56)$$

As the local electron density can be written as the average value, $\langle n \rangle$, in the vicinity of the point indicated by $\vec{r}'$, plus a perturbation, δn, the expected value of the differential scattering cross section takes the form

$$\langle \sigma \rangle = \left[\frac{k_0^2 \sin \chi}{4\pi n_c} \right]^2 [\Phi \langle n \rangle + \Phi \langle \delta n \rangle]$$ (10.57)

where

$$\Phi \langle n \rangle = \int_V \int_{V'} [\langle n(\vec{r}') \rangle \langle n^*(\vec{r}'') \rangle] \exp[j(\vec{k}_i - \vec{k}_r).(\vec{r}' - \vec{r}'')] \, d^3\vec{r}' d^3\vec{r}''$$ (10.58)

and $\Phi \langle \delta n \rangle$ is a similar function in which n is replaced by δn. The integral $\Phi \langle n \rangle$ represents the contribution arising from the average distribution in electron density while the integral $\Phi \langle \delta n \rangle$ represents the contributions due to fluctuations. Experimental observations[10.60] have indicated that in most cases the second integral is much more important than the first which can often be neglected.

Mathematically, the expression $\Phi \langle \delta n \rangle$ is the Fourier transform of the spatial correlation function of the fluctuations in electron density, and as such represents a power density spectrum which characterizes the turbulence. The measurement of the scattered energy at a given wavelength and in one particular direction determines one point on the Fourier spectrum with the wavenumber $2k_0 \sin (\theta/2)$, where θ is the smallest angle between $\vec{k}_i$ and $\vec{k}_r$. The complete spectrum can be obtained either by varying the radar frequency or the angle of observation. Figure 10.35 shows an arrangement of three focused antennae used at GM/DRL[10.61] for observations at different frequencies, and Figure 10.36 shows the antenna system used at CARDE to monitor the scattered signal in five different directions around the wake. Whatever the approach taken it is always convenient to illuminate the same volume of wake with the different antennae in order to simplify the task of data analysis.

When the turbulence is isotropic and the correlation length is small comparatively to the size of the illuminated volume of wake, the statistical behavior can be described by a one-dimensional correlation function and the corresponding Fourier spectrum is readily obtained. The usual approach is to assume again a realistic form of correlation function and adjust the descriptive parameters so as to match experimental results. Exponential and Gaussian laws are often considered as well as a more general law given by Tatarsky[10.62] and used notably by Pippert[10.60] in the analysis of field radar data, and by Guthart et al[10.63] in the analysis of laboratory data obtained on a plasma jet. Significant amounts of data concerning scattering from turbulent wakes as observed in ballistic ranges have not yet appeared in the open literature.

The correlation length so obtained determines the average size of the energy-containing eddies in the turbulent wake. On the other hand, if the fluctuations of free electrons do follow mass fluctuations then the amplitude and the form of the power spectrum determines the intensity of turbulence, the way the kinetic energy is distributed among the different eddies, modes of exchange of internal energy, and dissipation rates by viscous forces[10.62].

In addition to recording the amplitude of the scattered signal, it is also useful to record the phase as a function of time. In particular, when the phase changes arising from the time fluctuations of electron density are slow compared to the phase changes produced by the displacement of the eddies, the velocity component in the direction $(\vec{k}_i - \vec{k}_r)$ can be measured. The complete velocity spectrum characterizes the type of motion occurring in the turbulence.

REFERENCES

10.1	Koch, R.	*Mesure Radioélectrique de la Vitesse des Projectiles.* Onde Electrique, Vol.32, 1952, p.357.
10.2	Barlow, E.J.	*Doppler Radar.* Proc.I.R.E., Vol.37, 1949, p.340.
10.3	Primich, R.I.	*Microwave Techniques for Hypersonic Ranges.* Paper in Electromagnetic Effects of Re-Entry. Pergamon Press, 1961, p.186.
10.4	Musal, H.M. Jr. Primich, R.I. Blore, W.E. Robillard, P.E.	*Millimeter Radar Instrumentation for Studying Plasma Effects Associated with Hypersonic Flight.* General Motors Defense Research Laboratories, Technical Report 64-02J, 1964.
10.5	Collin, R.E. Brown, J.	*The Design of Quarter-Wave Matching Layers for Dielectric Surfaces,* Proc.I.E.E., Vol.103-C, Monogr. No.149 R, 1956, p.153.
10.6	Epis, J.J.	*Compensated Electromagnetic Horns.* Microwave Journal, Vol.4, 1961, p.84.
10.7	Parnell, G.W.	*On the Axial Phase Anomaly for Microwave Lenses.* J.Opt.Soc.Amer. Vol.48, 1958, p.643.
10.8	Pennelegion, L.	*Microwave Interferometry Studies in Free-Piston Gun Tunnels.* Advances in Hyper-velocity Techniques, Plenum Press, 1962, (Proc.Second Symp. on Hypervelocity Techniques, Denver, Colorado, March 1962).
10.9	Pennelegion, L.	*A Microwave Method of Determining the Displacement and Velocity of a Piston in a Hypersonic Gun Tunnel.* Nature, Vol.183, January 1959.
10.10	Hendrix, R.E.	*Microwave Reflectometry in Interior Ballistics.* Arnold Engineering Development Center, Technical Report 66-54, May 1964.
10.11	Hendrix, R.E.	*Microwave Measurement of Projectile Kinematics Within Launcher Barrels.* Arnold Engineering Development Center, Technical Report 62-213, November 1962.
10.12	Knapp, R.E. Hendrix, R.E.	*Experimental Projectile Kinematic Studies in a Two-Stage Light Gas Gun.* Arnold Engineering Development Center, Technical Report 65-60, March 1965.
10.13	Hruby, R.J.. Sander, R.C. Berggren, R.E.	*Microwave Technique for Measuring Projectile Time History in Light-Gas Guns.* Proc. of the IEEE, Second International Congress on Instrumentation in Aerospace Simulation Facilities. Stanford University, August 1966.
10.14	Lin, S.C. Teare, J.D.	*Rate of Ionization Behind Shock Waves in Air, II. Theoretical Interpretation.* Phys. Fluids, Vol.6, 1963, p.355.
10.15	Lin, S.C. Neal, R.A. Fyfe, W.J.	*Rate of Ionization Behind Shock Waves in Air, I. Experimental Results.* Phys. Fluids, Vol.5, 1962, p.1633.
10.16	Wilson, J.	*Ionization Rate of Air Behind High-Speed Shock Waves.* Phys. Fluids, Vol.9, 1966, p.1913.
10.17	Eschenroeder, A.Q. Daiber, J.W. Golian, T.C. Hertzberg, A.	*Shock Tunnel Studies of High-Enthalpy Ionized Airflows.* Proceedings of the AGARD Conference on "High Temperature Aspects of Hypersonic Flow", April 3-6, 1962, Pergamon Press, 1964.
10.18	Kornegay, W.	*Electron Density Decay in Wakes.* AIAA Journal, Vol.3, 1965, p.1819.
10.19	Labitt, M.	*The Measurement of Electron Density in the Wake of a Hypervelocity Pellet Over a Six-Magnitude Range.* MIT Lincoln Laboratory, Technical Report 307, April 15, 1963.
10.20	Hall, J.G. Eschenroeder, A.Q. Marrone, P.V.	*Blunt-Nose Inviscid Airflows with Coupled Nonequilibrium Processes.* J.Aerospace Sciences, Vol.29, 1962, p.1038.
10.21	Blottner, F.G.	*Nonequilibrium Laminar Boundary-Layer Flow of Ionized Air.* AIAA Journal, Vol.2, 1964, p.1921.
10.22	Eschenroeder, A.Q. Chen, T.	*Near-Wake Ionization Behind a Sphere in Hypersonic Flight. Part I: Reaction Kinetics,* General Motors Defense Research Laboratories Technical Report 65-01H, September 1965; *Part II: Influence of Flight Conditions,* General Motors Defense Research Laboratories Technical Report 65-01Q, December 1965.

10.23 Wen, K.S. *Preliminary Theoretical Results of Laminar Wake Ionization Behind Hypersonic*
      Chen, T. *Spheres and Cones.* General Motors Defense Research Laboratories Technical Report
                66-22, June 1966.

10.24 Lykoudis, P.S. *Recent Developments in the Fluid Mechanics of Hypersonic Wakes.* Rand Corporation
                      Report P-3451, November 1966.

10.25 Lykoudis, P.S. *A Review of Hypersonic Wake Studies.* AIAA Journal, Vol.4, 1966, p.577.

10.26 Eschenroeder, A.Q. *Kinetic Processes in Hypersonic Wakes.* Proceedings of the AGARD Specialists
                         Meeting on Fluid Physics of Hypersonic Wakes, held at Colorado State University,
                         Fort Collins, Colorado, May 10-12, 1967.

10.27 Slattery, R.E. *Range Contamination and its Effects on Measurements.* Proceedings of the Second
      Clay, W.E.   International Congress on Instrumentation in Aerospace Simulation Facilities,
      Worthington, W.C. Stanford University, August 29-31, 1966.

10.28 Heald, M.A. *Plasma Diagnostics With Microwaves.* John Wiley and Son, New York, 1965.
      Wharton, C.B.

10.29 Hockstim, A.R. *Charts for Microwave Propagation Through a Plasma.* General Dynamics, AE-0858, 1962.

10.30 Musal, H.M. *Plasma Frequency and Electron Collision Frequency Charts for Hypersonic Vehicle*
                   Equilibrium Flow Fields in Air. General Motors Defense Research Laboratory,
                   Technical Report 2096, December 1962.

10.31 Serbin, H. *Supersonic Flow Around Blunt Bodies.* Journal of the Aeronautical Sciences, Vol.25,
                  No.1, January 1958.

10.32 Stratton, J.A. *Electromagnetic Theory.* McGraw Hill, 1941.

10.33 Blore, W.E. *Experimental Verification of Scattering Coefficients for Metal Spheres.* Proc.
                   IEEE Vol.51, No.9, 1963, p.1270.

10.34 King, R. *The Scattering and Diffraction of Waves.* Harvard University Press, 1959.
      Wu, T.T.

10.35 Purcel, E.M. *The Radar Equation.* M.I.T. Radiation Laboratory Series, Vol.1, McGraw Hill, 1947.

10.36 Blore, W.E. *35 and 70 Gc CW Balanced-Bridge Model Measurement Radars.* Microwave Journal,
      Robillard, P.E. Vol.7, No.9, 1964.
      Primich, R.I.

10.37 Wetzel, L. *Precursor Ionization and Electron Diffusion From a Shock Front.* Physics of Fluids,
                  Vol.5, No.7, July 1962.

10.38 Murphy, E.L. *The Reduction of Electromagnetic Backscatter From a Plasma Clad Conducting Body.*
                    M.I.T. Lincoln Laboratory, Technical Report 589, September 1963.

10.39 Zivanovic, S. *Investigation of Precursor Ionization in Front of the Shock Waves of Hypersonic*
                     Projectiles. AIAA Conference, Preprint 63-458, August 1963.

10.40 Bachynski, M.P. *Free-Space Microwave Techniques for Plasma Measurements.* RCA Rev., Vol.25, No.2,
      Cloutier, G.G. 1964.

10.41 Balakhanov, V.Ya., *Determination of Plasma Parameters by Means of a Multi-Beam Radio-Interferometer.*
      Rusanov, V.D.   Atomnoya Energiya (USSR), Vol.18, No.5, 1965.
      Striganov, A.R.

10.42 Huddlestone, R. *Plasma Diagnostic Techniques.* Academic Press, New York, 1965.
      Leonard, S.L.

10.43 Primich, R.I. *Millimeter Wavelength Focused Probes and Focused Resonant Probes for Use in Studying*
      Hayami, R.A. *Ionized Wakes Behind Hypersonic Velocity Projectiles.* General Motors Defense
                    Research Laboratories Technical Report 63-217C, 1963.

10.44 McLeod, J. *A Method for Determining Profiles of Radial Electron Density and Collision Frequency*
      Zivanovic, S. *in the Wakes of Hypersonic Projectiles Using Transverse Microwave Probes.* General
                     Motors Defense Research Laboratories Report 64-02M, November 1964.

10.45 Hayami, R.A. *Wake Electron Density Measurements Behind Hypersonic Spheres and Cones.* Proceedings
      Primich, R.I. of the AGARD Specialists Meeting on Fluid Physics of Hypersonic Wakes, held at
                     Colorado State University, Fort Collins, Colorado, May 10-12, 1967.

10.46 Labitt, M.
Herlin, M.A.
Application of the Resonant Cavity Method to the Measurement of Electron Densities and Collision Frequencies in the Wakes of Hypervelocity Pellets. MIT Lincoln Laboratory Technical Report 248, October 1961.

10.47 Labitt, M.
Measurement of the Diameter of the Electronic Wake of Hypersonic Pellets. MIT Lincoln Laboratory Technical Report 342, January 1964.

10.48 Primich, R.I.
Hayami, R.A.
The Application of the Focused Fabry-Perot Resonator to Plasma Diagnostics. IEEE Trans. MTT Vol.12, 1964, p.33.

10.49 Hayami, R.A.
Kelley, K.J.
The Continuous Measurement of Rapid Changes in the Low-Level Ionization in the Wakes of Hypersonic Velocity Projectiles Using Open Microwave Resonators. Proceedings of the IEEE Second International Congress on Instrumentation in Aerospace Simulation Facilities, Stanford University, August 1966.

10.50 Hayami, R.A.
Auston, D.H.
Kelley, K.J.
Faulkner, J.R.
Fabry-Perot Resonators at 5Gc and 35Gc for Wake Ionization Measurement in a Free-Flight Ballistic Range. General Motors Defense Research Laboratories, Technical Report 65-19B, March 1965.

10.51 Auston, D.H.
Primich, R.I.
Hayami, R.A.
Further Considerations of the Use of Fabry-Perot Resonators in Microwave Plasma Diagnostics. Proc. Symposium on Quasi-Optics, New York, June 1964. Microwave Res. Inst. Symposia Ser. Vol.XIV, Polytechnic Press, Brooklyn, N.Y.. 1964, p.273.

10.52 Hayami, R.A.
Kelley, K.J.
The Measurement of Transient Ionization Levels Using Open Microwave Resonators. General Motors Defense Research Laboratories Technical Report 66-01K, July 1966.

10.53 Boyd, G.D.
Kogelnik, H.
Generalized Confocal Resonator Theory. Bell System Tech.J., Vol.41, 1962, p.1347.

10.54 Wilson, L.N.
The Far Wake Behavior of Hypersonic Spheres. General Motors Defense Research Laboratories Technical Report 66-19, June 1966.

10.55 Primich, R.I.
Robillard, P.E.
Wilson, L.
Hayami, R.A.
Zivanovic, S.
Radar Scattering From Wakes. General Motors Defense Research Laboratories Technical Report 65-01E, 1965.

10.56 Kirpatrick, A.
Heckman, D.
Cantin, A.
Wake Plasma Turbulence Study Using an Electrostatic Probe Array. AIAA Journal, Vol.5, 1967.

10.57 Albini, F.A.
Scattering and Absorption of Plane Waves by Cylindrically Symmetrical Underdense Zones. AIAA Journal, Vol.2, No.3, 1964, p.524.

10.58 Albini, F.A.
Nagelberg, E.R.
Scattering of a Plane Wave by an Infinite Inhomogeneous Dielectric Cylinder – An Application of the Born Approximation. Journal of Applied Physics, Vol.33, No.5, 1962.

10.59 Booker, H.G.
Gordon, W.E.
A Theory of Radio Scattering in the Troposphere. Proceedings I.R.E., Vol.38, No.4, 1950, p.401.

10.60 Pippert, G.F.
On the Structure of Wake Turbulence Deduced From Field Radar Measurements. AIAA Preprint 63-446, 1963.

10.61 Zivanovic, S.
Robillard, P.E.
Primich, R.I.
Radar Investigation of the Wake of Blunt and Slender Hypersonic Velocity Projectiles in the Ballistic Range. Proceedings of the AGARD Specialists Meeting on Fluid Physics of Hypersonic Wakes, held at Colorado State University, Fort Collins, Colorado. May 10-12, 1967.

10.62 Tatarsky, V.I.
Wave Propagation in a Turbulent Medium. McGraw-Hill Book Company, Inc., New York, N.Y., 1961.

10.63 Guthart, H.
Weissman, D.E.
Morita, T.
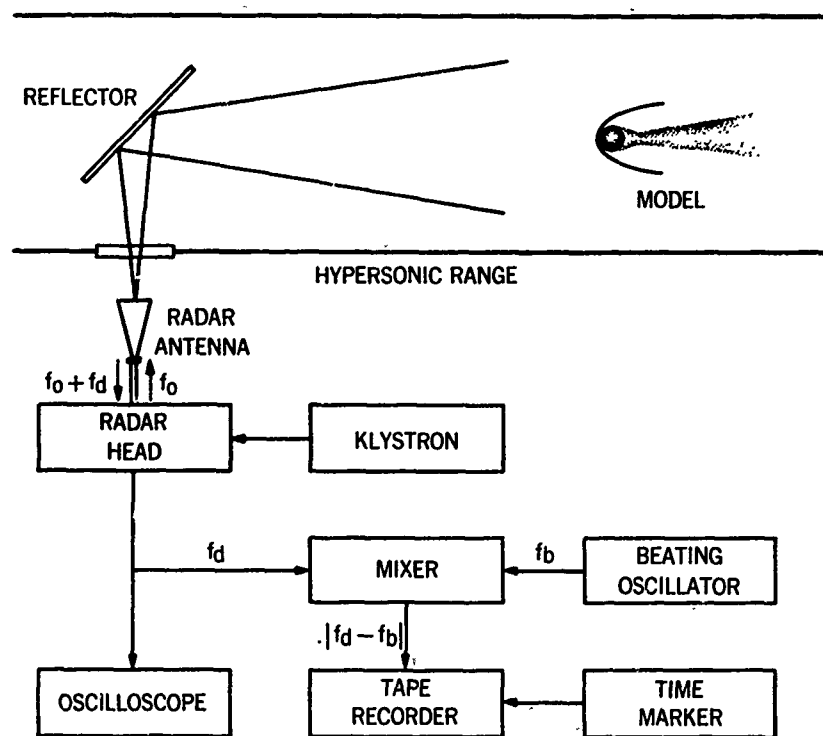*Microwave Scattering From an Underdense Turbulent Plasma.* Radio Science, Vol.I, No.11, 1966.

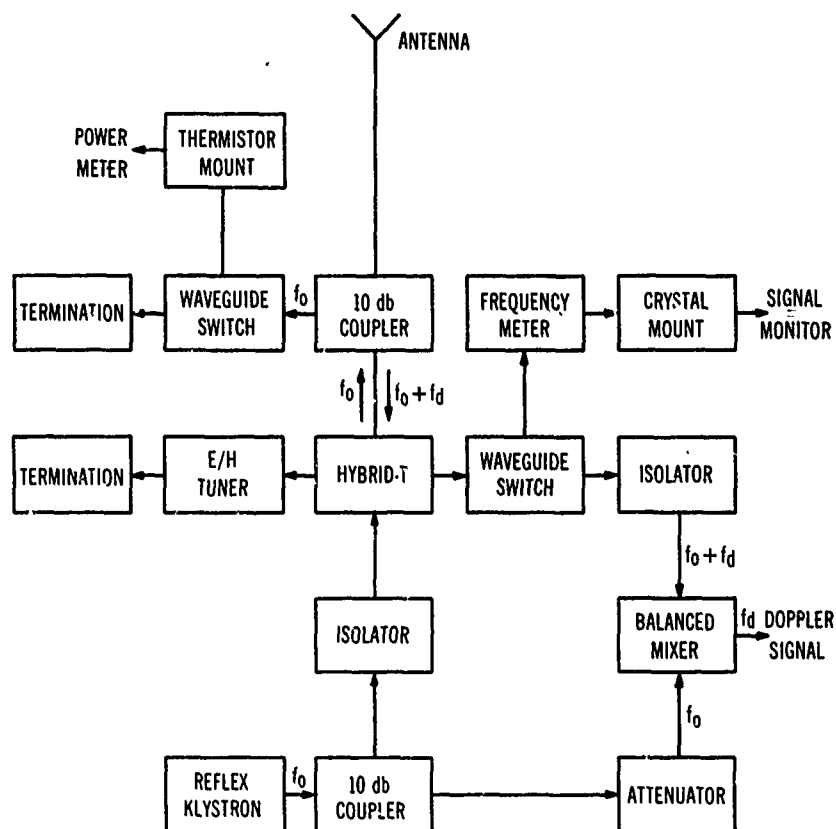Fig. 10.1 Schematic of Doppler-radar system used on hypersonic range

Fig. 10.2 CW-Doppler-radar microwave circuit

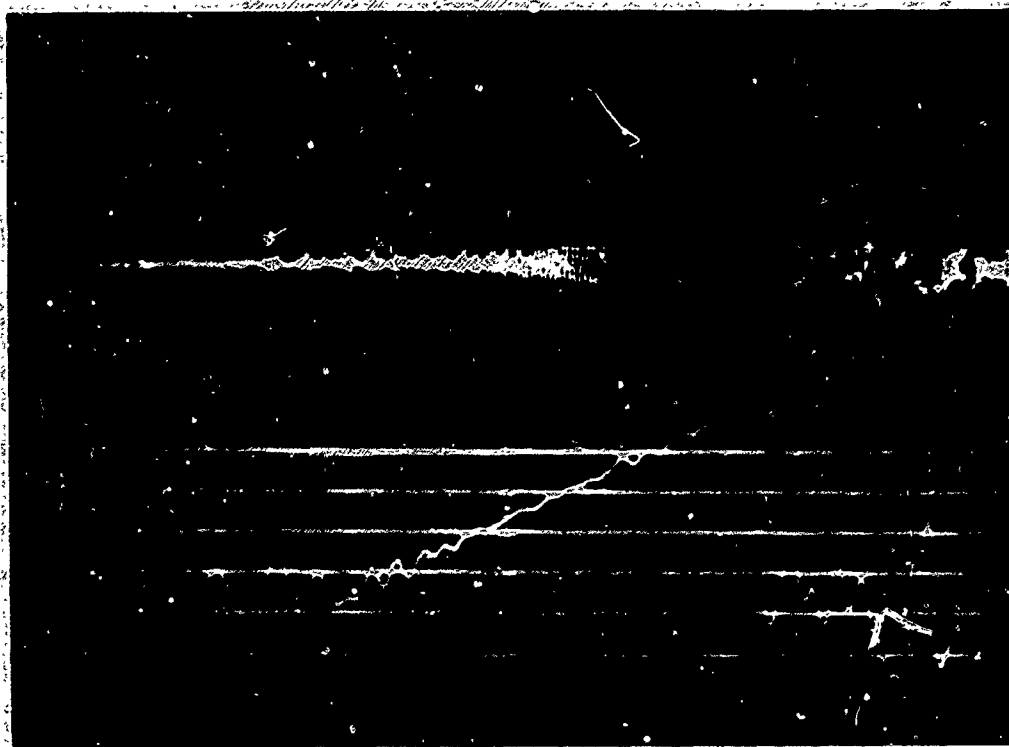

Fig. 10.3   Record of Doppler frequency shift played back from a magnetic tape (top curve) and output of
frequency discriminator (bottom trace) which is proportional to velocity. With reference to
the frequency-discriminator trace, the top calibration line represents a velocity of 4.39
km/sec and the bottom calibration line 4.56 km/sec, so that vertical scale is given by
approximately 27.5 m/sec per division of calibration. The horizontal scale is about 0.625
millisec per division (centimeter). The round was a 2.54-cm-sphere shot at a range pressure
of 76 torr
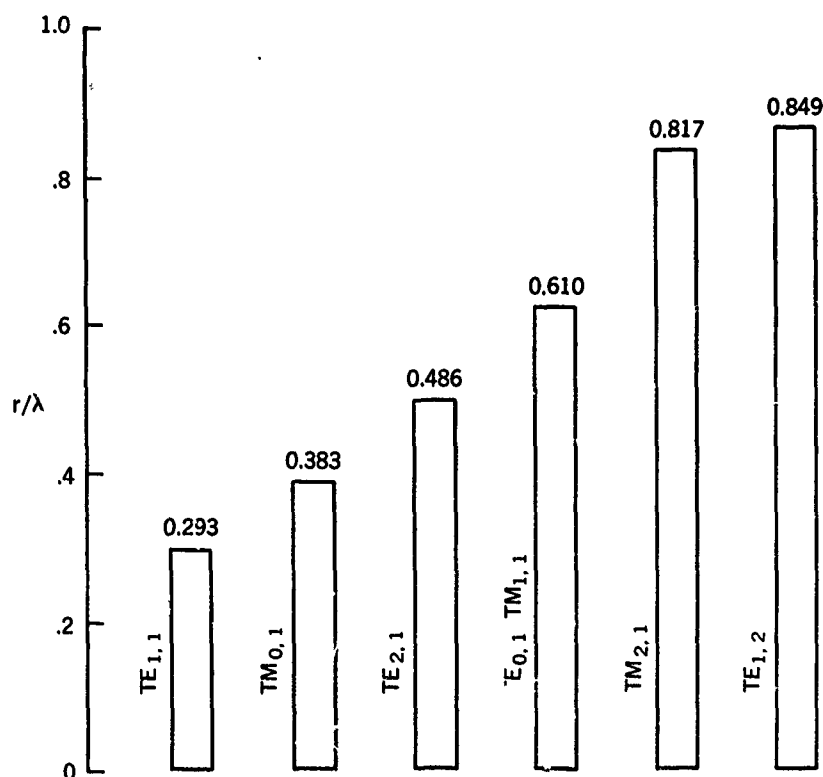
Fig. 10.4   The ratio of waveguide radius to free-space wavelength at cut-off for various modes in a circular
waveguide (after Moreno, "Microwave Transmission Design Data", Dover Publications, Inc.)
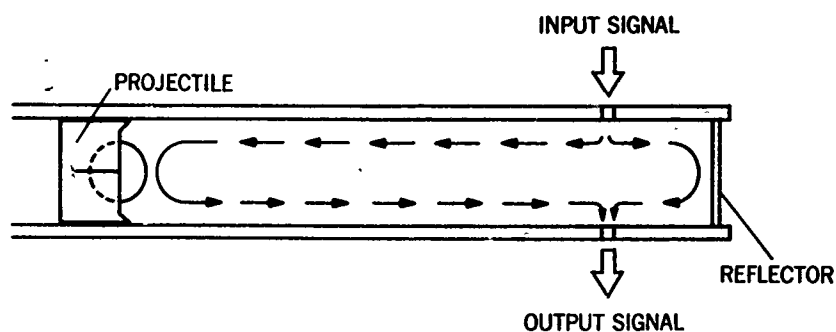
Fig. 10.5   Hybrid-T configuration for microwave measurement of projectile kinematics in a gun barrel
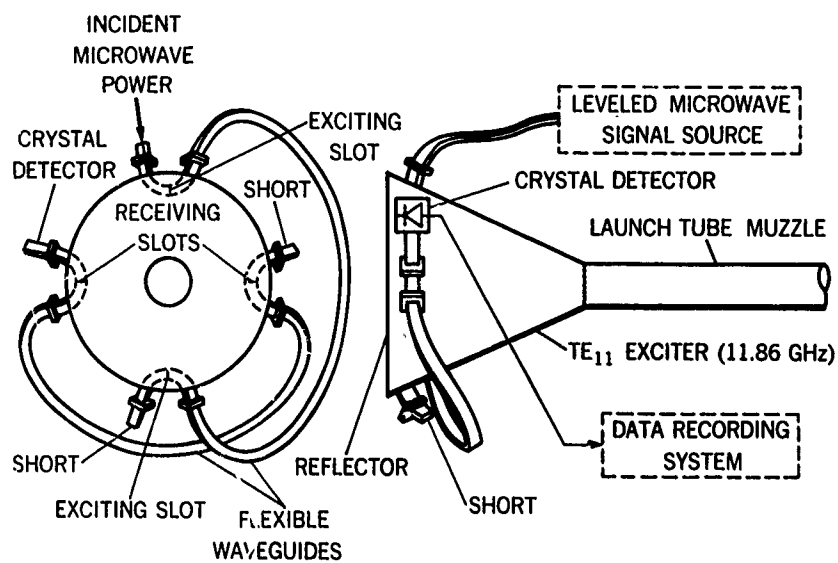

Fig. 10.6   Horn exciter for the TE_{11} mode microwave reflectometer on the Ames 25.4 mm light-gas gun
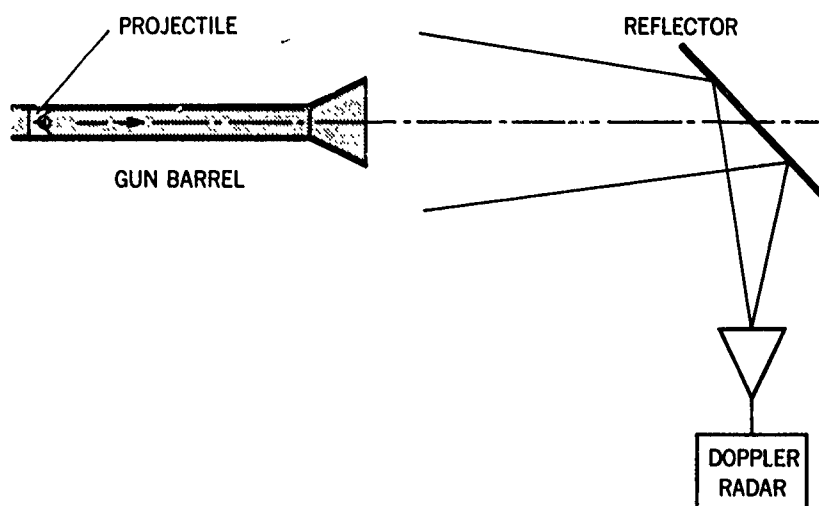

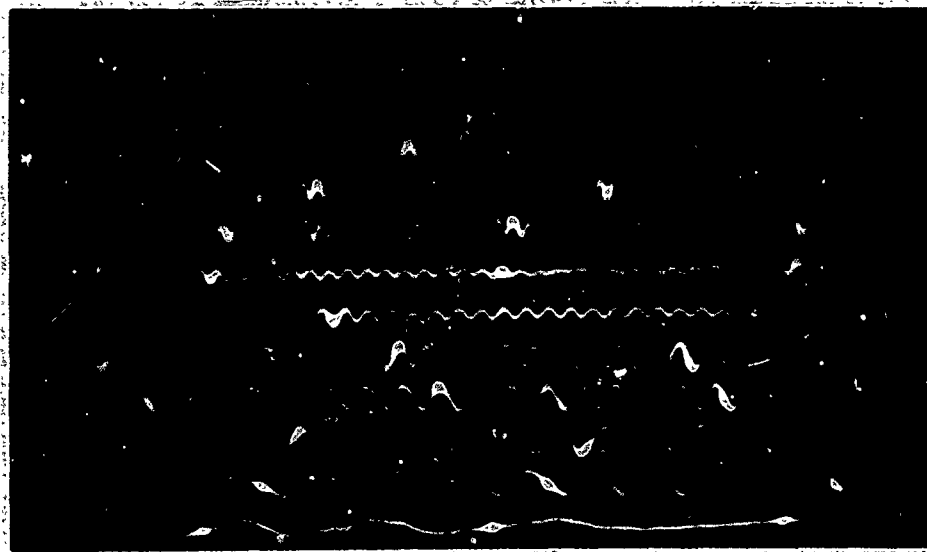Fig. 10.7   Doppler-radar configuration to study interior ballistics

Fig. 10.8   Multi-sweep oscilloscope record of the motion of a projectile in a gun barrel using the hybrid-T configuration.   The signal is displayed from left to right and from bottom to top.   Each cycle represents a projectile displacement of half a guide-wavelength
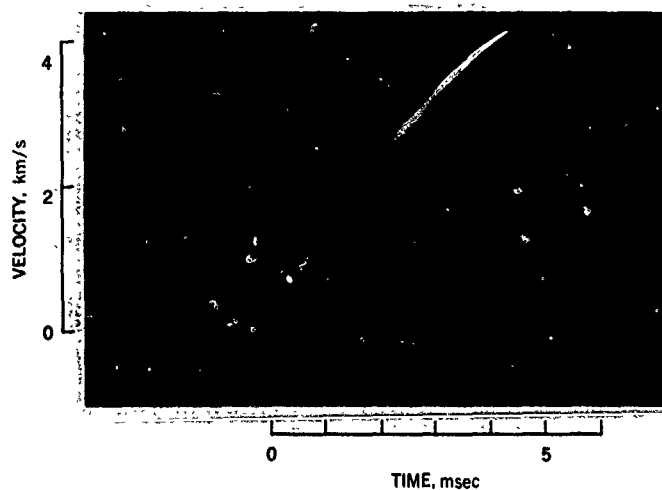

Fig. 10.9   Frequency-discriminator record of the velocity of the projectile in a gun barrel using the Doppler-radar configuration.   This record was obtained at CARDE at 9.95 GHz on a 38-mm-diameter gun barrel.   (Courtesy of L. Moir)

CASE (a)
PISTON SPEED 758 m/s
MODEL RELEASE PRESSURE
.68 kbar
MUZZLE SPEED 8.02 km/s

CASE (b)
PISTON SPEED 651 m/s
MODEL RELEASE PRESSURE
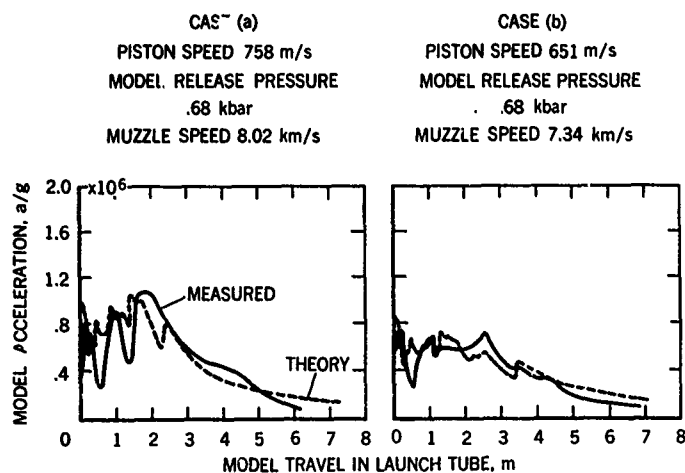.68 kbar
MUZZLE SPEED 7.34 km/s

Fig. 10.10   Typical results from gun-cycle measurements as obtained at Ames using the gun barrel as a microwave cavity
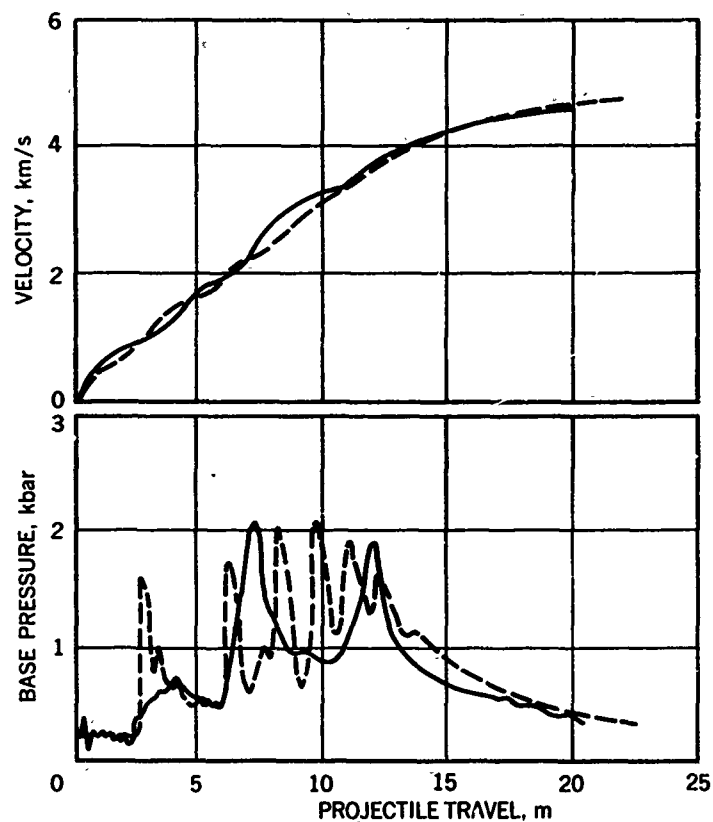
Fig. 10.11   Typical result from gun-cycle measurements as obtained at CARDE using a Doppler radar. The solid
curves are the experimental results. The dotted curves are theoretical predictions based on an
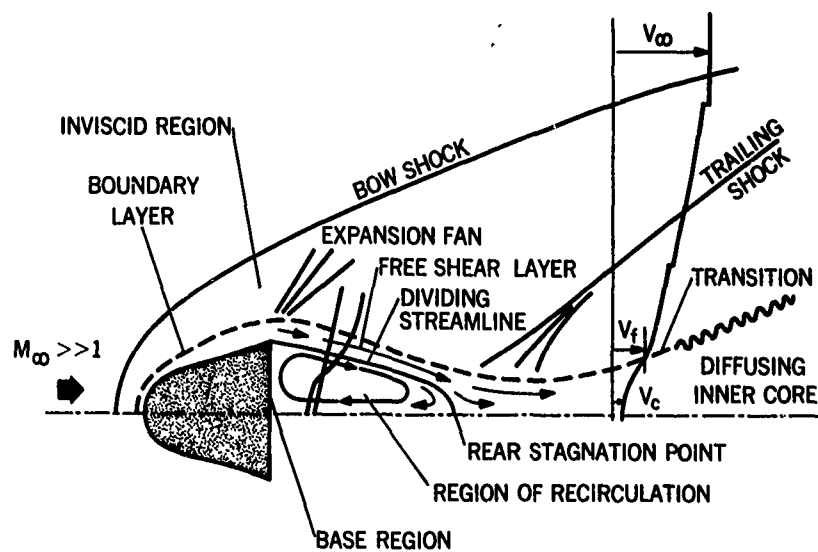approximate gas-dynamic model.   (Courtesy of M. Cloutier)

Fig. 10.12   Definition of the various regions of the flow field surrounding a hypersonic object. In the figure,
the model is assumed to be at rest, while the gas is flowing over it. V_∞, V_f, V_c represent
respectively the free stream velocity, the velocity at the turbulent front and the velocity on the
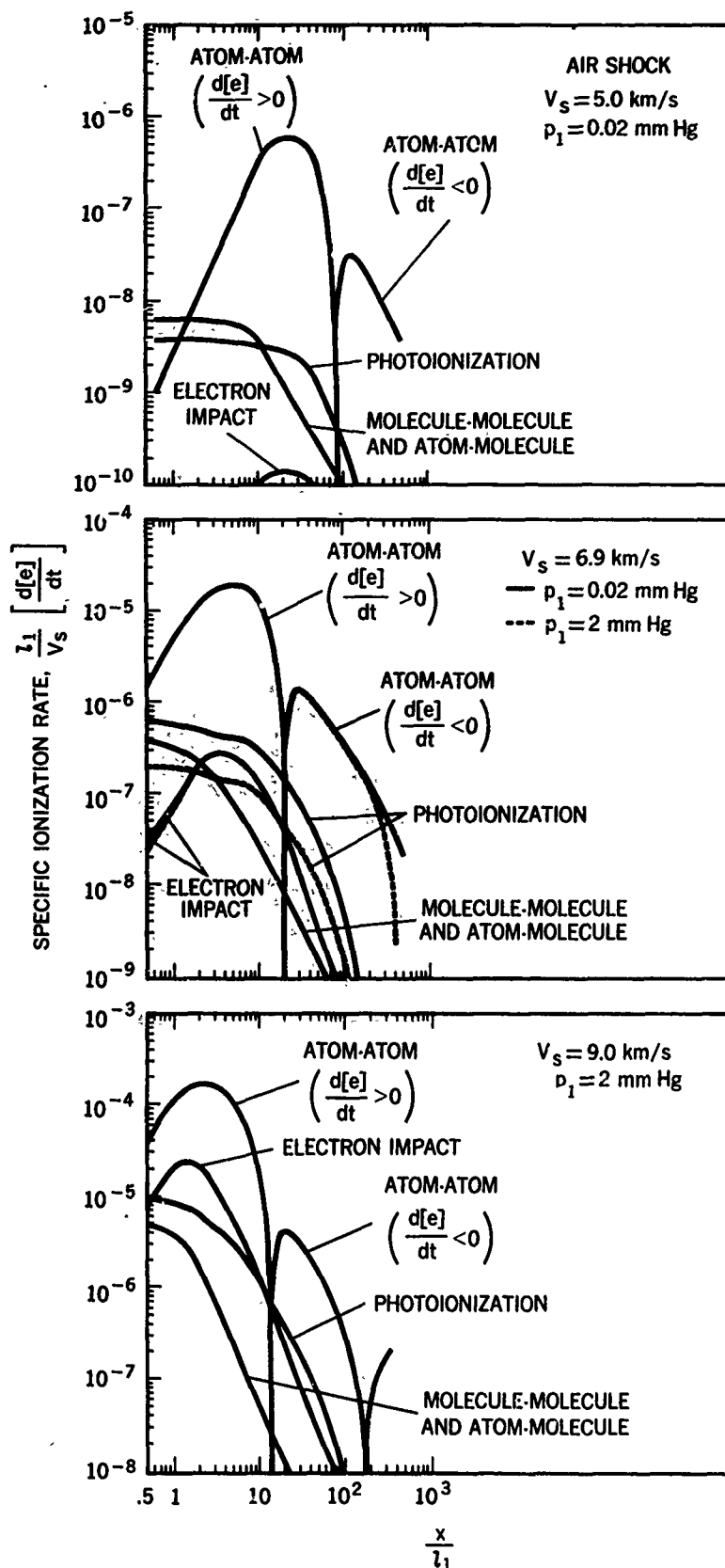wake centerline

Fig. 10. 13   Illustration of specific ionization rates for the various groups of ionization processes (atom-atom, electron impact, photoionization, etc.) as functions of distance behind the shock and for various shock velocities. Distance behind the shock is measured in numbers of upstream mean free paths, l_1 . The specific ionization rate is defined as the absolute value of the time rate-of-change of the normalized electron density, multiplied by the time it takes the shock to traverse one upstream mean free path, l_1/V_s . The initial air density is specified by the pressure, p_1 , at room temperature.   (By permission from "Rate of Ionization Behind Shock Waves in Air, II.   Theoretical Interpretation" by Lin and Teare in Phys. Fluids, Vol. 6, March 1963, p. 355)
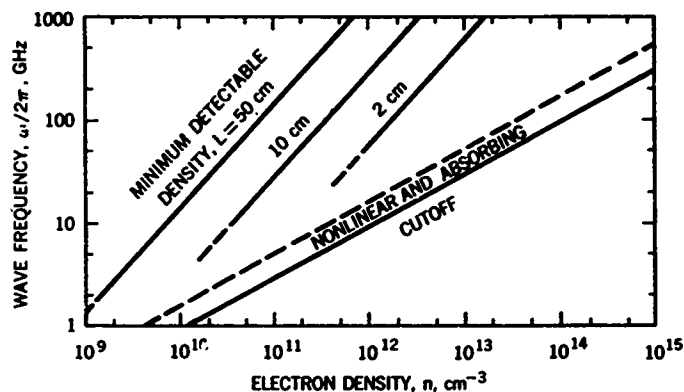
Fig. 10.14   Range of measurable electron density in a path length, L , using adiabatic phase shift analysis.
The term "nonlinear", as used here, means that the phase shift is not directly proportional to
average density. The minimum detectable densities assume a phase resolution of $\pi/10$, or $18°$.
(By permission from "Plasma Diagnostics with Microwaves" by Heald and Wharton, copyright 1965,
John Wiley & Sons, Inc.)

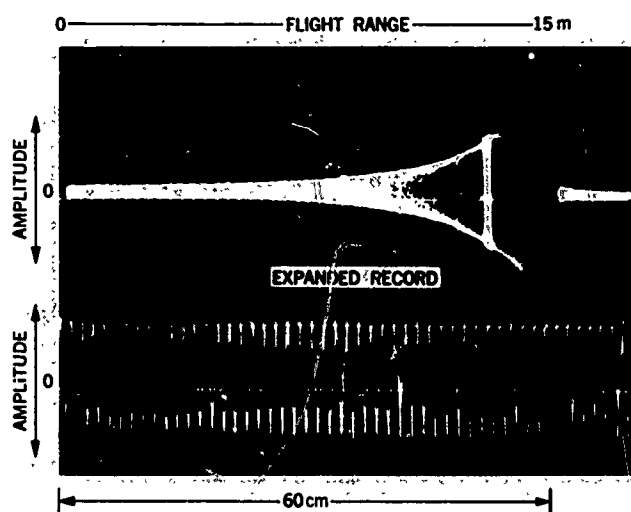Fig. 10.15   Oscilloscope display of CW-Doppler-radar record. The upper trace shows clearly the inverse-fourth-
power law, while the lower trace shows the Doppler frequency from which the model velocity can be
obtained.   (Courtesy of General Motors Corporation, Defense Research Laboratories)

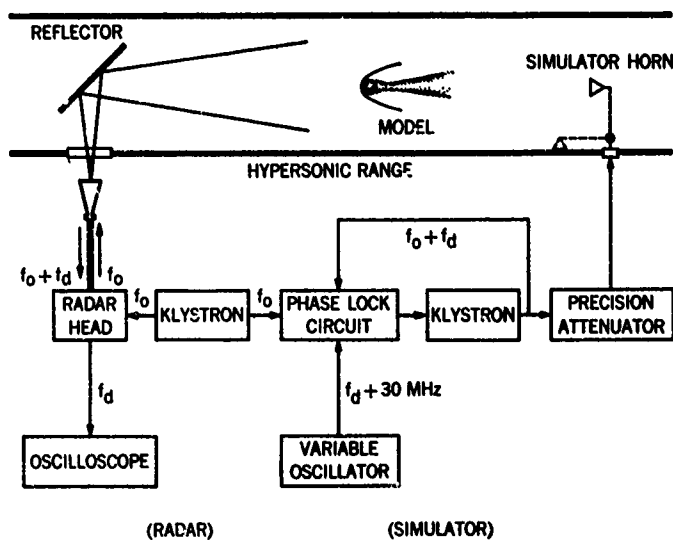Fig. 10.16   Schematic diagram of a CW-Doppler radar and simulator unit mounted in a hypersonic range
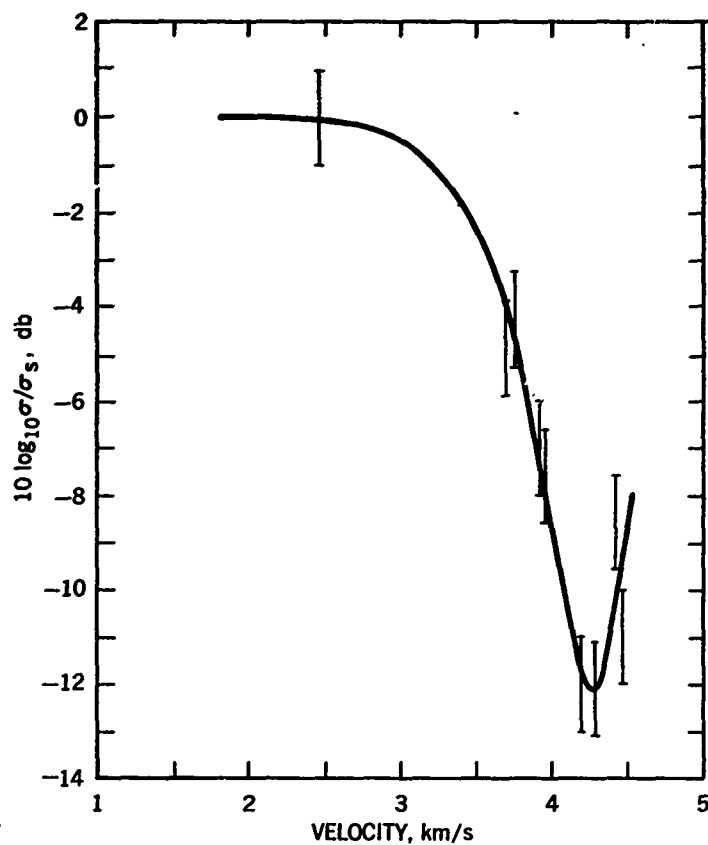
Fig. 10.17   Normalized dynamic radar cross-section as a function of model velocity for 2.5-cm metal spheres fired at a range pressure of 76 torr.   The radar frequency was 35 GHz
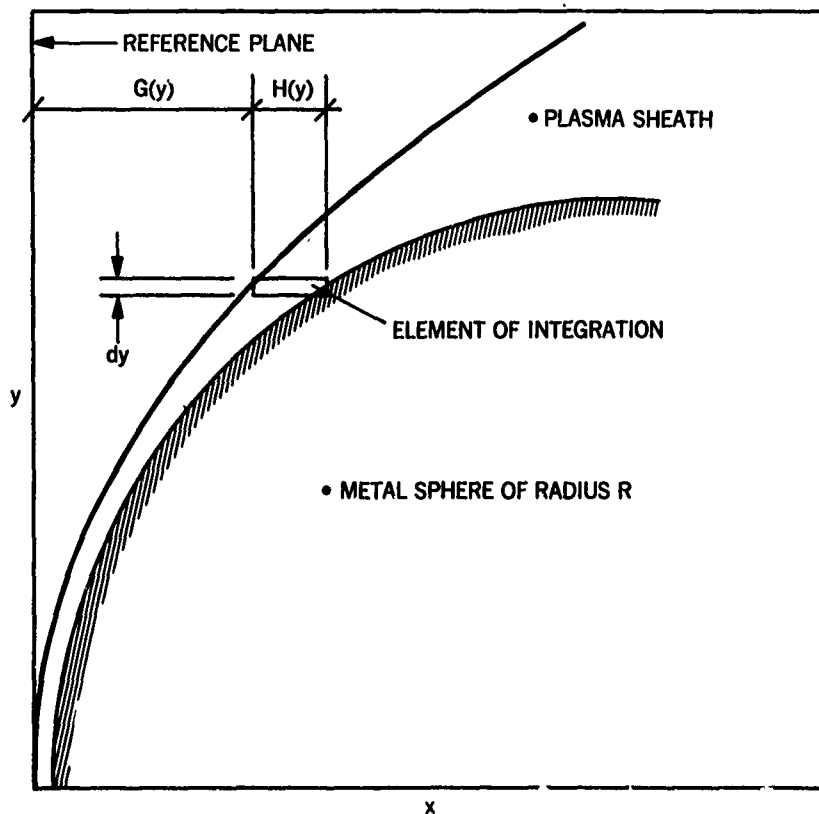
Fig. 10.18   Geometrical definition of the terms used in the radar cross-section integral given by Equation 10.28
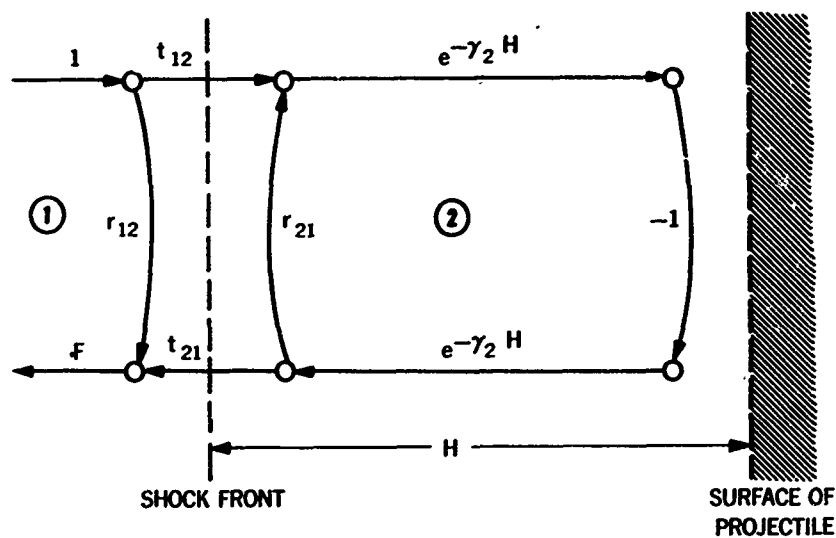
Fig. 10.19   Flowgraph of the multiple reflections occurring within the plasma sheath.
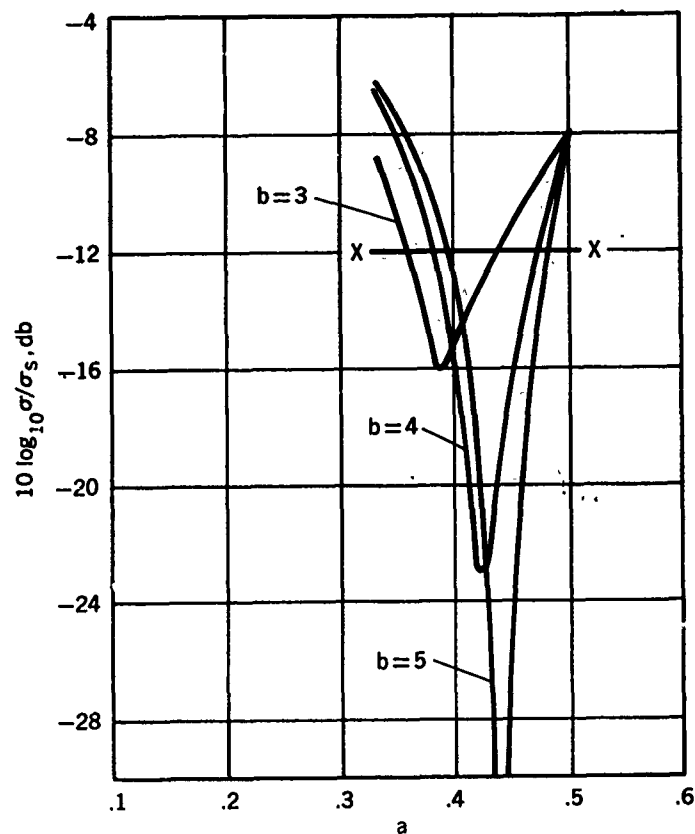
Fig. 10. 20   Influence of the radial electron-density profile of the plasma sheath upon the radar cross-section, σ . The electron-density function assumed is of the form $n = n_0 \exp (-y/aR)^b$, where y/R is the normalized radial distance
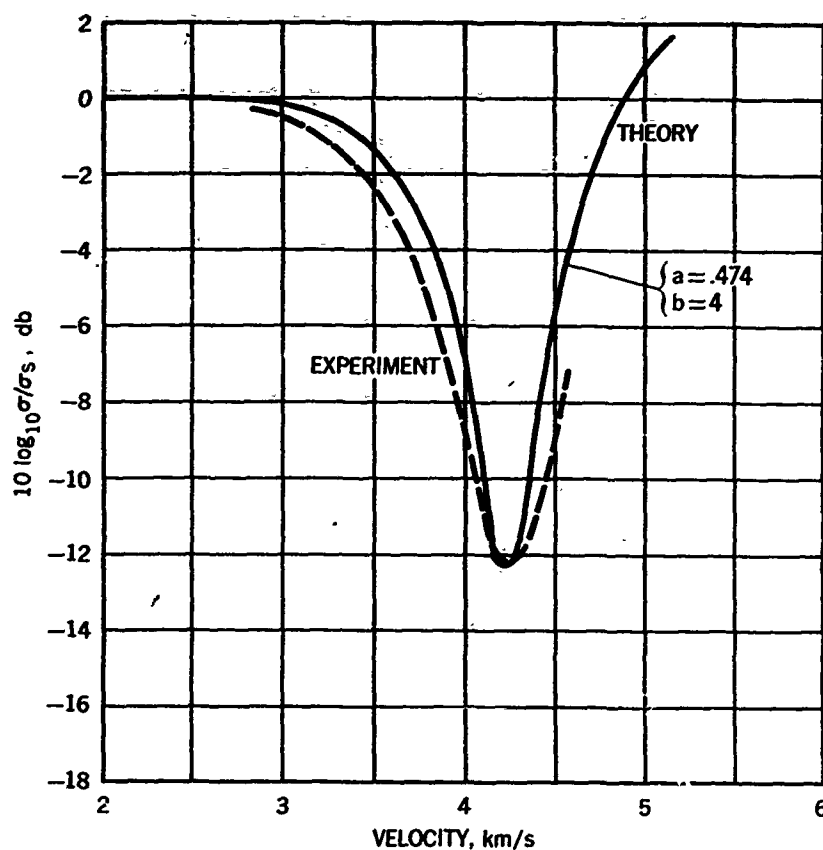
Fig. 10.21   This figure illustrates how well the observed variations in radar cross-section with projectile velocity can be explained on the basis of a simple two-parameter electron-density function
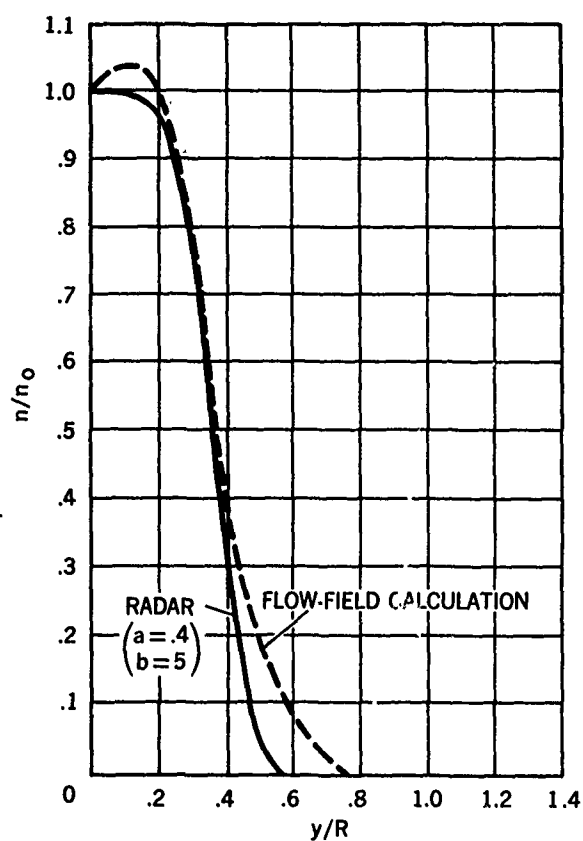
Fig. 10.22   Comparison between the radial electron-density function inferred from analysis of radar-cross-section data and that obtained from flow-field calculations
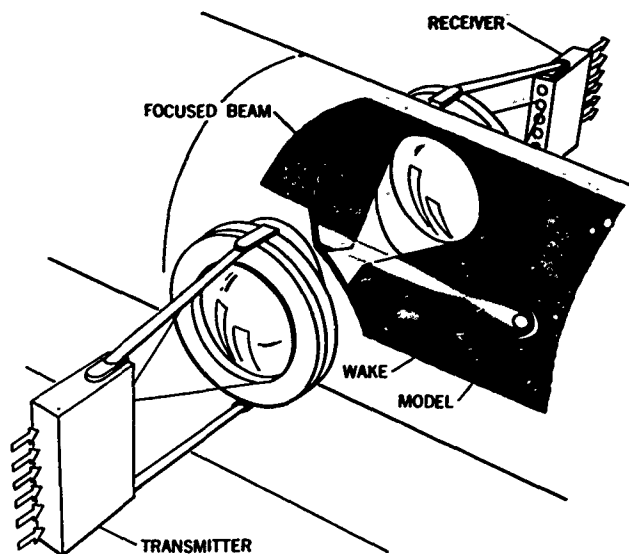
Fig. 10.23 Multi-beam focused-microwave interferometer for electron-density measurements in hypersonic wakes. (Courtesy of General Motors Corporation, Defense Research Laboratories)
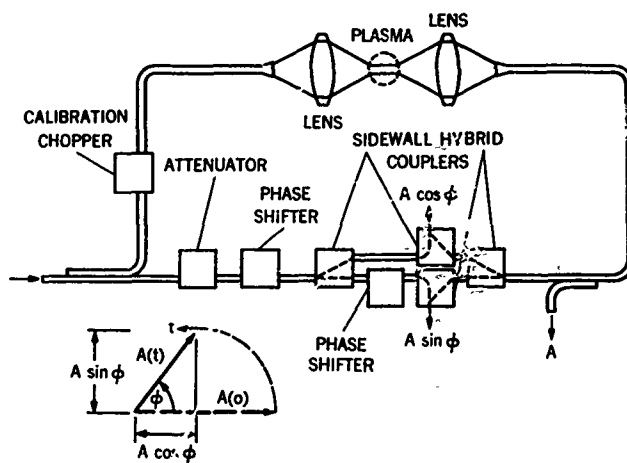
Fig. 10.24 Block diagram of microwave-interferometer circuit
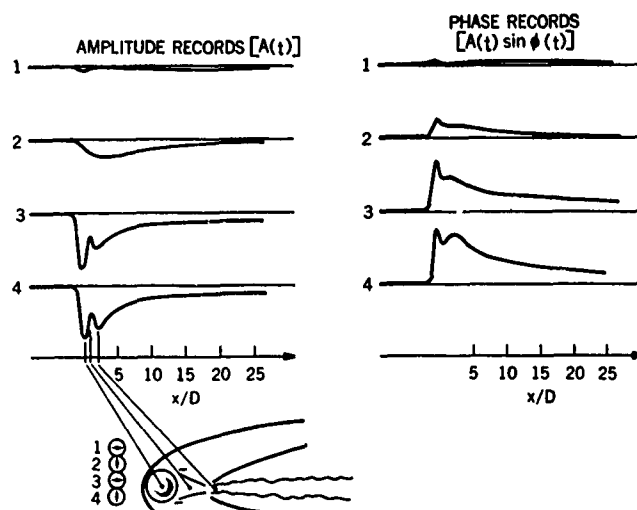
Fig. 10.25 Typical example of amplitude and phase records from a 4-channel microwave interferometer (x is distance behind projectile and D is diameter of the projectile)

ELECTRONS/cm^3

2 x 10^{12}
1 x 10^{12}
5 x 10^{11}
1 x 10^{11}
5 x 10^{10}

0   2   4   6   8   10   12   14

2.5 x 10^{12} x/D
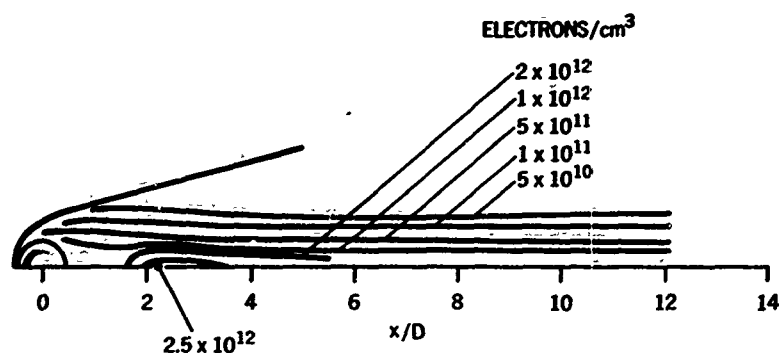
Fig. 10.26   Example of a map of constant-electron-density contours in the wake of a 2.5-cm-diameter polycarbonate
(Zelux) sphere fired at a velocity of 4.6 km/sec in air at a pressure of 100 mmHg

WAVEGUIDE
BEYOND CUTOFF
ENTRY AND EXIT TUBES

HYDROGEN GUN

IONIZED WAKE

PELLET
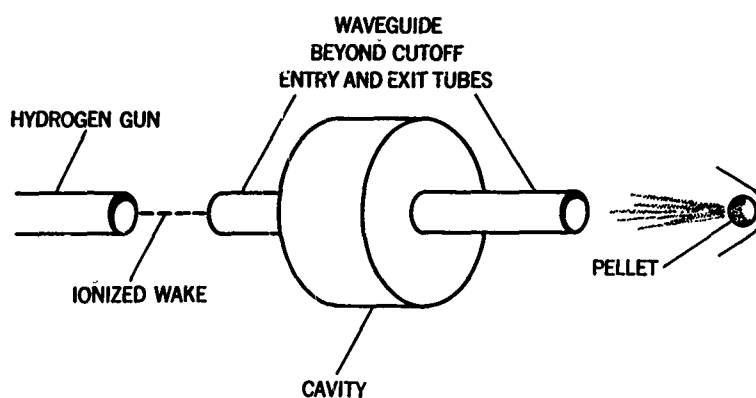
CAVITY

Fig. 10.27   Geometry of a UHF closed-resonant cavity experiment.   (Courtesy of Massachusetts Institute of
Technology, Lincoln Laboratory)

LINE
STRETCHER

VERNIER
PHASE
ADJUSTER

VERNIER
AMPLITUDE

PAD   PAD

CAVITY

M   TO "STANDARD"
RECEIVER

CIRCULATOR   EZ

M

OSCILLATOR
(441 MHz)   HYBRID

M   HYBRID
COUPLERS   M

EZ

SLOTTED
LINE   EZ

WAVEGUIDE BEYOND
CUTOFF ATTENUATOR

M   TO "DIFFERENCE"
RECEIVER

TO REFERENCE PHASE IN RECEIVERS

M   DENOTES MATCHED LOAD

EZ   DENOTES MATCHING TRANSFORMER
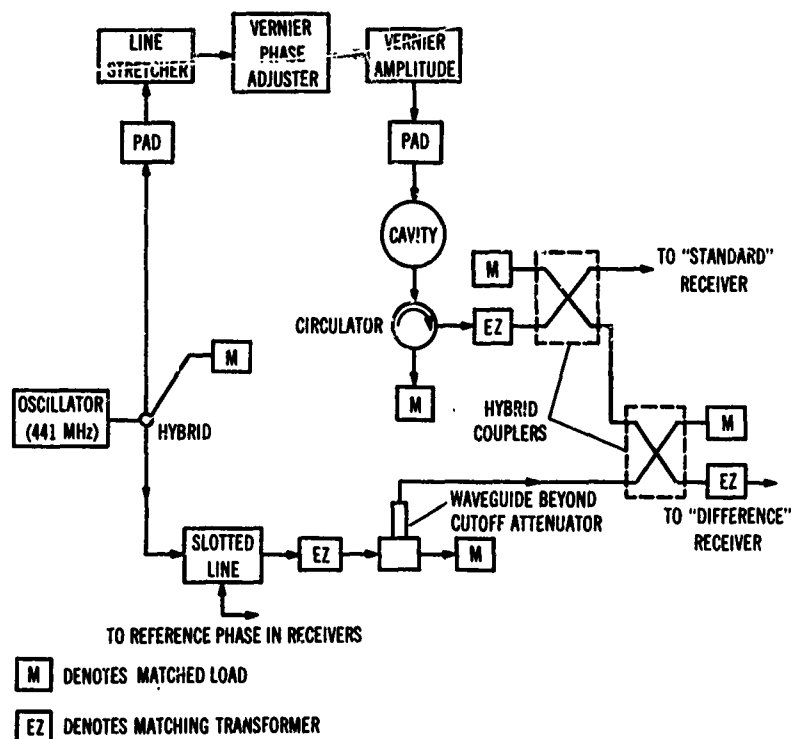
Fig. 10.28   Schematic block diagram of combination "standard" and "difference" circuit for resonant cavity.
(Courtesy of Massachusetts Institute of Technology, Lincoln Laboratory)

(a) RELATION OF CAVITY TO WAKE

(b) E-LINES IN CAVITY

SECTION A-A
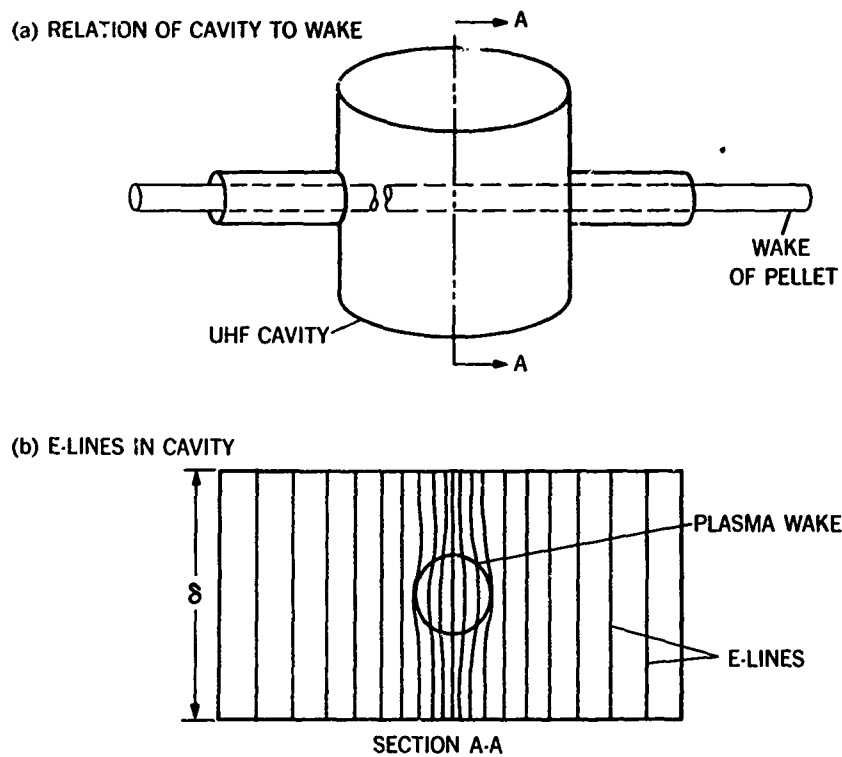
Fig. 10.29   Geometry for a cavity plasma-wake-diameter measurement.   (Courtesy of Massachusetts Institute of Technology, Lincoln Laboratory)
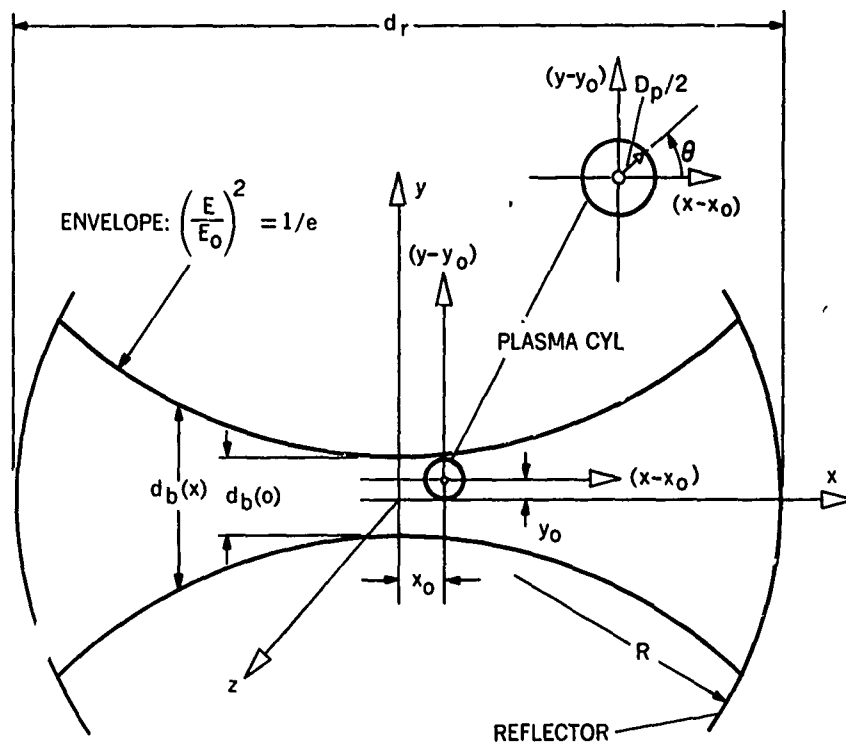
Fig. 10 30   Schematic of operation of open resonator.   (Courtesy of General Motors Corporation, Defense Research Laboratories)

Fig. 10.31   Block diagram of swept-frequency resonator system and sample of photographic record.   (Courtesy of General Motors Corporation, Defense Research Laboratories)

Fig. 10.32   Block diagram of phase-recording open-resonator system.   (Courtesy of General Motors Corporation, Defense Research Laboratories)

Fig. 10.33   Doppler-radar measurements of turbulent-wake velocity behind 15-mm spheres, at a range pressure of 100 torr and velocity of 5.65 km/sec, as a function of axial distance from the body, measured in body diameters.   The wake velocity, V_w, is normalized to the projectile velocity, V_∞.   (Courtesy of General Motors Corporation, Defense Research Laboratories)

464

Fig. 10.34   Illustration of the scattering geometry considered by Albini.   (Aftei Albini, "Scattering and Absorption of Plane Waves by Cylindrically Symmetrical Underdense Zones," in AIAA Jour. Vol. 2, March 1964, p. 524)
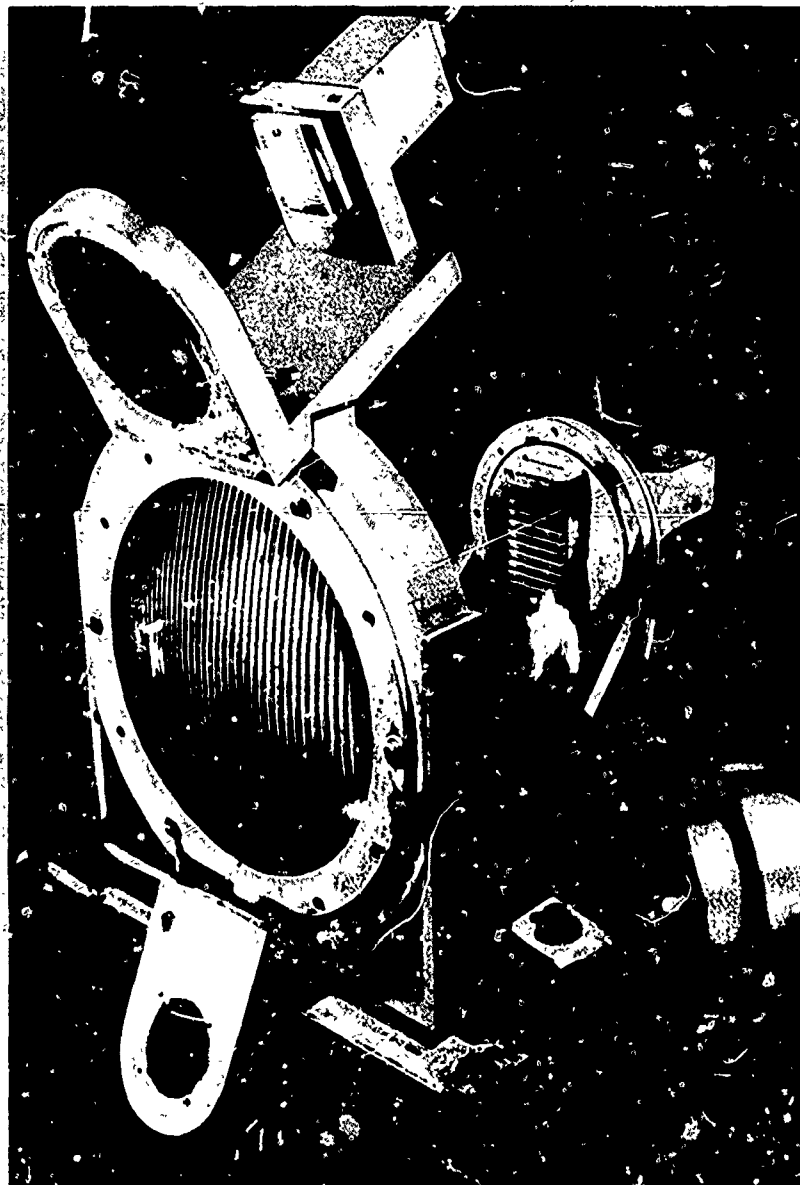
Fig 10 35   Photograph showing three of the four antennae used at GM/DRL in a four-frequency system for study of the turbulent wale.   Each antenna illuminates the same portion of wake.   The three frequencies considered here are 17 GHz 35 GHz and 70 GHz   (Courtesy of General Motors Corporation, Defense Research Laboratories)
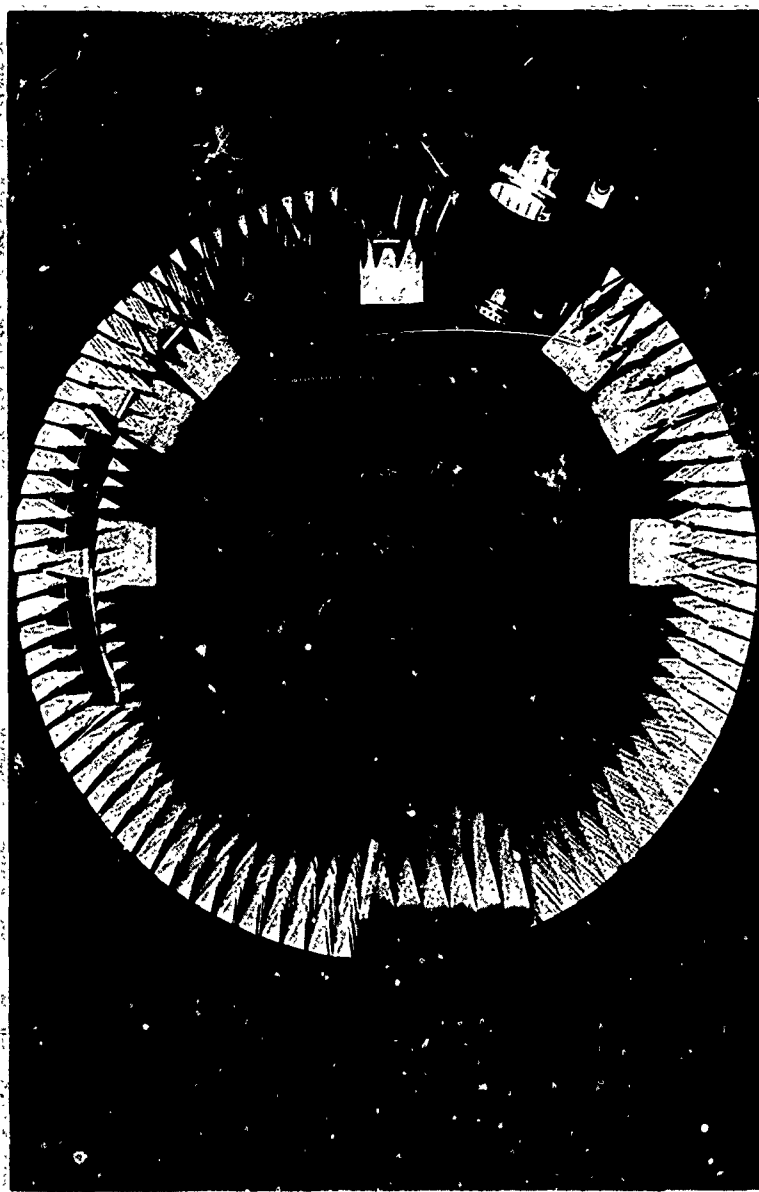
Fig. 10.36   Photograph of angular antenna system used at CARDE to study turbulent-wake scattering at 10 GHz

CHAPTER 11

POINT MEASUREMENTS IN THE WAKE

by

L. Tardif, C. LaHaye, D. Heckman, D. Ellington and J. G. G. Dionne

Canadian Armament Research and Development Establishment,
Quebec, Canada

POINT MEASUREMENTS IN THE WAKE

L.Tardif, C.LaHaye, D.Heckman, D.Ellington and J.G.G.Dionne

11.1 INTRODUCTION

The wakes of projectiles fired in ballistic ranges bear a very close resemblance to those produced by larger bodies flying at very high altitudes. If the flight velocity and Reynolds number are duplicated, the viscous wake of the model should closely simulate that of the larger vehicle, except for two, well-recognized effects: (1) The higher pressure needed to match the Reynolds number on a small model leads to differences in equilibrium composition of the wake, including the equilibrium degree of ionization. (2) For processes which are governed by other than binary scaling, the chemical kinetic effects will differ between model and vehicle.

In addition, far downstream from the model, wakes in the ballistic range may be disturbed by reflections of bow and wake shock waves from the range walls and equipment. The reflected waves have been observed to displace the wake and to affect significantly the temperature, mass density, and electron density measurements. This interference can best be studied at low pressures, where laminar wakes may be achieved. Absorbing materials on the walls can help to suppress reflections. The best results have been obtained with anechoic-type Fiberglas wedges. Acoustic Fiberglas and urethane foam blanket treatments become inefficient at low pressures. But in studies to date complete suppression has not been obtained.

Therefore, the detailed study of wakes in ballistic ranges must be viewed as an effort to understand the physical processes which govern the behavior, and to verify theory, but not as a valid simulation of all features of the wakes of large entry bodies at high altitudes. In Chapter 10, the use of microwave techniques to determine electron density in the wake was discussed. Since the best spatial resolution possible with conventional microwave frequencies is comparable to the wake diameter, this technique leaves a need for improved spatial resolution. Even if higher microwave frequencies were available (wavelengths in the millimeter range), the response to the ionized wake would be improper, because the plasma frequency would be too low.

In order to study the detailed structure of wakes, therefore, several measurements of wake properties by other means have been tried. These techniques, grouped under the title "Point Measurements in the Wake," are the subject of this chapter. The objectives of these measurements are to determine local variations in velocity, temperature, density, and electron population. Most of the methods described have been tried only recently and are therefore evolving rapidly.

The four techniques included are each based on a distinctive principle, some of which have been applied in other kinds of test facilities. They are: spark tracing of ionized paths to determine velocity, electrostatic (Langmuir) probe measurement of the wake plasma, heat transfer (hot wire or cooled film) anemometry, and electron beam excitation of the flow to determine density from optical radiation emitted. The special features of these techniques for ballistic range studies will be noted, and their capabilities and limitations given, consistent with the present state of their development.

11.2 VELOCITY-PROFILE DETERMINATION BY USE OF SEQUENTIAL SPARKS

11.2.1 Description of Experimental Technique

The technique of using sequences of sparks for the measurement of flow velocities has been treated by various authors[11.1,11.2]. This technique is a quantitative flow visualization experiment which operates on a very simple principle. When an electric spark is produced between a pair of electrodes, a low resistance ionized path is created between the electrodes and appreciable ionization persists for about 0.1 millisecond. Subsequent sparks produced during this time interval will follow the ionized path made by the first spark. When a series of sparks of short duration are made across the wake of the projectile at properly selected time intervals, the ionized path due to the first spark is displaced at the velocity of the gases in the wake and each succeeding spark reilluminates the ionized path. By open shutter photography of the spark traces, a profile of the displacement of the gas is obtained and the wake velocity profile can be calculated knowing the time interval between the sparks.

To produce the sparks, 90 kilovolt pulses of 0.8 microsecond duration have been used across the electrodes and a maximum current of 20 amperes is measured in the discharge[11.3,11.4]. These high-voltage pulses can drive the spark across gaps of 12 to 18 cm at pressures from 10 to 200 torr. The time interval between the sparks can be adjusted to any value from 3 to 150 microseconds. A typical train of pulses may consist of a series of four pulses at intervals of 3 microseconds to form the spark path, followed by a series of 4 pulses at properly selected time intervals. It has been found experimentally that large curvatures of the spark path may reduce the accuracy

of the measurement. These large curvatures can be avoided by restricting the time intervals between spark firings. Satisfactory results are obtained when the wake displacement between two firings of the spark is 10 to 20% of the viscous wake width.

With the recent development of a method to select the position of the spark in an array of electrode pairs, it is possible to measure multiple radial profiles in the wake of the same projectile. Figure 11.1 shows the stereo photographs of the three sequences of sparks made in the wake of a 2.5 cm aluminum sphere travelling at 4.4 km/sec at ambient pressure of 40 torr. These three sequences were made at axial distances of 450, 1000 and 2400 body diameters using spark intervals of 35, 75 and 150 microseconds respectively. The switching of the spark position is made in the following way: The three anodes (top electrodes in Figure 11.1) are connected in parallel and the +90 kilovolt trains of pulses are applied to the anodes. The cathodes are insulated from one another and a 10 microsecond, -30 kilovolt pulse is applied to the cathode at which the spark is to occur. The reliability of the spark switching depends on synchronization of the positive pulses fed to the anodes with the negative pulses on the cathodes. The switching also depends on the fact that between sequences, the old spark path is convected out of the electrode region by movement of the wake. Switching of the spark position has been achieved after intervals as short as 0.75 millisecond.

Preliminary measurements have indicated that the sparks do not necessarily pass through the center of the wake along a straight path and therefore, a three-dimensional record of the spark path is required. This has been produced by a precision stereo system consisting of two cameras whose optical axes lie in the horizontal plane and intersect at the center of the electrode gap. One camera looks downrange at 60 degrees from the flight axis, while the other looks in an uprange direction, also 60 degrees from the flight axis. Horizontal and vertical reference lines are provided to define the geometry. A film reader reproducing the range geometry is used to perform the three-dimensional analysis of the spark traces. The flight trajectory of the projectile with respect to the spark paths is determined to an accuracy of 2.5 mm from the X-ray shadowgraph system.

11.2.2 Data-Reduction Method

An example of the data reduction procedure is given using the sequence of sparks shown in Figure 11.2. In this case, a series of sparks was made at a distance of 600 body diameters behind a 2.5 cm diameter aluminum sphere travelling at 4.4 km/sec at an ambient pressure of 40 torr. The sequence of 7 sparks at 40 microsecond intervals is shown together with a Schlieren photograph taken immediately after the occurrence of the fourth spark. It is seen that, in this case, the diameter of the turbulent wake is greater than the electrode gap.

In order to obtain velocity profiles from these data, it is necessary first of all to locate accurately the flight path of the projectile with respect to the horizontal reference lines. The plates from the stereo spark cameras are then mounted in the stereo projector reading assembly which is aligned by using the vertical and horizontal reference lines. The co-ordinates of numerous points of each spark in the xz and yz planes are determined by standard photogrammetric techniques. Projections of the sparks are shown in Figure 11.3 where the x axis is the direction of flight, the z axis is the vertical direction and the y axis is horizontal. This figure shows the displacement of three of the sparks in the yz plane and it is seen that none of them passes through the axis of the wake which was displaced about 1 cm to the right of the electrodes. This was the case for all seven firings of the spark in this sequence. The velocities are computed by measuring the distance between points on consecutive spark traces and dividing by the measured time intervals between the sparks. It is assumed in the analysis that the velocity in the z direction is zero.

Graphs of the resulting velocity profiles obtained from every pair of consecutive sparks are shown in Figure 11.4. The notation V_{23} means the velocity profile computed from the second and third sparks. No measurements are shown closer than 0.3 body diameters from the axis, because the sparks did not pass through the center of the wake. Averages of the profiles shown are usually used for further analysis.

Data which have been gathered by this technique behind spheres travelling at supersonic and hypersonic velocities are reported in References 11.3 and 11.4. Comparisons with data obtained by an alternate technique, an electrostatic probe array, will be made in a later section.

11.3 ELECTROSTATIC-PROBE MEASUREMENTS

Electrostatic probes have also been used to investigate turbulent wake plasmas, but they present some difficulty in the interpretation of the probe current. The requirement of high enough air density to make the wake turbulent in the ballistic range prevents operation at sufficiently low pressures for the established collisionless probe theory to be applicable and an appropriate continuum theory is not yet established.

Typically, the ion collection theories available indicate that the probe current depends on electron and ion temperatures, pressure, probe voltage, etc., as well as on charge density. If the flow were in thermal equilibrium, then the ratio of the rms electron density fluctuation compared to the mean electron density would be so much larger than similar ratios for temperature and other variables that it could be assumed that the observed probe current fluctuations (under proper bias) are dominated by charge density fluctuations. Under these conditions it could be assumed that statistical analysis of the probe current signals would determine the statistics of the charge density fluctuations. However, it appears that the wake is very often not in equilibrium for conditions studied in ballistic ranges and the ratio of the rms probe current to the mean current is small enough to cast doubt at this stage of our knowledge on the assumption that charge density fluctuations dominate the process.

Nevertheless, it has been observed at Lincoln Laboratories[11.5] that the mean current to an electrostatic probe in a wake follows the mean electron density, and there is some supporting evidence from turbulent flame study at Stanford Research Institute[11.6] that a major contribution to fluctuations in probe current is due to fluctuations in charge density, at least in the case of thermal equilibrium.

Of course some results can be obtained with probes which do not depend on the interpretation of the probe current. For example in measurements of convection velocity, velocity fluctuations, and to a lesser extent, time scales of the turbulence, the electrons in the wake may be considered as a kind of passive contaminant or tracer.

The final objective of electrostatic probe work in turbulent wakes is to measure mean electron density and the characteristics of electron density fluctuations. The most valuable results to date, however, have been obtained by exploring other promising avenues, in particular, velocity. At CARDE, beginning with the use of single probes, it was realized that interpretation of a probe signal time history in terms of a spatial pattern would require the use of Taylor's hypothesis and a suitable mean wake velocity. Rather than rely on the results of another experiment, an attempt was made to measure wake velocity with a device consisting of two probes aligned parallel to the line of flight. When this technique gave promise of success, it was only a short series of steps to the adaptation of the classical two-probe technique, one fixed and one moving, used to investigate turbulence in steady jets[11.7]. The analogous technique is an electrostatic probe array technique of the type in use at CARDE to investigate wake turbulence in the ballistic range[11.8].

Figure 11.5 shows a typical axial electrostatic probe array consisting of five equidistantly spaced electrostatic probes mounted in a thin support with the probe tips aligned along the flight trajectory so as to present a minimum interference to the flow. Because of projectile trajectory dispersion, the radial distance of the wake axis from the tips of the probes is only approximately determined when the projectile is fired. After the passage of the projectile, the wake grows onto the array. As the wake is convected past, it is seen in sequence by the first probe in the array, then the second, third, fourth and fifth. To achieve synchronization of the signals needed in the data reduction, the signals of each of the four last probes are recorded individually on a Fastax film along with the signal of the first probe. Figure 11.6 shows a typical example of the four pairs of probe signals from five probes (P_1 designates the first probe, P_2, P_3, P_4 and P_5 the following probes). The signals on each film are digitized and a cross-correlation curve of each probe signal with the signal of the first is obtained.

Because of the decay of the mean wake velocity and the decay of the mean electron density in the wake, the sets of electrostatic probe signals are divided into short segments. The normal length of a correlated interval of signal is about 0.5 millisecond, which corresponds to a change of axial distance behind the projectile of about 30 body diameters. Figure 11.7 gives an example of a family of cross-correlation curves from a given set of probe signal segments. The envelope drawn over the four cross-correlation curves represents the autocorrelation in the moving frame[11.7] from which a time scale measuring the temporal change of the turbulence pattern can be inferred. The points of tangency between the cross-correlation curves and the envelope measure the time lag arising before the pattern which first passed the first probe P_1 arrives at successive probes. By plotting the distance between pairs of probes as a function of the time lags obtained corresponding to the various points of tangency, we arrive at a curve such as the one given in Figure 11.8. The slope of the straight line fitting the points is a measure of the convection velocity of the wake past the array of probes. Successive sets of signal segments provide successive estimates of the velocity history along the wake at a given radial distance thereby allowing a complete profile of normalized wake velocity versus axial distance to be plotted[11.9].

Recent work at CARDE[11.10] has indicated that the spacing between the pairs of probes in an axial array cannot be reduced beyond the point where succeeding probes see a flow disturbed by the preceding probe. Further investigation of this effect has been carried out by Ghosh and Richard at RCA Victor Research Laboratories[11.11].

11.4 COMPARISON OF VELOCITY DATA FROM SEQUENTIAL SPARK PHOTOGRAPHS AND PROBE ARRAYS

Wake velocity data from sequential spark photographs is in the form of velocity profiles as a function of radius at fixed axial distances in the wake (Fig.11.9). Convection velocities from the electrostatic probe array, on the other hand, are obtained in the form of velocity profiles as a function of axial distance behind the base at a fixed distance from the axis of the wake. In order to permit comparison of the experimental results from the two techniques, a large number of radial profiles at various axial distances, as measured by the spark technique, may be transformed into axial profiles. The normalized mean velocities are plotted and interpolated to obtain velocity data at selected radial distances, say, 0.1, 0.2, 0.3, 0.4, etc., body diameters, for various axial positions. The axial distributions of data points thus obtained can be compared directly with the axial distributions of data points obtained by the probe array at the same radial distance.

Such a comparison has been made with data collected at CARDE. Because of scatter in the sequential spark data due to turbulence, which masks differences resulting from various ambient conditions, relatively large variations in ambient conditions have been tolerated in the data used to obtain the axial distributions of velocity, in order to increase the statistical confidence. Radial profiles measured behind 2.5-cm-diameter spheres travelling at velocities between 3.6 and 4.6 km/sec were used because the normalized wake velocity shows a very weak dependence on projectile velocity in that range of velocities. Measurements made at pressures varying between 20 and 76 torr have been utilized despite the appreciable dependence of the wake velocity on pressure. Assuming a linear dependence of wake velocity on ambient pressure, however, the distribution of data points is reasonably balanced giving an average pressure of 40 torr. A total of 40 radial profiles were used in the formation of these distributions of points. A least mean squares fit of an equation of the form

$$V_w/V_\infty = a + b \log (x/d) ,$$

where a and b are functions of radial position, was made on the distribution of velocity data points at each preselected radial distance. This particular form of equation has no theoretical justification, but fits the data very well. Figure 11.10 shows a typical example of the semilogarithmic least mean squares fit (open circles and full line) of the sequential spark wake velocity data at a radial distance of 0.7 body diameter. The scatter of the data points is attributable in part to the large range of ambient conditions included in the data. Note that data are presented for axial distances from 130 to 1000 body diameters. The comparison with the electrostatic probe array results obtained behind a 6.9-cm titanium sphere travelling at 4.6 km/sec at an ambient pressure of 20 torr is shown by the filled data points and dashed line. The scatter of the probe array data points is typical of the velocity fluctuations that can be observed on a single measurement of an axial velocity profile. More measurements at the same conditions may change the scatter; however, the agreement between the results obtained by the sequential spark and the probe array techniques is remarkably good.

Comparison of the results of these two techniques with the results of an integrated wake velocity measuring technique - the sequential Schlieren photograph method of Herrmann et al.[11.12] - is indicative of the advantage of point measurements. The Schlieren technique averages the wake velocities through the wake and across the velocity profile[11.13], and consequently underestimates the wake velocity on the axis[11.10,11.13].

11.5 COOLED-FILM-ANEMOMETER MEASUREMENTS

An application of hot wire anemometry to the study of the turbulent characteristics of projectiles in free flight was made by Fox, et al.[11.14], employing a constant temperature anemometer to study the wake of 0.22 calibre rifle bullet travelling at supersonic speed in a ballistic range. These measurements were aimed primarily at determining the frequency content of the wake and from the measured power spectral density, the microscale and integral scale of the turbulence were determined as functions of axial distance downstream.

In the hypersonic wake the environmental temperature may exceed the operating temperature of conventional hot wires and it becomes attractive to consider the use of the cooled film anemometer developed by Fingerson[11.15]. An experimental application of this technique at CARDE has employed two anemometers at different temperatures to determine both temperature and velocity.

In the cooled-film constant temperature anemometer, the sensing element consists of a tiny pyrex-U-tube, 0.15 mm in diameter, through which a cooling fluid can be circulated (Fig.11.11). A platinum film, one micron thick and 1 mm long, is deposited on one limb of the U-tube and electrical contact is provided by a gold coating on the rest of the tube. With the coolant circulating through the sensor, the platinum film is maintained at constant resistance (and hence constant temperature) by means of a bridge circuit (of which the sensor forms a branch) and a feedback system.

In the absence of any heat transfer between the film and the environment, electrical power supplied to the film element is dissipated by the coolant circulating through the sensor. When this element is exposed to environmental conditions such that a power transfer Q_{ENV} occurs between the environment and the element, the power supplied to the element electrically, Q_{PS} , is adjusted so that the power dissipation to the coolant Q_{WATER} is unaltered. In this way fluctuations in bridge voltage are related to changes in the environmental conditions. The power balance described is indicated schematically in the lower part of Figure 11.11.

In the two-temperature method, two sensing elements, each controlled by its own heat flux system, are placed in close proximity to each other and to the predicted flight path of the projectile. The sensing elements are maintained at two different but constant temperatures and the two outputs are recorded simultaneously on the same Fastax film. The signals from the two probes can be analyzed to yield wake temperature and velocity as functions of distance behind the projectile.

The analysis is based on an empirical relation between Nusselt number, Nu, and Reynolds number, Re, of the probe cylinder, and the assumption of constant pressure in the wake. One relationship employed is that due to Collis and Williams[11.16] which was obtained for the cooling of heated cylinders at relatively low environment temperatures and under subsonic incompressible flow conditions in undissociated air. This relationship is

$$\text{Nu}_f (T_e/T_f)^m = a + b (\text{Re}_f)^n , \tag{11.1}$$

where subscript f refers to so-called film conditions or conditions in the boundary layer of the cylinder. (The effective boundary layer temperature T_f is usually taken as the mean of the sensor and environment temperatures.) The environment temperature is T_e , and a , b , m and n are empirical constants given below:

Re_f	a	b	m	n
0.02-44	0.24	0.56	0.17	0.45
44-140	0	0.48	0.17	0.51

The Nusselt number in Equation (11.1) is defined as $h_c d/k_f$, where h_c is the heat transfer coefficient corrected for slip flow effects, and is related to the uncorrected coefficient, h, by the relation

$$\frac{1}{h_c} = \frac{1}{h} - 2 \frac{(Kn)(d)}{k_s} . \tag{11.2}$$

Here, Kn is the Knudsen number evaluated at the sensor temperature, T_s, d is the cylinder diameter, and k_s and k_f are the fluid conductivities at temperatures T_s and T_f. Also, the heat transfer coefficient, h, is related to the power input, Q, from the environment to the sensor, by the definition

$$h = \frac{Q}{\pi d\, l\, (T_e - T_s)} . \tag{11.3}$$

where l is the cylinder length.

With these definitions and the usual definition of Reynolds number based on diameter, Equation (11.1) may be expanded to obtain the fluid velocity past the sensor in terms of the temperatures, sensor dimensions, and fluid properties.

$$V = \frac{\nu_f}{d}\left[\frac{1}{b}\left(\frac{Q}{[\pi l k_f(T_e - T_s) - 2\,(k_f/k_s)\,KnQ]\,(T_f/T_e)^m} - a\right)\right]^{1/n} . \tag{11.4}$$

For two sensors operating at the same point in the fluid, but at different constant temperatures denoted by subscripts 1 and 2, two equations of the form of equation (11.4) pertain. The velocity V may be eliminated between them and the resulting equation solved for the environment temperature T_e. An iterative technique for solution of the equations has been described by Ellington and Trottier[11.17] and the method programmed for solution using a digital computer. A pair of values (T_e, V) is computed from each input pair (Q_1, Q_2).

It became evident at an early stage that the method suffered from inaccuracies introduced in the calibration, measurement, recording, reading and analysis phases of the experiment. These inaccuracies were such as to produce an unacceptably large cumulative error in the final determination of wake temperature and velocity. For ease of performing an error analysis Equation (11.4) has been written in a simplified form

$$Q_1 = (T_e - T_{s_1})\left(\frac{V}{Z_1}\right)^{1/2} \tag{11.5}$$

$$Q_2 = (T_e - T_{s_2})\left(\frac{V}{Z_2}\right)^{1/2} \tag{11.6}$$

for the two sensors respectively corresponding to the Collis and Williams correlation for $44 < Re_f < 140$ ($n \simeq 1/2$ and $a = 0$). It has been assumed that the term containing the Knudsen number may be neglected. Then, $Z_{1,2}$ is defined

$$Z_{1,2} = \frac{\nu_{f_{1,2}}}{d_{1,2}b^2\pi^2 l_{1,2}^2 k_{f_{1,2}}^2 (T_{f_{1,2}}/T_e)^{0.34}} . \tag{11.7}$$

For a given ambient pressure, over the range of realizable values of T_{s_1}, and T_{s_2}, the values of Z do not vary by more than a few percent for typical values of T_e likely to be encountered in the hypersonic wake. Thus we take

$$Z_1 = Z_2 = Z ,$$

and from Equations (11.5) and (11.6) obtain

$$T_e = \frac{KT_{s_2} - T_{s_1}}{K - 1} \tag{11.8}$$

and

$$V = \frac{ZQ_2^2(K-1)^2}{(T_{s_2} - T_{s_1})^2} , \tag{11.9}$$

where we have defined the parameter K.

474

$$K = \frac{Q_1}{Q_2} = \frac{T_e - T_{s_1}}{T_e - T_{s_2}}.$$ (11.10)

The fractional error in K is related to fractional errors in Q_1 and Q_2. Assuming $|\Delta Q_1/Q_1| = |\Delta Q_2/Q_2| = |\Delta Q/Q|$, we note that the maximum error in K occurs when

$$\frac{\Delta Q}{Q} = -\frac{\Delta Q_1}{Q_1} = \frac{\Delta Q_2}{Q_2}.$$

The resulting errors in T_e and V are given by

$$\frac{\Delta T_e}{T_e} = \pm 2 \frac{\Delta Q}{Q} \left(\frac{KT_{s_2}}{KT_{s_2} - T_{s_1}} - \frac{K}{K-1} \right)$$ (11.11)

and

$$\frac{\Delta V}{V} = \pm 2 \frac{\Delta Q}{Q} \left(\frac{K+1}{K-1} \right).$$ (11.12)

Equations (11.11) and (11.12) have been evaluated as functions of K for various combinations of sensor temperatures. Figure 11.12 is appropriate to sensor temperatures $T_{s_1} = 400°$ K and $T_{s_2} = 700°$ K. It will be seen that the values $(\Delta T_e/T_e)/(\Delta Q/Q)$ increase sharply for values of K between about zero and 2.

With distilled water coolant and laminar coolant flow, the platinum film temperature cannot much exceed 450° K. This is because the high mass flow rate through the sensor required to accommodate the higher film temperatures without coolant boiling may cause transition to turbulence in the coolant flow, which produces the equivalent of electrical noise in the bridge circuit. Under hypersonic wake environmental conditions of T_e = 1000° K, and T_{s_1} = 400° K and T_{s_2} = 500° K, the maximum realizable value of K is about 1.2. Under these conditions, the error analysis shows that 10% error in the measured heat transfer signals can result in a maximum error in estimated wake temperature of 60% and a maximum error in estimated wake velocity of 220%. The corresponding figures for T_{s_1} = 600° K, T_{s_2} = 800° K, T_e = 1000° K are 8% and 60% on temperature and velocity respectively, corresponding to a 10% error in measured signal.

Consequently, some effort has been expended to increase the maximum operating sensor temperature and also to improve the accuracy of the measurement. With regard to the former, it has been found that with the use of a coolant of higher viscosity than that of water, the mass flow of coolant can be increased to accommodate a higher sensor temperature before the coolant flow becomes turbulent. Temperatures in excess of 800° K have been obtained in this way, with the use of fluids such as Fluorolube FS.

The use of Fluorolube in one of the sensors also permits the power dissipation to the coolant to be equalized for the two sensors. This is necessary, because as can be shown analytically, the frequency response of the system is proportional to the power dissipation to the coolant.

Trials have been made using sensor temperatures of 400° K (water coolant) and 700° K (Fluorolube). Under these circumstances the frequency response of the two sensors is reasonably matched. Figure 11.13 shows typical temperature results using the two temperature methods in the inviscid region of the wake and in the viscous core. Although the mean temperature values are probably reasonable, the fluctuations observed are still subject to question. It has been decided that further progress in this technique will require the additional precision capability of digital data recording. However, some residual error may be expected to remain because of the physical impossibility of putting the two sensors in precisely the same small fluid element.

11.6 ELECTRON-BEAM EXCITATION TO DEFINE DENSITIES IN WAKE

When a beam of electrons traverses low density air, a small number of electrons collide with nitrogen molecules leaving the nitrogen in an excited state. In dropping down to the ground state (almost instantaneously), the excited molecules emit radiation, and the intensity of the radiation is a measure of the gas density in any small volume from which the fluorescence is observed. At gas densities low enough to prevent non-radiative de-excitation processes, the light output is a linear function of gas density and electron beam current.

This technique has been successfully used in the study of densities in shock tubes and shock tunnels (Refs.11.18, 11.19,11.20). It is also applicable to the measurement of mass density in the wakes of hypersonic projectiles. The technique is capable of temporal and spatial resolution without mechanically interfering with the wake flow. Because the electrons are attenuated and scattered by oxygen and nitrogen molecules, ambient pressures at which the technique can be used are restricted to less than 10 torr. This pressure limitation permits measurements of average density in both laminar and turbulent regimes, but reduces the capability of the technique to measure fluctuations at densities corresponding to the turbulent regime.

A detailed analysis of the excitation emission processes was reported by Muntz[11.21], and Camac[11.22]. Davidson and O'Neill[11.23] have made a complete spectrographic study of the radiation. The bulk of radiation is emitted by the second positive system of the neutral nitrogen molecule $N_2(2+)$ and by the first negative system of the singly ionized nitrogen $N_2^+(1-)$. For pressures above one torr, which are of most interest, the intensity is found to be both stronger and more linear from the $N_2(2+)$ system than that from the $N_2^+(1-)$. Tests conducted in pure nitrogen at pressures up to 10 torr have shown that the intensity of the $N_2(2+)$ system is more linearly dependent than is the case in air.

A density measuring apparatus which has been used at CARDE is illustrated in Figure 11.14. A 100 Kev beam generator, capable of a beam current of one milliampere has multiple pumping stages allowing operation at test section pressures up to 10 torr. The light collecting and field defining system consists of a quartz lens and a slit defining a 1.2 mm by 12 mm field of view with its smaller dimension along the beam direction. The photodetector thus measures the fluorescence originating in a cylindrical volume geometrically defined by the field of view and the beam diameter and spectrally limited by an interference filter centered at $3375\overset{o}{A}$ with half-peak bandwidth of $55\overset{o}{A}$ and a transmission of 45%.

Calibration under static conditions at room temperature and various nitrogen pressures ranging from 0.5 to 10 torr has shown some departure from an exact linear dependence. The calibration data can be fitted by

$$S \simeq k \frac{a\rho}{a + \rho},$$
(11.13)

where S is the output signal from the photodetector

  k is a normalizing factor

  a is a parameter to fit the curve shape

  ρ is the gas density.

By a least mean squares fit of the calibration data points, the value of a can be determined. The determination of the normalizing factor k is more difficult as this value depends on various experimental and instrumental parameters such as the solid angle of the light collecting system, amplifier gain and detector sensitivity, as well as filter and lens transmission. However k can be determined by measuring the fluorescence intensity under ambient conditions just prior to the arrival of the projectile. Then

$$S_\infty = k \frac{a\rho_\infty}{a + \rho_\infty}.$$
(11.14)

Equation (11.13) is solved to define the density ratio normalized to ambient conditions,

$$\frac{\rho}{\rho_\infty} = \frac{aS}{\rho_\infty (ka - S)},$$
(11.15)

and k is determined from Equation (11.14).

The parameter, a , is related to the quenching efficiency of the gas and may have a temperature dependence. Shock tube results of Camac[11.22] however, have shown the temperature effect to be negligible at temperatures of interest in wakes at velocities of the order of 4 km/sec.

Typical measurements of average density as a function of downstream distance in the wake are shown in Figure 11.15. These densities were obtained along the axis of wakes of 6.9-cm-diameter titanium spheres fired at 4.6 km/sec in nitrogen and air atmospheres at 8.0 torr[11.24],[11.25]. Correction for the reduced attenuation of the beam in the presence of the wake would lower these densities slightly. Recent wake density computations performed by K.S. Wen et al.[11.26] allowing variable diffusivity along the turbulent wake have shown excellent agreement with these experimental results for axial distances from 10 to 1000 body diameters.

As noted in the Introduction, the techniques described above are all of very recent origin. It is expected that they are capable of further development and improvement. It also seems clear that other, similar measurement techniques could be identified and developed. The possibilities for such direct measurements in the near vicinity of free flight models is a new direction for ballistic range instrumentation, which will perhaps be further exploited in the future.

REFERENCES

11.1. Bomelburg, H.J.   *The Electric Spark Method for Quantitative Measurements in Flowing Gases.* AFOSR
       Herzog, J.   TN-59-273, ASTIA AD212707, University of Maryland 1959.
       Weske, J.R.

11.2. Frungel, F.B.A. *High Speed Pulse Technology,* Vol. II, Academic Press, New York 1956, pp 162-182.

11.3. LaHaye, C.   *Radial and Axial Velocity Profiles of Hypersonic and Supersonic Wakes Measured by*
       Léger, E.G.   *the Sequential Spark Method.* Conference Proceedings No. 19 of the AGARD Specialists
       Lemay, A.   Meeting on the Fluid Physics of Hypersonic Wakes, held at Colorado State University,
                        May 10-12, 1967.

11.4. LaHaye, C.   *Wake Velocity Measurements Using a Sequence of Sparks.* AIAA Journal Vol. 5, No. 12,
       Léger, E.G.   pp 2274-76, December 1967.
       Lemay, A.

11.5. Slattery, R.E.   Private Communication, 1967.

11.6. Guthart, H.   *Measurements of the Charged Particles of an Equilibrium Turbulent Plasma,* Physics of
       Weissman, D.E.   Fluids Vol. 9, No. 9, pp 1766-1772, September 1966.
       Morita, T.

11.7. Fisher, H.J.   *Correlation Measurements in a Non-Frozen Pattern of Turbulence,* J. Fluid Mech. 18,
       Davies, P.O.A.L. pp 97-116, January 1964.

11.8. Kirkpatrick, A. *Wake Plasma Turbulence Study Using an Electrostatic Probe Array,* AIAA Journal, Vol. 5,
       Heckman, D.   No. 8, pp 1494-95, August 1967.
       Cantin, A.

11.9. Heckman, D.   *Convection Velocity Measurements in Hypersonic Sphere Wakes,* AIAA Journal, Vol. 6
       Cantin, A.   No. 4, pp 750-52, April 1968.
       Emond, A.
       Kirkpatrick, A.

11.10. Heckman, D.   *Some Results of Electrostatic Probe Measurements in the Turbulent Wake of Hypersonic*
       Emond, A.   *Spheres,* AIAA Preprint 68-689, June 1968.
       Sevigny, L.

11.11. Ghosh, A.K.   *Probe Geometry Effect on Turbulent Plasma Diagnostics,* RCA Victor Research Report
       Richard, C.   No. 3.900.11, May 1968.

11.12. Herrmann, J.   *Some Statistical Properties of Turbulent Wakes,* Conference Proceedings No. 19 of
       Clay, W.G.   the AGARD Specialists Meeting on the Fluid Physics of Hypersonic Wakes, held at
       Slattery, R.E.   Colorado State University, May 10-12, 1967.
       Richardson, R.E.

11.13. Herrmann, J.   *Measured Properties of the Wakes of Hypersonic Cones,* AIAA Preprint 68-687, June
       Slattery, R.E.   1968.
       Clay, W.G.

11.14. Fox, J.   *Hot Wire Measurements of Wake Turbulence in a Ballistic Range,* AIAA Journal, Vol. 5,
       Webb, W.H.   No. 1, pp 99-102, January 1967.
       Jones, B.G.
       Hammit, A.G.

11.15. Fingerson, L.   *Instruction Manual, Heat Flux System Model 1000A,* Thermosystems, Inc., St. Paul, Minn.

11.16. Collis, D.C.   *Two Dimensional Convection from Heated Wires at Low Reynolds Numbers,* J. Fluid Mech.
       Williams, M.J.   6, 3, pp 357-384, October 1959.

11.17. Ellington, D.   *Studies of Turbulence in the Wakes of Hypersonic Spheres under Simulated Reentry*
       Trottier, G.   *Conditions,* Conference Proceedings No. 19 of the AGARD Specialists Meeting on the
                        Fluid Physics of Hypersonic Wakes, held at Colorado State University, May 10-12, 1967.

11.18. Muntz, E.P.   *Electron Excitation Applied to the Experimental Investigation of Rarefied Gas Flows,*
       Marsden, D.J.   Third International Rarefied Gas Dynamics Symposium (J.A. Laurmann, ed.), Vol.II,
                        pp 495-526, 1963, Academic Press Inc., New York, N.Y.

11.19. Muntz, E.P.   *A Study of Laminar Near Wakes,* AIAA Journal, Vol. 4, No. 6, pp 961-968, June 1966.
       Softley, E.S.

11.20. Rothe, D.E. *Electron Beam Studies of the Diffusive Separation of Helium-Argon Mixtures in Free Jets and Shock Waves.* UTIAS Report No. 114, July 1966, Institute for Aerospace Studies, University of Toronto, Toronto, Canada.

11.21. Muntz, E.P. *Measurements of Rotational Temperature, Vibrational Temperature and Molecule Concentration in Non-Radiating Flows of Low Density Nitrogen.* UTIAS Report No. 71, April 1961, University of Toronto, Toronto, Canada.

11.22. Camac, M. *Boundary Layer Measurements with an Electron Beam,* R.R. 273, AVCO Everett Res. Lab., Everett Mass, Ju¹ 1967.

11.23. Davidson, G.
O'Neill, R. *The Fluorescence of Air and Nitrogen Excited by 50 Kev Electrons,* Air Force Cambridge Research Lab. AFCRL-64-466, May 1964.

11.24. Dionne, J.G.G.
Sadowski, C.M.
Tardif, L.
Vanoverschelde, J.E.H. *Mass Density Measurements in Hypersonic Wakes,* Conference Proceedings No. 19 of the AGARD Specialists Meeting on the Fluid Physics of Hypersonic Wakes, held at Colorado State University, May 10-12, 1967.

11.25. Tardif, L.
Dionne, J.G.G. *Density Distribution in Turbulent and Laminar Wakes,* AIAA Journal, Vol. 6, No. 10, pp 2027-2029, Oct. 1968.

11.26. Wen, K.S.
Chen, T.
Lien, B. *A Theoretical Study of Hypersonic Sphere Wakes in Air and Comparison with Experiments,* AIAA Preprint 68-703, June 1968.
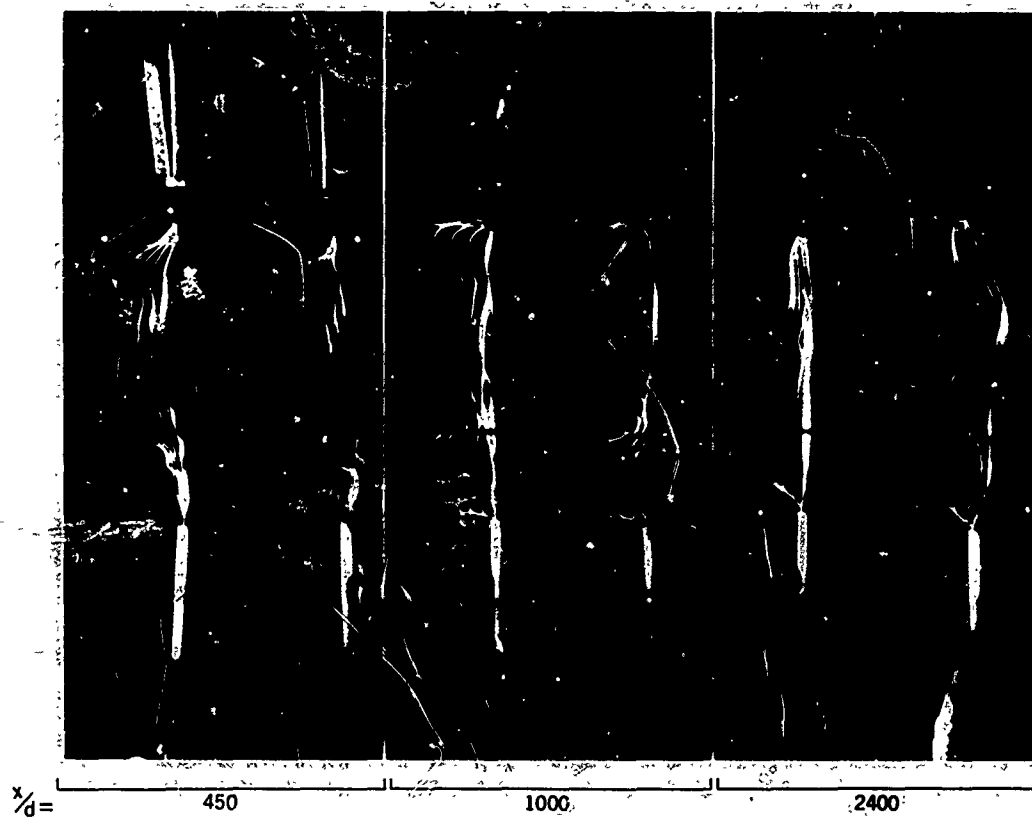
Fig. 11.1 Stereo-photographs of three sequences of sparks made at axial distances of x/d = 450, 1000 and 2400 behind a 2.5-cm-diameter aluminum sphere.
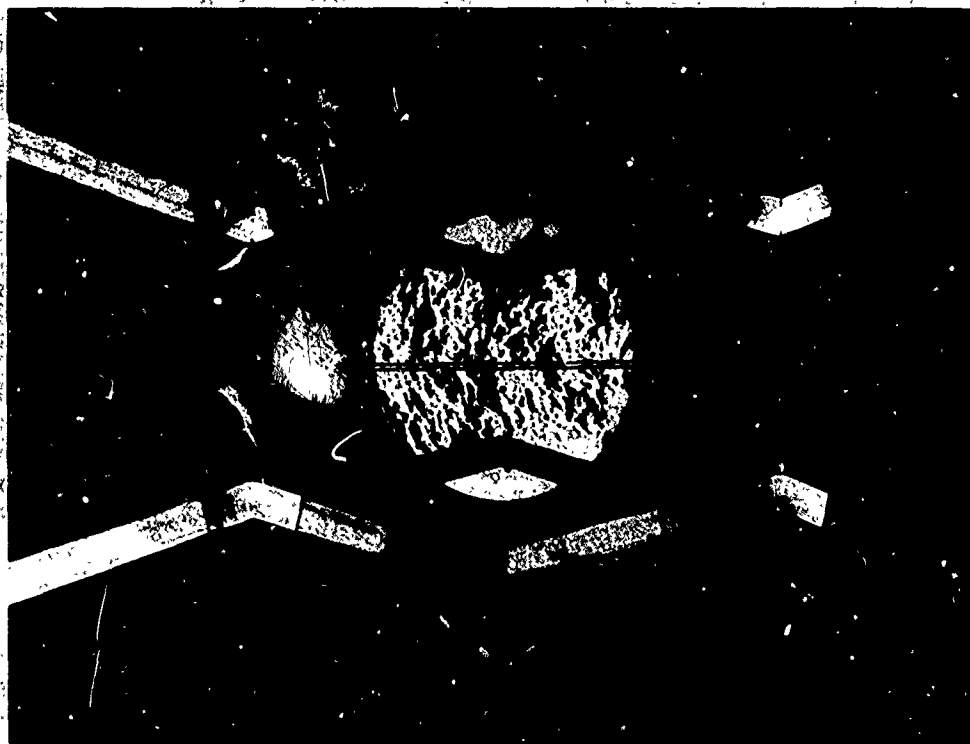

Fig. 11.2 Stereo-photographs of a sequence of sparks obtained behind a 2.5-cm-diameter aluminum sphere.
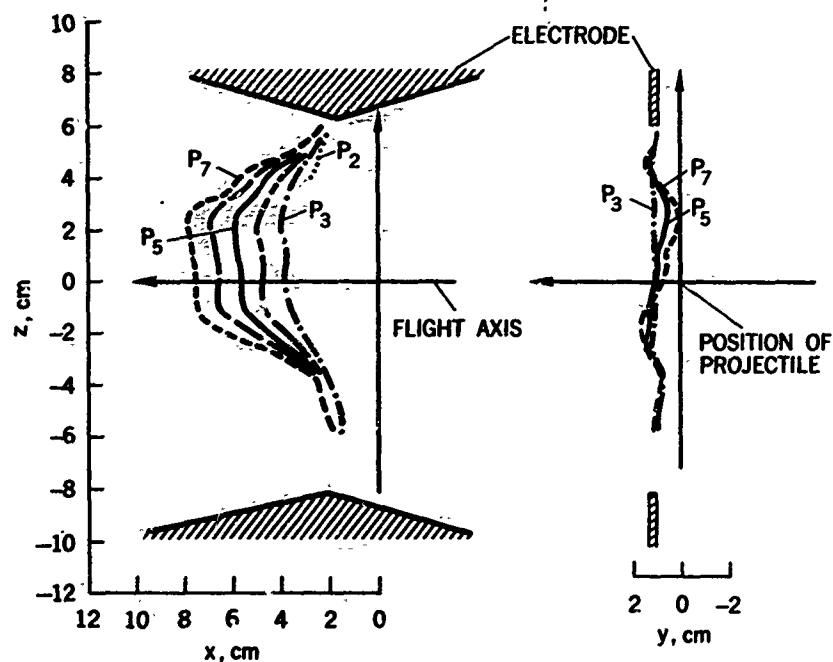
Fig.11.3 Projections in the xz (axial) and yz (lateral) plane of the series of sparks of Fig.11.2.
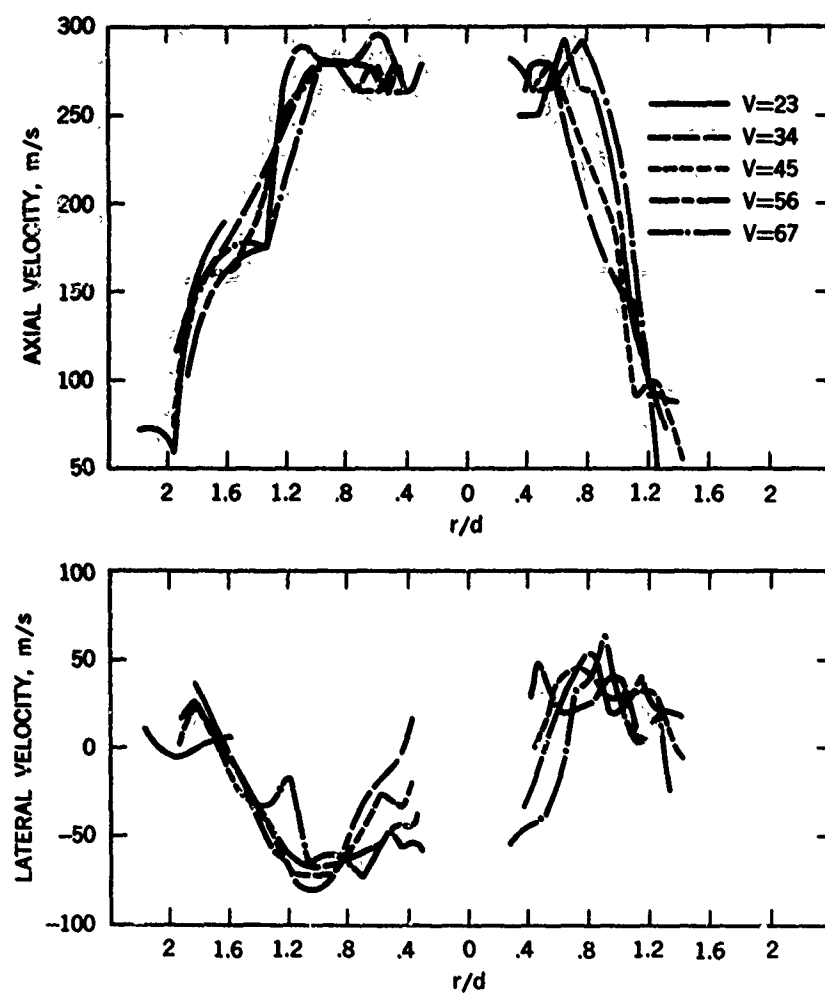

Fig.11.4 Radial profiles of the axial and lateral wake velocities obtained from the spark photographs of Fig.11.2.

480

Fig. 11.5   Axial array of electrostatic probes.

P1-P2

P1-P3

P1-P4

P1-P5

136   201   265
                x/d
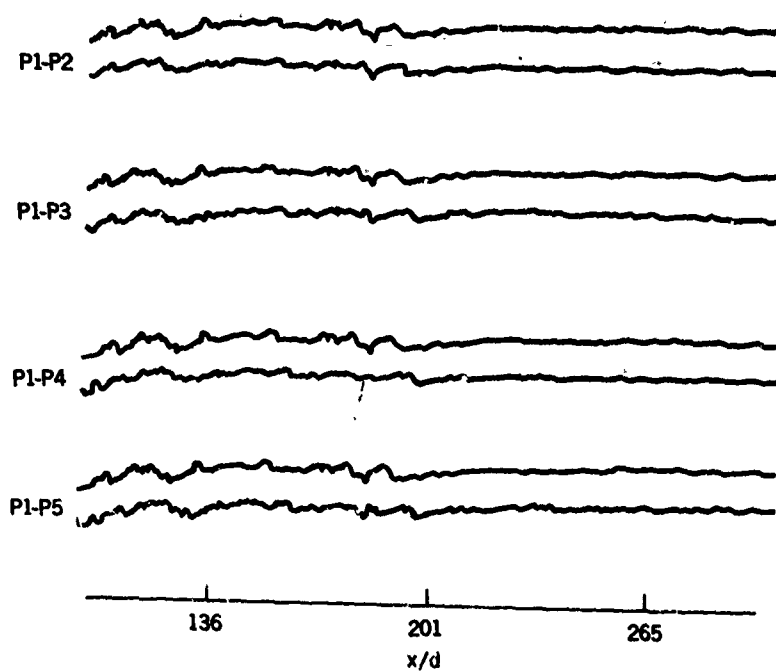
Fig. 11.6   Segments of a set of typical electrostatic-probe axial-array current signals obtained behind a 6.9-cm
Ti   sphere.

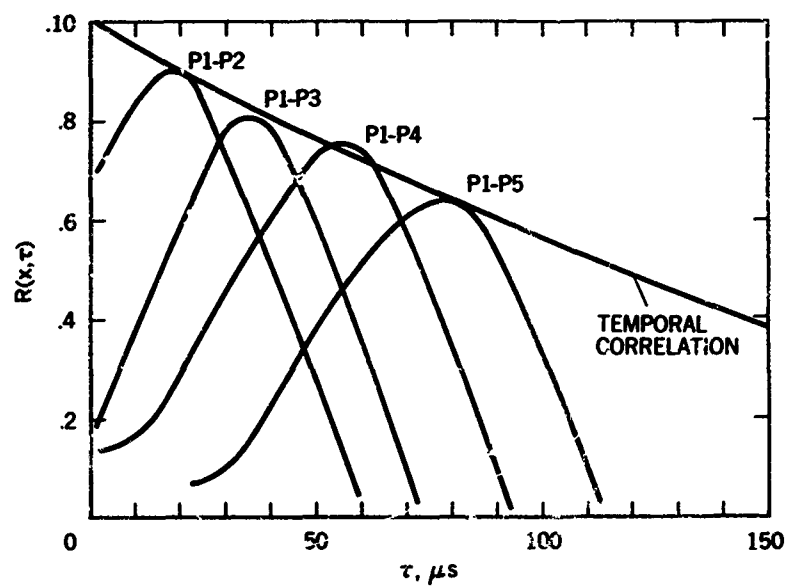V_∞ = 4.4 km/sec ; p_∞ = 9.3 torr :   r/d = 0.6 .

Fig.11.7   Family of cross-correlation R(x,τ)   curves obtained from corresponding 0.5-millisecond sections of the probe-current signals shown in Fig.11.6.
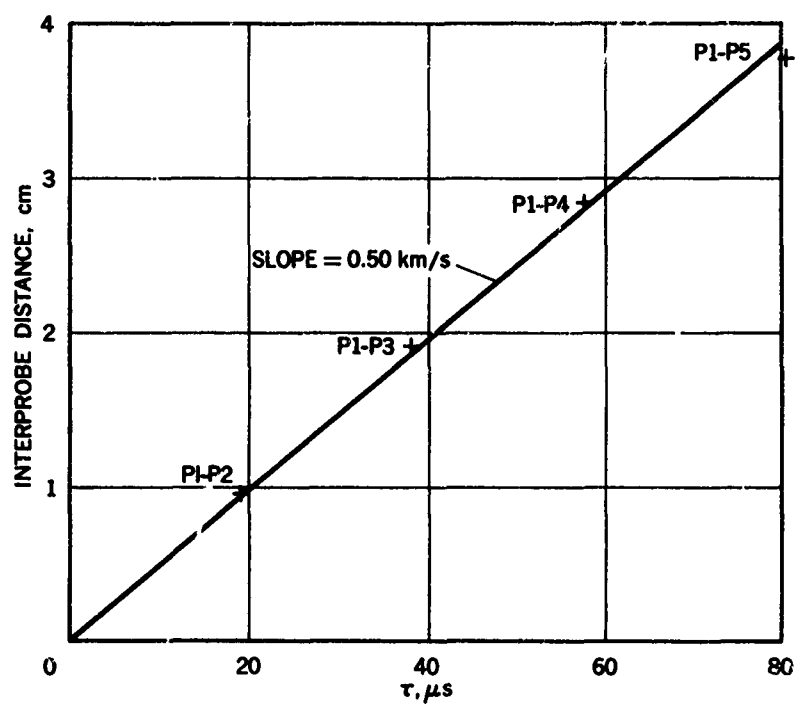
Fig.11.8   Convection-velocity determination from the data shown in Fig.11.7.
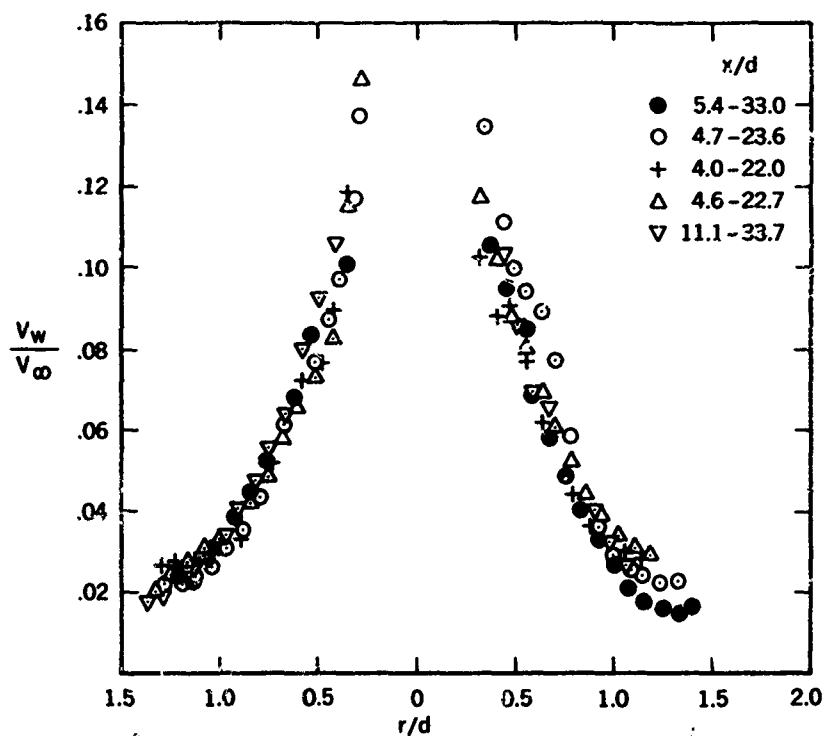
Fig.11.9(a)   Velocity profiles of the inviscid portion of the wake measured in the region of 4.0 to 37 body
diameters behind 2.5-cm-diameter aluminum spheres.

$$V_\infty = 1.2 \text{ km/sec} ; \qquad p_\infty = 100 \text{ torr} .$$
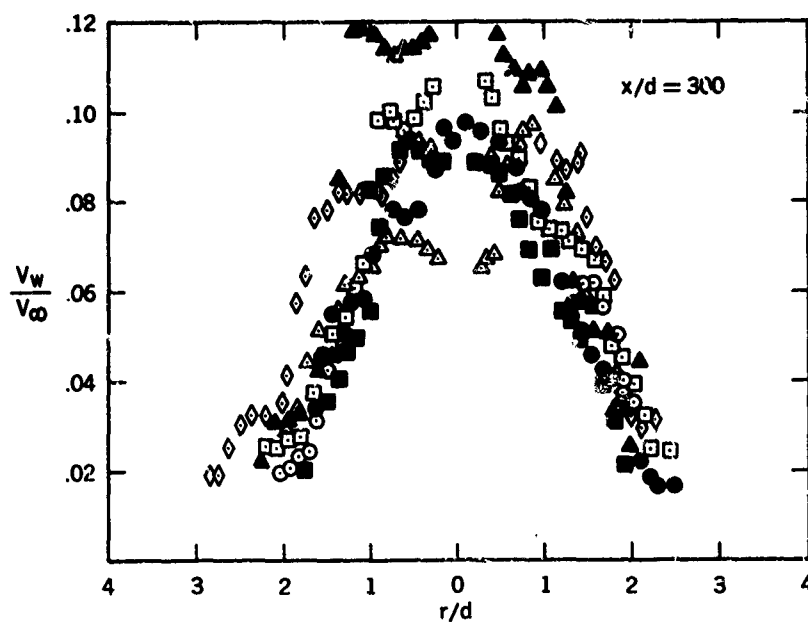
Fig.11.9(b)   Velocity profiles of the turbulent core of the wake measured at an axial distance of 300 body
diameters behind 2.5-cm-diameter spheres.

$$3.6 \leqslant V_\infty \leqslant 4.6 \text{ km/sec} ; \qquad p_\infty = 40 \text{ torr} .$$
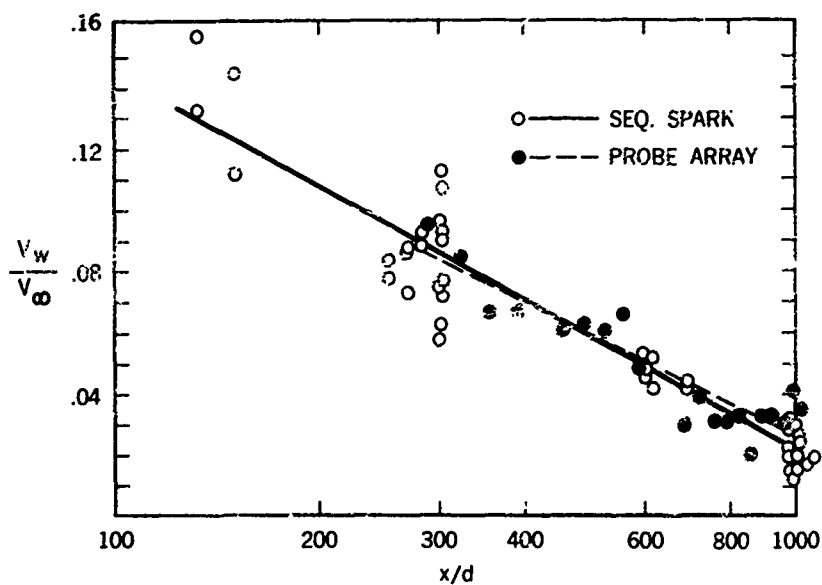
Fig.11.10 Semilogarithmic rms fits of sequential-spark and probe-array normalized wake-velocity data, comparéd
at r/d = 0.7.

$(p_\infty d \approx 100 \text{ torr-cm})$
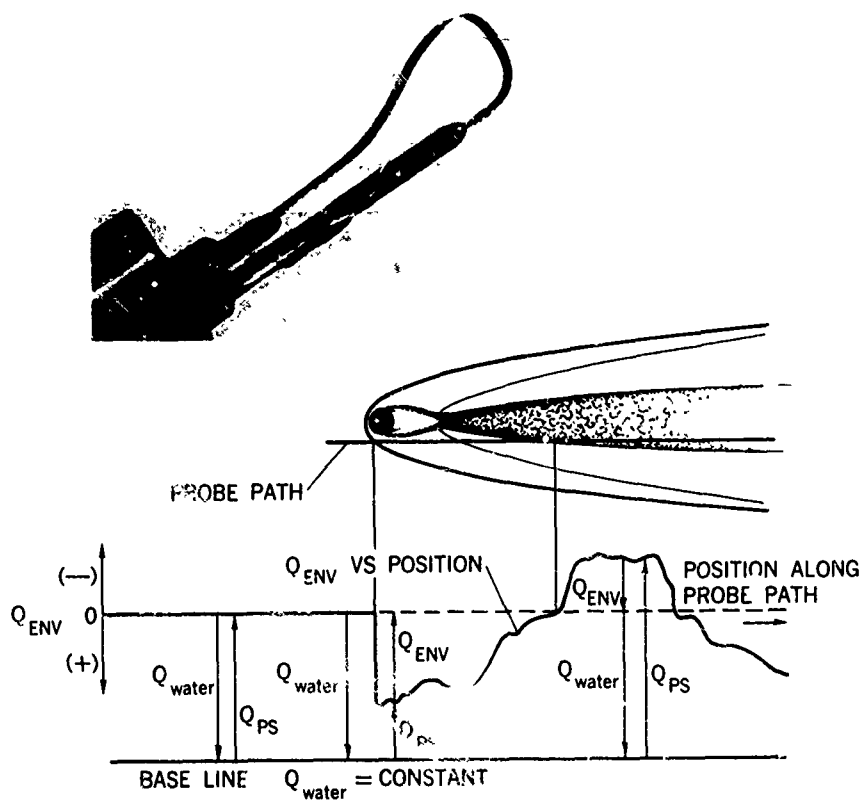
Fig.11.11 Cooled-film anemometer, typical heat-flux power balance. (The insert shows the sensor element.)
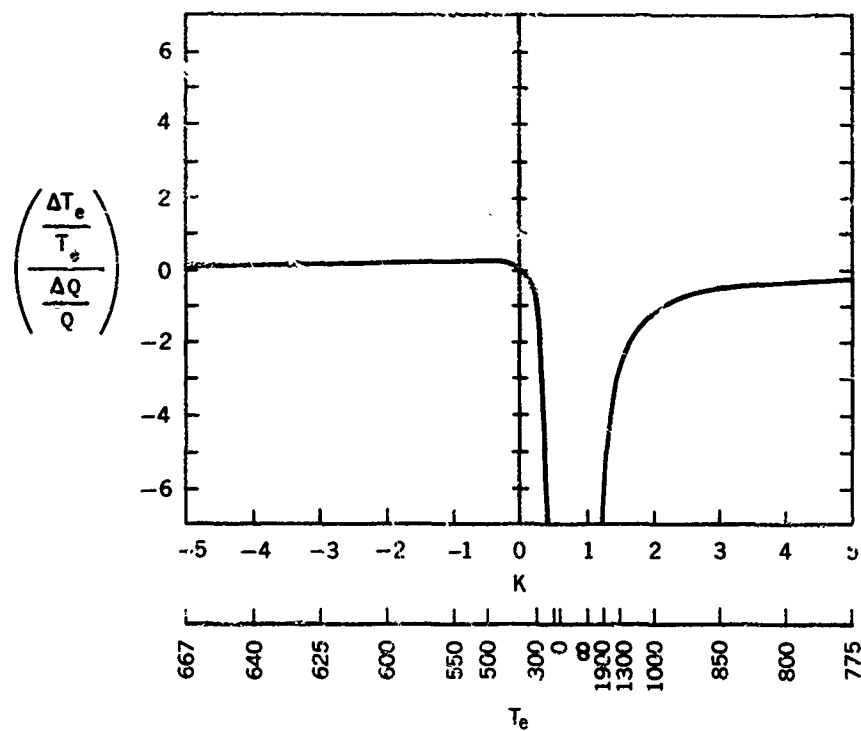
Fig.11.12   Fractional errors in the flow temperature due to errors in the heat-transfer data as a function of the heat-transfer ratio, K , for two sensors operating at temperatures of 400° K and 700° K .
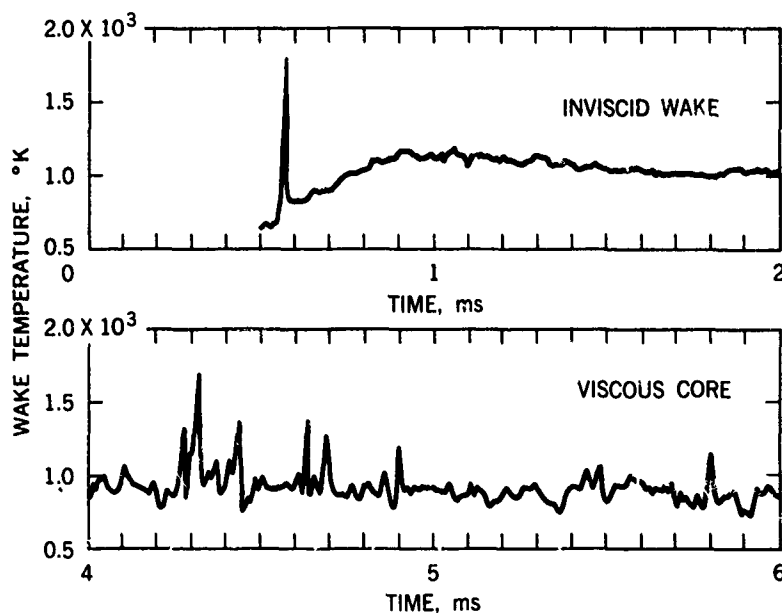
Fig.11.13   Temperature in the inviscid wake and viscous core.

$$V_\infty \ = \ 4.5 \ km/sec \ ; \qquad p_\infty \ = \ 75.9 \ torr \ ; \qquad r/d \ \simeq \ 2.2 \ .$$
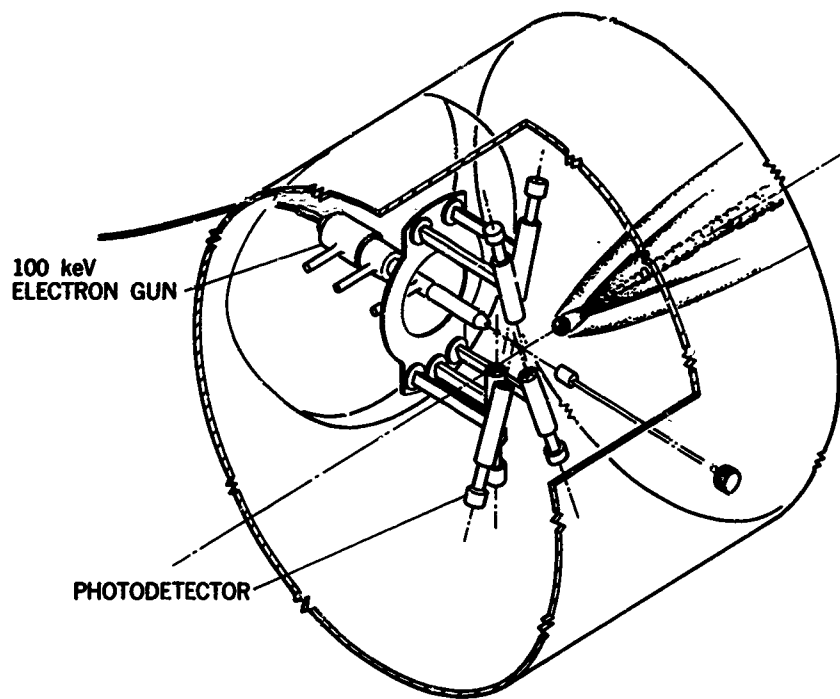
Fig. 11.14   Schematic of electron-beam equipment at CARDE.
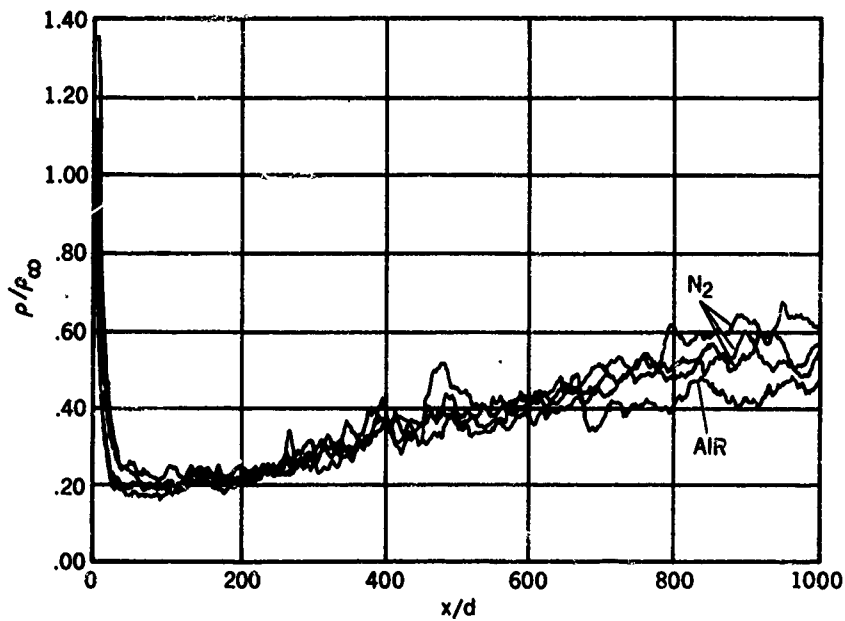
Fig. 11.15   Typical measurements of mass density normalized to free-stream density near the wake axis   (r/d < 0.5) as obtained with the electron-beam equipment.

CHAPTER 12

CONVECTIVE-HEATING MEASUREMENTS

by

Gary T. Chapman, Layton Yee,
Dale L. Compton, and Max E. Wilkins

NASA-Ames Research Center

CONVECTIVE-HEATING MEASUREMENTS

Gary T.Chapman, Layton Yee,
Dale L.Compton, and Max E.Wilkins

12.1 INTRODUCTION

Ballistic ranges and free-flight tunnels have only infrequently been used to measure convective heating because of the difficulty of determining the rate of temperature rise of the model surface in flight. Although considerable effort has been made to develop miniature active telemetry systems for this purpose, the lack of data obtained shows the difficulty of this approach. A brief description is given of what has been done and what the future holds in store for active telemetry. However, three methods of determining heat-transfer rates have been developed to the level of producing reportable data in the last 15 years for use in ballistic ranges; one is based on passive telemetry, while the other two are completely different in approach. Other convective heating data have been deduced from studies of recovered ablated models. These techniques will be summarized in this chapter.

The passive telemetry system[12.1] uses the electromagnetic coupling between two coils, an energized (signal) coil in the model which flies through a fixed coil (antenna) in the ballistic range. The coil in the model is energized by the output of a thermocouple, and in turn induces a current in the pickup coil in the range. The pickup coil output is proportional to the current from the thermocouple and hence to the surface-temperature rise. By firing the model through a series of coils placed along boresight a temperature-time history of the model is obtained and from this the heat transfer can be inferred.

The second method involves calorimetric measurement of the total aerodynamic heat in the recovered model, immediately after it has been decelerated from a high initial velocity by aerodynamic drag[12.2]. Since the heat content of the recovered model is accurately measured in a calorimeter, a series of tests at various launch velocities can be analyzed to yield heat-transfer rates. One of the limitations of this method is that, if the heating rate to the model becomes high enough (e.g., by increasing launch velocity) the model will begin to melt and lose material so that the calorimeter will fail to measure the total heat input. This particular limitation becomes the basis for the third method.

The third method is based on the detection of the time of onset of melting of the model[12.2]. The onset of melting on free-flight models can be fairly reliably detected, since the molten material runoff apparently forms a fine opaque mist which yields a shadow image in the range photographs. Surface melting on the model ordinarily occurs first where the heating rate is highest — at the stagnation point for most models. The time at which melting first occurs is a measure of the stagnation-point heating rate.

These three methods are basically independent of each other and each has inherent advantages and disadvantages. It should be noted that all three are applicable with most guns and ballistic facilities. Each places its own set of requirements on range size, pressure levels, and auxiliary equipment.

12.2 ACTIVE TELEMETRY

Considerable effort has been expended (notably, M.Letarte et al., of Canadian Armament Research and Development Establishment, and P.L.Clemens et al., of von Kármán Gas Dynamics Facility, ARO, Inc.) on active telemetry systems to measure heat-transfer rates. The telemeters used are typically transistorized FM-FM systems with a carrier frequency of about 60 MHz, and a subcarrier frequency of about 50 KHz. Thin-film gages have been the most frequently used temperature sensor for these systems.

The development of an active telemetry system for high-velocity launches has been hampered by the fragility of the electronic components built into the models. Transistors, for instance, are unusable in their off-the-shelf state and must be carefully potted. With careful selection of suitable components and tedious manufacture, active telemetry models have been tested successfully. The acceleration loads have been limited to about 200,000 g (quite modest by light-gas-gun standards), which resulted in launch velocities of less than 3 km/sec. The use of integrated circuits might overcome many difficulties of the past; unfortunately, however, there is evidence that above 4 km/sec the ionized sheath around the model will impair the data transmission in the case of blunt-nosed models.

Clemens has compiled a comprehensive bibliography on telemetry suitable for ballistic-range use[12.3]. His survey listed 30 references chronologically from June 1954 to July 1962, including the extensive work of Letarte.

12.3 PASSIVE TELEMETRY

The models used in passive-telemetry heat-transfer tests contain a copper-constantan thermocouple, the active element, connected in series with a low-resistance coil, as shown in Figures 3.31 and 12.1. The hot junction, located at the nose of the model in Figure 12.1, is formed by the copper-calorimeter nose cap and the constantan wire core, which also joins a copper disk buried in the model (the cold junction). The small copper coil, wound on an insulating form, joins the disk to the edge of the calorimeter.

The detector is a multi-turn, single-layer, center-tapped, coil wound on a cylindrical dielectric form and enclosed by an electrostatic shield to minimize spurious signals caused by the model's static charge, its ionized flow field, and wake. A photograph of a pickup coil with its shield and support is shown in Figure 12.2.

The experimental setup shown in Figure 12.3 illustrates one of several identical detector stations. The magnetic field caused by current flow in the small coil in the model induces an e.m.f. on the pickup coil. This signal, recorded on a differential-input oscilloscope, is proportional to the current flowing in the excited coil and to the rate of change of mutual inductance between the two coils. Since all these parameters are either known before the flight or are measured during the flight of the model, the temperature history of the calorimeter can be determined. A representative signal is shown in Figure 12.4. Only the central feature (i.e., the antisymmetric rise, fall, and return to zero) is of importance. The other signals are electromagnetic interference picked up from the firing of sparks in the shadowgraph stations.

12.3.1 Analysis

The voltage induced in the pickup coil by the moving model is given by Faraday's law

$$e = -10^{-6} \frac{d(MI)}{dt} , \qquad (12.1)$$

where

e = e.m.f. induced in the pickup coil, volt

M = mutual inductance between the coils, μH

I = current flowing in the model coil, A.

If the current is assumed to be constant during the short passage time in the coil, the voltage induced in the pickup coil is

$$e = -10^{-6} I \frac{dM}{dt} . \qquad (12.2)$$

The mutual inductance between the two coils may be expressed[12.4] as

$$M = 0.00986 \frac{a^2 N_a N_A}{b} \left(\frac{x + b}{\sqrt{[(x+b)^2 + A^2]}} - \frac{x - b}{\sqrt{[(x-b)^2 + A^2]}} \right) , \qquad (12.3)$$

where

a = radius of model coil, cm

A = radius of pickup coil, cm

$2b$ = length of pickup coil, cm

N_a = number of turns of model coil

N_A = number of turns of pickup coil

x = axial distance between the centers of the coils, cm.

With the appropriate coil dimensions substitued into Equation (12.3), M is defined. Equation (12.3) may then be differentiated with respect to x, and this derivative substituted into Equation (12.2) (after transforming Equation (12.2) from time to distance as an independent variable by $dM/dt = V dM/dx$) to give

$$e = -8.826 \times 10^{-6} IV \{[(x + 1.905)^2 + 25.806]^{-3/2} - [(x - 1.905)^2 + 25.806]^{-3/2}\} . \qquad (12.4)$$

In order to reduce the data from the peak voltage recorded on the oscilloscope, Equation (12.4) is differentiated to find the value of x for which e is maximum. The substitution of this value of x into Equation (12.4) yields

$$e_{max} = kIV , \qquad (12.5)$$

where, for the particular coil dimensions of Reference 12.1, $k = 3.78 \times 10^{-8}$ volt sec/ampere cm. The value of e_{max} can be determined from the oscilloscope record, V (cm/sec) can be calculated from the time distance

history recorded in shadowgraphs and on electronic timers. Thus, I , the current flowing through the model coil can be determined. The product of I and the known circuit resistance of the model gives the voltage output of the thermocouple. The temperature rise of the nose cap can then be obtained from a copper-constantan thermocouple calibration curve.

The preceding calculations are valid only when the model axis and pickup coil axis coincide. For off-center shots, the voltage induced in the coil is still given by Equation (12.2); however, the expression for M (Eqn(12.3)) must be modified to account for the radial distance between the axes of the two coils. This expression has been evaluated on a digital computer[12.1]. The result of this evaluation, as applied to the coils in that reference, is shown in Figure 12.5 as a correction-factor plot. This curve was verified experimentally by measuring the mutual induction (using a probe coil with a measured current to simulate the model coil in off-center positions), as shown by the experimental points.

The raw experimental data give a temperature-time history of the inner surface of the copper-cap calorimeter. To compute the heat-transfer rate at the stagnation point, the following assumptions are made:

(a) Temperature is uniform across the thickness of the copper cap.

(b) Conduction along the cap may be neglected.

(c) Conduction past the inner surface of the copper cap may be neglected.

The heat-transfer rate, $\dot{q}$, is obtained from the measured rate of rise of model surface temperature through the expression

$$\dot{q} = \frac{kl}{\alpha} \frac{dT}{dt} , \qquad (12.6)$$

where

α = thermal diffusivity of copper

k = thermal conductivity of copper

l = thickness of the nose cap

T = measured temperature.

Assumption (a) is intimately related to the finite response time of the copper calorimeter cap. It has been shown[12.1] that the error incurred in making this assumption is less than 2 percent. Assumption (b) is satisfied because the heat-transfer rate over the entire front surface of the copper cap does not vary by more than 5 percent. Assumption (c) is fulfilled because the boron nitride behind the copper cap is a good heat insulator; the constantan stem is not only small but a relatively poor heat conductor (conductivity about 1/20 of that of copper) as well.

12.3.2 Design Factors

The working equations which define the signals to be expected indicate the significant parameters for designing the models and antennas, and selecting test conditions. Because the expected signals are small (less than 10 mV), it is important to optimize the design of the model and the antenna to obtain a favorable signal-to-noise ratio.

From Equations (12.2) and (12.3), the signal is proportional to the current in the model coil, the number of turns, and the square of its radius. The maximum allowable coil radius is fixed by the model size; and the maximum ampere-turns is obtained when the coil resistance is one-half that of the thermocouple. The constantan wire which forms the hot junction largely determines the circuit resistance. However, this wire must necessarily be small to minimize heat conduction away from the calorimeter, even though a larger wire would increase the signal potential of the model and facilitate its fabrication.

The coil form in the model must be a good insulator, and it must not deform when heat is applied to the nose cap to silver-solder the hot junction and the coil. Boron nitride, while not a strong structural material, fulfilled the requirements adequately when supported by an aluminum alloy afterbody.

The circuit resistance was accurately measured with a Wheatstone bridge before final assembly. Epoxy cement was used to join all nonelectrical surfaces and fill all voids.

To achieve efficient coupling with the model coil, the pickup coil should have a large number of turns and a small radius, as indicated by Equation (12.3). In practice, however, the number of turns is limited by the corresponding increase in the amount of noise picked up by a more sensitive coil. Moreover, it is desirable for the coil to have a high resonant frequency to insure flat response, which also limits the number of turns of the coil. The coil should be critically damped with a resistor whose value can be determined experimentally.

The size of the pickup coil is determined by the dispersion of the gun-launched models; that is, a coil too small would not only be more susceptible to damage from erratic launches, but the correction for off-center flights would be more critical. With the radius of the pickup coil four times the usual dispersion at the last coil station of successful launches, the off-center correction was found to be usually less than 10 percent.

12.3.3 Comparison With Other Techniques

The accuracy of the heat-transfer measurements using this technique is believed to be comparable to that made using calorimeter heat-transfer gages in shock tubes. (Some experimental data are shown in Figure 12.15.) Since the radiated field is essentially d.c., it is unaffected by the ionized sheath around the model, so that the technique is usable at hypersonic speeds. The hot thermocouple junction can be located in areas other than the stagnation region, e.g., on the afterbody, where this technique would have a distinct advantage over conventional wind-tunnel tests because of the absence of sting effects. On the debit side, the models are fragile, difficult to manufacture, and difficult to launch at high speeds. The vulnerability of the pickup coils to damage from model impacts is also an expensive nuisance.

12.4 CATCHER-CALORIMETER TECHNIQUE

The heat content of ballistic-range models can be determined by capturing them in a calorimeter after flight[12.2,12.6]. The test arrangement for this catcher-calorimeter technique is shown schematically in Figure 12.6. The model, held in a completely enclosing sabot, on being launched from the gun emerges from the sabot and enters the range, where it is photographed in spark-shadowgraph stations while decelerating. The model scale, model material, air density, and range length are selected so that the model slows below a speed of about a hundred meters per second before entering a catcher. The model decelerates to zero-forward velocity by piercing many sheets of paper and then falls through a funnel into the calorimeter, where its total heat content is measured.

As the model decelerates during its flight, a major portion of its kinetic energy is converted to heat in the surrounding air by virtue of the strong bow shock wave; some of the energy is delivered to the model surface by boundary-layer convection. The rates of energy loss and model heating are highly variable along the trajectory, and the analysis must allow for this.

12.4.1 Heat-Input Analysis

The instantaneous average heating rate over the model surface, $\dot{q}_{av}$, is defined as

$$\dot{q}_{av} = \frac{1}{A_w} \int_{A_w} \dot{q}_l \, dA_w \, . \tag{12.7}$$

where $\dot{q}_l$ is the local heat-transfer rate, and A_w is the wetted area of the body. The functional relationship between $\dot{q}_{av}$, free-stream density, model scale, and velocity, for laminar flow, is taken as[12.5]

$$\dot{q}_{av} = K \left(\frac{\rho_\infty}{r}\right)^{\frac{1}{2}} V^n \, , \tag{12.8}$$

where ρ_∞ is the free-stream density, r is a reference length (e.g., radius of curvature at the stagnation point), V is the flight speed, and K and n are constants to be determined.

The total aerodynamic heat transfer to a model during a given trajectory can be expressed as

$$Q_{aero} = A_w \int_0^t \dot{q}_{av} \, dt' \, , \tag{12.9}$$

where t is the time of flight.

The equation relating velocity and time is

$$\frac{dV}{dt} = -\rho_\infty C_D A \frac{V^2}{2m} \, ,$$

where

    m = model mass

    A = reference area

    C_D = drag coefficient.

This equation may be used to write Equation (12.9) in terms of V as the independent variable.

Then, from Equations (12.8) and (12.9), we obtain

$$Q_{aero} = \frac{-K2mA_w}{A(\delta_\infty r)^{\frac{1}{2}}} \int_{V_L}^{V_{catch}} \frac{V^{n-2}}{C_D} \, dV \, . \tag{12.10}$$

Since the velocity history and drag coefficient are known, evaluation of Q_{aero} depends only on a selection of n and K. The procedure for selecting n and K, to obtain a best fit to the experimental data, is normally

a least-squares procedure using differential corrections. For the case of constant drag coefficient Equation (12.10) has the simple form

$$Q_{aero} = \frac{K2mA_W}{AC_D(n-1)(\delta_\infty r)^{\frac{1}{2}}} \left(V_L^{n-1} - V_{catch}^{n-1}\right) .$$ (12.11)

12.4.2 Design Factors and Equipment

The design of tests which employ this technique requires that the model scale and material, range length, and ambient density be selected to slow the model to a suitable recovery speed by the time it reaches the catcher. This can readily be done by use of the equation which gives the velocity variation with distance flown for constant drag coefficient, which is

$$\frac{V}{V_L} = \exp\left[-\frac{\rho_\infty A}{2m}C_D x\right] .$$ (12.12)

This equation is plotted to show the velocity variation with the dimensionless distance $(\rho_\infty AC_D/2m)x$ in Figure 12.7. Similarly, in Equation (12.8), $\dot{q}_{av}$, and in Equation (12.9), Q_{aero}, are functions of velocity only, other test conditions being given. Hence they may be universally plotted against the dimensionless distance. Thus $\dot{q}_{av}$ has been given in Figure 12.7 in ratio to its value at launch and Q_{aero} in ratio to Q_{aero} at the catcher, which makes it unnecessary to specify K. The exponent n, however, has, for illustrative purposes, been assigned the value 3.15 (Ref.12.5). This figure may be used for the case of a constant drag coefficient and a heating rate which is dependent on the velocity to the 3.15 power, to design a total-heat-transfer experiment for any particular combination of model, test conditions, and ballistic-facility. For example, a 0.635-cm-diameter aluminum hemisphere at 1 atm ($C_D = 0.9$ and $\rho_\infty A/2m = 0.1$ meter^{-1}) takes on 95 percent of the heat and loses 78 percent of its velocity in 16 meters of flight. It can be seen from this figure that the major portion of the heating occurs when the velocity is still relatively high, a result of the near-cubic dependence of heating rate on velocity.

Calculations must also be performed to determine that the model does not begin to melt, since heat would then be discarded in the melted and vaporized material and would not all be found in the model at recovery. This requirement does not hold, however, if one wishes to study the heat that is absorbed by the remaining part of an ablated model.

12.4.2.1 Sabot Design

The sabot, in addition to its usual functions of supporting the model during the launch and providing a seal between model and launch barrel, also must be designed to minimize heating to the model from three unwanted sources: (1) barrel friction, (2) the compressed gas in front of the sabot, and (3) the hot propellant gas behind the sabot. The protection provided by a conventional split sabot alone against the driver gas has been found to be inadequate; the propellant gases can pass along the parting planes of the split sabot and scorch the model. This leakage can be largely prevented by a thin disk gas seal behind the sabot (see Section 3.4.1.1). The total enclosure of the model within the sabot and the evacuation of the launch barrel will control or eliminate heating from gas in front of the model. With plastic sabots, barrel friction is small and the heat generated at the barrel wall and conducted to the model is negligible during the very brief acceleration stroke. Hence, with suitable design, spurious heat inputs in the gun can be made small compared to Q_{aero}.

12.4.2.2 Catcher and Funnel

The catcher is designed to stop models flying at subsonic speed, intact and without appreciably altering their total heat content. A suitable catcher developed in the study reported in Reference 12.6 consists of many (50-100) sheets of building paper hung on a rack. Sheets are spaced so that the model will fall freely between any two sheets into the funnel.

The funnel is formed of wrapping paper with steep sides to minimize transit time. Squaring the corners reduced the tendency of the model to spiral down the funnel, because spiraling increases the descent interval and hence permits additional heat loss from the model to the funnel and the air.

12.4.2.3 Calorimeter Description and Analysis

A very sensitive type of calorimeter is required, since the heat deposited by a small model may be of the order of a joule (0.001 Btu). One type possessing the desired sensitivity and accuracy is the conduction calorimeter in which the temperature difference across a known thermal conductance is measured as a function of time for as long a time period as any sensible temperature difference exists. Such a calorimeter is shown schematically in Figure 12.8. The differential equation for the conductive heat transfer from the source to the isothermal sink (of large heat capacity) is

$$\frac{dQ}{dt} = K_1[T_A(t) - T_B] .$$ (12.13)

Thus

$$Q = \Delta Q = K_1 \int_0^\infty [T_A(t) - T_B] \, dt .$$ (12.14)

In practice a finite integration limit can replace the infinite limit on the integral in Equation (12.14). If properly selected, this finite truncation has a negligible effect on the results.

In the technique described here, the calorimeter consists of a thin cup into which the model drops, a heat sink to absorb the heat, and a controlled conduction path between the cup and heat sink. Figure 12.9 is a quarter-sectional view of such a calorimeter. To obtain a large value of $T_A(t)$ with a small heat input, it is important to keep the heat capacity of the cup very low. To obtain rapidly a spatially uniform equilibrium temperature with the hot model, a high thermal diffusivity is required in the cup material. A small thin silver cup meets these requirements. The cup is instrumented with several thermocouples on the bottom exterior. All but one of these are connected in series with the reference junctions located in the heat sink. The remaining thermocouple is used to determine absolute temperatures.

The heat sink is constructed of two large blocks of phosphor bronze. The silver cup is suspended in a cavity in the lower block. The purpose of two large blocks is to provide sufficient heat capacity that the temperature level T_B in Equation (12.13) does not change more than a few thousandths of a degree while temperatures are being recorded. Buried in the lower portion of the lower block are several iron-constantan thermocouples which utilized the heat sink as a constant temperature reference mass; all but one of these are the reference junctions for the cup thermopile, and the remaining one is used to record absolute temperature. The model enters the cup through a conical hole in the upper block. This hole is lined with a low conductivity material to minimize any heat transfer due to contact with the model as it drops through to the cup.

The conduction path between the cup and heat sink consists of small support arms made of low-conductivity material, such as epoxy resins. These are fastened between the cup and the rim of the cavity. The conductivity of these supports (proportional to the value of K_1 in Equation (12.13)) is made such that the major portion of the heat from the hot model is transferred to the heat sink in a few minutes. It is necessary to use very fine thermocouples on the cup to minimize both their heat capacity and their conductivity between the cup and the heat sink. The excess volume of the cavity can be filled with foamed plastic to minimize free convection.

The output of the thermopile is proportional to the instantaneous temperature difference $T_A(t)-T_B$. This output, in millivolts, is recorded on a strip chart recorder (or other suitable device) from which portions of a typical trace are shown in Figure 12.10. The integral under this temperature difference – time curve is proportional to the heat transfer. Measurements of heat inputs as low as 10^{-2} joule were found to be possible with such equipment[12.6]. The development of this highly sensitive and accurate calorimeter made this test technique possible since, as noted, heat quantities to be measured may range down to a joule.

To calibrate the calorimeter, preheated models are dropped into it to determine the constant K_1 in Equation (12.14) and to determine the effects of several variables on K_1 such as model geometry, model orientation in cup, model material, and nonuniform temperatures in the model, etc. The value of K_1 was found to be insensitive to these variables.

12.4.3 Reduction of Total-Heat-Transfer Data

The reduction of the total heat-transfer data proceeds from an energy balance. The thermal energy, Q, added to the calorimeter by the model is obtained directly from the area under the temperature versus time curve of the calorimeter and the calibration constant K_1. This increment of energy consists of two parts, the energy due to aerodynamic heating, Q_{aero}, and the energy due to possible temperature differences between the model and the calorimeter prior to launching the model. The increment in energy, ΔQ, can be expressed as

$$\Delta Q = Q_{aero} + mc(T_{Mi} - T_{Ai}) , \qquad (12.15)$$

where m is the mass of the model, c is the specific heat of the model material, and T_{Mi} and T_{Ai} are the prelaunch model and calorimeter temperatures, respectively. Equation (12.15) may be solved for Q_{aero}. It is assumed that there are no extraneous heat sources. This assumption is justified if proper precautions are taken. (See Section 12.4.5 for the details of these precautions.) The initial model temperature is evaluated from the gun temperature prior to launch. To assure that the model attains the gun temperature, it is loaded as much as an hour prior to launch.

12.4.4 Typical Results

Some typical total heat-transfer data obtained with such a calorimeter technique are shown in Figure 12.11, where total aerodynamic heat input, Q_{aero}, is plotted as a function of launch velocity V_L for eight independent tests. These results are for a 0.635-cm-diameter aluminum hemisphere tested at 1 atm free-stream pressure. These data were analyzed to obtain the constant and exponent in the heat transfer Equation (12.8) by fitting Equation (12.11) to the data. From this, the instantaneous heat-transfer rates averaged over the wetted surface area may be plotted against velocity as in Figure 12.12. The experimental curve (solid line) is compared with a theoretical curve (dashed line) obtained using the stagnation-point results of Reference 12.7, together with the distributions of Reference 12.8, for the case of zero base heat transfer. It can be seen that the agreement is good.

12.4.5 Error Analysis

The accuracy of the total heat-transfer measurements depends primarily upon the accuracy of the calorimeter measurements and the size of extraneous heat sources and sinks. The calorimeter precision can be determined from

calibration by examining sensitivity and repeatability. The extraneous sources of heating to be considered are:

1. Heating from gases in front of the model while the model is traversing the launch tube.

2. Heating caused by propellant gas leaking through the sabot to the model.

3. Heat loss due to long subsonic flight.

4. Heating and/or cooling during capture in the catcher and funnel.

As noted earlier, the complete enclosure of the model within the sabot, and the partial evacuation of the launch tube, are believed to essentially eliminate heating resulting from item 1. The heating resulting from item 2 can be as high as 100 percent of Q_{aero} when no gas seal is used. The effectiveness of the gas seal in reducing this heating can be ascertained from the repeatability of data from several test shots with various seal designs. The heat lost from the model during the low-speed portion of the flight (when the wall temperature may be greater than the recovery temperature) has been found to be small[12.6].

The model may be heated or cooled by friction and conduction as it passes through the catcher and funnel combination. This can be studied experimentally with models preheated to a known temperature and fired at low speeds into the catcher from a compressed air gun placed inside a temperature-controlled oven. Since the amount of energy stored in the model before launch is known, the overall effect of the catching process on the total heat transfer can be evaluated. Reference 12.6 has reported on the basis of such tests that errors of the order of 10 percent of the aerodynamic heating can be introduced in the catcher. This small error, once defined, can be reconciled.

The sum of the estimated errors due to items 1 through 4, in the total heat input measurements of Q_{aero} reported in Reference 12.6, are listed below for three different velocities. As expected, the percentage error diminishes as the launch velocity, and hence, Q_{aero}, increases.

Launch velocity (km/sec)	Error range (percent)	
1.7	+13	−15
2.3	+ 8	−10
3.3	+ 6	− 8

Because of the method of data reduction used, it is difficult to estimate the accuracy of the heating rates, $\dot{q}_{av}$. The maximum expected error could be larger than the maximum error in the total heat-transfer measurements. As can be seen from Figure 12.12, the difference between the heating rates obtained from the present technique and from well-established theory, for the case of a hemisphere, is near the maximum estimated error in the total heating measurements. However, a part of the disagreement is due to base heating, and as such, should not be classified as measurement error. Thus, it appears that the technique is accurate to the order of 10 percent under the conditions described. This is comparable to the accuracy of more conventional heat-transfer-measurement techniques.

The technique is applicable to determination of heat transfer in gases other than air. Measurement of heat absorbed by ablating bodies can be used to evaluate transpiration blockage effects. Local heating to selected model regions can in principle be measured on segmented models which come apart on entering the catcher if mechanical devices can be designed to allow only the part of interest to enter the calorimeter. Thus, for example, if the blunt tip of a conical model is separated from the parent body by deceleration loads in penetrating the paper sheets, and if a proper sized screen is placed over the calorimeter entrance, only the tip enters the calorimeter, and tip heating is measured.

As noted earlier, the velocity limit of this technique may be imposed by the begining of melting in the stagnation region. This limitation to the catcher-calorimeter technique becomes the basis for the melting-onset technique.

12.5 MELTING-ONSET TECHNIQUE

This technique uses the time of onset of melting in the stagnation region of small metal models as a measure of the stagnation-point heating rate[12.2,12.11]. A sabot-held model is gun-launched at high velocity into either still air or an oncoming airstream. Heating is experienced by the model as it decelerates. This heating serves to raise the temperature of the model and, if heating is prolonged, at some point along its flightpath the surface of the model will begin to melt. Melting occurs first in the stagnation region, where the heating rate is highest. Since the viscosity of the metal used (aluminum) is low, the metal flows off the model surface and into the wake. This liquid aluminum runoff produces a partially opaque screen which is visible in the wake region in spark shadow-graphs. If the free-stream density and model size are adjusted correctly, melting can be made to begin during the portion of the model flight through the instrumented test section of the range; thus, the time at which melting first occurs can be determined from successive shadowgraphs. With the time of melting-onset known, the stagnation-point heating rate can be determined by solving the heat-conduction equation for the model interior. This technique is described in detail in the following sections.

12.5.1 Analysis

In order to relate the melting-onset time to the heat-transfer rate, it is necessary to solve the heat-conduction equation for the interior of the model. Calculations have shown that for the short flight times typical of small ballistic ranges (a few milliseconds) the appreciably heated layer within the model is thin (less than 10 percent of the model diameter), and that the one-dimensional form of the heat-conduction equation can be used. The boundary conditions are those for a semi-infinite slab, initially at uniform temperature, heated on its exposed surface with a time-dependent heating rate. The time dependence of the heating rate arises because of the changing free-stream conditions and velocity along the flightpath.

The equations to be solved are

$$
\left.
\begin{aligned}
a \frac{\partial^2 T}{\partial y^2} &= \frac{\partial T}{\partial t}, \quad y > 0, \ t > 0 \\
T(y,0) &= T_1 \\
-K\left(\frac{\partial T}{\partial y}\right)_{y=0} &= \dot{q}_{st} = \dot{q}_{st}(t).
\end{aligned}
\right\}
\tag{12.16}
$$

where T is the temperature, t is time, y is distance into the model surface, K is thermal conductivity, a is thermal diffusivity, and $\dot{q}_{st}$ is the heat-transfer rate at the stagnation point.

The solution of this system is well known and can be written with the aid of Duhamel's integral[12.9]. The surface temperature, T_w, is given by

$$
T_w - T_1 = \left(\frac{a}{\pi}\right)^{\frac{1}{2}} \frac{1}{K} \int_0^t \dot{q}(t - \tau) \frac{d\tau}{\tau^{\frac{1}{2}}}.
\tag{12.17}
$$

Thus if the heating rate is known as a function of time, the surface-temperature variation with time may be calculated. Under the assumption of constant free-stream density (e.g., when the model is flown into still air) and constant drag coefficient, one form of the trajectory equation is

$$
V = \frac{1}{(\rho_\infty A C_D/2m)t + \dfrac{1}{V_L}}.
\tag{12.18}
$$

Since the velocity does not change greatly over the trajectory under conditions chosen for this kind of test, the stagnation-point heating rate may be approximated by a less general form of Equation (12.8)

$$
\dot{q}_{st} = \gamma V^3,
\tag{12.19}
$$

where γ depends on ρ_∞ and the body size.

If Equations (12.17), (12.18), and (12.19) are combined, the equation for surface temperature may be written

$$
T_w - T_1 = \frac{\dot{q}_{st_L}}{K V_L^3}\left(\frac{a}{\pi}\right)^{\frac{1}{2}} \int_0^t \frac{d\tau}{\left[\rho_\infty A C_D/2m)(t-\tau) + \dfrac{1}{V_L}\right]^3 \tau^{\frac{1}{2}}}.
\tag{12.20}
$$

where $\dot{q}_{st_L}$ is the heating rate at the beginning of flight. This may be integrated to give

$$
T_w - T_1 = \frac{2\dot{q}_{st_L}}{K}\left(\frac{at}{\pi}\right)^{\frac{1}{2}} \left\{ \frac{d^2}{8(bt+d)^2}\left[\frac{2(bt+d) + 3d}{d^2} + \frac{3}{2\sqrt{bt(bt+d)}} \ \log_e \left[\frac{\sqrt{(bt+d)} + \sqrt{(bt)}}{\sqrt{(bt+d)} - \sqrt{(bt)}}\right]\right]\right\}
$$

$$
= \frac{2\dot{q}_{st_L}}{K}\left(\frac{at}{\pi}\right)^{\frac{1}{2}} \beta
\tag{12.21}
$$

where

$$
b = \frac{\rho_\infty A C_D}{2m}, \quad d = \frac{1}{V_L},
\tag{12.22}
$$

and β is the term in braces $\{\}$. Equation (12.21) is a closed-form solution for the time dependence of the stagnation-point surface temperature for models fired into still air.

When models are fired through the tunnel-starting-transient flow into a counterflow airstream, it is no longer possible to obtain a closed-form solution and Equation (12.17) must be integrated numerically. The integral is improper at its lower limit and thus unsuitable for numerical integration. A slight alteration of this equation removes the singularity to give

$$T_w - T_i = 2 \left(\frac{a}{\pi}\right)^{\frac{1}{2}} \frac{1}{K} \int_0^{\sqrt{t}} \dot{q}_{st}(t-\tau) d(\sqrt{\tau}) \ . \tag{12.23}$$

The numerical integration of Equation (12.23) is best performed on a computer. Equation (12.23) will allow the surface temperature to be computed as a function of time for counterflow airstream operation if the heating rates along the flightpath are known. Reference 12.7 should be consulted for details of this procedure.

12.5.2 Facilities and Test Equipment

No special equipment is required for this experiment. The model (material and geometry) and the test conditions must be selected such that melting occurs in the instrumented test section of the facility which is required to be equipped with shadowgraph stations.

A simple design criterion for estimating these conditions can be obtained on the basis of a constant velocity flight (i.e., constant heat-transfer rate). If $\beta = 1$, the model surface-temperature rise is given from Equation (12.21) as

$$T_w - T_i = \frac{2\dot{q}_{st}}{K} \left(\frac{at}{\pi}\right)^{\frac{1}{2}} \ . \tag{12.24}$$

Solving for the time to reach melting temperature, setting $x = Vt$ where V is the constant velocity, and using Equation (12.19) gives

$$x_{melt} = \frac{\pi}{a} \left(\frac{[T_{melt} - T_i]K}{2\gamma}\right)^2 \frac{1}{V^5} \ , \tag{12.25}$$

where x_{melt} is the approximate distance from the gun at which melting begins.

Equation (12.25) allows one to choose the model material, size, and free-stream density for a particular size facility and launch velocity. For example, a 0.635-cm-diameter aluminum hemisphere launched at 7.4 km/sec into air at a free-stream pressure of 70 torr begins to melt in about 7 meters of travel.

12.5.3 Typical Results

The shadowgraphs[12.11] shown in Figure 12.13 illustrate the evidence of melting onset. The model is an aluminum hemisphere 0.635 cm in diameter launched at 7.4 km/sec into air at 70 torr. Six data stations are shown with the corresponding temperatures calculated with Equation (12.21) and the heat-transfer rates of Reference 12.10. No melting is noted in stations one and two, but in station three there is a line of molten material seen coming off the rear of the model. The temperature of the stagnation point is calculated to be 921°K. This is in good agreement with the known melting point of aluminum (7075-T6), which is 911°K. Results from several tests of this type are shown plotted in Figure 12.14. Shown here is the actual observed time to melting onset (abscissa) compared with the theoretical computed time (ordinate). The bar length indicates error bands of the observations. The agreement is very good. A summary of results collected using this technique is shown in Figure 12.15. The shaded area represents some of the available shock-tube data[12.10, 12.12, 12.13].

12.5.4 Error Considerations

As with all heat-transfer techniques, sources of error in this technique are difficult to evaluate completely. If the results in Figure 12.14 are considered, the deviation of the heating rate from the average is +9 and −13 percent. Part of this can be accounted for by the fact that the model is observed only at discrete times along the flightpath, and therefore, melting onset is always observed sometime after it might first have been observed. On the average this error is −6 percent for the particular test facility used to obtain these results (1.2-meter intervals between stations and approximately 7 meters from gun muzzle to melting onset. Therefore, other sources of error, such as changes in heating during launch, changes in sabot separation from run to run, and angle of attack must account for the remainder of the scatter in these results.

12.5.5 Remarks

This technique, which measures local heating rates, is relatively simple to use and has been used at velocities in excess of earth-escape velocity. Testing times are of the order of 10 to 100 times longer than in shock tubes at the higher speeds. There are, however, sources of error, particularly when the countercurrent airstream is used, which are difficult to assess. In general, the accuracy of the technique can be considered acceptable but not extraordinary. Its principal virtue is that by being different from techniques used in other types of laboratory facilities, it offers an independent method for obtaining experimental data.

Possible applications of the technique are the measurement of heat transfer in planetary gases, the study of the effects of surface catalysis on heat transfer, and, by the provision of low-melting-temperature alloy inserts, the measurement of heat-transfer rates to other parts of the model.

12.6 STUDIES OF SURFACE ABLATION ON RECOVERED MODELS

12.6.1 Model-Recovery Techniques

The techniques of recovering the models used in the catcher-calorimeter tests[12.6] have been applied to plastic models which have suffered moderate ablation as well. The surfaces of the recovered models reveal the extent of the ablation as well as the nature of the flow processes responsible for the ablation, provided that negligible damage is done by the recovery. The first quantitative studies of this kind were done using the paper-arresting device described in Section 12.4.2.2, but only mass-loss data were obtainable since the surface features on the models were removed by passage through the paper sheets. Far superior results were subsequently obtained by simply allowing the model to come almost to rest under aerodynamic deceleration alone[12.14-12.17].

12.6.2 Range Requirements

A plastic model that has decelerated to low speed will frequently stray erratically far from boresight. It is desirable therefore to install a large open-ended tube in the range to guide the model during the last part of its flight to the backstop. The tube aids in model recovery and prevents damage from impacts of the model with down-range shadowgraph stations. Although the model can slide or ricochet along the tube, the damage thus incurred is usually minor and the terminal collision can be postponed until the velocity is reduced sufficiently that the model can impact the backstop without further damage.

Although all of the recovered models from aeroballistic ranges have been fired horizontally and recovered inside airtight enclosures, it seems attractive to consider firing small-scale models vertically in the open air and recovering them after they fall to the ground. This procedure would allow the use of heavier and/or more slender models which will not decelerate sufficiently to be recovered intact within the length of the ballistic range. In a sense this technique is being used in long exterior guided-missile test ranges, where recovery of entry bodies has been effected.

12.6.3 Experimental Requirements

The most critical ballistic requirement for these tests is that the model surface not be marred after preparation for the test. Aside from obvious precautions in handling, this requires great care in the design and construction of sabots to insure that no propellant gas penetrates along the parting surfaces to erode the test surfaces. A sabot used for this type of testing is illustrated in Figure 3.34. It has been found possible to prevent gas leakage by use of a thin obturation cup at the sabot base or by use of thin films of polyester plastic inside the sabot.

During the acceleration in the launch tube the hydrostatic pressure in the model-sabot assembly greatly exceeds the normal working stress for these materials. Voids along the parting surfaces of the sabot fingers near the plastic model can result in permanent deformation of the model surface. When such voids do exist, the damage done so roughens the model that the flight results lose much of their meaning. An alternative design eliminates the fingers, and thus the joints, by use of a one-piece paraffin wax casting covering the front of the model. In addition to aligning the model inside the launch tube, the wax can be matched in density to that of the plastic model reducing the possibility of model failure. On launching, the wax separates from the model quickly because of its low melting point. It is necessary to use a rigid pusher plug behind the wax-encapsulated model.

A somewhat less obvious requirement on the sabot is that all of it separate quickly from the model after emergence from the gun. If even a small part flies along in the near wake, the model base drag will be decreased and the total mass effectively increased. The resulting reduced deceleration leads to excessive ablation, and the occasional collisions will disturb the natural oscillations of the test body.

12.6.4 Experimental Observations

The quantitative studies of the changes wrought by ablation of these models include:

(a) Total mass removal

(b) Local mass removal

(c) Percent of surface covered by triangular areas of transitional and turbulent boundary-layer flow

(d) Stagnation-point mass removal and change of radius of curvature

(e) Identification of tracks of longitudinal vortices in the boundary layer

(f) Discovery of spatially fixed excessive-heating patterns

The first four items are of direct interest to the designer of heat-protection systems, because they document the actual performance of real ablating surfaces under realistic flows. The last two appear to give clues which may lead to far better understanding of important, somewhat orderly, processes in both laminar and turbulent boundary-layer flows over ablating bodies.

The interpretation of measured total mass loss is highly uncertain except for tests in which it is quite clear that the boundary-layer flow was either all laminar or all turbulent during the high-speed part of the flight.

Where the flow has been turbulent on parts of the surface from time to time, it is particularly desirable to establish a reference axis from which measurements can document the surface recession over the entire body. This has been done for 30° half-angle solid plastic cones having a base diameter of 1 cm by using the base plane and a hole in its center to establish a central axis before the test. By use of this hole and the base plane to position the model, silhouette photographs (e.g., Figure 12.16) can be taken before and after tests with such precision that variations in surface recession can be resolved to ±25 microns.

Figure 12.17 shows surface recession measurements from an acetal (Delrin) plastic cone fired at an initial velocity of 5.3 km/sec. A visual examination of the surface of this particular model disclosed cne turbulence wedge (a triangular area with increased mass-loss) similar to that shown in the upper picture of Figure 12.18. The surface-recession measurements in Figure 12.17 are for a cone generator (ray) along the center of this wedge, and for two other rays 10° and 180° away from the wedge. Predicted surface-recession profiles for continuously laminar and turbulent flow are also shown for comparison with the measurements. All the measurements indicate laminar flow near the nose of the model. The measurements along the wedge show transition to turbulent flow within the wedge. The measurements along the 10° ray show transition after this generator enters the wedge, while the measurements along the 180° ray indicate nearly laminar flow. These comparisons show that useful interpretations can be made from measurements of local mass-loss.

On a recovered model the sculpture produced by the airflow is sometimes remarkably detailed and reveals features some of which clearly define characteristics of the overlying boundary-layer flow, such as longitudinal vortices and areas of turbulent flow resulting from roughness. In cases where the sculpturing tends to preserve or accentuate the flow features responsible, the end result is also available for study. Figures 12.18 and 12.19 are photographs of these features. Their quantitative interpretation is not completely understood but early efforts are detailed in References 12.14 through 12.17.

If high resolution photographs can be taken while the model is still in high speed flight, it should be possible to relate the profile changes and sculpture to the flow conditions and history with greater confidence. Furthermore, if it is unnecessary to recover the model without damage, it should be possible to study the profiles and surfaces of slender models, which would not otherwise decelerate sufficiently, and to study the phenomena over broader ranges of Reynolds number.

The detailed study of shadowgraphs and laser photographs for measurement of profile changes has been attempted[12.18,12.19]. Serious attempts to observe the sculpturing process during flight have not yet been made, but the possibility does not seem remote. Figure 12.20 is a reflected-light laser photograph of a slender bimetal cone in flight at a velocity of 3.9 km/sec. The resolution of detail in the metal surface features, the clarity of the bimetal joint, and the sharpness of the profile demonstrate that the state-of-the-art required for such real-time photography is probably in hand.

500

REFERENCES

12.1   Yee, Layton.   *Ballistic-Range Measurements of Stagnation-Point Heat Transfer in Air and in Carbon*
       Bailey, Harry E.   *Dioxide at Velocities up to 18,000 feet per second.* NASA TN D-777, 1961.
       Woodward, Henry T.

12.2   Compton, Dale L.   *Two New Free-Flight Methods for Obtaining Convective-Heat-Transfer Data.* AIAA
       Chapman, Gary T.   Aerodynamic Testing Conference, Washington, DC, March 9-10, 1964.

12.3   Clemens, Paul L.   *Bibliography: Radio Telemetry to Survive High Accelerations.* AEDC-TDR-63-36,
                                   February 1963.

12.4   Terman,   *Radio Engineering.* 2nd edition. McGraw-Hill, 1937.
       Frederick Emmons

12.5   Chapman, Dean R.   *An Approximate Analytical Method for Studying Entry Into Planetary Atmospheres.*
                                   NACA TN 4276, 1958.

12.6   Chapman, Gary T.   *Measurement of the Heat Transfer to Bodies of Revolution in Free-Flight by Use of*
       Jackson, Charles T. Jr *a Catcher Calorimeter.* NASA TN D-1890, 1963.

12.7   Fay, J.A.   *Theory of Stagnation Point Heat Transfer in Dissociated Air.* J. Aero. Science, Vol.25,
       Riddell, F.R.   No.2, February 1958, pp.73-85.

12.8   Stine, Howard A.   *Theoretical and Experimental Investigation of Aerodynamic-Heating and Isothermal*
       Wanlass, Kent   *Heat-Transfer Parameters on a Hemispherical Nose With Laminar Boundary Layer at*
                                   Supersonic Mach Numbers. NACA TN 3344, 1954.

12.9   Carslaw, H.S.   *Conduction of Heat in Solids.* 2nd edition. Oxford University Press, London, 1959.
       Jaeger, J.C.

12.10 Hoshizaki, H.   *Heat Transfer in Planetary Atmospheres at Super-Satellite Speeds.* ARS J., Vol.32,
                                   No.10, October 1962, pp.1544-51.

12.11 Compton, Dale L.   *Free-Flight Measurements of Stagnation-Point Convective Heat Transfer at Velocities*
       Cooper, David M.   *to 41,000 ft/sec.* NASA TN D-2871, June 1965.

12.12 Rose, P.H.   *Stagnation Point Heat Transfer Measurements in Partially Ionized Air.* Res. Rep.
       Stankevics, J.O.   143, Avco-Everett Res. Lab., April 1963.

12.13 Offenhartz, E.   *Stagnation Point Heat Transfer Measurements at Super-Satellite Speeds.* J. of Royal
       Weisblatt H.   Aero. Soc., Vol.66, No.613, January 1962, p.54.
       Flagg, R.F.

12.14 Wilkins, Max E.   *Evidence of Surface Waves and Spreading of Turbulence on Ablating Models.* Tech.
                                   Note, AIAA J., Vol.3, No.10, October 1965, pp.1963-1966.

12.15 Wilkins, Max E.   *Boundary-Layer Transition on Ablating Cones at Speeds up to 7 km/sec.* AIAA J.,
       Tauber, Michael E.   Vol.4, No.8, August 1966, pp.1344-1348.

12.16 Canning, Thomas N. *Boundary-Layer Phenomena Observed on the Ablated Surfaces of Cones Recovered After*
       Wilkins, Max E.   *Flights at Speeds up to 7 km/sec.* AGARD Specialists' Meeting on Fluid Physics of
       Tauber, Michael E.   Hypersonic Wakes, Colorado State Univ., Fort Collins, Colorado, May 10-12, 1967.

12.17 Canning, Thomas N. *Ablation Patterns on Cones Having Laminar and Turbulent Flows.* AIAA J. Tech. Note,
       Wilkins, Max E.   AIAA J., Vol.6, No.1, January 1968, pp.174-175.
       Tauber, Michael E.

12.18 Palkin, S.N.   *Investigation of the Ablation of Low-Melting-Temperature Models on a Ballistic Facility.*
       Reznikov, u.T.   (Issledovanie unosa massy legkoplavkikh modelei na ballisticheskoi ustanovke).
       Studenkov, A.M.   In book "Aerophysical Studies of Supersonic Flows". (Aerofizicheskie Issledovaniia
       Bykov, V.N.   Sverkhzvukovykh-Techenii) ed. Iu. A. Dunaev. Moscov, Isdatel'stvo Nauka, 1967.

12.19 Collins, D.J.   *Microsphere Ablation in a Free-Flight Range.* AIAA J., Vol.5, September 1967,
       Rogers, W.K.   pp.1684-1685.
       Sangster, D.K.

COPPER
CALORIMETER

2024-T4
ALUMINUM

BORON NITRIDE

HOT JUNCTION

CONSTANTAN
CORE

COLD JUNCTION

COPPER
DISK   COIL

INSULATION

5.59 mm D

MODEL WEIGHT — 0.2g
NOSE RADIUS — 2.79mm
NOSE THICKNESS — 0.190mm
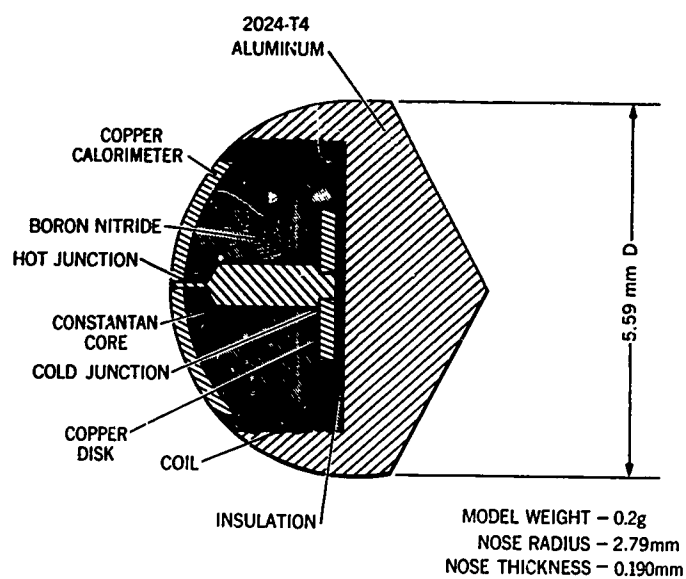
Fig.12.1   Thermocouple model

DEBRIS SHIELD

DIRECTION OF
MODEL FLIGHT

ELECTROSTATIC
SHIELD
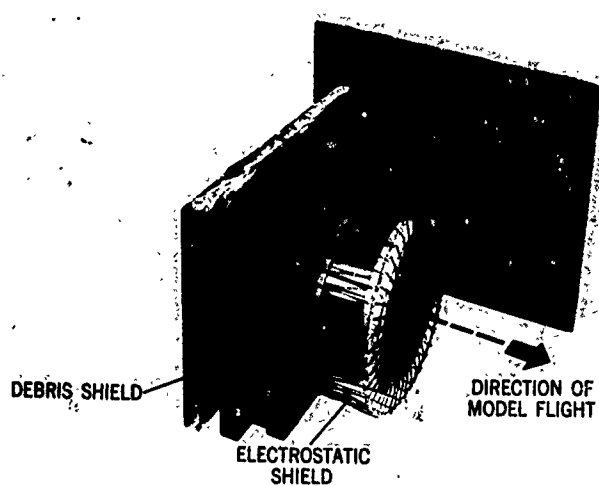
Fig.12.2   Pickup-coil assembly; coil diameter = 10 cm

400 TURN CENTER-TAPPED
PICK-UP COIL WITH
ELECTROSTATIC SHIELDING

ELECTRONIC TIMER

SPARK

A   B

DIFFERENTIAL
INPUT
OSCILLOSCOPE

SHADOWGRAPH

LIGHT-GAS GUN
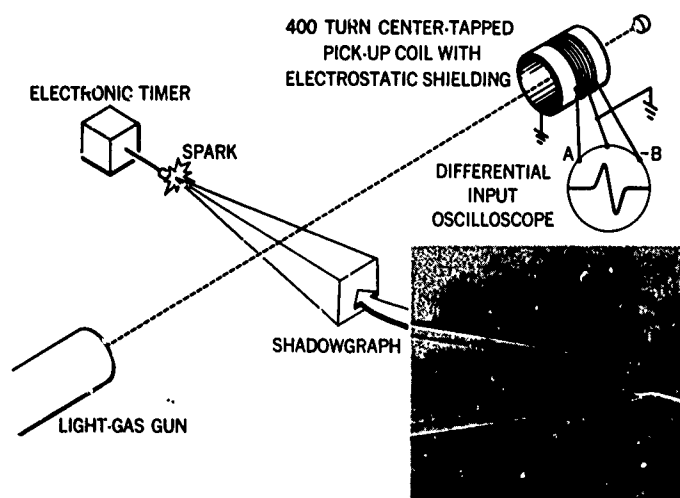
Fig.12.3   Experimental setup

502
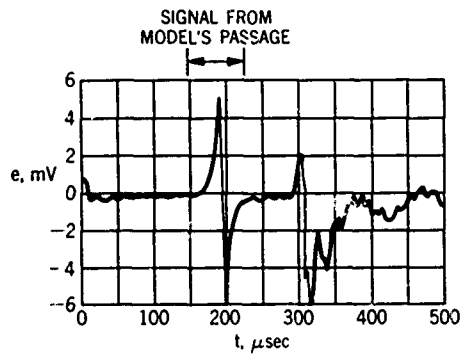
Fig. 12.4   Oscillogram of signal
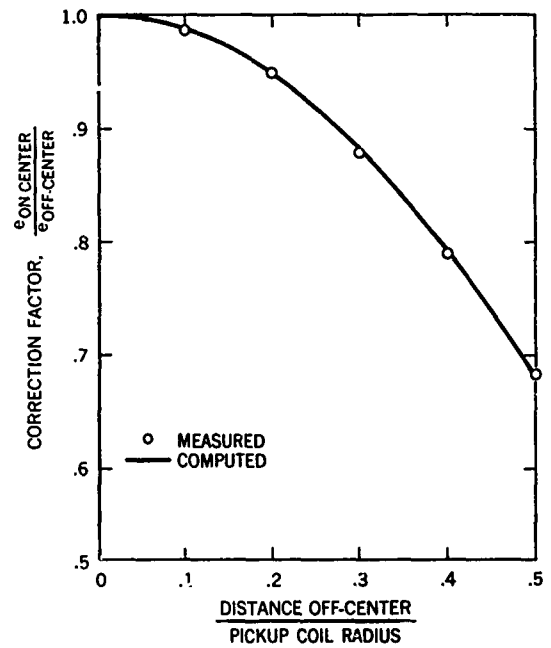
Fig. 12.5   Correction for off-center shot

$$\left(\frac{\text{Pickup coil R}}{\text{Model coil R}} = 23.5\right)$$
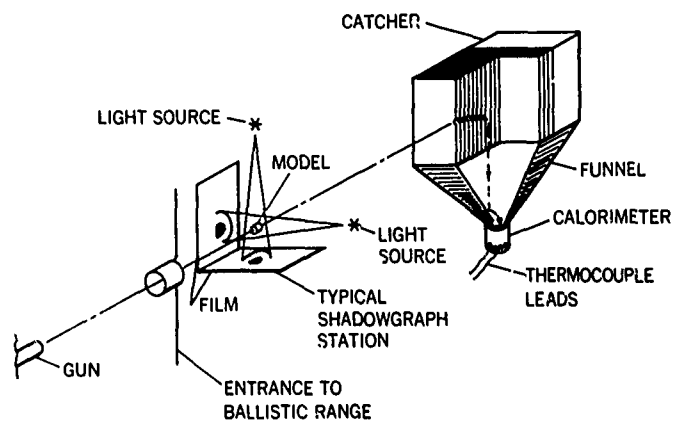
Fig. 12.6   Schematic drawing of test setup
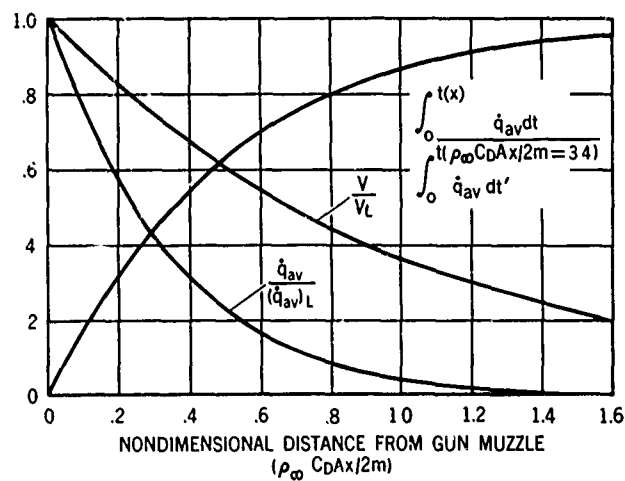
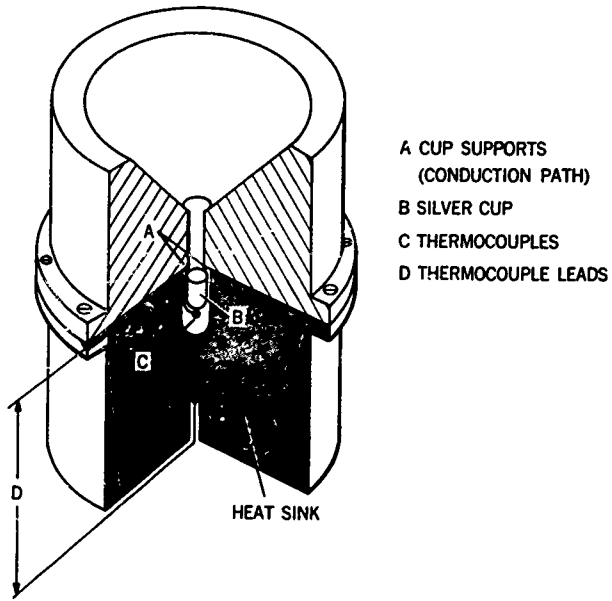Fig. 12.7   Variations in heating and velocity with distance from the gun

A CUP SUPPORTS
(CONDUCTION PATH)
B SILVER CUP
C THERMOCOUPLES
D THERMOCOUPLE LEADS
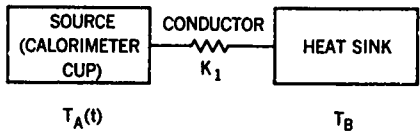
Fig.12.8   Block diagram of calorimeter

Fig.12.9   Quar⸱ᵉⁱ ᵉᵉᶜtional drawing of the calorimeter
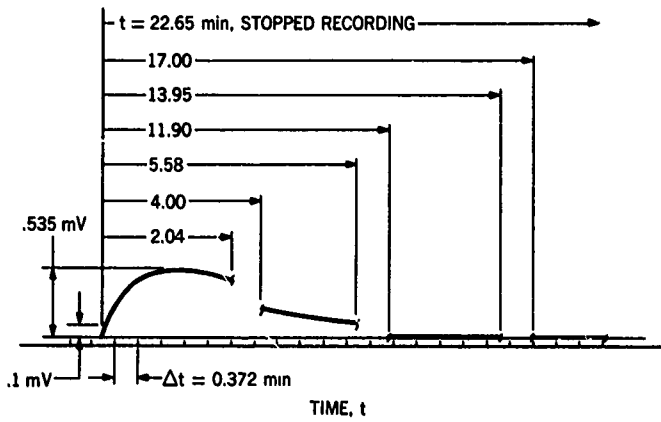
Fig.12.10   Typical calorimeter output trace
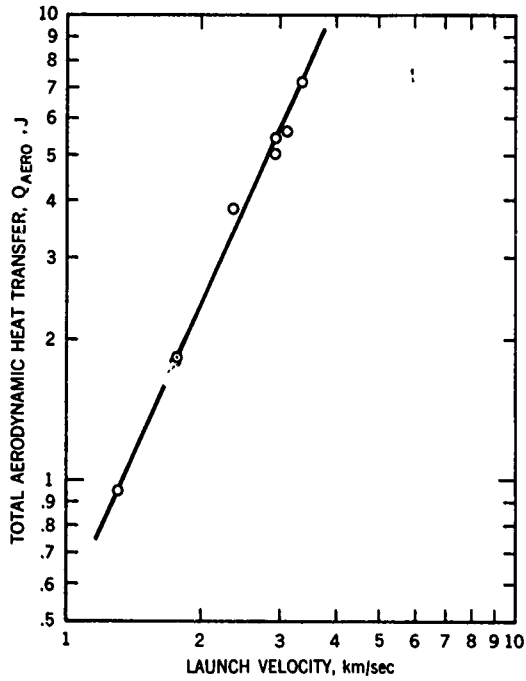
Fig.12.11   Heat transfer to a 0.635-cm-
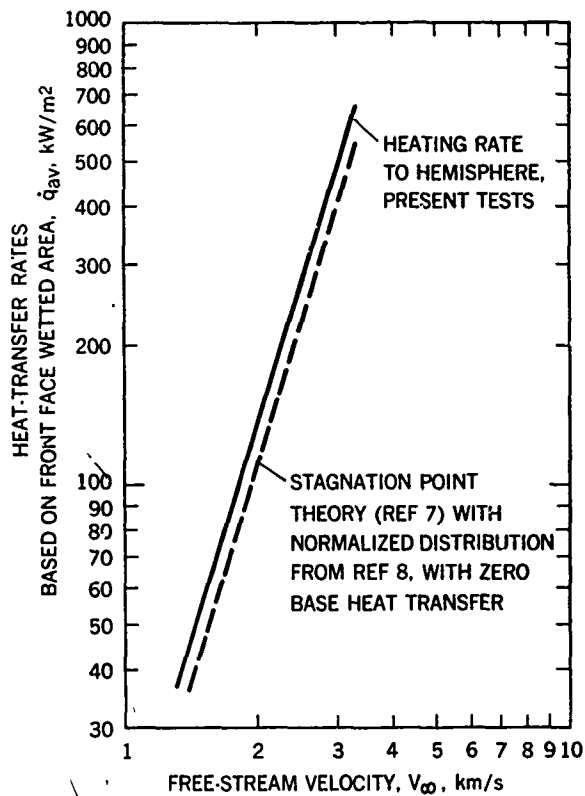diameter hemisphere at 1-atmosphere
free-stream pressure

HEAT-TRANSFER RATES BASED ON FRONT FACE WETTED AREA, $\dot{q}_{av}$, kW/m²

1000
900
800
700
600
500
400

300

200

100
90
80
70
60
50

40

30

HEATING RATE TO HEMISPHERE, PRESENT TESTS

STAGNATION POINT THEORY (REF 7) WITH NORMALIZED DISTRIBUTION FROM REF 8, WITH ZERO BASE HEAT TRANSFER

1   2   3   4   5 6 7 8 9 10

FREE-STREAM VELOCITY, V_∞, km/s

Fig. 12.12   Comparison of the experimental and theoretical heat-transfer rates, based on front-face wetted area, for a 0.635-cm-diameter hemisphere

STA. 1; t = 0.634 ms;
$T_W = 822°K$

STA. 2; t = 0.807 ms;
$T_W = 875°K$

STA. 3; t = 0.983 ms;
$T_W = 921°K$
(MELTING FIRST OBSERVED)

STA. 4; t = 1.161 ms;
$T_W = 959°K$

STA. 5; t = 1.341 ms;
$T_W = 993°K$

STA. 6; t = 1.523 ms;
$T_W = 1021°K$

ALUMINUM (7075-T6) MELTING TEMP. = 911°K
$V_L = 7.4$ km/s
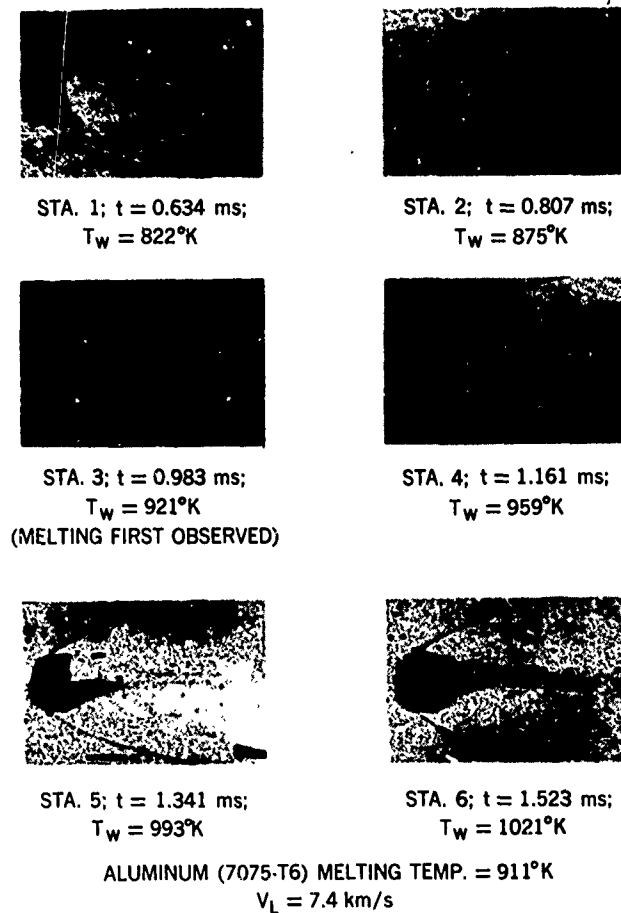
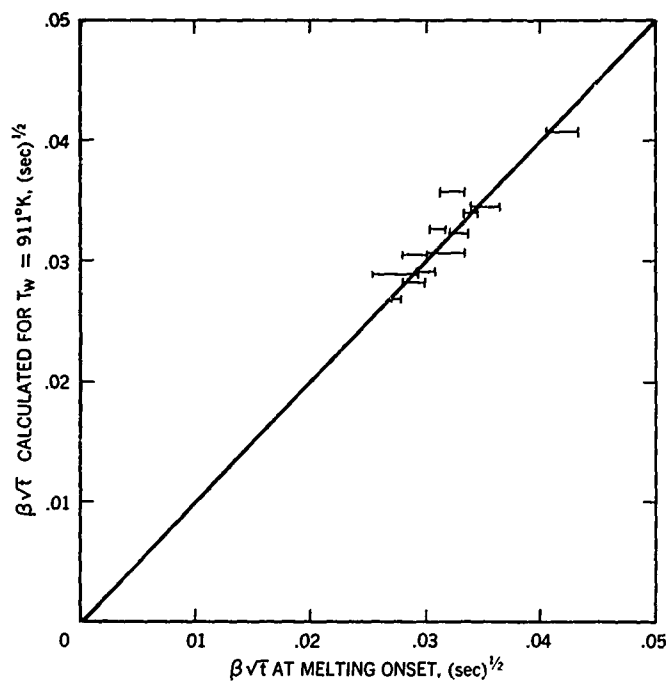Fig. 12.13   Shadowgraphs showing onset of melting

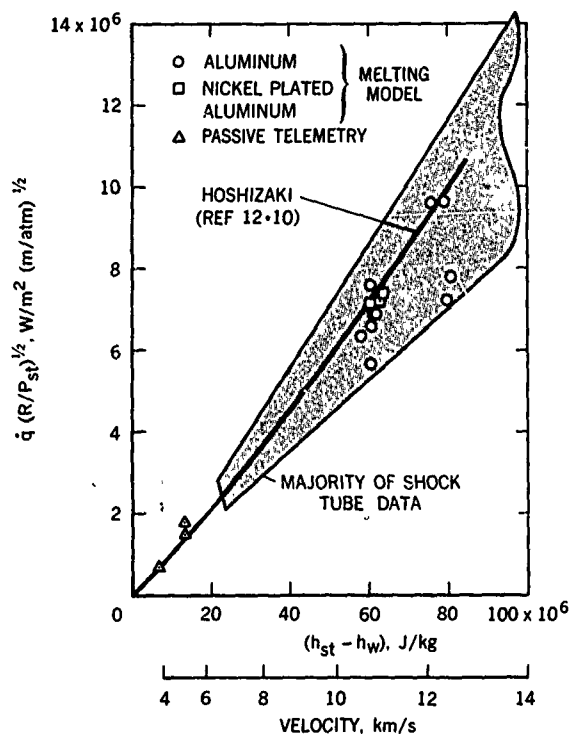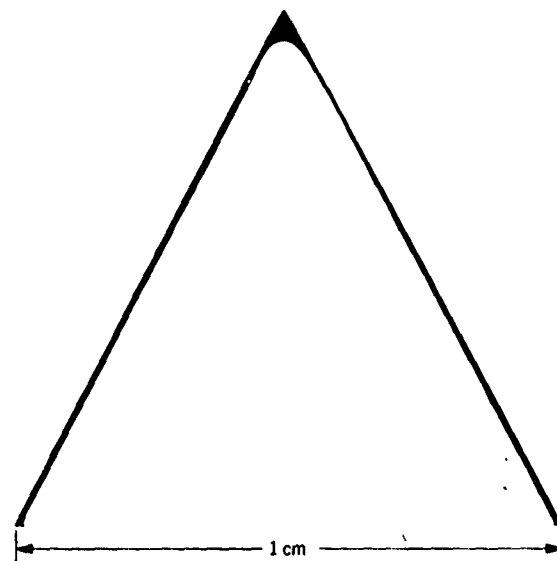Fig.12.14   Correlation plot for 7.3 km/sec data

Fig.12.15   Summary of results; h_{st} = stagnation
enthalpy , h_w = wall enthalpy , R = nose radius ,
P_{st} = stagnation pressure

Fig.12.16   Before and after silhouettes of Delrin
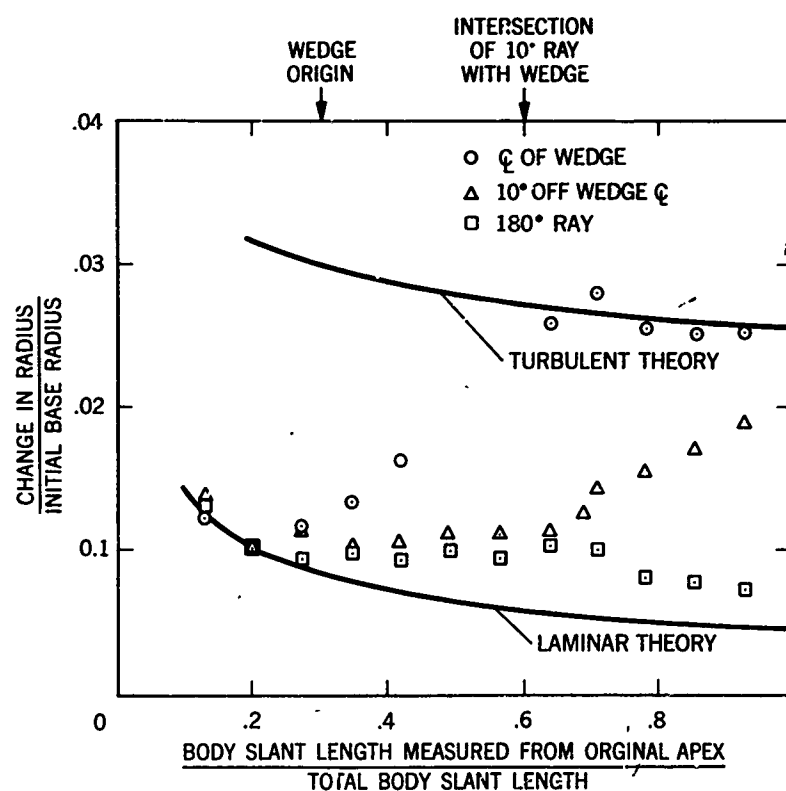(acetal) model; launch velocity, 6.4 km/sec

Fig.12.17   Surface recession profiles of a 30° half-angle conical Delrin model with turbulence wedges. Launch velocity, 5.3 km/sec; mass loss, 3.80%; slant-length Reynolds number based on boundary-layer-edge properties at launch, 5.3×10^6; range pressure, 1 atm air
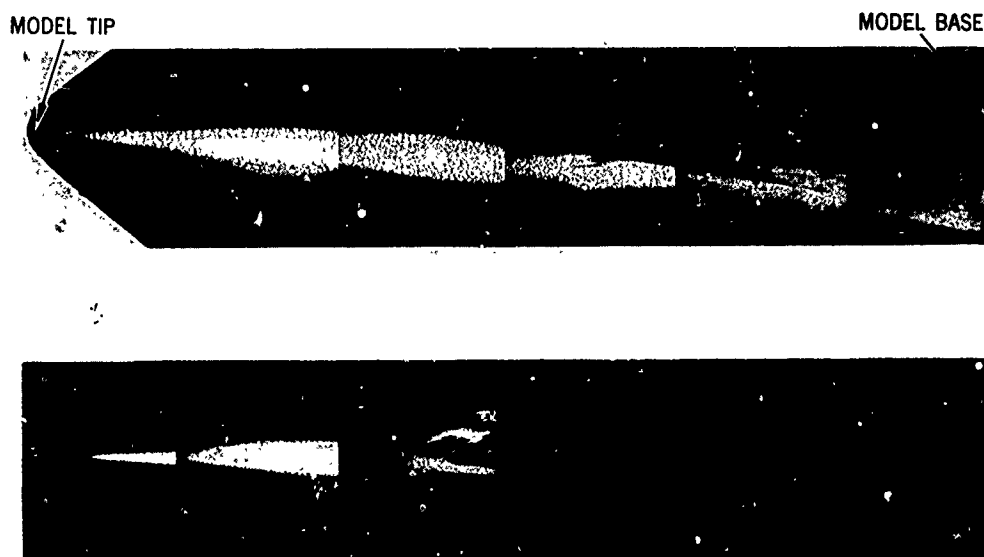

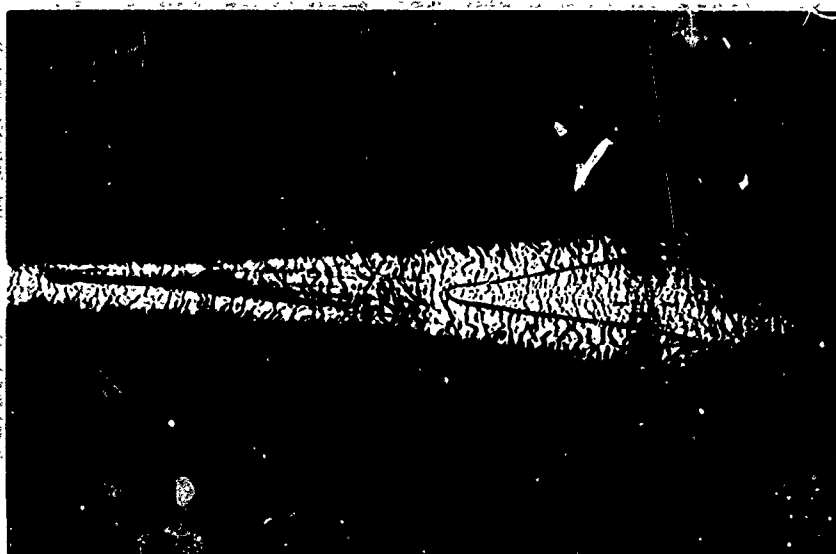Fig.12.18   Photomicrographs of surfaces of recovered Lexan (polycarbonate) models

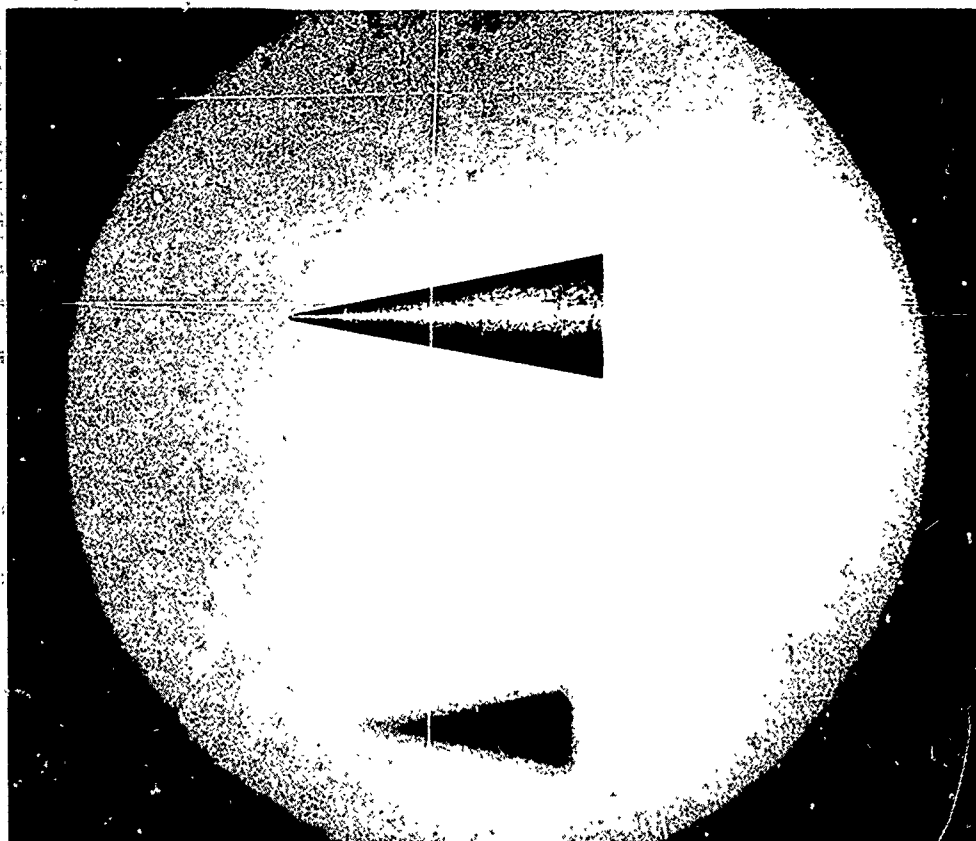Fig. 12.19   Turbulence wedge on recovered Lexan model

Fig. 12. 20   Reflected-light photograph of a 10-degree semi-angle cone in the VKF 1000-ft Hypervelocity Range, exposed with a 20-nsec laser pulse. Model is constructed with a copper nose and aluminum afterbody. Base diameter = 25.4 mm; velocity = 3.9 km/sec; range press. = 49 mm Hg.   (Courtesy of von Kármán Gas Dynamics Facility, Arnold Engineering Development Center.)

NATIONAL DISTRIBUTION CENTRES FOR UNCLASSIFIED AGARD PUBLICATIONS

Unclassified AGARD publications are distributed to NATO Member Nations
through the unclassified National Distribution Centres listed below

BELGIUM
General J. DELHAYE
Coordinateur AGARD – V.S.L.
Etat Major Forces Aériennes
Caserne Prince Baudouin
Place Dailly, Bruxelles 3

CANADA
Director of Scientific Information Services
Defence Research Board
Department of National Defence – 'A' Building
Ottawa, Ontario

DENMARK
Danish Defence Research Board
Østerbrogades Kaserne
Copenhagen Ø

FRANCE
O.N.E.R.A. (Direction)
29, Avenue de la Division Leclerc
92, Châtillon-sous-Bagneux

GERMANY
Zentralstelle fur Lüftfahrtdokumentation
und Information
Maria-Theresia Str. 21
8 München 27
Attn: Dr Ing. H.J. RAUTENBERG

GREECE
Hellenic Armed Forces Command
D Branch, Athens

ICELAND
Director of Aviation
c/o Flugrad
Reykjavik

ITALY
Aeronautica Militare
Ufficio del Delegato Nazionale all' AGARD
3, P. le del Turismo
Roma/Eur

LUXEMBOURG
Obtainable through BELGIUM.

NETHERLANDS
Netherlands Delegation to AGARD
National Aerospace Laboratory, NLR
Attn: Mr A.H. GEUDEKER
P.O. Box 126
Delft

NORWAY
Norwegian Defense Research Establishment
Main Library, c/o Mr P.L. EKERN
P.O. Box 25
N-2007 Kjeller

PORTUGAL
Direccao do Servico de Material
da Forca Aerea
Rua de Escola Politecnica 42
Lisboa
Attn: Brig. General Jose de Sousa. OLIVEIRA

TURKEY
Turkish General Staff (ARGE)
Ankara

UNITED KINGDOM
Ministry of Technology Reports Centre
Station Square House
St. Mary Cray
Orpington, Kent BR5 3RE

UNITED STATES
National Aeronautics and Space Administration (NASA)
Langley Field, Virginia 23365
Attn: Report Distribution and Storage Unit

———————— ★ ★ ★ ————————

If copies of the original publication are not available at these centres, the following may be purchased from:

Microfiche or Photocopy	*Microfiche*	*Microfiche*
Clearinghouse for Federal Scientific and Technical Information (CFSTI) Springfield Virginia 22151, USA	ESRO/ELDO Space Documentation Service European Space Research Organization 114, Avenue de Neuilly 92, Neuilly-sur-Seine, France	Ministry of Technology Reports Centre Station Square House St. Mary Cray Orpington, Kent BR5 3RE England

The request for microfiche or photocopy of an AGARD document should include the AGARD serial number, title, author or editor, and publication date. Requests to CFSTI should include the NASA accession report number.

Full bibliographical references and abstracts of the newly issued AGARD publications are given in the following bi-monthly abstract journals with indexes:

Scientific and Technical Aerospace Reports (STAR)
published by NASA,
Scientific and Technical Information Facility,
P.O. Box 33, College Park,
Maryland 20740, USA

United States Government Research and Development
Report Index (USGDRI), published by the Clearinghouse
for Federal Scientific and Technical Information,
Springfield, Virginia 22151, USA